TalentDetector

TalentDetector2025_Summer
INTERNATIONAL STUDENTS SCIENTIFIC CONFERENCE

Scientific editor:
Mirosław Bonek

Department of Engineering Materials and Biomaterials,
Faculty of Mechanical Engineering,
Silesian University of Technology
23-25 June 2025
Gliwice, Poland

Katedra Materiałów
Inżynierskich i Biomedycznych

Katedra Materiałów Inżynierskich i Biomedycznych
Wydział Mechaniczny Technologiczny
Politechnika Śląska
ul. Konarskiego 18a, 44-100 Gliwice tel. +48 (32) 2371322

Redakcja techniczna i skład komputerowy:
dr h.c. dr hab. inż. Mirosław Bonek, prof. PŚ

Recenzenci:
M. Bonek, W. Borek, A. Drygała, K. Gołombek, A. Kania, M. Kciuk, M. Król, L. Kuchariková, S. Lesz, K. Lukaszkowicz, G. Matula, C. Meran, M. Musztyfaga-Staszuk, D. Pakuła, O. Polishchuk, M. Polok-Rubiniec, M. Spilka, M. Sroka, M. Staszuk, M. Szindler, A. Śliwa, T. Tański, E. Tillová, M. Uhríčik, A. Włodarczyk-Fligier, B. Ziębowicz

Materiały są opublikowane na podstawie oryginałów dostarczonych przez Autorów, zaopiniowanych przez Zespół Recenzentów.

Wydano za zgodą:
Kierownika Katedry Materiałów Inżynierskich i Biomedycznych
Wydziału Mechanicznego Technologicznego
Politechniki Śląskiej

Wydawca:
Katedra Materiałów Inżynierskich i Biomedycznych
Wydział Mechaniczny Technologiczny
Politechnika Śląska
Gliwice 2025

Wszystkie opublikowane materiały stanowią utwór podlegający ochronie na mocy prawa autorskiego. Utwór ten w całości ani we fragmentach nie może być powielany ani rozpowszechniany za pomocą urządzeń elektronicznych, mechanicznych, kopiujących, nagrywających i innych. Ponadto utwór ten nie może być umieszczany ani rozpowszechniany w postaci cyfrowej zarówno w Internecie, jak i w sieciach lokalnych, bez pisemnej zgody posiadacza praw autorskich.

Seria wydawnicza:
Prace Katedry Materiałów Inżynierskich i Biomedycznych
Wydział Mechaniczny technologiczny
Politechnika Śląska
Publikacja: czerwiec 2025

ISBN 978-83-65138-44-6

INTERNATIONAL STUDENTS SCIENTIFIC CONFERENCE

TALENTDETECTOR2024_SUMMER

SILESIAN UNIVERSITY OF TECHNOLOGY, GLIWICE, POLAND

23-25 JUNE 2025

The International Student Scientific Conference TalentDetector2025_Summer aims to integrate the student and scientific community dealing with topics related to material technologies. It is a place that gives the opportunity to exchange experiences, knowledge, skills and present current scientific achievements, developing and expanding students' interests in the field of materials engineering, surface engineering, biomaterials and biomedical engineering, nanotechnology, pro-ecological technologies and computer materials science. The conference allows for the presentation of projects conducted with the industry as part of the activities of Student Scientific Circles, doctorates, projects implemented in the form of PBL - Project Based Learning as part of the Excellence Initiative - Research University at the Silesian University of Technology, projects in the framework of EURECA PRO/European University in Responsible Consumption and Production and international bilateral cooperation between Universities.

CONFERENCE ORGANIZER

Materials Science Circle of the Association of Alumni of the Silesian University of Technology, Gliwice, Poland

CONFERENCE CO-ORGANIZER

Department of Engineering Materials and Biomaterials, Faculty of Mechanical Engineering, Silesian University of Technology, Gliwice, Poland

INTERNATIONAL SCIENTIFIC COMMETTEE

prof. Mirosław Bonek dr h.c., Silesian University of Technology, Gliwice, Poland - *President of the International Scientific Commette*

prof. Marcin Adamiak, Silesian University of Technology, Gliwice, Poland
prof. Sedat Alkoy, Gebze Technical University, Gebze, Turkey
prof. Rafał Babilas, Silesian University of Technology, Gliwice, Poland
prof. Stela Dinescu, University of Petroșani, Petroșani, Romania
prof. Ahmet Durgutlu, Gazi University, Ankara, Turkey
prof. Boris Gitolendia, Georgian Technical University, Tbilisi, Georgia
prof. Afrim Gjelaj, University of Pristina, Pristina, Kosovo
prof. Adam Grajcar, Silesian University of Technology, Gliwice, Poland
prof. Alexander Horn, Laserinstitut Hochschule Mittweida, Mittweida, Germany
prof. Volkan Kılıçlı, Gazi University, Ankara, Turkey
doc. Lenka Kuchariková, University of Zilina, Zilina, Slovakia
prof. Martin Kusy, Slovak Technical University in Bratislava, Trnava, Slovakia
prof. Grzegorz Matula, Silesian University of Technology, Gliwice, Poland
prof. Janusz Mazurkiewicz, Silesian University of Technology, Gliwice, Poland
prof. Serhii Matiukh, Khmelnitskyi National University, Khmelnitskyi, Ukraine
prof. Cemal Meran, Pamukkale University, Denizli, Turkey
prof. Oleh Polishchuk, Khmelnitskyi National University, Khmelnitskyi, Ukraine
prof. Mykola Skyba, Khmelnitskyi National University, Khmelnitskyi, Ukraine
prof. Tomasz Tański, Silesian University of Technology, Gliwice, Poland
doc. Miroslava Tavodova, Technical University in Zvolen, Zvolen, Slovakia
prof. Eva Tillova, University of Zilina, Zilina, Slovakia
prof. Zheng Zhanguo, SCISE Yanshan University, Qinhuangdao, China

ORGANIZING COMMETTEE

Chairman
prof. Mirosław Bonek dr h.c.

prof. Klaudiusz Gołombek
prof. Sabina Lesz
prof. Małgorzata Musztyfaga-Staszuk
prof. Daniel Pakuła
prof. Marek Sroka
prof. Marcin Staszuk
prof. Agata Śliwa
prof. Adam Zarychta
dr. Aleksandra Drygała
dr. Rafał Honysz
dr. Aneta Kania
dr Monika Kciuk
dr. Mariusz Król
dr. Magdalena Polok-Rubiniec
dr. Magdalena Szindler
dr. Marek Szindler
dr. Anna Włodarczyk-Fligier
Amadeusz Dziwis MSc
Wojciech Mikołejko MSc
Sichale Worku Fita MSc

TalentDetector HISTORY

The International Student Scientific Conferences TalentDetector from 11 edition (since 2018) have been a place for the exchange of experience, knowledge, skills and presentation of students' current scientific achievements in the field of materials engineering, surface engineering, biomaterials and biomedical engineering. As part of the conference, two international scientific monographs, TalentDetector_Summer and TalentDetector_Winter, are published annually, which already contain over 680 scientific articles resulting from the implementation of PBL, EURECA PRO, Students Scientific Cyrcles projects and projects with secondary school students with international authors. Participation in the form of presentations and posters in TalentDetector International Student Scientific Conferences allows members of the project teams to integrate the student and scientific community of the Silesian University of Technology as well as young staff from foreign research centres in Austria, China, Czech Republic, Ethiopia, Ghana, Georgia, Iran, Romania, Slovakia, Ukraine and Turkey, dealing with topics related to materials technologies.
Scientific monographs are prepared based on articles, mostly with international authors, reviewed by an international scientific committee.
The initiative of the cyclical organization of the International Student Scientific Conference TalentDetector significantly expands activities in the field of student education, organizational and popularization activities for the scientific community related to materials engineering at the national and international level.

Thanks to extensive international cooperation, over 220 articles were published free of charge.

Number of cooperating universities: 13

Gazi University, Ankara, Turkey
Gebze Technical University, Gebze, Turkey
Georgian Technical University, Tbilisi, Georgia
Khmelnitskyi National University, Khmelnitskyi, Ukraine
Laserinstitut Hochschule Mittweida, Mittweida, Germany
Pamukkale University, Denizli, Turkey
Silesian University of Technology, Gliwice, Poland
Slovak Technical University in Bratislava, Trnava, Slovakia
Technical University in Zvolen, Zvolen, Slovakia
University of Petroșani, Petroșani, Romania
University of Pristina, Pristina, Kosovo
University of Zilina, Zilina, Slovakia
Yanshan University, Qinhuangdao, China

The history of TalentDetector in numbers:

2018
TalentDetector 2019 (Gliwice)
Number of articles: 59
Number of authors: 206
Number of countries: 1

2021
TalentDetector2021_Winter (Gliwice)
Number of articles: 37
Number of authors: 134
Number of countries: 2

TalentDetector2021_Summer (Zawiercie)
Number of articles: 57
Number of authors: 173
Number of countries: 3

2022
TalentDetector2022_Winter (Gliwice)
Number of articles: 79
Number of authors: 179
Number of countries: 4

TalentDetector2022_Summer (Wisła)
Number of articles: 79
Number of authors: 176
Number of countries: 4

2023
TalentDetector2023_Winter (Gliwice)
Number of articles: 73
Number of authors: 143
Number of countries: 6

TalentDetector2023_Summer (Brenna)
Number of articles: 105
Number of authors: 173
Number of countries: 9

2024
TalentDetector2024_Winter (Gliwice)
Number of articles: 82
Number of authors: 135
Number of countries: 7

TalentDetector2024_Summer (Gliwice-Zilina)
Number of articles: 84
Number of authors: 147
Number of countries: 8

2025
TalentDetector2024_Winter (Gliwice)
Number of articles: 95
Number of authors: 173
Number of countries: 9

Katedra Materiałów Inżynierskich i Biomedycznych
Wydział Mechaniczny Technologiczny
Politechnika Śląska
ul. Konarskiego 18a, 44-100 Gliwice tel. +48 (32) 2371322

Redakcja techniczna i skład komputerowy:
dr h.c. dr hab. inż. Mirosław Bonek, prof. PŚ

Recenzenci:
M. Bonek, W. Borek, A. Drygała, K. Gołombek, A. Kania, M. Kciuk, M. Król, L. Kuchariková, S. Lesz, K. Lukaszkowicz, G. Matula, C. Meran, M. Musztyfaga-Staszuk, D. Pakuła, O. Polishchuk, M. Polok-Rubiniec, M. Spilka, M. Sroka, M. Staszuk, M. Szindler, A. Śliwa, T. Tański, E. Tillová, M. Uhríčik, A. Włodarczyk-Fligier, B. Ziębowicz

Materiały są opublikowane na podstawie oryginałów dostarczonych przez Autorów, zaopiniowanych przez Zespół Recenzentów.

Wydano za zgodą:
Kierownika Katedry Materiałów Inżynierskich i Biomedycznych
Wydziału Mechanicznego Technologicznego
Politechniki Śląskiej

Wydawca:
Katedra Materiałów Inżynierskich i Biomedycznych
Wydział Mechaniczny Technologiczny
Politechnika Śląska
Gliwice 2025

Wszystkie opublikowane materiały stanowią utwór podlegający ochronie na mocy prawa autorskiego. Utwór ten w całości ani we fragmentach nie może być powielany ani rozpowszechniany za pomocą urządzeń elektronicznych, mechanicznych, kopiujących, nagrywających i innych. Ponadto utwór ten nie może być umieszczany ani rozpowszechniany w postaci cyfrowej zarówno w Internecie, jak i w sieciach lokalnych, bez pisemnej zgody posiadacza praw autorskich.

Seria wydawnicza:
Prace Katedry Materiałów Inżynierskich i Biomedycznych
Wydział Mechaniczny technologiczny
Politechnika Śląska
Publikacja: czerwiec 2025

ISBN 978-83-65138-44-6

TalentDetector
23th-25th June 2025
Gliwice-Brenna, Poland
DEPARTMENT OF ENGINEERING MATERIALS AND BIOMATERIALS
FACULTY OF MECHANICAL ENGINEERING
SILESIAN UNIVERSITY OF TECHNOLOGY
INTERNATIONAL STUDENTS SCIENTIFIC CONFERENCE

Contents

Effects of Atomic Layer Deposition Temperature on the Formation of ZnO Nanolayers for Improved Solar Cell Efficiency
Elizabeth Addae, Wojciech Sitek, Marek Szindler 1

The Effect of Current-Assisted Lacquer Coating on The Corrosion Resistance of Electrolytically Nickel-Plated Surfaces
Yasin Akgun, Koray Guler, Yener Kilic, Cemal Meran 6

Design and production of a multi-layer composite material dedicated to insoles for professional running shoes
Krystian Albrecht, Agnieszka J. Nowak 14

Investigating the Response of PBF-LB/M AlSi10Mg and AlSi12Mg to Direct Aging: A Microstructural and Microhardness Study
Augustine Nana Sekyi Appiah, Przemysław Snopiński, Evans Atioyire, Marcin Adamiak 22

The effect of nickel on the austenite formation in LPBF Duplex stainless steel
Beatrice Naa Ayeley Ardayfio, Zbigniew Brytan 29

Wytwarzanie kompozytów ceramika-metal opartych na materiałach odpadowych infiltrowanych stopami metali lekkich
Jennifer Badora, Michał Głogowski, Julia Muszyńska, Julia Pindur, Karolina Romberg, Martin Mikolajčík, Zuzana Šurdová, Lenka Kuchariková, Mateusz Lis, Klaudiusz Gołombek 35

The methodology for calculating order value and pricing printed products in the "Print-Expert" automated management system
Tea Baramashvili, Nini Baidoshvili 41

Comparison of Au Deposition Methods on Ti: Effect of Surface Preparation on the Quality of Ti–Au Layers
Oktawian Bialas 47

Structure and corrosion resistance of $CoCrFeNiNb_xMo_y$ near-eutectic high entropy alloys
Jakub Bicz, Krzysztof Matus, Rafał Babilas 51

Kompozyty hydrożelowe na osnowie polietylenu
Marcin Bilewicz, Michał Rak, Igor Zdebel, Weronika Gębska,
Michał Gwóźdź, Katarzyna Mazik 57

Design and Development of Prototype Mobile Platforms
Franciszek Borgosz, Michał Plok, Michał Łubko 63

Analysis of the properties of composite materials made from components derived from renewable resources
Katarzyna Borowiecka, Agnieszka J. Nowak 71

Optimization of semiconductor layer thickness in dye-sensitized solar cells
Jakub Budzynowski, Oskar Górka, Judyta Drygała, Aleksandra Drygała 79

The Effect Of Magnetic Field On Welding Arc Field During Sheet Metal Welding
Berranur Ceker, Sezai Kunan, Murat Mat, Cemal Meran 86

Innovative laser surface treatment technology for engineering materials
Julia Chudy, Bartosz Filip, Szymon Szeja, Kacper Krysiak,
Katarzyna Furman, Mirosław Bonek, Eva Tillova 94

Computationally Assisted Laser and Heat Treatment Processes for Surface Property Optimization
Julia Chudy, Bartosz Filip, Szymon Jędrzejewski, Matusz Paluch, Mirosław Bonek 104

Designing of universal testing machine simulator for remote education purposes
Xiyue Cui, Rafał Honysz 111

A Visual Platform for PC Hardware Configuration
Shiyang Dai, Linkun Xiao, Yifan Wu 119

Research on the loss of efficiency of an internal combustion engine
Olha Drobot, Oleg Polishchuk, Oleg Babak, Mirosław Bonek 125

Influence of print parameters on mechanical properties. Modifications of components made using 3D printing technology
Bartosz Filip, Zbigniew Brytan 134

Materials used for recording of music played on a gramophone
Paweł Foltyn, Hanna Krymiec, Magdalena Maślanka, Wiktor Liszka,
Bogusław Ziębowicz, Anna Ziębowicz 141

The Relationship Between Laser Technology and Eco-Friendly Cutting with PDM/PLM Systems and the Lean Six Sigma Approach in Production Engineering
Katarzyna Furman, Dominik Towarnicki, Mirosław Bonek 149

Structure and wear resistance of PVD TiN/TiAlN coating applied on a cemented carbide substrate
Rafał Gabryś, Magdalena Polok-Rubiniec, Anna Włodarczyk-Fligier, Aneta Kania 153

Design and Development of a Solar Sintering System for Powder Metallurgy
Maciej Gajdemski, Marcin Kowalik, Błażej Tomiczek 157

Development of biodegradable composite based on PLA matrix with the addition of material acquired from Symbiotic Cultures of Bacteria and Yeast (SCOBY)
Adrianna Hadyk, Wojciech Smołka, Jakub Osiewała, Olivia Mikolajec, Julia Kuliś 163

Porovnanie vlastností polotovarov z polymérneho kompozitu používaného pri termoformovaní
Rastislav Hanulík, Lenka Markovičová, Mirosław Bonek 170

Cutting of Future - Lasers in Modern Manufacturing
Magdalena Hulbój, Emilia Put, Mirosław Bonek 178

Functional properties of CrN coating obtained by PVD on aluminum alloy surface AlSi9Cu3
Justyna Janoszka, Natalia Puchała, Petr Jánský, Anna Smetanova, Michal Lattner, Antonin Kříž, Marcin Staszuk, Daniel Pakuła 186

Practical Applications of Laser Marking in Manufacturing Industry
Dawid Jarysz, Jan Wypiór, Mirosław Bonek 196

Pro-ecological Laser Cutting Technology
Szymon Jędrzejewski, Bartosz Nikiel, Kamil Oleksy, Matusz Paluch, Dominik Towarnicki, Mirosław Bonek, Oleh Polishchuk 203

Evaluation of selected mechanical properties of Astaloy CrS material produced by sinterhardening process
Dmitriy Koblik, Miroslava Ťavodová, Monika Vargová 211

The use of laser technology in the processing of modern steels in the automotive industry
Tomasz Kołodziej, Wiktor Rudek, Mirosław Bonek 217

Secondary use of powder materials in additive manufacturing technologies
Dominik Krisak, Lenka Zavodna, Jiří Hajnys, Martyna Urbańska, Kinga Stępska, Jan Wypiór, Olaf Pradelok, Krzysztof Olszak, Vojtěch Macejko, Eliška Posmyková, Mariusz Król, Agnieszka J. Nowak 231

Investigation of the Effect of Busbar Number on Solar Cell Characteristics
Alicja Król, Wiktoria Wilczak, Jakub Jabłoński, Cyprian Chowaniec, Kadir Ozdemir, Onur Dodak, Emir Kaan Ozbay, Wojciech Filipowski, Cemal Meran, Małgorzata Musztyfaga-Staszuk 240

Design and production of gradient materials using additive technology – 3D printing
Patryk Krzempek, Mateusz Miarecki, Radosław Kos, Emilia Krzystanek, Krzysztof Goczoł, Marek Gazda, Dominik Krišák, Agnieszka J. Nowak, Mariusz Król 249

Design and Field Testing of a Synchronized Camera–LiDAR–IMU System for Real-World Dataset Collection
Tomasz Kukuczka, Michał Polończyk 256

Farebné leptanie grafitických liatin
Denis Kulas, Alan Vaško, Mirosław Bonek 260

Automatic Granule Feeding Line For Cable Manufacturing: Design And Implementation
Batuhan Kurt, Cem Samet Kartal, Cemal Meran, Koksal Ilhan, Fatih Oztekin 267

Wpływ rodzaju anody lampy RTG podczas badań dyfrakcyjnych warstw napawanych laserowo na dokładność pomiarów
Waldemar Kwaśny, Wojciech Kała, Bartłomiej Kazek, Damian Janicki, Aleksander Lisiecki 273

Optimization of engineering material selection using expert system
Ruojia Li, Rafał Honysz 283

Analysis of the Influence of Mold Temperature on the Physical Properties of Low-Density Polyethylene
Mateusz Lis, Katarzyna Młynarek-Żak 291

Microstructural and chemical characterisation of norfloxacin
Paulina Lukaszkowicz, Tiara Ogórek, Ewa Adamek, Wojciech Baran, Magdalena Szindler, Klaudiusz Gołombek 295

Organization of the CNC machine operator’s position
Marcin Majnusz, Martyna Gawlas, Aneta Kania, Magdalena Polok-Rubiniec, Anna Włodarczyk-Fligier 299

Studies on performance properties of CrN coating obtained by PVD on austenitic steel surface X2CrNiMo17-12-2
Tobiasz Markowicz, Jakub Pluskota, Beniamin Sobczak, Petr Jánský, Anna Smetanova, Michal Lattner, Antonin Kříž, Daniel Pakuła, Marcin Staszuk 305

Investigation of nozzle temperature impact on surface roughness and mechanical properties of FDM-printed CF-PEEK components
Getu Koro Megersa, Wojciech Sitek, Agnieszka J. Nowak 317

Korózna odolnosť nehrdzavejúcej ocele AISI 316L po plazmovej nitridácii
Erik Meliš, Viera Zatkaliková 325

AGV localisation in the process of mapping the room floors
Jakub Mlaskawa, Krzysztof Paszek 333

Standardized Experimental Method for Evaluating Aircraft Checklist Interfaces in IFR Simulation
Dariusz Myszor, Magda Mrozik, Mateusz Pietraszko, Michał Sujkowski, Aleksandra Gruszka, Piotr Pulit 341

Comparative Analysis of Paper vs. Avionics-Integrated Checklists Based on Pilot Feedback
Dariusz Myszor, Magda Mrozik, Mateusz Pietraszko, Michał Sujkowski, Aleksandra Gruszka, Piotr Pulit 349

Shaping the microstructure and properties of duplex stainless steels manufactured via LPBF additive technology
Antonina Olszewska, Wiktoria Wanczura, Kamil Czajkowski, Bartosz Jagla, Kacper Toman, Oleksander Knysh, Aleksander Kolšovský, Mengistu Jemberu Dagnaw, Zbigniew Brytan, Jana Bidulská 358

Near-Infrared Vein Visualization System with Integrated DLP Projection and Adaptive Image Enhancement Algorithms
Marcin Paszkuta, Agnieszka Szczęsna, Wirginia Likus, Jakub Antonowicz, Kamil Ceglarski, Artur Szaboń, Mateusz Róg, Aleksandra Wąsek, Sebastian Tkacz 366

Poruchy valivých ložísk
Mária Pilarčíková, Eva Tillová, Miroslaw Bonek 371

Computer simulation of the mechanical properties of a wood chipping knife during the production of wood chips
Jakub Polis, Jakub Bicz, Radosław Trojnar, Daniel Pella, Filip Bejm, Amadeusz Dziwis, Agata Śliwa, Marek Sroka, Jan Komendák, Samuel Zachar, Miroslava Tavodova 377

Creating an effective cooling system for the loading zone of a 3D printer screw extruder when printing with composite mixtures
Andrii Polishchuk, Mirosław Bonek, Oleh Polishchuk, Serhii Matiukh, Svitlana Lisevich, Artem Tostiuk 385

Structure and phase transformations of Mg-Zn-Ca alloys containing Ag and Au obtained by mechanical alloying
Julia Popis, Oktawian Bialas, Oliwia Starczewska, Małgorzata Karolus, Sabina Lesz 394

Laser Technology in Microfabrication and Optics
Katarzyna Ptasznik, Wiktoria Gamla, Mirosław Bonek 398

Optimization of numeric keyboard interfaces based on signals from eye tracking components build in virtual reality goggles
Maja Rudnicka, Michał Lasak, Szymon Sadza 406

Modernization and development of transport applications of an autonomous airship
Maja Rudnicka, Michał Lasak, Franciszek Borgosz 413

Wytrzymałościowa analiza numeryczna łomu wykonanego z różnych materiałów inżynierskich oraz jego wizualizacja
Adam Schwarz, Łukasz Buszka, Łukasz Mann, Amadeusz Dziwis, Wojciech Mikołejko, Agata Śliwa 419

Ergonomic assessment of the carpenter's workplace using the NIOSH method and the concept of robotics application
Marcin Sitko, Monika Spilka 424

Research on stone material from mining waste dumps for use in construction materials
Barbara Słomka-Słupik, Jakub Piasecki 432

Thermal analysis of aircraft double-pane windows
Haoxiang Song, Ruyu Shi, Xiyue Cui 438

Analysis of reactive power compensation in a 100/15kV station and the suitability of using capacitor banks in the network
Szymon Szeja 446

Analiza numeryczna własności mechanicznych wspornika schodowego
Mateusz Szojda, Bianka Wyrobek, Agata Śliwa, Marek Sroka 454

Influence of tin and niobium on the morphology of calcium phosphate nanowires
Yao M. Tsekpo, E. Atioyire, Weronka Smok, Paweł Jarka, Tomasz Tański 462

Energy saving technologies for obtaining high purity neon and helium
Irine Ugrekhelidze, Tamaz Isakadze 470

Laser tattoo removal by Q-switch lasers
Martyna Urbańska, Kinga Stępska, Mirosław Bonek 474

Study of strength properties of components made of recyclate doped filaments
Martyna Urbańska, Kinga Stępska, Jan Wypiór, Olaf Pradelok, Krzysztof Olszak, Vojtěch Macejko, Eliška Posmyková, Mariusz Król, Jiří Hajnys 483

Microstructure and Hardness Evaluation of Additive Materials Applied by Hardfacing by Welding Technology
Monika Vargová, Miroslava Ťavodová 492

Vplyv veľkosti plastickej deformácie a teploty rekryštalizačného žíhania na tvrdosť a štruktúru vybraných konštrukčných materiálov
Jozef Vicena, Milan Uhríčik, Mirosław Bonek 501

Určenie príčiny a následný návrh náhrady poistnej skrutky v kolennej endoprotéze
Richard Vidrich, Ronald Bašťovanský, Peter Palček, Mirosław Bonek 509

Six-degree-of-freedom robotic arm design
Qilin Wang, Fan Yang, Yining Huang, Wenhao Zhu, Chaoyue Yang 517

Passivation of steel: protection mechanism and comparison of chemical methods
Łucja Wantuch, Monika Kciuk 528

AGV auto levelling system for autonomous floor mapping
Krzysztof Witek, Krzysztof Paszek, Ernest Antolak, Justyna Paszek 532

The influence of sea water on the properties of ship steel covered with a protective coating
Anna Włodarczyk-Fligier, Magdalena Polok-Rubiniec, Aneta Kania 540

Finite Element Analysis of Single-Cell Ti6Al4V and TiZrNb Structures: Investigating Thickness and Porosity Effects for Scaffold Design Applications
Sichale Worku Fita, Mirosław Bonek, Sebastian Sławski, Anna Woźniak 545

Numerical analysis of the load on the surface of a wood chipping tool
Zuzanna Zielińska, Łukasz Lomania, Katarzyna Ptasznik, Kajetan Kojm, Wiktoria Borowiec, Wojciech Mikołejko, Agata Śliwa, Marek Sroka, David Varholík, Peter Očovský, Miroslava Tavodova 553

Analysis of the properties of multilayer composite materials dedicated for yacht hulls
Zuzanna Żaczek, Agnieszka J. Nowak 562

Characterisation of materials used in construction for damp-proofing and waterproofing
Ewelina Kaputa-Kuc, Ewa Jonda, Marek Sroka 570

Analysis of the properties of multilayer composite materials dedicated for yacht hulls
Maryam Soleimani, Wojciech Sitek, Magdalena Szindler 577

Influence of external friction on amplitude dependences of internal friction of steel
Yuliia Sokolan, Kateryna Sokolan, Oleg Polishchuk, Mirosław Bonek 583

TalentDetector
23th-25th June 2025
Gliwice-Brenna, Poland
DEPARTMENT OF ENGINEERING MATERIALS AND BIOMATERIALS
FACULTY OF MECHANICAL ENGINEERING
SILESIAN UNIVERSITY OF TECHNOLOGY
INTERNATIONAL STUDENTS SCIENTIFIC CONFERENCE

Effects of Atomic Layer Deposition Temperature on the Formation of ZnO Nanolayers for Improved Solar Cell Efficiency

Elizabeth Addae [a], Wojciech Sitek [b], Marek Szindler [c]

Scientific and Didactic Laboratory of Nanotechnology and Material Technologies, Faculty of Mechanical Engineering, Silesian University of Technology, Towarowa 7 Str., 44-100 Gliwice, Poland; Elizabeth.Addae@polsl.pl
Scientific and Didactic Laboratory of Nanotechnology and Material Technologies, Faculty of Mechanical Engineering, Silesian University of Technology, Towarowa 7 Str., 44-100 Gliwice, Poland; Wojciech.Sitek@polsl.pl
Scientific and Didactic Laboratory of Nanotechnology and Material Technologies, Faculty of Mechanical Engineering, Silesian University of Technology, Towarowa 7 Str., 44-100 Gliwice, Poland; Marek.Szindler@polsl.pl

Abstract: The semiconductor photoanode is crucial to device efficiency, and zinc oxide (ZnO) has emerged as a promising alternative to titanium dioxide (TiO_2) due to its higher electron mobility and versatile nano-structuring capabilities.
This study explores the deposition of ZnO on FTO-glass substrates using Atomic Layer Deposition (ALD), focusing on how deposition temperature affects thin film quality. ALD enables precise, uniform deposition of ZnO thin films with excellent chemical stability—ideal for Dye Sensitized Solar Cells (DSSCs) devices. Scanning Electron Microscopy (SEM) and Energy Dispersive X-ray Spectroscopy (EDS) analysis revealed that thin films deposited at 200°C showed greater crystallinity, homogeneity, and Zn incorporation compared to those at 100°C. These results emphasize the importance of deposition temperature in optimizing ZnO layer properties and demonstrate that ALD-deposited ZnO is a stable and efficient semiconductor for enhancing DSSC

Keywords: EDS analysis, ZnO photoanode, ALD, Morphology, Deposition Temperature

1. INTRODUCTION

Dye-sensitized solar cells (DSSCs) are a strong substitute for conventional silicon-based photovoltaic technology providing special benefits that meet both pragmatic energy requirements and concerns regarding the environment. The ecologically conscious production method of DSSCs is among their most noteworthy advantages. These types of solar cells are more sustainable than traditional solar cells since they are made with low-energy methods and contain plentiful, non-toxic components. The fact that they are effective in low light is another significant benefit. DSSCs, in contrast to conventional solar cells, continue to function in indoor lighting,

cloudy conditions, and diffused light. This makes it possible to generate energy consistently in a greater variety of settings [1].

DSSCs work via a photoelectrochemical process in which sunlight is absorbed by a photosensitizer dye, which then introduces electrons into the conduction band of a semiconductor [2]. A redox mediator in the electrolyte regenerates the oxidized dye molecules, completing the circuit as these electrons go through the semiconductor to the anode. Compared to conventional silicon-based solar cells, this arrangement offers advantages by enabling the decoupling of the processes involved in light absorption and charge transport. A standard DSSC is composed of a counter electrode, an electrolyte with a redox couple, a monolayer of sensitizing dye, a mesoporous semiconductor layer, and a transparent conducting oxide (TCO) substrate. Because the semiconductor layer is mesoporous, it has a large surface area for dye adsorption, which increases the effectiveness of light absorption [2,3].

With distinct benefits that may improve device performance, zinc oxide (ZnO) has become a strong substitute for titanium dioxide (TiO_2) in dye-sensitized solar cells (DSSCs). Because ZnO has more electron mobility than TiO_2, charge transport in the photoanode is more effective. In DSSCs, this characteristic may result in lower electron recombination rates and increased total efficiency. ZnO has a broad direct bandgap of around 3.3 eV and excellent electron mobility, allowing for efficient charge transfer within the photoanode. Furthermore, ZnO can potentially be produced into a range of nanostructures, including nanowires, nanorods, and nanotubes, employing low-temperature and cost-effective processes. These nanostructures provide a large surface area for dye adsorption and can provide direct paths for electron transport, therefore reducing recombination losses. This capacity to modify the shape of ZnO nanostructures enables adjustment of light scattering and absorption characteristics, potentially improving the overall photovoltaic efficiency of DSSCs.

Atomic Layer Deposition (ALD) provides atomic-level control over thin film thickness and composition, allowing for the creation of homogenous ZnO layers with customized characteristics. This accuracy is critical for optimizing the electrical properties of the semiconductor layer, which has a direct influence on the efficiency of the DSSC. Furthermore, ZnO thin films produced by ALD show excellent chemical stability, especially in the acidic conditions common to DSSC electrolytes. This stability keeps the device's performance steady over time and extends its operating longevity [4].

2. METHODOLOGY

The FTO glass substrates were cleaned in order to remove any impurities that would impair the quality and adherence of the thin film. The FTO substrates were successively immersed for ten to fifteen minutes in ultrasonic baths containing acetone, isopropanol, and deionized water. The substrates were cleaned and then dried using nitrogen gas.

The atomic layer deposition (ALD) process using the Picosun R-200 system began by introducing diethylzinc (DEZ) vapor into the reaction chamber for a brief pulse lasting approximately 0.1 seconds. During this step, DEZ molecules chemisorbed onto the available reactive sites on the surface of the FTO-glass substrate, initiating the formation of the first half of the ZnO monolayer. Following this precursor exposure, the chamber was purged with an inert carrier gas—typically nitrogen—for about 4 seconds. This purge step effectively removed any unreacted DEZ molecules and gaseous by-products, thereby preventing any unwanted gas-phase reactions in the subsequent steps.

Next, water vapor was introduced into the chamber as the oxidizing agent, also for a short pulse of 0.1 seconds. The water molecules reacted with the adsorbed DEZ layer on the substrate surface, completing the surface reaction and forming a uniform monolayer of zinc oxide (ZnO). To conclude the cycle, a second purge step was carried out using inert gas to eliminate any excess water vapor and remaining reaction by-products from the chamber. This careful sequencing ensured self-limiting surface reactions and high-quality layer formation, essential for the uniform growth of ZnO thin films in ALD. These steps were repeated until 500 cycles of thin films were achieved however at different deposition temperatures – 100^0C and 200^0C as demonstrated in Figure 1.

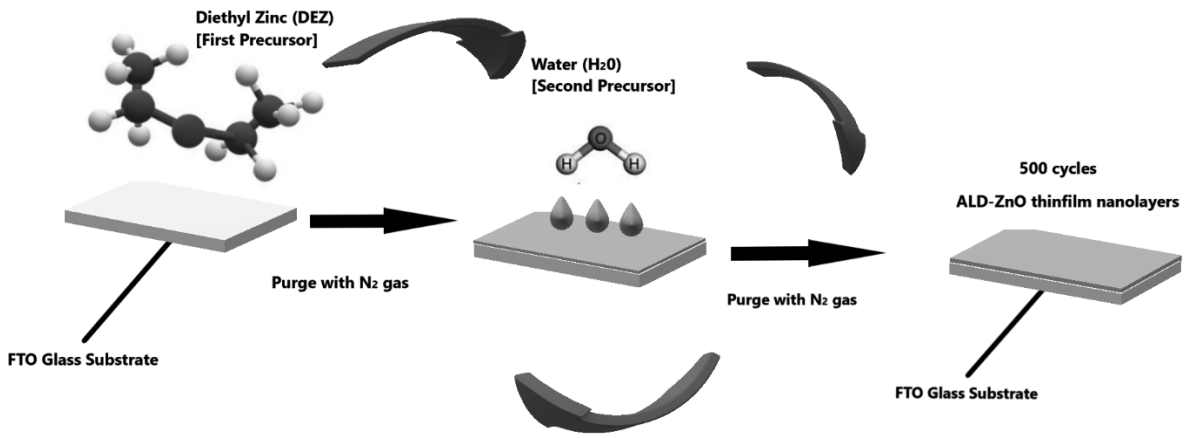

Figure 1. Deposition of ZnO nanolayer thin-films via ALD method

3. RESULTS

As seen in Figure 2, the SEM images generated a visible trend in b) and c) with change in deposition temperature. Despite equal deposition cycles, *FTO-ZnO 500cycles-200^{o}C* exhibits a more defined and homogeneous layer.

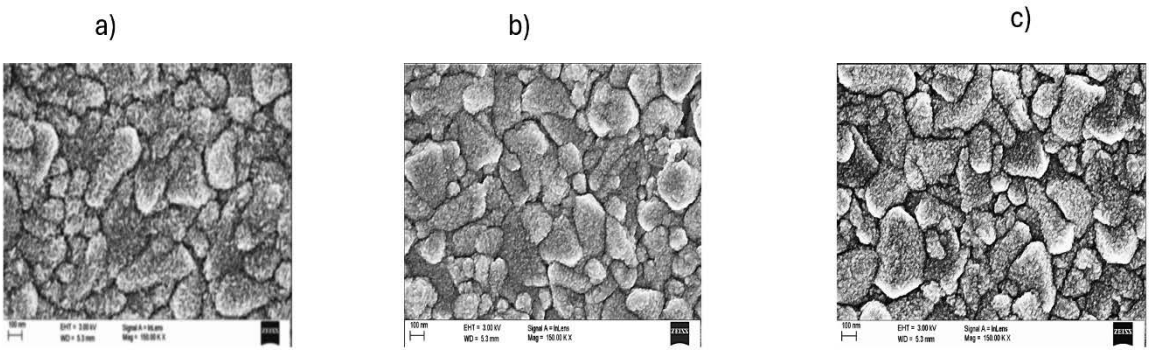

Figure 2. SEM image analysis of a) pure FTO-ZnO glass b) FTO-ZnO 500cycles-100^{o}C c) FTO-ZnO 500cycles-200^{o}C

One possible explanation for the observed variations in film morphology lies in the differences in deposition temperature during the ALD process. As illustrated in the trend across the images, there is a clear increase in structural definition with rising temperature. This is because temperature plays a crucial role in facilitating gas-phase chemical reactions, which are essential for the layer-by-layer growth characteristic of atomic layer deposition [5].
Higher deposition temperatures generally lead to more crystalline and smoother films, as well as an accelerated growth rate. This is due to increased kinetic energy, which improves the reactivity and mobility of precursor molecules on the substrate surface. From these observations, it can be concluded that temperature is a key parameter influencing the quality and efficiency of ZnO thin film deposition via ALD. Specifically, deposition temperature of 200°C is more ideal, as it can produce uniform film growth, and optimize the overall physical and chemical properties of the ZnO metal oxide layer.
Figure 3 contains the Energy Dispersive Spectroscopy (EDS) elemental graphs with their corresponding weight and atomic percentage values found in all three samples. Pure FTO glass samples showed zero peaks for Zn with correlating 0.0% for both the elemental weight and atomic values. These recorded values prove that the FTO glass substrates do not contain any ZnO structures.

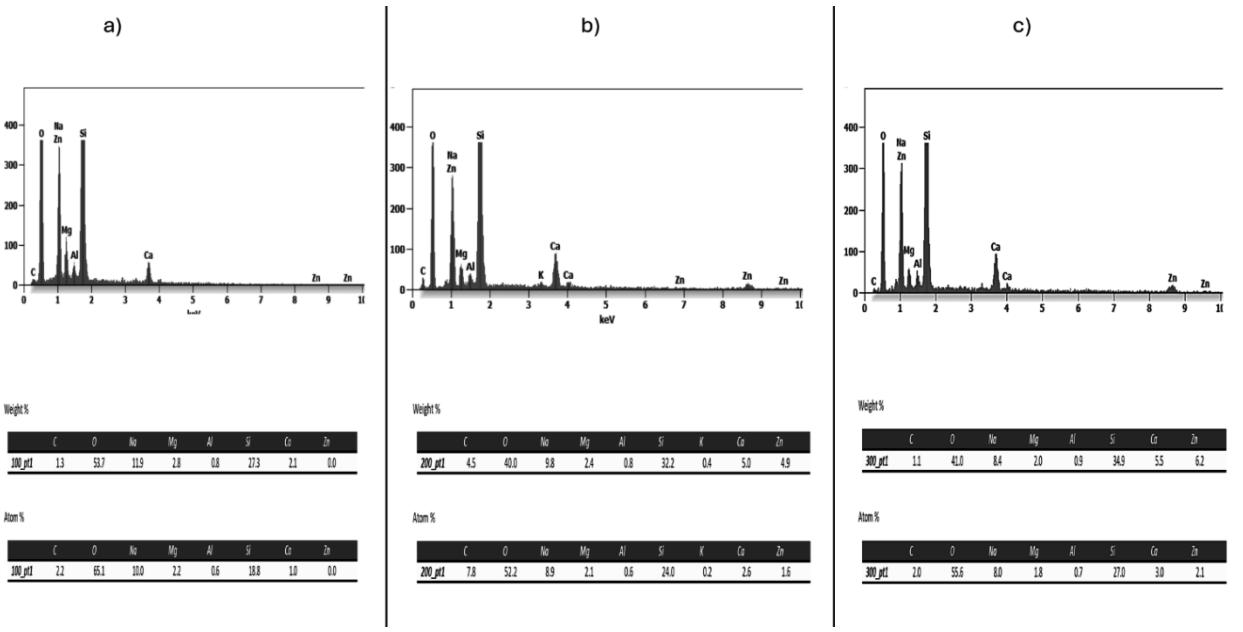

Figure 3. EDS element analysis of a) pure FTO-ZnO glass b) FTO-ZnO 500cycles-100°C c) FTO-ZnO 500cycles-200°C

However, Zn values were recorded in Figure 3b) and c) with *FTO-ZnO 500cycles-100°C* showing 4.9% weight of Zn and *FTO-ZnO 500cycles-200°C* showing *6.2%* weight of Zn. Despite equal deposition cycles, samples deposited at 200°C retained more Zn particles than samples deposited at 100°C. This could be due to the fact that ZnO thin films deposited at higher temperatures tend to exhibit a slower overall growth rate per ALD cycle. This reduced growth rate allows for finer control over film thickness, enabling the deposition of more precisely tailored and homogeneous layers [6]. The deceleration in growth is attributed to the enhanced desorption of excess precursor molecules and by-products at elevated temperatures, which helps maintain the self-limiting

nature of the ALD process. As a result, each cycle contributes a consistent and well-defined atomic layer to the film. Moreover, higher deposition temperatures improve the mobility and surface reactivity of the adsorbed species, leading to better packing density and more uniform film coverage across the substrate. This enhanced uniformity is particularly valuable in applications requiring thin, conformal coatings—such as in photovoltaics and nanoelectronics—where consistency in film thickness and material properties directly influences device performance. Therefore, operating at elevated temperatures not only refines the structural integrity of ZnO thin films but also promotes the formation of continuous, pinhole-free layers with superior uniformity [7].

4. CONCLUSION

According to the obtained results, data analysis shows that the quality of ZnO films generated by ALD is significantly influenced by the deposition temperature. Even after going through the same number of deposition cycles, the sample that was deposited at 200°C had a more uniform, well-defined layer and had a greater zinc content than the sample that was placed at 100°C. Improved surface mobility and precursor reactivity at higher temperatures are responsible for this, since they increase homogeneity and enable more precise control over layer thickness. A deposition temperature of about 200°C is therefore ideal for producing high-quality, well-structured ZnO thin films that are appropriate for optoelectronic and photovoltaic applications.

BIBLIOGRAPHY

1. J. B. Baxter and E. S. Aydil, “Nanowire-based dye-sensitized solar cells,” Applied Physics Letters, vol. 86, no. 5, p. 053114, Jan. 2005, doi: 10.1063/1.1861510
2. Grätzel, M. Dye-Sensitized Solar Cells. *Journal of Photochemistry and Photobiology C: Photochemistry Reviews* 2003, *4*, 145–153, doi:10.1016/S1389-5567(03)00026-1.
3. O’Regan, B.; Grätzel, M. A Low-Cost, High-Efficiency Solar Cell Based on Dye-Sensitized Colloidal TiO2 Films. *Nature* 1991, *353*, 737–740, doi:10.1038/353737a0.
4. I. Jang, K. Song, J.-H. Park, and S.-G. Oh, “Enhancement of Dye Adsorption on TiO2 Surface through Hydroxylation Process for Dye-sensitized Solar Cells,” Bulletin of the Korean Chemical Society, vol. 34, Oct. 2013, doi: 10.5012/bkcs.2013.34.10.2883.
5. K. Roelofs et al., “Effect of Al2O3 Recombination Barrier Layers Deposited by Atomic Layer Deposition in Solid-State CdS Quantum Dot-Sensitized Solar Cells,” The Journal of Physical Chemistry C, vol. 117, pp. 5584–5592, Feb. 2013, doi: 10.1021/jp311846r.
6. H.-M. Cheng, W.-H. Chiu, C.-H. Lee, S.-Y. Tsai, and W.-F. Hsieh, “Formation of Branched ZnO Nanowires from Solvothermal Method and Dye-Sensitized Solar Cells Applications,” J. Phys. Chem. C, vol. 112, no. 42, pp. 16359–16364, Oct. 2008, doi: 10.1021/jp805239k.
7. X. Wang, M. Ahmad, and H. Sun, “Three-Dimensional ZnO Hierarchical Nanostructures: Solution Phase Synthesis and Applications,” Materials, vol. 10, no. 11, Art. no. 11, Nov. 2017, doi: 10.3390/ma10111304

TalentDetector

23th-25th June 2025
Gliwice-Brenna, Poland

DEPARTMENT OF ENGINEERING MATERIALS AND BIOMATERIALS
FACULTY OF MECHANICAL ENGINEERING
SILESIAN UNIVERSITY OF TECHNOLOGY

INTERNATIONAL STUDENTS SCIENTIFIC CONFERENCE

The Effect of Current-Assisted Lacquer Coating on The Corrosion Resistance of Electrolytically Nickel-Plated Surfaces

[1]Yasin Akgun, [1]Koray Guler, [1]Yener Kilic, [2]Cemal Meran

[1]Student, Pamukkale University, Faculty of Engineering, Department of Mechanical Engineering, Denizli, Turkey
[2]Prof.Dr., Pamukkale University, Faculty of Engineering, Department of Mechanical Engineering, Denizli, Turkey, Email: cmeran@pau.edu.tr

Abstract: This study investigates the effect of the electrophoretic lacquer coating process on the corrosion resistance of electrolytically nickel-plated surfaces using an experimental approach. The research involved a detailed analysis of nickel-plating processes and parameters. The corrosion performance of different coating combinations was then compared. The potential of flow lacquering to improve the corrosion resistance of nickel-plated surfaces was also evaluated. The experimental process was carried out systematically, including preparing the nickel-plating baths, meticulously applying the coatings, and conducting corrosion tests. The findings demonstrate that the current lacquering process positively impacts the corrosion resistance of nickel-plated surfaces, contributing to the metal plating industry and the field of materials science.

Keywords: Electrolytic Nickel Plating, Current-Assisted Lacquer Coating, Corrosion, Corrosion Testing

1. INTRODUCTION

When metal materials used in industrial applications are exposed to harsh environmental conditions and chemical effects, they lose their physical and chemical properties over time and corrode. Corrosion is a serious problem that not only causes material loss, but also adversely affects the functionality and safety of systems. For this reason, various protective methods have been developed to extend the life of metals such as iron, steel, brass and copper. One of these methods is surface coating technologies, [Url-1].

Electrolytic nickel plating, which is widely preferred among surface coating techniques, stands out by providing both decorative and functional properties on metal surfaces. Electrolytic nickel coatings provide protection against corrosion as well as advantages such as wear resistance, gloss and surface hardness. However, the long-term corrosion resistance of these coatings may not be sufficient in some application areas. For this reason, it is aimed to further improve the performance of the coating with additional surface treatments that can be applied after coating.

Current lacquering, one of the prominent methods in this context, is a method applied on electrolytic coated surfaces and aims to limit the contact of the material with environmental factors by forming a thin, impermeable film layer on the surface. The lacquering process is especially important in terms of providing chemical resistance and protection against atmospheric corrosion, [Url-2].

2. SURFACE COATING

Electrolytic nickel plating is a process in which a uniform layer of a nickel-phosphorus alloy is deposited on a substrate. Electrolytic plating differs from this as it uses an external electric current to achieve the deposition. This process offers many advantages such as increased corrosion resistance, higher durability and maintaining the thickness of the coating on complex shapes. Electrolytic nickel coatings form a dense, continuous and uniform coating that acts as an effective barrier against corrosive elements such as moisture, chemicals and salts, [Url-3].

Electrophoretic lacquer coating is a coating method applied to metal surfaces to provide durability, aesthetic appearance and long-lasting protection. This process is carried out by homogeneously applying a water-based lacquer solution to the metal surface with the help of an electrical current. Electrophoretic coating is frequently preferred especially in the automotive, white goods and electronics sectors, [Url-4].

High corrosion resistance, environmental friendly low volatile organic compound content, and excellent surface coating quality are among the outstanding features of this method.

The basic polymers used in these processes are acrylic urethanes, but it is the polyurethane polymer that primarily forms the coatings. Although epoxy, one of the other polymers, has good properties, it does not provide the appearance, hardness, corrosion resistance and sub-surface adhesion normally expected from the final lacquer layer in a balanced manner, [Url-5].

Advantages of Lacquer Coating;

- High Durability
- Aesthetic Appearance
- Environmentally Friendly Formulation
- Chemical Resistance
- Ease of Use

ASTM G31-21 is a standardized test method for evaluating the corrosion behaviour of metals and alloys by immersion in liquid media. This standard provides for the corrosion of specimens by complete immersion for a specified period in solutions of specified temperature and chemical composition, especially under laboratory conditions. ASTM G31 has undergone several revisions since it was first published, and this version, updated in 2021, has increased the reliability of the standard by providing clearer and more repeatable criteria on issues such as the frequency of solution changes, the use of stirred systems, and surface preparation procedures. During the test, the pH, temperature and composition of the solution should be kept constant, and the environment should be set either stationary or stirred. ASTM G31-21 is widely used by industry, academia and research organizations worldwide, particularly in material selection, quality control, surface coating performance analysis and new alloy development, [Url-6].

3. MATERIALS AND METHODS

3.1 Surface Preparation

Structural steel specimens with a dimensions of 2x20x20 mm, were cut with a 100 mm long band saw. The burrs were cleaned in the sanding machine. The specimens were washed with gasoline to remove the dirt and particles adhering to the specimens during the deburring process. The samples were thrown into a cauldron full of sawdust, separated from the gasoline and dried. The samples were suspended on hangers and the preliminary preparations for surface cleaning were completed, Figure 1.

a **b** **c** **d**

Figure 1. Surface Preparation Stages a-) Cutting of Samples b-) Deburring of Samples c-) Cleaning of Samples with Gasoline d-) Drying with Sawdust

The samples were cleaned in a cleaning bath containing cyanide, sodium hydroxide (caustic) and soda for 1 minute. The specimens were cleaned on the principle of cathodic cleaning to remove heavy oils and dirt. After rinsing, sulfuric acid and rinsing again, the samples were ready for nickel plating. The samples were cleaned in a cleaning bath containing cyanide, sodium hydroxide (caustic) and soda for 1 minute. Heavy oils and dirt were removed from the samples cleaned in the cathodic cleaning principle, Figure 2.

Figure 2. Cleaning Bath

After rinsing, sulfuric acid and rinsing again, the samples were ready for nickel plating, Figure 3.

a **b** **c**

Figure 3. a-) 1st Rinse Water b-) Sulfuric Acid c-) 2nd Rinse Water

3.2 Electrolytic Nickel Plating

The object, which was 5.3 volts, 273 amps, 55 °C, 5 metres long and weighed 4 tons, was kept in the pool for 20 minutes and nickel-plated. Plastic balls in the nickel bath maintain the bath temperature. The samples were removed from the nickel bath and rinsed twice, after which the nickel-plated sample was prepared, Figure 4.

a **b** **c**

Figure 4. Nickel Plating Stages a-) Nickel Bath b-) 1st and 2nd Rinsing Tanks c-) Nickel Plated Samples

3.3 Current-Assisted Lacquer Coating

For better strength of nickel-plated materials, current lacquering is performed. Nickel and nickel-chrome plated samples were subjected to 1st and 2nd rinsing in the lacquering chamber. Pre-cleaning was performed prior to pickling with acid. The samples cleaned with rinsing and rinsed water to remove the acid were taken to the lacquering chamber.

The Electrophoretic Lacquer Reducer, which is set to T2 program, performs the lacquering process in 34 seconds as soon as it reaches 4.0 amps and 30 volts after a short preparation phase. After the lacquering process, the samples were rinsed again.

After the lacquering process was completed, the samples were taken to the oven to be baked. After baking at 171°C for 45 minutes, the samples were placed on a cooling rack for cooling, Figure 5.

a **b** **c**

Figure 5. a-) Rinsing Pools b-) Lacquering Process c-) Samples baked at 171°C

4. EXPERIMENTAL STUDIES

4.1 Solution Preparation

A 5% solution of sodium chloride (NaCl) and distilled water was used as the test medium. The solution was prepared in the proportions specified in ASTM G31-21. According to the standard, the pH value is required in the range of 6.5 - 7.2. In the solution we prepared, our pH value was 7.13. The ambient temperature was kept at room temperature (25 ± 2 °C), [Url-6].

4.2 Preparation of Specimens for Testing

The specimens to be subjected to corrosion testing were prepared as specified in ASTM G31-21 prior to testing. The specimens were cleaned with distilled water to remove oxide layers and foreign particles from the surface. The surface roughness of each sample was checked. The samples were weighed with a precision balance and the initial weight and thickness measurements with a micrometre were recorded.

4.3 Corrosion Test Stages

The prepared specimens were placed vertically so that they were completely submerged in the solution. Care was taken to avoid contact between the specimens and the vessel walls. Each specimen was kept in the solution at room temperature for 168 hours. Ambient conditions were checked at regular intervals throughout this period.

At 12-hour intervals, the samples were removed from the solutions, dried with a blow dryer and the solutions were mixed. The stirring of the solutions was done both to provide fluctuation and to disperse the particles settling to the bottom.

At 24-hour intervals, the weight and thickness of the samples were measured and recorded.

At 48-hour intervals, the solutions were renewed, and the pH was checked. The ropes on which the samples were hung were changed.

At the end of the test period, the samples were removed from the solution and cleaned in accordance with ASTM G1 standard. For this purpose, the specimens were immersed in a 10% solution of HCl and distilled water to remove corrosion products.

5. CONCLUSION AND EVALUATION

Nickel Plated Sample

The post-treatment surface roughness (Ra) values of the samples coated at 5.3 V - 237 A and 2.2 V - 32 A were measured as 0.640 µm and 0.593 µm, respectively, and increased compared to the initial values, Table 1. This increase indicates microstructural irregularities that may occur on the coating and deterioration in coating quality, Figure 6.

Table 1. Nickel Plated Sample Data

Voltage (V) and Current (A) Values	Weight (grams)		Surface Roughness (µm)		Thickness (mm)	
	First	Final	First	Final	First	Final
5.3 V – 237 A	63	62	0.454	0.640	1.190	1.151
2.2 V – 32 A	63	62	0.449	0.593	1.160	1.150
8.0 V – 135 A	66	66	0.266	0.268	1.210	1.178

Voltage (V) and Current (A) Values	First	Final
5.3 V 237 A	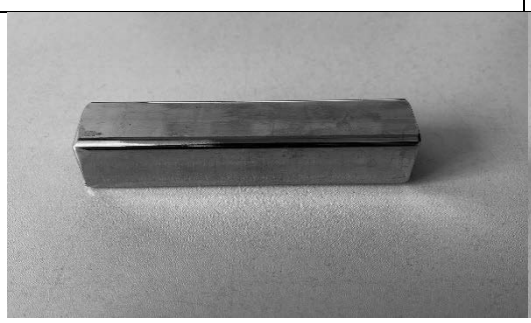	
2.2 V 32 A	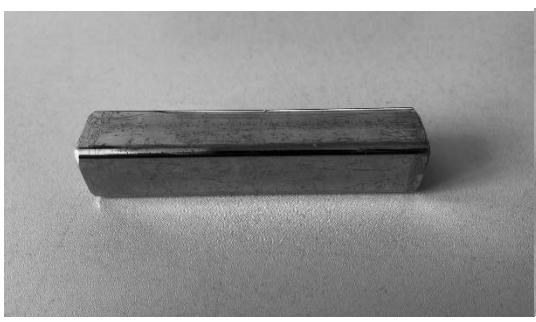	
8.0 V 135 A		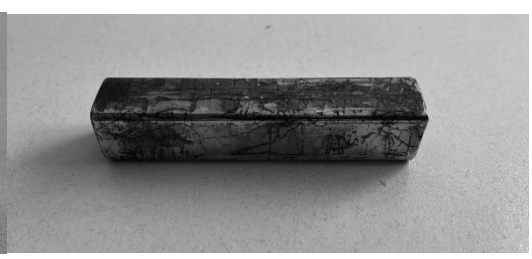

Figure 6. First and Final Images of Nickel Plated Sample

On the other hand, the Ra value remained constant in the sample coated at 8.0 V - 135 A condition and gave the most stable result in terms of surface roughness. When the thickness values were analyzed, a slight decrease was observed in all samples, indicating deformations due to surface oxidation after coating. Weight data show slight differences between the samples. While all samples had a bright, smooth and homogeneous surface before the process, serious discoloration, dulling and surface deterioration were observed in the samples coated with 5.3 V and 2.2 V in the post-treatment images. This indicates uneven nickel distribution and oxidation formation on the plating surface.

Nickel + Lacquer Coated Sample

Specimens exposed to 30 and 45 minute firing times showed an increase in surface roughness after corrosion in both cases. The 45-minute baked specimen initially had a lower roughness, but after the test, it reached a similar Ra value to the 30-minute specimen, Table 2.

Table 2. Nickel + Lacquer Coated Sample Data

Baking Times (min)	Weight (grams)		Surface Roughness (µm)		Thickness (mm)	
	First	Final	First	Final	First	Final
30	63	63	0.183	0.300	1.197	1.182
45	64	63	0.161	0.301	1.185	1.160

Baking Times (min)	First	Final
30		
45		

Figure 7. First and Final Images of Nickel + Lacquer Coated Sample

This indicates that the longer baking time causes microscopic degradation in the coating structure and the surface becomes more irregular, Figure 7. Thickness measurements also support the data and both samples showed a decrease after the test.

Especially in the 45-minute sample, the decrease in coating thickness is more pronounced. When the weight measurements were analyzed, no change was observed in the 30-minute sample, while a loss of 1 gram occurred in the 45-minute sample. These results show that the coatings baked for longer periods of time show less resistance to corrosion effects and weakening in their protective properties. After corrosion, physical changes such as discoloration, dulling and surface deterioration were observed more clearly, especially in the 45-minute sample. When all the data obtained are evaluated together, it is concluded that the 30-minute baking time protects the coating integrity and corrosion resistance more effectively, Figure 7.

BIBLIOGRAPHY

Url-1 https://www.fafvana.com.tr/nikel-nedir-nerelerde-kullanilir-ozellikleri-nelerdir/
Url-2 https://www.galvanoteknik.net/form/dosyalar/08.pdf
Url-3 https://kingsunmachining.com/tr/blog/electroless-nickel-vs-stainless-steel/
Url-4 https://www.deltagalvano.com.tr/index.php/elektroforetik-lak/
Url-5 https://en.wikipedia.org/wiki/Electrophoretic_deposition
Url-6 https://www.laboratuar.com/testler/metal-test-laboratuvari/astm-g31-metallerin-daldirma-korozyon-testi/

TalentDetector
23th-25th June 2025
Gliwice-Brenna, Poland
DEPARTMENT OF ENGINEERING MATERIALS AND BIOMATERIALS
FACULTY OF MECHANICAL ENGINEERING
SILESIAN UNIVERSITY OF TECHNOLOGY
INTERNATIONAL STUDENTS SCIENTIFIC CONFERENCE

Design and production of a multi-layer composite material dedicated to insoles for professional running shoes

Krystian Albrecht [1], Agnieszka J. Nowak[2]

[1] Student Science Club "HEAD TO HEAD" operating at the Department of Scientific and Didactic Laboratory of Nanotechnology and Material Technologies at the Faculty of Mechanical Engineering, Silesian University of Technology in Gliwice, Poland
[2] Scientific and Didactic Laboratory of Nanotechnology and Material Technologies, Silesian University of Technology, Konarskiego 18A, 44-100, Gliwice, Poland

Abstract:
This article presents the results of research and analysis on developing a multilayer composite material dedicated to use as insoles in professional running shoes. The work aimed to improve the performance parameters of the inserts through layered systems using polymer matrix composites and various types of reinforcement. An experimental evaluation of selected material variants in bending resistance (three-point bending test), impact strength (Charpy method) and microscopic structure analysis was carried out. The impact of the configurations used on the mechanical behaviour of the inserts was evaluated, as well as their potential to improve comfort and biomechanical performance. The results obtained allowed us to determine the optimal parameters of the composites, taking into account weight minimization, improvement of shock absorption and increase of the user's energy efficiency. The conducted research and its results contribute to further developing technology for producing advanced sports footwear using composite materials. The conclusions from the research allow for optimising the design of the inserts based on advanced composite materials and indicate the directions for further development of products in this category.

Keywords: composite materials, mechanical properties, running shoe insoles

1. INTRODUCTION

The dynamic development of materials science in recent decades has contributed to the emergence of advanced technologies for designing and manufacturing structures with high mechanical performance. One of the effects of this development is the popularization of composite materials, the origins of which date back to the early twentieth century. Composites – a combination of two or more components with different physicochemical properties – have been developed to overcome the limitations of traditional materials such as metals, wood and plastics, which, despite their many advantages, often do not meet the requirements of modern applications in terms of strength-to-weight ratio, durability or resistance to environmental factors.

Initially, composite materials were mainly used in the aerospace, automotive and construction industries [1]. Thanks to progressive miniaturization, better availability and the development of processing technologies, composites are also increasingly used in the sports industry – including the construction of bicycles, sports rackets, protectors, and footwear elements. Particular attention was paid to the possibility of using advanced composite structures to produce insoles for running shoes, which are responsible for the user's cushioning, stabilization and biomechanical support.
Traditional insoles, usually made of materials such as EVA foam or polyurethane, have limited durability, stiffness, and energy efficiency [2]. In response to these limitations, sandwich structures are increasingly being developed, in which the use of fiber-reinforced polymer composites (e.g., glass, carbon) allows for better mechanical parameters while maintaining low weight and high comfort of use.

2. PURPOSE AND SCOPE OF WORK

The study aimed to develop a multi-layer composite material intended for use as an insole in professional running shoes. The basic matrix material was epoxy resin Epidian® 652, while carbon, aramid, and hybrid fabrics played the reinforcing phase role. The main research objective was to determine the influence of the type and configuration of the reinforcing phase on the mechanical properties of the manufactured laminates and indicate the optimal solution for biomechanical applications.
Five material variants were created and differentiated in structure and type of reinforcement used as part of the work. The composites were prepared by manual lamination, obtaining layered systems with controlled geometry and thickness. The scope of work performed:
• development and execution of five configurations of composite laminates using Epidian® 652 resin and various reinforcing fabrics,
• preparation of samples for mechanical tests following PN-EN ISO 178:2006,
• microscopic analysis of the topography of fabrics used as reinforcement,
• conducting three-point bending tests to determine the modulus of elasticity and bending strength,
• performing impact tests using the Charpy method to assess the resistance to dynamic cracking,
• microscopic analysis of the surface of the damage of the samples after mechanical tests,
• assessment of the effectiveness of individual configurations in the context of their possible use in the structures of sports insoles,
• comparative analysis of the results and formulation of technical and design conclusions.

3. RESEARCH METHODOLOGY

As part of the work, comprehensive research was carried out to characterize the mechanical properties of the developed layered composites in detail. Five configurations of reinforcing layers embedded in the Epidian® 652 epoxy resin matrix were analyzed. The research included mechanical tests and microscopic analysis of the components and fractures of the samples after the tests.

3.1. Three-point bending test

One of the main stages of verifying the properties of the composites was the three-point bending test, which allowed the determination of parameters such as flexural strength, elastic modulus, and limit strain of the specimen. The tests were carried out in accordance with method B of PN-EN ISO 178:2006, taking into account amendment A1:2005.

Five sets of samples, five elements each, in cuboids measuring 80 mm × 25 mm, were prepared for the study. The spacing of the supports was 40 mm. The tests were performed at a speed of 2 mm/min using the Shimadzu AGX kN10D testing machine, which enables the testing of various materials, including plastics, composites, and metals [3, 4]. Figure 1 shows an example of the placement of the test sample.

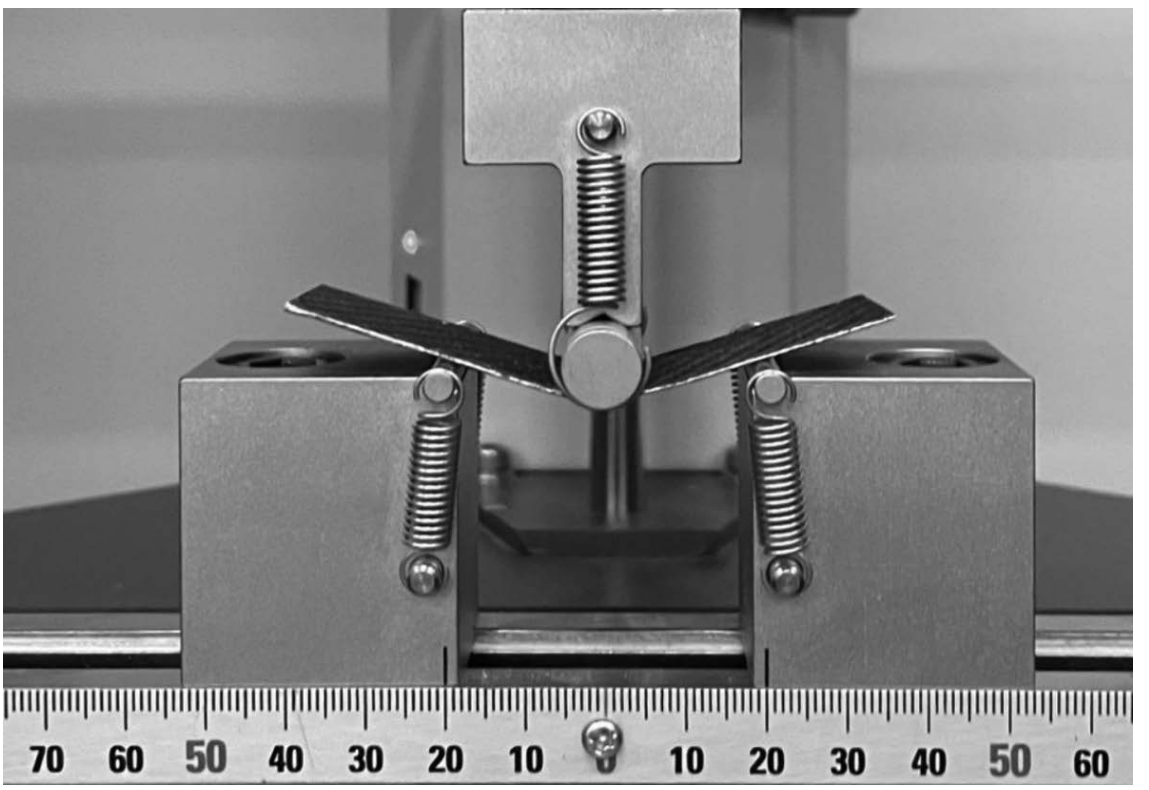

Figure 1. Sample during the three-point bending test [own study]

3.2 Charpy impact test

The composites' dynamic resistance was assessed per the PN-EN ISO 179-1/1f:2010-07 standard using a ZwickRoell HIT25P Charpy hammer with a nominal energy of 5 J. Each of the five material configurations was tested based on three samples with dimensions of 80 mm × 14 ± 2 mm × 1.18 ± 0.12 mm. The samples were fixed in the device holder, and the hammer was struck in the middle of the samples. In order to reproduce the real operating conditions as best as possible, the impact has been directed to the plane of the insert, which corresponds to the loads generated during running. The spacing of the supports during the test was 40 mm. A diagram of the sample assembly is presented in Figure 2.

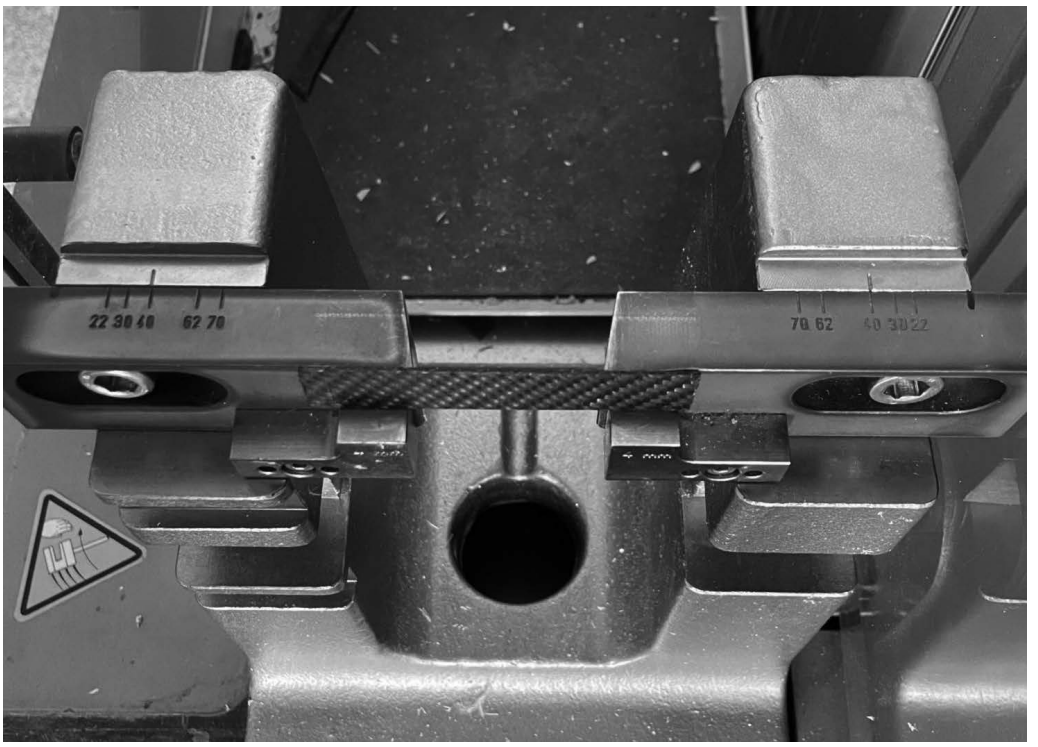

Figure 2. A fitting for testing placed on an impact testing device [own study]

3.2 Microscopic analysis

For an in-depth assessment of the structure of the composites, microscopic observations of both reinforcing fabrics and mechanical fractures were performed. The Leica DVM6 A digital optical microscope enabled 2D and 3D analysis at 50× and 100× magnifications. The arrangement and orientation of fibres in individual layers were analysed, as well as possible structural defects such as microcracks, uneven fibre distribution, inclusions of foreign bodies or surface damage.

In addition, the samples' fractures after three-point bending studies (Tab. 1) were observed to identify the dominant failure mechanisms. Particular attention was paid to the fracture initiation location and damage propagation along the composite layers.

Table 1. Fractures of specimens after three-point bending [own study]

	Rectangular 3x WW fitting after three-point bending test, 100x bend location, side view [own study]

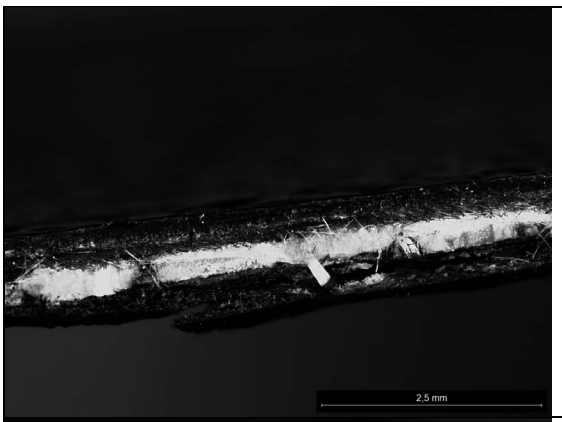	*Rectangular WAWg fitting after three-point bending test, 100x bend location, side view [own study]*
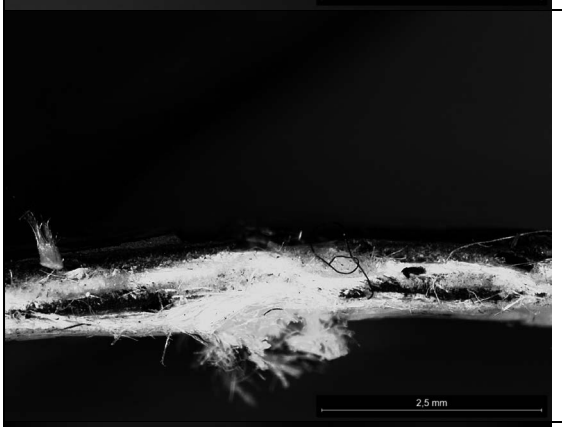	*Rectangular HAWg fitting after three-point bending test, 100x bend location, side view [own study]*
	Rectangular fitting 3x H after three-point bending test, 100x bend location, side view [own study]

c.d. Table 2. Fractures of specimens after three-point bending [own study]

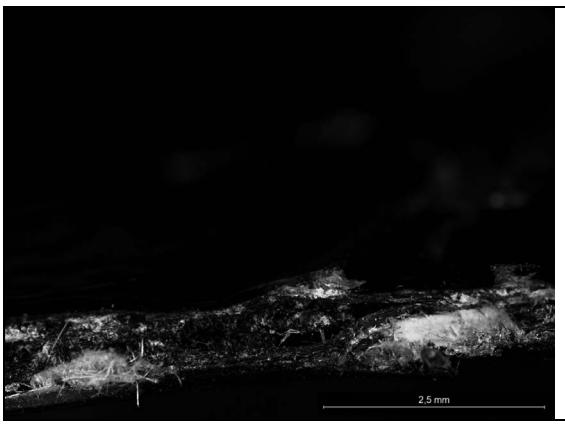

Rectangular HHWg fitting after three-point bending test, 100x bend location, side view [own study]

4. DISCUSSION OF RESEARCH RESULTS

4.1. Three-point bending

Five types of laminates were tested with three-point bending while maintaining the same number of layers. Five samples were made for each series, and the mean values of bending stress, strain for maximum force, flexural strength and Young's modulus are listed in a table 2 and presented graphically in the Figure 3.

Table 3. Averaged results obtained during three-point bending test

Type of laminate	Strain for max. forces; %	Endurance for bending; MPa	Modulus of elasticity; GPa	Stress bending; MPa
3x WW	2,02 ± 0,25	390,87 ± 49,41	20,97 ± 3,72	165,56 ± 16,77
WAWg	2,18 ± 0,7	272,05 ± 133,66	11,83 ± 11,59	113,57 ± 14,33
HAWg	1,15 ± 0,58	107,16 ± 50,45	10,27 ± 2,97	79,86 ± 35,27
3x H	2,18 ± 1,19	254,99 ± 87,27	18,88 ± 7,64	139,16 ± 23,82
HHWg	2,25 ± 1,16	113,86 ± 86,68	8,19 ± 8,72	79,55 ± 14,37

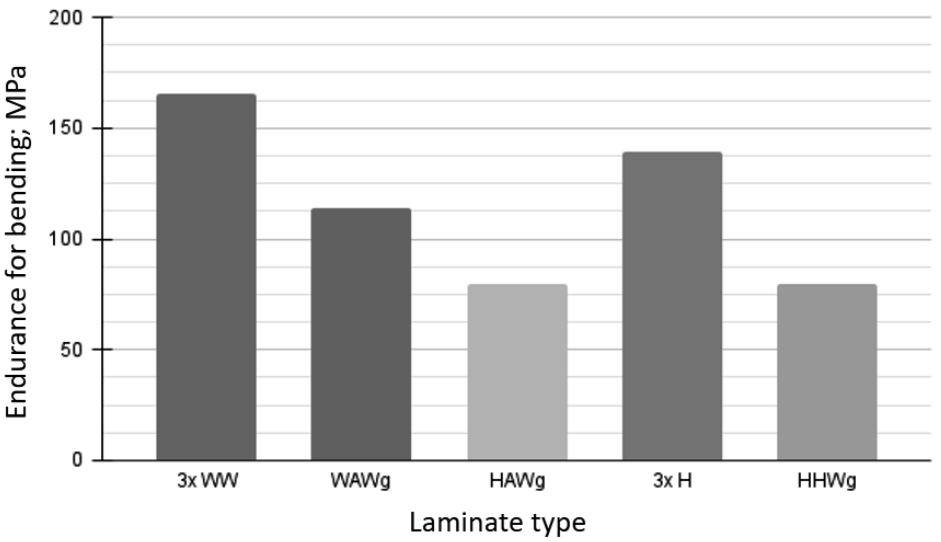

Figure 3. Diagram showing averaged bending stress results

The highest mechanical parameters were obtained for the carbon fabric-reinforced laminate (3x WW), which achieved an average bending stress of 165.56 ± 16.77 MPa. For the WAWg variant, this value was 113.57 ± 14.33 MPa (a decrease of 31.4%), while HAWg and HHWg laminates obtained much lower values – 79.86 ± 35.27 MPa and 79.55 ± 14.37 MPa, respectively. The laminate consisting of three layers of hybrid fabric (3x H) achieved a moderate bending stress of 139.16 ± 23.82 MPa. The comparison of the results shows that the stiffness and strength of laminates strongly depend on the type and arrangement of reinforcing fabrics. Laminates containing carbon fabrics were characterized by higher strength than hybrid and aramid systems, which confirms their suitability for structures requiring high rigidity while maintaining low weight.

4.2. Impact test

The results of the impact tests carried out using the Charpy method (Tab. 3 and Fig. 4) showed significant differences in the energy absorption capacity of the analyzed laminates. The highest average impact strength was obtained for the 3x H laminate – 44.07 ± 12.92 kJ/m², an increase of 23.6% compared to the reference variant 3x WW (35.67 ± 25.30 kJ/m²).

Table 4. Results obtained during the impact test

Type of laminate	Energy absorbed in case of fracture; J	Width sample; mm	Sample thickness; mm	Toughness; kJ/m^2
3x WW	0,70 ± 0,76	14,91 ± 4,02	1,28 ± 0,14	35,67 ± 25,30
WAWg	0,62 ± 0,05	12,58 ± 1,18	1,15 ± 0,15	43,19 ± 3,47
HAWg	0,53 ± 0,21	13,45 ± 2,00	1,11 ± 0,07	35,60 ± 16,28
3x H	0,72 ± 0,44	13,95 ± 2,80	1,16 ± 0,24	44,07 ± 12,92
HHWg	0,66 ± 0,31	14,79 ± 1,03	1,20 ± 0,27	38,86 ± 25,91

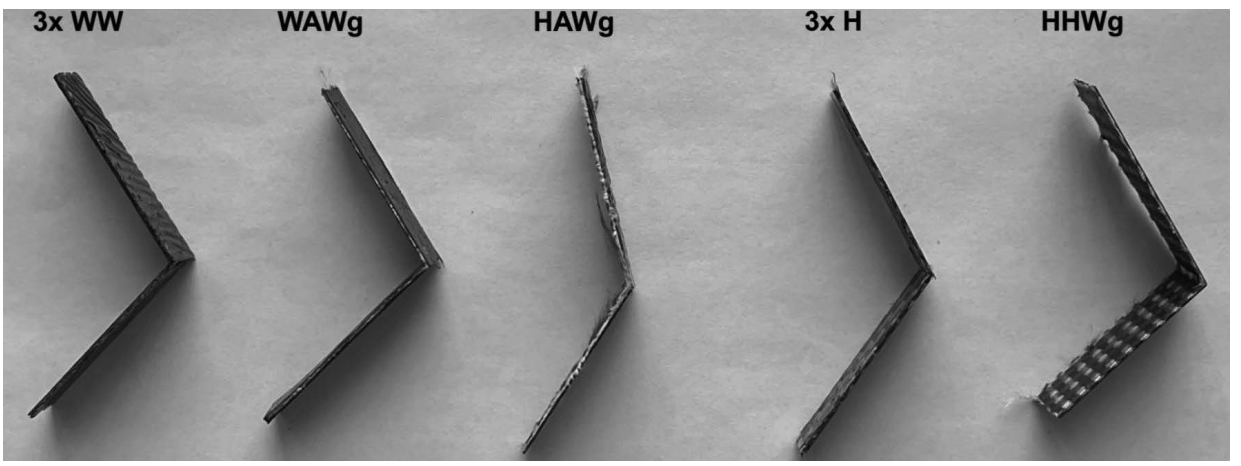

Figure 4. Specimens after impact testing [own study]

The second highest value was the WAWg laminate – 43.19 ± 3.47 kJ/m², while the HHWg laminate reached 38.86 ± 25.91 kJ/m². The lowest impact score was achieved by the HAWg variant – 35.60 ± 16.28 kJ/m².

The results indicate that laminates containing hybrid fibres, especially 3x H, showed the best compromise between stiffness and resistance to impact loading. This suggests their potential in footwear areas particularly exposed to dynamic loads, such as landing zones during running. For each sample tested, an H-hinge refraction was observed.

5. CONCLUSION

The research confirmed the significant effect of the type and configuration of the reinforcing phase on the mechanical properties of composite laminates intended for insoles in professional running shoes. The best strength properties were obtained for the laminate reinforced with three layers of carbon fabric (3x WW), which showed the highest stiffness and bending resistance. The highest impact strength was found for the 3x H laminate, proving its high energy absorption capacity under dynamic loads. WAWg and 3x H laminates offer a well-balanced mechanical performance, combining stiffness with flexibility, making them versatile solutions for different running styles and user preferences. Despite lower strength parameters, materials such as HAWg and HHWg can be used where greater flexibility and adaptation of the insole to specific biomechanical conditions are required. The results indicate that composites with hybrid fabric layers have the potential for applications in professional sports, especially in areas that require a compromise between comfort, cushioning, and energy efficiency. The developed solutions provide a solid basis for further research into optimising insert geometry and using new types of composite matrices and reinforcements.

ACKNOWLEDGEMENT

The present study was produced as part of the activities of the Student Science Club "HEAD TO HEAD" operating at the Department of Scientific and Didactic Laboratory of Nanotechnology and Material Technologies at the Faculty of Mechanical Engineering, Silesian University of Technology in Gliwice.

BIBLIOGRAPHY

1. Dobrzański LA., Non-metallic engineering materials. Silesian University of Technology Publishing House (2008).
2. Website: havel–composite.pl index.php/menu/produkty/type/tkaniny_szklane Date of access: 20.05.2025
3. Grabian J., Ślączka W., and Przetakiewicz W.; Multifunctional layered composite materials for hulls of selected units operated in inland navigation conditions; *Advances in Mechanical and Materials Engineering* 35.298 (3) (2018): 297-308.
4. Jastrzębska M., and Jurczak W.; Modern composite materials for the production of sports and recreational equipment;Logistics 3 (2012).
5. Błędzki AK., Gorący K., and Urbaniak M.; Possibilities of recycling and utilization of polymer materials and composite products; *Polimery* 57.9 (2012): 620-626.

TalentDetector

23th-25th June 2025
Gliwice-Brenna, Poland

DEPARTMENT OF ENGINEERING MATERIALS AND BIOMATERIALS
FACULTY OF MECHANICAL ENGINEERING
SILESIAN UNIVERSITY OF TECHNOLOGY

INTERNATIONAL STUDENTS SCIENTIFIC CONFERENCE

Investigating the Response of PBF-LB/M AlSi10Mg and AlSi12Mg to Direct Aging: A Microstructural and Microhardness Study

Augustine Nana Sekyi Appiah[a], Przemysław Snopiński[a], Evans Atioyire[b], Marcin Adamiak[a]

[a] Silesian University of Technology, Faculty of Mechanical Engineering, Department of Engineering Materials and Biomaterials
[b] University of Ghana, CBAS, School of Engineering Sciences, Department of Materials Science and Engineering, email: augustine.appiah@polsl.pl

Abstract: This study investigates the effect of direct aging (DA) at 180°C for 6 hours on the microstructure and microhardness of laser-based powder bed fusion of metals (PBF-LB/M) manufactured AlSi10Mg and AlSi12Mg alloys. Microstructural characterization via SEM confirmed the retention of the fine cellular PBF-LB/M structure post-DA, alongside the formation of nanoscale, intra-cellular precipitates predominantly composed of Si within the α-Al matrix. The direct aging treatment resulted in a slight increase in Vickers microhardness for both alloys. AlSi10Mg hardness increased from an as-built value of approximately 115.1 $HV_{0.3}$ to 117.7 $HV_{0.3}$ after aging. Similarly, the AlSi12Mg alloy showed a hardness increase from approximately 107.4 $HV_{0.3}$ to 109.7 $HV_{0.3}$. These findings indicate that low-temperature direct aging induces precipitation hardening through the formation of Si-rich nanoprecipitates, while preserving the characteristic fine PBF-LB/M microstructure.

Keywords: additive manufacturing, heat treatment, cellular microstructure

1. INTRODUCTION

Laser-based powder bed fusion of metals (PBF-LB/M), a prominent metal additive manufacturing (AM) technology, enables the fabrication of complex metallic components with high design freedom. Among the processable materials, aluminum-silicon-magnesium alloys, particularly AlSi10Mg, have become a benchmark due to their excellent processability, good strength-to-weight ratio, and corrosion resistance [1]. The rapid solidification inherent to the PBF-LBM/M process results in a unique, non-equilibrium microstructure characterized by fine cellular or dendritic α-Al grains supersaturated with silicon, enclosed by a continuous eutectic Si network. This fine structure imparts high strength to the material in its as-built state [2].

To further optimize mechanical properties and relieve internal stresses, post-process heat treatments are essential. While a conventional T6 treatment (solutionizing, quenching, and artificial aging) [3] is effective, it can be energy-intensive and risk part distortion at high solutionizing temperatures. An alternative and more economical route is direct aging (DA),

which involves heating the as-built part directly to the aging temperature. This approach aims to leverage the supersaturated solid solution created during the PBF-LB/M process to induce precipitation of strengthening phases, primarily nanoscale Si-rich constituents, without destroying the fine as-built cellular morphology [4].

This study investigates the effect of a direct aging heat treatment at 180°C for 6 hours on two closely related alloys: the widely used AlSi10Mg and the higher-silicon variant, AlSi12Mg, both produced by PBF-LB/M. The objective is to characterize and compare the resulting microstructural evolution and the corresponding change in Vickers microhardness. By analyzing the samples using light optical microscopy (LOM) and scanning electron microscopy (SEM), this work aims to elucidate the influence of post-PBF-LB/M direct aging heat treatment on the precipitation hardening response and microstructural stability of PBF-LB/M Al-Si-Mg alloys.

2. METHODOLOGY

The starting materials for this investigation were commercially acquired, gas-atomized AlSi10Mg, and AlSi12Mg powders from Sigma Aldrich. Test samples were manufactured from these powders using a laser-based powder bed fusion of metals (PBF-LB/M) technique on a Trumpf TruPrint system. Subsequent direct aging heat treatments were conducted in a laboratory resistance furnace at 180°C for 6 hours for each sample. For microstructural analysis, specimens were prepared using standard metallographic procedures and examined via LOM with an AxioVision optical microscope and SEM using an EVO 15 MA instrument. The mechanical response to heat treatment was evaluated through Vickers microhardness measurements performed on an FM-ARS 9000 microhardness tester.

3. RESULTS AND DISCUSSION

3.1 Microstructure

LOM was used to investigate the general microstructure of the PBF-LB/M AlSi10Mg and AlSi12Mg alloys in their as-built condition and after direct aging (DA), as presented in Figure 1. For the AlSi10Mg alloy, the as-built microstructure on the XZ plane (Figure 1A) clearly exhibited characteristic semi-circular or fish-scale-like melt pool boundaries [5], delineating successive laser passes, while the XY plane (Figure 1B) revealed the laser scan traces in the melt pool. After the direct aging treatment, the AlSi10Mg alloy on the XY plane (Figure 1C) largely preserved this melt pool morphology at this LOM scale, though subtle variations in etching response might suggest stress relief or early-stage precipitation. Similarly, the as-built AlSi12Mg alloy displayed distinct melt pool boundaries on the XZ plane (Figure 1D) comparable to AlSi10Mg. Following direct aging, the AlSi12Mg microstructure on the XY plane (1F) also showed that the primary solidification features remained largely unchanged. Overall, the LOM observations confirmed the typical heterogeneous microstructure produced by the PBF-LB process for both alloys and indicated that the direct aging treatment at 180°C for 6 hours did not induce major changes in these coarser microstructural features. The primary influence of this aging, namely the precipitation of fine strengthening phases within the α-Al matrix, is anticipated

to occur at a much finer scale, therefore a higher magnification technique – SEM – was used for detailed observation.

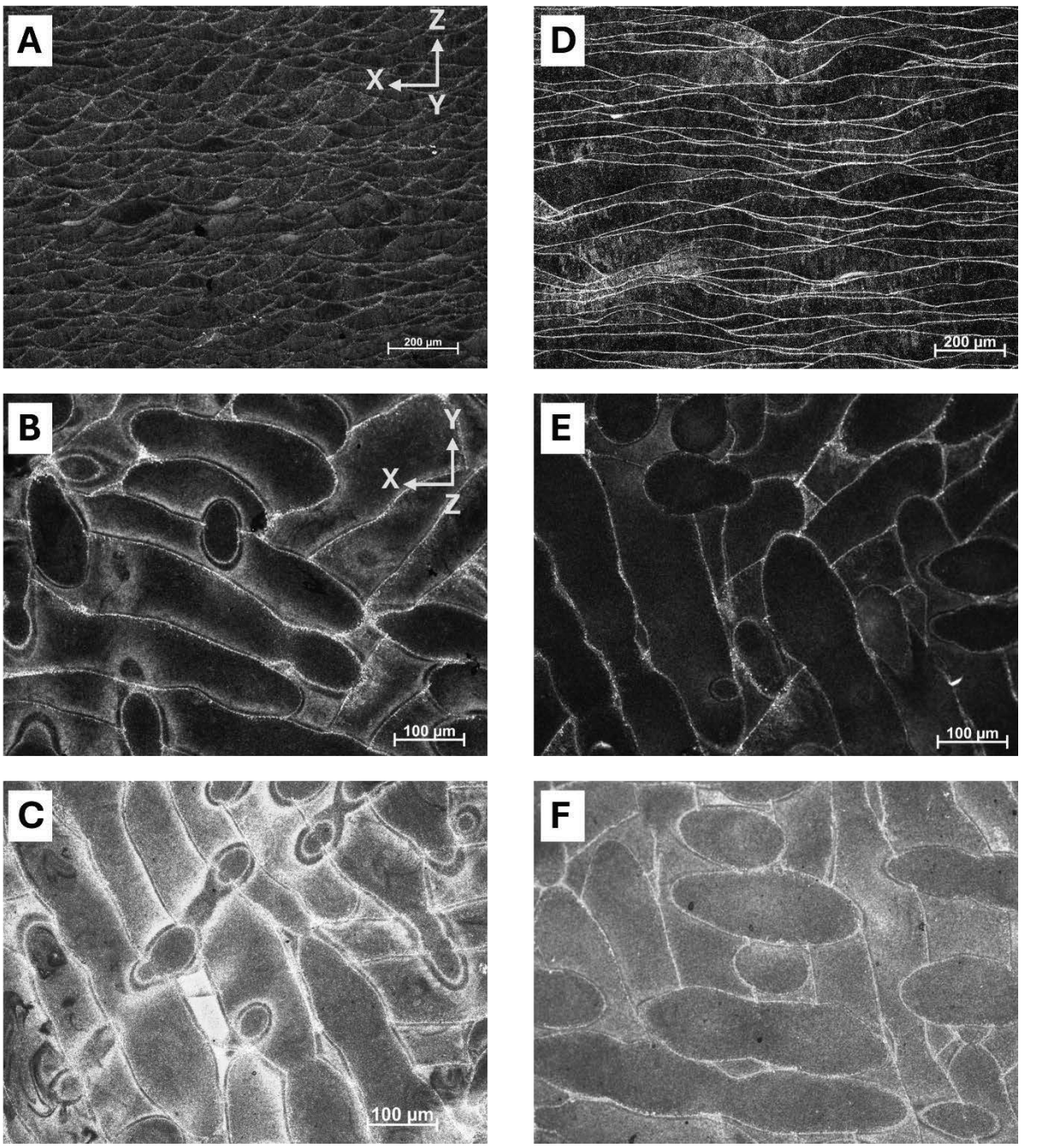

Figure 1. Microstructure of examined samples under the light optical microscope (LOM) A. as-built AlSi10Mg in the XZ plane, B. as-built AlSi10Mg in the XY plane, C. DA AlSi10Mg in the XY plane, D. as-built AlSi12Mg in the XZ plane, E. as-built AlSi12Mg in the XY plane, and F. DA AlSi12Mg in the XY plane

The results from SEM observations are presented in Figure 2.

For the PBF-LB/M AlSi10Mg alloy, the as-built condition shown in Figure 2A at lower magnification revealed typical PBF-LB/M features, including distinct regions within the melt pool (MP) such as coarser cellular structures (MP Coarse), finer cellular structures (MP Fine), and the heat-affected zone (HAZ). A higher magnification of the MP Fine region (Figure 2B) detailed the characteristic fine cellular α-Al matrix, with individual cells measuring approximately 0.88 ± 0.17 μm, delineated by a continuous or semi-continuous network of fine, interconnected eutectic Si particles.

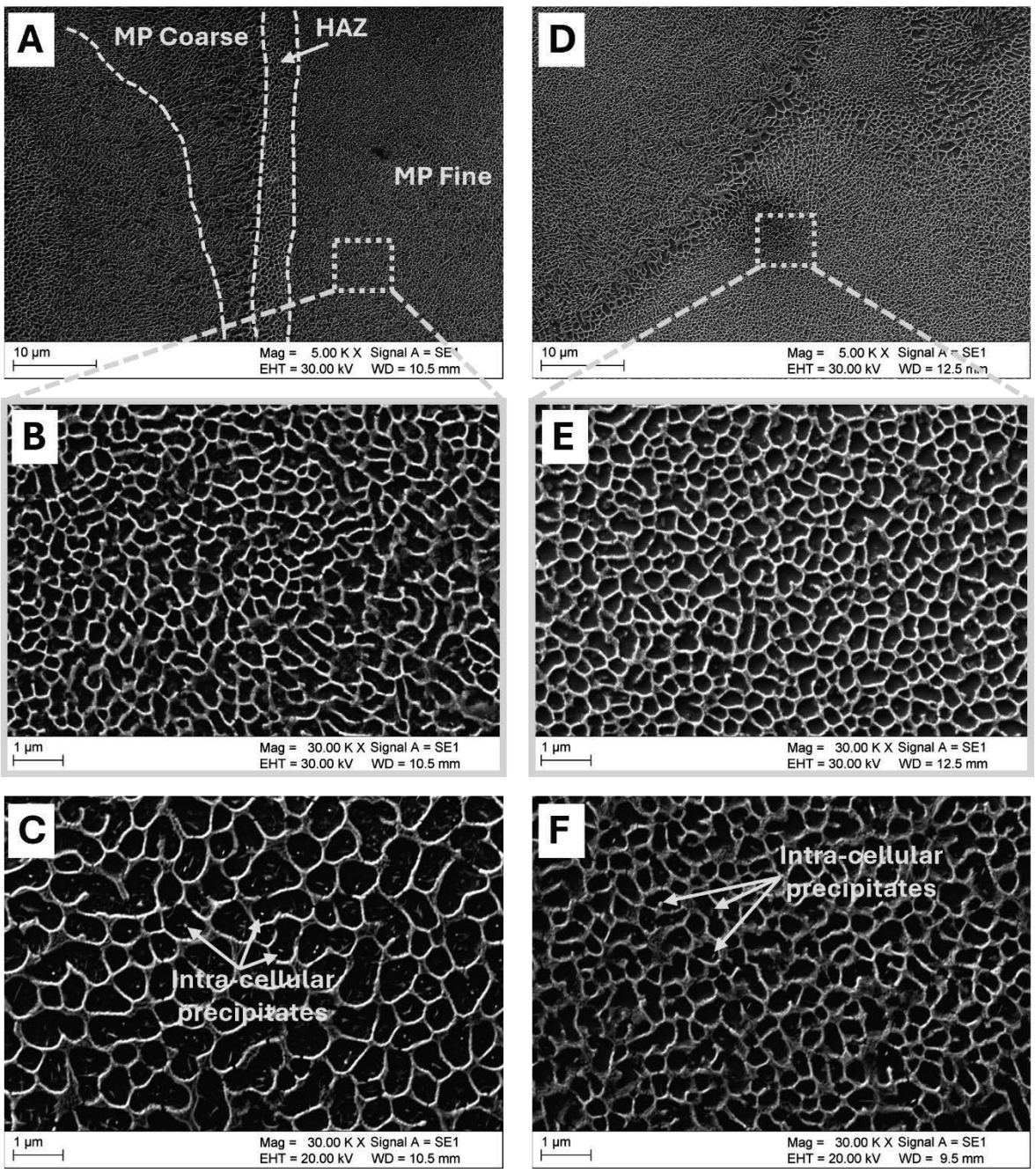

Figure 2. Microstructure of examined samples under the scanning electron microscope (SEM) A,B. AlSi10Mg in the as-built condition, C. AlSi10Mg after DA, D,E. AlSi12Mg in the as-built state, and F. AlSi12Mg after DA.

Following the direct aging treatment at 180°C for 6 hours, the AlSi10Mg microstructure (Figure 2C) showed that the overall cellular morphology and α-Al cell integrity were well-preserved, with the eutectic Si network largely retaining its as-built morphology. Significantly, as highlighted in Figure 2C, fine intra-cellular precipitates are observed within the α-Al cells, indicating the response to the thermal treatment. According to Park et. al. [6], these nanoscale precipitates are predominantly composed of Si.

Similarly, the PBF-LB/M AlSi12Mg alloy's, as-built microstructure (Figure 2D at lower magnification and Figure 2E at higher magnification) displayed a fine cellular solidification structure, with α-Al cells, measuring approximately 1.36 ± 0.38 μm, outlined by a well-defined eutectic Si network. After direct aging, the AlSi12Mg microstructure (Figure 2F) also demonstrated good thermal stability of these as-built features, with the fine cellular structure and eutectic Si network remaining largely unchanged from the as-built condition and, importantly, also exhibiting fine intra-cellular precipitates within the α-Al cells, as indicated. The direct observation of fine intra-cellular precipitates within the α-Al cellular interiors in the aged samples (Figures 2C and 2F) provides evidence of the diffusion-controlled precipitation of nanoscale constituents, which is reported as a key mechanism for an expected increase in mechanical properties [6].

3.2 Microhardness

The Vickers microhardness of the PBF-LB/M AlSi10Mg and AlSi12Mg alloys were evaluated in both the as-built condition and after the DA treatment with the results summarized in Table 1.

Table 1. Vickers microhardness results for the PBF-LB/M AlSi10Mg and AlSi12Mg alloys before and after direct aging heat treatment

Measured Point	Vickers Microhardness			
	AlSi10Mg	DA AlSi10Mg	AlSi12Mg	DA AlSi12Mg
1	116.79	118.49	107.31	105.28
2	116.79	115.59	110.05	109.7
3	114.47	119.91	111.46	109.76
4	113.33	116.2	105.99	103.41
5	116.79	115.58	108.67	118.14
6	117.98	122.16	105.99	115.48
7	111.11	118.66	105.99	103.16
8	113.33	118.03	108.67	109.4
9	110.02	116.19	104.68	108.42
10	120.41	115.88	104.68	114.39
Mean	115.102	117.669	107.349	109.714
Standard dev.	3.056926	2.078694	2.178878	4.798336

In the as-built state, the AlSi10Mg alloy exhibited a mean microhardness of 115.10 ± 3.06 $HV_{0.3}$, which increased to 117.67 ± 2.08 $HV_{0.3}$ following the direct aging treatment. For the AlSi12Mg alloy, the as-built samples presented a lower mean microhardness of 107.35 ± 2.18 $HV_{0.3}$, which subsequently rose to 109.71 ± 4.80 $HV_{0.3}$ after the same DA treatment. Thus, AlSi10Mg

demonstrated higher microhardness than AlSi12Mg in both the as-built and direct-aged conditions. The slight increase in hardness for both alloys; approximately 2.23% for AlSi10Mg and 2.20% for AlSi12Mg, is attributed to the precipitation of the observed nanoscale intra-cellular Si-rich constituents. While both alloys responded positively to the aging treatment with a comparable relative increase in hardness, the direct aging treatment led to a slight reduction in hardness scatter for AlSi10Mg, whereas AlSi12Mg showed an increase in standard deviation, potentially suggesting a slightly less uniform distribution or size of these Si precipitates under these specific aging conditions. The observed increases in hardness, therefore, correlate with the SEM observations of this fine, predominantly Si, intra-cellular precipitate formation, confirming the occurrence of precipitation hardening due to these nanoscale Si-rich phases.

4. CONCLUSION

This study investigated PBF-LB/M AlSi10Mg and AlSi12Mg alloys direct-aged at 180°C for 6 hours. The treatment successfully preserved the fine PBF-LB/M cellular microstructure while inducing the formation of nanoscale, intra-cellular precipitates predominantly composed of Si. This resulted in a slight Vickers microhardness increase for both AlSi10Mg (from approximately 115.1 $HV_{0.3}$ to 117.7 $HV_{0.3}$) and AlSi12Mg (from approximately 107.4 $HV_{0.3}$ to 109.7 $HV_{0.3}$), with AlSi10Mg consistently exhibiting higher hardness. The findings demonstrate that this low-temperature direct aging facilitates slight precipitation hardening via these Si-rich nanoprecipitates without significantly altering the fine as-fabricated PBF-LB/M microstructure.

FUNDING

The research was funded by the National Science Centre, Poland based on the decision number 2021/43/D/ST8/1 946. This project has received funding from the European Union's Horizon under the Marie Skłodowska-Curie Actions MSCA Staff Exchanges grant agreement No. 101129996.

BIBLIOGRAPHY

[1] Z. Liao, L. Zhang, X. Huang, and D. J. Jensen, "Microstructural and textural gradients in SLM-manufactured AlSi10Mg after low-draught cold-rolling and heat treatment," presented at the Journal of Physics: Conference Series, IOP Publishing, 2023, p. 012038.

[2] A. Salandari Rabori and V. Fallah, "Room temperature strain rate sensitivity of as-built 3D printed AlSi10Mg by laser powder bed fusion," *Mater. Lett.*, vol. 320, p. 132395, Aug. 2022, doi: 10.1016/j.matlet.2022.132395.

[3] N. T. Aboulkhair, I. Maskery, C. Tuck, I. Ashcroft, and N. M. Everitt, "The microstructure and mechanical properties of selectively laser melted AlSi10Mg: The effect of a conventional T6-like heat treatment," *Mater. Sci. Eng. A*, vol. 667, pp. 139–146, 2016.

[4] H. Tang *et al.*, "Effects of direct aging treatment on microstructure, mechanical properties and residual stress of selective laser melted AlSi10Mg alloy," *J. Mater. Sci. Technol.*, vol. 139, pp. 198–209, Mar. 2023, doi: 10.1016/j.jmst.2022.08.032.

[5] P. Snopiński, A. N. S. Appiah, O. Hilšer, and M. Kotoul, “Investigation of Microstructure and Mechanical Properties of SLM-Fabricated AlSi10Mg Alloy Post-Processed Using Equal Channel Angular Pressing (ECAP),” *Materials*, vol. 15, no. 22, p. 7940, 2022.

TalentDetector
23th-25th June 2025
Gliwice-Brenna, Poland
DEPARTMENT OF ENGINEERING MATERIALS AND BIOMATERIALS
FACULTY OF MECHANICAL ENGINEERING
SILESIAN UNIVERSITY OF TECHNOLOGY
INTERNATIONAL STUDENTS SCIENTIFIC CONFERENCE

The effect of nickel on the austenite formation in LPBF Duplex stainless steel

Beatrice Naa Ayeley Ardayfio[a], Zbigniew Brytan[a]

[a] Silesian University of Technology, Faculty of Mechanical Engineering, Department of Engineering Materials and Biomaterials, email: BeatriceNaaAyeleyArdayfio@polsl.pl

Abstract: Duplex stainless steel samples were fabricated using laser powder bed fusion (LPBF), the raw materials used were standard 2507 DSS powder and 3%Ni admixed 2507 DSS powder. The samples underwent post processing treatment (solution annealing) after printing. Unique microstructure and morphology were examined using scanning electron microscopy and energy dispersive x-ray spectroscopy. The results showed as-printed SDSS sample are primarily dominated by ferrite with little traces of austenite but after solution annealing the nucleation of austenite phases form within the sample. An increase in nickel content before printing elevated the nucleation of austenite within the overall sample and more pronounced after solution annealing, leading to a balance in the austenite and ferrite phase with the sample.

Keywords: 2507 duplex stainless steel, laser powder bed fusion (LPBF), solution annealing

1. INTRODUCTION

Duplex stainless steels (DSS) are characterized by a unique microstructure that consists of approximately equal proportions of ferrite (α) and austenite (γ), which enables these materials to exhibit impressive mechanical properties, such as high strength, excellent toughness, and outstanding resistance to corrosion. This combination of attributes makes DSS particularly suitable for various challenging environments such as high stress and harsh corrosive environments [1]. Super duplex stainless steels (SDSS) are a further development of DSS and are advanced corrosion-resistant alloys designed for use in even more demanding environments. They belong to the duplex family but exhibit enhanced performance in highly aggressive media, including seawater and acidic solutions. Their elevated PREN (Pitting Resistance Equivalent Number), typically above 40, ensures superior durability in chloride-rich and acidic conditions.
The composition of duplex stainless steels plays a fundamental role in determining the microstructural balance between ferrite and austenite phases. Chromium (Cr) serves as a ferrite stabilizer, promoting ferrite formation within the matrix, while nickel (Ni) acts as an austenite stabilizer, encouraging the formation of austenite. Therefore, adjusting the Cr/Ni ratio is essential for fine-tuning the phase distribution, which directly influences the mechanical properties and performance of the alloy in various applications [2], [3].

The process of solution annealing is a crucial heat treatment method that enhances the microstructural properties of duplex stainless steels. When the material is heated to a temperature

typically ranging from 1000°C to 1120°C and subsequently quenched, multiple beneficial transformations occur. Solution annealing aids in dissolving undesirable secondary phases, such as sigma or chi phases, thereby promoting a homogeneous microstructure and leading to uniform phase distribution between ferrite and austenite. This homogeneity is vital for achieving optimal mechanical properties and improving corrosion resistance [4], [5].

Furthermore, post-solution annealing can enhance the toughness and corrosion resistance of duplex stainless steels. The removal of precipitates and the reformation of a balanced microstructure facilitate increased toughness, yielding materials that are better able to resist localized corrosion in aggressive environmental conditions. Moreover, stabilizing the austenite content through solution annealing increases the ductility of the duplex stainless steel, thus improving the performance under stress [6].

A critical issue in the Laser Powder Bed Fusion (LPBF) of super duplex stainless steels (SDSS) is the microstructural imbalance caused by the process's inherently high cooling rates. During LPBF, solidification occurs rapidly which suppresses the δ-ferrite to austenite transformation, resulting in an as-built microstructure that is nearly fully ferritic. This imbalance undermines the defining duplex character of SDSS, which relies on a roughly equal phase distribution of ferrite and austenite to achieve its superior mechanical properties and corrosion resistance. The lack of sufficient austenite, particularly in critical areas such as grain boundaries, can degrade toughness and corrosion behavior. Moreover, the absence of a balanced duplex structure may also lead to localized weaknesses, especially under mechanical stress or in corrosive environments such as seawater or chemical plants. To restore the desired microstructure, a post-process solution annealing heat treatment is typically required, promoting austenite re-precipitation and achieving phase equilibrium. However, this adds complexity and cost to the LPBF workflow, and if not precisely controlled, may introduce additional phase instabilities or grain coarsening. These challenges underscore the importance of optimizing both LPBF parameters and alloy composition to mitigate phase imbalance and enhance the performance of SDSS components [7], [8], [9].

This study investigates the behaviour of standard SDSS and 3%Ni admixed SDSS powders after solution annealing. Also, the effect of nickel is understudied to determine if an increase of nickel content as an alloying element can affect the development of austenite in the creation of heterogeneity (ferrite and austenite phases) within the sample during LPBF manufacturing.

2. METHODOLOGY

2.1 Sample fabrication

The powder used in the study were in two batches. The first powders used were standard 2507 super duplex stainless steel SDSS with a d_{90} of 52.10 μm and the second batch of powders had an addition of 3%Ni wt. (SDSS+3%Ni). The powder studied had the composition as presented in Table 1.

Table 1. Chemical composition of studied SDSS composition

Sample ID	Alloying elements, wt.%.							
	Cr	Ni	Mo	Mn	Si	Cu	C	N
SDSS	25.2	6.3	3.8	0.4	0.30	0.15	0.016	0.35
SDSS+3%Ni	24.44	9.1	3.69	0.39	0.29	0.14	0.016	0.35

The powder mix was prepared by mixing in a Turbula mixer for 20 min. The fabrication of horizontal samples (10x10x55) was conducted using an AM125 Renishaw printer, with the following process parameters: laser power of 180 W, hatch distance of 120 µm, layer thickness of 30 µm, and scan speed of 300 mm/s. These settings correspond to a volumetric energy density of approximately 166 J/mm³. A meander scanning strategy was employed, characterised by a rotation of 67° between successive layers. The samples were then heat treated at temperature of 1050℃ for 15 minutes and subsequently quenched in water. These samples were labelled the solution annealed.

2.2 Characterization technique

Scanning electron microscopy (SEM) was used to view the different morphologies and phases present before and after solution annealing. The Zeiss SEM microscope was employed. To quantify the chemical composition of the samples before and after solution annealing, energy dispersive x-ray spectroscopy (EDS) was used. Samples were denoted as printed (AS) for samples of 2507 SDSS composition without any modifications and 3%Ni+SDSS for mixture alloyed with nickel. Samples denoted with solution annealing (SA) are samples after post processing (solution annealing).

3. RESULTS AND DISCUSSION

3.1 Scanning Electron Microscopy

Figure 1 presents scanning electron micrographs of 2507 SDSS and 3% Ni + SDSS before and after solution annealing. From Figure 1a, it can be observed that the standard 2507 SDSS has large grains and grain boundaries accompanied by a few pores. Also, cellular grain networks are also present which is a characteristic of 3D printing processing where alloying element segregation take place, and alloying element like silicon concentrates on the grain boundaries.

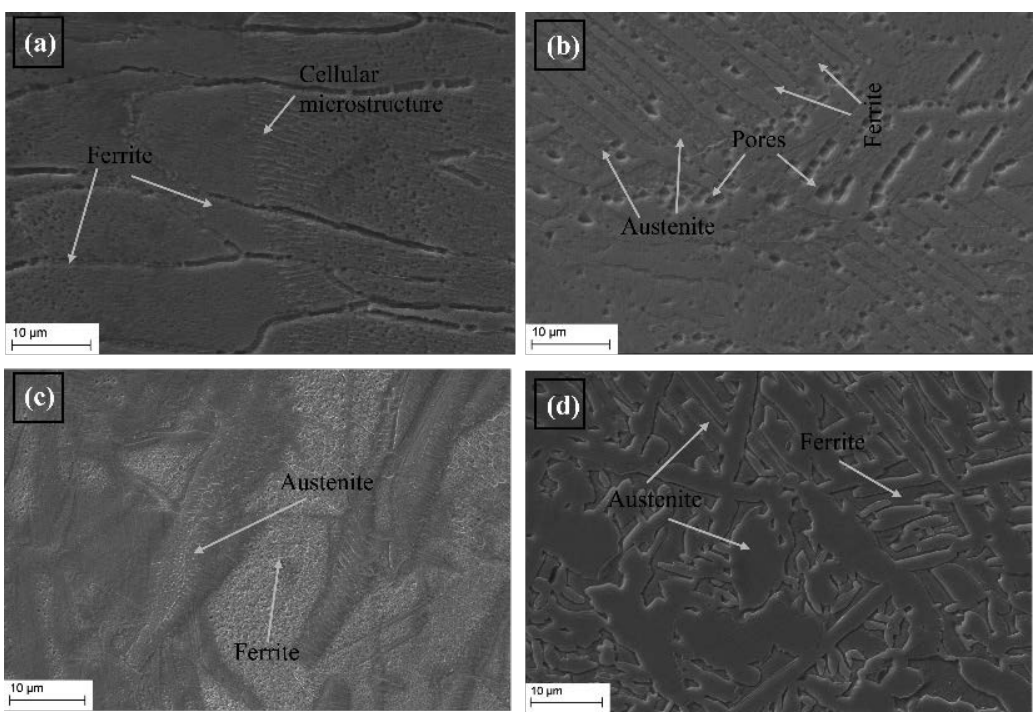

Figure 1. SEM image showing morphology of 3D printed SDSS a) as printed SDSS b) solution annealed SDSS, c) as printed 3%Ni+SDSS d) solution annealed 3%Ni+SDSS

Phases present within Figure 1a indicate mainly ferrite with little growth of austenite. But after solution annealing, Figure 1b shows two phases present accompanied by some porosity that results from the etching process. The phases present in Figure 1b are clearly distinctive, showing the ferrite matrix and austenite phases of form of plate-shaped austenitic grains. Figure 1c shows SDSS+3%Ni composition in as printed state. This microstructure presented predominantly distinctive phases; one phase forms a columnar dendrite growing in different directions (austenite) in a ferrite matrix. Figure 1d shows a SDSS+3%Ni after solution annealing. It is observed that a new nucleation of grains has formed from the matrix. This creates a clearer distinction between the phases present within the material after solution annealing with more austenite formation. The austenite is more pronounced; the grain boundary austenite is coarse and intra granular plate-shaped austenite grains are well distinguished.

From the scanning electron micrographs, it can be concluded that solution annealing improves the dual phase fraction of standard SDSS after printing. Moreover, the addition of nickel also contributed to the phase balance since it increased the visibility and growth of austenite present.

3.2 Energy dispersive x-ray spectroscopy (EDS)

With SEM, the phases present could not be accurately determined. So, using EDS through compositional analysis of chromium (ferrite former) and nickel (austenite formers) present, quantitative evidence is obtained to distinguish between the phases present in SDSS before and after solution annealing. Figure 2 (a)-(d) shows the EDS analysis results. From Figure 2a, it is observed that the amount of Cr within the sample is higher compared to the Ni amount present indicating a ferrite dominant sample with traces of austenite. Figure 2b, is the solution annealed SDSS, this sample contains an average amount of Cr and Ni as shown in Table 2 indicating the presence of austenite in the ferrite matrix. The addition of Ni to the SDSS sample in Figure 2c increased the amount of austenite present in the overall sample when compared to Cr amount relatively. After solution annealing as shown in Figure 2d the austenite phase increased as well as the nickel percentage. The chromium percentage reduced as the nickel weight percentage increased. Figure 3(b) and (d) representing the line scan analysis of major alloying elements of SDSS through the region of few grains. The fluctuation of nickel and chromium may be observed when scan is passing through austenitic and ferritic grains.

Detailed analysis inside austenitic and ferritic grains revel alloying element partitioning between phases. The austenite is enriched in nickel, while ferrite in chromium. The detailed analysis of chemical composition in each phase is presented in Table 2.

Table 3 shows the general compositional analysis and when compared to Table 2 the increase in nickel and chromium content is evident. Due to operational errors the consistency in compositions in Table 1 may vary to that of Table 2 and 3 in relation to the standard DSS measurements.

Table 2. Detailed chemical composition of both phases in the SDSS and SDSS+3Ni

Sample ID	Alloying elements, wt.%.						
	Phase	Si	Cr	Mn	Fe	Ni	Mo
SDSS-SA	austenite	0.4	26.8	0.2	62.6	6.2	3.9
	ferrite	0.5	27.2	0.2	62.9	5.4	3.9
3%Ni+SDSS-SA	austenite	0.4	24.8	0.2	60.8	11.7	3.0
	ferrite	0.4	28.3	0.3	61.2	4.6	3.7

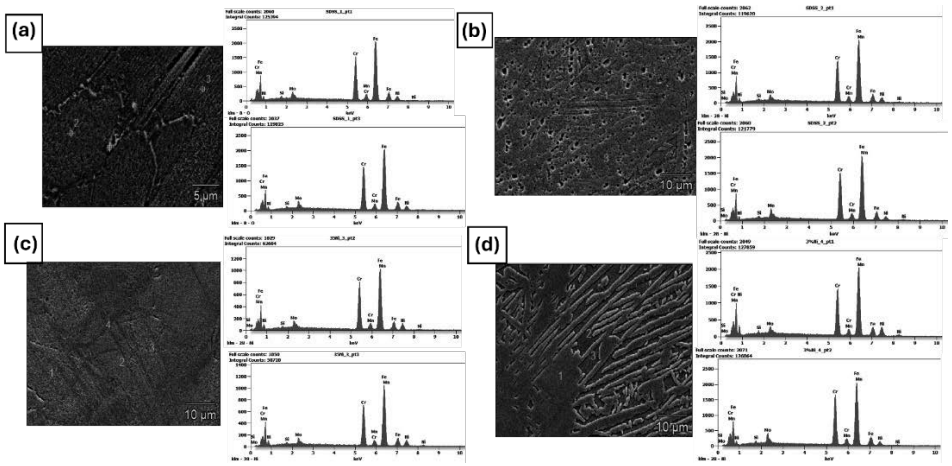

Figure 2. (a) SDSS-AP, (b) SDSS-SA, (c) 3%Ni+SDSS-AS and (d)3%Ni+SDSS-SA

Table 3. Summary of EDS analysis on samples (a)-(d) in wt%

Sample ID	Alloying elements, wt.%.					
	Si	Cr	Mn	Fe	Ni	Mo
SDSS-AS	0.43	27.03	0.13	62.9	5.8	3.73
SDSS-SA	0.47	27.27	0.37	62.7	5.57	4.0
3%Ni+SDSS-AS	0.43	27.2	0.23	60.8	7.1	4.2
3%Ni+SDSS-SA	0.4	26.15	0.15	61.25	8.33	3.73

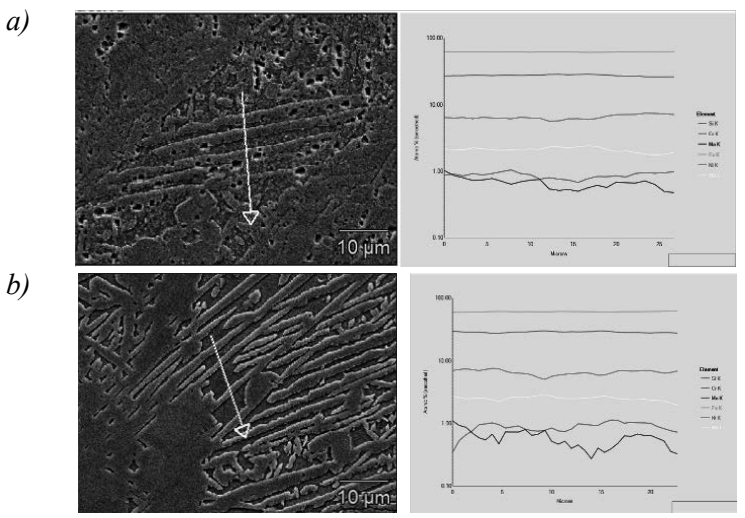

Figure 3. EDS line scan analysis of a) SDSS-SA, b) 3%Ni + SDSS-SA

4. CONCLUSION

The as-printed microstructure of LPBF super duplex stainless steel exhibits a non-equilibrium morphology, characterized by large, columnar grains and cellular substructures typical of rapid solidification. These features include a ferrite-dominant matrix with limited austenite presence and visible elemental segregation. After solution annealing, the microstructure transforms into a more balanced duplex structure with clearly defined ferrite and plate-like austenite grains. The heat treatment promotes recrystallization and grain refinement, enhancing phase definition and homogenization.

The EDS analysis revels clear elemental partitioning between the two phases. In SDSS after solution annealing, the austenite phase contains 6.2 wt.% Ni, while the ferrite phase contains 5.4 wt.% Ni, indicating a preferential enrichment of nickel in the austenitic regions. In the 3%Ni-modified SDSS, this partitioning becomes more pronounced: austenite contains 11.7 wt.% Ni, while ferrite has only 4.6 wt.% Ni. Chromium shows the opposite trend, with ferrite enriched up to 28.3 wt.% Cr, compared to 24.8 wt.% Cr in austenite. This partitioning reflects the thermodynamic role of nickel as an austenite stabilizer and chromium as a ferrite stabilizer. Molybdenum remains relatively stable between the phases but slightly favours ferrite. These results confirm that thermal treatment enhances the redistribution of alloying elements, reinforcing phase stability and distinction.

The addition of 3 wt.% nickel to SDSS significantly increases the formation and stability of the austenitic phase during both solidification and heat treatment. In the as-printed condition, nickel promotes earlier nucleation of austenite, which forms as columnar dendrites within the ferritic matrix. After solution annealing, the austenite fraction increases notably, with coarse grain boundary austenite and well-formed intragranular plate-like structures clearly visible.

ACKNOWLEDGEMENT

This research was funded by EU Horizon MSCA (Grant 101129996, SynAM) and Polish Ministry of Science and Higher Education (PMW 5783/HE/2024/).

REFERNCES

1. N. Mayoral, L. Medina, R. Rodríguez-Aparicio, A. Díaz, J. M. Alegre, and I. I. Cuesta, “Process Parameter Optimisation in Laser Powder Bed Fusion of Duplex Stainless Steel 2205,” *Appl. Sci.*, vol. 14, no. 15, 2024, doi: 10.3390/app14156655.
2. D. M. Kemény, B. Sándor, B. Varbai, and L. T. Katula, “The effects of arc voltage and shielding gas type on the microstructure of wire arc additively manufactured 2209 duplex stainless steel,” *Adv. Mater. Sci.*, vol. 23, no. 4, pp. 62–82, 2023.
3. H. Park and B. C. De Cooman, “Creep-Induced Microstructure Evolution of Type 2205 Duplex Stainless Steel during Continuous Annealing Processing,” *steel Res. Int.*, vol. 85, no. 5, pp. 756–770, 2014.
4. A. B. Başyiğit, A. Kurt, “The effects of nitrogen gas on microstructural and mechanical properties of TIG weldeds 32205 duplex stainless steel,” *Metals*, vol. 8, no. 4, p. 226, 2018.
5. L. Atia and M. Bamberger, “Development of coated electrodes for welding of Super Duplex steel,” *Heliyon*, vol. 6, no. 1, 2020.
6. C. Payares-Asprino, “Prediction of mechanical properties as a function of welding variables in robotic gas metal arc welding of duplex stainless steels SAF 2205 welds through artificial neural networks,” *Adv. Mater. Sci.*, vol. 21, no. 3, pp. 75–90, 2021.
7. M. Mirz, S. Herzog, C. Broeckmann, and A. Kaletsch, “Influence of the L-PBF Process Atmosphere on the Microstructure and Tensile Properties of AISI 318LN Duplex Stainless Steel,” *J. Manuf. Mater. Process.*, vol. 6, no. 2, 2022.
8. C. Cui *et al.*, “Laser Additive Manufacturing of Duplex Stainless Steel via Powder Mixture,” *Journal of Manufacturing and Materials Processing*, vol. 6, no. 4. 2022.
9. M. L. Köhler, J. Kunz, S. Herzog, A. Kaletsch, and C. Broeckmann, “Microstructure analysis of novel LPBF-processed duplex stainless steels correlated to their mechanical and corrosion properties,” *Mater. Sci. Eng. A*, vol. 801, no. September 2020, 2021.

TalentDetector
23th-25th June 2025
Gliwice-Brenna, Poland
DEPARTMENT OF ENGINEERING MATERIALS AND BIOMATERIALS
FACULTY OF MECHANICAL ENGINEERING
SILESIAN UNIVERSITY OF TECHNOLOGY
INTERNATIONAL STUDENTS SCIENTIFIC CONFERENCE

Wytwarzanie kompozytów ceramika-metal opartych na materiałach odpadowych infiltrowanych stopami metali lekkich

Jennifer Badora[a], Michał Głogowski[b], Julia Muszyńska[a], Julia Pindur[a], Karolina Romberg[a], Martin Mikolajčík[c], Zuzana Šurdová[c], Lenka Kuchariková[c], Mateusz Lis[d], Klaudiusz Gołombek[e]

[a] studentka Politechniki Śląskiej, Wydział Mechaniczny Technologiczny, ul. Konarskiego 18A, 44-100 Gliwice
[b] student Politechniki Śląskiej, Wydział Automatyki, Elektroniki i Informatyki, ul. Akademicka 16, 44-100 Gliwice
[c] University of Zilina, Faculty of Mechanical Engineering, Department of Materials Engineering, Slovak Republic
[d] Politechnika Śląska, Wydział Mechaniczny Technologiczny, Laboratorium Naukowo-Dydaktyczne Nanotechnologii i Technologii Materiałowej
[e] Politechnika Śląska, Wydział Mechaniczny Technologiczny, Laboratorium Badania Materiałów, email: klaudiusz.golombek@polsl.pl

Streszczenie: W pracy wytworzono i zbadano kompozyty o osnowie ceramicznej – oparte na porowatych szkieletach ze szkła odpadowego, modyfikowanego popiołem lotnym oraz infiltrowanych ciekłym stopem aluminium.

Abstract: The aim of the study was to manufacture and study ceramic matrix composites based on porous skeletons made of waste glass modified with fly ash and infiltrated with liquid aluminium alloy.

Słowa kluczowe: kompozyty, szkło spienione, popiół lotny, infiltracja

1. WSTĘP

Materiały kompozytowe stanowią szeroko rozpowszechnioną grupę materiałów inżynierskich. Kompozyty o osnowie ceramicznej stosuje się np. do produkcji elementów konstrukcyjnych w budownictwie, przemyśle lotniczym i kosmicznym, przemyśle automotive, medycynie, na narzędzia, izolacje cieplne. Szczególną grupą są kompozyty funkcjonalne ceramiczno-metalowe charakteryzujące się specjalnymi własnościami, które ukierunkowują te materiały na dedykowane zastosowania. Powszechne stosowanie kompozytów na bazie osnowy ceramicznej wynika z ich wyjątkowych własności wytrzymałościowych w wysokiej temperaturze, stabilności termicznej, chemicznej oraz doskonałej odporności na ścieranie i utlenianie. Ze względu na wyżej wymienione własności materiały ceramiczne wymagają

zastosowania specjalnych metod wytwarzania. Brak ciągliwości wyklucza kształtowanie przez odkształcenie plastyczne, wysoka twardość i kruchość ogranicza możliwości obróbki materiałów przez cięcie czy szlifowanie [1-10]. Szczególną rolę w wytwarzaniu kompozytów ceramiczno-metalowych odgrywają metody metalurgii proszków oraz infiltracji bezciśnieniowej lub ciśnieniowej. Infiltracja porowatych szkieletów jest nowoczesną odmianą technologii odlewania, łączącą techniki odlewnicze – proces infiltracji oraz metalurgię proszków – wytwarzanie porowatych szkieletów spiekanych. Proces otrzymywania funkcjonalnych kompozytów ceramiczno-metalowych z zastosowaniem metod infiltracji charakteryzuje się wysoką wydajnością, możliwością adaptacji procesu do masowej produkcji, możliwością uzyskania elementów o dokładnym odwzorowaniu kształtów i powierzchni, pozwala na zastosowanie szerokiej gamy osnowy ceramicznej jako szkieletu i materiałów osnowy, do których zaliczyć można aluminium i jego stopy [11-15]. Ważnym aspektem związanym z wytwarzaniem tego typu kompozytów jest możliwość zastosowania modelu gospodarki w obiegu zamkniętym (GOZ), dzięki wykorzystaniu materiałów pochodzących z recyklingu: odpadów szklanych oraz popiołów lotnych, do wytworzenia ceramicznego szkieletu, co ma niewątpliwie korzystny wpływ na środowisko oraz ograniczy składowanie odpadów.

Celem badań było opracowanie i wytworzenie funkcjonalnych kompozytów ceramiczno-metalowych opartych na szkielecie ze szkła spienionego modyfikowanego popiołem lotnym oraz stopach aluminium wykorzystując metodę infiltracji.

2. MATERIAŁ I METODYKA BADAŃ

Materiał do badań

Do wytworzenia kompozytów ceramiczno-metalowych wykorzystano materiały wsadowe pochodzące z odpadów: stłuczkę szklaną oraz popioły lotne ze spalania biomasy, a także stop aluminium. Materiały do badań przedstawiono na rysunku 1.

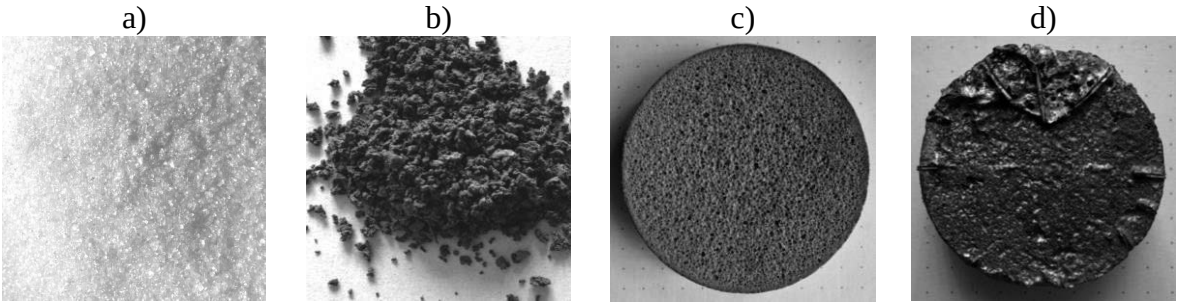

Rys. 1. Materiały: a) stłuczka szklana, b) popiół lotny; c) pianka; d) pianka po infiltracji
Figure 1. Materials: a) glass cullet, b) fly ash; c) foam glass; d) infiltrated glass foam

W pierwszym etapie prac przygotowano proszek stłuczki szklanej pochodzącej z szyb typu float i popiół lotny otrzymany ze spalania biomasy o frakcji <45μm oraz glicerynę jako środek spieniający i lepiszcze. Następnie odważono składniki za pomocą wagi laboratoryjnej firmy Radwag i przygotowano wypraski mieszaniny proszku zmielonego szkła i popiołu lotnego z gliceryną w proporcjach przedstawionych w tablicy 1. Wypraski poddano obróbce cieplnej w temperaturze 800°C przez 30 minut, uzyskując piankę o założonej porowatości. Po obróbce

cieplnej pianki obrabiano mechanicznie. Tak przygotowane pianki poddano infiltracji w temperaturze 750°C, przy ciśnieniu azotu 30 bar, w czasie 10 minut.

Tablica 1. Oznaczenie próbek
Table 1. Sample designations

Oznaczenie	Zawartość szkła [%]	Zawartość popiołu [%]	Zawartość gliceryny [%]
K94-5-1	94	5	1
K91-8-1	91	8	
K89-10-1	89	10	

Zrealizowano następujące etapy badawcze: wytworzono i przygotowano do infiltracji szkielety ceramiczne oparte na spienionym szkle; dobrano stop metali lekkich – stop aluminium do infiltracji ze względu na zastosowanie; dobrano optymalne warunki infiltracji ciekłym metalem porowatych szkieletów ceramicznych; wytworzono funkcjonalne kompozyty ceramiczno-metalowe; zbadano strukturę wytworzonych kompozytów. Obserwację struktury próbek wykonano wykorzystując mikroskop cyfrowy stereoskopowy Leica DVM6 Digital oraz wysokorozdzielczy skaningowy mikroskop elektronowy ZEISS SUPRA 35 wyposażonym w detektor składu chemicznego EDS.

3. WYNIKI BADAŃ

Badania powierzchni i mikrostruktury wykonano na zgładach metalograficznych na mikroskopie świetlnym i stereoskopowym oraz w wysokorozdzielczym skaningowym mikroskopie elektronowym. Mikrostruktury badanych kompozytów przedstawiono na rysunkach 2-3, a analizy składu chemicznego EDS na rys. 4-6.

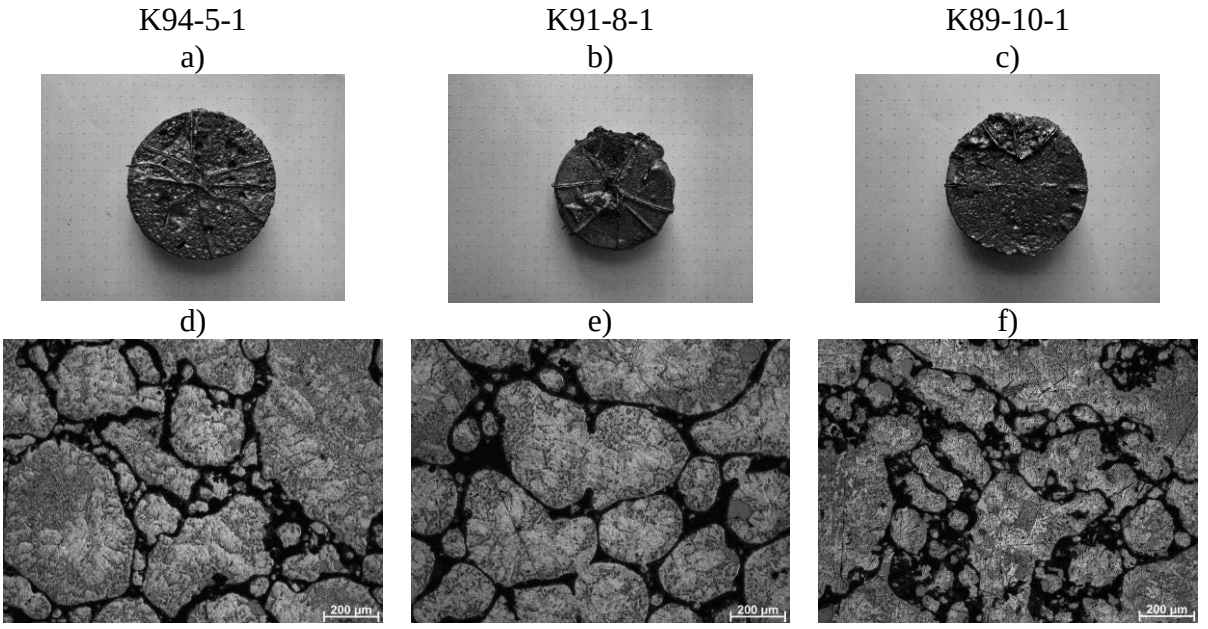

Rys. 2. Struktura badanych próbek; mikroskop: a-c) stereoskopowy; d-f) świetlny
Figure 2. Structure of tested specimens; microscope: a-c) *stereoscopic; d-f) LM*

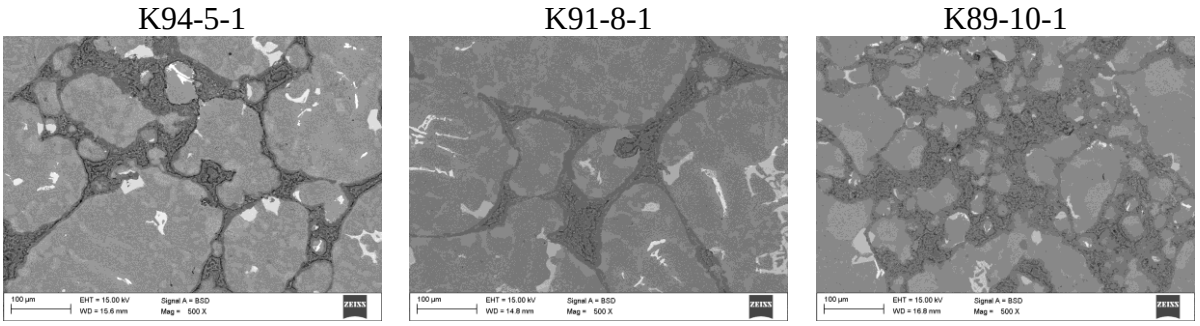

Rys. 3. Mikrostruktura badanych próbek, HRSEM
Figure 3. Microstructure of tested specimens, HRSEM

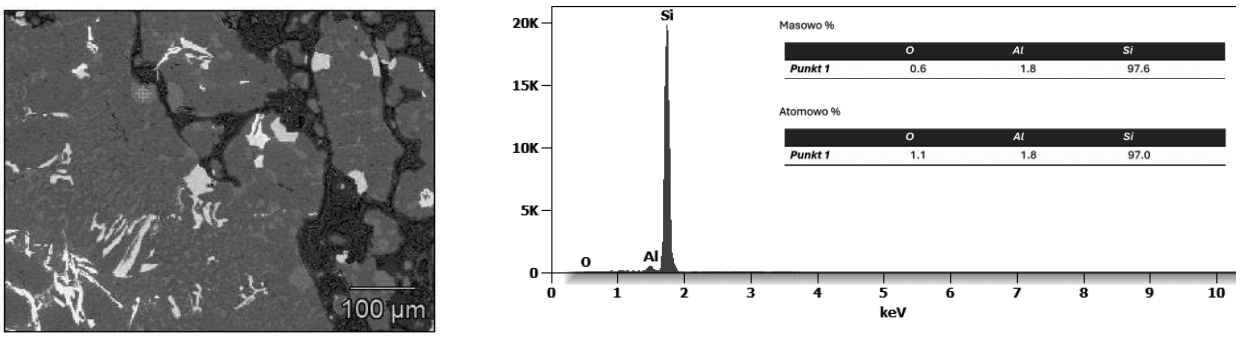

Rys. 4. Wyniki analizy EDS z zaznaczonego obszaru dla próbki K94-5-1
Figure 4. Results of the EDS analysis from the marked area of specimen K94-5-1

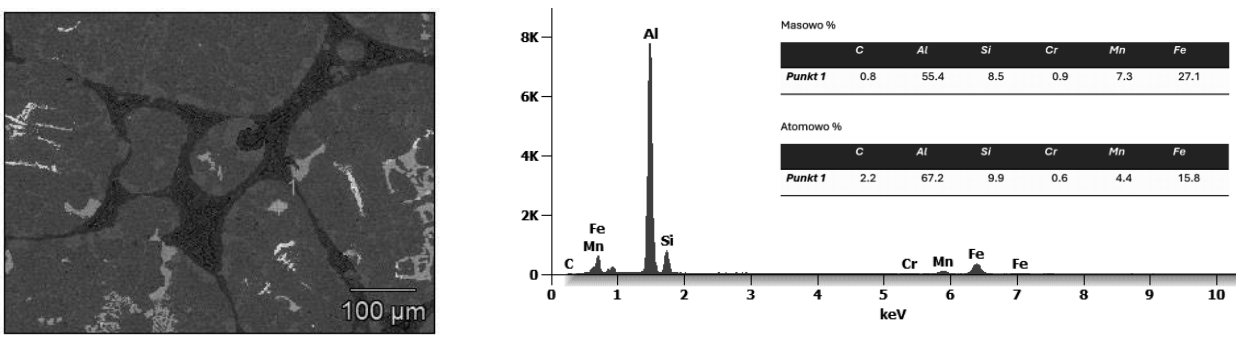

Rys. 5. Wyniki analizy EDS z zaznaczonego obszaru dla próbki K91-8-1
Figure 5. Results of the EDS analysis from the marked area of specimen K91-8-1

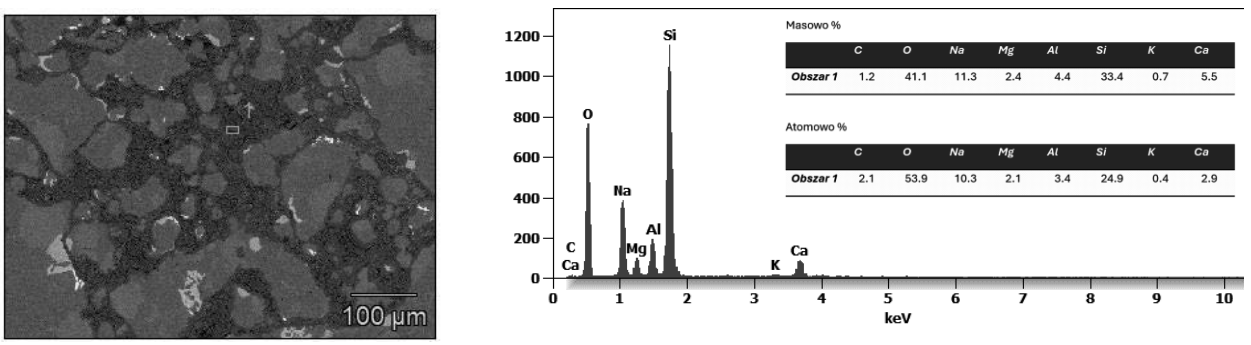

Rys. 6. Wyniki analizy EDS z zaznaczonego obszaru dla próbki K89-10-1
Figure 6. Results of the EDS analysis from the marked area of specimen K89-10-1

4. PODSUMOWANIE I WNIOSKI

Na podstawie wykonanych badań stwierdzono, że możliwe jest wytworzenie kompozytów ceramiczno-metalowych opartych na piankach ceramicznych uzyskanych z mieszaniny stłuczki szklanej i popiołu lotnego, infiltrowanych stopem aluminium. W ramach badań określono optymalne parametry wytwarzania kompozytu ceramika-metal: temperaturę infiltracji 750°C, ciśnienie azotu wynoszące 30 bar, czas 10 minut. Zbyt wysoka temperatura może doprowadzić do degradacji pianek pod ciężarem stopu aluminium, natomiast zbyt niska temperatura prowadzi do niekompletnej infiltracji.

Badania metalograficzne przeprowadzone z wykorzystaniem mikroskopii świetlnej i skaningowej mikroskopii elektronowej wykazały, że struktura uzyskanych kompozytów jest jednorodna, a infiltracja szklanego szkieletu skutecznie wypełniła puste przestrzenie – pory, tworząc kompozytową strukturę ceramicznego szkieletu wypełnionego stopem aluminium. Zaobserwowano bardzo niewielki udział porów nie wypełnionych stopem aluminium, co świadczy o prawidłowym doborze parametrów wytwarzania pianek szklanych oraz procesu infiltracji. Na podstawie analizy składu chemicznego w mikroobszarach metodą rozproszonego promieniowanie rentgenowskiego EDS stwierdzono, że struktura wytworzonych kompozytów składa się z ceramicznego szkieletu zawierającego takie pierwiastki jak: C, O, Na, Mg, Al, Si, K, Ca pochodzące ze szkła i popiołu oraz stopu aluminium szczelnie wypełniającego przestrzenie porów, zawierającego takie pierwiastki jak: Al, Si, Mn, Cr, Fe.

LITERATURA

1. M. Ciecińska, D. Dorosz, Technologia szkła. Właściwości fizykochemiczne, Polskie Towarzystwo Ceramiczne, Kraków, 2002.
2. M. Kaczorowski, A. Krzyńska, Konstrukcyjne materiały metalowe, ceramiczne i kompozytowe, wyd. 2 popr., Oficyna Wydawnicza Politechniki Warszawskiej, Warszawa, 2017.
3. S.J. Kowalski, Inżynieria materiałów porowatych, Wydawnictwo Politechniki Poznańskiej, Poznań, 2004.
4. Y. Attila, M. Güden, A. Taşdemirci, Foam glass processing using a polishing glass powder residue, Ceramics International, nr (5), t. 39, (2013) 5869–5877.
5. A. Zawada, I. Przerada, M. Lubas, J. Iwaszko, Izolacyjne materiały spieniane na bazie surowców wtórnych, Materiały Ceramiczne, nr (2), t. 69, (2017) 132–137.
6. J.P. Wu, A.R. Boccaccini, P.D. Lee, M.J. Kershaw, R.D. Rawlings, Glass ceramic foams from coal ash and waste glass: Production and characterisation, Advances in Applied Ceramics, nr (1), t. 105, (2006) 32–39.
7. H.R. Fernandes, D.U. Tulyaganov, J.M.F. Ferreira, Production and characterisation of glass ceramic foams from recycled raw materials, Advances in Applied Ceramics, nr (1), t. 108, (2009) 9–13.
8. R.K. Dhir, J. de Brito, G.S. Ghataora, C.Q. Lye, Production and Properties of Glass Cullet, 2018.
9. J. Bai, X. Yang, S. Xu, W. Jing, J. Yang, Preparation of foam glass from waste glass and fly ash, Materials Letters, t. 136, (2014) 52–54.
10. P. Chakartnarodom, P. Ineure, Foam glass development using glass cullet and fly ash or rice husk ash as the raw materials, Key Engineering Materials, t. 608, (2014) 73–78.

11. C.A. Leon-Patiño, R.A.L. Drew, Role of metal interlayers in the infiltration of metal–ceramic composites. Curr. Opin. Solid State Mater. Sci. 9, (2005) 211–218.
12. J.-J. Sha, Z.-Z. Lu, R.-Y. Sha, Y.-F. Zu, J.-X. Dai, Y.-Q. Xian, W. Zhang, D. Cui, C.-L. Yan, Improved wettability and mechanical properties of metal coated carbon fiber-reinforced aluminum matrix composites by squeeze melt infiltration technique. Trans. Nonferrous Met. Soc. China, 31, (2021) 317–330.
13. M. Pawlyta, B. Tomiczek, L.A. Dobrzański, M. Kujawa, B. Bierska-Piech, Transmission electron microscopy observations on phase transformations during aluminium/mullite composites formation by gas pressure infiltration. Mater. Charact., 114, (2016) 9–17.
14. G. Matula, J. Krzysteczko-Witek, B. Tomiczek, Application of ceramic injection moulding and pressure infiltration to the manufacturing of alumina/AlSi10Mg composites. Arch. Metall. Mater., 63, (2018) 2101–2106.
15. K. Konopka, M. Szafran, Fabrication of Al_2O_3–Al composites by infiltration method and their characteristic, J. Mater. Processing Technol., 175, (2006) 266–270.

PODZIĘKOWANIA

Badania wykonano w ramach XII edycji projektów badawczych zorientowanych projektowo – PBL (Project Base Learning) we współpracy z uczelnią zagraniczną – Uniwersytetem w Żylinie, Słowacja, realizowanych na Politechnice Śląskiej w programie Inicjatywa Doskonałości – Uczelnia Badawcza.

TalentDetector
23th-25th June 2025
Gliwice-Brenna, Poland
DEPARTMENT OF ENGINEERING MATERIALS AND BIOMATERIALS
FACULTY OF MECHANICAL ENGINEERING
SILESIAN UNIVERSITY OF TECHNOLOGY
INTERNATIONAL STUDENTS SCIENTIFIC CONFERENCE

The methodology for calculating order value and pricing printed products in the "Print-Expert" automated management system

Tea Baramashvili[a], Nini Baidoshvili[b]

[a] PhD Degree in Mechanical Engineering and Technology, Professor, at Georgian Technical University, Faculty of Transport Systems and Mechanical Engineering, Georgia
email: baramashvili.t@gtu.ge
[b] Vocational student, at Georgian Technical University, Faculty of Transport Systems and Mechanical Engineering, Georgia
email: niiinbaidoshvili@gmail.com

Abstract: The cost of printed products is a significant indicator of a company's operations. The choice of cost calculation methodology can be a key factor in making optimal management decisions. This article discusses an automated management software system capable of calculating the cost of printed products and determining order prices. It calculates the unit cost and displays the total order cost**.** Gathering this information allows for the analysis of the actual costs of digital printing in the shortest possible time.

Keywords: Production Facility, Printed Products, Cost, Automation, Expenses, Printing, Method.

1. INTRODUCTION

Cost calculation is the determination of expenses in monetary form for the production of a unit or a group of units of products, or for specific types of production. This allows for the determination of the actual or planned cost of an object or item and serves as the basis for its valuation.

Printing, on the one hand, can be attributed to the production of consumer goods, while on the other hand, to the service sector. As a rule, it combines elements from both, in varying proportions within each completed printing order: this depends on the customer, type, circulation, and production time. A printing house produces tangible items, but most often it is a unique printed product required in a certain quantity by a specific date. Therefore, standard pricing approaches cannot exist, unlike, for example, in a typical shop or factory. Here, complex differentiated prices must be used, depending on various conditions, starting from the product type and circulation, and ending with the timeframe. The pricing principles used in practice can be divided into two main types: the first based on market principles, and the second on the cost of product production. In the first case, prices are determined by analyzing the local market and the offers of existing competitors.

Functional expenses can be: technological (for technological processes of product production), for technical maintenance (to create conditions for production, equipment, repairs, transport, etc.), and for management (for the functioning of management personnel, accounting, etc.). Depending on the volume of production, all expenses can be divided into two groups: variable and fixed. Variables are expenses that directly depend on the volume of production: paper and materials, employee wages for work, electricity, transportation services, etc. Fixed expenses include: insurance premiums, maintenance costs for buildings, structures, and equipment, etc. Accordingly, according to the method of attribution to production cost, all are divided into direct and indirect expenses. Direct expenses are calculated based on norms, are associated with the production of a specific product, and are directly included in its cost. Indirect expenses are associated with the activities of the enterprise as a whole and cannot be attributed to the cost of a specific product. They are distributed according to certain types of products or orders, based on production volume in standard hours, production labor intensity, direct or basic wages of main producers, and other principles.

The article provides an approximate list of calculation items (production cost calculation): Material expenses; Costs of purchased products and semi-finished goods; Basic wages for production employees; Additional wage expenses for workers (bonuses, internship benefits, etc.); Social security and safety contributions; General production expenses (equipment depreciation, service and transportation expenses, general workshop expenses); General business expenses (administrative expenses, deductions for general business property, maintenance costs for general business fixed assets, and other general business and non-production expenses); Sales expenses (packaging, transportation, advertising, marketing research, selling expenses, etc.); Enterprise development expenses.

The full cost method considers all expenses and sets the product's selling price according to the "cost plus fixed profit" system. The return on investment method means that the company sets the selling price to ensure the required profit on investment. In the direct costing method, variable and fixed expenses are recorded separately, and the calculation does not determine the total cost, but only variable expenses. The selling price is formed by adding an amount to this calculated value that includes fixed expenses and normal profit. The direct cost method allows you to consider product demand and does not require complex allocation of overhead costs. To get the price using the simplest direct cost method, you need to calculate all variable expenses and add a determined percentage of profit. Can you imagine the reaction of a typography manager who is forced, for example, to calculate the cost of 1000 magazines?

It must be said that, in reality, the aforementioned pricing methods have much in common. Price lists are usually not set individually for each circulation of a certain type of product but are calculated by adding the cost of each technological operation used in the production of that product. The cost of this operation has already been tested at the market level. Given that technological operations depend in one way or another on the type of equipment, circulation size, complexity of readiness, etc., the first type of prices (by price, functional characteristics, resource consumption, cost, etc.) are considered. Moreover, the more factors a price list takes into account, the closer the classic calculation of prices will be to norms. But you cannot overdo it: a too detailed price list will turn out to be a complex, cumbersome structure that is inconvenient to use. In practice, printing houses often use fairly simple formulas to calculate the prices of individual operations, including only linear dependencies: the finished price multiplied by the circulation of the used sheet. At the same time, the finished price includes all fixed expenses, and the price of the used sheet includes variable expenses. The circulation is divided into many ranges, and in each of them, they enter this formula with their own

coefficients. The most advanced printing houses choose these coefficients so that there are no gaps (or price jumps) within the chosen circulation boundaries. Managers need at least Excel, or better yet, a calculator program on a computer or website.

Let's discuss the process of distributing pricing in price lists for each technological operation and determining the coefficients for calculation formulas in automated programs, using „Print-Expert“ software as an example.

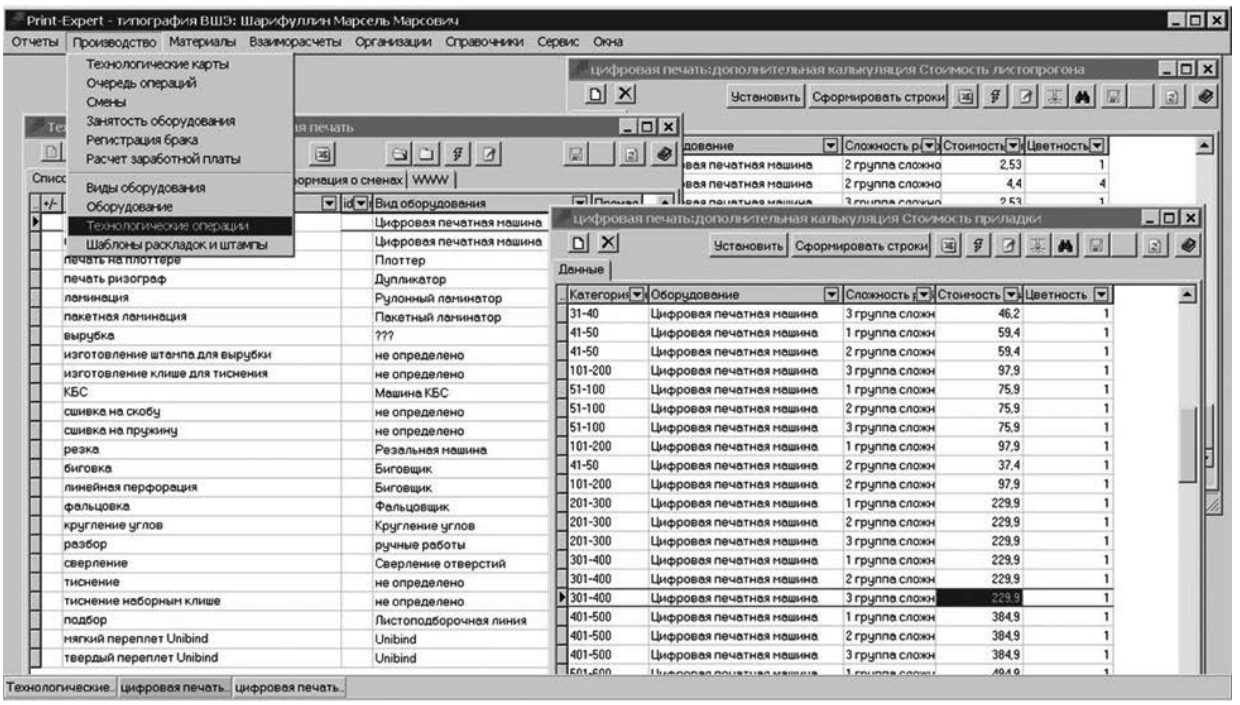

Figure 1. Inputting Calculation Coefficients for Technological Operation Cost Calculation Formulas in the „Print-Expert“ Automated Management System

To stabilize their business, printers aim to transition to calculations based on norms (regardless of their complexity), but completely rejecting price lists would be incorrect due to the existence of a concept like "market price." If calculating production costs according to norms turns out to be lower than the market price, the enterprise will simply lose additional profit and appear unserious in the eyes of colleagues. If it's higher, then demand will be lower. Therefore, the best solution is to combine these two types of pricing within a single accounting program. For example, by performing a preliminary calculation of the order value according to the market price list and immediately calculating the estimated production cost. The program should automatically compare the obtained figures and show the higher value to the manager as the recommended price. This way, the printing house will be protected from accepting an unprofitable order even at the initial stage.

The Use of Automation

Working with complex price lists requires an automated program. Calculation "according to norms" is generally impossible without an integrated automated production control system (APCS). In this case, it's necessary to define and select not only the optimal types of

technological operations but also the consumables and time for each of them. Labor costs, deductions, direct general production costs, and many others must be taken into account.

As a specific example, let's consider the „Aurora-Print" printing house, which specializes in producing paper bags and calendars. The developer of the „Print-Expert" software for the automated system had to write thousands of lines of code to calculate prices for all types of paper bags within a single program window. Previously, managers performed calculations using a „semi-manual" method from dozens of Excel spreadsheets, considering all possible types of package types, printing technology, and finishing. They spent a lot of time on this and regularly made mistakes, leading to lost profits for the enterprise. Thanks to the use of the „Print-Expert" program, calculations now take minutes, and price ranges have disappeared. It should be noted that due to the multitude of manual operations at „Aurora-Print" printing house, most products are still calculated using automated pricing, although some atypical product types and processing are already calculated according to standards, as the control system allows for this. The acceleration of calculations alone enabled this printing house to almost double its production load during the pre-New Year season.

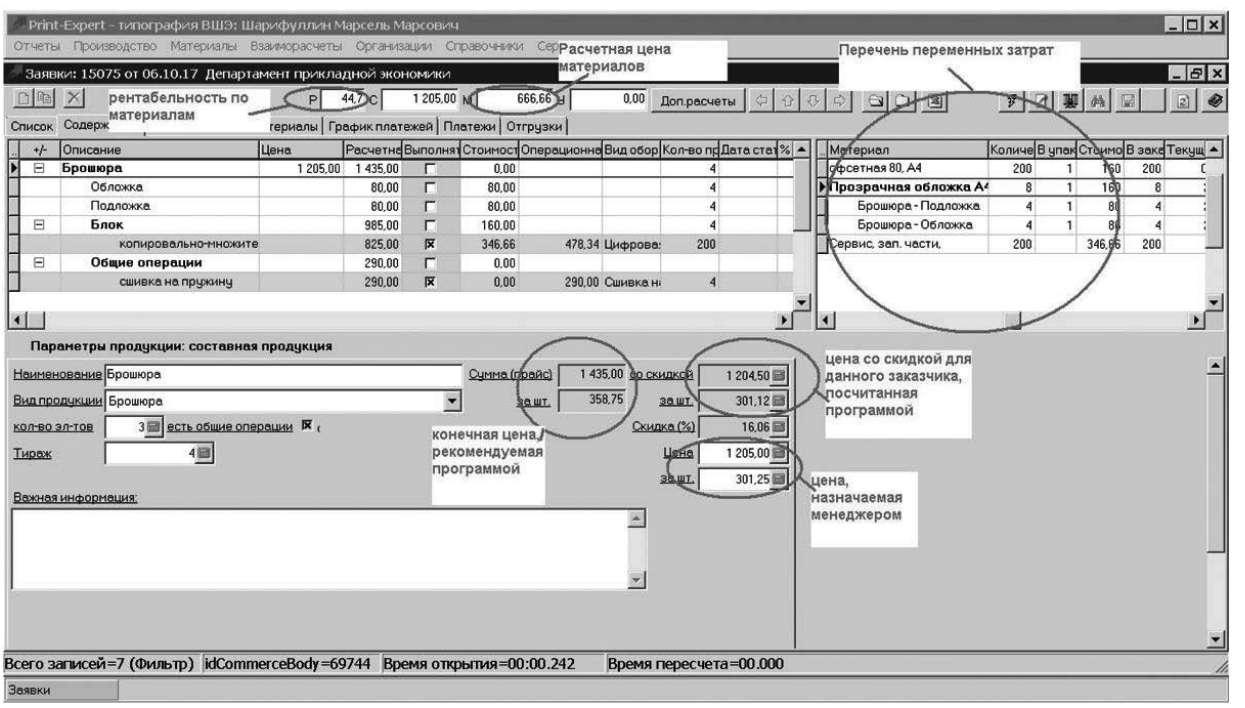

Figure 2. Calculating Order Prices in the „Print-Expert" Automated Management System

In some cases, the system simply includes only the basic variable costs (expenses for consumed materials, semi-finished products, outsourcing operations, and partial employee wages), and all other costs are added as a fixed percentage. Even such a rough estimate saves the printing house from unprofitable orders. After filling in the order parameters, the manager sees a list of completed technological operations, a list of materials needed for the order, the estimated cost of the order based on materials, and recommended prices. Based on this data, the manager sets the order price and sees its profitability level. The program won't allow the manager to set a price below a certain threshold.

Real-Time Cost Analysis

Additionally, when fulfilling each specific order, the automated system must accurately calculate the real costs, right down to the value of the actual quantity of materials consumed (at their purchase price). It then ultimately shows the real profitability of the job. By analyzing the data received, the printing house management can adjust its price list coefficients or standard data, bringing the calculated figures closer to reality.

Streamlined Calculation with „Print-Expert“

This program makes it easy to calculate prices for a vast assortment of printed products, regardless of complexity or volume in the price list. Typically, when implementing an automated management system in a printing house, the operator simply provides the pricing algorithms to the developer. The developer then configures them in the program so managers can instantly get a product's cost in the „Print-Expert“ program window by simply filling in all order parameters in the specially designated fields.

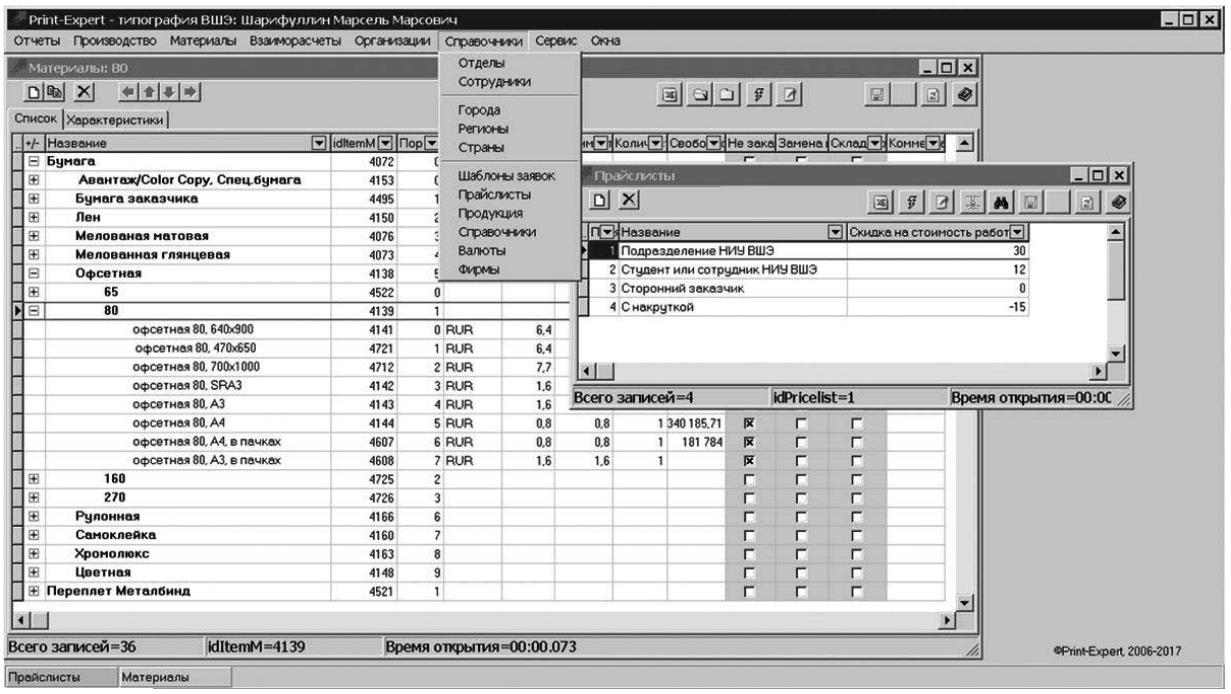

Figure 3. In the „Print-Expert" automated management system, the accounting cost of materials and discounts are adjusted for certain groups of clients.

Calculation according to „Print-Expert“ norms can be done in various ways: based on production norms and time norms, considering costs with and without readiness, in accounting departments, taking into account a percentage of circulation, considering material consumption that is difficult to attribute to specific orders, considering service costs, amortization, general production and business expenses, and so on. This can be estimated (preliminary) and actual. The result of the preliminary calculation appears immediately in the same window as the price calculation and allows managers to apply discounts based on prices for specific or group customers. For example, when performing a preliminary calculation of the cost of a digital order in the automated PrintExpert program, the concept of accounting cost is used. This prevents complicating the manager's work by selecting a specific MTC. A printing house may have a large fleet of different digital machines, and the manager may not know which one will

actually print the order. When the order is fulfilled, the printing equipment notes the specific digital printing machine and the actual paper consumption in the automated system. After this, the ACS calculates the actual cost and shows the full cost of the order. Collecting this information allows for further analysis of the actual costs of digital printing and adjustment of the contract accounting cost.

The price within the automated management system is also easily adjusted (moreover, without developer involvement) when the level of market competition changes. Markup and discount rates are easily adjusted not only by product type but also by season, client importance, and any other aspect the printing house wishes to implement.

2. CONCLUSION

We live in an era of rapid information and technological change. The volume of information in the world grows sixfold annually, while corporate data volume increases by a staggering 50 times. What comes next is unknown. The Fourth Industrial Revolution has already begun, printing technologies have rapidly shifted from brochures to digital printing, and within digital, from electrographic systems to inkjet UV solutions. Each new technology brings its own economics to the production process. To understand the situation, it's necessary to control the processes ongoing within the enterprise.

In modern automated management systems, everything is connected to a single system. Calculations made by the manager are immediately checked for consistency when execution is marked in production. As soon as the contractor enters information, the program displays a comparison of calculated and actual data.

BIBLIOGRAPHY

1. Research and Modeling of the Label Sticking Mechanism - T. Baramashvili, J. Uplisashvili, "Transport and Mechanical Engineering" – ISSN 1512-3537, No. 2(39) 2017, Tbilisi, p. 5-12.
2. J. Uplisashvili, N. Javakhishvili, T. Baramashvili - Inversion and its use, "Technical University" publishing house, Tbilisi, 2013.
3. Uplisashvili J., Natbiladze N., "Geometrical Foundations of Printing Machine's Movable Spatial Systems," Tbilisi, 2009.
4. "Offset Printing Machines," Printing Systems of HEIDELBERG, Moscow, MSUP Publishing, 1999.
5. https://www.britannica.com/topic/textile/Dyeing-and-printing
6. https://cen.acs.org/business/consumer-products/new-textile-dyeing-methods-make/96/i29
7. https://textilevaluechain.in/in-depth-analysis/articles/textile-articles/types-of-dyeing-and-printing-with-their-inovations/

TalentDetector

23th-25th June 2025
Gliwice-Brenna, Poland

DEPARTMENT OF ENGINEERING MATERIALS AND BIOMATERIALS
FACULTY OF MECHANICAL ENGINEERING
SILESIAN UNIVERSITY OF TECHNOLOGY

INTERNATIONAL STUDENTS SCIENTIFIC CONFERENCE

Comparison of Au Deposition Methods on Ti: Effect of Surface Preparation on the Quality of Ti–Au Layers

Oktawian Bialas[a*]

[a] Politechnika Śląska, Laboratorium Badania Materiałów, ul. Konarskiego 18A, 44-100 Gliwice
*email: oktawian.bialas@polsl.pl

Abstract: The study compared two approaches to gold deposition on titanium substrates: (I) PVD with ion beam surface cleaning using the Plasmonique system and (II) conventional sputtering under reduced pressure without surface activation. The aim was to evaluate the effect of both approaches on coating adhesion, homogeneity, and performance after laser treatment. The results showed that ion cleaning prior to PVD significantly improves coating adhesion and reduces delamination. In contrast, coatings deposited without surface activation exhibited visible structural defects, including blistering and poor continuity. Laser processing further emphasized these differences, with ion-cleaned layers showing better thermal stability and resistance to degradation. These findings highlight the critical importance of surface preparation in achieving high-performance Ti–Au coatings for functional and biomedical applications.

Keywords : PVD, sputtering, TiAu, Ion cleaning, adhesion, top layer

1. INTRODUCTION

The Ti–Au system remains the subject of numerous studies due to its attractive properties, such as biocompatibility, corrosion resistance, and high thermal stability [1–4]. However, the effectiveness of the final layer depends not only on the materials used but also on the choice of deposition technology and the quality of substrate surface preparation. Applications of TiAu layers include biomedical technologies, protective functional coatings, and microengineering applications [5–7]. In this study, the influence of surface preparation prior to gold deposition via physical vapor deposition (PVD) was compared: PVD following ion cleaning (Plasmonique) versus conventional sputtering without surface activation [8,9]. The evaluation focused on differences in layer adhesion, behavior after laser processing, and observable signs of delamination.

2. Methodology

The substrates used were 7 mm thick discs of CP Ti, mechanically prepared according to the following protocol: grinding (grit size 220–1200 grit/mm²), diamond polishing (9–1 μm), and final OPU polishing on an MD-Chem disc.

2.1 PVD Deposition After Ion Cleaning

The process was carried out under high vacuum conditions. Immediately prior to deposition, the surface was subjected to ion cleaning (argon glow discharge) to remove oxides and surface contaminants. Subsequently, a gold layer was deposited to a programmed thickness using a Plasmonique device.

2.2 Sputter Coating Without Surface Activation

For comparison, Au layers were also deposited using conventional sputtering under standard vacuum conditions (~10^{-3} mbar) without prior ion cleaning, using a Leica EM SCD050 system.

2.3 Laser Processing

Both sets of samples underwent laser modification using a picosecond laser A-355 (Oxford Lasers). The parameters were selected to achieve a comparable visual melting effect while maintaining controlled absorption conditions.

2.4 Microscopic Analysis

Surface analysis was performed using a Zeiss Supra 25 scanning electron microscope, focusing on uniformity, melting behavior, and the presence of surface defects.

3. RESULTS

The layers obtained via PVD with ion cleaning (Variant I) showed high uniformity and good adhesion to the substrate. No signs of delamination or cracking were observed (Fig. 1b).

In contrast, the layers obtained by conventional sputtering without surface activation (Variant II) exhibited localized blistering, delamination, and discontinuities (Fig. 1a). Morphological analysis indicated weakened adhesion resulting from the presence of oxide layers and the lack of proper surface activation.

Laser processing also revealed differences in layer behavior. Coatings deposited after ion cleaning withstood localized heating better and showed no degradation in the molten area (Fig. 1d), unlike the conventionally sputtered layers, which detached from the substrate in some areas (Fig. 1c).

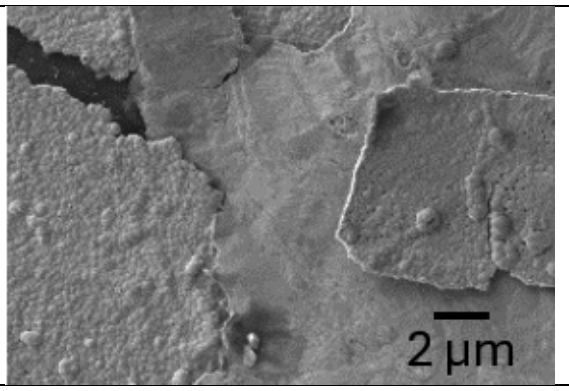

(a)

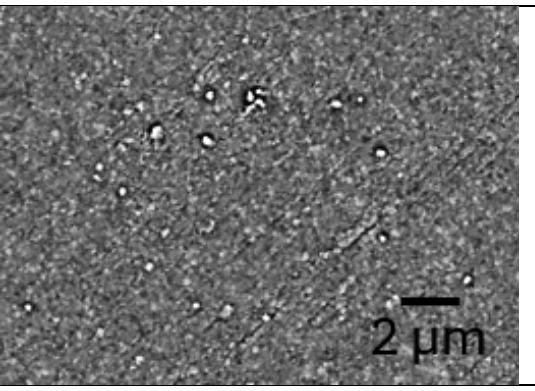

(b)

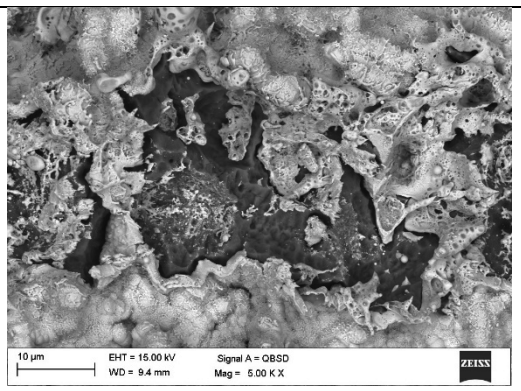

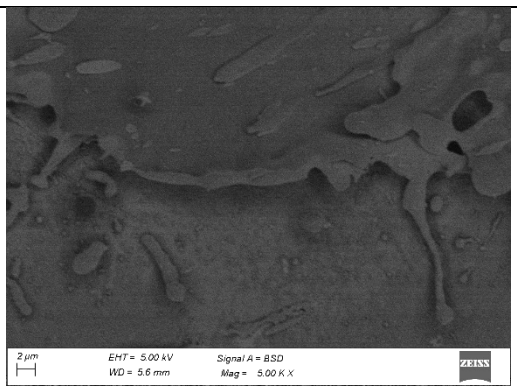

(c) (d)

Fig. 1. SEM images of samples: (a) coating applied at low pressure without surface activation, (b) coating deposited after ion activation under high vacuum, (c) laser processing of a material without adhesion to the substrate, (d) laser processing showing alloying effect.

4. SUMMARY

Ion cleaning prior to PVD deposition using the Plasmonique device enabled the formation of layers with high adhesion, continuity, and resistance to delamination. Conversely, conventional sputtering without appropriate surface preparation led to significant structural defects and poor coating quality. Based on the conducted research, the following conclusions can be drawn:

- Ion cleaning prior to PVD significantly improves coating quality and durability.
- Layers deposited without surface activation tend to delaminate.
- PVD coatings (Plasmonique) exhibit better resistance to localized laser modification.
- Proper surface preparation before deposition is crucial for the durability and functionality of Ti–Au layers.

LITERATURE

[1] Bialas, O., Poloczek, T., Lis, M., Skowronek, A., Górka, J., and Adamiak, M., 2021, "Laser Assisted Size Reduction of Gold (Au) Particles onto a Titanium (Ti) Substrate Surface," Applied Sciences, 11(18), p. 8755. https://doi.org/10.3390/app11188755.

[2] Akmal, M., Jeong, W., and Ryu, H. J., 2023, "Ti-Zr-Nb Based BCC Alloy Containing Mo Prepared by Laser Directed Energy Deposition—ω Phase and Cellular Structure," Journal of Alloys and Compounds, 969, p. 172306. https://doi.org/10.1016/j.jallcom.2023.172306.

[3] Bialas, O., Kunwar, A., Taratuta, A., Skonieczna, M., Matus, K., and Adamiak, M., 2025, "Surface Engineering of Ti13Zr13Nb Biomaterial Alloy with Gold Via Laser Melting for Enhanced Biocompatibility and Functional Performance," Metall Mater Trans A, 56(6), pp. 2235–2251. https://doi.org/10.1007/s11661-025-07763-y.

[4] Bialas, O., Appiah, A. N. S., Wala, M., Kunwar, A., Woźniak, A., Nuckowski, P. M., Simka, W., Råback, P., and Adamiak, M., 2023, "Laser Assisted Fabrication of Mechanochemically

Robust Ti3Au Intermetallic at Au-Ti Interface," Engineering Science and Technology, an International Journal, 42, p. 101413. https://doi.org/10.1016/j.jestch.2023.101413.

[5] Balazic, M., Kopac, J., Jackson, M. J., and Ahmed, W., 2007, "Review: Titanium and Titanium Alloy Applications in Medicine," IJNBM, 1(1), p. 3. https://doi.org/10.1504/IJNBM.2007.016517.

[6] Asserghine, A., Filotás, D., Nagy, L., Souto, R. M., and Nagy, G., 2022, "Do Titanium Biomaterials Get Immediately and Entirely Repassivated? A Perspective," npj Mater Degrad, 6(1), p. 57. https://doi.org/10.1038/s41529-022-00270-0.

[7] Buffinton, C. M., Tong, K. J., Blaho, R. A., Buffinton, E. M., and Ebenstein, D. M., 2015, "Comparison of Mechanical Testing Methods for Biomaterials: Pipette Aspiration, Nanoindentation, and Macroscale Testing," Journal of the Mechanical Behavior of Biomedical Materials, 51, pp. 367–379. https://doi.org/10.1016/j.jmbbm.2015.07.022.

[8] Zhou, X. W., Johnson, R. A., and Wadley, H. N. G., 2004, "Misfit-Energy-Increasing Dislocations in Vapor-Deposited CoFe/NiFe Multilayers," Phys. Rev. B, 69(14), p. 144113. https://doi.org/10.1103/PhysRevB.69.144113.

[9] Alcázar, J. C. B., Lemos, R. M. J., Conde, M. C. M., Chisini, L. A., Salas, M. M. S., Noremberg, B. S., Motta, F. V. da, Demarco, F. F., Tarquinio, S. B. C., and Carreño, N. L. V., 2019, "Preparation, Characterization, and Biocompatibility of Different Metal Oxide/PEG-Based Hybrid Coating Synthesized by Sol–Gel Dip Coating Method for Surface Modification of Titanium," Progress in Organic Coatings, 130, pp. 206–213. https://doi.org/10.1016/j.porgcoat.2019.02.007.

ACKNOWLEDGMENTS

This work is the result of research project no. 2022/45/N/ST8/01004 funded by the National Science Center, Poland

TalentDetector
23th-25th June 2025
Gliwice-Brenna, Poland
DEPARTMENT OF ENGINEERING MATERIALS AND BIOMATERIALS
FACULTY OF MECHANICAL ENGINEERING
SILESIAN UNIVERSITY OF TECHNOLOGY
INTERNATIONAL STUDENTS SCIENTIFIC CONFERENCE

Structure and corrosion resistance of $CoCrFeNiNb_xMo_y$ near-eutectic high entropy alloys

Jakub Bicz[a], Krzysztof Matus[b], Rafał Babilas[c]

[a] Student of Silesian University of Technology, Faculty of Mechanical Engineering
e-mail: jakubic839@student.polsl.pl
[b] Silesian University of Technology, Faculty of Mechanical Engineering, Materials Research Laboratory
[c] Silesian University of Technology, Faculty of Mechanical Engineering, Department of Engineering Materials and Biomaterials

Abstract: In this work, $CoCrFeNiNb_xMo_y$ high entropy alloys with variable niobium and molybdenum content (x = 0.35 or 0.4; y = 0.25 or 0.3) were prepared by using the induction melting in a form of ingots. The structure was investigated by the scanning electron microscopy method. Electrochemical measurements were performed in 5% NaCl solution at a temperature of 25 °C to assess the corrosion resistance. Mechanical properties were examined by the Vickers microhardness test. The $CoCrFeNiNb_{0.4}Mo_{0.3}$ alloy showed the best corrosion resistance in the 5% NaCl solution, showing the lowest values of the corrosion current density (114 nA/cm^2) and the highest polarization resistance (261 kΩcm^2). The highest hardness with a value of 457 HV_1 was obtained for the $CoCrFeNiNb_{0.4}Mo_{0.25}$ ingot.

Keywords: High entropy alloys, Eutectic composition, Corrosion resistance, Hardness

1. INTRODUCTION

The high entropy alloys represent a novel class of metallic materials which has been intensively developed in recent years. In order to achieve a high value of configurational entropy, their design involves use of five or more elements, with each in the content of 5 - 35 at.%. The increased configurational entropy favours the formation of solid solution phases, reducing their mixing free energy [1,2]. As a result of their exceptional properties, such as superior high-temperature strength [3], excellent corrosion resistance [4] and irradiation resistance [5], high entropy alloys characterize with wide range of possible applications in numerous fields, such as aerospace, chemical, and power generation sectors. Initially, the objective of the design of high entropy alloys was being to search for alloys characterized by single phase solid solution structures [2]. However, alloys exhibiting single phase face-centred cubic (FCC) structure generally characterized by rather low strength, whereas those with body-centred cubic (BCC) structure show limited ductility [3]. As a promising method to solve this issue, concept of

eutectic high entropy eutectic alloys was proposed [6]. The dual-phase eutectic structure, combining solid FCC solution with the BCC solid solution or intermetallic phases, enables one to obtain an excellent strength-ductility balance, simultaneously allowing alleviation of common castability problems [6,7].
In previous work, high-entropy eutectic alloys were developed basing on the unitary alloying of the CoCrFeNi alloy by niobium and molybdenum [8,9]. In particular, $CoCrFeNiNb_{0.5}$ characterize with advantageous properties, including the compressive strength of 2200 MPa simultaneously at 17% plasticity [10]. Moreover, both niobium and molybdenum can positively affect the corrosion resistance of CoCrFeNi-based high entropy alloys, improving the stability of passivation layer by promoting the generation of Cr_2O_3 [11,12]. Furthermore, the method of eutectic high entropy eutectic alloys through synergistic alloying was recently proposed [13], based on the possibility of formation of infinite solid solutions between molybdenum, niobium, tantalum, and wolframium. Consequently, this work aims to investigate the structure and corrosion behaviour of near-eutectic $CoCrFeNiNb_xMo_y$ alloys (x = 0.35 or 0.4; y = 0.25 or 0.3) designed on the work [13].

2. MATERIALS AND METHODS

Alloys were prepared by the induction melting method, using elements with the 99.99 wt.% purity. The process was carried out using an NG-40 induction generator in an argon atmosphere. Ingots were solidified with a low cooling rate and ceramic crucibles from Al_2O_3 were used. The microstructure of ingots and plates was analysed using the Zeiss Supra 35 high-resolution scanning electron microscope (SEM). The hardness of the alloys was measured using a Future Tech FM-7000 Vickers hardness tester with a dwell time of load of 1000 g for a 15 s. To evaluate their corrosion resistance, the samples were subjected to potentiodynamic polarization measurements, conducted in the 5% NaCl solution. An Autolab 302N potentiostat equipped with a three-electrode measuring system was used for the study. A saturated calomel electrode (SCE) was used as the reference electrode, platinum wire was used as the counter electrode, and the material being tested was the working electrode. During electrochemical measurements, changes in open-circuit potential (E_{OCP}) were recorded in a stabilisation time of 3600 s, followed by polarization measurements in the range of – 400 mV to 400 mV, with a scan rate of 0.001 V/s. On the basis of the results obtained, the corrosion potential (E_{corr}), corrosion current density (jcorr), and polarization resistance (R_p) were determined with the use of the Tafel extrapolation method.

3. RESULTS AND DISCUSSION

The microstructures of the alloys investigated are shown in Figure 1. The results suggest the dual-phase structure of the alloys. According to the publication of Tsau et al. [14] the darker phase can be identified as a face-centred cubic solid solution of CoCrFeNi that is characterized with low solid solubility of niobium and molybdenum, while the brighter phase is an intermetallic Laves phase, exhibiting a hexagonal closed-packed structure. In the case of the $CoCrFeNiNb_{0.35}Mo_{0.25}$ alloy, the microstructure is composed of FCC solid solution dendrites between the lamellar eutectic. Similarly, precipitates of the Laves phase can also be observed. The $CoCrFeNiNb_{0.35}Mo_{0.3}$ and $CoCrFeNiNb_{0.4}Mo_{0.25}$ alloys characterise with more homogenous structure – resulting from an increased volume content of the eutectic structures, although the presence of the bulk Laves phase can still be observed. In turn, for the

CoCrFeNiNb$_{0.4}$Mo$_{0.3}$ alloy, numerous dendrites constituted of the Laves phase can be observed, suggesting its hypereutectic composition.

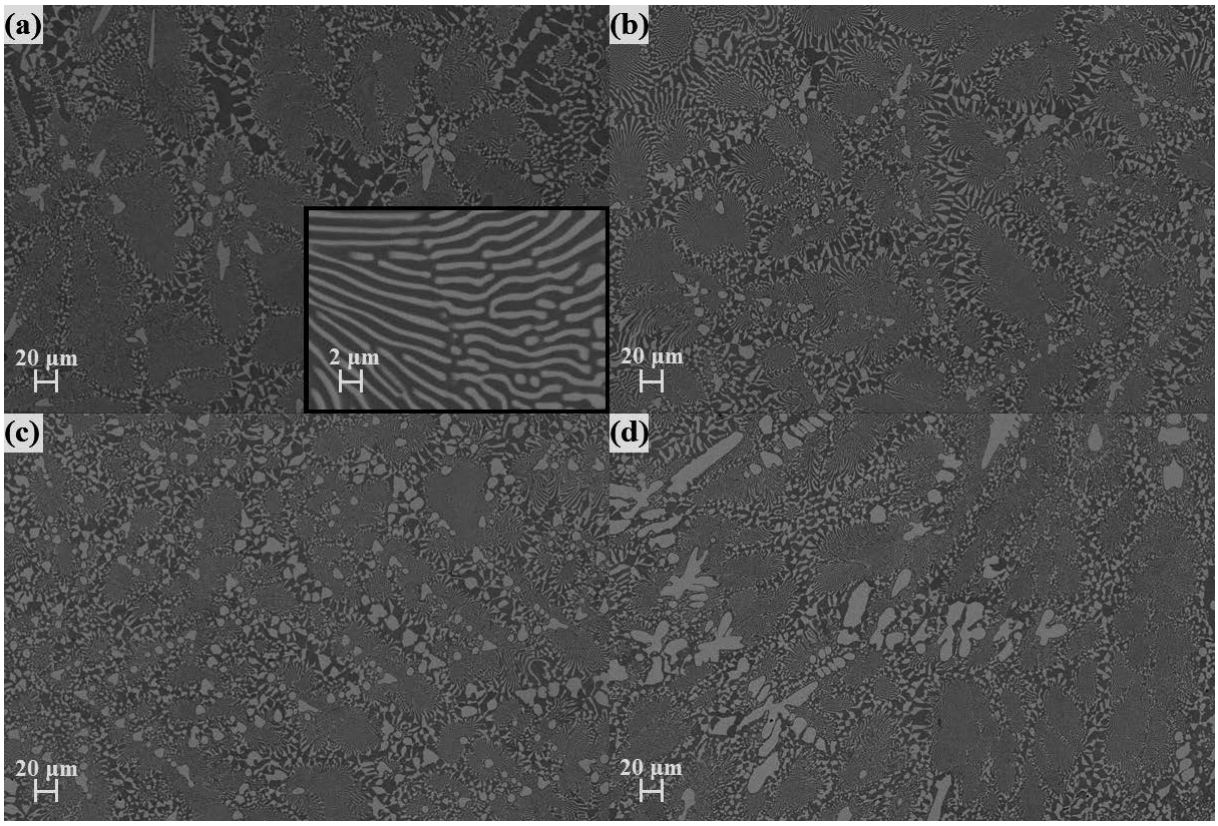

Figure 1. Microstructures of the CoCrFeNiNb$_{0.35}$Mo$_{0.25}$ (a), CoCrFeNiNb$_{0.35}$Mo$_{0.3}$ (b), CoCrFeNiNb$_{0.4}$Mo$_{0.25}$ (c), CoCrFeNiNb$_{0.4}$Mo$_{0.4}$ (d) alloys in the as-cast state

The results of the hardness tests of the CoCrFeNiNb$_x$Mo$_y$ alloys in the as-cast state are presented in Figure 2. All of the alloys investigated are characterised with comparable values of hardness, varying in a relatively narrow range of 448 to 457 HV$_1$. However, a noticeably lower standard deviation can be observed for CoCrFeNiNb$_{0.35}$Mo$_{0.3}$, which can be attributed to its more homogeneous microstructure. Compared to the CoCrFeNi base alloy, which exhibits a hardness of approximately 135 HV [15], a substantial increase in hardness can be observed. That effect can be assigned mainly to the secondary phase strengthening, which results from the precipitation of the Laves phase, and, to a lesser extent, also to the strengthening of the solid solution of the FCC phase by solute niobium [16].

The corrosion resistance of the alloys investigated was evaluated on the basis of electrochemical measurements, performed in the 5% NaCl solution at a temperature of 25 °C. Changes in open-circuit potential as a function of time (a) and potentiodynamic polarization curves (b) for the as-cast alloys are shown in Figure 3. The parameters obtained as a result of the measurements conducted are summarized in the Table 1. Based on the tests conducted, it can be stated that the best corrosion resistance characterizes the CoCrFeNiNb$_{0.4}$Mo$_{0.3}$ alloy. It is confirmed by the lowest corrosion current density (114 nA/cm^2) and the highest polarisation resistance (261 kΩcm^2). However, in terms of polarization resistance, also CoCrFeNiNb$_{0.35}$Mo$_{0.25}$ and CoCrFeNiNb$_{0.4}$Mo$_{0.25}$ alloys are also characterized with similar values of R_p, in both cases exceeding 250 kΩcm^2. In turn, the higher corrosion potential

recorded for $CoCrFeNiNb_{0.35}Mo_{0.3}$ and $CoCrFeNiNb_{0.4}Mo_{0.3}$ alloys can be attributed to a higher concentration of molybdenum with a more positive standard potential (Mo/Mo^{2+} – 0.2 V vs. standard hydrogen electrode) [17].

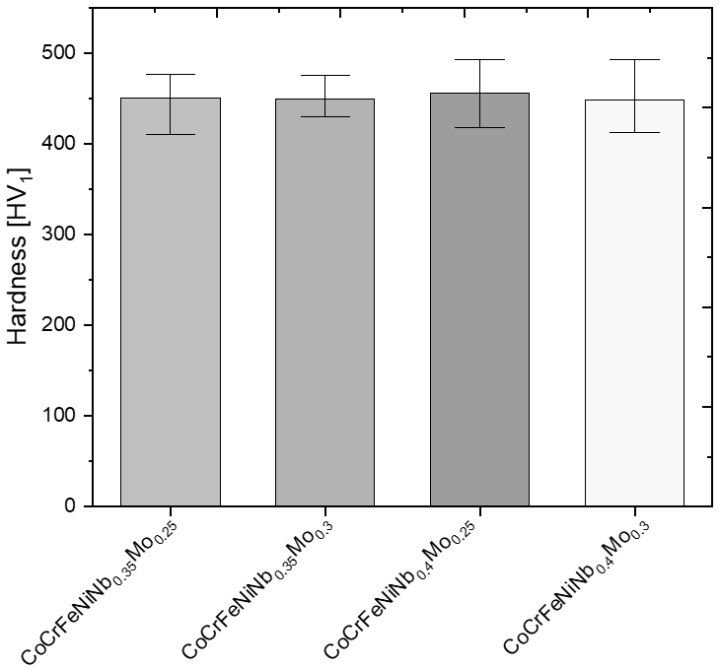

Figure 2. Variation of Vickers hardness of the $CoCrFeNiNb_xMo_y$ alloys in as-cast state

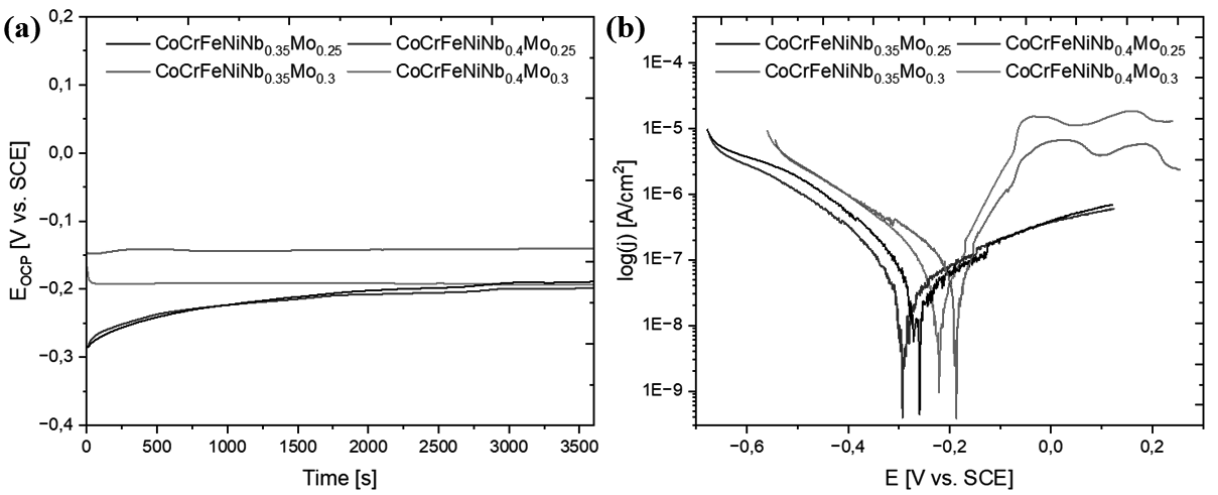

Figure 3. Changes of open-circuit potential (a) and potentiodynamic polarization curves (b) of $CoCrFeNiNb_xMo_y$ alloys in 3.5% NaCl solution at 25 °C

Table 1. Results of the electrochemical tests conducted in the 5% NaCl solution at 25°C

Alloy	E_{corr} [mV]	j_{corr} [nA/cm^2]	R_p [kΩcm^2]
$CoCrFeNiNb_{0.35}Mo_{0.25}$	−273	892	252
$CoCrFeNiNb_{0.35}Mo_{0.3}$	−191	588	112
$CoCrFeNiNb_{0.4}Mo_{0.25}$	−292	632	252
$CoCrFeNiNb_{0.4}Mo_{0.3}$	−223	114	261

4. CONCLUSIONS

The significant volume content of the eutectic structure was confirmed for all of the alloys tested, indicating their near-eutectic composition. However, for the CoCrFeNiNb$_{0.35}$Mo$_{0.25}$ alloy, the presence of FCC solid solution FCC dendrites can be observed, indicative of its hypoeutectic composition, while, in the case of the CoCrFeNiNb$_{0.4}$Mo$_{0.3}$ dendrites composed of the Laves phase, can be observed, which allows us to describe that alloy as hypereutectic. A slight influence of variation in the concentration of niobium and molybdenum was found, simultaneously all alloys characterise with high values of hardness with the maximum value of 457 HV$_1$ obtained for CoCrFeNiNb$_{0.4}$Mo$_{0.25}$ ingot. The CoCrFeNiNb$_{0.4}$Mo$_{0.3}$ alloy showed the best corrosion resistance in the 5% NaCl solution, showing the lowest values of the corrosion current density (114 nA/cm^2) and the highest polarization resistance (261 kΩcm^2).

ACKNOWLEDGEMENTS

The work was supported by the National Science Centre of Poland under research project no. 2022/47/B/ST8/02465.

BIBLIOGRAPHY

1. B.S. Murty, J.W. Yeh, S. Ranganathan, P.P. Bhattacharjee, High Entropy Alloys – second edition, Elsevier, Amsterdam, 2019.
2. D.B. Miracle, O.N. Senkov, A critical review of high entropy alloys and related concepts, Acta Materialia 122, 2017, p. 448-511.
3. T. Sonar, M. Ivanov, E. Trofimov, A. Tingaev, I. Suleymanova, An overview of microstructure, mechanical properties and processing of high entropy alloys and its future perspectives in aeroengine applications, Materials Science for Energy Technologies 7, 2024, p. 35-60.
4. Z. Zhou, H. Li, Y. Liu, T. Niu, H. Li, Effect of Ti on the corrosion behavior of (FeCrCoNi)$_{100-x}$Ti$_x$ alloy, Corrosion Science 209, 2022, 110807.
5. Y. Lin, T. Yang, L. Lang, Ch. Shan, H. Deng, W. Hu, F. Gao, Enhanced radiation tolerance of the Ni-Co-Cr-Fe high-entropy alloy as revealed from primary damage, Acta Materialia 196, 2020, p. 133-143.
6. Y. Lu, Y. Dong, S. Guo, L. Jiang, H. Kang, T. Wang, B. Wen, Z. Wang, J. Jie, Z. Cao, H. Ruan, T. Li, A promising new class of high-temperature alloys: eutectic high-entropy alloys, Scientific Reports 4, 2014, p. 1-5.
7. J. Liu, b , Z. Li, D. Lin, Z. Tang, X. Song, P. He, S. Zhang, H. Bian, W. Fu, Y. Song, Eutectic high-entropy alloys and their applications in materials processing engineering: A review, Journal of Materials Science & Technology 189, 2024, p. 211-246.
8. H. Jiang, K. Han, X. Gao, Y. Lu, Z. Cao, M.C. Gao, J.A. Hawk, T. Li, A new strategy to design eutectic high-entropy alloys using simple mixture method, Materials & Design 142, 2018, p. 101-105.
9. Y. Guo, L. Liu, Y. Zhang, J. Qi, B. Wang, Z. Zhao, J. Xiang, A superfine eutectic microstructure and the mechanical properties of CoCrFeNiMo$_x$ high-entropy alloys, Journal of Materials Research 33, 2018, p. 1-8.

10. B. Chanda, J. Das, Composition Dependence on the evolution of nanoeutectic in $CoCrFeNiNb_x$ ($0.45 \leq x \leq 0.65$) high entropy alloys, Advanced Engineering Materials 20, 2017, 1700908.
11. Ch. Liu, Y. Gao, K. Chong, F. Guo, D. Wu, Y. Zou, Effect of Nb content on the microstructure and corrosion resistance of $FeCoCrNiNb_x$ high-entropy alloys in chloride ion environment, Journal of Alloys and Compounds 935, 2023, 168013.
12. C. Dai, T. Zhao, C. Du, Z. Liu, D. Zhang, Effect of molybdenum content on the microstructure and corrosion behavior of $FeCoCrNiMo_x$ high-entropy alloys, Journal of Materials Science & Technology 33, 2020, p. 64-73.
13. X. Ye, H. Lei, X. Liu, G. Zhao, J. Feng, J. Chen, B. Li, D. Fang, N. Gao, Design synergistic alloying CoCrFeNi eutectic high entropy alloy based on infinite solid solution, Materials Letters 343, 2023, 134395.
14. C.H. Tsau, Y.H. Chen, M.C. Tsai, The Effects of Niobium and Molybdenum on the Microstructures and Corrosion Properties of $CrFeCoNiNb_xMo_y$ Alloys, Materials 15, 2022, 2262.
15. T. Shun, L. Chang, M. Shiu, Microstructure and mechanical properties of multiprincipal component $CoCrFeNiMo_x$ alloys, Materials Characterization 70, 2012, p. 63-67.
16. W.H. Liu, J.Y. He, H.L. Huang, H. Wang, Z.P. Lu, C. T. Liu, Effects of Nb additions on the microstructure and mechanical property of CoCrFeNi high-entropy alloys, Intermetallics 60, 2015, p. 1-8.
17. J.A. Dean, Lange's Handbook of Chemistry, 15th Edition, McGraw-Hill, 1999.

TalentDetector
23th-25th June 2025
Gliwice-Brenna, Poland
DEPARTMENT OF ENGINEERING MATERIALS AND BIOMATERIALS
FACULTY OF MECHANICAL ENGINEERING
SILESIAN UNIVERSITY OF TECHNOLOGY
INTERNATIONAL STUDENTS SCIENTIFIC CONFERENCE

Kompozyty hydrożelowe na osnowie polietylenu

Marcin Bilewicz*, Michał Rak, Igor Zdebel, Weronika Gębska, Michał Gwóźdź, Katarzyna Mazik

Politechnika Śląska, Wydział Mechaniczny Technologiczny, Katedra Materiałów Inżynierskich i Biomedycznych, Gliwice, *email: marcin.bilewicz@polsl.pl

Streszczenie: W artykule przedstawiono badania nad kompozytem hydrożelowym – materiale na osnowie polimerowej zawierającym materiał hydrożelowy. Otrzymane w ten sposób materiały mogą znaleźć specjalistyczne zastosowania w sektorze medycznym, budowlanym czy też sadowniczym. Materiały będą miały na celu gromadzenie wody/wilgoci i stopniowe jej uwalnianie. Przyszłe zastosowanie może obejmować modyfikację hydrożeli lub wykorzystanie różnych typów do bardziej zaawansowanych zastosowań w opatrunkach na rany, inżynierii tkanek i rusztowań.
Abstract: The article presents research on a hydrogel composite - a polymer-based material containing a hydrogel material. The materials obtained in this way can find specialized applications in the medical, construction or horticultural sectors. The materials will be aimed at accumulating water/moisture and gradually releasing it. Future applications may include the modification of hydrogels or the use of different types for more advanced applications in wound dressings, tissue engineering and scaffolds.

Słowa kluczowe: materiały funkcjonalne, hydrożel, polimery

1. WPROWADZENIE

Materiały hydrożelowe należą do grupy materiałów funkcjonalnych, zwanych w nomenklaturze zagranicznej jako smart, które mogą być superabsorbentami wody i innych cieczy. Według Water Utility Journal [1] hydrożel może wchłonąć do 400 razy więcej niż jego pierwotna waga. Ta właściwość materiału może być wykorzystywana w kompozytach polimerowych [2-3]. Zastosowanie różnych proporcji materiałów i różnych metod przetwarzania otwiera szereg możliwości uzyskania funkcjonalnych kompozytów z możliwością kontrolowania wilgotności i absorpcji wody [4-5].

2. BADANIA I WYNIKI

Do przygotowania mieszanek kompozytowych wykorzystano mieszankę polimeru-polietylenu (PE) i materiału hydrożelowego (poliakrylanu sodu) o różnym stosunku. Stosunek

ten wynosił 2% wag., 4% wag., 6% wag. i 8% wag. Zastosowano dwa rodzaje technologii, a mianowicie: pierwsza - wytłaczanie, gdzie masterbatch poddawano wysokim szybkościom ścinania przy użyciu podwójnej wytłaczarki; druga - formowanie wtryskowe – polimer o różnym stosunku mieszano z hydrożelem i wtryskiwano do wnęki formy z kompleksem ustawień, takich jak ciśnienie wtrysku, ciśnienie docisku, przeciwciśnienie i temperatury chłodzenia. Próbki po procesie wytłaczania i formowania wtryskowego przechowywano przez 24 godziny w wodzie mineralnej (około 300 mg/l minerałów i wody zdemineralizowanej (rys. 1). Obserwacja próbek po wytłaczaniu ujawnia obecność cząstek hydrożelu pokrytych polimerem, cząstki są równomiernie rozmieszczone wewnątrz polimeru. Zaobserwowano, że w niektórych miejscach z powodu nieciągłości powłoki polimerowej hydrożel wyrósł po przechowywaniu w wodzie demineralizowanej.

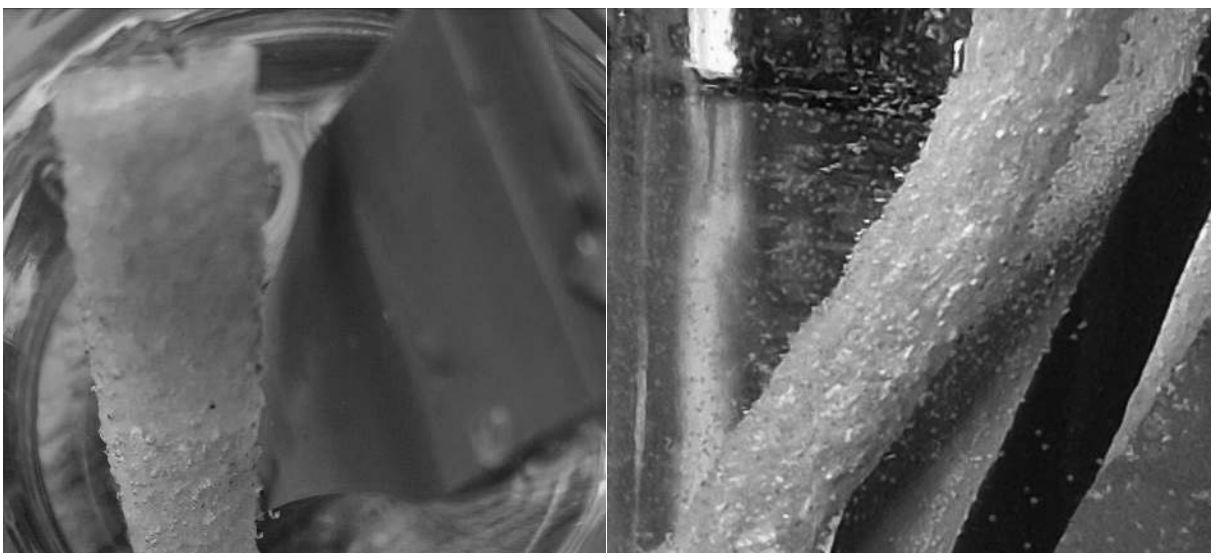

Rysunek 1. Próbki przechowywane w wodzie: zdemineralizowanej (po lewej), zmineralizowanej (po prawej).
Figure 1. Samples kept in the water: demineralized (left), mineralized (right).

Cząsteczki są nasycone wodą i czasami oddzielają się od materiału (rys. 2, górna próbka). Dostęp wody do cząstek hydrożelu wewnątrz kompozytu jest znacznie trudniejszy w próbkach wtryskiwanych. Symetria wtrysku powoduje, że cząstki znajdują się wewnątrz próbki, pozostawiając warstwę zewnętrzną w postaci polimeru bez dostępu do cząstek hydrożelu (rys. 3).

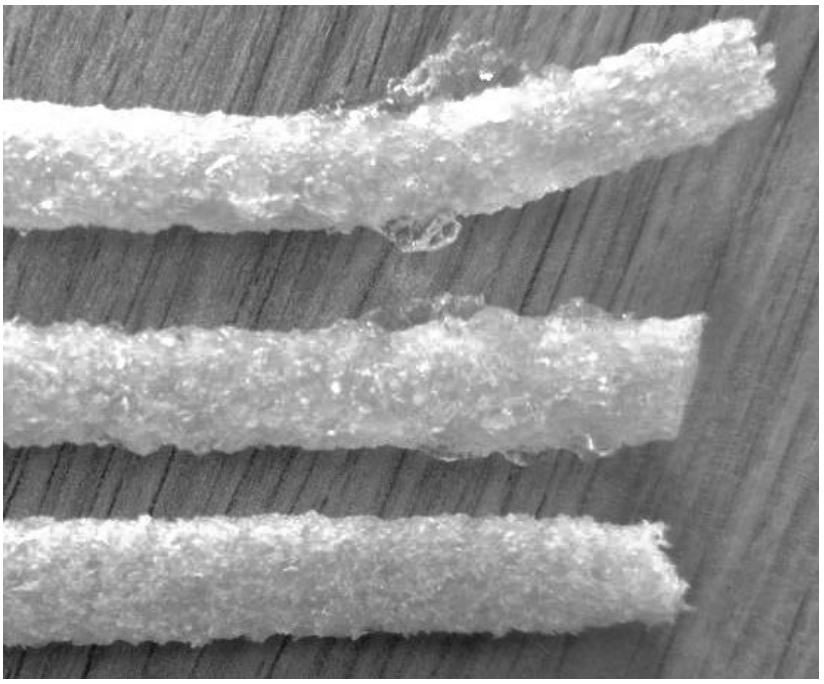

Rysunek 2. Nasycone cząsteczki hydrożelu po przechowywaniu w wodzie demineralizowanej (próbka górna), wodzie zmineralizowanej (próbka środkowa), bez wody (próbka dolna)
Figure 2. Saturated particles of hydrogel after keeping in demineralized water (top sample), mineralized water (middle sample), no water (bottom sample)).

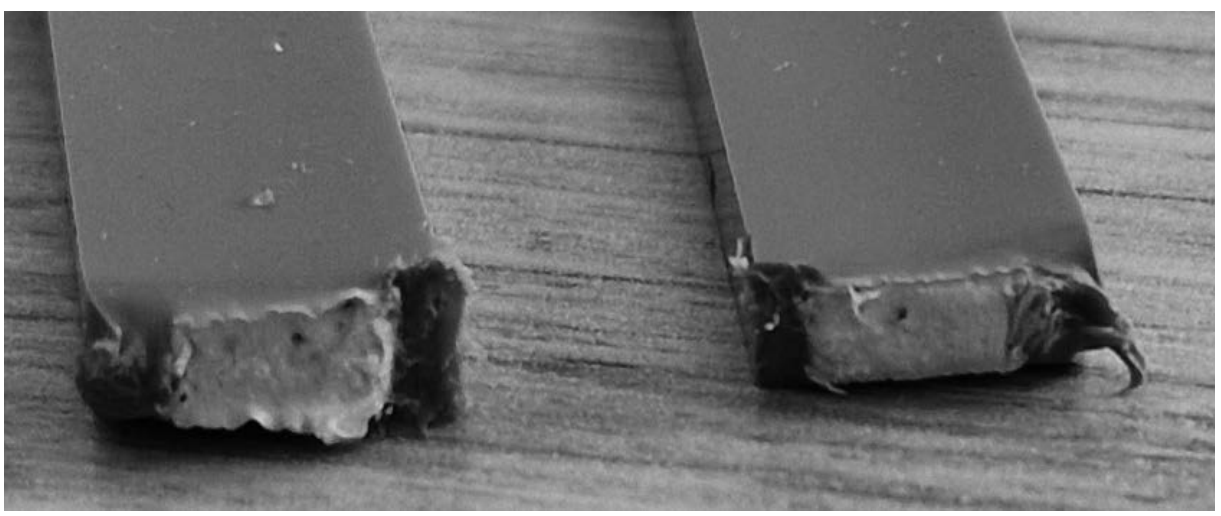

Rysunek 3. Przekrój wtryskiwanych próbek. Brak widocznych cząstek hydrożelu
Figure 3. Cross section of injected samples. No visible hydrogel particles in outer part of sample.

Próbki uzyskane po wytłaczaniu, w których hydrożel był nasycony, zbadano pod mikroskopem stereoskopowym (rys. 4).

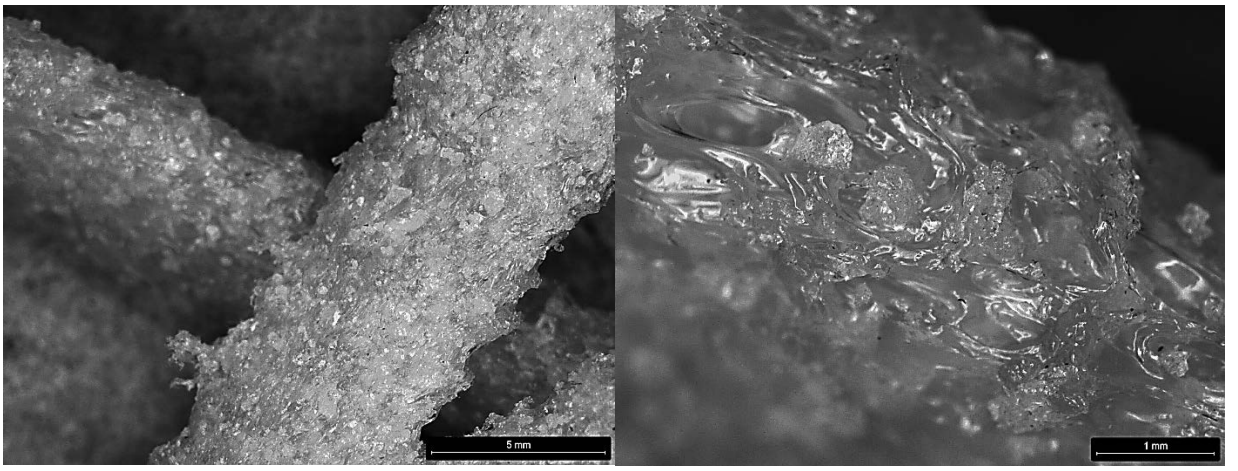

Rysunek 4. Próbki po wytłaczaniu obserwowane za pomocą mikroskopii stereoskopowej. Cząsteczki hydrożelu są zlokalizowane wzdłuż przepływu polimeru (dół).
Figure 4. Samples after extrusion observed using stereoscopic microscopy. Hydrogel particles are located along flow of polymer (bottom).

W celu zwiększenia kontrastu między cząsteczkami polimeru i hydrożelu zastosowano pigment koloryzujący (rys. 5).

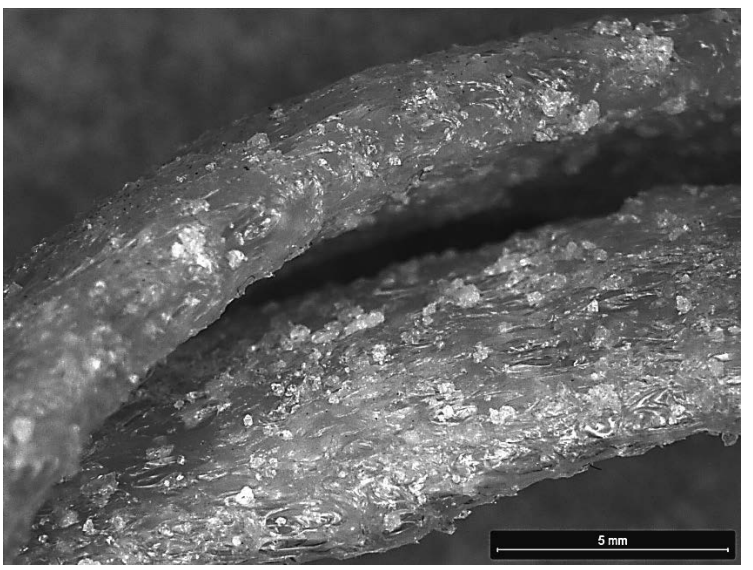

Rysunek 5. Próbki po wytłaczaniu obserwowane za pomocą mikroskopii stereoskopowej. Osnowa polimerowa została zabarwiona za pomocą pigmentu. Cząsteczki hydrożelu znajdują się wzdłuż przepływu polimeru.
Figure 5. Samples after extrusion observed using stereoscopic microscopy. Polymer matrix was coloured using pigment. Hydrogel particles are located along flow of polymer.

Aby sprawdzić wytrzymałość formowanych wtryskowo próbek o różnym stosunku cząstek hydrożelu (2% wag., 4% wag., 6% wag., 8% wag., 10% wag.). Wyniki przedstawiono na poniższych wykresach (rys. 6-10).

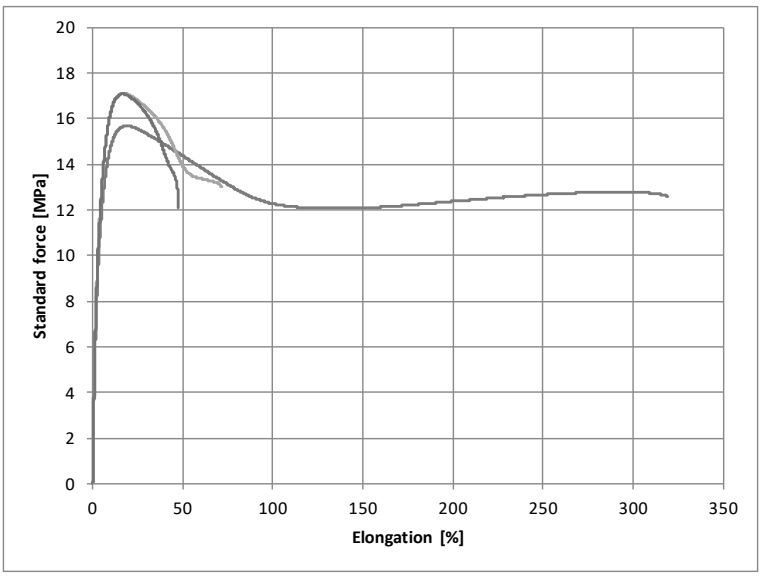

Rysunek 6. Krzywa wytrzymałości na rozciąganie próbki PE z zawartością wagową cząstek hydrożelu wynoszącą 2%.
Figure 6. Tensile test curve of PE sample with 2wt% of hydrogel particles.

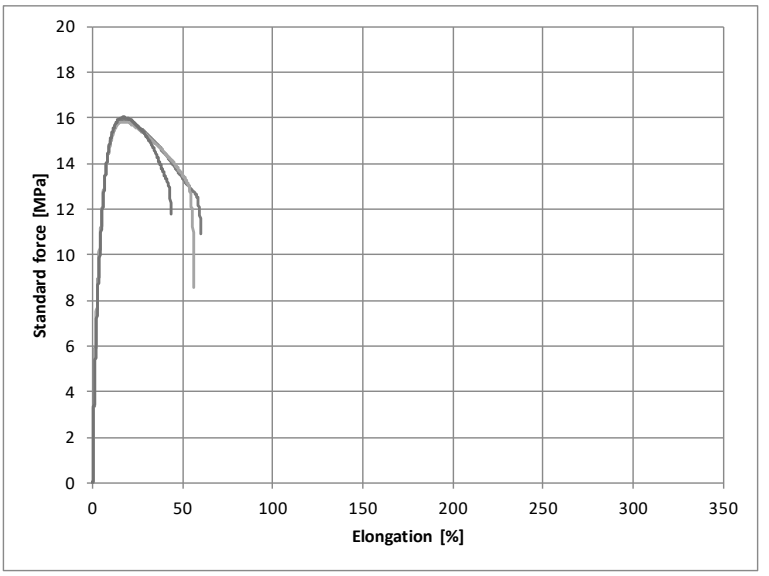

Rysunek 7. Krzywa wytrzymałości na rozciąganie próbki PE z zawartością wagową cząstek hydrożelu wynoszącą 4%.
Figure 7. Tensile test curve of PE sample with 4wt% of hydrogel particles.

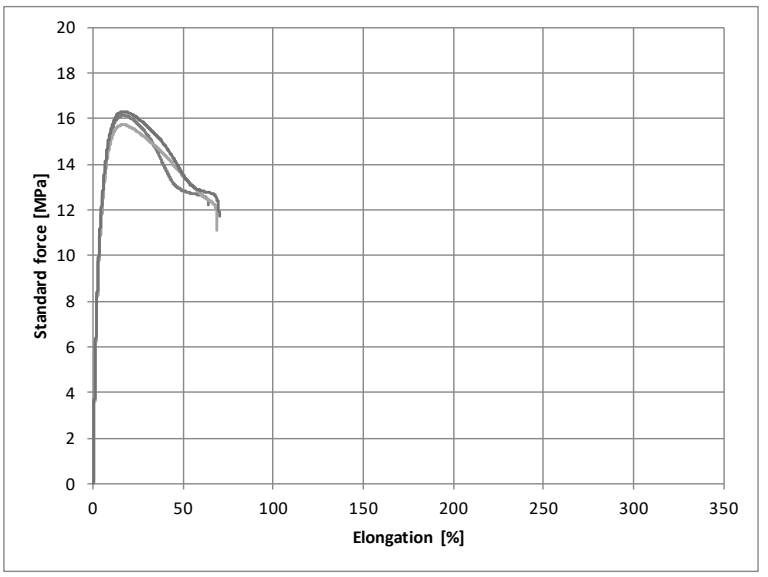

Rysunek 8. Krzywa wytrzymałości na rozciąganie próbki PE z zawartością wagową cząstek hydrożelu wynoszącą 6%.
Figure 8. Tensile test curve of PE sample with 6wt% of hydrogel particles.

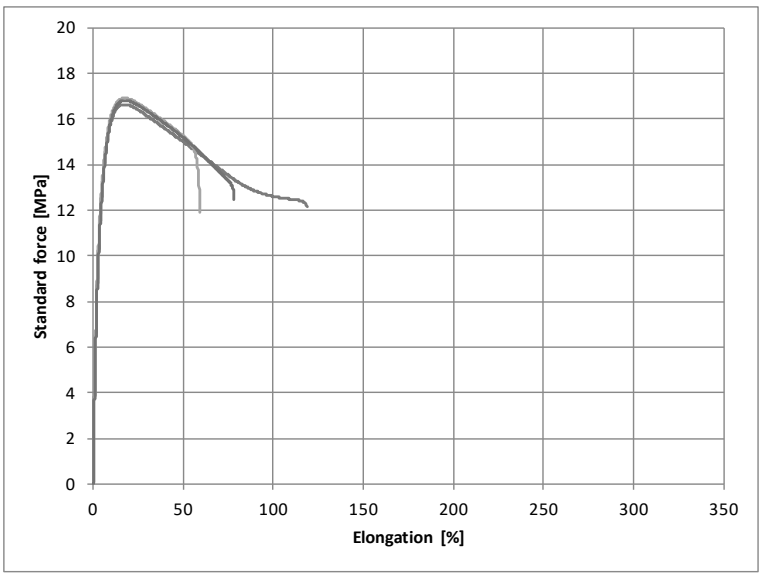

Rysunek 9. Krzywa wytrzymałości na rozciąganie próbki PE z zawartością wagową cząstek hydrożelu wynoszącą 8%.
Figure 9. Tensile test curve of PE sample with 8wt% of hydrogel particles.

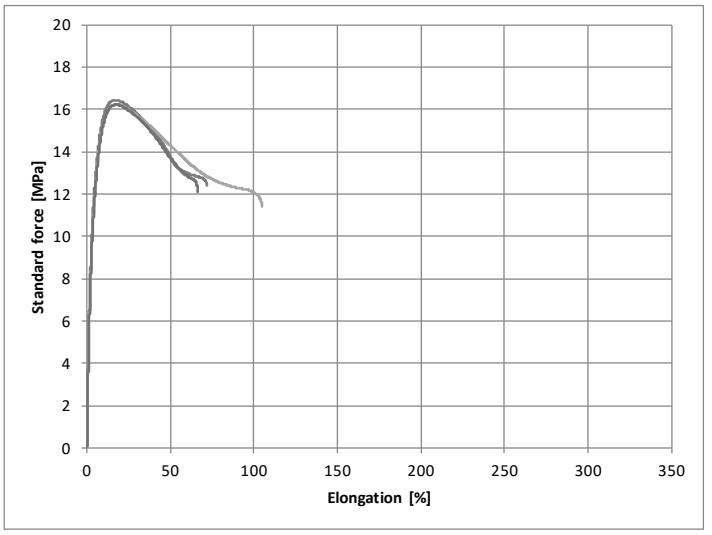

Rysunek 10. Krzywa wytrzymałości na rozciąganie próbki PE z zawartością wagową cząstek hydrożelu wynoszącą 10%.
Figure 10. Tensile test curve of PE sample with 10wt% of hydrogel particles.

3. WNIOSKI

Z krzywych wytrzymałości na rozciąganie widać, że cząsteczki hydrożelu nie wpływają znacząco na wytrzymałość. Dla próbek z domieszką 2% wag. cząsteczek hydrożelu można zaobserwować, że jedna z próbek wykazała znacznie dłuższą drogę rozciągania. Może to wynikać z niejednorodnego wymieszania materiałów, szczególnie w przypadku najmneijszej zawartości hydrożelu. Wraz ze wzrostem zawartości cząsteczek hydrożelu zobserwowano nieznacznie wydłużenie drogi rozciągania. Adhezja pomiędzy cząstkami hydrożelu a osnową polimerową jest warta bliższego zbadania. Konieczne są również dalsze prace nad zaprojektowaniem układu o strukturze porowatej lub innego układu ułatwiającego dostęp wody do cząsteczek wewnątrz kompozytu hydrożelowego.

BIBLIOGRAFIA

1. K. Lal, U. Singh, D. M. Denis, S. Srivastava, A. Ranjan, The role of polymers in increasing water use efficiency, E.W. Publications, Water Utility Journal 27, 2021, 15-26.
2. K. Susheel, Polymeric Hydrogels as Smart Biomaterials, Springer International Publishing Switzerland, 2016.
3. H. Li, V. Silberschmidt, The Mechanics of Hydrogels: Mechanical Properties, Testing, and Applications, Woodhead Publishing, 2022.
4. J. P. Davim, Biomedical Composites: Materials, Manufacturing and Engineering, De Gruyter, 2013.
5. M. Bilewicz, I. Zdebel, M. Rak, W. Gębska, M. Gwóźdź, Kompozyty hydrożelowe otrzymywane technologią formowania wtryskowego jako materiały typu smart, XXI Konferencja Naukowo-Techniczna Polimery i kompozyty konstrukcyjne, Wydawnictwo Katedry Mechaniki Teoretycznej i Stosowanej, 2024

TalentDetector
23th-25th June 2025
Gliwice-Brenna, Poland
DEPARTMENT OF ENGINEERING MATERIALS AND BIOMATERIALS
FACULTY OF MECHANICAL ENGINEERING
SILESIAN UNIVERSITY OF TECHNOLOGY
INTERNATIONAL STUDENTS SCIENTIFIC CONFERENCE

Design and Development of Prototype Mobile Platforms

Franciszek Borgosz[a], Michał Plok[b], Michał Łubko[c]

[a] Silesian University of Technology, Faculty of Automatic Control, Electronics and Computer Science, SKN vFly, SKN SpaceCoffe
[b] Silesian University of Technology, Faculty of Automatic Control, Electronics and Computer Science, SKN vFly, SKN SpaceCoffe
[c] Michał Łubko, Silesian University of Technology, Faculty of Automatic Control, Electronics and Computer Science, SKN vFly, SKN SpaceCoffe
email: franek.borgosz@gmail.com

Abstract: This article presents the design of a prototype mobile modular platforms intended to carry out autonomous operations in the future iterations.

Keywords: mobile platform, modularity, design

1. INTRODUCTION

This paper presents the technical foundation and development process of a modular mobile platform designed to perform autonomous tasks in its future iteration. The project involves the design and prototyping of a wheeled platform system equipped with appropriate computational hardware, sensor arrays, and actuation components necessary for future intended autonomous operation.

The platform design places emphasis on modularity in the mechanical design so that components can be changed quickly. The modular design promotes quick prototyping and future modification for a wide range of applications, such as the introduction of sensors or modification of the drive system. The component mounts and chassis were CAD designed to enable the 3D printing of interchangeable and upgradeable parts with ease.

From an electronic standpoint, the system incorporates a processing unit, along with dedicated modules for motion control, as well as sensors environmental sensing.

The project provides a foundation for iterative development, with the ability to try and test different autonomous navigation algorithms on a physical platform with expandable capabilities.

2. DESIGN

The design process of the mobile platform followed an iterative, modular approach to ensure flexibility, ease of assembly, and compatibility with various sensor and hardware configurations.

The platform's mechanical structure was divided into interchangeable modules, including separate units for the chassis, sensor mounts, drive train, and control unit housing. Each module was designed with standardized mounting points and dimensions to support quick hardware swaps and configuration changes. This modularity enables the platform to be adapted for different operational requirements or upgraded as more advanced components become available. [3]

The drivetrain was designed to support various wheel and motor configurations, and the electronics bay was structured to accommodate different processing units and power sources. This modular framework not only accelerates development cycles but also supports experimental work and educational use, where components may be reused or repurposed across different projects.

In the near future we plan on designing various other propulsion methods for the platform, among them swing arm suspension or nature-inspired propulsion, such as mechanical legs. This will allow us to compare the capabilities of our designs, as well as choose the best-suited one for our research purposes. [1,2]

2.1 Wheel and Motor Mount

Motor mounts are designed in the spirit of modularity, therefore the can be easily changed or modified without changing any other major components. Mounts are connected to the main body via a dovetail joint. This type of connection provides a secure and stable connection while being easy to design parts around it. They are secured in place by two bolts, which prevent the mounts from sliding.[2] (Figs. 1-2)

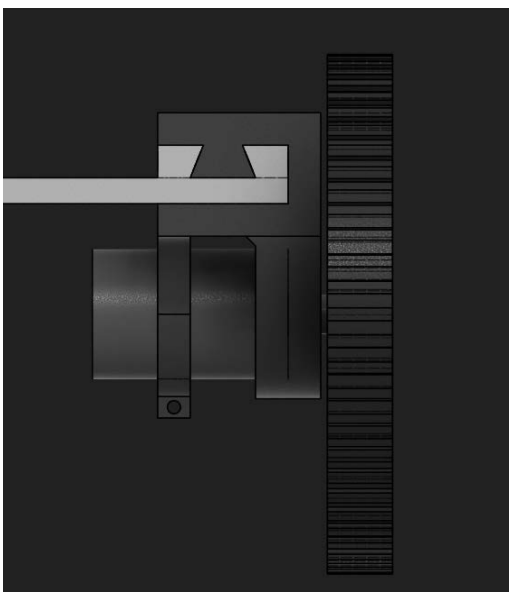

Figure 1. Motor Mount on a Dovetail Rail Mount (Front view)

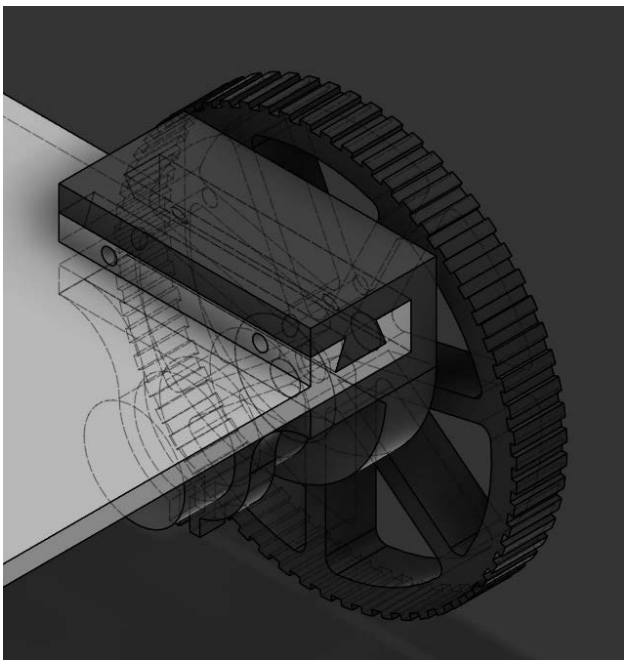

Figure 2. Motor Mount on a Dovetail Rail Mount (Diagonal view)

2.2 Sensor Adjustable Mount

Sensor mounts were designed to be easily swapped and adjustable, similarly to motor mounts it utilises a dovetail joint. Their design can be easily altered to suit the given sensor and allows us to quickly change the sensor's angle as required. (Figs. 3-4)

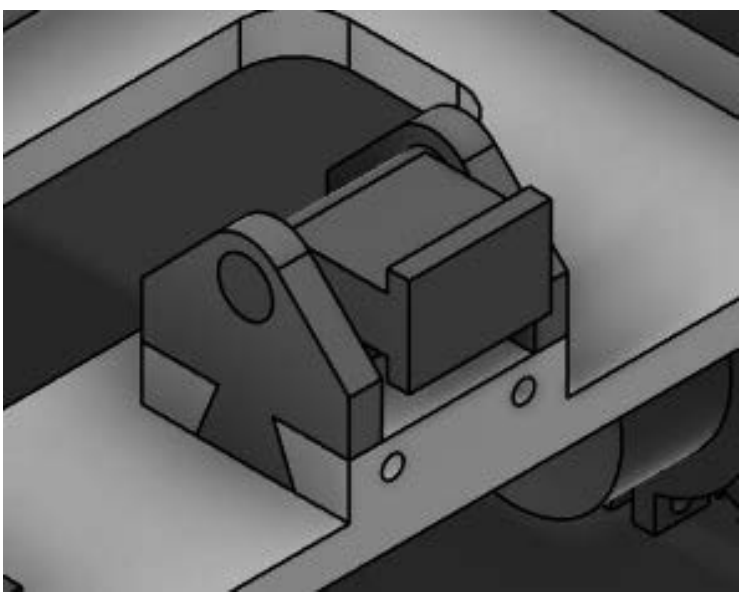

Figure 3. Sensor Mount on a dovetail joint (Diagonal view)

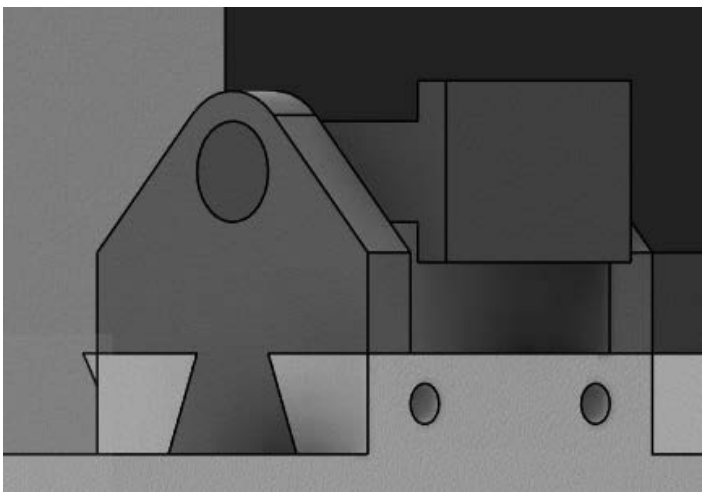

Figure 4. Sensor Mount on a dovetail joint (Side angled view)

2.3 Electronics Bay

Electronics bay is designed to allow quick and easy change of all control systems without the need to disassemble multiple components as well as protecting the delicate circuits from the elements. (Fig. 5)

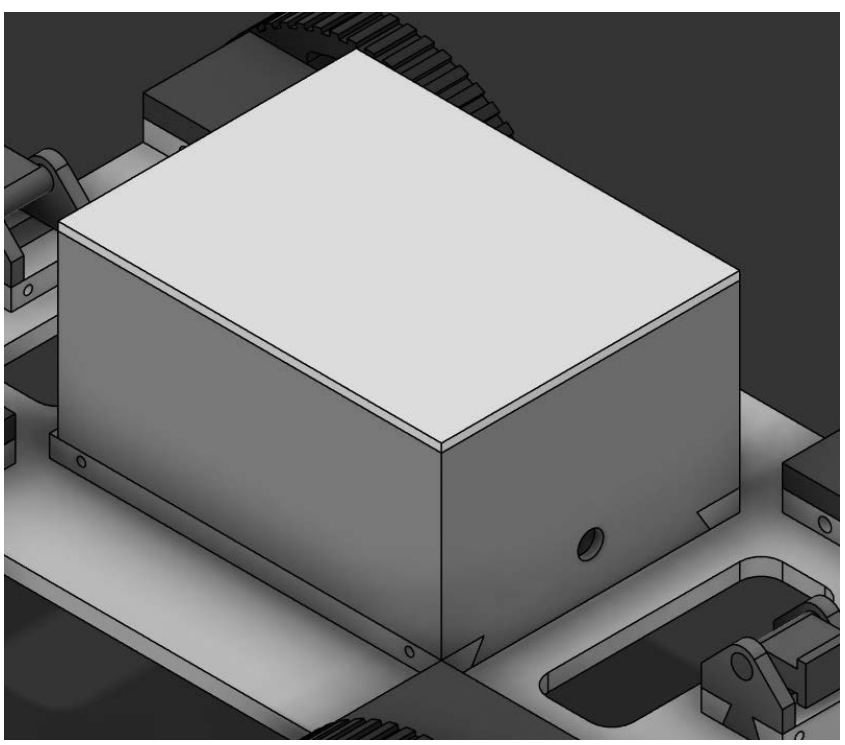

Figure 5. Electronics Bay (diagonal view)

2.4 Whole Mobile Platform Assembly View

As shown in the below featured pictures the whole assembly is highly modular and easy to modify as need be, while maintaining durability and ease of assembly. (Figs. 6-9)

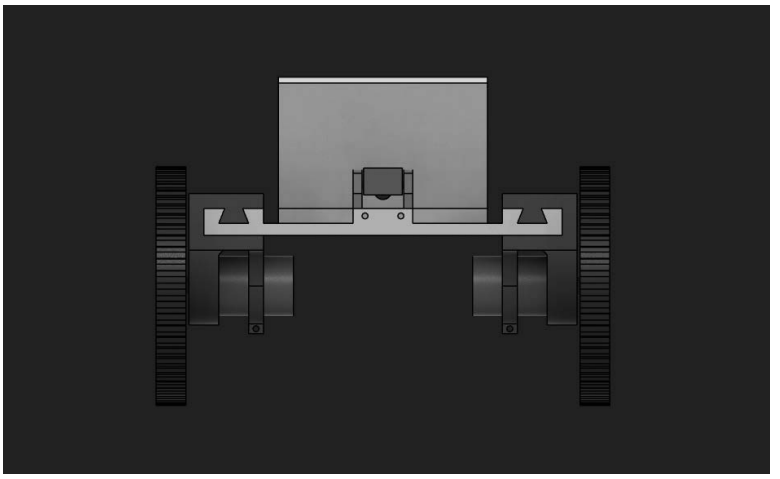

Figure 6. Mobile Platform (Top side view)

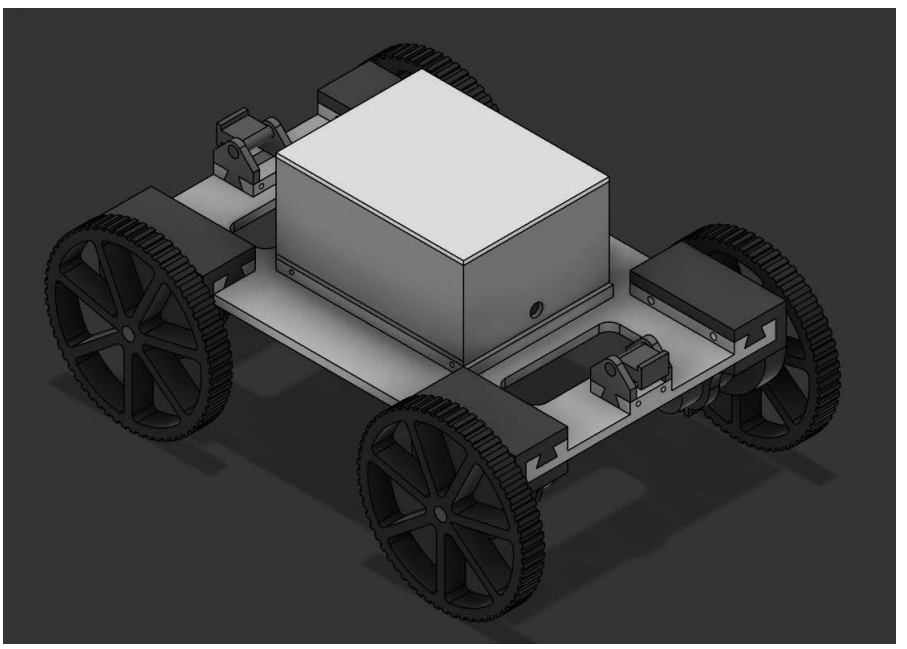

Figure 7. Mobile Platform (Front view)

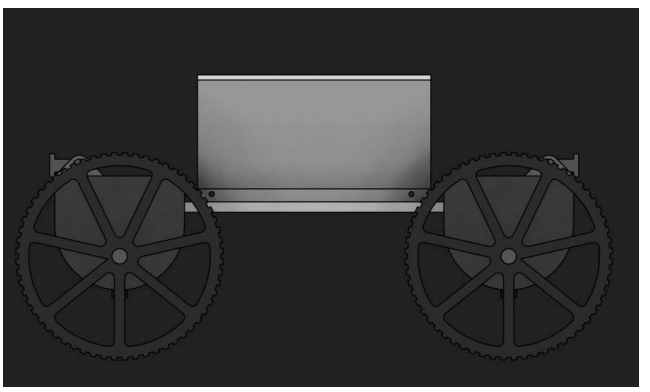

Figure 8. Mobile Platform (Side view)

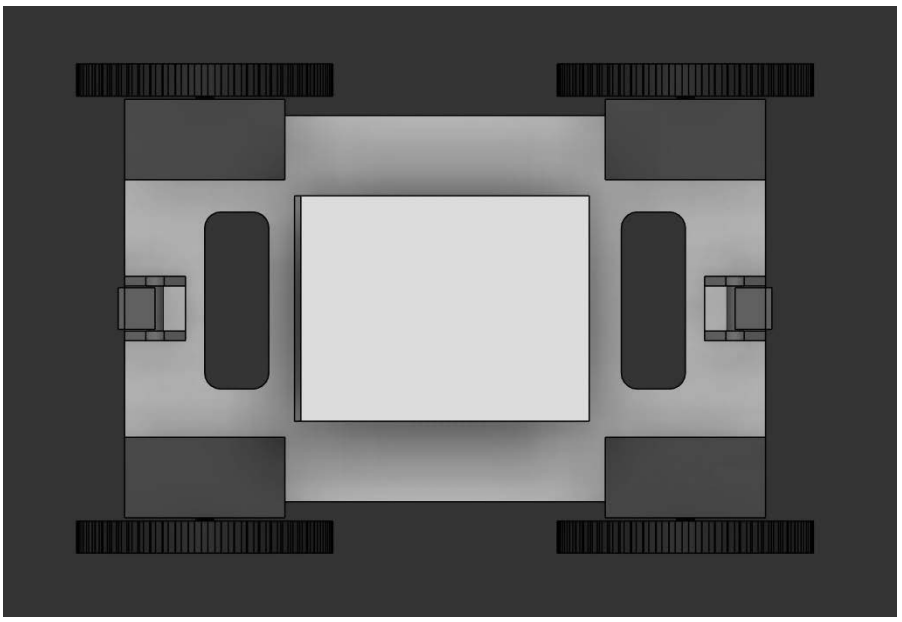

Figure 9. Mobile Platform (Top view)

3. FUTURE FURTHER DEVELOPMENTS

Future development of the mobile platform will focus on enhancing its autonomous capabilities and expanding its hardware and software modularity. Planned improvements include the integration of more advanced sensor systems, such as LiDAR, to enable more accurate environment mapping and obstacle detection. On the software side, implementation of neural network-based control systems will allow for autonomous navigation in dynamic environments. [4]

To support these advancements, the processing architecture will be upgraded to accommodate more computationally intensive tasks. Additional focus will be placed on improving the platform's energy management system to allow for longer operation times and more efficient power distribution.

The modular design will also be extended to support rapid swapping of functional modules, enabling the platform to serve as a testbed for various research and educational applications. This adaptability will make it possible to reconfigure the platform in the matter of minutes to make it suitable to the given task. Ultimately, these developments aim to transform the platform from a basic prototype into a versatile tool for experimentation in autonomous systems. [3]

4. CONCLUSION

This project led us to a design of a prototype mobile platform tailored for executing autonomous tasks in the future. The design prioritizes adaptability and ease of maintenance, allowing for straightforward integration of additional components or replacement of existing ones as technological requirements evolve. This flexible architecture not only simplifies

hardware and software development but also supports iterative testing and enhancement. As a result, the platform offers a robust foundation for continued research and educational use, and is well-positioned to accommodate future upgrades, modifications, and expanded functionality.

BIBLIOGRAPHY

1. NASA, *Exploration Rover Concepts and Development Challenges*, Glenn Research Center Report, 2015.
2. A. S. Bhat, "Design and Analysis of Mars Rover Wheel", *International Research Journal of Engineering and Technology*, vol. 10, no. 5, pp. 1–6, 2023.
3. R. Siegwart, I. R. Nourbakhsh, and D. Scaramuzza, *Introduction to Autonomous Mobile Robots*, 2nd ed., MIT Press, 2011.
4. K. Walas and D. Nowicki, "Designing Modular Mobile Robots – A Software and Hardware Perspective," *Journal of Automation, Mobile Robotics & Intelligent Systems*, 2020.

TalentDetector
23th-25th June 2025
Gliwice-Brenna, Poland
DEPARTMENT OF ENGINEERING MATERIALS AND BIOMATERIALS
FACULTY OF MECHANICAL ENGINEERING
SILESIAN UNIVERSITY OF TECHNOLOGY
INTERNATIONAL STUDENTS SCIENTIFIC CONFERENCE

Analysis of the properties of composite materials made from components derived from renewable resources

Katarzyna Borowiecka[1], Agnieszka J. Nowak[2]

[1] Student Science Club "HEAD TO HEAD" operating at the Department of Scientific and Didactic Laboratory of Nanotechnology and Material Technologies at the Faculty of Mechanical Engineering, Silesian University of Technology in Gliwice, Poland
[2] Scientific and Didactic Laboratory of Nanotechnology and Material Technologies, Silesian University of Technology, Konarskiego 18A, 44-100, Gliwice, Poland

Abstract: This work presents the terminology related to polymeric materials of petrochemical and renewable origin, such as composites with biodegradable thermoplastic matrix reinforced with particles from natural components. Proportions were prepared, and twenty compositions of biodegradable composite materials with a matrix consisting of bioplasts GF 106/02 and GS 2189, reinforced with walnut shell and quercetin, were produced. Static tensile and hardness tests, microscopic observations and differential scanning calorimetry were carried out for all the produced materials.

Keywords: Polymer materials, thermoplastics, thermoplastic matrix composites, biodegradable materials

1. INTRODUCTION

Polymeric materials are widely used in the automotive, construction, aerospace, and packaging industries, primarily due to their good mechanical properties, low weight, chemical resistance, and ease of processing thermoplastics. The low melting temperature of these polymers enables energy-efficient processing and cost reduction.
Nowadays, there is a clear need to reduce waste, especially in the packaging industry, where single-use, petrochemical-based plastics are a significant source of persistent waste. However, biodegradable polymers do not match them in terms of performance and are significantly more expensive. A promising solution lies in composite materials, which, through natural reinforcements, achieve improved mechanical properties while remaining biodegradable.
In this study, composites based on two biodegradable polymers approved for food contact were developed and reinforced with walnut shells and quercetin. Mechanical and thermal analyses were conducted to assess their properties. The research methodology was described, and the results were presented.

2. POLIMER AND COMPOSITE MATERIALS

Polymeric materials are divided into two main categories: elastomers and plastomers. Elastomers are characterized by very high elastic deformation under low stress. When the force is removed, they return to their original shape. In contrast, plastomers exhibit much smaller deformations. Depending on their thermal behaviour, plastomers are classified as thermoplastics or thermosets. Thermoplastics can be repeatedly moulded into specific shapes, as they become pliable when heated. Thermosets, on the other hand, undergo permanent cross-linking after being shaped at elevated temperatures, which prevents further reshaping without damaging the material's structure [1-3].

Polymeric materials can also be classified based on their origin. Petrochemical-based polymers are produced from non-renewable resources such as crude oil and natural gas. They degrade very slowly, which negatively impacts the environment. Polymers derived from renewable sources generally have slightly lower mechanical properties, but they biodegrade much more quickly, making them more environmentally friendly [4].

Composite materials consist of at least two different components (Fig. 1). Depending on their volume fraction, the material may exhibit properties similar to one of the components or entirely new characteristics. A composite is composed of a matrix, which holds the reinforcement in place and maintains structural integrity, and a filler phase, which determines the material's mechanical properties [5].

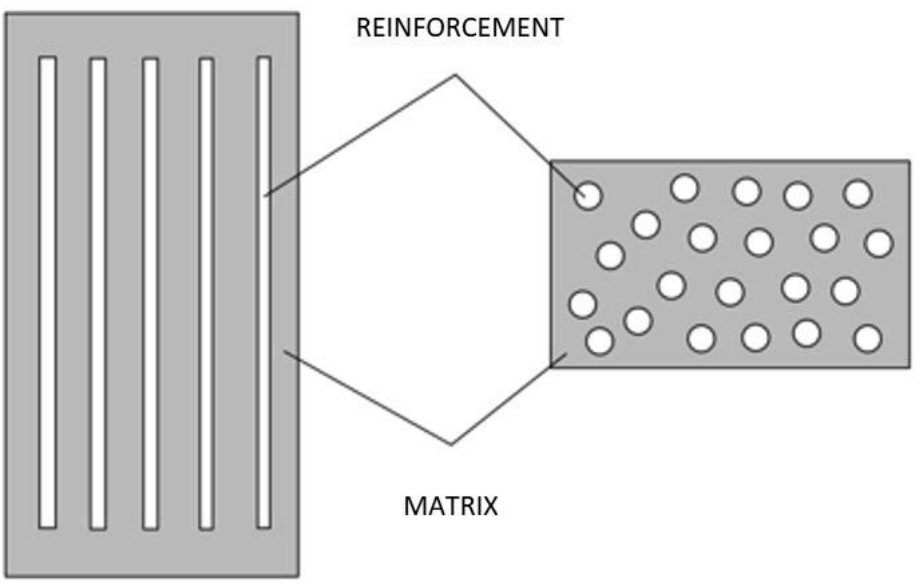

Figure 1. Composite construction diagram [5].

We distinguish between metal matrix composites and non-metal matrix composites, the latter of which are further divided into polymer matrix composites and ceramic matrix composites.

Polymer matrix composites are used to reduce weight and increase chemical resistance. Additionally, they provide vibration damping and serve as electrical insulators [1-3].

3. EXPERIMENT

3.1 Used materials

Four different materials were used in various proportions to create composite materials (Tab. 1). The first is BIOPLAST GF 106/02, a thermoplastic biodegradable polymer. It is used to produce products using the blown film extrusion method. The second one is BIOPLAST GS 2189, a thermoplastic polymer. As a previous material, it has excellent flow properties and is completely biodegradable under industrial composting conditions. This polymers were used as a matrix for the materials. For composite reinforcement, ground walnut shells were used, which provide mechanical properties of materials, and quercetin, which has antibacterial properties.

Table 1. *Percentage and mass share of individual components in the tested samples*.*

No.	Symbol of the sample	A, %	B, %	C, %	D, %	A, g	B, g	C, g	D, g
1.	A100	100	-	-	-	37,50	-	-	-
2.	B100	-	100	-	-	-	40,50	-	-
3.	A80 B20	80	20	-	-	30,00	8,10	-	-
4.	A60 B40	60	40	-	-	22,50	16,20	-	-
5.	A20 B80	20	80	-	-	7,50	32,40	-	-
6.	A40 B60	40	60	-	-	15,00	24,30	-	-
7.	A99 C1	99	-	1	-	33,75	-	0,48	-
8.	B99 C1	-	99	1	-	-	36,45	0,48	-
9.	A79 B20 C1	79	20	1	-	29,63	8,10	0,48	-
10.	A59 B40 C1	59	40	1	-	22,13	16,20	0,48	-
11.	A20 B79 C1	20	79	1	-	7,50	31,99	0,48	-
12.	A40 B59 C1	40	59	1	-	15,00	23,90	0,48	-
13.	A79 C1 D20	79	-	1	20	29,63	-	0,48	2,88
14.	B79 C1 D20	-	79	1	20	-	31,99	0,48	2,88
15.	A59 C1 D40	59	-	1	40	22,13	-	0,48	5,76
16.	B59 C1 D40	-	59	1	40	-	23,90	0,48	5,76
17.	A59 B20 C1 D20	59	20	1	20	22,13	8,10	0,48	2,88
18.	A20 B59 C1 D20	20	59	1	20	7,50	23,90	0,48	2,88
19.	A39 B20 C1 D40	39	20	1	40	14,63	8,10	0,48	5,76
20.	A20 B39 C1 D40	20	39	1	40	7,50	15,98	0,48	5,76

* Legend to table 1:

- A - BIOPLAST GF 106/2
- B - BIOPLAST GS 2189
- C – quercetin
- D - ground walnut shells

3.2 Preparation of composite materials

Initially, the composite material granulate was produced through homogenization in a Zamak Mercator VM-30 kneader. The process was carried out in two consecutive stages. The first stage involved mixing at a paddle speed of 5 rpm at a temperature of 190 °C for 10 minutes. Next, the mixing speed was increased to 10 rpm for an additional 10 minutes.

The next stage involved forming the composite material into standardized specimens for mechanical testing. For this purpose, injection moulding technology was used with a Zamak Mercator IM-15 laboratory injection moulding machine. The process parameters are presented in Table 2. The injection temperature was increased when processing materials containing ground walnut shells to facilitate the moulding process. Two types of samples were used::

- Paddle-shaped specimens with a thickness of 2 mm for tensile testing,
- Discs with a diameter of 30 mm and a thickness of 8 mm for hardness testing.

Table 1. *Parameters of injection molding.*

Type of material	Injection temperature, °C	Form temperature, °C	Pressure, bar	Injection time, s
Materials without walnut shells	190	40	4,5	3
Materials with walnut shells	195	40	4,5	3

4. REASERCH METODOLOGY

In this study, strength tests of the manufactured composite materials were carried out, including a static tensile test and hardness testing, differential scanning calorimetry, and microscopic observation of the fracture surfaces of the samples.

The static tensile test was carried out using a Shimadzu AGX-V universal testing machine following the PN-EN ISO 527-2 standard. The test involved axial stretching of the mounted specimen until it broke. Three measurements were performed for each composite. The tensile speed was 2 mm/min. The Young's modulus and tensile strength were calculated.

The hardness testing of the produced composite materials was performed using the ball indentation method on a Zwick/Roell 3106 hardness tester in accordance with the ISO 2039-1 standard. The test specimens were discs with a thickness of 8 mm. The measurement time was 30 seconds. Hardness was automatically determined by the device.

Differential Scanning Calorimetry (DSC) was performed using a DSC3 Mettler Toledo device, operating within a temperature range of -90°C to 700°C. The tested samples, weighing between 6–10 mg, were heated at a rate of 10°C/min. The glass transition temperature was measured in the range of 20°C to 200°C. The measurement value was taken from the thermogram curves during the third heating cycle. The first two cycles were conducted to stabilize the values.

A Leica DM light microscope was also used to observe the fracture surfaces of the samples obtained from the static tensile test and examine their structure.

5. RESULTS

5.1. Static tensile test

The highest tensile strength was observed in pure Bioplast GS 2189 (Fig. 2), while the lowest was recorded for Bioplast GF 106/02 containing 40% walnut shell filler and 1% quercetin. Among the filled materials, the best results were achieved with the A20 B79 C1 composition. An increase in walnut shell content leads to reduced tensile strength due to the oversaturation of the matrix with the reinforcing phase, which introduces natural stress concentrators that disrupt the material's continuity. The addition of quercetin has a minimal effect on the composite's properties, with observed changes falling within the measurement device's margin of error.

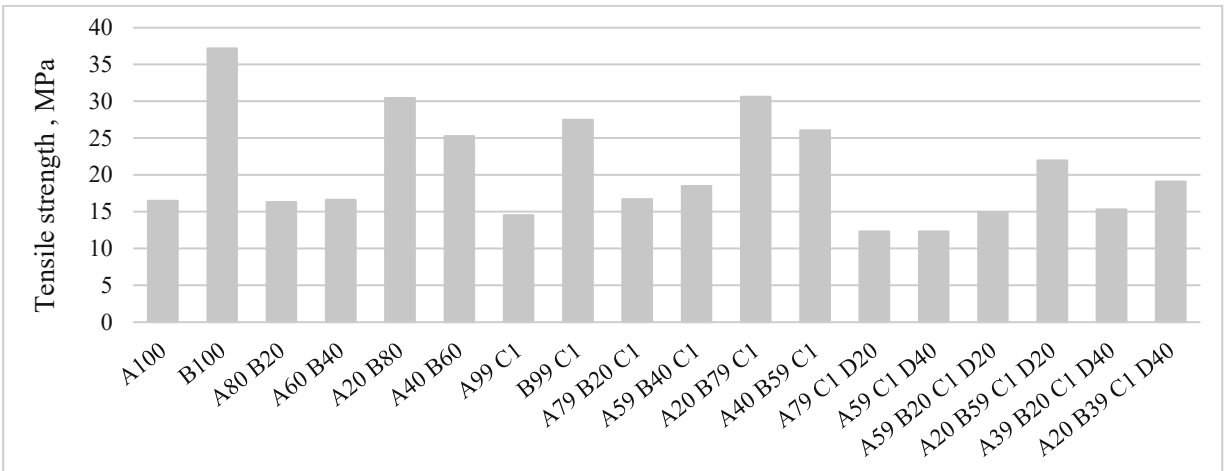

Figure 2. Tensile strength of composite materials.

The composition B99 C1 exhibited the highest Young's modulus, while the lowest was found in pure Bioplast GF 106/02. Increasing walnut shell content negatively affects this property. Among the walnut shell-filled composites, the highest value was obtained for A20 B59 C1 D20, although it was still 24% lower than that of B99 C1.

5.2. Hardness test

The hardness of the materials varies significantly depending on the type of polymer matrix used (Tab. 3). Composites with a matrix primarily composed of Bioplast GS 2189 are considerably harder than those based on Bioplast GF 106/02. Pure Bioplast GS 2189 exhibited the highest hardness among all the tested samples. The addition of a small amount of quercetin has only a slight effect on the material's hardness..

Table 2. *Results of hardness tests.*

No.	Sample name	Applied load, N	Hardness, N/mm^2	Standard deviation
1.	A100	-	-	-
2.	B100	358	87,58	1,54
3.	A80 B20	49	15,65	1,10
4.	A60 B40	49	19,43	2,10
5.	A20 B80	132	47,58	1,94
6.	A40 B60	132	33,40	3,83

7.	A99 C1	49	18,38	1,34
8.	B99 C1	132	58,95	4,17
9.	A79 B20 C1	49	12,97	2,03
10.	A59 B40 C1	49	19,83	1,13
11.	A20 B79 C1	132	48,93	5,68
12.	A40 B59 C1	132	38,08	1,33
13.	A79 C1 D20	49	14,68	0,40
14.	B79 C1 D20*	-	-	-
15.	A59 C1 D40	49	15,28	0,17
16.	B59 C1 D40*	-	-	-
17.	A59 B20 C1 D20	49	17,85	0,92
18.	A20 B59 C1 D20	132	45,58	4,36
19.	A39 B20 C1 D40	132	27,48	1,03
20.	A20 B39 C1 D40	132	45,25	3,20

5.3. Differential scanning calorimetry

As a result of the differential scanning calorimetry (DSC) analysis, it can be observed that composites composed of both bioplasts exhibit two glass transition temperatures— a lower one corresponding to Bioplast GF 106/02 and a higher one to Bioplast GS 2189 (Fig. 3). The highest glass transition temperature was recorded for the A59 B20 C1 D20 composition. The maximum safe operating temperature of the produced composite materials ranges from 100.97°C for B79 C1 D20 to 112.66°C for A20 B80. Additionally, the broadened single peak observed in figure 3 suggests improved processability of these materials. To confirm this assumption, melt flow index (MFI) testing should be performed on the selected composites.

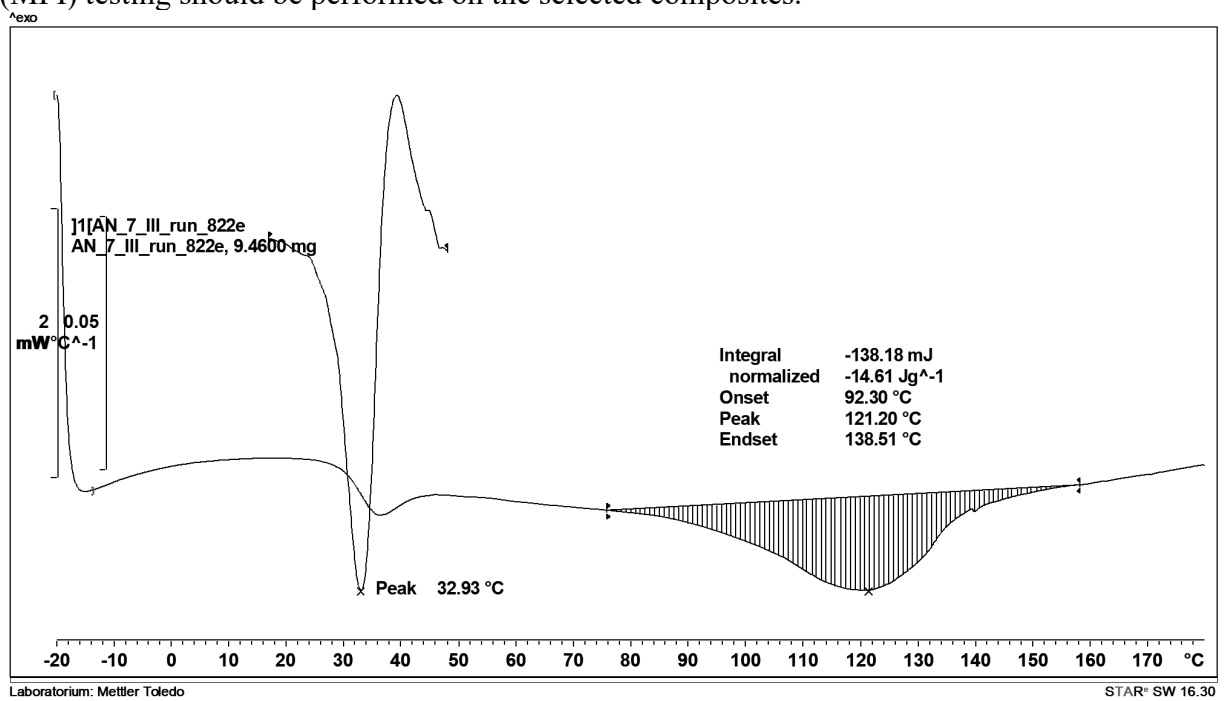

Figure 3. DSC thermogram for composite A99 C1.

5.4. Microscopic observations

In the fracture surface images, the reinforcement particles are evenly distributed within the matrix (Fig. 4a). After fracture, the break surface appears irregular, and in some samples, air bubbles formed during the injection molding process are visible (Fig. 4b).

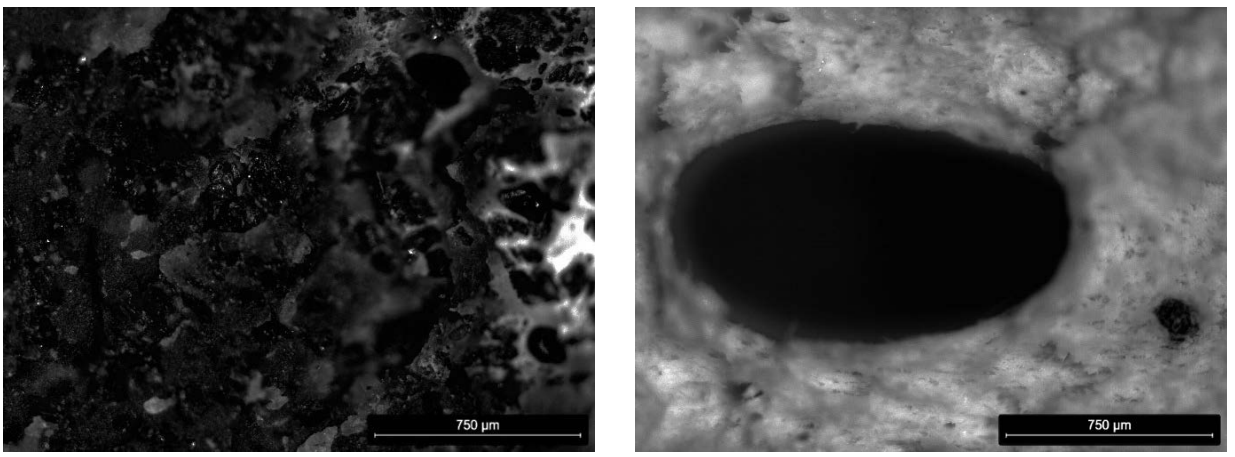

Figure 4. Fracture surface images of the composites: a) composite A59 C1 D40, b) composite A20 B79 C1

6. CONCLUSION

Due to their high costs and production challenges, biodegradable polymers are not competitive with petrochemical-based polymers. By creating composites from renewable thermoplastics with natural reinforcements, such as walnut shells and quercetin, we can improve processing properties and reduce costs in an environmentally friendly way.

The A20 B79 C1 composition demonstrated the highest tensile strength among all the produced biodegradable composite materials. Hardness testing showed that materials based on the GS 2189 bioplastic matrix are harder than those based on GF 106/02. Microscopic observations revealed a uniform distribution of the reinforcement within the matrix, along with defects such as air bubbles formed during the manufacturing process. Differential scanning calorimetry (DSC) revealed two glass transition temperatures for some composites, indicating that the bioplastics did not become compatible with each other after the homogenization process. Insufficient homogenization may negatively affect the processing of these materials, requiring operation within a narrow processing window.

ACKNOWLEDGEMENT

The present study was produced as part of the activities of the Student Science Club "HEAD TO HEAD" operating at the Department of Scientific and Didactic Laboratory of Nanotechnology and Material Technologies at the Faculty of Mechanical Engineering, Silesian University of Technology in Gliwice.

BIBLIOGRAPHY

1. Dobrzański LA., Fundamentals of Materials Science, Silesian University of Technology Publishing House, Gliwice 2012
2. https://www.businesswaste.co.uk/your-waste/packaging-waste-recycling/packaging-waste-facts-and-statistics/ (dostęp 15.04.2025)
3. PN-EN ISO 527-2 Tworzywa sztuczne - Oznaczanie właściwości mechanicznych przy rozciąganiu.Gołębiewski, J., Gibas, E., & Malinowski, R. (2008). Selected biodegradable polymers, production, properties, applications. Polymers, 53(11-12), 799-807.
4. Śledziona J., Fundamentals of Composite Technology, Silesian University of Technology Publishing House, Gliwice 1998
5. Wróbel G., Polymers and Structural Composites, Silesian University of Technology Publishing House, 2008

TalentDetector
23th-25th June 2025
Gliwice-Brenna, Poland
DEPARTMENT OF ENGINEERING MATERIALS AND BIOMATERIALS
FACULTY OF MECHANICAL ENGINEERING
SILESIAN UNIVERSITY OF TECHNOLOGY
INTERNATIONAL STUDENTS SCIENTIFIC CONFERENCE

Optimization of semiconductor layer thickness in dye-sensitized solar cells

Jakub Budzynowski[a], Oskar Górka[a], Judyta Drygała[b], Aleksandra Drygała[c]

[a] Student, Silesian University of Technology, Faculty of Mechanical Engineering, Konarskiego 18a, 44-100 Gliwice, Poland
[b] Student, Silesian University of Technology, Faculty of Architecture, Akademicka 7, 44-100 Gliwice, Poland
[c] Silesian University of Technology, Faculty of Mechanical Engineering, Department of Engineering Materials and Biomaterials, Konarskiego 18a, 44-100 Gliwice, Poland
email: aleksandra.drygala@polsl.pl

Abstract: Dye-sensitized solar cells (DSSCs) are third-generation photovoltaic devices that offer an attractive alternative to silicon-based technologies due to their simpler fabrication processes, lower production costs, and ability to operate under low-light conditions. One of the key components of a DSSC is the photoanode, which includes a semiconductor layer responsible, in particular, for transporting electrons from the dye to the conductive layer. In this work, the thickness of the semiconductor layer made of titanium dioxide was optimized. The surface topography of TiO_2 and the electrical properties of the dye-sensitized solar cell were analyzed.

Keywords: renewable energy, photovoltaics, dye-sensitized solar cells, photoanode, semiconductors

1. INTRODUCTION

Contemporary energy challenges stemming from the limited availability of fossil fuels and the urgent need to reduce greenhouse gas emissions, are accelerating the development of technologies that utilize renewable energy sources. In this context, photovoltaics—particularly novel concepts such as dye-sensitized solar cells (DSSCs), categorized as third-generation photoelectrochemical devices—has garnered significant attention [1, 2, 3].

DSSCs represent an intriguing alternative to conventional silicon solar cells due to their relatively low fabrication costs, straightforward manufacturing processes, ability to operate under diffuse or low-intensity light, and the potential for flexible device architectures. Additional advantages include the tunability of the dye sensitizer and the possibility of employing various semiconductor materials, enabling the tailoring of device properties for specific applications. However, DSSCs also present limitations, such as lower energy-conversion efficiencies compared to silicon technologies, limited long-term operational stability, and challenges related to the chemical stability of the electrolyte system [4, 5].

Structurally, a DSSC comprises several key components (Fig. 1) [6, 7]:

- **photoanode**: a substrate (e.g. glass) coated with a transparent conductive oxide (TCO) layer, onto which a mesoporous metal-oxide film—most commonly titanium dioxide—is deposited. Dye molecules are adsorbed onto the TiO_2 surface to harvest incident photons,
- **electrolyte**: typically a non-aqueous solvent containing a redox couple and additives to enhance ionic mobility, filling the interelectrode space and facilitates charge transport,
- **counter-electrode (cathode)**: a substrate (e.g. glass) coated with a TCO, onto which a catalytic layer—most commonly platinum—is deposited. This layer facilitates the reduction of the oxidized redox species in the electrolyte. Due to platinum's high cost and limited availability, carbon-based materials such as expanded graphite, carbon nanotubes, and graphene have been proposed as alternative catalysts.

The generation of electrical current in a DSSC involves several key steps: light absorption by the dye, injection of electrons into the conduction band of TiO_2, transport of charge through the external circuit, and regeneration of the dye's ground state via the redox reaction in the electrolyte [7, 8].

The significance of DSSCs in the field of photovoltaics is primarily related to their application potential in niche areas such as building-integrated photovoltaic systems, portable devices, and smart windows. Although these devices do not directly compete with silicon solar cells in terms of efficiency or long-term stability, their unique properties such as visual aesthetics, semitransparency, and performance under low-light conditions – make them well-suited for applications where conventional solutions are less effective or impractical [9,10]. In this study, the influence of the TiO_2 semiconductor layer thickness on the electrical properties of dye-sensitized solar cells was investigated.

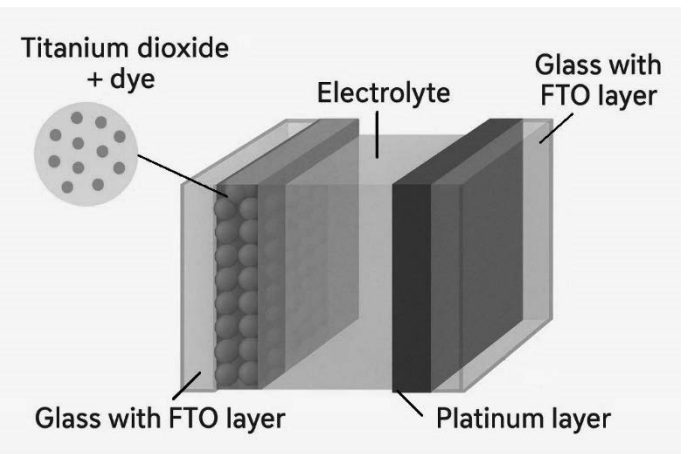

Figure 1. Scheme of the dye-sensitized solar cell structure [6, 7]

2. MATERIALS AND METHODS

Dye-sensitized solar cells were fabricated with one, three, and five semiconductor layers of TiO_2. Glass substrates (25 × 25 mm, 7 Ω/□) supplied by Sigma-Aldrich were used. The substrates were cleaned sequentially in a detergent solution and ethanol in an InterSonic IS-5.5 ultrasonic bath. After each cleaning step, the substrates were dried with compressed air prior to TiO_2 deposition via screen printing, using GreatCell Solar's 18NR-T Titania Paste and a Printing

Machine MS 300 FRO printer. Between successive printing steps, the samples were stabilized for 15 minutes, then dried in a Pol-Eko SLW53STD oven at 105 °C for 5 minutes.

For counter-electrode preparation, a platinum layer was screen-printed onto fluorine-doped tin oxide (FTO)-coated glass substrates and dried under the same conditions (100 °C, 5 minutes). All printed layers were subsequently sintered at 500 °C for 30 minutes in a Nabertherm P330 furnace. The photoanodes were immersed in GreatCell Solar's synthetic N719 dye for 24 hours, after which excess dye was removed with ethanol.

To estimate the semiconductor layer thickness, photoanodes were fractured at the printed area. Surface and cross-sectional topographies of the photoanode were examined by scanning electron microscopy (SEM) using a Zeiss Supra 25 instrument in InLens mode at an accelerating voltage of 3 kV. The photoanode and counter-electrode were assembled into a cell, and EL-HPE electrolyte was introduced between the electrodes. The electrical properties of the fabricated DSSCs was characterized by current–voltage measurements under simulated solar illumination using a Photo Emission Tech Solar Simulator (model SS150AAA). Prior to testing, the system was calibrated against a reference solar cell.

3. RESULTS

In this study, photoanodes with one, three, and five TiO_2 semiconductor layers—with an active area of 0.42 cm^2—were prepared. Macroscopic observations of the photoanodes before and after dye sensitization (Figs. 2 and 3) revealed that increasing the number of printed layers results in reduced transparency of photoanode Following sensitization, the color of the TiO_2 layer changes from milky white to burgundy. After the deposition of five layers, it becomes non-uniform, with visible defects, indicating insufficient adhesion to the substrate.

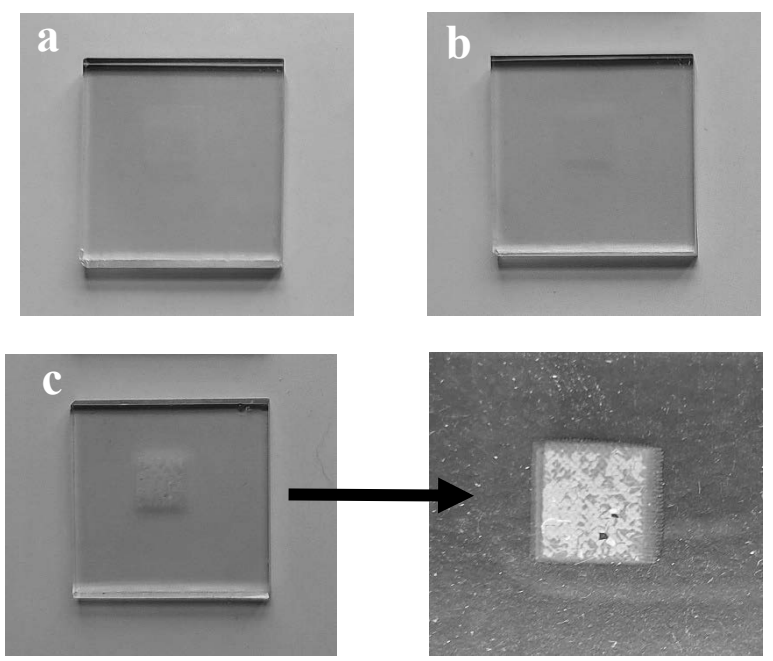

Figure 2. FTO coated glass with a) one b) three c) five printed TiO_2 layers before dyeing

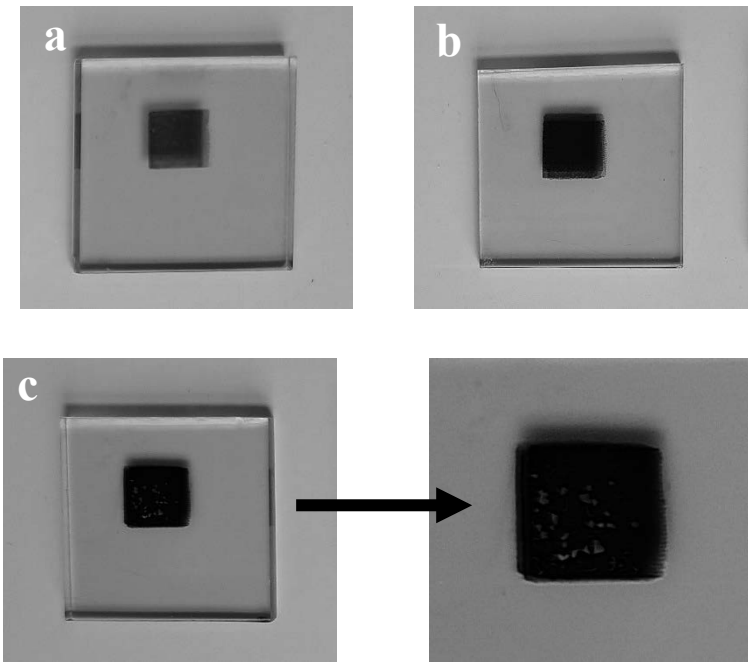

Figure 3. FTO coated glass with a) one b) three c) five printed TiO_2 layers after dyeing

Figure 4 presents the surface topography of the photoanode at the interface between the deposited titanium dioxide layer and the conductive FTO film. Characteristic grains of fluorine-doped tin oxide (FTO) with irregular shapes and sizes not exceeding 270 nm were observed. The screen-printed titanium dioxide layer exhibits a granular morphology, with TiO_2 nanoparticles forming randomly distributed agglomerates.

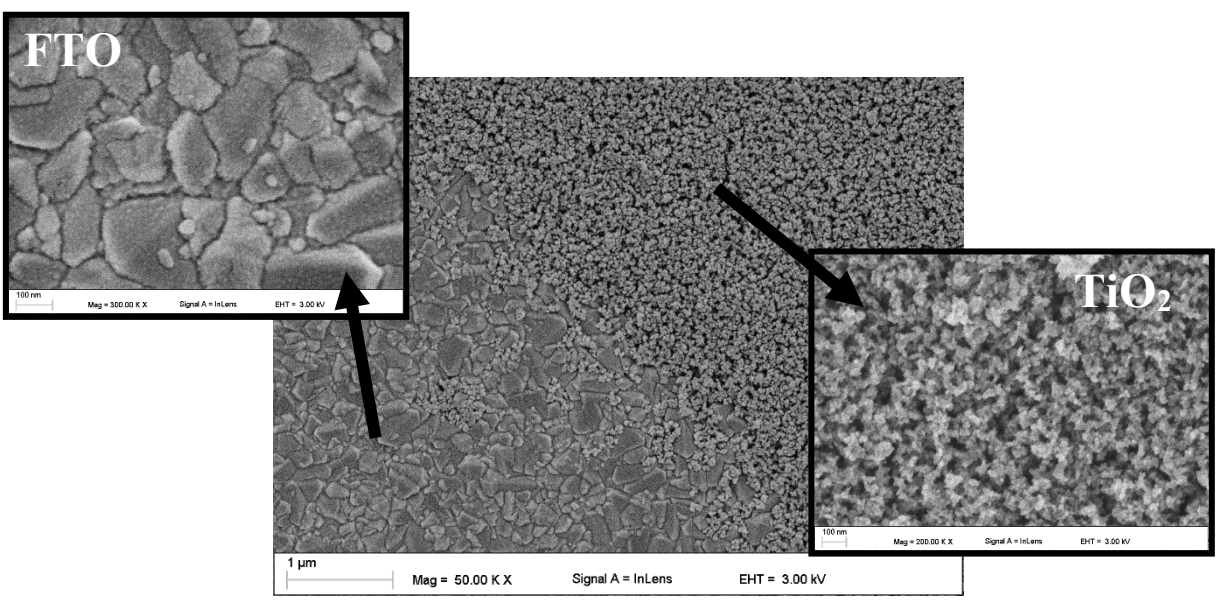

Figure 4. Surface topography of DSSC photoanode (SEM)

Figures 5–7 show the cross-sections of photoanodes containing one, three, and five deposited TiO_2 layers. The FTO layer thickness is approximately 550 nm, consistent with the manufacturer's specification. Regardless of the number of print passes, the titanium dioxide layer maintains a porous structure, which facilitates efficient adsorption of the dye responsible for light harvesting. It was observed that the thickness of the semiconductor film increases proportionally with the number of print cycles: one, three, and five layers yielded film thicknesses of approximately 4.05 µm, 12.11 µm, and 18.7 µm, respectively.

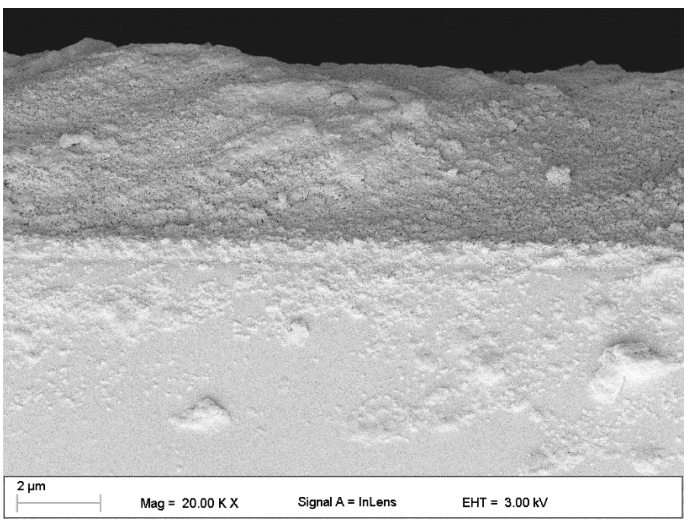

Figure 5. Cross section of photoanode with one printed layer of TiO_2 (SEM)

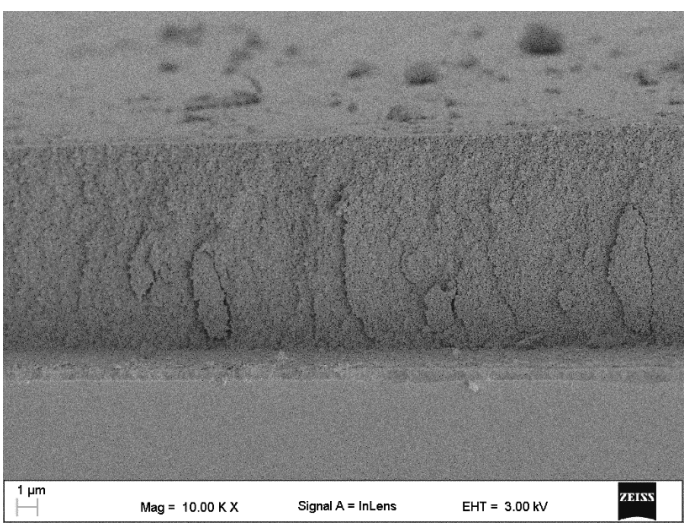

Figure 6. Cross section of photoanode with three printed layers of TiO_2 (SEM)

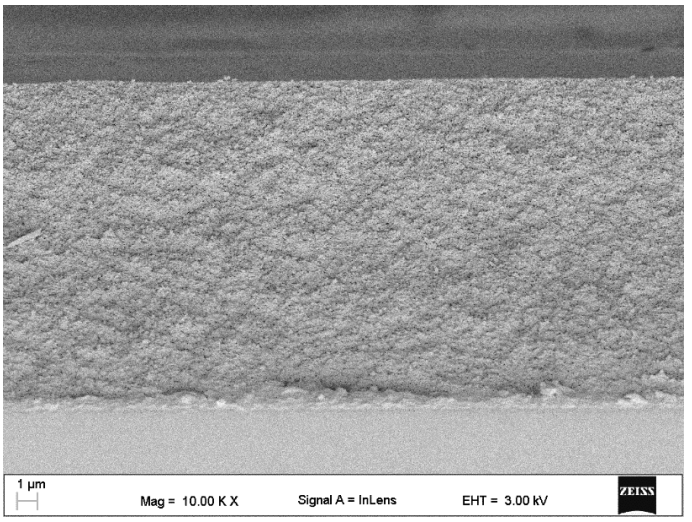

Figure 7. Cross section of photoanode with five printed layers of TiO_2 (SEM)

Table 1 summarizes the electrical properties of the TiO_2-based dye-sensitized solar cells as a function of semiconductor-layer thickness. The highest power-conversion efficiency (4.76 %) was obtained for the device with three printed layers (about 12.11 µm). In comparison to the DSSC with only one printed layer, a slight increase in open-circuit voltage (U_{oc}) by 8 mV was observed, along with a significant increase in short-circuit current (I_{sc}) by 2.57 mA. As a result, the cell exhibits higher efficiency and maximum power output. However, it is characterized by the lowest fill factor (FF), equal to 0.46. The dye-sensitized solar cell with five printed layers demonstrated the lowest performance among all tested devices. This is most likely due to the excessive thickness of the semiconductor layer, which led to the formation of cracks and weakened adhesion to the substrate. Furthermore, it was observed that increasing TiO_2 layer thickness significantly enhances the short-circuit current with only negligible variations in open-circuit voltage.

Table 1. Electrical properties of DSSCs base on photoanode with different number of TiO_2 printed layers, where I_{max} – current at the P_{max}, U_{max} – voltage at the P_{max}

Liczba nadrukowanych warstw	I_{sc} [mA]	U_{oc} [mV]	P_{max} [mW]	FF [-]	η [%]
1	3.87	671.10	1.34	0.52	3.20
3	6.39	679.10	2.01	0.46	4.76
5	2.64	660.30	0.85	0.49	2.02

4. CONCLUSIONS

Although DSSCs do not match silicon solar cells in terms of efficiency and long-term stability, their unique attributes—such as aesthetic appeal, semi-transparency, and high performance under low light condition—make them well suited for applications where conventional technologies are less effective or impractical. In this work, the thickness of the semiconductor layer was

optimized. On one hand, a thicker layer allows adsorption of a greater amount of dye; on the other hand, it impedes charge transport. Analysis revealed that titanium dioxide nanoparticles form numerous agglomerates with irregular shapes. The thickness of a single screen-printed TiO_2 layer was estimated at approximately 4.05 μm. The deposition of five layers led to extensive defects and insufficient adhesion. The highest efficiency, 4.76 %, was achieved for DSSCs employing a photoanode with three printed semiconductor layers.

BIBLIOGRAPHY

1. Źródła energii w Polsce (2023), ZPE, https://zpe.gov.pl/a/zrodla-energii-w-polsce/DZ9m3Dvd0, 2025r.
2. E. Klugmann-Radziemska, Technologiczny postęp w fotowoltaice, Czysta energia, 5 (2014).
3. M. Davykoza, R. Szafran, Barwnikowe mikroogniwa fotowoltaiczne, Zeszyty Energetyczne, VII (2020) 429-440.
4. Y. Ren, D. Zhang, J. Suo, Y. Cao, F. T. Eickemeyer, N. Vlachopoulos, S. M. Zakeeruddin, A. Hagfeldt, M. Grätzel, Hydroxamic acid pre-adsorption raises the efficiency of cosensitized solar cells, Nature 613 (2023) 60-65.
5. A. Garwol, (2024), Możliwości rozwoju technologii wytwarzania energii elektrycznej za pomocą modułów fotowoltaicznych, Journal of Konbin, 54, 3 (2024), 27-40.
6. E. Schab-Balcerzak, P. Gnida, Modyfikacje ogniw barwnikowych w kierunku poprawy ich sprawności, Przegląd Elektrotechniczny, 10 (2023) 247-250.
7. K. Siuzdak, M. Klein, K. Łapiński, A. Cenian, Barwnikowe ogniwa słoneczne, Rynek energii, 5 (2015) 75-83.
8. K. Dyndał, G. Lewińska, K. Marszałek, Generacje ogniw fotowoltaicznych, Fotowoltaika, Wydawnictwo Akademii Górniczo-Hutniczej, Kraków, 2021.
9. D. Czułyt et al., Obserwacje makro- i mikroskopowe fotoanody barwnikowego ogniwa słonecznego, TalentDetector2023_Summer: International Students Scientific Conference, Brenna, Poland, 26th June 2023, Bonek Mirosław (*red.*), Prace Katedry Materiałów Inżynierskich i Biomedycznych, 2023, Gliwice, Politechnika Śląska, (2023) 184-192.
10. K. Barczak et al., Wpływ grubości warstwy półprzewodnikowej na własności optoelektryczne barwnikowych ogniw fotowoltaicznych, TalentDetector2023_Summer: International Students Scientific Conference, Brenna, Poland, 26th June 2023, Bonek Mirosław (*red.*), Prace Katedry Materiałów Inżynierskich i Biomedycznych, 2023, Gliwice, Politechnika Śląska, (2023) 41-48.

TalentDetector

23th-25th June 2025
Gliwice-Brenna, Poland

DEPARTMENT OF ENGINEERING MATERIALS AND BIOMATERIALS
FACULTY OF MECHANICAL ENGINEERING
SILESIAN UNIVERSITY OF TECHNOLOGY

INTERNATIONAL STUDENTS SCIENTIFIC CONFERENCE

The Effect Of Magnetic Field On Welding Arc Field During Sheet Metal Welding

Berranur Ceker[1], Sezai Kunan[1], Murat Mat[1], Cemal Meran[2]

[1]Student, Pamukkale University, Faculty of Engineering, Department of Mechanical Engineering, Denizli, Turkey
[2]Prof.Dr., Pamukkale University, Faculty of Engineering, Department of Mechanical Engineering, Denizli, Turkey, cmeran@pau.edu.tr

Abstract: This study experimentally investigated the use of magnets for workpiece clamping as an alternative to traditional mechanical clamps in welding processes, regarding the effects of the induced magnetic field on arc behaviour and weld quality. Parameters such as magnet position, torch-to-magnet distance, welding current and arc length were systematically evaluated. The results showed that the position of the magnet relative to the welding axis is a critical factor in arc deflection. These findings provide essential control parameters for the effective implementation of magnet-assisted clamping systems, thereby improving weld quality and production efficiency.

Keywords: Arc Welding, Ark Blow, Magnet, Weld Quality, Magnetic Field.

1. INTRODUCTION

Welding technologies are widely used across various industrial sectors, including manufacturing, construction, automotive and shipbuilding. They are one of the fundamental pillars of industrialisation. Arc welding is a particularly effective and widely adopted method of joining two metal components by converting electrical energy into heat. The electric arc is at the core of the welding process and directly influences weld quality and overall process efficiency. However, instabilities in the arc, particularly arc blow, can adversely affect the reliability of the welding operation and the mechanical properties of the final product.

Arc blow is defined as the deflection of the arc's linear trajectory due to external influences. This often results in weld defects, inadequate penetration and structural irregularities. The primary cause of such deviations is the presence of magnetic fields in the welding zone. The interaction between the welding current and the workpiece's geometric and magnetic properties can lead to arc deflection, which makes the process more difficult to control and contributes to quality issues, particularly in automated welding systems. This study investigates the influence

of magnetically induced arc blow on the arc zone and explores ways to optimise arc blow behaviour by adjusting specific parameters.

2. ARC WELDING AND ARC BLOW

The effects of magnetic fields on welding processes have been studied extensively for many years, revealing that this interaction varies depending on material type, welding current level, workpiece geometry, and magnetization. Particularly in ferromagnetic metals, significant arc deflections can occur due to magnetic forces during welding. These deviations often lead to production errors, rework requirements, and consequently, waste of time, labor, and materials. The influence of external magnetic fields on both the weld seam and the heat-affected zone (HAZ) has been clearly demonstrated, especially in MAG welding processes involving test plates of 10–15 mm thickness, where the highest penetration and lowest hardness values were observed at around 20 gauss. An increase in magnetic field intensity was found to decrease HAZ hardness, highlighting the impact of magnetic fields on the mechanical properties of welds [1].

Research on the parameters used in electric arc welding methods has shown that process variables such as welding speed, current intensity, electrode diameter, groove geometry, and welding position significantly affect weld quality and performance. As the arc length increases, so does the arc voltage, leading to irregular and shallow welds, higher spatter, and an increased risk of arc blow. The electrode travel angle also plays a crucial role in arc blow, and managing these parameters carefully is essential to minimize welding defects such as cracking, fracture, and separation [2].

In addition, the technical parameters of arc welding machines have been extensively analyzed regarding their effects on weld seam geometry and quality. Experimental studies have shown that current and voltage values are decisive for weld width, depth, and penetration, while welding speed and electrode diameter significantly influence seam geometry. These findings underscore the critical role of optimizing machine parameters to enhance the mechanical strength and quality of welds [3].

When evaluating the mechanical properties of different welding methods used in ship steel joining, it has been observed that arc blow during arc welding significantly affects weld pool shape and seam smoothness. Controlling arc length has emerged as a key parameter for ensuring weld quality and structural integrity. These findings highlight the need for careful parameter selection in critical applications such as shipbuilding [4].

Similarly, studies on various welding methods in shipbuilding have shown that arc blow disrupts arc stability, leading to quality issues in the weld seam. Arc deflection due to magnetic fields can result in weld shape irregularities, ultimately compromising material strength and hardness in ship structures [5].

In conclusion, the effects of magnetic fields on arc behavior during welding are complex and multidimensional. Parameters such as welding current, travel speed, wire feed rate, magnet location, torch-to-magnet distance, and magnet strength must be experimentally investigated, and the relationships among these variables should be systematically established. Based on the resulting data, the underlying causes of arc blow can be better understood, and practical solutions can be developed to control this phenomenon. Such studies offer valuable contributions to both academic research and industrial practice by improving weld quality, enhancing process efficiency, and reducing overall production costs. Ultimately, welding operations can become more reliable, effective, and sustainable.

2. MATERIAL AND METHODS

In this study, the effect of magnetic fields on the welding arc during sheet metal arc welding was investigated experimentally. Gas Metal Arc Welding (GMAW) was performed on standard sheet metal specimens. The study was conducted in two main phases: In the first phase, welding parameters were kept constant while the position of the magnet and the direction of the magnetic field were varied. In the second phase, the magnet position was fixed, and parameters such as welding current, voltage, and travel speed were altered.

Arc deflection, weld seam quality, and penetration depth were evaluated through visual inspection and measurements. Based on the findings, appropriate welding setups and process parameters were identified to mitigate the effects of the magnetic field.

To assess the influence of magnetic fields, magnet models with load capacities of 100 kg and 1000 kg were used. These magnets, with pulling forces of 100 kgf (980 N) and 1000 kgf (9800 N), were positioned at different angles to observe arc deflections [6]. The magnets were also utilized for clamping the workpieces, and their effects on the welding process were evaluated. Photographs of the 100 kg and 1000 kg magnets used in the experiments are presented in Figure 1.

Figure 1. The 100 and 1000 kg magnetic lifters used for clamping during welding experiments [8].

The welding operations were carried out using industrial welding automation systems, which offer high precision and repeatability. The robotic welding application enabled control over the arc behavior under varying magnetic field conditions. The welding machine used during the experiments is shown in Figure 2.

Figure 2. The welding robot used during the experiments.

Another device used during the experiments was the gaussmeter. The gaussmeter is a fundamental instrument used to measure the intensity of magnetic fields. It determines the magnitude of the field by detecting the induction generated by the magnetic field on a fine wire coil. The magnetic field measurement device used in this study is equipped with a Hall effect probe and is capable of performing precise measurements within the range of 0–1999 mT. The measurement results are critical for investigating the effect of the magnetic field on the welding arc. The gaussmeter used during the experiments is shown in Figure 3.

Figure 3. Gaussmeter used for magnetic field measurement during the experiments.

3. EXPERIMENTAL RESULTS

The artificial magnetic field was generated using industrial magnets with lifting capacities of 100 kg and 1000 kg, available within the company where the experiments were conducted. These magnets created different magnetic field intensities, thereby producing an artificial magnetic effect on the test specimen during the welding process. A high-precision gaussmeter was employed to measure the applied magnetic field. Magnetic field intensity measurements on all test pieces were performed along the welding axis and at a 5 mm distance from the torch, as well as 3 mm above the surface of the test plate. During the measurements, the Hall probe was positioned both perpendicular and parallel to the magnetic flux lines; in each position, measurements were repeated with small angular adjustments until the maximum value was recorded. The placement of the probe within the experimental setup and its position relative to the magnets are illustrated in Figure 4.

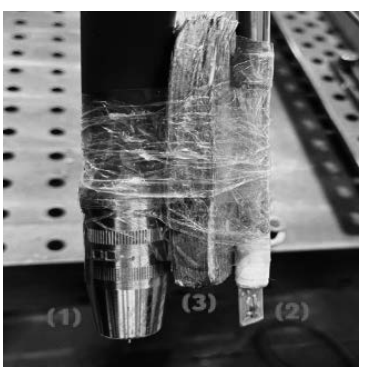

Figure 4. (1) Welding torch, (2) Gaussmeter probe, (3) Fixing clamp.

In the initial experimental phase, it was observed that increasing the welding speed under the artificial magnetic field led to a reduction in heat input and the amount of molten metal, which consequently decreased the weld seam height. Additionally, arc deflection diminished, and spatter formation was minimized. Higher welding speeds mitigated the adverse effects of the magnetic field, thereby enhancing weld quality. The welding image related to this experiment is presented in Figure 5.

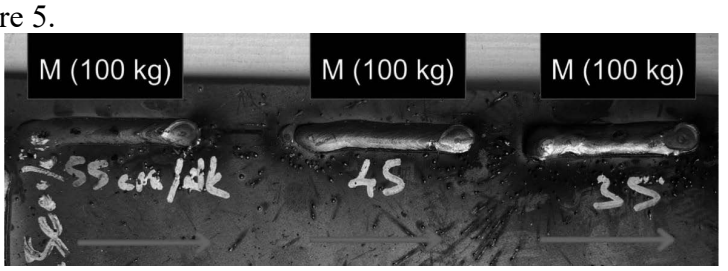

Figure 5. The weld seam image obtained from the variable welding speed experiment.

In the second phase of the experiment, the position of the magnet was evaluated. Within Scenario 1, the operator aligned the welding torch to move directly toward the center of the magnet placed on the plate, effectively aligning the torch with the direction of the magnetic field. In this configuration, no significant arc deviation was observed, and the weld seam quality was maintained, allowing the welding process to be completed safely and in a controlled manner. The corresponding weld image is presented in Figure 6.

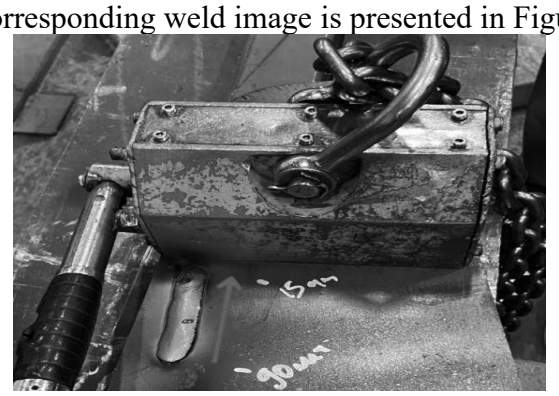

Figure 6. Weld seam image obtained during the approach toward the magnet placed on the plate.

Within Scenario 2, the magnet was placed on the side surface of the plate, and no significant deviation in the weld seam was observed. However, spatter blow in the direction of the magnet occurred, and the magnetic field strength was measured to be approximately 13.80 mT. Although the overall weld quality was maintained, it is recommended to be cautious of spatter accumulation. The corresponding weld image is presented in Figure 7.

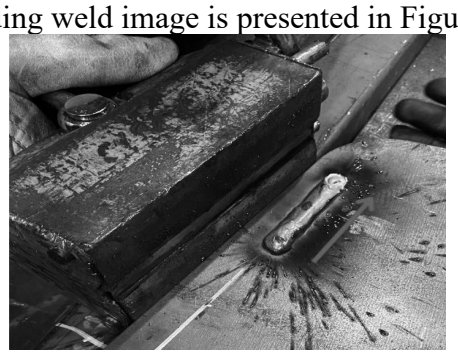

Figure 7. Weld seam image obtained with the magnet positioned horizontally along the thickness (side) of the plate.

In Scenario 3, due to the direct intersection of the welding path by the opposite poles of the magnet, the magnetic field was oriented perpendicularly along the welding arc, resulting in a noticeable deviation and an unstable weld seam. Both attraction and arc blow effects were observed, with the magnetic field strength reaching 19.03 mT, adversely affecting weld stability. This configuration significantly reduced weld quality and is therefore not recommended. The related weld image is presented in Figure 8.

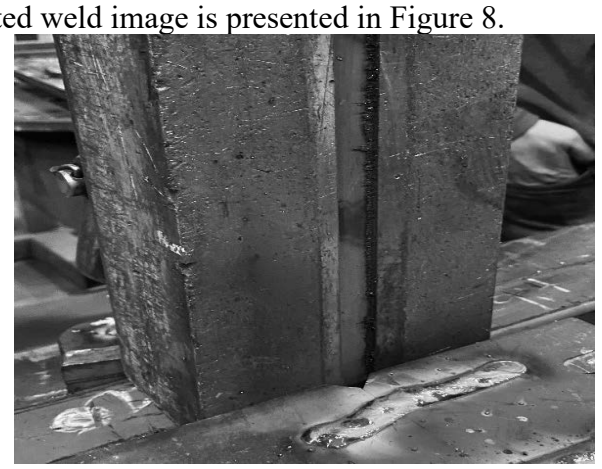

Figure 8. Weld seam image obtained during welding with the magnet positioned vertically on the side (thickness edge) of the plate.

In Scenario 4, placing the magnet on the bottom surface of the plate prevented the welding process from proceeding properly. The arc was deflected downward, no weld seam was formed, and surface integrity could not be achieved. The magnetic field strength was measured at 15.7 mT, and this configuration caused significant instability in the welding process. Positioning the magnet on the underside of the workpiece is not recommended due to its negative impact on process safety and weld quality. The corresponding weld seam image is presented in Figure 9.

Figure 9. Weld seam image obtained during welding with the magnet positioned beneath the plate.

In the third experimental phase, the distance-dependent effect of the magnetic field was investigated comparatively. Throughout the experiment, the magnet's position remained unchanged; it was placed horizontally on the side surface of the plate with its attracting face aligned parallel to the welding direction. The distance between the torch and the magnet was

evaluated across four scenarios, gradually reduced to 80 mm, 60 mm, 40 mm, and 20 mm, respectively. The resulting weld seam images are presented in Figure 10.

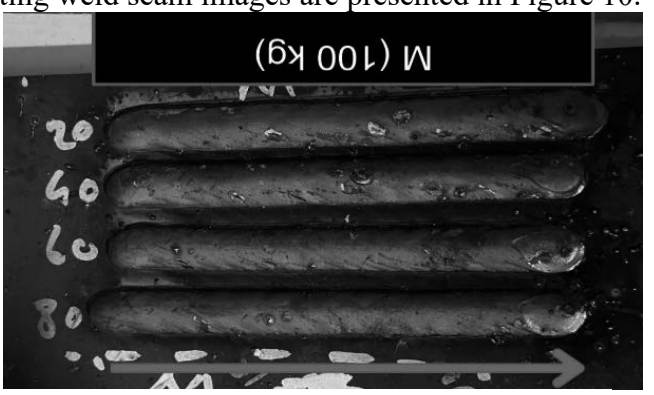

Figure 10. Weld seams obtained at varying distances from the magnet.

In the fourth experimental phase, the effects of different electrode extension lengths on weld quality under an artificial magnetic field were investigated. The most stable and deviation-free result was obtained with a wire extension of 16 mm, during which the magnetic field values remained within safe limits (before: 9.72 mT, during: 13.71 mT). At 20 mm, arc deflection was observed at the beginning but gradually decreased as welding progressed. At 26 mm, significant deflection and disruption of weld seam integrity occurred. Overall, as wire extension increased, initial arc deflection tended to rise, but this effect diminished over time with increased heat input. The 16 mm extension emerged as the most suitable value for optimal performance. The corresponding weld seam images are presented in Figure 11.

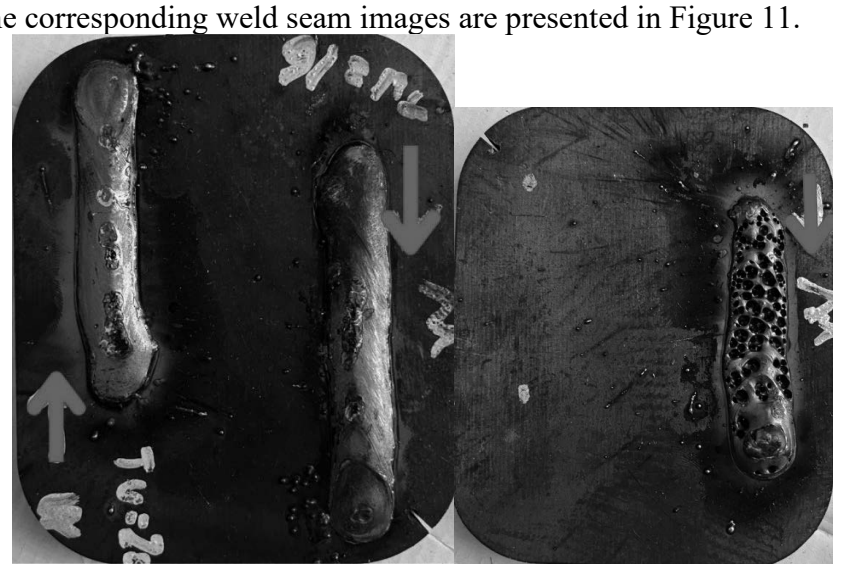

Figure 11. Appearance of arc welding seams at 16 mm, 20 mm, and 26 mm wire extensions in the variable wire length experiment.

In the fifth experimental phase, an increase in current was observed, resulting in higher wire feed rate and melting rate. This contributed to a more stable molten pool, significantly reducing spatter, particularly at 266 A. The reinforcement height decreased with the rising current, reaching 2.0 mm at 266 A, producing a flatter and mechanically preferred weld profile. Gaussmeter measurements confirmed that the magnetic field remained below 9 mT before welding and under 14 mT during welding, indicating the system operated within magnetic limits. These findings suggest that the magnet did not create a critical threshold causing

magnetic deflection; however, the magnetic field increased with current. Consequently, an appropriate current increase under artificial magnetic fields reduced weld spatter and improved arc stability, while maintaining magnetic field strength within safe limits. The weld image for this experiment is presented in Figure 12.

Figure 12. Weld seams obtained at different current levels.

4. CONCLUSION

Based on these results, when performing welding operations under artificial magnetic fields, the positioning of the magnet must be carefully planned as a priority. Other parameters should then be optimized within appropriate limits to complement overall weld quality. A general assessment of the parameters reveals the following:

- Most influential parameter on the welding process: Magnet position
- Second most influential parameter: Distance between the torch and the magnet
- Moderately influential parameters: Welding speed and current intensity
- Least directly influential, but significant at the beginning of the process: Wire extension (arc length)

The experimental study successfully reduced arc deflection—one of the most critical issues affecting quality in the manufacturing process. As a result, labor costs were reduced and production quality was improved, enhancing customer satisfaction and creating opportunities to expand market share.

BIBLIOGRAPHY

1. Türkocağı, İ. "MAG kaynak yönteminde dış manyetik alanların kaynak dikiş formuna ve ITAB'a etkisi", Doctoral Thesis, Institute of Science, İstanbul Teknik University, İstanbul, 1991.
2. Uslu, S. "Ark kaynak parametrelerinin optimizasyonu", Master's Thesis, Institute of Science, Sakarya University, Sakarya, 2010.
3. Bişmişer, G. "Elektrik ark kaynak makine özelliklerinin kaynak dikiş geometrisi üzerindeki etkileri", Master's Thesis, Institute of Science, Marmara University, İstanbul, 2001.
4. Süzen, A. "Gemi saclarının kaynak bağlantılarında kaynak parametrelerinin dikiş geometrisine etkisinin incelenmesi", Master's Thesis, Institute of Science, Sakarya University, Sakarya, 2009.
5. Asarkaya, M. "Gemi inşasında kullanılan kaynak yöntemlerinin mekanik özelliklere etkisi", Master's Thesis, Institute of Science, Sakarya University, Sakarya, 2006.
6. Netlift. General Introduction Catalog [Promotional Brochure]. https://www.netlift.com.tr/Uploads/GenelDosya/genel-netlift-3099-d.pdf, 2025.

TalentDetector
23th-25th June 2025
Gliwice-Brenna, Poland
DEPARTMENT OF ENGINEERING MATERIALS AND BIOMATERIALS
FACULTY OF MECHANICAL ENGINEERING
SILESIAN UNIVERSITY OF TECHNOLOGY
INTERNATIONAL STUDENTS SCIENTIFIC CONFERENCE

Innovative laser surface treatment technology for engineering materials

Julia Chudy [a], Bartosz Filip [a], Szymon Szeja [b], Kacper Krysiak [b], Katarzyna Furman [a], Mirosław Bonek [c], Eva Tillova [d]

[a] Student, Silesian University of Technology, Faculty of Mechanical Engineering, Department of Engineering Materials and Biomaterials
email: julichu884@polsl.pl, bf313885@student.polsl.pl, katafur136@student.polsl.pl
[b] Student, Silesian University of Technology, Faculty of Electrical Engineering:
email: kacpkry923@student.polsl.pl, szymsze085@student.polsl.pl
[c] Silesian University of Technology, Faculty of Mechanical Engineering, Department of Engineering Materials and Biomaterials
[d] University of Žilina, Faculty of Mechanical Engineering, Department of Materials Engineering

Abstract: The purpose of this study was to try to remelt the surface layer of HS6-5-3-8 high-speed steel using laser power: 0.7 kW, 1.4 kW, 1.7 kW and 2.1 kW. Subsequently, the chemical composition was analyzed and changes in the material's structure were evaluated. In addition, hardness measurements, surface roughness and microstructure analysis were performed.

Keywords: materials, laser treatment, high speed steels

1. INTRODUCTION

High speed steels are a unique group of tool steels, characterized by their high alloying element content, ledeburitic structure after casting, and special heat treatment to achieve secondary hardness. Although they make up a small percentage of the world's steel production, their technical importance remains high due to their unique properties - high hardness, wear resistance and high hardenability and ductility. Originally used in machining tools, today they are also used in machine components where high durability is required. The emergence of high-speed steels in the early 20th century revolutionized the metalworking industry, and the following decades brought intensive development in chemical composition, manufacturing technology and heat treatment. Scientific research has optimized both their properties and production costs. Nowadays, there are also efforts to unify them within the framework of international standards.

The purpose of this paper is to study the effect of laser remelting and alloying of the surface layer of high-speed steel on its structure, hardness, roughness and chemical composition.

1.1. Characteristics of high-speed steels HS6-5-3-8

HS6-5-3-8 steel has a higher carbon content and high cobalt content, so it has excellent hardness, wear resistance and high-temperature capability. Due to the presence of tungsten, molybdenum and vanadium, the steel exhibits a secondary hardness effect, and the addition of cobalt improves thermal conductivity and structural stability during tempering. The chemical composition is shown in Table 1 [1].

Table 1. Chemical composition of HS6-5-3-8 steel (according to PN-EN ISO 4957:2002)

Steel grade	C [%]	Cr [%]	W [%]	Mo [%]	V [%]	Co [%]	Si [%]	P [%]	S [%]
HS6-5-3-8	1.28	4.2	6.3	5.0	3.0	8.4	1.09	0,015	0,010

1.2. Heat treatment of HS6-5-3-8 steel

Heat treatment of HS6-5-3-8 steel included an austenitizing process carried out in a salt bath furnace and a two-stage tempering in a chamber furnace under a protective atmosphere of argon. The samples were heated in stages, performing isothermal stops at 650°C and 850°C, each lasting 15 minutes. Austenitizing was then carried out at 1180°C for 30 minutes, after which the samples were cooled in hot oil. After quenching, the material was tempered twice - each cycle lasting 2 hours at 560°C. Detailed heat treatment parameters are shown in Table 2 [2]. After heat treatment, the samples were sandblasted and machined on a magnetic grinder.

Table 2. Heat treatment conditions of the tested steel.

Type of operation	**Conditions of operation**	**Temperature, °C**	**Time, h**
Annealing	Annealing was performed in a chamber furnace with a protective atmosphere of argon, followed by cooling with the furnace.	800	8
Hardening	Austenitizing was carried out in salt bath furnaces using step heating at 650ºC and 850ºC for 15 minutes; continuous cooling in hot oil (110ºC).	1180	0,5
Tempering	Double tempering was performed in a chamber furnace with an argon protective atmosphere.	560	2x2

2. LASERS – OPERATING PRINCIPLES, DEVELOPMENT HISTORY, STRUCTURE AND PROPERTIES OF LASER RADIATION

Lasers (Light Amplification by Stimulated Emission of Radiation) operate based on quantum processes involving the interaction between electromagnetic radiation and matter. The fundamental concept is the stimulated emission of photons when atoms or molecules in an excited state are induced to release energy by incoming photons of the same energy level.

In a laser medium, energy is supplied to elevate electrons from a lower energy level (E_0) to a higher one (E_1). These excited electrons can return to the ground state spontaneously

(spontaneous emission) or by stimulated emission, which is the basis of laser action. During stimulated emission, a photon of specific energy ($\Delta E = h\nu$) interacts with an excited atom and causes the emission of another photon with the same phase, direction, frequency, and polarization.

A necessary condition for laser generation is achieving a population inversion, where more atoms occupy the excited state than the ground state. This is typically accomplished through various pumping mechanisms such as electrical discharge, optical pumping, or chemical reactions.

The emitted photons are then amplified within an optical resonator composed of two mirrors. One mirror is fully reflective, while the other is partially transparent to allow coherent laser light to exit the system. The constructive interference of the reflected photons results in a coherent and focused beam of high intensity.

3. PREPARATION OF SAMPLES

Samples made of HS6-5-3-8 steel, which were subjected to standard heat treatment and laser remelting, were cut perpendicular to the remelting direction using a Discotom-2 device by Struers (Figure 1). The cutting disc was water-cooled.

The cut samples were hot-mounted in a thermosetting resin for 12 minutes—7 minutes of heating the resin and 5 minutes of cooling the samples. Metallographic specimens were prepared by grinding with abrasive papers and mechanically polishing with diamond pastes using Struers equipment, and then etched using reagents. The etching time was selected experimentally for each type of surface layer of the examined material.

Figure. 1. Struers Discotom-2 cutting machine and Struers LaboPol-5 grinding and polishing machine

Table 3. Chemical Composition of the Etchants Used

No.	Chemical Composition of Etchant and Etching/Polishing Conditions	Application of the Etchant
1	5 cm^3 nitric acid and 100 cm^3 ethyl alcohol; temperature 20°C, time 5–20 s	Chemical etching of metallographic specimens; reveals structure and grain boundaries of primary austenite

2	490 cm³ orthophosphoric acid, 50 g chromic acid anhydride, and 5 cm³ sulfuric acid; temperature 20°C, time 2–4 s, voltage 30 V, current density approx. 6 A/cm²	Electrolytic polishing of thin foils using a modified Bolmann method
3	50 cm³ perchloric acid and 1000 cm³ glacial acetic acid; temperature 12°C, time 5–15 s, voltage approx. 20 V, current density approx. 3 A/cm²	Jet electrolytic polishing of 3 mm diameter discs using a Tenupol device

4. STUDY DESCRIPTION

The research was conducted on cobalt high-speed steel with increased carbon content, grade HS6-5-3-8, with a composition compliant with the PN-EN ISO 4957:2002 standard.

Fig. 2 Shape and dimensions of the sample used for laser surface remelting.

4.1 Heat treatment of HS6-5-3-8 steel

The heat treatment of HS6-5-3-8 steel involved austenitizing the samples in a salt bath furnace and tempering in a chamber furnace under a protective argon atmosphere. The samples were gradually heated to the austenitizing temperature, with isothermal holding at 650°C and 850°C for 15 minutes. Austenitizing was performed at 1180°C for 30 minutes, followed by hot oil quenching. Post-hardening, the samples were double-tempered, each cycle lasting 2 hours at 560°C. After heat treatment, the samples were sandblasted and mechanically finished on a magnetic grinder.

4.2 Laser remelting process of high-speed steel

High-power HPDL Rofin DL 020 diode laser was used for remelting the tested steel. This high-power, versatile device is commonly used in materials engineering for cladding, welding, remelting, and surface alloying.

Fig. 3 High-power HPDL Rofin DL 020 diode laser.

Remelting and surface alloying were carried out with power ranging from 0.7 to 2.1 kW. Remelted tracks were produced on each sample surface over a length of 55 mm. The laser beam dimensions focused on the material surface were 1.8×6.8 mm. The working focal length (measured from the protective glass surface in the head) was 92 mm. Remelting was performed perpendicular to the longer side of the focused beam with a multimode energy distribution, allowing a wide bead face to be formed [4].

Preliminary tests determined that the maximum stable processing speed was 0.5 m/min. Further tests were conducted at a constant remelting speed, varying the laser beam power from 0.7 to 2.1 kW during surface remelting. Argon shielding gas at a flow rate of 20 l/min through a ring nozzle (Ø 12 mm), directed opposite to the remelting direction, ensured complete protection of the remelt zone.

4.3 Metallographic examinations

Metallographic studies were conducted using a Leica MEF4A metallographic microscope (Fig. 4) with the Leica-Qwin computer image analysis system at magnifications from 100× to 1000× and with the DSM-940 scanning electron microscope (SEM) by Opton. Thickness measurements of individual zones of the surface layer and grain surface area were performed with the Leica-Qwin system. Results concerning average grain size and dendrite length in specific zones were statistically analyzed.

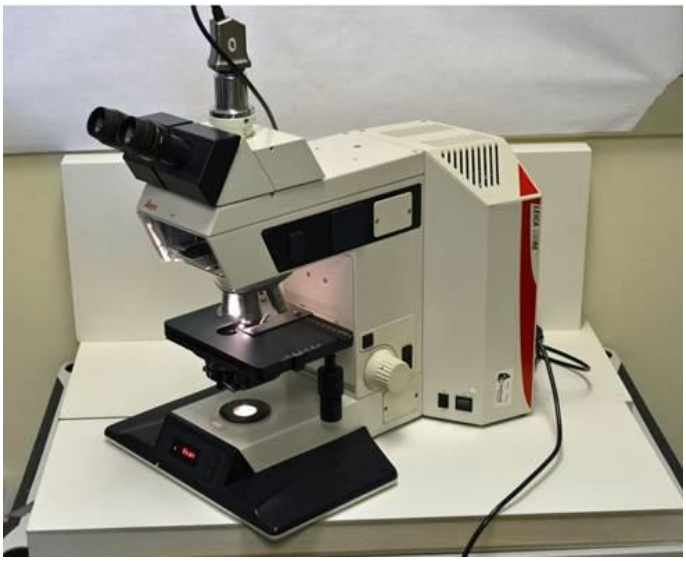

Fig. 4 Leica MEF4A metallographic microscope.

4.4 Rockwell hardness testing

Hardness tests were carried out according to PN-EN ISO 6508-1:2002 [5] using the C scale on a DUH 202 dynamic ultramicrohardness tester from Shimadzu. Ten measurements were performed per condition, and the average value was calculated. The tests were conducted under a load of 0.1 N, making sufficient impressions across the cross-section of each sample corresponding to the depth of structural changes in the surface layer. Results were statistically analyzed. Hardness was measured on ground and mechanically polished end faces of the samples.

Microhardness measurements were made along lines perpendicular to the surface, aligned with the bead axis. The schematic positioning of the measurement points is presented in Fig. 5.

Fig. 5 Shimadzu DUH 202 dynamic ultramicrohardness tester.

5. RESULTS AND DISCUSSION

5.1 Surface layer of the remelted sample

Evaluation of the remelting process was based on analysis of images from the DSM-940 SEM (Opton) and measurements of the depth and width of the remelted zone in HS6-5-3-8 steel samples processed with different laser powers. The analysis helped determine the influence of process parameters on the formation of the melted track. Figs. 6 and 7 show images of the remelted zone at a constant speed of 0.5 m/min and multimodal energy distribution, which ensures a wide bead face. A clear change in the shape of the remelted zone, consisting of the remelted zone, heat-affected zone (HAZ), and base material, is observed.

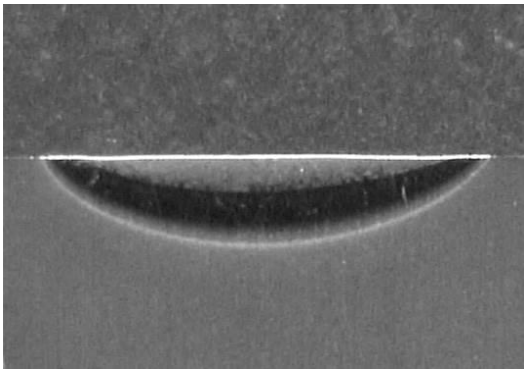

Fig. 6 Surface layer of HS6-5-3-8 steel after remelting with the following parameters: scanning speed – 0.5 m/min, beam power – 1.7 kW

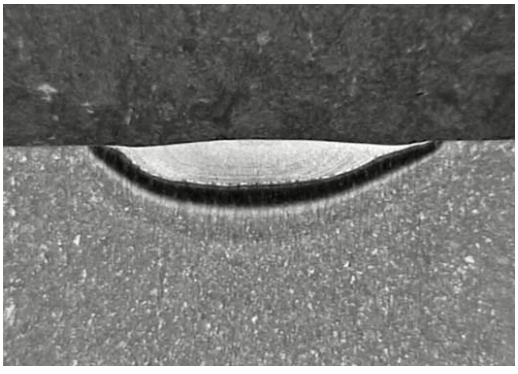

Fig. 7 Surface layer of HS6-5-3-8 steel after remelting with parameters: scanning speed – 0.5 m/min, beam power – 2.1 Kw

With a laser power of 0.7 kW, the remelting depth was approx. 0.4 mm, and at 2.1 kW, it reached approx. 1.1 mm. The power density of the laser beam significantly affects the remelting depth. As the power density increases, the base material's contribution grows, indicating deeper remelting, as shown in Fig. 8.

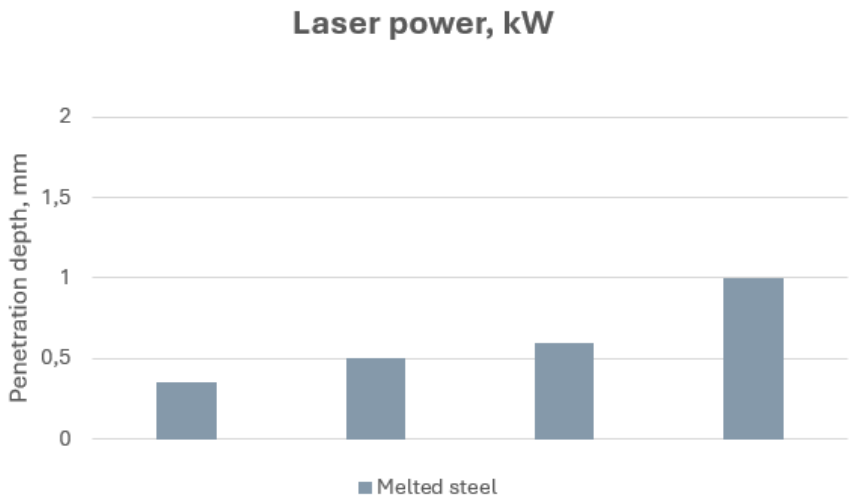

Fig. 8 Effect of laser power on the depth of the remelted zone of the surface layer of HS6-5-3-8 steel after laser remelting with laser powers of 0.7 kW, 1.4 kW, 1.7 kW, and 2.1 kW, at a constant remelting speed of 0.5 m/min

5.2 Remelted bead surface of HS6-5-3-8 steel

The laser surface remelting resulted in a cross-sectional track shape corresponding to the laser beam's energy distribution. Tracks were produced on each sample surface over a length of 55 mm. The beam dimensions on the material surface were 1.8×6.8 mm, and the working focal length was 92 mm. The processing was conducted perpendicular to the longer beam axis with multimodal energy distribution for a wide bead face.

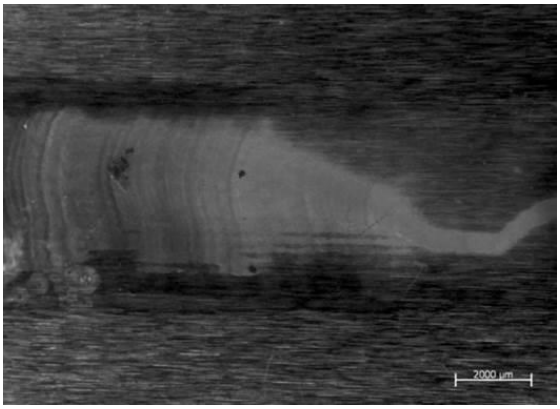

Fig. 10 View of the surface after remelting of HS6-5-3-8 steel, laser power 0.7 kW

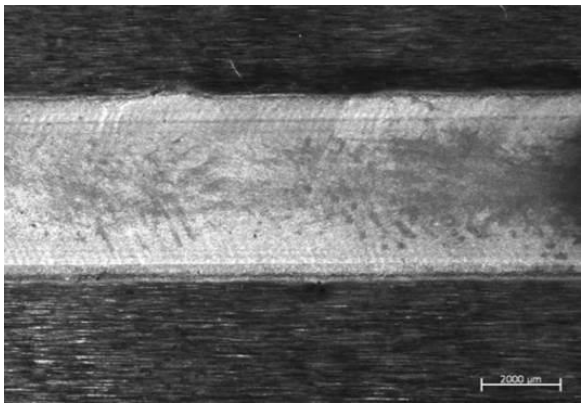

Fig. 11 View of the surface after remelting of HS6-5-3-8 steel, laser power 1.4 kW

As shown in Fig. 12, higher laser power resulted in smoother track surfaces and more distinct remelting boundaries compared to those produced with lower power (Fig. 10).

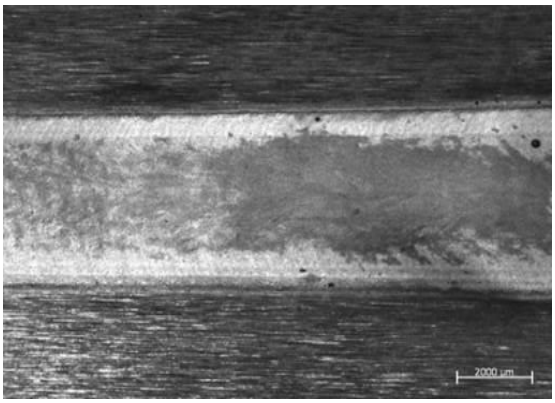

Fig. 12 View of the surface after remelting of HS6-5-3-8 steel, laser power 1.7 kW

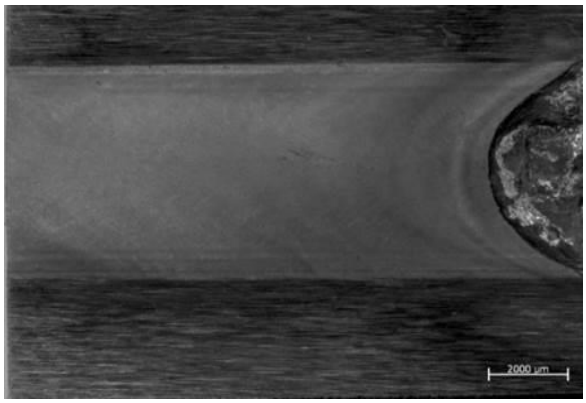

Fig. 13 View of the surface after remelting of HS6-5-3-8 steel, laser power 2.1 Kw

5.3 Surface roughness of the high-speed steel layer

After laser remelting, rough surface areas were observed. This may result from oxidation and evaporation of material from the surface layer, correlating with the remelt zones. The smoothest surface was obtained at 0.7 kW, and the roughest at 2.1 kW, as shown in Fig. 14. Laser power plays a crucial role—surface roughness increases with beam power.

Macroscopic observations suggest that additional finishing is needed to reduce surface roughness. Surface porosity may serve as micro-reservoirs for lubricants, reducing the friction coefficient in moving parts.

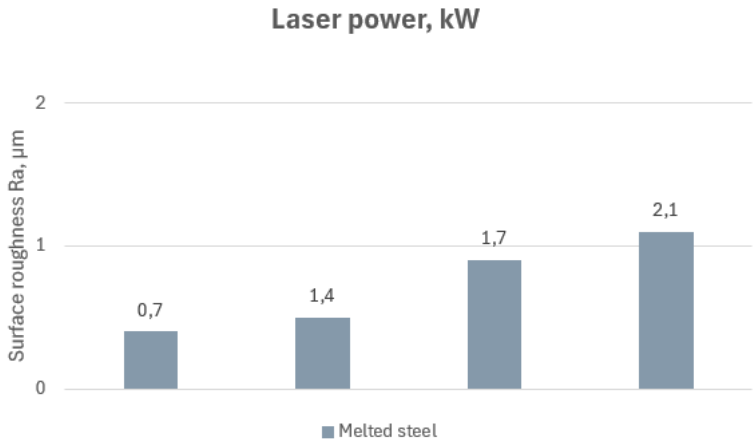

Fig. 14. Influence of laser power on surface roughness of HS6-5-3-8 steel after laser remelting at 0.7 kW, 1.4 kW, 1.7 kW, 2.1 kW and a constant speed of 0.5 m/min.

5.4 Surface layer hardness of high-speed steel

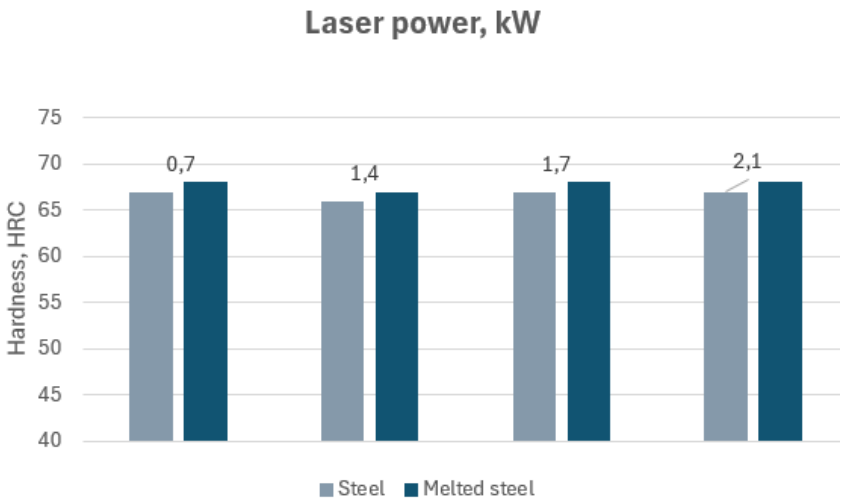

Fig. 15 Changes in average surface hardness of HS6-5-3-8 steel after laser remelting at various powers (0.7 kW, 1.4 kW, 1.7 kW, 2.1 kW), with a constant speed of 0.5 m/min.

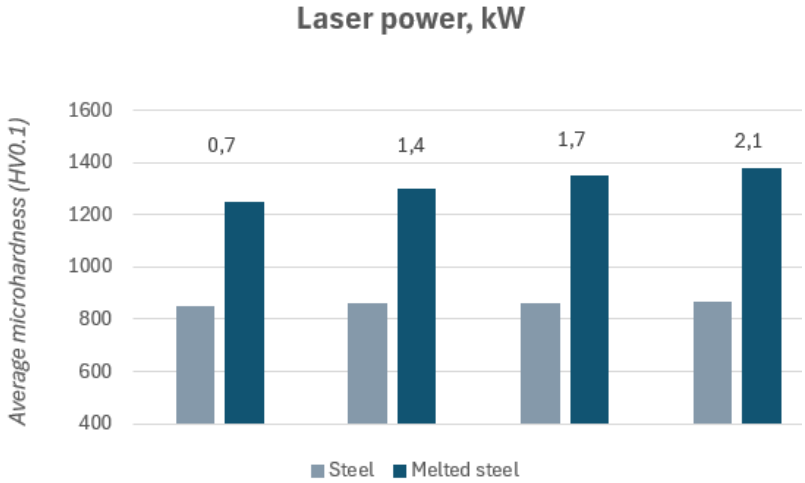

Fig. 16 Average microhardness of the surface layer of HS6-5-3-8 steel after laser remelting at the same powers and speed.

Microhardness was measured linearly across the cross-section from the bead face toward the base material using a DUH 202 Shimadzu tester under 0.1 N load. Measurements matched the structural depth changes, and results were presented graphically for selected laser power densities.

Fig. 16 shows microhardness of the base material (approx. 850 HV0.1) and the average microhardness of the surface layer after laser remelting at different powers. With increased remelting depth, the hardness rises due to significant structural refinement, which strengthens the surface.

The lowest hardness (approx. 1300 HV0.1) was observed at 0.7 kW, and the highest (approx. 1400 HV0.1) at 2.1 kW, with a difference of about 100 HV0.1. The relative hardness increase after remelting, compared to the base material, was about 30%.

6. CONCLUSIONS

The study demonstrated that laser surface treatment significantly influences the structural and mechanical properties of HS6-5-3-8 high-speed steel. As the laser power increased from 0.7 kW to 2.1 kW, the depth of the remelted zone also increased, reaching up to 1.1 mm.

The surface morphology changed noticeably, with higher powers producing smoother and more defined remelt tracks. However, increased power also led to higher surface roughness, likely due to oxidation and material evaporation, although this roughness could be beneficial for applications requiring lubricant retention. Additionally, the laser treatment enhanced the microhardness of the surface layer by approximately 30% compared to the base material, with values rising from around 1300 HV0.1 to 1400 HV0.1 as a result of microstructural refinement.

These findings confirm that laser remelting is an effective method for improving surface hardness and durability in engineering materials.

ACKNOWLEDGEMENTS

The work was created as part of project based learning - PBL, in the 12th competition under the Initiative of Excellence - Research University, Silesian University of Technology, Gliwice, Poland and as part of project of Students Scientific Circle of Laser Surface Treatment under the Initiative of Excellence - Research University, Silesian University of Technology, Gliwice, Poland.

BIBLIOGRAPHY

1. PN-EN ISO 4957:2002 to "Stale narzędziowe - Wymagania"
2. M. Bonek, Technologie laserowe w inżynierii powierzchni, Politechnika Śląska
3. A. Pindor, W. Gorzkowski, A. Szymacha : Feymana wykłady z fizyki. Tłumaczenie z j. ang. Książki p.t. „ The Feyman Lectures on Physics, Volume III, Massachusetts, U.S.A., 1965.
4. A. Klimpel, Technologie laserowe: spawanie, napawanie, stopowanie, obróbka cieplna i cięcie, Wydawnictwo Politechniki Śląskiej, Gliwice 2012.
5. Norma PN-EN ISO 6507-1, Metale. Pomiar twardości sposobem Rockwella. Część 1, Metoda badań (skale A, B, C, D, E, F, G, H, K, N, T)

TalentDetector
23th-25th June 2025
Gliwice-Brenna, Poland
DEPARTMENT OF ENGINEERING MATERIALS AND BIOMATERIALS
FACULTY OF MECHANICAL ENGINEERING
SILESIAN UNIVERSITY OF TECHNOLOGY
INTERNATIONAL STUDENTS SCIENTIFIC CONFERENCE

Computationally Assisted Laser and Heat Treatment Processes for Surface Property Optimization

Julia Chudy [a], Bartosz Filip [a], Szymon Jędrzejewski [a], Matusz Paluch [a], Mirosław Bonek[b]

[a] Silesian University of Technology, Faculty of Mechanical Engineering, Department of Engineering Materials and Biomaterials
[b] Silesian University of Technology, Faculty of Mechanical Engineering, Department of Engineering Materials and Biomaterials
email: miroslaw.bonek@polsl.pl

Abstract: Laser material processing techniques, including remelting, hardening, and surface texturing, offer unprecedented control over the microstructural and mechanical properties of engineering materials. These processes are characterized by rapid thermal cycles, leading to unique phase transformations and the development of metastable microstructures. The integration of classical heat treatment concepts with laser-based technologies, supported by advanced simulation methods such as Phase Field, Molecular Dynamics, and CALPHAD, enables accurate prediction and control of process outcomes. This study highlights the synergy between experimental laser processing and computational modeling, emphasizing the predictive capabilities of digital tools in optimizing surface modifications, enhancing performance, and ensuring structural integrity of modern engineering materials.

Keywords: laser surface modification, heat treatment, simulation, CALPHAD, molecular dynamics, phase field method, microstructure evolution, surface engineering,

1. INTRODUCTION

The dynamic development of modern industry and increasing performance expectations for materials have led to a growing interest in high-precision thermal and mechanical processing technologies. Among them, laser-based methods such as remelting, surface hardening, alloying, and texturing have emerged as highly effective tools for modifying material surfaces without altering their overall geometry. These processes are distinguished by rapid thermal cycling—heating rates of up to thousands of kelvins per second—causing highly localized phase changes, residual stress formation, and microstructural evolution on the surface layers [1, 3].
In parallel, heat treatment remains a foundational metallurgical process aimed at enhancing mechanical properties and stabilizing internal stresses. While conventional heat treatment operates on a macroscopic scale with gradual temperature changes, laser processing achieves similar goals through precise, highly localized energy input, affecting the same fundamental parameters: phase composition, grain structure, and dislocation density. The combination of

both approaches offers a deeper understanding of how to engineer material properties, especially when supported by predictive simulations [1].
Advanced computational tools are now an essential part of modern materials science, providing insight into microstructural transformations at both atomic and mesoscopic levels. Simulation techniques such as the Phase Field method, Molecular Dynamics, and CALPHAD modeling bridge the gap between experimental laser treatment and theoretical prediction. This allows for the design of tailored surface layers with specific hardness, wear resistance, or thermal stability. The convergence of laser technology and simulation not only supports the development of next-generation materials but also accelerates innovation in sectors such as aerospace, biomedical, energy, and automotive industries [4][5].

2. FUNDAMENTALS OF LASER MATERIAL PROCESSING

The laser as an energy source is characterised by high power density, a small heat-affected zone and the possibility of local and controlled surface modification [2]. Depending on the parameters (power, exposure time, beam diameter), the laser can cause melting and rapid solidification of the surface, phase transformations and the formation of intrinsic stresses and crystallographic textures [1].

3. KINETICS OF PHASE TRANSITIONS DURING LASER PROCESSING

During laser remelting, materials are subjected to extremely rapid heating (up to thousands of K/s) and equally rapid cooling [3]. Under such conditions, non-diffusive transformations, such as martensitic, and nucleation and grain growth can occur according to the Johnson-Mehl-Avrami-Kolmogorov equation [4][5]. High cooling rates favour the formation of metastable phases, such as residual austenite or fine carbides.

4. COMPUTER-AIDED MATERIALS SCIENCE IN LASER PROCESSING ANALYSIS

4.1. Phase Field Method

The phase field method allows the simulation of the phase transformation front on a microscopic and macroscopic scale. It allows prediction of grain morphology after solidification, carbide dissolution and crystallisation, and dendrite formation [6][7].

4.2. Molecular dynamics method

Molecular dynamics operates at the atomic scale, modelling the behaviour of atoms under varying conditions of temperature and stress. It allows analysis of nucleation, movement of interfacial boundaries and formation of crystal defects [8].

4.3. CALPHAD (Calculation of Phase Diagrams)

The CALPHAD method is used to calculate phase equilibria in multicomponent systems under varying thermodynamic conditions [9][10]. It can be used to design chemical compositions and predict phase stability under laser remelting conditions.

4.4 Examples of use

Typical applications for steel processing methods can be divided into the following groups:

- Tool steels - laser remelting improves wear resistance by forming a fine-grained martensitic layer [2];
- NiTi alloys - control of the martensitic transformation allows modification of the shape memory effect [3];
- Nickel superalloys - control of γ' phase precipitation increases high-temperature strength [11].

5. HEAT TREATMENT AS A TOOL FOR STRUCTURAL STABILIZATION AND PERFORMANCE IMPROVEMENT

Heat treatment is a metallurgical process involving controlled heating and cooling cycles to alter a material's physical and, occasionally, chemical properties without changing its shape. This manipulation is primarily aimed at enhancing mechanical properties such as hardness, strength, toughness, ductility, wear resistance, and machinability. Beyond property enhancement, heat treatment also serves to relieve internal stresses induced by prior manufacturing processes like cold working, welding, or casting. The ability to mitigate manufacturing-induced defects is a critical aspect of heat treatment. The consistent emphasis on both improving mechanical properties and relieving internal stresses highlights a dual functionality of heat treatment. It is not solely about imparting new, desirable characteristics but also about correcting or mitigating undesirable states, such as residual stresses and distortions, which are inherently introduced during various fabrication steps. This capability ensures the integrity and dimensional stability of components post-manufacturing. Therefore, heat treatment is an essential part of quality control, playing a crucial role in preventing premature failure and ensuring the reliability of engineered components. This proactive mitigation of defects is as vital as the optimization of material properties [12].

5.1 The Interplay of Microstructure and Material Properties

The core science behind heat treatment lies in its ability to alter the material's microstructure—the arrangement and characteristics of its constituent crystals or phases. These microstructural changes directly dictate the final mechanical properties, such as hardness, strength, ductility, and durability. By precisely controlling temperature, cooling rate, and time, engineers can manipulate phase transformations, leading to desired changes in the metal's properties. For instance, heating a metal to a high temperature, below its melting point, excites its atoms, allowing the crystal structure to change. The subsequent cooling rate then determines the final microstructure and properties. This fundamental understanding of microstructure-property relationships is paramount for achieving specific material characteristics through heat treatment processes [12-15].

5.2 Metallurgical Transformations

Heat treatment fundamentally relies on inducing controlled phase transformations within the material's microstructure. Phases are physically distinct materials within metals, each possessing unique properties, and their presence dictates the overall properties of an alloy [16]. Common phase transformations occurring during heat treatment include [12-17]:

- **Allotropic Transformation:** This involves a change in the crystal structure of a material without altering its chemical composition. A classic example is iron, which transforms from a body-centered cubic (BCC) ferrite phase to a face-centered cubic (FCC) austenite phase upon heating above approximately 912°C, and reverts upon cooling.
- **Eutectoid Transformation:** This is a transformation where a single solid phase transforms into two or more different solid phases upon cooling from an elevated temperature. In steels, the eutectoid transformation of austenite (a solid solution of carbon in iron) into a lamellar mixture of ferrite and cementite, known as pearlite, occurs at around 727°C during slow cooling.
- **Precipitation Transformation:** This involves the formation of sub-micron sized particles (precipitates) of one phase within an existing matrix phase. These precipitates impede dislocation movement, thereby enhancing the material's strength and hardness.[1] This process, often called age hardening, is crucial for strengthening alloys like aluminum-copper systems (e.g., Al_2Cu precipitates in an aluminum matrix) and certain steels and copper alloys.
- **Martensitic Transformation:** Unlike the other transformations, martensitic transformation is diffusionless, meaning it occurs through a rapid, shear-like atomic shift rather than atomic diffusion. In steel, this transformation occurs when austenite is rapidly cooled (quenched) to prevent diffusion-dependent transformations, resulting in a hard and brittle martensite phase. This transformation is key to hardening steels, though it typically requires subsequent tempering to improve toughness.

All phase transformations, except for martensitic transformation, involve diffusion, where atoms rearrange themselves within the crystal lattice over time to form new phases. The kinetics of these transformations are critical for heat treatment design.

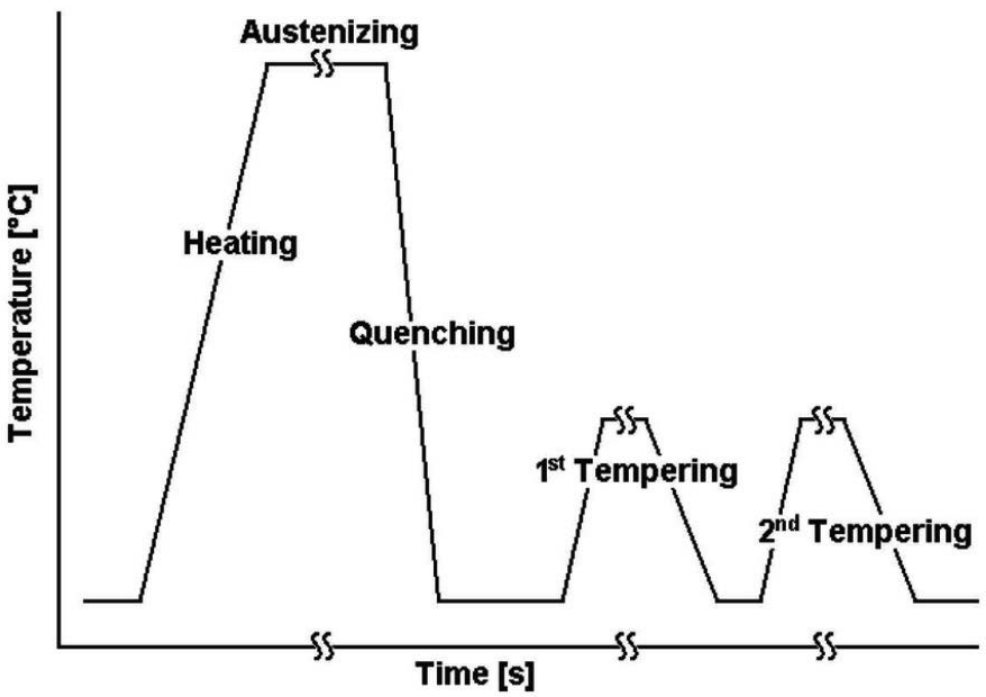

Figure 1 Variation of temperature in a typical heat treatment process [18]

6. INTEGRATION OF LASER PROCESSING AND THERMOMECHANICAL SIMULATIONS IN MATERIALS ENGINEERING

The convergence of laser technology with the simulation of thermomechanical processing of engineering materials represents a significant advancement in modern material engineering. Both disciplines aim to manipulate the microstructure and mechanical properties of materials through controlled thermal and mechanical inputs, albeit using different approaches. Laser processing—including cutting, hardening, cladding, or surface texturing—relies on the precise application of focused thermal energy, which induces rapid heating and cooling cycles. These phenomena closely resemble those observed in classical heat treatment methods such as quenching or tempering, but occur on a much smaller time and spatial scale. The resulting effects, such as martensitic transformations, grain refinement, and residual stress development, require careful thermal modeling to predict and control [18, 19].

6.1 Role of Simulations in Predicting Thermal and Mechanical Responses

Simulations of heat treatment and plastic deformation processes provide critical insight into thermal gradients, stress-strain distributions, and phase transformation kinetics under varying process conditions. When applied to laser processing, these simulation techniques allow for precise prediction of heat-affected zones (HAZ), thermal conductivity effects, or thermal expansion-induced distortions. Numerical models, such as finite element analysis (FEA) and computational thermodynamics (e.g., CALPHAD), are particularly useful for forecasting microstructural evolution and mechanical performance after laser exposure. Furthermore, when laser-induced deformation is employed—such as in laser forming or laser shock peening—the understanding of plastic flow and stress wave propagation becomes crucial, drawing directly from principles of plasticity simulations and dynamic material behavior [21-23].

6.2 Synergy in Process Optimization and Property Tailoring

Integrating these domains enables the development of advanced processing strategies that optimize laser parameters (e.g., beam power, scanning speed, pulse duration) to achieve targeted mechanical outcomes. For example, simulating thermal cycles during laser surface modification can help avoid undesirable effects like thermal fatigue or cracking by adjusting energy input profiles. Similarly, by coupling mechanical deformation models with localized laser heating data, one can predict residual stress distributions and evaluate the structural integrity of treated components. This interdisciplinary synergy enhances not only process control and repeatability but also supports the tailoring of material properties for applications in high-performance sectors such as aerospace, automotive, or energy. Ultimately, the integration of laser technologies with thermomechanical process simulation facilitates a more comprehensive and predictive approach to engineering material performance [21-23]

7. SUMMARY

The interplay between laser processing and heat treatment represents a powerful convergence of classical metallurgical science with modern technological advancement. Laser-based methods enable highly controlled, localized alterations of surface properties, while simulation

tools offer predictive insight into the microstructural outcomes of such treatments. The integration of modeling techniques—Phase Field, Molecular Dynamics, and CALPHAD—allows engineers to design thermal cycles with precision, optimizing phase composition and mechanical properties without excessive trial-and-error experimentation.
This combined approach supports the development of "digital twins" in material processing, where virtual simulations mirror real-world results, significantly reducing costs and improving reliability. It fosters more intelligent, efficient, and sustainable engineering of advanced materials tailored for high-performance applications. Ultimately, by uniting physical experimentation with computational science, researchers can better predict and manipulate the complex phenomena that govern material behavior during laser treatment, ensuring enhanced durability, stability, and performance in engineered components.

ACKNOWLEDGEMENTS

The work was created as part of project based learning - PBL, in the 12th competition under the Initiative of Excellence - Research University, Silesian University of Technology, Gliwice, Poland and as part of project of Students Scientific Circle of Laser Surface Treatment under the Initiative of Excellence - Research University, Silesian University of Technology, Gliwice, Poland.

BIBLIOGRAPHY

1. W.M. Steen, J. Mazumder, Laser Material Processing, 4th ed., Springer, London, 2010.
2. N.B. Dahotre, S.P. Harimkar, Laser Fabrication and Machining of Materials, Springer, New York, 2008.
3. T. DebRoy, H.L. Wei, J.S. Zuback, T. Mukherjee, J.W. Elmer, J.O. Milewski, et al., Additive manufacturing of metallic components – Process, structure and properties, Progress in Materials Science 92 (2018) 112–224.
4. D.A. Porter, K.E. Easterling, M.Y. Sherif, Phase Transformations in Metals and Alloys, 3rd ed., CRC Press, Boca Raton, 2009.
5. J.W. Christian, The Theory of Transformations in Metals and Alloys, 3rd ed., Pergamon, Oxford, 2002.
6. W.J. Boettinger, J.A. Warren, C. Beckermann, A. Karma, Phase-field simulation of solidification, Annual Review of Materials Research 32 (2002) 163–194.
7. S.M. Allen, J.W. Cahn, A microscopic theory for antiphase boundary motion and its application to antiphase domain coarsening, Acta Metallurgica 27(6) (1979) 1085–1095.
8. D. Frenkel, B. Smit, Understanding Molecular Simulation: From Algorithms to Applications, 2nd ed., Academic Press, San Diego, 2001.
9. N. Saunders, A.P. Miodownik, CALPHAD (Calculation of Phase Diagrams): A Comprehensive Guide, Pergamon, Oxford, 1998.
10. L. Kaufman, H. Bernstein, Computer Calculation of Phase Diagrams, Academic Press, New York, 1970.
11. C. Körner, Additive manufacturing of metallic components by selective electron beam melting – a review, International Materials Reviews 61(5) (2016) 361–377.

12. Heat Treating Metal Parts: A Comprehensive Guide - The Federal Group USA, Dostęp z dnia: maja 21, 2025, https://www.tfgusa.com/heat-treating-metal-parts/
13. An Overview of Heat Treatment Methods & Their Benefits | Fractory, Dostęp z dnia: maja 21, 2025, https://fractory.com/heat-treatment-methods/
14. Principles of Heat Treatment Training | Industrial Materials eLearning Course - Amatrol, Dostęp z dnia: maja 21, 2025, https://amatrol.com/product/principles-of-heat-treatment/
15. The Science Behind Metal Heat Treating: Understanding Microstructures and Material Properties, Dostęp z dnia: maja 21, 2025, https://jfheattreatinginc.com/2023/08/the-science-behind-metal-heat-treating-understanding-microstructures-and-material-properties/
16. Phase Transformations in Metals - metallurgy article, otwierano: maja 21, 2025, https://www.imetllc.com/phase-transformations-in-metals/
17. Kaymak, Yalcin. (2007). Simulation of metal quenching processes for the minimazation of distortion and stresses. 10.25673/4872.
18. C. S. Montross, T. Wei, L. Ye, G. Clark, Y. W. Mai: Laser Shock Processing and Its Effects on Microstructure and Properties of Metal Alloys: A Review, *International Journal of Fatigue*, Vol. 24, No. 10, 2002
19. M. M. Mirsalehi, M. R. Razfar, M. H. Sadeghi: Recent Advances in the Laser Forming Process: A Review, *Metals*, Vol. 10, No. 11, 2020
20. A. S. Azar, M. R. Razfar: Thermomechanical Process Simulation and Experimental Validation for Multilayer Laser Cladding Additive Manufacturing of Inconel®718, *Materials*, Vol. 16, No. 7, 2023
21. Z. Ding, H. Wang, J. Luo, N. Li: A review on forming technologies of fibre metal laminates, *International Journal of Lightweight Materials and Manufacture*, Vol. 4, No. 1, 2021
22. X. Ren, H. Zou, Q. Diao, C. Wang, Y. Wang, H. Li, T. Sui, B. Lin, S. Yan: Surface modification technologies for enhancing the tribological properties of cemented carbides: A review, *Tribology International*, Vol. 180, 2023

TalentDetector

23th-25th June 2025
Gliwice-Brenna, Poland

DEPARTMENT OF ENGINEERING MATERIALS AND BIOMATERIALS
FACULTY OF MECHANICAL ENGINEERING
SILESIAN UNIVERSITY OF TECHNOLOGY

INTERNATIONAL STUDENTS SCIENTIFIC CONFERENCE

Designing of universal testing machine simulator for remote education purposes

Xiyue Cui[a], Rafał Honysz[b]

[a] Student of Mechanical Engineering, Silesian University of Technology, Faculty of Mechanical Engineering, Department of Engineering Materials and Biomaterials
email: xc304823@student.polsl.pl
[b] Silesian University of Technology, Faculty of Mechanical Engineering, Department of Engineering Materials and Biomaterials
email: rafal.honysz@polsl.pl

Abstract: This article describes the developed virtual simulator of a universal testing machine. The model is intended to be a remote teaching aid used in classes with students and to familiarize them with its structure, mode of operation and methodology of performing experiments on a real machine.

Keywords: Virtual Simulation; Universal Testing Machine; SolidWorks Modeling

1. INTRODUCTION

The current study reported the planning and conduct of an online virtual universal testing machine simulator in view of the increase in demand for virtual lab teaching. SolidWorks is utilized for much of the major mechanical components including ball screw mechanism, worm and worm gear, bevel gears, and linear guide rails comprising the system to visualize the logical physical structure and motion behaviour of a testing machine. The parameters of the virtual system allow to simulate correctly the process of a tensile test of the material, include the clamping of samples, the beam-driven loading, the force application and the output of the result. The upper beam has threaded holed for diverse options; the lower beam is simply guided in duct excitations through the screw drive, so that the vertical arrangement is always ensured during testing.

For simulation studies using SolidWorks Simulation module, two of these common materials, PLA and Copper were chosen. The results demonstrated the capacity of the system to emulate the mechanical reactions and stress-strain characteristics of materials in tension loading. To make the system interactive, a control panel with three operational buttons was implemented along with a monitor interface to set parameters and visualize results. It also recommends SolidWorks Composer for a higher degree of interactivity in presentation.

This virtual simulator provided within this solution may be a real, replicable, and scalable resolution for mechanical engineering education within the even be an answer to associate degree implementation of remote or hybrid learning settings. Potentially, more advanced simulation

platforms such as COMSOL, or Abaqus or might be integrated with dynamic fracture visualization with improved non-linear material modelling potential to increase the fidelity and learning capacity of the system in the future.

2. DESIGNING OF UNIVERSAL TESTING MACHINE

In order to meet the needs of different materials and different teaching demonstration, the beam is designed as a variable speed structure. The speed is adjusted by a motor to achieve the switching of the beam speed from low speed observation to fast loading. For the minimum speed, we select it as 50mm/min. This speed is suitable for teaching demonstration, it is enough slow to observe the changes of some details in the tests. Also this speed is usually used for tensile tests for some metal materials. For the maximum speed we choose 200mm/min. The merit of this speed is it can show experimental results in near real time. Same with using it for the right soft materials, such as rubber or plastic. Beam speed between 50 mm/min-200 mm/min. This range is suitable for any occasion, actually. This also ensures the virtual UTM can revert to conservative laboratory conditions, or more energetic industrial testing and yet satisfy the education requirement, which achieves the desired balance between accuracy and enumeration. For the maximum testing force, consider that the universal testing machine is used for educational testing online, so we determine the maximum testing force is 100kN, this force is enough for stretch, compression and some basic mechanical properties testing. At the same time, 100kN can simulate some industrial device operation, which can help students get in touch with the real engineering environment in a virtual platform. It can not only improve the authenticity of education, but also can lay a good foundation for students to enter the laboratory later in the work. Most universal testing machines are floor-standing double-column vertical, in this project, we also design it as floor-standing double-column vertical. About the size of universal testing machine. We consider the layout of transmission system, structural strength and centre of gravity stability, we determine the size of this universal testing machine as 800mm×500mm×2100mm. The size is reasonable in education, it keeps the engineering representativeness of the actual equipment and considers the efficiency and requirements of the remote platform.

Core components are built and driven by functional requirement. The strategy simultaneously builds a mechanically representative structure, manages to characterise functional properties with sufficient accuracy, whilst achieving a relative level of computational efficiency in the full approximation of the multi-body dynamic and detailed structural conduction during an approximation drift. The design principles of this approach centres around a single backbone of minimal complexity for a given task (functional requirements) so as to minimize an unnecessary computational load, albeit with guaranteed fidelity. This particular simplification, namely function-driven simplification, specifically addresses practical needs, by determining the key components that are important for the behaviour of the system and eliminating those components that make insignificant contributions to the system behaviours with respect to the salient performance feature. During mechanical modelling, they can be approximated or abstracted because some geometric details might not be relevant for how the complete object behaves. This enhances the model's precision and computational efficacy, enabling faster analysis and validation. Furthermore, this approach is well suited for multi-disciplinary engineering problems like integrated simulation problems encompassing structural mechanics, heat transfer, and fluid dynamics. In these cases, it is extremely important to blend the attributes of the several fields to make sure that the resulting model satisfies the functional specifications of each subsystem and

preserves a global computational efficiency. Therefore, the simplified function-driven approach offers a solid solution of modern engineering design in balancing accuracy and efficiency. In this project, I used SolidWorks for structural modelling, assembly, and motion simulation analysis. After completing the 3D modelling of each key component and auxiliary structure, all components were assembled in SolidWorks software to build a complete 3D assembly model of the universal material testing machine. During the assembly process, the installation sequence and structural logic of the actual equipment were strictly followed to ensure the continuity of the power path between the transmission units and the accuracy of the installation position. At the same time, the matching tolerances and connection forms involved in the assembly relationship were reasonably simplified, and the models in the standard library were directly called for some connectors to ensure the accuracy of the size. Through this assembly model, the spatial layout and functional connection between the various systems in this design can be intuitively displayed. The final assembly is shown on figure 1:

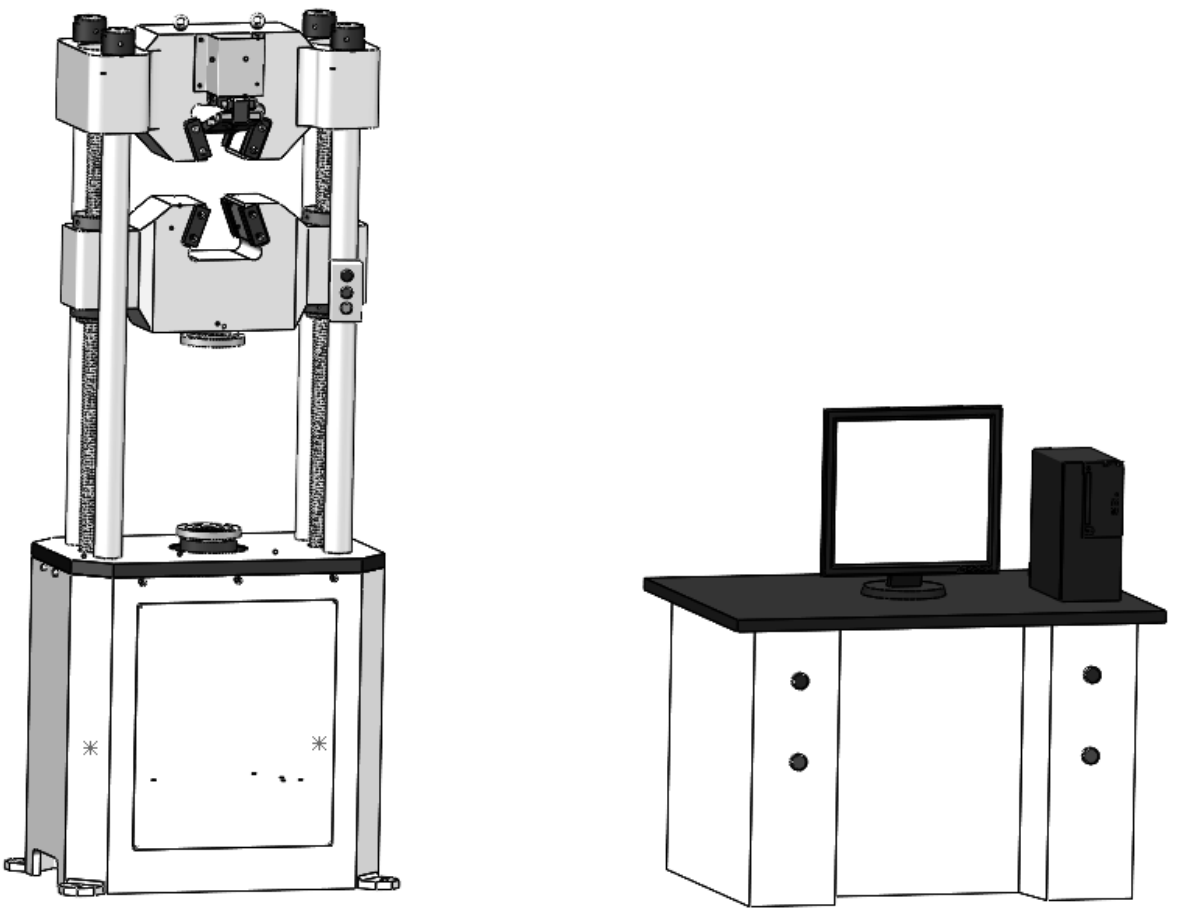

Figure 1. The completed assembly of the Universal Testing Machine

3. USER MANUAL

The virtual UTM model is engineered to replicate the functionality of a physical universal testing machine, enabling users to conduct various types of mechanical tests, including tensile,

compression, and flexural testing, entirely within a digital setting. This capability renders it an indispensable tool for educational institutions, research facilities, and industries where hands-on access to testing equipment may not always be practical. For example, students studying materials science or engineering can gain practical insights into material behavior without needing access to costly laboratory equipment.

This chapter functions as a comprehensive user manual, providing detailed guidance on operating the virtual universal testing machine (UTM) model developed in this project. The main purpose of this manual is to assist users in effectively launching, navigating, controlling, and interacting with the virtual environment. Through these steps, it ensures that the system can be utilized for its intended applications, such as teaching, demonstrations, or simulations, while maintaining ease of use and clarity.

3.1. Enter the Simulation Interface and familiar with the structure

Lauch the SolidWorks and open the main simulation window. After launching the simulation interface, users have the option to activate the exploded view, a feature that provides an in-depth, visual exploration of the internal assembly of the machine. This function is particularly useful for gaining a comprehensive understanding of how the various components are arranged and interconnected within the system. By enabling the exploded view, users can clearly observe the spatial relationships and functional integration of key elements such as the motor, transmission units, crossbeam, and guide rails.

Additionally, educators can utilize this feature to explain complex mechanical concepts in a more accessible manner, bridging the gap between theoretical knowledge and practical application.

3.2. Select a test sample

Choose a sample material from the available list, which typically includes options such as PLA, aluminum, copper, steel, or other materials commonly tested in engineering applications. Each material comes with predefined mechanical properties, including yield strength, ultimate tensile strength, elongation at break, and modulus of elasticity. These properties are stored within the system's database and are automatically applied when a specific material is selected.

This automated approach not only simplifies the testing process but also enhances accuracy by minimizing human error. Furthermore, it enables users to quickly switch between different materials and compare their behaviors under identical testing conditions. Such functionality is particularly valuable in educational settings, where students can gain hands-on experience observing how varying mechanical properties influence material performance during tensile tests. It also proves beneficial in professional environments, allowing engineers to efficiently evaluate material suitability for various applications.

3.3. Start the tensile test

Once the sample material has been selected, press the “Start Test” button on the control panel. This action triggers the simulated tensile process, beginning with the activation of the lower beam's motion. In the virtual environment, the movement of the lower beam is controlled precisely according to predefined parameters such as test speed and maximum displacement. Users can adjust these settings prior to starting the test to simulate different loading conditions.

3.4. Clamp and load process

As the test begins, the upper and lower fixtures securely hold the specimen in place. The clamping mechanism ensures that the sample remains stable throughout the loading process, replicating the precision required in real-world testing environments. Following clamping, the lower beam moves downward at a controlled speed, applying axial tension to the material. During this process, users can observe the deformation of the sample material in real time (figure 2).

a) b)

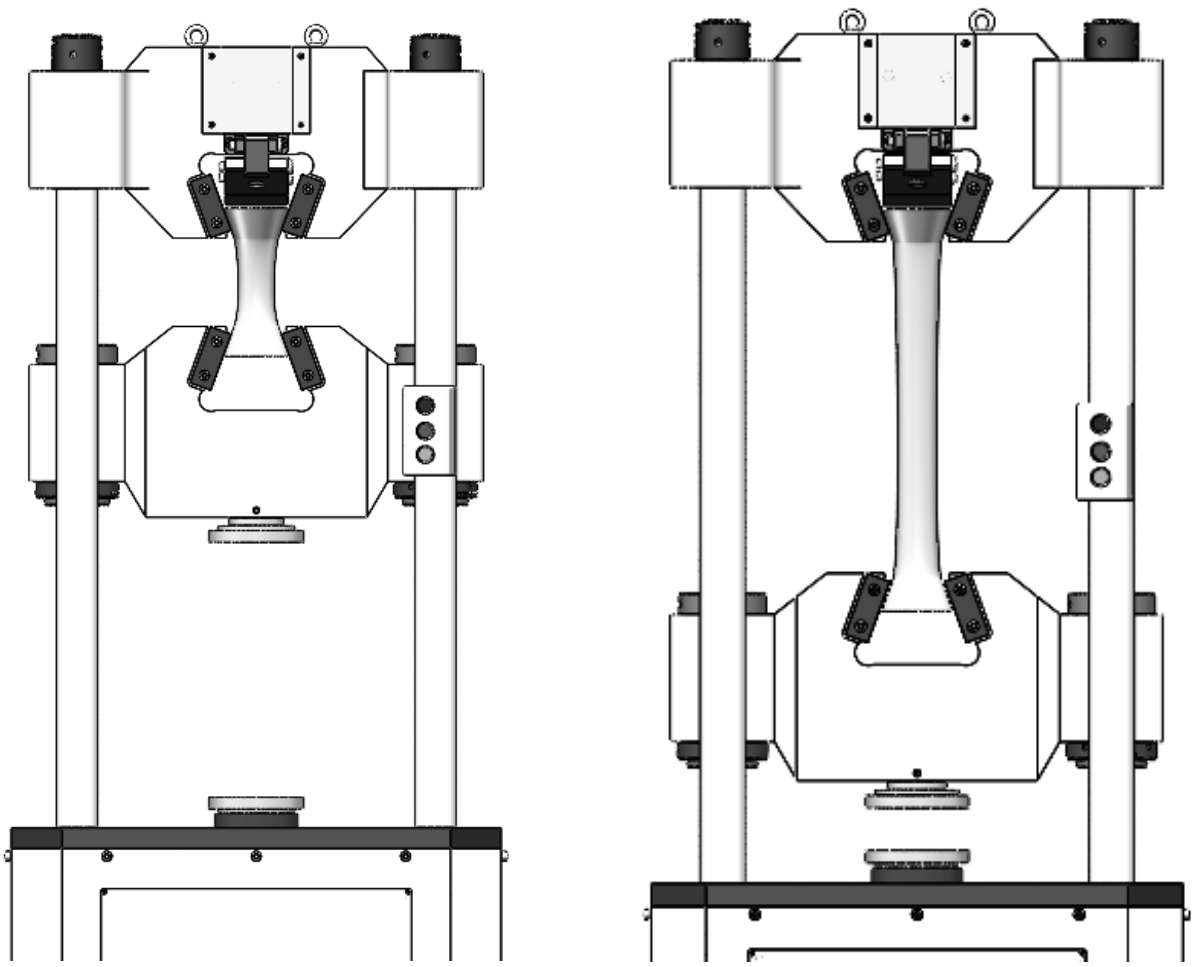

Figure 2. The sample a) before and b) after testing

3.5. Show the result

After the loading process is completed, the system automatically generates and displays a stress-strain curve, providing a visual representation of the specimen's behavior under tension. Then, these results can be compared against theoretical predictions or experimental data from physical tests to validate the accuracy of the simulation.

4. PERFORMANCE ANALYSIS AND APPLICATION VALUE

This study successfully built a virtual universal testing machine with complete functions. The main structural components such as guide rails, columns, and bases are based on rigid connections to ensure force stability and deformation control during loading. The test force is transmitted vertically through the ball screw, reducing transmission clearance and structural vibration. This design uses a five-stage transmission system of "servo motor, continuously variable transmission, worm and worm gear, bevel gear pair, ball screw" to complete the power conversion from rotation to linear motion. The transmission ratio, power loss and mechanical efficiency of each level have been theoretically calculated. The transmission ratios of each level are reasonably distributed to achieve a total transmission ratio of about 55.6, which effectively meets the technical requirements of a beam speed range of 50–200 mm/min, the range covers the test speed range of conventional materials such as tension, compression, shear, etc. In the virtual model, the influence of different loading rates on the deformation behavior of the specimen can be simulated by adjusting the input motor speed. and a maximum loading force of 100 kN. Then the system intends to use a servo motor as the power source, which can achieve precise control of loading speed and loading force.

In the context of the continuous development of distance learning, virtual simulation equipment provides a new way for experimental teaching. In traditional material mechanics experiments, students often find it difficult to intuitively understand the structural composition and power transmission path of the universal testing machine. The model developed in this design has good integration and network adaptability, and can be deployed as an online interactive experimental tool through a web page or teaching platform. It supports students to complete structure observation, test loading operations, parameter adjustment, etc. remotely, and realizes multiple operations such as magnification, slicing, rotation, explosion, loading, etc., effectively improving the sense of participation and operational authenticity of remote experiments. In summary, the virtual universal material testing machine not only meets the teaching and demonstration requirements in terms of performance indicators, but its design ideas and structural architecture also have strong adaptability and scalability. It integrates a variety of technical means such as engineering structure modelling, transmission theory analysis, three-dimensional virtual simulation and remote interactive control, providing a feasible solution for the development of new engineering experimental teaching methods. In the future, this design model is expected to be integrated with technologies such as AI analysis, simulation measurement and control, and big data feedback, and further expanded into the basic module of the "smart experimental teaching platform" to promote the modernization of engineering education.

5. CONCLUSION

In this project, a virtual universal testing machine was designed and developed by SolidWorks. The main objective of this project is to support remote education and improve the efficiency of teaching for materials testing principles by providing an accessible, interactive, and comprehensive learning tool. This virtual UTM serves as a bridge between theoretical knowledge and practical application, allowing students and educators to explore complex material behaviours without the requirement for physical laboratory equipment. The core of this system incorporates mechanical design principles to ensure the accuracy and availability of the virtual components. This includes detailed modelling of structural elements such as crossbeams, linear

guides, and transmission systems, which are important for achieving the functionality of a physical UTM. Throughout the development process, high attention was paid to modelling the structural framework with high accuracy. This included detailed representations of key components such as the upper and lower beams, linear guide rails, and sample fixtures. Each component was meticulously designed to ensure that its dimensions, material properties, and functional characteristics closely mirrored those of a physical universal testing machine. For instance, the upper beam was modelled to provide rigid support for clamping fixtures, while the lower beam, which is movable, was equipped with mechanisms for both tensile and compression testing. The linear guide rails were carefully engineered to ensure smooth vertical motion without lateral deviation, thereby maintaining alignment during testing. To achieve controlled linear motion, a complete multi-stage transmission system was designed and implemented. This system consists of several critical components: a servo motor for precise rotational control, a variable-speed gearbox to adjust torque and speed, a worm gear set for efficient power transfer, a bevel gear for directional changes in motion, and a ball screw for converting rotational motion into linear displacement. Each stage of the transmission system was thoroughly calculated to ensure optimal performance under varying load conditions. This integration of components ensures that the virtual UTM can replicate the controlled linear motion necessary for accurate material testing. At the same time, the platform allows users to assemble the virtual UTM from individual components, the platform provides hands-on experience in understanding how each part contributes to the overall functionality of the machine. This function is particularly valuable for students studying mechanical engineering or materials science, as it allows them to visualize and operate complex parts or assemblies in a controlled digital environment. Overall, this project demonstrates the potential of integrating modern technology with traditional technology concept to create innovative solutions for education. Whether used by students, educators, or industry professionals, the virtual UTM provides a versatile platform for exploring and understanding the principles of materials testing in a safe, cost-effective, and engaging manner.

BIBLIOGRAPHY

1. L.A. Dobrzański, R. Honysz, The idea of material science virtual laboratory, Journal of Achievements in Materials and Manufacturing Engineering 42/1-2 (2010) 196-203.
2. Xiao Ting, Zheng Yuan, Qiu Zhiyong, et al. Design of virtual simulation experiment for tokamak plasma physics[J]. Experimental Technology & Management, 2025, 42(1).
3. Sun Jianjun, Zhang Yingjie, Ba Yu, et al. Discussion on high voltage virtual simulation experiment teaching[J]. Experimental Science and Technology, 2022, 20(2): 52-56.
4. Li Linlu, Tang Xiaohong, Zhao Yongfeng. Application and prospects of simulated medical education in prenatal ultrasound teaching[J]. China Medical Education Technology, 2022, 36(2).
5. Song Libing, Wang Yingwei, Shang Guoyin. Development and training application of virtual drill simulation system for coal mine disaster emergency rescue[J]. China Mining, 2024, 33(S1): 219-222, 229.
6. Yang Xiao, Ren Hongxiang, Lian Jingjing, et al. VR interactive 3D virtual ship modeling and simulation[J]. China Navigation, 2022, 45(1): 37-42, 49.
7. Han Chenghao, Ma Jilin, Liu Jialun, et al. Design and application of ship intelligent navigation system based on virtual simulation test platform[J]. China Navigation, 2023, 46(1): 148-154.

8. Liu Wenyong, Chen Yi, Liu Yiwu, et al. Research on the construction of virtual simulation course system for polymer materials and engineering major[J]. Integration of Industry and Education, 2024, 6(7): 8-16.
9. Lai, Joel Weijia, and Kang Hao Cheong. Adoption of virtual and augmented reality for mathematics education: A scoping review. IEEE Access 10 (2022): 13693-13703.
10. Sun Liangxu, Li Linlin. Research on virtual simulation experiment platform for network engineering[J]. Experimental Science and Technology, 2023, 21(2): 34-38.
11. Dou Dongyang, Li Chang, Wang Qili, et al. Virtual simulation experiment design for crack fault diagnosis of vibrating screen beam for engineering education certification[J]. Experimental Technology & Management, 2024, 41(7).
12. Gao Ruqian, Zhang Jun, Xiang Yuxuan, et al. Development of plunger pump practical teaching system based on virtual reality technology[J]. Creative Education Studies, 2024, 12: 738.
13. Zhang Min, Wen Fuan, Liu Junbo. Connotation and characteristics of high-quality virtual simulation experiment teaching courses[J]. Experimental Technology & Management, 2022, 39(3).
14. Wang Zichang. Research on ship driving simulation combined with virtual reality technology[J]. Ship Science and Technology, 2023, 45(19): 181-184.
15. Chen Hao, Cui Quanwei, Guo Liqun, et al. Design and development of bending-torsion combined virtual simulation experiment based on Unity3D[J]. Experimental Science and Technology, 2024.
16. Zhang Shanshan, Li Qinhua, Xue Yukun, et al. Application and prospects of virtual reality technology in eye diseases[J]. Journal of Xi'an Jiaotong University (Medical Sciences), 2024, 45(3).
17. Ramaseri Chandra, Ananth N., Fatima El Jamiy, and Hassan Reza. A systematic survey on cybersickness in virtual environments. Computers 11.4 (2022): 51.
18. Rojas-Sánchez, Mario A., Pedro R. Palos-Sánchez, and José A. Folgado-Fernández. Systematic literature review and bibliometric analysis on virtual reality and education. Education and Information Technologies 28.1 (2023): 155-192.
19. Mao Xiaoyan, Ye Hua, Yang Zhi, et al. Application of LabVIEW in signal and system virtual simulation experiment teaching[J]. College and Job, 2024, 13: 2134.
20. Peng Bo, Yuan Sannan, Wo Yumin. Research and application of virtual simulation system based on digital twin[J]. Computer Measurement & Control, 2023, 31(10).

TalentDetector
23th-25th June 2025
Gliwice-Brenna, Poland
DEPARTMENT OF ENGINEERING MATERIALS AND BIOMATERIALS
FACULTY OF MECHANICAL ENGINEERING
SILESIAN UNIVERSITY OF TECHNOLOGY
INTERNATIONAL STUDENTS SCIENTIFIC CONFERENCE

A Visual Platform for PC Hardware Configuration

Shiyang Dai, Linkun Xiao, Yifan Wu

Silesian University of Technology, Faculty of Mechanical Engineering
email: sd304824@student.polsl.pl

Abstract: With the continuous development of the computer hardware market and the growing public familiarity with hardware components, an increasing number of users seek to build customized desktop systems that align with their specific functional and aesthetic preferences. However, the lack of access to physical retail spaces limits users' ability to directly inspect hardware appearance and evaluate performance. Moreover, many users encounter difficulties in assessing dimensional compatibility and performance matching among components. Beyond practical considerations, the assembly process itself appeals to users interested in technical exploration and hands-on experience, fostering both knowledge acquisition and a sense of achievement.
In response to these demands, this project proposes a computer assembly visualization platform that offers precise three-dimensional representations of user-defined configurations. The platform is designed to support personalized customization, incorporating key functions such as dimensional compatibility verification and hardware price trend analysis, thereby providing a comprehensive solution for individualized system assembly.

Keywords: hardware, compatibility, visualization platform, configurations, customization

1. INTRODUCTION

With the growth of the computer hardware market and increasing user awareness, more individuals seek to build custom PCs tailored to their needs. However, most users lack access to physical stores where they can evaluate the appearance and compatibility of components in person. Matching dimensions and performance between parts remains a common challenge. Additionally, PC assembly appeals to users interested in hands-on experience and technical exploration, offering both knowledge and a sense of accomplishment.
To address these needs, we developed a visual PC assembly platform. The system presents user-selected configurations in a 3D environment, supports personalized customization, and offers features such as compatibility checks and price trend analysis.

2. CONCEPT OVERVIEW

We present user-selected PC configurations through 3D visualization, enabling users to intuitively explore the full build. The platform also provides compatibility evaluation and customizable aesthetics, helping users create machines that balance performance with personal design preferences. Future development will include a "direct-to-build" mode and expert consultation features, offering professional advice. Users will be able to choose cost-effective components while customizing their appearance to suit individual tastes.

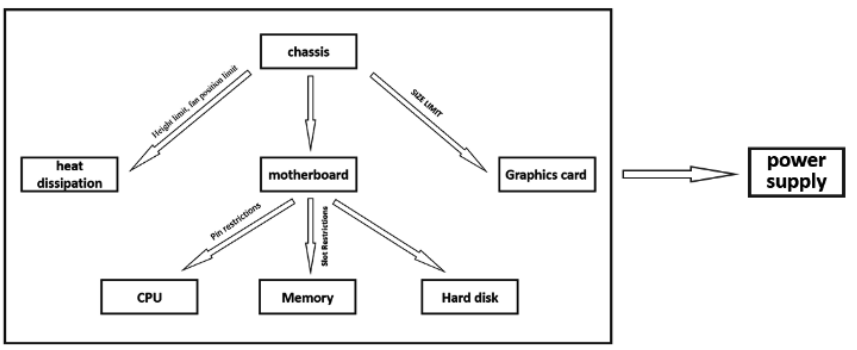

Figure 1. Deposition of Al_2O_3 monolayer by ALD method

3. TECHNICAL KEY ASPECTS

3.1 PyQt5-Based UI Design for PC Assembly Platform

A user-friendly interface designed with PyQt5 to enhance the interactive experience during PC assembly, ensuring intuitive component selection and system configuration.

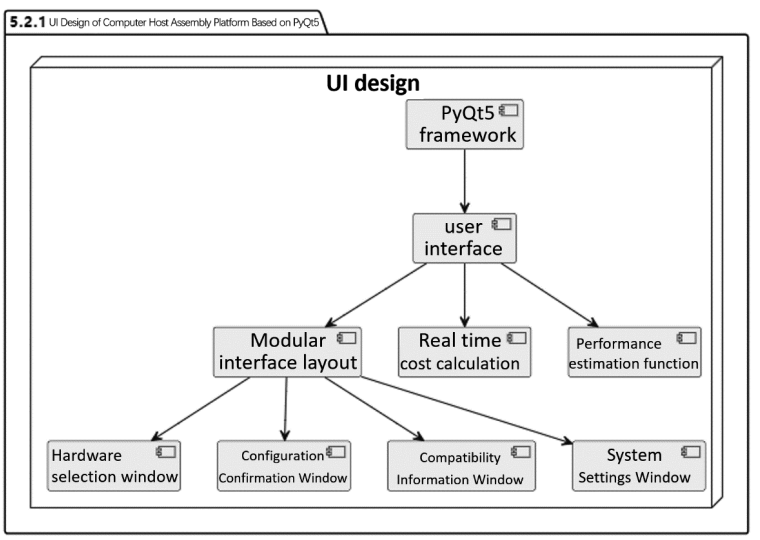

Fig 2 UI design of the platform

3.2. Hardware Compatibility Detection and Performance Prediction Algorithm

Leveraging a comprehensive hardware specification database, we implement a performance prediction model powered by machine learning. This model analyzes extensive historical data on hardware combinations to estimate the expected performance of user-customized configurations, enabling optimal balance between budget and performance.

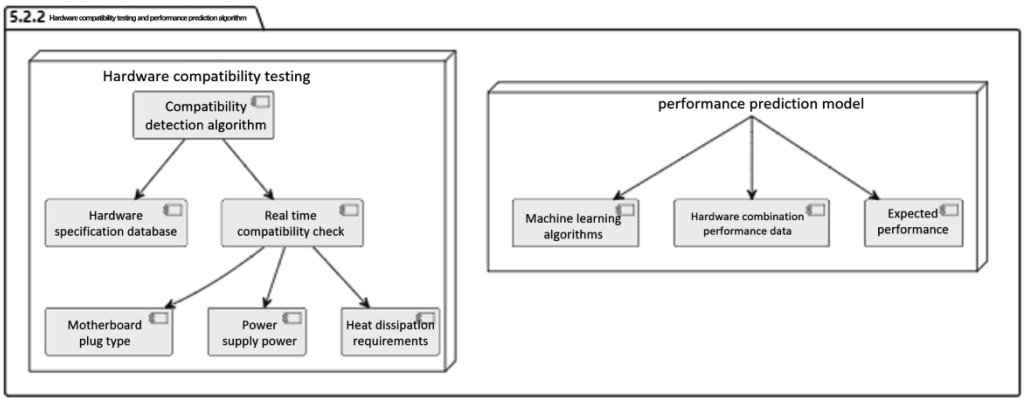

Fig 3 Hardware Compatibility Checking Algorithm

3.3. Integration of Third-Party APIs and Services

Incorporates price comparison APIs, user review/rating systems, and logistics tracking services to help users identify cost-effective options, strengthen purchasing confidence, and streamline the order fulfillment process with accurate delivery information.

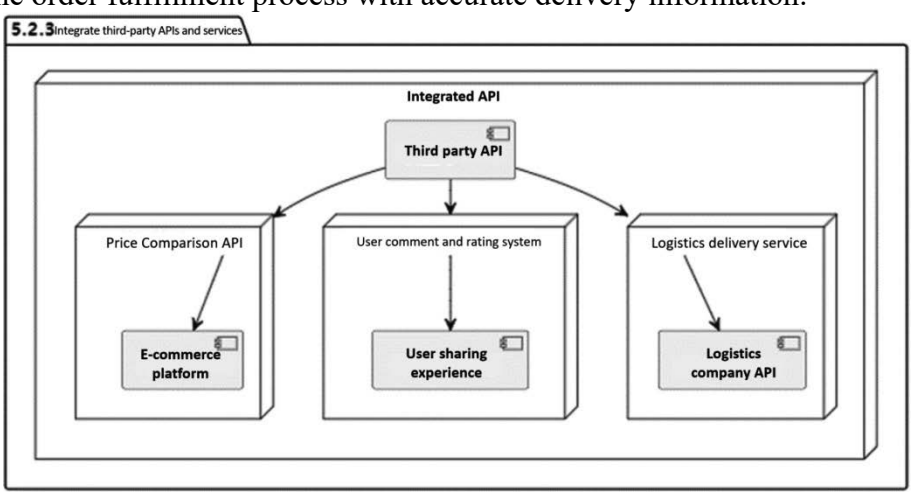

Fig 4 Integrated API

3.4. Personalized Hardware Recommendation System

Combines collaborative filtering (based on users' historical preferences) with scenario-specific optimization to suggest tailored hardware combinations aligned with the user's intended usage.

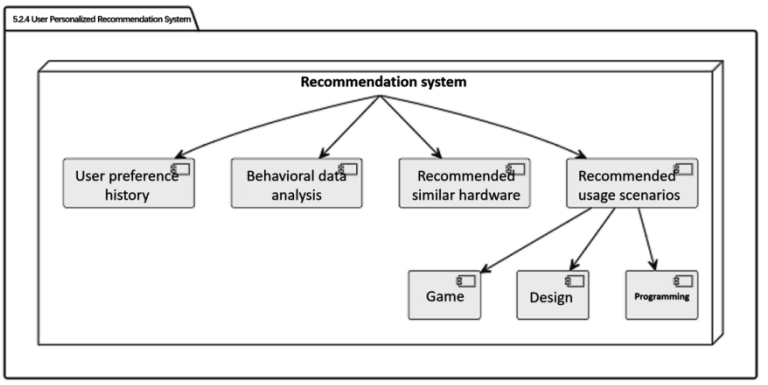

Fig 5 Recommendation System

3.5. Hardware-Software Co-Validation Testing

A preemptive diagnostic framework to identify and mitigate potential system failures through integrated stress testing and protocol validation.

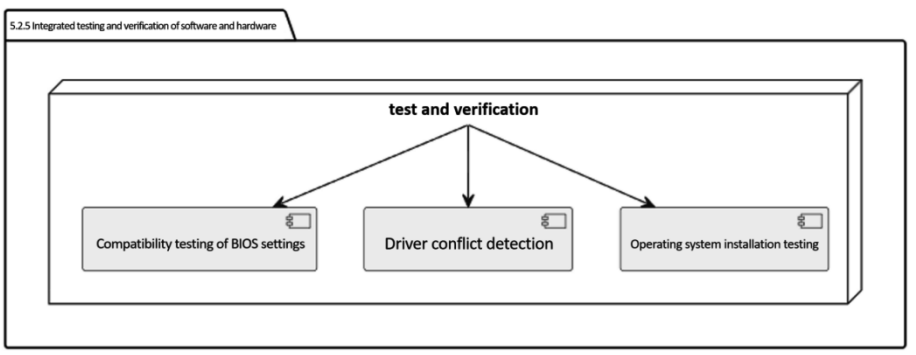

Fig 6 Test and Verification

3.6. Security and Privacy Protection Measures

Implements encrypted storage/transmission (AES-256) and industry-standard security protocols (SSL/TLS) to safeguard transactional data integrity and user privacy.

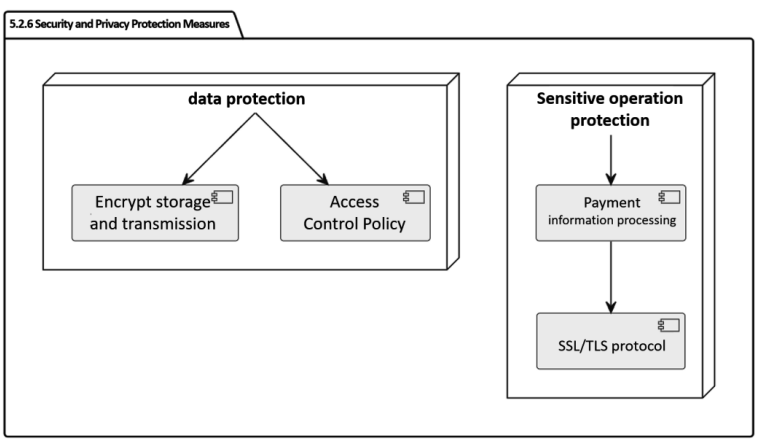

Fig 7 Security and Privacy Protection Measures

Descriptions of tables justified: in Polish (simple text) and in English (italics), as shown in the example below. Board border ½ point, width 16 cm.

4.DIRECTIONS FOR USING

Launch the application and navigate to the login interface. New users should select "Register" to create an account, which requires entering basic personal information.
After successful registration, log in using your credentials.

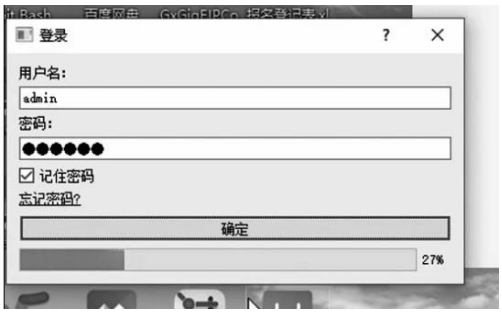

Fig 8 Account Setting

4.2.Main Interface Operation

The main interface features a left-side panel listing essential PC assembly components (e.g., chassis, graphics card, motherboard).

Click on any component in the list to display its corresponding 3D model in the right-side panel.

The 3D visualization provides real-time simulation of the assembly process, allowing users to inspect component fit and compatibility.

4.3.Interactive Features

Use mouse controls to rotate, zoom, and pan the 3D model for detailed examination.

The system automatically highlights potential compatibility issues between selected components.

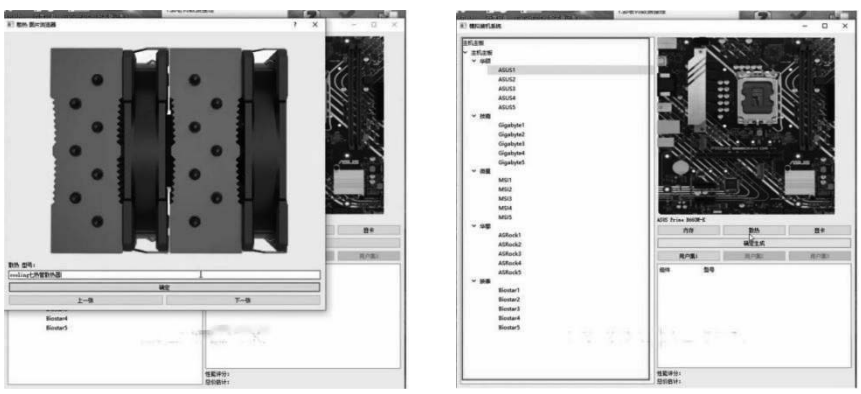

Fig 9 Select Hardware

After the user completes the configuration, the platform simulates the assembled case, including the insertion of the graphics card and motherboard integration. In the lower-right

section of the interface, users can access estimated performance scores and total cost, calculated based on the lowest market prices for each component. A detailed breakdown is available upon selection.

Below the 3D visualization module, a community section enables users to share feedback, evaluate builds, and view configurations created by others. Each user can save up to three custom builds in a personal storage area accessible via the 3D model interface.

A membership system offers additional benefits, including increased save slots and a VIP badge for enhanced visibility in community interactions. Once a configuration is finalized, users can either purchase components individually for self-assembly or opt for platform-supported assembly. In the latter case, the hardware is professionally assembled, tested, and safely delivered to the user's address.

5. SUMMARY

This project presents a hardware configuration visualization platform developed using the Python 3.x environment, with PyQt5 for the graphical user interface. The system integrates Matplotlib and PyQtGraph to offer intuitive performance and compatibility visualizations, while Three.js enables interactive 3D modeling of assembled computer systems, enhancing user engagement and comprehension. These technologies ensure reliability, scalability, and an optimized user experience.

Targeted primarily at university students and tech-savvy young consumers, the platform addresses the growing demand for customizable, high-performance PC builds. Its robust technical foundation supports flexible feature expansion and aligns with current trends in visual computing and intelligent configuration. The market potential is considerable, with wide applicability ranging from hobbyist users to professional hardware analysts. The system's visual clarity and interactive capabilities position it as a competitive solution in the evolving tech landscape, offering promising prospects for large-scale adoption and economic benefit.

BIBLIOGRAPHY

1. Fitzpatrick, Martin. Create GUI Applications with Python & Qt5 (PyQt5 Edition): The hands-on guide to making apps with Python. Martin Fitzpatrick, 2020.
2. Sial, Ali Hassan, Syed Yahya Shah Rashdi, and Abdul Hafeez Khan. "Comparative analysis of data visualization libraries Matplotlib and Seaborn in Python." International Journal 10.1 (2021): 277-281.
3. Thomas, Stephen. SSL andTLS essentials. New York, Wiley, 2000.
4. Sauter, Nicholas K., et al. "New Python-based methods for data processing." Biological Crystallography 69.7 (2013): 1274-1282.
5. Raschka, Sebastian, Joshua Patterson, and Corey Nolet. "Machine learning in python: Main developments and technology trends in data science, machine learning, and artificial intelligence." Information 11.4 (2020): 193.
6. Gu, Xiaodong, et al. "Deep API learning." Proceedings of the 2016 24th ACM SIGSOFT international symposium on foundations of software engineering. 2016.

TalentDetector
23th-25th June 2025
Gliwice-Brenna, Poland
DEPARTMENT OF ENGINEERING MATERIALS AND BIOMATERIALS
FACULTY OF MECHANICAL ENGINEERING
SILESIAN UNIVERSITY OF TECHNOLOGY
INTERNATIONAL STUDENTS SCIENTIFIC CONFERENCE

Research on the loss of efficiency of an internal combustion engine

Olha Drobot[a], Oleg Polishchuk[b], Oleg Babak[c], Mirosław Bonek[d]

[a]Khmelnytskyi National University, Faculty of Engineering Mechanics, Khmelnytskyi, Ukraine, e-mail: pion12208@gmail.com.
[b]Khmelnytskyi National University, Faculty of Engineering Mechanics, Khmelnytskyi, Ukraine email: opolishchuk7l @gmail.com.
[c]Khmelnytskyi National University, Faculty of Engineering Mechanics, Khmelnytskyi, Ukraine, e-mail: ang.babak:@gmail.com.
[d]Silesian University of Technology, Faculty of Mechanical Engineering, Gliwice, Poland

A**bstract:** The methods of studying damage to valves of the gas distribution mechanism of an internal combustion engine are described. Analysis of damage that occurred in the valves and led to their deformation and destruction showed that the cause is not the long-term operation of the valves, when the material exhausts its service life. Damage to the valves occurred as a result of significant compressive forces that acted for a short time. It was established that the destroyed valves did not experience wear of the working surfaces during operation and lost their operability due to the short-term action of significant dynamic loads. Cracks that formed on the surface of the valve plates suggest that the valve could have undergone deformations even during adjustment.

When adjusting the valves after installing them in the socket, the values of the linear gaps must be maintained. Underestimating these dimensions leads to overheating of the valves, an increase in their dimensions due to thermal expansion, and when the gap practically disappears, the valves freeze. The result is a loose fit of the valve in the seat, overheating of the head and its destruction.

Keywords: internal combustion engine, valve, valve head, thermal clearance, valve adjustment, destruction, macrostructural analysis, cracks, chips.

1. INTRODUCTION

An internal combustion engine is a set of mechanisms and systems that perform various functions. Their reliability and durability, along with productivity and efficiency, are the main criteria for evaluating modern technology. One of the most loaded components in the operation of an internal combustion engine (ICE) is the valve mechanism.

The valve, by opening and closing the hole in the cylinder head, it ensures the intake of the working mixture and the exhaust of exhaust gases, thanks to which the car can move.

The valve has a simple geometry, and its design ensures smooth exhaust of gases due to the optical transition of the rod to the head.

The selected radius of curvature provides conditions for complete release or filling of the combustion chamber.

The operating conditions of the valve are quite harsh - it is under the influence of exhaust gas pressure and high temperatures. The exhaust valve head of gasoline engines can heat up to 900 ° C, in diesel engines - up to 700 ° C. The intake valve operates in less harsh conditions. It heats up to 300°C.

Exhaust gases create significant pressure on the valve head. To reduce pressure on the valve, its head is made smaller than that of the intake valve.

Reliable operation of the valves is ensured by a rational choice of materials for their manufacture.

Valves are made of two parts - heat-resistant steel is chosen for the head (40X9S2, 40X10S2M, 40X14H14V2M), and carbon steel (steel 40, 45) for the rod. -12X18H9T, 45X14H14V2M, 45X22H4M3 chamfer hardness HRC 32 - 45, rod HRC 43-65. Austenitic steels are coated with a layer of 0.7 - 1.5 mm thick stellite with a hardness greater than HRC 70

The intake valve operates in less harsh conditions. It heats up to lower temperatures due to the removal of part of the heat from the valve and its components by the fuel that is injected into the combustion chamber. This ensures smaller temperature differences in the operation of the intake valve.

A layer of hard alloy with a thickness of 1.5 ... 2.5 mm is applied to the surface of the exhaust valve head, which increases the corrosion resistance of the valve.

Intake valves are made of less alloyed medium carbon steel grades (Gas distribution mechanism - intake valves: steel 40X, 45X, 45XN, 50XN, 40X9S2, 40X10S2M, 30X13N7S2).

The valve streamline should be more perfect, which helps to increase the speed of entry and exit of the fuel mixture charge.

The valve head is mainly flat, for powerful engines operating with increased loads, the heads are made concave. This shape of the head helps to reduce the mass of the part and the inertial forces that arise during operation.

For better cooling of the exhaust valve during operation, it is provided to make it hollow from the inside. The cavity is filled with a metal with a low melting point, most often sodium. When the valve head is heated, liquid sodium vapor rises to the upper, colder part, taking on a significant amount of heat, which is given to the less heated part of the rod. Extreme operating conditions can contribute to the exhaust valves jamming in the hole of the guide sleeve.

The operation of a piston engine is based on the supply of a fuel-air mixture to the cylinders and the removal of exhaust gases. These functions are performed by the intake and exhaust valves, opening alternately to supply the working mixture to the cylinders and to release the already used mixture. In the operation of this group of parts, there is one very important area - the thermal gap between the camshaft cam and the valve mechanism part that opens the valve. The operating conditions of the valve mechanism parts, and mainly the valves, are very harsh. The valves are heated to 800 - 900 ° C, their rods are lengthened, and the dimensions of the gaps that should be between their ends and cams are reduced. To compensate for this expansion, a thermal gap is assigned, the adjustment of this gap is carried out after each set for each group of engine mileage of the car. Manufacturers recommend adjusting the valve clearance after – 60… 80 thousand km of the car’s mileage, but it is not harmful to do it after a shorter period of operation.

With a reduced clearance, the valve does not fully perform its function – the sealing of the combustion chamber and its insulation from the intake and exhaust tract is not ensured. Leakage of the combustion chamber through an open valve causes a decrease in compression and the entry of high-temperature gases into the intake or exhaust tract. The thermal load on the valve increases due to its loose fit to the seat, which is a violation of the main condition for its cooling.

This has a particularly harmful effect on the exhaust valves. If the intake valves are cooled by the fuel-air mixture supplied to the cylinders, the exhaust valves come into contact with exhaust gases that have a high temperature (2500 ° C) and for them, cooling in the area of contact with the seat is of crucial importance. Poor cooling of the valve due to a small thermal gap leads to its overheating and destruction (burnout). The ingress of the ignited fuel-air mixture into the exhaust tract causes deterioration of the catalyst or its destruction, and then catastrophic damage to the cylinders by abrasive dust.

When the thermal gap increases, the impact action of the camshaft on the valve mechanism occurs, which causes untimely and incomplete opening of the valve, and the filling of the cylinder with the fuel-air mixture deteriorates, which reduces engine performance and power.

The thermal gap is quite small - 0.1 -0.4 mm. It is determined using a set of feelers with an accuracy of hundredths of a millimeter. The value of the thermal gap for the intake and exhaust valves is different, which is determined by the operating conditions of these valves. The operating conditions of the exhaust valves are more stressful, they heat up to higher temperatures, and therefore the change in size is more significant, therefore the thermal gap for them is larger.

Valve adjustment must be provided by the engine design. Engines that are equipped with hydraulic compensators - devices for automatic adjustment of the thermal gap, do not require manual intervention to adjust the valves.

During the operation of the car, such malfunctions may occur in the gas distribution mechanism as poor valve fit to the seat, incomplete valve opening, stretching of the drive chain links.

A sign of incomplete valve opening is knocking in the engine and a drop in power. The cause of this malfunction is a large gap between the valve stem and the rocker arm tip.

The malfunctions of the gas distribution mechanism also include wear of the camshaft gears, an increase in the longitudinal displacement of the camshaft and sticking of the valves due to the deposition of resinous substances on their rods.

The detected malfunctions must be eliminated in the following way: remove the carbon deposits, replace the broken spring, rinse the tarred valve rods with gasoline. The disturbed gap between the valve stem and the rocker arm tip is restored by adjustment. If the parts of the gas distribution mechanism are significantly worn, the engine is repaired.

An increase in the gap causes knocking of the valves, and a decrease causes a flash in the carburetor or pops in the muffler. With a large gap, the amount of valve lowering decreases and the duration of its opening is shortened, as a result of which the filling of the cylinder with a combustible mixture and the removal of combustion products from it deteriorate, and the engine power decreases.

Stretching the drive chain leads to a violation of the gas distribution phases, which makes it difficult to start the engine and reduces its power.

2. FORMULATION OF THE PROBLEM

To determine the causes of valve destruction and failure of the internal combustion engine of the Mercedes car. To achieve the set goal, the following tasks were solved: determining the composition of the material and its structure; conducting a macrostructural and factographic analysis of the obtained fragments; conducting metrological determinations of the geometric characteristics of the valve surface; based on the conducted studies, establishing the cause of premature valve destruction and failure of the internal combustion engine.

3. PRESENTING MAIN MATERIAL

When studying the condition of the destroyed valves and establishing the causes of their destruction, knowledge of the vehicle design, their technical operation and diagnostics; standardization, interchangeability and technical measurements; materials science and the basics of the theory and technology of heat treatment; mathematical statistics and the theory of the experiment was used.

The carbon content in the material of the provided valve fragments was determined according to GOST 22536.1-88 using the AN-7529 device (Fig. 1).

Figure 1 - Gas analyzer AN - 7529

The presence of alloying elements was determined according to GOST 28033-89 by the X-ray fluorescence method on the Spectroscan device.

Hardness and microhardness measurements were performed on TR 5006 (Fig. 2) and PMT – 3 (Fig. 3).

Figure 2 - Hardness tester TR 5006

Figure 3 - Microhardness tester PMT-3

The surface type and nature of the fracture were studied by macrostructural analysis using the MBS-9 device (Fig. 4).

Microstructural analysis was carried out on the MIM-10 microscope using the traditional method (Fig. 5). Photographing and processing of digital information was carried out using computer programs.

Figure 4 - Microscope MBS-9

Figure 5 - Microscope MIM – 10

4. THE RESULT OF WORK

General view of damaged valves (Fig. 6).

Figure 6 – Damaged valves of a Mercedes car

The chemical composition of the valve material is presented in Table 1.

Table 1 - Content of chemical elements

Material	Chemical composition, %							
	C	Cr	Mn	Mo	Si	Ti	Cu	Ni
Valve fragments	0,42	9,8	0,65	0,74	2,2	до 0 15	-	до 0,3
Steel grade 40X10C2M	0,35-0,45	9- 10,5	до 0,8	0,7- 0,9	1,9 -2,6	до 0,2	до 0,3	до 0,6

A visual inspection of the provided valve fragments showed that the main signs of the causes of destruction, such as oxidation, carbon deposits, which are usually the main cause of destruction of surface layers and valve wear, were not detected.

The valve was destroyed not from burnout, but as a result of the mechanical effect of applied forces (Fig. 7, 8).

The valve's service life after MOT (technical inspection) was not tens of thousands of kilometers, but only 100 km, after which the valve was damaged.

On the working surface of the valve plate, as a result of emergency operating conditions, scratches, cracks, and chips were found. No wear was found on the working surfaces of the valve head and stem.

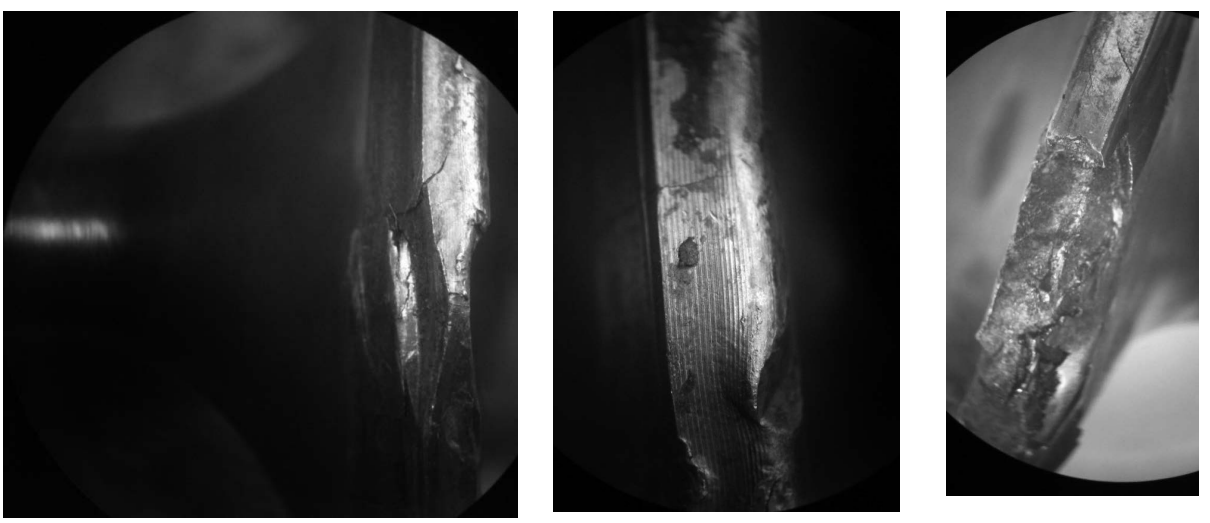

Figure 7 - Cracks in the valve plate

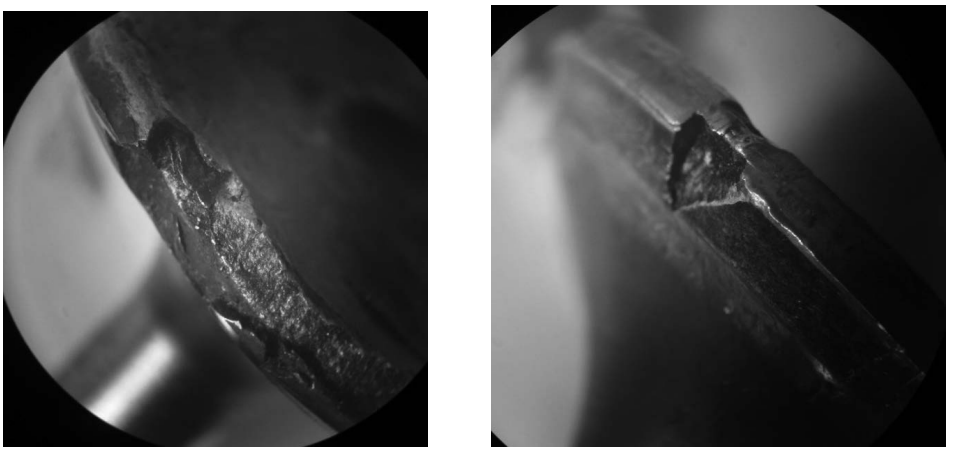

Figure 8 – Chips, gouging out of a dent in the valve plate

A trace of its seizure with the valve was found on the surface of the piston, apparently this happened at the moment when the exhaust valve jammed in the hole of the guide sleeve. The valve overheated greatly, oxidized, cracks formed, which led to its destruction.

The piston could destroy the valve during an impact when it jammed in the upper position. The displaced end of the valve rested with its edge on the piston. As a result of the impact, cracks appeared, which caused the destruction of the valve head and its separation from the rod.

A trace of the valve was found on the surface of the piston, which was formed as a result of the mutual impact contact of the piston with the plate (Fig. 9).

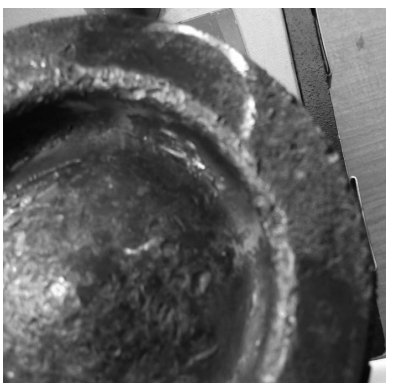

Figure 9 – Trace on the piston surface due to the valve impact

The valve rods also underwent deformation and destruction (Fig. 10).

Thus, the diameter values of the rods changed. The diameter of one of the rods in the lower part near the plate has a size of 8.52 mm, and in the upper part – 8.46 mm; the second rod – respectively - 8.48 and 8.46 mm. Such changes in size could have occurred only as a result of the action of significant compressive stresses, which, apparently, arose during the contact of the valve with the piston.

Figure 10 – Damaged valve stems

Figure 11 – Consequences of valve destruction – damaged turbine.

The destruction of the valves and their failure caused damage to the turbine (Figure 11). The destroyed valve fragments entered the combustion chamber, as a result of which the turbine blades were damaged and deformed.

5. CONCLUSIONS

The valve defects that caused the failure of the internal combustion engine are described. It was found that the cause of valve failure is not structural or technological defects, but unprofessional vehicle maintenance.

The chemical composition of the valve material meets the requirements of the standard. The loss of performance and destruction of the valve occurred under the influence of short-term dynamic loads. A sharp increase in dynamic loads occurred due to a small thermal gap between the valve and the piston, which was unqualifiedly set during regular maintenance, or during assembly work of the car.

It is recommended to adjust the thermal gaps (valve adjustment) according to one of the options that corresponds to the design features of the car engine.

ACKNOWLEDGEMENTS

The work was created as part of project based learning - PBL, in the 12th competition under the Initiative of Excellence - Research University, Silesian University of Technology, Gliwice, Poland.

BIBLIOGRAPHY

1. Buchynskyi M.Ya., Horyk O.V., Chernyavskyi A.M., Yakhin S.V. Fundamentals of machine creation / [Edited by O.V. Horyk, Doctor of Technical Sciences, Professor, Honored Worker of Public Education of Ukraine]. – Kharkiv: Publishing House “NTMT”, 2017. – 448 p. : 52 ill.
2. Kyslykov V.F., Lushchyk V.V. Construction and operation of cars: Textbook. — 6th ed. – K.: Lybid, 2006. – 400 p.
3. Ludchenko O.A. Maintenance and repair of automobiles: Textbook. – K.: Znannia - Press, 2003. – 511 p.

4. Drobot O.S., Pidgaichuk S.Ya., Borovyk L.V. Technology of structural materials and fundamentals of materials science in technical systems of state border protection. Textbook. Recommended by the Academic Council of the National Academy of the State Border Service of Ukraine named after B. Khmelnytsky. Khmelnytsky. NADPSU, 2019. 264 p.
5. Aftandylyants E. Materials science. Textbook/ Yevheniy Aftandylyants, Oksana Zazimko, Kostyantyn Lopatko. – Lira K. 2013. – 107 p.
6. Materials science. Textbook: educational and methodological complex for students of full-time and part-time studies / A.V. Haliko, O.V. Kuzyk, V.M. Kropivny, A.V. Kropivna, L.A. Molokost – Kirovograd: KOD, 2015. – 168 p.

TalentDetector
23th-25th June 2025
Gliwice-Brenna, Poland
DEPARTMENT OF ENGINEERING MATERIALS AND BIOMATERIALS
FACULTY OF MECHANICAL ENGINEERING
SILESIAN UNIVERSITY OF TECHNOLOGY
INTERNATIONAL STUDENTS SCIENTIFIC CONFERENCE

Influence of print parameters on mechanical properties. Modifications of components made using 3D printing technology

Bartosz Filip[a], Zbigniew Brytan[b]

[a] Student, Silesian University of Technology, Faculty of Mechanical Engineering, Department of Engineering Materials and Biomaterials
email: bf313885@polsl.pl
[b] Silesian University of Technology, Faculty of Mechanical Engineering, Department of Engineering Materials and Biomaterials

Abstract: The work describes the verification of the influence of selected process parameters and modification methods on the mechanical properties of 3D printed components. Particular attention was paid to the use of crosslinking techniques for enhancing the structural integrity of parts made from PLA and PETG materials. In addition, a Finite Element Method (FEM) analysis was conducted to simulate mechanical loading conditions and evaluate the behavior of the printed parts under stress. The combination of experimental testing and numerical simulation enabled a comprehensive assessment of how material selection, printing parameters, and post-processing modifications influence the final performance of the components.

Keywords: FDM, PLA, PET, MES, CAD, 3D Printing

1. INTRODUCTION

3D printing technology, which is one of the fastest growing areas of incremental manufacturing. It is playing an increasingly important role in design, prototyping and low-volume production. With the ability to create physical models quickly, it enables efficient testing, optimisation and customisation of products. A number of the advantages of 3D printing listed above, combined with the lack of need for expensive machinery and tooling, significantly increase the availability and prevalence of these methods. The focus of this paper is on 3D printing by filament extrusion (continuous filament material), based on polymers is referred to as the FDM (Fused Deposition Modelling) method. The main issue in determining the suitability of components made using the FDM method is the analysis of strength properties. Changing the individual parameters of the printing process, including the printing speed and temperature of the extruded mass, as well as the use of crosslinking modifications, are the main components of the analyses.

1.1. TEST MATERIAL – PLA AND PET-G

PLA (polylactic acid) is an important biopolymer derived from renewable sources such as starch and sugars, mainly from corn. Production involves the fermentation of glucose into lactic acid, followed by its polymerization. PLA exhibits mechanical properties similar to PET and is suitable for standard polymer processing methods such as injection molding and extrusion [1]. Prusament PLA filament from Prusa Polymers was used in the study, characterized by high quality and stability of the printing process. The material works well for rapid prototyping and production of functional components. The specific properties of the material used during the tests are presented in table 1.

Table 1. Declared properties of PLA material (filament) [2].

Material properties	Typical value	Test of method
Melt Flow Rate MFR [g/10 min] (1)	*9–11*	*ISO 1133*
Density [g/cm³]	*1,24*	*ISO 1183*
Tensile strength (yield strength) [MPa]	*57 ± 1*	*ISO 527*

(1) 2.16 kg; 210°C
(2) 24 °C; relative humidity 22 %

PET-G is a modified version of PET, enriched with glycol (usually CHDM), which improves its mechanical and thermal properties, while maintaining transparency and food contact safety. The material has good strength, flexibility and heat resistance. Prusament PETG filament from Prusa Polymers, designed for FDM/FFF printing, with high precision (diameter of 1.75 mm ± 0.02 mm), was used in the work. The recommended printing parameters are nozzle temperature of 250°C and table temperature of 80°C, with speeds up to 200 mm/s [3]. The material works with a variety of work surfaces, making it versatile and practical for engineering applications. The specific properties of the material used during the tests are presented in table 2.

Table 2. Declared properties of PET-G material (filament) [4].

Material properties	Typical value	Test of method
Melt Flow Rate MFR [g/10 min] (1)	*-*	*ISO 1133*
Density [g/cm³]	*1,27*	*ISO 1183*
Tensile strength (yield strength) [MPa]	*46 ± 1*	*ISO 527*

(1) 2.16 kg; 210°C
(2) 24 °C; relative humidity 22 %

1.2 TECHNOLOGY FDM

Fused Deposition Modeling (FDM) technology is one of the most common 3D printing methods, especially popular among hobbyists and small businesses. It involves the layering of molten thermoplastic material (e.g. PLA, PETG) through a moving nozzle. A number of process parameters affect the quality and properties of the prints, such as:

- Orientation of the raster - affects the stress distribution and strength of the part;
- Printing speed - determines precision, layer adhesion and production time;
- Fill density - determines stiffness and material consumption;
- Layer thickness - determines accuracy and printing time;
- Extrusion and table temperature - are crucial for layer bonding and dimensional stability of the model [5].

Choosing the right parameters is crucial for achieving high quality and durability of printed parts.

1.3 RADIATION CROSSLINKING

Electron beams are commonly used in the radiation treatment of polymers as an alternative to gamma radiation from the cobalt-60 isotope. Ionizing radiation, especially gamma radiation, is used, among other things, to sterilize and crosslink plastics to improve their mechanical and thermal properties. The process of radiation cross-linking is an economical method of strengthening cheaper and more easily processed polymers, increasing their durability, heat resistance and strength. By adjusting the irradiation dose, it is possible to precisely control the level of cross-linking and even selectively modify specific areas of the component. Cross-linked polymers are characterized by, among other things, non-fusibility, insolubility, reduced swelling and increased stiffness [6].

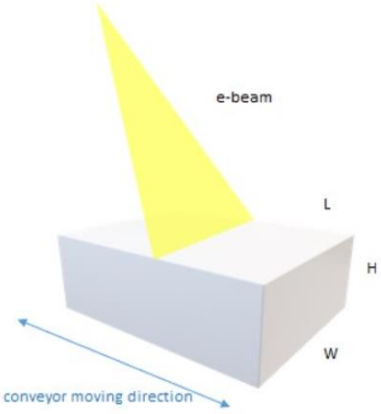

Figure 1 Radiation diagram

1.4 FEM ANALYSIS DETAILS

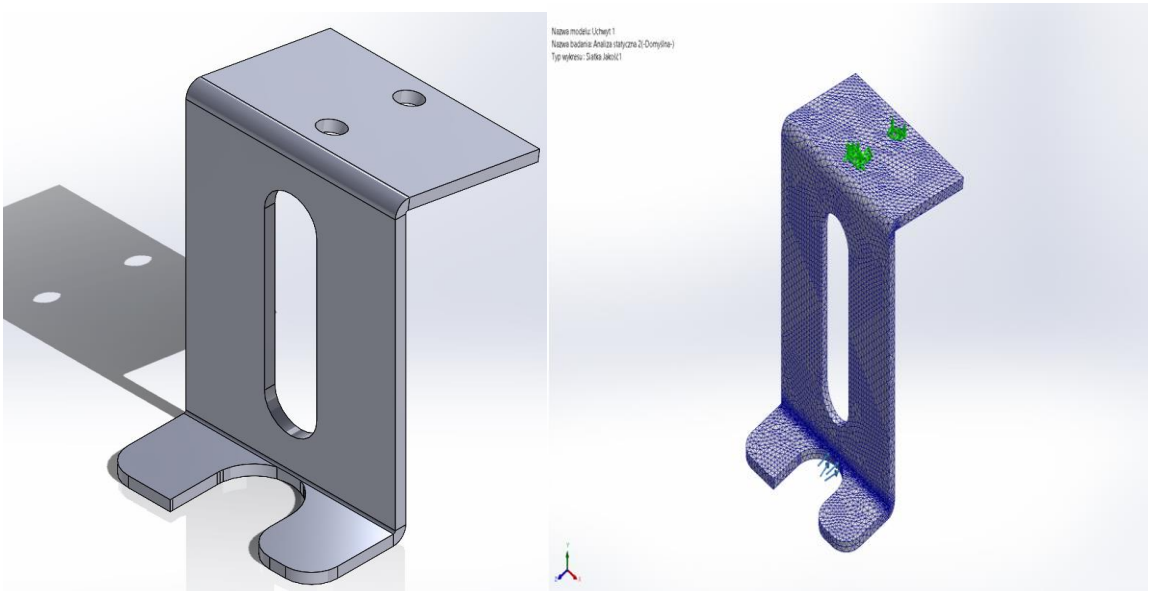

Figure 2 Solid mesh generated for the purposes of FEM analysis.

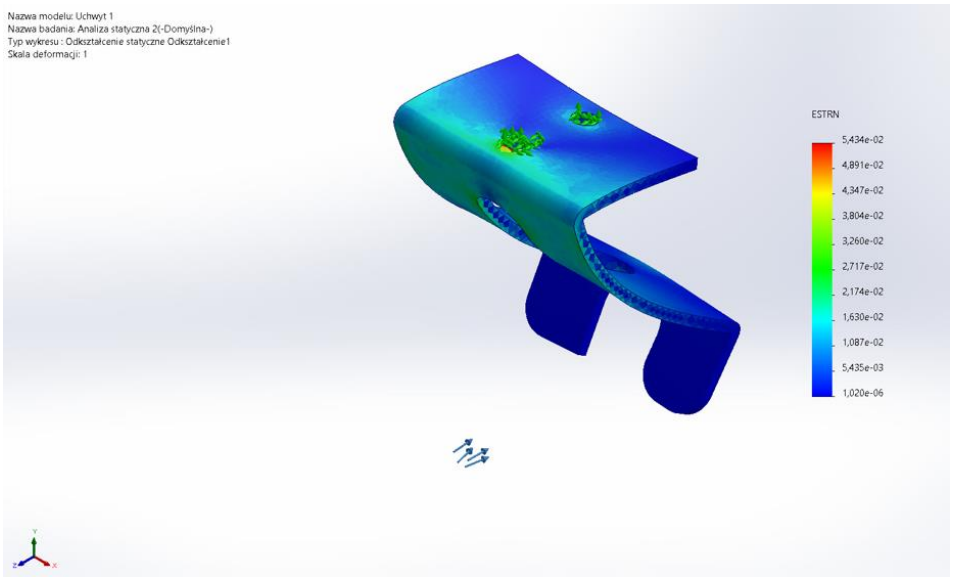

Figure 3 Analysis of element deformation using FEM analysis.

1.5 SUMMARY OF VALUES MEASURED DURING THE TESTS

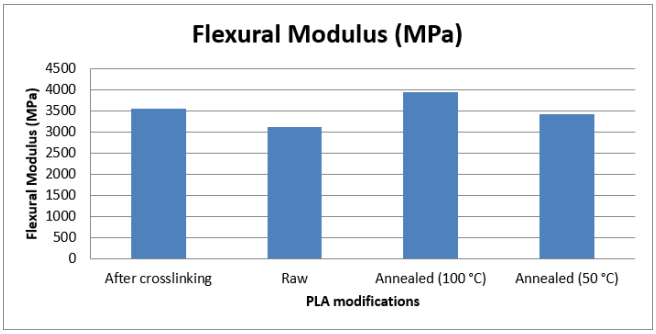

Figure 4 Flexural Modulus of PLA

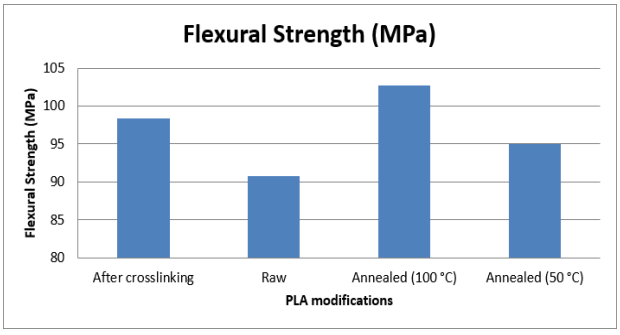

Figure 5 Flexural Strength of PLA

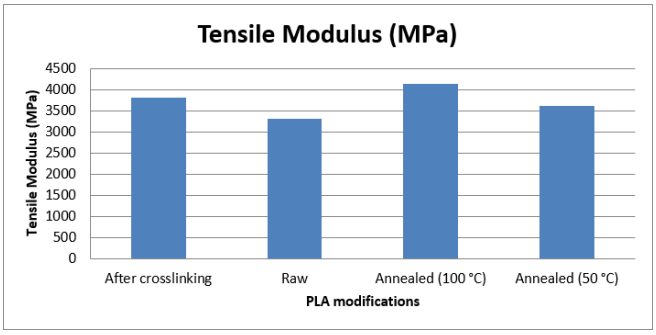

Figure 6 Tensile Modulus of PLA

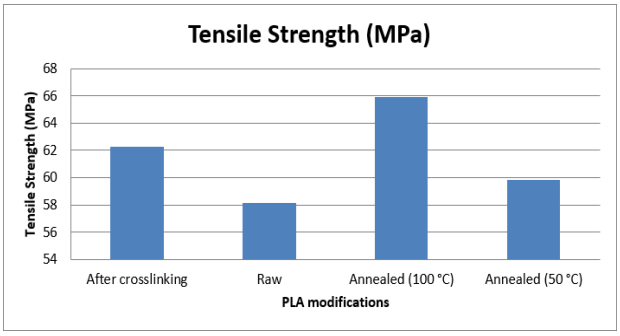

Figure 7 Tensile Strength of PLA

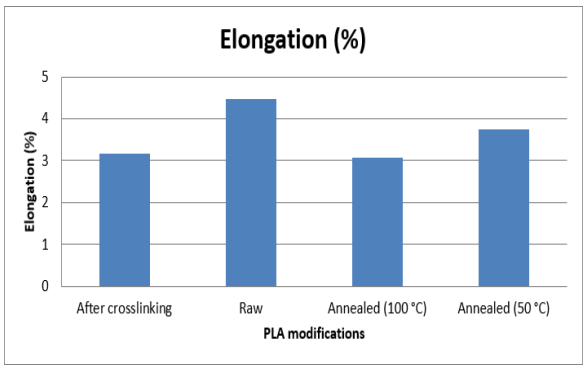

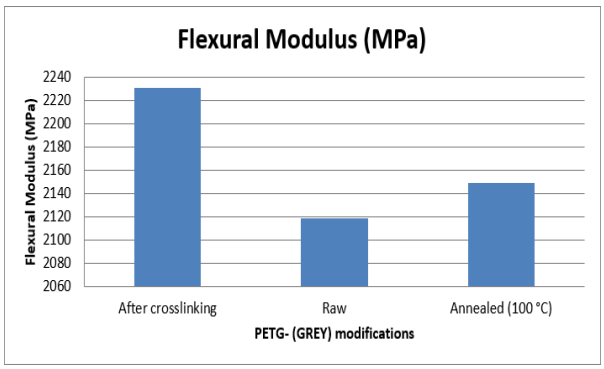

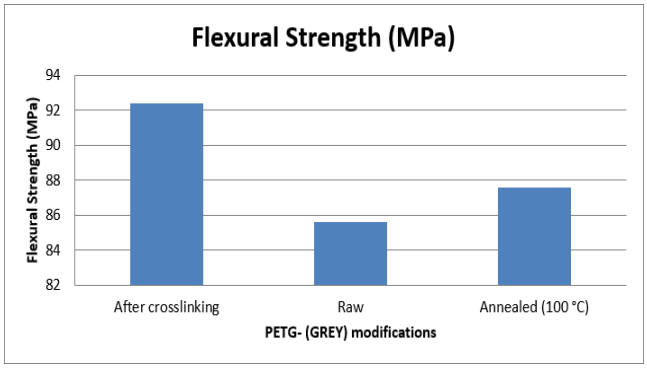

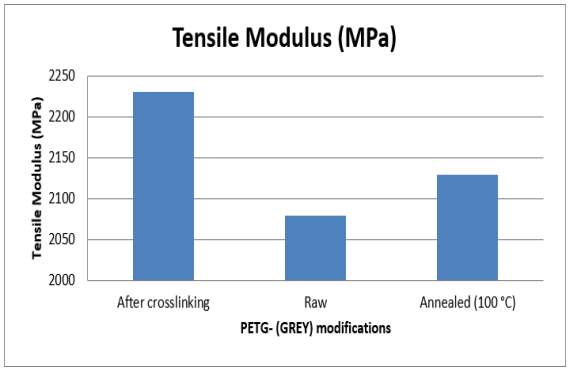

Figure 8 Elongation of PLA
Figure 9 Flexural Modulus of PETG(GREY)
Figure 10 Flexural Strength of PETG(GREY)
Figure 11 Tensile Modulus of PETG(GREY)
Figure 12 Tensile Strength of PETG(GREY)
Figure 13 Flexural Modulus of PETG(BLACK)
Figure 14 Elongation of PETG(GREY)
Figure 15 Flexural Strength of PETG(BLACK)

Figure 16 Tensile Modulus of PETG(BLACK)
Figure 17 Tensile Strength of PETG(BLACK)

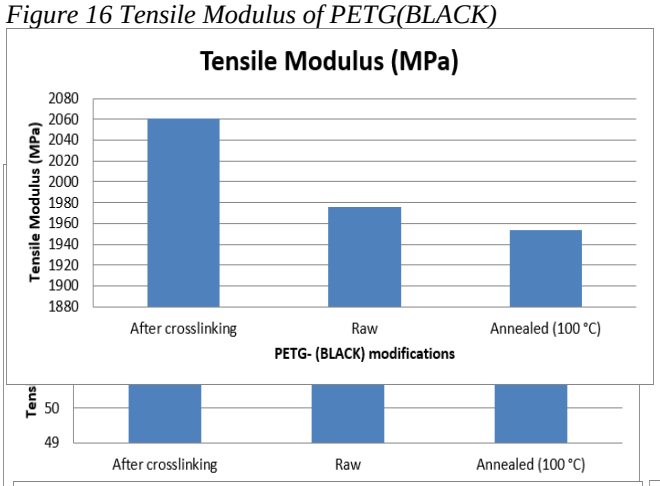

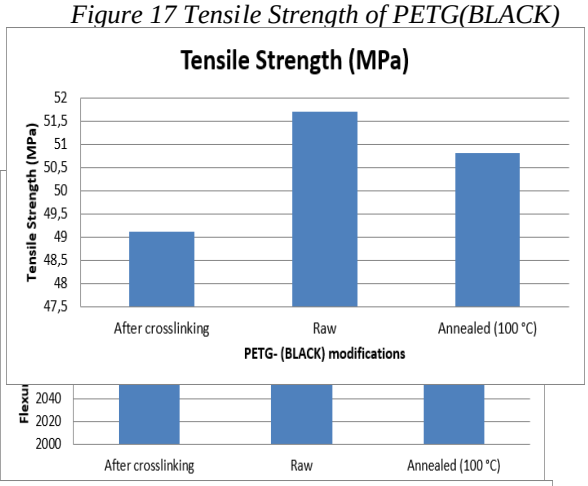

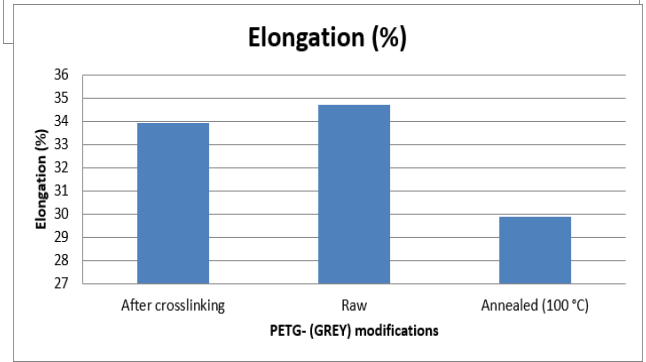

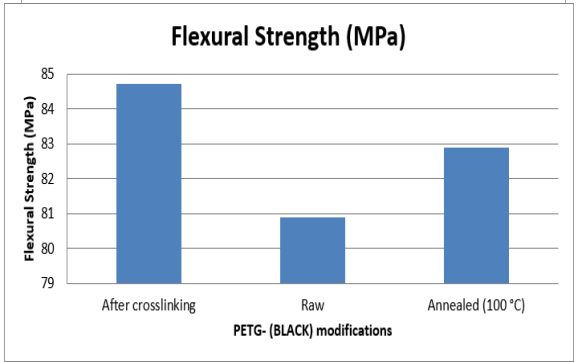

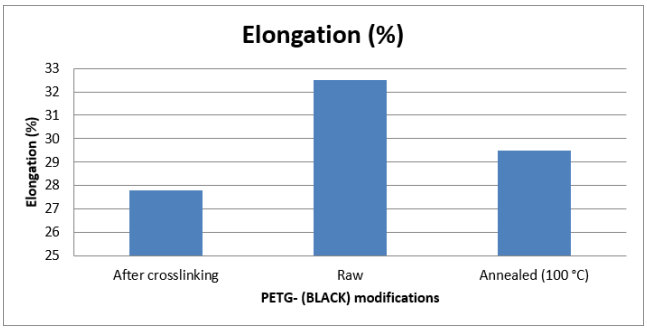

Figure 18 Elongation of PETG(BLACK)

2. SUMMARY

Selecting the optimal material for manufacturing components using the FDM method requires an integrated analysis of mechanical properties and numerical simulation results. Parameters such as elastic modulus, bending strength and deformation capacity are of key importance, as they determine the behaviour of the component under load. FEM analysis indicates the presence of significant bending stresses, which, in combination with the results of strength tests, allows for an informed choice of material configuration. The use of PLA after annealing at 100°C ensures the highest stiffness and resistance to deformation, meeting the design requirements resulting from modelling. The integration of experimental data with computational analysis provides the basis for rational optimisation of the printing process and the design of functional components.

ACKNOWLEDGEMENTS

The work was created as part of project based learning - PBL, in the 12th competition under the Initiative of Excellence - Research University, Silesian University of Technology, Gliwice, Poland and as part of project of Students Scientific Circle of Laser Surface Treatment under the Initiative of Excellence - Research University, Silesian University of Technology, Gliwice, Poland.

BIBLIOGRAPHY

1. Mohanty AK, Misra M, Drzal Lawrence TD, Selke SE, Harte BR, Hinrichsen G, et al. “Natural Fibers, Biopolymers and Biocomposites: An Introduction” 2005; 1, 15-50 (dostęp z dnia: 27.04.2025)
2. Technical datasheet Prusament PLA by Prusa Polymers, Version: 1.1, Last update: 16-02-2022
3. https://www.simplify3d.com/resources/materials-guide/petg/,
4. Technical datasheet Prusament PLETG by Prusa Polymers, Version: 1.1, Last update: 16-02-2022

5. Chacón, J. M., et al. (2017). Additive manufacturing of PLA structures using fused deposition modelling: Effect of process parameters on mechanical properties and their optimal selection. Materials & Design
6. International Atomic Energy Agency (IAEA), Radiation Processing of Polymers, IAEA-TECDOC-1420, Vienna, 2004.

TalentDetector
23th-25th June 2025
Gliwice-Brenna, Poland
DEPARTMENT OF ENGINEERING MATERIALS AND BIOMATERIALS
FACULTY OF MECHANICAL ENGINEERING
SILESIAN UNIVERSITY OF TECHNOLOGY
INTERNATIONAL STUDENTS SCIENTIFIC CONFERENCE

Materials used for recording of music played on a gramophone

Paweł Foltyn[a], Hanna Krymiec[b], Magdalena Maślanka[b], Wiktor Liszka[b], Bogusław Ziębowicz[c], Anna Ziębowicz[d]

[a] Faculty of Mechanical Engineering, Study group Science with Culture, Silesian University of Technology, Konarskiego 18A , 44-100 Gliwice, Poland;
email: pf316706@student.polsl.pl
[b] Faculty of Energy and Environmental Engineering, Study group Science with Culture, Silesian University of Technology, Konarskiego 18, 44-100 Gliwice, Poland;
email: hk318029@student.polsl.pl, mm317677@student.polsl.pl, wl318036@student.polsl.pl
[c] Faculty of Mechanical Engineering, Department of Engineering Materials and Biomaterials, Silesian University of Technology, Konarskiego 18A , 44-100 Gliwice, Poland;
email: boguslaw.ziebowicz@polsl.pl
[d] Faculty of Biomedical Engineering, Department of Biomaterials and Medical Device Engineering, Silesian University of Technology, Roosevelta 40, 41-800 Zabrze, Poland;
email: anna.ziebowicz@polsl.pl

Abstract: The article presents a historical overview related to the materials used for recording sound over the past 150 years, starting from the beginning of global phonography initiated by Édouard-Léon Scott de Martinville, Thomas Alva Edison, Alexander Graham Bell, and Emile Berliner's work. These materials are: paper and carbon soot, tin foil, beeswax, celluloid, ebonite, bakelite, shellac, polyvinyl chloride, polyethylene. This study is part of the research conducted by the study group Science with Culture operating at the Faculty of Mechanical Engineering and at the Student Cultural Center Mrowisko.

Keywords: vinyl record, turntable, materials, paper and carbon soot, tin foil, beeswax, celluloid, ebonite, bakelite, shellac, polyvinyl chloride, polyethylene, music, sound.

1. INTRODUCTION

The first preserved recording of sound to this day is the recording of the French song *Au clair de la lune*, made in 1860. It was written on paper coated with carbon soot and was not intended for playback. The recording was made by a device called the phonautograph (Fig. 1a), invented by Édouard-Léon Scott de Martinville, a bookseller and printer by profession. Privately, de Martinville was fascinated by the mechanical recording of sound. The phonautograph consisted of a membrane that moved a stylus - writing on paper coated with carbon soot. Scott de Martinville didn’t foresee the possibility of playing back such sound - he was fascinated by the lines appearing on paper, which were recordings of acoustic waves. The recordings created in

this way would be merely a curiosity, if it weren't for the fact that in 2008 scientists from Lawrence's laboratory in Berkeley, California, became interested in recreating them. After receiving their images from the institute in Paris, which is responsible for their storage, the scientists reproduced the sound recorded by the phonautograph. The earliest proved to be a recording of a French song - presumably performed by the inventor himself. In the following years, Thomas Edison, who patented the phonograph (Fig.1b) that allowed for the recording and playback of sound, and Alexander Graham Bell, who patented the graphophone (Fig. 1c), returned to this topic. These devices, despite many improvements, caused problems in everyday use. In 1887, the matter was addressed by Emil Berliner, who constructed the first gramophone (Fig. 1d) and prototypes of vinyl records, which were shellac discs. He decided to seriously engage in their production and sales, which brought the product to a wide audience. Various material solutions were used for music playback on these devices. [1-6]

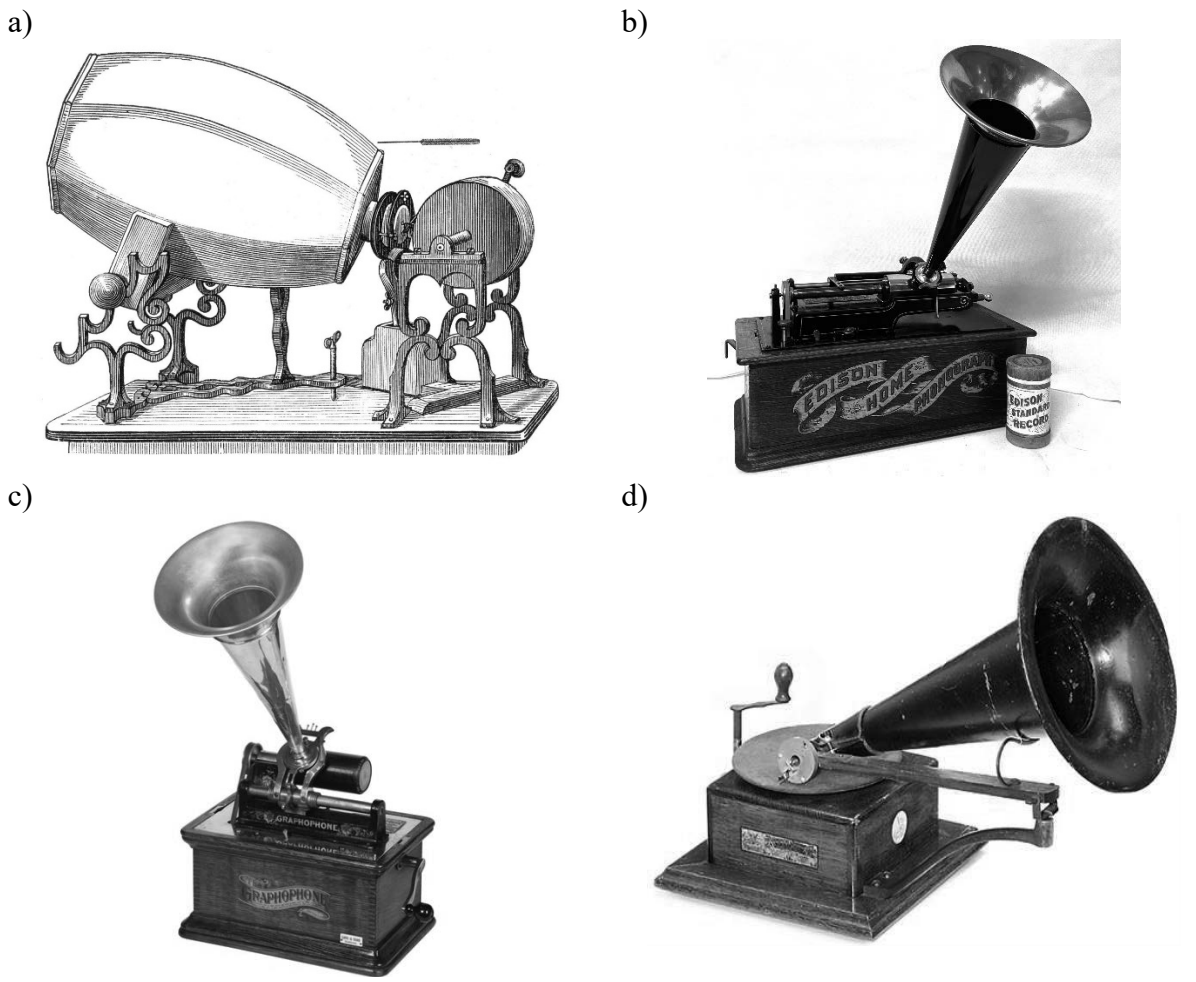

Figure 1. View of: a) phonautograph, b) phonograph, c) graphophone, d) gramophone [7]

1.1. Materials used for recording of music played on a gramophone

1.1.1. Paper and carbon soot (Fig. 2)

Leon de Martinville was the first to record an image of sound waves. He recorded sound visually on a phonautograph through a tube and a membrane, which vibrated and moved a stylus – this in turn left a mark on a paper cylinder covered with carbon soot. [8]

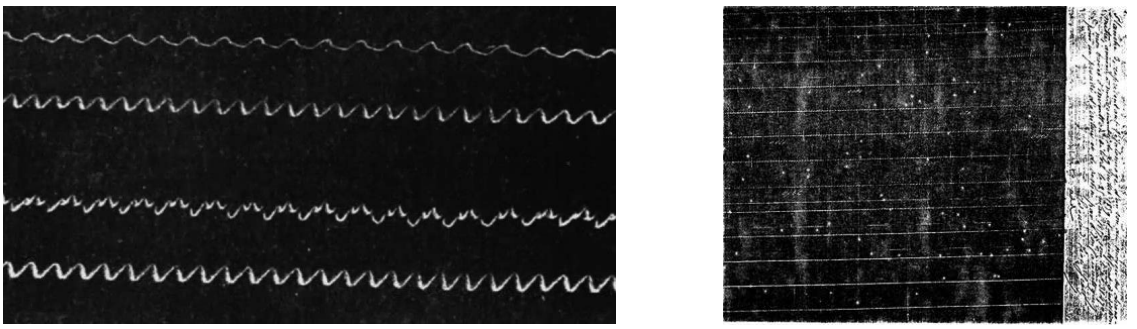

Figure 2. Surface of paper and carbon soot cylinder [7]

1.1.2. Tin foil (Fig. 3)

In the history of sound recording technology, tin foil played an absolutely fundamental role, being the first practical material that allowed for the preservation and reproduction of acoustic waves. In 1877, Thomas Alva Edison constructed the phonograph – a device that used a thin layer of tin foil wrapped around a rotating cylinder. The mechanism of action was based on converting acoustic waves into vibrations of a thin membrane, which moved a needle that engraved a spiral groove in the soft surface of the tin foil wound around the rotating cylinder. During playback, the needle moving in the engraved groove caused the membrane to vibrate again, enabling a faithful reproduction of the recorded acoustic signal. The physical properties of tin foil were crucial for this application. This material, due to its softness and plasticity, allowed for quick and precise reproduction of even slight changes in membrane vibration amplitude. However, its brittleness, susceptibility to tearing and deformation significantly limited the durability of the recording. Each subsequent playback resulted in gradual degradation of sound quality, and after several cycles, the material often suffered complete destruction. An additional difficulty was the recording process itself — the foil required precise winding onto a cylinder, and any imperfections led to the emergence of noise and signal distortions. Despite operational limitations, the use of tin foil marked a breakthrough in the history of recording technology. The first recording made on Edison's phonograph was a recording of the children's rhyme *Mary Had a Little Lamb* played back with a characteristic, distorted sound that, despite its low quality, made a huge impression on the audience of that time. However, the introduction of tin foil was experimental rather than industrial. This medium was too fragile and unstable to allow for mass production of recordings. Yet, without the pioneering use of tin foil, breaking through the technical barrier in the field of sound recording would not have been possible. It laid the foundation for the development of subsequent recording and playback technologies. [8]

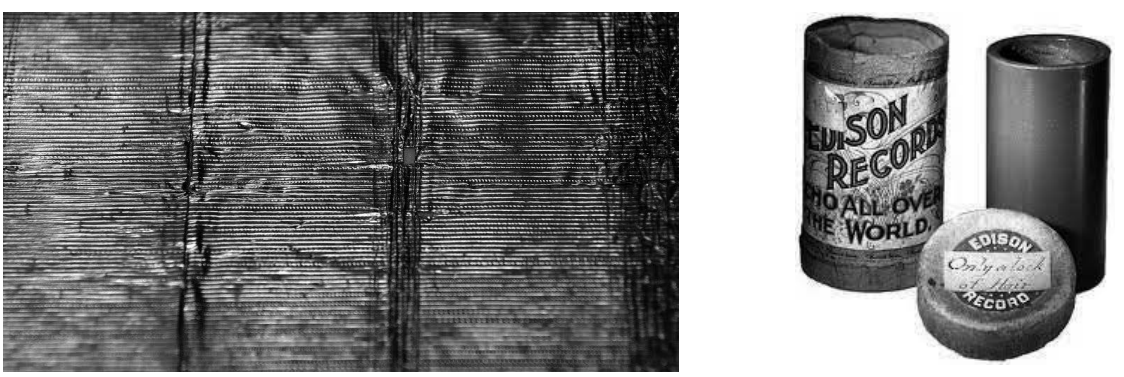

Figure 3. Tin foil cylinder [7]

Beeswax (Fig. 4)

Alexander Graham Bell and Charles Sumner Tainter at Volta Laboratory worked on other methods of sound recording. They replaced tin foil with paper coated with a mixture of beeswax and paraffin, which later transformed into a cylinder made entirely of wax. Instead of using an indent recording, they employed surface recording, where a sharp needle "engraved" sound waves into the wax. The thicker layer of wax allowed for the erasure of the cylinder's surface to replace the recording with another one. The device used for recording and playback of sound was called a graphophone, which was an improved version of Edison's phonograph. Due to the properties of wax, the cylinders wore out after several uses; in later years, their lifespan was extended by using harder wax. [8]

Figure 4. Beeswax cylinder [7]

1.1.3. Celluloid (Fig. 5)

Celluloid, invented in the 1860s by John Wesley Hyatt as a substitute for expensive ivory, was one of the first synthetic plastics. This material was created by combining cellulose nitrate with camphor, which acted as a plasticizer, giving the structure flexibility and elasticity. Celluloid exhibited unique physical properties: it was lightweight, transparent, relatively resistant to cracking and abrasion. It softened at around 90°C, making it easy to mold in industrial processes, but at the same time, it made it susceptible to deformation under elevated temperatures. In the context of the development of sound recording technology, celluloid played a groundbreaking role from the beginning of the 20th century. It was used, among other things, in the production of durable phonograph cylinders, particularly known under the Blue Amberol brand of Edison Records. These cylinders, unlike earlier wax carriers, allowed for hundreds of playback without significant loss of sound quality. Thanks to its plasticity, celluloid enabled a very accurate reproduction of the microstructures of phonographic grooves, which significantly improved the quality of recorded and played sound material. However, celluloid also had significant drawbacks that limited its long-term use. The biggest issue was its high flammability, resulting from the high content of cellulose nitrate. This material could ignite at relatively low temperatures or from a spark. Additionally, when exposed to UV light and higher temperatures, celluloid underwent gradual degradation: it shrank, cracked, and released harmful chemicals such as nitrogen oxides. Nevertheless, the introduction of celluloid marked a breakthrough in the accessibility of music for a wider audience. It enabled the mass production of sound recording media, which significantly contributed to the development of the phonographic industry. [10, 11]

Figure 5. Celluloid cylinder [7]

1.1.4. Ebonite

Ebonite, also known as hard rubber, is a plastic obtained by the strong vulcanization of natural or synthetic rubber with the addition of 25-30% sulfur. It was patented in 1851 by Nelson Goodyear. It has a density of 1.1–1.3 g/cm³ and belongs to the group of rubber materials known as duramers - it is hard, wear-resistant, but also brittle. In gramophones, ebonite was mainly used in the early development of audio technology, including the production of phonograph records, mechanical components, and electrical insulators. Due to its properties, it effectively damped vibrations, which was important for improving sound quality. [11]

1.1.5. Bekelite (Fig. 6)

Bakelite is the first synthetic thermosetting plastic, invented in the early 20th century by Leo Hendrik Baekeland. Bakelite is a phenol-formaldehyde resin that becomes very hard but relatively brittle after curing, and it is resistant to heat, chemicals, and electric current. The production of bakelite sheets was based on the condensation process of phenol with formaldehyde in the presence of an acidic or basic catalyst. This process took place in two stages: 1. Synthesis of phenol-formaldehyde resin (prepolymer) where phenol and formaldehyde were heated in the presence of a catalyst to produce a sticky material known as novolak or resol, 2. Molding and curing. Bakelite sheets were most commonly produced in the form of laminates, where the resin saturated layers of fabric or paper, and then the whole was pressed and cured. [11]

Figure 6. Bakelite records [7]

1.1.6. Shellac (Fig. 7)

Shellac records were made from natural resin derived from cochineal insects of the Kerriidae family. The resin was mainly harvested in India and then refined to produce shellac. In the production of gramophone records, shellac was combined, for example, with clay materials, quartz, slate dust, or barium sulfate; the proportions in which they were used and the exact composition varied between factories. The sound was first recorded onto a wax matrix, which was then coated with several layers of metal. This created a negative of the record, from which shellac copies intended for playback were pressed. Due to the brittleness of the material, shellac records were susceptible to cracking or chipping. After some time, soot was added to the components, which gave the record a black color and increased its durability. [8,11]

Figure 7. Shellac records [7]

1.1.7. Polyvinyl chloride (PVC) (Fig. 8)

PVC was synthesized in 1872 by German chemist Eugen Baumann after extended investigation and experimentation. The polymer appeared as a white solid inside a flask of vinyl chloride that had been left on a shelf sheltered from sunlight for four weeks. In the early 20th century, the Russian chemist Ivan Ostromislensky and Fritz Klatte of the German chemical company Griesheim-Elektron both attempted to use PVC in commercial products, but difficulties in processing the rigid, sometimes brittle polymer thwarted their efforts. Waldo Semon and the B.F. Goodrich Company developed a method in 1926 to plasticize PVC by blending it with various additives including the use of dibutyl phthalate by 1933. The result was a more flexible and more easily processed material that soon achieved widespread commercial use. It has thermoplastic properties, characterized by high mechanical strength (abrasion resistance), good flexibility, and resistance to the action of many solvents. Due to its properties, since the early 1950s, it has been the best and only material for the production of phonograph records. It is a phenomenon on a global scale. [12]

1.1.8. Polyethylene (Fig. 9)

High-density polyethylene (HDPE) is a thermoplastic material that gained popularity in the second half of the 20th century. It is resistant to chemicals, lightweight, and flexible, and sufficiently resistant to abrasion and scratches. It is mainly used for the production of picture

discs, and in the past, sound postcards and inserts for music magazines (paper soaked in polyethylene). [13]

Figure 8. Vinyl (PVC) records [7]

Figure 9. Picture discs [7]

2. SUMMARY

The 150-year period of audio recording (music) can be divided into two equal periods. The first is the period of searching for the right material and format of the gramophone record lasting until the early 1950s. The second is the time of PVC dominance. This period has already lasted for over seventy years and does not seem to be ending with any spectacular revolution. Of course, various other music carriers are in use, but alongside them, the vinyl record is still in use. The modern gramophone record was first presented in 1948 by Columbia Records (Fig. 10). [13]

Figure 10. Advertisement for a vinyl record from 1948 [7]

Its characteristic features, which are still in effect today, are:– made of plasticized polyvinyl chloride with various additives– recorded in mono and stereo (system 45/45)– mass-produced and machine-pressed from metal matrices– fine-grooved (groove four times smaller than in shellacs)– played at a speed of 33.1/3 revolutions per minute– about 45 minutes of recording– any colours (use of dyes). [13]

BIBLIOGRAPHY

1. Historia Gramofonu (dostęp 29.05.2025r.) https://voiceshop.pl/pl/n/16.
2. Krótka historia audio – fonograf, fonoautograf, telegraf i gramofon (dostęp 20.05.2025r.) https://www.rms.pl/aktualnosci/sprzet/1051-krotka-historia-audio-fonograf-fonoautograf-telegrafon-i-gramofon.
3. M. Kominek, Zaczęło się od fonografu, Polskie Wydawnictwo Muzyczne, Kraków, 1986.
4. A. Fogg, Adaptery, Państwowe Wydawnictwa Techniczne, Warszawa, 1957.
5. T. Olszewski, Książka o winylach, Wydawnictwo Polvinyl sp z o.o., 2023.
6. M. Anniss, P. Fuller, Winyle – podręcznik miłośnika winylów, Wydawnictwo Bellona, Warszawa, 2019.
7. www.wikipedia.org
8. https://www.firstsounds.org/sounds/scott.php (dostęp 29.05.2025r.)
9. https://www.americanhistory.si.edu/press/fact-sheets/early-sound-recording-collection-and-sound-recovery-project (dostęp 29.05.2025r.)
10. L. Jeffrey L., American Plastic: A Cultural History, Rutgers University Press, 1995.
11. O. Welch, W. L. Welch, From Tin Foil to Stereo: Evolution of the Phonograph. Howard W. Sams & Co., 1976.
12. A. Millard, America on Record: A History of Recorded Sound. Cambridge University Press, 1995.
13. P. Gronow, I. Saunio, An International History of the Recording Industry. Cassell, 1998.

TalentDetector
23th-25th June 2025
Gliwice-Brenna, Poland
DEPARTMENT OF ENGINEERING MATERIALS AND BIOMATERIALS
FACULTY OF MECHANICAL ENGINEERING
SILESIAN UNIVERSITY OF TECHNOLOGY
INTERNATIONAL STUDENTS SCIENTIFIC CONFERENCE

The Relationship Between Laser Technology and Eco-Friendly Cutting with PDM/PLM Systems and the Lean Six Sigma Approach in Production Engineering

Katarzyna Furman[a], Dominik Towarnicki[a], Mirosław Bonek[b]

[a] Silesian University of Technology, Faculty of Mechanical Engineering, Department of Automation of Technological Processes and Integrated Manufacturing Systems
email: katafur136@student.polsl.pl, domitow239@student.polsl.pl
[b] Silesian University of Technology, Faculty of Mechanical Engineering, Department of Engineering Materials nd Biomaterials

Abstract: This paper examines the integration of eco-friendly laser cutting technology into strategies for efficient operations in manufacturing enterprises. It highlights how fiber laser systems, when combined with advanced digital tools such as CAM, MES, and PLM systems, enhance production efficiency, reduce energy consumption, and support sustainable development goals. Furthermore, the application of methodologies like Lean Six Sigma, effective supply chain management, and structured data systems ensures that laser cutting processes align with modern business demands. This fusion of technology and strategic management supports not only environmental responsibility but also operational excellence, positioning enterprises to meet the challenges of Industry 4.0.

Keywords: Eco-friendly laser cutting, fiber lasers, operational efficiency, CAM systems, Lean Six Sigma, sustainability, Industry 4.0, supply chain optimization, digital manufacturing, smart production.

1. INTRODUCTION

In today's competitive industrial environment, enterprises are under increasing pressure to innovate, reduce costs, and operate sustainably. One technological advancement that aligns with these demands is the adoption of eco-friendly laser cutting systems—especially fiber lasers—which are recognized for their high energy efficiency, precision, and adaptability. When integrated with modern production management tools such as Computer-Aided Manufacturing (CAM), Product Data Management (PDM), and Manufacturing Execution Systems (MES), these technologies significantly enhance the agility and sustainability of production processes.

At the same time, strategic frameworks like Lean Six Sigma and the broader digital transformation of manufacturing (Industry 4.0) emphasize the need for data-driven decision-making, waste minimization, and operational transparency. The fusion of eco-friendly laser

cutting technologies with such strategies not only helps companies reduce their environmental footprint but also supports continuous improvement, regulatory compliance, and market competitiveness.
This paper explores how environmentally conscious laser cutting solutions serve as a foundation for efficient and modern enterprise operations, and how their application contributes to the holistic development of sustainable industrial practices.

2. COMPUTER-AIDED PRODUCTION MANAGEMENT

The integration of eco-friendly laser cutting technology with Computer-Aided Manufacturing (CAM) systems enhances production efficiency and sustainability. Fiber laser cutting machines, known for their precision and energy efficiency, can be seamlessly incorporated into CAM workflows.

- **Energy Efficiency**: Fiber lasers convert up to 70% of electrical energy into laser light, significantly reducing energy consumption compared to traditional CO_2 lasers.
- **Material Optimization**: Advanced nesting software in CAM systems ensures optimal material usage, minimizing waste.
- **Real-Time Monitoring**: Integration with Manufacturing Execution Systems (MES) allows for real-time monitoring and control, leading to improved quality and reduced downtime.

3. LEAN SIX SIGMA IN PRODUCTION INVOLVEMENT

Implementing Lean Six Sigma methodologies in laser cutting processes leads to continuous improvement and waste reduction. The DMAIC (Define, Measure, Analyze, Improve, Control) framework is particularly effective:

- **Define**: Identify areas where laser cutting can reduce environmental impact.
- **Measure**: Collect data on energy consumption, material waste, and process efficiency.
- **Analyze**: Determine root causes of inefficiencies or waste.
- **Improve**: Implement process changes, such as optimizing cutting parameters or upgrading equipment.
- **Control**: Establish monitoring systems to maintain improvements.

This structured approach ensures that laser cutting operations are both efficient and environmentally responsible.

4. SUPPLY CHAIN MANAGEMENT

Eco-friendly laser cutting technology positively impacts supply chain management by enhancing sustainability and efficiency:

- **Reduced Waste**: Precision cutting minimizes scrap, leading to cost savings and less environmental impact.
- **Energy Savings**: Lower energy consumption reduces operational costs and carbon footprint.

- **Regulatory Compliance**: Adopting green technologies helps companies meet environmental regulations and standards.
- **Customer Satisfaction**: Sustainable practices can improve brand image and meet customer demand for environmentally responsible products.

5. PRODUCTION DATA MANAGEMENT SYSTEMS (PDM/TDM/PLM)

Integrating laser cutting technology with PDM, TDM, and PLM systems enhances data management and process optimization:

- **PDM (Product Data Management)**: Centralizes design and process data, ensuring consistency and traceability.
- **TDM (Tool Data Management)**: Manages tool information, optimizing usage and maintenance schedules.
- **PLM (Product Lifecycle Management)**: Oversees the entire product lifecycle, facilitating continuous improvement and innovation.

These systems enable better decision-making, reduce errors, and support sustainable manufacturing practices.

6. STRATEGIES FOR EFFICIENT OPERATIONS IN ENTERPRISES

The use of eco-friendly laser cutting technology for engineering materials is closely related to strategies for efficient operations in enterprises, as both aim to increase efficiency, reduce costs, improve quality, and minimize environmental impact. Here's how they are connected:

- **Sustainable Development as a Strategic Element**

Eco-friendly technologies, such as fiber laser cutting, are less energy-intensive and generate less waste compared to traditional methods.
In modern business strategies, environmental responsibility is becoming a key competitive advantage and a part of brand image.

- **Process Efficiency**

Laser cutting is a fast, precise, and automated technology, enhancing operational efficiency.
Companies implementing strategies like Lean, Kaizen, or Just-in-Time focus on waste elimination – laser technology supports this by reducing material waste and errors.

- **Resource and Cost Savings**

Laser cutting optimizes both energy and material usage (e.g., through nesting and high energy efficiency).
Efficient business strategies focus on cost optimization and profitability, which are supported by modern laser systems.

- **Digitalization and Automation**

Laser cutting systems can be easily integrated with CAM, MES, and ERP systems, supporting digital transformation and real-time process monitoring.
Efficient operational strategies increasingly rely on automation and smart production management to quickly respond to market changes.

- **Innovation and Competitiveness**

Implementing eco-friendly technologies demonstrates modernity and innovation, enhancing a company's market position.

Growth-oriented business strategies emphasize the adoption of advanced solutions that increase customer value and differentiate the company.
Eco-friendly laser cutting not only supports environmental protection but also fits perfectly into strategies for efficient, modern, and sustainable business management, making it a cornerstone of Industry 4.0.

ACKNOWLEDGEMENTS

The work was created as part of project based learning - PBL, in the 12th competition under the Initiative of Excellence - Research University, Silesian University of Technology, Gliwice, Poland and as part of project of Students Scientific Circle of Laser Surface Treatment under the Initiative of Excellence - Research University, Silesian University of Technology, Gliwice, Poland.

LITERATURE

1. Kumar, A., Kumar, A., & Kumar, A. (Eds.). (2024). *Laser-Based Technologies for Sustainable Manufacturing*.
2. George, M. L., Rowlands, D., Price, M., & Maxey, J. (2005). *The Lean Six Sigma Pocket Toolbook: A Quick Reference Guide to Nearly 100 Tools for Improving Quality and Speed*. McGraw-Hill.
3. Chopra, S., & Meindl, P. (2018). *Supply Chain Management: Strategy, Planning, and Operation* (7th ed.).
4. Stark, J. (2015). *Product Lifecycle Management: 21st Century Paradigm for Product Realisation* (3rd ed.). Springer.
5. Porter, M. E., & Kramer, M. R. (2011). *Creating Shared Value*. Harvard Business Review.

TalentDetector
23th-25th June 2025
Gliwice-Brenna, Poland
DEPARTMENT OF ENGINEERING MATERIALS AND BIOMATERIALS
FACULTY OF MECHANICAL ENGINEERING
SILESIAN UNIVERSITY OF TECHNOLOGY
INTERNATIONAL STUDENTS SCIENTIFIC CONFERENCE

Structure and wear resistance of PVD TiN/TiAlN coating applied on a cemented carbide substrate

Rafał Gabryś[a], Magdalena Polok-Rubiniec[b], Anna Włodarczyk-Fligier[b], Aneta Kania[b]

[a] Students of Industrial Mechatronics, Silesian University of Technology, Faculty of Mechanical Engineering
[b] Silesian University of Technology, Faculty of Mechanical Engineering, Department of Engineering Materials and Biomaterials
email: magdalena.polok-rubiniec@polsl.pl

Abstract: This paper presents the results of tests on the surface topography and abrasive wear resistance of a PVD TiN/TiAlN coating deposited on a WC cemented carbide substrate. The non-uniform structure of the tested coating and its good abrasion resistance were found.

Keywords: PVD coatings, thopography, pin-on-disc

1. INTRODUCTION

Physical vapor deposition (PVD) is a technological process consisting in evaporating atoms or molecules of a material from a solid or liquid source and then transporting them in the form of a vapor through a vacuum or gas environment of low pressure and condensing them on the substrate. The use of increasingly new and advanced approaches in the design of coatings, such as multilayer, nanocrystalline, metastable or multicomponent layered materials cured with a solution, enable the protection of tools operating under very extreme and complex load conditions [1,2].

During the cutting process, the working surfaces of cutting tools are in constant contact with the surfaces of the machined material and the chip moving relative to them. The phenomena occurring on the surfaces of both the cutting tools and the machined material are the main reason for the wear process of cutting tools, which is the cause of the loss of the cutting ability of the tool. The most common phenomena causing the wear of cutting tools include: mechanical abrasion, adhesion, diffusion and chemical phenomena - oxidation [3]. During the cutting process, high stresses and loads are also created, as a result of which the tool matrix is quickly worn out and the efficiency of the machining process of the machined materials is reduced. For this reason, the use of protective coatings plays a key role in improving the properties and extending the service life of cutting tools. The use of a protective coating reduces friction and interaction between the tool material and the machined object. A properly prepared anti-wear layer with properties such as: high hardness, chemically neutral and antioxidant, produced on the tool surface, should prove effective even in the most demanding

working conditions [4]. The introduction of protective coatings to the market has led to a breakthrough in improving the properties of cutting tools. The creation of a barrier in the form of a coating has made it possible to limit the interaction between the chip and the tool material, and the hardness, thermal stability and chemical inertness of the cutting edge have also been increased. Currently, over 90% of all cemented carbide tools are applied using the PVD method, i.e. physical vapor deposition, or its combinations [5].

2. MATERIAL AND METHODOLOGY

The tests were performed on samples in the form of 10 mm diameter rods made of WC type cemented carbide with multilayer TiN/TiAlN type PVD coatings applied. The coatings were produced using the PVD SPUTTER method (sputtering).

The test samples made of coated carbide rods were cut into slices with the dimensions: 10 mm in diameter and 3 mm thick, using a universal tool grinder.

The surface topographies of the TiN/TiAlN coatings were observed on a Supra 35 scanning electron microscope at an accelerating voltage of 15.00 kV.

The abrasive wear resistance test was performed using the pin-on-disc method in accordance with the ASTM G99-95a standard [6], using a CSM Instruments tribometer.

The test used a counter-sample made of ZrO_2 with a diameter of 6 mm. The tests were carried out in an air atmosphere at room temperature. During the pin-on-disc test, a stationary ball was pressed against a disc rotating in a horizontal plane with a force of 5.0 N, the speed of rotation of the disc with the sample was 5 cm/s, the distance was 5000 cycles, and the friction radius was 3 mm. During the pin-on-disc test, the friction coefficient between the counter-sample and the disc is measured.

Observations of the abrasion profile trace of the coatings formed during pin-on-disc were performed on a Leica DVM6 A digital microscope for 2D and 3D imaging and analysis, at magnifications: 25x, 170x and 150x.

Wear track width measurements were performed using a stereomicroscope to measure the volume of coating material worn during the pin-on-disc test. Ten measurements were taken on each sample and the average was taken. The volume of material consumed due to friction was calculated using formula (1) in accordance with ASTM G99-95a [6].

$$V = \frac{\pi \cdot R \cdot D^3}{6 \cdot r} \qquad (1)$$

where:
V – average volume of material worn as a result of friction [mm^3],
R – friction radius [mm],
D – abrasion width [mm],
r – ball radius [mm].

3. RESULTS AND DISCUSSION

As a result of observations of the surface topography of the tested coatings, numerous irregularities were noticed, as well as precipitations in the form of drops (fig. 1), which may be related to the applied coating method.

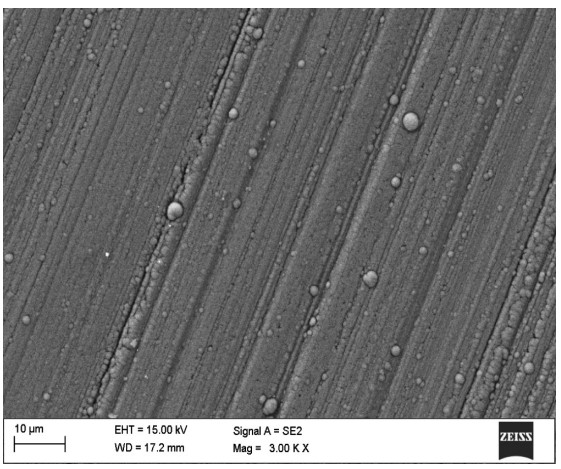

Figure 1. Surface topography of TiAlN coating on WC cemented carbide substrate

The abrasive wear resistance tests of the TiN/TiAlN coating (fig. 2) were carried out using the pin-on-disc method at room temperature. During the test, the course of changes in the coefficient of friction between the ZrO_2 ball and the tested sample was recorded. The graph shows the running-in effect, which disappears with time. The value of the coefficient of friction (fig. 2) increases from 0.6 to 0.75, and its average value remains at about 0.7.

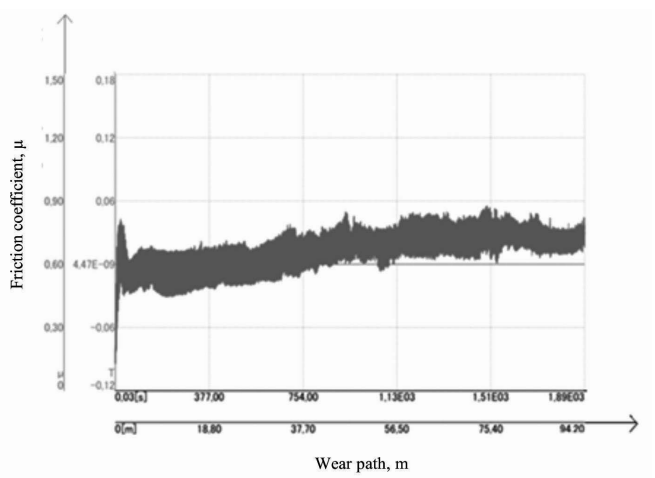

Figure 2. The course of changes in the coefficient of friction for the coating TiN/TiAlN.

As a result of observing the wear traces created during the pin-on-disc test for the TiN/TiAlN coating (fig. 3 a, b), unevenness and depressions were observed along the entire length of the track as well as differences in their degree of wear. The average width of the wear

marks for the TiN/TiAlN coating is 219,12 μm, the volume of material used calculated according to formula (1) is 0,00551 mm^3.

The average width of the wear marks for the TiN/TiAlN coating is 219,12 μm, the volume of material used calculated according to formula (1) is 0,00551 mm^3.

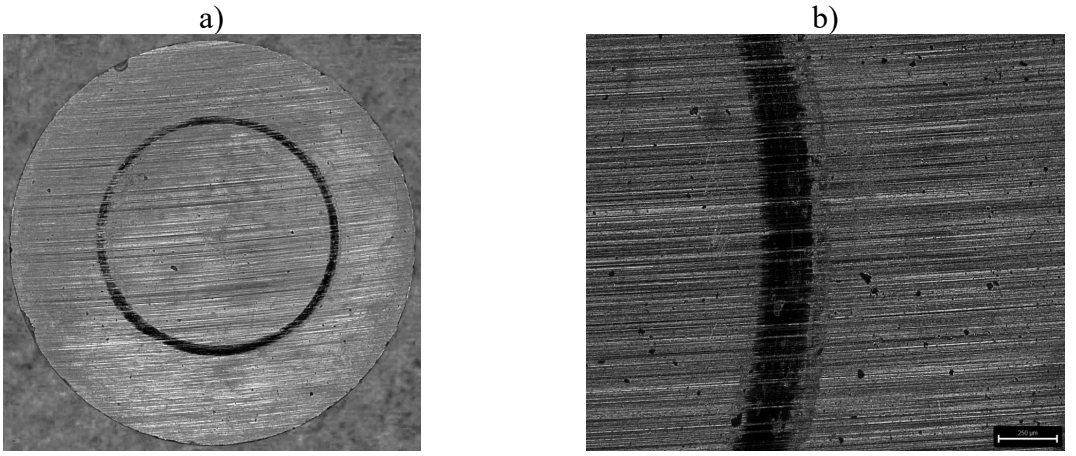

Figure 3. Wear trucks on the surface of the tested samples for the TiN/TiAlN coating, a)-mag.25x, b) - mag. 175x

4. SUMMARY

Observations of the surface topography of the tested TiN/TiAlN coatings indicate the presence of surface irregularities that could have been created during cutting of the WC rod. Numerous drops were also found to have been created during the process of applying the coatings using the physical vapor deposition method (PVD). The friction coefficient value for the tested TiN/AlTiN coating is on average 0.7.

BIBLIOGRAPHY

1. D. M. Mattox, Physical Vapor Deposition (PVD) Processes, Society of Vacuum Coaters, A/buquerque, N.M., 2002.
2. H. Holleck, V. Schier, Multilayer PVD coatings for wear protection, Surface and Coatings Technology 76-77 (1995) 328-336
3. Y. Deng, W. Chen, B. Li, Ch. Wang, T. Kuang, Y. Li, Physical vapor deposition technology for coated cutting tools: A review, Ceramics International 46, (2020) 18373–18390.
4. G. Wolfe, C. Petrosky, D.T. Quinto, The role of hard coatings in carbide milling tools, Journal of Vacuum Science & Technology 4 (1986) 24-29
5. A. Inspektor, P. A .Salvador, Architecture of PVD coatings for metal cutting applications: A review, Surface & Coatings Technology 257 (2014) 138-153
6. Norma ASTM G99-95a, Standard Test Method for Wear Testing with a Pin-on-Disk Apparatus, 1995.

TalentDetector
23th-25th June 2025
Gliwice-Brenna, Poland
DEPARTMENT OF ENGINEERING MATERIALS AND BIOMATERIALS
FACULTY OF MECHANICAL ENGINEERING
SILESIAN UNIVERSITY OF TECHNOLOGY
INTERNATIONAL STUDENTS SCIENTIFIC CONFERENCE

Design and Development of a Solar Sintering System for Powder Metallurgy

Maciej Gajdemski[a], Marcin Kowalik[a], Błażej Tomiczek[b]

[a] Student of Industrial Automation and Robotics, Silesian University of Technology, Faculty of Mechanical Engineering, Konarskiego 18A, 44-100 Gliwice, Poland
[b] Silesian University of Technology, Faculty of Mechanical Engineering, Scientific and Didactic Laboratory of Nanotechnology and Material Technologies, Konarskiego 18A, 44-100 Gliwice, Poland
email: blazej.tomiczek@polsl.pl

Abstract: The article describes design and development of a solar-powered sintering system intended for use in powder metallurgy applications. The device utilizes a Fresnel lens to concentrate solar radiation and achieve the high temperatures required for the sintering of metal and ceramic powders. The supporting structure was designed in a CAD environment and consist of dual-axis adjustable frame, allowing continuous alignment of the lens with the Sun's trajectory. Custom 3D-printed joints and connectors were designed and produced taking into account optimization for rigidity and precise fit. The system allows for both solar tracking and thermal control during sintering, demonstrating a low-cost, sustainable alternative to traditional high-temperature furnaces. The construction confirms the feasibility of combining additive manufacturing and solar energy to create efficient, and ecologically responsible material processing equipment.

Keywords: Solar sintering, powder metallurgy, additive manufacturing

1. INTRODUCTION

This work presents an innovative methodology for utilizing solar energy in modern powder metallurgy, specifically in sintering metallic and ceramic materials. The conceptual foundation of the system is based on the focused concentration of solar radiation using a Fresnel lens, enabling the attainment of high temperatures necessary for sintering without reliance on conventional thermal sources [1]. This approach aligns with global efforts to decarbonize high-temperature industrial processes and offers a sustainable alternative for materials processing [2], [3]. The Fresnel lens is integrated into a dual-axis solar tracking structure in the described system, utilizing an industrial-grade controller typically used in photovoltaic applications. Due to their reduced mass and compact geometry, Fresnel lenses offer a distinct advantage over traditional spherical lenses - they maintain comparable optical efficiency while being significantly lighter, which is especially beneficial for integration into mobile or automated tracking systems [4]. This configuration enables accurate alignment of the optical axis with the apparent solar motion

throughout the day, ensuring consistent and maximized irradiance at the focal point. The system architecture guarantees that the concentrated solar flux remains spatially fixed on the sintering surface despite the Sun's trajectory, which is critical for maintaining thermal uniformity during processing.

The system employs dual control architectures. The primary subsystem governs the real-time alignment of the optical axis via light-intensity sensors arranged co-planarly with the Fresnel lens. By employing angularly isolated photodetectors separated by baffles, crosstalk is eliminated, thereby enabling high-resolution feedback and precise adjustment of actuators along orthogonal axes. This guarantees spatial constancy of the focal point on the sintering surface throughout the solar day. The secondary control subsystem maintains precise temperature control inside the sintering chamber. A key challenge in solar-based sintering is the real-time regulation of process temperature, which must remain within a narrow window to avoid detrimental effects such as internal stress accumulation, microcracking, or surface melting. A fast-response thermocouple embedded directly beneath the sample provides continuous feedback to a microcontroller unit, which actuates a mechanical shutter system to modulate the incident thermal flux dynamically. The sintering module is equipped with an active cooling system to enhance thermal uniformity and protect critical components. A water-circulating thermal management loop, based on a dual-walled crucible with integrated cooling jackets, stabilizes thermal gradients and extends the durability of heat-exposed components. The simplicity of the system—utilizing convective mixing between hot and ambient water in a buffer tank—proves adequate due to the short duration of sintering cycles, avoiding the need for more complex radiative or forced convective exchangers.

The application of concentrated solar energy in powder metallurgy offers a range of potential advantages, including a significant reduction in sintering time and processing temperature while still enabling full densification of the material [5]. Compared to conventional resistance or furnace-based sintering, solar-driven systems have demonstrated the ability to achieve equivalent or superior results in a fraction of the processing time [5, 6]. Furthermore, these systems inherently produce steep thermal gradients and rapid cooling rates, which favour the formation of fine-grained, non-equilibrium microstructures with enhanced mechanical properties [7], [8].

The described method represents a confluence of optical engineering, automation, thermal sciences, and advanced manufacturing. It constitutes a viable, ecologically responsible pathway for processing high-performance sintered materials, in alignment with contemporary directives in materials science and sustainable engineering.

2. CONSTRUCTION DESIGN

The construction design process was handled using the CAD software Autodesk Fusion, the result of which is presented in Figure 1. The project assumptions were to make a simulated design to visualize the key aspects of the construction, that is, the use of the Fresnel lens, the sintering chamber, and the movement mechanism for adjusting the position of the lens.

2.1 General description of the structure

The main structural elements were designed using aluminium extruded profiles, which were chosen due to their favourable combination of low weight, high stiffness, and modularity. These profiles provide not only mechanical strength but also simplify the assembly process, as they

allow the use of standard connectors and enable future adjustments or modifications without the need for welding or machining. Aluminium also helps minimize thermal expansion and deformation under outdoor conditions, essential when working with concentrated solar energy.

Figure 1. Construction design

The overall geometry of the system resembles a truncated square pyramid, with the larger top surface intended to support a large Fresnel lens and the smaller bottom surface positioned to contain the sintering chamber. This specific shape was chosen to facilitate optimal solar radiation focusing while maintaining a structurally efficient and compact design. The pyramid is a rigid frame that keeps the lens and the chamber aligned along the optical axis. Additionally, this geometry supports effective heat concentration within a relatively small focal zone.

To ensure that the Fresnel lens remains perpendicular to the incoming sunlight throughout the day, the entire pyramid structure must be able to follow the Sun's movement across the sky. For this reason, a base frame was developed, which supports the pyramid and allows it to rotate in two axes. This dual-axis rotation system is necessary for tracking the Sun both in azimuth (east-west) and elevation (up-down), maximising the efficiency of solar energy collection during the sintering process. A robust shaft is mounted vertically on a square metal plate at the base of the system. This plate provides a wide footprint, significantly enhancing the stability of the entire setup and allowing it to be placed on various flat surfaces. The shaft is designed to be compatible with a standard M30 thread, which enables secure and precise mounting of the main structure. This also simplifies potential disassembly and transport of the system.

To achieve controlled movement, two linear actuators are integrated into the design. The first actuator rotates the base frame around the central shaft, allowing the system to track the Sun from east to west. The second actuator is positioned to push or pull one side of the pyramid structure, tilting it along the vertical axis and thus adjusting the elevation angle. This setup ensures smooth and accurate alignment of the Fresnel lens with the direction of sunlight during the entire sintering process. Such a configuration not only increases the system's thermal efficiency but

also extends the possible duration of its operation during the day. In summary, the design is compact, modular, and fully adjustable. It allows for efficient solar energy utilisation to reach the high temperatures required for metal powder sintering while maintaining mechanical simplicity and structural stability.

2.2 CAD designing

The design comprises primary elements, joints, and connectors prepared for 3D printing. This allows us to test the dimensions and movement of components about each other. By using the assembly functions of CAD software, there is a possibility to verify how the connections fit between 3D printed elements and other parts, as well as simulate joint movements and collision risks. The simulation of assembly joint movements has been helpful in the design process in assessing the placement of actuators that allow smooth movement without risk of collision.

2.3 3D printed parts

Different types of connections and joints were designed to connect extrusion profiles. There are two possibilities for connecting to an extrusion profile – one is by sliding inside the groove, and the other is by inserting inside one of the ends. The image Figure 2 shows different types of joints connecting extrusion profiles. One (on the bottom) allows rotation in two axes, holds the frame, and is supposed to tilt the construction, while the second rotation axis's purpose is to accommodate the angle of truncated square pyramid walls. The second joint (seen on the top) is a ball-type joint, allowing easy frame element position adjustment. This type of joint is only for connecting, and no rotation axis is required; that is why it is locked in place by a nut-type element after fitting the components. The holes in 3D printed parts are prepared for fastening with screws that hold the elements in place with extrusion profiles and allow rotation in case of tilt angle joint element. Implementing 3D printing in construction made assembly more customizable and allowed for a fast prototyping process. Actual mass and shape may sometimes vary in the case of physical elements compared to a simulation, which is why constant adjustments of connections were needed. By 3D printing the joints, the prototyping process was shortened due to the elimination of ordering and fitting different types of connections. Higher cost-effectiveness was achieved because of the lower cost of 3D printed parts compared to ordered aluminium joints.

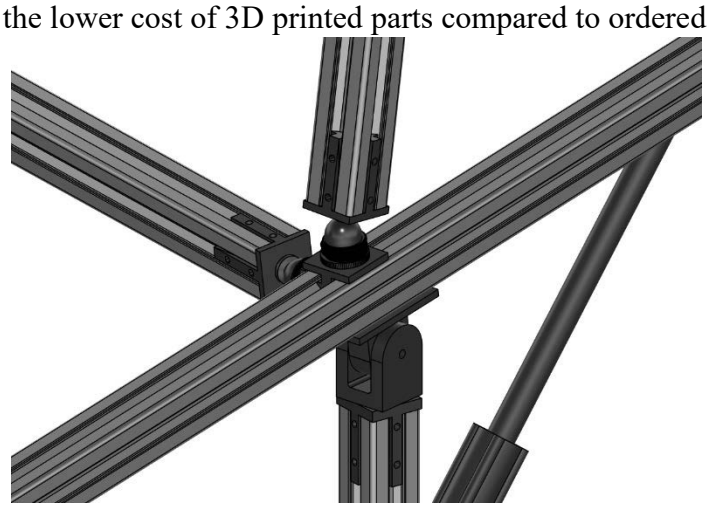

Figure 2. Modelled joints and connections

3. MANUFACTURED PARTS

The 3D-printed parts used in the construction assembly were manufactured using FDM (Fused Deposition Modeling) technology. These components were designed to integrate with the aluminium extrusion profiles and provide custom functionality, such as support brackets, mounting adapters, and mechanical connectors. All printed elements were tested virtually within the CAD environment before fabrication, ensuring proper fit and functionality within the assembled structure. The manufactured parts are shown in Figure 3, which presents the implementation of a tilt joint and a mounting bracket for a reinforcing brace.

Figure 3. Manufactured parts implemented in the construction

The printing process used a high infill percentage (around 80–100%) to achieve maximum mechanical strength and dimensional stability. Most of the printed components were designed to match the aluminium frame profiles and included built-in slots and tolerances to ensure a snug press-fit or bolt-on connection. Where necessary, slight post-processing was performed, such as removing support material or lightly sanding contact surfaces to improve fit. Design optimizations were introduced to reduce material usage while maintaining mechanical rigidity, such as reinforcing ribs and filleted corners in high-stress areas. These manufactured parts simplified the assembly process and provided a cost-effective and customizable way to realize non-standard geometries that would be difficult or expensive to machine using traditional methods. Their successful integration into the system confirmed the effectiveness of combining 3D printing with modular aluminium framing in developing functional solar sintering equipment.

4. SUMMARY AND CONCLUSIONS

Developing a comprehensive CAD model was a crucial step in successfully realising the solar sintering device. The 3D model enabled detailed visualisation of the entire construction, allowing for early detection of potential design conflicts and a clear understanding of the spatial relationships between system components. Thanks to the parametric nature of the CAD environment, custom joints and hinges were precisely adapted to the aluminium frame, ensuring structural compatibility and ease of assembly.

The CAD model also served as a platform for simulating the movement of the dual-axis tracking mechanism. These kinematic simulations were essential for verifying the range of

motion and mechanical correctness of the rotation system, ensuring the lens could maintain perpendicular alignment with the Sun throughout the day.

Based on the validated design, dedicated components were manufactured using 3D printing technology. The printed parts were optimised to fit seamlessly with the main structure, offering reliable mechanical performance while significantly simplifying the fabrication and assembly process. Using the CAD model thus streamlined the transition from concept to physical prototype and ensured the system's functional integrity from the outset.

ACKNOWLEDGMENTS

This publication was supported by the Excellence Initiative—Research University program implemented at the Silesian University of Technology in 2025. The authors would like to thank the project team members, Adam Brzoza, Maciej Bąkowicz, Kamil Pietrus, and Stanisław Bujak, for their valuable contributions to the preliminary stages of the project. In addition, the authors would like to thank Dr Marek Kremzer for his assistance in selecting the FDM printing parameters for the designed components and Dr Magdalena Szindler and Dr Marek Szindler for their consultation on choosing an appropriate Fresnel lens.

BIBLIOGRAPHY

1. D. Y. Goswami, *Principles of Solar Enginieering*, Boca Raton: CRC Press, 2015.
2. European Comission, *Photovoltaic Solar Energy: Development and Current Research*, Luxembourg: Office for Official Publications of the European Union, 2009.
3. E. Krajewska, J. Kuta , M. Pietruszka, O. Sobek, B. Łagosz, M. Ziółkowska, M. Szindler, B. Tomiczek, M. Szindler: *Stereolithography in the design and manufacturing of Fresnel lenses*, International Students Scientific Conference TalentDetector 2025-Winter, Gliwice
4. Fresnel Technologies, Inc., *Fresnel Lens Brochure*, Fresnel Technologies, Inc., Fort Worth, Texas, 2014.
5. G. Herranz, A. Romero, V. de Castro, G.P. Rodríguez: *Processing of AISI M2 high speed steel reinforced with vanadium carbide by solar sintering*, Materials and Design 54, 934–946, 2014.
6. A. Cañadilla, A. Romero, G. P. Rodríguez, G. Matula, Ł. Krzemiński, B. Tomiczek: *Manufacturing copper complex parts using an innovative Printing-Debinding-Solar Sintering (PDSS) process*, Journal of Manufacturing Processes 134, 851-865, 2025.
7. E. A. Olevsky, *Theory of sintering: from discrete to continuum*, Material Science and Engineering 23/2, 1998.
8. L. A. Dobrzański, G. Matula, *Podstawy metalurgii proszków i materiały spiekane*, Gliwice: International OCSCO World Press, 2012 (in polish)

TalentDetector
23th-25th June 2025
Gliwice-Brenna, Poland
DEPARTMENT OF ENGINEERING MATERIALS AND BIOMATERIALS
FACULTY OF MECHANICAL ENGINEERING
SILESIAN UNIVERSITY OF TECHNOLOGY
INTERNATIONAL STUDENTS SCIENTIFIC CONFERENCE

Development of biodegradable composite based on PLA matrix with the addition of material acquired from Symbiotic Cultures of Bacteria and Yeast (SCOBY)

Adrianna Hadyk [a,b], Wojciech Smołka [a,b], Jakub Osiewała [c], Olivia Mikolajec [d], Julia Kuliś [d]

[a] Student of Silesian University of Technology, Faculty of Chemistry, Department of Organic Chemistry, Bioorganic Chemistry and Biotechnology
[b] Student of Silesian University of Technology, Faculty of Energy and Environmental Engineering, Department of Environmental Biotechnology
[c] Student of Silesian University of Technology, Faculty of Mechanical Engineering, Department of Engineering Processes Automation and Integrated Manufacturing Systems
[d] Student of Silesian University of Technology, Faculty of Architecture, Department of Fine Arts and Design
e-mail: adrihad566@student.polsl.pl

Abstract: The aim of the study was to develop a biodegradable composite with PLA matrix with the addition of the material derived from kombucha cellulose, representing an exciting breakthrough in design and material science. It involves identifying the most favorable environment for the growth of SCOBY (*Symbiotic Culture of Bacteria and Yeast*) to obtain a material with the best possible properties. The article discusses the process of SCOBY cultivation, the production of PLA-SCOBY composite and the results of the tests of ion chromatography for tea fungus medium. The results of a static tensile strength tests of PLA-SCOBY composite were presented. Biodegradation of composites with a share of 5, 10 and 15% of SCOBY was also discussed.

Keywords: kombucha cellulose, biodegradable materials, SCOBY, composites, industrial design

1. INTRODUCTION

The tea fungus (*Medusomyces gisevii L.*), also known as kombucha, is a complex symbiotic microbiological structure that is gaining increasing attention as a source of innovative bio-based materials. It is primarily composed of bacterial cellulose produced by acetic acid bacteria such as *Gluconacetobacter xylinus* [1]. Numerous microorganisms are immobilized within its structure, including bacteria from the genera *Gluconacetobacter*, *Acetobacter*, *Lactococcus*, *Lactobacillus*, and *Clostridium*, as well as yeasts such as *Saccharomyces*, *Brettanomyces*, *Torulopsis*, *Zygosaccharomyces*, *Schizosaccharomyces*, and *Candida* [1,2]. The composition of

the microflora is variable and depends on cultivation conditions, which makes the tea fungus a versatile raw material [1].
The traditional use of kombucha is the production of a fermented beverage, valued for its prophylactic and medicinal properties [3]. The fermentation process, which includes three stages—lactic, alcoholic, and acetic—leads to an increase in the polyphenol and flavonoid content, as well as the antioxidant capacity of the liquid [4]. Nevertheless, bacterial cellulose, the main component of the tea fungus, represents a promising material for industrial applications. The layered cellulose structures produced by kombucha are characterized by flexibility, durability, and hypoallergenic properties, making it an attractive natural material [4].
In recent years, research has been increasingly undertaken to develop biodegradable polymer composites in which natural materials are used as fillers. The aim of this approach is to improve biodegradability, decrease of weight, reduce costs and obtain a beneficial effect on health and the natural environment. The properties of natural materials are a promising alternative to synthetic fillers [5,6]. Examples of natural fillers include coir, banana, kenaf, sugarcane fibers and so on [6] and wallnut shells [7]. The previously mentioned SCOBY material has also been described in the literature as a potential candidate for applications in composite materials. For example, Muralidharan et al. [8] indicated the potential use of laminate with the addition of kombucha cellulose for biodegradable tableware. Arteaga-Ballesteros et al. [5] developed composites based on polylactide (PLA) with the addition of kombucha. The aim of this study was to produce SCOBY material and then use it as a filler in PLA-based composites.

2. MATERIALS AND METHODS

2.1. SCOBY cultivation

The cultivation of the kombucha SCOBY (*Symbiotic Culture of Bacteria and Yeast*) was carried out using cultures obtained from two independent producers. The purpose of this approach was to optimize cultivation conditions and compare the quality and growth rate of the biofilm depending on the source of microorganisms. The initial cultures (primary cultivations) were established using a classic black tea extract, prepared by steeping tea in boiled water. Once the infusion had cooled, sugar was added at a ratio of 300 grams per 2 liters of liquid, creating a nutrient-rich medium with easily assimilable sugars essential for microbial development. A starter culture contained in the purchased SCOBY was added to each prepared portion of the medium. This starter included active strains of acetic acid bacteria and yeast, which immediately initiated the fermentation process, converting sugars into organic acids, carbon dioxide, and other metabolites. Simultaneously, the formation of a new layer of biofilm began — the characteristic gelatinous SCOBY structure, composed primarily of bacterial cellulose. The addition of the starter also ensured that the pH of the medium remained within the optimal range of 3.5–4.5, which is crucial for the proper course of fermentation and for preventing the growth of undesirable microorganisms.
The pH level was monitored using two methods: a digital pH meter and litmus paper. Prior to measurement, the pH meter electrodes were properly calibrated using standard buffer solutions. The electrodes were then immersed in the solution, and the values displayed on the device were recorded. In parallel, litmus paper was used — a strip was dipped into the solution and its color

was compared against a reference scale. If the pH value was too high, it was adjusted by adding small amounts of apple cider vinegar until a value of 3.5 was achieved.
The prepared primary cultures were distributed into four laboratory beakers with a volume of 5 liters and two flat trays measuring 40 × 60 cm, allowing observation of differences in biofilm development depending on the shape of the container. All vessels were covered with gauze secured by rubber bands to protect the cultures from insects and environmental contaminants while allowing gas exchange. The cultures were then incubated for a period of three weeks.
To examine the effect of temperature on fermentation and SCOBY formation, one beaker and one tray were placed in a laboratory incubator, where a constant temperature of 27°C was maintained. The remaining vessels were kept at room temperature (approximately 21–23°C). Additionally, ethanol was introduced at a concentration of 1 mg/ml into one of the trays incubated outside the incubator to analyze its effect on the development of microorganisms and the structure of the forming biofilm.
After the incubation period, which lasted approximately three weeks, the resulting SCOBYs were thoroughly rinsed with clean water to remove any residual medium and potential contaminants. They were then left to air-dry on a clean surface. Fig.1 presents the process of preparing SCOBY cultures. Depending on the needs of further research, the dried SCOBY was grounded.

Figure 1. Development of the first SCOBY cultures, October 2024.

2.2. Ion chromatography of the SCOBY medium

Analysis of a sample of tea fungus medium after three weeks of fermentation was carried out by ion chromatography using a Dionex AQUION instrument. The sample was subjected to a 1:10 dilution with deionized water and then analyzed using AS9HC 9mM 45mA 26min. The injection volume was 25 µL, and the total analysis time was 25 minutes.

2.3. Production of composite material based on PLA with the addition of SCOBY

The PLA (*polylactic acid*) was selected as the polymer matrix of the composite. The material was initially introduced in the form of transparent granules, which were subsequently melted using a thermoplastic injection molding machine. Once the PLA reached a molten state, finely ground SCOBY biomass was gradually added in three different concentrations—5%, 10%, and 15% by weight. The blending process was carried out until a homogenous mixture was

achieved, resulting in a viscous, paste-like mass. This mixture was then allowed to solidify under controlled conditions before being mechanically fragmented using hand tools such as a hammer to achieve a granule size suitable for further processing. The composite pieces were then reprocessed using a laboratory-scale injection molding machine. In this step, the material was once again plasticized and injected into molds to produce uniform samples shaped as standard tensile test specimens, commonly referred to as "dog-bone" samples. These samples served as the starting material for subsequent mechanical testing. Notably, the experiments highlighted the influence of SCOBY preparation and cultivation conditions on the quality of the resulting biocomposites. Variability in the texture, moisture content, and particle size of the SCOBY biomass appeared to significantly affect the consistency and performance of the final product. These findings underscore the need for further research aimed at standardizing the SCOBY cultivation process and improving composite formulation techniques. Fig. 2. presents an image of dried SCOBY material and the composite samples for tensile strength tests.

a) 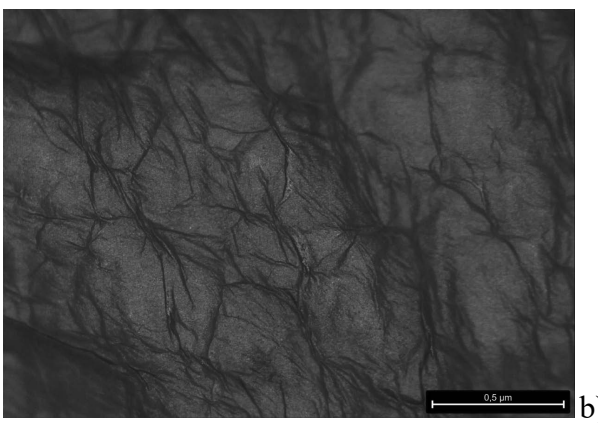

b) 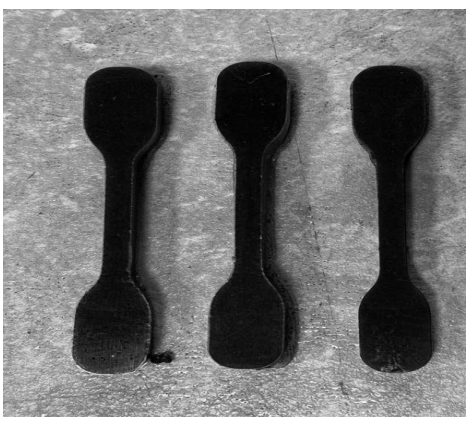

Figure 2. The image showing the SCOBY after drying (a), and the produced PLA-SCOBY composite in the form of samples for static tensile strength test.

2.4. Tensile strength testing

Mechanical testing was conducted to assess the tensile properties one composite made of PLA and 10% SCOBY by weight. Testing was performed using a universal tensile testing machine (Zwick/Roell Z020) under ambient conditions.

2.5. Biodegradation analysis

To assess the environmental impact and decomposition characteristics of the materials, a preliminary biodegradation study was carried out under controlled composting conditions. Samples of SCOBY-only and PLA-SCOBY composites were buried in a moist soil matrix at 25°C and monitored over a 12-week period. Visual inspection, weight loss measurements, and observations were recorded every two weeks. Results demonstrated that SCOBY-only materials showed a rapid biodegradation rate, with over 60% mass loss after 6 weeks. PLA composites exhibited slower degradation, depending on the PLA content. Composites with 5% PLA retained partial structural integrity after 12 weeks, while those with 15% PLA showed minimal decomposition, highlighting the importance of PLA ratio in balancing durability and environmental responsibility.

3. RESEARCH RESULTS

The results of ion chromatography (Fig.3) showed the presence of fluoride, chloride and sulfate ions at the following concentrations: fluoride - 34.38 mg/L (retention time: 4.06 min), chloride - 1.49 mg/L (retention time: 6.10 min) and sulfate - 1.81 mg/L (retention time: 17.27 min). The total sum of the determined ions was 37.69 mg/L. Particular attention was paid to the very high level of fluorine, which should not be present in such quantities in the test medium. Fluorine is present in black tea and its concentration can be as high as 6 mg/1 L. Such a high value of fluorine, seen in the graph, could be the result of preparing the tea bite medium from too much black tea. Other possible reasons for the elevated fluoride concentration are contamination of the water used to prepare the medium, or laboratory contamination, such as washing laboratory glassware with fluoride-containing detergents or rinsing it with fluoridated water. Another possible explanation is the effect of the tea fungus on the concentration of fluoride in the fermentation medium, since some acetic acid bacteria can accumulate ions of this element. In addition, it is possible that the tea used to prepare the medium contained higher-than-standard amounts of fluorine, which may be due to growing conditions and the age of the leaves - older leaves accumulate higher amounts of this element.

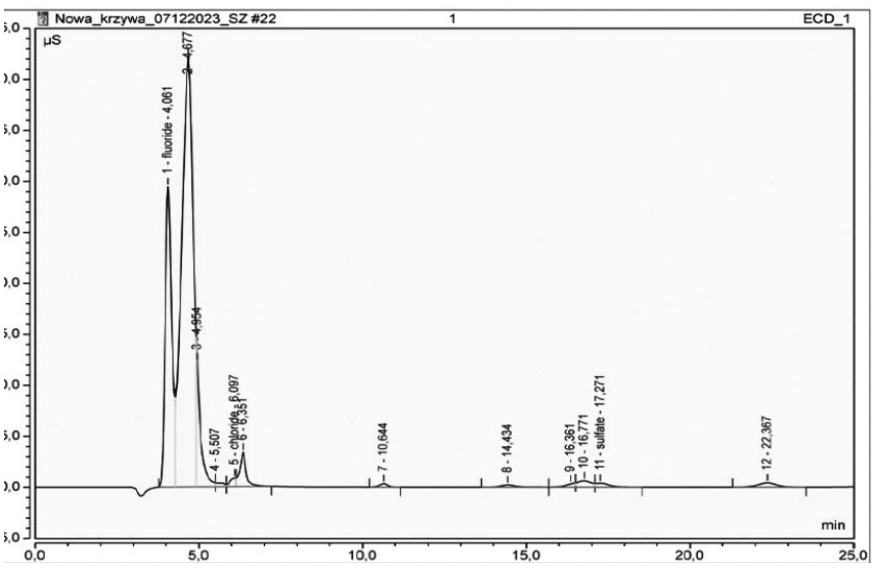

Figure 3. Ion chromatogram of the tea fungus medium after three weeks of fermentation, showing the presence of fluoride, chloride, and sulfate ions.

The static tensile strength tests of composite with the addition of 10% SCOBY was carried out for three samples. The average tensile strength was 47.3 ± 0.8 MPa with the strain of 3.6 ± 1.1%. Fig. 4. presents a tensile strength stress-strain curve. According to literature [9], tensile strength of PLA ranges from 39.9 to 52.5 MPa. According to Agaliotis et al. [10], the maximum strain stress of 3D printed pure PLA was 56.7 ± 2.3 MPa. It can be assumed that the 10% of SCOBY addition has not significantly affected the tensile strength, however further research should be carried out in the future.

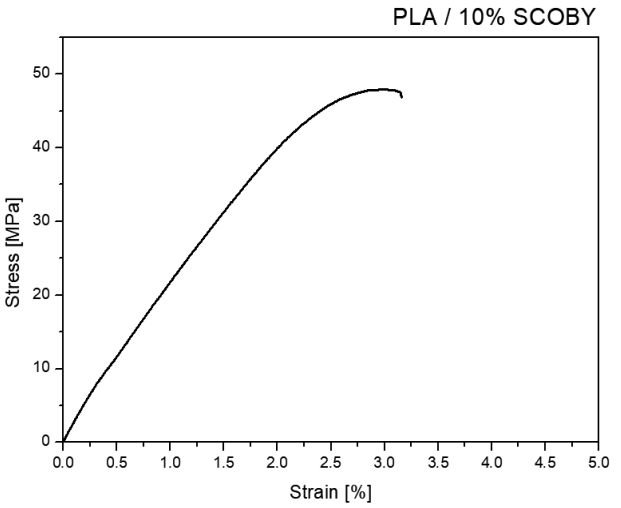

Figure 4. Tensile strength stress–strain curve of the PLA-SCOBY (10% by weight) composite.

4. SUMMARY

The results of the cultivation experiments revealed several important relationships between environmental and procedural variables and the rate and extent of SCOBY growth. One of the most significant findings was the influence of the size of the starter culture on the final biomass yield. Larger initial SCOBY fragments introduced into the medium produced a visibly thicker and heavier layer of bacterial cellulose after the standard three-week incubation period. This correlation highlights the importance of optimizing inoculum volume for efficient scaling of the material production process.

Temperature was another critical factor affecting the development of the kombucha culture. Samples incubated at a constant temperature of 27–28°C in a laboratory incubator exhibited a significantly accelerated growth rate and produced denser and more uniform cellulose layers compared to those kept at ambient room temperature (approximately 21–23°C). The increased metabolic activity of the microbial community under elevated temperature conditions contributed to a more rapid fermentation process and facilitated the synthesis of bacterial cellulose.

To investigate the potential impact of ethanol on SCOBY formation, 1 mg/mL of ethanol was introduced into one of the culture trays. However, the addition of alcohol did not significantly affect the rate or quality of cellulose production. The resulting SCOBY was comparable in size and texture to those grown in ethanol-free conditions, suggesting that this concentration of ethanol neither inhibited nor enhanced microbial activity or cellulose biosynthesis in a meaningful way.

The static tensile strength tests showed that the SCOBY addition probably does not significantly affect the deterioration of mechanical properties, however, further research should be carried out in this direction. It is possible that the biodegradation of PLA-SCOBY composites can be largely improved without deterioration of mechanical properties.

BIBLIOGRAPHY

[1] E.A. Flyurik, O.S. Ermakova, Medusomyces gisevii L.: Cultivation, composition, and application. Foods and Raw Materials 11 (2023) 563–572.

[2] A.J. Marsh, O. O'Sullivan, C. Hill, R.P. Ross, P.D. Cotter, Sequence-based analysis of the bacterial and fungal compositions of multiple Kombucha (tea fungus) samples, Food microbiology 38 (2014) 171-178.
[3] N.P. Shah, Functional cultures and health benefits, International Dairy Journal 17 (2007) 1262-1277.
[4] C.J. Greenwalt, R.A. Ledford, K.H. Steinkraus, Determination and characterization of the antimicrobial activity of the fermented teaKombucha, LWT-Food Science and Technology 31 (1998) 291-296.
[5] B. Arteaga-Ballesteros, A. Guevara-Morales, E. Martín-Martínez, U. Figueroa-López, H. Vieyra, Composite of polylactic acid and microcellulose from kombucha membranes, e-Polymers, 21 (2020) 015-026.
[6] P. Jagadeesh, M. Puttegowda, Y.G. Thyavihalli Girijappa, S.M. Rangappa, S. Siengchin, Effect of natural filler materials on fiber reinforced hybrid polymer composites: An Overview, Journal of Natural Fibers, 19 (2022) 4132–4147.
[7] A. Włodarczyk-Fligier, M. Polok-Rubiniec, B. Chmielnicki, Polypropylene-matrix polymer composites with natural filler, Archives of Metallurgy and Materials, 66 (2021) 313–319.
[8] V. Muralidharan, C.R.T. Jebathomas, S. Sundaramoorthy, B. Madhan, S. Palanivel, Preparation and evaluation of novel biodegradable Kombucha cellulose-based multi-layered composite tableware. Industrial Crops and Products 215 (2024) 118629.
[9] G. Gao, F. Xu, J. Xu, Z. Liu, Study of Material Color Influences on Mechanical Characteristics of Fused Deposition Modeling Parts, Materials, 15 (2022) 7039.
[10] E.M. Agaliotis, B.D. Ake-Concha, A. May-Pat, J.P. Morales-Arias, C. Bernal, A. Valadez-Gonzalez, P.J. Herrera-Franco, G. Proust, J.F. Koh-Dzul, J.G. Carrillo, E.A. Flores-Johnson, Tensile Behavior of 3D Printed Polylactic Acid (PLA) Based Composites Reinforced with Natural Fiber. Polymers, 14 (2022), 3976.

TalentDetector

23th-25th June 2025
Gliwice-Brenna, Poland

DEPARTMENT OF ENGINEERING MATERIALS AND BIOMATERIALS
FACULTY OF MECHANICAL ENGINEERING
SILESIAN UNIVERSITY OF TECHNOLOGY

INTERNATIONAL STUDENTS SCIENTIFIC CONFERENCE

Porovnanie vlastností polotovarov z polymérneho kompozitu používaného pri termoformovaní

Rastislav Hanulík[a], Lenka Markovičová[a], Mirosław Bonek[b]

[a] Žilinská univerzita v Žiline, Strojnícka fakulta, Katedra materiálového inžinierstva, Univerzitná 8215/1, 010 26 Žilina, Slovak Republic
[b] Silesian University of Technology, Faculty of Mechanical Engineering, Department of Engineering Materials and Biomaterials, ul. Konarskiego 18A, 44-100 Gliwice, Poland
email: hanulik3@stud.uniza.sk, lenka.markovicova@fstroj.uniza.sk

Abstrakt: Príspevok provnáva vlastnosti polotovarov z polymérneho kompozitu používaného pri termoformovaní. Cieľom práce bolo testovanie a porovnanie vlastností dvoch polotovarov (starý „S" a nový „N") z polymérneho kompozitu plneného talkom (mastenec) určených na termoformovanie a vyhodnotenie zmeny vybraných mechanických vlastností (skúška ťahom, skúška tvrdosti podľa Shora, nasiakavosť a korózna skúška pod napätím) vzoriek vystavených expozícii v rôznych prostrediach (olej, benzín, kyselina sírová) po dobu 14, 28 a 35 dní.

Získané výsledky jasne potvrdzujú, že materiál „N" vykazuje horšie mechanické vlastnosti a nižšiu odolnosť voči pôsobeniu agresívneho prostredia, čo vedie k vyššej kazivosti počas výroby. Naopak, materiál „S" vykazuje vyššiu stabilitu a je vhodnejší pre aplikácie vyžadujúce dlhodobú mechanickú a chemickú odolnosť.

Kľúčové slová: polymér, kompozit, polymérne kompozity, polypropylén, termoformovanie

1. ÚVOD

Polymérne kompozity predstavujú špičkovú triedu materiálov, ktoré spôsobujú revolúciu v mnohých priemyselných odvetviach na celom svete. Tieto kompozity sú skonštruované kombináciou polymérnej matrice s vystuženými materiálmi ako sú vlákna alebo častice, aby sa dosiahli zlepšené mechanické, tepelné a elektrické vlastnosti. Všestrannosť polymérnych kompozitov vyplýva z ich schopnosti prispôsobiť vlastnosti na základe špecifických požiadaviek. S vlastnosťami, ktoré môžu prekonať vlastnosti tradičných materiálov, ako sú kovy a keramika, polymérne kompozity ponúkajú jedinečnú rovnováhu pevnosti, nízkej hmotnosti a odolnosti voči korózii.

Odvetvie letectva, automobilového priemyslu, stavebníctva a športových potrieb patrí k mnohým, ktoré ťažia z mimoriadnych vlastností polymérnych kompozitov. Ako výskum neustále napreduje, polymérne kompozity sú prísľubom pre ešte rozmanitejšie a inovatívnejšie aplikácie, ktoré poháňajú pokrok v rôznych oblastiach.

Aj napriek tomu, že využitie plastov v rôznych priemyselných odvetvia je prínosom z hľadiska energetického (šetria energetické zdroje a znižujú množstvo exhalátov) a ekonomického (šetria surovinové zdroje), nemožno zabúdať na fakt, že aj polymérne materiály degradujú. Mnohé z nich pri degradačných procesoch uvoľňujú nízkomolekulové zlúčeniny, ktoré môžu škodiť zdraviu, ohrozovať životné prostredie alebo dokonca môžu byť i toxické.

Nielen tieto ich vlastnosti však ohrozujú životné prostredie. Vývoj smeruje k výrobe stabilných plastov a tie nestrácajú stabilitu ani po opotrebovaní či skončení životnosti výrobku, keď sa stávajú odpadom, ktorý sa umiestňuje na skládkach, zaberá obrovský objem, čím sa stáva nebezpečným. Je preto dôležité poznať vlastnosti plastov v rôznych degradačných prostrediach, či dochádza k ich podstatnej zmene a tým zabrániť hromadeniu plastového odpadu a šetriť životné prostredie. V tomto prípade hovoríme o starnutí plastov [1-8].

2. EXPERIMENTÁLNA ČASŤ

Ako experimentálny materiál bol použitý polymérny kompozit plnený minerálom mastencom, známejším ako talk. Tento kompozit patrí medzi kompozitné materiály na báze časticových plnív a je tvorený polypropylénom, termoplastom známeho pre svoju vysokú pevnosť, odolnosť voči chemikáliám a dobrú spracovateľnosť, s 20 % prídavkom mastenca (PP+20T). Pridanie mastenca môže zmeniť vlastnosti plastov, ako napr. tvarovanie, zmrašťovanie, povrchovú tvrdosť, modul ohybu, pevnosť v ťahu, rázovú pevnosť, teplotu pri tepelnom pretváraní, proces tvarovania a rozmerová stabilitu výrobkov.

Dodávateľom materiálu bola spoločnosť Vitalo Slovakia s.r.o., ktorá sa špecializuje na výrobu krytov autobatérií pre elektromobily pomocou technológie termoformovania.

Obr. 1 Finálny výrobok z polymérneho kompozitu plnený talkom po termoformovaní
Figure 1. Final product made of polymer composite filled with talc after thermoforming

Pri dlhodobejšom používaní polotovarov od externého dodávateľa začala firma Vitalo zaznamenávať výrobné chyby.

Medzi hlavné problémy patrilo:

- zvrásnenie povrchu (tzv. "sopeľ"), (obr. 2a),
- praskanie hotových produktov (obr. 2b).

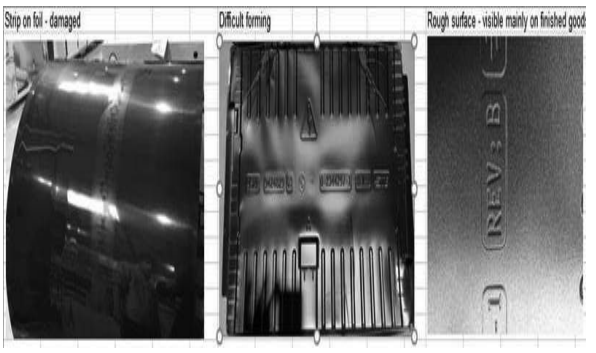

a) zvrásnenie povrchu (sopeľ)

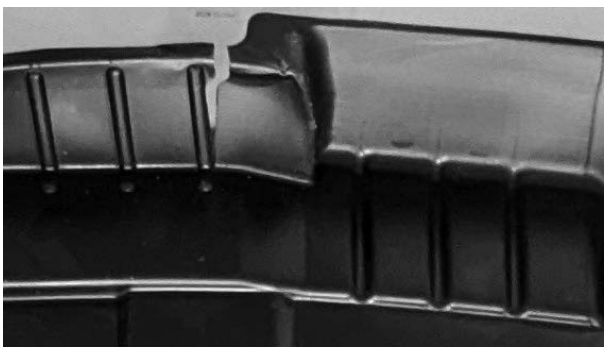

b) praskanie

Obr. 2 Výrobné chyby
Figure 2. Manufacturing defects

Tieto chyby poukazovali na možnú degradáciu materiálu alebo zmenu jeho vlastností. Z tohto dôvodu boli vytvorené dve skupiny vzoriek: "S" (starý materiál) - bez výraznejších výrobných chýb a "N" (nový materiál) s vyššou chybovosťou. Vzorky boli ďalej označované podľa smeru výroby fólie: "V" (v smere výroby), "H" (proti smeru výroby).

Napríklad označenie „V1S 14 benzín“ znamená: vzorka vyrezaná v smere odvíjania fólie (V), prvá v poradí (1), z materiálu "S", namáčaná v prostredí benzínu po dobu 14 dní. Cieľom experimentu bolo posúdiť rozdiely vo fyzikálno-mechanických vlastnostiach medzi týmito dvoma typmi materiálov, najmä vplyvom chemického a mechanického zaťaženia počas vystavenia rôznym prostrediam.

Na analýzu boli zvolené štyri základné experimentálne metódy:

- skúška ťahom,
- skúška tvrdosti podľa Shore D,
- skúška nasiakavosti,
- skúška korózie za napätia.

Tieto metódy poskytujú komplexný pohľad na správanie sa kompozitu v rôznych podmienkach.

Skúška ťahom je jednou z najdôležitejších metód na posúdenie mechanickej pevnosti materiálu. V súlade s normou STN ISO 527-1 sa počas skúšky pôsobí na skúšobné teleso ťahovou silou, až kým nedôjde k jeho pretrhnutiu. Počas skúšky sa merajú tri hlavné parametre:

- Pevnosť v ťahu (σM) – maximálne napätie, ktoré materiál znesie pred pretrhnutím.
- Predĺženie pri pretrhnutí – pomer predĺženia vzorky ku pôvodnej dĺžke.
- Youngov modul pružnosti – udáva tuhosť materiálu, teda pomer medzi napätím a deformáciou.

Vzorky boli rozmerov 115 x 25 mm, s hrúbkou 2,5 mm. Každý typ materiálu bol testovaný na piatich vzorkách. Skúška sa realizovala na univerzálnom trhacom stroji ZDM 30, s maximálnym zaťažením do 300 kN. Správne upnutie skúšobnej tyče je kľúčové - os tyče musí byť totožná s osou pôsobiacej sily, aby nedochádzalo k nesymetrickému zaťaženiu. Výsledkom je tzv. ťahová krivka, ktorá znázorňuje závislosť medzi napätím a deformáciou.

Rôzne typy polymérov vykazujú rôzne krivky - zatiaľ čo elastoméry vykazujú vysoké predĺženie pri nízkom napätí, termoplasty naopak dosahujú vysoké napätie už pri nízkom predĺžení.

Tvrdosť podľa Shoreho je ďalším významným mechanickým parametrom. Meraná bola tvrdosť podľa stupnice Shore D, ktorá je určená na tvrdé plasty podľa normy STN EN ISO 868. Princíp metódy spočíva v zatlačení indentora do povrchu vzorky.

Indentor má vrcholový uhol 30° a zakrivenie s polomerom 0,1 mm. Hĺbka vtlačenia sa meria priamo v stupňoch Shore. Podmienky merania: minimálna hrúbka vzorky: 6 mm, vzdialenosť meraného miesta od okraja: minimálne 12 mm, čas odčítania po pritlačení: 15 sekúnd a zaťaženie pre zvýšenie presnosti: závažie 5 kg.

Skúška nasiakavosti slúži na posúdenie chemickej odolnosti materiálu. Vzorky boli ponorené do troch rôznych kvapalín:

- kyselina sírová (H2SO4),
- motorový olej,
- benzín.

Dĺžka expozície bola stanovená na 14, 28 a 35 dní. Po uplynutí týchto intervalov sa zmerala zmena hmotnosti vzorky. Prírastok hmotnosti poukazuje na množstvo absorbovanej kvapaliny. Pozorovania zahŕňali: zmenu hmotnosti, povrchové zmeny (napr. zmatnenie, deformácia, farebné zmeny), vytvorenie prasklín alebo bubliniek.

Skúška korózie za napätia simuluje kombinované pôsobenie mechanického napätia a agresívneho chemického prostredia. Táto metóda je veľmi citlivá a často sa využíva pri posudzovaní dlhodobej spoľahlivosti plastov. Vzorka sa predopne mechanickým zaťažením (napr. ohyb alebo natiahnutie), následne sa na krátku dobu (2 minúty) vystaví pôsobeniu kvapaliny a pozoruje sa vznik trhlín alebo povrchových defektov.

3. VÝSLEDKY EXPERIMENTOV A DISKUSIA

Z výsledkov skúšky ťahom (obr. 3) vyplýva, že materiál označený ako „S“ (starý) dosahoval lepšie mechanické vlastnosti. Jeho priemerná pevnosť v ťahu bola vyššia a predĺženie pri pretrhnutí väčšie než u materiálu „N“ (nový). To poukazuje na lepšiu kohéznu štruktúru materiálu „S“. Vzorky materiálu „N“ vykazovali vyššiu variabilitu výsledkov, čo potvrdzuje nižšiu homogenitu materiálu a možný vplyv recyklátu alebo zmeneného zloženia.

Z týchto rozdielov vyplýva, že nový materiál má nižšiu mechanickú stabilitu, čo môže byť príčinou pozorovaných výrobných problémov, ako sú praskliny a deformácie pri následnom tvarovaní.

Tvrdosť materiálu (obr. 4) bola vyššia u starého typu „S“. Tvrdosť sa postupne s rastúcou dĺžkou expozície vo všetkých kvapalinách znižovala, čo naznačuje degradáciu materiálu. Najvýraznejší pokles tvrdosti bol zaznamenaný po 35-dňovom pôsobení kyseliny sírovej. Z týchto údajov vyplýva, že chemické prostredie významne ovplyvňuje povrchovú integritu a odolnosť kompozitu.

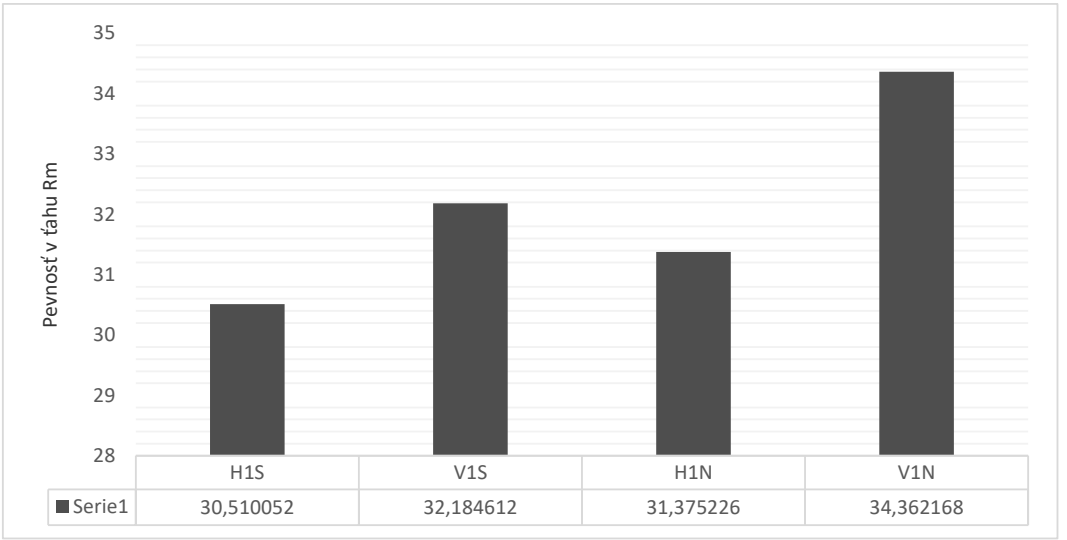

Obr. 3 Porovnanie pevnosti v ťahu
Figure. 3 Comparison of tensile strength

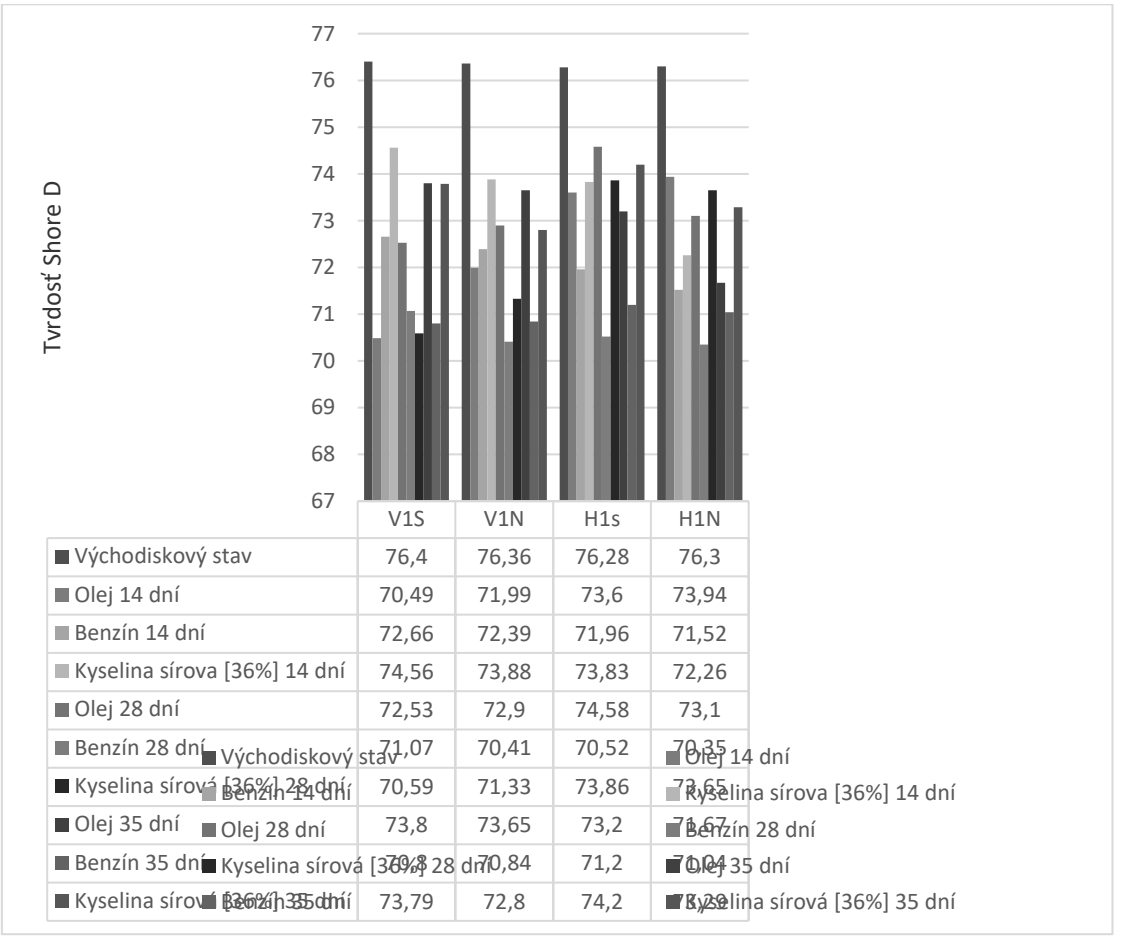

Obr. 4 Porovnanie tvrdosti kompozitu po dobu 14, 28 a 35 dní
Figure 4. Comparison of composite hardness after 14, 28 and 35 days

Merania nasiakavosti (tab. 1, tab. 2 a tab. 3) preukázali, že materiál „N“ je viac náchylný na absorpciu kvapalín. Vzorky v kyseline zaznamenali najväčší nárast hmotnosti.

Tab. 1 Nasiakavosť H_2SO_4 - 14, 28, 35 dní
Table 1. H_2SO_4 absorption - 14, 28, 35 day

	m [g]	**m_1[g]**	**Δm [%]**
14 dní			
V1S	0,26743	0,26811	0,25
V1N	0,28192	0,28257	0,23
H1S	0,24649	0,24722	0,30
H1N	0,26846	0,26921	0,28
28 dní			
V1S	0,26274	0,26324	0,19
V1N	0,2714	0,27177	0,14
H1S	0,27336	0,27404	0,25
H1N	0,27157	0,27213	0,21
35 dní			
V1S	0,26035	0,26067	0,12
V1N	0,23691	0,23709	0,08
H1S	0,26660	0,26701	0,15
H1N	0,29155	0,29216	0,21

Tab. 2 Nasiakavosť olej - 14, 28, 35 dní
Table 2. Oil absorption - 14, 28, 35 day

	m [g]	**m_1[g]**	**Δm [%]**
14 dní			
V1S	0,25801	0,25893	0,36
V1N	0,25452	0,25528	0,30
H1S	0,25912	0,25996	0,32
H1N	0,26656	0,26759	0,39
28 dní			
V1S	0,26447	0,26576	0,49
V1N	0,28475	0,2875	0,97
H1S	0,256	0,25714	0,45
H1N	0,25122	0,25226	0,45
35 dní			
V1S	0,27411	0,2747	0,22
V1N	0,24783	0,24819	0,15
H1S	0,25350	0,25392	0,17
H1N	0,26128	0,26180	0,20

Tab. 3 Nasiakavosť benzín - 14, 28, 35 dní
Table 3. Gasoline absorption - 14, 28, 35 day

	m [g]	**m_1[g]**	**$_{\Delta}$m [%]**
14 dní			
V1S	0,26112	0,26623	1,96
V1N	0,24250	0,24755	2,08
H1S	0,25912	0,27034	4,33
H1N	0,27282	0,27837	2,034
28 dní			
V1S	0,25099	0,27612	10,01
V1N	0,25733	0,28226	9,69
H1S	0,27208	0,29481	8,35
H1N	0,25685	0,28524	11,05
35 dní			
V1S	0,26420	0,28743	8,79
V1N	0,27341	0,29216	6,86
H1S	0,25976	0,28017	7,86
H1N	0,25355	0,27380	7,99

Porovnanie všetkých kvapalín ukázalo, že najagresívnejšia bola kyselina, nasledovaná olejom a benzínom. Výraznejšie zmeny hmotnosti a povrchu boli zaznamenané pri dlhšom čase pôsobenia. To poukazuje na potrebu testovania materiálu pred jeho aplikáciou v chemicky náročných prostrediach.

Materiál „N“ vykazoval nižšiu odolnosť voči korózii za napätia (tab. 4). Trhliny sa objavili už po krátkodobom kontakte s kvapalinami. U materiálu „S“ sa nevyskytli žiadne alebo len minimálne poškodenia.

Tab. 4 Korózia za napätia - účinok kvapaliny na vznik trhlín (pôsobenie 2 minúty)
Table 4. Stress corrosion - effect of liquid on crack formation (exposure time 2 minutes)

	V1S	**V1N**	**H1S**	**H1N**
5% HCl	√	X	X	X
5% HNO_3	X	X	X	X
5% H_2SO_4	X	X	X	√
5% NaOH	X	X	X	X

Najväčšie poškodenie spôsobila kyselina sírová, zatiaľ čo benzín mal najmenší vplyv. Výsledky dokazujú, že starý materiál má vyššiu odolnosť voči kombinovanému mechanickému a chemickému zaťaženiu.

Tab. 5 Korózia za napätia - namočenie vzorky po dobu 2 minúty
Table 5. Stress corrosion - sample soaking for 2 minutes

	V1S	**V1N**	**H1S**	**H1N**
5% HCl	X	√	X	X
5% HNO_3	X	X	X	√
5% H_2SO_4	√	√	X	√
5% NaOH	X	X	X	X

Získané výsledky jasne potvrdzujú, že nový materiál „N“ vykazuje horšie mechanické vlastnosti a nižšiu odolnosť voči pôsobeniu agresívneho prostredia, čo vedie k vyššej kazivosti počas výroby. Naopak, materiál „S“ vykazuje vyššiu stabilitu a je vhodnejší pre aplikácie vyžadujúce dlhodobú mechanickú a chemickú odolnosť.

POĎAKOVANIE

Príspevok vznikol v rámci riešenia spoločného slovensko-poľského projektu Project Based Learning ako výsledok spolupráce medzi Politechnikou Slaskou, Gliwice a Žilinskou univerzitou v Žiline a projektov KEGA 004ŽU-4/2023, KEGA 009ŽU-4/2023 a KEGA 016ŽU-4/2023.

BIBLIOGRAPHY

1. Liptáková, T. a kol. Polymérne konštrukčné materiály. EDIS, 2012, 189s.
2. Fričová, O. Polymérne materiály. Štruktúra a vnútorné interakcie v polyméroch. Košice, 2019, 68 s. [CD-ROM]. ISBN 978-80-553-3365-6
3. Švorčík, V. Struktura a vlastnosti polymerů. On-line
4. Běhálek, L. Polyméry. 2014. https://publi.cz/books/180/Cover.html
5. Termoplasty, Reaktoplasty, Elastoméry. https://topden.sk. [Online] https://topden.sk/termoplasty-reaktoplasty-elastomery/.
6. Williams, J. The science and technology of composite materials. https://www.science.org.au. [Online] https://www.science.org.au/curious/technology-future/composite-materials.
7. Krizberg, J., Gutakovskis, V. Kompozitné materiály, 2016.
8. Brabazon, D. Encyclopedia of Materials: Composites. 2021 Elsevier, 978-0-12-819731-8.

TalentDetector

23th-25th June 2025
Gliwice-Brenna, Poland

DEPARTMENT OF ENGINEERING MATERIALS AND BIOMATERIALS
FACULTY OF MECHANICAL ENGINEERING
SILESIAN UNIVERSITY OF TECHNOLOGY

INTERNATIONAL STUDENTS SCIENTIFIC CONFERENCE

Cutting of Future - Lasers in Modern Manufacturing

Magdalena Hulbój, Emilia Put, Mirosław Bonek

Silesian University of Technology, Faculty of Mechanical Engineering, Department of Engineering Materials and Biomaterials
email: ep309683@student.polsl.pl, mh309664@student.polsl.pl

Abstract: The article describes the development and application of laser cutting technology in industrial production. It presents a comparison between traditional mechanical, plasma cutting, oxyfuel cutting and modern laser-based techniques. It analyses the advantages and disadvantages of each approach, with a particular focus on efficiency, precision, cost, and environmental impact. The article also includes a comparative table of cutting methods and highlights the economic and technical benefits of implementing laser cutting systems in various industries.

Keywords: laser cutting, mechanical cutting, plasma cutting, oxy-fuel cutting

1. INTRODUCTION

Modern industry is constantly seeking solutions to enhance the efficiency, precision, and costeffectiveness of production processes. One significant technological breakthrough that has profoundly impacted these areas is the application of lasers, particularly in material cutting. Laser technology, once considered an expensive novelty just a few decades ago, has now become a cornerstone of modern production lines.This article focuses on comparing cutting processes before the laser era with current automated methods based on precise light beams. We will analyse how the use of lasers has contributed to increased production efficiency, reduced material waste, and lowered operational costs. Special attention will be given to the economic aspect, presenting specific financial benefits resulting from the implementation of this technology.Collected data and observations lead to a clear conclusion: the application of laser technology in industrial cutting significantly improves efficiency, quality, and profitability of production. This solution not only streamlines processes but also enables companies to achieve tangible savings and greater competitiveness in the market. Additionally, laser cutting minimizes environmental impact by reducing waste and lowering energy consumption, aligning with sustainable development goals.

2. MECHANICAL CUTTING [1]

Mechanical cutting is a material processing process that uses physical force to precisely divide the material. Methods such as shearing, sawing, and punching are among the oldest and most commonly used in industries worldwide. They utilize cutting tools like blades or punches to achieve the desired results.

2.1 Advantages of Mechanical Cutting [1]

One of the main advantages of mechanical cutting is the low initial investment cost. Mechanical cutting systems are generally cheaper to purchase compared to more advanced technologies, such as laser cutting. This makes them an attractive option for small and medium-sized enterprises that want to invest in efficient solutions with a limited budget.

Another advantage is the simplicity of operation. Mechanical cutting methods are relatively easy to master and do not require advanced technical knowledge. This allows for quick employee training to operate cutting machines, which is important in dynamic production environments.

2.2 Disadvantages of Mechanical Cutting [1]

Despite its numerous advantages, mechanical cutting also has its drawbacks. One of them is tool wear. Blades, punches, and dies gradually become dull during use, requiring regular replacement or sharpening. This leads to additional maintenance costs, potential production downtime, and the need for skilled personnel to service the equipment.

Another disadvantage is limited precision. Mechanical cutting methods can struggle to achieve high accuracy, especially with complex shapes or narrow tolerances. As a result, fine or intricate cuts may require additional operations such as grinding or polishing to meet the required quality standards.

It is also important to consider the possibility of material deformation. The physical contact with cutting tools can lead to distortions, especially when working with delicate or thin materials. This is particularly problematic in industries where material integrity is crucial, such as the aerospace or electronics industries.

2.3 Applications of Mechanical Cutting [1]

Mechanical cutting is used in various industrial sectors. In metal manufacturing, it is used for precise cutting of sheets, rods, or pipes. Depending on the material’s thickness and type, different techniques such as shearing, band sawing, or disc cutting are applied. It is important to select the appropriate method based on the material's characteristics and production requirements.

In the food industry, particularly in fruit farming, mechanical cutting is used to shape the crowns of fruit trees. This allows for a uniform and predictable tree structure, which enhances light penetration to the crown and the formation of flower buds. As a result, the fruits are

more uniform in size and quality. However, it should be noted that mechanical cutting in orchards requires proper machine preparation and adaptation to the specific needs of the crops.

3. PLASMA CUTTING [2], [3], [4]

Plasma cutting involves melting a narrow gap in metal objects using a stream of plasma. The principle of plasma cutting is based on utilizing the extremely high temperature of the plasma, along with the very high velocity of the gas exiting the nozzle of the plasma torch. This stream melts and simultaneously blows the metal out of the cutting gap.

3.1 Advantages of Plasma Cutting [2], [3]

Laser cutting offers the ability to cut all types of metals. It provides cutting speeds up to five to six times faster than oxy-fuel cutting, particularly for metals with a thickness of less than 25 mm. One of the key advantages is that it does not require preheating of the material before starting the cutting process.

It enables faster piercing of low-carbon steel sheets up to approximately 65 mm thick, as well as high-alloy steels and aluminum up to around 50 mm. Due to the significantly higher cutting speed and the highly concentrated heat source, the heat-affected zone is narrower. This results in higher cutting precision, reduced thermal distortion, and a narrower kerf width. Laser cutting also prevents edge melting when cutting materials with thicknesses as low as 0.5 mm. It allows cutting in all positions and even under water. The process supports precise and efficient beveling of structural steel plates up to 30 mm thick.Additionally, it facilitates greater automation of the cutting process, which allows for the production of both flat and three-dimensional components of various shapes. There is also a reduced risk in the welding workspace, as the process does not require flammable or explosive gases.

3.2 Disadvantages of Plasma Cutting [2], [4]

The disadvantages of plasma cutting include the higher cost of welding station equipment compared to oxy-fuel cutting. The process generates high noise levels, especially when cutting in open air, and produces intense light radiation from the plasma arc. It also emits large amounts of harmful gases, fumes, and welding dust that pose health risks.

Additionally, plasma cutting can cause changes in the chemical composition and structure within the heat-affected zone of the material being cut. Maintaining perpendicular edges can be challenging, and the process requires a reliable source of electrical energy to operate effectively.

3.3 Applications of Plasma Cutting [4]

Additionally, plasma cutting is less suitable for achieving high precision, particularly when it comes to intricate or complex cuts. While plasma cutting is efficient for thicker materials, it struggles to achieve the fine tolerances needed for more detailed and precise cuts. The precision of plasma cutting is generally lower than that of laser cutting, making it challenging to achieve narrow tolerances. In industries that require highly detailed cuts or tight

specifications, such as electronics or medical device manufacturing, plasma cutting may not be the best option.

Despite these limitations, plasma cutting remains one of the most widely used technologies, particularly in applications where speed, efficiency, and cutting of thick materials are priorities. It is commonly used in industries where large components need to be cut quickly, and precision is not the primary concern. However, in cases where greater precision is required or when the quality of the cut edges is critical, alternative cutting methods such as laser cutting may be more appropriate.

3. OXY-FUEL CUTTING [3]

Oxy-fuel cutting is a process used to separate metal by locally burning it in a stream of pure oxygen, aided by a heat source—typically a gas flame.
To initiate cutting, the metal must be preheated to its ignition temperature, which for lowcarbon and low-alloy steels is approximately 1300–1350°C.

Only carbon steels and low-alloy steels meet the necessary conditions for oxy-fuel cutting. As the content of carbon or alloying elements such as chromium (Cr), silicon (Si), and tungsten (W) increases, the cutting process becomes more difficult. Therefore, cutting cast iron, high-alloy steels, or non-ferrous metals is generally not feasible using this method, except with specialized techniques.

Carbon steels with a carbon content of up to 0.7% (with a pearlitic structure) can be cut without significant issues. When the carbon content exceeds this level, cutting becomes more challenging, and preheating to around 200°C is necessary. In the case of low-alloy steels, preheating is required when the carbon content is above 0.3%.Oxy-fuel cutting is usually performed with universal torches, which can also be used for welding when fitted with a cutting attachment**.**

4.1 Advantages of Oxy-fuel Cutting [9]

Oxyfuel gas cutting offers several benefits over other metal cutting techniques like sawing, milling, and arc cutting. One of its main advantages is the ability to cut steel more quickly than with traditional machining methods. It is also a cost-effective solution for cutting complex shapes and thick sections that would be difficult or expensive to machine. The basic equipment required for oxyfuel cutting is relatively inexpensive compared to mechanical tools, and it is portable enough for field use. During cutting, the torch direction can be easily adjusted within a small radius, and large plates can be cut in place by moving the torch rather than the material itself. Additionally, this method is economically viable for preparing plate edges, especially for bevel and groove weld joints.

4.2 Disadvantages of Oxy-fuel Cutting [9]

Oxyfuel gas cutting of metals has several notable disadvantages. Dimensional tolerances are significantly poorer compared to machine tool capabilities. The process is commercially

limited primarily to cutting steel and cast iron, although some other readily oxidized metals like titanium can also be cut.

The use of preheat flames and the expulsion of red-hot slag pose fire and burn hazards to both personnel and equipment. The combustion of fuel and oxidation of the metal generate fumes that require proper exhaust systems and adequate ventilation. Cutting of hardenable steels may necessitate preheating, postheat treatment, or both, in order to preserve the metallurgical structure and mechanical properties near the cut edges.

Additionally, special process modifications are required when cutting high alloy steels and cast iron.

4.3 Applications of Plasma Cutting [4]

In practice, there are three main types of oxy-fuel cutting: separating cuts, surface cutting (also known as gouging), and oxygen lance cutting. The most commonly used method is separating or straight-line cutting. Surface cutting is primarily used for creating grooves or beveling weld joints before welding. Oxygen lance cutting is applied in situations where deep holes need to be pierced, such as in heavy industrial applications.

5. LASER CUTTING [5], [6]

Laser cutting is a non-contact process that uses a concentrated laser beam to melt, burn, or vaporize materials along a specified cutting line. Laser cutting systems are capable of cutting a wide range of materials, including metals, plastics, wood, ceramics, and composites. There are several types of lasers used in industrial cutting, with the most popular being CO_2 lasers and fibber lasers.

Laser cutting systems utilize a highly concentrated laser beam to focus intense Energy on a small area of the material. This localized energy causes the material to melt, vaporize, or burn, resulting in a clean and precise cut. The laser beam is typically directed through a lens that focuses it onto the material. The speed and intensity of the beam can be adjusted depending on the material being cut, allowing for precise control over the process.

5.1 Advantages of laser cutting [5], [6],[8]

The advantages of laser cutting include precision and accuracy. Laser cutting is known for its high precision and ability to cut materials with extremely tight tolerances. It can achieve cutting widths as small as 0.1 mm, which is significantly more accurate than traditional cutting methods. Speed is another advantage; laser cutting is faster than most traditional methods, especially when cutting thinner materials. The high cutting speed results in shorter cycle times, leading to higher productivity and reduced production costs.
Minimal material waste is another benefit. The narrow kerf (cut width) generated by the laser means that less material is wasted during the cutting process. This is particularly advantageous when working with expensive materials such as stainless steel or titanium. Tool wear is eliminated because laser cutting is a non-contact process, meaning there is no physical

interaction between the cutting tool and the material. This eliminates the need for tool replacement or maintenance, reducing costs and downtime associated with tool wear.

Versatility is also a key advantage; laser cutting is highly versatile and can be used to cut a wide range of materials, including metals, plastics, wood, ceramics, and composites. It can also handle both thin and thick materials, making it suitable for various applications across different industries. Despite the initial investment cost, the long-term economic benefits of laser cutting often outweigh the upfront expense. Laser cutting systems offer several economic advantages:
Reducing operational costs: Laser cutting systems are faster than traditional cutting methods, meaning fewer labour hours are needed to produce a given number of parts. This reduces labour costs and improves operational efficiency. Additionally, the high precision of laser cutting reduces the need for finishing operations such as grinding or polishing, further lowering costs.
Lower maintenance costs, laser cutting systems require less maintenance than mechanical or thermal cutting systems. Since there are no physical tools that wear out, the need for frequent tool replacement or sharpening is significantly reduced.
This decreases downtime and maintenance costs, which can be significant expenses in mechanical cutting systems.
Material utilization, laser cutting is more efficient in terms of material utilization thantraditional methods. The narrow kerf generated by the laser minimizes material waste, which can significantly reduce raw material costs. Advanced nesting software can optimize part placement, further improving material utilization.

5.2 Disadvantages of Laser Cutting [5], [6],[8]

Despite its numerous advantages, laser cutting does have some limitations. The most frequently mentioned drawback is the high initial investment cost associated with purchasing and installing laser cutting systems. For small businesses, this may pose a significant entry barrier. However, this investment often pays off in the long term due to lower operating costs and increased production efficiency. Another limitation lies in the difficulty of processing certain highly reflective materials such as copper or brass, which may require specialized laser sources or additional machine settings. In some cases, when cutting very thick materials, alternative cutting methods may be necessary to achieve optimal results.

5.3 Applications of Laser Cutting [5], [6],[7]

Laser cutting is widely used across various industrial sectors due to its precision, speed, and versatility. In the automotive industry, it is employed for cutting body components, engine parts, and other precision mechanical elements. In the aerospace sector, the technology is used for processing lightweight yet durable metal alloys, while maintaining minimal material deformation. In the medical field, laser cutting enables the production of intricate surgical instruments and miniature components for diagnostic devices. The electronics industry uses it for cutting printed circuit boards and device enclosures. In the textile and fashion industries, laser cutting allows for precise patterns on fabrics and leather. Additionally, in interior design and architecture, it facilitates the customization of decorative and structural elements. The adaptability of laser cutting makes it suitable for both mass production and individualized, high precision projects.

Cutting method	Material thickness	Cut quality	Cutting speed	Shape flexibility	Advantages	Disadvantages
Laser cutting	From 0.5 mm to over 30 mm	High precision, low edge roughness, minimal burr formation	High	High, capable of cutting intricate shapes and small holes	High precision, ability to cut various materials, no tool	Higher initial investment and operational costs
Plasma cutting	Up to 38 mm manually, up to 150 mm with CNC control	Higher roughness, requuires additional finishing	High for thick sheets	Limited precision; difficulties with small holes and complex shapes	Fast cutting speed, lower equipment and perational costs	Lower precision, larger heataffected zone, requires additional finishing
Oxy-Fuel cutting	1-1,000 mm	High roughness, requires additional finishing	Low, requires preheating	Limited shape flexibility;ch allenge with small holes and intricate countours	Low equipment cost, ability to cut very thick materials	Low cut quality, high material consumption requires additional finishing

6. CONCLUSION

In conclusion, laser cutting has established itself as a leading-edge technology in the field of material processing. Its ability to produce clean, precise cuts with minimal thermal distortion and material waste has revolutionized manufacturing processes across a wide range of industries. Unlike mechanical, plasma and oxy-fuel cutting methods, laser cutting ensures high accuracy, narrow kerf widths, and repeatability, making it ideal for industries where product consistency and tight tolerances are crucial. The initial cost of implementing laser cutting systems, including machine acquisition and operator training, is relatively high compared to more traditional methods.

However, this upfront investment is often offset by significant long-term advantages. These include lower operational costs, reduced need for finishing operations, higher throughput, and longer machine uptime due to the lack of physical tool wear. Furthermore, advanced software integration enables optimization of material usage through intelligent nesting, contributing to improved sustainability and material savings.

Laser cutting also supports a wide variety of materials — including metals, plastics, wood, ceramics, and composites — and can be adapted to both thin and thick sections. This versatility allows for its deployment in numerous sectors such as automotive manufacturing, aerospace engineering, electronics, medical device fabrication, and the design and architecture industries. Its role in high-precision component fabrication, customized product creation, and even artistic design highlights its multifaceted applications.

Moreover, laser technology aligns with the goals of Industry 4.0 by integrating seamlessly with digital manufacturing systems, robotics, and smart production environments. As global industry continues to prioritize sustainability, efficiency, and quality, laser cutting is expected to remain at the forefront of technological advancement in fabrication and processing.

Given its numerous advantages and expanding applicability, laser cutting is not only a modern alternative to traditional methods but also a future-proof solution for manufacturers seeking to remain competitive in an increasingly demanding and dynamic market.

ACKNOWLEDGEMENTS

The work was created as part of project of Students Scientific Circle of Laser Surface Treatment under the Initiative of Excellence - Research University, Silesian University of Technology, Gliwice, Poland.

BIBLIOGRAPHY

1. Łukasz Bohdal „Procesy Cięcia i Wykrawania elementów ze stali elektrotechnicznych” 2025r.
2. Czupryński Artur; Rzeźnikiewicz Agnieszka “Specjalne technologie spawalnicze w ćwiczeniach laboratoryjnych cz.2” Publisher: Politechnika Śląska, Gliwice 2020r.
3. Mazur, Marceli “Podstawy spawalnictwa” Publisher: Politechnika Śląska, Gliwice 1999r.
4. Sianos, Juliusz “Spawanie gazowe i cięcie termiczne” Publisher: Politechnika Śląska, Gliwice 1981r.
5. Andrzej Klimpel “Technologie laserowe: spawanie, napawanie, stopowanie, obróbka cieplna i cięcie” Publisher: Politechnika Śląska, Gliwice 2012r.
6. Andrzej Klimpel “Nowoczesne lasery i technologie laserowe w inżynierii spawalnictwa” Publisher: Politechnika Śląska, Gliwice 2023r.
7. M.N. Avadhanulu „An Introduction to Lasers Theory and Application” Publisher: S. Chand 2001r.
8. J. Radhakrishan, Sunil Pathak „Advanced Engineering of Materials Through Lasers” 2022r.
9. Mr. Rohit Manglik “Manufacturing Technology” Publisher: EduGorilla Publication, 2024r.

TalentDetector
23th-25th June 2025
Gliwice-Brenna, Poland
DEPARTMENT OF ENGINEERING MATERIALS AND BIOMATERIALS
FACULTY OF MECHANICAL ENGINEERING
SILESIAN UNIVERSITY OF TECHNOLOGY
INTERNATIONAL STUDENTS SCIENTIFIC CONFERENCE

Functional properties of CrN coating obtained by PVD on aluminum alloy surface AlSi9Cu3

Justyna Janoszka[a], Natalia Puchała[a], Petr Jánský[b], Anna Smetanova[b], Michal Lattner[c], Antonin Kříž[c], Marcin Staszuk[d], Daniel Pakuła[d]

[a] Student of Faculty of Mechanical Engineering, Silesian University of Technology, Poland
[b] Student of Faculty of Mechanical Engineering, Jan Evangelista Purkyně University in Ústí nad Labem, Czech Republic
[c] Professor of Mechanical Engineering, Jan Evangelista Purkyně University in Ústí nad Labem, Czech Republic
[d] Professor of Engineering Materials and Biomaterials, Silesian University of Technology, Poland

Abstract: The work was carried out during the 12th edition of PBL within the framework of international cooperation. The study presents the results of research on the structure and functional properties of a chromium nitride (CrN) coating applied to AlSi9Cu3 aluminum alloy using the physical vapor deposition (PVD) method. The study investigated the structure, surface topography, adhesion, and tribological properties of the coating.

Keywords: CrN coating, AlSi9Cu3 alloy, functional properties

1. INTRODUCTION

The AlSi9Cu3 aluminum alloy is characterized by good corrosion resistance and high strength. While maintaining low weight, it is used in the automotive and aerospace industries. To enhance the mechanical resistance of the alloy, protective coatings are applied.

These coatings play a key role in enhancing the durability and surface resistance of tools and machine components to wear and mechanical loads. Particularly important in this context are hard coatings such as CrN, applied using PVD methods, which, due to their functional properties, find wide application.

As demonstrated by the authors in work [1], the CrN coating deposited on the AlSi9Cu3 substrate exhibits the highest load-bearing capacity and wear resistance under both dry and lubricated conditions. This is attributed to its optimal thickness, increased hardness, adhesion, and surface roughness. When oil lubrication is applied, the coating shows superior load-carrying capability and a lower coefficient of friction under high loads compared to DLC and GLC coatings [1]. In industrial applications, such as stamping tools made from tool steel, the use of chromium nitride (CrN) coatings significantly reduces material wear and decreases the force required for the stamping process. This indicates the coating's effectiveness in reducing frictional resistance, which in turn contributes to extended tool service life [2]. Furthermore, research by the authors in study [3] showed that the CrN coating offers higher resistance to crack propagation,

better cohesion, and improved adhesion compared to coatings such as AlCrN, making it more suitable for applications subjected to high contact pressures [3]. In comparative studies [4] with other coatings (TiN, TiB_2), the CrN coating demonstrated the highest hardness, elastic modulus, and the best spallation resistance, which is reflected in the lowest coefficient of friction and wear during tribological testing. Furthermore, combining the CrN coating with an FeCoNiAlSi layer deposited using the HVOF method significantly improves mechanical and tribological properties [5]. However, under conditions of intensive hydrogen saturation—as shown in studies on aluminum alloys coated with CrN—the coating may undergo delamination, negatively impacting its durability [6]. The optimal CrN layer thickness is critical: an increase up to approximately 0.8 μm results in elevated compressive stresses and improvements in both mechanical and tribological performance. In contrast, increasing the thickness (e.g., to 1.2 μm) leads to the formation of microcracks and spallation, which reduces wear resistance and promotes abrasive–oxidative wear mechanisms [7]. The application of CrN coatings enhances wear resistance, and their effectiveness depends on the linear sliding speed—the lower the speed, the longer the coating service life [8]. The objective of this work is to present the functional properties of CrN coating obtained via the PVD process on an AlSi9Cu3 aluminum alloy substrate.

2. MATERIALS AND METHODOLOGY

The study utilized AlSi9Cu3 aluminum alloy samples both uncoated and coated with a CrN layer deposited by the PVD method.

The structure, surface topography, and wear or damage traces were analyzed using a ZEISS SUPRA 35 scanning electron microscope operating at an electron high tension (EHT) of 15 kV, employing secondary electron (SE) detection. Additionally, chemical composition microanalysis of the surface was performed using an energy-dispersive X-ray spectrometer (EDS).

Both coated and uncoated substrates were subjected to tribological testing using a "ball-on-plate" method on a device by CSM Instruments. During the tests, the samples moved in a reciprocating motion at a speed of 10 cm/s along a 6 mm track. The counterbody was a tungsten carbide ball pressed against the surface under constant loads of 1 N and 3 N, respectively. The tribological tests were conducted at a temperature of 25°C and a relative humidity of 50%. Material wear was evaluated using a Taylor Hobson Surtonic contact profilometer.

To assess the adhesion and mechanical resistance of the coating, scratch testing was performed using the Revetest RST^3 system from Anton Paar. The tests were conducted twice, under loads of 30 N and 100 N. Additionally, adhesion was evaluated using the Rockwell indentation test with an Ernst AT 250X hardness tester. Conical diamond indenters were used to make impressions at three load levels: 60 kp, 100 kp, and 150 kp, with three indentations performed at each load level. The extent of damage was evaluated using a descriptive scale (Fig. 1), taking into account the number and length of radial cracks, the presence of spallation, and the continuity of the material around the indentation. The size and nature of damage around the indentations were analyzed using a Tescan VEGA 3 SEM equipped with a Bruker EDX analyzer, as well as with an Olympus OLS 5000 confocal laser microscope.

The fretting test was carried out using a Bruker UMT TriboLab system. A 6 mm diameter cemented carbide (WC-Co) ball was used as the counterbody, moving over the sample surface at a speed of 5 cm/s. The tests were conducted under normal loads ranging from 1 to 5 N, with test durations varying from 0.5 to 14 minutes.

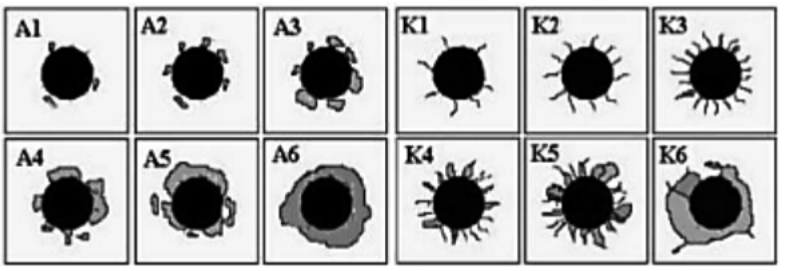

Fig. 1 Evaluation of coating failure around the indentation on Rockwell Test

3. RESULTS

The CrN coating was uniformly deposited and adheres tightly to the substrate. It exhibits a columnar structure oriented perpendicular to the substrate surface (Fig. 2a). The average coating thickness is approximately 1.3471 μm. The surface of the coating shows a granular morphology, with visible irregularities in the form of scratches, which may partially reflect the substrate's surface texture. Additionally, isolated irregular chromium particles, which condense on the surface during the deposition process, are also visible (Fig. 2b).

a) b)

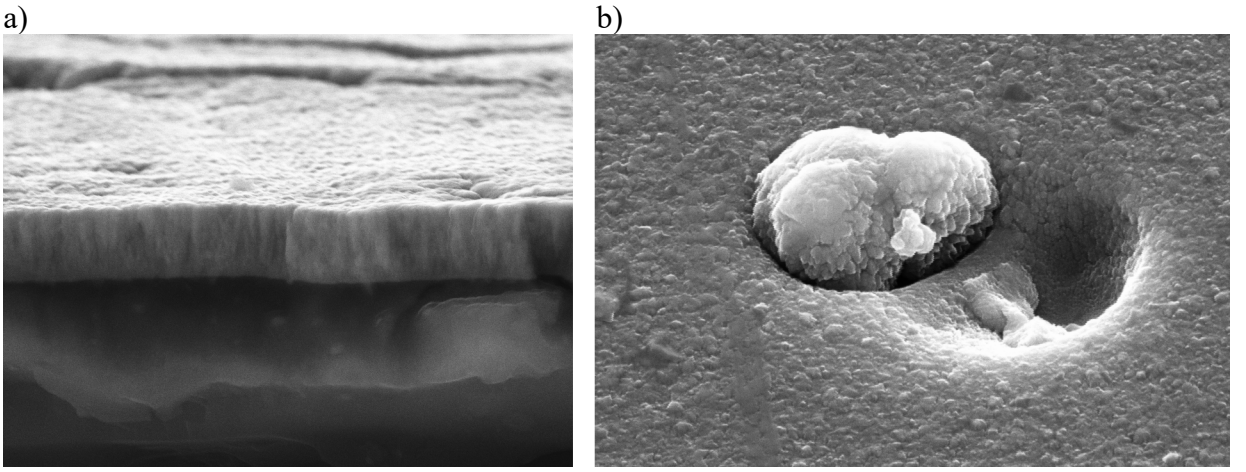

Fig. 2 Surface topography of the CrN coating on the aluminum alloy: a) coating breakthrough, b) presence of chromium-rich particulates

Based on the analysis of wear track profiles (Fig. 3), the average worn surface area and material loss volume were determined. The quantitative data presented in Table 1 indicate that for the uncoated aluminum alloy, material loss values at 1 N and 3 N loads are comparable (Fig. 4). The application of the CrN coating at a 1 N load significantly reduced wear, decreasing both the wear track area (0.0045 mm^2) and material loss volume (0.0269 mm^3) by nearly 50% compared to uncoated samples.

However, at a 3 N load, the coating's effectiveness was substantially reduced—the wear track area increased to 0.0277 mm^2 and the material loss volume to 0.1663 mm^3. Microscopic observations indicate that the higher load caused mechanical degradation of the CrN coating, leading to localized fragmentation. The resulting hard debris acted as an abrasive medium, intensifying the abrasive wear mechanism of the aluminum substrate. Consequently, increasing the normal load to 3 N resulted in more than a fivefold increase in both wear area and volume in the coated samples.

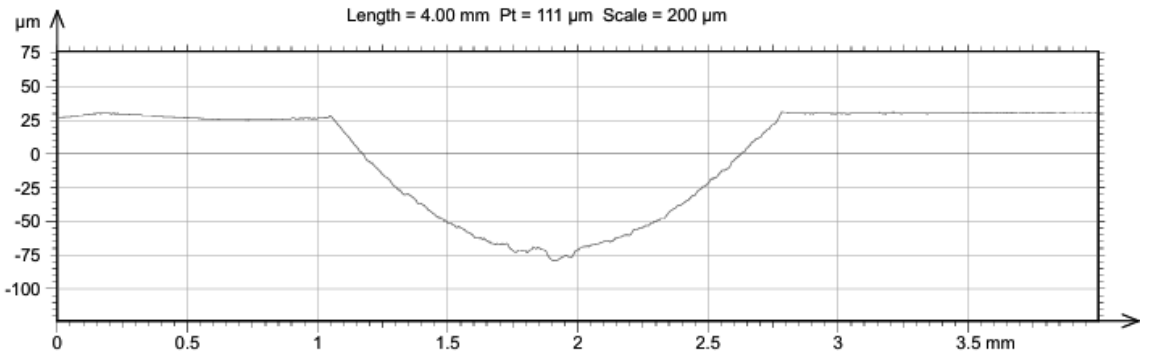

Fig. 3 Surface profile obtained from contact profilometry measurements on the coated alloy, applied load: F = 3 N

Table 1 Average surface area, abrasion volume, friction coefficient and standard deviation for samples

Coating	Normal load [N]	Area [mm^2]	Volume [mm^3]	Average friction coefficient [µ]	Standard deviation
-	1	0,0082	0,0491	0,3603	0,2261
CrN		0,0045	0,0269	0,3694	0,2328
-	3	0,0081	0,0485	0,2709	0,1801
CrN		0,0277	0,1663	0,3333	0,2186

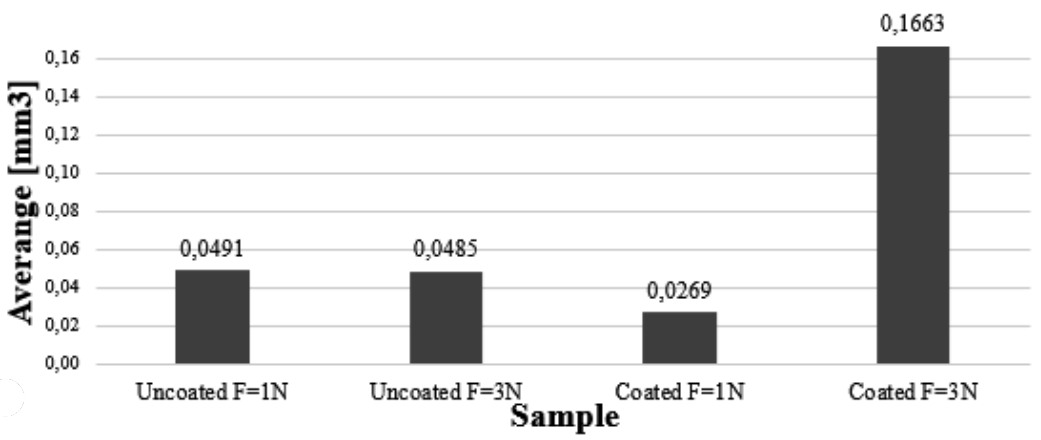

Fig. 4 Average abrasion volume of CrN coated and uncoated AlSi9Cu3 alloy at different loads

During wear resistance tests of the CrN-coated aluminum alloy at a 3 N load, an increase in the average coefficient of friction (COF) of approximately 0.1 was observed compared to the uncoated material. Both the coated and uncoated alloy exhibited variability in the COF during the initial phase of the test. This was followed by a decrease and temporary stabilization—around 0.40 for the uncoated aluminum and approximately 0.55 for the CrN-coated alloy. Later in the test, the COF increased again in both cases and stabilized at a higher level (Fig. 5).

At a load of 1 N, the COF value for the CrN-coated aluminum alloy was slightly lower than that of the uncoated substrate, suggesting the coating's effectiveness in reducing friction under lower loads.

The application of a protective CrN coating on the aluminum alloy substrate demonstrated high effectiveness under a 1 N load, reducing the intensity of tribological wear. The wear track on the coated substrate surface was relatively uniform, indicating stable contact conditions and reducing microscopic damage. In contrast, the uncoated aluminum alloy exhibited pronounced surface irregularities and localized material loss, indicative of severe adhesive and abrasive wear mechanisms (Fig. 6).

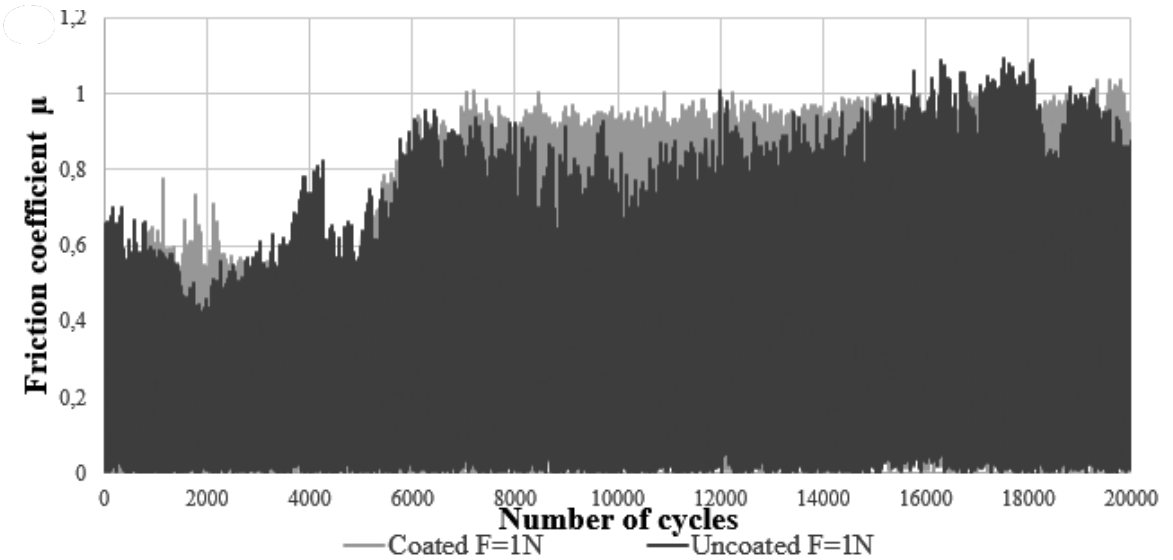

Fig. 5 Coefficient of friction (COF) as a function of the number of cycles for coated and uncoated aluminum samples, applied load: F = 3 N

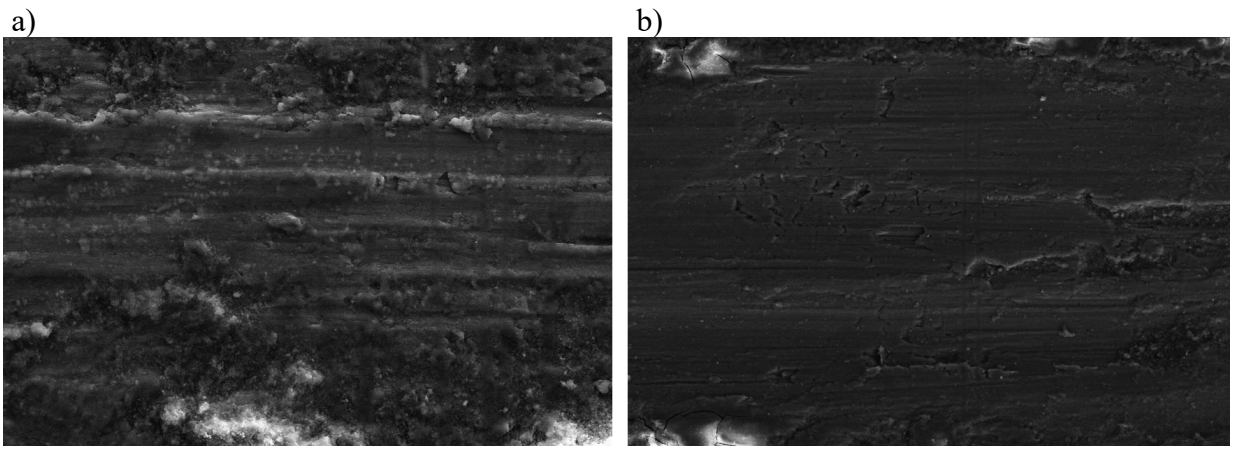

Fig. 6 SEM profiles of wear tracks under a 1 N load: a) uncoated sample, b) CrN-coated sample

Increasing the load to 3 N intensified the degradation of the CrN coating. Fragmentation of the protective layer was observed, along with an increased contribution of abrasive wear mechanisms caused by hard particles detached from the coating, which acted as abrasives against the soft aluminum substrate. This suggests that at higher loads, mechanical degradation of the hard coating on the soft substrate progresses faster than the coating's protective properties can counteract wear, resulting in a significant decline in its effectiveness.

SEM microscopic analysis and EDS microanalysis of the AlSi9Cu3 sample coated with CrN revealed significant differences in surface condition depending on the location along the scratch path. Initial signs of coating damage and localized substrate exposure were observed at a load of approximately 11 N. In the analyzed Area 1, the dominant EDS signal was aluminum, clearly indicating complete removal of the coating and exposure of the substrate alloy, thus confirming the occurrence of severe mechanical damage. In contrast, in Area 2, elements characteristic of the CrN coating—chromium, nitrogen, and trace amounts of silicon—were still detected, indicating the preservation of the protective layer continuity in this region and its resistance to load within this part of the wear track (Fig. 7).

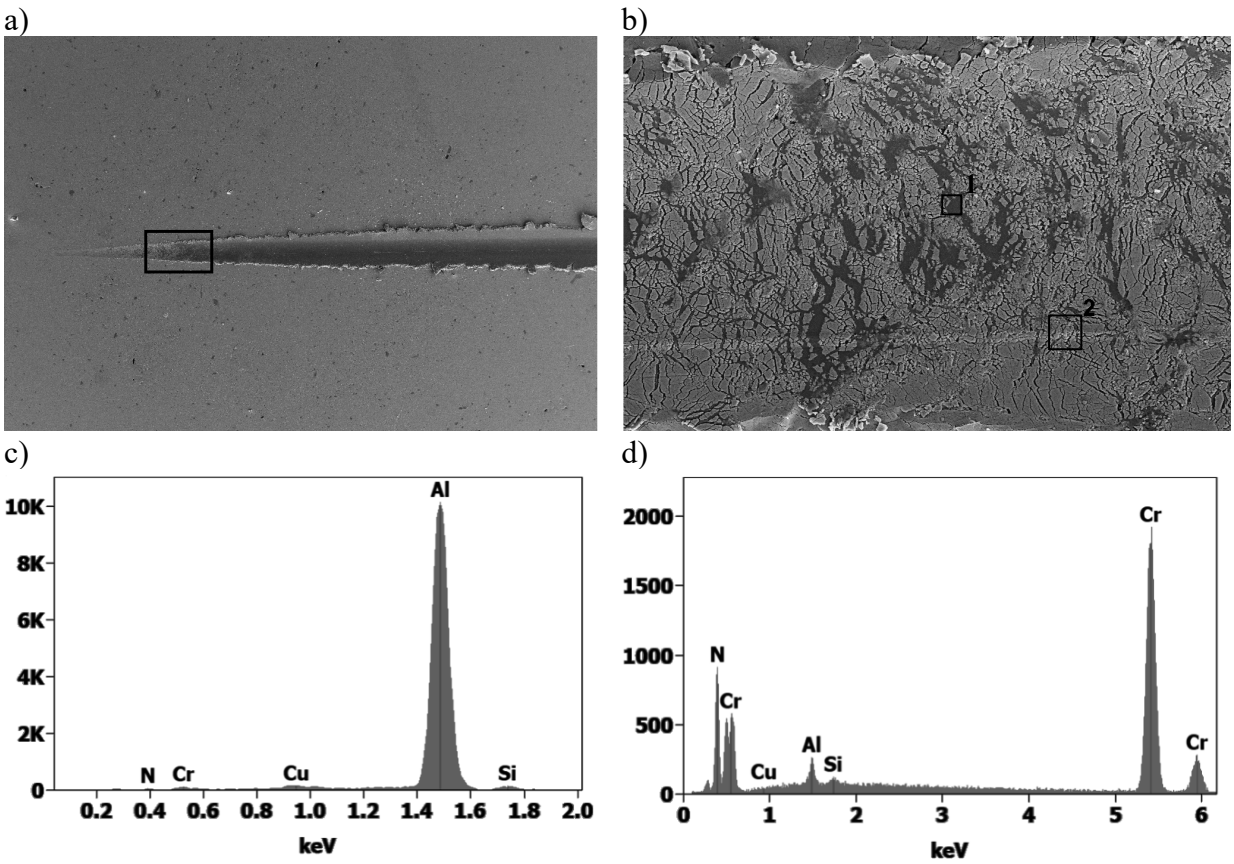

Fig. 7 SEM - coated aluminum sample after scratch test (30 N): a)general view of the scratch, b)fragment of the scratch trace, c)EDS analysis from area 1, d)EDS analysis from area 2

During the scratch test with progressively increasing load up to 30 N, a systematic increase in the friction force (F_t) was observed in response to the rising normal load (F_n), which is characteristic of progressive damage to the surface layer. In the initial phase of the test, the acoustic emission (AE) remained at a low, stable level, indicating the absence of significant defects in the coating structure and good adhesion to the substrate. Around the load of 20 N, a distinct increase in the AE signal was recorded, which can be interpreted as the onset of localized coating degradation, including microcracking, delamination, or initiation of coating detachment from the substrate. In the final phase of the test, a sharp rise in both F_t and AE was observed, indicating complete failure of the protective coating continuity and a transition of the tribological contact to the substrate material level (Fig. 8).

In the fretting test, the uncoated AlSi9Cu3 substrate exhibited a very high coefficient of friction ($\mu = 2.45 \pm 2.08$) and significant surface wear (depth of 38 μm, width of 440 μm) after only 0.5 minutes of operation. Strong adhesive bonding, plastic deformation, and formation of hard tribological layers were observed. The application of the CrN coating significantly reduced friction—with a load of 5 N and a test duration of 14 minutes, the coefficient of friction decreased to $\mu = 0.65 \pm 0.19$. Nevertheless, complete degradation of the coating and substrate damage occurred (depth of 86 μm, width of 1300 μm), indicating limited durability of the coating under prolonged contact conditions (Table 2).

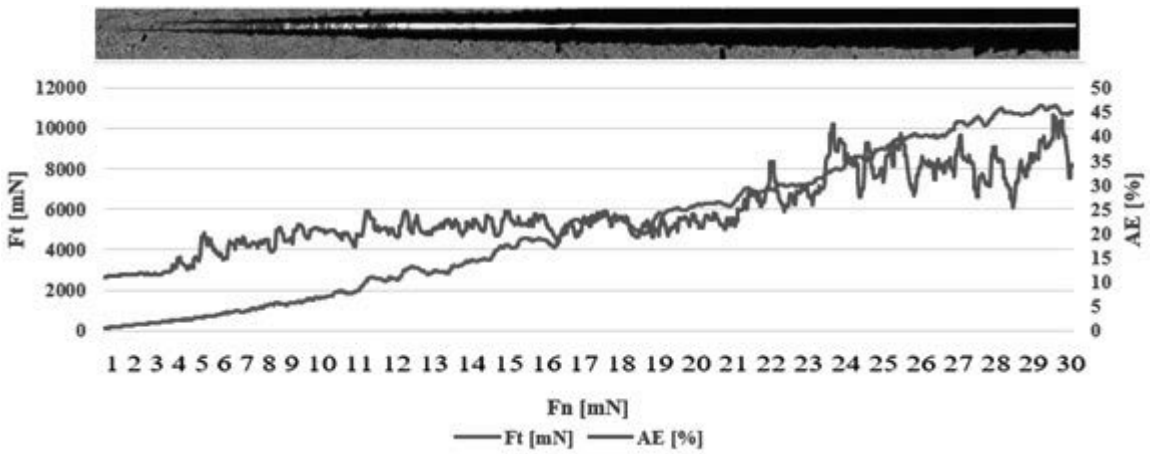

Fig. 8 Friction force (Ft) and acoustic emission (AE) as a function of normal force (Fn)

Table 2 Friction coefficient values obtained from the fretting test

Sample	Substrate	Coating	Test parameters			Test results		
			Speed [cm/s]	Load [N]	Duration [min]	COF μ [-]	Depth [μm]	Width [μm]
1	AlSi9Cu3	-	5	1	0,5	2.45 ± 2.08	440	38,04 ± 3,20
2	AlSi9Cu3	CrN	5	5	14	0.65 ± 0.19	1300	85,99 ± 6,30
3	AlSi9Cu3	CrN	5	2	2	1.81 ± 0.92	1000	77,60 ± 6,63
4	AlSi9Cu3	CrN	5	1	2,5	1.02 ± 0.75	520	30,39 ± 2,93

At lower loads of 2 N and 1 N and shorter test durations, a gradual increase in the coefficient of friction (μ = 1.81 and 1.02, respectively) was observed, along with less pronounced but still significant wear (Table 2). Even at 1 N, coating penetration and substrate damage occurred, indicating that CrN coating does not provide effective protection against fretting on the soft AlSi9Cu3 alloy. The results suggest that although the CrN coating reduces friction, its durability is limited by the low deformation resistance of the substrate. Under all test conditions, coating breakthrough was observed, which restricts its applicability in fretting environments.

Figure 9 shows characteristic morphological features such as irregular cracks and a directional structure indicative of material brittleness. At higher magnification, distinct grain boundaries and microcracks are visible, confirming the brittle nature of the structure.Figure 10 presents the wear analysis of the AlSi9Cu3 alloy surface coated with CrN after the fretting test (F = 5 N, t = 14 min). Figure 10a depicts the wear track with three measurement lines, for which depth profiles are shown in graphs (b). Significant indentations and surface irregularities are visible, confirming intensive layer degradation and coating breakthrough to the substrate.

The adhesion test of the CrN coating using the comparative Rockwell method revealed progressive coating damage with increasing load (Table 3). At the lowest load (60 kp, HRA), limited cohesive cracking and minimal signs of delamination were observed, resulting in a rating of K2/A1. The indentation diameter measured 905 ± 2 μm, with damage localized around the impression. Increasing the load to 100 kp (HRD) caused a noticeable increase in damage, with delamination appearing at the edges of the indentation and more pronounced radial cracks (K2/A2, diameter 1183 ± 9 μm). The most severe changes occurred at 150 kp (HRC), where a dense network of cohesive cracks and extensive coating delamination were recorded (K3/A2, diameter 1470 ± 12 μm).

Figure 11 shows the appearance of the indentation after the Rockwell test on the CrN coating at a load of 60 kp (HRA). Image (a) displays extensive cohesive cracking within the indentation,

while the enlarged view in image (b) reveals coating delamination and a network of microcracks at the indentation boundary, indicating localized detachment of the coating from the substrate.

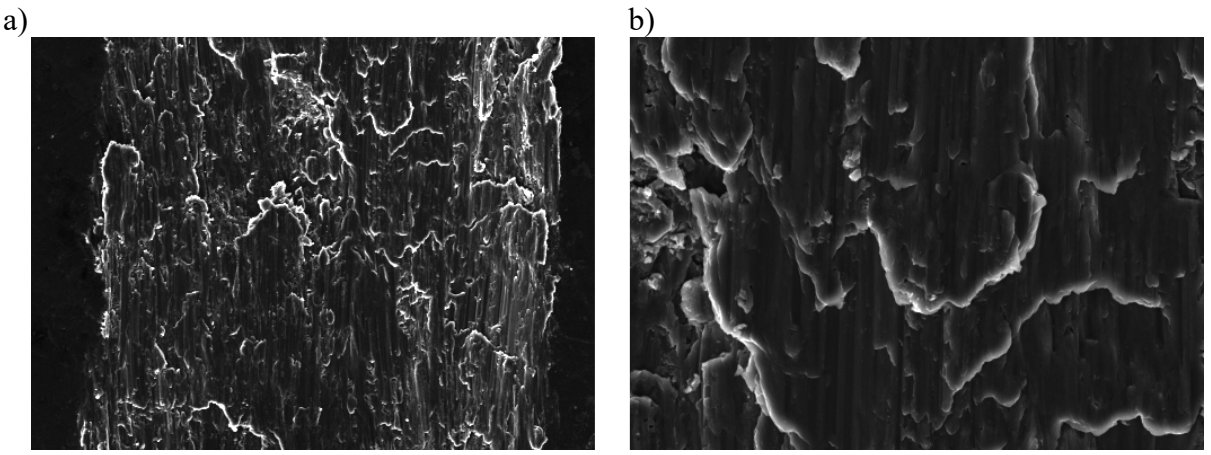

Fig. 9 Micrographs of the AlSiCu alloy surface: a) image showing the general morphology of cracks and directional structure, b) image revealing grain boundaries and presence of microcracks indicative of material brittleness

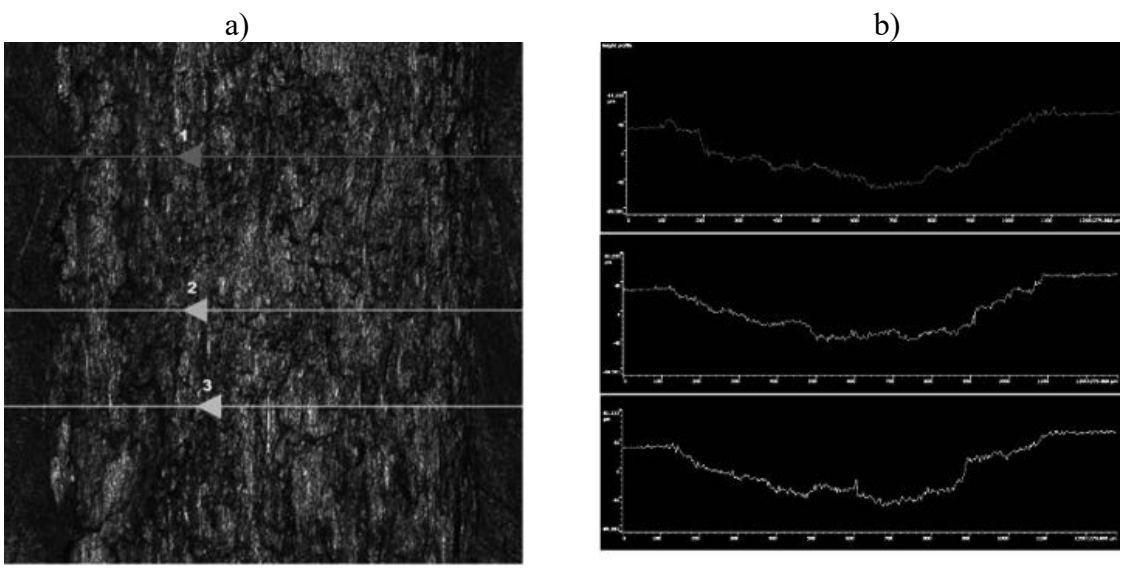

Fig. 10 Depth profiles of surface wear on the AlSi9Cu3+CrN alloy (F = 5 N, t = 14 min): a) SEM image showing the wear track with marked measurement lines; b) corresponding depth profiles obtained by profilometry

Table 3 Results of the Rockwell test performed on an AlSi9Cu3 substrate with a CrN layer.

Test parameters		**Test results**	
Marking	**Load size [kp]**	**Indentation diameter [µm]**	**Assigned number**
HRA	60	905 ± 2	K2/A1
HRD	100	1183 ± 9	K2/A2
HRC	150	1470 ± 12	K3/A2

Figure 12 illustrates characteristic damages observed after the Rockwell adhesion test. In image (a), numerous cohesive cracks are visible within the coating layer, propagating in various directions, indicating significant internal stresses and brittle fracture behavior of the material.

Image (b) shows delamination of the layer, i.e., its detachment from the substrate, with clear layer separation and an irregular crack line. The observed damage suggests low mechanical load resistance of the coating and potentially weak adhesion to the substrate.

a) b)

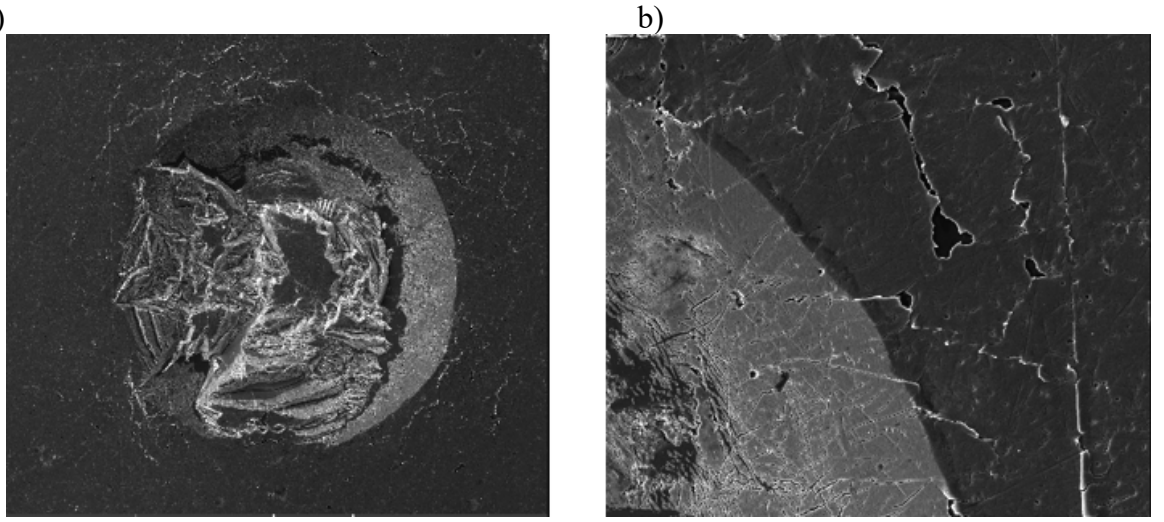

Fig. 11 The appearance of the indentation after the Rockwell test on the CrN coating under a load of 60 kp (HRA): a) reveals extensive cohesive cracking within the indentation, while image, b coating delamination and a network of microcracks at the indentation boundary, indicating local detachment of the layer from the substrate

a) b)

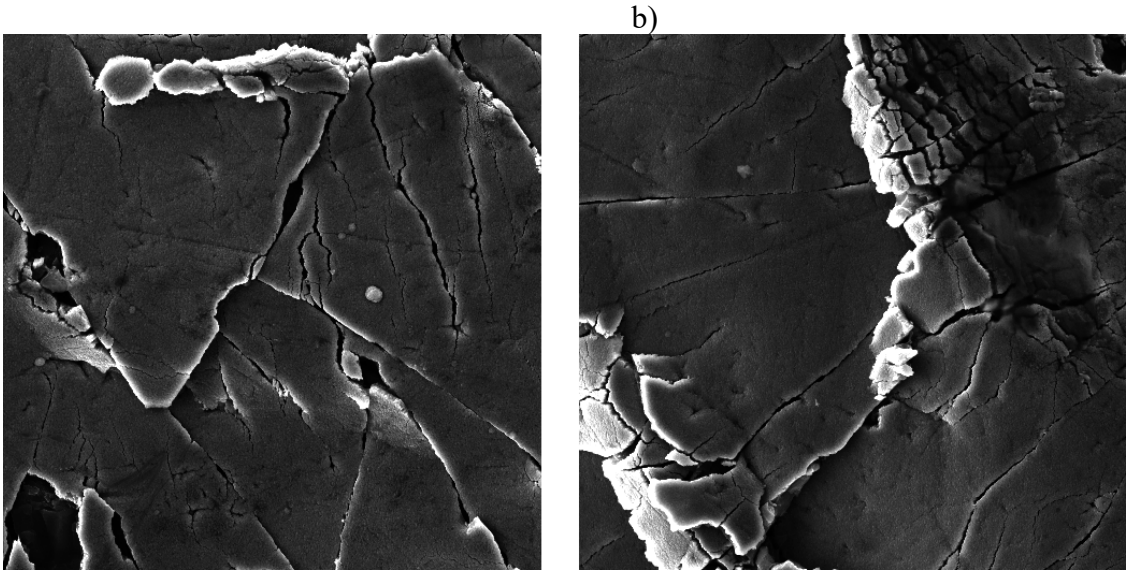

Figure 12 Coating damage after the Rockwell test (HRC): a) displays cohesive cracks indicating high stresses and brittleness, b) reveals delamination with irregular cracking, weak adhesion and low mechanical resistance

4. CONCLUSIONS

- The CrN coating is characterized by a columnar structure and uniform adhesion to the substrate, with an average thickness of 1.35 μm. Topographical analysis revealed a granular structure and isolated chromium particles, indicating localized imperfections in the deposition process.

- The coating demonstrated protective effectiveness under friction conditions at lower loads, reducing volumetric wear by up to 50% at a load of 1 N. At a higher load of 3 N, rapid degradation of the coating and increased wear were observed.
- The main wear mechanisms were abrasive wear and delamination. At higher loads, the cracking CrN coating acted as a hard abrasive, leading to damage of the soft aluminum substrate.
- The scratch test showed that the first damages to the CrN coating appeared at approximately 11 N, with complete degradation occurring around 20 N. The increase in friction force and acoustic emission confirms the progressive destruction of the protective layer and exposure of the substrate.
- The fretting test revealed a significant decrease in the friction coefficient (from $\mu = 2.45$ to $\mu = 0.65$) after applying the CrN coating; however, in all variants, damage to the coating occurred, especially with longer test duration and higher load.
- The Rockwell test confirmed good adhesion of the CrN coating (K2/A1 at 60 kp), but with increasing load (up to 150 kp), progressive loss of cohesion and delamination (K3/A2) were observed, indicating the dominance of degradation mechanisms under high contact stress.

ACKNOWLEDGEMENTS

This work was produced as part of the project implemented within the framework of project-oriented education – PBL, in the XII competition under the Excellence Initiative - Research University program, at the Silesian University of Technology.

BIBLIOGRAPHY

1. Z. Li, X. Guan, Y. Wang, J. Li, X. Cheng, X. Lu, L. Wang, Q. Xue, Comparative study on the load carrying capacities of DLC, GLC and CrN coatings under sliding-friction condition in different environments, *Surface & Coatings Technology* vol. 321, (2017), 350–357.
2. R. Edis, T. Sinmazcelik, A. T. Erturk, Measuring applied force and energy consumption in deep drawing die sets: An experimental and numerical analysis of CrN and CrTiN PVD coating effects, *Surface & Coatings Technology* vol. 224, (2024).
3. S. M. Aktarer, Y. Sert, T. Küçükomeroğlu, Investigation of structural, hardness, adhesion, and tribological properties of CrN and AlCrN coatings deposited on cylinder liner, *Surface & Coatings Technology* vol. 253, (2025), 1–17.
4. T. Narayana, S. S. Saleem, Comparative investigation and characterization of the nano-mechanical and tribological behavior of RF magnetron sputtered TiN, CrN, and TiB_2 coating on Ti6Al4V alloy, *Surface & Coatings Technology* vol. 193, (2024).
5. K. Li, L. Shao, W. Li, L. Shang, R. Li, Y. Zhang, Q. Song, C. Wang, C. Zhang, Superior wear resistance of CrN film by PVD/HVOF structure design, *Surface & Coatings Technology* vol. 209, (2025).
6. D.-H. Shin, S.-J. Kim, Effect of hydrogen charging on the wear resistance of CrN-coated Al alloy for hydrogen valve of fuel cell electric vehicles, *Surface & Coatings Technology* vol. 62, (2023).
7. J. Wang, X. Tao, X. Zhang, F. Tian, Z. Huang, W. Tian, J. Chen, The influences from CrN transition layer thickness to the tribological and corrosion performance of DLC films, *Surface & Coatings Technology* vol. 155, (2025).
8. J. Janoszka, N. Puchała, N. Zaręba, M. Staszuk, D. Pakuła, Tribological properties of CrN coating applied to aluminum alloy substrate, *Talent Detector Winter*, (2025).

TalentDetector

23th-25th June 2025
Gliwice-Brenna, Poland

DEPARTMENT OF ENGINEERING MATERIALS AND BIOMATERIALS
FACULTY OF MECHANICAL ENGINEERING
SILESIAN UNIVERSITY OF TECHNOLOGY

INTERNATIONAL STUDENTS SCIENTIFIC CONFERENCE

Practical Applications of Laser Marking in Manufacturing Industry

Dawid Jarysz [a], Jan Wypiór [b], Mirosław Bonek [c]

[a] Production Engineering and Management student, e-mail: dj309666@student.polsl.pl
[b] Production Engineering and Management student, e-mail: jw309692@student.polsl.pl
[c] Silesian University of Technology, Faculty of Mechanical Engineering, Department of Engineering Materials and Biomaterials

Abstract: The article provides a comprehensive overview of laser marking technology [1] in the manufacturing industry, starting with a discussion of the basic mechanisms of operations (ablation, burn marking, annealing) and the three main types of laser sources (CO_2, fiber, UV/green) used to mark various materials. The following sections describe applications of the method in key industries: automotive (marking of engine parts and plastic components), electronics and semiconductor (micro marking of wafer and PCBs with minimal thermal impact), aerospace (meeting stringent traceability standards for marking titanium alloys, aluminum and composites) and medical (marking of surgical instruments and implants according to UDI). It then discusses the benefits of durability, precision and automation of the process, as well as pointing out limitations such as capital costs, the need to match the laser to the material, and concludes with ongoing directions.

Keywords: Laser, Laser marking, materials, technologies, identification, automotive industry

1. INTRODUCTION

Laser marking is currently one of the fastest growing technologies used in the manufacturing industry. [2] But what makes this technology such a breakthrough in so many different industries? The fact that it involves permanently applying various types of markings - from simple serial numbers to QR barcodes to logos or even complex graphics - by applying a laser beam to the surface of a material. Compared to traditional marking methods such as thermal printing, mechanical engraving or self-adhesive stickers, laser marking is characterized by extremely high durability and resistance to external factors (abrasion, heat, chemicals), as well as very precise reproduction of details and the possibility of full automatization.

As producers in various industries face increasingly complex product traceability requirements - whether for regulatory reasons or for quality, safety or logistics management - laser marking technology is gaining increasing importance. This paper provides a comprehensive overview of practical applications of laser marking in the manufacturing industry, including a description of the mechanisms of operation and available laser types, a discussion of major industry implementations, an analysis of advantages and limitations, characteristics of leading

system suppliers, examples of process parameters, and prospects for further development of this technology. This is something we want to examine in a broader context and discuss in our article thoroughly and in detail.

2. METHOD OF PROCESS OPERATION

The essential mechanism of laser mark making is the interaction of the concentrated laser beam with the surface of the material. Depending on the type of laser, parameters such as power, pulse duration or operating frequency, as well as the characteristics of the material itself (metal, plastic, ceramic, wood, glass), effects varying in depth, contrast and appearance can be obtained. One of the most common methods is ablation, [3] which is the evaporation of the top layer of the material, resulting in engraving into the material (for example, in the case of steel or aluminum). Another common form is "scorching" or burn marking, which involves locally changing the color of a surface due to high temperature (used with plastics, wood, paper), resulting in a dark mark on a lighter background. For applications requiring high color contrast or near-thermal exposure, UV lasers or green lasers are used, [3] which operate at shorter wavelengths and induce a local change in the chemical structure of the surface (e.g., oxidation of metal, modification of plastic dye), resulting in a black, white or even colored mark without deep damage to the material.

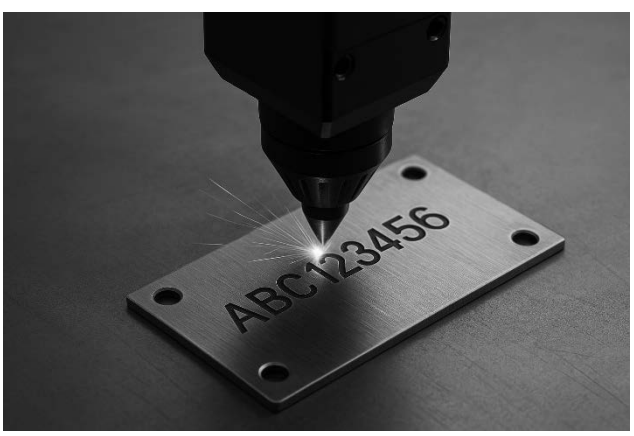

Figure 1. Laser Marking Machine in Action

3. VARIOUS TYPES OF LASERS AND THEIR INTENDED USE

In industrial practice, three types of lasers are generally used for marking: CO_2 lasers, fiber lasers, and UV or green lasers.[3] CO_2 lasers, operating at a wavelength of about 10.6 μm, are excellent for marking organic materials such as wood, cardboard, rubber and most plastics (ABS, PMMA, polyvinyl PVC; however, PVC should be avoided due to the release of toxic gases during processing). Their main advantage is the relatively low cost of purchase and operation, as well as simplicity of operation - only ventilation or exhaust extraction is usually required. The disadvantage, on the other hand, is the relatively poor performance on pure metals such as aluminum and copper, which largely reflect radiation of this wavelength.

For this reason, if metal marking is necessary, fiber lasers, emitting a beam with a wavelength of about 1.06 μm, are more often used. Fiber lasers are characterized by high energy efficiency, low maintenance costs (no gas exchange, longevity of the light source - up to 100,000 hours of operation), as well as very high power density, which allows marking metals (steel, aluminum, titanium alloys) with excellent contrast and high speed (on the order of several hundred millimeters per second).In addition, the short pulse durations (often in the nanosecond or picosecond range) make it possible to reduce thermal impact, which is important for thin electronic components, for example. This can also be used in medicine, an industry where time and precision are the things that count most.

A third type used especially in the electronics and medical industries are UV lasers (wavelength ~355 nm) and green lasers (532 nm). Due to their short wavelengths, they are strongly absorbed by many plastics and thin layers of paint coatings or dyes

4. INDUSTRIES WHERE MARKING IS ACTIVELY USED

4.1 Automotive industry

Laser marking technology has found its way into almost every manufacturing industry, especially where permanent traceability and high quality marks are required. In the automotive industry, for example, laser marking has long been the standard - engine parts such as cylinder heads, engine blocks, crankshafts or connecting rods must be marked with legible two-dimensional codes or serial numbers so that, in the event of a malfunction, the production batch, location and date of manufacture can be quickly identified.

Automobile manufacturers such as Ford, Toyota and General Motors have successfully implemented laser marking systems in plants producing cast, stamped or milled parts - the fiber laser beam makes it possible to obtain a high-contrast, friction- and heat-resistant mark that does not smear even during multi-stage heat treatment (annealing) and painting. [8]

Figure 2. Automotive Brake Disc Rotor

What is important here is the integration of the marking station with the MES (Manufacturing Execution System), which allows the automatic transmission of information about the VIN (Vehicle Identification Number), production change and batch, and subsequent archiving in a central database. It's also worth noting that in the automotive industry, in addition to the marking of metal parts, plastic components are increasingly being lasered - for example, filter housings,

interior components (dashboard panels, trim) or electrical wiring - usually using CO_2 or UV lasers. This avoids sticking traditional labels, which could become unstuck or abraded by high temperatures in the engine compartment or body.

4.2 Airline industry

In the aerospace segment, the situation is similar, but the requirements are even more stringent. Fuselage shells, wing components, landing gear, engine parts, as well as aircraft interior components must be permanently and unambiguously marked in accordance with a number of SAE standards (AS478, among others) or FAA requirements. Laser marking on titanium, stainless steel or carbon composite components ensures that the markings will survive both heat and chemical treatment, as well as extreme vibration and varying pressures during flight. Boeing, for example, uses fiber lasers to mark turbine rotors and jet engine components, where the marked area can be exposed to temperatures as high as 600 °C and contact with aggressive chemicals. Airbus, on the other hand, has implemented a UV laser marking system based on UV lasers at its A350 plant, which has made it possible to apply smaller but high-contrast codes on composite fuselage components without risking damage to the material's structure. As a result, each structural part of the aircraft is assigned a unique set of data - manufacturer, batch number, year of manufacture, material certificate - which, in a potential service campaign situation, allows specific components to be quickly located and replaced.

Figure 3. Aerospace Turbine Blade

4.3 Marking in the healthcare industry

In the medical industry, the introduction of UDI (Unique Device Identification) by the FDA in the US and an EU directive has led to the mandatory permanent marking of every medical device - from simple surgical instruments to orthopedic implants to disposable items such as catheters and syringes.[7] These marks must survive repeated sterilization processes (autoclave,

plasma, chemicals), must not release any chemical residues or compromise the structure of the material, especially when we are talking about implants implanted in the patient's body. In practice, this means using fiber lasers to spot-engrave batch numbers or DataMatrix codes on stainless steel or titanium instruments, as well as UV lasers to mark plastic components such as sample containers, infusion bags or diagnostic equipment components.

Figure 4. Medical Surgical Scalpel (UDI Marking)

4.4 Labeling in the food industry

In the food and packaging industry, laser marking is increasingly replacing thermal printing or stickers, especially for ink-sensitive products such as food and pharmaceuticals. The use of CO_2 lasers makes it possible to quickly and permanently apply best-before dates, barcodes or lot numbers to cardboard packaging, cartons or corrugated cardboard.

Recent years have also seen the introduction of concepts for marking the actual surface of food products - for example, low-power lasers for creating patterns on fruit peels (apples, pears), allowing additional information (code of origin, date of harvest) without the need for any labels. While this is still a niche, it is gaining popularity due to the growing trend of zero waste and avoiding plastic. Personally, I find this solution innovative and interesting, while I have some reservations about the frequency of use. On the products shown below, i.e. kiwi or watermelon, the solution makes sense and does not differ from the standard in any way. However, on fruits such as apples, pears, i.e. products eaten whole, without peeling, such an inscription will rather discourage and worry customers. Appropriate steps would have to be taken to promote such a solution as safe for health.

Figure 5. Kiwi with "BIO" Laser Mark and PET Bottle with Laser-Etched Best-Before Date

5. ADVANTAGES OF LASER MARKING

Laser marking has a number of undeniable advantages that make it an increasingly popular choice for manufacturers. First of all, the resulting markings are permanent - resistant to abrasion, heat, chemicals and UV radiation; there is no risk that the serial number or batch code will precipitate, chip or rub off over time during further processing. In addition, the process itself is non-contact (no friction or mechanical pressure), which eliminates the risk of micro-cracks or deformation, as is the case with traditional mechanical engraving. The laser guarantees very high repeatability - with the determination of optimal parameters of power, pulse time and scanning speed, the same mark can be obtained millions of times in identical quality. [4]

With no ink, inks or stickers to consume, the process complies with the principles of “clean manufacturing” - it generates no waste and only a minimal amount of fumes or smoke. [4] It is this longevity of the process's applicability-another way of amortizing the investment-that spreads out over many years of reliable use. [5]

6. DISADVANTAGES OF LASER MARKING

The first drawback, an obvious one that comes to mind almost immediately, is the cost of purchasing marking stations. Another limitation is that laser marks are mostly superficial - their depth rarely exceeds several tens of micrometers. In applications where extreme abrasion resistance must be achieved (for example, deep nameplates for industrial machinery operated in very harsh conditions) or when a very large depth of drilling is required, the laser may not be sufficient and it is sometimes necessary to use deep CNC engraving. On the organizational side, it is worth considering staff training and the development of maintenance procedures - although modern fiber lasers are relatively maintenance-free, they do require periodic checks on the condition of the optics, the tightness of the seals and the operation of the cooling system.

7. PROSPECTS OF USING LASER MARKING - "SO I BOUGHT A LASER AND NOW WHAT'S NEXT?”

In terms of development prospects, several trends and directions can be noted that will bring further evolution of laser marking in the coming decade. First, there is growing interest in technologies that enable marking on curved or irregular surfaces. Second, solutions based on cloud-based analytics and artificial intelligence are beginning to appear, which automatically select optimal laser parameters depending on changes in factors such as humidity, temperature or material hardness. [6] These systems can predict how the process is going. Of course, they can't replace a skilled operator, but they can certainly help with parameter selection. [9]

8. SUMMARY

In conclusion, it is worth noting that laser marking is a versatile and durable solution for a variety of industries - from automotive, electronics, aerospace and medicine to the food industry. By precisely selecting the type of laser and the parameters of the process, markings resistant to abrasion, chemicals or extreme temperatures are obtained, with flexibility and the possibility of

full automation. [10] While the investment in advanced systems (especially UV or fiber) can be costly, the lack of the need for ink or labels and the low operating costs mean that it quickly pays for itself in the form of increased productivity and certainty of production traceability. Looking ahead, developments in 3D technology, integration with the cloud and artificial intelligence systems will enable further improvements, as well as new opportunities.

ACKNOWLEDGEMENTS

The work was created as part of project of Students Scientific Circle of Laser Surface Treatment under the Initiative of Excellence - Research University, Silesian University of Technology, Gliwice, Poland.

BIBLIOGRAPHY

1. Laser treatment of the surface layer of 32CrMoV12-28 and X40CrMoV5-1 steels, Autor: Dobrzański, Leszek Adam; Labisz, Krzysztof; Jonda, Ewa, artykuł
2. https://www.researchgate.net/publication/281192318_Laser_Marking_Methods#read
3. https://www.linxglobal.com/wp-content/uploads/2023/06/csl60-laser-white-paper-6pp-lores.pdf
4. https://www.datalogic.com/upload/white_papers/2016_WP_LASER%20MARKING_EN.pdf
5. https://www.troteclaser.com/pl/zasoby/faqs/jak-znakowac-laserem
6. https://pl.wikipedia.org/wiki/Laser
7. https://www.nashvillelaserstudio.com/laser-marking#:~:text=barcodes
8. https://www.yupeclaser.com/the-7-applications-of-laser-technology-in-industrial-manufacturing/
9. https://www.asme.org/topics-resources/content/7-top-applications-of-lasers-in-manufacturing
10. https://www.automator.com/en-us/laser-marking-industrial-applications

TalentDetector
23th-25th June 2025
Gliwice-Brenna, Poland
DEPARTMENT OF ENGINEERING MATERIALS AND BIOMATERIALS
FACULTY OF MECHANICAL ENGINEERING
SILESIAN UNIVERSITY OF TECHNOLOGY
INTERNATIONAL STUDENTS SCIENTIFIC CONFERENCE

Pro-ecological Laser Cutting Technology

Szymon Jędrzejewski [a], Bartosz Nikiel [a], Kamil Oleksy [a], Matusz Paluch [a], Dominik Towarnicki[a], Mirosław Bonek[b], Oleh Polishchuk [c]

[a] Students of Silesian University of Technology, Faculty of Mechanical Engineering
[b] Silesian University of Technology, Faculty of Mechanical Engineering, Department of Engineering Materials and Biomaterials
[c] Khmelnytskyi National University, Faculty of Mechanical Engineering, Transport and Architecture, Khmelnytskyi, Ukraine

Abstract: This study compares four cutting methods—laser, plasma, guillotine, and mechanical punching—for producing steel components used in transport baskets. Each method was evaluated based on dimensional accuracy, surface quality, efficiency, and environmental impact. A multi-criteria analysis showed that laser cutting achieved the highest overall score, offering excellent precision, minimal waste, and high production speed. The results confirm laser cutting as the most effective and sustainable option for this application.

Keywords: laser treatment, laser cutting, cutting technologies, environmental impact

1. INTRODUCTION TO LASER CUTTING TECHNOLOGY

The landscape of modern manufacturing is continuously evolving, driven by demands for increased precision, efficiency, and, crucially, environmental sustainability. High-power laser technology has emerged as a pivotal tool in this evolution, offering distinct advantages in material processing, particularly in cutting and welding applications. Its non-contact nature, high energy density, and precise control capabilities distinguish it from conventional methods, making it an indispensable component in industries ranging from aerospace and automotive to electronics. This theoretical introduction aims to provide a comprehensive overview of laser cutting technology, from its foundational principles and historical development to its inherent eco-friendly attributes and future advancements [1].

1.1.Fundamental Mechanisms and Advantages of Laser Cutting

Laser cutting is fundamentally an advanced, non-contact machining process that achieves material separation by irradiating the workpiece with a high-energy density laser beam, causing localized melting, vaporization, or burning. To fully comprehend the "pro-ecological" advantages of laser cutting, it is essential to contextualize it against the environmental and health impacts associated with conventional material processing techniques. This section

provides a comparative overview of mechanical, plasma, and waterjet cutting methods, highlighting their respective environmental considerations. One of the most substantial environmental contributions of laser cutting is its remarkable ability to minimize material waste [4]. Unlike conventional mechanical methods such as sawing or punching, which frequently generate considerable amounts of scrap material, laser cutting employs precise, high-energy beams to vaporize or melt only the necessary material [5]. This results in significantly less excess material.

The precision of laser cutting is further amplified by advanced nesting software, which optimizes the layout of cuts on a raw material sheet to maximize material utilization. This technology ensures that virtually every inch of valuable raw material is efficiently used, a particularly crucial benefit when working with expensive metals or other high-value resources. This inherent precision also dramatically reduces the incidence of defective parts, thereby minimizing the need for rework or corrections. In traditional processes, inaccuracies often lead to discarded parts, resulting in wasted materials, processing time, and energy. The alignment of laser cutting with lean manufacturing principles, which prioritize the elimination of waste and streamlining of production processes, further solidifies its eco-friendly credentials [5].

The precision and material optimization offered by laser cutting not only lead to a reduction in waste but also translate directly into economic advantages. Maximizing material usage and minimizing rework contribute to lower production costs [5]. Furthermore, the absence of physical tools that wear out eliminates the recurring costs associated with tool replacement, as the laser beam itself serves as the cutting instrument [4]. This synergy between environmental benefits (waste reduction) and economic advantages (cost savings) makes eco-friendly laser cutting a compelling business case, driving its adoption beyond mere regulatory compliance and towards a more sustainable and profitable manufacturing paradigm.

1.2. Energy Efficiency and Reduced Carbon Emissions

Laser cutting generally exhibits higher energy efficiency compared to many traditional cutting methods, consuming less power for effective operation. Among laser types, fiber lasers are particularly noteworthy for their exceptional energy efficiency, consuming significantly less power than CO2 lasers. Their long diode lifespans, approximately 100,000 hours, contribute to long-term energy savings and reduced maintenance requirements [4, 6]. The inherent speed of laser cutting, coupled with its accuracy, contributes to reduced machine operational times. This translates directly into lower overall energy consumption during the production process and, consequently, a reduction in carbon emissions. Modern laser cutting systems are increasingly designed with energy-saving features, such as standby modes and optimized beam delivery systems, further enhancing their energy performance [5]. A significant aspect of the reduced carbon footprint stems from the non-contact nature of laser cutting. Traditional methods rely on physical tools that undergo a life cycle of manufacturing, transportation, and eventual disposal, each stage contributing to carbon emissions. Laser cutting, by eliminating tool wear, bypasses these associated lifecycle emissions from tool production and disposal. This absence of tool wear is a substantial, though often overlooked, contributor to a reduced carbon footprint and decreased resource depletion, positioning laser cutting as a more holistically sustainable choice throughout the entire manufacturing process lifecycle. The reduced need for consumables and maintenance further lowers emissions over the equipment's lifespan [4, 5].

2. INDEPENDENT WORK

The present study investigates the effectiveness of various cutting technologies for thin steel components, with the primary goal of comparing laser cutting against traditional mechanical and thermal methods. The selected component is characterized by a simple, flat geometry that enables direct, objective evaluation of edge quality, dimensional accuracy, production efficiency, and environmental impact.

2.1. Description of the Component and Selected Cutting Methods

The research compares four distinct cutting methods, each applied to produce identical test pieces. For each method, cutting parameters such as speed, power, and tool clearance were strictly controlled. Following production, samples from each batch were tested for dimensional accuracy, surface quality, cutting speed, and post-processing requirements. An illustration of the target application is shown in Figure 1.

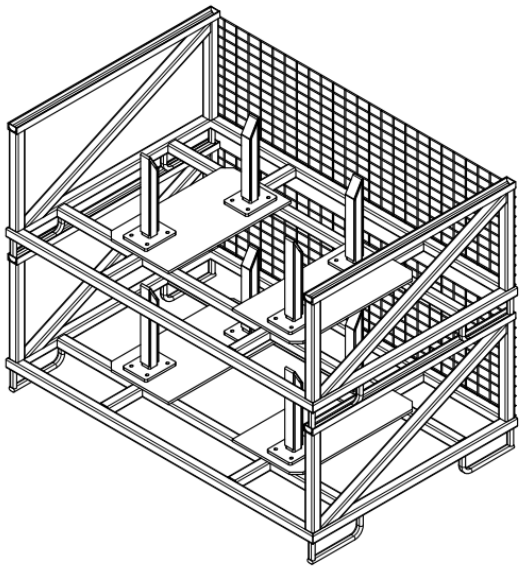

Figure 1 Diagram of stacking transport containers used in the automotive industry

The methods were also analyzed for material waste, noise emission, operator workload, and energy consumption. The produced elements are intended to be used as components in the manufacturing of a steel transport basket, designed for industrial storage and logistics applications. The design and technical documentation were provided to the cutting department, where several product series were manufactured using the four methods mentioned above.

Cutting Method No. 1
Initially, it was decided to use a BLM GROUP LS 5 laser cutting machine for the production of this component. The following parameters were applied during the cutting process:

- Nozzle distance from the sheet: 0.7 [mm]
- Assist gas used: nitrogen
- Gas pressure: 19 [bar]
- Cutting speed: 2500 [mm/min]
- Focal offset: -2.5 [mm]
- Power: 2000 [W]

Cutting Method No. 2
Next, a second series of products was manufactured using the HYPERFORMANCE PLASMA HPR130XD plasma cutter. During the process, the machine was calibrated with the following parameters:

- Torch-to-sheet distance: 1.5 [mm]
- Plasma gas used: oxygen
- Shielding gas used: oxygen
- Plasma gas flow rate: 92 [l/min]
- Shielding gas flow rate: 5 [l/min]
- Arc voltage: 123 [V]
- Cutting speed: 1160 [mm/min]

Cutting Method No. 3
The next technology tested was mechanical cutting using guillotine shears. The production of the components took place in three stages: first, the sheet metal was cut into strips of equal width; then, the resulting long pieces were cut into smaller rectangles matching the overall dimensions of the finished product. In the final stage, each metal plate was chamfered on both sides at a 45° angle.
The process used a VIMERCATI CSI 3050x6 guillotine shear. The cutting parameters were as follows:

- Cutting speed: 85 [mm/s]
- Power: 7500 [W]
- Clearance used: 0.3 [mm]
- Pressure applied: 18,000 [kg]

Cutting Method No. 4
Finally, it was decided to produce a series using punching, which is a specialized mechanical cutting method. Before the actual cutting, the sheet metal was divided into strips, similarly to the previous method. The prepared semi-finished product was then fed into a mechanical press, where it was given its final shape using special punches.
The process utilized a SANGIACOMO PRESSE T 63R CE machine. The following parameters were applied during the process:

- Cutting speed: 15 [strokes/min]
- Power: 5500 [W]
- Clearance used: 0.3 [mm]
- Pressure applied: 20,000 [kg]

3. ANALYSES AND RESEARCH CARRIED OUT

The elements produced using these methods were then decided to be tested. For this purpose, several products were randomly selected from each batch and delivered to the quality department. There, they were subjected to non-destructive visual tests, during which their dimensional correctness was checked and their surfaces were checked for possible discontinuities and deformations. Next, the individual production processes used to produce the discussed element were carefully examined. Based on the observations and analyses, a table was created comparing the features and parameters – Table 1.

	Selected features	Cut No. 1	Cut No. 2	Cut No. 3	Cut No. 4
1	Cutting tool	laser beam	plasma jet	cutting knives	punch
2	The nature of the cut	Laser cutting	gas cutting	mechanical cutting	mechanical cutting
3	Heat Affected Zone	small	big	lack	lack
4	Impact on the surface layer	small	big	small	small
5	Parallelism of cutting	big	mean	mean	big
6	Surface roughness after cutting	All right	mean	mean	mean
7	Dimensional accuracy	All right	mean	mean	All right
8	Cutting speed	big	mean	small	big
9	Need for further processing	rarely	Sometimes	rarely	rarely
10	Repair and operating costs	medium	medium	small	big
11	Environmental factors	low noise; emission of harmful radiation and oxides	high noise; emission of harmful radiation and oxides	medium noise	big noise
12	Approximate unit time	3 seconds	8 seconds	18 seconds	4 seconds
13	Amount of waste produced (scrap)	small	small	small	small
14	Number of employees in the position	1	1	3	3
15	Number of pieces produced per shift	9000	3375	1500	6750

Table 1 Comparative list of features and parameters used in cutting processes.

The specification of parameters and features for each cutting method performed allowed us to select the values that most significantly affect the quality of the manufactured product. In order to estimate the impact of the applied method on the quality level of the manufactured products, point optimization was performed, in which selected data was compiled and calculations were made on them - Table 2.

	K1	**K2**	**K3**	**K4**	**K5**	**Σ kn**	**W1**	**W2**	**W3**	**W4**	**Wmax**
K1		0.5	0.4	0.3	0.4	1.6	2	2	1	1	3
K2	0.5		0.4	0.5	0.3	1.7	3	2	1	3	3
K3	0.6	0.6		0.6	0.5	2,3	3	2	1	3	3
K4	0.7	0.5	0.4		0.4	2	3	2	1	2	3
K5	0.6	0.7	0.5	0.6		2.4	2	2	2	2	3
						Σ (kn · Wn)	26	18.4	15.6	25.6	30
						IN%	**86.7**	**66.7**	**41.3**	**74.7**	**100**

Table 2 Point optimization for the four tested cutting processes.

Based on all selected features, five criteria were created:

- K1 – criterion 1: Cutting surface roughness;
- K2 – criterion 2: Parallelism of the cutting surface;
- K3 – criterion 3: Dimensional accuracy;
- K4 – criterion 4: Cutting speed;
- K5 – criterion 5: Need for further processing.

The cutting methods analyzed for optimization purposes were given the following abbreviations:

- W1 – cut no. 1 (BLM GROUP LS5 laser cutter);
- W2 – cut no. 2 (HYPERFORMANCE PLASMA HPR130XD plasma cutter);
- W3 – cut no. 3 (VIMERCATI CSI 3050x6 scissor guillotine);
- W4 – cut no. 4 (SANGIACOMO PRESSE T 63R CE mechanical press).

Then, each criterion was compared numerically with the remaining four. In this comparison, it was assumed that the sum of the two weights of the analysed criteria is 1, and their weights are selected based on the importance of one criterion over the other, e.g. it was found that criterion K1, due to the quality requirements of the product, is less important than criterion K5, therefore K1 was given a weight of 0.4, while K5 was assigned a weight of 0.6. The remaining activities were carried out in an analogous manner.
In this way, four coefficients (kn) were created for each criterion, which were then summed up and recorded in the column marked with the symbol **Σ kn**. Then, each criterion was considered in relation to all possible variants (1-4). The symbol W max was used to define the maximum weight value that can be assigned to the tested ratio of the criterion to the cutting method. The correctness of the criterion in the tested variant (Wn) was assessed according to the scale:

- 1 – small;
- 2 – average;
- 3 – large.

Next, the result values for each variant were determined by summing the products (Σ kn · Wn) calculated for each criterion. In this way, numerical data were obtained, which were then divided by W max to obtain percentage values (W%), based on which it was estimated that the most suitable manufacturing method, based on the analyzed criteria, is laser cutting 86.7%. An alternative method may also be cutting on dies, which in the optimization carried out obtained a result of 74.7%. The other two methods: plasma cutting and cutting on guillotine shears obtained significantly lower results, 66.7% and 41.3%, respectively.

4. SUMMARY

The aim of the conducted research was to assess the impact of the applied cutting methods on the quality of the manufactured component and to determine which production method would be the most advantageous for actual manufacturing. Based on the literature review and the conducted experiments, it has been demonstrated that the use of laser technology allows for the production of this component with minimal material losses and ensures the highest productivity. Moreover, the products obtained through this process exhibit very high quality. This conclusion is based on analyses supported by dedicated observations and measurements. The tools and instruments used in these evaluations allowed for precise and visual inspection of the studied criteria. Additionally, it was proven that in each of the tested manufacturing methods, to varying degrees, there are components that require finishing or rework. Therefore, it is recommended to establish a dedicated station for the inspection and selection of manufactured parts.

5. CONCLUSIONS

- Based on the analyses, observations, and measurements, the following conclusions were drawn:
- Observations using a stereoscopic microscope showed that elements produced through mechanical cutting have a macrostructure with varying surface roughness and surface defects. The presence of these features often necessitates finishing operations. In the case of plasma cutting, deposits formed along the edges, and early signs of corrosion were visible at the cutting site, which also frequently affects further processing.
- Measurements of surface parallelism and dimensional accuracy confirmed that the components produced by punching and laser cutting best met these criteria. Products cut with guillotine shears showed the greatest dimensional deviations and the least parallelism of cutting surfaces.
- The use of a laser cutter allows for the highest manufacturing speeds. This technology enables the production of the largest number of components while requiring the involvement of only one operator. Other methods involve significantly longer cycle times or require more personnel.
- The applied point-based analysis made it possible to compare and evaluate all examined criteria. For each selected criterion, relevant tests and observations were conducted, enabling an accurate assessment through point-based optimization. Based on this analysis, it was concluded that laser technology is the most suitable method for producing the component, achieving a score of 86.7%, the highest result. Conversely, guillotine cutting was found to be the least effective method, scoring only 41.3%.
- Among the manufactured components, there are some that require finishing operations. Therefore, it is recommended to establish a selection station. Such a setup would allow for the quicker elimination of products that do not meet the required quality standards and direct them to further processing.

ACKNOWLEDGEMENTS

The work was created as part of project based learning - PBL, in the 12th competition under the Initiative of Excellence - Research University, Silesian University of Technology, Gliwice, Poland and as part of project of Students Scientific Circle of Laser Surface Treatment under the Initiative of Excellence - Research University, Silesian University of Technology, Gliwice, Poland.

BIBLIOGRAPHY

1. Research progress on the application of high-power laser ... - Frontiers, Dostęp z dnia: maja 21, 2025, https://www.frontiersin.org/journals/physics/articles/10.3389/fphy.2025.1595077/full
2. Genna, Silvio, Erica Menna, Gianluca Rubino, and Vincenzo Tagliaferri. 2020. "Experimental Investigation of Industrial Laser Cutting: The Effect of the Material Selection and the Process Parameters on the Kerf Quality" Applied Sciences 10, no. 14: 4956. https://doi.org/10.3390/app10144956
3. Badoniya, Pushkal. (2018). CO2 Laser Cutting of Different Materials-A Review. International Journal of Engineering and Technical Research. 5. 2103-2115.
4. Advantages of laser cutting compared to traditional cutting techniques | justlaser.com, Dostęp z dnia: maja 21, 2025, https://www.justlaser.com/en/blog/advantages-of-laser-cutting-compared-to-traditional-cutting-techniques/
5. Environmental Benefits of Laser Cutting - Stephens Gaskets, Dostęp z dnia: maja 21, 2025, https://www.stephensgaskets.co.uk/environmental-benefits-laser-cutting-minimising-waste-reducing-carbon-footprint
6. The Sustainability Advantage of Lasers - Matthews Marking Systems, Dostęp z dnia: maja 21, 2025, https://matthewsmarking.com/blog/the-sustainability-advantage-of-lasers/

TalentDetector
23th-25th June 2025
Gliwice-Brenna, Poland
DEPARTMENT OF ENGINEERING MATERIALS AND BIOMATERIALS
FACULTY OF MECHANICAL ENGINEERING
SILESIAN UNIVERSITY OF TECHNOLOGY
INTERNATIONAL STUDENTS SCIENTIFIC CONFERENCE

Evaluation of selected mechanical properties of Astaloy CrS material produced by sinterhardening process

Dmitriy Koblik[a], Miroslava Ťavodová[b], Monika Vargová[b]

[a]GEVORKYAN, a.s., Slovakia
[b]Technical University in Zvolen, Faculty of Tehnology, Department of Manufacturing Technologies and Quality Management
email: dmitriy.koblik@gevorkyan.sk, tavodova@tuzvo.sk, monika.vargova@tuzvo.sk

Abstract: The article describes the evaluation of the mechanical properties of the Astaloy CrS material with a low alloying volume of chromium and molybdenum. Astaloy CrS samples with different Ni contents were studied, the mechanical properties - tensile strength, yield strength and ellongation, HRB, HRC and HV10 hardness after the sinterhardening process were compared. The influence of additional high-temperature sintering on the mechanical properties was evaluated. From the experimental results, it can be concluded that for the studied material it is possible to obtain a tensile strength higher than 900 MPa and a hardness higher than 33 HRC.

Keywords: sintering, sinterhardening, high-temperature sintering, Astaloy CrS, mechanical properties

1. INTRODUCTION

Powder metallurgy (PM) is a term covering a wide range of ways in which materials or components are made from metal powders. PM processes are sometimes used to reduce or eliminate the need for subtractive processes in manufacturing, lowering material losses and reducing the cost of the final product [1,2]. This process finds extensive applications in the automotive field, meeting the demand for complex and multifunctional parts, e.g. engine, transmission, brake, chassis and electromagnetic components [1,2,3]. This occurs especially often with small metal parts, like gears for small machines. Some porous products, allowing liquid or gas to permeate them, are produced in this way. They are also used when melting a material is impractical, due to it having a high melting point [4].

The powder metallurgy process consists of mixing elemental or alloy powder, compacting the mixture in a die and then sintering or heating the resultant shape in a controlled atmosphere. Powder metallurgy is a highly developed method of manufacturing ferrous and nonferrous materials. It is a chip less working process. This process is cost effective in producing simple or complex part in manufacturing rates which can range from a few hundreds to several thousands parts per hour. Due to high cost of die and equipment this process is suitable for mass production only. The basic steps involved in the production process are:

- Preparation of powder or powders of desired composition.

- Mixing and blending – Powder are mixed thoroughly and blended to ensure desired property.
- Compacting the powders into desired shape and size and providing strength to the parts.
- Sintering – Green compacts are heated at elevated temperature to impart strength.

To continue to expand PM into new industrial areas and applications, materials with enhanced properties produced in cost-effective way are needed. One of such methods is sinterhardening process, which includes classic sintering followed by fast cooling [5]. It allows to achieve high mechanical properties in comparison with standard sintering due to formation of a martensitic structure.

Compared with the traditional die casting process, it shows the advantages of less manufacturing processes, higher material utilization rate and higher dimensional accuracy [6,7]. In addition, PM technology can increase the supersaturation of alloying elements, refine the microstructure, and eliminate segregation of the alloys.

When evaluating materials for any application, understanding their mechanical properties is crucial, as these characteristics dictate how the material will perform under different types of loads and conditions. Whenever we select a material, it is tailored to the application. For powder metal components, several key mechanical properties should be considered, including hardness, tensile strength, yield strength and elongation [8].

In this article a solution and application of the sinterhardening process was described based on a new material Astaloy CrS. To increase hardenability and strength, additional alloying with low Ni content was used. Achieved properties allows the material to be successfully used in moderately loaded applications and assemblies and is also comparable to such frequently used and more expensive materials as Distaloy DH and Astaloy CrM [9].

2. MATERIALS AND METHODS

The chemical composition and densities are shown in Table 1. Chemical elements Cr and Mo are added to the base material Astaloy CrS by pre-alloyed method, Ni and C are admixed.

Table 1. Chemical composition and densities of the used powder mixes

	Cr (%)	Mo (%)	Ni (%)	C (%)	Compacting density ($g.cm^{-3}$)
Astaloy CrS-1Ni-7.0	0.85	0.15	1.00	0.85	7.0
Astaloy CrS-1Ni-7.2	0.85	0.15	1.00	0.85	7.2
Astaloy CrS-2Ni-7.0	0.85	0.15	2.00	0.85	7.0
Astaloy CrS-2Ni-7.2	0.85	0.15	2.00	0.85	7.2

Samples for testing tensile strength and elongation (Fig.1) according to ISO 2740:2023 [10], with a length of 90 mm were pressed on a Dorst hydraulic press (Technologies GmbH, Germany) (Fig. 2a,) at a density of 7.0 and 7.2 $g.cm^{-3}$.

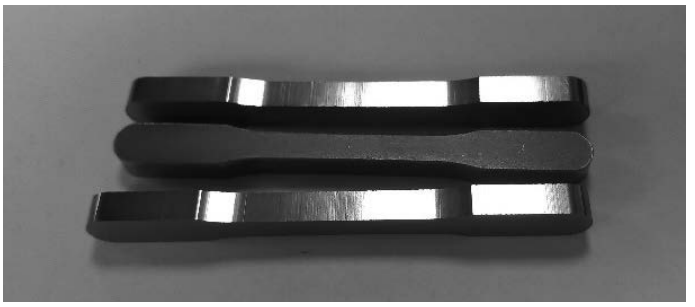

Figure 1. Samples for testing mechanical properties

The sinter hardening process was carried out in a Mahler (Mahler GmbH, Germany) conveyor belt furnace with a cooling zone (Fig.2b,).

a, b,

Figure 2. Hydraulic Dorst press (a,); Mahler conveyor belt furnace (b,)

Conditions of experiment are shown in Table 2.

Table 2. Conditions of sinterhardening and high-temperature sintering

	Sintering temperature (°C)	Sintering time (minutes)	Protective sintering atmosphere
Sinterhardening	1 200	20	mix 90 % nitrogen 10 % hydrogen
High-temperature sintering		30	

After sinterhardening the samples were tempered at a temperature of 200 °C for 1 hour in air. Tensile strength and elongation were measured by Hoganas on tensile machine Olssen (Tinius Olssen testing machine company, USA) according to ISO 6892:2019 [11]. Hardness was measured on universal hardness tester InnovaTest (InnovaTest Europe BV, The Netherlands) according to ISO 6507-1:2023 [12] and ISO 6508-1:2023 [13].

3. RESULTS

The results of measuring the basic mechanical properties and hardness by different methods (HV, HRB/HRC) are in Tables 3 and 4.

Table 3. Mechanical properties of samples processed by sinterhardening

Material	HV10	HRC	HRB	Tensile strength (MPa)	Yield strength (MPa)	Elongation (%)
Astaloy CrS-1Ni-7.0	228	-	96	688	568	0.65
Astaloy CrS-1Ni-7.2	264	23	-	825	638	1.09
Astaloy CrS-2Ni-7.0	315	32	-	794	709	0.35
Astaloy CrS-2Ni-7.2	386	35	-	944	785	0.49

Table 4. Mechanical properties of samples processed by high-temperature + sinterhardening

Material	HV10	HRC	HRB	Tensile strength (MPa)	Yield strength (MPa)	Elongation (%)
Astaloy CrS-1Ni-7.0	220	-	93	795	570	1.83
Astaloy CrS-1Ni-7.2	279	22	-	929	653	2.00
Astaloy CrS-2Ni-7.0	309	33	-	1028	791	0.81
Astaloy CrS-2Ni-7.2	400	37	-	1152	832	1.08

The results of measuring the mechanical properties are in tables 3 and 4. The material Astaloy CrS-2Ni-7.2 has the greatest hardness after high-temperature sintering + sinterhardening. The hardness of samples with Ni 2% composition is significantly higher compared to materials with Ni 1%. The increase in hardness due to the increase in compacting density is smaller than when the Ni content is increased. The hardness of the samples after sinterhardening and high-temperature sintering + sinterhardening has a small difference, 6.1% when measured by the Vickers method, 5.7% when measured by the Rockwell method, which shows that additional sintering does not have a great effect on the hardness of the samples. Also, the reason for the slight difference in hardness may be carbothermal reduction of chromium oxides at higher temperatures which uses the combined carbon as reducing agent. The carbon forms CO (and some CO_2) being transferred into the gaseous phase [14]. The Figure 3a,b, shows graphs showing the difference in hardness between sinterhardening and high-temperature sintering + sinterhardening samples.

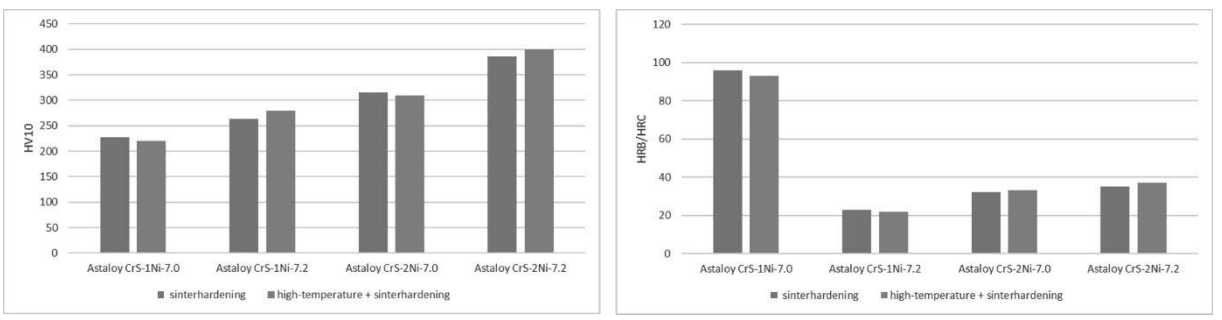

a, b,

Figure 3. Difference in hardness between sinterhardening and high-temperature sintering + sinterhardening samples – HV10 (a,); HRB/HRC (b,)

Material Astaloy CrS-2Ni-7.2 has the highest tensile strength after high-temperature sintering + sinterhardening. Tensile strength certainly increases with increasing compaction density, Ni content and addition of high-temperature sintering. The material Astaloy CrS-1Ni-7.2 has the greatest elongation after high-temperature sintering + sinterhardening. Elongation is increased by increasing the compacting density, adding high-temperature sintering, and decreasing the Ni content. The reason for the difference in tensile strength and elongation is the difference in microstructure, which will be described below (Fig.4).

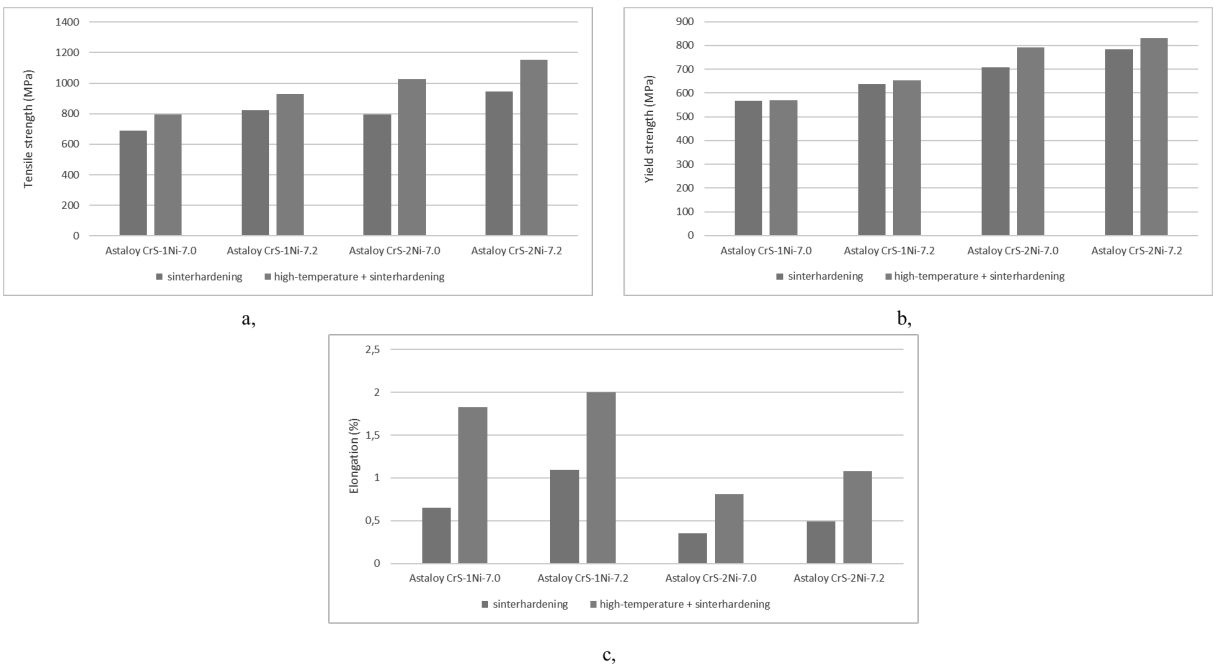

Figure 4. Comparing of mechanical properties sinterhardening and high-temperature sintering + sinterhardening samples - tensile strength (a,); yield strength (b,); elongation (c,)

CONCLUSION

Powder metallurgy is a metal-forming process of ferrous-powdered materials performed by pressing and sintering metal powder compacts near to net shape of the final component. It allows very complex geometries and intricate features. It is now widely acknowledged as a superior way of producing high-quality sintered, structural components for a large array of applications in different industries.

Lean pre-alloyed Cr-Mo material Astaloy CrS with addition of Ni and C can be processed by sinterhardening process, tensile strength greater than 900 MPa and hardness greater than 33 HRC can be achieved directly after sinterhardening and after combination with high-temperature sintering. Material has great good compressibility due to low content of Cr and Mo, density 7.2 g.cm^{-3} can be obtained by single compacting which provides higher mechanical properties, better tightness and corrosion resistance of material [15].

BIBLIOGRAPHY

1. P. Ramakrishnan Automotive Applications of Powder Metallurgy. In Advances in Powder Metallurgy, Elsevier: Amsterdam, The Netherlands, (2013) 493-519.
2. A. Fujiki Present State and Future Prospects of Powder Metallurgy Parts for Automotive Applications. Mater. Chem. Phys. 2001, 67, 298-306.
3. Z. Tan et al. New Development of Powder Metallurgy in Automotive Industry, J. Cent. South Univ. 2020, 27, 1611-1623.
4. O. Erdem The Development and Applications of Powder Metallurgy Manufacturing Methods in Automotive Industry. Int. J. Eng. Res. Dev. 2017, 9, 100-112.
5. R.J. Causton, J.J. Fulmer Sinter-Hardening Low-Alloy Steels, Advances in Powder Metallurgy & Particulate Materials - 1992, Vol. 5, p. 17, Metal Powder lndustries Federation, Princeton, NJ.
6. S. Abhishek, et al. A review of reinforcements and process parameters for powder metallurgy-processed metal matrix composites. Materials Today: Proceedings (2023).
7. P. Yu et al. Interfacial reaction during the fabrication of Ni60Nb40 metallic glass particles-reinforced Al based MMCs. Materials Science and Engineering: A 444.1-2 (2007): 206-213.
8. M. Qi, et al. Superior mechanical properties and microstructural evolution of powder metallurgy 2195 Al-Li alloy subjected to hot extrusion. Journal of Alloys and Compounds 962 (2023): 171184.
9. Iron and steel powders for sintered components – Hoganas Handbook for Sintered Components, p.348, 395.
10. ISO 2740:2023 Sintered metal materials, excluding hardmetals – Tensile test pieces.
11. ISO 6892-1:2019 Metallic Materials – Tensile testing – Part 1: Method of test at room temperature.
12. ISO 6507-1:2023 Metallic materials – Vickers hardness test – Part 1: Test method.
13. ISO 6508-1:2023 Metallic materials – Rockwell hardness test – Part 1: Test method.
14. S. Kremel, H. Danninger, Y. Yu Powder Metallurgy Progress, vol. 2, 2002, no.4, p.211.
15. G.F. Bocchini The influence of porosity on the characteristics of sintered materials, The International Journal of Powder Metallurgy, 22, 3, 1986, pp.185-202.

TalentDetector

23th-25th June 2025
Gliwice-Brenna, Poland

DEPARTMENT OF ENGINEERING MATERIALS AND BIOMATERIALS
FACULTY OF MECHANICAL ENGINEERING
SILESIAN UNIVERSITY OF TECHNOLOGY

INTERNATIONAL STUDENTS SCIENTIFIC CONFERENCE

The use of laser technology in the processing of modern steels in the automotive industry

Tomasz Kołodziej[a], Wiktor Rudek[a], Mirosław Bonek[b]

[a] Students of the 5th Secondary School named after Andrzej Struga in Gliwice, ul. Górnych Wałów 29, 44-100 Gliwice, Poland
email: tomelkolodziej@gmail.com , wiktor.rdk@gmail.com
[b] Silesian University of Technology, Faculty of Mechanical Engineering, Department of Engineering Materials and Biomaterials, ul. Konarskiego 18A, 44-100 Gliwice, Poland
email: miroslaw.bonek@polsl.pl

Abstract: This article explores the application of laser technologies in the processing of modern steels within the automotive industry. It presents the principles of laser operation and the key types of industrial lasers used for cutting, welding, surface hardening, additive manufacturing, and marking. Emphasis is placed on the advantages and limitations of laser-based processing, as well as its integration with Industry 4.0 concepts such as digital twins, AI-based monitoring, and predictive maintenance. The article further investigates the use of laser techniques in the fabrication of electric vehicles and sustainable manufacturing practices. Recent technological developments and challenges are discussed, offering a perspective on future directions and innovations.

Keywords: laser processing, automotive industry, high-strength steels, Industry 4.0, additive manufacturing

1.INTRODUCTION

Laser technology currently represents one of the key tools in modern industrial processes, particularly in the field of engineering material processing. Although initially associated primarily with applications in optics and medicine, its physical and functional properties have enabled wide expansion into the area of materials engineering. A laser, being a source of monochromatic and coherent electromagnetic radiation, generates a highly focused light beam with high energy density. This allows for precise interaction with a material without the need for direct contact between the tool and the surface, significantly minimizing tool wear and thermal deformation. The origins of laser technology date back to 1960, when T. H. Maiman constructed the first operational ruby laser. Since then, laser-based solutions have undergone intensive development, both in terms of design and applications. Today, depending on the type of active medium used, various types of lasers are employed, including gas lasers (e.g., CO_2), solid-state lasers (e.g., Nd:YAG), diode lasers and fiber lasers. Each of these exhibits different beam parameter ranges and interaction characteristics with materials, allowing for their

adaptation to a wide variety of technological tasks. From the perspective of the materials industry-particularly the automotive sector-laser technologies offer a range of significant advantages. These include high precision in cutting and shaping, the ability to perform joints with a reduced heat-affected zone, selective heat treatment (such as surface layer hardening), as well as durable marking and surface structuring. In addition, the integration of laser systems with production lines enables process automation, aligning with the principles of Industry 4.0. This article presents an overview of selected issues related to laser technology in the context of processing modern structural materials. The authors outline the fundamental principles of laser operation, typical configurations used in production engineering, and areas of application-with particular emphasis on the automotive industry, which is one of the most advanced and dynamic users of this technology.

2. TECHNOLOGIES OF LASER PROCESSING USED IN THE AUTOMOTIVE INDUSTRY

2.1. Fiber Laser

Fiber lasers are solid-state devices in which the active gain medium is an optical fiber doped with rare-earth elements such as ytterbium (Yb^{3+}). The laser beam is generated through stimulated emission, then transmitted via a flexible fiber to the processing head (fig.1). This setup enables a small, high-quality focal spot and allows for precise, high-speed processing of materials.

Due to their efficiency, reliability, and compact design, fiber lasers are widely used in the automotive sector. Their main applications include:

Cutting of advanced high-strength steels (AHSS) used in vehicle structures.
Welding of body parts, exhaust components, and seat reinforcements.
Surface treatment, such as cleaning or texturing.
Engraving and marking of parts for traceability.

Advantages:
High electrical-to-optical efficiency.
Long operational lifespan and low maintenance.
Excellent beam quality for precision tasks.
Compact, modular design suitable for automation.

Limitations:
Higher initial cost for high-power systems.
Limited effectiveness on non-metallic or transparent materials.

These lasers are particularly effective for processing modern steels used in vehicle safety and lightweight construction, where high strength and precision are crucial [1,2].

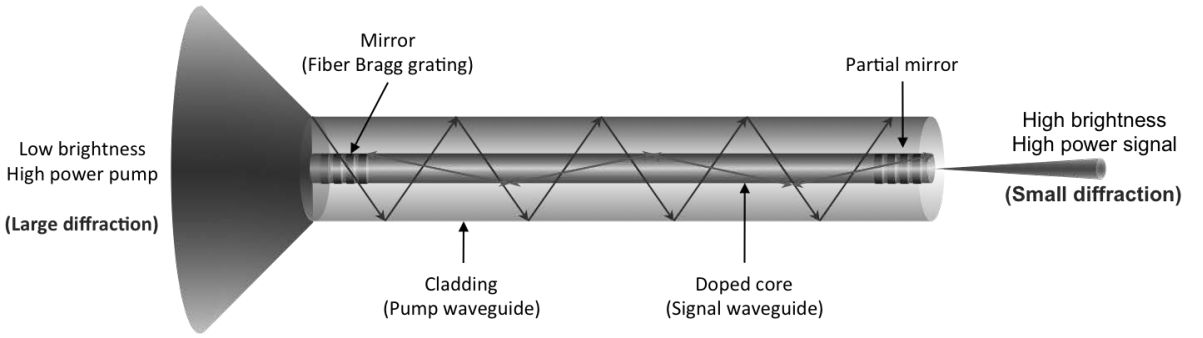

Fig.1. Schematic of a fiber laser system [21]

2.2. Diode Laser

Diode lasers are compact (fig.2), semiconductor-based devices that generate laser light via electron-hole recombination within a p-n junction. Their high efficiency, small size, and ease of integration make them valuable tools in manufacturing, especially where lower laser power is sufficient.[3]

In the automotive industry, diode lasers are widely applied in:

Plastic welding (e.g., dashboard modules, sensor housings).

Brazing of body-in-white components (e.g., tailgates, roof frames).

Surface treatment of lightweight structural parts (e.g., aluminum profiles).

Paint stripping and surface activation for adhesive bonding.[1,3]

Advantage:

High electro-optical efficiency.

- Compact and cost-effective.
- Easily integrated with automation systems.
- Suitable for temperature-sensitive substrates.

Limitations

- Lower beam quality compared to fiber lasers.
- Limited power output for deep penetration welding.
- Susceptible to temperature drift and beam divergence.

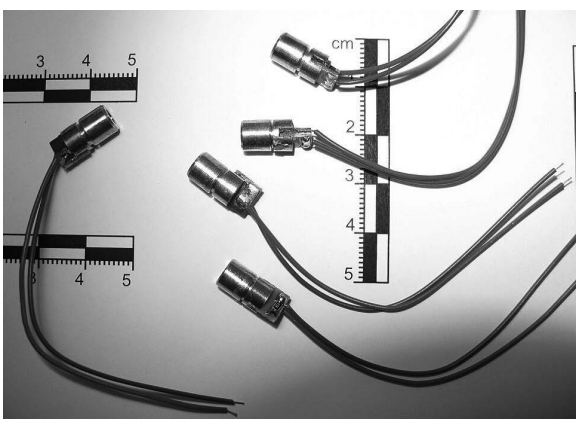

Fig. 2. Typical design of a diode laser [22]

Due to these characteristics, diode lasers are ideal for tasks requiring moderate power, high precision, and minimal thermal distortion. Their implementation in automotive body assembly and electronic component integration underscores their industrial value [1].

2.3. CO_2 Lasers

CO_2 lasers (fig.3) are gas lasers that utilize a carbon dioxide gas mixture excited by electrical discharge to emit infrared radiation, typically at a wavelength of 10.6 μm. These lasers are known for their high power and efficiency in processing both metallic and non-metallic materials [1]. In the automotive industry, CO_2 lasers have historically been applied in various manufacturing operations, such as:

Cutting non-metallic components like plastics, composites, and interior trim materials.
Welding and cutting steel sheets in the production of car body elements.
Surface cleaning and paint stripping prior to joining processes.
Marking and engraving components for traceability and quality control [3].

Advantages

Effective for cutting thicker materials at high speeds.
High energy efficiency in continuous operation.
Compatibility with a broad range of materials.

Limitations

Bulky design and complex beam delivery systems using mirrors.
Lower efficiency when processing highly reflective metals like aluminum and copper.
More difficult integration in flexible robotic systems compared to fiber lasers [1], [3].

Although increasingly replaced by fiber lasers in many automotive applications, CO_2 lasers remain relevant in certain niche processes, particularly those involving non-metallic components or where high cutting power is required [1], [3].

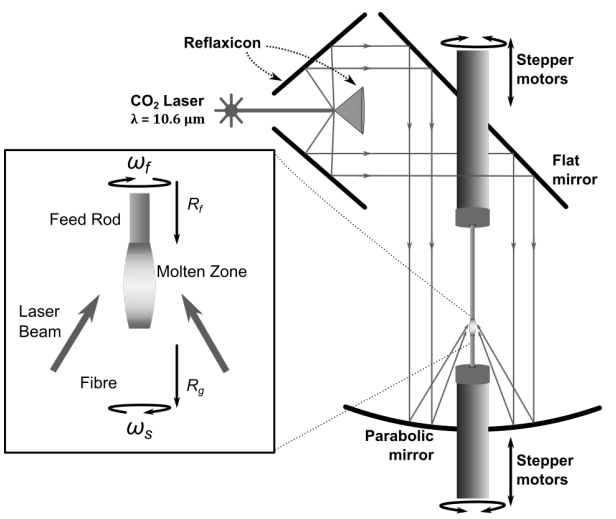

Fig. 3. Schematic of a CO_2 laser system [23]

2.4. Solid-state lasers (Nd:YAG, DISK, SLAB)

Solid-state lasers utilize a solid gain medium, typically a crystal or glass doped with rare earth ions, to generate laser light. Among these, **Nd:YAG (neodymium-doped yttrium**

aluminum garnet) lasers are prominent in industrial applications, emitting light at a wavelength of 1064 nm. They can operate in both continuous and pulsed modes, offering versatility in processing methods [1].

In the automotive industry, solid-state lasers are employed in various applications:

Precision welding of thin automotive sheet metals, especially in areas requiring high accuracy.

Drilling and structuring of hard materials used in powertrain and engine components.

Marking of engine parts, VIN codes, and small metallic components for traceability.

Surface texturing to enhance adhesive bonding in assembly lines [1], [2].

Advantages

High beam quality enabling precise energy concentration.

Compatibility with optical fibers (notably for Nd:YAG), facilitating robotic delivery systems.

Effective for both deep penetration welding and fine micromachining.

Limitations

Thermal management challenges due to heat accumulation in the solid medium.

Higher maintenance requirements compared to fiber lasers.

Generally higher initial investment cost than CO_2 lasers [1].

Advancements in solid-state laser technology have led to the development of disk and slab lasers, which offer improved thermal management and beam quality. Disk lasers, in particular, have found increased adoption in automotive manufacturing due to their robustness and efficiency in high-precision tasks [4].

3. MAIN LASER-BASED OPERATIONS IN THE AUTOMOTIVE INDUSTRY

3.1. Laser cutting of car bodies and structural components made from advanced high-strength steels

The modern automotive industry increasingly relies on Advanced High-Strength Steels (AHSS) and Ultra High-Strength Steels (UHSS) to balance crash safety with vehicle lightweighting. However, their high strength makes conventional machining difficult due to increased tool wear and geometric limitations. Laser cutting offers an effective alternative, enabling precise shaping of complex parts with minimal heat-affected zone (HAZ) and high edge quality [1] (Fig.4). Using a focused fiber laser beam, this process melts or vaporizes material locally. Controlled via CNC or robotic systems, laser cutting is widely applied in the serial production of body and chassis parts, including door pillars, reinforcement beams, crumple zones, and elements made from DP, TRIP, or CP steels [5]. The method supports weight reduction without compromising structural integrity, improving fuel economy and reducing CO_2 emissions. It also enhances fitment precision and weldability while minimizing risks of microcracking or edge hardening [6]. Nonetheless, laser cutting involves high equipment costs and technical challenges when working with reflective or layered materials. Stable processing conditions, surface cleanliness, and proper fume extraction are essential for maintaining quality and safety [7].

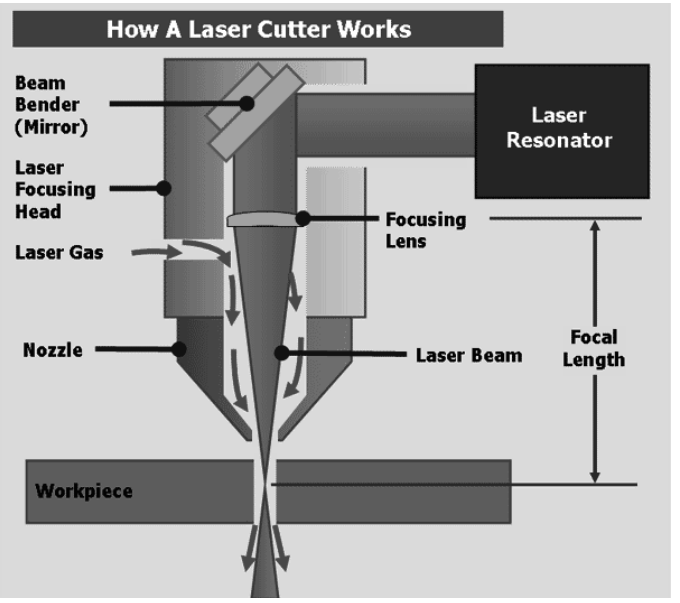

Fig.4. Laser cutting of car body components.

3.2. Surface hardening of engine and powertrain components

Laser surface hardening is a precise thermal treatment method that enables the selective hardening of the surface layer of steel components without altering the mechanical properties of their core. This technology is widely applied in the automotive industry, particularly in engine and powertrain components such as shafts, gears, bushings, and cams [8]. The process involves heating the surface to the austenitization temperature using a laser beam, followed by self-quenching through heat conduction into the cooler interior of the material. As a result, a hard martensitic layer with a thickness ranging from 0.3 to 2 mm is formed, while the core retains its ductility and fracture resistance [9]. The main advantages of this method include a significant increase in wear and fatigue resistance, without the need for a quenching bath and with minimal geometric distortion. The process is fully automated and can be integrated into production lines [10]. However, limitations include high equipment costs, the need for precise parameter calibration, and a restricted hardening depth [11]. Laser surface hardening offers an optimal compromise between durability and fatigue resistance, making it a key tool in the design of durable and lightweight next-generation automotive components.

3.3. Laser marking and component traceability

Laser marking plays a critical role in ensuring component traceability in the modern automotive industry. This technology enables the permanent inscription of serial numbers, DataMatrix codes, or QR codes onto the surfaces of parts using a fiber or UV laser beam. The process is non-contact, and the resulting markings are resistant to abrasion, chemicals, and thermal influences [3]. Laser marking is widely applied to engine components, drivetrain systems, body structures, and electronic parts to ensure comprehensive tracking of their origin and service history. This technology supports quality management systems, logistics, and warranty processes. Due to its high precision and compatibility with production line integration, marking can be performed rapidly without disrupting manufacturing continuity. Among the limitations are the need for proper surface preparation and challenges associated with marking components with irregular geometries [10].

3.4. Laser processing as a method for repair and remanufacturing of components.

Laser-based remanufacturing processes-particularly in the form of laser cladding-represent an advanced method for the repair and reinforcement of worn or damaged steel components. This technology enables the precise deposition of thin metallic alloy layers onto component surfaces using a focused laser beam, which locally melts both the substrate material and the applied powder or wire feedstock. The resulting coating exhibits strong adhesion, high hardness, and excellent wear resistance, while generating a minimal heat-affected zone and inducing virtually no geometric distortion [2]. Laser cladding is employed in the refurbishment of shafts, gears, cam surfaces, and valve seats in high-performance, industrial, and premium-class vehicles, where the cost of replacement parts and stringent quality requirements justify the use of advanced repair technologies (Fig.5). Owing to its capacity for localized processing and preservation of the original core properties, this method significantly extends component lifespan and reduces material waste [11]. However, the technology is not without limitations. Key challenges include the high cost of equipment, the necessity of meticulous surface preparation, and the requirement for precise control over process parameters such as powder feed rate, laser energy input, and scanning path.

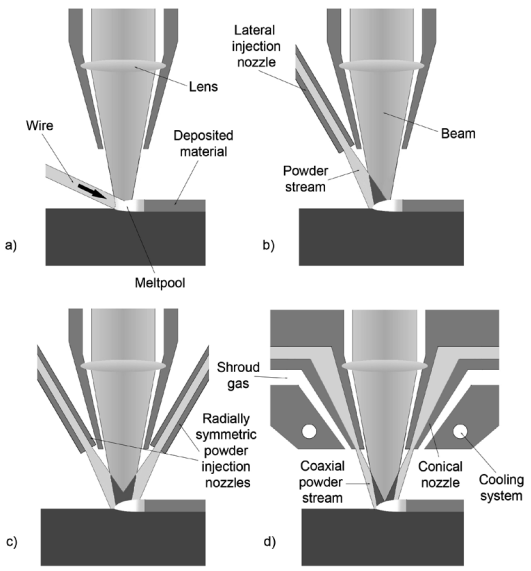

Fig.5. Diagram of the laser cladding process with powder feeding.

3.5. Laser processing of car body components made from advanced lightweight steels.

Modern automotive engineering strives for maximum vehicle weight reduction while maintaining high standards of safety and durability. A key response to these demands is the increasing use of hybrid structures combining advanced high-strength steels with lightweight aluminum alloys. However, such material pairings present significant technological challenges due to the substantial differences in the physicochemical properties of the constituent metals. Laser processing-particularly in the form of welding, brazing, or selective melting-offers a promising solution, enabling precise and controlled joining of complex material combinations [5]. Owing to the localized energy input and the ability to finely control beam parameters, laser technology helps to mitigate the formation of brittle intermetallic phases, hot cracking, and

excessive thermal stresses. In the automotive industry, this approach is employed in the joining of steel-aluminum sheets in door, trunk, roof, and pillar structures, as well as in the hybrid assembly of body panels in electric vehicles. Furthermore, integration with vision and robotic systems enhances both the precision and repeatability of the process [3]. Nevertheless, certain limitations must be addressed, including the need for thorough surface preparation, stringent requirements for the selection of processing parameters and interlayer materials (e.g., buffer layers), and the necessity of rigorous quality control of dissimilar metal joints.

4. ADVANTAGES AND DISADVANTAGES OF LASER TECHNOLOGY

4.1. Advantages

Laser-based manufacturing technologies offer several key benefits that make them especially attractive in the automotive industry. These advantages arise from the unique physical characteristics of laser beams and the level of process control they allow [1], [5]:

• **High precision and repeatability** - Laser beams can be focused to micrometer-scale diameters, enabling highly accurate material processing with minimal deviation.

• **Non-contact processing** - No mechanical force is applied to the workpiece, minimizing tool wear and mechanical distortion.

• **Reduced heat-affected zone (HAZ)** - Concentrated energy input limits thermal influence on surrounding material, which is critical for processing high-strength steels [6].

• **Versatility** - A single laser source can be used for cutting, welding, hardening, marking, or surface structuring.

• **Automation and integration** - Laser systems are easily integrated into robotic and CNC platforms, making them well-suited for automated, high-volume production lines.

• **Material and energy efficiency** - Precise energy delivery reduces waste and supports environmentally friendly production practices.

• **Improved component performance** - Laser surface treatments (e.g., hardening, texturing) enhance wear resistance, fatigue life, and joining quality [8], [10].

4.2. Disadvantages

Despite their many strengths, laser technologies also present specific challenges and limitations that must be considered during design and implementation [1], [9], [11]:

• **High initial investment** - Laser systems, especially high-power or specialized units, require significant capital expenditure and long-term return calculations.

• **Material limitations** - Certain reflective materials, like copper or aluminum, are more difficult to process with conventional laser wavelengths and require specific adjustments [7].

• **Complexity of process control** - Laser parameters must be finely tuned to material properties, which demands expertise and precise calibration to avoid defects such as cracking or incomplete fusion.

• **Maintenance and safety** - Optical systems and laser sources require periodic maintenance. Additionally, high-power lasers necessitate strict safety protocols to prevent accidents.

• **Limited penetration depth in surface treatments** - In processes like surface hardening, the achievable hardening depth is typically shallower compared to traditional thermal methods [8].

• **Dependency on surface conditions** - Laser performance can be influenced by surface cleanliness, coating presence, or oxidation, requiring careful preparation.

5. FUTURE

5.1. Integration with industry 4.0

The advent of Industry 4.0 has catalyzed a paradigm shift in manufacturing, characterized by the integration of cyber-physical systems, real-time data analytics, and advanced automation. In this context, laser technologies have evolved beyond standalone tools to become integral components of intelligent manufacturing systems, particularly in the automotive sector.

Smart Laser Systems and Real-Time Monitoring

Modern laser systems are increasingly equipped with advanced sensors and real-time monitoring capabilities. These enhancements enable immediate feedback and adjustments during processing, ensuring optimal performance and quality. For instance, the incorporation of multisensor fusion techniques allows for comprehensive monitoring of laser-material interactions, facilitating in-situ quality control and defect correction in processes like laser-directed energy deposition [12].

Predictive Maintenance and Operational Efficiency

The integration of Internet of Things (IoT) technologies with laser systems facilitates predictive maintenance strategies. By continuously monitoring equipment health and performance metrics, manufacturers can anticipate maintenance needs before failures occur, thereby minimizing downtime and extending equipment lifespan [13].

Digital Twins and Simulation

The concept of digital twins-virtual replicas of physical systems-is gaining traction in laser-based manufacturing. These digital models allow for simulation and optimization of processes before actual implementation, reducing trial-and-error in production and accelerating time-to-market. In laser additive manufacturing, digital twins have been employed to predict melt pool behavior and optimize process parameters in real time [14].

Integration with Artificial Intelligence

Artificial intelligence (AI) and machine learning algorithms are being integrated with laser systems to enhance adaptability and decision-making. These technologies enable laser systems to learn from data, predict outcomes, and adjust parameters autonomously, thereby improving process reliability and product quality [15].

In summary, the integration of laser technologies with Industry 4.0 principles is transforming automotive manufacturing. By enabling smarter, more responsive, and efficient production processes, this synergy is setting new standards for quality and innovation in the industry.

5.2. Advanced laser types

Recent advancements in laser technologies have introduced innovative systems that significantly improve the precision, flexibility, and efficiency of automotive manufacturing processes. These next-generation lasers are particularly valuable in addressing the industry's increasing demand for lightweight structures, multi-material assemblies, and high-speed production.

Adjustable Ring Mode (ARM) Fiber Lasers

ARM fiber lasers enable dynamic control over beam profile distribution, enhancing weld quality in dissimilar and high-strength steels used in automotive body structures. This flexibility allows manufacturers to reduce spatter, improve penetration, and achieve higher reproducibility in difficult welding scenarios [16].

Laser-Hybrid Welding

By combining the deep penetration of laser welding with the filler capabilities of arc welding, laser-hybrid welding provides faster welding speeds and greater weld stability. It is widely implemented in the production of car bodies, door frames, and underbody components where structural integrity and cost-efficiency are critical [16].

Ultrafast Lasers

Ultrafast lasers, operating in the picosecond and femtosecond regimes, allow for high-precision micromachining with negligible thermal effects. In automotive applications, they are used for micro-drilling of fuel injector nozzles and surface texturing of sealing surfaces, where minimal distortion is essential [17].

Laser-Based Additive Manufacturing

Laser additive manufacturing, particularly Laser Rapid Manufacturing (LRM), enables the production of complex metal components directly from CAD data. This technology supports lightweight design and customization in automotive prototyping and small-batch production while reducing material waste [18].

Laser Direct Structuring (LDS)

LDS enables the integration of conductive paths onto three-dimensional plastic parts by selectively activating surface areas with a laser. This technique is used in the production of compact electronic modules in vehicles, including control panels and sensor housings, contributing to design flexibility and space efficiency [18].

These advanced laser types are driving innovation in automotive production by enabling smarter materials processing, higher product quality, and greater adaptability to evolving design and performance requirements.

5.3. Applications in electric vehicles and lightweight design

The rapid growth of the electric vehicle (EV) market and the increasing emphasis on lightweight vehicle construction have accelerated the adoption of advanced laser technologies. These processes support the automotive industry's strategic goals of reducing emissions, increasing energy efficiency, and improving structural performance.

Battery Module Fabrication

Laser welding plays a key role in the assembly of EV battery modules and packs, particularly in joining copper and aluminum components such as busbars, terminals, and cooling plates. Due to their ability to deliver precise energy input with minimal heat-affected zones, fiber and ultrafast lasers ensure reliable, repeatable welds that maintain the electrical and thermal performance of battery systems [19]. New beam-shaping techniques and wavelength-tuned lasers (e.g. green lasers for copper) further enhance process stability in these highly reflective materials.

Lightweight Body Structures

Weight reduction remains a critical objective in EV design to maximize range and efficiency. Laser welding and cutting are extensively applied to process high-strength steels and lightweight materials such as aluminum and magnesium alloys. Hybrid structures

combining different metals can be joined effectively using laser-based solutions, contributing to body-in-white mass reduction without compromising crash safety [16], [18].

Structural Bonding and Surface Preparation

Lasers are also used to texture or clean surfaces prior to adhesive bonding. In EV manufacturing, this is particularly useful in preparing surfaces for battery enclosures, sealing elements, and structural adhesives, ensuring high bond strength and long-term durability [20].

Thermal Management Components

Efficient thermal management is essential in EVs, especially for battery systems and power electronics. Lasers enable microchannel creation and precision welding of thin-sheet heat exchangers, improving cooling system performance while maintaining low component mass [19].

The integration of laser technologies in EV manufacturing enhances product quality, enables compact designs, and supports the development of modular, scalable vehicle architectures. As electrification advances, the demand for highly specialized, flexible, and efficient laser processing solutions is expected to grow significantly.

5.4. Sustainability and green manufacturing

Laser technologies have become increasingly important in the pursuit of sustainable manufacturing in the automotive industry. Their efficiency, precision, and versatility support eco-friendly practices in areas such as energy use, material efficiency, process emissions, and waste reduction.

Energy Efficiency and Emission Reduction

Laser systems, particularly modern fiber lasers, demonstrate high electrical-to-optical conversion rates. Their precise, localized heating leads to minimal energy loss and lower emissions compared to conventional thermal processing techniques [1], [9]. In mass production, this translates into significant reductions in overall energy consumption and carbon footprint.

Material Efficiency and Process Waste Minimization

Laser cutting and welding offer high accuracy and minimal heat-affected zones, enabling the reduction of excess material, scrap, and secondary machining steps. These benefits improve material utilization and reduce industrial waste [6], [9].

Support for Lightweight Construction

The ability of lasers to join dissimilar materials and process advanced high-strength steels is essential in lightweight vehicle design, which remains a core strategy for reducing fuel consumption and CO_2 emissions across the vehicle lifecycle [6], [8].

Reduction of Hazardous Chemicals

Laser cleaning replaces abrasive or chemical-based surface preparation with a clean, dry, and non-contact alternative, minimizing the use of solvents and associated environmental hazards [9].

Alignment with Smart and Green Manufacturing

As highlighted in recent reviews of laser integration into Industry 4.0 environments, smart laser systems not only increase productivity but also allow real-time process monitoring and optimization for energy and material savings, supporting broader green manufacturing goals [19].

In summary, laser technologies offer a sustainable path forward for automotive production by supporting energy-efficient, material-saving, and cleaner manufacturing methods.

5.5. Challenges and outlook

Despite the significant progress in laser-based technologies for automotive manufacturing, several challenges remain that may affect their broader adoption and long-term impact. These include economic, technical, and organizational aspects that must be addressed to fully realize the potential of laser systems in next-generation production environments.

Economic and Investment Barriers

High initial costs of advanced laser systems - particularly for high-power or ultrafast variants - remain a barrier to adoption, especially for small and medium-sized manufacturers. Although operating costs are lower due to efficiency and reduced tool wear, the return on investment depends heavily on production scale and utilization rate [1], [19].

Integration Complexity and Knowledge Gap

The effective deployment of laser technologies within Industry 4.0 frameworks requires expertise in optics, robotics, process control, and data analysis. Many production environments face a knowledge gap when it comes to integrating these systems with digital twins, predictive maintenance platforms, or real-time quality control. Bridging this skills deficit will be crucial for future competitiveness [12], [15].

Material and Process Limitations

While lasers offer precise and versatile processing capabilities, certain materials - such as copper or highly reflective alloys - remain challenging to process efficiently with conventional wavelengths. Moreover, some applications still suffer from limited penetration depth, sensitivity to surface conditions, or difficulties with real-time process control in high-speed production [6], [9].

Standardization and Safety

With the growing use of laser technologies comes the need for standardized safety protocols and process certification, especially when lasers are used in human-robot collaborative environments. Enhanced training, certification schemes, and compliance frameworks will be critical to ensure workplace safety and process reliability [1].

Future Outlook

Ongoing advancements in beam shaping, wavelength modulation, AI-assisted control systems, and hybrid processes are expected to further expand the capabilities of industrial lasers. Their role in enabling smart, efficient, and environmentally responsible manufacturing will continue to grow, particularly in light of the automotive industry's shift toward electrification, modularity, and sustainability [19].

In conclusion, while laser technologies are already transforming automotive manufacturing, addressing current limitations through interdisciplinary innovation and workforce development will be key to unlocking their full industrial potential in the decades ahead.

6. CONCLUSIONS

Laser technologies have firmly established themselves as a fundamental tool in modern automotive manufacturing. Their precision, efficiency, and adaptability enable a wide range of processes - from cutting and welding to surface treatment and additive manufacturing - supporting both high-performance requirements and sustainable production goals.

The integration of laser systems into smart, digitally connected environments reflects their compatibility with Industry 4.0 principles. In parallel, their role in lightweight design, electric vehicle production, and green manufacturing aligns with broader shifts in the industry.
While economic and technical challenges remain - including investment costs, material constraints, and workforce training - ongoing innovations in beam control, monitoring, and automation continue to expand the potential of laser processing.
Looking forward, lasers are expected not only to enhance existing manufacturing practices but to drive transformative change across the automotive sector, playing a key role in the transition to more intelligent, sustainable, and modular vehicle production.

ACKNOWLEDGEMENTS

This work was created as part of the project implemented within the framework of project-orientated education, the PBL project implemented with secondary school students, in the V competition under the Excellence Initiative - Research University programme, at the Silesian University of Technology and as part of project of Students Scientific Circle of Laser Surface Treatment under the Initiative of Excellence - Research University, Silesian University of Technology, Gliwice, Poland.

BIBLIOGRAPHY

[1] Steen, W.M., & Mazumder, J. (2010). Laser Material Processing (4th ed.). Springer.
[2] Bonek, M., & Dobrzanski, L.A. (2010). Characterization Performance of Laser Melted Commercial Tool Steels. Archives of Materials Science and Engineering, 43(2), 69-76.
[3] Bonek, M., Lisiecki, A. (2014). Analysis of Laser Welding of Car Body Elements Using Diode Lasers. Archives of Foundry Engineering, 14(2), 15-20.
[4] Disk lasers for automotive applications. (2012). *Laser Focus World*. Retrieved from https://www.laserfocusworld.com/industrial-laser-solutions/article/14216445/disk-lasers-for-automotive-applications
[5] Lathabai, S. (Ed.). (2020). Laser-Based Manufacturing. Elsevier.
[6] Tomków, J., Fydrych, D., Rogalski, G. (2020). Application of Fiber Lasers for Cutting Advanced High-Strength Steels. Archives of Metallurgy and Materials, 65(2), 525-530.
[7] Weber, R., Graf, T. (2013). Industrial laser cutting of high-strength steels - Process challenges and solutions. Physics Procedia, 41, 526-531.
[8] Duflou, J. R., et al. (2010). Laser hardening of steels. CIRP Annals, 59(2), 593-617.
[9] Kaplan, A. F. H. (2016). Laser heat treatment: Fundamentals and applications. Journal of Laser Applications, 28(2), 022202.
[10] Yilbas, B. S., et al. (2012). Laser treatment of engine components. Surface and Coatings Technology, 206(8-9), 2433-2441.
[11] Seeliger, H. W., Wolf, M. (2018). Advances in laser surface hardening. Journal of Materials Processing Technology, 259, 202-208.
[12] Chen, L., Yao, X., Liu, K., Tan, C., & Moon, S. K. (2023). Multisensor fusion-based digital twin in additive manufacturing for in-situ quality monitoring and defect correction. *arXiv preprint arXiv:2304.05685*. https://arxiv.org/abs/2304.05685

[13] Permanova Lasersystem. (n.d.). Connected laser processes for efficient production in Industry 4.0. Retrieved from https://www.permanova.se/en/connected-laser-processes-for-efficient-production-in-industry-4-0/
[14] Liu, N., Li, X., Rajanna, M. R., Reutzel, E. W., Sawyer, B., Rao, P., ... & Yu, Y. (2024). Deep neural operator enabled digital twin modeling for additive manufacturing. *arXiv preprint arXiv:2405.09572*. https://arxiv.org/abs/2405.09572
[15] Karkaria, V., Goeckner, A., Zha, R., Chen, J., Zhang, J., Zhu, Q., ... & Chen, W. (2024). Towards a digital twin framework in additive manufacturing: Machine learning and Bayesian optimization for time series process optimization. *arXiv preprint arXiv:2402.17718*. https://arxiv.org/abs/2402.17718
[16] Coherent. (2022). Advanced Fiber Lasers Improve Automotive Welding. Retrieved from https://www.coherent.com/news/blog/advanced-fiber-lasers-improve-automotive-car-welding
[17] Wikipedia contributors. (2024). Ultrafast laser. In *Wikipedia, The Free Encyclopedia*. Retrieved from https://en.wikipedia.org/wiki/Ultrafast_laser
[18] Wikipedia contributors. (2024). Laser rapid manufacturing. In *Wikipedia, The Free Encyclopedia*. Retrieved from https://en.wikipedia.org/wiki/Laser_rapid_manufacturing
[19] Reisch, C., & Müller, J. (2020). Laser-based manufacturing in the age of Industry 4.0. *Procedia CIRP*, 93, 234-239. https://doi.org/10.1016/j.procir.2020.04.019
[20] Rofin-Sinar. (2019). Laser Applications for Electric Vehicle Manufacturing. Retrieved from https://www.rofin.com/fileadmin/user_upload/documents/whitepapers/laser-ev-manufacturing.pdf
[21] Wikimedia Commons. (2021). Schematic diagram of high power fiber laser using a double-clad fiber. Retrieved from https://commons.wikimedia.org/wiki/File:Schematic_diagram_of_high_power_fiber_laser_using_a_double-clad_fiber.png
[22] Wikimedia Commons. (2008). Red diode laser modules. Retrieved from https://commons.wikimedia.org/wiki/File:Red_diode_laser_modules.jpg
[23] Wikimedia Commons. (2015). Schematic illustration of a possible configuration of a LFZ setup . Retrieved from https://commons.wikimedia.org/wiki/File:LFZ.svg
[24] Wikimedia Commons. (2016). how Laser Cutting Works Retrieved from https://commons.wikimedia.org/wiki/File:Infographic-how-laser-cutting-works.gif
[25] Wikimedia Commons. (2008). Laser Cladding nozzle configurations. Retrieved from https://commons.wikimedia.org/wiki/File:Laser_Cladding_nozzle_configurations.jpg

TalentDetector
23th-25th June 2025
Gliwice-Brenna, Poland
DEPARTMENT OF ENGINEERING MATERIALS AND BIOMATERIALS
FACULTY OF MECHANICAL ENGINEERING
SILESIAN UNIVERSITY OF TECHNOLOGY
INTERNATIONAL STUDENTS SCIENTIFIC CONFERENCE

Secondary use of powder materials in additive manufacturing technologies

Dominik Krisak[a], Lenka Zavodna[a], Jiří Hajnys[a], Martyna Urbańska[b], Kinga Stępska[b], Jan Wypiór[b], Olaf Pradelok[b], Krzysztof Olszak[b], Vojtěch Macejko[b], Eliška Posmyková[b], Mariusz Król[c], Agnieszka J. Nowak[d]

[a] Department of Machining Assembly and Engineering Metrology, Faculty of Mechanical Engineering, VSB – Technical University Ostrava, Ostrava, Czech Republic.
email: dominik.krisak@vsb.cz
[b] Politechnika Śląska, Wydział Mechaniczny Technologiczny, Inżynieria Produkcji i Zarządzania,
[c] Politechnika Śląska, Wydział Mechaniczny Technologiczny, Katedra Materiałów Inżynierskich i Biomedycznych, e-mail: mariusz.krol@polsl.pl
[d] Politechnika Śląska, Wydział Mechaniczny Technologiczny, Laboratorium Naukowo-Dydaktyczne Nanotechnologii i Technologii Materiałowych

Abstract: This study investigates the potential for reprocessing waste PA12 powder from selective laser sintering (SLS) technology. The theoretical part focuses on material degradation mechanisms, analytical methods for evaluating polymer properties, and a review of current approaches to PA12 recycling. As a promising solution for material reuse, filament extrusion for FDM/FFF technology is proposed. In the experimental part, the feasibility of producing filament from recycled PA12 using a low-cost extruder was verified, followed by an assessment of the printability and mechanical properties of the printed parts.

Keywords: Powder, PA12, SLS, FDM, Recycling

1. INTRODUCTION

Additive Manufacturing (AM), or 3D printing, has become a cornerstone of modern production due to its ability to create complex geometries directly from digital models without the need for traditional tooling. Among AM methods, Selective Laser Sintering (SLS) stands out for its high mechanical performance and design freedom, achieved through the layer-wise sintering of polymer powders—most commonly Polyamide 12 (PA12)—by a laser beam [1,2]. Its growing industrial adoption is driven by the ability to produce functional parts without support structures and with minimal material waste during the printing of the part itself.

Despite these advantages, SLS technology faces a significant sustainability challenge due to the large proportion of unsintered powder that accumulates during each print cycle. Although this material is not directly fused into the final part, it is exposed to elevated temperatures throughout the process. The following section provides a detailed analysis of how this residual

powder degrades over time, including its declining crystallinity, formation of spherulites, and associated effects on flowability and mechanical integrity [2,3].

Given the high cost of SLS-grade powders and increasing environmental concerns, researchers have begun exploring secondary uses for thermally degraded PA12. One promising pathway is the transformation of waste powder into filament for Fused Deposition Modeling (FDM) or Fused Filament Fabrication (FFF)—technologies that are more accessible and less sensitive to minor material variations [4]. This approach represents a potential step toward circular material flows in additive manufacturing ecosystems.

In this context, the presented study evaluates the feasibility of recycling degraded PA12 powder into functional FDM filament. Using a low-cost single-screw laboratory extruder, the material was processed and subsequently used to fabricate 3D printed test specimens. These were analyzed to assess both mechanical performance and print quality, forming the basis for practical recommendations on waste reuse.

2. WASTE POWDER

One of the most commonly used materials in Selective Laser Sintering (SLS) technology is polyamide 12 (PA12)-based powder. However, during a single printing cycle, only 5–15% of the material is actually used for printing, while the remaining 85–95% remains unused. Although this unused powder can theoretically be reused, repeated exposure to high temperatures leads to its gradual degradation.

To ensure dimensional stability during the printing process, the surrounding powder must be preheated to a temperature close to its melting point, which induces physical and chemical changes. This includes a reduction in crystallinity (by up to 6% after three recycling cycles) and the growth of spherulites—crystalline structures formed by entangled molecular chains. This development increases the molecular weight of the powder, reduces its flowability, and deteriorates its mechanical and thermal properties [3, 5].

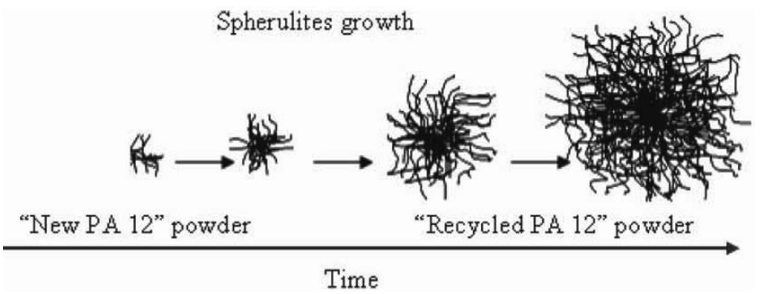

Figure 1. Growth of spherulites in fresh and recycled PA12 powder over time [3]

As a result of these changes, the reusability of unsintered powder is limited. The powder must be regularly replenished with fresh material; otherwise, the quality of the prints may deteriorate. Failure to maintain the optimal mixing ratio can lead to visual defects such as orange peel— a rough, uneven surface caused by irregular shrinkage. Severely degraded powder should be completely discarded.

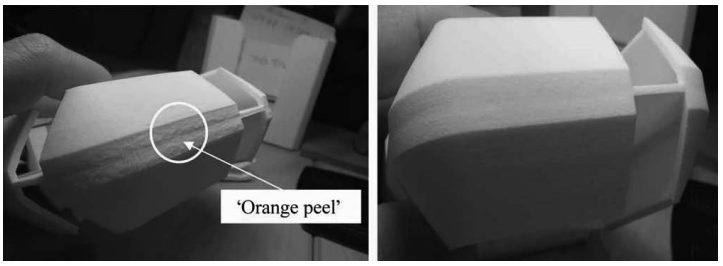

Figure 2. Orange peel on the surface of a defective printed part (left) compared to a quality part (right) [3]

3. EXPERIMENT

3.1 Starting Material – Polyamide 12 (PA12)

For filament extrusion, waste polyamide powder EOS PA 2200 (PA12) was used, obtained during the unpacking of parts after printing using SLS technology. This material is typically removed from the surface of printed parts in the unpacking chamber and collected via an overflow pipe into containers for disposal or further processing.

Based on findings from the literature review, the input material was not dried prior to extrusion, as in this specific case, drying had no significant effect on the quality of the resulting filament.

3.2 Measuring MFR of waste powder

To assess the usability of waste PA12 powder for filament production, it was necessary to evaluate its suitability for the extrusion process, specifically through melt flow rate (MFR) measurement. In cooperation with Fillamentum Manufacturing Czech s.r.o., MFR testing was carried out on pure waste PA2200 powder, a 50/50 blend with virgin material, and pure virgin powder.

The testing was conducted according to the ČSN EN ISO 1133-1 standard at a temperature of 190 °C and a load of 2.16 kg. The results are presented in Table 1.

Table 1. Results of MFR measures of PA2200 powder

PA 2200	MFR ISO 1133 D 190 °C / 2,16 kg
New	14 g/10 min
50/50	7,6 g/10 min
Waste	0,35 g/10 min

A comparison with the literature shows that the MFR of recycled PA12 varies significantly depending on the number of prior uses in the SLS process. For example, Feng [5] reports a value of 6.99 g/10 min, while Pham [3] measured 13.5 g/10 min for powder used three times. These differences confirm that the properties of waste powder are not consistent, and therefore it is advisable to measure the MFR individually for each batch intended for extrusion.

For comparison, the typical input PA12 material used for filament production by Fillamentum has an MFR value of 4.0 g/10 min, whereas the tested waste powder showed a value of 0.35 g/10 min, indicating lower flowability, yet still sufficient for the extrusion process.

3.3 Preparation of Granulate

Due to its poor flow properties, the fine waste powder was not most suitable for direct extrusion. Therefore, in cooperation with the Slovak University of Technology in Bratislava, it was processed into granulate form. Two particle size fractions were prepared with d_{50} = 1 mm and d_{50} = 1.8 mm, and the particle size distribution was analyzed for both. Then for reference, particle size distribution of powder was added as seen in Figure 3.

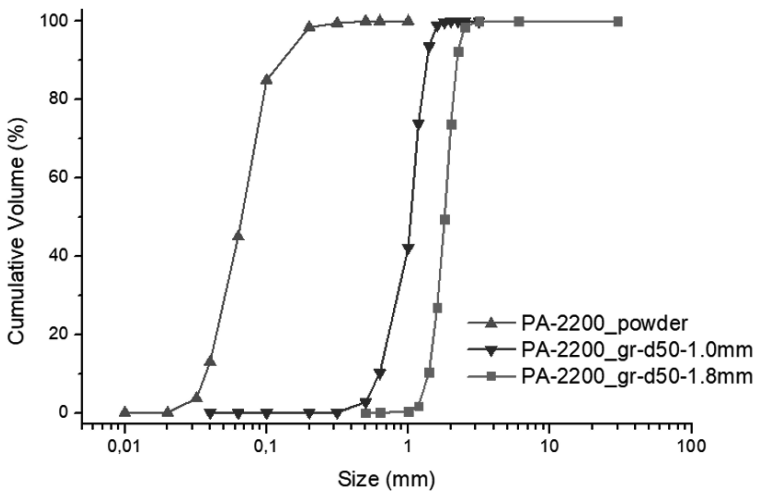

Figure 3. Particle distribution of granulates and powder

The decision to convert the material into granulate form was based on findings from the literature review, with the aim of improving its processability during filament extrusion. The results were subsequently compared with the extrusion performance of the untreated powder.

3.4 Used Extruder

For filament extrusion, a single-screw prototype extruder with flood feeding was used, designed based on a DIY concept. The objective was to verify the feasibility of assembling a compact and low-cost device suitable for experiments with various materials.

The design emphasized the use of FDM 3D printing for manufacturing structural components and the use of readily available parts instead of specialized and expensive components typically intended for industrial-scale extrusion. The device was developed within the Protolab 3D Printing Center, and its design is shown in Figure 4.

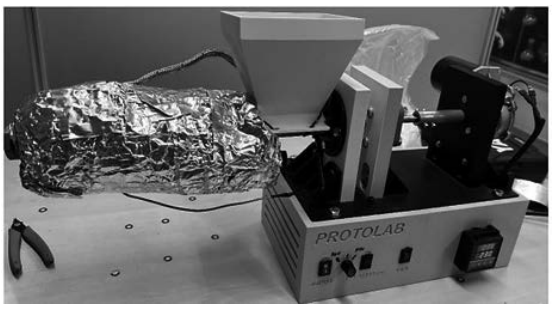

Figure 4. Extruder prototype used for Extrusion

4. EXTRUSION PROCESS

Filament extrusion began with preheating the extruder to 230 °C to melt any residual material and prevent damage to the equipment when starting the screw. After cleaning, a small amount of fresh material was fed in, and the temperature was adjusted according to the type of input material.

Initial tests with waste PA 2200 powder were conducted at temperatures ranging from 230 to 260 °C and confirmed both the continuous material flow and the functionality of the device. However, the extruder soon showed a tendency to overfill, as larger quantities of powder caused the screw to stall due to insufficient motor torque and the presence of only a single heating zone.

In such cases, it was necessary to manually remove some of the material and push the molten plastic through by hand. Based on these findings, all subsequent experiments were carried out using small, controlled doses of input material, which ensured a stable extrusion process.

4.1 Extrusion test with Ø1,75 mm nozzle

After the device's run-in, extrusion tests were conducted using untreated waste PA 2200 powder and two granulate types. Multiple rounds were needed due to electric motor overheating, which reduced performance (Table 2).

In the first run, melt built up between the screw end and nozzle. Introducing new material pushed out the overheated melt, which flowed rapidly and failed to form a solid filament (Figure 5).

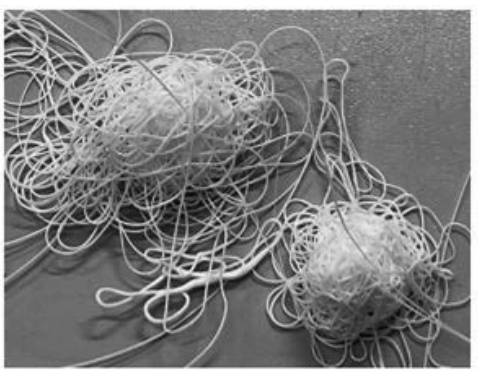

Figure 5. Overheated material

Table 2. Extrusion test results with Ø1,75 mm nozzle

Extrusion – PA 2200 Powder - Ø1,75 mm				
Run	Temperature [°C]	Dose of material [g]	Motor power [%]	Result
1	215	15	25	X
2	215	30	25	OK
3	215	30	50	X
4	207	30	25	X
5	207	15	50	OK
Extrusion – Granulate 1 - Ø1,75 mm				
1	207	30	50	X
2	207	30	25	X
3	215	30	25	OK
Extrusion – Granulate 2 - Ø1,75 mm				
1	215	30	25	X
2	220	15	50	OK

A similar issue occurred during the third run. This time combined with an excessively high extrusion speed. In the fourth run, the extruder became clogged due to incorrect material dosing.

When switching from powder to granulate, the equipment had to be purged of sintered residues, which also resulted in colour changes in the extruded output (see Figure 6). The first two tests with Granulate 1 were unsuccessful—the first due to rapid material outflow, and the second again due to clogging.

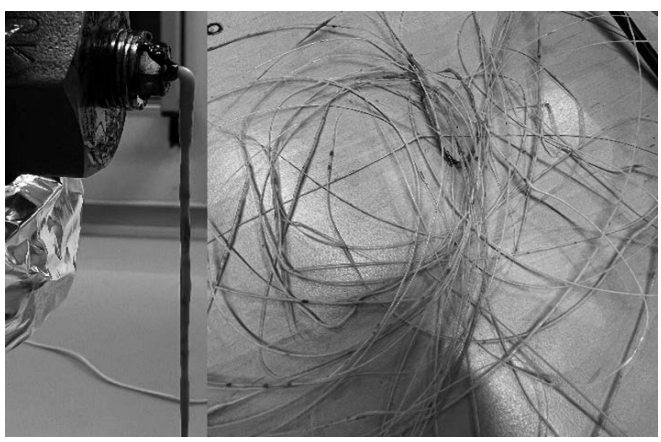

Figure 6. Filament extruded in cleaning process

The initial extrusion attempt with Granulate 2 was unsuccessful—the material did not pass through the nozzle. However, after adjusting the parameters, successful extrusion was achieved. In some runs (see Table 2), only half the standard material dose was used, as a large amount of residual material remained in the chamber after previous clogging.

The successful runs were subsequently subjected to diameter measurements of the extruded filament, with the results presented in the following section.

4.2 Extrusion test with *Ø2 mm nozzle*

During the replacement of the extrusion head cover, residual material was cleaned out while the system was still hot. This also confirmed a design flaw—an excessive gap between the screw and the head opening, which causes turbulence and melt accumulation, contributing to clogging.

The installation of the new cover was straightforward and carried out using standard tools. Due to the high temperature, increased caution was necessary during handling. In the following extrusion, the device had to be tilted, as without the nozzle, material adhered to the inner wall of the cover. Thanks to previous testing, suitable parameters were adjusted more quickly (see Table 3), but even so, issues with overheated melt appeared during the initial runs of all materials.

It proved beneficial to use a stabilizing dose when changing materials.For the powder material, weak flow was observed during the third run, which required an increase in motor power. Successful extrudates were measured, labeled, and documented.

Table 3. Extrusion test results with Ø2 mm nozzle

Extrusion – PA 2200 powder - Ø2 mm				
Run	Temperature [°C]	Dose of material [g]	Motor power [%]	Result
1	215	30	25	X
2	215	30	10	OK
3	207	30	25	X
4	207	30	50	OK
Extrusion – Granulate 1 - Ø2 mm				
1	207	30	25	X
2	215	30	25	OK
Extrusion – Granulate 2 - Ø2 mm				
1	215	30	25	X
2	215	30	50	OK

4.3 Extrusion Results

For diameter measurement of the extruded filaments, a 4-meter segment was taken from each sample and marked at 20 cm intervals. Each measurement thus included 20 individual values, with samples selected from the visually most stable sections of the strand.

Measurements were conducted optically using a Mitutoyo TM-505B microscope equipped with a DeltaPix HDMI16MDPX camera. The results for the Ø1.75 mm nozzle are presented solely in graphical form (see Figure 7).

The measurements show that PA 2200 produced a more stable diameter at 207 °C and 25% motor power. Granulate 2 resulted in a slightly smaller diameter but demonstrated relatively consistent behavior. The highest variation in diameter was recorded for Granulate 1.

A similar measurement was carried out for the Ø2 mm nozzle, with results presented exclusively in graphical form (see Figure 8). The most stable diameter was again achieved at 207 °C and 25% motor power. Comparable results were obtained with Granulate 1 at 215 °C. Although Granulate 2 reached values close to 1.75 mm, it exhibited significant diameter fluctuations even over short segments.

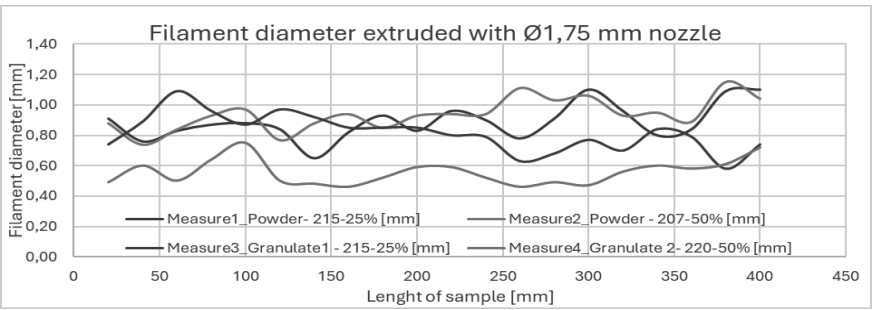

Figure 7. Filament diameter fluctuations with Ø1,75mm nozzle

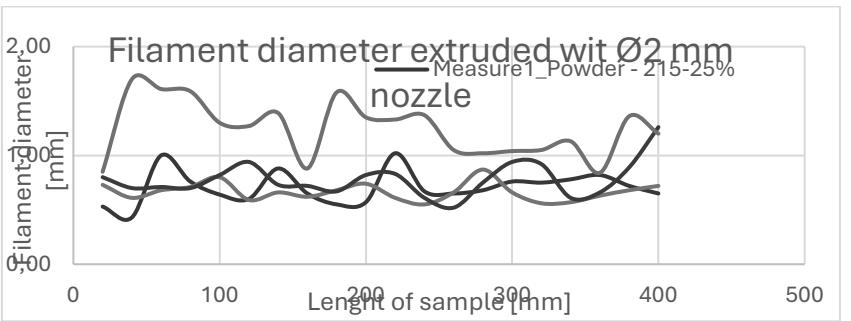

Figure 8. Filament diameter fluctuations with Ø1,75mm nozzle

5. CONCLUSION

This study explored the potential of recycling PA12 waste powder from SLS technology into filament for FDM printing. Theoretical research outlined the challenges of PA12 degradation and reviewed low-cost extrusion methods. A DIY single-screw extruder was built and tested with both raw powder and granulated waste material. MFR measurements confirmed that under specific conditions, recycled PA12 is suitable for extrusion.

Although continuous filament was produced, diameter instability and extrusion issues were observed due to equipment limitations. The most stable results were achieved at 207 °C and 25% motor power, yet the filament still lacked the dimensional precision needed for FDM use. However, its internal structure was like commercial filaments, showing promise for further development.

Overall, the findings confirm that PA12 powder waste can be reused for extrusion, but consistent quality requires more advanced equipment. Still, the study demonstrates the feasibility of low-cost recycling as a basis for future sustainable material research.

ACKNOWLEDGEMENT

The present study was produced as part of the activities of the Student Research Group "GYROID" operating at the Department of Engineering and Biomedical Materials at the Faculty of Mechanical Engineering, Silesian University of Technology in Gliwice.

Publication supported by the Excellence Initiative - Research University program implemented at the Silesian University of Technology, 2025.

BIBLIOGRAPHY

1. Gibson, I.; Rosen, D.; Stucker, B.; Khorasani, M. *Additive Manufacturing Technologies*; Springer International Publishing: Cham, 2021; ISBN 978-3-030-56126-0.
2. Schmid, M. *Laser Sintering with Plastics*; Carl Hanser Verlag GmbH & Co. KG: München, 2018; ISBN 978-1-56990-683-5.
3. Pham, D.T.; Dotchev, K.D.; Yusoff, W.A.Y. Deterioration of Polyamide Powder Properties in the Laser Sintering Process. *Proc Inst Mech Eng C J Mech Eng Sci* 2008, *222*, 2163–2176, doi:10.1243/09544062JMES839.
4. Su, A.; Al'Aref, S.J. History of 3D Printing. In *3D Printing Applications in Cardiovascular Medicine*; Elsevier, 2018; pp. 1–10.
5. Feng, L.; Wang, Y.; Wei, Q. PA12 Powder Recycled from SLS for FDM. *Polymers (Basel)* 2019, *11*, 727, doi:10.3390/polym11040727.

TalentDetector

23th-25th June 2025
Gliwice-Brenna, Poland

DEPARTMENT OF ENGINEERING MATERIALS AND BIOMATERIALS
FACULTY OF MECHANICAL ENGINEERING
SILESIAN UNIVERSITY OF TECHNOLOGY

INTERNATIONAL STUDENTS SCIENTIFIC CONFERENCE

Investigation of the Effect of Busbar Number on Solar Cell Characteristics

Alicja Król[a], Wiktoria Wilczak[a], Jakub Jabłoński[a], Cyprian Chowaniec[a], Kadir Ozdemir[b], Onur Dodak[b], Emir Kaan Ozbay[b], Wojciech Filipowski[a], Cemal Meran[b], Małgorzata Musztyfaga-Staszuk[c]

[a] Silesian University of Technology, Faculty of Automatic Control, Electronics and Computer Science, Akademicka 16 street, 44-100 Gliwice, Poland, email: wojciech.filipowski@polsl.pl
[b] Pamukkale University, Faculty of Engineering, Department of Mechanical Engineering, Kinikli Campus, 20160 Pamukkale, Turkiye, email: cmeran@pau.edu.tr
[c] Silesian University of Technology, Faculty of Mechanical Technology, Materials investigating laboratory, Konarskiego 18A street, 44-100 Gliwice, Poland,
email: malgorzata.musztyfaga@polsl.pl

Abstract: The aim of the electrical and structural analysis of silicon solar cells is to identify the reproducibility of the obtained parameter properties and potential defects in the investigated material. This process enables confirmation of the material's properties or facilitates quick repairs and elimination of issues, thereby contributing to a reduction in financial costs.

Keywords: solar cell, photovoltaic structure, photovoltaics

1. INTRODUCTION

Increasing the share of renewable energy sources in electricity generation is one of the most essential steps toward building a sustainable future. Among renewable energy options, solar power has become increasingly prominent in recent years due to its accessibility and applicability as a clean energy source. The rise in global investments and the proliferation of solar power plants clearly demonstrate the sector's potential for growth. The global share of solar energy in total electricity capacity rose from 0.8% in 2010 to 10.6% in 2021, while its contribution to production increased from 0.2% to 3.7% over the same period [1].

In this context, the rapid advancement and potential of solar energy have driven intensive research and development into various photovoltaic (PV) technologies. The Chinese market, which leads globally, continues to dominate both new and cumulative capacity, having added 106 GW (accounting for 44% of new capacity) and reaching a cumulative capacity of 414.5 GW [2]. The development of high-efficiency technologies plays a critical role in meeting renewable energy targets. These technologies include organic solar cells, amorphous silicon (a-Si), and crystalline silicon (c-Si), which have laid the groundwork for subsequent innovations such as PERC, SHJ, perovskite, and tandem solar cells. At the core of these technologies lies the classification of solar cells by generation and their structural characteristics. First-generation (crystalline silicon), second-generation (thin-film, e.g., a-Si, CdTe, CIS/CIGS),

and third-generation (organic, dye-sensitized, or perovskite-based) solar cells each exhibit distinct differences in manufacturing techniques, efficiency levels, and costs. M. Green et al. (2019) investigated the laboratory efficiencies of these various technologies in their studies [3].

When evaluating different technologies, both efficiency and the balance of system (BOS) must be considered. BOS includes all components except the solar cell, such as wiring and mounting. The BOS penalty represents the extra costs associated with more efficient panels that need more expensive BOS components. Thus, solar technology assessment should consider both cell efficiency and total installed cost [4].

Despite the rise of newer technologies, first-generation silicon-based solar panels remain dominant, making up about 90% of the global PV market in 2023 [5]. Their popularity stems from silicon's high efficiency, durability, and mature manufacturing. Polycrystalline silicon cells are particularly prominent, generating 43.7% of revenue in 2023 [6]. These cells consist of layers including a glass top, antireflection coating, front contact, active p-n junction, and back electrode, each playing a role in sunlight absorption and transport. Conventional single-junction cells with optimal bandgaps have a maximum efficiency of 33.16%, known as the Shockley–Queisser limit [7].

The effective operation of these layers heavily depends on the production processes of silicon-the fundamental material in solar cells. The process starts with melting silicon in an arc furnace using natural quartz (SiO_2) and carbon. The resultant silicon is refined to solar-grade purity (>99.9999%) [8] and undergoes further processing to be used in PV production. Wafers are fabricated and then crystallized using the Czochralski method. After crystallization, the resulting ingots are sliced into thin wafers, which are surface-treated to prepare them for use in solar cell production [9].

The production cost of crystalline silicon solar cells has significantly decreased from 2 USD/Watt in 2010 to around 0.20–0.30 USD/Watt in 2020. Panel costs range from 0.40–0.60 USD/Watt, and when system installation is included, the total cost reaches approximately 1–1.5 USD/Watt. To further reduce these costs, new technologies and materials are continuously being developed and integrated into manufacturing processes [10].

Besides cost, it's crucial to analyze factors affecting solar cell performance. Electrodes collect and conduct current generated by sunlight, with transparent conductive oxides as front electrodes and metallic contacts at the rear. Electrode design must balance transparency and conductivity. Currently, screen printing is the main method for front-side metallization in crystalline silicon cells, with metal fingers about 100 μm wide. Optimizing this process can enhance efficiency and lower production costs [11].

Moreover, understanding the internal resistances within a solar cell is crucial for maximizing its efficiency. A solar cell functions electrically like a diode, and its performance is strongly influenced by series and shunt resistances [12–13]. Series resistance impedes current flow and reduces efficiency when high, while low shunt resistance, indicative of leakage currents, can also degrade performance. According to McIntosh and Honsberg (2000) and McMahon et al. (1996), shunt resistance may result from surface defects or edge leakage paths, both of which negatively impact efficiency and reduce the maximum output power. This leads to a drop in open-circuit voltage and fill factor [14].

Accurate characterization of these electrical parameters is vital to evaluate overall performance. Commonly used electrical tests include current–voltage (I–U) characterization, open-circuit voltage (V_{oc}), short-circuit current (I_{sc}), capacitance–voltage (C–U) profiling, and efficiency calculations. These tests provide essential insights into how solar cells perform under operational conditions, enabling optimization of performance metrics [15]. In addition to electrical analysis, structural evaluation is essential for ensuring high manufacturing quality

and improving efficiency. Techniques such as microscopy, surface profilometry, and fracture analysis are used to examine the structural properties of solar cells. Advanced methods like SEM, TEM, XRD, and AFM are employed to identify structural defects that may occur during fabrication. These analyses allow for quality control and help mitigate negative effects on cell performance [16]. Solar cells that successfully pass these processes are ready for deployment.

The aim of the paper is to perform electrical and structural investigations on silicon solar cells in order to identify the reproducibility of the obtained parameters and any potential defects in the tested material. This allows for confirmation of these properties or for quick repairs and elimination of issues, which contributes to reducing financial costs. The diagnostic tools used pave the way for innovation, as they enable the identification of problems that need to be addressed in the future, for example through the use of new materials.

2. MATERIALS

A typical silicon solar cell, shown on Figure 1, is a photovoltaic device consisting of a single p–n junction embedded within a crystalline silicon substrate.

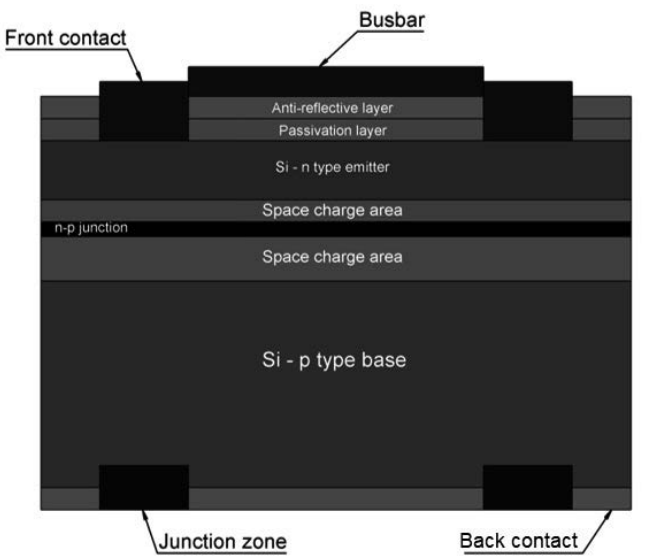

Figure 1. Schematic drawing of a single junction silicon solar cell

Single junction silicon solar cells absorb sunlight to generate electron-hole pairs and produce electricity across one energy bandgap. Their simple design, abundant material, and established manufacturing make them the most common in the market. However, their efficiency is limited to about 33% by the Shockley–Queisser limit. Despite this, improvements in surface passivation, light trapping, and doping have enhanced their practical performance, maintaining their role in renewable energy. The main layers are:

1. **Busbar**: Thick metal strips on the solar cell surface that collect and transfer electric current, reducing resistive losses.
2. **Anti-reflective layer**: Thin coating on the cell's front to reduce sunlight reflection, increasing light absorption and efficiency.
3. **Passivation layer**: Dielectric coating (e.g., Si_3N_4, SiO_2) that reduces surface recombination, enhancing efficiency.

4. **Si - n type emitter**: Doped silicon layer with excess electrons, forming part of the p-n junction for efficient charge flow.
5. **N–p junction**: Interface between n- and p-type silicon, creating an electric field for charge separation.
6. **Space charge area**: Depleted region around the junction with an electric field that drives electron-hole separation.
7. **Si - p type base**: Doped silicon layer with holes, forming the cell's foundation and collecting carriers.

3. MATERIALS USED FOR RESEARCHES

In this article, crystalline silicon solar cells with varying numbers of busbars were investigated. They are shown in Figure 2.

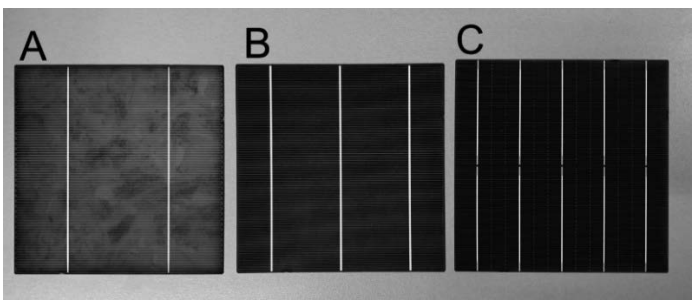

Figure 2. Silicon solar cells with: A) 2 busbars, B) 3 busbars, C) 5 busbars

4. METHODOLOGY

Structural analyses were performed using scanning electron microscopy (SEM). The experiment included surface topography and cross-sectional studies of the front electrode with a silicon substrate. Additionally, the chemical composition of selected fragments of the solar cell was analyzed using energy dispersive X-ray spectroscopy (EDS).

Efficiency and fill factor were determined using a setup with the SS150AAA solar simulator from Photo Emission Tech. The following parameters were measured of solar cells: U_{oc} (open-circuit voltage), I_{sc} (short-circuit current), U_m (voltage at maximum power), I_m (current at maximum power), P_m (maximum power), FF (fill factor), E_{ff} (conversion efficiency).

4. RESULTS

The solar cells shown in Figure 2 were measured using a solar light simulator. The light current-voltage (I–U) characteristics were measured along with key parameters such as U_{oc}, (I_{sc}), (P_m), and others. An example of the I-U characteristic for the solar cell shown in Figure 2B is presented in Figure 3.

Table 1. The characteristic parameters of the measured solar cells

No of busbars	I_{sc} [mA]	U_{oc} [mV]	P_m [mW]	FF [-]	E_{ff} [%]	$R_s@U_{oc}$ [mOhm]
2	7969.0	672.1	3133.2	0.585	15.54	18.3
3	8207.4	668.9	3315.9	0.604	16.09	15.6
5	8076.2	670.9	3665.6	0.677	17.91	10.4

The measured maximum power output of the measured solar cells shows an increasing trend with the number of busbars. This correlates with the progressively higher efficiency coefficients of the cells. However, particular attention should be paid to the series resistance values listed in the last column of Table 1. These values clearly decrease as the number of busbars in the cell increases. Although this relationship may seem intuitive, the easurement results clearly indicate a reduction in the series resistance of the solar cell with an increasing number of busbars. The visualizations of the key parameters of the solar cells are presented in Figure 4.

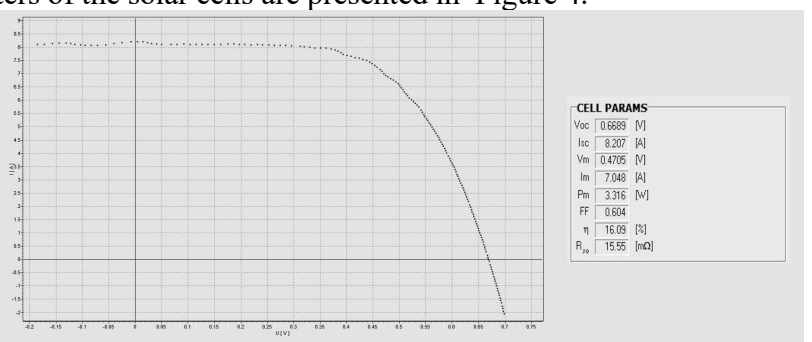

Figure 3. The current-voltage characteristic of the solar cell is shown in Figure 2B

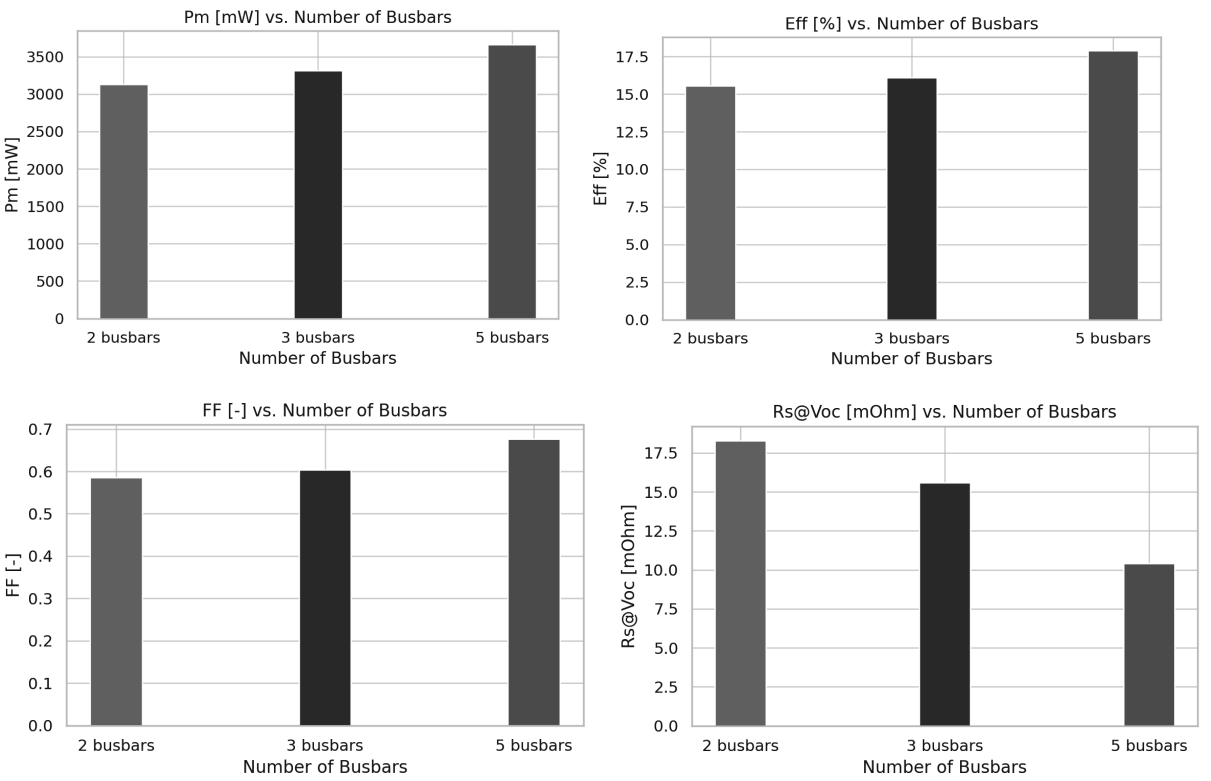

Figure 4. Visualization of the key parameters of the solar cells prepared based on Table 1

Figure 5 presents an example of the surface topography of the silicon of the investigated solar cells. Analyzing the silicon surface in Figures 5a and 5b, it can be concluded that the solar cell most likely underwent a texturing process in an acid solution with an appropriate concentration and volume ratio. It can be assumed that a solvent dedicated to this purpose was applied during the manufacturing process. Based on the further investigations conducted using a scanning electron microscope (Fig. 5c), it was determined that the average height of the pyramids on the textured surface is approximately 2.5 µm for this sample.

Figure 6 shows the topography of the front metallization of the investigated solar cells. Metalographic observations using a scanning electron microscope reveal that the morphology of the front electrode from the commercial silver paste samples exhibits a porous structure.

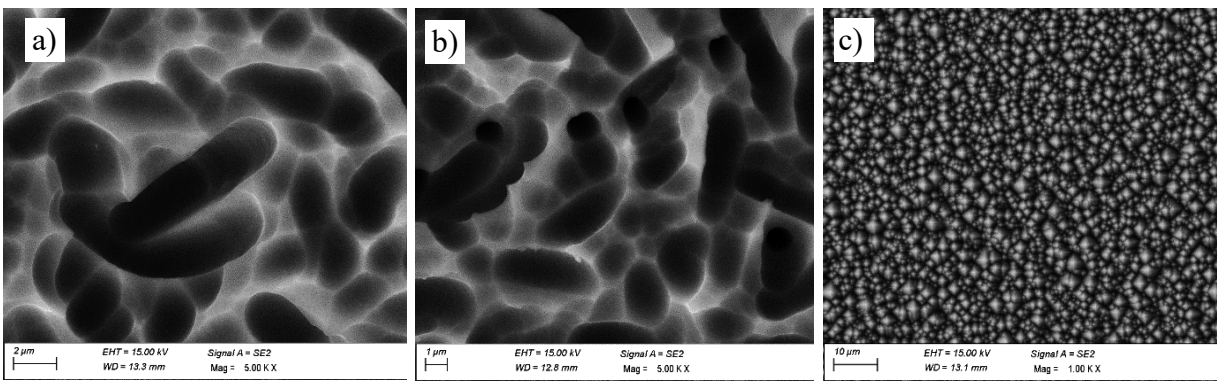

Figure 5. Surface topography of the silicon solar cell with: a) 2 busbars, b) 3 busbars, c) 5 busbars (SEM)

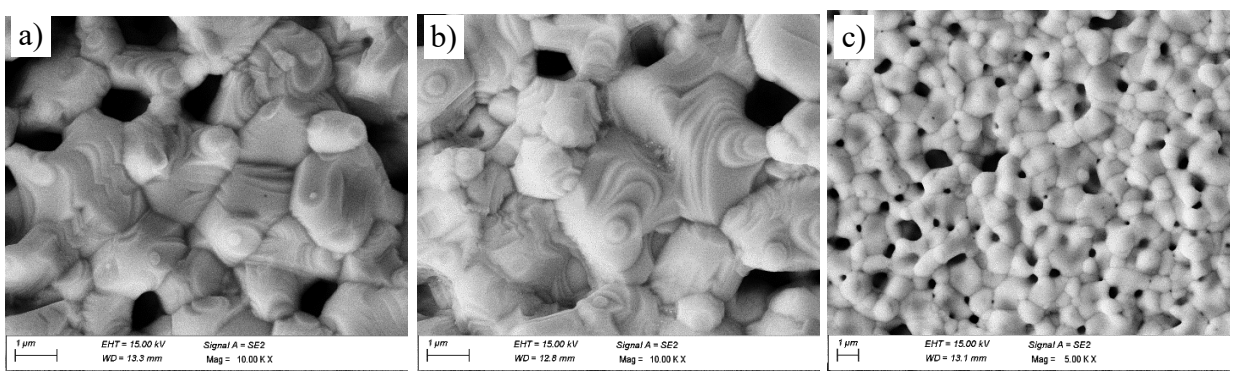

Figure 6. Surface topography of the front side metallization of solar cell with: a) 2 busbars, b) 3 busbars, c) 5 busbars (SEM)

Figure 7 presents the cross-sectional of the front metallization with silicon substrate of solar cells. Based on fractographic studies of all solar cells, it was found that the electrodes made from silver paste form porous and irregular continuous, with the silicon substrate.

In Table 2 and Figure 8, the results of the chemical composition analysis of selected fragments of the solar cell with two busbars are presented, performed using energy-dispersive X-ray spectroscopy.

Table 2. Chemical composition of selected areas within the solar cell (where: x1 – busbar, x2 – collecting finger, x3 – silicon substrate)

The area investigated	Weight fraction of elements , %		
	N	Si	Ag
X1			100
X2	6.8	93.2	
X3		1	99.0

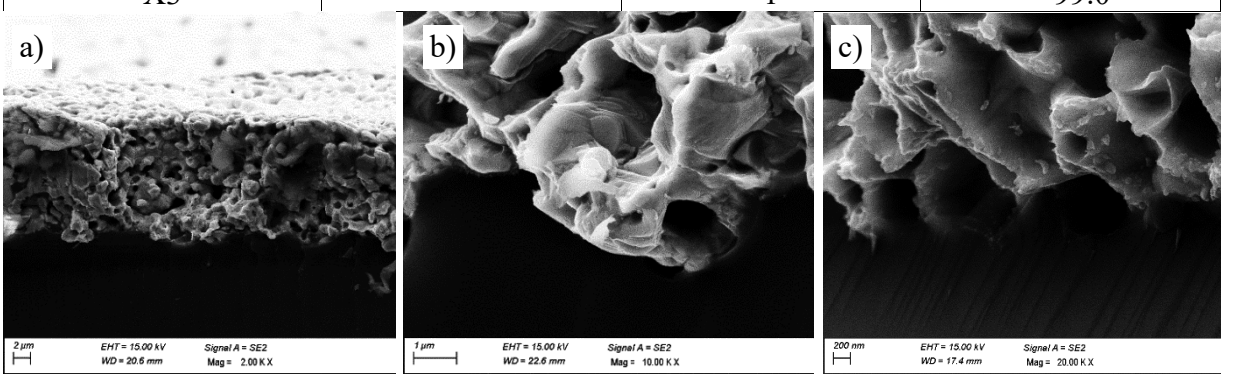

Figure 7. The cross-sectional surface area of the front electrode and the region where it connects with the silicon substrate of solar cells with: a) 2 busbars, b) 3 busbars, c) 5 busbars (SEM)

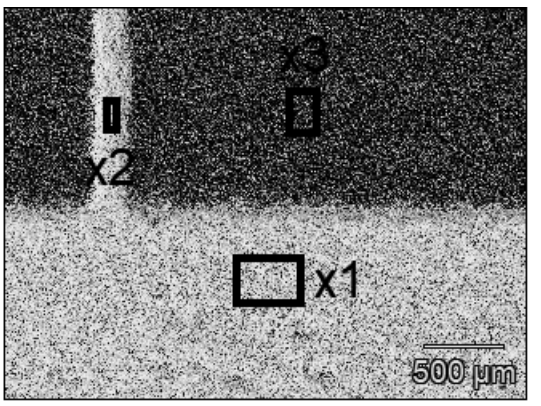

Figure 8. Graph of the dispersed X-ray radiation energy from selected micro-areas of the solar cell (x1 – busbar, x2 – collecting path, x3 – silicon substrate)

Based on the obtained investigation results, it was found that in area x1, silver is the predominant element. In area x2, silver also dominates, but trace amounts of silicon are present. Area x3 mainly consists of silicon with small quantities of nitrogen, which may result from surface passivation that could have been performed in an inert nitrogen (N_2) gas stream.

5. CONCLUSIONS

Based on the obtained research results, it was concluded that:

- increasing the number of busbars reduces the series resistance of the solar cell;
- with a similar cell design manufactured under comparable technological conditions, the reduction in series resistance leads to an increase in: maximum power, efficiency, and the fill factor of the current-voltage characteristic;

- the topography of the front electrode surface of the solar cells is characterized by a porous structure composed of numerous pores;
- the cross-section of the front metallization with the silicon substrate in the solar cells exhibits a porous and irregular structure with continuous cone-shaped connections;
- the chemical composition of the investigated solar cells, determined using the EDS method, confirm the presence of elements suitable for the Si with deposited layers.

ACKNOWLEDGMENT

This work was produced as part of the project implemented within the framework of project-oriented education – PBL, in the XII competition under the Excellence Initiative – Research University program, at the Silesian University of Technology.

BIBLIOGRAPHY

[1] Joshi, P., Rao, A. B., & Banerjee, R. Review of solar PV deployment trends, policy instruments, and growth projections in China, the United States, and India. Renewable and Sustainable Energy Reviews, 213, 115436, 2025.
[2] IEA-PVPS, L. S. (2023). Snapshot of global PV markets 2023. Report IEA-PVPS T1, 44.
[3] Green M., Hishikawa Y., Dulop E., Levi D.H., Hohl-Ebinger J., Yoshita M., Yo-Baillie A., Solar Cell Efficiency Tables (Version 53), Progress in Photovoltaics and Research and Applications, 27(1): 3-12, January 2019.
[4] Blieske, U., Müller-Ost, J., Meisenzahl, K., Grommes, E. M., Gecke, R., Schneble, N. Current and future trends in photovoltaic technology. In 2019 International Energy and Sustainability Conference (IESC) (pp. 1-5) 2019, IEEE.
[5] Cellura, M., Luu, L. Q., Guarino, F., & Longo, S. (2024). A review on life cycle environmental impacts of emerging solar cells. Science of the total environment, 908, 168019.
[6] Solar Cell Market Size, Share & Trends Analysis Report By Technology (Monocrystalline, Polycrystalline, CDTE, A-Si, CIGD), By Application (Residential, Commercial, Utility), By Region, And Segment Forecasts, 2024- 2030, (2022).
[7] Shockley, W., Queisser, H. (2018). Detailed balance limit of efficiency of p–n junction solar cells. In Renewable energy (pp. Vol2_35-Vol2_54). Routledge.
[8] Di Sabatino, M., Hendawi, R., & Garcia, A. S. (2024). Silicon solar cells: trends, manufacturing challenges, and AI perspectives. Crystals, 14(2), 167.
[9] Ranjan, S., Balaji, S., Panella, R. A., & Ydstie, B. E. (n.d.). Silicon solar cell production. Carnegie Mellon University, Department of Chemical Engineering.
[10] Woodhouse, M., Smith, B., Ramdas, A., & Margolis, R. (2020). Crystalline silicon photovoltaic module manufacturing costs and sustainable pricing: 1H 2018 benchmark and cost reduction road map (NREL/TP-6A20-72134). National Renewable Energy Laboratory.
[11] Drabczyk, K., Socha, R., Panek, P., & Mordarski, G. (2014). Electrodeposition of thin metallic layer for solar cell electrodes. Soldering & Surface Mount Technology, 26(1), 18-21.
[12] Dates on stage: https://www.pveducation.org/pvcdrom/solar-cell-operation/series-resistance
[13] Dates on stage: https://www.pveducation.org/pvcdrom/solar-cell-operation/shunt-resistance
[14] Mc Intosh KR, Honsberg CB (2000) The infl uence of edge recombination on a solar cell's I–V curve. Proceedings of 16th PVSEC, pp. 1651–1654.

[15] Electrical Characterization of Photovoltaic Materials and Solar Cells with the 4200A-SCS Parameter Analyzer. (n.d.).Dates on stage: https://www.tek.com/en/documents/application-note/electrical-characterization-photovoltaic-materials-and-solar-cells-4200a-s

[16] Schroder, D. K. Semiconductor Material and Device Characterization (3rded.). Wiley-Interscience, 2006.

TalentDetector
23th-25th June 2025
Gliwice-Brenna, Poland
DEPARTMENT OF ENGINEERING MATERIALS AND BIOMATERIALS
FACULTY OF MECHANICAL ENGINEERING
SILESIAN UNIVERSITY OF TECHNOLOGY
INTERNATIONAL STUDENTS SCIENTIFIC CONFERENCE

Design and production of gradient materials using additive technology – 3D printing

Patryk Krzempek[1], Mateusz Miarecki[1], Radosław Kos[1], Emilia Krzystanek[1], Krzysztof Goczoł[1], Marek Gazda[2], Dominik Krišák[2], Agnieszka J. Nowak[3], Mariusz Król[4]

[1] Student Science Club "HEAD TO HEAD" operating at the Department of Scientific and Didactic Laboratory of Nanotechnology and Material Technologies at the Faculty of Mechanical Engineering, Silesian University of Technology in Gliwice, Poland
[2] Department of Machining Assembly and Engineering Metrology, Faculty of Mechanical Engineering, VSB – Technical University Ostrava, Ostrava, Czech Republic.
[3] Scientific and Didactic Laboratory of Nanotechnology and Material Technologies, Silesian University of Technology, Konarskiego 18A, 44-100, Gliwice, Poland
[4] Department of Engineering Materials and Biomaterials, Faculty of Mechanical Engineering, Silesian University of Technology, 44-100 Gliwice, Konarskiego 18a, Poland

Abstract: The article describes the manufacturing process and the results of strength tests of newly developed gradient materials produced by incremental technology - 3D printing (FFF method). In particular, the focus was on assessing changes in the properties of the developed materials after applying the appropriate decomposition of one component in the other, thus obtaining a gradient of the tested properties. These results were compared with the materials used - reference samples. Models of standardized samples for strength tests considering the material gradient and reference samples were developed. Two thermoplastic materials that differ in elasticity, i.e., PLA CF, TPU, ABS, ASA and PETG CF, were used to produce the gradient material.

Keywords: gradient materials, thermoplastic, 3D printing, FFF method

1. INTRODUCTION

Gradient connections in materials engineering are innovative solutions that involve gradual change of material properties in a specific direction or area. The idea of gradient materials, also known as Functionally Graded Materials (FGM), is that the material's chemical composition and microstructure change smoothly to obtain the desired functional properties [1]. Thanks to this approach, it is possible to optimally adapt the material to specific working conditions, significantly improving its durability and mechanical and thermal resistance. Gradient materials are widely used in the aerospace, automotive, energy and biomedical industries [2]. They are critical where structural elements are subjected to complex, variable loads or aggressive environments. Using gradient connections avoids sharp transitions between different materials, which can lead to stress concentration and earlier damage. In 3D printing, these technologies

become extremely attractive due to the possibility of precise control of the production process parameters. 3D printing, also known as additive technology, is based on layered material deposition according to a digital model [3]. This enables the creation of complex geometries that would be very difficult or impossible to produce using conventional methods. 3D printing technology allows the use of a wide range of materials, including polymers such as PLA, ABS, PETG or nylon [4], as well as metals, ceramics and composite materials. A particularly interesting direction in the development of additive technologies is the printing of gradient materials. Thanks to the possibility of precise dosing of various materials during the production process, it is possible to obtain components with smooth changes in properties, ideally suited to specific application needs. For example, in metal 3D printing technology, gradient transitions between materials with different corrosion resistance, high strength or thermal conductivity are used [5]. This allows the creation of parts with complex functional properties, such as turbine blades, heat exchanger elements or medical implants. The development of gradient technologies in 3D printing is combined with advanced software for computer-aided design (CAD) and topological optimization [6]. Thanks to these tools, it is possible not only to determine the geometric structure of the detail precisely but also to plan the material distribution inside it.
To sum up, gradient connections and 3D printing are key technologies of the future. They offer extremely wide possibilities in the design and production of materials with unique functional properties. The integration of these technologies opens up new perspectives for the industry, allowing the production of elements that combine excellent mechanical, thermal, and chemical parameters while reducing costs and production time [7].

In light of the premises mentioned earlier, the main objective of the study was to obtain a comparative characterisation of gradient materials manufactured by the additive method using the 3D printing technology of the FFF type (Fused Filament Fabrication), taking into account specific design assumptions and parameters of the manufacturing process. This analysis focuses on assessing the influence of selected technological variables on the mechanical properties of the resulting structures, which is an essential step towards optimising the additive process and designing functionally diverse materials.

2. RESEARCH MATERIAL

In this type of research, it is essential to select materials for a specific application consciously. In the analyzed case, the decisive factor was the convergence of operating temperatures of materials with different levels of elasticity. Among the available options regarding technological parameters, the best-matched combination turned out to be PLA-CF and TPU for AMS. The properties of the filaments considered are included in Table 1.

Table. 1. *Data taken into account when selecting materials*

Filament	**Tensile strength; MPa**	**Deformation; %**	**Density; g/cm³**	**Operating temperature; °C**
PLA-CF	38 ± 4	8.4 ± 3.2	1.22	210-240
TPU for AMS	22.4 ± 0.6	＞650	1.26	220 - 240
TPU 95A HF	27.3 ± 0.8	＞650	1.22	220 - 240
ABS	33 ± 3	10.5 ± 1.0	1.05	240 - 270
ABS-GF	36 ± 3	6.3% ± 1.2	1.08	240 - 270
PETG-CF	35 ± 5	10.4 ± 0.6	1.25	240 - 270
ASA	37 ± 3	9.2 ± 1.4	1.05	240 - 270

3. RESEARCH METHODOLOGY

The advanced Autodesk Fusion 360 engineering software was used to develop geometric models, which enable parametric modelling of elements and their preliminary analysis regarding the adopted technological conditions. This program allows for precise mapping of design assumptions and their optimization in the context of the specificity of the additive process, which significantly affects the quality and repeatability of the manufactured structures. The additive manufacturing process of samples using the Bambu Lab X1 Carbon 3D printer with the AMS system, operating in FFF (Fused Filament Fabrication) technology. This device, equipped with two independent extruders and a closed working chamber, ensures the stability of the printing process parameters, which is particularly important in the case of materials requiring a controlled working environment. The technology used enables precise mapping of the designed gradient structures and allows the use of a wide range of thermoplastic materials

3.1. Development of material variants

All models were developed as cubes with dimensions of 10×10×10 mm, which allows for their easy comparison and use in experiments with controlled geometric conditions (Fig. 1).

Model No. 1: The sample is based on the structure of a cube with a spherical core. The outer part of the structure is made of PLA-CF, which provides high resistance to mechanical loads, such as compression, tension and impacts. Inside the cube, there is a spherical core made of TPU for AMS. TPU acts as a shock absorber, effectively absorbing kinetic energy and dissipating forces acting on the structure. Due to its flexibility, the TPU core can absorb energy from impacts or dynamic loads, which can improve the entire sample's resistance to mechanical damage.

Model No. 2: The sample is based on a honeycomb cube design. This design allows for even stress distribution throughout the model, which reduces the risk of local damage or cracks (Fig. 2).

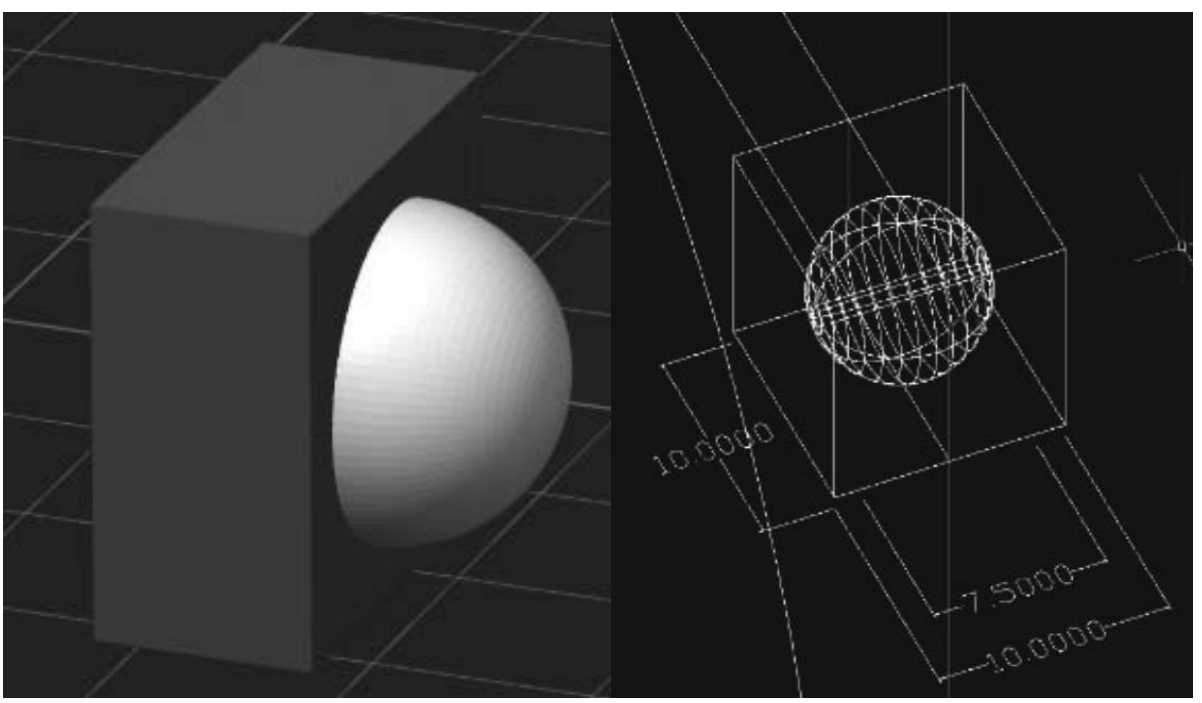

Figure 1. *Designed Model No. 1*

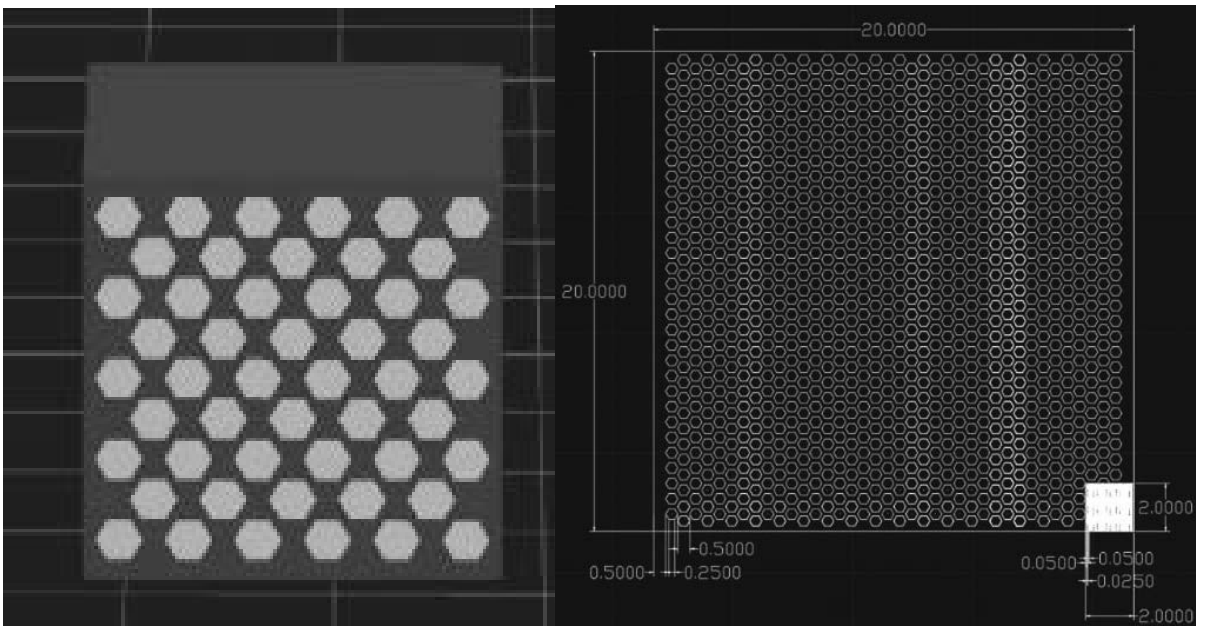

Figure 2. *Designed Model No. 2*

3.2 Sample production

The dimensions of the prepared models are matched to the geometry of the samples used for the static compression test, and they were selected based on the standard | PN-EN-ISO-604 2006 - Plastics | Determination of properties in compression. The process of preparing and manufacturing models was started in connection with the adopted material solutions. This process included preparing a 3D model, preparing a layered model and selecting printing parameters. Figure 3 presents a general scheme of activities carried out within the manufacturing process. The models made in the Fusion 360 program were saved in the STL file format. The first stage of making the hybrid sample models was to design a cube with dimensions of 10x10x10 mm per the indicated standard. The next stage of development is to create separate elements that make up the final hybrid model. This was done by applying mesh planes to the model wall and then manually selecting the mesh grids intended for later cutting out of the solid. The final stage of developing the hybrid 3D model was designing the opposite solid. Combining these two solids gives a whole cube, i.e. the model. 3D models prepared in this way are already suitable for importing to a program such as Slicer: Bambu Studio (Fig. 4). In the indicated software environment, the manufacturing process was calibrated so that hybrid models could be manufactured in an acceptable/correct manner. The changes introduced in the program are listed in Table 2.

Figure 3. *A diagram showing the sequence of activities performed in the 3D printing process*

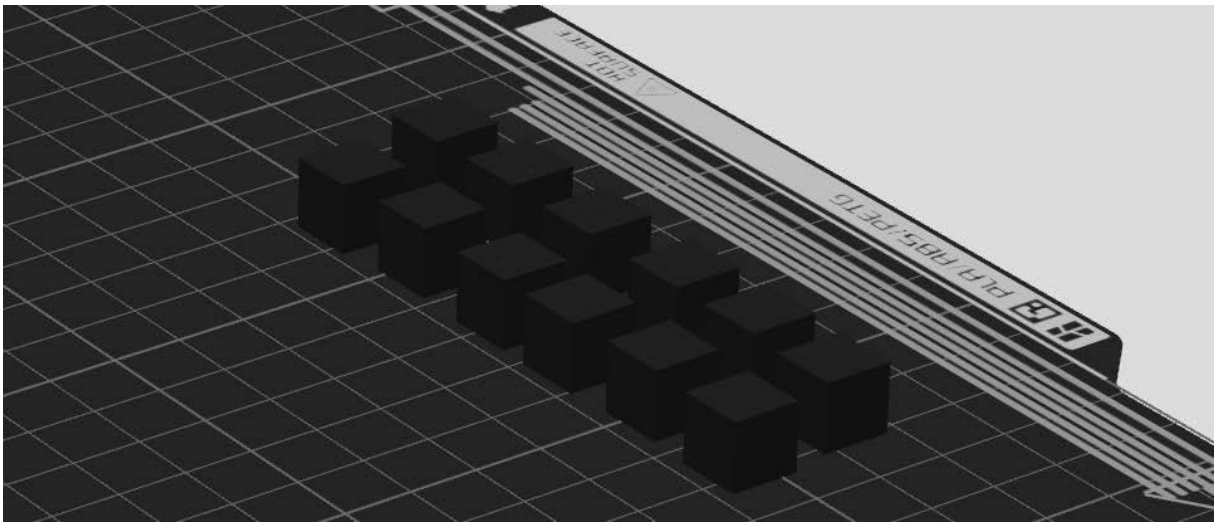

Figure 4. *Sets of elements after multiplication and optimal distribution - Bambu Studio software*

After preparing the printer control files, standardized sample packages were produced for static compression testing. Some samples were made of solid PLA or TPU, while others were created with a gradient transition between these two selected thermoplastic materials with a designed functional transition geometry. Example photos of the produced samples are shown in Figure 4.

Table 2. *Printing parameters in Bambu Studio settings.*

SPEED	
First Layer Speed	20mm/s
First Infill Layer	50mm/s
Outer Wall Speed	150mm/s
Inner Wall Speed	150mm/s
Infill Speed	150mm/s
Inner Infill Layer Speed	150mm/s
Vertical Coating Speed	80%
Slow Down on Overhangs	YES
Bridge Speed	50%
Gap Fill Speed	150mm/s
Support Speed	150mm/s
Connecting Support Layer Speed	80mm/s
Idle Speed	500m/s
ACCELERATION	
Normal Printing	10000mm/s^2
Idle Speed	10000mm/s^2
First Pass Layer	6000mm/s^2
First Layer	500mm/s^2
Outer Wall	5000mm/s^2
Inner Wall	0mm/s^2

Top Surface	2000mm/s^2
Infill	100%
WALLS	
Number of Hits Walls	2
Thin Wall Detection	NO
TOP/BOTTOM COATINGS	
Top Coating Layers	5
Top Coating Thickness	1mm
Top Coating Penetration	5
Lower Coating Layers	3
Density fill	100%
Lower shell layers	3
Lower shell thickness	0mm
Lower shell penetration	3
Internal solid fill pattern	Rectilinear
FILL	
Fill density	100%
Fill pattern	Rectilinear
Fill anchor length	400%
Maximum fill anchor length	20%

a) b)

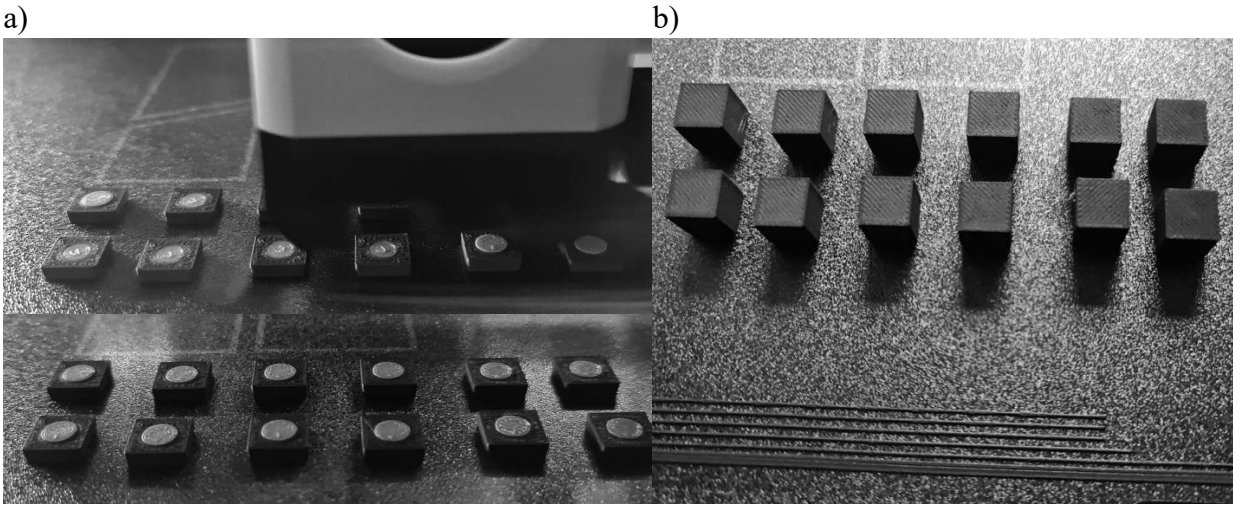

Figure. 4. *Sample photos showing: a) Model 1 samples during the production process, b) after completion.*

4. CONCLUSION

3D printing is an attractive alternative to many other manufacturing methods currently available. As an additive manufacturing technology, it has many advantages, thanks to which its popularity is growing logarithmically on the world market. The development of new gradient

materials can revolutionize the 3D printing market. Combining the advantages of two materials in one model using a gradient can affect a broader range of applications of a given model. This approach allows us to manipulate the material's properties to obtain properties best suited for a given application.

The developed geometries satisfactorily combine two different thermoplastic materials, creating a smooth transition from one material to another with varying stiffness obtained through additive techniques – adhesion tests were successful. Additionally, it was observed that using a fluid biaxial connection ensured better adhesion of the developed hybrid materials to each other than a uniaxial connection.

The future assessment of mechanical properties includes compression first after optimizing the geometry used, three-point bending, tension, and impact strength. Based on the results of the compression tests, the team will develop a model for entering the developed geometries into standardized samples for the above tests and then into real structures, taking into account their work in operating conditions. Strength tests enable a quantitative assessment of the load-bearing capacity and susceptibility of the structure to deformation and thus allow for a comprehensive characterization of the behaviour of the tested material under the influence of external forces. The obtained experimental data will constitute the basis for comparing the effectiveness of different technological configurations in the context of the obtained mechanical properties. Their analysis allows for formulating conclusions regarding the validity of specific process parameters. It indicates potential directions for further optimization of printing technology and/or gradient structures, especially in their practical application in environments requiring diverse mechanical characteristics within a single solid.

ACKNOWLEDGEMENT

The present study was produced as part of the activities of the Student Science Club "HEAD TO HEAD" operating at the Department of Scientific and Didactic Laboratory of Nanotechnology and Material Technologies at the Faculty of Mechanical Engineering, Silesian University of Technology in Gliwice.

Publication supported by the Excellence Initiative - Research University program implemented at the Silesian University of Technology, 2025.

BIBLIOGRAPHY

1. Naveed, N. (2021). Investigating the material properties and microstructural changes of fused filament fabricated PLA and tough-PLA parts. *Polymers*, *13*(9), 1487
2. Finnes T., HighDefinition 3D Printing – Comparing SLA and FDM Printing Technologies, "The Journal of Undergraduate Research" 2015, Vol. 13, Article 3;
3. Ślusarczyk P.;FDM Technology – CHAPTER 1 – What is it and what does it consist of…? centrumdruku3d.pl; day preview: 02.05.2025
4. Budzik G., Siemiński P.; Additive Techniques. 3D Printing. 3D Printers. Warsaw: Oficyna Wydawnicza PW 2023,
5. 2015;https://www.sciencedirect.com/science/article/pii/S2211812814008074 day preview: 02.05.2025
6. https://link.springer.com/article/10.1007/BF00549902 day preview: 12.05.2025
7. https://3dprinting.com/what-is-3d-printing/ day preview: 22.05.2025

TalentDetector
23th-25th June 2025
Gliwice-Brenna, Poland
DEPARTMENT OF ENGINEERING MATERIALS AND BIOMATERIALS
FACULTY OF MECHANICAL ENGINEERING
SILESIAN UNIVERSITY OF TECHNOLOGY
INTERNATIONAL STUDENTS SCIENTIFIC CONFERENCE

Design and Field Testing of a Synchronized Camera–LiDAR–IMU System for Real-World Dataset Collection

Tomasz Kukuczka [a], Michał Polończyk[b]

[a] Silesian University of Technology, Faculty of Automatic Control, Electronics And Computer Science, Department of Graphics, Department of Cybernetics, Nanotechnology and Data Processing
[b] Autonomos Systems Sp. z o. o.
email: tomasz.kukuczka@polsl.pl

Abstract: This paper presents the design and implementation of a mobile data acquisition platform inspired by the KITTI Vision Benchmark Suite. The developed system is equipped with four cameras, a 64-channel LiDAR, a GPS/IMU receiver, and a hardware synchronization module. The primary objective of the project was to develop a flexible and scalable platform capable of recording synchronized data from multiple sensors under real-world conditions. The collected data was intended for training machine learning models for depth estimation. Additionally, the platform enables the execution of validation tests for the designed models.
The paper outlines the component selection process, addresses implementation challenges, and details the applied hardware and software solutions. It also describes the custom mounting system and the procedures followed during field testing of the developed platform.

Keywords: VIDAR; autonomous vechicles; autonomous driving

1. INTRODUCTION

Datasets play a crucial role in the development of perception systems for autonomous vehicles. The KITTI Vision Benchmark Suite is one of the most recognized sources used for training and validating stereo vision and LiDAR processing algorithms [1].
The aim of VIDAR project was to design a proprietary data acquisition system capable of capturing synchronized information from multiple sensors, including cameras and LiDAR, under real-world environmental conditions. This system was used to collect a dedicated dataset and was subsequently integrated into a prototype platform to evaluate the performance of a proposed deep learning-based method for depth estimation in practical scenarios [3].

2. DESIGN ASSUMPTIONS AND COMPONENT SELECTION

After analyzing available RGB cameras equipped with global shutter sensors[5], the NileCAM25_CUXVR models were selected due to their high image quality, support for

hardware synchronization, and GMSL2 interface commonly used in automotive systems. Four cameras were deployed, each fitted with lenses offering different fields of view (FOV) to ensure heterogeneity in the camera setup. Compatibility with the NVIDIA Jetson AGX Xavier platform was also a key selection criterion, allowing for future use of the system in real-time depth estimation tasks.
For depth data acquisition, the Ouster OS1 LiDAR (Gen0/Gen1) was utilized in both 16- and 64-channel configurations. This sensor offers a range of up to 90 meters, a 45° vertical field of view, and a refresh rate of 10 Hz [2]. Additionally, the system includes a GPS/IMU unit for capturing inertial data, including the vehicle's acceleration and angular velocity.

Figure 1. Acquisition set (NILECam cameras, Ouster OS1 along with NVIDIA Jetson AGX).

3. SYSTEM IMPLEMENTATION

The camera handling application was developed in C++. Its primary function was to capture and store images in UYVY format, with configurable options for white balance, exposure time, and hardware synchronization. Although the OpenCV library was initially considered, the final implementation utilized V4L2 due to its superior performance. Enabling hardware synchronization required modifications to the camera driver and recompilation of the operating system kernel on the NVIDIA Jetson AGX Xavier platform.
Due to a manufacturing defect in the available LiDAR units—specifically, a trigger signal voltage of 300 mV instead of the expected 3.3 V—it was necessary to incorporate a Raspberry Pi Pico microcontroller. This microcontroller translated the strobe signal by detecting voltage transitions at a sampling frequency of 125 MHz, achieving a latency of approximately 100 µs.
The system was further extended with functionality to store LiDAR data in PLY format. The range of registered data was limited to the area covered by the cameras, which helped improve overall system performance. An IMU module was also integrated, allowing for full trajectory recording of the platform's motion [6].
The complete system was deployed on two test platforms: the autonomous EZ10 shuttle and a conventional Fiat Stilo passenger car. The EZ10 was used for controlled testing in closed environments along predefined routes, while the Fiat Stilo enabled data acquisition under real traffic conditions[4].

Figure 2. Platform installed on Stilo (on the right) and installed on EZ10 (on the left).

To install the cameras, LiDAR, and IMU on the platform, a custom mounting system was designed to enable precise positioning of the devices on the roofs of the test vehicles [7]. Several design approaches were considered (see Fig. 3). In the final version, aluminum profiles were selected as the mounting framework. Cameras were attached to these profiles using screws, which allowed for easy adjustment of their positions. Each camera was housed in a custom-designed, 3D-printed enclosure, which facilitated the mounting process and protected the camera against environmental elements.

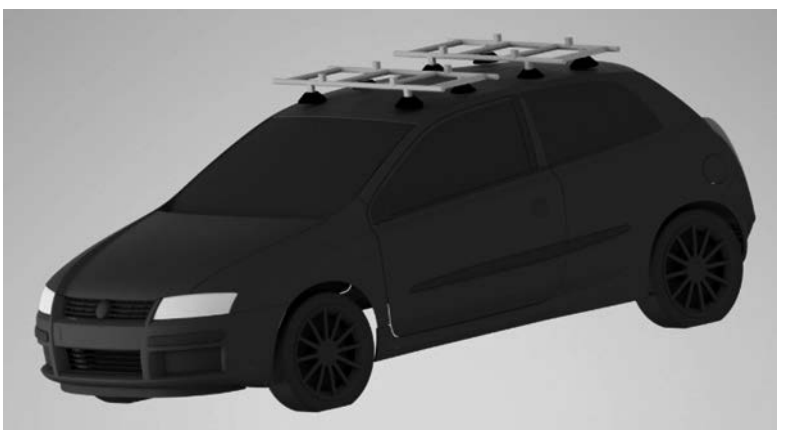

Figure 3. Concept of the system mounting system.

In the final version of the prototype, lenses providing fields of view (FOV) of 120° and 60° were used. The distance between the cameras with a 120° FOV was 45 cm, while the distance between the cameras with a 60° FOV was 15 cm.

4. SUMMARY

This paper presented the design and implementation of a mobile data acquisition platform for training and validating depth estimation models. The system integrates four hardware-synchronized RGB cameras, a 64-channel LiDAR, and a GPS/IMU module. Custom mounting hardware was developed to ensure precise sensor alignment. Data is recorded in real-world conditions and stored in synchronized formats suitable for machine learning applications. The

platform was deployed on two test vehicles and successfully used to collect datasets for deep learning-based depth estimation.

5. ACKNOWLEDGEMENTS

The publication/paper was based on the results of the project no. POIR.01.01.01-00-0123/20 co-financed by the European Union under the European Regional Development Fund - Smart Growth program 2014-2020.

BIBLIOGRAPHY

1. Geiger, Andreas, Philip Lenz, and Raquel Urtasun. "Are we ready for autonomous driving? the kitti vision benchmark suite." 2012 IEEE conference on computer vision and pattern recognition. IEEE, 2012.
2. Zhang, Ji, and Sanjiv Singh. "LOAM: Lidar odometry and mapping in real-time." Robotics: Science and systems. Vol. 2. No. 9. 2014.
3. Chen, Liang-Chieh, et al. "Deeplab: Semantic image segmentation with deep convolutional nets, atrous convolution, and fully connected crfs." IEEE transactions on pattern analysis and machine intelligence 40.4 (2017): 834-848.
4. M. Cordts et al., "The Cityscapes Dataset for Semantic Urban Scene Understanding," 2016 IEEE Conference on Computer Vision and Pattern Recognition (CVPR), Las Vegas, NV, USA, 2016, pp. 3213-3223, doi: 10.1109/CVPR.2016.350.
5. H. Caesar et al., "nuScenes: A Multimodal Dataset for Autonomous Driving," 2020 IEEE/CVF Conference on Computer Vision and Pattern Recognition (CVPR), Seattle, WA, USA, 2020, pp. 11618-11628, doi: 10.1109/CVPR42600.2020.01164.
6. P. Sun *et al*., "Scalability in Perception for Autonomous Driving: Waymo Open Dataset," *2020 IEEE/CVF Conference on Computer Vision and Pattern Recognition (CVPR)*, Seattle, WA, USA, 2020, pp. 2443-2451, doi: 10.1109/CVPR42600.2020.00252.
7. Liu, Zhenbin, et al. "LVI-fusion: A robust LiDAR-visual-inertial SLAM scheme." *Remote Sensing* 16.9 (2024): 1524.

TalentDetector
23th-25th June 2025
Gliwice-Brenna, Poland
DEPARTMENT OF ENGINEERING MATERIALS AND BIOMATERIALS
FACULTY OF MECHANICAL ENGINEERING
SILESIAN UNIVERSITY OF TECHNOLOGY
INTERNATIONAL STUDENTS SCIENTIFIC CONFERENCE

Farebné leptanie grafitických liatin

Denis Kulas[a], Alan Vaško[a], Mirosław Bonek[b]

[a] Žilinská univerzita v Žiline, Strojnícka fakulta, Katedra materiálového inžinierstva, Univerzitná 8215/1, 010 26 Žilina, Slovak Republic
[b] Silesian University of Technology, Faculty of Mechanical Engineering, Department of Engineering Materials and Biomaterials, ul. Konarskiego 18A, 44-100 Gliwice, Poland
email: kulas2@stud.uniza.sk, alan.vasko@fstroj.uniza.sk

Abstrakt: Článok sa zameriava na aplikáciu farebného leptania pri štruktúrnej analýze grafitických liatin, s cieľom priniesť nové poznatky o ich štruktúre, ako napr. zvýraznenie rozdielov v chemickom zložení mikrolokalít, alebo odlíšenie fáz, ktoré sú pri čierno-bielom leptaní ťažko alebo vôbec odlíšiteľné.

Analyzované boli 3 druhy grafitických liatin s odlišným tvarom grafitu. Potvrdilo sa využitie farebných leptadiel na farebné zvýraznenie štruktúrnych fáz. Z 5 použitých leptadiel sa najviac osvedčili leptadlá chróman sodný, Klemm I a molybdénan sodný, ktoré jednoznačne odlíšili fázy ako ferit, perlit, fosfidové eutektikum alebo farebne odlíšili meniace sa chemické zloženie tuhého roztoku.

Kľúčové slová: liatina, farebná metalografia, leptadlo, matrica.

1. ÚVOD

Farebné leptanie je najdôležitejším spôsobom vyvolania farebného kontrastu úpravou povrchu vzorky v metalografickej mikroskopii. Reakciou povrchu metalografického výbrusu a leptadla vzniká transparentný film premenlivej hrúbky, ktorý má funkciu interferenčného povlaku. Ak je pozorovaná vzorka pokrytá transparentným filmom, vzniká interferencia svetla v dôsledku rozdelenia odrazeného svetla na zložky odrazené na rozhraní vzduch - vrstva a na rozhraní kov - vrstva.

Hrúbka transparentného interferenčného povlaku vznikajúceho v dôsledku účinku leptadla závisí od chemického zloženia materiálu výbrusu, od chemického zloženia leptadla a doby leptania. Ak sú podmienky leptania (druh leptadla, doba leptania) konštantné a výrazne sa mení chemické zloženie jednotlivých mikrolokalít, bude sa meniť aj hrúbka vzniknutého povlaku v závislosti od chemického zloženia mikrolokality a v dôsledku toho aj farba jednotlivých mikrolokalít už pri osvetlení vo svetlom poli.

Chemické zloženie leptadiel je zvolené tak, aby bolo možné vytvoriť povlaky s meniacou sa hrúbkou asi v rozmedzí 100 až 150 nm, s využiteľnou závislosťou hrúbky povlaku od chemického zloženia skúmaných štruktúrnych zložiek.

Najdôležitejšie farebné leptadlá je možné rozdeliť do 3 skupín:

1. pyrosiričitanové leptadlá (Klemm, Beraha, Lichtenegger-Bloech, Bloech-Wedl);
2. molybdénové leptadlá (molybdénan sodný, kyselina molybdénová);
3. horúce leptadlá (pikrát sodný, chróman sodný) [1-3].

2. EXPERIMENTÁLNA ČASŤ

Pre experimenty (metalografickú analýzu) sa vybrali vzorky 3 grafitických liatin:

- perliticko-feritická liatina s lupienkovým grafitom ⟹ ozn. LLG
- feriticko-perlitická liatina s červíkovitým grafitom ⟹ ozn. LČG
- feriticko-perlitická liatina s guľôčkovým grafitom ⟹ ozn. LGG

Na proces grafitizácie majú najväčší vplyv uhlík a kremík, pričom ich účinok je približne rovnocenný. To znamená, že ak sa zvýši množstvo jedného z týchto prvkov, je potrebné znížiť množstvo druhého, aby sa zachoval rovnaký stupeň grafitizácie.

Na obr. 1. sa nachádza grafické znázornenie mechanických vlastností použitých liatin a ich porovnanie. Najvyššie mechanické charakteristiky dosahuje liatina s guľôčkovým grafitom s pevnosťou v ťahu R_m = 547 MPa, dohovorenou medzou klzu $R_{p0,2}$ = 412 MPa a ťažnosťou A = 5 %. Najnižšie mechanické vlastnosti má liatina s lupienkovým grafitom.

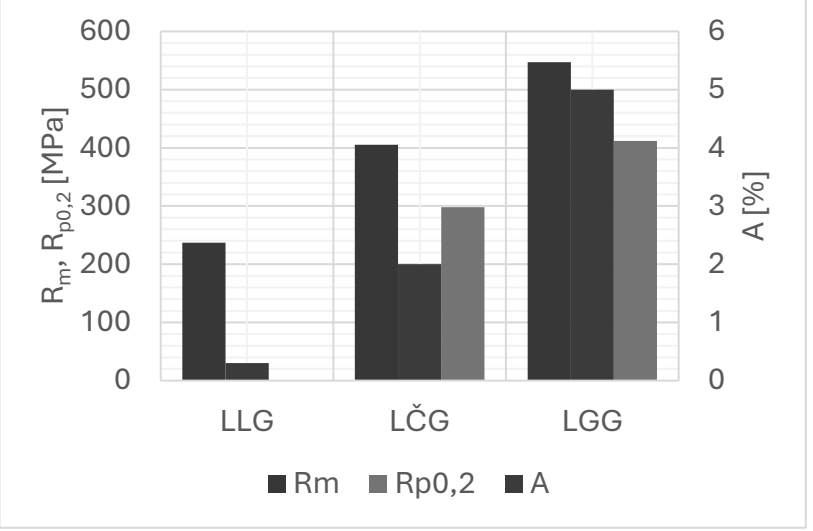

Obr. 1. Mechanické vlastnosti použitých liatin
Figure 1. Mechanical properties of used cast irons

Hodnotenie mikroštruktúry vzoriek sa uskutočnilo na optickom mikroskope Neophot 32. Pre zhotovenie fotodokumentácie bol použitý program NIS-Elements AR 5.20.

Pre čiernobiele leptanie bol použitý 3 % Nital, ktorého zloženie pozostáva z 4,8 ml kyseliny dusičnej a 95,2 ml alkoholu. Leptanie grafitických liatin prebiehalo potieraním povrchu vzoriek pomocou vaty namočenej v leptadle s časom leptania približne 5 sekúnd.

Pri farebnom leptaní bolo aplikovaných päť farebných leptadiel, a to chróman sodný, Klemm I, Kalling´s 2, molybdénan sodný a Beraha-Martenzit (tab. 1).

Chróman sodný sa ako leptadlo môže použiť pre všetky druhy liatin, pričom citlivo reaguje na odmiešavanie hlavných prvkov v dôsledku iného chemického zloženia. Klemm I reaguje na odmiešavanie hlavných prvkov, rozpustených v austenite, resp. vo ferite. Kalling´s 2 sa používa na leptanie ADI liatin, pre rozlíšenie karbidov, grafitu a základnej kovovej matrice. Molybdénan sodný umožňuje odlíšiť v štruktúre cementit, fosfidy a ferit. Patrí do skupiny molybdénových leptadiel a používa sa pri liatinách predleptaných Nitalom. Základný roztok treba ďalej okysliť na pH 2,5-3 pomocou kyseliny dusičnej. Beraha-Martenzit umožňuje odlíšiť v štruktúre bainit a martenzit a patrí do skupiny pyrosiričitanových leptadiel. Po každom leptaní sa naleptané vzorky dôkladne opláchli vodou, destilovanou vodou a vysušili horúcim vzduchom.

Tab. 1. Zloženie a čas leptania použitých farebných leptadiel
Table 1. The composition and time of etching used colour etchants

Leptadlo	Zloženie	Čas leptania
Chróman sodný	35 g hydroxid sodný + 100 ml vody, 5 g oxid chrómový	4,5 min.
Klemm I	100 ml tiosíran sodný + 2 g pyrosiričitan draselný	3-5 min.
Kalling´s 2	5 g chlorid meďnatý + 100 ml kyselina chlorovodíková + 100 ml alkohol	6 s.
Molybdénan sodný	1 g molybdénan sodný + 100 ml vody, kyselina dusičná	1 min.
Beraha-Martenzit	83 g vody + 17 g kyselina chlorovodíková, 2 g pyrosiričitan draselný, 2 g hydrogenfluorid amonný	8 s.

3. VÝSLEDKY

Mikroštruktúra liatin po čierno-bielom leptaní je dokumentovaná na obr. 2.

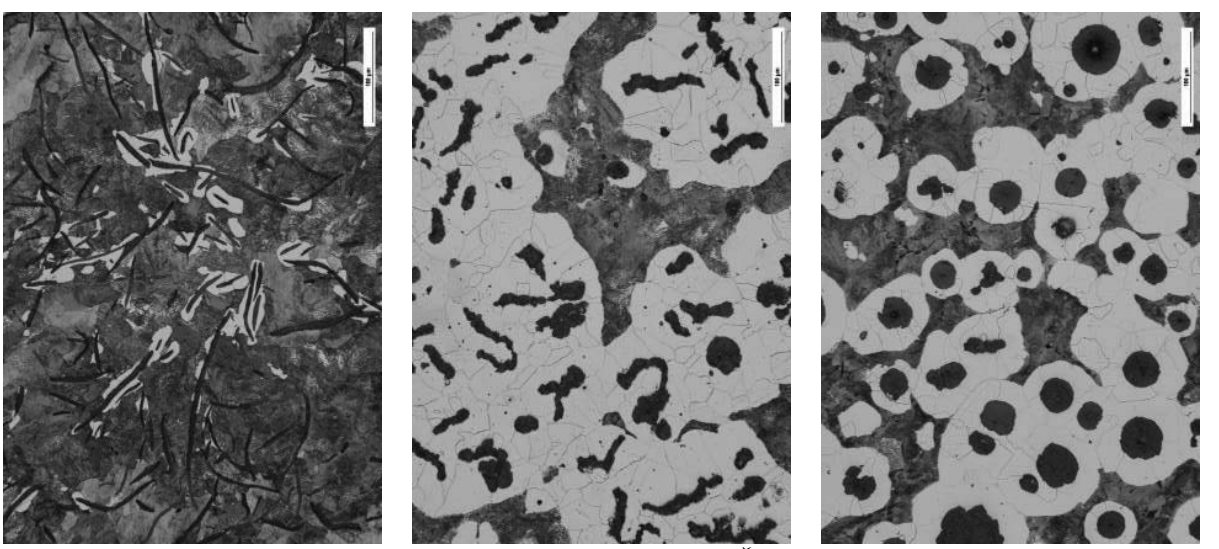

a) perliticko-feritická LLG *b) feriticko-perlitická LČG* *c) feriticko-perlitická LGG*

Obr. 2. Mikroštruktúra liatin po čiernobielom leptaní, lept. 3 % Nital
Figure 2. Microstructure of cast irons after black and white etching, etch. 3 % Nital

Na obr. 3. sú zobrazené mikroštruktúry grafitických liatin po aplikácii farebného leptania pomocou chrómanu sodného. Liatina s lupienkovým grafitom (obr. 3a) vykazuje farebný kontrast matrice, ktorý zahŕňa odtiene od svetlomodrej, cez žltú, až po červeno-fialovú. Svetlomodrá farba v okolí grafitických častíc poukazuje na prítomnosť feritu, zatiaľ čo žlté až červeno-fialové oblasti predstavujú perlit. V prípade liatiny s červíkovitým grafitom (obr. 3b) sa v okolí grafitu objavujú farby od žltej cez modrozelenú až po fialovú, ktoré reprezentujú ferit, pričom sivohnedé odtiene vyznačujú perlit. Liatina s guľôčkovým grafitom (obr. 3c) má matricu s farebným prechodom od béžovej po svetlohnedú (ferit), zatiaľ čo tmavohnedé až modré oblasti predstavujú perlit.

Na vzorkách po farebnom leptaní chrómanom sodným neboli pozorované žiadne ďalšie fázy, napr. fosfidové eutektikum, cementit a iné karbidy.

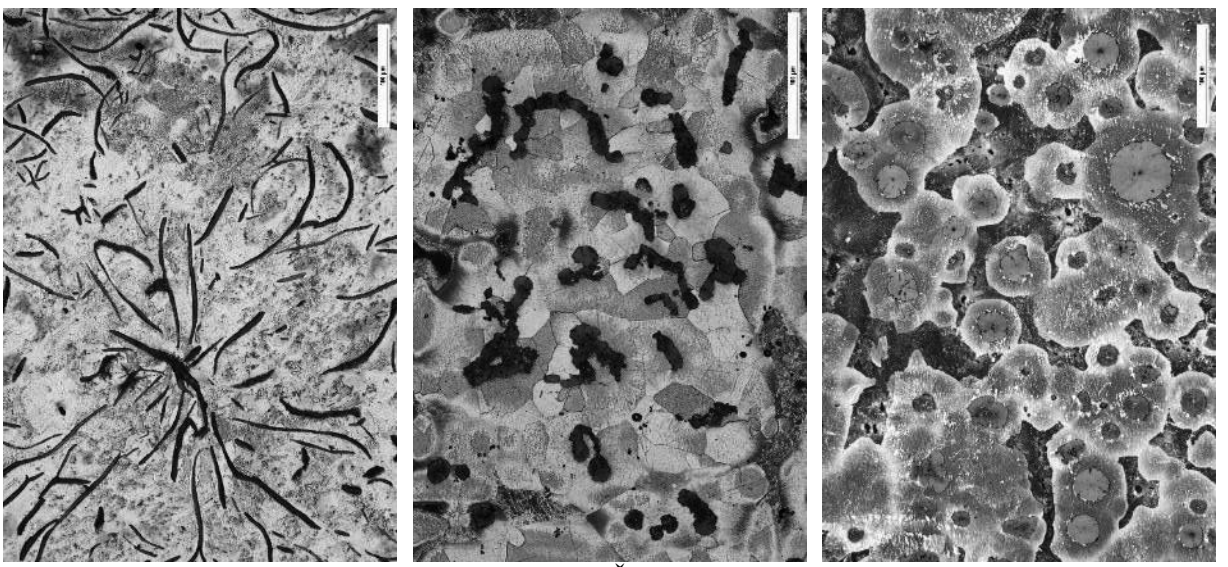

a) LLG b) LČG c) LGG

Obr. 3. Mikroštruktúra liatin po farebnom leptaní chrómanom sodným
Figure 3. Microstructure of cast irons after coloured etching by sodium chromate

Obr. 4. dokumentuje mikroštruktúru liatin po farebnom leptaní leptadlom Klemm I. Liatina s lupienkovým grafitom (obr. 4.a) má farebnú matricu od béžovej po sivo-hnedú, kde béžová vyznačuje ferit a sivá až sivo-hnedá perlit. Lamely perlitu sú jemne modrasté.

Pri liatine s červíkovitým grafitom (obr. 4.b) sú zvýraznené hranice zŕn a matrica prechádza od bielej po modrú farbu. Ferit má bielu až hnedú farbu, perlit modrú. Biele sfarbenie v okolí grafitu vyznačuje vyšší obsah kremíka, hnedé odtiene reprezentujú vyšší obsah mangánu.

Liatina s guľôčkovým grafitom (obr. 4.c) má podobné spektrum – ferit je biely až hnedý, perlit modrý. Biely odtieň blízko grafitu značí vyšší obsah kremíka, hnedé farby vo väčšej vzdialenosti od grafitu vyznačujú vyšší obsah mangánu.

Po farebnom leptaní leptadlom Klemm I neboli pozorované žiadne ďalšie fázy, napr. fosfidové eutektikum, cementit a iné karbidy.

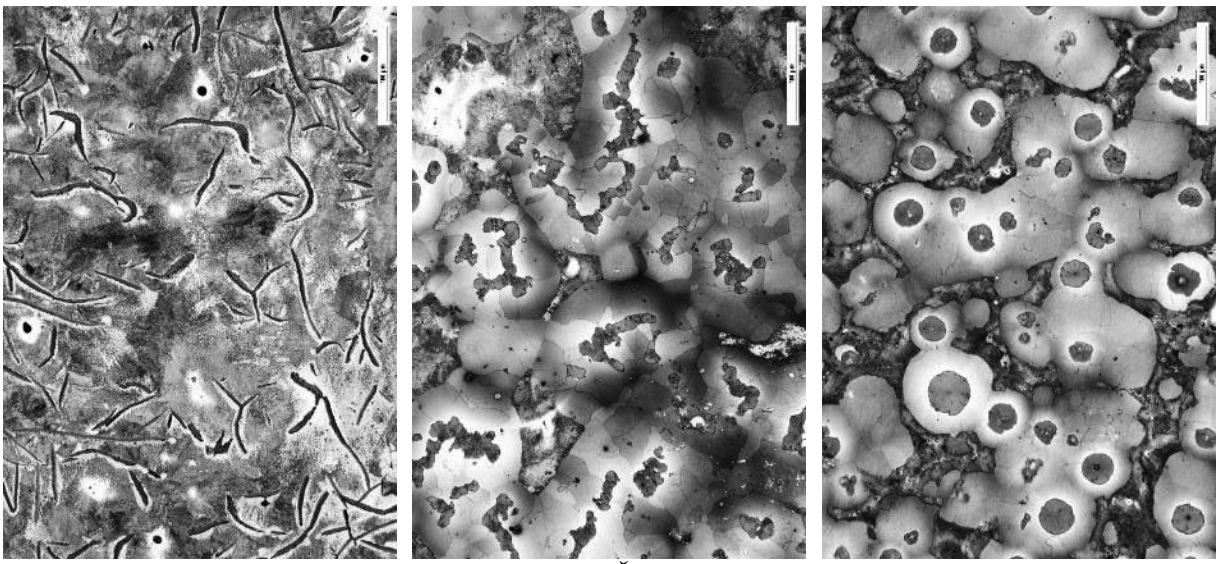

a) LLG *b) LČG* *c) LGG*

Obr. 4. Mikroštruktúra liatin po farebnom leptaní leptadlom Klemm I
Figure 4. Microstructure of cast irons after coloured etching by Klemm I

Na obr. 5 je dokumentovaná aplikácia leptadla Kalling´s 2. Leptanie liatiny s guľôčkovým grafitom neposkytlo farebné rozlíšenie fáz - štruktúra vyzerá podobne ako po leptaní pomocou 3 % Nitalu. Obr. 5a zobrazuje mikroštruktúru po leptaní leptadlom Kalling´s 2, zatiaľ čo obr. 5b zobrazuje tú istú oblasť po leptaní, ale aj s použitím polarizovaného svetla. V tomto prípade sú štruktúrne zložky čiastočne farebne odlíšené: ferit má odtiene od žltej po modrú a perlit sa javí sivohnedo až zelene.

Po leptaní leptadlom Kalling´s 2 neboli pozorované žiadne ďalšie fázy, napr. fosfidové eutektikum, cementit a iné karbidy.

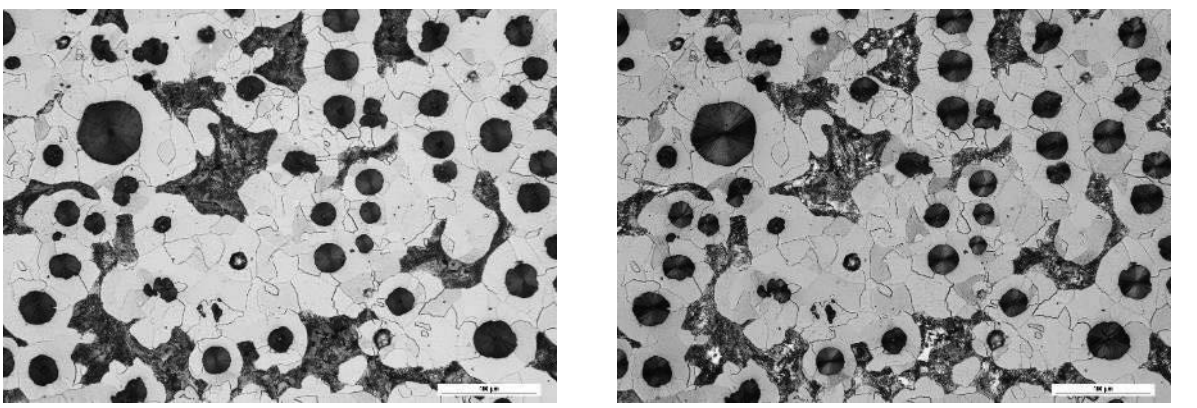

a) LGG, lept. Kalling´s 2 *b) LGG, lept. Kalling´s 2 + polarizované svetlo*

Obr. 5. Mikroštruktúra LGG po farebnom leptaní leptadlom Kalling´s 2
Figure 5. Microstructure of nodular cast iron after coloured etch. by Kalling´s 2

Obr. 6. zobrazuje mikroštruktúry liatin po farebnom leptaní molybdénanom sodným. V prípade liatiny s lupienkovým (obr. 6a), červíkovitým (obr. 6b) aj guľôčkovým grafitom (obr. 6c) sa matrica sfarbila od bielej po hnedosivú - ferit sa javí ako biely, perlit ako hnedosivý. Pri liatinách s červíkovitým a guľôčkovým grafitom bolo navyše pozorované modré sfarbenie grafitu.

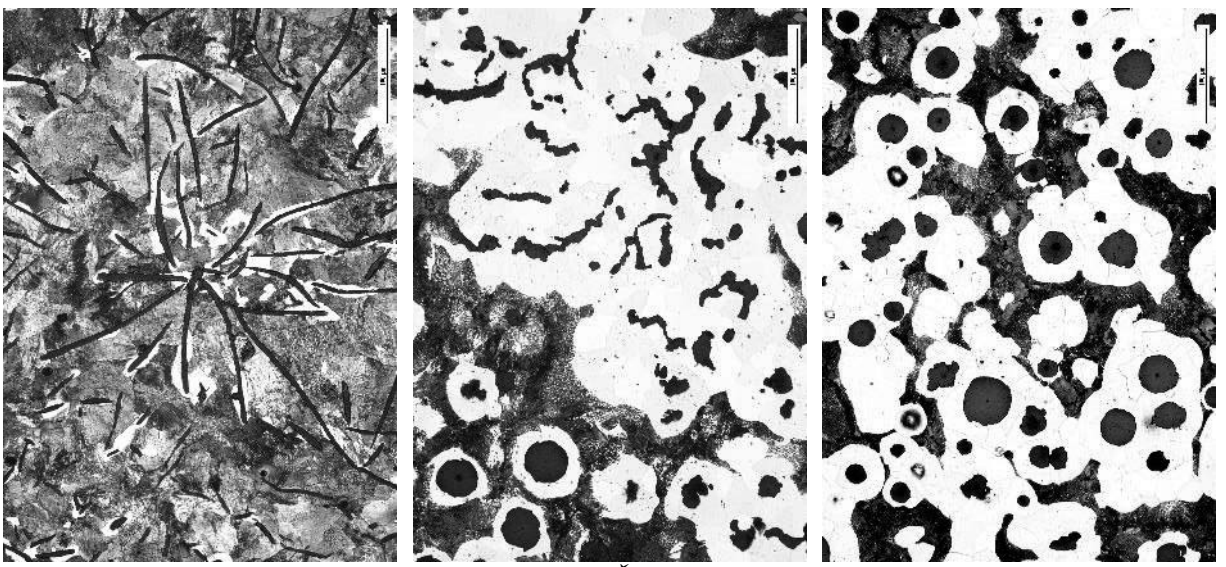

) LLG *b) LČG* *c) LGG*

Obr. 6. Mikroštruktúra liatin po farebnom leptaní molybdénanom sodným
Figure 6. Microstructure of cast irons after coloured etch. by sodium molybdate

Obr. 7 reprezentuje mikroštruktúru liatiny s lupienkovým grafitom po leptaní molybdénanom sodným. Na okraji vzorky bola pozorovaná ďalšia fáza, a to fosfidové eutektikum (oranžovo-hnedé sfarbenie), ktoré sa v štruktúre vyskytuje pri zvýšenom obsahu fosforu. Perlit je sivý, pričom jeho lamely majú modrasté sfarbenie.

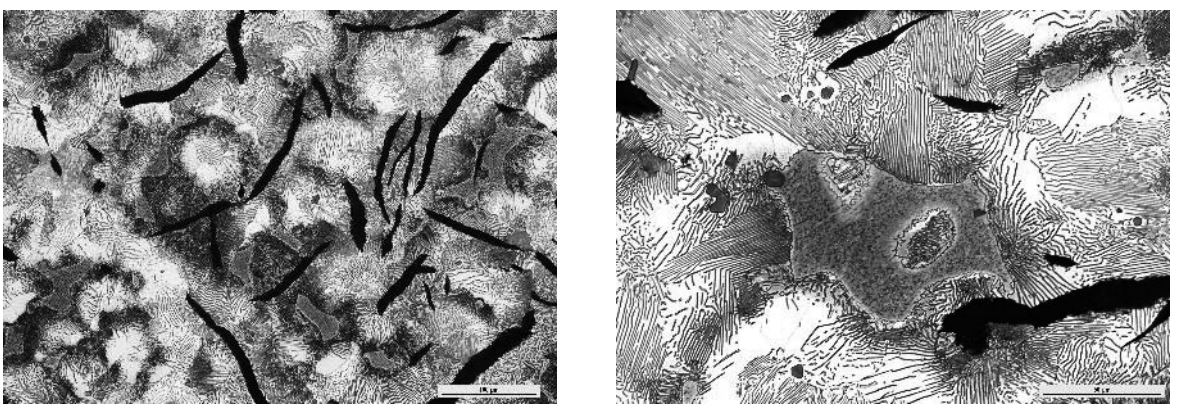

a) LLG *b) LLG, detail fosfidového eutektika*

Obr. 7. Mikroštruktúra LLG po farebnom leptaní molybdénanom sodným
Figure 7. Microstructure of lamellar cast iron after coloured etching by sodium molybdate

V článku nie sú uvedené fotografie mikroštruktúr po farebnom leptaní leptadlom Beraha-Martenzit, pretože toto leptadlo neposkytlo požadované farebné rozlíšenie štruktúrnych fáz matrice liatin. Mikroštruktúry grafitických liatin po leptaní pomocou leptadla Beraha-Martenzit boli totožné s výsledkami získanými čiernobielym leptaním pomocou 3 % Nitalu. Leptadlo Beraha-Martenzit je určené najmä na zvýraznenie štruktúrnych fáz ako bainit a martenzit, ktoré sa však v skúmaných mikroštruktúrach grafitických liatin nevyskytovali, a preto nebolo možné dosiahnuť požadovaný farebný kontrast.

Z výsledkov realizovaných experimentov vyplýva:

- Farebné leptanie je využiteľné pri zvýraznení a odlíšení jednotlivých štruktúrnych fáz grafitických liatin;
- Z 5 aplikovaných leptadiel (chróman sodný; Klemm I; Kalling´s 2; molybdénan sodný a Beraha-Martenzit) sa najviac osvedčili leptadlá chróman sodný, Klemm I a molybdénan sodný. Tieto leptadlá jednoznačne odlíšili štruktúrne fázy ako sú ferit, perlit, fosfidové eutektikum alebo farebne odlíšili meniace sa chemické zloženie tuhého roztoku.

Farebné leptanie sa dá využiť na zvýraznenie rozdielov v chemickom zložení mikrolokalít alebo na odlíšenie matrice liatin, ktoré sú pri použití čierno-bieleho kontrastu ťažko odlíšiteľné, príp. sa vôbec nedajú odlíšiť. Farebný kontrast zároveň výrazne doplní výrazové prostriedky a zvýši (posilní) informačnú hodnotu svetelnej metalografickej mikroskopie.

POĎAKOVANIE

Príspevok vznikol v rámci riešenia spoločného slovensko-poľského projektu Project Based Learning ako výsledok spolupráce medzi Politechnikou Slaskou, Gliwice a Žilinskou univerzitou v Žiline a projektov KEGA č. 004ŽU-4/2023 a KEGA č.009ŽU-4/2023.

ZOZNAM POUŽITEJ LITERATÚRY

1. Skočovský, P., Podrábský, T., 2001. Farebná metalografia zliatin železa. EDIS, 68 s., ISBN 80-7100-911-3.
2. Skočovský, P., Podrábský, T., 2005. Grafitické liatiny. EDIS, 168 s., ISBN 80-8070-390-6.
3. Vaško, A., 2022. Advantages of colour etching in quality control of graphitic cast irons. In: Production Engineering Archives. vol. 28, issue 4, p. 319-324, ISSN 2353-7779.

TalentDetector
23th-25th June 2025
Gliwice-Brenna, Poland
DEPARTMENT OF ENGINEERING MATERIALS AND BIOMATERIALS
FACULTY OF MECHANICAL ENGINEERING
SILESIAN UNIVERSITY OF TECHNOLOGY
INTERNATIONAL STUDENTS SCIENTIFIC CONFERENCE

Automatic Granule Feeding Line For Cable Manufacturing: Design And Implementation

Batuhan Kurt[1], Cem Samet Kartal[1], Cemal Meran[2], Koksal Ilhan[3], Fatih Oztekin[3]

[1]Student, Pamukkale University, Faculty of Engineering, Department of Mechanical Engineering, Denizli, Turkey [2]Prof.Dr., Pamukkale University, Faculty of Engineering, Department of Mechanical Engineering, Denizli, Turkey, cmeran@pau.edu.tr
[3]Nexans Turkey Industry, R&D Center, Denizli, Turkey

Abstract: In modern industrial production, the seamless and efficient flow of raw materials is essential for maintaining product quality and operational efficiency. This study presents the design and analysis of an automated granule feeding system specifically developed for a cable manufacturing factory, integrating both dilute and dense phase pneumatic conveying technologies to optimize flexibility and performance. Utilizing industrial-grade components such as roots-type blowers, stainless steel transport pipes, directional valves, silos, and granule loading units, the system is engineered to meet the factory's daily production capacity with high efficiency. Detailed calculations— including air velocity, pressure drop, pipe diameter, and solid-to-gas ratio—validate the system's capability for reliable operation. Developed as part of a senior thesis at Pamukkale University's Mechanical Engineering Department, the system aims to replace traditional forklift-based material transport, thereby minimizing human error, enhancing workplace safety, reducing production downtime, and supporting energy efficiency goals. Continuous improvements were made based on technical feedback from the factory's maintenance team, ensuring alignment with production continuity and sustainability objectives. This study exemplifies the effective application of pneumatic conveying systems in industrial cable manufacturing, highlighting its potential contribution to smart, energyefficient, and safe production environments aligned with Industry 4.0 principles

Keywords: Pneumatic Conveying, Blower, SLR, Granule, Pressure Drop

1. INTRODUCTION

The continuous and efficient delivery of raw materials, such as polymer granules used in cable production, is vital for ensuring high-quality output and operational continuity. Traditional methods relying on manual or forklift-based transport introduce risks such as human error, safety hazards, and production interruptions. To address these challenges, a fully automated granule feeding system was designed, integrating dilute and dense phase pneumatic conveying technologies. This system eliminates the inefficiencies of manual handling, reduces the carbon footprint through electricpowered operations, and incorporates automation

infrastructure compatible with Industry 4.0 standards. The thesis, conducted by Batuhan Kurt and Cem Samet Kartal under the supervision of Prof. Dr. Cemal Meran at Pamukkale University in 2024-2025, provides a detailed engineering solution for modern cable manufacturing facilities.

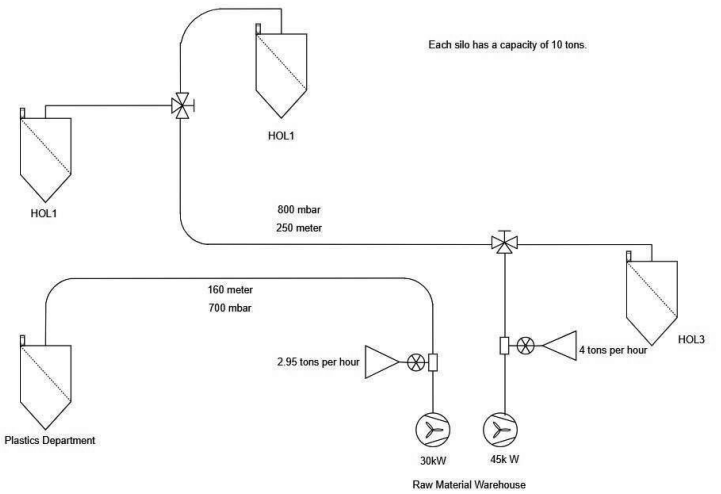

Figure 1. Schematic representation of dilute and dense phase lines

1.1. Importance and Objective

The primary objective of this study is to develop an automated system that ensures a reliable, safe, and efficient supply of granule materials from storage to cable production lines. By leveraging pneumatic conveying, the system minimizes human intervention, enhances safety, and optimizes material flow. [1] The dual-mode approach— combining dilute phase for high-speed, long-distance transport and dense phase for controlled, low-speed transfer— addresses varying operational needs, ensuring flexibility and energy efficiency. [2]

1.2 Role of Granule Feeding in Cable Manufacturing

In cable production, polymer granules (e.g., PVC, PE, XLPE) are critical for insulation and sheathing processes. These granules must be delivered consistently to extruders to ensure uniform coating and high-quality output. Manual feeding methods are labor-intensive, prone to errors, and disrupt production continuity.[5] Automated systems, particularly those using pneumatic conveying, offer a solution by enabling synchronized material delivery to multiple production lines, reducing contamination risks, and improving workplace safety. [3]

2. METHODOLOGY

The thesis adopts a systematic approach to design an automated granule feeding system tailored to the needs of a cable manufacturing facility. The methodology includes:

▪Literature Review: A comprehensive review of pneumatic conveying systems, focusing on dilute and dense phase technologies, was conducted to establish the theoretical foundation.
▪System Design: Key components such as hoppers, rotary valves, blowers, and pipelines were selected and optimized based on material properties and operational requirements.

▪Engineering Calculations: Parameters such as pipe diameter, air velocity, solid loading ratio (SLR), pressure drop, and blower power were calculated to ensure system efficiency.
▪Performance Evaluation: The system's performance was analyzed in terms of capacity, energy efficiency, and operational reliability.

3. SYSTEM DESIGN

The proposed system integrates several critical components to ensure seamless granule transport:

3.1 System Components

▪Hopper: Designed with a conical or pyramidal shape to facilitate smooth granule flow, preventing blockages and ensuring consistent material delivery.[8]
▪Rotary Valve: Provides controlled granule feeding into the pneumatic line while maintaining system pressure and preventing air leaks.[3]
▪Pneumatic Pipeline: Constructed from corrosion-resistant stainless steel, optimized for minimal pressure loss and durability.[4]
▪Blower: Supplies the necessary air pressure and flow rate, with centrifugal blowers selected for their efficiency in dilute phase systems.[7]
▪Filtration Elements: Cyclone separators and dust filters remove fine particles from the air stream, ensuring system cleanliness and compliance with environmental standards.[2]
▪Directional Valves: Enable flexible routing of granules to multiple production lines, enhancing operational versatility. [6]
▪PLC and Sensors: A programmable logic controller (PLC) with integrated sensors monitors parameters like pressure, flow rate, and material levels, ensuring real-time system optimization. [9]

3.2 Dilute vs. Dense Phase Conveying

The system employs both dilute and dense phase conveying to address different operational needs:
▪Dilute Phase: Operates at high air velocities (20 m/s) with a low solid-to-gas ratio (SLR = 3.2), suitable for long-distance, high-capacity transport (65 tons/day). It requires higher energy but offers simplicity and reliability.
▪Dense Phase: Uses lower air velocities (8 m/s) with a higher SLR (15), ideal for shorter distances and abrasive materials (23 tons/day). It minimizes wear and energy consumption but requires more complex control systems.

4. ENGINEERING CALCULATIONS

The system design is supported by detailed calculations to ensure optimal performance:

4.1 Mass Flow Rate

▪Dilute Phase: 65,000 kg over 22 hours yields a mass flow rate of 0.821 kg/s.
▪Dense Phase: 23,000 kg over 5 hours results in 1.111 kg/s.

4.2 Air Mass Flow Rate

Using the SLR, air mass flow is calculated as:

▪Dilute Phase: 0,821/3,2 = 0,256 kg/s

▪Dense Phase: 1,111/15 = 0,0741 kg/s

4.3 Volumetric Flow Rate

The air density was assumed to be 1.225 kg/m³.

▪Dilute Phase: 0,256 / 1,225 = 0,209 m^3/s

▪Dense Phase: 0,0741 / 1,225 = 0,0605 m^3/s

4.4 Pipe Diameter

Pipe cross-sectional area is calculated as ($A(m^2) = Q(m^3/s) / v (m/s)$), where (v) is air velocity:

▪Dilute Phase: ($A=0,209 / 20 = 0,01045\ m^2$), yielding a diameter of 115 mm (standardized to 129 mm per EN ISO 1127).

▪Dense Phase: ($A = 0,0605 /8 = 0,0076\ m^2$), yielding a diameter of 98 mm (standardized to 104 mm).

4.5 Pressure Drop

Pressure drop calculations account for air friction, solid effects, vertical lift, and elbow losses:

Air Friction Loss: Using the Darcy-Weisbach equation, ($\Delta P_{air} = f(L/D)\rho v^2/2$).

- Dilute: 6272 Pa
- Dense: 1998 Pa

Solid Effect Loss: ($\Delta P_{solid}=K*SLR*\Delta P_{hava}$).

▪Dilute: 8028 Pa

▪Dense: 11,993 Pa

Vertical Lift Loss:

($\Delta P_{vercial}=\rho_{material}.gh$).

▪Dilute: 47,088 Pa

▪Dense: 64,746 Pa

Elbow Loss: ($\Delta P_{Elbow}=Kb\rho v^2\ n/2$).

▪Dilute: 784 Pa

▪Dense: 188.16 Pa

Total Pressure Drop:

▪Dilute: 62.1 kPa

▪Dense: 78.9 kPa

4.6 Blower Power

(P (kW) = (Q ΔP) / (η 1000)

Q: Air flow rate (m^3/s) ΔP: Total pressure drop (Pa)

η: Blower efficiency (usually taken as 65–75%)

▪Dilute Phase: (P =0,2454*62172,16/(0,7*1000)= 21,79 kW) (standardized to 30 kW).

▪Dense Phase: (P = 0,007854*78926,50/(0,7*1000)= 45 kW)

5. COST ANALYSIS

5.1 Energy Costs

The system's energy consumption was compared to forklift-based transport:
Forklift: Consumes 2,578 liters of diesel monthly (125,000 TL or €2,825), equating to 1,250,000 TL (€28,263) annually.
Pneumatic System:
▪Dilute Phase: 660 kW/day (17,160 kW/month, 90,246 TL or €2,050).
▪Dense Phase: 225 kW/day (5,820 kW/month, 30,770 TL or €700).
Total: 121,017 TL (€2,750) monthly, 1,452,000 TL (€33,000) annually. The pneumatic system is approximately 15% more energy-efficient than forklifts.

5.2 Initial Investment Costs Dilute Phase:

Total: 768,902 TL (€17,475)
Key components: 30 kW blower (200,000 TL), 180 m stainless steel pipe (180,000 TL), cyclone separator (200,000 TL).
▪Dense Phase: Total: 906,296 TL (€20,597)
Key components: 45 kW blower (250,000 TL), 300 m stainless steel pipe (300,000 TL).
▪Ancillary Equipment: 87,300 TL, including flanges, valves, and safety systems.

5.3 Performance and Cost Evaluation

The dilute phase system is more cost-effective for high-capacity, long-distance transport, while the dense phase system reduces wear and maintenance costs for abrasive materials. The higher initial cost of the dense phase system (18% more than dilute) is offset by lower operational costs and longer equipment lifespan.

6. RESULT AND DISCUSSION

6.1 Challenges and Solutions

The designed system successfully overcomes the challenges of manual granule transport by delivering 65 tons/day in dilute phase and 23 tons/day in dense phase with optimized air velocities and minimal pressure losses, ensuring high efficiency. It enhances workplace safety through closed-loop conveying that eliminates dust and contamination risks. Sustainability is achieved by using electric-powered blowers, which significantly reduce the carbon footprint compared to diesel forklifts. Furthermore, the system incorporates PLC-based automation for real-time monitoring and adaptability, aligning with Industry 4.0 smart factory standards.

The automatic granule feeding system presented in this thesis offers a robust solution for cable manufacturing, combining dilute and dense phase pneumatic conveying to achieve high efficiency, safety, and sustainability. The system's design, supported by rigorous engineering calculations and cost analysis, demonstrates its feasibility for industrial applications. By reducing reliance on manual transport, minimizing energy consumption, and integrating Industry 4.0 technologies, the system sets a benchmark for modern material handling in cable production. Future work could explore further optimization of blower efficiency and integration with IoT for enhanced real-time analytics.

BIBLIOGRAPHY

1. Cabrejos, F. J., & Klinzing, G. E. (1994). *Powder Technology*, 79(3), 173-186.
2. Hilgraf, J. (2015). *Pneumatic Conveying Systems: Design, Selection, and Troubleshooting*. Wiley-VCH
3. Marcus, R. D. (2010). *Pneumatic Conveying Design Guide*. Elsevier.
4. Clyde Bergemann. (2020). *Bulk Materials Handling Systems Catalog.* Clyde Bergemann
5. Rhodes, M. (2003). *Introduction to Particle Technology*. Wiley.
6. Shen, X., et al. (2019). *Powder Technology*, 345, 189-208
7. Vismec (n.d.). Centralized Material Feeding Systems. https://www.vismec.com/
8. Khan, A. A., & Richardson, J. F. (2001). Gas-solid flows in dilute phase pneumatic conveying systems.
9. Siemens**,** *SIMATIC S7-1500 Automation System – System Manual*. Erlangen, Germany: Siemens AG, 2018.

TalentDetector

23th-25th June 2025
Gliwice-Brenna, Poland

DEPARTMENT OF ENGINEERING MATERIALS AND BIOMATERIALS
FACULTY OF MECHANICAL ENGINEERING
SILESIAN UNIVERSITY OF TECHNOLOGY

INTERNATIONAL STUDENTS SCIENTIFIC CONFERENCE

Wpływ rodzaju anody lampy RTG podczas badań dyfrakcyjnych warstw napawanych laserowo na dokładność pomiarów

Waldemar Kwaśny [a], Wojciech Kała[b], Bartłomiej Kazek [b], Damian Janicki [a], Aleksander Lisiecki [a]

[a] Wydział Mechaniczny Technologiczny, Katedra Spawalnictwa, Politechnika Śląska,
e-mail: waldemar.kwasny@polsl.pl; damian.janicki@polsl.pl; aleksander.lisiecki@polsl.pl
[b] Student kierunku Mechanika i Budowa Maszyn: Technologie Spawalnicze, Politechnika Śląska,
e-mail: wk302493@student.polsl.pl; bk303868@student.polsl.pl

Abstract: The aim of this study was to conduct X-ray examinations to assess the structure of laser-cladded layers. As part of the project, samples made of AISI 316L steel and an additional material in the form of Oerlikon Amdry MetcoAdd 316L-D metallic powder were used. The laser cladding process was carried out using a Trumpf Trudisk 3302 disk laser. The technological parameters of cladding included, among others, laser beam power, cladding speed, and powder feed rate. The prepared samples were subjected to metallographic observations and mechanical tests, including Vickers hardness measurements. Structural analysis was performed using X-ray diffraction (XRD), allowing for the identification of phases present in the cladded layer and the determination of residual stress values. The examinations were conducted using X-ray tubes with copper and cobalt anodes, enabling the evaluation of the influence of wavelength on the analysis results.

Streszczenie: Celem poniższej pracy było przeprowadzenie badań rentgenowskich w celu oceny struktury warstw napawanych laserowo. W ramach pracy wykorzystano próbki wykonane ze stali AISI 316L oraz materiał dodatkowy w postaci proszku metalicznego Oerlikon Amdry MetcoAdd 316L-D. Proces napawania laserowego przeprowadzono przy użyciu lasera dyskowego Trudisk 3302 firmy Trumpf. Parametry technologiczne napawania obejmowały między innymi moc wiązki laserowej, prędkość napawania oraz natężenie podawania proszku. Przygotowane próbki poddano obserwacjom metalograficznym oraz badaniom mechanicznym, w tym pomiarom twardości metodą Vickersa. Analiza strukturalna została przeprowadzona przy użyciu dyfrakcji rentgenowskiej (XRD), pozwalając na identyfikację faz występujących w warstwie napawanej i określenie wartości naprężeń własnych. Badania wykonano z zastosowaniem lamp rentgenowskich o anodzie miedzianej oraz kobaltowej, co umożliwiło ocenę wpływu długości fali na uzyskane wyniki.

Słowa kluczowe: Napawanie, napawanie laserowe, napoina, badania XRD, twardość.

1. WSTĘP

Modyfikacja powierzchni polega na celowej zmianie właściwości zewnętrznej warstwy materiału, takiej jak jej utwardzenie, amorfizacja, wprowadzenie pierwiastków stopowych, wytworzenie struktury metastabilnej czy nałożenie dodatkowej warstwy. Do takich procesów wykorzystuje się technologie spawalnicze, np. laser lub wiązkę elektronów, które dzięki wysokiej koncentracji energii wprowadzają zmiany mikrostrukturalne na niewielkiej głębokości metalu [1-4].

Nanoszenie warstw lub powłok realizuje się w następujących celach:

- Regeneracja elementów – uzupełnianie ubytków powstałych w wyniku eksploatacji, takich jak pęknięcia, wytarcia, odpryski, korozja czy kawitacja.
- Poprawa właściwości powierzchni – nadawanie powierzchni określonych cech fizycznych, mechanicznych i chemicznych, np. zwiększonej odporności na ścieranie, korozję, poprawy twardości czy zmniejszenia współczynnika tarcia. Takie działania mogą być stosowane zarówno w regeneracji elementów, jak i w procesach produkcyjnych jako zaplanowany etap technologiczny.
- Poprawa estetyki – nanoszenie warstw dekoracyjnych, np. miedzi lub innych metali, poprzez metalizację natryskową, co pozwala na zwiększenie walorów wizualnych wyrobu.

Napawanie jest procesem, który polega na precyzyjnym stopieniu metalurgicznym napoiny z materiałem rodzimym. Udział materiału podłoża w napoinie może wynosić nawet do 60%. Proces ten wykorzystuje różnorodne źródła ciepła, takie jak płomień gazowy, łuk elektryczny, łuk plazmowy czy wiązka lasera, które umożliwiają stapianie materiału dodatkowego w postaci drutu, pręta, taśmy lub proszku.

Podczas napawania możliwe jest uzyskanie warstw o grubości od 0,05 mm do ponad 100 mm w jednym przejściu. Napoiny wyróżniają się wysoką jednorodnością metalurgiczną i strukturalną, choć w przypadku napawania utwardzającego stopami o dużej twardości dopuszcza się występowanie pęknięć jako naturalnego efektu procesu [1-4].

2. MATERIAŁY WYKORZYSTANE DO BADAŃ

Materiałem podstawowym wykorzystanym podczas napawanie była stal AISI 316Lo niskiej zawartości węgla. Skład chemiczny oraz właściwości fizyczne stali przedstawiono w tabeli 1 oraz 2. (Stal AISI 316L klasyfikowana również jako Stal 1.4404) [5].

Tabela 1. Skład chemiczny stali AISI 316L [5]

Pierwiastek	C	Si	Mn	P	Cr	Mo	Ni	Cu	N
Max	0,030	1,0	2,0	0,045	18,5	3,0	14,0	0,30	0,10

Tabela 2. Właściwości fizyczne stali AISI 316L [5]

Właściwość	Wartość
Gęstość	8,0 [kg/dm^3]
Przewodność cieplna w 20°C	15 [W/(m*k)]
Opór elektryczny w temperaturze 20°C	0,75 [(Ω*mm^2)/m]
Ciepło właściwe w temperaturze 20°C	500 [J/(kg*K)]

Jako materiał dodatkowy zastosowany w celu wytworzenia napoiny, wykorzystano proszek metaliczny na bazie stali austenitycznej o składzie chemicznym zbliżonym do stali AISI 316L. Ziarnistość proszku wynosi 45 - 90 μm, skład chemiczny proszku oraz właściwości przedstawiono w tabelach 3 oraz 4 [6].

Tabela 3. Skład chemiczny proszku Oerlikon Amdry MetcoAdd 316L-D [6]

Pierwiastek	C	Mo	Cr	Ni	Inne
Zawartość [%]	<0,03	2	18	12	<1,0

Tabela 4. Właściwości Oerlikon Amdry MetcoAdd 316L-D [6]

Właściwości	Wartość	Jednostka
Wytrzymałość na rozciąganie, XY	668÷672	[MPa]
Granica plastyczności, XY	533÷563	[MPa]
Wydłużenie przy zerwaniu, XY	43÷47	[%]
Twardość (VHN 300g)	193÷239	[HV]
Gęstość względna	>99,6	[%]

3. PROCES NAPAWANIA LASEROWEGO

Próbę napawania przeprowadzono na zautomatyzowanym laserze dyskowym Trudisk 3302 firmy Trumpf. Parametry lasera dyskowego zostały przedstawione w tabeli 5, natomiast parametry wykorzystane podczas badań zostały zestawione w tabeli 6. Sterowanie odbywa się za pomocą numerycznego układu pozycjonowania głowicy laserowej oraz blachy poddanej napawaniu (Rysunek 1).

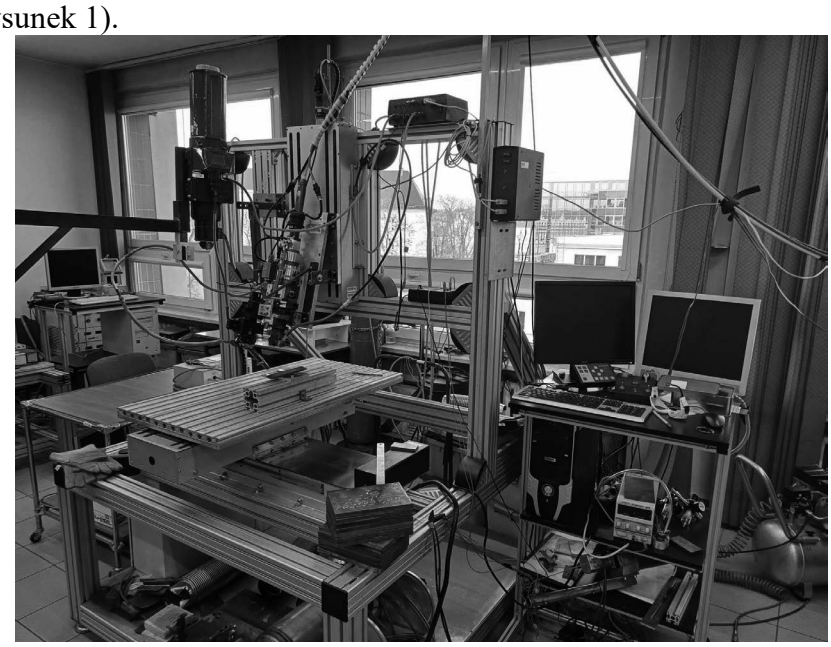

Rysunek 1. Stanowisko badawcze wyposażone w laser dyskowy Trudisk 3302 firmy Trumpf

Tabela 5. Parametry lasera dyskowego Trudisk 3302 firmy Trumpf

Znamionowa moc wyjściowa (promieniowanie ciągłe) [W]	3300
Regulacja mocy wyjściowej [W]	80-3300
Długość fali promieniowania [mm]	1030
Długość ogniskowa [mm]	200
Średnica ogniska wiązki [µm]	200
Współczynnik jakości wiązki BPP [mm/mrad]	8

Podczas napawania laserowego:
- ognisko wiązki laserowej znajdowało się 30mm nad powierzchnią,
- średnica dyszy wynosiła 1,6mm,
- proces napawania prowadzony był wielościegowo na zakładkę 35%,
- gazem osłonowym oraz transportującym był argon.

Tabela 6. Parametry z jakich skorzystano podczas napawania

Moc wiązki laserowej [W]	Prędkość napawania [m/min]	Natężenie podawania proszku [g/min]	Położenie ogniska względem przetapianej powierzchni	Proszek
1000	0,1	7	+30	Oerlikon Amdry MetcoAdd 316L-D

4. OBSERWACJE METALOGRAFICZNE

Badania mikroskopowe zostały wykonane z wykorzystaniem mikroskopu Nikon Eclipse MA100N. Zdjęcia próbki napawanej proszkiem Oerlikon Amdry MetcoAdd 316L-D przedstawiają mikrostrukturę warstwy napawanej, lini wtopienia, strefy przejściowej oraz materiału rodzimego przy powiększeniach x100, x200 oraz x500 (Rysunek 2-3).

a) 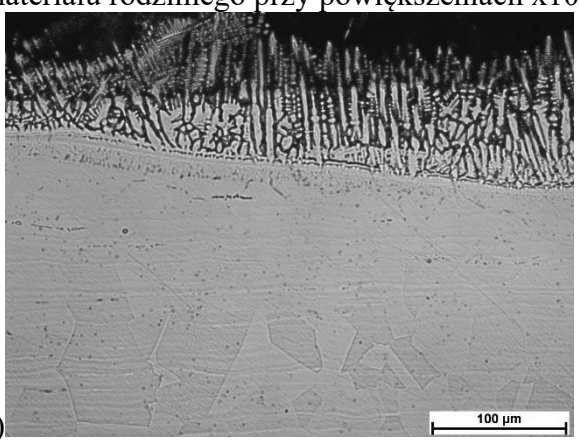

b) 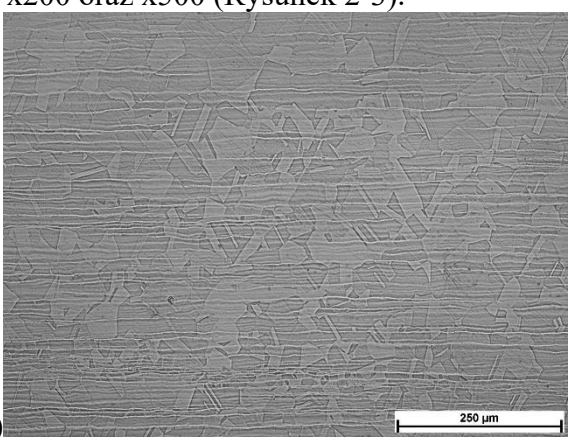

Rysunek 2. Zdjęcia mikroskopowe a) Strefy przejściowej wraz z materiałem rodzimym (x200) b) Materiału rodzimego (x100)

a) 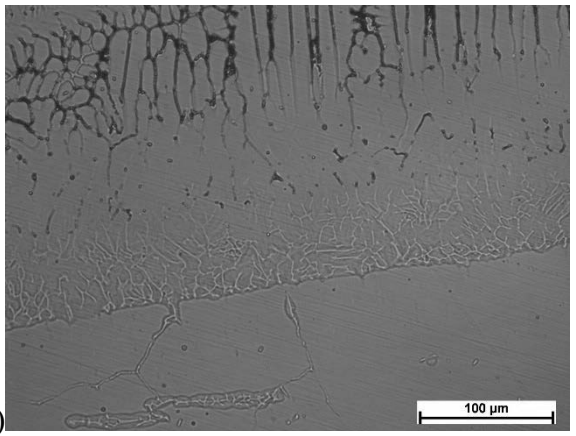

b) 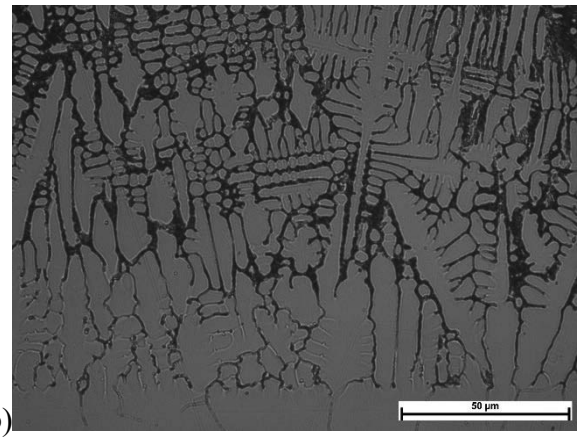

Rysunek 3. Zdjęcia mikroskopowe a) Linii wtopienia wraz ze strefą wpływu ciepła (x200) b) Linii wtopienia (x500)

5. POMIARY TWARDOŚCI

Pomiary twardości przeprowadzono na mikrotwardościomierzu FM-810. Badaniu podlegały: warstwa napoiny, strefa przejściowa oraz materiał rodzimy. Dla lica napoiny wykonano 4 , dla strefy przejściowej 2 natomiast dla materiału rodzimego 6 pomiarów. Próby wykonywane były przy obciążeniu o masie 0,2 kg oraz docisku obciążenia wynoszącym 12 sekund. Wyniki badania twardości zamieszczono w tabeli 7.

Uśrednione wyniki badań pomiaru twardości wykazały, że twardość warstwy napawanej wynosi 297 HV, SWC plasuje się na poziomie 260 HV, natomiast twardość materiału rodzimego wynosi 200 HV.

Tabela 7. Wyniki badania twardości

Pomiar	Twardość [HV0,2]
1	240
2	297
3	311
4	341
5	261
6	258
7	215
8	224
9	188
10	200
11	183
12	188

6. BADANIE SKŁADU FAZOWEGO I POMIAR NAPRĘŻEŃ METODAMI RTG

Rentgenowską analizę fazową przeprowadzono na dyfraktometrze rentgenowskim X'PERT PRO z wykorzystaniem lampy o anodzie miedzianej oraz kobaltowej (λ_{Cu} = 1,5405 Å, λ_{Co} = 1,79021 Å) zasilanej napięciem 40kV, o natężeniu prądu żarzenia 30mA. W badaniach wykorzystano detektor paskowy X Celerator po stronie wiązki ugiętej. Pomiary naprężeń analizowanej warstwy wykonano techniką $\sin^2\psi$ w oparciu o firmowy program XPert Stress Plus, który zawiera bazy danych niezbędne do obliczeń wartości stałych materiałowych. Ze względu na wykorzystany materiał podłoża oraz skład chemiczny proszku wykorzystanego do napawania na uzyskanych dyfraktogramach (Rysunek 4-5, 7-8) zidentyfikowano refleksy od Feγ dla materiału podłoża oraz refleksy od Feγ i Cr_7C_3 dla warstwy napawanej (lampa Cu i Co). Na rysunkach 6 i 9 przedstawiono nałożone dyfraktogramy zidentyfikowane dla materiału podłoża oraz napoiny dla dwóch długości promieniowania zastosowanych w trakcie badań.

Na podstawie pomiarów naprężeń (Rysunek 10-11) stwierdzono zdecydowanie wyższą wartość naprężeń ściskających w warstwie napawanej w odniesieniu do materiału podłoża. Szczegółowe wyniki pomiaru naprężeń (lampa Cu i Co, kierunek badań) zamieszczono w tabelach 8 oraz 9.

Tabela 8. Zestawienie wartości naprężeń podłoża ze stali AISI 316L w kierunku równoległym oraz prostopadłym do kierunku napawania.

Anoda lampy rentgenowskiej	Naprężenia (w kierunku równoległym do kierunku napawania)	Naprężenia (w kierunku prostopadłym do kierunku napawania)
Cu	-386,7 ± 215,2 MPa	-429,8 ± 126,4 MPa
Co	-417,9 ± 53,9 MPa	-353,3 ± 65,6 MPa

Tabela 9. Zestawienie wartości naprężeń warstwy napawanej w kierunku równoległym oraz prostopadłym do kierunku napawania.

Anoda lampy rentgenowskiej	Naprężenia (w kierunku równoległym do kierunku napawania)	Naprężenia (w kierunku prostopadłym do kierunku napawania)
Cu	-1090 ± 230 MPa	-1088 ± 197,1 MPa
Co	-1169,4 ± 109,6 MPa	-1159 ± 84,8 MPa

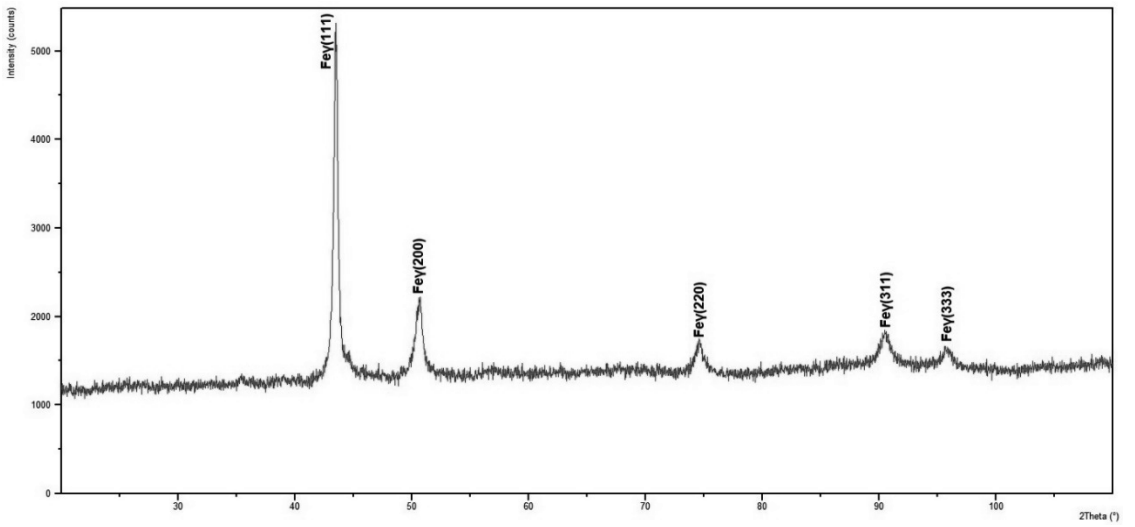

Rysunek 4. Dyfraktogram stali AISI 316L (λ_{Cu} = 1,5405 Å)

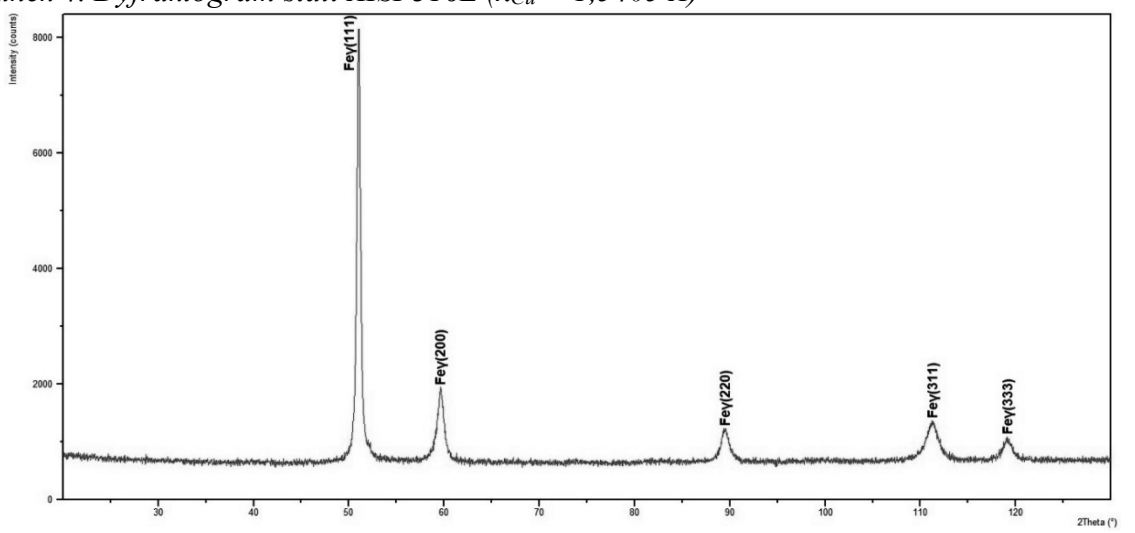

Rysunek 5. Dyfraktogram stali AISI 316L (λ_{Co} = 1,79021 Å)

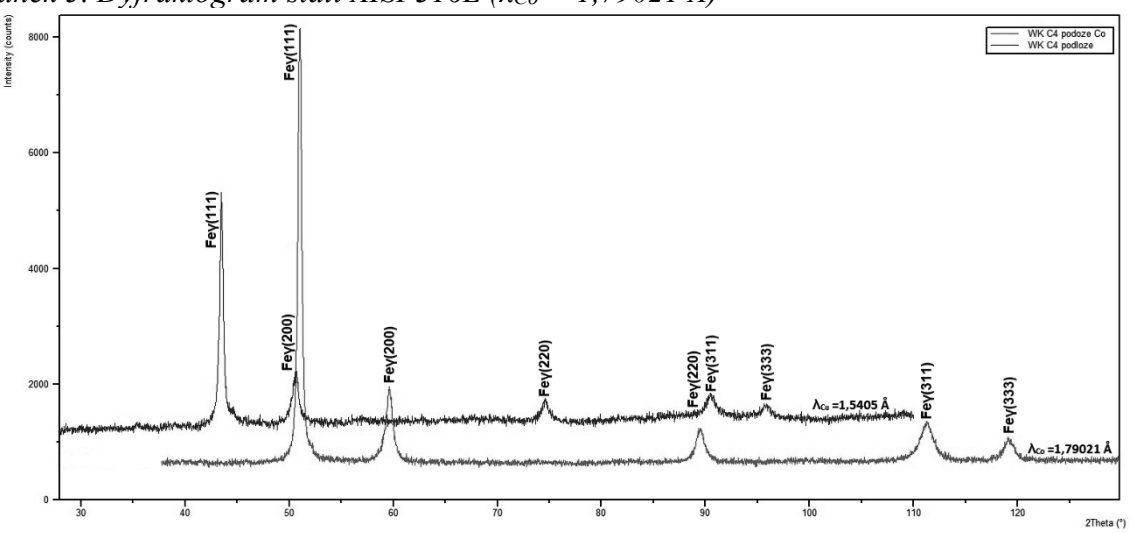

Rysunek 6. Nałożone dyfraktogramy stali AISI 316L (Lampy Cu oraz Co)

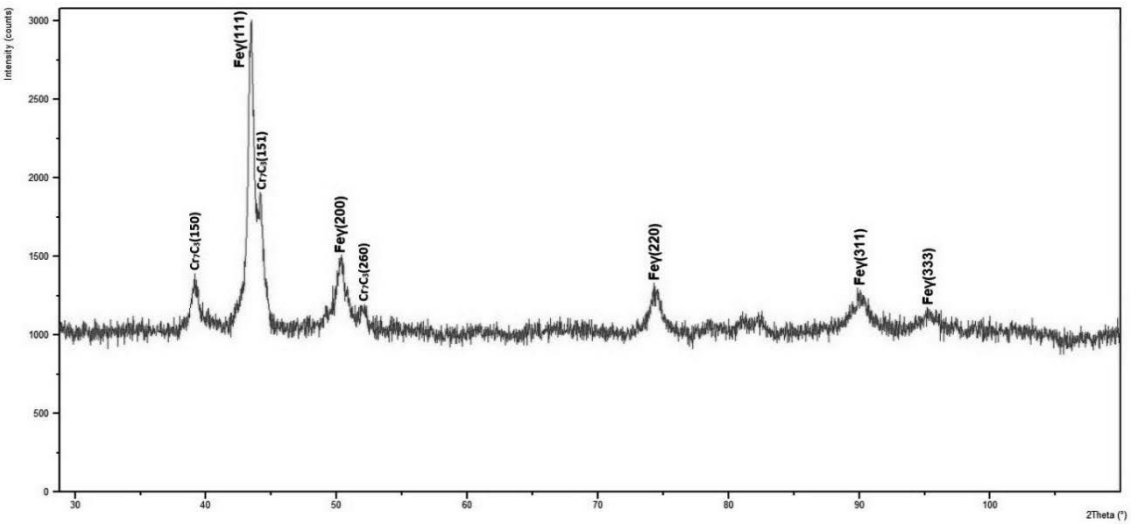

Rysunek 7. Dyfraktogram warstwy napawanej (λ_{Cu} = 1,5405 Å)

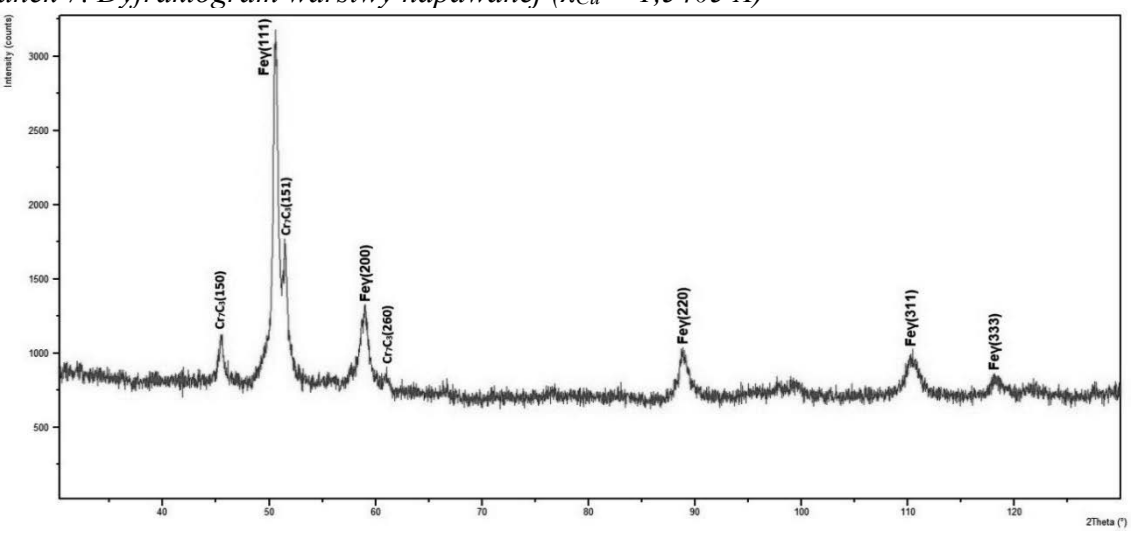

Rysunek 8. Dyfraktogram warstwy napawanej (λ_{Co} = 1,79021 Å)

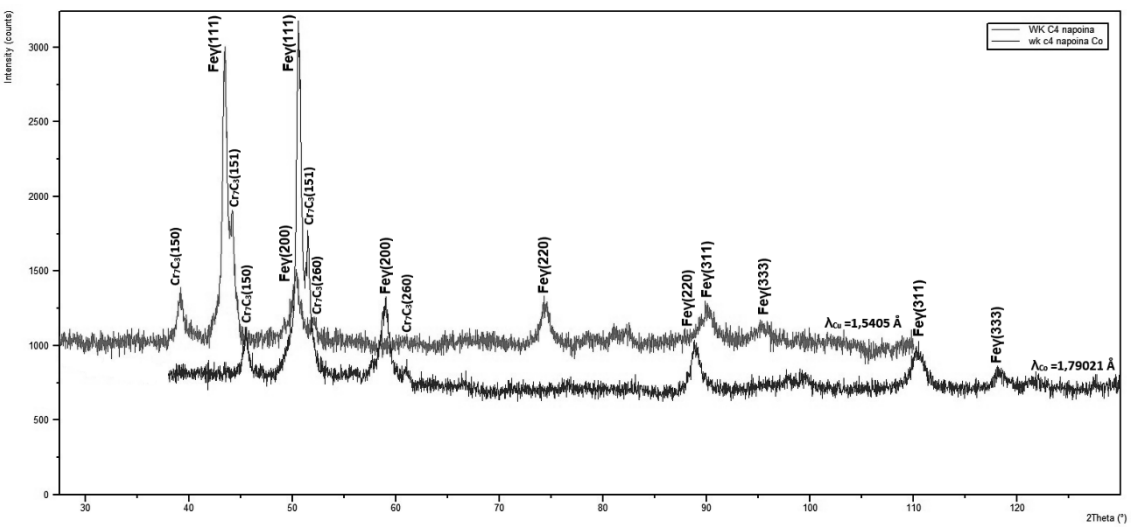

Rysunek 9. Nałożone dyfraktogramy warstwy napawanej (Lampy Cu oraz Co)

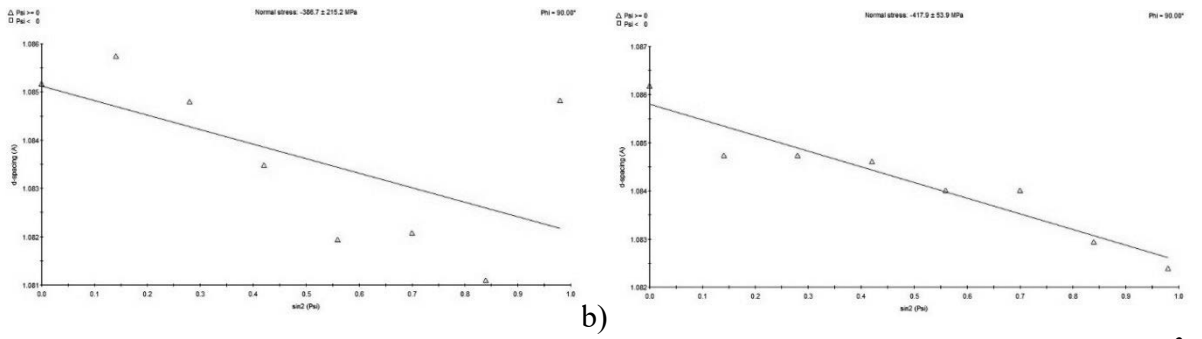

a) b)

Rysunek 10. Wykres zmian położenia refleksu Feγ (311) stali AISI 316L w funkcji $sin^2\psi$ a) zgodnie z kierunkiem napawania, λ_{Cu} = 1,5405 Å b) zgodnie z kierunkiem napawania, λ_{Co} = 1,79021 Å

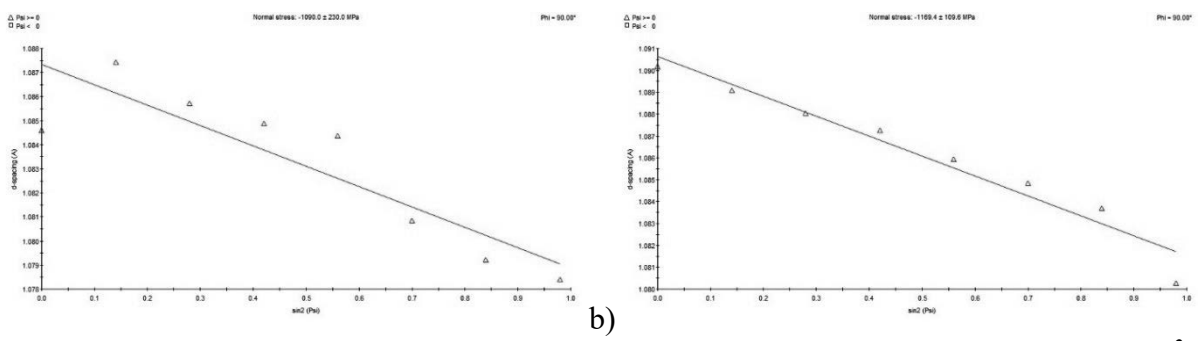

a) b)

Rysunek 11. Wykres zmian położenia refleksu Feγ (311) warstwy napawanej w funkcji $sin^2\psi$ a) zgodnie z kierunkiem napawania, λ_{Cu} = 1,5405 Å b) zgodnie z kierunkiem napawania, λ_{Co} = 1,79021 Å

7. WNIOSKI

Wyniki badań pomiaru twardości wykazały, że twardość warstwy napawanej wynosi 297 HV, SWC 260 HV, natomiast twardość materiału rodzimego wynosi 200 HV.

Badania rentgenowskie wykazały, że w strukturze analizowanej napoiny występuje Feγ oraz węgliki chromu zidentyfikowane niezależnie od anody lampy rentgenowskiej zastosowanej w trakcie pomiaru.

Na podstawie pomiarów naprężeń stwierdzono zdecydowanie wyższą wartość naprężeń ściskających w warstwie napawanej w odniesieniu do materiału podłoża.

Porównując obie długości promieniowania zastosowane podczas badań XRD można stwierdzić, że w przypadku napoiny nie stwierdzono większych różnic pomiędzy uzyskanymi rezultatami. Dla materiału podłoża wykonanego ze stali AISI 316L stwierdzono na dyfraktogramach zarejestrowanych dla lampy Co niższe wartości poziomu tła oraz zdecydowanie większe intensywności zarejestrowanych refleksów w odniesieniu do badań RTG przeprowadzonych z wykorzystaniem lampy Cu. W przypadku pomiaru naprężeń (materiał podłoża, napoina) uzyskano wyniki obarczone mniejszym błędem, przy wykorzystaniu lampy o anodzie kobaltowej.

LITERATURA

1. K. Ferenc; Spawalnictwo, 2016
2. A. Klimpel, J. Dziubiński; Technologia napawania, 1983
3. W.Chrzanowski, W.Napadłek, Z.Bogdanowicz; Analiza wpływu parametrów napawania laserowego LMD na wybrane właściwości napoin wytworzonych z proszku HS6-5-2c na stali 1.4923. Wydawnictwo: Wojskowa Akademia Techniczna im. Jarosława Dąbrowskiego, vol. 72, nr 1, 2023
4. Y.Gao, Y.Liu, L.Wang, X.Yang, T.Zeng, L.Sun, R.Wang; Microstructure evolution and wear resistance of laser cladded 316L stainless steel reinforced with in-situ VC-Cr7C3; Surface and Coatings Technology, vol 435, 15 April 2022
5. https://stalespecjalne.com.pl/oferta/stale-nierdzewne/1-4404.html ; 20.01.2025 r.
6. https://mymetco-europe.oerlikon.com/en-us/product/metcoadd316ld ; 20.01.2025 r.

TalentDetector

23th-25th June 2025
Gliwice-Brenna, Poland

DEPARTMENT OF ENGINEERING MATERIALS AND BIOMATERIALS
FACULTY OF MECHANICAL ENGINEERING
SILESIAN UNIVERSITY OF TECHNOLOGY

INTERNATIONAL STUDENTS SCIENTIFIC CONFERENCE

Optimization of engineering material selection using expert system

Ruojia Li[a], Rafał Honysz[b]

[a] Student of Mechanical Engineering, Silesian University of Technology, Faculty of Mechanical Engineering, Department of Engineering Materials and Biomaterials,
email: rl304827@student.polsl.pl
[b] Silesian University of Technology, Faculty of Mechanical Engineering, Department of Engineering Materials and Biomaterials
email: rafal.honysz@polsl.pl

Abstract: The article describes an expert system developed using Python. The system is designed to optimize the selection of engineering materials. It integrates physical, chemical, and mechanical parameters of materials with rules based on expert experience to achieve intelligent matching and recommendation of materials under specific operating conditions. Two typical case studies of engineering materials selection optimization are presented.

Keywords: Expert System; Selection of Engineering Materials; Knowledge Base; Multi-criteria decision-making; Intelligent Optimization

1. INTRODUCTION

In modern engineering design and manufacturing processes, material selection plays a decisive role in product performance, cost control, and service life. Traditional material selection relies on the personal experience and expertise of engineers, which often leads to low decision-making efficiency, weak information integration, and high subjectivity. These shortcomings make it difficult to achieve a comprehensive balance of multiple performance indicators in complex engineering environments. To address this issue, this paper proposes an expert system-based optimization method for engineering material selection. An expert system is an artificial intelligence technology that simulates the thinking process of human experts and is mainly composed of a knowledge base, inference engine, user interface, and interpreter. This system integrates the physical, chemical, and mechanical performance parameters of materials with expert experience rules to achieve intelligent matching and recommendation of materials under specific working conditions.

In this study, a database was designed using SQLite and JSON, and an expert system was developed using the Python logic programming language for optimizing engineering material selection. In this expert system, you can manage materials and make optimized selections. Two common case studies for engineering material selection optimization are presented, and the

designed expert system was used for optimization. Material options were evaluated and ranked through rule-based reasoning and weighted analysis techniques.

Experimental results show that the system can quickly and accurately recommend materials that meet design requirements across several typical engineering cases, significantly improving the scientific basis and efficiency of material selection. Additionally, the system demonstrates good scalability and maintainability, supporting dynamic updates of new material information and continuous optimization of expert rules. This research offers a new approach to intelligent material selection in the engineering field and holds broad application prospects. Future work may further incorporate machine learning algorithms to enable self-learning and optimization in the material selection process, thereby enhancing the system's intelligence and adaptability.

2. THE PURPOSE OF DEVELOPING THE EXPERT SYSTEM

The motivation behind developing this expert system originated from the growing complexity in engineering material selection, which involves balancing multiple, often conflicting, performance criteria such as tensile strength, corrosion resistance, density, and cost. In many real-world applications, engineers are faced with overwhelming amounts of data and inconsistent information, making manual selection inefficient and prone to errors.

My primary purposes in developing this expert system were:

- To digitize and automate the decision-making process of material selection using expert knowledge and real data.
- To reduce the dependence on traditional manual methods and individual experience, which are often subjective and inconsistent.
- To improve the accessibility of material knowledge for students, junior engineers, and practitioners lacking domain-specific expertise.
- To promote intelligent engineering practices, where AI-based decision systems support real-time analysis and feedback.

Moreover, I wanted to create a flexible, updatable, and user-friendly system that allows users to input their requirements, assign weights to different parameters, and get ranked material suggestions—ultimately improving both the efficiency and scientific accuracy of material selection in practical engineering.

To build the expert system, I employed the following tools:

- SQLite: This tool was used to implement the rule-based reasoning mechanism. It is particularly suitable for building expert systems due to its support for knowledge representation and inference.
- JSON: This tool is used to set rules for the database and data storage, and it can also visualize the data.
- Python (optional if used): Python is a logical language for the overall structure, using Python to incorporate all database rules and integrate information to write logic that ultimately forms the interactive page, which is the main tool in the entire expert system.

The logical framework of the expert system was designed based on a forward-chaining inference mechanism. This means:

- Facts are entered by the user (e.g., material requirements such as strength, weight, cost).
- The inference engine matches these facts with the rules in the knowledge base.
- New facts are inferred, ultimately leading to the recommendation of the most suitable material.

In the design of the expert system, I defined a series of rule-based logic conditions to simulate expert-level decision-making. These rules formed the inference engine of the system and were implemented using Python. The rule definitions included logical evaluations of user inputs against stored material data. Each rule considered:

- Minimum acceptable tensile strength
- Maximum allowable density
- Required corrosion resistance level
- Maximum budgeted cost per kilogram
- User-defined weights for each parameter.

3. DESIGNING OF THE EXPERT SYSTEM

In the past, many traditional materials were widely used in engineering, but now they are being replaced by newer ones. This change is mainly because people want lighter products and better performance. There was a time when metals were the main choice in mechanical design, and not knowing about other materials wasn't a big problem. But things have changed quickly. Now, engineers have more material options than ever before. When choosing materials, we shouldn't just stick with something like steel just because it's what we've always used. It's important to begin with a full list of possible materials. If we don't do this, we might miss better options. When looking at new materials, we need to stay open-minded. New materials can lead to better designs, new products, and improved versions of current ones with higher performance and lower cost. Usually, more than one material can work for the same use, and the final decision is a balance between pros and cons. Since there are so many materials and many factors to consider, picking the right one can be quite challenging.

Choosing the right material usually means finding the best match between the material's properties, the process used to shape it, and what the design needs. These properties and processes must work well together. A key step in material selection is understanding how the material relates to the function it needs to perform. The system supports the management and matching query of materials through the graphical interface. Database information is synchronized to materials.json files, ensuring data durability and ease of viewing. Building an expert system involves the following steps:

- Build a database(by SQLite and Json)
- Code Construction(by Python)
- Generate interactive page(by Tkinter module built-in with Python)
- Optimization of engineering material selection(By Designed Expert System)

The Expert System for Optimization of Engineering Material Selection is a desktop application designed to help engineers, students, and designers select the right engineering materials based on mechanical and economic criteria. It also displays all existing materials in the database, and can be added, edited, and deleted through interactive pages. It uses a weighted scoring system to recommend the best matching materials from a database of 50+ commonly used engineering materials (fig.1).

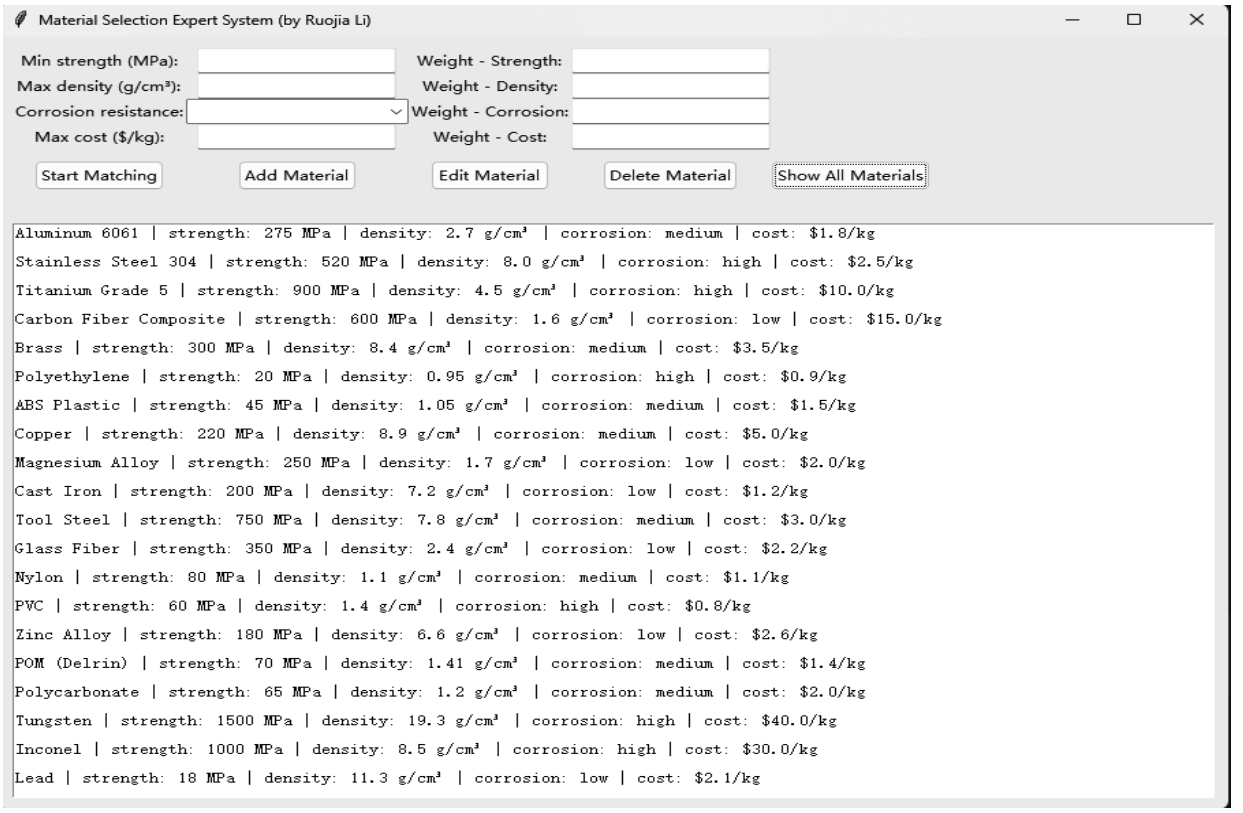

Figure 1. A list of some material properties included in database

4. APPLICATION EXAMPLES

4.1. Material optimization for aluminum table legs (with strength calculation)

When optimizing the material for the legs of an aluminum table, the goal is to find a balance between strength, weight, stability, cost, and appearance. Since the tabletop is made of aluminum, the legs should ideally match it in style and performance. However, using pure aluminum may not always be the best choice, so optimization involves exploring better or more suitable options.

Information for the case table:

- Table type: Engineering aluminum table Tabletop
- Size: 1200 mm × 600 mm
- Tabletop weight (including items): 50 kg
- Number of table legs: 4
- Maximum static load each table leg needs to bear (including safety factor of 1.5):

$$F = \frac{50 \times 9.81 \times 1.5}{4} \approx 184N$$

Assuming the table leg is a hollow circular tube structure (common design), with the following dimensions:

- Outer diameter D = 30 mm
- Wall thickness t = 2 mm

- Material: 6061-T6 aluminum alloy
- Length L = 720 mm

Critical buckling load (using Euler's buckling theory):

$$P_{cr} = \frac{\pi^2 EI}{(KL)^2} \qquad E = 69Gpa \qquad K = 1 \qquad I = \frac{\pi(D^4 - d^4)}{64} \qquad d = D - 2t = 26mm$$

Calculations :

$$I \approx 17380mm^4 \qquad P_{cr} \approx 720N$$

The safety load of 720 N is much greater than the actual load of 184 N, meeting the strength and stability requirements, with a sufficient safety factor. And Then We use the Designed Expert System to opzimite the material selection For the use of everyday chairs, the material strength has the largest weight. The weight of density is as large as the proportion of corrosion resistance and the proportion of cost:

- Strength: 35 – for a table to carry a table top + books + items, it must be structurally stable and not deformed, but the load is usually lower than of a chair.
- Density (Weight): 15 – the legs must be stable and not wobbly or collapse. It is a guarantee of basic safety and functionality.
- Corrosion-resistance: 25 – in household environments, where there is frequent exposure to moisture or beverages, corrosion resistance can extend service life, especially in kitchens or balconies.
- Cost: 25 – due to the large size of the table and the large amount of materials, cost control is more important, so the cost weight is slightly higher than that of the chair.

According to the expert system, we found that Aluminum 7075 is the most suitable material for the table (fig 2):

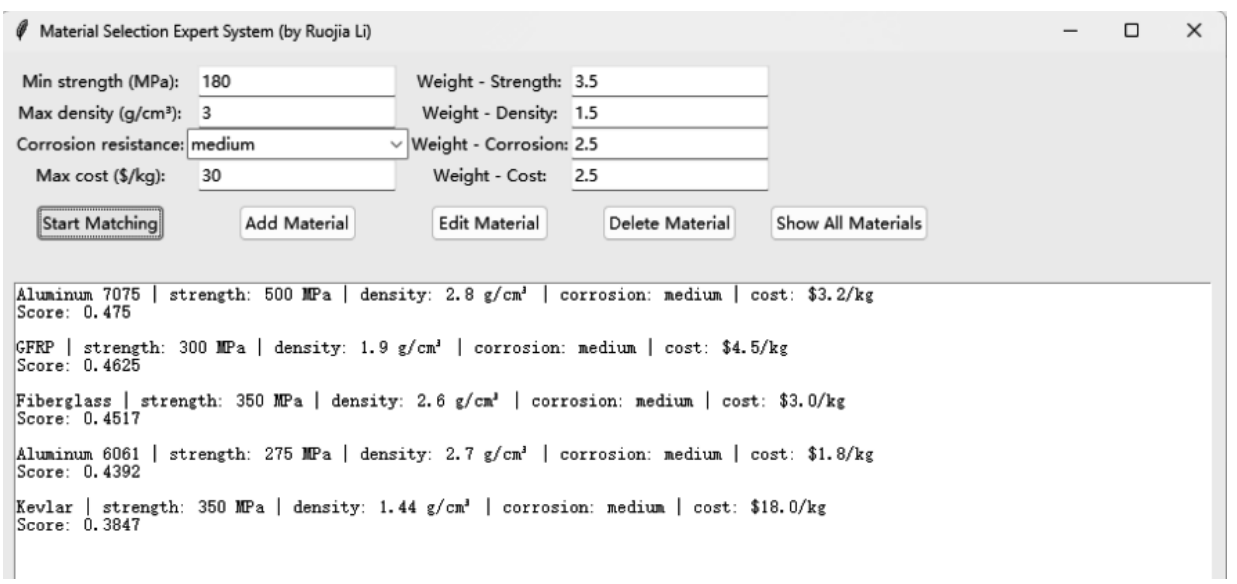

Figure 2. Optimization of materials selection of chairs

4.2. Material Optimization for Selection of materials for drone body.

Select a material as the main structural material (airframe) for the drone, balancing the following key indicators:

- Strength: High
- Cost: The lower, the better
- Corrosion Resistance: At least medium

Candidate materials from the database (with strength calculation). We have selected materials that meet the following criteria:

- Strength ≥ 100 MPa (ensure structural rigidity)
- Density ≤ 5.0 g/cm³ (lightweight)
- Corrosion Resistance: At least medium
- Moderate cost(considering mass production)

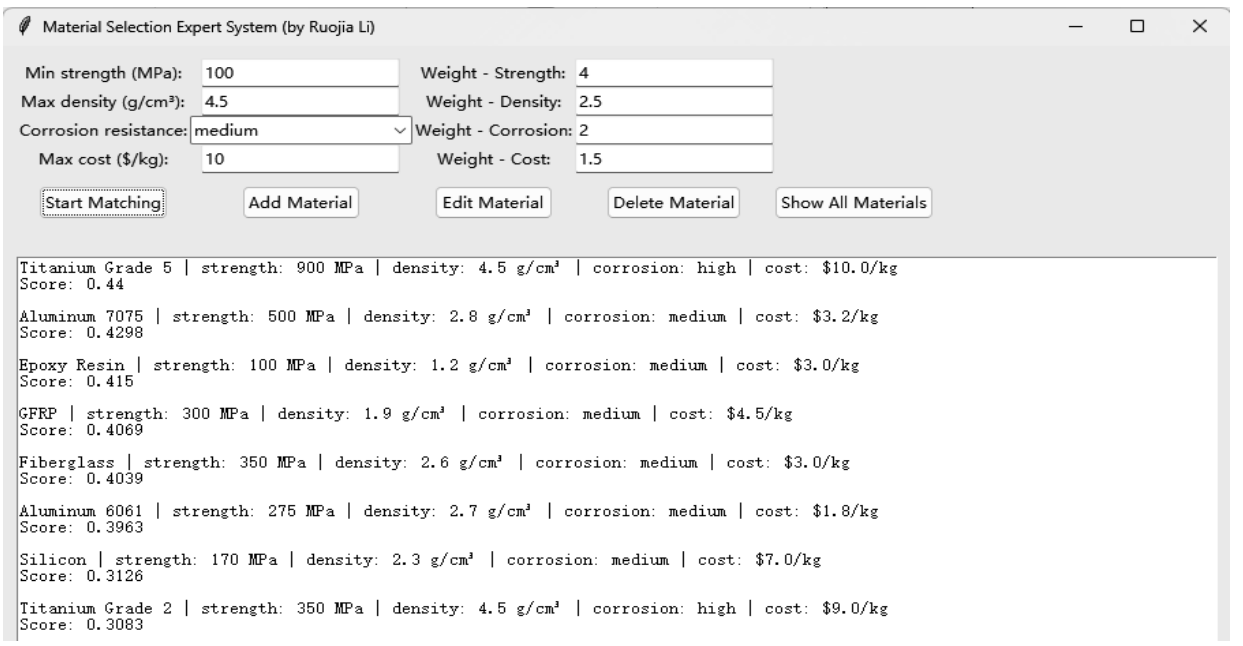

Figure 3. Optimization of materials selection of drone body

According to the analysis from the above expert system, Titanium Grade 5 is the most suitable material for the fuselage of drones.

5. CONCLUSION

In this paper, the research content mainly focuses on improving the engineering material selection process through expert systems. After comparing with traditional ways such as manually searching for materials by experience and rules of thumb, it was found that these ways do not take into account some important factors such as environment and durability in the long term, which will inevitably lead to an increase in costs in the later stage of engineering and finally cause the failure of the project. For example, if only the strength is emphasized when choosing

the skin material of the aircraft but its fatigue resistance is ignored, then it will inevitably lead to unsafe consequences.

An expert system can make full use of various kinds of data (such as mechanical performance, cost, sustainability) plus logical inference algorithms to evaluate materials more comprehensively. The improved sequence quadratic programming algorithm has been used for raw material selection in complex industrial uses, reducing the total decision-making time by more than 40%.

Furthermore, it was found that the advantages of using expert systems are obvious when there are contradictions among objects, such as battery supplier selection for electric vehicles. The relationship between them is balanced by the system, while conventional methods have difficulty finding a solution due to fragmented or incomplete information. Similar projects conducted in the construction industry calculated the embedded carbon emissions for different materials and helped the company reduce the carbon emission of its concrete mix by 22% without compromising structural strength.

However, there were some shortcomings regarding applying the expert system: delaying updating knowledge would affect accuracy; for example, adding a new polymer material like organogel conductors (with good stretchability) into the knowledge base would be ignored although it was the best option.

Nonetheless, experts said that since green innovation projects such as photovoltaic building materials had rich datasets, the utilization of expert systems using fuzzy decision-making methods could still identify feasible low-carbon solutions. And the application results differed according to their applications' types. For instance, when evaluating high-voltage power transmission equipment selections, the accuracy reached 96%. But when applied to nanocomposite-related projects, the value was about 78%, probably because the number of involved parameters increased.

Another interesting case would be using the experts' systems to support simulation of hydrogen-based steelmaking routes to forecast energy consumption to help policymakers search for de-carbonization solutions. They demonstrated that experts' systems could not only reach faster decisions but may also help narrow some knowledge gaps between different subjects; i.e., transferring medical techniques such as knowledge graphs into materials fields will improve more efficiently titanium alloy's process knowledge bases. Finally, they illustrated their work's useful contribution by confirming another multi-criteria-making idea: e.g., in assisting with the shortest period narrowing one underground pumped storage power station site from 15 best-fit selections by specialists' advisors, despite heavy dependency on the nature and quantity of input facts about them being still dominant.

Some material standard expert systems could apply better multi-criteria-decision-modes-assist functions if utilizing real-world cases; such evidence came out at last during evaluating studies performed about sustainability in rural spaces over China or establishing new battery standards as New energy electric cars. Therefore, we confirmed this study showing how critical and relevant AI material science is today among other things besides proving more examples exist where it may already be applied successfully together in complex engineering projects.

The next work can continue to deeply develop in many aspects. For example, although the expert system has realized material selection, it may be more favourable when combined with artificial intelligence. The existing database of materials should also be expanded.

BIBLIOGRAPHY

1. L.A. Dobrzański, R. Honysz, The idea of material science virtual laboratory, Journal of Achievements in Materials and Manufacturing Engineering 42/1-2 (2010) 196-203.
2. Liu Yiming, et al. Machine Learning for Perovskite Solar Cells and Component Materials: Key Technologies and Prospects. Adv Funct Mater 33(17), 2023.
3. Wang Xinyi, et al. Performance of ChatGPT on the Chinese national medical licensing examination. Journal of medical systems, 2023, 47(1): 86.
4. Nafei A, Amirhossein A Z, Smarandache F. Neutrosophic autocratic multi-attribute decision making strategies for building material supplier selection[J]. Buildings, 2023, 13(6): 1373.
5. Huan Xu, et al. Mainstream optimizing strategies of cathode materials for sodium-ion batteries. Small Structures 3.4:2100217 (2022)
6. Qishuang W, Zhou C. A multi criteria decision making scheme to select the manufacturer of electric vehicles (EVs) by Chinese Government departments and Public Authorities[J]. Environmental Science and Pollution Research, 30(4):10540–10559.
7. He X, et al. An optimization model of a selected raw material process for the complex industry with the improvement of sequential quadratic programming algorithms[J]. International Journal Of Computational Intelligence Systems, Ijcis.ISSN:1875-6883.103.
8. Guo L, Liang J Q, Shi G H, et al. Automatic Building of the Machining Process Knowledge Base from a Knowledge Graph[C], Springer International Publishing.
9. Urrea C, Henríquez G, Jamett M. Development of an expert system to select materials for the main structure of a transfer crane designed for disabled people[J]. Expert Systems with Applications, 2015, 42(1): 691–697.
10. Wang, Zhuo, et al. Data-driven materials innovation and applications. Advanced Materials 34.36 (2022): 2104113.
11. Yuan Zheng, et al. Application of multi-criteria decision-making analysis to rural spatial sustainability evaluation: A systematic review. International Journal of Environmental Research and Public Health. 19(11): 6572. 2022.
12. Xiao Q, et al. Plant Metabolomics: A New Strategy and Tool for Quality Evaluation of Chinese Medicinal Materials. Chinese Medicine. 2022;17(1):45.
13. Gao, Chaochao, et al. Innovative materials science via machine learning. Advanced Functional Materials 32.1 (2022): 2108044.
14. Liu Liu, et al. Akb-48: A real-world articulated object knowledge base. In Proceedings of the IEEE/CVF Conference on Computer Vision and Pattern Recognition 2022.
15. Masood SH, Soo A. A rule based expert system for rapid prototyping system selection[J]. Robotics and Computer-Integrated Manufacturing, 2002, 18(3–4): 267–274.
16. Wang Xiaochen, Wang Siyi. Exploring Chinese EFL learners' engagement with large language models: A self-determination theory perspective. Learning and Motivation, 87, 2024, 102014.
17. Xuan Liu, et al. Adaptation of Feature Selection Algorithms for Classification of Chinese Text. Systems 11(9), 2023, p.483.
18. Khan M. I., Siddiquee A. N., et al. An expert system prototype for material selection in aerospace structures[J]. Advances in Materials Science and Engineering, 2020
19. Kar A. Expert System for Process Selection and Operation Optimization[D]. University of Maryland, 1986.
20. Altay, İ. R.. Development of an Expert System for Corrosion Resistant Material Selection. Master's Thesis, Middle East Technical University.,1998
21. Kumar A, Singh R, Singh R. Genetic Algorithm-Based Data-Driven Process Selection System for Additive Manufacturing in Industry 4.0[J]. Materials, 2024, 17(18): 4544.

TalentDetector
23th-25th June 2025
Gliwice-Brenna, Poland
DEPARTMENT OF ENGINEERING MATERIALS AND BIOMATERIALS
FACULTY OF MECHANICAL ENGINEERING
SILESIAN UNIVERSITY OF TECHNOLOGY
INTERNATIONAL STUDENTS SCIENTIFIC CONFERENCE

Analysis of the Influence of Mold Temperature on the Physical Properties of Low-Density Polyethylene

Mateusz Lis[a], Katarzyna Młynarek-Żak[b]

[a] Silesian University of Technology, Faculty of Mechanical Engineering, Nanotechnology and Materials Technology Scientific and Didactic Laboratory
[b] Silesian University of Technology, Faculty of Mechanical Engineering, Department of Engineering Processes Automation and Integrated Manufacturing Systems
email: mateusz.lis@polsl.pl

Abstract: The aim of this study was to investigate the influence of mold temperature on the mechanical properties and crystalline structure of low-density polyethylene (LDPE). For the experiments, samples were injection molded at mold temperatures of 50 °C, 60 °C, and 70 °C. Tensile tests and thermal analysis using Differential Scanning Calorimetry (DSC) were performed. The results showed that an increase in mold temperature leads to a decrease in tensile strength. The highest tensile strength (10.95 MPa) was recorded for samples molded at 50 °C. Total elongation was highest for the 60 °C series. The DSC analysis revealed slight differences in the degree of crystallinity – the highest (46.7%) was observed for samples molded at 70 °C. The results indicate that mold temperature affects the mechanical properties of LDPE, while its impact on the degree of crystallinity is relatively minor.

Keywords: mold temperature, LDPE, tensile strength, crystallinity.

1. INTRODUCTION

Low-density polyethylene (LDPE) is widely used in industries such as packaging, electrical engineering and the production of everyday consumer goods [1]. It offers good mechanical properties, high flexibility and excellent chemical resistance. Its molecular structure, characterized by branched chains, makes LDPE especially sensitive to variations in processing conditions, which in turn affects the physical properties of the molded parts [2]. Therefore, it is essential to investigate the impact of injection molding parameters on the end-use properties of LDPE products. In polymer processing, mold temperature is one of the key technological parameters determining the quality and properties of the final products. This parameter must be carefully considered during process optimization, as it significantly affects the material's microstructure, the dimensional accuracy of mold reproduction and the residual stresses formed during processing. Mold temperature is particularly critical in the case of semi-crystalline polymers, where differences in crystallization behavior can directly influence the final performance characteristics of the product [3, 4].

The aim of this study is to analyze the influence of mold temperature on selected mechanical properties of injection-molded parts made from LDPE. The study uses standardized specimens, conforming to norms relevant to tensile testing of polymers.

2. MATERIALS AND RESEARCH METHODOLOGY

The subject of the research was low-density polyethylene (LDPE) of the Resinex PE RXP 1002 NATURAL grade, in the form of a micrometric powder, with a melt flow index (MFI) of 22 g/10 min.

The materials for testing were produced using a twin-screw micro extruder EHP 15 by Zamak Mercator and a mini injection molding machine IM 15 by Zamak Mercator. In the extruder, the tested polymer was plasticized and homogenized, after which the polymer melt was transferred to the plasticizing system of the injection molding machine, which was maintained at a temperature of 180 °C. The material was then injected into a mold heated to 50 °C, 60 °C and 70 °C. The injection time of the material into the mold was 10 seconds, which was sufficient to counteract the injection shrinkage effect. Test specimens were prepared according to the dimensions specified in the PN/EN ISO 527-2:2012 standard – type 1BA. The samples were then subjected to tensile testing using a Zwick/Roell Z020 universal testing machine, with a crosshead speed of 50 mm/min and an initial grip separation of 30 mm, 10 measurements were performed for each temperature series.

To evaluate the influence of mold temperature on the crystalline structure of the low-density polyethylene, Differential Scanning Calorimetry (DSC) measurements were carried out using a DSC Q2000 instrument by TA Instruments. The mass of the analyzed samples ranged from 10 to 23 mg. Samples were conditioned at 10 °C and the heating process ended upon reaching 180 °C. The tests were conducted in an argon atmosphere, at a heating rate of 10 °C/min. The results of the analysis were recorded as a function of (W/g)/temperature. The enthalpy of melting related to the loss of crystalline structure served as the basis for determining the degree of crystallinity.

3. RESEARCH RESULTS

The results of tensile strength tests performed on standardized specimens made from low-density polyethylene (LDPE) are presented in Figure 1. Based on the obtained data, it was concluded that the technological parameter of mold temperature influences the mechanical properties under investigation.

The highest tensile strength was observed in the series of samples molded at the lowest mold temperature, i.e., 50 °C, with a maximum value of 10.95 MPa. It was noted that tensile strength decreases as mold temperature increases. Specifically, the tensile strength dropped by 4.3% for samples molded at 60 °C, and by 5% for those molded at 70 °C, compared to the reference at 50 °C. The lowest total elongation was recorded for the samples molded at 70 °C, with a value of 155.9%. The highest total elongation was observed for the samples molded at 60 °C, showing a 21% increase compared to the 70 °C series. For the samples molded at 50 °C, total elongation was 13.2% higher than that of the series produced at the highest mold temperature (70 °C).

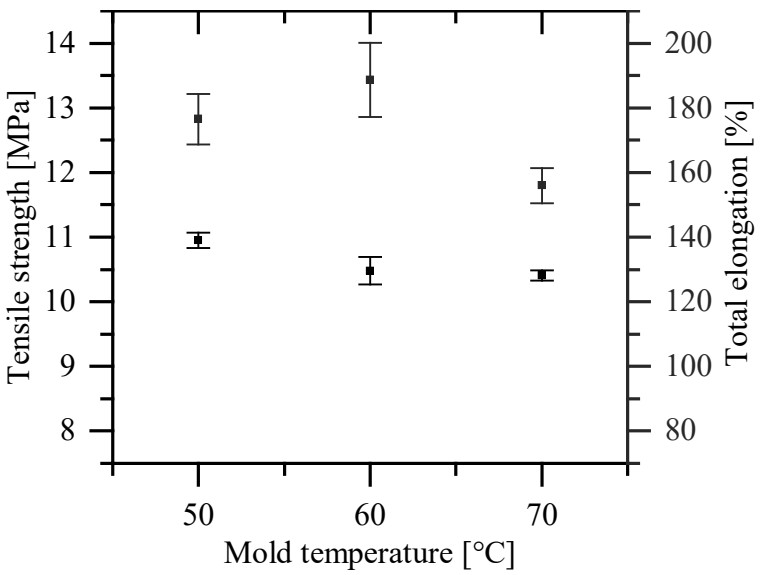

Figure 1. Graph of tensile strength and total elongation as a function of mold temperature

Table 1 presents the results of measurements obtained using Differential Scanning Calorimetry (DSC) for low-density polyethylene (LDPE) samples molded at different mold temperatures. Based on the conducted analysis, it was found that the lowest degree of crystallinity was observed in the samples molded at 60 °C, while the highest crystallinity was recorded for the samples molded at 70 °C. However, the difference between these two series is only 2% (0.9 percentage points). The melting temperature of the crystalline phase was the same for the samples molded at 60 °C and 70 °C, but was 1.4 °C lower (1.3%) for the series of samples molded at 50 °C.

Table 1. Effect of mold temperature on the melting temperature and degree of crystallinity of low-density polyethylene

Mold temperature [°C]	Melting temperature [°C]	Melting enthalpy [J/g]	Degree of crystallinity [%]
50	107	132.4	46.2
60	108.4	131.4	45.8
70	108.4	134	46.7

3. SUMMARY

The aim of the study was to determine the influence of mold temperature on the mechanical properties and crystalline structure of injection-molded samples made from low-density polyethylene (LDPE) and test specimens were produced at three different mold temperatures: 50 °C, 60 °C and 70 °C. Tensile test results showed that increasing mold temperature leads to a decrease in tensile strength. The highest tensile strength (10.95 MPa) was recorded for specimens molded at 50 °C. At 60 °C and 70 °C, tensile strength decreased by 4.3% and 5%, respectively. In terms of total elongation, the highest value was observed for the 60 °C series, while the lowest was recorded for specimens molded at 70 °C. Differential Scanning Calorimetry (DSC) analysis

revealed that the highest degree of crystallinity (46.7%) was observed in samples molded at 70 °C, while the lowest (45.8%) was at 60 °C. However, the differences between these values were minor (0.9 percentage points). Based on conducted study, it was found that mold temperature affects the mechanical properties of LDPE, with lower mold temperatures enhancing tensile strength. However, the influence on the degree of crystallinity is relatively small.

The presented research was carried out as part of the Development of Research Potential project No. 10/110/BKM25/0092 BKM-701/RTL2/2025, funded by the Silesian University of Technology.

BIBLIOGRAPHY

1. C. Leyva-Porras, A. Balderrama-Aguilar, Y. Estrada-Ávila, I. Espelosín-Gómez, M. Mendoza-Duarte, C. Piñón-Balderrama, M. Zenaida Saavedra-Leos, I. Estrada-Moreno, Injection Molding of Low-Density Polyethylene (LDPE) as a Model Polymer: Effect of Molding Parameters on the Microstructure and Crystallinity, Polymers 13 (2021) 3597.
2. K. Chrissafis, D. Bikiaris, Can nanoparticles really enhance thermal stability of polymers? Part I: An overview on thermal decomposition of addition polymers, Thermochimica Acta, Volume 523, 2011.
3. P. Zengeya, K. Mao, V. Goodship, The effects of cooling rate (mould temperature) on HDPE gears produced through injection moulding, Wear, Volumes 530–531, 2023.
4. Dejian Zou, Tongmin Yu, Chunzheng Duan, The role of mold temperature in changing molecular chain morphology of flowing melt, Applied Surface Science, Volume 572, 2022.

TalentDetector
23th-25th June 2025
Gliwice-Brenna, Poland
DEPARTMENT OF ENGINEERING MATERIALS AND BIOMATERIALS
FACULTY OF MECHANICAL ENGINEERING
SILESIAN UNIVERSITY OF TECHNOLOGY
INTERNATIONAL STUDENTS SCIENTIFIC CONFERENCE

Microstructural and chemical characterisation of norfloxacin

Paulina Lukaszkowicz[a], Tiara Ogórek[a], Ewa Adamek[b], Wojciech Baran[b], Magdalena Szindler[c], Klaudiusz Gołombek[d]

[a] Medical University of Silesian in Katowice, Faculty of Pharmaceutical Sciences in Sosnowiec, Student Scientific Club at the Department of Inorganic Chemistry
email: s86990@365.sum.edu.pl; s87046@365.sum.edu.pl
[b] Medical University of Silesian in Katowice, Faculty of Pharmaceutical Sciences in Sosnowiec, Department of Inorganic Chemistry
email: eadamek@sum.edu.pl; wbaran@sum.edu.pl
[c] Silesian University of Technology, Faculty of Mechanical Engineering, Department of Engineering Materials and Biomaterials
email: magdalena.szindler@polsl.pl
[d] Silesian University of Technology, Faculty of Mechanical Engineering, Materials Research Laboratory
email: klaudiusz.golombek@polsl.pl

Abstract: The research subject was the microstructural and chemical characterisation of norfloxacin. The compound was characterised using scanning electron microscopy (SEM), energy-dispersive spectroscopy (EDS), and Fourier transform infrared spectroscopy (FTIR) for morphological, chemical composition, and functional group studies, respectively.

Keywords: norfloxacin, SEM, EDS, FTIR

1. INTRODUCTION

Since the discovery of penicillin by Alexander Fleming and its use in industrialisation, commercialisation and pharmacotherapy, many other groups of antibiotics have been discovered [1]. These substances have become common remedies for diseases caused by bacteria, mycoplasmas and chlamydia. They have also found their use in industry, animal husbandry and aquaculture [2, 3]. Different groups of these substances are used in antibacterial therapy. We can divide antibiotics by origin (natural, synthetic) or mechanism of action. By mode of action, we distinguish between antibiotics that inhibit cell wall synthesis (β-lactam antibiotics), inhibit protein synthesis (aminoglycoside antibiotics, macrolide antibiotics), disrupt cell membrane function (polypeptide antibiotics), inhibit specific biochemical processes (sulfonamides) and inhibit DNA synthesis (fluoroquinolones) [4].

Fluoroquinolones (FQs) are synthetic chemotherapeutics with a broad spectrum of biocidal activity. They are commonly used to treat infections in humans and animals. FQs work by

inhibiting two key bacterial enzymes—gyrase (topoisomerase II) and topoisomerase IV—which play important roles in DNA replication, transcription, recombination, and repair. Currently, pharmacotherapy mainly uses second-, third-, and fourth-generation fluoroquinolones [5].

Norfloxacin (NOR), or 1-ethyl-6-fluoro-4-oxo-7-piperazine-1-ylquinolin-3-carboxylic acid, is a nalidixic acid derivative belonging to the second generation of fluoroquinolones. The structure of this drug is a modification of the 4-quinoline system, to which a piperazine ring was added at the C-7 position and a fluorine atom at the C-6 position (Fig. 1). Thanks to this modification, there is an increased penetration of the drug into the bacterial cell and then its binding to the GryA-DNA complex (DNA gyrase) and ParC-DNA (topoisomerase IV). In the NOR molecule, functional groups are important for its activity, i.e., a carboxyl group at the C-3 position and a ketone group at the C-4 position. Their presence is essential for the formation of drug-enzyme-DNA complexes. The discovery of NOR became a turning point in synthesising new drugs from the FQ group [6].

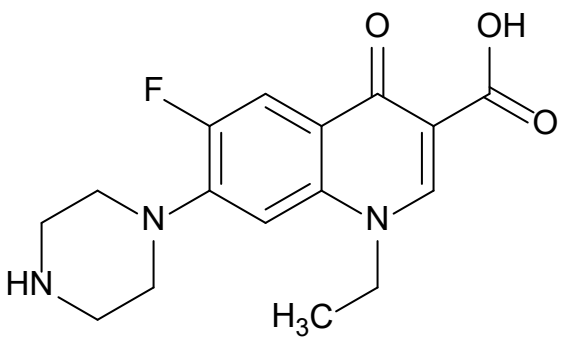

Figure 1. Structure of norfloxacin

2. MATERIALS AND METHODS

The material used for the study was norfloxacin ($C_{16}H_{18}FN_3O_3$), a drug from the fluoroquinolone group. The compound was used in the study in solid form (powder). The norfloxacin was characterised using scanning electron microscopy (SEM) and Fourier transform infrared spectroscopy (FTIR) techniques. FTIR analysis was performed by a Nicolet 6700 FTIR spectrophotometer (Thermo Scientific). The spectra were recorded in absorption mode using ATR (Attenuated Total Reflection) in the 500 to 4000 cm^{-1} region with 2 cm^{-1} resolution. The morphology and chemical composition of the norfloxacin were examined using a high-resolution scanning electron microscope (SEM) HRSEM SUPRA 35 by Zeiss, equipped with an EDS detector. The accelerating voltage was in the range of 10-20 kV. A secondary electron detector SE and a backscatter electron detector BSE were used for the study. Chemical composition analyses in micro-areas were performed using the EDS detector with Pathfinder software.

3. RESULTS AND DISCUSSION

The SEM study found that norfloxacin powder particles exhibit a regular shape similar to a cuboid (Fig. 2). The particle size of norfloxacin varies, ranging from several micrometres to about 250 μm. The chemical composition tests performed using the EDS detector confirmed the

presence of individual elements included in the analysed material. The results of the EDS analysis of the chemical composition demonstrate the high chemical quality of norfloxacin. The presence of carbon may be related to the phenomenon of contamination (Fig. 3).

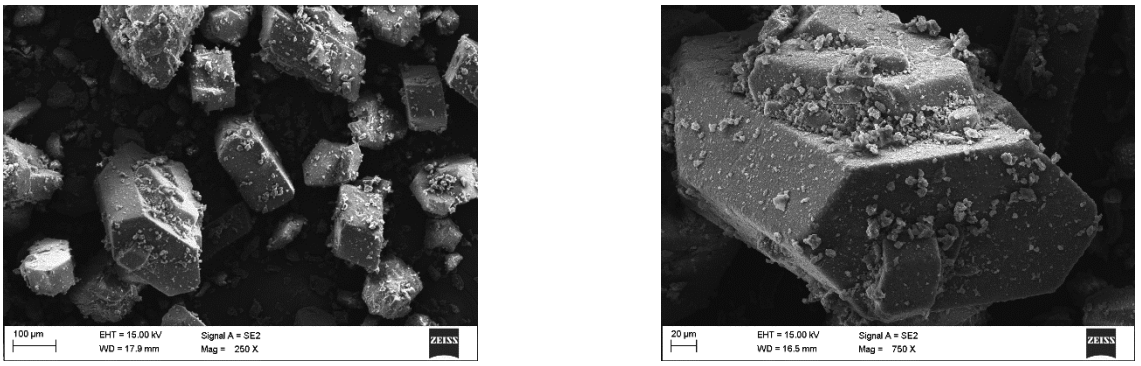

Figure 2. SEM surface morphology image of norfloxacin

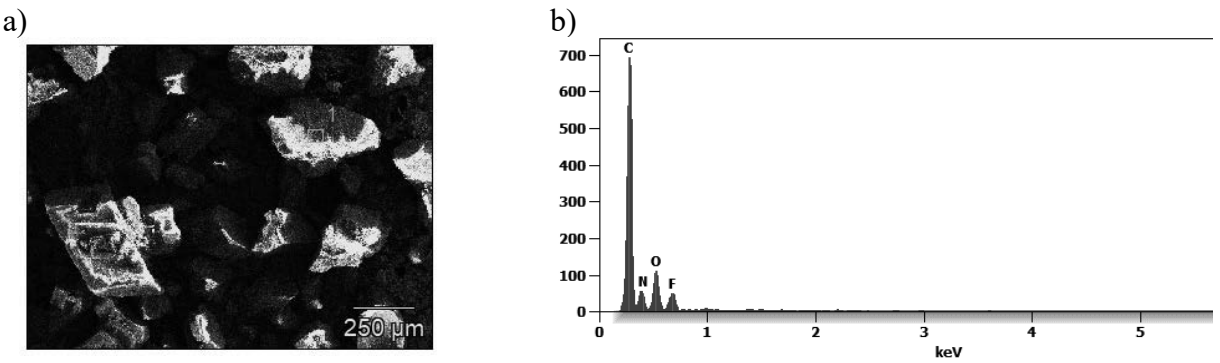

Figure 3. Norfloxacin particles: a) surface morphology image (SEM), b) EDS spectrum of the area as in fig. a

The FTIR spectrum obtained from norfloxacin shows all the characteristic peaks of the investigation material (Fig. 4).

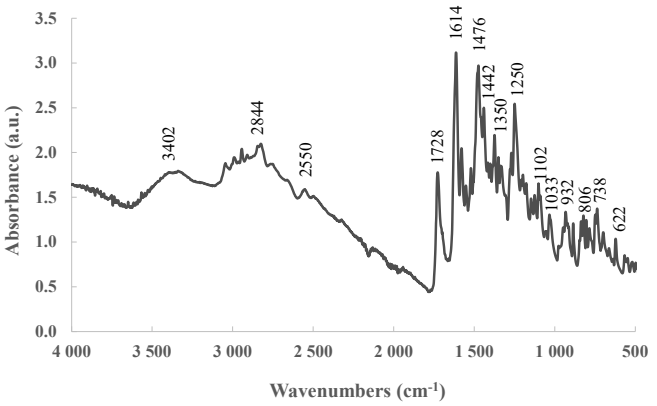

Figure 4. FTIR spectra of norfloxacin

The registered spectrum, at a wavenumber from 3500 to 3300 cm^{-1}, shows a band of stretching vibration bonds for NH. The infrared peak intensity at 2844 and 2550 cm^{-1} corresponds to asymmetric and symmetric CH_2 stretch. Another absorption band at 1728 and 1350 cm^{-1} was observed, corresponding to the C=O and C-O stretching vibrations. The peak at 1614 cm^{-1} should be assigned to the N-H bending vibration of quinolones. The peaks in the region 1500-1250 cm^{-1} represented the stretching vibration of the O-C-O group and the bending vibration of the O–H group. The absorption band between 1050 and 1000 cm^{-1} was assigned to the C–F group [7, 8].

4. CONCLUSION

The comprehensive SEM, EDS, and FTIR investigation results show that norfloxacin particles are characterised by sizes ranging from tens to hundreds of nanometers and high chemical purity. The studied material contains functional groups typical of norfloxacin. Scanning electron microscopy, EDS, and FTIR spectroscopy can be used in the pharmaceutical field to analyse the chemical composition, surface topography, and impurities in the studied materials.

BIBLIOGRAPHY

1. S. Zheng, Y. Wang, C. Chen, X. Zhou, Y. Liu, J. Yang, Q. Geng, G. Chen, Y. Ding, F. Yang, Current progress in natural degradation and enhanced removal techniques of antibiotics in the environment: A review, International Journal of Environmental Research and Public Health 19/17 (2022) 10919.
2. M. Bilal, S. Mehmood, T. Rasheed, H.M.N. Iqbal, Antibiotics traces in the aquatic environment: persistence and adverse environmental impact, Current Opinion in Environmental Science & Health 13 (2020) 68-74.
3. F. Wang, J. Gao, W. Zhai, J. Cui, D. Liu, Z. Zhou, P. Wang, Effects of antibiotic norfloxacin on the degradation and enantioselectivity of the herbicides in aquatic environment, Ecotoxicology and Environmental Safety 208 (2021) 111717.
4. A. Adler, D.E. Katz, D. Marchaim, The continuing plague of extended-spectrum β-lactamase-producing Enterobacteriaceae infections, Infectious Disease Clinics of North America 30/2 (2016) 347-375.
5. W. Janiec (red.), Kompendium farmakologii, Wydawnictwo Lekarskie PZWL, Warszawa, 2011.
6. National Center for Biotechnology Information. PubChem Compound Summary for CID 4539, Norfloxacin. https://pubchem.ncbi.nlm.nih.gov/compound/Norfloxacin [retrieved May 10, 2025].
7. S. Sahoo, C.K. Chakraborti, P.K. Behera, S.C. Mishra, FTIR and Raman spectroscopic investigations of a norfloxacin/carbopol934 polymeric suspension, Journal of Young Pharmacists 4/3 (2012) 138-145.
8. S. Chaturvedi, V.K. Agarwal, A. Verma, N. Verma, S. Singh, Comparative evaluation of natural and semi-synthetic superdisintegrants in the formulation of oro-dispersible tablets of norfloxacin, International Journal of Pharmacy and Pharmaceutical Sciences 4/3 (2012) 576-583.

TalentDetector

23th-25th June 2025
Gliwice-Brenna, Poland

DEPARTMENT OF ENGINEERING MATERIALS AND BIOMATERIALS
FACULTY OF MECHANICAL ENGINEERING
SILESIAN UNIVERSITY OF TECHNOLOGY

INTERNATIONAL STUDENTS SCIENTIFIC CONFERENCE

Organization of the CNC machine operator's position

Marcin Majnusz[a], Martyna Gawlas, Aneta Kania[b], Magdalena Polok-Rubiniec[b], Anna Włodarczyk-Fligier[b]

[a] Student of Engineering and Material Technologies, Silesian University of Technology, Faculty of Mechanical Engineering
email: mm303344@student.polsl.pl
[b] Silesian University of Technology, Faculty of Mechanical Engineering, Department of Engineering Materials and Biomaterials
email: aneta.kania@polsl.pl

Abstract: The article presents the organization of the production station in company X to increase ergonomics and work safety. The analysis includes the use of FMEA (Failure Mode and Effects Analysis) method, which allowes the identification of critical places and design of a two-stage operator protection system in the form of a safety curtain and safety buttons. As a result of the implemented changes, the production line was improved, safety at the production station was increased and employee absenteeism caused by accidents at work was reduced.

Keywords: work safety, FMEA analysis, two-stage safety system, safety curtain, safety buttons

1. INTRODUCTION

Modern production plants strive to maximize efficiency while ensuring safety and comfort of work. The organization of the production work position plays a key role in achieving these goals. A well-designed workstation allows not only to increase the efficiency of the process, but also to minimize the risk of accidents. Proper adaptation of the work position to requirements of ergonomics and occupational health is an indispensable factor that has a direct impact on the comfort and safety of operators. Work safety is one of the key aspects that must be taken into account when designing work stations, especially in the automotive industry, where technological and regulatory requirements change dynamically.

In this work, the assembly station was analyzed and evaluated, and optimal health and safety measures were designed, taking into account both ergonomic and technical aspects. The implementation of a safety curtain and safety buttons allows for a significant reduction in the risk of accidents, increasing operator safety.

2. ORGANIZATION AND SAFETY OF WORK POSITIONS

The organization of workstations plays an important role in the enterprise, and the key resource of every organization is human capital [1]. Effective planning of the workstation requires the proper combination of safety measures and appropriate methods of their use, what allows the implementation of tasks in an optimal and effective manner [2,3].

The aim of well-organized assembly stations is to achieve high efficiency, which has a positive impact on both the efficiency and the quality of the operations performed. The key role is played by the appropriate arrangement of elements that the employee must have under control or he has interaction.

Occupational safety is an important element in organizational management, especially in sectors related to human-robot collaboration, where the risk of accidents or incidents is increased. Identification of all hazards that may occur at the workplace and effective risk assessment are the foundation for building a safe environment for employees and minimizing potential losses for the company. Designing a safe workplace where the employee has constant contact with devices of increased risk is a great challenge. The correct application of appropriate safety standards and directives is extremely important [4-6].

When organizing a work position, it is also necessary to analyze all the loads that may occur during work. The workstation should enable the employee to perform work while maintaining a natural body posture. Improper design of the workstation can lead to many problems, including musculoskeletal system diseases or eye diseases. For this reason, an important factor is the organization of the work position adapted to physical, biomechanical and psychophysical needs of the employee [7,8].

3. FMEA ANALYSIS FOR A SELECTED WORK POSITION

Company X decided to focus on the complete elimination of the risk related to human errors and the consequences of accidents at work. In accordance with the FMEA (Failure Mode and Effects Analysis) methodology, the highest risk indicator (RPN – Risk Priority Number) was determined (Tab. 1). In order to eliminate the risk at the selected workstation, FMEA analysis was performed (Tab. 2). The analysis was performed on a workstation requiring the cooperation of an operator with an industrial robot.

Table 1. Criteria for risk analysis

RPN = O · S · D					
Occurrence	**O**	**Severity**	**S**	**Detection**	**D**
Does not occur	1	Imperceptible	1	Certain	1
Very slight	2-3	Minor effects	2-3	Large	2-3
Insignificant	4-6	Moderate effects	4-6	Significant	4-6
Moderate	7-8	Serious consequences	7-8	Slight	7-8
Frequent	9-10	Critical effects	9-10	Very low	9-10

Table 2. FMEA sheet for the operator's position

No.	Stage of the process	Function	Type of failure	Effect of failure	Cause	Current status				Remedial measures
						O	S	D	RPN	
1	Loading of parts	Placing parts in the molds	Operator enters the robot's work area	Risk of collision with the robot, accident at work	Lack of physical access protection, operator staying in the robot's work area	9	5	5	**225**	Safety curtain installation
2	Transport of parts by the robot	Transport of parts from the mold to the CNC machine	Inadequate gripping of the part by the robot	Damage to the part	Inadequate calibration of the gripper, failure of the loading mechanism	7	4	4	112	Regular calibration of the gripper
3	Machining on a CNC machine	Precision machining of parts	Dimensions not in accordance with requirements	Incorrect machining parameters	Incorrectly written program, tool failure	7	4	5	140	Regular checking of the CNC program
4	Washing of parts	Cleaning of parts	Insufficient cleaning of the surface	Incorrect parameters	Lack of automatic control, failure of the washing system	5	4	4	80	Optimization of washer parameters
5	Drying of parts	Drying of parts	Lack of proper drying	Damage of transport rollers	Too short drying time, material deformation	5	4	4	80	Adding humidity sensors
6	Transport to quality control	Transport of parts on transport rollers	Blockage of part on the line	Contamination of transport rollers	Lack of flow monitoring, inappropriate transport conditions	5	3	5	75	Regular cleaning of transport rollers
7	Quality control	Evaluation of detail quality	Missing product defects	Fatigue, routine or lack of experience	Lack of vision system, too large tolerances	7	4	4	112	Implementation of the vision system

4. TWO-STAGE SECURITY SYSTEM

4.1. Safety curtain

Based on the results of the FMEA analysis, the area with the highest risk of collision was identified. The greatest risk occurred at the stage of loading parts into the molds. A decision was made to implement a safety curtain. The frame and housing of the curtain were made of stainless steel, which is perfectly suited to an environment with increased humidity. Powder coating was carried out in the warning color – orange "RAL 2000". The protective profiles were made of aluminum, ensuring lightness, corrosion resistance and resistance to damage. Then, infrared transmitting diodes and receivers were selected, which in the event of a beam interruption send information to the robot control station. The protective screens, which are designed to protect the diodes and receivers from dirt and damage, were made of tempered glass (Fig. 1).

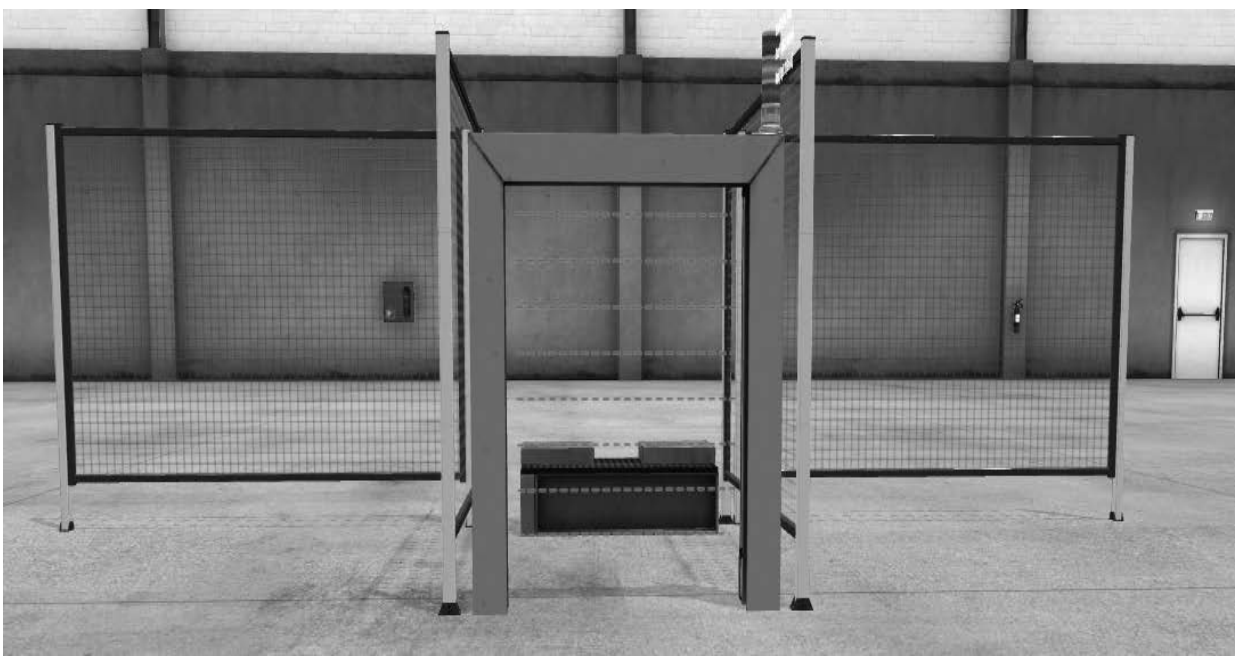

Figure 1. Safety curtain (drawing made in Factory IO)

4.2. Safety buttons

The design of the safe workstation has been enriched with buttons that play an important role in ensuring the operator's safety (Fig. 2):

- the red button signals, through illumination, exceeding the safety zone caused by the interruption of the sensor beam. Information is provided directly to the operator's table, where the buttons are located. In this case, the robot changes its operating mode, interrupting its activities and providing protection to the operator.
- the green button is intended to inform the machine that the operator has left the dangerous zone of the robot's work. The operator must press the green button to resume the robot's work. If the button is not pressed, the robot remains in the stopped state.

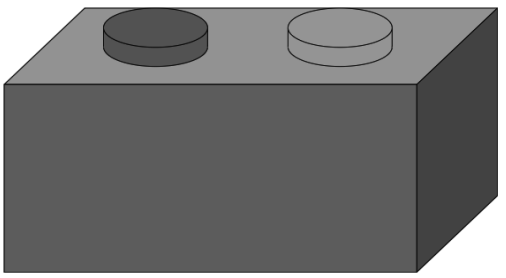

Figure 2. Security buttons – side view (drawing made in Microsoft Visio)

The two-stage safety system at the analysed work position, consisting of a light curtain and safety buttons, supports operators in their work, eliminating the risk of a serious accident. Even in the event of a failure of one of the elements, the system provides protection to the operator, due to two independent levels of protection. The operating principles of the system are presented below (Fig. 3):

– The first stage of the system is a safety curtain, which uses light beams to monitor the dangerous area of the robot's work. In the event of an interruption of the light beam, a red button is illuminated on the operator's table, signaling an intrusion into the robot's work zone, and the machine's operation is automatically stopped. The light curtain area has been designed in such a way that the information is sent immediately, thanks to the low response time of 20 ms.
– Leaving the detection zone by the curtain should be confirmed with the green button located on the operator's table. This is an additional safeguard, thanks to which the robot cannot start its work until the operator confirms his presence at the work position. This process is enriched with mutual interlocks which, after receiving information from the light curtain and signaling with the green safety button, allow the robot to resume work.

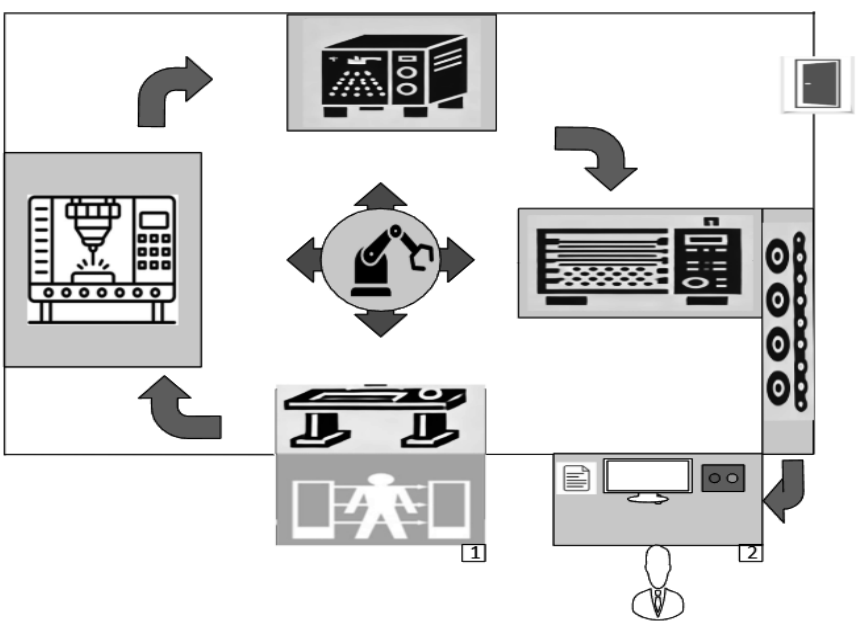

Figure 3. Technological process with proposed improvements, 1 – safety curtain, 2 – safety buttons.

5. CONCLUSIONS

Modernizations at the operator's station were proposed and implemented based on the results of the FMEA analysis. It concerned the possibility of collision between the operator and the robot during assembly of parts into molds. That indicated the need to introduce appropriate safeguards and changes at the workstation. After a thorough risk analysis, it was decided to modernize the work position and implement the two-stage safety system in the form of a protective curtain and safety buttons, which will minimize the possibility of human errors and potential accidents at work. The safety system project was developed taking into account all important ergonomic aspects, including: providing support to the operator in daily duties, maintaining the correct body posture of the operator, increasing the comfort of work performed. Engineering solutions minimize the risk of injuries resulting from repetitive movements and statistical load.

Adherence to the above-mentioned recommendations can contribute to achieving success in the automotive industry, as well as a significant reduction in the number of accidents at work.

BIBLIOGRAPHY

1. J. Pyka, Organization and sustainable management of the work environment; https://www.gwsh.pl/content/biblioteka/org/zeszyty/ag/zn12/ZN12AG_15Pyka.pdf, 2025.
2. P. Kiełbasa, P. Budyn, K. Klamka, F. Kadłuczka, K. Nalepa, Ergonomic evaluation of the geometry of the workstation, Agricultural Engineering 11 (2007) 93-100.
3. P. Kalinowska, A. Polak-Sopińska, A. Mączewska, Ergonomic analysis of the assembly station, Scientific Papers of the Małopolska University of Economics in Tarnów 3/39 (2018) 67-83.
4. PN-EN ISO 12100:2012. Machinery Safety – General Design Principles – Risk Assessment and Risk Reduction, PKN, Warsaw, 2012.
5. J.R. Etherton, Industrial machine systems risk assessment: A critical review of concepts and methods, Risk Analysis: An International Journal 27/1 (2007) 71-82.
6. P. Krupa, P. Gawłowicz, Computer-aided design of a safe robot workstation, Scientific Papers of Poznan University of Technology. Organization and Management (2017) 1-8.
7. K. Byrska-Bienias, M. Zemczak, The use of augmented reality in shaping job positions, in. Innovations in production management and engineering, Polish Society for Production Management 2 (2017) 435-446.
8. K. Jach, M. Kuliński, Basics of ergonomic work station, LAB Laboratories, Equipment, Research 15 (2010) 30-32.

TalentDetector

23th-25th June 2025
Gliwice-Brenna, Poland

DEPARTMENT OF ENGINEERING MATERIALS AND BIOMATERIALS
FACULTY OF MECHANICAL ENGINEERING
SILESIAN UNIVERSITY OF TECHNOLOGY

INTERNATIONAL STUDENTS SCIENTIFIC CONFERENCE

Studies on performance properties of CrN coating obtained by PVD on austenitic steel surface X2CrNiMo17-12-2

Tobiasz Markowicz[a], Jakub Pluskota[a], Beniamin Sobczak[a], Petr Jánský[b], Anna Smetanova[b], Michal Lattner[c], Antonin Kříž[c], Daniel Pakuła[d], Marcin Staszuk[d]

[a] Student of Silesian University of Technology, Faculty of Mechanical Engineering, Konarskiego 18A, 44-100 Gliwice, Poland
email: tm307633@student.polsl.pl, jp307654@student.polsl.pl, bs308653@student.polsl.pl
[b] Student of Jan Evangelista Purkyně University in Ústí nad Labem, Faculty of Mechanical Engineering, Pasteurova 3544/1, 400 96 Ústí nad Labem-město, Czech Republic
email: petr.jansky3@gmail.com, Smetanova.ana@seznam.cz
[c] Jan Evangelista Purkyně University in Ústí nad Labem, Faculty of Mechanical Engineering, Pasteurova 3544/1, 400 96 Ústí nad Labem-město, Czech Republic
email: Michal.Lattner@ujep.cz, antonink1970@gmail.com
[d] Silesian University of Technology, Faculty of Mechanical Engineering, Department of Engineering Materials and Biomaterials, Konarskiego 18A, 44-100 Gliwice, Poland
email: daniel.pakula@polsl.pl, marcin.staszuk@polsl.pl

Abstract: This article was written as a part of a PBL project. It investigates the performance properties of CrN coating deposited by physical vapor deposition (PVD) on 316L austenitic steel. Tribological properties were tested using ball-on-plate method. Wear mechanisms were analyzed using contact profilometer and scanning electron microscopy (SEM). Topographical studies were conducted using atomic force microscopy (AFM). Scratch test, fretting test, and Rockwell test were also conducted.

Keywords: 316L, Tribology, PVD, CrN, SEM, AFM, Scratch test, Fretting test, Rockwell test

1. INTRODUCTION

Stainless steel, due to high corrosion and wear resistance, good mechanical properties and ability to adapt to different environments, has a wide range of applications in many areas of not only engineering, but also everyday life [1,2].

One of the representatives of this steel grade is 316L steel (X2CrNiMo17-12-2), which is used in the transportation and petrochemical industries and is also often applied in biomedical engineering. This steel owes its very good corrosion resistance to its high chromium content, which supports the formation of a protective passive layer on the substrate surface. In addition to chromium, nickel is also important, thanks to which the austenite structure is stabilized,

resulting in 316L steel having a single-phase austenitic structure. Other characteristics of this steel are also very good mechanical properties and weldability [3-7].

However, 316L steel also has its disadvantages. Due to its low carbon content, the steel has a low hardness, which also affects its susceptibility to abrasion and scratching, resulting in weaker mechanical properties, increased susceptibility to wear and limiting its use at high temperatures. Another disadvantage of 316L stainless steel, which significantly affects its use, is also its poor tribological properties. In order to improve the individual properties of 316L steel, its surface is coated with appropriately selected coatings. One of these is the CrN coating [4,8,9].

The application of CrN chromium nitride coatings is now a widely used method of changing the surface properties of components such as machining and forging tools, casts, as well as various mechanical components. Numerous studies carried out on this coating have shown that its application largely improved the corrosion resistance of the coated parts and provided a reduction in the coefficient of friction. CrN coatings provide good adhesion on iron-based alloys, high microhardness and a significant improvement in wear resistance [10-13].

The aim of this research is to investigate the performance properties of PVD coatings deposited on 316L austenitic steel substrates.

2. MATERIALS AND METHODOLOGY

Base material used in tests was austenitic stainless steel 316L. Rods with diameter of 20 mm were cut into slices roughly 7 mm thick and prepared for coating by grinding and polishing. Suitably prepared substrates were then coated with CrN coating in PVD process.

Tribological properties of coated and uncoated substrates were tested using tribometer from CSM Instruments using ball-on-plate method with parameters shown in table 1.

Table 1. Parameters used for the study of tribological properties

Sample number	Substrate	Coating	Parameters				
			Number of cycles	Normal load [N]	Path [mm]	Acquisition rate [Hz]	Linear speed $\left[\frac{cm}{s}\right]$
1	316L	-	20000	7.5	6	10	10
2		CrN					
3		-		10			
4		CrN					

Tests were conducted in temperature 25°C and humidity of 50%. Counter-sample used in tests was a tungsten carbide ball with a diameter of 6mm.

Paths created during tests were measured with Tayler Hobson Surtronic profilometer.

The scratch test was conducted using Revetest RST^3 machine from Anton Paar. Scratches were made while applying force linearly increasing from 1 N to 100 N and from 1 N to 200 N.

Wear mechanisms were also tested using fretting test method. Parameters used during tests are shown in table 2. Tests were conducted for substrates with CrN coating and for test samples with no coating. Tungsten carbide ball with a diameter of 6mm was used as a counter-sample.

Table 2. Parameters used for the fretting test

Sample	Substrate	Coating	Speed [cm/s]	Load [N]	Test duration [min]
1	316L	-	5	2	13
2		CrN			120

Adhesion of a coating was tested using Rockwell method, in which coating is pierced with an indenter, after creating the indentation, the evaluation follows by assigning an adhesion and cohesion rating to the indentation according to figure 1, where K parameter evaluates cohesion of the coating and A parameter its adhesion.

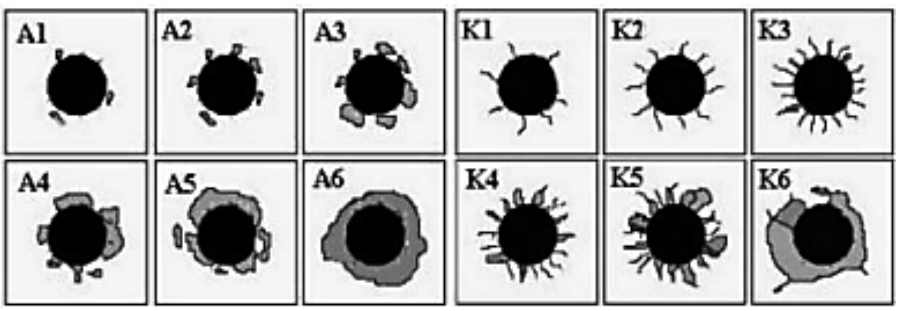

Fig. 1. Evaluation of thin film damage around the indentation.

Tests were conducted using three different shape indenters and different load values. Used parameters and number of indentations is shown in table 3.

Table 3. Parameters used for the Rockwell test

Label	Load [kp]	Number of indentations
HRA	60	3
HRB	100	
HRC	150	

Wear mechanisms which took place during tests were investigated using scanning electron microscopy SEM using EHT voltage of 15 kV at magnifications ranging from 20 to 5000 times and using secondary electron (SE) detectors. Chemical composition analysis of certain areas was conducted using X-ray energy dispersive spectroscopy EDS.

3. RESULTS

Study of surface topography of the coating was conducted using scanning electron microscopy SEM and atomic force microscopy AFM (Fig. 2). It shows typical chromium nitride CrN coating obtained in PVD process topography, there also are some craters which are production defects and some scratches which are residues from process of surface preparation by grinding and polishing.

a) b)

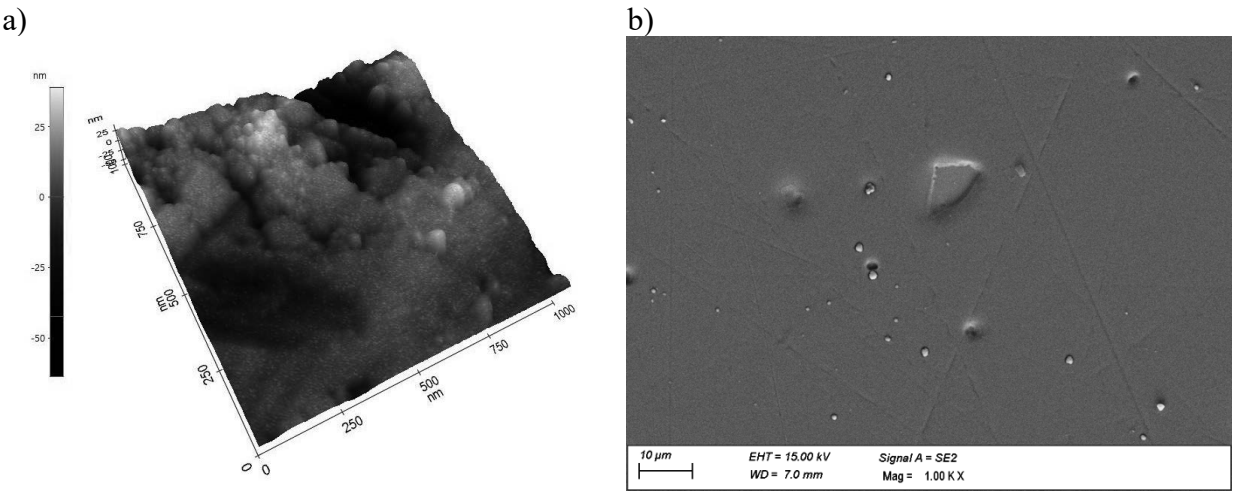

Fig. 2. CrN coating topography a) AFM [13], b) SEM.

Figure 3 shows graphs of the change in friction coefficient μ as a function of the number of cycles (20000) for the uncoated surface (a) and the CrN-coated surface (b). Two levels of normal load were considered for each case: 7.5 N (green) and 10 N (red).

The coefficient of friction for the uncoated surface increases steadily in the initial cycles from 0 to 6000, after which it reaches a value of about 0.65-0.75. For 7.5 N, the coefficient of friction is initially lower (about 0.5), but over time approaches the level observed at 10 N. For 10 N, the coefficient of friction reaches high values more quickly (0.7-0.8), indicating stronger tribological wear.

The initial increase in the coefficient of friction for the coated surface is similar to that for the uncoated surface but reaches a lower level of approximately 0.6-0.7. For 7.5 N, the coefficient of friction initially increases rapidly, but quickly stabilizes at a level of approximately 0.6-0.65. For a force of 10 N, the coefficient of friction is greater than 7.5 N and reaches a value of approximately 0.7-0.75.

a) b)

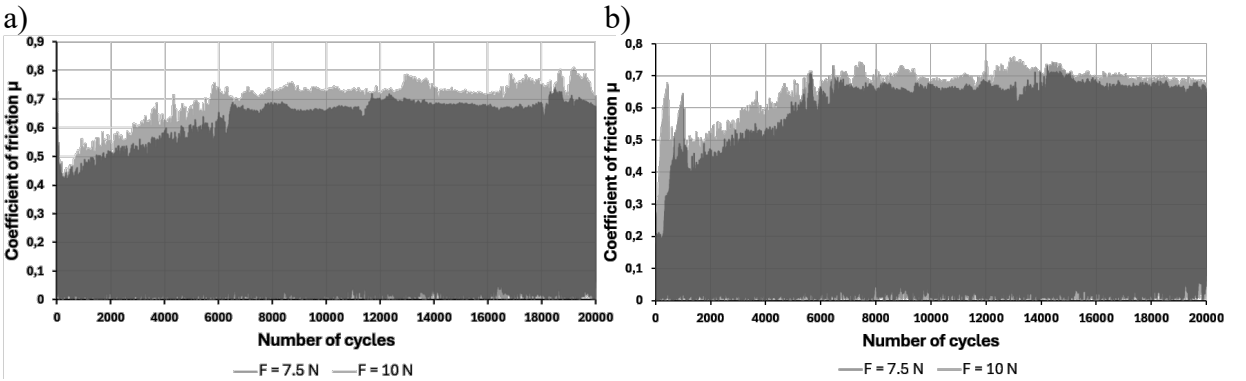

Fig. 3. Friction coefficient as a function of the number of cycles for the steel substrate a) uncoated, b) coated.

Measurements done with contact profilometer show that in case of substrates with CrN coating the change in load used in tests on a tribometer from 7.5 N to 10 N resulted in significant increase in depth of the wear trace by about 30 μm. Wear profile for steel substrates are shown in figure 4.

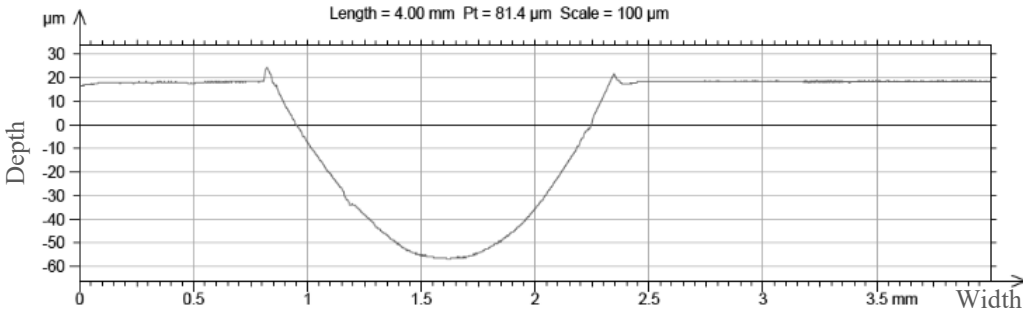

Fig. 4. Profile of steel with coating received from contact profilometer measurements, normal load 10 N.

Table 4 summarizes the average area and volume of the wear section for all steel substrates. Figure 5 illustrates the comparison of the wear volumes of all substrates.

Both the area and volume of the cavities are smaller for the coated substrates (2 and 4) than for the uncoated substrates (1 and 3), clearly indicating the effectiveness of the CrN coating in reducing wear. The highest volume reduction was recorded for sample 3 (uncoated, 10 N) - 0.431 mm^3. The smallest was recorded for sample 2 (CrN, 7.5 N) - 0.257 mm^3.

The effect of the load is significant. Increasing the normal force from 7.5 N to 10 N results in a clear increase in the wear volume, regardless of the presence of the coating. The CrN coating reduces volumetric wear by approximately 14% for 7.5 N and 9% for 10 N relative to uncoated substrates.

Table 4. Average area and volume of cavities created on steel samples

Sample number	Coating	Normal load [N]	Area [mm^2]	Volume [mm^3]
1	-	7.5	0.050	0.298
2	CrN		0.043	0.257
3	-	10	0.072	0.431
4	CrN		0.065	0.391

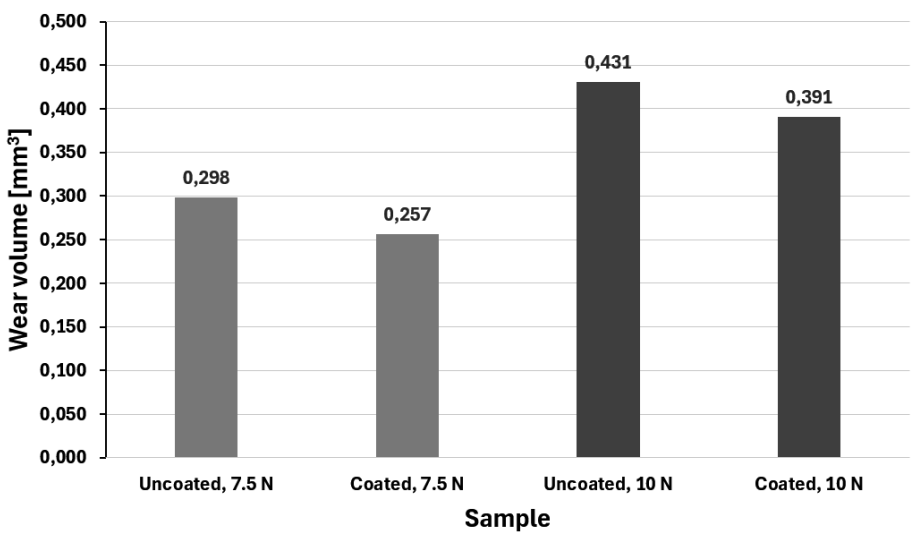

Fig. 5. Comparison of surface wear volume of steel samples for different normal loads.

Studies of surface topography of wear traces obtained in test using load of 7.5 N and 10 N were conducted using SEM (Fig. 6). They show expected damage to the coating. Wear mechanisms were the same and showed no change when the load was changed. Studies done using EDS confirmed that the coating was worn through, showing presence of iron (area x2) which came from the base material. Spectroscopy conducted for area which appears to be white (area x2) showed that it has oxidized during testing. In that area there are also some reflexes from tungsten which most likely comes from tungsten carbide counter sample.

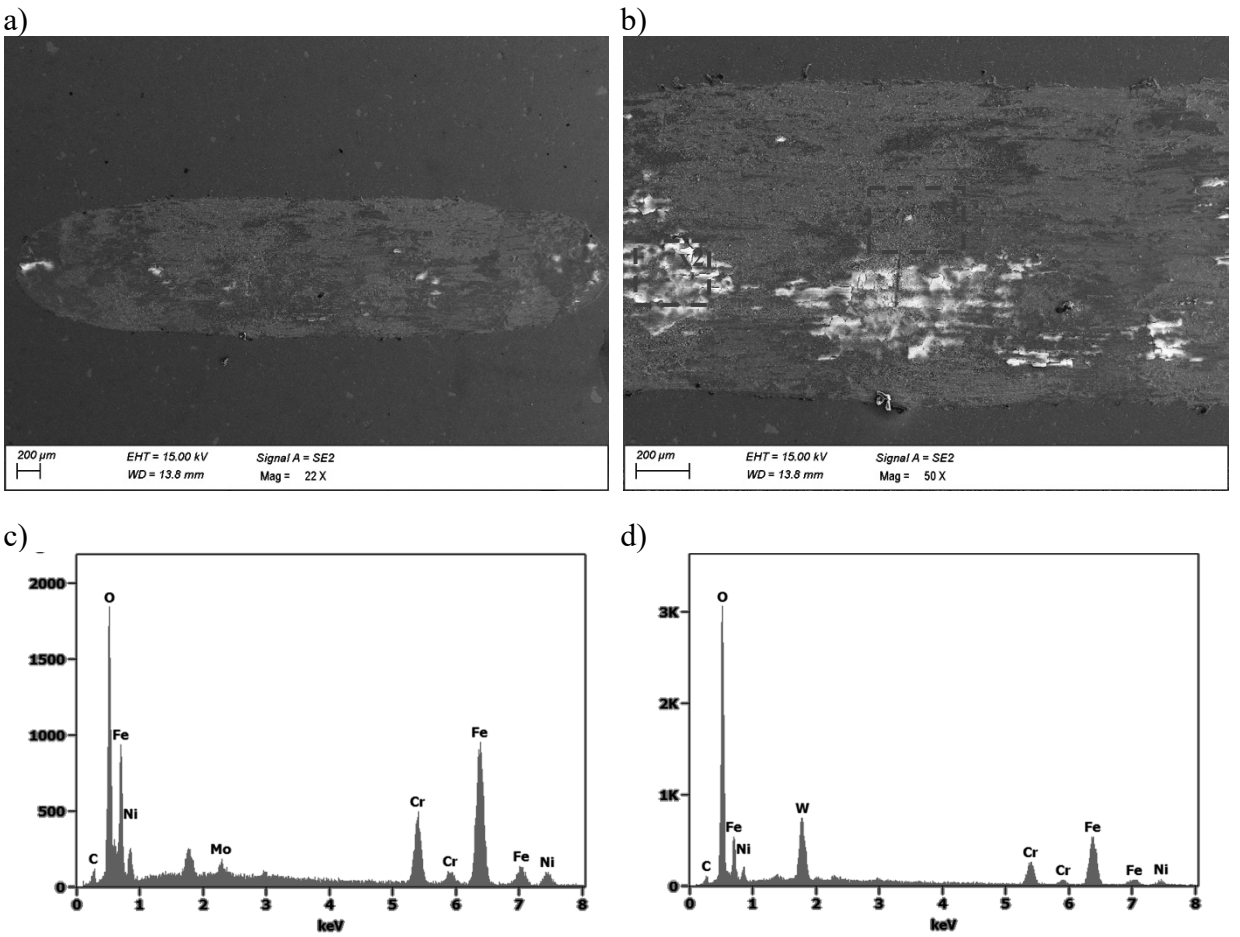

Fig. 6. a) Wear trace after the ball-on-plate test at normal load equal 7.5 N for 316L steel with CrN coating, b) Close-up of the damage on the coating surface. c) EDS analysis from the x1 micro-area. d) EDS analysis from the x2 micro-area.

The scratch test didn't reveal any clear point at which coating failed, based on SEM analysis of the scratch mark it was concluded that the failure happened when the load reached the value of 35N. Graphs obtained during test are shown in figure 7. They show increasing drag force *Ft* and value of acoustic emission *AE* relative to linearly rising normal force *Fn*.

SEM studies of a scratch mark obtained in a scratch test show that in a place that corelates to a normal force of about 35N during testing, lighter areas started to appear, in those places EDS analysis showed a presence of elements coming from base material which signifies the failure of the coating. Higher loads resulted in proportionally greater damage to the coating. Fragments of scratch trace are shown in figure 8.

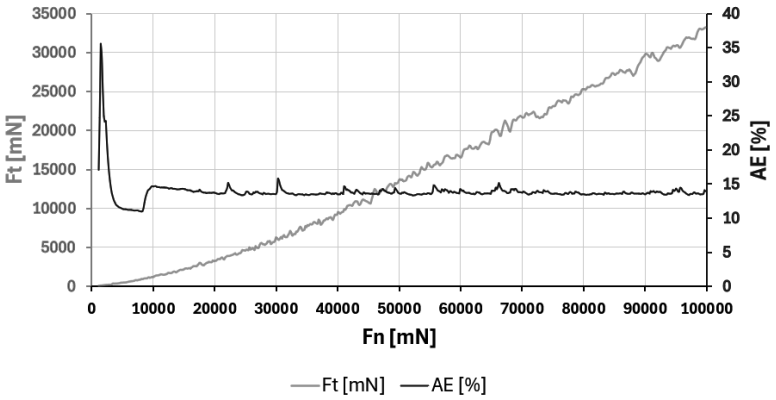

Fig. 7. Scratch test results with increasing load up to 100 N.

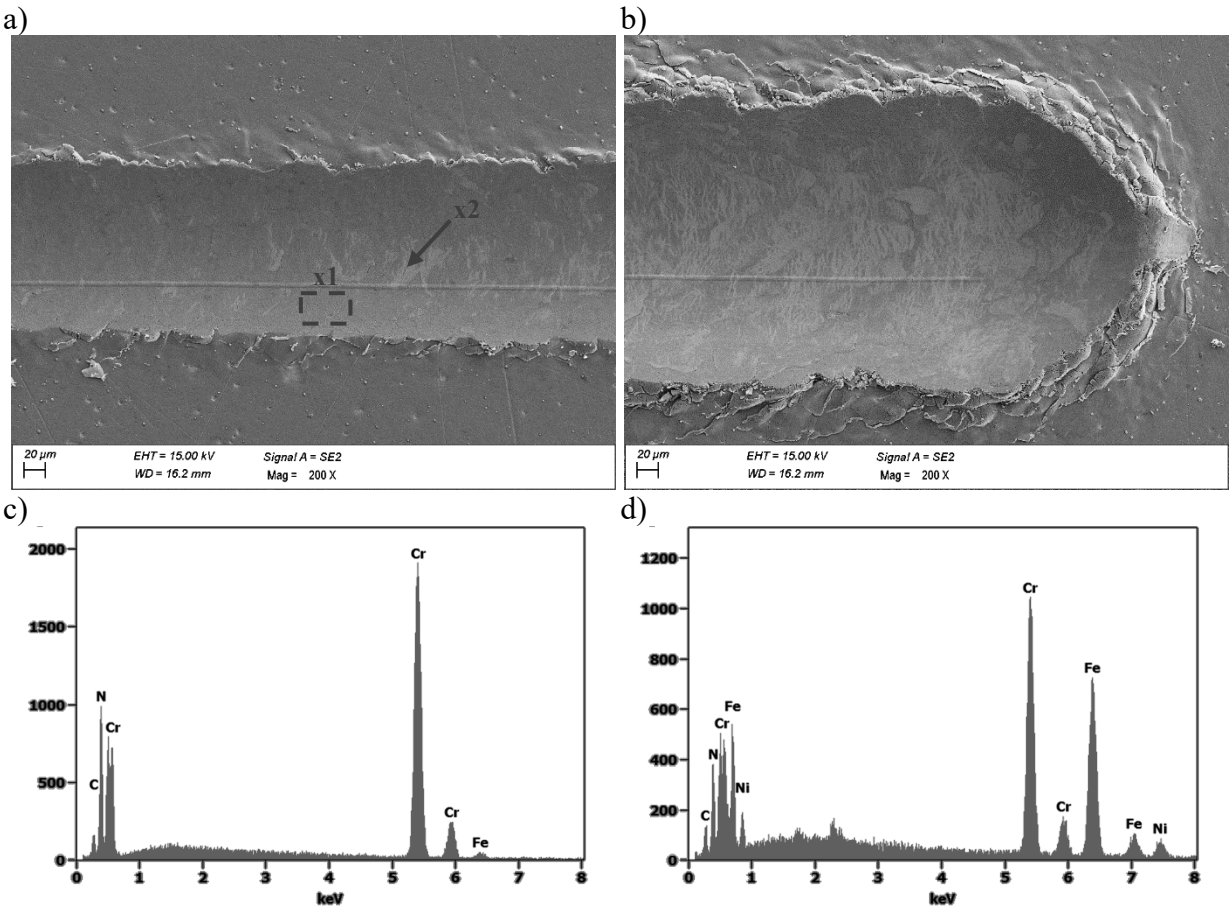

Fig. 8. a) Fragment of scratch trace (~35 N) after the scratch test at for 316L steel with CrN coating, b) End of scratch trace (100 N) after the scratch test for 316L steel with CrN coating. c) EDS analysis from the x1 micro-area. d) EDS analysis from the x2 micro-area.

Fretting test display how the value of the coefficient of friction changes depending on the duration of the test and presence of a coating on a substrate. The profile of friction coefficient graphs is shown in figure 9. In case of substrate without coating average friction coefficient was 0.85 ± 0.16, and as for substrate with CrN coating it was almost three times higher and amounted to 2.98 ± 1.77. Average values of friction coefficients and the wear trace dimensions are shown in table 5.

Table 5. Fretting test results on 316L substrate

Sample	Substrate	Coating	Test results		
			COF μ	Width [μm]	Depth [μm]
1	316L	-	0.85 ± 0.16	680	17.06 ± 0.92
2		CrN	2.98 ± 1.77	450	0.57 ± 0.04

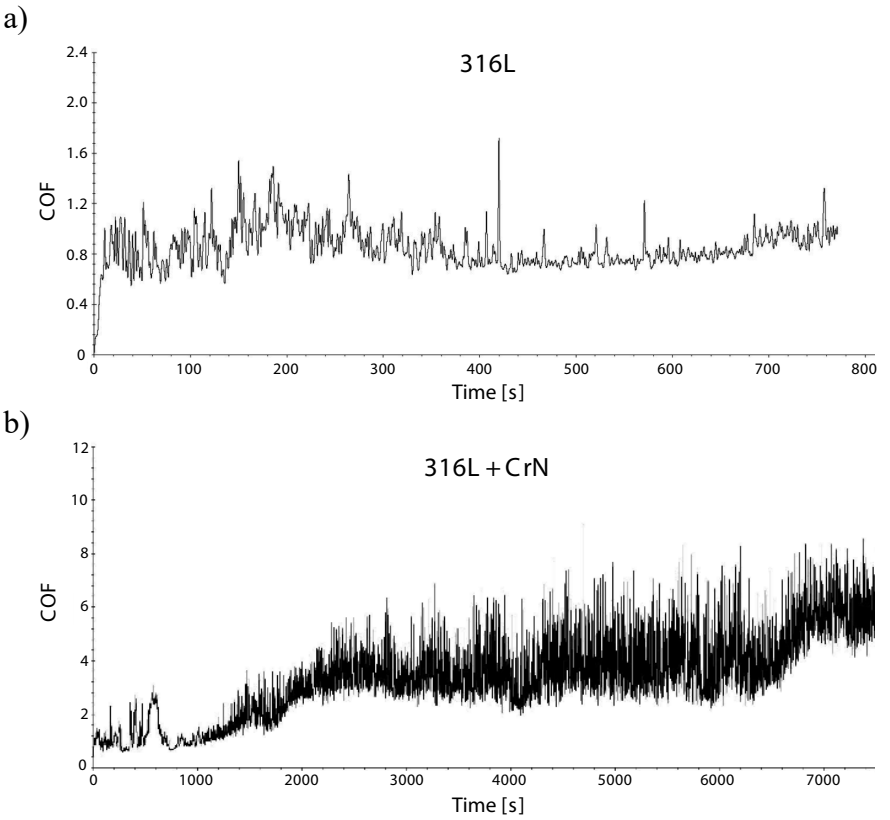

Fig. 9. Friction coefficient profile of a) 316L steel without coating, b) 316L steel with CrN coating.

The studies on structure of wear traces for substrates with and without coatings were conducted using SEM. They showed that in case of uncoated substrate small particles can be observed in the images. These may represent fragments of the carbide ball or oxides of the base material. In both cases, these particles likely participated in the fretting process and contributed to accelerated wear.

In case of the coated substrate the morphology study revealed a smooth surface which signifies that the coating did not fail during testing. However, in isolated areas, cracks in the coating can be seen. These may have been caused by small fragments of the WC-Co ball being pressed into the surface or contact fatigue of the coating due to prolonged cyclic loading.

Measurements of dimensions of wear traces show that for a substrate without a coating an average width is 680 μm and an average depth measured with profilometer is 17.06 ± 0.92 μm. The coating had a great impact on test results, decreasing an average width of a wear trace to 450μm and its depth to 0.57 ± 0.04 μm proving that the coating works as intended.

SEM photos of surface studies and profiles of wear traces are shown in figure 10.

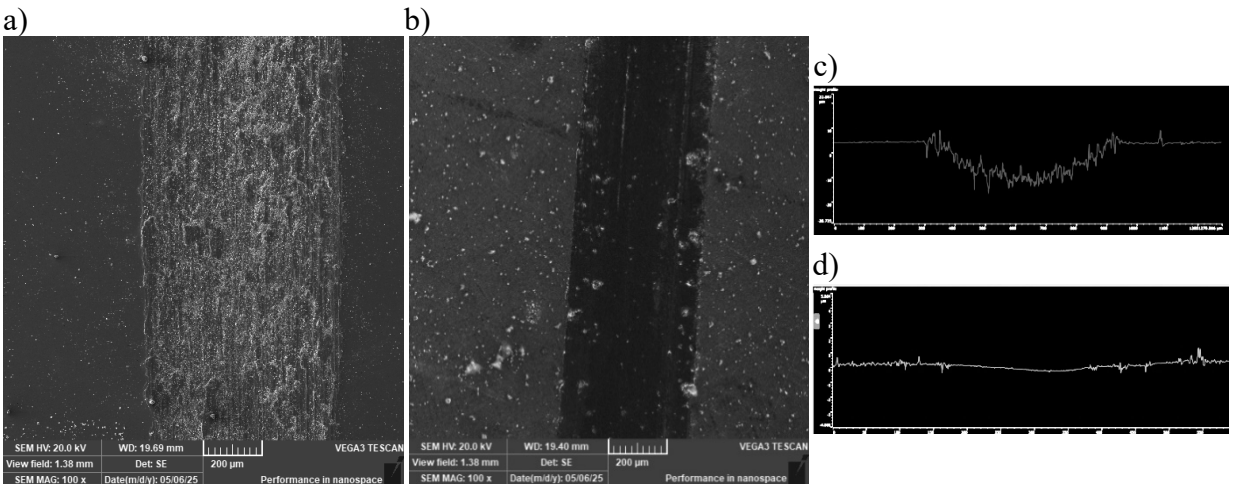

Fig. 10*. Surface wear of 316L steel after fretting test a) without coating, b) with CrN coating. Depth profiles of surface wear on 316L steel c) without coating, d) with CrN coating.*

Figure 11 shows the indentation after the Rockwell test conducted test conducted at HRA load (60 kp), the average diameter of indentations was about 650µm.

After the tests at this load the CrN coating stayed intact without any signs of delamination, only small cohesive cracks were observed near the edges of the indentation, indicating slight internal stress within the coating but no failure at the interface. These results indicate excellent adhesion and very good cohesive strength of the CrN coating at low mechanical loads.

When the load was increased to HRB (100 kp), no significant difference in coating behavior was observed compared to the lower load (HRA). These results confirm that the CrN coating on 316L steel maintains excellent adhesion and high cohesive integrity even under moderate mechanical loading.

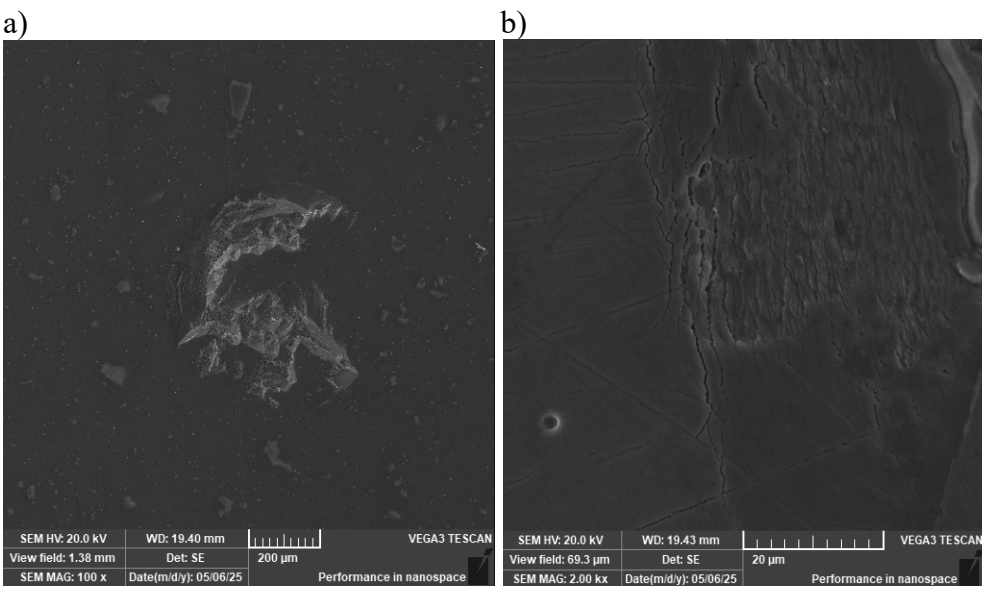

Fig. 11. a) Appearance of indentation after Rockwell test on 316L steel with CrN coating (HRA load), b) Minor cohesive cracks around the indentation (HRA load).

Figure 12 shows the surface of a 316L steel substrate with the CrN coating after the Rockwell test performed at the HRC load (150 kp). The average diameter of the indentations at this load level was approximately 840 μm.

At that load no significant coating delamination was visible around the indentations, even at this highest applied load. Only cohesive cracks were observed, becoming apparent under high magnification. The number of cohesive cracks was higher than in the lower load conditions, indicating increasing internal stress but still no adhesive failure. These results confirm the excellent adhesion and very good cohesion of the CrN coating even under high mechanical stress, making it suitable for demanding applications where both surface durability and resistance to crack propagation are essential.

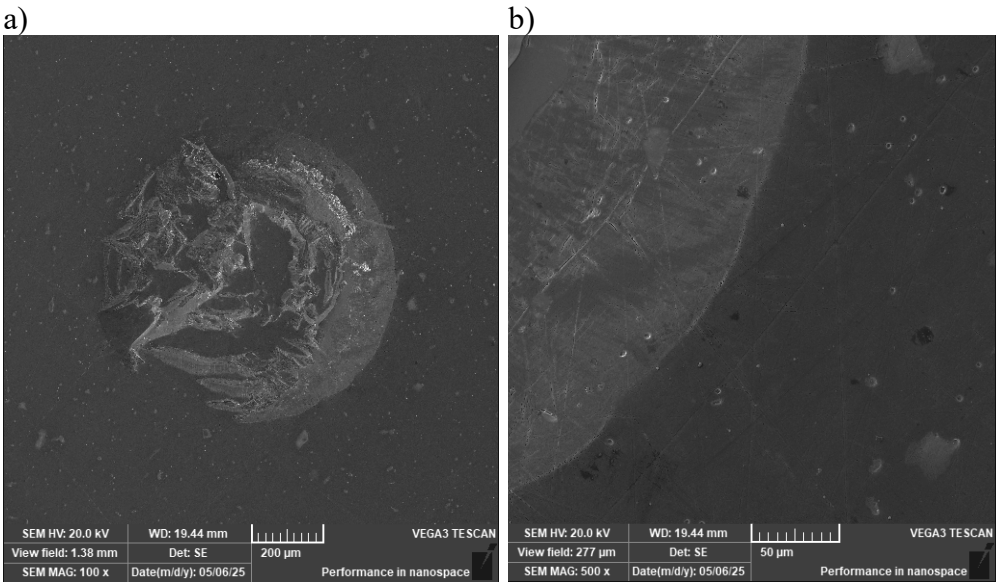

Fig. 12. a) Appearance of indentation after Rockwell test on 316L steel with CrN coating (HRC load), b) Minor cohesive cracks around the indentation (HRC load).

Table 6 summarizes the results obtained from the Rockwell test conducted on the 316L steel substrate with CrN coating. Each indentation shown in the previous figures was evaluated and assigned an adhesive and cohesive rating according to the reference scale presented in figure 1.

Table 6. Results of the Rockwell test on 316L substrate with CrN coating

Test label	Load [kp]	Average indentation diameter [µm]	Assigned rating
HRA	60	650	K1/A0
HRB	100	700	K1/A0
HRC	150	840	K2/A0

4. CONCLUSIONS

Based on the conducted research, it was shown that:

- The increase in normal load leads to proportionally increased wear. This is reflected in a higher coefficient of friction and increased wear.

- During the scratch test, coating penetration was observed at a load of approximately 35 N, indicating good adhesion to the substrate.
- The CrN coating shows a beneficial effect on the tribological properties of the coated steel surface, both in terms of reducing the coefficient of friction and reducing material wear.
- The presence of the CrN coating shows high mechanical properties (good adhesion to the substrate and abrasion resistance), higher than the uncoated substrate.
- The AISI 316L + CrN system demonstrated very high resistance to fretting wear. The CrN coating withstood the applied mechanical stress and remained intact throughout the test.
- The observed increase in the coefficient of friction and its high standard deviation were likely caused by carbide ball fragments or surface polishing of both the coating and the ball. This hypothesis could be further verified by SEM analysis of the carbide ball.
- The CrN coating exhibited excellent cohesion and adhesion to the AISI 316L substrate, with no signs of delamination even under high mechanical load.

ACKNOWLEDGEMENTS

This work was produced as part of the project implemented within the framework of project-oriented education – PBL, in the XII competition under the Excellence Initiative – Research University program, at the Silesian University of Technology.

BIBLIOGRAPHY

1. W. Zhu, Z. Xu, Z. Su, Y. Li, A. Yi, J. Zheng, J. Zhu, K. Li, K. Chen, Z. Liao, W. Li, Mechanical property and biocompatibility of multilayer Ti-DLC films with different Ti target power by hybrid PVD/PECVD on 316L stainless steel, Surface & Coatings Technology 496 (2025) 131672.
2. K. Chen, Y. Pan, G. Tang, D. Liang, H. Hu, X. Liu, Z. Liang, Facile fabrication of TiN coatings to enhance the corrosion resistance of stainless steel, Surface & Coatings Technology 494 (2024) 131450.
3. M. Staszuk, D. Pakuła, Ł. Reimann, A. Kloc-Ptaszna, K. Lukaszkowicz, Structure and properties of the TiN/ZnO coating obtained by the hybrid method combining PVD and ALD technologies on austenitic Cr-Ni-Mo steel substrate, Surfaces and Interfaces 37 (2023) 102693.
4. S. Indupuri, P. Sai Kiran, R. Kumar, Ch. Satish, A. Kumar Keshri, High-temperature tribological behavior of plasma sprayed GNPs-reinforced YSZ coating over 316L stainless steel, Materials Today Communications 41 (2024) 110451.
5. C. Zhao, Y. Bai, Q. Yan, B. Li, Enhanced corrosion resistance of laser powder bed fusion 316L stainless steel by modifying the microstructure through heat treatment, Journal of Materials Research and Technology 36 (2025) 7158-7171.
6. J. Xu, L. He, S. Cheng, X. Fang, Cryogenic mechanical properties and tribological behaviors of AISI stainless 316L steel cooled by liquid nitrogen, Cryogenics 147 (2025) 104058.
7. M. Staszuk, Investigations of CrN+Cr2O3/TiO2 coatings obtained in a PVD/ALD hybrid method on austenitic 316L steel substrate, Vacuum 207 (2023) 111653.

8. V.J.S.N. Prasad, F. Mayanglambam, P.N.V.V.L. Primila Rani, Pamu Dobbidi, Silver-doped ZrO2-TiO2 nanocomposite coatings on 316L stainless steel for enhanced corrosion resistance and bio applications, Surface & Coatings Technology 493 (2024) 131203.
9. A.F. Yetim, H. Tekdir, K. Turalioglu, M. Taftali, T. Yetim, Tribological behavior of plasma-sprayed Yttria-stabilized zirconia thermal barrier coatings on 316L stainless steel under high-temperature conditions, Materials Letters 336 (2023) 133873.
10. Y.L. Su, S.H. Yao, On the performance and application of CrN coating, Wear 205 (1997) 112-119.
11. T. Polcar, N.M.G. Parreira, R. Novák, Friction and wear behaviour of CrN coating at temperatures up to 500 °C, Surface & Coatings Technology 201 (2007) 5228–5235.
12. Y. Qiu, S. Zhang, B. Li, Y. Wang, J.-W. Lee, F. Li, D. Zhao, Improvement of tribological performance of CrN coating via multilayering with VN, Surface & Coatings Technology 231 (2013) 357-363.
13. T. Markowicz, J. Pluskota, B. Sobczak, D. Pakuła, M. Staszuk, Tribological studies of CrN coating obtained by PVD on austenitic steel surface X2CrNiMo17-12-2, Talent Detector International Students Scientific Conference, Volume 1, Winter (2025) p. 275-282.

TalentDetector

23th-25th June 2025
Gliwice-Brenna, Poland

DEPARTMENT OF ENGINEERING MATERIALS AND BIOMATERIALS
FACULTY OF MECHANICAL ENGINEERING
SILESIAN UNIVERSITY OF TECHNOLOGY

INTERNATIONAL STUDENTS SCIENTIFIC CONFERENCE

Investigation of nozzle temperature impact on surface roughness and mechanical properties of FDM-printed CF-PEEK components

Getu Koro Megersa[a], Wojciech Sitek[a], Agnieszka J. Nowak[a]

[a] Silesian University of Technology, Faculty of Mechanical Engineering, Scientific and Didactic Laboratory of Nanotechnology and Materials Technologies
email: getu.megersa@polsl.pl; wojciech.sitek@polsl.pl; agnieszka.j.nowak@polsl.pl

Abstract: This study investigates the effects of nozzle temperature on the surface roughness, tensile properties, and ball indentation hardness of carbon fiber-reinforced polyether ether ketone (CF-PEEK) components fabricated via fused deposition modeling (FDM). Specimens were printed at nozzle temperatures of 390 °C and 420 °C and subsequently evaluated for surface roughness, tensile strength, and ball indentation hardness. Results showed that increasing the nozzle temperature reduced surface roughness by 19.5% and increased maximum tensile stress and ball indentation hardness by 6.4% and 6.5%, respectively, while the elongation at break remained nearly unchanged. Fractographic analysis revealed enhanced interlayer bonding and reduced void content at higher temperature. Statistical analysis confirmed that the differences in mean values for maximum stress, hardness, and surface roughness between the two nozzle temperatures were significant ($p < 0.001$).

Keywords: CF-PEEK, Nozzle temperature, Surface roughness, Mechanical properties

1. INTRODUCTION

Carbon fiber (CF) is a prevalent reinforcing material used to enhance the properties of the PEEK matrix. The addition of CF significantly improves the mechanical performance of pure PEEK, thereby increasing its relevance for applications such as dental implants [1]. While PEEK alone offers biocompatibility, radiolucency, and an elastic modulus closer to natural bone than titanium, its relatively low stiffness limits its ability to withstand physiological loads [2]. Incorporating carbon fibers into PEEK enhances its stiffness and strength, aligning PEEK modulus more closely with cortical bone, thereby reducing stress shielding and improving the durability and performance of dental implants. Additive manufacturing (AM) techniques, particularly Fused Deposition Modeling (FDM), have gained significant importance in producing customized dental implants [3]. These methods allow for the direct fabrication of complex, patient-specific geometries from digital models, offering cost efficiency and reduced material waste compared to traditional manufacturing approaches. However, the mechanical performance and surface quality of FDM-printed CF-PEEK parts are highly dependent on factors such as

carbon fiber content, fiber orientation, and process parameters [3–5]. Among these, nozzle temperature is critical, as it governs the polymer's melt viscosity during extrusion, directly influencing filament fusion and interlayer adhesion, which in turn determine the part's mechanical and surface properties [4,6].

Numerous studies have shown the influence of nozzle temperature on surface quality and mechanical properties across various materials. Naganaboyina et al. [7] specifically investigated its effects on CF-PEEK prints, while Wang et al.[1] and Hanemann et al. [6] studied both PEEK and CF-PEEK, concluding that nozzle temperature critically impacts surface roughness and mechanical strength [8]. Further research by Tseng et al. [9], Gao et al.[5], and Sikder et al.[4] also analyzed PEEK, confirming its impact on tensile and flexural behavior. However, research specifically addressing the effect of nozzle temperature on the hardness of CF-PEEK remains limited, representing a critical gap in literature.

In this study, the effects of nozzle temperatures (390 °C and 420 °C) on the surface roughness, tensile strength, and ball indentation hardness of CF-PEEK components fabricated via fused deposition modeling (FDM) were investigated, providing insights into how nozzle temperature influences the surface and mechanical properties of printed parts.

2. MATERIALS AND METHODS

Specimens were fabricated using KetaSpire® PEEK CF10 LS1 AM filament (10 wt.% short carbon fiber, diameter 1.75 mm, density 1.33 g/cm³, melting point 343 °C), supplied by 3DGence (Przyszowice, Poland). The filament was dried at 150 °C for 4 hours prior to printing to remove moisture.

2.1. Specimen fabrication

CAD models of the specimens were designed in SolidWorks 2021 according to ISO standards (see Figure 1). The models were sliced using 3DGence SLICER 4.0 software. Specimens were printed on a 3DGence INDUSTRY F420 FDM printer with consistent parameters across all samples. Printing was performed in a horizontal build orientation with a ±45° raster angle, 100% infill density using a line pattern, and 3 perimeter walls. A 0.4 mm nozzle diameter and bead width (0% overlap) were used. The chamber temperature was maintained at 50 °C, the build platform at 190 °C, print speed was set to 18 mm/s, and layer thickness was 0.1 mm. Two nozzle temperatures, 390 °C and 420 °C, were selected based on prior studies to investigate their influence on the properties of CF-PEEK parts [10,11]. During printing, 3DGence ESM-10 support material was employed. After printing, specimens were allowed to cool naturally in air.

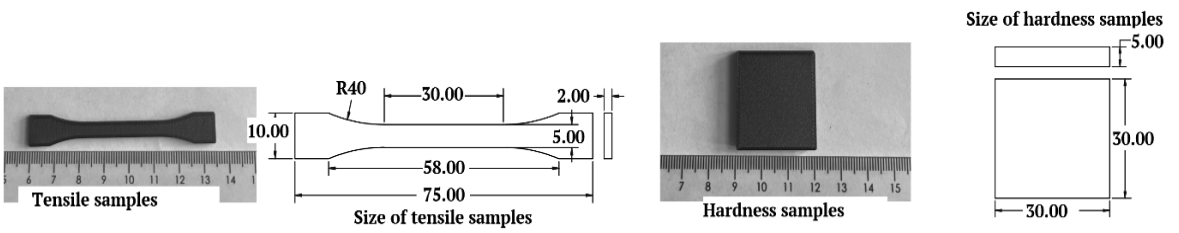

Figure 1. The shapes and dimensions (in mm) of hardness samples and tensile samples

2.2. Mechanical Testing

Tensile tests were performed in accordance with ISO 527-2:2012 on four specimens for each nozzle temperature using a Shimadzu AGSX universal testing machine at a crosshead speed of 5 mm/min. Hardness measurements were carried out following ISO 2039-1:2001 standards using a Zwick 3106 tester equipped with a 5 mm steel ball indenter. A load of 358 N was applied for 30 seconds during each indentation. For each nozzle temperature, four specimens were tested, with five indentations performed on each specimen. To prevent overlapping effects, the indentations were spaced at a minimum distance of three times the indentation diameter. Hardness values (H, N/mm²) were calculated based on the depth of each indentation.

2.3. Surface roughness

The surface roughness of the top surface of CF-PEEK hardness samples was evaluated to assess the influence of nozzle temperature on surface characteristics. A total of four samples were used: two printed at a nozzle temperature of 390°C and two at 420°C. Surface roughness was measured using the contact method with a Surtronic 25 surface roughness tester, following the ISO 4288 standard. The Ra parameters were used to quantify surface roughness, with a cut-off value of 0.8 mm and an evaluation length of 4 mm. Measurements were taken perpendicular to the build direction, as indicated in Figure 2.

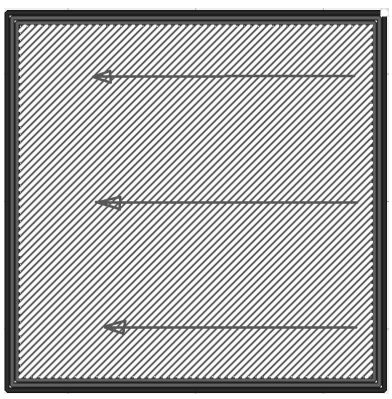

Figure 2. Direction and position of surface roughness measurement on the top surface of CF-PEEK samples.

2.4. Fractographic Analysis

The fracture surfaces of the tensile specimens were analyzed using a field emission scanning electron microscope (FE-SEM) operated at an accelerating voltage of 15 kV. Micrographs were initially acquired at a magnification of 150×, with selected regions of interest further magnified up to 250× to enable a more detailed assessment of the fracture morphology.

2.5. Statistical Analysis

Statistical analysis was performed using OriginPro 2024 software. The normality of data distribution was evaluated with the Shapiro-Wilk test, and differences between groups were assessed for statistical significance using a two-sample t-test.

3. RESULTS AND DISCUSSION

3.1. Surface roughness

The surface roughness (R_a) of CF-PEEK specimens was measured on the top surface perpendicular to the build orientation, intersecting deposited filaments at 45°. As shown in Table 1, roughness decreased significantly with higher nozzle temperature: specimens printed at 390°C exhibited an average R_a of 5.39 ± 0.33 µm, while those at 420°C measured 4.34 ± 0.28 µm, representing a 19.5% reduction. The reduction in surface roughness with increasing nozzle temperature observed in this study aligns with previous research. Hanemann et al. reported that for FDM-printed CF-PEEK with 10 wt.% carbon fiber, average surface roughness (R_a) decreased from 10 µm at 460°C to 7 µm at 510°C. In contrast, pure PEEK showed an initial increase in R_a from 16 µm at 420°C to 18 µm at 440 °C, followed by a slight decrease to 17 µm at 485 °C [6].

Increasing nozzle temperature in FDM improves surface quality by enhancing filament melting and molecular diffusion, which strengthens interlayer bonding and reduces voids [8,12]. At low temperatures, high melt viscosity hinders material flow, causing uneven deposition and higher roughness [6]. As temperature rises, better flow leads to more uniform layers and smoother surfaces [6,13]. However, exceeding the optimal temperature range can cause excessive fluidity, disrupting material placement and weakening bonding, which increases roughness [14,15]. For PEEK, Baek et al. observed increased roughness above 380 °C due to poor adhesion [15], while Pulipaka et al. noted similar effects beyond 405 °C linked to unstable flow and filament inconsistency [14].

Table 1. Average surface roughness (R_a) of FDM-printed specimens measured perpendicular to the build direction (mean ± SD).

Nozzle temperature (°C)	Roughness Ra (µm)
390	5.39 ± 0.33
420	4.34 ± 0.28

Figure 3 shows surface roughness profiles with R_a values near the group averages in Table 1.

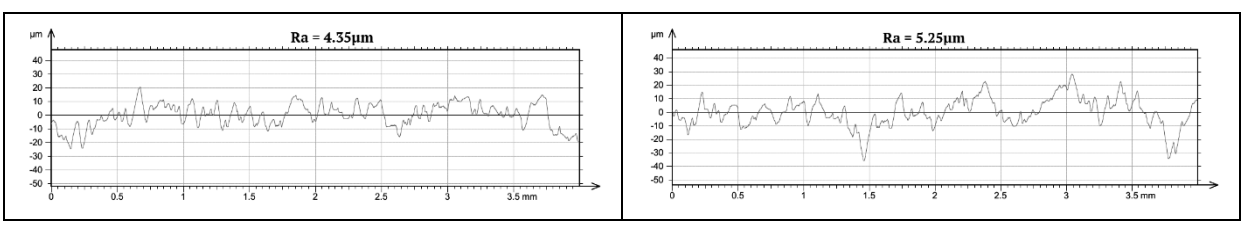

Figure 3. Surface roughness profiles of CF-PEEK specimens: (a) nozzle temperature 390 °C and (b) nozzle temperature 420 °C, showing measured Ra values close to the group averages.

3.2. Mechanical Properties Analysis.

3.2.1. Ball indentation hardness

Table 2 presents the ball indentation hardness values (N/mm²) of FDM-printed CF-PEEK specimens at different nozzle temperatures. The results indicate that increasing the nozzle temperature from 390 °C to 420 °C leads to a 6.5% improvement in hardness. Specimens printed

at 420 °C exhibited a higher mean ball indentation hardness of 83.39 N/mm², compared to 78.37 N/mm² for those printed at 390 °C. Nozzle temperature has a significant impact on the hardness of carbon fiber-reinforced parts produced with FDM, as it affects melt flow and fiber-matrix bonding [1]. Higher temperatures improve interlayer adhesion and fiber dispersion, resulting in a denser, more uniform structure with higher hardness. Conversely, low temperatures lead to incomplete melting, poor bonding and higher porosity, which reduces hardness [16]. However, excessively high temperatures can degrade the polymer matrix or impair the surface quality, which has a negative effect properties [8].

Table 2. Mean ball indentation hardness values (N/mm²).

Nozzle Temperature (°C)	Ball Indentation Hardness (N/mm²)
390	78.37 ± 4.16
420	83.39 ± 3.43

3.2.2. Tensile Mechanical Properties

Tensile tests demonstrate the influence of nozzle temperature on the mechanical behavior of the printed specimens. At 390 °C, the specimens reached a maximum load of 778.60 ± 24.28 N, while those printed at 420 °C achieved 834.24 ± 21.87 N. As the nozzle temperature increases, the specimens exhibit greater strength and stiffness. Figure 4a shows that all specimens fractured within the gauge length, while Figures 4b and 4c illustrate the load–displacement behavior, characterized by an initial elastic region followed by plastic deformation.

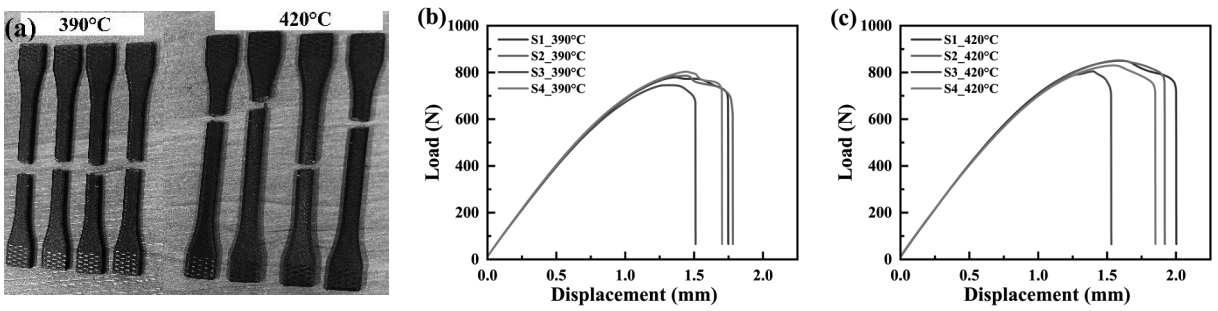

Figure 4. (a) Specimen appearance after tensile testing and corresponding load–displacement behavior of CF-PEEK specimens; (b) specimen printed at 390°C; (c) specimen printed at 420°C.

According to tensile test results (table 3), higher tensile properties were recorded with specimens printed at 420°C, which exhibited a maximum stress of 83.68 ± 1.39 MPa, an elastic modulus of 4.83 ± 0.06 GPa, and a stress at break of 71.32 ± 1.87 MPa. The elongation at break remained similar between the two temperatures, with 3.14 ± 0.34% at 420°C and 3.13 ± 0.27% at 390°C, indicating comparable ductility. In contrast, specimens printed at 390°C showed slightly lower mechanical performance, with a maximum stress of 78.12 ± 1.26 MPa, an elastic modulus of 4.71 ± 0.03 GPa, and a stress at break of 65.48 ± 3.84 MPa. The reduced performance at the lower temperature is likely due to increased voids and weaker interlayer bonding between deposited layers [9,13]. Elevated nozzle temperatures increase the thermal energy of polymer chains, reducing melt viscosity and enhancing material flowability. The improved flow behavior allows the material to flow into void spaces more effectively, thereby decreasing void content and increasing the interlayer contact area. This enhanced contact facilitates polymer chain diffusion, ultimately resulting in stronger interlayer bonding. Tseng et al. reported that, for

specimens fabricated via FDM using PEEK, increasing the nozzle temperature from 370°C to 390°C led to a significant reduction in porosity from 14% to 2.6%, along with enhancements in tensile modulus (+5.6%) and ultimate tensile strength (+46.9%) [9]. Similarly, Gao et al. observed a reduction in porosity from 3.22% to 0.29% in horizontally printed PEEK specimens as the nozzle temperature increased from 390°C to 420°C, with tensile strength reaching 82.31 MPa at 420°C [13].

Table 3. Average tensile properties.

Nozzle Temperature (°C)	Maximum Stress (MPa)	Young's Modulus (GPa)	Elongation at Break (%)	Stress at Break (MPa)
390	78.63 ± 1.21	4.71 ± 0.04	3.13 ± 0.26	65.47 ± 4.36
420	83.68 ± 1.36	4.83 ± 0.07	3.14 ± 0.36	71.82 ± 2.23

In addition to void content reduction, higher nozzle temperatures enhance chain mobility during solidification, promoting molecular alignment and leading to increased crystallinity. The resulting higher crystallinity and stronger intermolecular bonding contribute to improved mechanical properties, while reduced ductility may occur due to restricted polymer chain mobility in the more ordered structure [7]. Gao et al. also showed that elevating the nozzle temperature from 380°C to 480°C increased the crystallinity from 16.2% to 32.9%, which contributed to more compact molecular arrangement and stronger intermolecular interactions [13]. The SEM micrography shown in Figure 5 confirms all of these phenomena. The cross-sectional micrograph of the specimen printed at 390 °C reveals poor fusion between layers and a distinct layer boundary, attributed to the rapid solidification of CF-PEEK filaments at lower temperatures. However, excessive temperatures risk degradation and poor print quality, while too low temperatures cause incomplete melting and clogging [4]. Additionally, triangular voids are evident, which significantly reduces the mechanical properties of the 3D-printed specimens (Figure 5a). In contrast, specimens printed at 420 °C featured no visible layer boundaries and demonstrated improved fiber–matrix interaction. The deposited filaments fused more effectively, indicating stronger filament-to-filament bonding (Figure 5b). Although voids were still present, their quantity was reduced compared to specimens printed at 390°C.

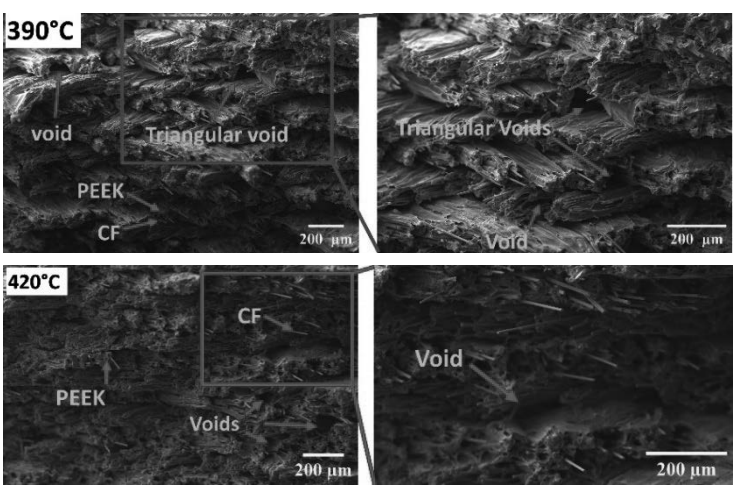

Figure 5. SEM image of the fractured surface at 150× magnification with an enlarged view (250×) of the marked region.

3.3. Statistical Analysis

The normality of the experimental data for maximum stress, ball indentation hardness, and surface roughness was assessed using the Shapiro–Wilk test at a 5% significance level. For all measured properties at nozzle temperatures of 390°C and 420°C, the test results yielded p-values greater than 0.05, indicating no significant departure from normality. Consequently, the assumption of normality was retained for all datasets, supporting the application of parametric statistical analyses in subsequent evaluations.

Two-sample t-tests were conducted to evaluate the effect of nozzle temperature (390°C and 420°C) on the maximum stress, ball indentation hardness, and surface roughness of the printed specimens, with all tests performed at a 95% confidence level. The maximum stress significantly increased from a mean of 78.63 MPa at 390°C to 83.68 MPa at 420°C ($p < 0.001$), indicating a statistically significant difference between the two means (Figure 6a). Similarly, ball indentation hardness exhibited a statistically significant increase from a mean of 78.37 to 83.39 with increasing nozzle temperature ($p < 0.001$) (Figure 6b). Surface roughness (R_a) demonstrated a significant decrease from a mean of 5.39 μm to 4.34 μm as the temperature increased, with a p-value less than 0.001 (Figure 6c). These results confirm that nozzle temperature exerts a significant influence on the mechanical properties and surface quality of the printed specimens.

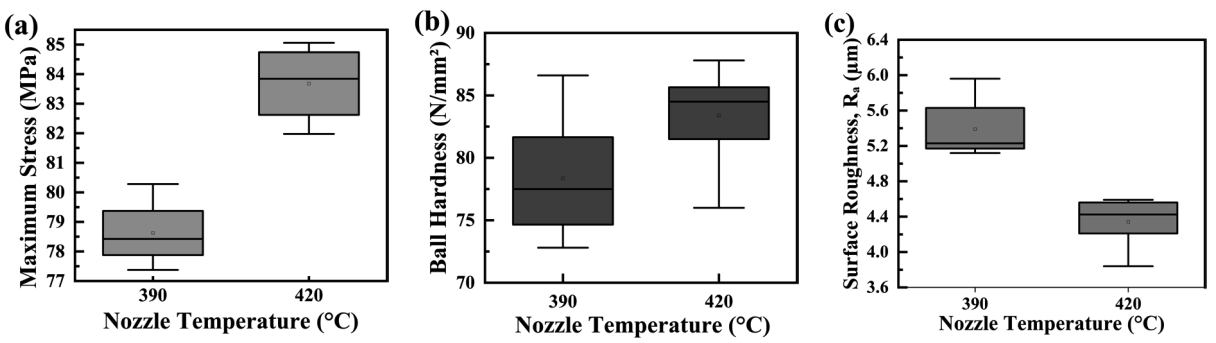

Figure 6. a) Maximum stress, b) Ball indentation hardness, c) Surface roughness.

4. CONCLUSION

Increasing the nozzle temperature from 390 °C to 420 °C significantly improves the surface roughness and mechanical properties of FDM-printed CF-PEEK. Specifically, surface roughness decreased by 19.5%, ball indentation hardness increased by 6.5%, maximum tensile stress improved, and stress at break was enhanced, while elongation at break remained consistent. SEM analysis revealed better interlayer fusion and reduced voids at higher temperatures. Statistical analysis confirmed these changes were significant, demonstrating that nozzle temperature critically influences surface quality, hardness, and tensile strength of CF-PEEK prints.

BIBLIOGRAPHY

[1] P. Wang, B. Zou, S. Ding, L. Li, C. Huang, Effects of FDM-3D printing parameters on mechanical properties and microstructure of CF/PEEK and GF/PEEK, Chinese Journal of Aeronautics 34 (2021) 236–246.

[2] X. Han, D. Yang, C. Yang, S. Spintzyk, L. Scheideler, P. Li, D. Li, J. Geis-Gerstorfer, F. Rupp, Carbon Fiber Reinforced PEEK Composites Based on 3D-Printing Technology for Orthopedic and Dental Applications, JCM 8 (2019) 240.
[3] S.Y. Sonaye, V.K. Bokam, A. Saini, V.V. Nayak, L. Witek, P.G. Coelho, S.B. Bhaduri, M.C. Bottino, P. Sikder, Patient-specific 3D printed Poly-ether-ether-ketone (PEEK) dental implant system, Journal of the Mechanical Behavior of Biomedical Materials 136 (2022) 105510.
[4] P. Sikder, B.T. Challa, S.K. Gummadi, A comprehensive analysis on the processing-structure-property relationships of FDM-based 3-D printed polyetheretherketone (PEEK) structures, Materialia 22 (2022) 101427.
[5] S. Gao, R. Liu, H. Xin, H. Liang, Y. Wang, J. Jia, The Surface Characteristics, Microstructure and Mechanical Properties of PEEK Printed by Fused Deposition Modeling with Different Raster Angles, Polymers 14 (2021) 77.
[6] T. Hanemann, A. Klein, S. Baumgärtner, J. Jung, D. Wilhelm, S. Antusch, Material Extrusion 3D Printing of PEEK-Based Composites, Polymers 15 (2023) 3412.
[7] H.P.S. Naganaboyina, P. Nagaraju, S.Y. Sonaye, V.K. Bokam, P. Sikder, In-house processing of carbon fiber-reinforced polyetheretherketone (CFR-PEEK) 3D printable filaments and fused filament fabrication-3D printing of CFR-PEEK parts, Int J Adv Manuf Technol 128 (2023) 5011–5024.
[8] P. Wang, B. Zou, H. Xiao, S. Ding, C. Huang, Effects of printing parameters of fused deposition modeling on mechanical properties, surface quality, and microstructure of PEEK, Journal of Materials Processing Technology 271 (2019) 62–74.
[9] J.-W. Tseng, C.-Y. Liu, Y.-K. Yen, J. Belkner, T. Bremicker, B.H. Liu, T.-J. Sun, A.-B. Wang, Screw extrusion-based additive manufacturing of PEEK, Materials & Design 140 (2018) 209–221.
[10] V. Gupta, N.I. Thiruselvam, D.M. Kulkarni, V.V. Chaudhari, S. Suraj, Anisotropy and deformation heterogeneity in additive manufactured carbon-reinforced PEEK, J Mech Sci Technol 37 (2023) 2871–2880.
[11] V. Mohammad, S. Yang, Extrusion-based additive manufacturing of PEEK for biomedical applications, Virtual and Physical Prototyping 10 (2015) 123–135.
[12] P. Wang, B. Zou, S. Ding, Modeling of surface roughness based on heat transfer considering diffusion among deposition filaments for FDM 3D printing heat-resistant resin, Applied Thermal Engineering 161 (2019) 114064.
[13] J. Gao, W. Li, J. Wang, X. Wang, C. Sha, K. Zhao, Comprehensive analysis of fused deposition modeling process conditions for enhancing mechanical properties and surface quality of 3D-Printed poly-ether-ether-ketone, Polymer Testing 134 (2024) 108432.
[14] A. Pulipaka, K.M. Gide, A. Beheshti, Z.S. Bagheri, Effect of 3D printing process parameters on surface and mechanical properties of FFF-printed PEEK, Journal of Manufacturing Processes 85 (2023) 368–386.
[15] I. Baek, O. Kwon, C.-M. Lim, K.Y. Park, C.-J. Bae, 3D PEEK Objects Fabricated by Fused Filament Fabrication (FFF), Materials 15 (2022) 898.
[16] M.-H. Hsueh, C.-J. Lai, K.-Y. Liu, C.-F. Chung, S.-H. Wang, C.-Y. Pan, W.-C. Huang, C.-H. Hsieh, Y.-S. Zeng, Effects of Printing Temperature and Filling Percentage on the Mechanical Behavior of Fused Deposition Molding Technology Components for 3D Printing, Polymers 13 (2021) 2910.

TalentDetector

23th-25th June 2025
Gliwice-Brenna, Poland

DEPARTMENT OF ENGINEERING MATERIALS AND BIOMATERIALS
FACULTY OF MECHANICAL ENGINEERING
SILESIAN UNIVERSITY OF TECHNOLOGY

INTERNATIONAL STUDENTS SCIENTIFIC CONFERENCE

Korózna odolnosť nehrdzavejúcej ocele AISI 316L po plazmovej nitridácii

Erik Meliš[a], Viera Zatkaliková[a]

[a] Žilinská univerzita v Žiline, Strojnícka fakulta, Katedra materiálového inžinierstva, Univerzitná 8215/1, 010 26 Žilina, Slovak Republic
email: melis2@stud.uniza.sk, viera.zatkalikova@fstroj.uniza.sk

Abstract: Príspevok sa zaoberá hodnotením austenitickej nehrdzavejúcej oceli AISI 316L s povrchovou úpravou. Hodnotená bola korózna odolnosť pomocou potenciodynamickej polarizačnej metódy, meraná mikrotvrdosť a analyzovaná mikroštruktúra vzoriek východiskového stavu a v stave po plazmovej nitridácii pri 530°C po dobu 24 hodín.

Z výsledkov vyplýva, že vzorky nitridovanej ocele AISI 316L nie sú vhodné pre oblasti s agresívnym prostredím obsahujúcim chloridy. Tvar potenciodynamických polarizačných kriviek u plazmovo nitridovaných vzoriek zodpovedá tvaru kriviek pre aktívne korodujúci kov, čo svedčí o strate pasívneho správania sa materiálu. Pre zlepšenie koróznych vlastností testovanej ocele so súčasne zachovaným zvýšením tvrdosti by bolo najvhodnejšie použiť nízkoteplotnú plazmovú nitridáciu.

Keywords: nitridácia, nehrdzavejúca oceľ 316L, plazmová nitridácia, bodová a jamková korózia

1. ÚVOD

Austenitické nehrdzavejúce ocele patria k najpoužívanejším druhom nehrdzavejúcich ocelí. Ich hlavnými prísadovými prvkami sú Cr (18-25%) a austenitotvorný nikel (8-20%). Vhodný pomer medzi obsahmi týchto prvokov zabezpečuje austenitickú štruktúru týchto ocelí. Najbežnejšie sú ocele AISI 304 a AISI 316.

Oceľ AISI 316 v porovnaní s AISI 304 obsahuje molybdén a vyššie percento niklu. Vyznačuje sa vynikajúcou odolnosťou proti korózii, ktorá je vďaka prídavku molybdénu porovnateľne lepšia ako odolnosť austenitických ocelí. Molybdén zlepšuje aj mechanické vlastnosti za tepla a odolnosť voči tzv. lokálnej korózii, najmä v prítomnosti chlóru a chloridov. Nikel má tiež pozitívny vplyv na koróznu odolnosť, hlavne v prítomnosti kyseliny sírovej. Okrem toho poskytuje ťažnosť a tvárnosť, vďaka čomu je austenit stabilný.

Cieľom nitridácie je vytvoriť vrstvu na povrchu legovaných ocelí. Vytvorená vrstva si udržuje vysokú tvrdosť a odolnosť proti oteru aj za zvýšených teplôt z dôvodu vysoko disperzných nitridov legujúcich prvkov s vysokou príbuznosťou k dusíku. Súčiastky po nitridácii je možné ešte tepelne spracovať, ale nie vždy je to pravidlom. Hrúbka vrstvy vytvorená nitridovaním pre konštrukčné ocele 0,2 až 0,4 mm alebo 0,7 až 0,8 mm.

Plazmová nitridácia (alebo iónová nitridácia) je plazmaticky podporované termochemické cementovanie. Plazmou nazývame ionizované plyny, ktoré vznikajú elektrickým výbojom v plyne. Pri plazmovej nitridácii sa elektrický prúd vedie plynom, pričom stena pece slúži ako anóda a nitridovaná súčasť ako katóda. Tok elektrického prúdu vytvára anomálny modrofialový výboj, ktorý počas procesu rovnomerne pokrýva povrch nitridovanej súčiastky. Vlastný proces nitridovania prebieha interakciou medzi povrchom nitridovanej súčiastky a plazmovým plynom.

2. EXPERIMENTÁLNA ČASŤ

Ako experimentálny materiál bola použitá oceľ AISI 316L zakúpená v spoločnosti ITALINOX Slovakia, vo forme plechu s rozmermi 2 x 1 m a hrúbkou 1,5 mm, z ktorého boli nastrihané vzorky obdĺžnikového tvaru s rozmermi 15 x 40 mm (obr. 1). Spracovanie ocele pozostávalo z kontinuálneho liatia v elektrickej oblúkovej peci, rozpúšťacieho žíhania pri teplote 1050°C a ochladenia na vzduchu. Povrchová úprava 2B (hladký matný povrch) bola získaná žíhaním a morením po mierne hladiacom valcovaní (www.italinox.sk).

Obr. 1 Skúšobná vzorka AISI 316L
Figure 1. Test specimen AISI 316L

Vzorky boli nitridované v spoločnosti RÜBIG SK Prievidza. Proces nitridovania trval 24 hodín pri teplote 530°C, kde bolo súčasťou aj nahrievanie zariadenia 2 hodiny z teploty 510°C na 530°C a odprašovanie argónom. Po procese nitridovania nasledovalo chladnutie v peci na teplotu 160°C. Po dosiahnutí tejto teploty došlo k vyrovnaniu tlaku na atmosferický tlak.

Pred nitridovaním boli vzorky opláchnuté demineralizovanou vodou a etanolom a vysušené prúdom vzduchu. Vzorky po ukončenom procese nitridácie sú dokumentované na obr. 3.

Na vzorkách po plazmovej nitridácii boli následne realizované skúšky:

- Skúška mikrotvrdosti - Zwick Roell;
- Metalografická analýza;
- Potenciodynamická polarizačná skúška.

Potenciodynamický polarizačný test je jednou z najrozšírenejších techník používaných na meranie koróznej odolnosti vzoriek. Charakterizuje priebeh elektrochemických alebo korózných procesov na kovoch a ich zliatinách na základe merania závislosti prúdovej hustoty od potenciálu. Potenciál vzorky je postupne posúvaný anodickým smerom (alebo aj smerom

katodickým), z čoho vyplýva, že vzorka sa čiastočne správa ako anóda a vďaka tomu koroduje. Táto metóda dobre určuje rýchlosť aktívnej/pasívnej korózie pri rôznych potenciáloch.

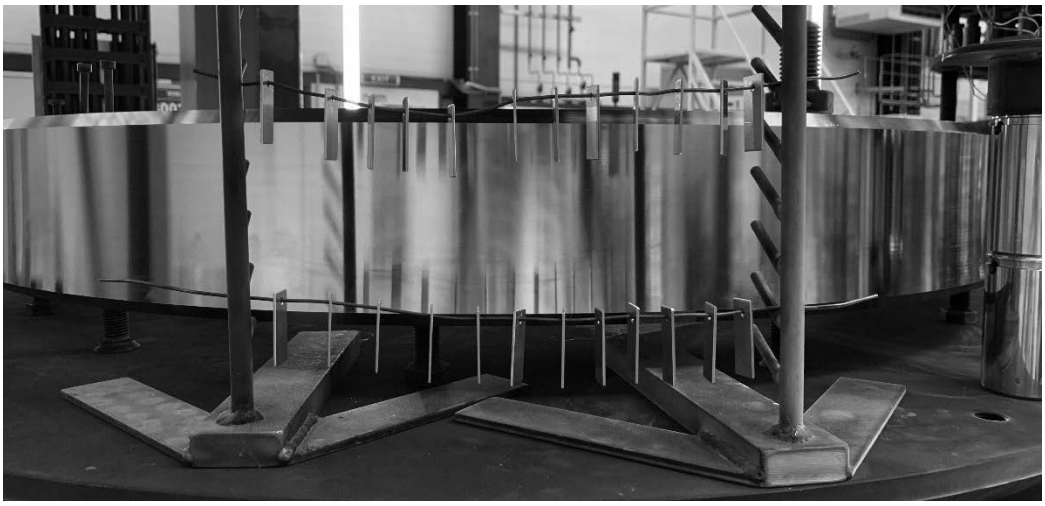

Obr. 2 Pripravené vzorky
Figure 2. Prepared samples

Potenciodynamickou polarizačnou metódou sa merala korózna odolnosť východiskového stavu materiálu a po plazmovej nitridácii. Používal sa korózny systém BioLogic s meracou jednotkou VSP a s trojelektródovou koróznou celou. Vzorky boli pripravené tak, aby boli v čo najlepšom stave (t.j. bez mechanického poškodenia, rovnomerne nitridované). Rozsah potenciálov pri potenciodynamickej polarizácii bol od -300 mV až po +800 mV oproti voľnému potenciálu (OCP = open circuit potencial) ustálenému pred meraním. Rýchlosť zmeny potenciálu bola 1 mV/s. Každé meranie sa opakovalo aspoň 3-krát pre spresnenie výsledkov a ich kontrolu. Po skončení procesu sa v softvéri EC-LAB vyhodnotili vykreslené krivky.

3. VÝSLEDKY

Hlavným cieľom bolo zistiť koróznu odolnosť nehrdzavejúcej ocele AISI 316L po plazmovej nitridácii pri teplote 530°C po dobu 24 hodín, pomocou potenciodynamickej polarizačnej metódy. Aby sa dalo posúdiť, ako na koróznu odolnosť po plazmovej nitridácii vplývala koncentrácia chloridov v koróznom prostredí, testovalo sa v dvoch roztokoch NaCl s koncentráciami 0,5 mol/dm^3 (0,5 M roztok) a 0,05 mol/dm^3 (0,05 M roztok).

Plazmová nitridácia vzoriek bola vykonaná v spoločnosti Rübig SK. Samotný proces nitridovania trval 24 hodín a nitridovalo sa pri teplote 530°C. Vzorky po nitridovaní vykazovali čierny matný povrch.

Prvá skúška, ktorá bola na nitridovaných vzorkách následne realizovaná bolo meranie mikrotvrdosti. Mikrotvrdosť sa merala na východiskovom stave austenitickej nehrdzavejúcej oceli AISI 316L a následne aj na materiáli po plazmovej nitridácii. Na meranie mikrotvrdosti bol použitý mikrotvrdomer s mikroskopom Zwick Roell. Na východiskovom materiáli sa robilo 15 vtlačkov pod uhlom 45° (obr. 3). Mikrotvrdosť ocele vo východiskovom stave dosiahla približne rovnaké výsledky, ako dosahujú austenitické nehrdzavejúce ocele AISI 316L (v priemere 198 HV) (tab. 1). Po meraní na východiskovom stave nasledovalo meranie vzoriek po plazmovej nitridácii. Robených bolo na každej vzorke 25 vtlačkov pod uhlom 45° (obr. 4).

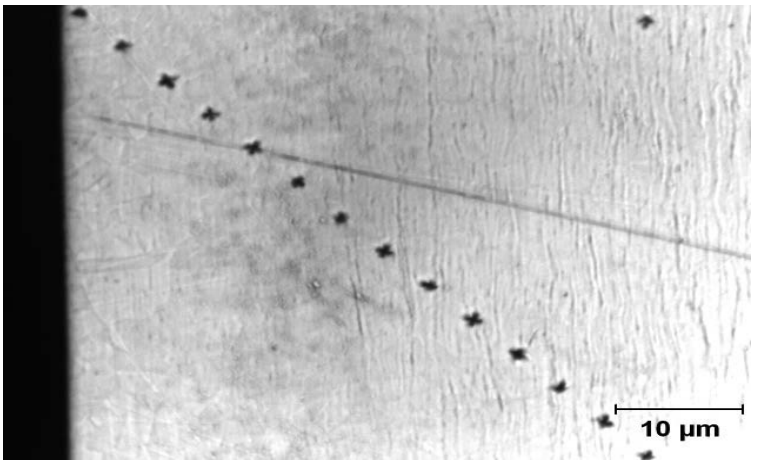

Obr. 31 Východiskový materiál (AISI316L) po meraní mikrotvrdosti
Figure 3. The experimental material (AISI 316L) after microhardness measurement

Na obr. 2 je zároveň dokumentovaný tmavo sivý nitridovaný pás, na ktorom je mikrotvrdosť výrazne vyššia v porovnaní s materiálom pod nitridovanou vrstvou (tab.1). Nitridovaná vrstva dosiahla tvrdosť 1575 HV, zatiaľ čo za ňou bola nameraná mikrotvrdosť 240 HV. Celkový priemer dosiahol hodnotu 721 HV. Nitridovaný materiál dosiahol výrazne vyššiu tvrdosť ako východiskový stav materiálu AISI 316L. Vysoká tvrdosť materiálu po nitridácii pri teplotách vyšších ako 500°C súvisí so vznikom nitridov chrómu, ktoré vznikajú za týchto podmienok a výrazne zvyšujú tvrdosť materiálu (Lanzoni et. al., 2014).

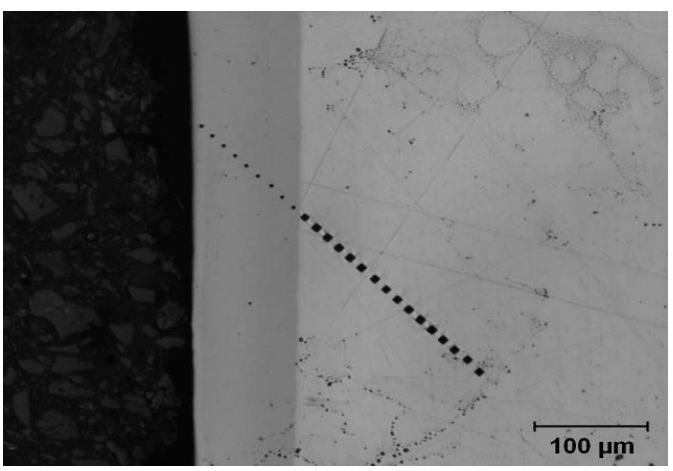

Obr. 4 Priečny rez nitridovanou vrstvou po meraní mikrotvrdosti
Figure 2. Cross section of the nitrided layer after microhardness measurement

Hodnoty v tab. 1 sú priemerné hodnoty a sú pre východiskový stav materiálu (VS), pre stav po plazmovej nitridácii (PN celková), pre nitridovanú vrstvu (PN nitridovaná) a pre vrstvu pod nitridačnou vrstvou (PN bez nitridácie). Porovnateľnú hodnotu mikrotvrdosti nitridovanej vrstvy na oceli AISI 316L po plazmovej nitridácii pri 520 °C uvádzajú tiež autori (de Araújo et. al., 2019).

Tab. 1 Priemerné hodnoty mikrovrdosti materiálu
Tabelle 1. Materials microhardness (average values)

	mikrotvrdosť [HV 0,5]
VS	198
PN celková	721
PN nitridovaná	1575
PN bez nitridácie	240

Po skúške mikrotvrdosti nasledovala metalografická analýza, pomocou ktorej sa hodnotila mikroštruktúra vzoriek pred plazmovou nitridáciou a po nitridácii. Vzorky na štruktúrnu analýzu bolo pripravené štandardným spôsobom, t.j. brúsené, leštené a leptané leptadlom Kalings2. Po naleptaní bola štruktúra pozorovaná a dokumentovaná na mikroskope Neophot 32 v programe NIS Elements.

Mikroštruktúra východiskového stavu materiálu ocele AISI 316L je dokumentovaná na obr. 5. Pozorujeme polyedrické zrná austenitu, bez zreteľných vtrúsenín. V štruktúre sú prítomné viaceré dvojčatá, ktoré mohli vzniknúť pri valcovaní alebo žíhaní.

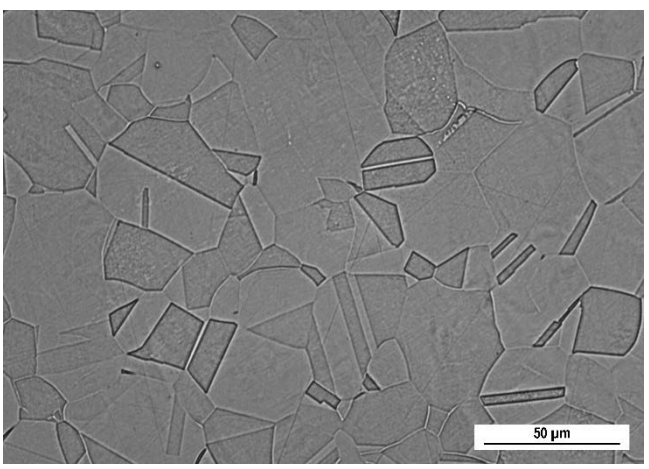

Obr. 5 Mikroštruktúra ocele AISI 316L (východiskový stav), lept. Kallings2
Figure 5. Microstructure of AISI 316L steel (initial state), etch. Kallings2

Mikroštruktúra ocele po plazmovej nitridácii je zobrazená na obr. 6. Na okraji priečneho rezu je zreteľne viditeľná nitridovaná vrstva, ktorá má po naleptaní leptadlom Kallings2 tmavú farbu. Na rozdiel od tmavo sfarbenej nitridovanej vrstvy na obr. 5, nitridovaná vrstva zobrazená na nenaleptanej vzorke pri meraní mikrotvrdosti má sivú farbu, bez viditeľných jednotlivých zón (obr. 4).

Po vyhodnotení mikroštruktúry boli na vzorkách ocele AISI 316L vo východiskovom stave a po plazmovej nitridácii realizované korózne potenciodynamické skúšky s cieľom stanoviť koróznu odolnosť. Korózna odolnosť bola hodnotená v dvoch roztokoch (0,5M a 0,05M roztok chloridu sodného) pomocou korózneho systému BioLogic s mernou jednotkou VSP a trojelektródovou koróznou celou. Po skončení procesu sa v softvéri EC-LAB vyhodnotili vykreslené krivky v semilogaritmických súradnicich (log. prúdovej hustoty i v závislosti od potenciálu E) a následne sa vybrala reprezentatívna krivka z každého merania.

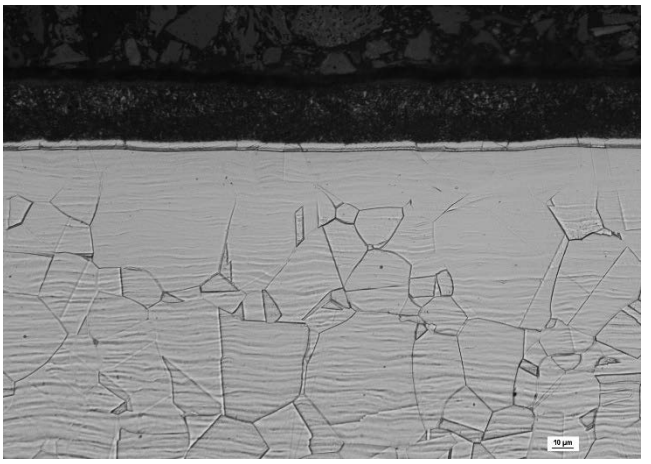

Obr. 6 Mikroštruktúra ocele AISI 316L po plazmovej nitridácii - priečny rez, lept. Kallings2
Figure 6. Microstructure of AISI 316L steel after plasma nitriding - cross section, etch. Kallings2

Reprezentatívne krivky pre východiskový stav materiálu AISI 316L sa vložili do spoločného grafu pre lepšie porovnávanie (obr. 7).

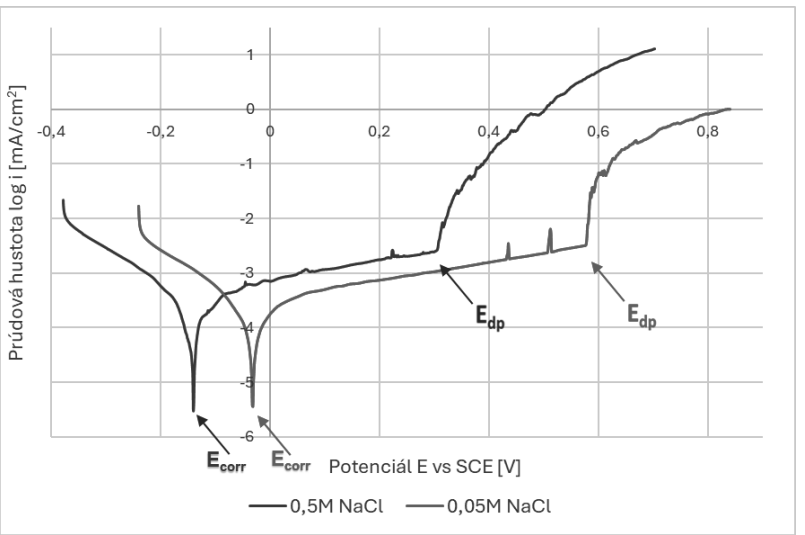

Obr. 7 Potenciodynamické krivky pre vzorky vo východiskovom stave
Figure 7. Potentiodynamic curves for samples in the initial state

Z tvaru kriviek vyplýva, že ide o typické krivky pre pasivovateľné kovy, kde sa nachádza po prechode z katódovej strany cez bod E_{corr} na anódovú stranu kriviek výrazná oblasť pasivity. Pri takomto tvare kriviek je dôležitou elektrochemickou charakteristikou depasivačný potenciál E_{dp} ktorý sa určuje ako potenciál pri ktorom začína prudký trvalý nárast prúdovej hustoty. Pri dosiahnutí potenciálu E_{dp} dochádza k narušeniu pasívnej vrstvy na povrchu ocele, spôsobenému prienikom chloridových aniónov cez oslabené miesta až na povrch materiálu pod pasívnou vrstvou. Čím je depasivačný potenciál vyšší, tým je vyššia odolnosť proti lokálnej bodovej korózii (Szklarska-Smialowska 2005). Namerané hodnoty E_{corr} a E_{dp} pre východiskový stav materiálu v 0,5M a 0,05M roztoku NaCl sú zobrazené v tab. 2.

Tab. 2 Elektrochemické charakteristiky vzoriek vo východiskovom stave
Tabelle 2. Electrochemical characteristics of samples in the initial state

	E_{dp} = depasivačný potenciál [V vs SCE]	**E_{corr} = korózny potenciál [V vs SCE]**
0,5M roztok NaCl	0.305	-0,140
0,05M roztok NaCl	0.577	-0.033

Ako možno vidieť z porovnania kriviek (obr. 7) a hodnôt E_{corr} a E_{dp} (tab. 1), oceľ AISI 316L vo východiskovom stave má vyššiu koróznu odolnosť v 0,05 M roztoku NaCl ako v 0,5 M roztoku. Vyššia koncentrácia chloridových aniónov v roztoku zvyšuje možnosť ich prieniku cez oslabené miesta pasívnej vrstvy a iniciáciu bodovej korózie. Negatívny vplyv rastúcej koncentrácie chloridov v roztokoch NaCl na kvalitu pasívnej vrstvy austenitických ocelí potvrdili tiež autori: Rustandi, et al., 2017, Zatkalíková, Markovičová, 2019.

Reprezentatívne korózne krivky vzoriek po plazmovej nitridácii, čo umožňuje ich lepšie porovnanie na jednom mieste dokumentuje graf na obr. 8.

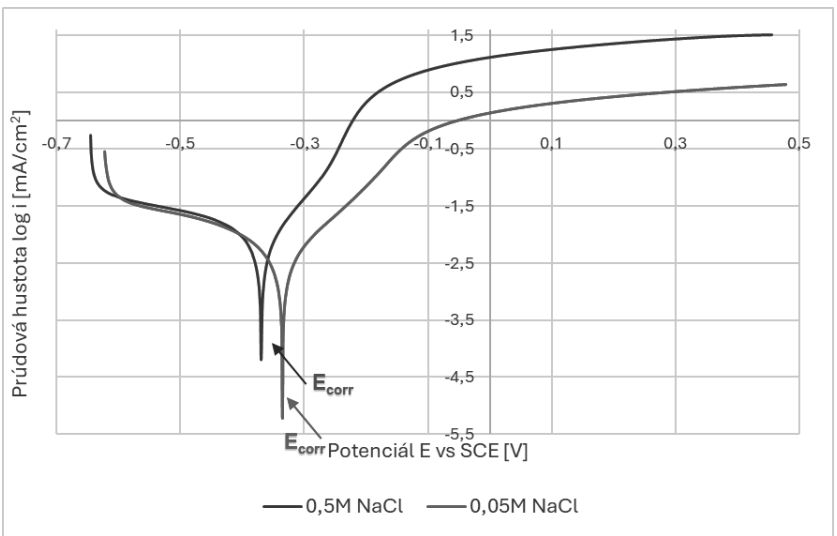

Obr. 8 Potenciodynamické krivky pre vzorky po plazmovej nitridácii
Figure 8. Potentiodynamic curves for samples after plasma nitridation

Tvar kriviek sa v tomto prípade výrazne líši od tvaru kriviek pre východiskový stav (obr. 7) a zodpovedá tvaru, ktorý je charakteristický pre aktívne korodujúci kov. Zrejme to súvisí so vznikom nitridov chrómu, ktoré sú typické pri vysokoteplotnej nitridácii a spôsobujú ochudobnenie povrchovej vrstvy o chróm a zhoršenie kvality pasívnej vrstvy (Saravan 2007) (Mukherjee 2004). Podobné výsledky, t.j. výrazné zhoršenie koróznej odolnosti, až stratu pasívneho správania austenitických ocelí v roztokoch NaCl po plazmovej nitridácii nad 500°C pri potenciodynamickej polarizácii pozorovali tiež autori: de Araújo, et. al., 2019 a Kartikasari, et. al., 2017.

V prípade potenciodynamických kriviek, ktoré nemajú na anódovej vetve oblasť pasivity sú základnými elektrochemickými charakteristikami na posúdenie koróznej odolnosti korózny potenciál, ktorý je mierou termodynamickej stability materiálu v danom prostredí (vyšší E_{corr} znamená vyššiu termodynamickú stabilitu) a korózna prúdová hustota i_{corr}, ktorá charakterizuje kinetiku korózneho procesu (vyššia prúdová hustota znamená vyššiu koróznu rýchlosť). Tieto

parametre sa určujú tzv. Tafelovou analýzou pomocou softvéru EC-LAB. Hodnoty korózných potenciálov, korózných prúdových hustôt a korózných rýchlostí, ktoré boli tiež súčasťou výsledkov Tafelovej analýzy (sú určené podľa i_{corr}) sa nachádzajú v tab. 3.

Tab. 3 Elektrochemické charakteristiky vzoriek po plazmovej nitridácii
Tabelle 3. Electrochemical characteristics of samples after plasma nitridation

	E_{corr} = korózny potenciál [V vs SCE]	**i_{corr} = Korózna prúdová hustota [µA/cm^2]**	**v_{corr} = Korózna rýchlosť [mm/rok]**
0,5M roztok NaCl	-0,368	3,027	0,035
0,05M roztok NaCl	-0,334	1,730	0,020

Korózne potenciály pre krivky po plazmovej nitridácii dosahujú nižších hodnôt čo predstavuje horšiu termodynamickú stabilitu oproti vzorkám východiskového stavu. Podľa autora (Groysman, 2009) sa korózne rýchlosti pod 0,01 mm/rok vo všeobecnosti pokladajú za nízke a svedčia o vysokej koróznej odolnosti materiálu. Podľa toho sú korózne rýchlosti vzoriek po plazmovej nitridácii (0,02 mm/rok pre 0,05M roztok a 0,035 mm/rok pre 0,5M roztok) získané pomocou softvéru EC-LAB Tafelovou extrapoláciou výrazne vyššie ako hraničná hodnota 0,01 mm/rok a preto takto upravenú oceľ AISI 316L neodporúčame na dlhodobé použitie do prostredí obsahujúcich chloridy, ani v prípade, že je ich koncentrácia veľmi nízka.

Získané výsledky ukázali, že vzorky po plazmovej nitridácii pri teplote 530°C po dobu 24 hodín vykazujú rádovo nižšiu odolnosť voči korózii a nehodia sa do agresívnych prostredí.

POĎAKOVANIE

Príspevok vznikol v rámci riešenia spoločného slovensko-poľského projektu Project Based Learning ako výsledok spolupráce medzi Politechnikou Slaskou, Gliwice a Žilinskou univerzitou v Žiline a projektov KEGA 004ŽU-4/2023, KEGA 009ŽU-4/2023 a KEGA 016ŽU-4/2023.

BIBLIOGRAPHY

1. http://www.sjf.tuke.sk/inmf/NW/moznosti/nitridovanie.html
2. Liptáková T., Bodová korózia nehrdzavejúcich ocelí. 2009. ISBN 978-80-554-0083-9
3. ŠEVČÍKOVÁ J. a HAGAROVÁ M., Povrchové inžinierstvo. Košice: Hutnícka fakulta technickej univerzity, 2007. 109 s. ISBN 978-80-8073-901-0.
4. IŽDINSKÁ Z., Nitridovanie Strojnícka fakulta STU. 2011
5. HADZIMA, B. 2008. Korózia a povrchové úpravy. Prednášky z predmetu. 2008.

TalentDetector
23th-25th June 2025
Gliwice-Brenna, Poland
DEPARTMENT OF ENGINEERING MATERIALS AND BIOMATERIALS
FACULTY OF MECHANICAL ENGINEERING
SILESIAN UNIVERSITY OF TECHNOLOGY
INTERNATIONAL STUDENTS SCIENTIFIC CONFERENCE

AGV localisation in the process of mapping the room floors

Jakub Mlaskawa[a], Krzysztof Paszek[b]

[a] Silesian University of Technology, Faculty of Automatic Control, Electronics and Computer Science, Automatic Control and Robotics Student
[b] Silesian University of Technology, Faculty of Automatic Control, Electronics and Computer Science, Department of Telecommunications and Teleinformatics
email: Krzysztof.Paszek@polsl.pl

Abstract: This article discusses the localisation technique used in AGVs (automated guided vehicles) for floor mapping. The positioning methods, which involve rotary LiDAR and wheel encoders, were fitted to the specific construction of the AGV and its operational requirements. Additionally, the article illustrates the real-time visualisation of the SLAM (simultaneous localisation and mapping) algorithm on a mobile device wirelessly connected to the AGV.

Keywords: SLAM, AGV, positioning, mobile application

1. INTRODUCTION

Modern AGVs require reliable and accurate localisation systems to navigate within unknown and dynamic environments while meeting system-specific performance criteria.

Over the years, various positioning methods have been developed, as UWB (ultra-wideband) technology, which is resistant to interference due to its use of wide-spectrum radio pulses and is considered one of the most effective alternatives [1]. Other solutions include Wi-Fi-based approaches, such as footprinting, which involves comparing the measured signal strength to a constructed map of signal strength patterns [2]. GNSS (global navigation satellite system), although widely used especially outdoors, is unsuitable for indoor applications due to the low or even no satellite signals [3]. Radar-based localisation is another option, although less common due to its relatively low spatial resolution. The common but not very accurate system used inside is INS (inertial navigation system), in which the position error rises in time [4].

Among these, rotating laser scanners (light detection and ranging, LiDAR) have become the most widely used solution [5]. They operate similarly to radar but use light beams instead of radio waves. Despite its versatility and accuracy, LiDAR presents certain challenges. Transparent or irregular surfaces, as well as particles such as dust or smoke, can lead to measurement errors and interfere with mapping and localisation processes. The generated point cloud has been utilised in various positioning and mapping algorithms to enhance the accuracy and support integration with the implemented navigation system logic.

2. POSITIONING

SLAM is a fundamental problem that emerged with the advancement of robotics and autonomous systems operating in unknown, dynamic environments [6]. It involves the use of various sensors and algorithms to create a map of the surroundings and to determine the object's position within that discovered environment.

The SLAM algorithm operates in an endless loop, which involves acquiring data from environmental sensors and odometry, estimating the actual position based on odometry information, and comparing it with sensor data from the environment to verify if it matches the predicted position. This process is then repeated, and the map and estimated position are updated accordingly (see Figure 1).

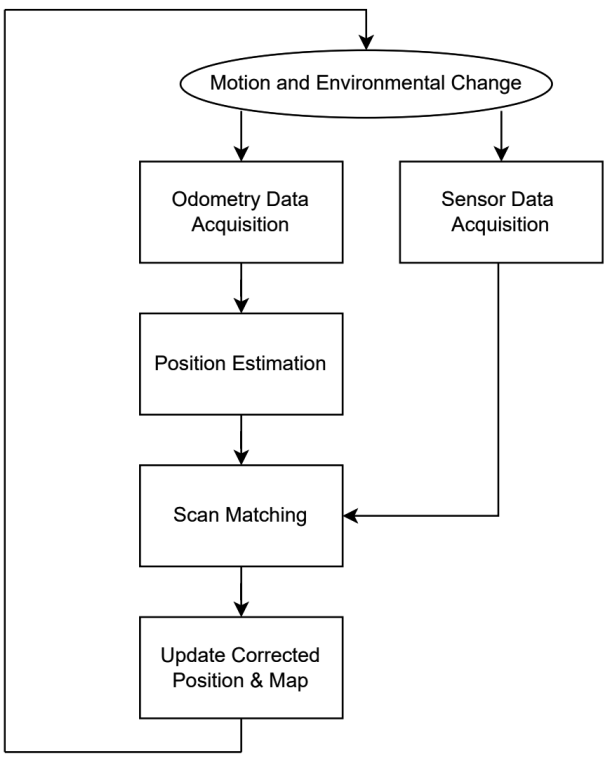

Figure 1. Block diagram of the SLAM algorithm

Each iteration of the SLAM loop requires the acquisition of odometry information and sensor readings from the environment. The selection of sensors depends on the type of algorithm used and the specific requirements of the system. Odometry data can be obtained from wheel encoders or an IMU (inertial measurement unit). For environmental data, the most commonly used devices are rotating laser scanners, which measure the time of flight from the device to obstacles using a laser beam within a limited or full 360-degree range, then calculate distances and usually produce a point cloud as the output.

Prediction of the vehicle's position begins with the use of odometry data. When wheel encoders are employed, displacement can be calculated based on the rotation angle and wheel diameter, producing a two-dimensional motion vector. In a system involving an IMU, especially accelerometers, such as those used in aerial vehicles, displacement is obtained by double integration of acceleration data over time, as these sensors measure acceleration along three axes. This results in a three-dimensional motion vector, which is crucial for vehicles like drones.

Based on the calculated displacement, the system predicts the vehicle's new position. However, correction is necessary, as relying solely on motion sensors can result in cumulative errors and divergence from the actual state. To prevent this, the predicted position is matched with environmental observations, such as a point cloud. Since environmental data are more reliable than odometry, they carry greater weight, helping to align the position more closely with its true location.

As the final step, the current values of the vehicle's position are updated, along with the map based on the latest observations of the surroundings. The algorithm then returns to the beginning of the loop, where data acquisition is performed again.

2.1. Test stand description

The AGV (see Figure 2) was built using an omnidirectional-wheeled platform specifically designed to reconstruct the floor of the room. The core principle of the system is to designate a grid of points within the room where the measurements are to be taken, then transfer information to the vehicle's control system about the movement to the nearest point. Afterwards, the measurement is performed, and the results are sent to the mobile application. The process is repeated until all designated points have been measured.

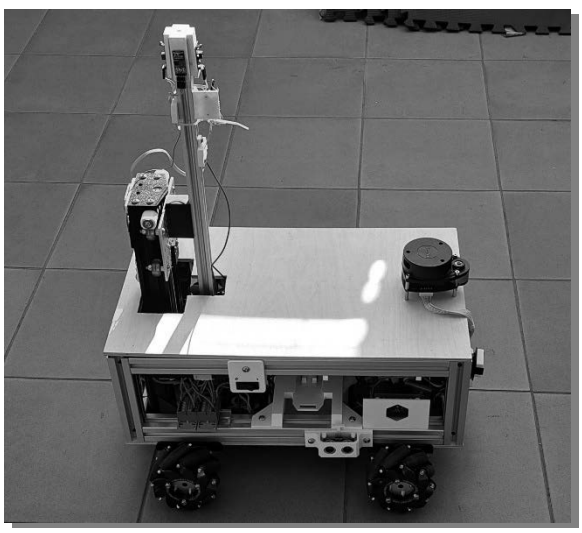

Figure 2. The platform used in the project

The platform was equipped with a LiDAR, IMU, wheel encoders, as well as distance and light beam sensors, enabling the acquisition of data for autonomous operation and effective obstacle avoidance. Sensor data processing and algorithm execution were handled by an Arduino Due and a Raspberry Pi 4, which communicated through a serial interface. Additionally, the Raspberry Pi broadcasts a Wi-Fi network to facilitate wireless communication with a mobile application.

The remaining hardware components supported the vehicle's movement and execution of the measurement tasks. The platform was equipped with four 12 V motors to drive omnidirectional wheels and, additionally, four stepper motors to control the vertical movement of a boom mechanism and to level the platform using three extendable support legs.

A key component for implementing the SLAM algorithm is the LiDAR. In this project, the RPLidar A1M8 model from Slamtec was used. It is a single-beam 2D LiDAR capable of performing 360-degree scans with a sampling rate of 8000 samples per second. The device was

connected to the Raspberry Pi via a USB-A interface, using an appropriate adapter wired to specific pins. Additional key specifications of the laser scanner were shown in Table 1.

Table 1. Key specifications of the RPLidar A1M8

Item	Unit	Typical
Distance Range	m	0.15-12
Angular Range	°	0-360
Distance Resolution	mm	<0.5 (<1.5 m)
		<1% of the distance (≥1.5 m)
Angular Resolution	°	≤1
Sample Duration	ms	0.125
Sample Frequency	Hz	≥8000
Scan Rate	Hz	1-10

The principle behind the device's measurement method is a laser triangulation based on reflected light. The device emits a laser beam in a defined direction, which is reflected by a surrounding object and received by its vision acquisition system. By receiving the ToF (time of flight) and angle of the reflected beam, the system calculates the distance to the object and its angular position relative to the LiDAR. This method, combined with the used hardware, offers an accuracy of better than 1% of the distance for objects located beyond 1.5 m, and better than 0.5 mm for close targets. The typical scan rate is relatively low – 5.5 Hz, yet it is sufficient to generate a dense enough point cloud for the SLAM algorithm to function effectively and respond promptly to dynamic changes in the environment.

3. AGV NAVIGATION

The project was developed using C and C++, implementing a SLAM algorithm along with the other functionalities necessary for communication with the project's other components. To implement core SLAM functionality, the BreezySLAM library was used, chosen for its independence from the ROS (robot operating system) [7]. However, modifications were required to adapt the code to the specific hardware and the design of the AGV used in the project.

Initially, the repository was not fully compatible with the RPLidar A1M8 model. Although example code was provided, the author acknowledged several known issues with its functionality. To resolve this, the official SDK (software development kit) from Slamtec was utilised, offering the necessary API for acquiring scan data and control the main functionalities of the device. As an initial step, it was essential to successfully retrieve and validate the point cloud to avoid further issues and ensure the input to the SLAM algorithm is correct. Since the LiDAR transmits data in the format of pair distance and angle, a transformation to a two-dimensional Cartesian coordinate system was necessary. It was performed using (1) and (2) for X and Y axes, respectively.

$$x = d \cdot \cos \alpha \tag{1}$$

$$y = d \cdot \sin \alpha \tag{2}$$

The calculated (x, y) points (obstacles in the surroundings) were then visualised using the OpenCV library, with a red dot indicating LiDAR localisation.

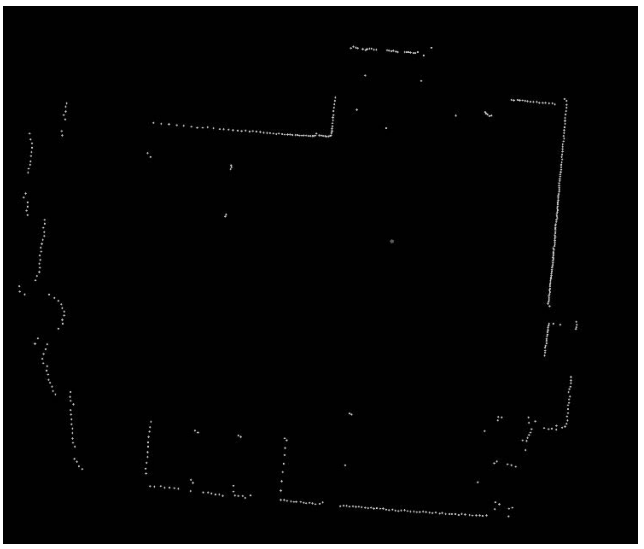

Figure 3. Visualisation of the point cloud

Original implementation primarily supported URG04LX and similar LiDAR sensors–scanners that return distance measurements at fixed, factory-defined angles. This allowed input data to consist solely of distances, with angles treated as constant parameters. However, the model used in this project lacks such precision, as the rotational speed of its scanning head varies due to mechanical and external factors. To address this, it was necessary to transmit angle values alongside distance measurements. Modifications were made to allocate an additional memory area for angles in the form of a one-dimensional vector, same as the structure used for distances. These values were then propagated through all layers of the API down to the core algorithm. Next required functionality involved freezing the SLAM algorithm during the platform's leveling process. Since a 2D LiDAR was used, any change in its tilt could alter the projected scan of the surroundings, potentially leading to significant disruptions in both mapping and localization accuracy. To prevent this, an Arduino – responsible for managing the leveling mechanism - sent start or stop signals through UART serial connection with Raspberry, enabling control over the pausing and resuming the algorithm. Adapting the system to the vehicle also required accounting for "false measurements" caused by the presence of the boom mechanism. It was necessary to remove a segment of scan data corresponding to points falling within the that angular range.

The angle α can be calculated using formula (3).

$$\alpha = arctan\left(\frac{\frac{77}{2}}{371.6}\right) \cdot \frac{180}{\pi} \approx 5.91° \tag{3}$$

Then, the angle should be multiplied by 2 to obtain the full angular span, and it was approximated to 12 degrees to account for measurement uncertainty. As a result, the resulting point cloud did not cover a full 360 degrees, but approximately 348 degrees. However, a small rotation or movement of the AGV was sufficient to eliminate the blind spot.

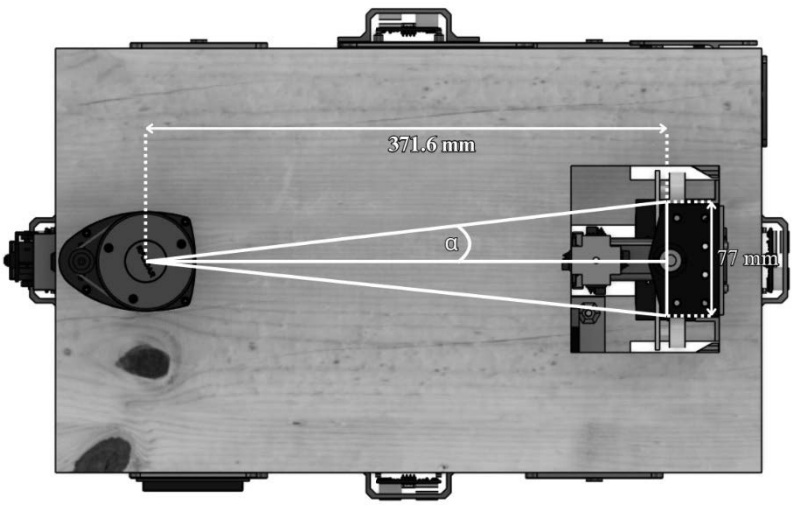

Figure 4. Dimensions of the distance between LiDAR and the probe

To achieve desirable algorithm accuracy, odometry data also needed to be provided. This was handled by a dedicated program thread that read the displacement reported by the Arduino since the last loop iteration. The Arduino calculated the two-dimensional vector using data from the encoders, taking into account the radius of the wheels. This whole communication was based on the serial port.

3.1. Mobile app description

The mobile application allows users to view the map generated by the SLAM algorithm, which was a key component of the platform's navigation system. This provided a real-time visualisation of the currently explored area and an initial overview of the room's layout.

The application offers several essential features for controlling the AGV and viewing its data. These include manual navigation, switching to autonomous mode, and visualising the mapped surface of the room. The most important functionality, in the context of this article, was displaying the map generated by the SLAM algorithm (see Figure 5), which served as the foundation for the navigation system. To enable this, a connection must be established. In this implementation, the Raspberry Pi operated as a server using the synchronous TCP (transmission control protocol), requiring the user to input the appropriate IP address and listening port.

Once the connection was established, the map was transmitted to the application. The image was structured as a two-dimensional array of 800 x 800 character values. Since each character equals 1 byte of memory, the image size was approximately 625 KB in binary form. To reduce the size of the map and improve transmission speed, the lossless RLE (run-length encoding) compression method was used, taking advantage of the large number of repeating values. This reduced the data size to around 150 KB – which was approximately 76% reduction. The data was then sent as a complete unit to the application socket.

The map utilised shades of grey to indicate the level of certainty regarding the presence of obstacles at specific locations. In this map (see Figure 5), white areas {1} corresponded to regions accessible to the AGV, while black areas {2} denoted obstacles that the navigation system needed to recognise and avoid. Areas of the environment that remained unexplored {3} were assigned intermediate values – grey, reflecting the lack of information about them.

Despite using low-cost hardware, the representation of the room map occurs in real-time on a mobile device. The key turned out to be the use of a method that reduces the size of the data packet, allowing for the smooth display of the transferred image.

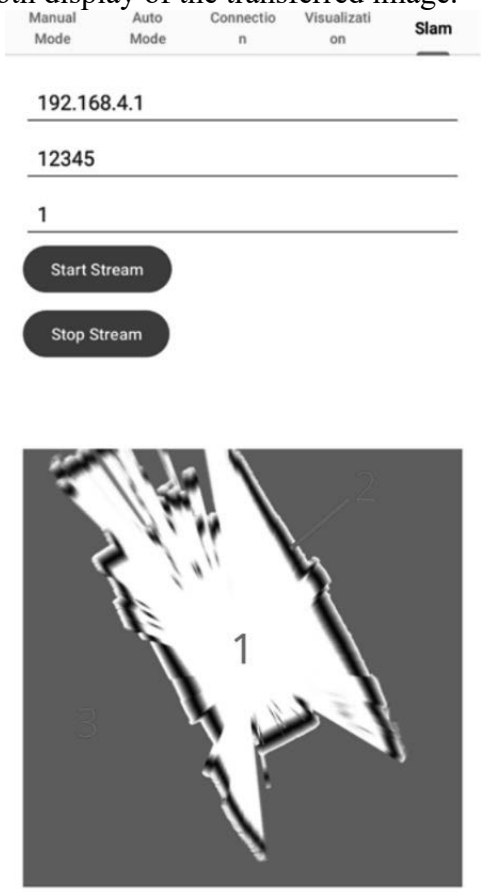

Figure 5. Mobile app SLAM visualisation

4. CONCLUSION

The project successfully accomplished localization and mapping for AGV navigation using a SLAM algorithm. The generated map accurately reflected the actual layout of the surrounding environment, and the estimated position demonstrated high precision, with accuracy up to a few centimetres. Despite being a budget model, the RPLidar A1M8 effectively collected point clouds that were efficiently processed by the algorithm. The connection with the mobile application operated smoothly, with minimal delay compared to real-time state. Although the Raspberry Pi had limited computing power, it managed to run the software efficiently, utilising the available resources effectively.

The project, while fully operational, still offers room for further development. One potential improvement is the implementation of loop closure within the SLAM algorithm. This technique involves recognising when the system returns to a previously visited location and applying corrections to the existing map, helping to reduce drift and improve overall accuracy.

In summary, the project established a foundational system for positioning, based on LiDAR scanner and odometry data, and map generation with clear potential for future enhancements.

ACKNOWLEDGEMENTS

This research was partially funded by the Polish Ministry of Science and Higher Education partially by Statutory Research, and partially by Young Researchers funds of the Faculty of Automatic Control, Electronics and Computer Science, Silesian University of Technology.
This research was supported by the Excellence Initiative – Research University program at the Silesian University of Technology 2025.

BIBLIOGRAPHY

1. K. Paszek, UWB System for Frequent Positioning of Moving Objects, in M. Themistocleous, N. Bakas, G. Kokosalakis and M. Papadaki,eds., Information Systems (2025) 299–310, doi:10.1007/978-3-031-81322-1_21.
2. H. Liu, H. Darabi, P. Banerjee and J. Liu, Survey of Wireless Indoor Positioning Techniques and Systems, IEEE Transactions on Systems, Man and Cybernetics, Part C (Applications and Reviews), 37 (2007) 1067–1080, doi:10.1109/TSMCC.2007.905750.
3. A. El-Rabbany, Introduction to GPS: The Global Positioning System, (2002).
4. D. Grzechca, K. Tokarz, K. Paszek and D. Poloczek, Using MEMS Sensors to Enhance Positioning When the GPS Signal Disappears, in N.T. Nguyen, G.A. Papadopoulos, P. Jędrzejowicz, B. Trawiński, & G. Vossen,eds., Computational Collective Intelligence (2017) 260–271, doi:/10.1007/978-3-319-67077-5_25.
5. A. Ziębiński and P. Biernacki, How Accurate Can 2D LiDAR Be? A Comparison of the Characteristics of Calibrated 2D LiDAR Systems, Sensors, 25 (2025, doi:10.3390/s25041211.
6. Y.-T. Wang, C.-C. Peng, A. Ravankar and A. Ravankar, A Single LiDAR-Based Feature Fusion Indoor Localization Algorithm, Sensors, 18 (2018), doi:10.3390/s18041294.
7. S. Bajracharya, BreezySLAM: A Simple, efficient, cross-platform Python package for Simultaneous Localization and Mapping, Washington Lee University, (2014).

TalentDetector
23th-25th June 2025
Gliwice-Brenna, Poland
DEPARTMENT OF ENGINEERING MATERIALS AND BIOMATERIALS
FACULTY OF MECHANICAL ENGINEERING
SILESIAN UNIVERSITY OF TECHNOLOGY
INTERNATIONAL STUDENTS SCIENTIFIC CONFERENCE

Standardized Experimental Method for Evaluating Aircraft Checklist Interfaces in IFR Simulation

Dariusz Myszor[a], Magda Mrozik[b], Mateusz Pietraszko[b], Michał Sujkowski[b], Aleksandra Gruszka[c], Piotr Pulit[d]

[a] Silesian University of Technology, Faculty of Automatic Control, Electronics and Computer Science, Department of Algorithmics and Software
[b] Silesian University of Technology, Faculty of Transport and Aviation Engineering, Department of Air Transport
[c] Silesian University of Technology, Faculty of Mechanical and Technological Engineering
[d] Silesian University of Technology, Faculty of Transport and Aviation Engineering, Department of Air Transport
email: dariusz.myszor@polsl.pl

Abstract: This article presents the methodology of an experimental study focused on evaluating the operational effectiveness of various types of aircraft checklists under IFR (Instrument Flight Rules) conditions. The study was conducted using a flight training device of FNTP II class, commonly used in pilot training. As a key part of the project, a custom data acquisition application was developed specifically for this research. The application allows for standardized and precise recording of pilot actions related to checklist execution, using timestamp-based tracking.
This structure enables detailed analysis of parameters such as response times, procedure compliance, total checklist interaction time, and time intervals between actions. The article outlines the flight scenario design, experimental setup, research tools used, and data recording strategy. It also discusses the flexibility of post-processing the collected data to support various analytical objectives.
The proposed methodology allows for comprehensive comparisons between different types of checklists—including paper-based, electronic, and avionics-integrated forms—highlighting their impact on procedure execution and identifying potential risks or advantages associated with each variant.
Keywords: human factor, IFR flight, flight simulation, aircraft checklist

1. INTRODUCTION

Ensuring safety in aviation remains a critical priority across all sectors of the industry. While technological development has significantly improved aircraft systems, avionics, and pilot training, human performance continues to be a dominant factor influencing flight safety. Numerous reports indicate that the majority of aviation accidents result from human errors, often

caused by decision-making issues, improper checklist use, or loss of situational awareness. These findings underline the necessity of evaluating how pilots interact with various types of procedures and interfaces, including flight checklists.

Checklists are an essential tool in flight operations, intended to reduce reliance on memory, structure pilot behavior, and enhance compliance with standard operating procedures. In modern cockpits, the introduction of electronic and avionics-integrated checklists raises new questions about their usability, efficiency, and operational effectiveness.

This article is part of a broader interdisciplinary research project focused on the operational effectiveness of different types of aircraft checklists in various scenarios and phases of flight. The study was conducted using a flight training device classified as FNTP II, replicating realistic IFR conditions. The key innovation described in this paper is the development of a custom software tool for timestamp-based data acquisition, allowing for precise and standardized analysis of pilot behavior during checklist execution.

1.1. Human Factor

Human performance is the most variable and often the most vulnerable element in the aviation safety chain [1]. According to data from the International Civil Aviation Organization (ICAO), the human factor contributes to 60–80% of aviation incidents and accidents worldwide. In general aviation, pilot error alone has been identified as the primary cause of up to 74.9% of all accidents [2, 3].

To understand and manage these risks, several conceptual frameworks have been developed. One of the most influential is the Swiss Cheese Model by James Reason, which illustrates how multiple latent failures and active errors can align across different system layers, ultimately leading to an accident if not mitigated [4].

Another widely adopted framework is the SHELL model (figure 1.), developed by ICAO, which maps out the interfaces between the pilot (Liveware) and other key system components: Software (procedures, checklists), Hardware (displays, controls), Environment (weather), and other Liveware (crew, ATC) [5]. The central idea of the SHELL model is that all mismatches or poorly managed interactions at any of these interfaces may result in degraded safety performance.

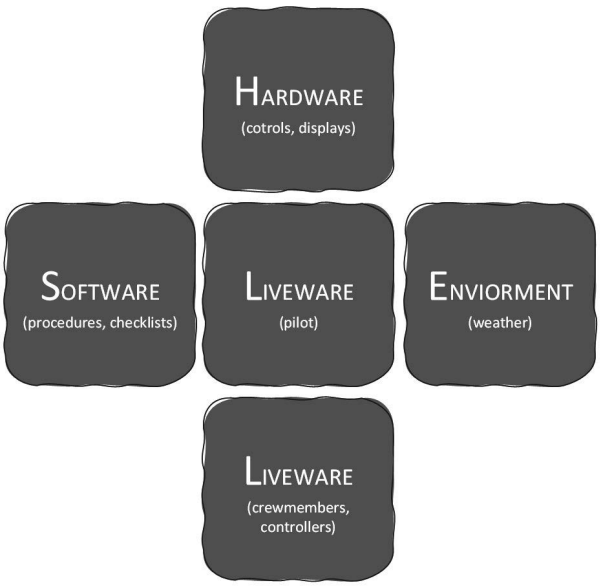

Figure 1. SHELL Model in Aviation

In the context of checklist usage, the pilot must often switch attention between managing aircraft systems, communicating with ATC, processing information from sensors and displays, and executing procedures – sometimes under high workload and time pressure. This is particularly evident during IFR operations.

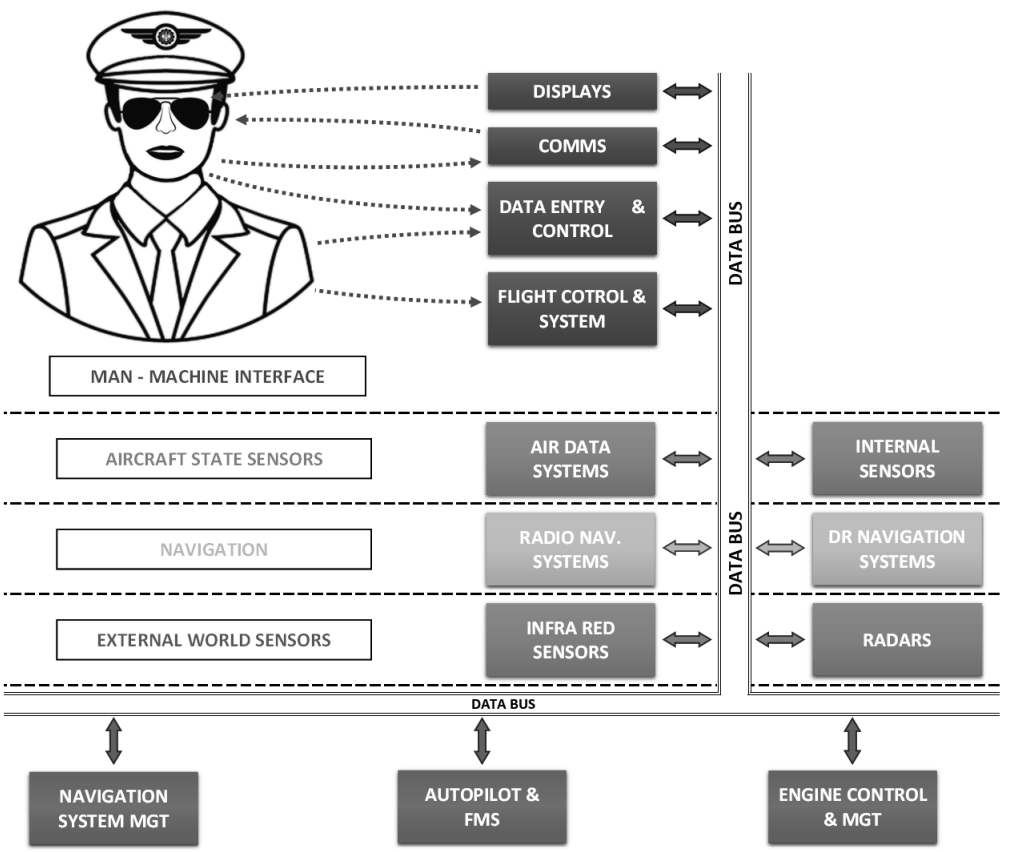

Figure 2. Interaction of the pilot with various aircraft systems

The figure 2. illustrates the complexity of real-time decision-making and the volume of information processed by the pilot. Each subsystem (navigation, FMS, communication, flight control) delivers critical data requiring attention and correct interpretation. If a checklist interface adds complexity or distracts from the primary flight task, it can compromise the safety margin.

1.2. Aviation operations safety

According to ICAO's official definition, "Safety is the state in which the risk of harm to persons or property damage is reduced to, and maintained at or below, an acceptable level through a continuing process of hazard identification and risk management" [1]. To meet this goal, aviation relies heavily on standardization – of procedures, interfaces, communication, and task management. Checklist design is part of this safety infrastructure. When properly implemented, checklists reduce variability in pilot behavior, ensure task completeness, and act as a fail-safe mechanism under stress or high workload.

However, as new technologies evolve and migrate into the cockpit—such as avionics-integrated checklists, touchscreens, or augmented reality – their impact on pilot performance must be carefully assessed. What enhances efficiency in one scenario may increase workload or cause confusion in another. The process of hazard identification must therefore include the way pilots interact with new types of digital checklists.

This article explores one aspect of that interaction by focusing on the methodology of standardized checklist evaluation under simulated IFR conditions. It sets the foundation for a broader analytical framework assessing both objective performance data and human-system compatibility in checklist usage.

2. METHODOLOGY

The research was supposed to measure the efficiency of different types of checklists. Two types were taken into consideration. First there were standard paper checklists, next built-in Garmin checklists.

To compare both checklist types, two similar but distinct IFR flight scenarios were designed. The objective was to obtain comparable results while preventing participants from memorizing procedures during the first flight and anticipating tasks in the second. Each participant completed two flights—one using a paper checklist and the other using Garmin checklists. Both the order of checklist types and the assignment of flight scenarios were randomized across participants, with an approximately equal (50/50) distribution. These measures aimed to minimize the influence of pilot anticipation and preparation, enabling a more accurate assessment of checklist effectiveness. In addition to using checklists, participants received in-flight instructions or hints from a simulated ATC, provided by a researcher communicating via radio.

2.1. IFR flight

IFR (Instrument Flight Rules) is a set of regulations that govern how a pilot operates an aircraft when flying primarily by reference to onboard instruments rather than external visual cues. IFR

is used during flights conducted in IMC (Instrument Meteorological Conditions), which refer to weather conditions where visibility is significantly reduced—making visual flight impractical or unsafe. These rules also apply to commercial jet operations on long-distance routes [1].

There are numerous regulations outlining the procedures and equipment required for IFR flight. In general, flying under IFR is considered challenging, particularly when conducted by a single pilot without additional crew support.

2.2. Flight scenario

The flight scenario was designed to be as simple as possible for an IFR operation. The participants were expected to put most of their attention into checklists and not distract themselves with complex piloting tasks. They were given a cold and dark aircraft already positioned on a runway at Zurich Airport. The entire scenario was structured to be completed strictly in accordance with the provided checklists. The first checklist involved the pre-flight procedure, during which participants inspected the aircraft and copied the departure clearance from Zurich Ground. This stage also included receiving general instructions about the expected flight profile. The next steps involved engine start-up and before take-off procedures, transitioning the aircraft from a cold and dark state to a ready-for-flight configuration. This included engine checks and obtaining take-off clearance from the tower. After that take-off took place (a stage of flight, when checklists are most of the times not used, but nevertheless useful if the plane is new to the pilot). Straight after that vectors were given by ATC. When the aircraft was stable in climb a specific checklist was supposed to be performed. The checklist was prepared by researchers. It was made in such a way, that it needed a completion of a long and complex procedure. During checklist execution, the researchers simulated an ATC interruption by requesting current speed and altitude, forcing participants to momentarily shift focus and then resume the checklist. This was the most important checklist, because it showed how pilots managed a long set of tasks, and what methods they used in order not to get lost during its execution. After checklist was finished pilot was expected to execute an approach briefing in accordance to approach chart. Its goal was to familiarize the pilots with approach type, and prepare them for landing. If there was not enough time to complete everything before the approach, ATC provided vectors to keep the plane nearby the final approach path.

At the end of the flight, after landing, pilots were instructed to stop on the runway and shutdown the aircraft according to the last checklist. The purpose of described procedure was to measure effectiveness of checklists in all phases of flight both on the ground and in flight. While the flight scenarios varied in detail between employed checklist types, they were similar enough to prevent participants from anticipating specific tasks or preparing procedural shortcuts.

3. RESEARCH TOOLS

The entire experiment was conducted on a non-certified FNTP II-class simulator, configured with a Cessna 172RG flight model. The data acquisition software was custom-developed by the research team.

3.1. Equipment and setup

The FNTP II simulator is widely used in flight training organizations for procedural and instrument flight instruction. The device meets all applicable simulator certification standards [2] and features a full-scale, interactive cockpit designed to simulate flight operations as realistically as possible. For the purposes of this study, the Cessna 172RG was selected—a simple, small aircraft that is fully IFR-certified [3]. It was chosen due to its ease of use, which was an important factor given the large number of study participants.

Custom checklists were developed by the research team for each phase of flight, ensuring consistency across all participants. The paper checklist were printed, laminated and formatted in order to fit into kneeboard. Electronical checklist were procedures written into Garmin GNS430.

Figure 5,6. Paper checklist used in research, Garmin GNS430 in checklist menu

Figure 5 presents the paper checklist used during the study. It was compact in format, allowing pilots to freely view and navigate all its sections. In contrast, Figure 6 shows the same procedures implemented within the Garmin avionics system [4]. In order to familiarize pilot with Garmin interface a brief training session was conducted.

3.2. Data acquisition and software

The custom-built application allowed researchers to create individual pilot profiles and systematically record performance data. Basic information such as total flight hours, age, and avionics experience was recorded at the beginning of each session. Then researchers were able to determine the flight progress by marking if every step of the procedure was correct, incorrect or omitted. Software made timestamps for every or these decisions, allowing further analysis of the data. After each flight NASA TLX survey was completed to determine pilot's fatigue, stress or exhaustion.

In the forementioned application, as shown in Figure 6, first the checklist was picked according to what the pilot was doing, and then checkboxes were clicked as the participant was flying. "Each checklist item could be marked as "OK" (correctly performed), "ERROR" (misperformed despite acknowledgment), or "OMITTED" (skipped without execution). The program also checked when any point was omitted.

4. CONCLUSIONS

This article presents a standardized and repeatable research methodology for evaluating pilot interaction with different types of aircraft checklists during an IFR-based experimental flight. The main achievement described in the study is the development and validation of a proprietary data acquisition application, designed to enable precise, objective, and consistent recording of pilot behavior throughout checklist execution.

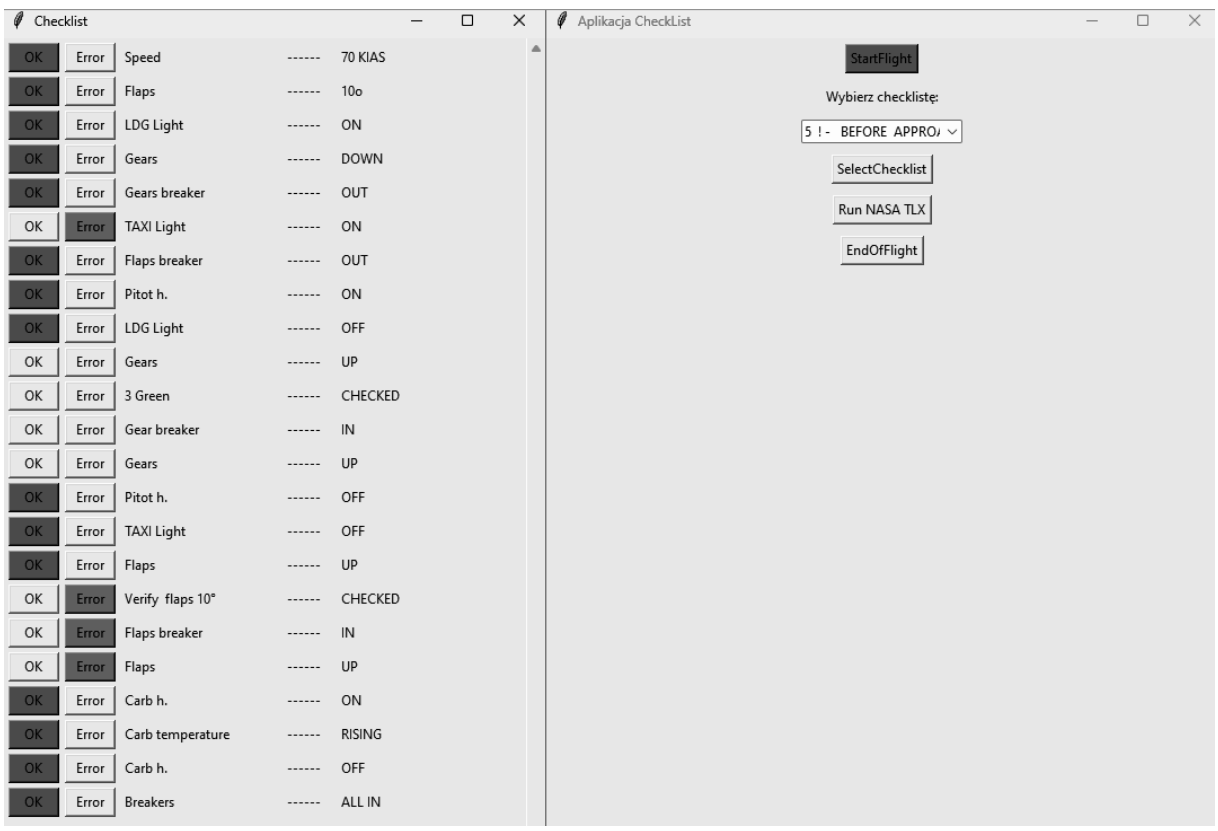

Figure 6. data acquisition program

The implemented system allows for the creation of individual user profiles and assigns timestamp markers to each checklist item—whether correctly executed, omitted, or performed incorrectly. This enables detailed time-based analysis, including response time for each checklist step, sequence compliance, average delay between actions, and total checklist handling time.
This data structure supports objective and quantitative comparisons between paper-based and electronic checklists, including those integrated into onboard avionics. The standardized logging

format enables the analysis of pilot behavior across different flight phases and scenarios, making the methodology scalable and applicable to broader experimental studies.
The proposed methodology has both scientific and practical value. It can be used in the design and validation of checklist formats, evaluation of training effectiveness, and identification of procedural risk areas. It enables researchers and practitioners to move beyond subjective user feedback and rely on measurable, verifiable performance metrics. As cockpit technology continues to evolve, tools of this nature may play a crucial role in assessing human–system interfaces under operational conditions.

BIBLIOGRAPHY

1. Smith et al., 2018; ICAO, 2019
2. AOPA AIR SAFETY FOUNDATION; 2006 NALL REPORT Accident Trends and Factors for 2005
3. Kozuba J. (2011), Impact of Human Factor on Likelihood of Aircraft Accident, Archives of Transport System Telematics, Vol. 4, Issue 2, May 2011, str. 29-36
4. Reason, James, E. Hollnagel, and J. Paries. "Revisiting the Swiss cheese model of accidents." Journal of Clinical Engineering 27.4 (2006): 110-115
5. Kiss C. "The Human Factors SHELL Model." Academia Edu 80, 2005
6. International Civil Aviation Organization, Doc 9859 Safety Management Manual, Fourth Edition, Canada, 2018

TalentDetector
23th-25th June 2025
Gliwice-Brenna, Poland
DEPARTMENT OF ENGINEERING MATERIALS AND BIOMATERIALS
FACULTY OF MECHANICAL ENGINEERING
SILESIAN UNIVERSITY OF TECHNOLOGY
INTERNATIONAL STUDENTS SCIENTIFIC CONFERENCE

Comparative Analysis of Paper vs. Avionics-Integrated Checklists Based on Pilot Feedback

Dariusz Myszor[a], Magda Mrozik[b], Mateusz Pietraszko[b], Michał Sujkowski[b], Aleksandra Gruszka[c], Piotr Pulit[d]

[a] Silesian University of Technology, Faculty of Automatic Control, Electronics and Computer Science, Department of Algorithmics and Software
[b] Silesian University of Technology, Faculty of Transport and Aviation Engineering, Department of Air Transport
[c] Silesian University of Technology, Faculty of Mechanical and Technological Engineering
[d] Silesian University of Technology, Faculty of Transport and Aviation Engineering, Department of Air Transport
email: dariusz.myszor@polsl.pl

Abstract: This article presents the results of a survey-based study on the subjective evaluation of two types of aircraft checklists used in general aviation: traditional paper checklists and avionics-integrated electronic checklists (Garmin GNS 430). The study was conducted following a simulated IFR flight in a Flight and Navigation Procedures Trainer (FNTP II), during which each participant used both checklist types – once in paper form and once in electronic form, with the order randomized. The questionnaire included questions related to intuitiveness, clarity, cognitive workload, and personal user preferences. The study group included pilots with varying levels of experience, which had a noticeable impact on their responses. While many participants found paper checklists more intuitive and easier to operate, others appreciated the integration of checklists into avionics systems, despite reporting occasional difficulties—especially with switching functions during navigation tasks. The results revealed significant variability in perceptions, highlighting that checklist design should be tailored to user profiles, taking into account operational familiarity and interface expectations. These findings underline the need for further investigation, particularly based on objective performance data, to comprehensively assess how checklist formats influence pilot performance and operational safety.

Keywords: aviation checklist, electronic checklist, survey study, flight simulation, pilot perception

1. INTRODUCTION

Modern civil aviation is mainly based on standardized operating procedures (SOPs) and checklists, the main purpose of which is to support crews in maintaining operational safety, both during normal flight operations, in abnormal and critical situations [1]. These tools are designed

primarily to ensure completeness, accuracy and usability in conditions of high stress and limited time to make decisions. Their effectiveness depends on a skilful balance between conciseness and detail, which forces aircraft designers and manufacturers, as well as air operators, to meet high functional requirements. Both in literature and operational practice, questions are increasingly being raised about the actual purpose and functionality of these tools. SOPs and checklists are developed not only by aviation technology experts and experienced pilots, but also by legal teams who place great emphasis on meeting the requirements of the letter of the law. There is a risk that the content of these documents may be partially determined by the need to limit legal liability, which may translate directly into the level of operational efficiency. Additionally, many procedures are created for a specific operation, which does not always reflect real conditions, such as sudden engine failure or difficult weather conditions. Analysing recommendations from post-accident analyses often leads to the expansion of procedures, which - although justified preventively - may result in their excessive complexity and limited usefulness in situations requiring a quick response.

1.1. Checklist versus human error

From the beginning of their use in aviation, checklists have played one of the key roles in the cockpit. The scope of their use has evolved with the development of aviation technology, as well as the complexity of the operations performed. Designed to limit human error to the greatest possible extent, they play the role of a tool that functions on the "do and check" and "do" principle[2] . An additional element is "memory items" which often require the pilot to recall from his own memory in a critical situation or when time is short.

1.2. Checklist types in aviation

For decades, paper checklists have found their place in both commercial and general aviation. Designed in a way that allows pilots to follow and perform subsequent steps, they have established a certain pattern of functioning in the cockpit. However, the dialogue on the use and practicality of electronic checklists is also increasingly being raised. Properly designed, they can allow for more effective time management of flight operations, as well as reduce the level of stress and distraction in the cockpit. Electronic checklists allow you to perform activities step by step, minimizing the possibility of making a mistake or the impossibility of performing any of the activities in the event of a disruption in the pilot's operational fluidity.

1.3. Objective and scope of the study

Abnormal situations, defined as events that deviate from the standard course of a flight operation, are often characterized by a high level of complexity, unpredictability, and stress. Such conditions are conducive to the crew making procedural errors, as well as correctly identifying the problem. Time pressure – especially during the approach and landing phases – is one of the most significant risk factors. One example is the emergency landing of US Airways flight 1549 on the Hudson River on January 15, 2009 [3]. In this case, the crew demonstrated composure and, despite losing thrust in both engines, had only a few minutes to take appropriate action and performed ditching. The time pressure to make the right decision and to take appropriate actions meant that the pilots were unable to find and fully complete all procedures and checklists. In opposite an example where time pressure did not play a major role is the story of Qantas flight

32 from 2010. During the aforementioned flight, an engine failure occurred on the Airbus A380. The crew had an adequate amount of fuel on board, and the presence of a second crew, who supported the actions during the failure, turned out to be an additional advantage. Despite the lack of excessive time pressure, operational procedures and checklists were not fully completed in this case either[4].

These cases indicate the limitations of current training process models, which, based on known and previously investigated incidents, create a pattern of action for crews, SOPs and checklists. Although this usually allows for a faster assessment of the situation and learning a specific scheme of actions, it limits cognitive functions and full analysis of a new, unexpected situation in which new elements and a separate time period occur.

The purpose of this article is to analyse the effectiveness of the application and execution of procedures, comparing the use of paper and electronic checklists during normal and abnormal situations in standard and unpredictable conditions. The study focuses on assessing the extent to which existing operational decision support tools fulfil their function in real, dynamic scenarios, and what implications this has for the design of future operational support systems, in particular electronic checklists.

2. METHODOLOGY

The primary objective of the study was to compare in perception two types of aviation checklists: traditional paper-based checklist and an electronic checklist integrated with avionics via a Garmin GNS 430 interface. The analysis focused on key aspects such as usability, intuitiveness, operational simplicity, and overall user comfort. All study participants took part in two similar simulator flights., each involving the use of a different checklist format, and subsequently assessed their experience based on individual perceptions. The goal was to gain insight into user preferences, identify the perceived strengths and limitations of each format, and evaluate how different type of checklist influences procedural execution, situational awareness, and pilot workload.

2.1. Paper checklists

The paper checklist was formatted as a single A4 sheet, foldable into three sections. It was laminated to enhance its durability and resistance to damage. The checklist could be placed on a kneepad or comfortably held in one hand.

Politechnika Śląska — C 172 RG NORMAL CHECKLIST

BEFORE START-UP R&D	
Preflight insp.	COMPLETE
Fuel selector	BOTH
Avionics	ON
Master	ON
Parking brake	SET
Cowl flaps	OPEN
Landing gear	GREEN
Breakers	ALL IN
Flight controls	FREE
Trims	T / O
Flaps	0°
ATIS	COPY
DEP. clearance	OBTAIN
Avionics	OFF

ENGINE START-UP R&D	
Mixture	RICH
Propeller	HIGH RPM
Carb h.	OFF
Throttle	1"
Master	ON
Beacon	ON
Prop aera	CLEAR
Primer	APPLY
Ignition	START
Oil press.	CHECK
Avionics master	ON
Radio	ON
XPDR	STB / ALT

Politechnika Śląska — C 172 RG NORMAL CHECKLIST

BEFORE TAKE-OFF R&D	
Parking brake	SET
Altimeters	SET
Trims	T / O
Flight controls	FREE
Fuel selector	BOTH
Throttle	1800 RPM
Mixture	RICH
L & R Magnetos drop	150 MAX / 50 DIFF
Propeller	CYCLE LOW - HIGH
Carb h.	CHECK DROP
Engine instruments	CHECK
Suction	CHECK
Throttle	1000 RPM
Radio	SET
Parking brake	OFF
T/O clearance	OBTAIN

TAKE-OFF	
Flaps	0°
Carb h.	OFF
LDG Light	ON
Flight controls	FREE
Power	FULL / 2700 RPM
Rotate	at 55 KIAS
Landing gear	RETRACT 50 ft
400 ft AAL	
Flaps	0°
Power	25 / 2500
LDG Light	OFF

Politechnika Śląska — C 172 RG NORMAL CHECKLIST

BEFORE APPROACH R&D	
Speed	70 KIAS
Flaps	10°
LDG Light	ON
Gears	DOWN
Gears breaker	OUT
TAXI Light	ON
Flaps breaker	OUT
Pitot h.	ON
LDG Light	OFF
Gears	UP
3 Green	CHECKED
Gear breaker	IN
Gears	UP
Pitot h.	OFF
TAXI Light	OFF
Flaps	UP
Verify flaps 10°	CHECKED
Flaps breaker	IN
Flaps	UP
Carb h.	ON
Carb temperature	RISING
Carb h.	OFF
Breakers	ALL IN

Figure 1. One of the two pages of the traditional paper-based checklist used.

2.2. Electronic checklists

The electronic checklist was integrated with the cockpit avionics (figure 2) and was located above the radio panel. To access it, the pilot had to manually activate the appropriate section. Each item in the checklist corresponding to the current flight phase was marked as completed using a button on the device.

Figure 2. Electronic checklist in the Garmin GNS 430.

2.3. After flight survey

An assessment of the use of different types of checklists was conducted among study participants shortly after they completed a simulator flight. The primary objective of the questionnaire was to gather subjective evaluations of the usability and effectiveness of different types of checklists used during a simulated flight.

3. RESULTS

Each of the 15 individuals involved in the study filled out a questionnaire within a few days following their simulation session. The questionnaire was distributed individually and was not anonymous. The study group consisted of pilots at various stages of their flight training, ranging from those who have about 45 flight hours to advanced trainees with more than 300 flight hours. Among the respondents, four were female, while the remaining participants were male.

The first survey item addressed the perceived ease of use of each checklist format. When asked which checklist was easier to use, 60% of respondents selected the traditional paper-based checklist, whereas 40% indicated the electronic version integrated into the cockpit avionics.

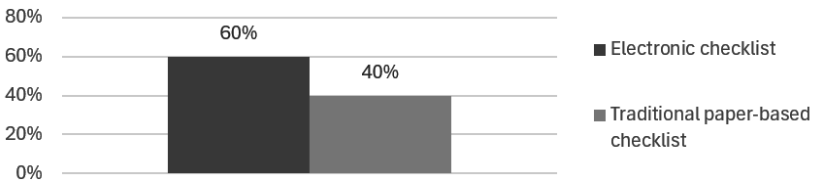

Figure 3. Responses to the question: "Which type of checklist was easier to use?"

Figure 4 presents the distribution of intuitiveness ratings for the traditional paper-based checklist and the electronic checklist. Participants rated each format on a 10-point scale, where 1 indicated "Not intuitive at all" and 10 represented "Very intuitive". The paper-based checklist received generally higher ratings, with a mean score of 6.87, while the electronic checklist was rated more variably, with a mean score of 5.20. The ratings for the paper-based checklist ranged from 1 to 10, with the majority of responses concentrated in the upper end of the scale. In contrast, the ratings for the electronic checklist were more evenly spread across the middle values of the scale, indicating greater variability in user perception.

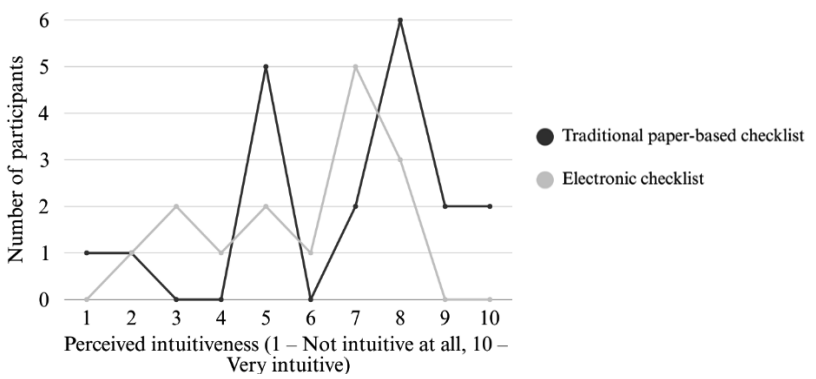

Figure 4. Distribution of intuitiveness ratings for the traditional paper-based checklist and the electronic checklist.

Figure 5 presents the distribution of participants' ratings concerning the visual clarity and structural organization of the two checklist formats. Each checklist was evaluated on a 10-point scale, where 1 corresponded to "Very difficult to follow and understand" and 10 to "Very clear and easy to follow". The traditional paper-based checklist received a slightly higher overall assessment, with a mean score of 7.80, while the electronic checklist obtained a mean score of 6.93. In both cases, responses tended to cluster toward the higher end of the scale.

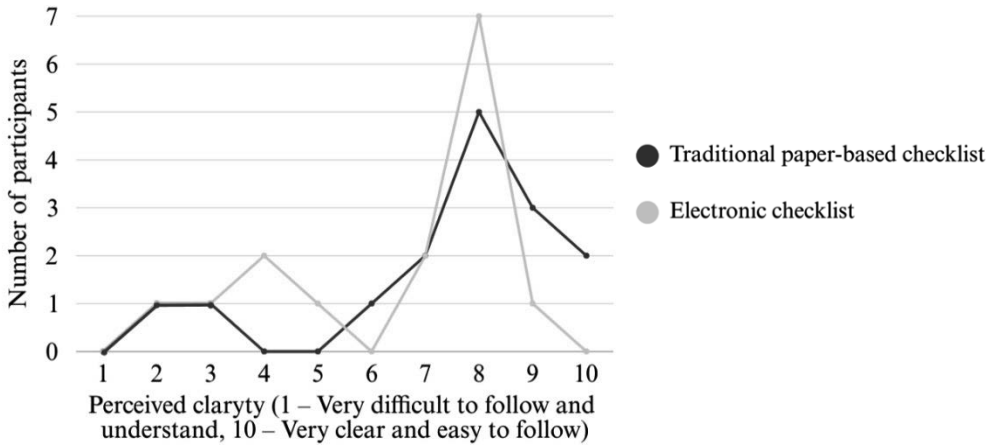

Figure 5. Distribution of visual clarity and structural organization ratings for the traditional paper-based checklist and the electronic checklist.

Figure 6 shows the responses to the question, "Did the use of the electronic checklist interfere with navigation tasks?" Of the 15 participants, less than half answered that it partially interfered, 5 said it interfered, and 3 indicated that it did not interfere.

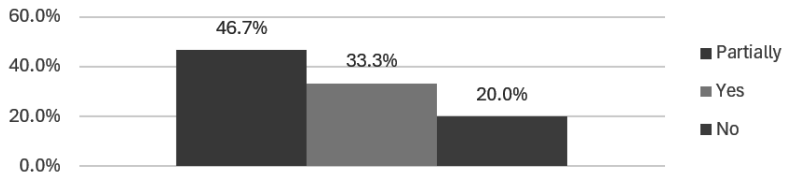

Figure 6. Response distribution to the question concerning interference of the electronic checklist with navigation tasks.

The next item in the questionnaire aimed to assess the perceived necessity of additional training prior to operating electronic checklist systems in a simulated flight environment. Out of 15 participants, 10 responded "Yes," indicating that, in their opinion, extended training in the use of the electronic checklist should be provided, while the remaining 5 stated that such training was not necessary.

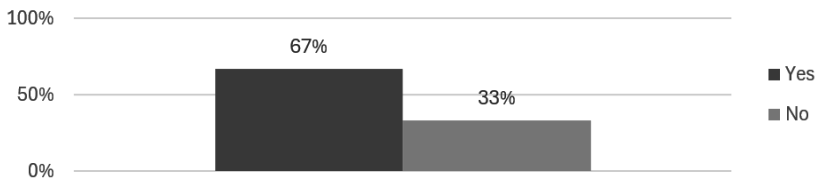

Figure 7. Response distribution to the question concerning whether the use of the electronic checklist should be preceded by special or extended training.

The subsequent section of the survey consisted of open-ended questions. The first asked participants to identify perceived disadvantages of using traditional paper-based checklists. Several recurring themes emerged from the responses. The vast majority pointed to difficulties in maintaining workflow continuity. Diverting attention or interrupting a task often led to a loss of orientation regarding the current checklist item. Participants also frequently mentioned the inability to mark completed steps, which made progress tracking more difficult. Physical

limitations of the paper format were also noted, including the risk of loss or damage. In addition, the need to flip through pages and search for the correct section was seen as distracting. Other concerns included the space occupied by the checklist in the cockpit and the need to use one hand to operate it.

The next open-ended question in the survey focused on the perceived advantages of using traditional, paper-based checklists. Participants indicated that this format was well known to them from earlier stages of flight training, which contributed to greater ease and confidence in its use. It was emphasized that the paper checklist allowed for quick and seamless transitions between sections, in contrast to the electronic version, which required familiarity with the interface. The main advantages were clarity, intuitiveness, and simplicity of use. All information was presented on a single page or in a logical, easy-to-follow sequence. Respondents also noted that the paper format could be adapted to individual preferences, such as attaching it to a kneeboard or positioning it at a convenient angle, which improved usability. A frequently mentioned benefit was the constant physical availability of the checklist – always "at hand" - without the need to perform additional actions such as operating a touchscreen or navigating through a digital system.

The subsequent open-ended question in the survey focused on the perceived advantages of using electronic checklists. The most frequently mentioned benefit was the ability to mark completed items, which helped participants keep track of their progress and reduced the probability of missing steps. Many respondents emphasized the constant availability of the checklist in a fixed, easily visible location, eliminating the need for additional illumination. Participants also highlighted that the integration of the checklist into the cockpit avionics reduced the number of loose items and eliminated the need to manipulate physical documents. This allowed for more efficient use of cockpit space - particularly around the kneeboard - contributing to a tidier and more ergonomic workspace. Some also emphasized that using an electronic interface felt more natural and intuitive, especially for younger pilots more accustomed to digital systems.

Table 1. Comparison of the main advantages and disadvantages of paper-based and electronic checklists.

	DISADVANTAGES OF A PAPER-BASED C/L	ADVANTAGES OF A PAPER-BASED C/L	DISADVANTAGES OF ELECTRONIC C/L	ADVANTAGES OF ELECTRONIC C/L
1	Difficulty in maintaining work continuity	Smooth transition between sections	Unintuitive interface	Ability to mark completed items
2	Inability to mark completed steps	Clarity, intuitiveness, and ease of use	Time-consuming switching between the C/L and navigation	Lower risk of missing steps
3	Risk of loss or damage	Easy access to the C/L, always readily available	Uncomfortable placement of the C/L	No need to handle physical documents

Despite several advantages, participants identified a range of limitations associated with the use of electronic checklists. A commonly cited concern was the need to divide attention between operating the device and maintaining situational awareness, particularly during critical phases of flight. Several participants noted that on the electronic system used during the simulation, only a portion of the checklist was visible at any given time, which complicated progress tracking and

increased the risk of omitting steps. In addition, switching between checklists often required leaving the navigation screen, reducing access to essential flight information. This was perceived as particularly problematic in single-screen cockpit configurations, where the checklist temporarily replaced navigation data, such as maps or flight plans. Other reported drawbacks included the non-intuitive interface, the need to remember specific operational procedures (e.g., how to launch the checklist). The requirement to repeatedly switch between the checklist and other avionics functions was described as time-consuming and, in some cases, stressful. Some respondents also highlighted ergonomic limitations, such as the need to reach farther across the cockpit to interact with the device. In longer procedures, maintaining arm position over the interface led to fatigue or discomfort.

In the final question (Figure 8.) regarding general preferences for the future format of checklists, more than half of the respondents selected the paper-based version, while the remaining participants opted for the electronic format. One respondent expressed no preference. Support for either format was mostly moderate - responses predominantly fell into the categories of "rather paper-based" or "rather electronic," with fewer participants choosing the more definitive options.

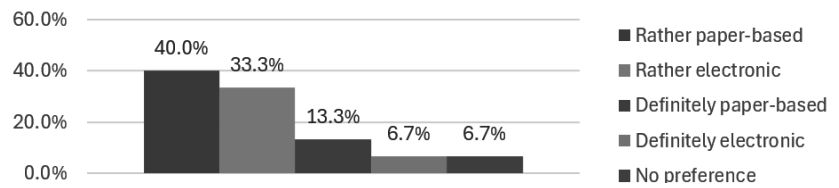

Figure 8. Response distribution to the question regarding general preferences for the future format of checklists.

4. CONCLUSIONS

The study focused on the subjective evaluation of two types of flight checklists – traditional paper-based and avionics-integrated electronic (Garmin GNS 430) – used during simulated IFR flights. According to the post-flight survey, the majority of participants rated the paper checklist as more intuitive, readable, and easier to operate. At the same time, a significant portion of respondents highlighted the advantages of the electronic checklist, such as the ability to mark completed steps and its fixed position within the cockpit – conveniently located and not requiring the pilot to look down or interrupt other tasks.

The results revealed clear differences in user perception, which may be influenced by experience level, operational habits, and individual preferences. Preliminary observations suggest that less experienced pilots, often more familiar with digital systems, tended to respond more positively to the electronic form, while experienced pilots favored the simplicity and predictability of paper-based checklists.

These findings indicate that the design of electronic checklists requires special attention to ergonomics, clarity, and cognitive load minimization. Such tools should be tailored to meet the needs of the widest possible group of users – even at the cost of reducing advanced functionality – if this ensures clarity, ease of use, and intuitive operation. Simplicity of interface and consistent logic must be prioritized regardless of the pilot's technical background.

It is important to emphasize that the presented results are based solely on subjective opinions. While they provide valuable insights into user preferences and impressions, they are insufficient to assess the operational effectiveness of checklist types. For a complete and reliable evaluation, the study must be extended with objective data such as task completion time, sequence accuracy, number of errors, or distraction levels. Only such a combined approach – integrating both subjective feedback and measurable performance indicators – can support meaningful conclusions about checklist efficiency in operational flight environments.

BIBLIOGRAPHY

1. VDI (Verein Deutscher Ingenieure). (2003). Menschliches Versagen: Erkennen und Vermeiden [Human Error: Recognition and Prevention]. VDI-Richtlinien 4001. Düsseldorf: VDI-Verlag.
2. Casner, S. M., Geven, R. W., & Williams, T. C. (2013). The effectiveness of airline pilot training for abnormal events. Human Factors, 55(3), 477–485. https://doi.org/10.1177/0018720812466897
3. National Transportation Safety Board (NTSB). (2010). Loss of Thrust in Both Engines After Encountering a Flock of Birds and Subsequent Ditching on the Hudson River, US Airways Flight 1549, Airbus A320-214, N106US, Weehawken, New Jersey, January 15, 2009. Aircraft Accident Report NTSB/AAR-10/03. Washington, DC: NTSB.
4. Australian Transport Safety Bureau (ATSB). (2012). In-flight uncontained engine failure – Airbus A380-842, VH-OQA, overhead Batam Island, Indonesia, 4 November 2010. Aviation Occurrence Investigation AO-2010-089. Canberra: ATSB.

TalentDetector
23th-25th June 2025
Gliwice-Brenna, Poland
DEPARTMENT OF ENGINEERING MATERIALS AND BIOMATERIALS
FACULTY OF MECHANICAL ENGINEERING
SILESIAN UNIVERSITY OF TECHNOLOGY
INTERNATIONAL STUDENTS SCIENTIFIC CONFERENCE

Shaping the microstructure and properties of duplex stainless steels manufactured via LPBF additive technology

Antonina Olszewska[a], Wiktoria Wanczura[a], Kamil Czajkowski[a], Bartosz Jagla[a], Kacper Toman[a], Oleksander Knysh[b], Aleksander Kolšovský[b], Mengistu Jemberu Dagnaw[a], Zbigniew Brytan[a], Jana Bidulská[b]

[a] Silesian University of Technology, Faculty of Mechanical Engineering, Department of Engineering Materials and Biomaterials, Gliwice, Poland
email: zbigniew.brytan@polsl.pl
[b] Institute of Materials and Quality Engineering, Faculty of Materials, Metallurgy and Recycling, Technical University of Košice, Košice, Slovakia

Abstract: This study investigates the effect of nickel addition and heat treatment on the microstructure, mechanical properties, and corrosion resistance of super duplex stainless steel (SDSS) processed by Laser Powder Bed Fusion (LPBF). Two powder compositions were analysed: standard SDSS and SDSS with 3 wt.% Ni. The as-printed microstructure was primarily ferritic due to rapid cooling, while solution annealing produced a balanced duplex structure. Mechanical testing showed improved ductility in as-printed SDSS+3%Ni and higher tensile strength after annealing. Both compositions reached ~30% elongation after heat treatment. Electrochemical tests confirmed improved corrosion resistance with heat treatment and further enhancement with nickel addition. SDSS+3%Ni exhibited more noble open circuit potentials and higher polarization resistance. These results demonstrate that nickel enrichment effectively improves phase balance, mechanical behaviour, and corrosion resistance in LPBF-processed SDSS.

Keywords: duplex stainless steel, LPBF, nickel, mechanical properties, corrosion resistance

1. INTRODUCTION

Duplex steels are a special type of stainless steel, created due to the existing demand for a combination of mechanical strength possessed by ferritic steels with corrosion resistance, which in turn is characterized by austenitic steels. The first attempts that were made to develop alloys combining both of these properties appeared already around the 1930s, but they gained industrial application only 50 years later - in the 1980s, when their chemical composition and manufacturing processes were appropriately improved [1].

A particularly important subclass within this family is the super duplex stainless steels (SDSS), which have attracted significant attention due to their exceptional combination of mechanical and corrosion-resistant properties. These alloys are characterized by an

approximately equal volume fraction of ferrite (α) and austenite (γ) phases, a balance that confers superior strength, high impact resistance, and excellent resistance to localized corrosion mechanisms such as pitting and crevice corrosion. The enhanced performance of SDSS stems from their refined chemical composition, which includes higher contents of chromium (typically 24–26 wt.%), molybdenum (3–5 wt.%), and nitrogen (up to 0.3 wt.%) compared to conventional DSS. These elements act synergistically: chromium and molybdenum improve resistance to chloride-induced pitting, while nitrogen stabilizes the γ-phase and enhances mechanical strength. [2,3].

The superior properties of SDSS make them ideal candidates for use in aggressive environments, such as those encountered in the chemical processing, desalination, and offshore oil and gas industries. However, achieving and maintaining the required phase balance is challenging due to the material's sensitivity to thermal history and compositional fluctuations. One of the main difficulties lies in the tendency of SDSS to form harmful intermetallic phases—such as sigma (σ) and chi (χ) phases—during prolonged exposure to intermediate temperatures, which can severely impair both ductility and corrosion resistance [2,3].

In response to these processing challenges, additive manufacturing (AM) technologies, especially Laser Powder Bed Fusion (LPBF), have been investigated as novel routes for fabricating SDSS components with complex geometries and tailored microstructures. LPBF involves the selective melting of fine metal powders layer-by-layer using a focused laser beam, providing high geometric resolution and control over local thermal gradients. However, the rapid solidification rates inherent to LPBF (~10^6 K/s) hinder the diffusion of γ-stabilizing elements like nickel and nitrogen, often resulting in as-built structures dominated by ferrite and depleted in austenite. Such unbalanced microstructures are associated with high hardness, low ductility, and diminished resistance to pitting corrosion due to chromium nitride precipitation [4-13].

To overcome these microstructural limitations, two primary optimization strategies are employed: post-process solution heat treatment and modification of the chemical composition of the powder feedstock. Solution annealing typically at 1050–1150 °C promotes the reformation of austenite, dissolution of secondary phases, and reduction of residual stresses, thereby improving mechanical and corrosion performance [9]. Alternatively, adjusting the alloy composition by increasing the nickel content is increasingly favoured. Nickel is a potent γ-phase stabilizer and has been shown to significantly enhance austenite formation during cooling, even under the rapid solidification conditions of LPBF. The presence of nickel also improves elongation, impact resistance, and corrosion behaviour, particularly in chloride-laden environments.

Recent studies demonstrate that in-situ alloying through powder blending, particularly by combining super duplex stainless steel powders like SAF 2507 with austenitic stainless steels such as AISI 316L, offers a practical method to tailor the chemical composition during the LPBF process. This technique allows controlled adjustment of the chromium equivalent to nickel equivalent ratio (Cr_{eq}/Ni_{eq}), a key parameter influencing phase stability in DSS. By fine-tuning this ratio, researchers have achieved near-equilibrium phase distributions, with nearly equal proportions of ferrite and austenite directly in the as-built microstructure[5].

This compositional adjustment mitigates the ferrite excess typically observed in LPBF-processed DSS due to rapid cooling, which otherwise hinders γ-phase formation. Notably, the incorporation of AISI 316L, rich in nickel and molybdenum, not only promotes austenite formation but also enhances pitting resistance and mechanical ductility. The resulting microstructure demonstrates significant improvements in hardness uniformity, tensile strength, elongation, and electrochemical stability when exposed to chloride environments. In-situ

alloying thus reduces the dependency on post-process heat treatments and provides a cost-effective route to microstructural and performance optimization, making it a viable strategy for industrial applications demanding high mechanical and corrosion performance.

Therefore, the current study aims to systematically evaluate the effect of nickel enrichment (3 wt.%) and subsequent solution annealing on SDSS processed via LPBF. The focus lies in assessing changes in phase distribution, grain morphology, hardness, tensile behaviour, and corrosion resistance in chloride-containing environments. The results aim to fill existing knowledge gaps and contribute practical guidelines for the reliable deployment of SDSS in advanced manufacturing applications using LPBF.

2. EXPERIMENT PROCEDURE

Super duplex stainless steel (SDSS) Ospray 2507 powder grade (1.4410), with a particle size range of 15–45 µm, was mixed with pure nickel powder (particle size: 22–45 µm) in proportions of 3 wt.% and 6 wt.%. The powders were blended for 20 minutes using a Turbula mixer. The resulting final compositions are presented in Table 1. The initial SDSS powder contains approximately 6 wt.% nickel, which increases to 9 wt.% in the composition designated as SDSS+3%Ni.

Table 1 Chemical composition of studied SDSS composition (

Designation	Alloying elements, wt.%.									
	Cr	Ni	Mo	Mn	Si	Cu	S	P	C	N
SDSS	25.2	6.3	3.8	0.4	0.30	0.15	0.001	0.024	0.016	0.35
SDSS+3%Ni	24.44	9.1	3.69	0.39	0.29	0.14	0.001	0.024	0.016	0.35

Horizontal samples for tensile testing (dog-bone shape) and Charpy impact testing were fabricated using an AM125 Renishaw printer, with the following process parameters: laser power of 180 W, hatch distance of 120 µm, layer thickness of 30 µm, and scan speed of 300 mm/s. These settings correspond to a volumetric energy density of approximately 166 J/mm³. A meander scanning strategy with a rotation of 67° between successive layers was applied. After fabrication, the samples underwent post-processing heat treatment by solution annealing at 1100 °C for 15 minutes, followed by rapid water quenching.

Microstructural characterization was carried out using scanning electron microscopy (SEM) and X-ray diffraction for phase identification. Mechanical property evaluation included hardness measurements (HRA), tensile testing and Charpy impact testing on unnotched samples. Corrosion resistance was assessed using potentiodynamic polarization measurements conducted via the Tafel extrapolation method. The tests were performed in a 3.5% NaCl aqueous solution at ambient room temperature to simulate chloride-rich environments commonly encountered in service conditions. The key corrosion parameters were determined, including corrosion potential (E_{corr}), corrosion current density (I_{corr}), and polarization resistance (R_{pol}). The Open Circuit Potential (OCP) was monitored for a duration of 60 minutes prior to polarization testing to ensure the electrochemical stabilization of the sample surface in the test environment.

3. RESULTS AND DISCUSSION

The as-printed super duplex stainless steel (SDSS) reveals an almost fully ferritic microstructure due to the rapid cooling rate of the laser powder bed fusion (LPBF) process. The X-ray diffraction pattern (Fig. 2) shows only a weak peak corresponding to the austenite – Fe-γ (111). After the solution annealing at 1100 °C for 15 min, the phase content becomes balanced, and strong peaks from both austenite and ferrite are visible in the XRD pattern. Quantitative analysis indicates that the austenite content is approximately 5% in the as-printed SDSS, increasing slightly to 7% in the SDSS+3%Ni composition. Solution annealing results in the formation of a well-balanced microstructure, with ferrite and austenite phases present in nearly equal proportions: 52% austenite in SDSS, increasing to almost 60% in SDSS+3%Ni.

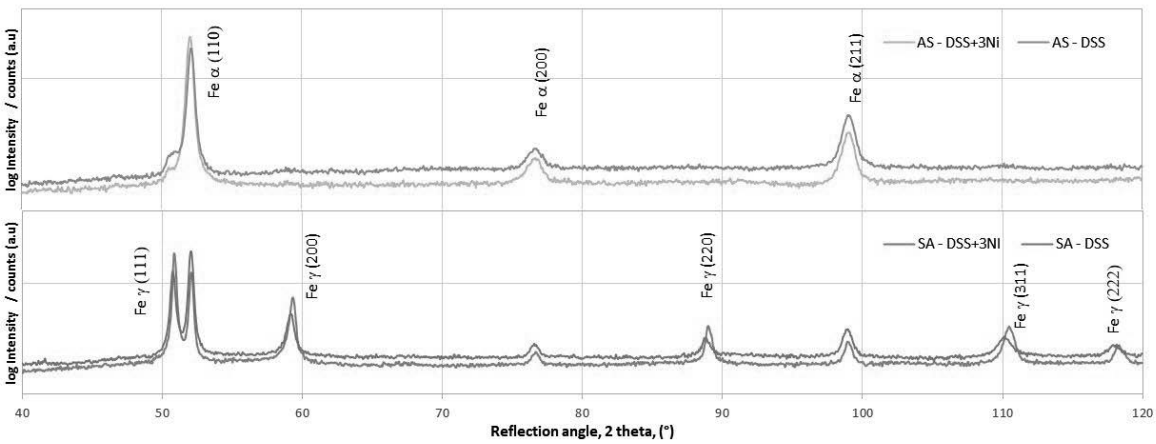

Figure 1. XRD patterns of as-printed (AS) and solution annealed (SA) super duplex stainless steel compositions: SDSS and SDSS+3%Ni.

The microstructure of LPBF-processed SDSS in the as-printed condition is predominantly ferritic for both compositions, as shown in Figures 2a and 2b. The ferritic grains exhibit elongated, columnar morphology oriented along the build direction, with smaller, rounded grains also observed. Additionally, grain boundary austenite (GBA) is likely present, contributing to the duplex character of the alloy. In the solution-annealed condition (Fig. 2c, 2d), a balanced and refined ferritic-austenitic microstructure was formed in both cases. However, for the SDSS+3%Ni composition, the austenite content is more pronounced. Austenitic grains form distinct islands, and a high number of fine acicular grains are homogeneously distributed throughout the microstructure.

When comparing the mechanical properties of the studied conditions (Table 2), it is evident that the SDSS+3%Ni composition exhibits higher ductility in the as-printed condition, due to its increased austenite content. The elongation after fracture for SDSS+3%Ni is approximately 7%, compared to 4.8% for standard SDSS (Fig. 3). The yield strength (Rp0.2) of SDSS+3%Ni is lower than that of standard SDSS, indicating an improved capacity for plastic deformation prior to fracture. In contrast, standard SDSS shows very similar values for yield strength and ultimate tensile strength (Rm), suggesting limited plastic deformation before failure. After solution annealing, the SDSS+3%Ni composition exhibits increased tensile strength compared to SDSS. The tensile strength increases from 860 MPa for SDSS to 890 MPa for SDSS+3%Ni. In terms of maximum elongation to fracture, both compositions exhibit similar values of approximately 30%.

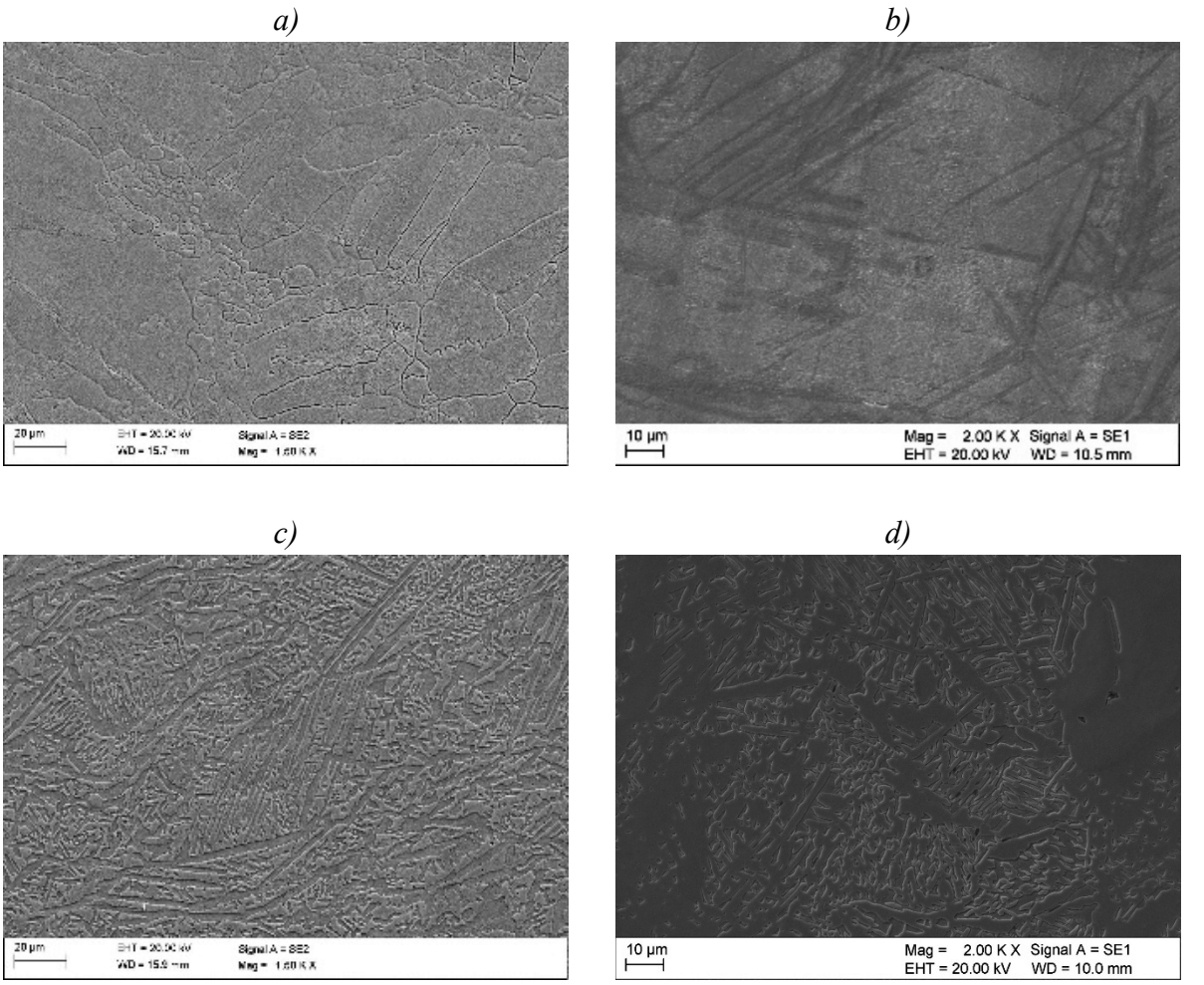

Figure 2. The microstructure of a) as-printed SDSS, b) as-printed SDSS+3Ni, c) solution-annealed SDSS and d) solution-annealed SDSS+3Ni

Table 2. Mechanical properties of the LPFB-manufactured super duplex stainless steels

Mechanical properties	SDSS as-printed	SDSS solution annealed	SDSS+3Ni as-printed	SDSS+3Ni solution annealed
HRA, core	69.92 ± 1.53	60.48 ± 2.49	72.20 ± 2.20	62.50±1.50
$Rp_{0.2}$, MPa	1310 ± 20	575 ± 8	1094±17	559 ±7.9
Rm, MPa	1390 ± 5	861 ± 3	1324±25	890 ± 1.9
A, %	4.8 ± 0.6	33.7 ± 0.5	6.8±1.9	29.6±0.8
Impact energy, J	103 ± 26.67	≥ 450	120± 14	≥ 450

The hardness of the as-printed samples is higher in both compositions (Table 2) due to strong internal stress concentrations resulting from the LPBF process. In contrast, solution annealing softens the material by promoting a balanced phase distribution and relieving residual stresses through uniform microstructural reformation. This heat treatment also has a significant effect on impact toughness, which is low in the as-printed condition but increases dramatically after solution annealing, reaching values ≥450 J (unnotched samples), indicating a substantial improvement in energy absorption and resistance to brittle fracture.

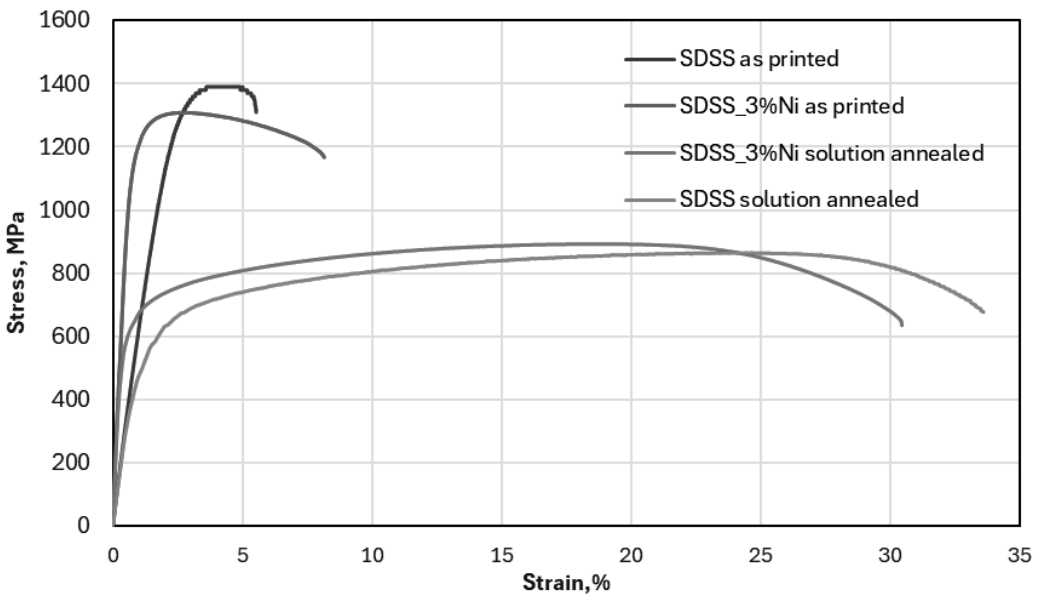

Figure 3. Stress–strain curves of LPBF-manufactured SDSS super duplex stainless steels

The corrosion resistance of LPBF-manufactured SDSS is influenced by chemical composition, phase content, and applied heat treatment. Results of the Tafel analysis and electrochemical parameters are summarized in Table 3. For the SDSS composition, solution annealing enhances corrosion resistance. The polarization resistance (R_{pol}) increases from 126 kΩ·cm² to 149 kΩ·cm² compared to the as-printed condition. Additionally, the open circuit potential (E_{OCP}) shifts towards more positive values, from –966 mV to –835 mV. A positive shift of E_{OCP} indicates a lower thermodynamic tendency for corrosion, reflecting a more stable and protective passive film on the material surface.

Table 3. The electrochemical parameters of LPBF manufactured SDSS

Mechanical properties	SDSS as-printed	SDSS solution annealed	SDSS+3Ni as-printed	SDSS+3Ni solution annealed
E_{OCP}, mV	- 966	-835	-350	-212
J_{corr}, μA/cm^2	140.63	131.89	237.18	114.19
E_{corr}, mV	-147.17	-136.35	-378.62	-250.63
R_{pol}, kΩ*cm^2	126.82	149.35	148.86	165.44

In comparison, the SDSS+3%Ni composition exhibits a significantly more positive E_{OCP}, ranging from –350 mV in the as-printed state to –212 mV after solution annealing. This improvement is attributed to the higher austenite content, which enhances passivity and electrochemical stability. The R_{pol} value also increases after heat treatment, from 149 kΩ·cm² to 165 kΩ·cm², indicating further improvement in corrosion resistance.

Comparison of polarization resistance confirms that SDSS+3%Ni exhibits higher R_{pol} values in both conditions compared to standard SDSS. For both compositions, solution annealing improves corrosion resistance, as reflected by increased R_{pol} and more noble E_{OCP} values.

All studied compositions demonstrated repassivation upon reversal of the polarization current. Among them, the solution-annealed SDSS exhibited faster repassivation compared to the as-printed condition, further supporting the beneficial effect of heat treatment on corrosion performance.

The results of this study demonstrate that both solution annealing and nickel addition significantly influence the microstructure, mechanical properties, and corrosion resistance of LPBF-processed super duplex stainless steels. The as-printed samples exhibited a predominantly ferritic microstructure, high hardness, low ductility, and limited impact toughness due to rapid solidification and residual stress accumulation. Solution annealing effectively transformed the microstructure into a balanced ferritic-austenitic phase composition, reducing hardness while substantially increasing ductility and impact toughness.

Nickel addition proved especially beneficial in the as-printed condition by promoting the formation of austenite, leading to improved ductility and lower yield strength, indicating enhanced plastic deformability. Furthermore, the SDSS+3%Ni composition exhibited superior corrosion resistance in both conditions, with more noble open circuit potentials and higher polarization resistance. These findings confirm that controlled nickel enrichment improves phase stability, mechanical performance, and electrochemical behaviour even without post-processing, making it a promising strategy for tailoring SDSS properties in additive manufacturing applications.

3. CONCLUSIONS

The microstructure of as-printed SDSS fabricated by LPBF is nearly fully ferritic, with minor amounts of grain boundary austenite. Solution annealing at 1100 °C for 15 min results in a balanced duplex microstructure, significantly increasing the austenite content to 52% in SDSS and up to 60% in SDSS+3%Ni. The addition of 3 wt.% Ni to the SDSS composition promotes austenite formation, both in the as-printed and heat-treated conditions, as confirmed by XRD and microscopy analysis.

Mechanical properties of SDSS+3%Ni show improved ductility in the as-printed state and increased tensile strength after solution annealing compared to standard SDSS. After solution annealing, both compositions reach elongation values near 30%, indicating excellent plasticity.

Corrosion resistance is significantly enhanced by solution annealing, as shown by increased polarization resistance and more noble open circuit potentials. SDSS+3%Ni consistently exhibits better electrochemical stability, associated with its higher austenite content and improved passivity.

The deliberate increase of nickel content by adding Ni powder to SDSS feedstock (SDSS_3Ni composition) is an effective alloying strategy, enhancing phase balance, improving corrosion resistance, and optimizing mechanical performance in both as-printed and heat-treated conditions.

ACKNOWLEDGEMENT

This paper is the result of a Project-Based Learning (PBL) initiative titled - Shaping the microstructure and properties of duplex stainless steels manufactured via LPBF additive technology.

BIBLIOGRAPHY

1. Gunn, R. N., Duplex Stainless Steels: Microstructure, Properties and Applications. Abington Publishing, 1997.
2. Nilsson, J. O., Super duplex stainless steels. Materials Science and Technology, 8(8), 1992, 685–700.
3. Sedriks, A. J. Corrosion of Stainless Steels (2nd ed.). Wiley-Interscience, 1996.
4. C. Xie, B. Li, G. Liu, J. Liu, H. Ying, D. Li, S. Wang, and L. Wang, "Study on the effect of solution treatment on mechanical and corrosion properties of SAF 2507 DSS produced by LPBF," *J. Mater. Res. Technol.*, vol. 26, 2023, 2070–2081.
5. Cui, C.; Becker, L.; Gärtner, E.; Boes, J.; Lentz, J.; Uhlenwinkel, V.; Steinbacher, M.; Weber, S.; Fechte-Heinen, R. Laser Additive Manufacturing of Duplex Stainless Steel via Powder Mixture. J. Manuf. Mater. Process. 2022, 6, 72.
6. H. Xiang, G. Chen, W. Zhao, and C. Wu, "Densification Behavior and Build Quality of Duplex Stainless Steel Fabricated by Laser Powder Bed Fusion," Metals, vol. 13, no. 4, p. 741, 2023.
7. W. Zhao et al., "Microstructure evolution in laser powder bed fusion melted 2205 duplex stainless steel using in-situ EBSD during uniaxial tensile testing," J. Mater. Res. Technol., vol. 33, pp. 2113–2124, 2024.
8. L. Karavias et al., "Tensile Properties and Fracture Analysis of Duplex (2205) and Super Duplex (2507) Stainless Steels, Produced via Laser Powder Bed Fusion Additive Manufacturing," Metals, vol. 14, no. 7, p. 838, 2024.
9. Chuqi Xie, Bolin Li, Guojie Liu, Jiyuan Liu, Hao Ying, Dong Li, Shenghai Wang, Li Wang, Study on the effect of solution treatment on mechanical and corrosion properties of SAF 2507DSS produced by LPBF, Journal of Materials Research and Technology, vol. 26, 2023, 2070-2081
10. K. P. Davidson, S. Singamneni, The mechanics of machining selective laser melted super duplex stainless steels, Journal of materials research and technology 2022;17, 601-611
11. Karl Davidson & Sarat Singamneni, Selective Laser Melting of Duplex Stainless Steel Powders: An Investigation, Materials and Manufacturing Processes, 2015, DOI: 10.1080/10426914.2015.1090605
12. Haghdadi, N; Laleh, Majid; Chen, H; Chen, Z; Ledermueller, C; Liao, X; et al., On the pitting corrosion of 2205 duplex stainless steel produced by laser powder bed fusion additive manufacturing in the as-built and post-processed conditions. Deakin University. Journal contribution 2021.
13. M. L. Köhler, J. Kunz, S. Herzog, A. Kaletsch, Ch. Broeckmann, Microstructure analysis of novel LPBF-processed duplex stainless steels correlated to their mechanical and corrosion properties, Materials Science and Engineering: A, Vol. 801, 2021, 140432.

TalentDetector
23th-25th June 2025
Gliwice-Brenna, Poland
DEPARTMENT OF ENGINEERING MATERIALS AND BIOMATERIALS
FACULTY OF MECHANICAL ENGINEERING
SILESIAN UNIVERSITY OF TECHNOLOGY
INTERNATIONAL STUDENTS SCIENTIFIC CONFERENCE

Near-Infrared Vein Visualization System with Integrated DLP Projection and Adaptive Image Enhancement Algorithms

Marcin Paszkuta[a], Agnieszka Szczęsna[a] ,Wirginia Likus[b], Jakub Antonowicz[c], Kamil Ceglarski[c], Artur Szaboń[c], Mateusz Róg[d], Aleksandra Wąsek[e], Sebastian Tkacz[f]

[a] Silesian University of Technology, Faculty of Automatic Control, Electronics and Computer Science, Department of Graphics, Computer Vision and Digital Systems
[b] Medical University of Silesia, Anatomy Department
[c] Silesian University of Technology, Faculty of Automatic Control, Electronics and Computer Science
[d] Medical University of Silesia, Anatomy Department
[e] Medical University of Silesia
[f] Silesian University of Technology, Faculty of Electrical Engineering
email: marcin.paszkuta@polsl.pl

Abstract: This article presents a vein detection and visualization system designed to enhance the accuracy and safety of venipuncture procedures. The system performs vein detection using a near-infrared (NIR) camera in conjunction with an infrared (IR) illuminator. It incorporates a Digital Light Processing (DLP)-based LED projector and adaptive image enhancement algorithms, such as Contrast Limited Adaptive Histogram Equalization (CLAHE), to improve vein visibility across a range of skin tones and lighting conditions. Powered by a Raspberry Pi 5 and equipped with an NIR camera and 850 nm NIR LEDs, the device enables real-time detection and on-body visualization. This study details the system's design, hardware integration, and algorithmic performance, and outlines future development directions, including AI-driven vein detection and multispectral imaging.

Keywords: Medical Imaging, Near-Infrared Technology, Vein Detection, Image Processing, DLP

1. INTRODUCTION

The growing demand for efficient venipuncture techniques in clinical settings highlights the need for innovative technological solutions that address anatomical variability and improve intravenous access. The Near-Infrared (NIR) vein visualization system exemplifies this innovation by utilizing hemoglobin's absorption characteristics at the optimal wavelength of 850 nm, enabling deeper tissue penetration and enhanced vein visibility [1]. This interaction between NIR light and biological tissues offers a transformative advantage in medical imaging, significantly improving patient safety and comfort during procedures [2]. The system integrates

a structured light DLP projection module with NIR-sensitive imaging tools and employs a Raspberry Pi 5 for processing, allowing for real-time feedback via projection. Adaptive image enhancement algorithms such as Contrast Limited Adaptive Histogram Equalization (CLAHE) dynamically adjust imaging outputs to accommodate various skin tones and ambient lighting conditions, effectively mitigating issues like motion artifacts and external interference. This sophisticated integration of hardware and software not only streamlines venipuncture procedures but also marks a pivotal shift in medical imaging and patient monitoring, opening new avenues for clinical applications and broader adoption in healthcare environments [3][4].

2. SYSTEM ARCHITECTURE AND COMPONENTS

The design of the near-infrared vein visualization system requires meticulous integration of various components, each playing a critical role in ensuring optimal performance. At the core of the architecture is the Raspberry Pi 5 (8GB), which serves as the primary processing unit, managing data flow and executing adaptive image enhancement algorithms. This module provides sufficient computational power to support AI-driven vein detection methods, as well as an augmented reality (AR) visualization module that enables real-time display of results directly on the patient's body.

A key component of the system is the DLP projection module (DLPDLCR2000EVM), based on the DLP2000 digital micromirror device (DMD). This micro-opto-electromechanical system (MOEMS) features an array of 640 × 360 aluminum micromirrors (16:9 aspect ratio), each with a 7.56 µm pitch, arranged in an orthogonal configuration. The integrated light engine uses red, green, and blue LEDs, collectively delivering approximately 20 lumens at a drive current of 320 mA—sufficient for clear vein visualization under standard ambient lighting conditions.

The compact form factor of the DLP2000 module allows for seamless integration into portable systems, offering high efficiency and low power consumption. These characteristics make it particularly well-suited for embedded applications such as the near-infrared vein visualization device.

Complementing this, a NIR-sensitive USB camera captures reflected light images. The camera transmits image data in Y8 format (8-bit grayscale), which simplifies processing by providing intensity information per pixel without additional color channels. This format is particularly well-suited for near-infrared imaging, where the primary concern is contrast and structural information rather than color fidelity. The use of Y8 format also reduces bandwidth requirements, enabling higher frame rates essential for real-time processing on the latest version of Raspberry Pi 5.

High-power NIR LEDs emitting light at a wavelength of 850 nm provide the necessary illumination for effective vein visualization [5]. Optical components, such as IR filters and LED lenses, shape the light beams for precise targeting. Furthermore, thermal management systems, alongside robust power management units using Li-ion batteries, ensure system stability during operation. This comprehensive architecture facilitates real-time visualization enhancements, essential for improving venipuncture success rates under various conditions like in the [6].

3. ADAPTIVE IMAGE ENHANCEMENT ALGORITHMS

The development of adaptive image enhancement algorithms is essential for the effectiveness of near-infrared (NIR) vein visualization systems, particularly in clinical settings where

precision is paramount. Techniques such as Contrast Limited Adaptive Histogram Equalization (CLAHE) are employed to optimize the contrast of vein images captured by NIR-sensitive cameras, addressing challenges posed by varying skin tones and fluctuating environmental lighting. An example result of the developed image processing is presented in Fig. 1. The left side shows the raw grayscale image captured by the NIR camera, while the right side displays the processed results. The veins are clearly visible, enabling subsequent detection and visualization steps.

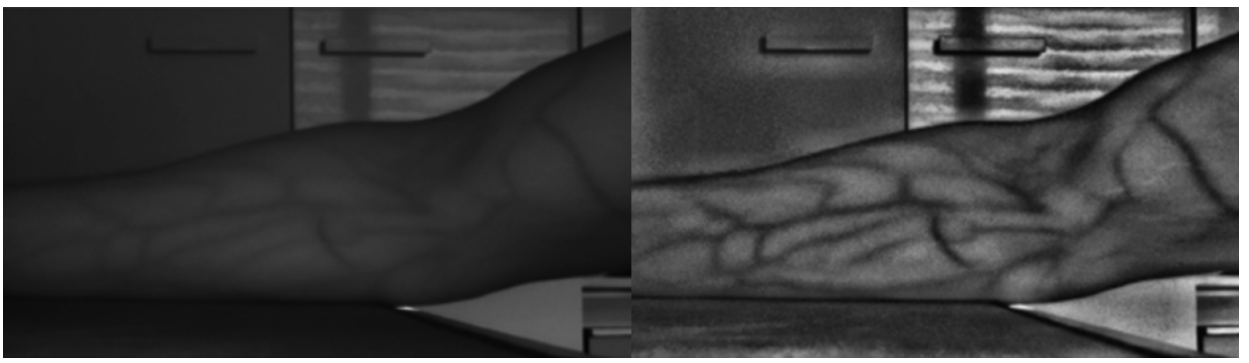

Figure 1. The raw image from the NIR camera (left) and its CLAHE-enhanced version (right).

The integration of image acquisition and real-time processing enables immediate projection of the enhanced image onto the patient's body, facilitating timely and accurate decision-making during procedures such as venipuncture. However, visual artifacts caused by ambient light interference and irregularities in infrared illumination often challenge classical algorithms, which may prove insufficient in maintaining image fidelity. In this context, AI-based models trained for vein detection offer a more robust and effective solution.
Effective image processing is therefore not just a supportive function but a fundamental component of the system, directly enhancing safety, efficiency, and reliability. Figure 2 illustrates the histograms of pixel intensity distribution before (left) and after processing (right). The applied image processing algorithms significantly enhance vein visibility while maintaining low image noise, thereby preserving overall image quality.

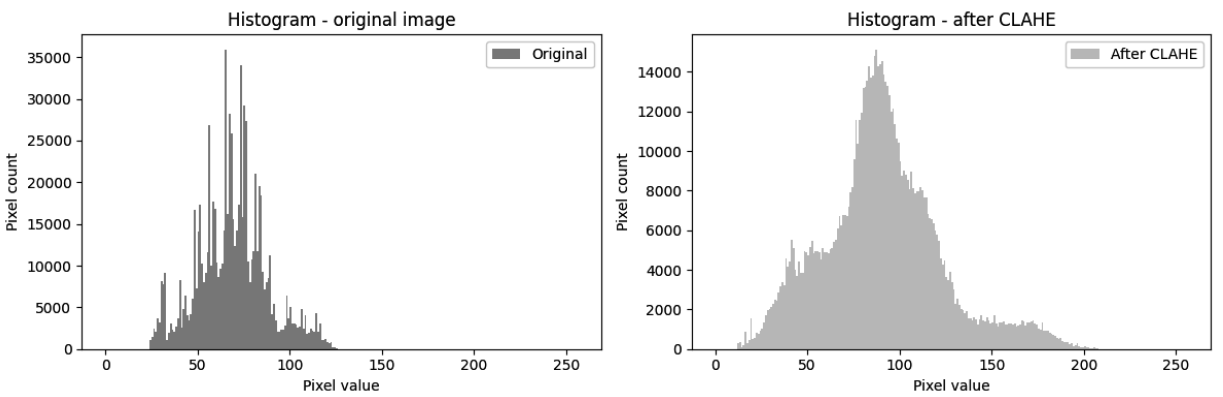

Figure 2. Histogram comparison showing the original image's pixel intensity distribution (left) and the CLAHE-enhanced image's broader value distribution (right), demonstrating improved contrast through adaptive histogram equalization (clip limit = 3.0, tile size = 8×8).

4. CONCLUSION

The development of the Near-Infrared (NIR) vein visualization system marks a significant advancement in venipuncture and medical imaging, offering improved accuracy and safety in clinical procedures. By integrating a DLP projection module with adaptive image enhancement techniques such as Contrast Limited Adaptive Histogram Equalization (CLAHE), the system enhances vein visibility across various skin tones and lighting conditions. Hemoglobin's peak absorption at the 850 nm NIR wavelength enables deeper tissue penetration and high-contrast imaging, addressing limitations of conventional methods.

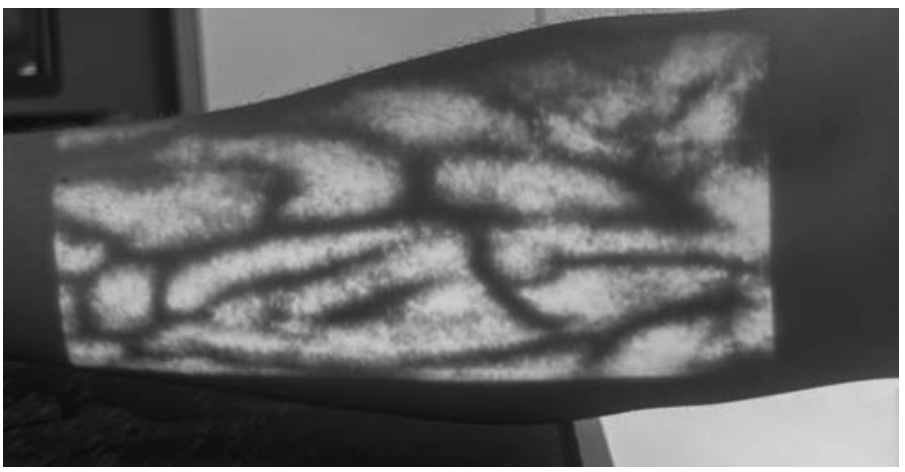

Figure 3. Processed image projected onto the patient's arm.

A Raspberry Pi 5 serves as the processing unit, paired with a NIR-sensitive USB camera and high-power NIR LEDs, while real-time feedback is delivered via an e-paper display to support clinical use. This setup not only increases intravenous access success rates but also reduces patient discomfort by minimizing repeated attempts. As noted in recent studies [4], the system shows strong potential for real-time applications, with future improvements like AI-driven vein detection and multispectral imaging expected to further enhance clinical utility by mitigating challenges such as motion artifacts and ambient light interference.
The project goal has been successfully achieved, with the developed device enabling direct visualization of veins on the patient's body. An example demonstrating the system in operation is shown in Fig. 3

5. FUTURE WORK

The designed vein detection algorithm, based on classical methods such as CLAHE (Contrast Limited Adaptive Histogram Equalization) and image binarization, delivers satisfactory results. However, varying lighting conditions may introduce artifacts and require manual parameter adjustments [7]. To address these limitations, an AI-based detection method is proposed. As part of the project, various NIR images of arms and hands will be captured, and the authors plan to compile these into a dedicated dataset to train the AI-based detection model.
During the research phase, several NIR light sources with different wavelengths were evaluated, and the selected configuration was found to meet the system's functional requirements. Nevertheless, future development will focus on optimizing the device for a more

compact and ergonomic form factor. Additionally, efforts will be directed toward achieving more uniform and controlled illumination to further enhance image quality and overall usability. These refinements aim to facilitate broader clinical adoption and improve the reliability of vein visualization in a wide range of medical environments.

ACKNOWLEDGMENTS

The research was financially suported by the PBL-IDUB project entitled “Opracowanie detektora żył z wykorzystaniem technologii obrazowania w bliskiej podczerwieni oraz uczenia maszynowego do wspierania procedur medycznych” under the Initiative of Excellence - Research University, Silesian University of Technology.

BIBLIOGRAPHY

[1] Abd Rahman, A. B., Juhim, F., Chee, F. P., Bade, A., & Kadir, F. (2022). Near Infrared Illumination Optimization for Vein Detection: Hardware and Software Approaches. Applied Sciences, 12(21), 11173. https://doi.org/10.3390/app122111173
[2] Cuper, N. J., Verdaasdonk, R. M., de Roode, R., de Vooght, K. M., Viergever, M. A., Kalkman, C. J., & de Graaff, J. C. (2011). Visualizing veins with near-infrared light to facilitate blood withdrawal in children. Clinical pediatrics, 50(6), 508–512. https://doi.org/10.1177/0009922810395932
[3] Yaprak, E., & Kayaalti-Yuksek, S. (2018). Preliminary evaluation of near-infrared vein visualization technology in the screening of palatal blood vessels. Medicina oral, patologia oral y cirugia bucal, 23(1), e98–e104. https://doi.org/10.4317/medoral.21996
[4] Fuksis, R., Greitans, M., Nikisins, O., & Pudzs, M. (2010). Infrared Imaging System for Analysis of Blood Vessel Structure. Elektronika Ir Elektrotechnika, 97(1), 45-48. Retrieved from https://eejournal.ktu.lt/index.php/elt/article/view/9943
[5] Ai, D., Yang, J., Fan, J., Zhao, Y., Song, X., Shen, J., Shao, L., & Wang, Y. (2016). Augmented reality based real-time subcutaneous vein imaging system. Biomedical Optics Express, 7(7), 2565. https://doi.org/10.1364/boe.7.002565
[6] Gunawan, I. P. A. S., Sigit, R., & Gunawan, A. I. (2019). Multi-Distance Veins Projection Based on Single Axis Camera and Projector System. EMITTER International Journal of Engineering Technology, 7(2), 444-466. https://doi.org/10.24003/emitter.v7i2.367
[7] Juric, S., & Zalik, B. (2014). An innovative approach to near-infrared spectroscopy using a standard mobile device and its clinical application in the real-time visualization of peripheral veins. BMC medical informatics and decision making, 14, 100. https://doi.org/10.1186/s12911-014-0100-z

TalentDetector
23th-25th June 2025
Gliwice-Brenna, Poland
DEPARTMENT OF ENGINEERING MATERIALS AND BIOMATERIALS
FACULTY OF MECHANICAL ENGINEERING
SILESIAN UNIVERSITY OF TECHNOLOGY
INTERNATIONAL STUDENTS SCIENTIFIC CONFERENCE

Poruchy valivých ložísk

Mária Pilarčíková[a], Eva Tillová[a], Miroslaw Bonek[b]

[a] Žilinská univerzita v Žiline, Strojnícka fakulta, Katedra materiálového inžinierstva, Univerzitná 8215/1, 010 26 Žilina, Slovenská republika
[b] Silesian University of Technology, Faculty of Mechanical Engineering, Department of Engineering Materials and Biomaterials, ul. Konarskiego 18A, 44-100 Gliwice, Poland
email: pilarcikova4@stud.uniza.sk, eva.tillova@fstroj.uniza.sk

Abstrakt: Valivé ložiská predstavujú kľúčové prvky v mnohých technických zariadeniach, kde ich spoľahlivosť priamo ovplyvňuje funkčnosť a životnosť celého systému. Napriek vysokým nárokom na výrobu a kvalitu použitých materiálov dochádza v praxi často k ich predčasnému zlyhaniu. Príspevok analyzuje najčastejšie sa vyskytujúce poruchy ložísk, identifikuje ich hlavné príčiny a poukazuje na význam pravidelnej kontroly kvality ložiskových ocelí. Zároveň poukazuje na dôležitosť preventívnych opatrení, správneho mazania, diagnostiky a technologickej disciplíny pri montáži ložísk, čím možno výrazne predĺžiť ich životnosť a znížiť riziko náhlych porúch.

Kľúčové slová: ložiská, poruchy ložísk, životnosť ložísk, akosť ložísk

1. ÚVOD

Valivé a klzné ložiská predstavujú kľúčové konštrukčné prvky širokého spektra strojov a zariadení, pričom ich spoľahlivosť priamo ovplyvňuje prevádzkovú bezpečnosť a životnosť zariadenia. Správna funkcia ložísk je dôležitá pre zabezpečenie plynulého a efektívneho chodu komplexných technologických celkov. Aj keď sú vyrábané z vysoko kvalitných ložiskových ocelí a modernými technologickými postupmi, v praxi často dochádza k ich predčasnému zlyhaniu. Tieto neočakávané zlyhania nie sú len nepríjemnosťou, ale predstavujú aj značné riziko pre samotné zariadenia, v ktorých sú ložiská aplikované. V extrémnych prípadoch môžu vyústiť až do rozsiahlych škôd na drahých komponentoch, alebo dokonca k úplnému zničeniu celých strojových systémov. Dôsledkom poruchy je neplánovaná odstávka zariadenia, zvýšené náklady na údržbu a značná strata produktivity. Aktívne monitorovanie stavu ložísk pomocou moderných diagnostických nástrojov, implementácia prediktívnej a pravidelnej údržby strojových zariadení je nevyhnutnosťou, ale aj ekonomicky racionálne riešenie. Ak už však dôjde k identifikácii chyby alebo porušenia funkčnosti ložiska, stáva sa prvoradou úlohou čo najrýchlejšie a najpresnejšie určiť príčinu a miesto vzniku daného problému. Len na základe dôkladnej analýzy je možné implementovať účinné nápravné opatrenia a zabrániť opakovaniu podobných situácií v budúcnosti. Žiaľ, súčasná prax v mnohých priemyselných odvetviach poukazuje na alarmujúci

fakt, že zlyhávanie zariadení v dôsledku vzniku porúch ložísk je stále veľmi rozšíreným javom. Preto je hlbšie pochopenie mechanizmov vzniku týchto porúch, ich klasifikácia a možnosti prevencie mimoriadne dôležité.[1,2]

2. DRUHY POŠKODENIA LOŽÍSK

Poruchy ložísk môžu byť spôsobené rôznymi faktormi, ktoré majú priamy vplyv na ich výkon a životnosť. Včasná identifikácia týchto problémov a prevencia porúch je kľúčová pre zaistenie efektívnej a bezpečnej prevádzky, pretože tieto poruchy môžu spôsobiť vážne technické problémy, ako sú zlyhania strojov a zariadení, čo vedie k neplánovaným prestávkam a nákladom na opravu.

Jednou z hlavných príčin zlyhania ložísk je prehriatie nad povolenú teplotu, ktoré vedie k zníženiu tvrdosti materiálu a znižuje jeho odolnosť voči opotrebovaniu a únavovému poškodeniu. Prehriatie môže nastať v dôsledku nesprávnej tepelnej regulácie alebo nadmerného zaťaženia. Dlhodobé vystavenie vysokým teplotám môže spôsobiť trvalé deformácie ložiska, čo vedie k rýchlejšiemu opotrebovaniu a nakoniec aj k jeho zlyhaniu.

Ďalšou významnou príčinou porúch je korózia farebných kovov a bronzov (obr. 1), ktoré sa používajú v niektorých častiach ložísk, najmä v klietkach a obaloch. Korózia vzniká vniknutím vody do maziva, príp. kondenzáciou pár a kapilárnou eleváciou, čo má za následok oxidačné a rozkladné produkty mazív, ktoré oslabujú materiál a znižujú jeho mechanické vlastnosti. Tieto chemické reakcie môžu znižovať životnosť ložísk a prispievať k ich predčasnému zlyhaniu. [1,3]

Obr. 1 Poškodenie ložiska koróziou [3]
Figure 1. Bearing damage due to corrosion [3]

Obr. 2 Falošné brinellovanie na vnútornom krúžku ložiska [5]
Figure 2. False brinelling on the inner ring of the bearing [5]

Medzi časté mechanické poškodenia patrí falošné brinellovanie (obr. 2), ktoré nastáva, keď zaťaženie ložiska prekročí hranicu pružnosti materiálu krúžku, ako aj vplyvom silných vonkajších vibrácií (mikropohybov). Teliesko sa nepretáča, len sa naklápa na strany cca o 2°. Tento jav vedie k vzniku vtlačkov na povrchu ložiskových dráh (v prípade guľôčkového ložiska sa na obežnej dráhe pod telieskom objaví priehlbina, u ložísk s čiarovým stykom sa objavia čiary v miestach pod zaťaženými telieskami), čo môže v konečnom dôsledku viesť až k únavovému lomu ložiska. Riešením je zabezpečenie kvalitného a nepretržitého mazania a pravidelné odstraňovanie tuhých častíc a nečistôt z obehového ložiskového oleja pomocou účinnej filtrácie.[1,4,5]

Podobné poškodenie môže nastať aj v prípade odlupovania (pitting - obr. 3), kedy dochádza k poškodeniu obežnej dráhy alebo valivých telies. Odlupovanie môže byť dôsledkom abnormálnych axiálnych síl alebo nesprávnej montáže, ako aj priehybu hriadeľa či nevhodného maziva.[1,6]

Obr. 3 Pitting, jamkové poškodenie na vnútornom krúžku ložiska [6]
Figure 3. Pitting on the inner ring of the bearing [6]

Nevhodný materiál a výroba ložiska tiež zohrávajú dôležitú úlohu pri vzniku porúch. Ak sa pri výrobe ložísk nepoužije správny materiál, môže to viesť k nevyhovujúcej mikroštruktúre, ktorá nie je dostatočne odolná voči prevádzkovým podmienkam. Nesprávna tepelno-chemická úprava materiálu alebo zlé spracovanie môže viesť k nerovnomernému rozloženiu karbidov, čo znižuje pevnosť ložiska.

Obr. 4 Povrch ložiska poškodený abrazívnym opotrebením [7]
Figure 4. Bearing surface damaged by abrasive wear [7]

Ďalším problémom je zlý výber a použitie ložiska, ďalej nesprávne mazanie, ktoré je jednou z najčastejších príčin porúch ložísk. Ak sa použije staré alebo nevhodné mazivo, alebo ak je jeho množstvo nedostatočné, vzniká zvýšené trenie, ktoré spôsobuje nadmerné opotrebovanie ložiska (obr. 4). Takisto kontaminácia maziva, ako je prítomnosť prachu, kovových častíc alebo iných nečistôt, môže viesť k abrazívnemu poškodeniu ložísk a výraznému skracovaniu ich životnosti. Okrem toho sa poruchy ložísk môžu vyskytnúť aj v dôsledku mechanických poškodení, ako sú abrazívne, adhezívne, erozívne alebo kavitačné opotrebovanie materiálu. Abrazívne opotrebovanie spôsobujú drobné častice - nečistoty, ktoré v spojení s mazivom pôsobia ako brúsna pasta a spôsobujú postupné vyhladzovanie nerovností obežnej dráhy a valivých teliesok. Nečistoty spôsobujúce tento druh opotrebovania môžu vnikať pri montáž, mazivom, zlým utesnením, rovnako pôsobia aj častice vznikajúce poškodzovaním povrchu ložiska (odlúpnutia). Adhezívne opotrebovanie je spôsobené nedostatočným oddelením dvoch kovových plôch mazivom. Dochádza k prenosu materiálu z jedného povrchu na druhý, resp. k jeho oddeľovaniu.

Ak ložisko nie je správne namontované alebo je vystavené nadmernému zaťaženiu, môže dôjsť k poškodeniu povrchu ložiska, čo vedie k jeho rýchlemu zlyhaniu. Taktiež vibrácie a rázové sily, ak sú príliš vysoké, môžu spôsobiť poškodenie ložiskového materiálu, ako sú vrypy alebo škrabance.[1,3,7]

Tieto faktory môžu významne ovplyvniť spoľahlivosť a akosť ložísk, čo vedie k prestávkam v prevádzke a vysokými nákladmi na opravu alebo výmenu. Z tohto dôvodu je dôležité venovať pozornosť kvalitnej výrobe ložísk, správnemu výberu materiálov a vhodnému mazaniu, aby sa minimalizovalo riziko zlyhaní.

3. ANALÝZA HLAVNÝCH PRÍČIN PORÚCH LOŽÍSK

Poruchy ložísk predstavujú komplexný problém v oblasti prevádzky strojov, pričom ich vznik je podmienený rôznorodými faktormi, ktoré môžu mať signifikantný vplyv na ich funkčnosť a celkovú životnosť. Analýzou širokého spektra potenciálnych príčin je možné identifikovať kľúčové faktory, ktoré s najväčšou pravdepodobnosťou vedú k zlyhaniu ložísk. V kontexte zabezpečenia spoľahlivej a efektívnej prevádzky strojového parku zohráva včasná diagnostika a implementácia účinných preventívnych opatrení nezastupiteľnú úlohu.

Možných príčin porúch ložísk je pomerne veľké množstvo a možno ich zhrnúť do týchto hlavných bodov (obr. 5):

- použitie nevhodného maziva 20 %,
- použitie starého maziva 20 %,
- nedostatok maziva v ložisku 15 %,
- prítomnosť tuhých nečistôt 19 %,
- nevhodná voľba ložiska 10 %,
- chyba pri montáži ložiska 5 %,
- prítomnosť tekutých nečistôt 5 %,
- použitý nevhodný konštrukčný materiál a výroba 1 %,
- následná porucha 5 %.

K týmto faktorom možno ešte priradiť výber a použitie nevhodného ložiska, nevhodného a nekvalitného tesnenia a utesnenie samotného ložiska. Pri aplikácii ložísk sa musí brať do úvahy aj pracovné prostredie, dôležitá je nízka relatívna vlhkosť, ochrana proti vniknutiu a kontaminácii mazacieho prostriedku vodou (ložiskový domček).

Medzi najfrekventovanejšie príčiny porúch ložísk patrí predovšetkým použitie nevhodného alebo degradovaného maziva, ako aj nedostatočné množstvo maziva v ložisku. Významným rizikovým faktorom je taktiež prítomnosť tuhých alebo tekutých kontaminantov v mazive, ktoré môžu abrazívne pôsobiť na funkčné plochy ložísk. Na mazanie ložísk sa používajú oleje a plastické mazivá (ďalej PM). Pre oba typy mazív platia pomerne prísne kritériá, ktoré sa musia plniť na 100 percent. Ložiskové oleje sú vyrobené na báze vysokokvalitných základových olejov. Základové oleje by mali mať vysokú tepelno-oxidačnú stabilitu, vysoký viskozitný index, vynikajúce mazacie, protioderové a protizadieracie vlastnosti, nesmú korodovať, peniť a nesmú obsahovať vodu a pod. Na mazanie ložísk sa používajú najmä plastické mazivá (asi 90 %) a ložiskové oleje (asi 10 %) z celkového množstva mazív použitých na mazanie ložísk, ktoré sú namontované v rôznych agregátoch. Iná situácia je v prípadoch, keď sú ložiská namontované v motoroch, automobiloch, turbínach, prevodovkách apod. Tu je opačný pomer, 90 % olej a 10 % PM.

Okrem toho, nevhodný výber ložiska pre danú aplikáciu a prevádzkové podmienky, a v neposlednom rade chyby, ktoré vznikli počas procesu montáže ložiska, predstavujú významné zdroje potenciálnych porúch. Pochopenie a eliminácia týchto hlavných príčin je kľúčové pre minimalizáciu rizika zlyhania ložísk a zabezpečenie ich dlhej a bezproblémovej prevádzky.[1,7]

Prehľad hlavných príčin porúch ložísk a ich percentuálne zastúpenie je vizualizovaný prostredníctvom Paretovho diagramu a Lorentzovej krivky na obr. 5.

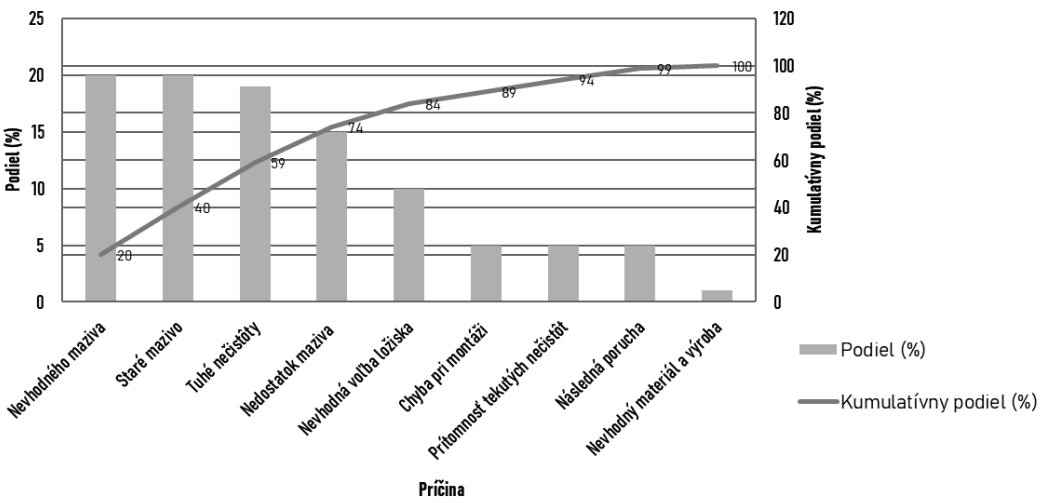

Obr. 5 Príčiny hlavných porúch ložísk
Figure 5. Causes of major bearing failures

4. MINIMALIZÁCIA RIZIKA PORÚCH LOŽÍSK

Zlyhanie ložísk predstavuje hrozbu pre plynulý a hospodárny chod strojových zariadení. Následky porúch sa neobmedzujú len na poškodenie samotných ložísk, často eskalujú až do deštrukcie ďalších nákladných komponentov a vyžadujú nákladné opravy. Dôsledkom sú predovšetkým prerušenia výrobného cyklu a zníženie celkovej efektivity prevádzky. Preto je implementácia účinných preventívnych opatrení, minimalizujúcich riziko týchto nežiaducich udalostí, absolútne kľúčová. Medzi základné preventívne stratégie patrí:

- *výber kvalitného a vhodného ložiska* (valivé, klzné, alebo pórovité, primeraná radiálna vôľa ložiska) pre aplikované strojné zariadenia;
- *výber kvalitných materiálov a mazív*: použitie ložiskovej ocele s optimálnou mikroštruktúrou a výber overeného maziva od renomovaného výrobcu, adekvátneho pre dané prevádzkové podmienky, tvorí základ dlhej a bezproblémovej životnosti ložísk. Neoddeliteľnou súčasťou je aj pravidelná kontrola a výmena maziva;
- *precízna a správna montáž a systematická údržba (dodržanie súosovosti, vhodné tesnenie):* ložiská musia byť inštalované s maximálnou opatrnosťou, kde sa eliminujú akékoľvek rázové sily a zabezpečí sa presná súososť s použitím vhodných tesniacich prvkov. Pravidelná údržba, zahŕňajúca kontrolu mazacieho systému, dopĺňanie maziva a čistenie, efektívne bráni kontaminácii a predčasnému opotrebeniu.
- *Aplikácia moderných diagnostických metód*: Včasná detekcia porúch prostredníctvom technickej a tribotechnickej diagnostiky (napr. analýza vibrácií, akustická diagnostika, rozbor maziva, stanovenie obsahu opotrebovaných kovov a kontaminantov) umožňuje realizovať nápravné kroky skôr, než dôjde k náhlemu výpadku zariadenia.

Dôsledné uplatňovanie týchto princípov výrazne redukuje frekvenciu porúch, predlžuje prevádzkovú životnosť ložísk a prispieva k stabilnej a nákladovo efektívnej prevádzke technologických systémov.[1,7]

POĎAKOVANIE

Príspevok vznikol v rámci riešenia spoločného slovensko-poľského projektu Project Based Learning ako výsledok spolupráce medzi Politechnikou Slaskou, Gliwice a Žilinskou univerzitou v Žiline a projektov KEGA č. 004ŽU-4/2023 a KEGA č.009ŽU-4/2023.

BIBLIOGRAFIA

1. Kuchariková L. et al., Kontrola kvality materiálov, Žilina : EDIS,2021, ISBN 978-80-554-1782-0
2. Konečná R., et al., Materiály II, Žilina : EDIS,2020, 978-80-554-1708-0
3. Bearing-news, Bearing failure RCA: Fretting, [online], https://www.bearing-news.com/bearing-failure-rca-fretting/
4. Reliability solutions, Understanding and preventing bearing damage [online], https://reliabilitysolutions.net/articles/brinelling-of-bearings/
5. NSK, Damage by type - False Brinelling, [online], https://www.nsk.com/eu-en/tools-resources/troubleshooting/damage-by-type/false-brinelling/
6. EATON, RWRG0016 - Front Countershaft Bearing Failure, [online], https://www.eaton.com/us/en-us/support/warranty-returns/eaton-commercial-vehicle-warranty/warranty-information/guidelines/rwrg0016.htm
7. Researchgate, Fault tree analysis of most common rolling bearing tribological failures, [online],https://www.researchgate.net/publication/314129554_Fault_tree_analysis_of_most_common_rolling_bearing_tribological_failures

TalentDetector
23th-25th June 2025
Gliwice-Brenna, Poland
DEPARTMENT OF ENGINEERING MATERIALS AND BIOMATERIALS
FACULTY OF MECHANICAL ENGINEERING
SILESIAN UNIVERSITY OF TECHNOLOGY
INTERNATIONAL STUDENTS SCIENTIFIC CONFERENCE

Computer simulation of the mechanical properties of a wood chipping knife during the production of wood chips

Jakub Polis[a], Jakub Bicz[a], Radosław Trojnar[a], Daniel Pella[a], Filip Bejm[a], Amadeusz Dziwis[a], Agata Śliwa[a], Marek Sroka[a], Jan Komendák[b], Samuel Zachar[b], Miroslava Tavodova[b]

[a] Silesian University of Technology, Faculty of Mechanical Engineering, Department of Engineering Materials and Biomaterials
email: jakupol064@student.polsl.pl, jakubic839@student.polsl.pl, radotro676@student.polsl.pl, dp316755@student.polsl.pl, fb316756@student.polsl.pl, amadeusz.dziwis@polsl.pl, agata.sliwa@polsl.pl, marek.sroka@polsl.pl
[b] Technical University in Zvolen, Faculty of Technology, Department of Manufacturing Technology and Quality Management
email: xkomendakj@is.tuzvo.sk, xzachars@is.tuzvo.sk, tavodova@tuzvo.sk

Abstract: Chopping machines are used to process lower-value wood and waste such as sawmill offcuts and logging residues. These machines cut wood across and along the grain to produce chips, which are used in the chemical, wood-processing, and energy industries. The required chip size varies by application, from fuel to fibreboard or paper production. Drum mowers, a common type of chopping machine, use a rotating drum with knives to chop wood. They are suitable for various types of wood waste and are comparable in performance to disc mowers, especially in the production of chips for burning or board manufacturing. The chopping knife is the key tool in these machines. It must be sharp and wear-resistant, and is typically made from tool steel, stainless steel, or powder metallurgy materials. Each material offers different properties in terms of hardness, durability, and corrosion resistance. The cutting process involves specific forces and angles that must be optimized to ensure efficient chip production and increase durability of the knife.

Keywords: Chopping machines; chopping knife; computer analysis; tool steel.

1. CHOPPING MACHINES

Chopping machines are used to process lower-value timber and wood waste such as sawmill trimmings, which arise from the processing of whole trunks into assortments, whether in forest or main timber stores, as well as waste arising from logging (branches, twigs, coniferous thinning etc.) Chopping machines are devices for the frictionless cutting of timber with a knife across the grain and at the same time to the necessary thickness along the grain. The output product of these machines is small pieces of wood called chips (Fig. 1) [1-3].

Figure 1. Wood chips [1].

The actual production of the chips can take place directly in the stand, at the collection points or in the factory. These are raw materials for further industrial processing in the chemical industry for the production of cellulose and paper, in the wood processing industry for the production of particleboard and fibreboard and in the energy industry as biomass (fuel) for heat production [2.3].
Depending on the purpose for which the wood chips are to be used, they must have the required dimensions and shape. For the production of fibreboard, the chips should be 20÷30 mm long and 3-5 mm thick. For charcoal production, chips 80÷120 mm long are used. In automatic combustion plants, the length of chips is controlled according to the type of boiler grate and loading equipment. If the chips are blown, a length of 6÷10 mm is required, with mechanical feeding the length is 12÷20 mm. For chemical processing of chips by sulphite method, the recommended length is 20-30 mm, thickness 3÷6 mm and for sulphate method the length should be 10-25 mm and thickness 3-5 mm [2,3].

1.1. Drum mower

It consists of a rotating drum, which has longitudinally positioned cutting blades around its circumference (Fig. 2a). The length of the chip is adjusted by the overlap of the knives. The quality of the chips is lower in these mowers because the cutting angle changes during the chopping process, which reduces the required length of the chips. The chopped wood is fed to the drum through the inlet chute, which is inclined at angles α1 and α2. A counter knife is fixed at the bottom of the chute. During cutting, the chips accumulate in the recesses under the blades and are thrown by centrifugal forces into the exhaust pipe sleeve or dropped under the drum onto the outfeed conveyor [2].
Drum mowers (Fig. 2b), unlike disc mowers, have the cutting tools mounted on the circumference of a rotating cylinder or double cone. The applications are varied and for different types of waste. However, it is mainly for processing waste such as sawmill offcuts, waste from the furniture industry, waste from plywood mills, veneer waste, etc. Due to the smaller dimensions of the chute, they are also used to process shorter waste (under 0.5 m). Today, drum mowers are equal in performance to other types of disc mowers and are mainly used in the production of chips for agglomerated boards and for incineration [2].

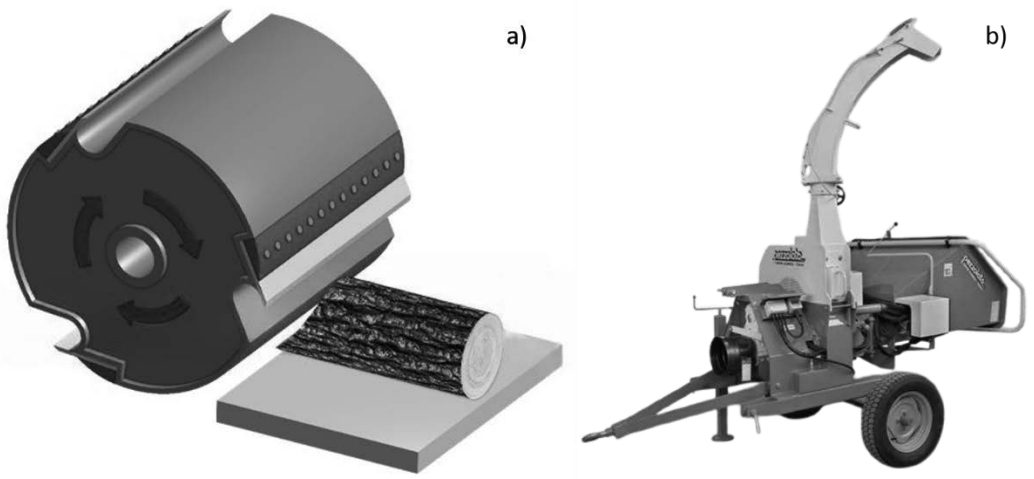

Figure 2. Drum mowers chopping knives mounted on a rotating drum [4]; b) Mower Pezzolato H780/200 [5].

2. CHOPPING KNIFE

The chopping knifes in wood chopping machines are used for cutting wood in the production of wood chips. This is produced by processing various materials such as logs, branches, stumps, bamboo or agricultural residues. Wood chips are mainly used as fuel [5,6].

2.1 MATERIAL OF CHOPPING KNIFES

Chopping knives are most often made of stainless tool steel or structural steel with increased hardness. However, they can also be made of various other materials, depending on the type of wood being processed and the operating conditions in which they will be used. It is important to ensure that the blade of the chopping knife remains sharp and wear-resistant in the long term, thus ensuring the quality and efficiency of the woodchip production process.Based on the materials used, chopping knives can be divided into several categories according to their physical and chemical properties such as wear resistance, strength, hardness, abrasion resistance, corrosion resistance and abrasive resistance. Each type of material has its advantages and disadvantages, so the selection of the right knife depends on the specific requirements of the production and the type of wood being processed [6].
Chopping knives can be divided into three main categories according to material. The first group consists of carbon steel knives, which are often used due to their low price and good cutting properties. However, they have the disadvantage of wearing out quickly, especially when in contact with hard or abrasive materials. The second type is alloy stainless steel knives, which are characterised by their high corrosion resistance, allowing them to be used even in wet environments. However, they are less hard and therefore less resistant to wear. The most durable knives are those made using powder metallurgy technology. They are characterised by high hardness, long service life and excellent cutting properties, making them ideal for demanding conditions. Their disadvantage is their higher price [6].

2.2 CHOPPING PROCESS

There are many different types of chopping knives where the important parameters of the knife are width, height and thickness. The knives come in several sizes, with widths of 175, 215 and 295 mm, depending on the model of chopper selected. There are different blade heights depending on the clearance between the blades of a given chopping machine. The Figure 6 shows the forces and angles applied during the wood chopping process. The main tool is the chopping knife, which removes material from the workpiece and creates a chip. This diagram is important for understanding the chopping mechanism and optimizing cutting conditions that affect tool life, surface quality and machining efficiency [6, 7].

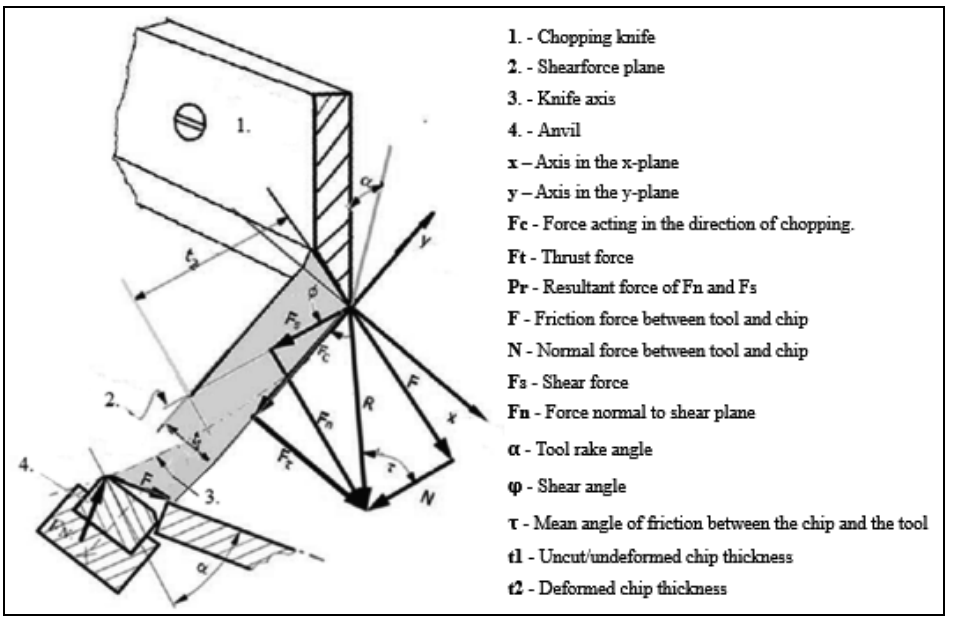

Figure 3. Knife cutting forces and chopping diagram [7].

3. MATERIALS AND METHODOLOGY

The analyzed component is a wood chopping knife made of X48CrMoV8-1-1 tool steel, with the chemical composition and properties given next in Table 1 and Table 2.

Table 1. Chemical composition of X48CrMoV8-1-1 steel [8].

Element	Min [%]	Max [%]
C	0.45	0.50
Cr	7.3	7.8
Mo	1.3	1.5
V	1.3	1.5
Si	0.7	0.9
Mn	0.35	0.45
P	-	0.02
S	-	0.005

The purpose of this study is to analyze the effect of a standard load of 3603 N on the surface of the chopping knife during operation. In addition, to evaluate the strength of the workpiece when the base load is exceeded, the model will be subjected to forces of 4143 N (i.e. +15% from the initial value) and 4683 N (i.e. +30% from the initial value).

Table 2. Mechanical and physical properties of X48CrMoV8-1-1 steel [9].

Property	Value
Young's modulu [GPa]	207
Poisson's ratio	0.28
Shear modulus [GPa]	79
Density [kg/m³]	7750
Tensile strength [MPa]	1135
Yield strength [MPa]	935
Coefficient of thermal expansion [K^{-1}]	$11*10^{-6}$
Thermal conductivity [W/(m*K)]	14
Specific heat [J/(kg*K)]	440

4. CAD GEOMETRIC MODEL

A model of wood chipping knife was made using SOLIDWORKS to carry out strength analysis by means of computer simulation. The designed wood chopping knife model is shown in Figure 1a.

5. BOUNDARY CONDITIONS

The following boundary conditions were adopted in the computer simulation:

- A finite element mesh was superimposed on the wood chopping knife model (Figure 1b),
- The model was loaded successively with forces of 3603 N, 4143 N and 4683 N, acting on the cutting edge of the blade at an angle of 36° (Figure 1c),
- The location of force application and immobilization geometry of the wood chopping knife are shown in Figure 1c.

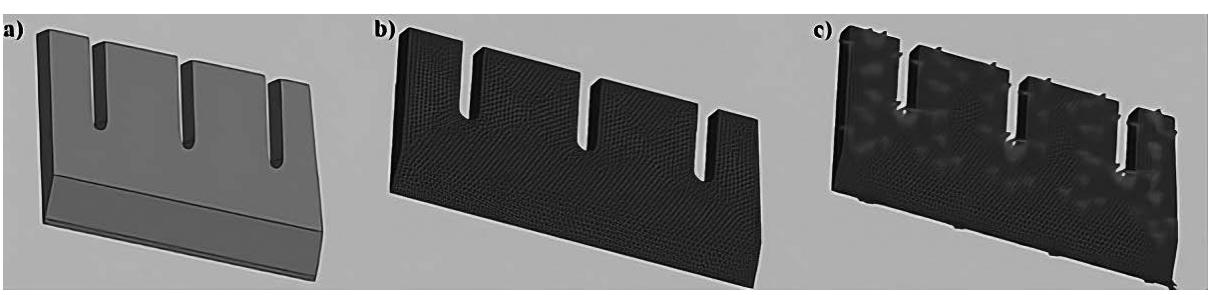

Figure 1. CAD model of wood chopping knife (a); with superimposed finite element mesh (b); with superimposed finite element mesh, visible direction of forces and immobilised knife geometry (c)

6. ANALYSIS OF RESULTS

Numerical stress analysis was performed based on the Huber-Mises hypothesis. After loading the component, stress diagrams were obtained, the values of which are expressed in MPa. Figure 2 shows the distribution of stresses developed during the given loading.

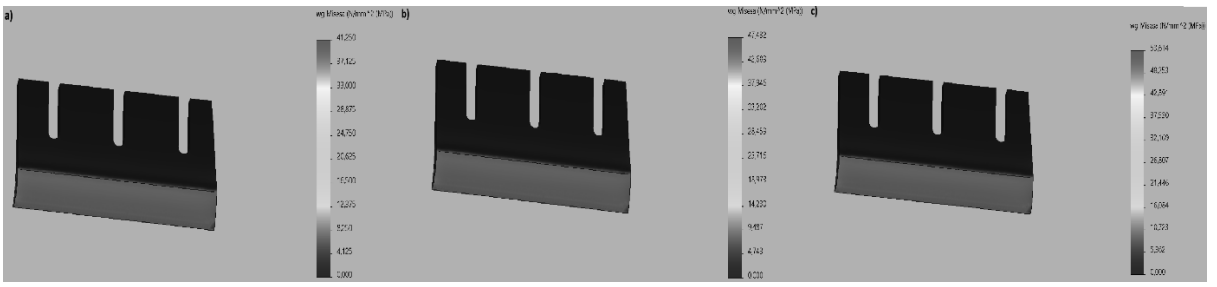

Figure 2. Huber-Mises stress reduction distribution of wood chipping knife at a force of (a) 3603 N, (b) 4143 N and (c) 4683 N.

The purpose of the subsequent computer simulation carried out was to determine the magnitude of the displacement under the application of a given force and to generate the displacement diagrams of the structure, which are shown in Figure 3.

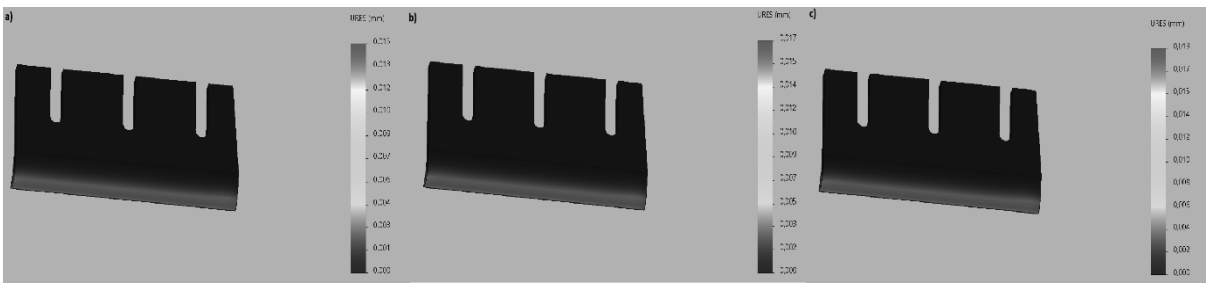

Figure 3. Displacement distribution of wood chipping knife at a force of (a) 3603 N, (b) 4143 N and (c) 4683 N.

The last simulation carried out was to determine the critical force causing the deformation. Figure 4 shows the equivalent deformation represented by the largest force required to deform the axis.

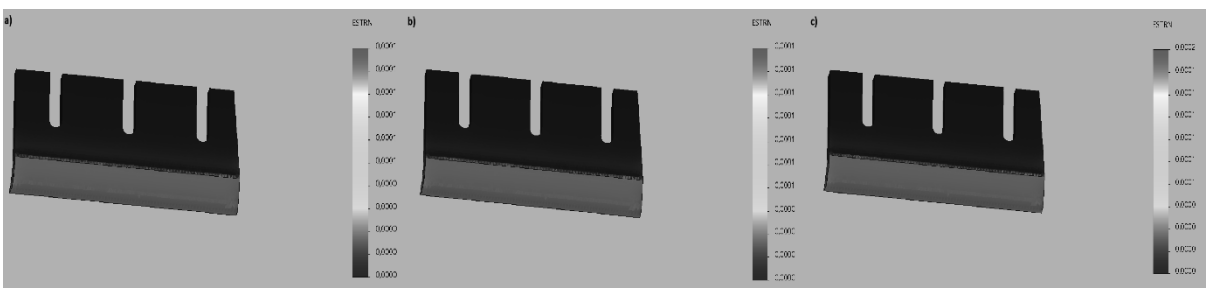

Figure 4. Equivalent deformation of wood chipping knife at a force of (a) 3603 N, (b) 4143 N and (c) 4683 N.

The overall results of the simulations performed are shown in Table 5.

Table 5. Summary of overall results from computer simulations carried out

Used force [N]	Maximum stress value [MPa]	Maximum displacement [mm]	Maximum deformation value
3603	41.253	0.015	$1*10^{-4}$
4143	47.432	0.017	$1*10^{-4}$
4683	53.614	0.019	$2*10^{-4}$

7. CONCLUSION

The results of the strength analysis show that as the applied force increases (from 3603 N to 4683 N), there is an almost linear increase in the value of maximum stress (from 41.25 MPa to 53.61 MPa) and maximum blade displacement (from 0.015 mm to 0.019 mm). This also applies to deformation and displacement.

X48CrMoV8-1-1 steel has a tensile strength of about 1000-1200 MPa (depending on the quenching and tempering condition) and a yield strength of about 900-1000 MPa after appropriate heat treatment. Concurrently, the maximum stress values obtained in the simulation (maximum ≈ 53.6 MPa) and therefore are many times lower than the yield strength of the steel (more than 900 MPa). This means that, in the analyzed load range, the knife operates in a safe zone, without the risk of permanent deformation or fracture.

The maximum blade displacement does not exceed 0.019 mm, even for the highest applied force (4683 N). Such a low deflection means that the cutting-edge geometry remains virtually unchanged during normal operation, resulting in precise cutting and minimized energy losses associated with deflection.

The deformation (a value of $1*10^{-4}$ for forces of 3603 N and 4143 N, and $2*10^{-4}$ for 4683 N) is at the micrometer level, again confirming that the material is not approaching yield strength and retains full elasticity.

The simulation confirmed that the blade made of X48CrMoV8-1-1 steel, when subjected to forces in the range of 3600-4700 N, performs its function without the risk of permanent deformation. Deformations and displacements are at the micrometric level, which guarantees edge stability and long-term blade life.

ACKNOWLEDGEMENT

This study was conducted as part of the project-oriented education - PBL, in the XII competition within the Excellence Initiative - Research University program.

BIBLIOGRAPHY

1. Drevná štiepka, 2025. Available at: https://microjob.sk/stavebne-tesarske-a-ine-remeselne-sluzby/drevna-stiepka_9514.html

2. KOVÁČ, Ján, Jozef KRILEK, Ján JOBBÁGY a Jiří DVOŘÁK. *Technika a mechanizácia v lesníctve: vysokoškolská učebnica*. Zvolen: Technická univerzita vo Zvolene, 2017. ISBN 978-80-228-3021-8.
3. MIKLEŠ, Milan. *Lesnícke stroje a zariadenia*. Zvolen: Technická univerzita vo Zvolene, 2011. ISBN 978-80-228-2302-9.
4. Industrial Wood Chippers, 2025. Available at: https://www.robsonforensic.com/articles/wood-chipper-expert-witness
5. Pezzolato H780/200, 2025. Available at: https://www.lectura-specs.cz/cz/model/komunalni-technika/odpadove-hospodarstvi-stepkovace-pezzolato/h-780-200-1038488
6. CHANGZHOU BINSHENG METALLURGICAL MACHINERY CORP., 2025. Chipping machine blades. Available at: https://www.industrialblades.cc/products/chipping-machine-blades.html
7. BELLO, R.S. Force Relations and Dynamics of Cutting Knife in a Vertical Disc Mobile Wood Chipper, 2011. ISSN 1583-1078. Available at: https://www.researchgate.net/publication/275642280_Force_Relations_and_Dynamics_of_Cutting_Knife_in_a_Vertical_Disc_Mobile_Wood_Chipper
8. https://virgamet.pl/oferta/1-2360-x48crmov811-stal-narzedziowa - access date 20.05.2025 r.
9. Solidworks material base

TalentDetector

23th-25th June 2025
Gliwice-Brenna, Poland

DEPARTMENT OF ENGINEERING MATERIALS AND BIOMATERIALS
FACULTY OF MECHANICAL ENGINEERING
SILESIAN UNIVERSITY OF TECHNOLOGY

INTERNATIONAL STUDENTS SCIENTIFIC CONFERENCE

Creating an effective cooling system for the loading zone of a 3D printer screw extruder when printing with composite mixtures

Andrii Polishchuk [a], Mirosław Bonek [b], Oleh Polishchuk [c], Serhii Matiukh [d], Svitlana Lisevich [e], Artem Tostiuk [f]

[a] Khmelnytskyi National University, Faculty of Mechanical Engineering, Transport and Architecture, Khmelnytskyi, Ukraine
email: andrepol215@gmail.com.
[b] Silesian University of Technology, Faculty of Mechanical Engineering, Department of Engineering Materials and Biomaterials, Gliwice, Poland
email: miroslaw.bonek@polsl.pl.
[c] Khmelnytskyi National University, Faculty of Mechanical Engineering, Transport and Architecture, Khmelnytskyi, Ukraine
email: opolishchuk7l@gmail.com.
[d] Khmelnytskyi National University, Faculty of International Relations and Law, Khmelnytskyi, Ukraine
email: matuh@khmnu.edu.ua.
[e] Khmelnytskyi National University, Faculty of Mechanical Engineering, Transport and Architecture, Khmelnytskyi, Ukraine
email: lisevichsv@gmail.com.
[f] Khmelnytskyi National University, Faculty of Engineering Mechanics, Khmelnytskyi, Ukraine
email: tvenergetik@gmail.com.

Abstract: The article considers the problem of overheating of the screw extruder housing during 3D printing with reinforced composite materials. Excessive thermal load arising from the operation of the heating element and friction of the composite mixture against the internal surfaces of the extruder leads to premature softening of the granules, sticking of the feed and deformation of polymer elements. An improved cooling system is proposed, which includes passive heat dissipation ribs, active air cooling by a fan and the installation of a thermal insulation barrier between the plasticization zone and the hopper. Three materials were investigated as thermal barriers : silicone, fluoroplastic and flubon - a composite material based on fluoroplastic with carbon fiber reinforcement. An experimental test of the thermal insulation properties of the specified materials under stable printing conditions was carried out. Flubon demonstrated the highest efficiency, which is explained by its reinforced structure and improved thermal insulation characteristics. The results of the study confirm the feasibility of using Flubon as a thermal protection element in the design of a screw extruder. The proposed technical solution increases the stability of operation, ensures high-quality supply of the composite mixture, and improves the reliability of 3D printing from reinforced materials.

Keywords: 3D printer, 3D printing, screw extruder, system cooling, thermal barrier, thermal insulation gasket.

1. INTRODUCTION

During 3D printing of reinforced composites by extrusion, one of the critical factors is overheating of the screw extruder housing. Heat is generated both due to the operation of the electric heater in the aluminum block and due to the intense friction of the reinforced polymer against the screw and barrel. Due to the high thermal conductivity of the materials (aluminum – 209.3 W/ m·K [1]; 40X steel – 74.4 W/ m·K [1, 2]), heat quickly spreads through the housing, which can lead to premature melting of one of the mixture elements even before the melt zone, a decrease in feed accuracy and an undesirable shift in the temperature profile.

This is especially critical for composites with fibrous fillers, which have increased abrasiveness and can impair heat transfer and cause uneven heating. Overheating of the housing also creates the risk of deformation of polymer assemblies, complicates granulate loading , reduces equipment life and threatens operator safety.

The implementation of an effective cooling system (air, liquid or combined) ensures thermal stability of the extruder, prevents thermal deformations and stabilizes the supply of reinforced material. This helps to increase the accuracy and repeatability of the printing process, reduce energy consumption and allows working with a wide range of composites, including those requiring strict temperature control.

Thus, the development of an extruder housing cooling system is of key importance for the reliable and safe operation of the equipment when printing with modern fiber composites.

2. FORMULATION OF THE PROBLEM

To develop a cooling system for the screw extruder housing of a 3D printer and ensure its compatibility with existing 3D printer designs.

3. PRESENTING MAIN MATERIAL

In a screw extruder of a 3D printer working with pellets or crushed reinforced composites, the melting zone performs the functions of a classic hotend, responsible for heating, melting, homogenizing and feeding the material through the nozzle [3, 4]. Temperature control of this zone is critical for flow stability, preventing clogging and maintaining print quality, especially when working with abrasive composites [5].

The largest number of studies is devoted to the thermodynamics of the hot end, while data on the heating of screw extruders for FDM printing are practically absent. However, the results of studies on hot ends can also be applied to the analysis of the melting zone of a screw extruder. In particular, in [6, 7] the influence of the hot end geometry on the pressure and material flow rate, as well as the temperature distribution, was estimated using the finite element method. In [8] the role of a thermal break was considered, which reduces heat loss and improves the energy efficiency of the system.

In works [9–12] the influence of cooling elements - fans, radiators and geometry of ventilation channels - on the thermal stability of the extruder and the uniformity of temperature

distribution is analyzed. These conclusions are relevant in the design cooling systems for reinforced composite processing areas that require precise temperature control.

In the first version of the screw extruder with composite mixture feed, the cooling of the housing was implemented using ribs placed on the upper part of the material cylinder. The air-cooled design was modeled in SolidWorks (Fig. 1, 2) [13].

Fig. 1. SolidWorks model of a material cylinder with air cooling fins

Fig. 2. General view of a material cylinder with air ribs cooling

The main purpose of the ribs on the material cylinder is to increase the heat transfer area in the polymer composite mixture feed zone to the screw. This allows to reduce heat transfer to the hopper and prevent premature melting of polymer matrix granules that have not yet entered the plasticization zone. However, during printing with materials such as TPU, PLA and ABS, particle sticking and blocking of their feed were observed, which indicates overheating of the upper part of the extruder [14]. In some cases, due to heat accumulation, even plastic elements of the hopper were deformed. Adjusting the heater temperature did not give a significant effect.

Therefore, passive air cooling with fins was insufficient. To increase heat transfer, active cooling with air flow from a fan was implemented. Turbine fan 1 (1.2 W, 50×50 mm) is installed in the upper part of the extruder (Fig. 3), and for local flow direction, a guide nozzle 2 was designed in SolidWorks [13].

The use of a fan allowed to reduce overheating of the polymer matrix, stabilize the temperature regime in the feed zone and increase the reliability of transporting the reinforced mixture to the melting zone. This positively affected the extruder productivity and the quality of the resulting products.

Fig. 3. Extruder with air cooling using a fan:
1-turbine fan; 2-directional nozzle

During 3D printing with composite mixtures based on ABS plastic in a screw extruder, a problem of granule sticking in the loading hopper was recorded. This caused a disruption in the stability of the material supply to the plasticization zone, blocking the transportation process and reducing the overall productivity of the extruder. The main reason turned out to be excessive thermal impact from the heated part of the extruder body, which was transmitted to the hopper. An increase in temperature in the feed zone led to partial melting or deformation of the polymer matrix granules before their contact with the screw, which is critical when working with reinforced composites that have different thermal conductivity and sensitivity to heat treatment.

To solve this problem, two technical improvements were implemented: installing an additional fan for active blowing of the hopper with an air flow and introducing a thermal barrier between the hopper and the heated zone of the extruder. The fan helped stabilize the temperature, but did not completely eliminate overheating. Therefore, the main measure was the development and installation of a heat-insulating gasket that physically separates the plasticization zone from the pellet feed zone. Such a thermal barrier performs several important functions: reduces heat transfer, stabilizes the conditions for transporting the composite, prevents thermal destruction of the pellets, and reduces the risk of deformation of the polymer parts of the hopper. In addition, this solution has a positive effect on the energy efficiency of the extruder, allowing to reduce heat losses.

Three materials were selected for the manufacture of the thermal barrier: silicone, PTFE (polytetrafluoroethylene) and Flubon - a fluorocarbon composite material developed at Khmelnytskyi National University. Silicone is a heat-resistant elastomer that can withstand temperatures up to 280–300 °C, has high flexibility, is resistant to moisture, ultraviolet radiation and aggressive environments. Its ability to absorb vibrations makes this material suitable for use in conditions of cyclic loads typical of 3D printing.

Fluoroplast-4 (PTFE) is a heat-resistant polymer with low thermal conductivity (0.252 W/ mK) and an extremely low coefficient of thermal expansion ($1 \cdot 10^{-5}$ / °C), which allows maintaining the stability of geometric dimensions when changing temperature. It also has high chemical resistance to acids, alkalis, solvents, as well as low adhesion and good antifriction properties, which is important when interacting with polymer mixtures in narrow gaps between parts.

Flubon is a composite material based on PTFE, modified with carbon fibers. It combines all the advantages of fluoroplastic, but thanks to reinforcement it acquires additional strength, reduces thermal expansion and has significantly improved anti-friction properties. In addition, flubon is characterized by high wear resistance, resistance to thermal destruction and water resistance, which makes it extremely suitable for use as a thermal barrier in the design of an extruder that works with aggressive composite materials. Studies have shown that the introduction of carbon fibers into fluoroplastic increases anti-friction properties up to 2000 times.

For experimental study of the thermal barrier efficiency, gaskets were made from all three materials with dimensions of 37×37 mm and a thickness of 2 mm, which corresponds to the structural dimensions of the extruder modeled in SolidWorks [13]. The silicone gasket was cut from a 20 mm thick sheet (Fig. 4, a), the fluoroplastic gasket was cut from a PTFE plate (Fig. 4, b), and the Flubon 15 gasket was made in the laboratory of polymer composites and lubricants of KhNU (Fig. 4, c) [26].

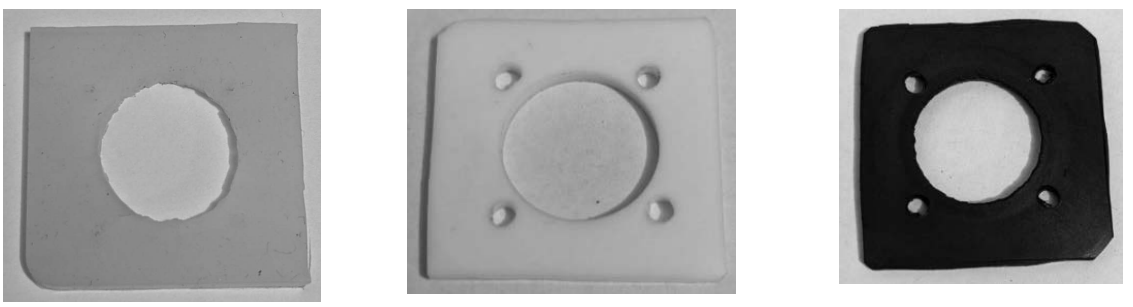

a b c

Fig. 4. Thermal insulation gaskets: a – silicone rubber; b – fluoroplastic 4; c – flubon 15

To assess the effectiveness of thermal insulation materials (Fig. 4), experimental studies were conducted to determine their real thermal conductivity under conditions close to the operation of a screw extruder for 3D printing of composites. The tests were carried out on an Anycubic 4 Max 3D printer Pro 2.0 with a closed housing, which ensures temperature stability during heating [27].

The platform temperature was set at 50 °C, after which thermal insulation pads made of silicone, fluoroplastic-4, and flubon were placed on it (Fig. 5). After thermal stabilization , the temperature of the worktable and the outer surfaces of the pads were measured using a thermal imager Walcom HT-03 [28]. The obtained outer surface temperatures were: silicone - 47.9 °C, fluoroplastic - 47.1 °C, flubon - 43.8 °C. Taking into account the platform temperature (51.4–51.9 °C), the temperature difference (ΔT) was determined, which reflects the efficiency of thermal insulation: flubon - 7.8 °C, fluoroplastic - 4.3 °C, silicone - 4.3 °C (Fig. 6).

Despite the fact that according to the literature, the thermal conductivity of fluoroplastic-4 is 0.252 W/ m K [23], and that of flubon 15 is 0.34…0.37 W/ mK [26], the experiment showed a better thermal insulation capacity of flubon. This can be explained by the additional influence of reinforcing fibers and structural features of the material. It is worth noting that the determination of exact thermal conductivity coefficients is not part of the task of this work; instead, the real efficiency of the thermal barrier in the conditions of working with composite raw materials was evaluated.

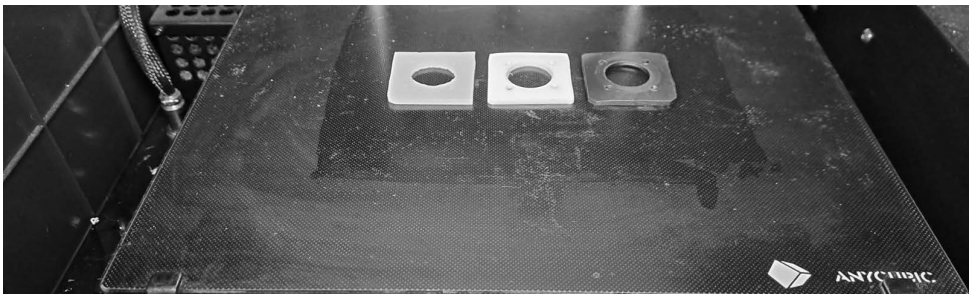

Fig. 5. Placement of thermal insulation pads on the 3D printer platform

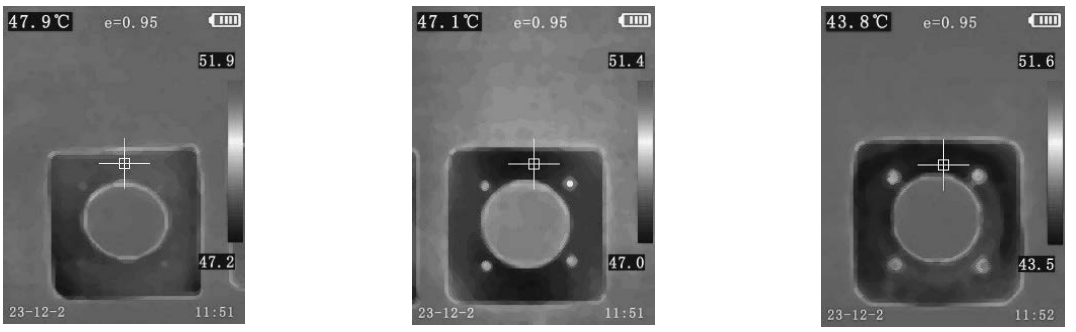

a b c

Fig. 6. Visual image of heating of gaskets: a-silicone; b-fluoroplastic 4; c-flubon 15

The general view of the screw extruder with an additional fan installed (40 W, 40×40 mm) is shown in Fig. 7, and the configuration with a thermal insulation gasket is shown in Fig. 8. The results confirm the feasibility of using Flubon as an effective thermal barrier when working with composite mixtures in 3D printing.

Fig. 7. General view of the extruder with an additional fan installed

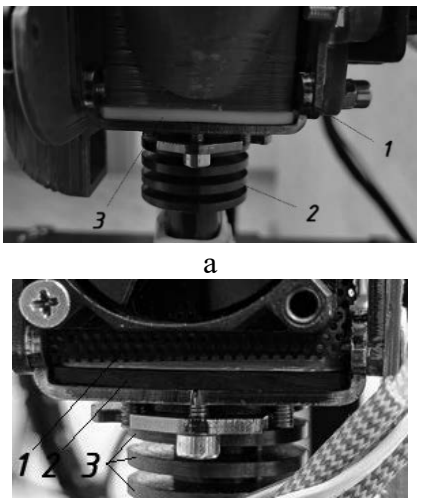

a

b

Fig. 8. General view of the extruder with the installed thermal insulation gasket: a-from fluoroplastic; b-from flubon ; 1-loading hopper; 2-cooling ribs; 3-thermal insulation gasket

Thus, installing a thermal barrier between the heated zone and the hopper is a justified engineering solution that increases the stability of the extruder, avoids defects in the transportation of composite raw materials, ensures thermal safety of assemblies, and improves the quality of the final product.

4. CONCLUSIONS

The study analyzed the impact of overheating of the screw extruder housing on the stability of the composite raw material feed during 3D printing and proposed engineering solutions to improve the thermal regime of its operation. It was found that when working with reinforced polymer composites, overheating of the feed zone can cause premature melting of polymer matrix granules, material sticking, deformation of polymer elements of the hopper and reduced extruder productivity of thermal barriers made of three materials: silicone, fluoroplastic-4, and flubon was conducted.

Experimental results showed that the lowest heat transfer is provided by the Flubon gasket, despite the fact that the nominal thermal conductivity coefficient of fluoroplastic is lower. This is explained by the reinforcement of Flubon with carbon fibers, which reduces thermal expansion and improves thermal insulation properties. It was found that the temperature on the outer surface of Flubon was the lowest among all tested materials (43.8 °C at a platform temperature of 51.9 °C), which indicates its high efficiency as a thermal insulation barrier.

In general, the installation of a thermal barrier made of Flubon in combination with a fan allowed to significantly improve the thermal regime of the extruder, ensure a stable supply of the reinforced composite mixture and increase the quality and reliability of 3D printing. The results can be used to improve the designs of extruders working with abrasive and heat-sensitive composites, taking into account the specifics of heat transfer and cooling in high-load areas.

GRATITUDE

The publication is the result of cooperation within the Visegrad Scholarship Program 2024/2025. The work was created as part of project based learning - PBL, in the 12th competition under the Initiative of Excellence - Research University, Silesian University of Technology, Gliwice, Poland.

BIBLIOGRAPHY

1. Thermal conductivity of metals: characteristics, methods of study. URL: https://interexpo.com.ua/rus/articles/cat_505-ff_0-items_2000-mode_full.html.
2. Basics of designing single-worm extruders: training. manual / I. O. Mikulonok, O. L. Sokolskyi, V. I. Sivetskyi, L. B. Radchenko. - K.: NTUU "KPI", 2015. - 200 p.

3. 3. Sizov V.D., Sorokvashin S.V. Basics of 3D printing [Electronic manual]. – 2018. – URL: https://cpto.dp.ua/public_html/posibnyky/osnovy_3d.pdf.
4. Manzhilevskyi O.D. Modern additive technologies of 3D printing. Features of practical application: study guide / O.D. Manzhilevskyi, R.D. Iskovich-Lototskyi. – Vinnytsia: VNTU, 2021. – 105 p.
5. Turner B.N., Strong R., Gold S. A. A review of melt extrusion additive manufacturing processes: I. Process design and modeling, Rapid Prototyping Journal, 20(3), 2014, pp. 192–204.. https://doi.org/10.1108/RPJ-01-2013-0012.
6. Sukindar N.A., Ariffin M.K.A., Baharudin B.T.H.T., Jaafar C.N.A., Ismail M.I.S. Analyzing the Effect of Nozzle Diameter in Fused Deposition Modeling for Extruding Polylactic Acid Using Open Source 3D Printing, Jurnal Teknologi, 78(10), 2016. - pp. 7–15.
7. Papon E.A., Sharif M.A.R., Haque A. Effect of Nozzle Geometry on Melt Flow Simulation and Structural Property of Thermoplastic Nanocomposites in Fused Deposition Modeling. Conference Paper, Thirty-second Technical Conference, West Lafayette, IN, USA, Oct. 23, 2017. https://doi.org/10.12783/asc2017/15339.
8. Gutiérrez Arias G., Jiménez Díaz F., Rúa Ramirez E., Valcarcel Guzman J. Thermal Analysis by Finite Elements of Hotends for 3D Printing by Fused Filament Fabrication. Periodica Polytechnica Mechanical Engineering, 65(2), pp. 129–133, 2021. https://doi.org/10.3311/PPme.16203.
9. Jerez-Mesa R., Travieso-Rodriguez J. A., Gomez-Gras G., Freixedes. J. Design of Open Source 3D Printer Extruder and Modelling of Thermal Performance with FEA. The 19th International Research/Expert Conference «Trends in the Development of Machinery and Associated Technology» (TMT), Barcelona, Spain, Jul. 22-23, 2015.
10. Jerez-Mesa R., Travieso-Rodriguez J. A., Corbella X., Busqué R., Gomez-Gras G. Finite element analysis of the thermal behavior of a RepRap 3D printer liquefier, Mechatronics, 36, 2016. - pp. 119–126.
11. Günel O., Koc E., Tiryaki G. Investigation of Heat Sink Geometry Effect on Cooling Performance for a FDM 3D Printer Liquefier. The International Conference on Energy and Thermal Engineering, Istanbul, Turkey, 2017, pp. 569–573.
12. Günel, O., Koc, E., Yavuz, T. "Investigation of Thermal Effect on 3D Printer Liquefier of different Cooling Fan Nozzle Geometry", In: International Conference on Energy and Thermal Engineering, Istanbul, Turkey, 2017, pp. 418–422.
13. Polishchuk A.O. Development of a screw extruder design for a 3D printer that uses granules or crushed polymer particles as raw materials. Technologies and engineering. 2023. No. 5.
14. Polishchuk O.S., Zozulya P.F., Polishchuk A.O. Generalized classification of filaments for 3D printing / Bulletin of the Khmelnytskyi National University. - 2017. - No. 6. - P.51-59.
15. Silicone rubber 2 mm. URL: http://surl.li/nooth.
16. Transparent silicone rubber sheet. URL: http://surl.li/nootv.
17. Extrusion System. URL: https://jetclay.com/project/open-source-clay-extrusion-system.
18. Jo J.H., Jo B.W., Cho W., Kim J.-H.. Development of a 3D Printer for Concrete Structures: Laboratory Testing of Cementitious Materials. International Journal of Concrete Structures and Materials. March. 2020. DOI: 10.1186/s40069-019-0388-2.
19. T. Lin, Z. Zhao, T. Wang, Ye-T. Pan. Three-Dimensional Printing of Large Ceramic Products and Process Simulation. Materials. 2023. №16. https://doi.org/10.3390/ma16103815.
20. Kurska T.M., Chernobay G.O., Eremenko S.B. Materials science and materials technology. Synopsis of lectures. - Kh.: UCZU, 2008. - 136 p.

21. Physical properties and technical characteristics of fluoroplastic. URL: http://kaprolon.com.ua/svojstva-i-harakteristiki-ftoroplasta/.
22. Properties and types of Fluoroplastics (Teflon). Basic information about fluoroplastics URL: https://baltro.cz/en/properties-and-types-of-fluoroplastics-teflon/.
23. Fluoroplast-4 (PTFE) URL: https://santex-kiev.com.ua/products/ftoroplast.
24. Polishchuk A., Polishchuk O., Lisevich S., Urbanyuk E., Rubanka M. Composite mixtures based on synthetic polymers and fillers and equipment for 3D printing with them. Bulletin of the Khmelnytskyi National University, Part 1. No. 2. 2023. - P. 104-110.
25. Composite materials URL: http://rts-ua.com/kompozitnye-materialy/.
26. Flubon URL: https://nauka.khmnu.edu.ua/flubon/.
27. Anycubic 4 Max Pro 2.0 3D printer: URL: http://surl.li/nvpgk.
28. Thermal imager for energy audit (80x60) WALCOM HT-03. https://simvolt.ua/teplovizor-dlya-energoauditu-80x60-walcom-ht-03/.

TalentDetector
23th-25th June 2025
Gliwice-Brenna, Poland
DEPARTMENT OF ENGINEERING MATERIALS AND BIOMATERIALS
FACULTY OF MECHANICAL ENGINEERING
SILESIAN UNIVERSITY OF TECHNOLOGY
INTERNATIONAL STUDENTS SCIENTIFIC CONFERENCE

Structure and phase transformations of Mg-Zn-Ca alloys containing Ag and Au obtained by mechanical alloying

Julia Popis[a], Oktawian Bialas[b], Oliwia Starczewska[c], Małgorzata Karolus[c], Sabina Lesz[a]

[a] Silesian University of Technology, Faculty of Mechanical Engineering, Department of Engineering Materials and Biomaterials
[b] Silesian University of Technology, Faculty of Mechanical Engineering, Materials Research Laboratory
[c] University of Silesia in Katowice, Faculty of Science and Technology, Institute of Materials Engineering, email: julia.popis@polsl.pl

Abstract: This study presents the research results on magnesium-based alloys $Mg_{65}Zn_{30}Ca_4Ag_1$ and $Mg_{65}Zn_{30}Ca_4Au_1$ produced by mechanical alloying. The study aimed to evaluate the effect of silver (Ag) and gold (Au) additions on the structure, thermal properties, and microstructure of the obtained materials. Phase analysis was carried out using X-ray diffraction (XRD), which enables the identification of the main crystalline phases present in the samples. Microstructural observations were performed using scanning electron microscopy (SEM) combined with energy-dispersive spectroscopy (EDS), allowing for the assessment of powder morphology and chemical homogeneity. Thermal properties were analysed by differential scanning calorimetry (DSC), identifying the temperatures of phase transformations. The results indicate different behaviour of the alloys depending on the noble metal addition on the microstructure and thermal properties, which may be important for further research on biodegradable magnesium-based materials for biomedical applications.

Keywords: Mg–based alloys, mechanical alloying, Ag, Au addition

1. INTRODUCTION

In recent years, there has been a growing interest in biodegradable materials for medical applications, especially in the context of temporary orthopedic implants and stents. Among them, magnesium alloys attract special attention, which are characterized by favorable mechanical properties, good biocompatibility, and the possibility of controlled degradation in the body environment. Modification of the chemical composition of magnesium alloys by adding noble elements, such as silver (Ag) or gold (Au), can lead to the improvement of their physicochemical properties, including microstructure, corrosion resistance, and biological properties. This work aimed to obtain $Mg_{65}Zn_{30}Ca_4Ag_1$ and $Mg_{65}Zn_{30}Ca_4Au_1$ alloys by mechanical alloying, where the elements were milled for 13 h, and their characterization using XRD, SEM/EDS, and DSC techniques.

2. METHODOLOGY

The $Mg_{65}Zn_{30}Ca_4Ag_1$ and $Mg_{65}Zn_{30}Ca_4Au_1$ alloys were prepared by mechanical synthesis. The powders were milled for 13 h. The crystalline phases were identified by X-ray diffraction (XRD) allowed for determining the phase composition and assessing the effect of mechanical alloying parameters on microstructure refinement. The particle morphology and their homogeneity were analysed using scanning electron microscopy (SEM), while the chemical composition of individual areas was assessed using energy dispersive spectroscopy (EDS). Thermal properties were analysed by differential scanning calorimetry (DSC), identifying the temperatures of phase transformations.

3. RESULTS

Figure 1 shows the results of XRD phase analysis of the $Mg_{65}Zn_{30}Ca_4Ag_1$ alloy after 13 h of MA. Figure 2 shows the results of XRD phase analysis of the $Mg_{65}Zn_{30}Ca_4Au_1$ alloy after 13 h of MA. For each of the alloys tested, the occurrence of $MgZn_2$ and $Mg_{51}Zn_{20}$ phases, as well as the solid solution of magnesium base αMg, was identified.

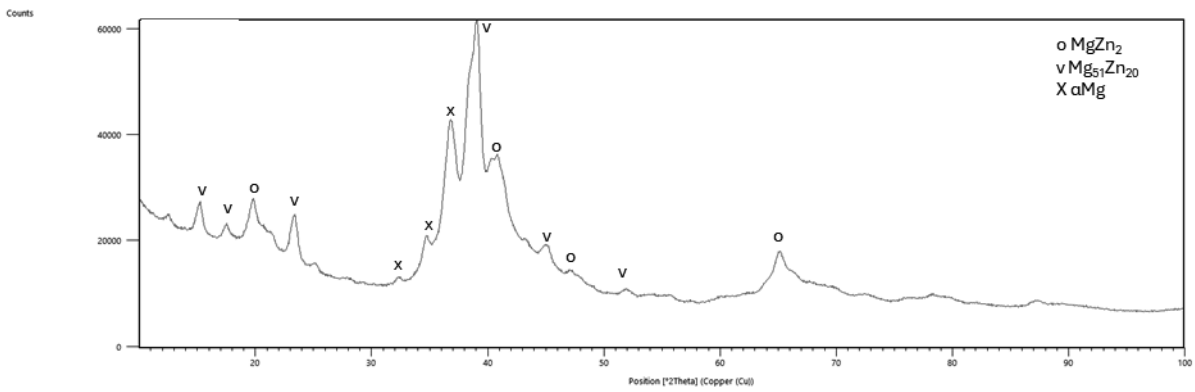

Figure 1. XRD patterns of $Mg_{65}Zn_{30}Ca_4Ag_1$ alloy powder after 13 h of milling time

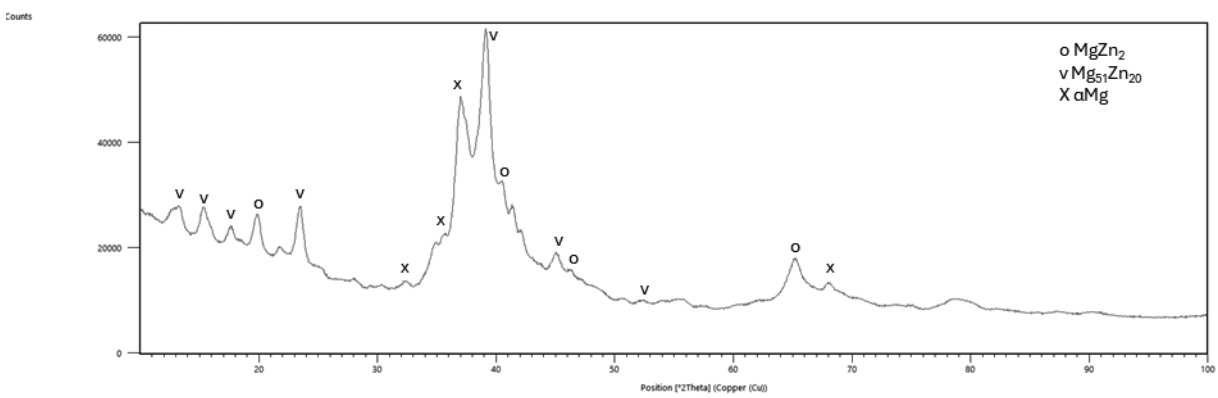

Figure 2. XRD patterns of $Mg_{65}Zn_{30}Ca_4Au_1$ alloy powder after 13 h of milling time

Figures 3 and 4 show the morphology of $Mg_{65}Zn_{30}Ca_4Ag_1$ and $Mg_{65}Zn_{30}Ca_4Au_1$ alloys after 13 h of MA. Visible are particles of irregular shape and varied size, with predominant fragmented, angular fragments. Characteristics are sharp edges and the presence of both larger agglomerates and finer fractions. On the surface of many particles, one can observe small

secondary structures, resulting from intensive crushing and fragmentation of the material during ball milling. The image indicates an advanced stage of mechanical synthesis, in which the particles are significantly fragmented and their active surface increases, which may affect further phase reactions and material properties.

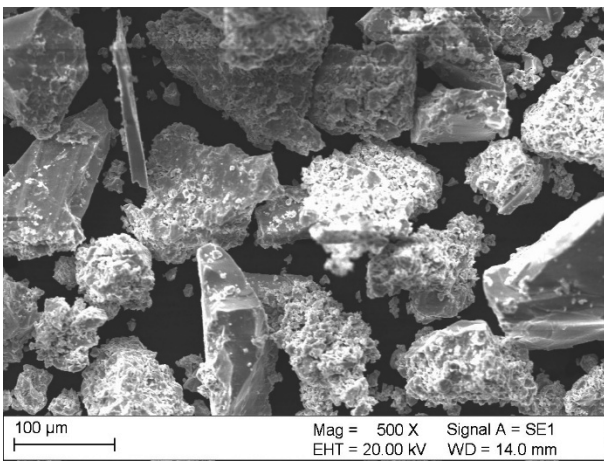

Figure 3. Morphology of $Mg_{65}Zn_{30}Ca_4Ag_1$ powders after 13 h of milling time

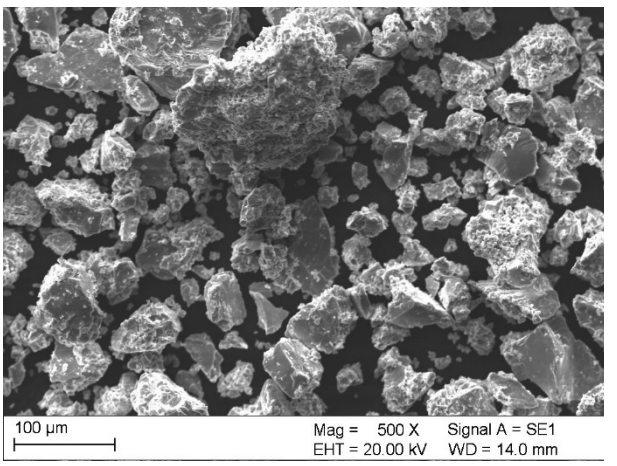

Figure 4. Morphology of $Mg_{65}Zn_{30}Ca_4Au_1$ powders after 13 h of milling time

Figures 5 and 6 show the analysis of $Mg_{65}Zn_{30}Ca_4Ag_1$ and $Mg_{65}Zn_{30}Ca_4Au_1$ alloys after 13 h of MA with a heating/cooling rate of 10˚C/min. The recorded DSC curves showed the presence of multi-stage phase transformations with different transition stages.

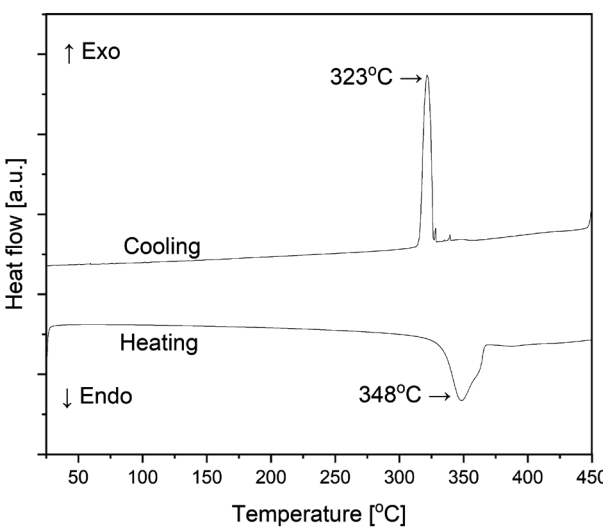

Figure 5. DSC curves for the $Mg_{65}Zn_{30}Ca_4Ag_1$ alloy after 13 h of milling time, heated and cooled at the rate of 10°C/min

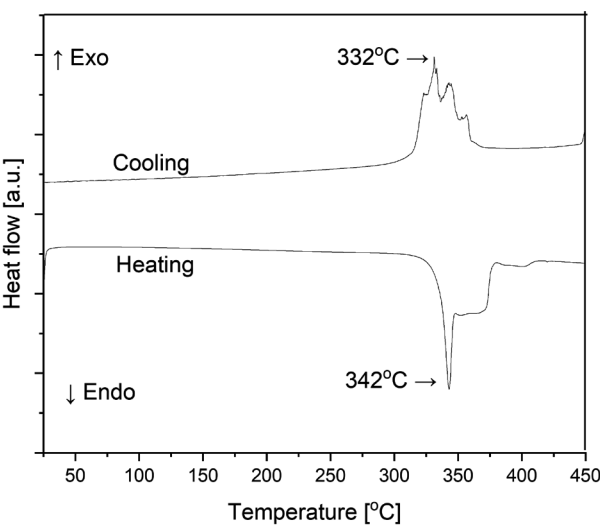

Figure 6. DSC curves for the $Mg_{65}Zn_{30}Ca_4Au_1$ alloy after 13 h of milling time, heated and cooled at the rate of 10°C/min

DSC curves showing the thermal effect accompanying the heating and cooling of the tested material. During the heating cycle, a clear endothermic effect was observed with a maximum at a temperature of about 348°C (Fig.5) and 342°C (Fig.6), which indicates the occurrence of a phase transformation requiring heat input, most likely related to the melting process or structural transformation in the alloy. During the cooling cycle, an exothermic effect was recorded with a

maximum temperature of about 323°C (Fig.5) and 332°C (Fig.6), indicating the reverse transformation – recrystallization or solidification of the material.

4. CONCLUSIONS

The paper presents the results of studies on the structure and phase transformations occurring in $Mg_{65}Zn_{30}Ca_4Ag_1$ and $Mg_{65}Zn_{30}Ca_4Au$ alloys obtained by mechanical synthesis. For each of the alloys studied, the occurrence of $MgZn_2$ and $Mg_{51}Zn_{20}$ phases, as well as the solid solution of magnesium base αMg, was identified. After 13 hours of mechanical synthesis, an advanced degree of fragmentation of particles of irregular shape and diverse size was observed, with dominance of sharp edges and the presence of secondary surface structures. The obtained morphology indicates a significant increase in the active surface of the particles, which may promote the intensification of further phase transformations and have a beneficial effect on the properties of the obtained materials. Analysis of DSC curves indicates the presence of reversible phase transformations in the tested alloys, which are accompanied by endothermic effects during heating (342–348°C) and exothermic effects during cooling (323–332°C). The observed phenomena suggest the occurrence of structural transformations characteristic of the studied system.

BIBLIOGRAPHY

1. J. Popis, O. Starczewska, M. Kremzer, K. Gołombek, M. Karolus, S. Lesz, Structural and thermal investigations of the ternary Mg–Zn–Ca system, JTAC, 2024;149:10647–10656. DOI:10.1007/s10973-024-13414-y.
2. JJ. Suñol, Mechanical Alloying: Processing and Materials, Metals, 2021;11;5,798, https://doi.org/10.3390/met11050798.
3. S. Lesz, M. Karolus, A. Gabryś, B. Hrapkowicz, W. Walke, W. Pakieła, K. Gołombek, J. Popis, P. Palček, Characteristics of Mg-Based Sintered Alloy with Au Addition, Mater. 2023;16,5,1915, https://doi.org/10.3390/ma16051915.

TalentDetector
23th-25th June 2025
Gliwice-Brenna, Poland
DEPARTMENT OF ENGINEERING MATERIALS AND BIOMATERIALS
FACULTY OF MECHANICAL ENGINEERING
SILESIAN UNIVERSITY OF TECHNOLOGY
INTERNATIONAL STUDENTS SCIENTIFIC CONFERENCE

Laser Technology in Microfabrication and Optics

Katarzyna Ptasznik[a], Wiktoria Gamla[a], Mirosław Bonek[b]

[a] Silesian University of Technology, Faculty of Mechanical Engineering, Department of Engineering Materials and Biomaterials
email: kp309682@student.polsl.pl, email: wg309661@student.polsl.pl
[b] Silesian University of Technology, Faculty of Mechanical Engineering, Department of Engineering Materials and Biomaterials

Abstract: The article discusses applications of laser technology in micromanufacturing and optics. Types of lasers, subtractive and additive micromachining techniques and integrated manufacturing systems are presented. Attention is given to the use of lasers
in microfluidics, medicine and optoelectronics, as well as to new developments such as chemical processes and open-loop microfabrication.

Keywords: laser technology, micromachining, micromanufacturing, optoelectronics, microfluidics, femtosecond lasers, 3D structures, Industry 4.0

1. INTRODUCTION

Laser technology has become one of the key tools used in modern micro-manufacturing and optics because of its exceptional precision, versatility and ability to low-temperature process a wide variety of materials. Contemporary applications include fields as diverse as microelectronics, optoelectronics, micromedicine, microfluidics and nanophotonics. Since the invention of the first laser by Theodor Maiman in 1960, the technology has undergone intensive development and undergone numerous transformations enabling its adaptation to micro- and nanoscale processes. A breakthrough was the introduction of ultra-short femtosecond pulses, which revolutionised micromachining by minimising thermal effects in the work zone. On an industrial scale, laser technology is characterised by high repeatability, non-contact machining and the possibility of automation, which significantly increases the efficiency of production processes. Its use allows micrometric accuracy to be achieved without the need for conventional mechanical tools, reducing tool wear and downtime. Thanks to these properties, lasers are becoming an indispensable element in the high-tech industry. [1,2]

2. FUNDAMENTALS OF LASER TECHNOLOGY

Understanding the basics of laser technology is key to its effective use in micromanufacturing. Lasers need to be tailored to specific materials or other requirements, and the most commonly used include:

• Femtosecond lasers - these emit ultra-short pulses (<1 ps), allowing precise processing of materials with minimal thermal impact. They are ideal for processing heat-sensitive materials such as polymers or glass. Such lasers include, for example, the Ti:Sapphire laser [3].

• UV lasers - thanks to their short wavelength (193 - 248 nm), they enable high resolution processing, which is particularly important in photolithography and micromachining. One such laser is excimer lasers, for example. [3]

• CO2 lasers - emit radiation in the infrared range (~ 10.6 μm) so they are mainly used for cutting and engraving non-metallic materials e.g. plastics.

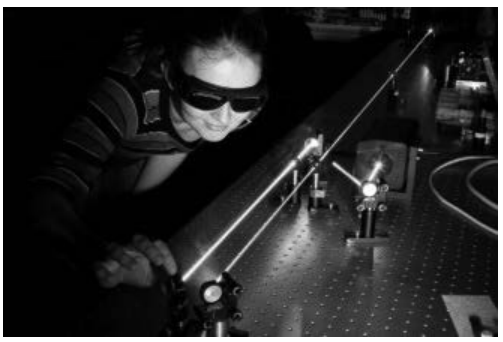

Figure 1 Laser Technologies [28]

It is not only the choice of the right laser that is crucial to the quality of micromachining, but also the technical parameters and these are:

• Wavelength: This determines the ability to focus the beam and the absorption by the material. Shorter wavelengths, e.g. UV, allow smaller spot sizes and therefore higher aspect ratios.

• Pulse duration: shorter pulse lengths, e.g. Femto or picosecond, minimise thermal effects, which is beneficial when treating heat-sensitive materials.

• Pulse power and energy: these determine the ability to remove material AND the depth of penetration. Higher pulse energy allows for deeper processing, but may increase the risk of thermal damage.

Another equally important technical parameter for micromachining is precision beam control systems and can be divided into:

• Galvo scanners: these enable the laser beam to be directed quickly and precisely to the surface of the material, which is important in processes requiring high speed and accuracy.

• Collimators: are used to parallelise the laser beam, which is important for maintaining a uniform energy distribution of the material surface.

• Focusing lenses: allow the beam to be focused to a very small size, which is essential for high precision.

3. LASER MICROPRODUCTION TECHNIQUES

Laser micromanufacturing is divided into subtractive (ablative) techniques, or those that focus on material removal, and additive, or material addition. Both groups are used in high-precision fields such as micro-optics and biomedical engineering.

Subtraction techniques are based on laser ablation, i.e. the local removal of material by intense heating and evaporation. Depending on the wavelength, pulse duration and material, it is possible to achieve very high precision without affecting the surrounding area.[4]
The most important substractive techniques include:

• Laser micro-cutting:

Allows very thin slits and precise shapes to be obtained in thin layers of metals, ceramics or glass. Used, for example, in the manufacture of medical implants and printed circuits. Femtosecond lasers are particularly valued because of their reduced heat-affected zone. [4]

Figure 1 – Laser micro-cutting [29]

• Laser micro-drilling:

Allows the creation of holes with diameters ranging from a few hundred nanometres to tens of micrometres, in both metallic and non-metallic materials. Drilling can be performed in pulses (one at a time) or by scanning the beam along a spiral or linear path. The technique is used in the manufacture of microfluidic filters and precision nozzles. [4]

• Surface texturing:

Involves modifying the topography of a surface to alter its properties, such as hydrophobicity, biological adhesion or friction. It is used, among others, in the medical industry to improve the integration of implants into tissue and in optics to create interference micrographs.

Examples of applications of these methods in microfabrication or optics include:
- Scribing of silicon wafers: Precision incision of wafers for subsequent separation.
- OLED glass cutting: Enables the creation of thin and precise shapes in delicate materials.
- Microchannel creation: Used in microfluidics to create high aspect ratio channels. [3]

Additive techniques involve the controlled application of material using laser beam energy. They enable complex 3D microstructures to be produced in a layered manner. The most commonly used techniques include:

• Two-Photon Polymerisation (TPP):

This technique uses a highly focused femtosecond laser beam in the near-infrared range to initiate polymerisation in light-curing resins. The two-photon phenomenon occurs only at the laser focus, allowing spatial structures to be created with a resolution of less than 200 nm. It is used in the manufacture of micro-optics, tissue scaffolds and micromechanical components. [5]

• Selective Laser Sintering (SLS):

Involves the spot sintering of a layer of powder (metal, ceramic or polymer) using a CO_2 laser or fibre laser. The process takes place layer by layer until a complete 3D microelement is obtained. This technique is widely used in the rapid prototyping of micromechanical components. [5]

4. INTEGRATED PRODUCTION SYSTEMS

Integrated laser-based manufacturing systems are now advanced platforms for automated micromachining. An example is the Newport Laser μFab system, which combines the functions of ablation, two-photon polymerisation and laser material deposition in a single device. This type of solution allows for the comprehensive production of microstructures without the need to change the technological environment.
A key feature of these systems is their modularity - it is possible to easily reconfigure depending on the material (glass, ceramics, polymers) and process. These systems are usually integrated with CAD/CAM software, allowing digital models to be accurately reproduced in the real material, while maintaining micrometric accuracy.
Such integrated solutions are part of the Industry 4.0 paradigm, enabling full automation and integration into production lines based on intelligent diagnostic and predictive systems.

5. APPLICATION OF LASER TECHNOLOGY

5.1. Microfluidics

In the development of microfluidics, laser technology plays a key role. Laser technology is particularly important for the fabrication and functionalisation of microstructures that are used in lab-on-a-chip devices.

• Laser micromachining:

Enables the creation of holes, microchannels and other structures with dimensions in the order of a few micrometres, in an extremely precise yet essential way to control the flow of fluids in microfluidics. The use of laser pulses, e.g. femtosecond or nanosecond, allows complex and intricate patterns to be made in a fast and reproducible manner. These patterns can be made in a variety of materials such as metals, polymers and glasses.

• Laser micromachining:

Like the examples above, it is also used for surface texturing. It is used, for example, to obtain oil micro- and nano-assemblies or structures to improve the flow properties and functionality of microfluidic systems. [5,6]

• Optical detection:

Microfluidics often uses lasers to detect biochemical reactions. This is done by, for example, excitation of fluorescence in flowing droplets containing enzymes, which allows fast and efficient analysis and detection of substances on very small volumes. [5,6]

5.2. Medicine and biomedical devices

In medicine, lasers are used in many fields due to their high precision, efficiency and minimal invasiveness. The most important applications of lasers in this field include:
• Laser surgery:
Laser surgery enables very precise cutting and coagulation of tissue. It is used in ophthalmology, dermatology, vascular surgery, neurosurgery or oncology, among others. Thanks to lasers, tumours, polyps and various types of cancerous lesions are removed. Lasers are also used to repair retinas and to improve vision. [7,8]
• Laser therapy:

Laser therapy is used to stimulate tissue regeneration, treat inflammation, pain, muscle injuries and chronic pain conditions, e.g. spine or tennis elbow. [9,10]
• Dermatology and aesthetic medicine:
In dermatology and aesthetic medicine, lasers are used for the removal of hyperpigmentation, scars, tattoos, hair, visible blood vessels, as well as for skin photorejuvenation treatments and microdermabrasion. [8,9]

5.3. Optoelectronics

One of the key pillars of modern optoelectronics is laser technology. Thanks to its unique properties such as coherence, high power, precision and the ability to modulate the beam, make laser technology widely applicable in many fields. The main areas of application are:
• Telecommunications and data transmission:
Lasers are the basis of fibre-optic communication systems. They enable the conversion of electrical signals into light pulses, which are then transmitted via optical fibres with very high bandwidth and minimal losses. This allows fast, secure and reliable data transmission over very long distances. [12-14]
• Medicine and diagnostics:
Laser technology is widely used in medicine and diagnostics. Among other things, it is used in diagnostic imaging (e.g. OCT - optical coherence tomography), therapy (e.g. laser skin therapy or laser surgery). Lasers are also used to detect tumours through laser-induced fluorescence. [12-14]
• Industry and automation:
In industry, lasers are used, among other things, for cutting, welding, marking materials, and as precision sensors and measurement transducers. [12,14,15]

6. NEW TRENDS AND RESEARCH DIRECTIONS

• Hybrid additive-subtractive systems:
In 2025, the latest trends and research directions in laser technology include the development of hybrid additive-subtractive systems, which combine incremental (additive) processes with material removal (subtractive). This allows for more complex and precise manufacturing of components. [16,17]
• Laser chemical processes (LCP) - etching, refractive index modification:
Laser chemical processes, such as etching or refractive index modification, are among the most rapidly developing areas of laser technology.
1. laser etching:
This is a non-contact method of marking and surface treatment that allows rapid, precise and permanent application of patterns or removal of material from a variety of substrates, including metals, glass or plastics. Compared to traditional chemical etching, laser etching is significantly faster, much greener and does not require the use of harmful chemicals. [18]
2. Refractive index modification:
The LIRIC (Laser Induced Refractive Index Change) technique uses ultra-short laser pulses, e.g. femtoseconds, to locally change the refractive index of optical materials without damaging their structure. [19]
• Open manufacturing systems - micro-fabrication under airborne conditions:

Today's laser systems allow accurate machining without the need for various chambers or protective gas atmospheres. This is a major simplification of the process that reduces costs and increases production flexibility, particularly in sectors that require great precision - electronics and medicine. Aerial microfabrication focuses its research, among other things, on minimising energy consumption through modern laser sources, making it a greener and more economical solution. [20]

7. ADVANTAGES AND LIMITATIONS OF THE TECHNOLOGY

• Precision, low heat affected zone (HAZ), rapid prototyping:
Advantages:
1. Precision:
Modern technologies such as precision laser cutting offer accuracy of up to +/- 0.01 mm, which is 5-10 times better than classic laser cutting methods. This makes it possible to realise extremely complex and delicate contours and micro-components. Precise process control allows for reliable and reproducible results. [21]
2. Low heat affected zone (HAZ):
Precision technologies such as welding and laser cutting minimise the heat-affected zone, so that the material retains its mechanical properties and deformation is significantly reduced. This is extremely important when processing thin, delicate and temperature-sensitive materials. [21,22]
3. Speed of prototyping:
Laser cutting allows rapid prototyping, reducing the time from design to finished part.[21,23]

Limitations:
1. limitations of precision and technology:
High precision is often associated with lower process speed - the higher the precision, the slower the cutting or welding progress. [21]
2. Heat affected zone (HAZ) - limitations:
Although current technologies minimise HAZ, it is still not always possible to completely eliminate the effect of heat on materials. [22]
3. Prototyping speed limitations:
Despite the high speed of individual prototypes, for mass production, precision laser cutting technology may not be cost-effective through slower speeds or higher unit costs. [24]

8. SUMMARY AND PROSPECTS FOR DEVELOPMENT

Laser technology has become a key tool in microfluidics and optics due to its precision, versatility and ability to process materials without contact. It is used in microfluidics, biomedical engineering and nanophotonics, among others. Modern systems combine subtractive and additive techniques, enabling the creation of 2D and 3D microstructures, and integrated platforms, such as Newport Laser μFab, are part of the Industry 4.0 trend.
Technology developments focus on process integration, laser chemistry and open working systems. These innovations increase efficiency, reduce costs and improve availability. The future will bring further miniaturisation and the use of lasers in micro-robotics, flexible electronics and

photonics. Despite technological challenges, the laser remains a pillar of modern manufacturing and innovation.

ACKNOWLEDGEMENTS

The work was created as part of project of Students Scientific Circle of Laser Surface Treatment under the Initiative of Excellence - Research University, Silesian University of Technology, Gliwice, Poland.

BIBLIOGRAPHY

[1] Sugioka, K., & Cheng, Y. (2014). *Ultrafast lasers—reliable tools for advanced materials processing*. Light: Science & Applications
https://www.nature.com/articles/lsa201430 (dostęp: 18.05.2025)
[2] Meijer, J., Du, K., Gillner, A., Hoffmann, D., Kovalenko, V., Masuzawa, (2002). *Laser machining by short and ultrashort pulses, state of the art and new opportunities in the micro-machining field*
https://www.sciencedirect.com/science/article/abs/pii/S0007850607616990?via%3Dihub (dostęp: 18.05.2025)
[3] Barkauskas M., Butkus V., Butkus S. (2017). Femtosecond lasers enable quality microfabrication. Laser Focus World
https://www.laserfocusworld.com/industrial-laser-solutions/article/14215960/femtosecond-lasers-enable-quality-microfabrication (dostęp: 18.05.2025)
[4] Chichkov, B. N., Momma, C., Nolte, S., von Alvensleben, F., & Tünnermann, A. (1996). *Femtosecond, picosecond and nanosecond laser ablation of solids*.
[5] Mahmood M.A, Popescu A.C, (2021). 3D Printing at Micro-Level: Laser-Induced Forward Transfer and Two-Photon Polymerization
https://www.mdpi.com/2073-4360/13/13/2034?utm_source (dostęp: 18.05.2025)
[6] https://www.gfms.com/pl-pl/machines/laser/laser-micromachining.html (dostęp: 04.05.2025)
[7] https://www.metrum.com.pl/lasery-w-medycynie-skok-w-przyszlosc-leczenia/ (dostęp: 04.05.2025)
[8] https://fizjoterapeuty.pl/medycyna/laseroterapia-zastosowanie-laserow-w-medycynie.html (dostęp: 04.05.2025)
[9] https://reh24.pl/baza-wiedzy-jak-dziala-laser-nowa-terapia-laserowa/ (dostęp: 04.05.2025)
[10] Pyszora, A., Adamczyk, A. (2005). Zastosowanie niskoenergetycznego promieniowania laserowego w leczeniu bólu. Polska Medycyna Paliatywna
[11] https://www.bogdanidermatologia.pl/produkty/lasery/ (dostęp: 04.05.2025)
[12] https://unisystem.com/pl/uni-abc/optoelektronika-podstawowe-informacje-i-przykladowe-zastosowania (dostęp: 05.05.2025)
[13] https://przemyslprzyszlosci.gov.pl/technologie/cyfrowe/fotonika-i-optoelektronika/ (dostęp: 05.05.2025)
[14] https://pl.wikipedia.org/wiki/Optoelektronika (dostęp: 05.05.2025)
[15] https://pl.loshield.com/news/what-are-the-applications-of-laser-technology-79464709.html (dostęp: 05.05.2025)

[16] https://magazynprzemyslowy.pl/artykuly/lasery-do-ciecia-7-potencjalnych-hitow-sprzedazowych-w-2025-roku (dostęp: 05.05.2025)
[17] https://staleo.pl/z-kraju-i-ze-swiata/artykuly/5822/raport-przeglad-rynku-wycinarek-laserowych-2025 (dostęp: 05.05.2025)
[18] https://www.keyence.eu/products/marker/laser-marker/resources/laser-marking-resources/laser-etching-a-complete-guide.jsp (dostęp: 08.05.2025)
[19] https://www.spiedigitallibrary.org/conference-proceedings-of-spie/12684/1268405/Laser-induced-refractive-index-change-writing-in-dehydrated-ophthalmic-materials/10.1117/12.2676240.short (dostęp: 08.05.2025)
[20] https://laser-adjatech.pl/2025/03/03/innowacje-laserowe-2025-wyprzedz-konkurencje/ (dostęp: 08.05.2025)
[21] https://www.hailtec.de/en/technologies/precision-laser-cutting/ (dostęp: 08.05.2025)
[22] Phani, K., M. (2024).Welding Process in Advanced Manufacturing. Integrative Journal of Conference Proceedings. (s. 1-8)
[23] https://www.3erp.com/blog/use-laser-cutting-sheet-metal-prototyping/ (dostęp: 08.05.2025)
[24] Zhou, L., Miller, J., Vezza, J., Mayster, M., Raffay, M., Justice, Q., Al Tamimi, Z., Hansotte, G., Devi Sunkara, L., Bernat, J. (2024). Additive Manufacturing: A Comprehensive Review. Sensors 2024. (s. 1-44)
[25] https://www.santanderopenacademy.com/pl/blog/zalety-i-wady-wspolczesnej-technologii.html (dostęp: 10.05.2025)
[26] https://www.istec.com/pl/korzysci-i-wyzwania-okresowego-i-ciaglego-monitorowania-drgan/ (dostęp: 15.05.2025)
[27] https://www.icareweb.com/pl/rozwiazania/wydajnosc-przemyslowa/kalibracja-pomiary/ (dostęp: 15.05.2025)
[28] https://forbot.pl/blog/wp-content/uploads/2021/01/laser_doswiadczenie_laboratorium-330x220.jpg
[29] https://dlaprodukcji.pl/wp-content/uploads/sites/8/2020/12/Mikroobrobka-laserowa-metali.jpg

TalentDetector

23th-25th June 2025
Gliwice-Brenna, Poland

DEPARTMENT OF ENGINEERING MATERIALS AND BIOMATERIALS
FACULTY OF MECHANICAL ENGINEERING
SILESIAN UNIVERSITY OF TECHNOLOGY

INTERNATIONAL STUDENTS SCIENTIFIC CONFERENCE

Optimization of numeric keyboard interfaces based on signals from eye tracking components build in virtual reality goggles

Maja Rudnicka[a], Michał Lasak[b], Szymon Sadza[c]

[a]Silesian University of Technology, Faculty of Automatic Control, Electronics and Computer Science, SKN SpaceCoffee, SKN vFly
email: maja.rudnicka@alogliwice.polsl.pl
[b]Silesian University of Technology, Faculty of Automatic Control, Electronics and Computer Science, SKN SpaceCoffee, SKN vFly
email: michal.lasak@alogliwice.polsl.pl
[c]Silesian University of Technology, Faculty of Automatic Control, Electronics and Computer Science, SKN SpaceCoffee, SKN vFly
email: szymon.sadza@alogliwice.polsl.pl

Abstract: This article presents results of tests of various numeric keyboard interfaces that were created in the Unity Engine. Those keyboards were navigated through utilizing virtual reality goggles with eye tracking sensors built into them.

Keywords: VR, Eye Tracking, eye activity

1. INTRODUCTION

This paper explores the development of various types of numeric keyboard interfaces designed for number entry using eye-tracking technology, all implemented within the Unity engine. Eye tracking[1] is a non-invasive technique for determining the direction of a user's gaze by detecting the reflection of infrared light from the eyes—pupils absorb a consistent amount of light, making them reliable reference points. Although eye-tracking technologies have existed for some time [3,7], only recently have they been integrated with virtual reality (VR) headsets[2,4]. This combination offers researchers new possibilities for alternative methods of computer input.

2. DESIGNS

The designs were developed using the Unity Engine [6]. A total of seven different layouts were created, each constrained to a maximum of 10 buttons per numeric keypad to ensure that every button remains comfortably sized. By focusing on a specific button, the system detects the relative position of the pupil with respect to that button [5]. This enables the system to determine which button the user has selected.

2.1 First design

It's a standard number keyboard design, but it lacks a "0", which makes the count of number combinations smaller. It's possible to implement a way to write zeros, for example if pressing "enter" would pass to the next number and zero is the default.

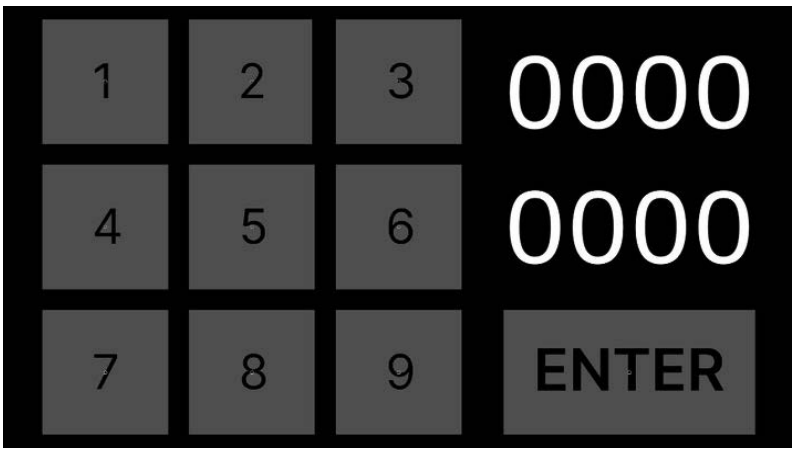

Figure 1. First Design of a BCI numerical keyboard

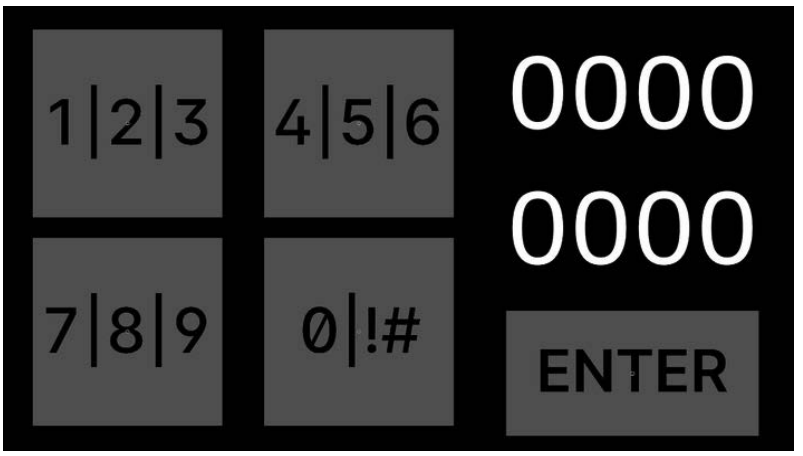

Figure 2. Second Design of a BCI numerical keyboard, in the main menu

2.2 Second design

The second design enables more precise and complex functionality, although it may operate more slowly compared to other implementations. However, it offers greater scalability, as none of the menus currently use the limit of ten buttons, allowing for additional features in the future. This design includes one main menu [Fig. 2] and several submenus [Figs. 3–4].

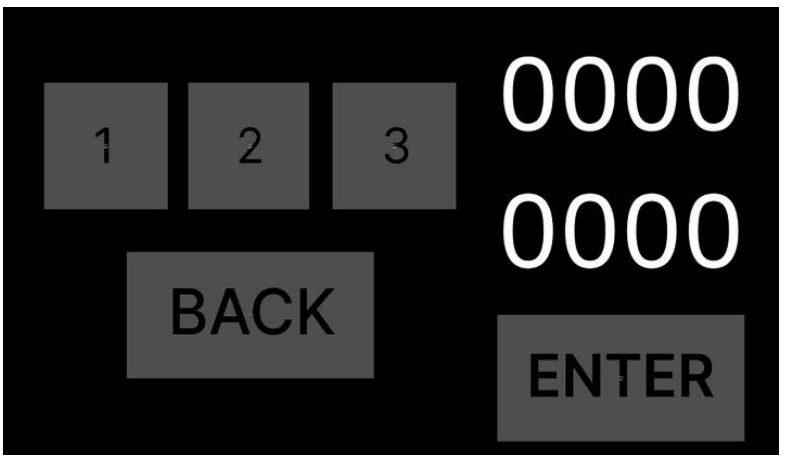

Figure 3. Second Design of a BCI numerical keyboard, in the first menu

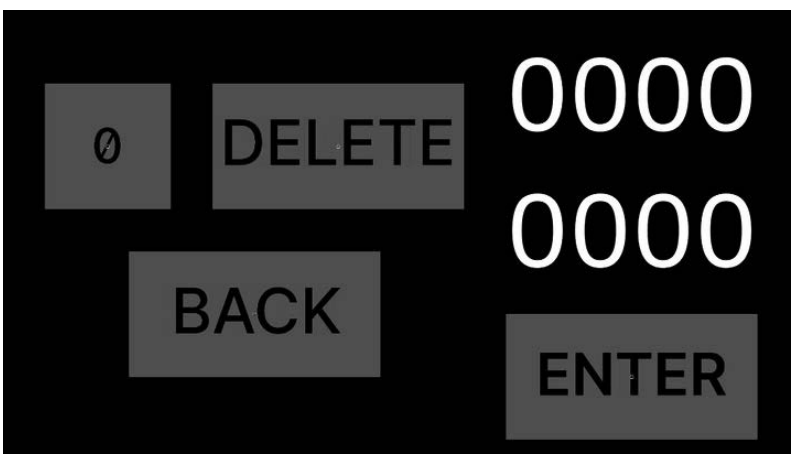

Figure 4. Second Design of a BCI numerical keyboard, in the last menu

2.3 Third design

The Third design is a blend between the first two, it uses similar menus as the Second Design, but it also has a typical layout that people are used to. It lacks the possibilities of the Second Design, but it can be advantages to those that are used to such.

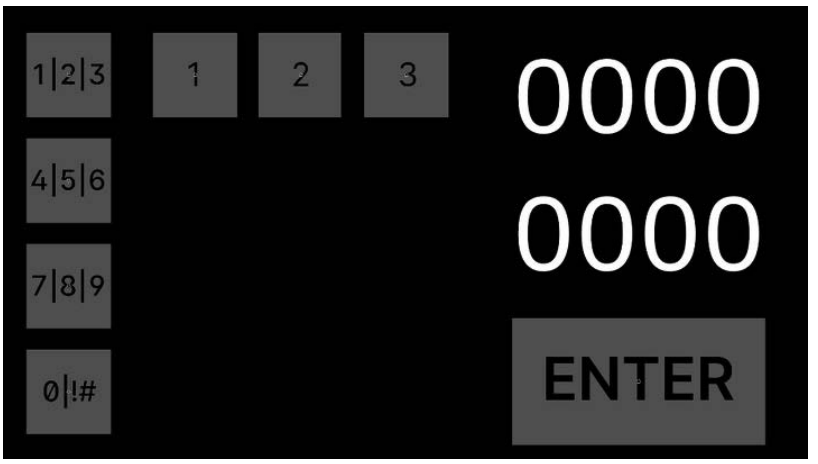

Figure 5. Third Design of a BCI numerical keyboard, with the first menu open

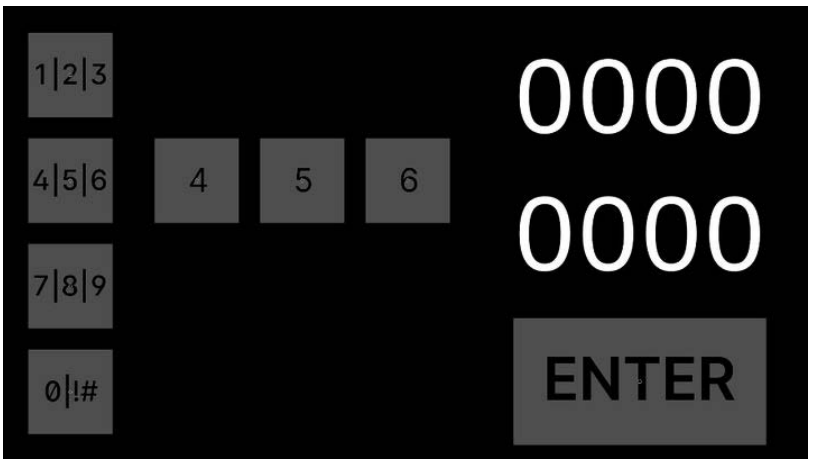

Figure 6. Third Design of a BCI numerical keyboard, with the second menu open

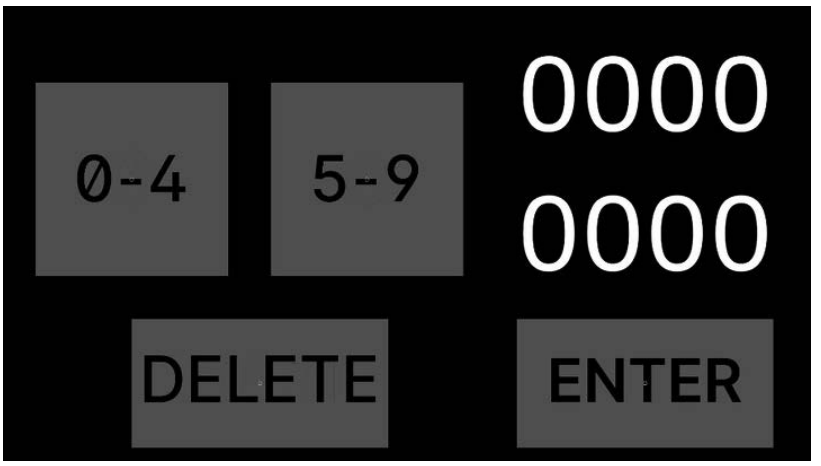

Figure 7. Fourth Design of a BCI numerical keyboard, with the main menu open

2.4 Fourth design

The Fourth Design is a simplified version of the Second, with only two menus and a simpler design. It still allows for some future improvement, but it is less flexible. It has a main menu [Fig.7] and two sub menus [Fig. 8]

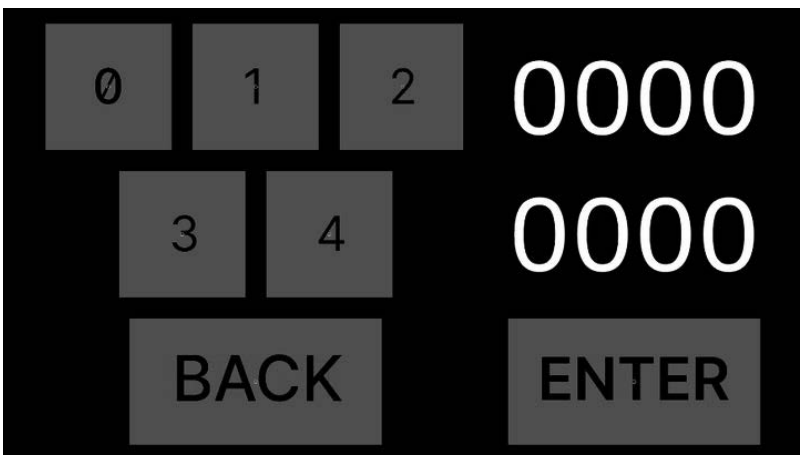

Figure 8. Fourth Design of a BCI numerical keyboard, with the first sub menu open

2.5 Fifth design

The Fifth Design is based on the First one, but with a zero instead of an enter, which provides another problem with the number selection, because every number can be selected only once.

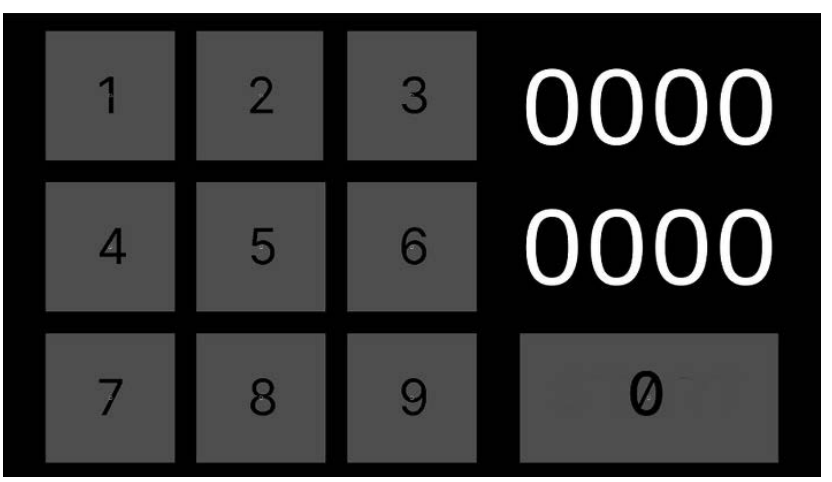

Figure 9. Fifth Design of a BCI numerical keyboard

2.6 Sixth design

The Sixth Design is a different version of the Fourth, with two menus in a circle. It is more intuitive, but allows for even less flexibility with additional buttons. It's reaching the 10 buttons limit.

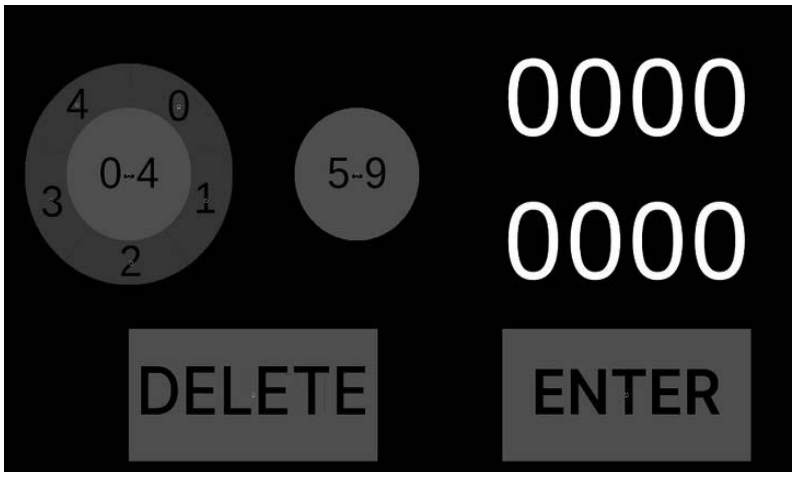

Figure 10. Sixth Design of a BCI numerical keyboard, with the first part expended

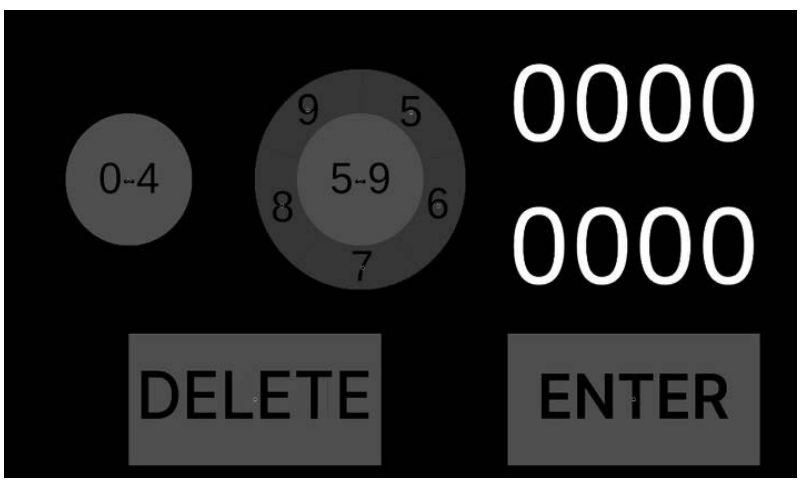

Figure 11. Sixth Design of a BCI numerical keyboard, with the second part expended

2.7 Seventh design

The Seventh Design is similar to the Fifth Design, it has a different layout, that could be more effective and intuitive.

3. FUTURE FURTHER DEVELOPMENTS

The next step of development is to test all of the designs and choose the best ones to develop them further. Few possible further developments include extending the program to include more combinations and buttons, that's especially likely, if the keyboards based on menus and submenus prove effective or if new designs become comfortable to use. Another way of development is a more personalized interface, customizable by the user, that would allow for the best effectiveness, but would require better calibration and would be less objective in tests.

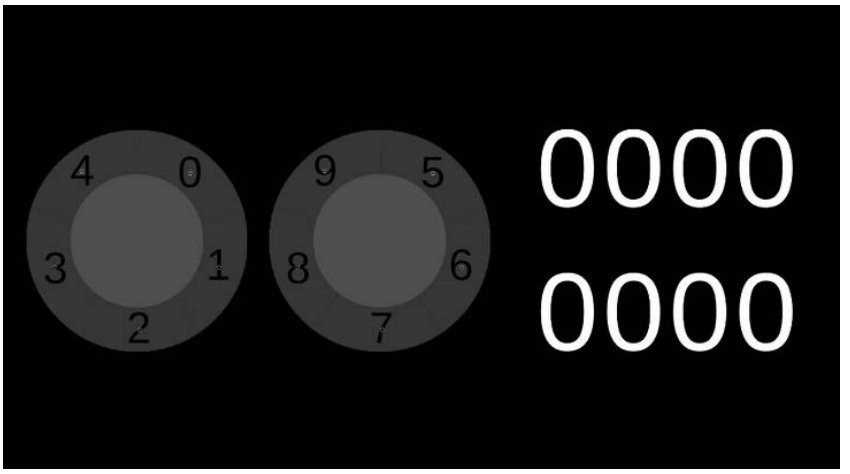

Figure 12. Seventh Design of a BCI numerical keyboard

4. CONCLUSION

Various designs of Eye Tracking numeric keyboard interfaces were developed within the Unity Engine, Each design offers unique features and trade-offs, ranging from simplicity to flexibility. The future of this technology lies in rigorous testing to identify the most effective designs for further refinement. These developments hold promise for improving accessibility and communication for individuals with disabilities, marking a significant step forward in Eye Tracking technology.

BIBLIOGRAPHY

1. Duchowski, A. T. (2017). *Eye Tracking Methodology: Theory and Practice* (3rd ed.). Springer. https://doi.org/10.1007/978-3-319-57883-5
2. VR headsets such as the HTC Vive Pro Eye or Meta Quest Pro now incorporate built-in eye-tracking sensors, enabling immersive gaze-controlled interfaces. *Example Study:* Pfeuffer et al. (2015), *Gaze+ Pinch Interaction in VR*.
3. Majaranta, P., & Räihä, K.-J. (2007). Text entry by gaze: Utilizing eye-tracking. *Proceedings of the ACM SIGCHI Conference on Human Factors in Computing Systems*, 2007, 1165–1172. https://doi.org/10.1145/1240624.1240807
4. Zhang, Y., Skadron, K., & Huang, T. S. (2020). Gaze typing: A comparative evaluation of eye-tracking input methods. *ACM Transactions on Computer-Human Interaction (TOCHI)*, 27(4), Article 26. https://doi.org/10.1145/3399706
5. LoPresti, E. F., Brienza, D. M., Angelo, J., & Gilbertson, L. (2008). Interface design for eye gaze input. *Assistive Technology*, 20(1), 12–22. https://doi.org/10.1080/10400435.2008.10131927
6. Portillo-Lara, R., & González, P. A. (2019). Unity for Human-Computer Interaction prototyping: A survey. *Journal of Computer Languages*, 52, 20–33. https://doi.org/10.1016/j.cola.2019.100711
7. Majaranta, P., & Bulling, A. (2014). Eye tracking and eye-based human–computer interaction. In *Advances in Physiological Computing* (pp. 39–65). Springer. https://doi.org/10.1007/978-1-4471-6392-3_3

TalentDetector
23th-25th June 2025
Gliwice-Brenna, Poland
DEPARTMENT OF ENGINEERING MATERIALS AND BIOMATERIALS
FACULTY OF MECHANICAL ENGINEERING
SILESIAN UNIVERSITY OF TECHNOLOGY
INTERNATIONAL STUDENTS SCIENTIFIC CONFERENCE

Modernization and development of transport applications of an autonomous airship

Maja Rudnicka[a], Michał Lasak[b], Franciszek Borgosz[c]

[a] Silesian University of Technology, Faculty of Automatic Control, Electronics and Computer Science, SKN SpaceCoffee
email: mrudnicka@spacecoffee.net
[b] Silesian University of Technology, Faculty of Automatic Control, Electronics and Computer Science, SKN SpaceCoffee
email: mlasak@spacecoffee.net
[c] Silesian University of Technology, Faculty of Automatic Control, Electronics and Computer Science, SKN SpaceCoffee
email: fborgosz@spacecoffee.net

Abstract: Autonomous airships have historically found their application in transport, before the technology was mostly abandoned. Since then, the demand for sustainable alternative transport solutions in the 21st century has reintroduced research on such aerial systems. More so, reviews point to blimps as a successful or even preferred platform in various missions, where heavier-than-air platforms have been commonly used. Due to its lightweight and low-risk character, airship technology proves useful in low-wind environments [1].
This paper presents the design, modernization attempts, and functional expansion of a small autonomous airship—ACCA (Autonomous Cargo Containment Airhsip), with the aim to apply it in short-range cargo transportation. The project focused on improving the airship prototype's propulsion and electronic systems, stabilizing the frame, as well as building the autonomous movement system which would ensure reliable navigation. The payload capacity was expected to be 5 kg. The results portray small autonomous airships as cost-effective and energy-efficient, contributing to the broader discourse on autonomous aerial transport. ACCA holds a prospect for scalable deployment in last-mile delivery and emergency logistics.

Keywords: Autonomous airship, autonomy, cargo, airship, blimp, aircraft, transport, innovation, modernization

1. INTRODUCTION

In recent years, an interest in sustainable and autonomous transport solutions has grown, particularly in the context of short-range logistics and last-mile delivery. Along with other types of innovative, modern transport solutions that have emerged, occurred a comeback to lighter-than-air airship technology. Its unique advantages, such as low energy consumption,

extended hovering-time capabilities, and minimal infrastructure requirements, seem attractive for utilizations in areas such as surveillance and telecommunications [2, 3].

While autonomous drones have seen much more widespread adoption, the challenges they face are predominantly caused by their limited payload, short operational time, and constraints by regulations. Airships may then work as a replacement in those specific missions where their stability and endurance outperform those of multirotor UAVs (unmanned aerial vehicles).

The ACCA project constituted the development and modernization of a small-scale autonomous airship based on a previous prototype. The main objective was to design a platform capable of transporting lightweight cargo (up to 5 kg), led by an autonomous steering program, with enhanced propulsion, high structural stability, and gas efficiency.

The following sections describe the construction of the airship, discussing key design challenges, as well as the electronic systems and autonomous navigation, finishing with a plan for future developments in the ACCA project.

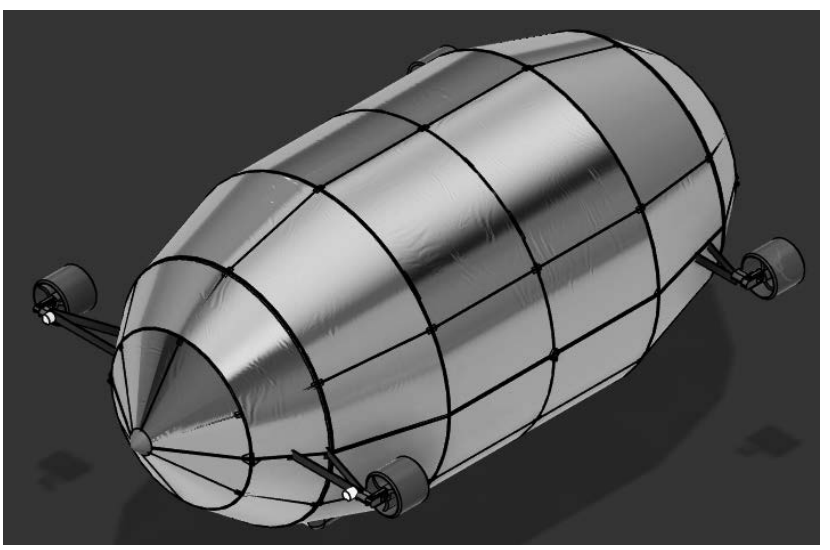

Fig. 1. ACCA airship render.

Fig. 2. ACCA airship realistic render.

2. CONSTRUCTION DESIGN

The structural design of the airship was created with the aim of maximizing lift efficiency while providing durability, modularity, and low total weight. The frame supporting the propulsion system, electronic components, and cargo attachment mechanism was built from durable carbon rods, wooden elements and 3D-printed parts, like fixings. This allows for precise adjustments during the testing phase and makes prototyping affordable. A modular gondola basket beneath the plating contains the main computing unit (Raspberry Pi 5), batteries, and main sensors. It was designed to allow quick access to the components. Stratospheric balloons filled with carrier gas mounted by the frame, under the plating, will lift the airship. The plating is meant to mitigate the risk arising from static electricity buildup on the external surfaces of the airship. The carrier gas during tests will be hydrogen [4], however public presentations will require the use of stable helium.

To complete the construction, it was necessary to determine the weight distribution and center-of-mass stabilization, since both are crucial for achieving flight stability and ensuring responsive autonomous navigation. To accommodate the airship's gas expansion and contraction during flight, the design also incorporates a flexible mounting system between the plating and the rigid body. The chosen approach to construction provides reliability in its functionality as well as facilitates the development of future airship iterations.

3. THE PROPULSION SYSTEM

The propulsion system for the airship was designed to be efficient and stable. It is integrated with the onboard autonomy framework. Each engine assembly consists of two servo motors connected with light-weight 3D printed brackets, at the end of which an electric motor is placed.

Brackets are interconnected with each other in a way that allows the engine to be rotated in two axes independently, providing the operator with a high degree of maneuverability and precision. This arrangement also allows for operations in enclosed environments or ones requiring constant corrections, such as facing angled winds.

Considering the vehicle's purpose as a lightweight cargo mover, capable of carrying payloads up to 5 kg, propulsion components were selected to balance thrust and the consumption of energy. The system comprises multiple electric motors, organized to ensure multidirectional steerability and stable hovering capabilities in low-wind environments. Custom-designed mounting arms, 3D-printed from lightweight composite filament, provide support for the motors and enable easy maintenance and adjustment. The drive system needs to integrate closely with the airship's control architecture, allowing the transition between manual override and fully autonomous flight modes. The propulsion units are powered by lithium-ion battery packs, selected because of their high energy density and weight-to-capacity ratio, which optimizes energy efficiency.

The airship's stability needs to be actively maintained during flight, particularly in response to changes in position, wind conditions, and payload distribution. To achieve this, the propulsion system adjusts thrust levels dynamically based on input from onboard sensors—positioning modules and inertial data. This is coordinated by the operating system.

Additionally, the configuration can be used for precise control of lift and forward motion—an essential for navigation during cargo pickup and delivery. The testing phase of the

propulsion system includes thrust calibration and performance assessment under different payloads and weather conditions, with a mission to improve flight process [5].

4. SYSTEM OPERATION AND CONTROL

The ACCA airship operates on an integrated control architecture that interconnects collecting data from the sensors, autonomous decision-making and real-time actuator management. At the core of the system is a Raspberry Pi 5 microcontroller which coordinates flight logic, sensor communication and propulsion commands. Onboard software includes custom modules for path planning, obstacle avoidance, altitude control and landing procedures. Navigation is based on a combination of a LIDAR module, a GPS positioning system and proximity sensors, enabling the airship to read its position accurately and respond dynamically to its environment. Control algorithms are implemented with the ability to switch between manual, semi-autonomous and fully autonomous modes, depending on mission requirements or operator intervention [6].

All critical telemetry is wirelessly transmitted to a base station for real-time monitoring and post-mission analysis. To enhance operational safety, redundant communication protocols and a basic fail-safe behavior module are included, so that the airship will perform an emergency landing in case of system failure or power loss. The operation protocols and control lay the groundwork for reliable and repeatable performance.

4.1. AUTONOMOUS NAVIGATION

The autonomy system is being developed with the goal of enabling fully self-directed flight, eliminating the need for continued human supervision. A core innovation the project presents is the use of a machine learning model trained to control the airship's navigation and basic task execution [7]. The training process focuses on achieving high performance using a minimal dataset, which reflects real-world constraints in collecting extensive flight data.

Instead of relying exclusively on rule-based logic, the system is designed to learn and adapt through exposure to curated flight scenarios, allowing it to handle tasks such as route following [8, 9], avoiding obstacles, and transport of lightweight cargo. The training is carried out on a dedicated computing unit configured for AI workloads, and the final model is later run on an onboard device designed to handle the operations directly on the airship.

Initial field tests are planned under favorable weather conditions to validate the model's behavior in hospitable environments. While traditional techniques such as sensor fusion and predefined flight routines remain available as fallback options, the target vision of the project is to implement an adaptable, learning-based autonomy system. This approach opens the path for further options, e.g. reinforcement learning in dynamic environments [10].

5. FUTURE DEVELOPMENTS

With further developments of the ACCA platform, several improvements are planned. The goal is to enhance the airship's reliability, autonomy system, and adaptability to real-world conditions. One major area of development is to expand the environmental research capabilities of the airship through integration of new sensors. These would include temperature, humidity, wind speed, and atmospheric pressure sensors, allowing the system to assess local weather

conditions and adapt its behavior accordingly. Real-time data about the weather conditions could be used to dynamically adjust flight parameters, delay missions in unsafe circumstances, or readjust the procedures for landing.

Additionally, future iterations of the autonomy framework are expected to be further developed by machine learning techniques for even more purposeful decision-making, including path optimization [10].

Other planned upgrades also include improving the energy management system, heavier payload support, and working on compatibility with intended ground docking stations. For the propulsion system, a PID-based control loop is being considered as an implementation for precise thrust vectoring and pitch stabilization.

6. CONCLUSION

This work presents the design, modernization, and functional expansion of the ACCA autonomous airship as a lightweight, energy-efficient platform for short-range cargo transport. Through the integration of the propulsion system, a stable structural framework, and an autonomy system, the airship proposes a feasible alternative to conventional UAVs, especially in some logistics scenarios. The current system focuses on the core functionality, but future developments aim to enhance the adaptability to dynamic environmental conditions, and to further improve system intelligence. The ACCA project makes its contribution to the growing body of research on lighter-than-air autonomous vehicles, clearing the pathway toward more innovative and sustainable aerial logistics solutions in the coming decade.

BIBLIOGRAPHY

1. Shantanu S. Bhat, Sreenatha G. Anavatti, Matthew Garratt, and Sridhar Ravi. 2024. Review of autonomous outdoor blimps and their applications. Drone Systems and Applications. 12: 1-21. DOI: https://doi.org/10.1139/dsa-2023-0052
2. N.J. Mayer, R.H. Krida, A review of lighter-than-air progress in the United States and its technological significance, Acta Astronautica, Volume 5, Issue 10, 1978, Pages 917-934, ISSN 0094-5765, DOI: https://doi.org/10.1016/0094-5765(78)90075-9.
3. Lin Liao, Igor Pasternak, A review of airship structural research and development, Progress in Aerospace Sciences, Volume 45, Issues 4–5, 2009, Pages 83-96, ISSN 0376-0421, DOI: https://doi.org/10.1016/j.paerosci.2009.03.001.
4. Bonnici, M., Tacchini, A. & Vucinic, D. Long permanence high altitude airships: the opportunity of hydrogen. *Eur. Transp. Res. Rev.* **6**, 253–266 (2014). DOI: https://doi.org/10.1007/s12544-013-0123-z
5. Miller, S. H., Fesen, R., Hillenbrand, L., Rhodes, J., Baird, G., Blake, G., ... & Zambrano, T. (2014). Airships: a new horizon for science. *arXiv preprint.* DOI: https://doi.org/10.48550/arXiv.1402.6706
6. Yang, Y., Wu, J., & Zheng, W. (2016). Positioning control for an autonomous airship. *Journal of Aircraft*, *53*(6), 1638-1646. DOI: https://doi.org/10.2514/1.C033709
7. Elfes, A. *et al.* (2002). Modelling, Control and Perception for an Autonomous Robotic Airship. In: Hager, G.D., Christensen, H.I., Bunke, H., Klein, R. (eds) Sensor Based

Intelligent Robots. Lecture Notes in Computer Science, vol 2238. Springer, Berlin, Heidelberg. DOI: https://doi.org/10.1007/3-540-45993-6_13

8. J. R. Azinheira, E. Carneiro de Paiva, J. G. Ramos and S. S. Beuno, Mission path following for an autonomous unmanned airship, Proceedings 2000 ICRA. Millennium Conference. IEEE International Conference on Robotics and Automation. Symposia Proceedings (Cat. No.00CH37065), San Francisco, CA, USA, 2000, pp. 1269-1275 vol.2, DOI: 10.1109/ROBOT.2000.844773.
9. Alexandra Moutinho, José Raul Azinheira, Ely C. de Paiva, Samuel S. Bueno, Airship robust path-tracking: A tutorial on airship modelling and gain-scheduling control design, Control Engineering Practice, Volume 50, 2016, Pages 22-36, ISSN 0967-0661. DOI: https://doi.org/10.1016/j.conengprac.2016.02.009.
10. Rottmann, A. (2012). Approaches to online reinforcement learning for miniature airships (Doctoral dissertation, Dissertation, Albert-Ludwigs-Universität Freiburg, 2012). DOI: urn:nbn:de:bsz:25-opus-88578

TalentDetector

23th-25th June 2025
Gliwice-Brenna, Poland

DEPARTMENT OF ENGINEERING MATERIALS AND BIOMATERIALS
FACULTY OF MECHANICAL ENGINEERING
SILESIAN UNIVERSITY OF TECHNOLOGY

INTERNATIONAL STUDENTS SCIENTIFIC CONFERENCE

Wytrzymałościowa analiza numeryczna łomu wykonanego z różnych materiałów inżynierskich oraz jego wizualizacja

Adam Schwarza, Łukasz Buszka[a], Łukasz Mann[b], Amadeusz Dziwis[c], Wojciech Mikołejko[c], Agata Śliwa[c]

[a] Uczniowie Zespołu Szkół Technicznych i Ogólnokształcących „Mechanik" w Tarnowskich Górach, email: misteradamowski@gmail.com, lukaszbuszka2@gmail.com
[b] Nauczyciel Zespołu Szkół Technicznych i Ogólnokształcących „Mechanik" w Tarnowskich Górach, email: l.mann@mechaniktg.pl
[c] Politechnika Śląska, Wydział Mechaniczny Technologiczny, Katedra Materiałów Inżynierskich i Biomedycznych,
email: amadeusz.dziwis@polsl.pl, wojciech.mikolejko@polsl.pl, agata.sliwa@polsl.pl

Streszczenie: W pracy dokonano analizy rozkładu naprężeń łomu wykonanego z trzech rodzajów stali: S253J, EN-AW 2117 oraz X33CrS16 obciążonego siłą 500 N. Symulacje wykonano w programie SolidWorks.

Abstract: The paper presents an analysis of stress distribution of a crowbar made of three types of steel: S253J, EN-AW 2117 and X33CrS16. The simulations were performed in the SolidWorks.

Słowa kluczowe: łom, rozkład naprężeń, odkształcenie, stal

1. WPROWADZENIE

Łom jest to narzędzie wykonane ze stali. Z jednej strony posiada zaostrzony szpic, z drugiej spłaszczenie z wygięciem pod kątem. Narzędzie to służy do rozbijania, kruszenia, podważania ciężarów itp. występują w różnych typach i kształtach, dopasowanych do konkretnych zastosowań. Łomy dzielimy na standardowe, płaskie, z hakiem, wąskie, a także łomy budowlane, wyburzeniowe i specjalistyczne, jak np. łomy ciesielskie czy brukarskie, które mogą być używane na budowach, przy pracach rozbiórkowych, wyciąganiu gwoździ, jak i w domu podczas majsterkowania. Łomy głównie wykonuje się ze stali narzędziowej [1,2]. Przykładowy łom został przedstawiony na rysunku 1.

Rys. 1 Łom [1].
Fig. 1 Crowbar [1].

2. ZAŁOŻENIE MODELOWE

W pracy poddano analizie statycznej łom wykonany z trzech rodzajów stali których dane materiałowe zawarto w tabeli1, pod naciskiem siły 500 N. Na rysunku 2 przedstawiono model łomu wraz z rzeczywistymi wymiarami podanymi w mm. Model geometryczny łomu został wykonany w programie SolidWorks. Na model geometryczny nałożono warunki brzegowe. W części do podważania zostało założone utwierdzenie stałe, natomiast siła 500 N została przyłożona na końcowej części łomu symulując podważanie elementu z siłą 50 kg co przedstawiono na rysunku 3. Na model geometryczny łomu została nałożona dokładna siatka bryłowa o rozmiarze elementu 6,9 mm oraz tolerancji 0,35 mm. W miejscach ugięcia siatka została zagęszczona co przedstawiono na rysunku 4.

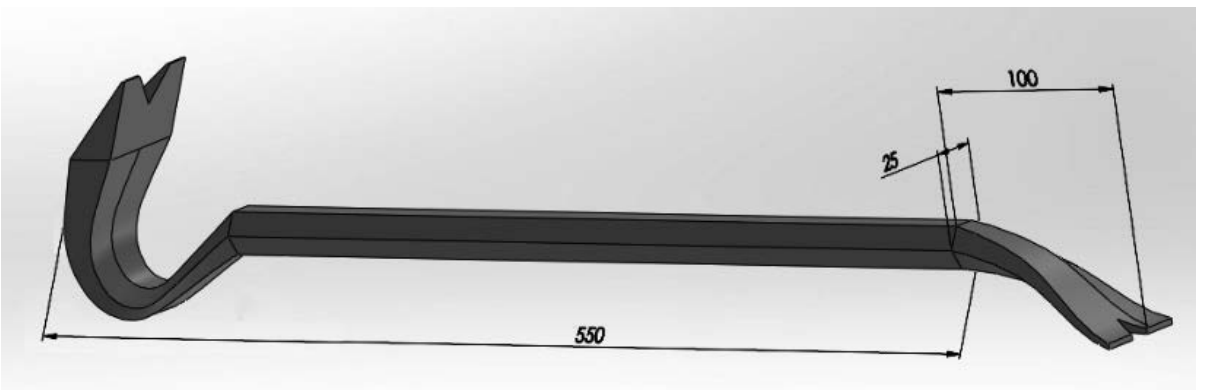

Rys. 2 Zwymiarowany model łomu.
Fig. 2 Dimensions of crowbar model.

Tablica 1 Własności materiałów użytych w symulacji [3,4].
Table 1 Material properties of materials used in simulation [3,4].

Symulacja:	**Materiał:**	**Granica plastyczności:**	**Współczynnik Poissona:**
1.	1.0037 (S253JR)	235 MPa	0.28
2.	3.1305 (EN-AW 2117)	165 MPa	0.33
3.	1.2085 (X33CrS16)	950 MPa	0.28

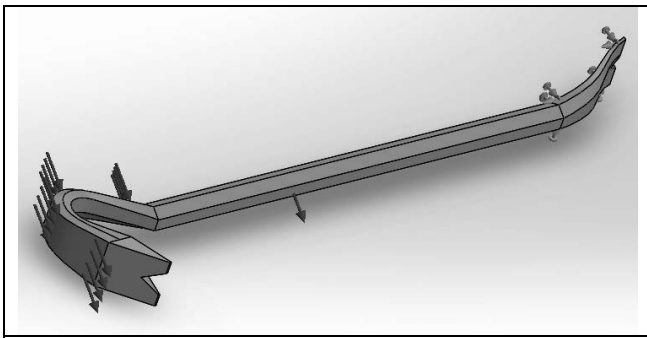

Rys. 3 Obciążenia i mocowanie.
Fig. 3 Loads and fix

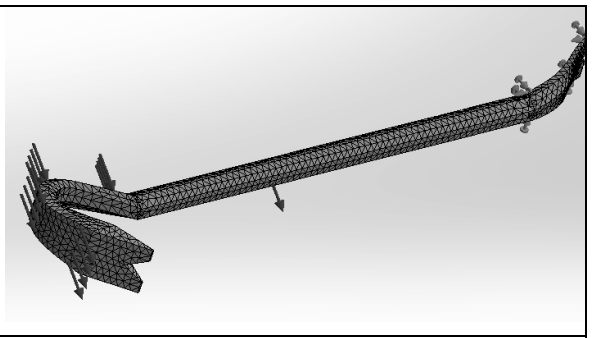

Rys. 4 Model z nałożoną siatką elementów skończonych.
Fig. 4 Mesh in model.

3. ANALIZA ROZKŁADU NAPRĘŻEŃ

Wyniki analizy przedstawiają rozkład naprężeń zredukowanych wg teorii Hubera von Misesa powstających w łomie podczas nadania siły nacisku 50 kg. Na rysunkach 5-8 zostały przedstawione wyniki przeprowadzonych symulacji. Największe naprężenia pojawiły się na łuku łomu w miejscu łączenia środkowej części z częścią utwierdzoną. Jest to spowodowane kumulowaniem się naprężeń.

W symulacji pierwszej (rys. 5, 6), w której wykorzystano stal konstrukcyjną S235JR o granicy plastyczności 235 MPa, maksymalna wartość naprężeń σ_{red} wyniosła 427 MPa. Stanowi to przekroczenie o 85% wytrzymałości materiału w jej krytycznym punkcie. Ponadto na połowie części środka łomu występują naprężenia zbliżone do granicy plastyczności stali S235JR. Następnie naprężenia zmniejszają się, aż do miejsca gięcia części tylnej gdzie minimalnie wzrastają z powodu kumulacji.

Symulację drugą wykonano dla łomu wykonanego ze stali narzędziowej X33CrS16 o granicy plastyczności 950 MPa. Jako, iż nie zostały zmienione warunki brzegowe to naprężenia w modelu się nie zmieniły. Największe naprężenie występujące przy mocowaniu elementu wynosi 429 MPa. Są to niemal połowę niższe naprężenia od dopuszczalnych.

Do wykonania trzeciej symulacji komputerowej naprężeń występujących w łomie wykorzystano stop aluminium przerobiony plastycznie EN-AW 2117. Jest to materiał o niskiej granicy plastyczności 165 MPa. Dopuszczalne naprężenia zostały ponad dwukrotnie przekroczone co prezentuje rysunek 7 i 8.

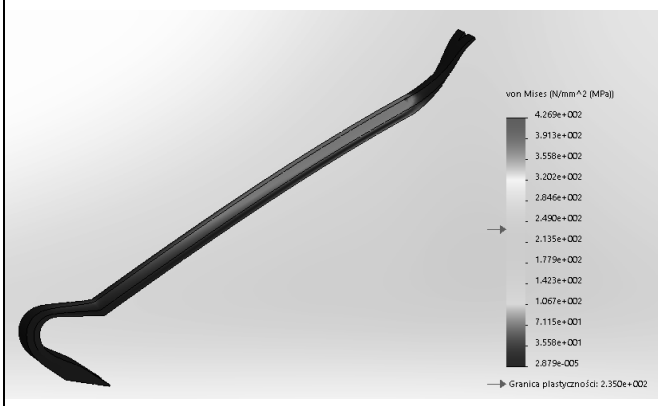

Rys.5 Barwna mapa naprężeń zredukowanych wg teorii Hubera von Misesa w rzucie izometrycznym
Fig. 5. A colorful map of stress reduced by the theory of Huber von Mises isometric

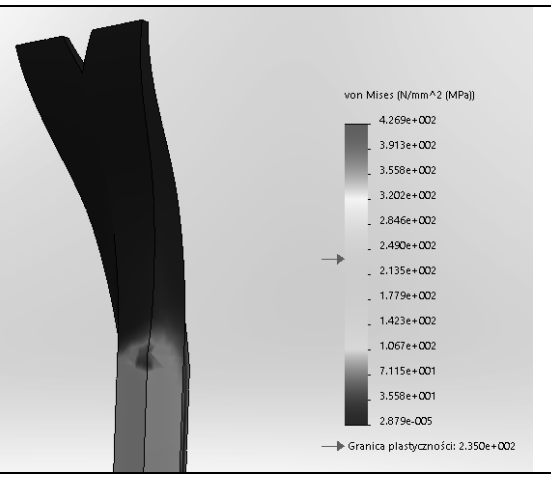

Rys. 6. Barwna mapa naprężeń zredukowanych wg teorii Hubera von Misesa w widoku przybliżonym na miejsce naprężeń maksymalnych
Fig. 6. colorful map of stress reduced by the theory of Huber von Mises to view the approximate location of maximum stress

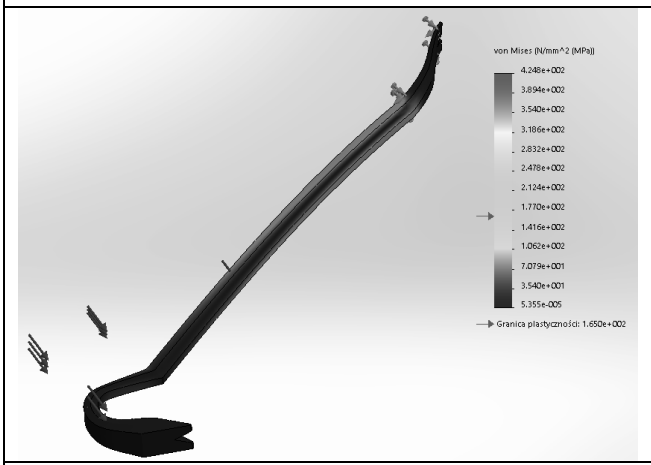

Rys.7 Barwna mapa naprężeń zredukowanych wg teorii Hubera von Misesa w rzucie izometrycznym
Fig. 7. A colorful map of stress reduced by the theory of Huber von Mises isometric

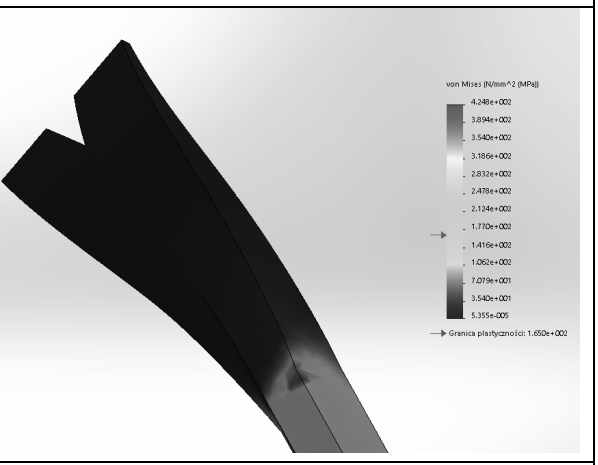

Rys. 8. Barwna mapa naprężeń zredukowanych wg teorii Hubera von Misesa w widoku przybliżonym na miejsce naprężeń maksymalnych
Fig. 8. colorful map of stress reduced by the theory of Huber von Mises to view the approximate location of maximum stress

4. PODSUMOWANIE

W pracy przedstawiono analizę numeryczną rozkładu naprężeń zredukowanych wg teorii Hubera von Misesa powstających w łomie podczas nadania siły nacisku 50 kg. Na

podstawie uzyskanych wyników można stwierdzić, iż stal S235JR oraz stop aluminium EN-AW 2117 nie nadają się do produkcji łomu, gdyż maksymalne naprężenia występujące w nim, znacznie przekraczają granicę plastyczności wymienionych materiałów. Łomy wykonuje się ze stali narzędziowych poddawanych obróbce cieplnej, dzięki której uzyskuje się wysokie własności plastyczne i wytrzymałościowe elementu. Analiza numeryczna przeprowadzona na modelu łomu wykonanego ze stali X33CrS16 w zupełności to potwierdza, gdyż w niej uzyskano najlepsze wyniki rozkładu naprężeń.

PODZIĘKOWANIA

Praca została wykonana w ramach projektu realizowanego z uczniami szkół średnich.

LITERATURA

[1] http://www.narzedzianonstop.pl/
[2] http://www.wikipedia.org/
[3] Leksykon materiałoznawstwa
[4] Biblioteka materiałów SolidWorks

TalentDetector
23th-25th June 2025
Gliwice-Brenna, Poland
DEPARTMENT OF ENGINEERING MATERIALS AND BIOMATERIALS
FACULTY OF MECHANICAL ENGINEERING
SILESIAN UNIVERSITY OF TECHNOLOGY
INTERNATIONAL STUDENTS SCIENTIFIC CONFERENCE

Ergonomic assessment of the carpenter's workplace using the NIOSH method and the concept of robotics application

Marcin Sitko[a], Monika Spilka[b]

[a] Student, Silesian University of Technology, Faculty of Mechanical Engineering, Department of Engineering Materials and Biomaterials
[b] Silesian University of Technology, Faculty of Mechanical Engineering, Department of Engineering Materials and Biomaterials
email: monika.spilka@polsl.pl

Abstract: The article concerns the ergonomic assessment of the carpenter's workplace and the possibility of using industrial robots in the transport of chipboards. An assessment of the employee's workload during lifting and carrying loads was carried out using the NIOSH method, and proposed actions to reduce the level of work arduousness. The use of a robot at the workplace eliminated the physical overload of the employee associated with the manual handling of large-sized chipboards.

Keywords: ergonomic assessment, carpenter's workplace, NIOSH method, robotics

1. INTRODUCTION

Safety refers to a situation in which risk or harm does not occur [1]. Council Directive 89/391/EEC requires that workplaces to be assessed in terms of hazards and the degree of risk to personnel [2]. This assessment should include ergonomic factors and identify opportunities for effective protective measures. Numerous statistical reports show that workers employed in the wood and sawmill industry suffer more often from musculoskeletal disorders, and ergonomic conditions are worse than in other sectors. Due to the combination of heavy manual work and relatively low use of machinery, the risk of accidents, injuries or work-related trauma in the carpentry industry is significantly higher than in other industries [3-6]. The solution to this problem may be the introduction of automation in the carpentry industry, due to the benefits that can be achieved at every stage of production, improving quality, efficiency and precision, which in turn contributes to reducing errors and increasing the company's competitiveness.

2. CHARACTERISTICS OF THE CARPENTER'S WORKPLACE

A carpenter's workshop with three employees, whose main activity is the production of furniture components was analysed. The production process involves both mechanical

processing and manual handling of heavy components during cutting, veneering, drilling and milling operations. The most commonly used raw material in furniture production is chipboard, which is a wood-based material created by pressing wood chips with the addition of synthetic glue under high pressure and at high temperature. The chipboard with a thickness of 18 mm is available in a wide range of sizes, but the standard size is 2800×2070 mm. The plate is rectangular, and its mass depends on its density. For standard chipboard, the density is approximately 650-700 kg/m³; the volume is 0.1042 m^3 and the weight (at a density of 700 kg/m³) is 72.94 kg.

3. APPLICATION OF THE NIOSH METHOD FOR ASSESSING WORKER LOAD DURING LIFTING AND CARRYING OF LOADS

Lifting and carrying heavy objects, such as chipboard, can cause a lot of strain on muscles and joints, especially the spine. Regularly performing such activities without following proper safety guidelines increases the risk of injuries and health issues such as back pain, muscle strain, or joint degeneration. To reduce the risk, rules and restrictions have been established regarding the permissible weight of items carried. Several factors are taken into account when assessing the risk [7]:

- lifting height – ideally, the plate should be at waist level, as lifting from the floor or above the head increases strain on the spine,
- distance from the body – the further away from the body the object being carried is, the greater the effort required to hold it, which can lead to injury,
- frequency of lifting – the more frequently this activity is performed during the day, the greater the risk of overloading,
- body twists – lifting and carrying plates with a twist of the torso increases the risk of back injury. It is advisable to rotate the whole body instead of twisting the torso alone,
- grip – a stable grip reduces the risk of dropping the plate and allows for better control over its handling,
- teamwork – if the plate is too heavy, it is better to lift it with two people, which significantly reduces the load on the spine and shoulders.

The reference mass (M_{ref}) refers to the maximum permissible weight of a load that can be lifted, as determined for a specific population. For the European population, these values are given in the PN-EN 1005-2 standard [8]. For the Polish population, the applicable limits are determined by national regulations contained in the Regulation of the Minister of Labour and Social Policy of 2000 (Journal of Laws of 2000, No. 26, item 313) [9].

Table 1 presents the reference mass values specified in the PN-EN 1005-2 standard for different population groups, taking into account three main areas of application:

- work at home, where the maximum reference mass ranges from 5 to 10 kg and applies to the entire population, except for children and the elderly in the case of the 5 kg limit;
- permanent work, for which the M_{ref} values range from 10 to 15 kg, with the 15 kg load taking into account the entire working population (including children and the elderly);
- occasional work, where the permissible values range from 25 to 40 kg; however, these apply only to experienced individuals with appropriate physical capabilities and training.

Additionally, the table includes the percentage share of the population able to lift specific loads, with values differing by gender. In the case of continuous work with a 25 kg load, 85% of the total population, 70% of women, and 90% of men are considered capable of lifting it.

These data serve as important guidelines in the design of workstations and manual handling support systems, taking into account user safety and ergonomics.

Table 1. Reference mass (M_{ref}) values for different user populations [7,8]

Application area	M_{ref} [kg]	Population [%]			Group in the population	
		F&M	F	M		
At home	5	Data not available			Children and older adults	The entire population
Permanent work	10	99	99	99	People working at home	
	15	95	90	99	Working population (+Y,+E)	The entire working population
Occasional work	25	85	70	90	Adult working population	
	30	Data not available			Qualified and trained personnel with appropriate capabilities	Skilled workers
	35					

where: F – women, M – men, Y – children, E – older adults

The body position during lifting loads is determined by a number of factors that directly influence the posture adopted. One of the key parameters is the vertical location (V), which defines the initial height at which the load is positioned. It refers to the vertical distance between the center points of the hands and the floor, measured at the start of the lift. This value, expressed in centimeters, is used to calculate the vertical location factor (V_M) according to the following formula [7]:

$$\boldsymbol{V_M = 1 - 0.003 \times |V - 75|} \quad (1)$$

Another important factor is the horizontal position (H), which means the horizontal distance between the center points of the hands and the center of the line connecting the ankles of the feet. On this basis, the coefficient of the distance of the grip of the object from the body axis (H_M) is determined, calculated according to the formula [7]:

$$\boldsymbol{H_M = 25/H} \quad (2)$$

The body position is also influenced by the vertical displacement (D), defined as the difference in height between the initial and final position of the lifted object. This value allows determining the vertical displacement coefficient (D_M) according to the relationship [7]:

$$\boldsymbol{D_M = 0.82 + (4.5)/D} \quad (3)$$

Another important parameter is the asymmetry angle (A), i.e. the angle between the sagittal plane and the asymmetry plane. It is expressed in degrees and takes into account the greatest body rotation, especially if the position of the feet changes between successive lifting or lowering of the load. On this basis, the asymmetry angle coefficient (A_M) is calculated using the formula [7]:

$$\boldsymbol{A_M = 1 - (0.0032 \times A)} \quad (4)$$

The parameter describing the time of performing an activity is the lifting repetition rate (F), i.e. the number of liftings performed in a given time. On its basis, the repetition frequency factor

(F_M) is determined, the value of which depends on the number of repetitions and the duration of the work. The FM coefficient values are included in the PN-EN 1005-2 standard.

Additional factors also influence the permissible load mass and the level of risk for musculoskeletal disorders. One of these is the grip coefficient (C_M), the value of which is determined according to Table 2. Other factors include the number of upper limbs engaged in the task, the number of workers involved in lifting, and the presence of additional tasks that place strain on the body. Considering these parameters enables a more accurate assessment of overload risk and allows for better adjustment of the permissible load weight to actual working conditions [7]:

- one-handed operation coefficient (O_M) – takes the value of 1.0 when both upper limbs are involved in lifting. When only one hand is used, the coefficient is 0.6;
- coefficient of activities performed by 2 people (P_M) – if the lifting task is performed by two people, the coefficient has a value of 0.85. For tasks performed individually, the coefficient is 1.0;
- other physical activity coefficient (A_T) – takes the value of 0.8 if there are additional activities that place physical strain on the body. In the absence of such tasks, the coefficient is 1.0.

Table 2. Grip coefficient (C_M) values depending on grip quality [7]

Grip description	Length ≤ 40 cm; height ≤ 30 cm; ability to grip well or the load has handles. Ability to easily carry loose objects and loads by grasping without excessive wrist bending.	Length ≤ 40 cm; height ≤ 30 cm, with poor grip or need to bend fingers at 90°. Ability to easily handle loose objects and loads by grasping and bending fingers at 90° without excessive wrist bending.		Length > 40 cm or height > 30 cm; objects difficult to lift or with an asymmetrical centre of mass; unstable or difficult to grasp; or need to be handled with gloves.
Grip quality	Good	Sufficient		Bad
C_M coefficient value	1.00	V<75 cm	V>=75 cm	0.90
		0.95	1	

Coefficients related to body position, repetition rate, and additional parameters are used to determine the allowable weight of the load to be lifted.

The recommended load weight limit (R_{ML}) is calculated using the NIOSH equation (5), which takes into account the factors listed. This formula allows to assess whether a given lifting activity is within safe limits for the health of the worker [7,10,11].

$$\boldsymbol{R_{ML} = M_{ref} \times V_M \times D_M \times H_M \times A_M \times C_M \times F_M \times O_M \times P_M \times A_T} \quad (5)$$

where:
M_{ref} – reference mass,
V_M – coefficient for the height of the initial position of the object [cm],
D_M – coefficient of the height difference between the initial and final position of the object [cm],
H_M – coefficient for the distance of the grasping point of the object from the body axis [cm],
A_M – asymmetry angle coefficient – torso twist angle during lifting [°],
C_M – grip coefficient,
F_M – frequency factor,
O_M – coefficient of activities performed with one upper limb,
P_M – coefficient of activities performed by 2 people,
A_T – other physical activity coefficient.

Based on the NIOSH equation, the risk associated with lifting activities can be assessed. The risk index (R_I) is calculated as follows [7]:

$$\boldsymbol{R_I = lifted\ weight\,[kg]/recommended\ weight\ limit\ value\ R_{ML}\,[kg]} \quad (6)$$

The risk index indicates the level of risk associated with lifting loads and their impact on worker health. The interpretation of the index value is as follows [7,12]:

- $R_I \leq 0{,}85$ – low risk (green zone): the risk of injury or occupational disease is minimal or at an acceptable level. No changes to the workplace are required;
- $0{,}85 < R_I < 1{,}0$ – medium risk (yellow zone): there is a moderate risk of occupational injury or disease, which may affect the entire employee population or only part of it. It is advisable to consider modifying the job or changing the work process;
- $R_I \geq 1{,}0$ – high risk (red zone): the risk of injury or occupational disease is significant and requires immediate redesign of the workplace to protect workers' health.

The NIOSH method was used to assess the level of physical overload of workers performing manual handling of panels, enabling the calculation of the risk index.

At the analyzed carpenter's workplace:

- weight lifted by one worker: 36.5 kg
- reference mass (M_{ref}): 23 kg
- vertical position (V): 70 cm
- horizontal position (H): 20 cm
- vertical displacement (D): 15 cm
- asymmetry angle (A): 45° (modified)
- lifting frequency: 3 times per hour
- grip quality: difficult ($C_M = 0.9$)
- work performed with both hands (O_M): 1.0
- work performed by 2 persons (P_M): 0.85
- no additional physical activities (A_T): 1.0

$V_M = 0.985$
$H_M = 1.25$
$D_M = 1.12$
$A_M = 0.856$
$F_M = 1.0$

$R_{ML} \approx 20.8$ kg
$R_I \approx 1.75$

The R_I result indicates a very high risk of injury (red zone). This means that the load significantly exceeds safe limits and poses a serious risk to workers' health. This level of physical load highlights the need to implement risk-reduction measures, such as automating the plate handling process, using appropriate support tools, and providing workers with proper ergonomic training. The introduction of such solutions will not only improve workplace safety and comfort but also enhance production efficiency by reducing sickness-related absenteeism and associated costs for the company.

3.1 Assessment of the impact of work on the musculoskeletal system at the carpenter's workplace

Manual work with chipboard in a carpentry workshop involves a great deal of physical strain on workers. Even with two people working together, each has to lift and carry pieces weighing around 36.5 kg, which far exceeds the recommended occupational safety standards. Performing such activities on a regular basis leads to fatigue, overload and a gradual weakening of the body, which can result in serious health problems and reduced work efficiency.

When lifting and carrying large plates, workers are often forced into awkward positions. In order to lift a heavy plate, they have to bend over, twist their torso and lift the load with their legs straight, which puts enormous strain on their backs, especially in the lower spine. Under such conditions, it is easy to develop overload and back pain, which can persist even after work. If these strains occur regularly, they can lead to a gradual weakening of the muscles that support the spine and changes that can cause chronic pain and reduced range of motion.

Lifting heavy objects requires considerable muscular effort from the hands and arms, which can lead to excessive tension and pain. Frequent overhead lifting and repetitive motions strain the shoulders, often resulting in stiffness, reduced range of motion, and difficulty raising the arms. Over time, this can weaken muscular strength and impair the ability to perform routine tasks. The wrists and hands are also subjected to high levels of strain, especially when gripping plates requires significant finger pressure. This can lead to pain, fatigue, and difficulty performing precise movements, all of which negatively affect both comfort and workplace safety.

Carrying large and heavy boards requires not only strength but also motor coordination. Frequent bending of the legs, dynamic torso rotations, and sudden changes in position put significant strain on the knee and hip joints, increasing the risk of overload. Prolonged work under these conditions can cause joint pain, stiffness, and a gradual reduction in joint stability. In extreme cases, microtrauma to soft tissues may occur, leading to long-term health issues and the need for rehabilitation. An additional hazard is the potential loss of balance while transporting large boards, which significantly increases the risk of falls and serious injury.

4. CONCEPT OF USING ROBOTICS TO REDUCE WORKERS' PHYSICAL WORKLOAD

To effectively reduce the risks associated with handling heavy and bulky wooden components, both organizational and technical solutions should be implemented. One of the key measures is the deployment of the Fezer VPL robot, which significantly reduces workers' physical workload and improves workplace safety [13].

Table 3 presents a comparison between manual handling of plates and handling assisted by a robot. The implementation of this solution leads to a significant reduction in injury risk, elimination of excessive physical effort, and increased efficiency and work comfort. Implementing the preventive measures in a furniture carpentry workshop will not only improve working conditions but may also enhance employee efficiency and comfort, ultimately benefiting both the workforce and the company in the long term.

Table 3. Assessment of the reduction in workers' physical load following robot implementation

Parameter	Manual lifting	With the Fezer VPL robot	Difference/Benefits
Weight lifted per worker	36.5 kg	~0 kg (the robot takes over the load)	Elimination of physical workload
Recommended lifting weight (R_{ML})	20.8 kg	-	Manual lifting far exceeds NIOSH methods
Overload indicator (R)	1.75 (high risk of injury)	~ 0	Significant risk reduction
Lifting frequency	3 times per hour	The robot performs all the work	Elimination of employee effort
Risk of musculoskeletal injuries	High	Minimal	Improving work ergonomics
Efficiency and speed of work	Limited by fatigue	Constant and high	Increased productivity
Precision plate manipulation	Limited, dependent on strength and coordination	High, thanks to the control system	Minimization of material damage
Impact on employee health	Risk of spine and joint injuries	No physical overload	Reduction in the number of sick leaves
Usability by individuals with physical limitations	Difficult	Full	Greater availability of workstations
Risk of dropping the plate	High	Close to zero	Elimination of material losses
Required number of employees	Minimum of 2 people	1 operator	Reduction of labor costs
Worker's energy expenditure	High	Minimal	Less fatigue and greater efficiency
Accessibility in confined spaces	Limited	Easier thanks to the compact design	Better mobility at the workstation

5. SUMMARY

The implementation of a robotic carpentry workplace will improve working conditions for carpenters by minimizing risk factors associated with handling heavy chipboard panels. Employees will experience less fatigue and be less exposed to the long-term effects of performing strenuous physical labor. The obtained results confirm the validity of applying robotics in the woodworking industry.

In the future, it is worth considering further improvements, such as the implementation of autonomous transport systems, which could further relieve employees and increase the efficiency of logistics processes.

BIBLIOGRAPHY

1. ISO 12100:2010. Safety of machinery – General principles for design – Risk assessment and risk reduction. International Organization for Standardization, Geneva, 2010.
2. Council Directive 89/391/EEC of 12 June 1989 on the introduction of measures to encourage improvements in the safety and health of workers at work. Official Journal of the European Communities, L 183, 29.06.1989, 1-8. https://eur-lex.europa.eu/legal-content/EN/TXT/?uri=CELEX%3A31989L0391
3. S.M. Qutubuddin, S.S. Hebbal, A.C.S. Kumar, An ergonomic study of work related musculoskeletal disorder risks in Indian Saw Mills, IOSR Journal of Mechanical and Civil Engineering 7/5 (2014) 7-13.

4. M.S. Rahman, A.H. Khan, M.S. Rahman, B. Biswas, Work-related musculoskeletal disorders: A case study of sawmill workers in Bangladesh, Current World Environment 14/2 (2019) 336-345.
5. C.A. Holcroft, L. Punnett, Work environment risk factors for injuries in wood processing, Journal of Safety Research 40/4) (2009) 247–255.
6. S. Vadivel, C. Subramaniyan, K. Muthukumar, T. Bharani, Ergonomic risk assessment of saw mill operator, Journal of Ergonomics 13/2 (2023) 1000328.
7. NIOSH method, https://www.ciop.pl/CIOPPortalWAR/appmanager/ciop/pl?_nfpb=true&_pageLabel=P620059861340178661073&html_tresc_root_id=300012898&html_tresc_id=300012978&html_klucz=32274&html_klucz_spis=
8. PN-EN 1005-2+A1:2010. Safety of machinery – Human physical performance – Part 2: Manual handling of machinery and component parts, Polish Committee for Standardization, Warsaw, 2010.
9. Regulation of the Minister of Labour and Social Policy of 14 March 2000 on occupational health and safety for manual handling operations, 2000. (Journal of Laws of the Republic of Poland, No. 26, item 313).
10. A step-by-step guide to using the NIOSH lifting equation for single tasks, https://ergo-plus.com/niosh-lifting-equation-single-task/
11. N.H. Kamarudin, S.A. Ahmad, M.K. Hassan, R.M. Yusuff, S.Z. Md Dawal, A review of the NIOSH lifting equation and ergonomics analysis, Advanced Engineering Forum 10 (2013) 214-219.
12. Load assessment during load handling, https://www.ciop.pl/CIOPPortalWAR/appmanager/ciop/pl?_nfpb=true&_pageLabel=P300018313355391822 78&html_tresc_root_id=300008716&html_tresc_id=300008717&html_klucz=19558&html_klucz_spis=
13. Fezer, https://www.assurich.com/en/vacuum-lifter/442-fezer-vacuum-tube-lifter-vacupowerlift-vpl.html

TalentDetector
23th-25th June 2025
Gliwice-Brenna, Poland
DEPARTMENT OF ENGINEERING MATERIALS AND BIOMATERIALS
FACULTY OF MECHANICAL ENGINEERING
SILESIAN UNIVERSITY OF TECHNOLOGY
INTERNATIONAL STUDENTS SCIENTIFIC CONFERENCE

Research on stone material from mining waste dumps for use in construction materials

Barbara Słomka-Słupik[a], Jakub Piasecki[b]

[a]Silesian University of Technology, Faculty of Civil Engineering, Department of Building Structures
email: Barbara.Slomka-Slupik@polsl.pl
[b] Student at the Silesian University of Technology, Faculty of Civil Engineering

Abstract: In response to the growing pressure to reduce CO_2 emissions in construction, an attempt was made to use waste rock from post-mining heaps as an alternative component in cement mixes. The aim of the study was to investigate the suitability of this material as a partial replacement for cement and sand in building mortars.

Keywords: concrete, aggregate, binder, mining, reclamation, mining

1. INTRODUCTION

A concrete mix is a combination of fine and coarse aggregate, sand, water, and cement, which, through the process of cement hydration, hardens into a material with properties similar to those of natural rock [1]. Currently, approximately 10 billion tons of concrete are consumed globally each year. This level of usage makes it the most widely used anthropogenic material in the world. European countries have set a goal to achieve net-zero emissions by 2050, which requires a substantial reduction in CO_2 emissions from concrete production. Efforts are underway to develop low-emission concretes, and the construction industry is increasingly incorporating eco-friendly materials that either supplement or replace conventional concrete components [2].
Among all the ingredients of concrete, cement has the highest carbon footprint. The cement industry is responsible for approximately 8% of global carbon dioxide emissions, making it one of the major contributors to greenhouse gas emissions. As other industrial sectors undergo transformations aimed at significantly reducing their emissions, inaction within the cement and concrete industry could become increasingly apparent and problematic [3].
One possible substitute for cement is gangue rock from post-mining waste dumps, which requires lower calcination temperatures than conventional cement. Utilizing gangue rock from mine waste heaps offers two major benefits, the first of which is environmental. These heaps began to form decades ago, at a time when available technologies did not allow for effective separation of coal and other valuable raw materials from the waste material. As a result, these wastes may contain a relatively high amount of carbon. Additionally,

improper compaction of these deposits and uncontrolled storage conditions can lead to spontaneous combustion. The second benefit is economic. As the name suggests, post-mining waste dumps are repositories of mining by-products. With proper utilization and optimization of the processing methods, these materials may prove to be more financially viable for manufacturers compared to standard materials.
In light of the above, the aim of this study was to investigate the use of stone material from post-mining waste dumps as a potential raw material in mortar production. Particular attention was given to evaluating its suitability as a component or partial substitute for binder or aggregate in concrete.

2. MATERIALS AND METHODS

After being transported to the Laboratory of the Faculty of Civil Engineering at the Silesian University of Technology, the rock samples collected from the post-mining waste dump were initially dried and crushed (Fig. 1a). Subsequently, the aggregates were placed on trays and subjected to drying in an oven (Fig. 1b) at a temperature of 105°C for a period of 7 days to ensure complete removal of free water. This step was crucial for the accuracy of subsequent analyses, as the presence of moisture could have affected the mass of the samples as well as the efficiency of grinding and sieving processes.

a) b)

Figure 1. Gangue samples: a) crushed, b) placed in a dryer

A Los Angeles-type mill and seven metal grinding balls, each weighing 2 kg, were used for the milling process. The crushed material was then sieved using a set of sieves mounted on a laboratory shaker. The aggregate was not rounded but crushed, with a predominantly platy fracture surface. The results of the sieve analysis, along with the mesh sizes used, are presented in Table 1. The bulk density of the aggregate was determined using the hydrostatic weighing method and averaged 1.97 g/cm³. The water absorption of the aggregate was also tested and did not exceed 5% of its mass – an important parameter indicating the potential absorption of mixing water. It was assumed that mortar samples would be prepared to investigate a fundamental parameter of hardened mixtures – compressive strength. This test is conducted according to the PN-EN 196-1 standard [4], which specifies the use of standard sand (1350 grams), water (225 grams), and cement (450 grams). We assumed the preparation of a reference cement mortar as well as modified versions. In the modified mixes, standard sand was replaced with waste dump aggregate in the 0 – 0.25 mm fraction. Part of the cement was replaced with stone material from the dump in the 0.25 mm – 1.00 mm fraction,

which was dried at 105°C and then calcined at 750°C or at 850°C. The mix compositions are shown in Table 2.

The calcination temperatures were selected based on thermogravimetric analysis and microscopic observations, which revealed the presence of clay and inert phases. These findings suggested the potential for producing pozzolanic binders. Microscopic images of the dump rock material dried at 105°C and sized to 0.5 mm are shown in Fig. 2, and the thermograph of the < 0.25 mm fraction is shown in Fig. 3.

Table 1. Results of sieve analysis

Sieve [mm]	Mass on sieve [g]	Percentage [%]	Cumulative Mass [g]	Percentage Retained [%]	Percentage Passing [%]	Cumulative Percentage
16,00	692,7	8,0	692,7	8,0	92,0	8,0
8,00	1648,8	19,1	2341,5	19,1	72,9	27,1
4,00	2066,8	23,9	4408,3	23,9	49,0	51,0
2,00	1620,4	18,7	6028,7	18,7	30,3	69,7
1,00	1142,0	13,2	7170,7	13,2	17,1	82,9
0,50	575,2	6,7	7745,9	6,7	10,4	89,6
0,25	325,8	3,8	8071,7	3,8	6,7	93,3
0,00	576,7	6,7	8648,4	6,7	0,0	100,0
SUM	8648,4	100	-	100	-	-

Table 2. Composition of mortar mixtures

Sample	Aggregate [g]		Binder [g]				Water [g]	
	Standard Aggregate	Waste Dump Aggregate - Substrate	Cement	Waste Dump Material Dried at 105°C	Waste Dump Material Calcined at 750°C	Waste Dump Material Calcined at 850°C	Standard	Additional
Z0	1350	0	450	0	0	0	225	0
Z1	1350	0	337,5	0	0	112,5	225	34
Z2	1350	0	337,5	0	0	112,5	225	0
Z3	1350	0	337,5	112,5	0	0	225	0
Z4	0	1370	450	0	0	0	225	116
Z5	1350	0	405	0	45	0	225	0

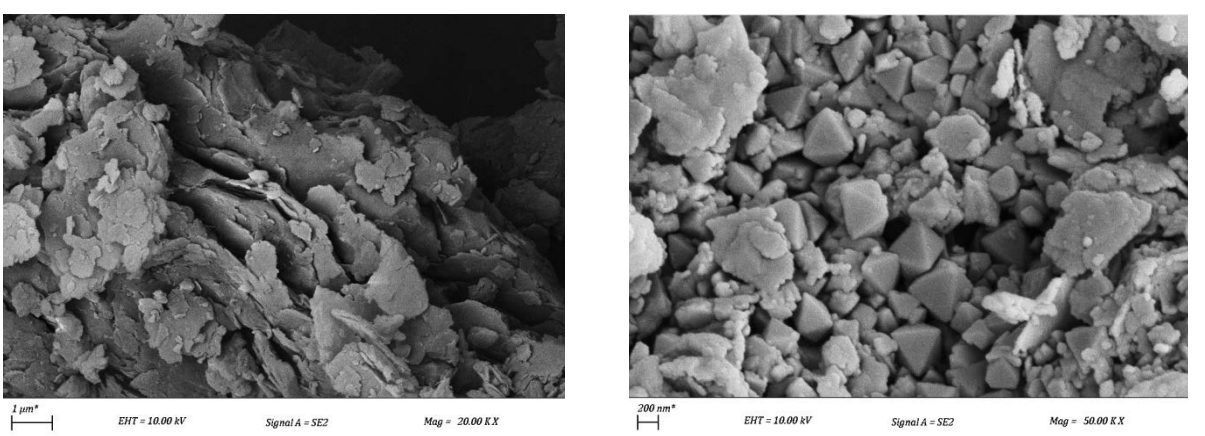

a) b)

Figure 2. Microscopic images of gangue: a) clay phase, b) carbonate or quartz phase

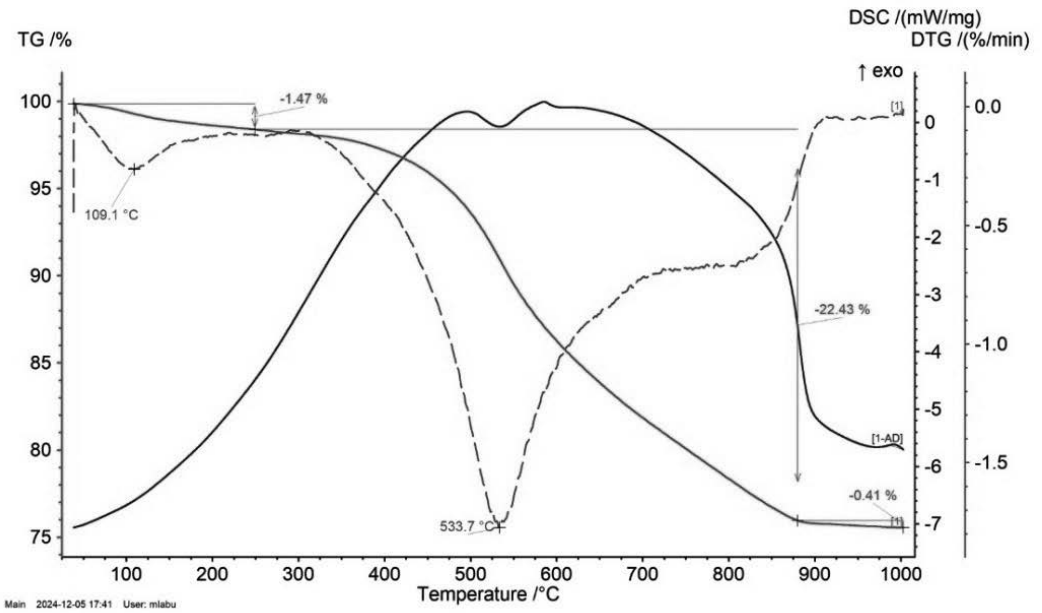

Figure 3. Thermograph of an aggregate sample with a fraction of 0–0.25 mm. Curves: TG – pink continuous, DTG – green dashed, DSC – blue continuous

The first mass loss effect, with a peak at 109°C (Fig. 3), indicated the dehydration of clay minerals. The endothermic reaction with a peak at 534°C was associated with the dehydroxylation process of these phases.

All six mixtures were prepared in a manner similar to the following procedure: the waste dump aggregate was dry-mixed with cement for 30 seconds, then water was added and mixed for another 30 seconds at low speed. Standard aggregate was then added and mixed for an additional 30 seconds. Flowability was tested using a flow table (Fig. 4). The mortars were cast into molds measuring 40 mm × 40 mm × 160 mm (Fig. 5).

In two cases described in Table 2 (mortars Z1 and Z4), due to their plastic consistency, it was necessary to add a greater amount of water. Additional water was added until a satisfactory consistency was achieved.

Figure 4. Flow test

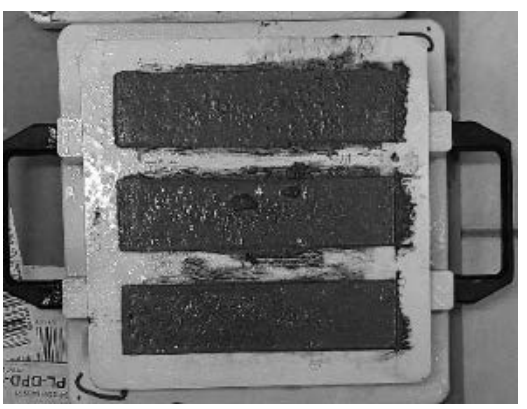

Figure 5. Fresh mortar in mold

3. RESULTS AND ANALYSIS

The compressive strength of the mortars was tested after 7, 28, and 84 days of curing. The results are presented in Figure 6.

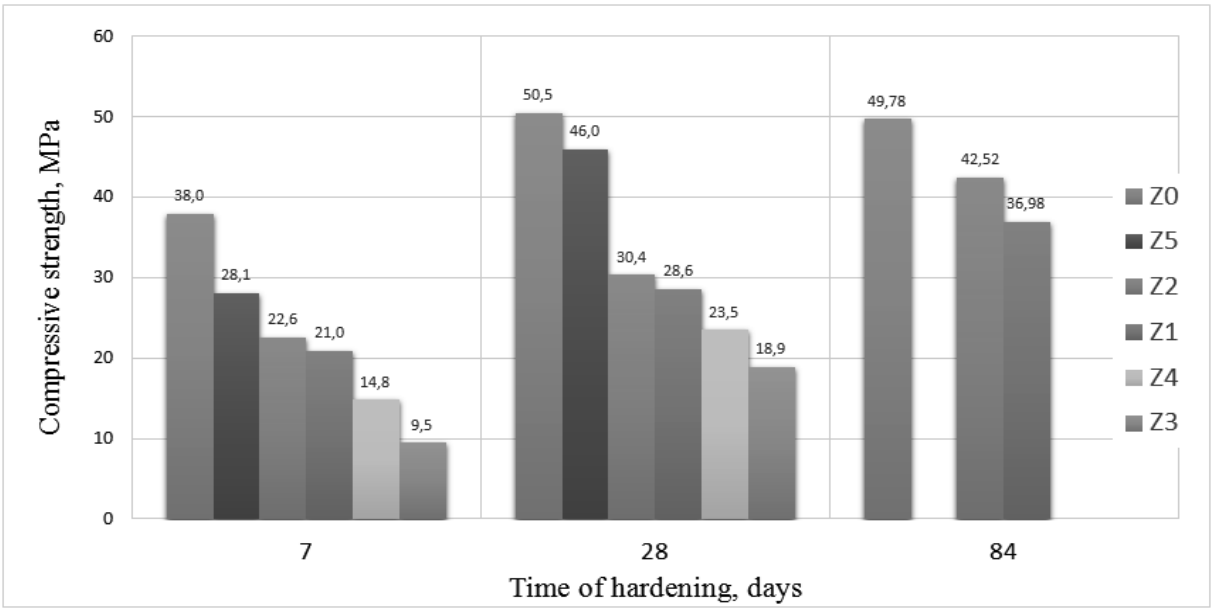

Figure 6. Compressive strength of samples after 7, 28 and 84 days of hardening

As, the aim of the study was to evaluate the effect of adding waste material from post-mining spoil heaps, subjected to thermal treatment at different temperatures, on the strength of construction mortars, we obtained the following results.

The experiment included six samples: Z0 (reference) and Z1–Z5 with various modifications of the cementitious and/or aggregate composition. The unmodified mortar Z0 reached its maximum compressive strength after 28 days, with no significant increase observed in subsequent days. In contrast, the strength of the other mixtures continued to increase over time due to prolonged pozzolanic reactions.

Compared to Z0:

- sample Z1 achieved approximately 73% of Z0's strength after 84 days.
- sample Z2 achieved approximately 85% of Z0's strength after 84 days.
- sample Z3 achieved approximately 37% of Z0's strength after 28 days.
- sample Z4 achieved approximately 40% of Z0's strength after 28 days.
- sample Z5 achieved approximately 92% of Z0's strength after 28 days.

The analysis of mortars hardening through pozzolanic reactions is challenging due to the prolonged nature of these processes, however, such reactions can potentially result in higher strength than hydration reactions, which govern the hardening of ordinary cement. Sample Z2 achieved the highest strength among all modified mortars at 84 days. The absence of additional water had a positive impact on strength (compare Z1 and Z2).

Sample Z3 exhibited the lowest strength after 4 weeks, as the stone material was not calcined and thus not activated. Replacing standard sand with anthropogenic aggregate in Z4 caused a reduction in strength, likely because this aggregate was naturally mechanically weaker.

The higher strength of Z4 compared to Z3 after 4 weeks was probably due to the greater amount of cement.
Interpretation: The mixture Z5 demonstrated very promising properties – already after 28 days it reached 91% of the strength of the Z0 mixture. This is significant and suggests that the calcination temperature of 750°C might be optimal for pozzolanic activation, even better than 850°C. This level of additive replacement did not significantly reduce strength, confirming that a lower percentage of cement substitution could be a viable approach to reduce cement consumption without compromising quality.

5. SUMMARY AND CONCLUSIONS

The conducted research clearly demonstrated that waste material from post-mining spoil heaps, subjected to appropriate thermal treatment, can effectively function as a pozzolanic additive in cement mortars, positively influencing their mechanical properties.
The best results were obtained in sample Z5, where 10% of cement was replaced with material calcined at 750°C, after 28 days, this sample reached as much as 92% of the strength of the reference sample, indicating a high pozzolanic activity of the material at this temperature. Equally promising was the 25% replacement of cement with material calcined at 850°C (Z2), which after 84 days achieved 85% of the reference strength.
On the other hand, the material dried at 105°C – used in mixture Z3 – did not exhibit binding or pozzolanic properties, as evidenced by its significantly lower strength.
Further studies are necessary to optimize the percentage substitution of the mass of cement and the calcination temperature.

Acknowledgments: This work was carried out thanks to funding from the PBL XI project, as part of the IDUB program at the Silesian University of Technology. We are grateful to Professor Małgorzata Labus for conducting the thermogravimetric analyses, as well.

LITERATURE

1. Raczkiewicz, W. (2012). Beton–materiał budowlany znany od wieków. *Przegląd Budowlany 83.10*, 13-18.
2. Strona internetowa: *Future-builders.com*. (2025, Kwiecień 15). Pobrano z lokalizacji Co po betonie? Branża budowlana kontra zmiany klimatu.: https://future-builders.com/posts/co-po-betonie-branza-budowlana-kontra-zmiany-klimatu
3. Strona internetowa: *ccus.pl*. (2025, Kwiecień 12). Pobrano z lokalizacji Nowe technologie wychwytu CO_2 w przemyśle cementowym: https://ccus.pl/nowe-technologie-wychwytu-co2-w-przemysle-cementowym
4. PN-EN 196-1 Metody badania cementu -- Część 1: Oznaczanie wytrzymałości

TalentDetector
23th-25th June 2025
Gliwice-Brenna, Poland
DEPARTMENT OF ENGINEERING MATERIALS AND BIOMATERIALS
FACULTY OF MECHANICAL ENGINEERING
SILESIAN UNIVERSITY OF TECHNOLOGY
INTERNATIONAL STUDENTS SCIENTIFIC CONFERENCE

Thermal analysis of aircraft double-pane windows

Haoxiang Song[1, 2], Ruyu Shi, Xiyue Cui[1, 2]

[1] Yanshan University, School of Mechanical Engineering, Qinhuangdao, China
email: hs304830@student.polsl.pl, rs304829@student.polsl.pl, xc304823@student.polsl.pl
[2] Silesian University of Technology, Faculty of Mechanical Engineering, Department of Engineering Materials and Biomaterials

Abstract: This report presents a comprehensive thermal analysis of aircraft double-pane windows. It begins by introducing the structure and materials used, including polycarbonate, laminated glass, and polyimide. Using SolidWorks modeling and thermal simulation, the study examines heat conduction and thermal stress distribution under temperature gradients. The results show that double-pane windows offer excellent insulation, noise reduction, safety, and energy efficiency. Finally, suggestions for structural optimization and maintenance are proposed to enhance durability and safety.

Keywords: Aircraft windows, Heat conduction, Material selection, Finite element analysis

1. INTRODUCTION

Aircraft double-glazed structures consist of two layers of glass, the inner and outer, called the outer and middle layers, with a certain air layer between these two layers. The thickness of the air layer is usually between 8-12 mm. The two layers of glass are connected by a rubber seal to form an airtight space. In addition to the outer and middle layers, there is also an inner layer, which is not a structural element, and whose main function is to separate the passenger from the middle load-bearing window.

1.1. The role of double glazing

The main role of aircraft double glazing is to keep warm and prevent dust. First of all, double glazing can effectively prevent the temperature difference between inside and outside the cabin from affecting the temperature inside the cabin. When an aircraft is flying at a high altitude, the temperature difference between inside and outside the cabin may reach dozens of degrees, and if the aircraft windows are installed with only one layer of glass, the water vapour inside the cabin will condense into small water droplets on the glass[1], which will affect the temperature inside the cabin. And double glazing can effectively prevent this from happening.

Secondly, double glazing can prevent dust and impurities from entering the cabin. Aircraft in flight may encounter a variety of dust and impurities, double-glazing can effectively prevent these impurities from entering the cabin, to ensure the cleanliness of the cabin.

1.2. Advantages of double glazing

Aircraft double glazing has several significant advantages that make it widely used in modern aviation. The following are the main advantages of aircraft double glazing:
(1) Excellent thermal insulation performance: the air layer between the double glazing forms an effective thermal insulation layer that can effectively prevent the transfer of heat. When flying at high altitude, the temperature outside the aircraft is extremely low, while the inside of the cabin needs to be maintained at a suitable temperature. The design of double glazing can significantly reduce the heat loss caused by the temperature difference between inside and outside, thus improving the insulation effect inside the cabin and creating a more comfortable flight environment for passengers and crew.
(2) Good sound insulation: The double-glazed structure can effectively reduce the transmission of external noise, including engine noise, airflow noise and so on. This not only improves the quietness of the cabin, which helps passengers to rest and relax, but also reduces the health risk of the crew being exposed to high noise levels for a long period of time.
(3) High Strength and Safety: Double glazing has higher structural strength and impact resistance than single glazing. This design can effectively prevent external objects from damaging the cabin interior and improve flight safety. In addition, even in the event of damage to the outer glass, the inner glass retains its structural integrity, providing additional protection for passengers and crew.
(4) Outstanding dust and cleanliness: The double-glazed structure effectively prevents dust and other small particles from entering, keeping the porthole clean and transparent. This not only improves the clarity of the pilot's vision and helps ensure flight safety, but also reduces the frequency and cost of cleaning and maintenance.
(5) Energy saving and environmental protection: As double glazing has excellent thermal and acoustic insulation properties, it reduces the aircraft's reliance on air-conditioning systems and noise suppression systems, thereby reducing energy consumption and emissions and helping to realize the sustainable development of the aviation industry.

2. AIRCRAFT DOUBLE WINDOW MODEL

2.1. Double window model

First of all, we use solidworks modelling to build a roughly aircraft double window model, aircraft window glass is generally composed of three layers of glass, including the outer window, the middle window and the inner window. Among them, the thickness of the outer window is about 8mm, which mainly plays a protective and thermal insulation role; the thickness of the middle window is about 3mm, which is to buffer and cushion the pressure; there is an 8mm air layer between the outer window and the middle window; and the thickness of the inner window is 2mm, which is to prevent the glass from cracking and reduce the weight.

Fig. 1. Double window model

2.2. Double-pane window modelling materials

A double-pane aircraft window structure usually consists of an outer layer, a middle layer and an inner layer. The outer layer is usually made of polycarbonate material, which has impact and pressure resistance properties. The middle layer is generally made of laminated glass, which is used to enhance the strength and thermal insulation properties of the glass. The inner layer is generally composed of a polymer material such as polyimide, which is used to protect the glass from splash problems in case of breakage. This structural design can effectively improve the safety and thermal insulation performance of aircraft windows.

Outer layer of polycarbonate material:
Polycarbonate (PC) is a polymer material widely used in the aerospace industry [2]for outer windows. Its main characteristics and advantages are as follows:
(1) High impact resistance: The impact strength of Polycarbonate is about 250 times that of glass, and it maintains good toughness even at low temperatures. It can withstand impacts such as bird strikes and hailstones that may be encountered in flight, providing excellent protection.
(2) Lightweight: The density of polycarbonate is about 1.2 g/cm³, much lighter than traditional glass, which helps to reduce the overall weight of the aircraft and improve fuel efficiency.
(3) Good heat resistance: Polycarbonate remains stable in the range of -40°C to 120°C, is not easy to deform, and adapts to extreme temperature changes in high-altitude flight.
(4) High transparency: The light transmittance is as high as 88%-92%, comparable to glass, ensuring a clear view for passengers and pilots.
(5) Excellent processing performance: Easy thermoforming and machining, can be made into a variety of complex shapes of window components.
(6) UV protection: Adding anti-ultraviolet coating can effectively block ultraviolet radiation and extend the service life of the material.
Medium Laminated Glass:
Laminated glass (Laminated Glass) is a multi-layer composite glass[3] made of one or more layers of polyvinyl butyral (PVB) film sandwiched between two or more pieces of glass, made by high temperature and high pressure, with the following characteristics and advantages:

(1) High strength and safety: The structural strength of laminated glass is high, even if it is broken, it can maintain the integrity, because the PVB film can stick to the fragments, preventing the glass from flying apart and reducing the harm to passengers.
(2) Good thermal insulation performance: The PVB layer in the middle has a low thermal conductivity, which effectively reduces heat transfer, improves thermal insulation and keeps the temperature stable in the cabin.
(3) Good sound insulation: PVB film can effectively block the transmission of sound, reduce the noise outside the aircraft such as engine noise, airflow noise, etc. into the cabin, providing a quiet flight environment.
By choosing polycarbonate and laminated glass as the material for aircraft double-paned windows, not only can it significantly improve the safety and durability of the windows, but also effectively improve thermal insulation performance, to meet the demand for high-performance materials in modern aviation.

3.THERMAL ANALYSIS OF AIRCRAFT DOUBLE PANE WINDOW MODEL

3.1. Thermal conductivity analysis

The thermal conduction performance of double glazing mainly depends on its material, thickness, air layer thickness and sealing performance. Due to the existence of the air layer, the double glazing effectively prevents the direct conduction of heat. In addition, the thermal insulation performance of double glazing can be further improved by adopting glazing materials with low thermal conductivity and optimised sealing structures.
Thermal conductivity of external window: The thermal conductivity of external window is 4.064W/(mK)[4], which can be calculated as: 4.064 W/(mK) / 0.0254 m = 160W/(m^2*°C) under the condition of temperature gradient of 57°C per inch.
Thermal conductivity of the centre window: The thermal conductivity of the centre window is 5.08 W/(mK), which can be calculated as: 5.08 W/(mK) / 0.0254 m = 200W/(m^2*°C) for a temperature gradient of 57°C per inch.
Thermal conductivity of the inner window: The thermal conductivity of the inner window is 0.00061976 W/(mK), and at a temperature gradient of 57°C per inch, the thermal conductivity of the inner window can be calculated as: 0.00061976 W/(mK) / 0.0254 m = 0.0244 W/(m^2*°C)

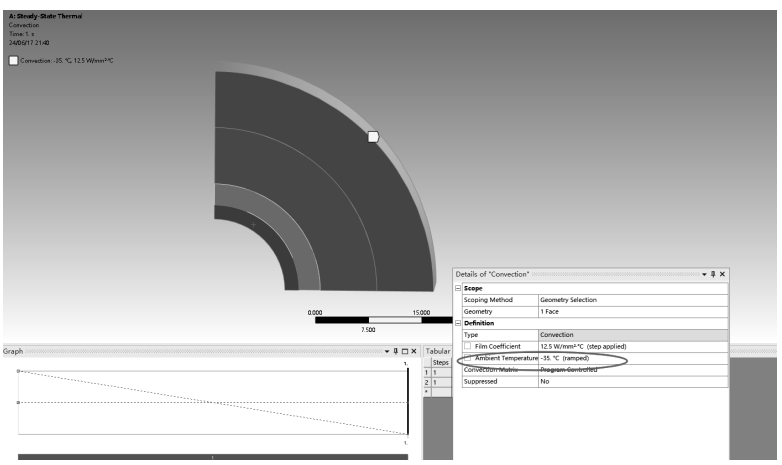

Fig. 2. The temperature of outside

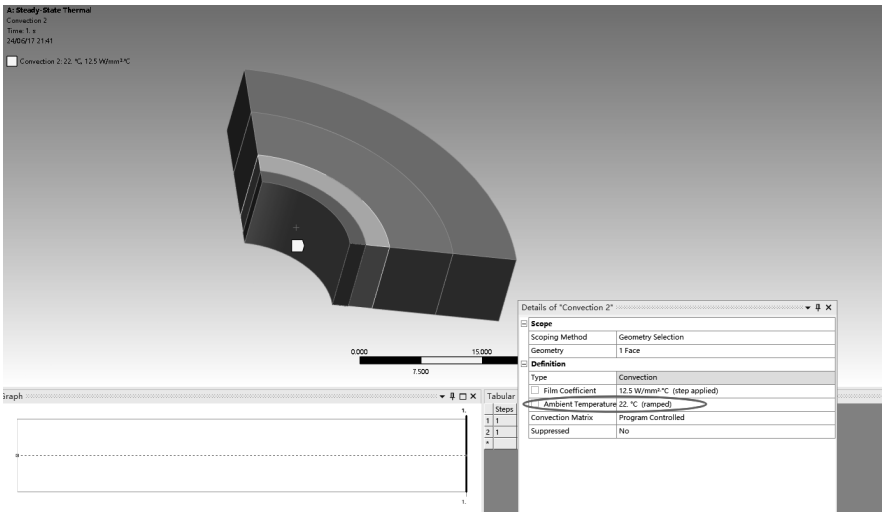

Fig. 3. The temperature of inside

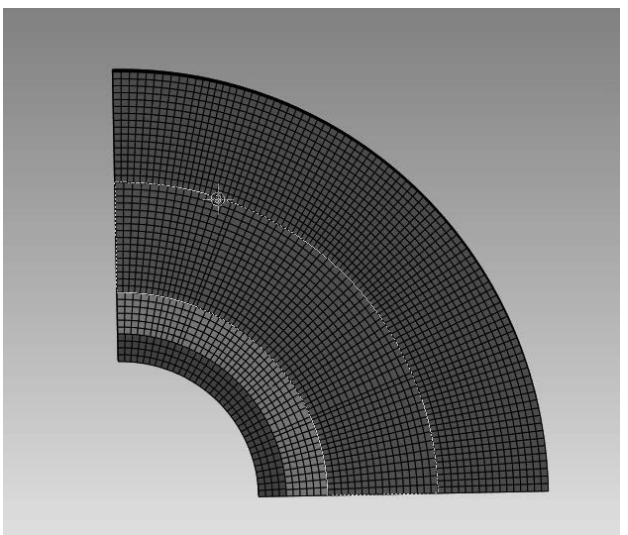

Fig. 4. The meshing of double window model

3.2. Characteristics of thermal stress distribution

Thermal stresses are generated when double glazing is subjected to a temperature gradient[5]. The distribution of thermal stresses is mainly characterised by high stresses in the edge region and relatively low stresses in the centre region. This distribution may have an impact on the strength and stability of double glazing, and therefore needs to be fully considered and assessed during the design and manufacturing process.
Under the influence of temperature gradient, thermal stresses are generated in double glazing.

Thermal stress distribution is characterised mainly by:
Higher stress in the edge region: Due to the uneven stress in the edge region, thermal stress is concentrated, which may lead to cracks or breakage at the stress concentration points.
Relatively small stress in the central region: the distribution of thermal stress in the central region is more uniform, less concentrated stress points.

This distribution characteristic needs to be fully considered during the design and manufacturing process to prevent potential structural damage and safety hazards.

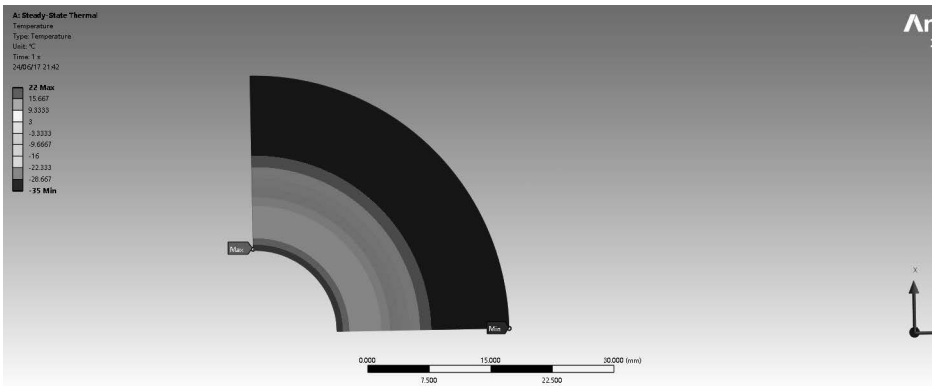

Fig. 5. Distribution of thermal stress

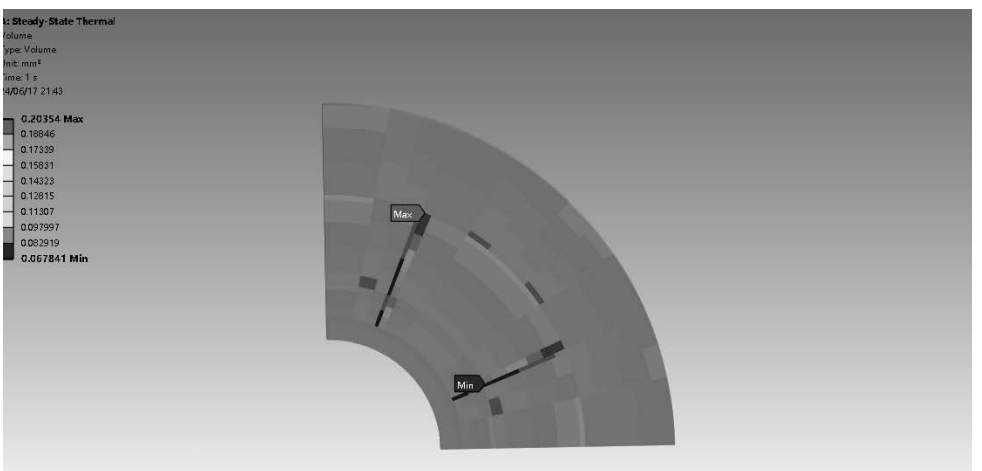

Fig. 6. Distribution of volume changes

3.3. Effect of temperature gradient

The temperature gradient is the difference in temperature between the inner and outer sides of the double glazing. This temperature difference will have an impact on the performance of double glazing, such as leading to the generation and uneven distribution of thermal stresses. Therefore, when designing and using double glazing, the effects of temperature gradients need to be fully considered and measures taken to control and optimise them.
Temperature gradient refers to the temperature difference between the inner and outer sides of double glazing.

This temperature difference can have the following effects on the performance of double glazing:
Lead to thermal stress generation: the greater the temperature difference, the greater the thermal stress generated, which may lead to glass deformation or cracking.
Affects material properties: different materials have different coefficients of expansion over temperature gradients, which may lead to separation or stress concentration at the interface.

Therefore, when designing and using double glazing, it is necessary to give full consideration to the effects of temperature gradients and take appropriate measures to control and optimise them, such as selecting materials with similar coefficients of thermal expansion and improving the sealing structure.

3.4. Thermal insulation effect

Through the heat conduction test and comparative analysis of the double glass, it can be found that the double glass has the following superior heat insulation effect compared with the single glass:
Effectively reduce the temperature change: the temperature change of the inner side of the double glass is significantly smaller than that of the single glass, which can better maintain the stability of the temperature in the cabin.
Improve passenger comfort: Effectively reduce the impact of temperature difference between inside and outside the cabin on passenger comfort, providing a more comfortable flight environment.
Reduce energy consumption: Due to the superior thermal insulation performance, it can reduce the load on the air-conditioning system, lowering energy consumption and achieving energy-saving effects.

4. AIRCRAFT DOUBLE-PANE WINDOW OPTIMISATION AND MAINTENANCE

To address the thermal and safety limitations of double glazing, the following improvements are recommended:
Enhance structural design to improve sealing and insulation;
Use advanced materials and technologies to reduce thermal conductivity;
Increase resistance to impact and fatigue for better safety;
Implement regular inspection and maintenance systems.
Routine inspections are essential to detect cracks, scratches, or other damage that could affect performance. Damaged sections should be repaired or replaced promptly.Cleaning is also important, as accumulated dust or dirt can reduce visibility and potentially harm the glass. Proper cleaning methods and tools should be used to maintain transparency.Moisture resistance must be ensured by keeping the glazing dry and checking seals regularly to prevent water ingress and related issues like corrosion.Finally, repairs and replacements must be performed by qualified aviation technicians who can assess and address problems accurately.

5. SUMMARY

Through a comprehensive analysis of the thermal performance of aircraft double glazing, it can be found that double glazing has significant advantages in terms of heat preservation and insulation, but at the same time, there are also some problems that need to be improved and optimised. In the future, with the development of new materials and technologies as well as the continuous improvement of design methods, it is believed that the performance of double glazing will be further improved and perfected, providing more reliable guarantee for the comfort and safety of aircraft.

REFERENCES

1. O. Aydin, "Determination of optimum air-layer thickness in double-pane windows," *Energy and Buildings*, vol. 32, no. 3, pp. 303–308, 2000.
2. NASA, "Optical Characterization of Window Materials for Aerospace Applications," NASA Technical Reports Server, 2015.
3. Pilkington, "Glass and Thermal Stress," [Online]. Available: https://www.pilkington.com/en/us/architects-page/glass-information/functions-of-glass/glass-and-thermal-stress
4. Sanco, "Glass fracture due to thermal stresses," 2020. [Online]. Available: https://www.sanco.de/fileadmin/user_upload/inhaltsseiten/downloads/EN/SANCO_thermischer_Glasbruch_04-2020_EN_Web.pdf
5. Pilkington, "Glass and Thermal Stress," [Online]. Available: https://www.pilkington.com/en/us/architects-page/glass-information/functions-of-glass/glass-and-thermal-stress
6. A. Rana et al., "Thermal performance of double and triple glazed windows: Experimental results from lab and in-situ measurements," *Energy and Buildings*, vol. 159, pp. 282–295, 2018.

TalentDetector

23th-25th June 2025
Gliwice-Brenna, Poland

DEPARTMENT OF ENGINEERING MATERIALS AND BIOMATERIALS
FACULTY OF MECHANICAL ENGINEERING
SILESIAN UNIVERSITY OF TECHNOLOGY

INTERNATIONAL STUDENTS SCIENTIFIC CONFERENCE

Analysis of reactive power compensation in a 100/15kV station and the suitability of using capacitor banks in the network

Szymon Szeja

Silesian University of Technology, Faculty of Electrical Engineering
email: szymsze085@polsl.pl

Abstract: The article describes the compensation of reactive power of one of the power stations in southern Poland. The feasibility of connecting or disconnecting the capacitor bank was analyzed.

Keywords: reactive power, transformer, capacitor bank

1. INTRODUCTION

This article focuses on the analysis of reactive power compensation in a 110/15 kV station in southern Poland. The presented data are true, provided by the power grid operator Tauron dystrybucja SA. Unfortunately, this data cannot be public, therefore for the purposes of presenting the article the name of the station has been changed (working name: GLIWICE (GLW)).

2. COMPENSATION ANALYSIS

110/15 kV Gliwice (GLW) station operates as a two-section. A BKR1 capacitor bank is installed in section S1, which is powered by a 16 MVA 2-winding 110/15 kV transformer TR1.

A BKR2 capacitor bank is installed in section S2, which is powered by a 16 MVA 2 - winding 110/15 kV transformer TR2, but the bank is not working.

The analysis of the transformer load in the 110/15 kV Gliwice (GLW) station in SCADA WN shows that since 01.08.2022, transformers TR1 and TR2 have been operating in hidden reserve (both transformers TR1 and TR2 are loaded, and the 15 kV clutch is switched off).

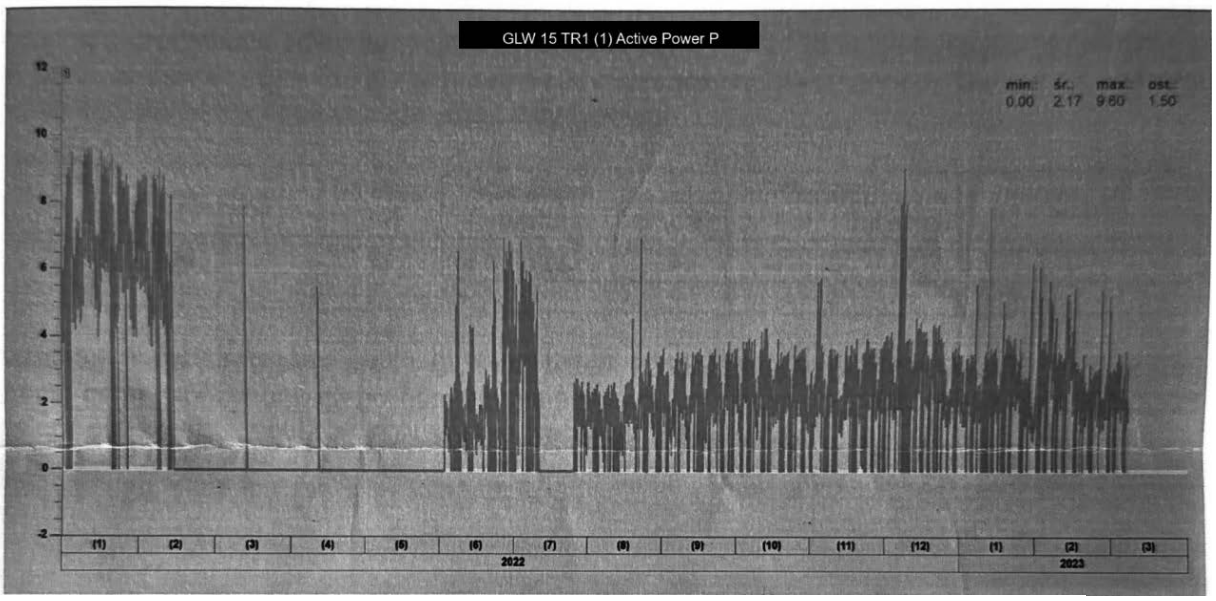

Chart 1. P=f(t) graph in the period from 01.01.2022 to 07.03.2023 - transformer TR1

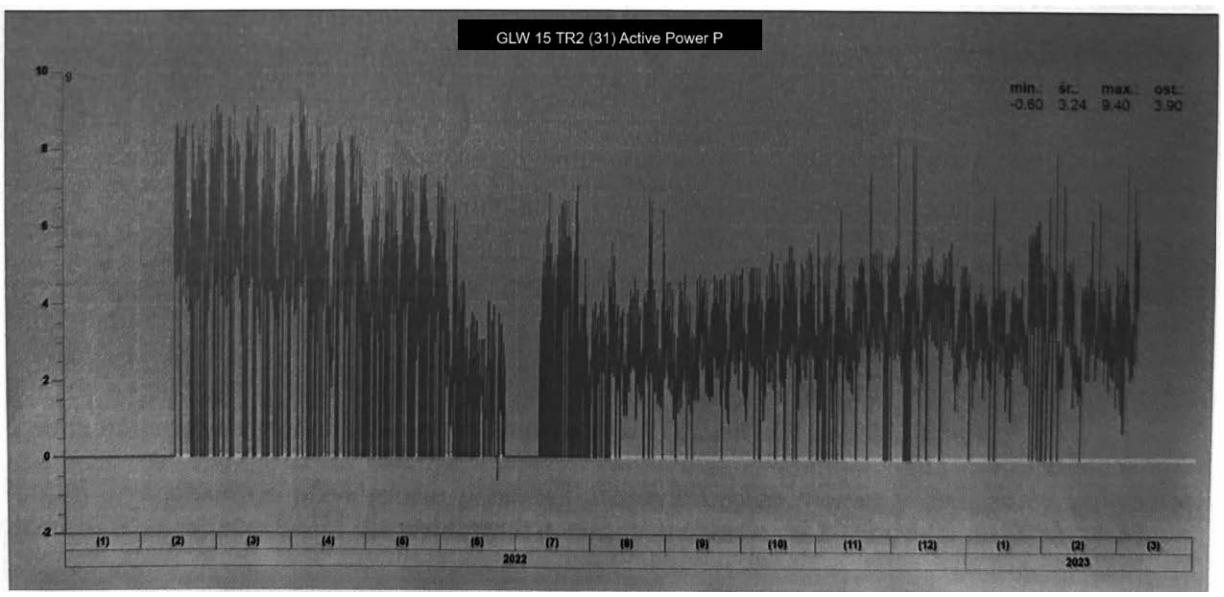

Chart 2. P=f(t) graph in the period from 01.01.2022 to 07.03.2023 - transformer TR2

Therefore, the analysis was carried out for a 7-month operating cycle of the above-mentioned transformers in the period from 01.08.2022 to 28.02.2023.

2.1. S1 SECTION

According to the operation program of the 110 kV power grid of Tauron Dystrybucja SA for the summer of 2022, the BKR1 capacitor bank with a power of Q_{BKR1} = -1.08MVAr should operate continuously throughout the week.

Table 1. Work schedule – summer 2022

station name	voltage [kV]	battery power [Mvar]	work schedule		
			6.00-22.00	22.00-6.00	days off
Gliwice	15	Nr 1 1,08	+	+	+
		Nr 2 0	+	-	-

According to the operation program of the 110 kV power grid of Tauron dystrybucja SA for the winter of 2022/23, the BKR1 capacitor bank with a power of Q_{BKR1} = -1.08MVAr should operate continuously throughout the week.

Table 2. Work schedule – winter 2022/23

station name	voltage [kV]	battery power [Mvar]	work schedule		
			6.00-22.00	22.00-6.00	days off
Gliwice	15	Nr 1 1,08	+	+	+
		Nr 2 0	+	-	-

However, the current waveforms IBKR1 = f(t) of the BKR1 capacitor bank indicate that the operation of this bank deviated from the adopted work schedule. In the period from 01.08.2022 to 28.02.2023, the battery operated continuously, but did not work on weekends.

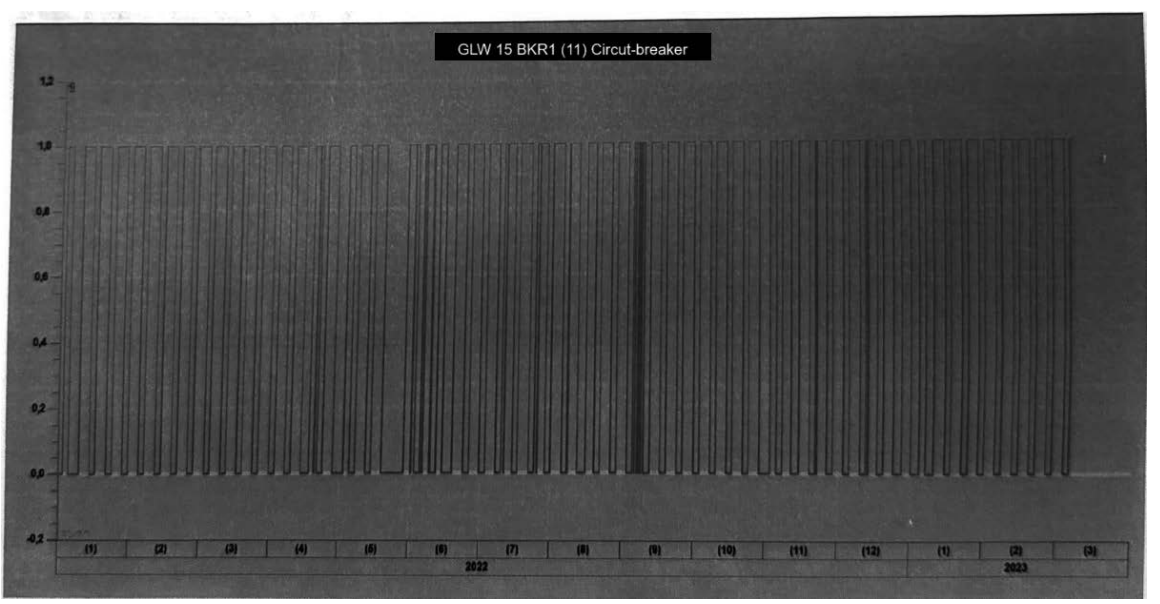

Chart 3. Circuit breaker BKR1 = f(t) engagement graph in the period from 01.01.2022 to 07.03.2023

Below are example waveforms showing the switching moments of the BKR1 capacitor bank circuit breaker for selected months in the period from 01/08/2022 to 31/12/2022.

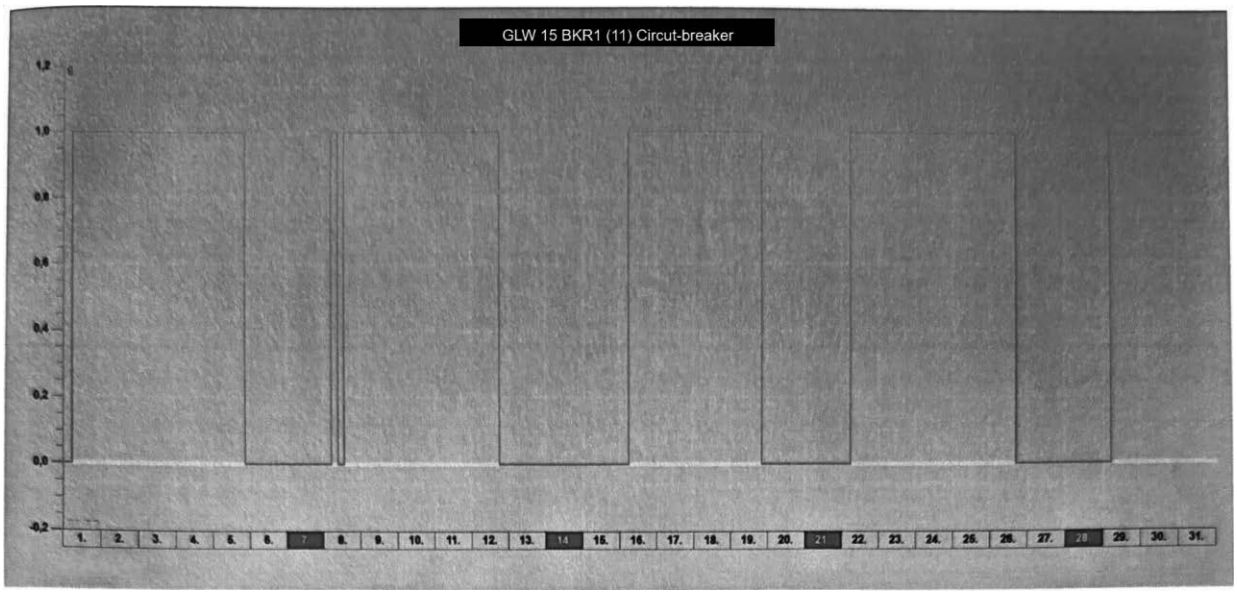

Chart 4. Circuit breaker BKR1 = f(t) engagement graph – 08.2022

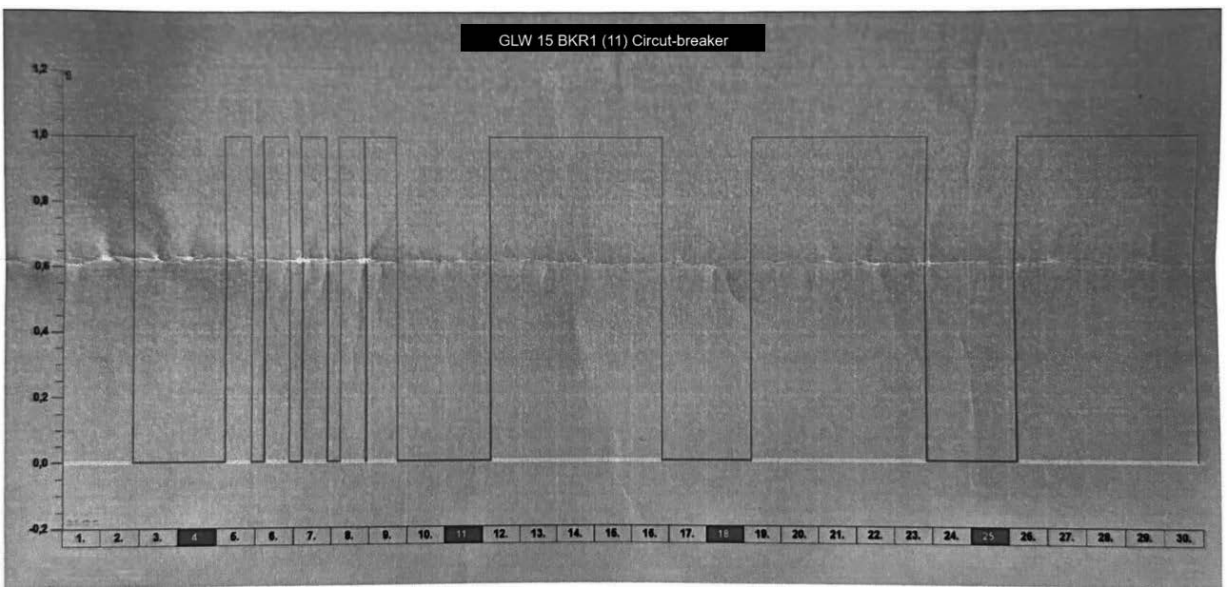

Chart 5. Circuit breaker BKR1 = f(t) engagement graph – 09.2022

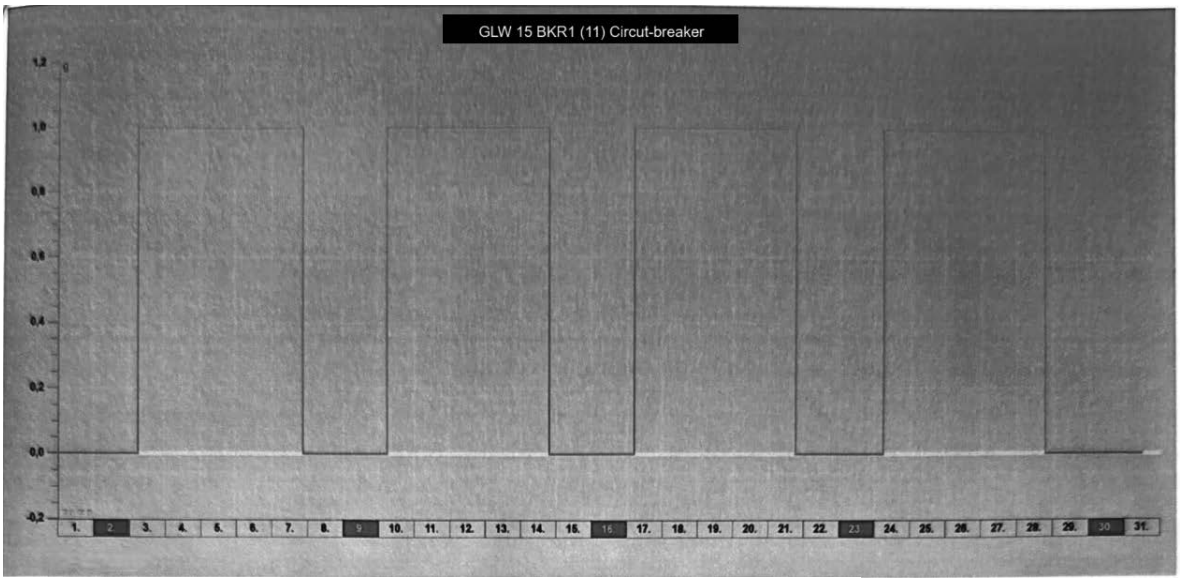

Chart 5. Circuit breaker BKR1 = f(t) engagement graph – 10.2022

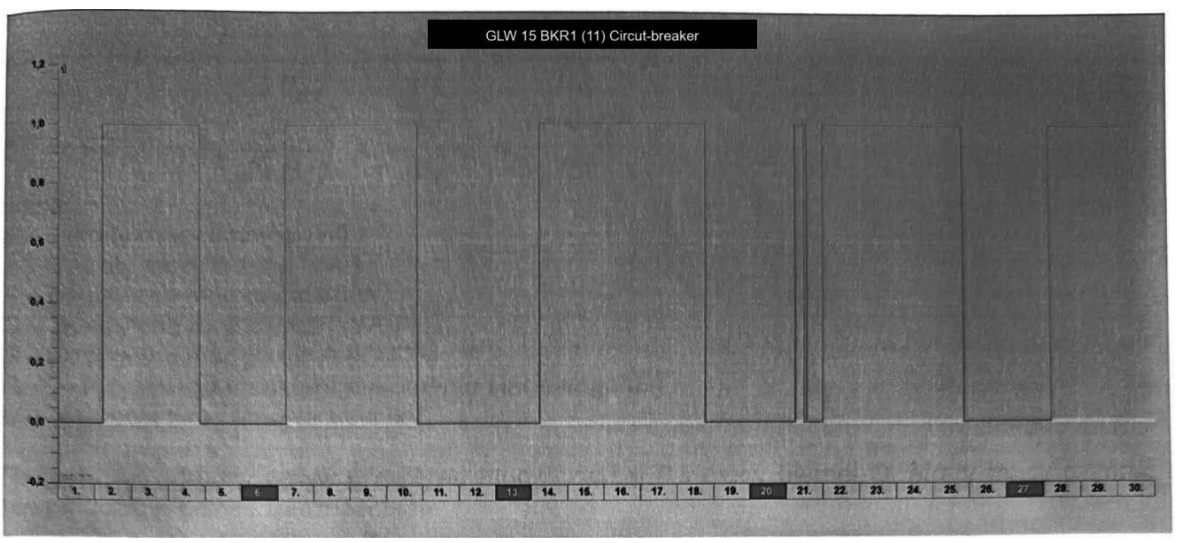

Chart 6. Circuit breaker BKR1 = f(t) engagement graph – 11.2022

The reactive power load graphs of section S1 in the period from 01.08.2022 to 28.02.2023 show that the section is loaded with reactive power Q of a capacitive nature. During this period, section S1 was loaded with reactive power with an average value of Q1 = -0.75 MVAr.

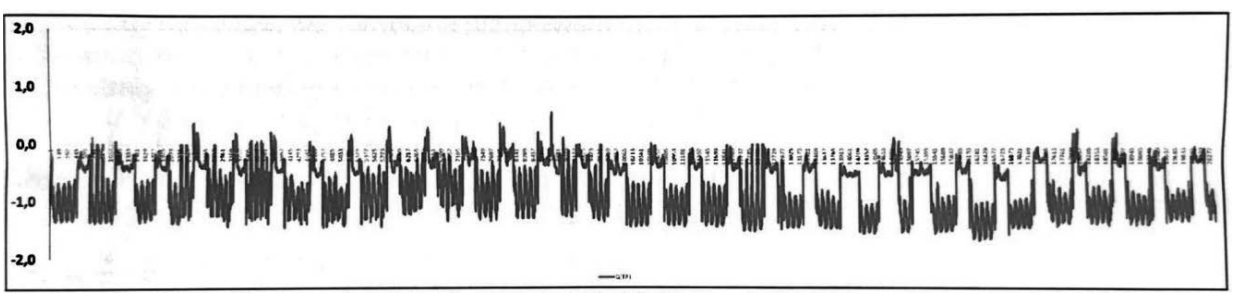

Chart 7. Q1 = f(t) graph in the period from 01.08.2022 to 28.02.2023 - section S1 (actual mileage)

Below is a simulation of the load of section S1 with reactive power Q1sym = f(t) in the period from 01.08.2022 to 28.02.2023 in the event that the capacitor bank used was disconnected (average value Q1symsr = -0.08 MVAr).

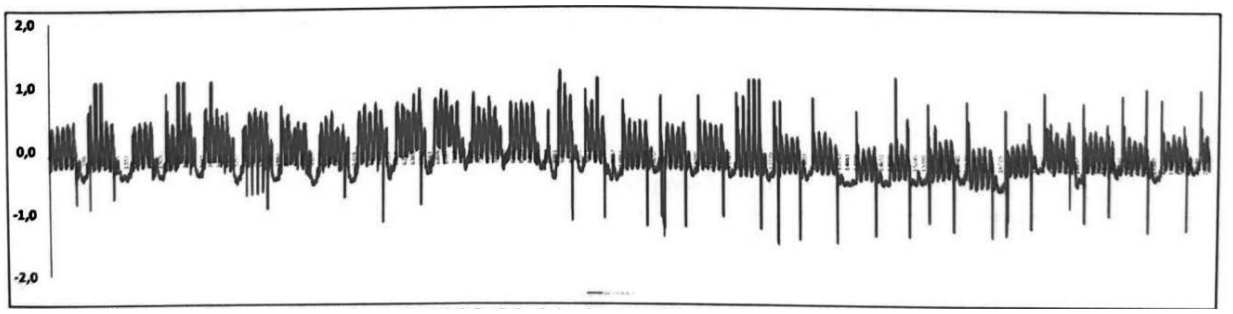

Chart 8. Q1 = f(t) graph in the period from 01.08.2022 to 28.02.2023 - section S1 (capacitor bank shutdown simulation)

3. THE INFLUENCE OF REACTIVE POWER OF THE USED CAPACITOR BATTERY ON POWER LOSSES

The load losses of active and reactive power occurring in the network element are:

$$\Delta P = 3I^2R = 3(\frac{S}{\sqrt{3}U_n})^2 R = \frac{S^2}{U_n^2}R = \frac{P^2+Q^2}{U_n^2} R$$

$$\Delta Q = 3I^2X = 3(\frac{S}{\sqrt{3}U_n})^2 X = \frac{S^2}{U_n^2}X = \frac{P^2+Q^2}{U_n^2} X$$

ΔP - active power losses [W]
ΔQ - reactive power losses [Var]
P - Transmitted active power [kW]
Q - Transmitted reactive power [kVAr]
S - Transmitted apparent power [kVA]
R, X - Resistance and reactance of the network element [Ω]
U_n - rated network voltage [kV]

Considering the separate influence of the active power flow P and reactive power flow Q, the active and reactive power losses can be described by the following relations:

$$\Delta P = \frac{P^2+Q^2}{U_n^2} R = \frac{P^2}{U_n^2}R + \frac{Q^2}{U_n^2}R = \Delta P_a + \Delta P_r$$

$$\Delta Q = \frac{P^2+Q^2}{U_n^2} X = \frac{P^2}{U_n^2}X + \frac{Q^2}{U_n^2}X = \Delta Q_a + \Delta Q_r$$

ΔP_a - Active power losses due to active power flow [W]
ΔP_r – Active power losses caused by reactive power flow [W]
ΔQ_a - Reactive power losses caused by active power flow [Var]
ΔQ_r – Reactive power losses due to reactive power flow [VAr]
Considering power losses originating only from reactive power flow, they can be defined as:
active power losses caused by reactive power flow:

$$\Delta P_r = \frac{Q^2}{U_n^2} R$$

Reactive power losses caused by reactive power flow:

$$\Delta Q_r = \frac{Q^2}{U_n^2} X$$

Since in our case U, R, X are constant, the level of losses is determined only by the reactive power flow Q and in particular Q^2.

4. SIMULATION FOR SECTION S1

The table below presents the analysis results for different variants of the capacitor bank operation. For each variant, the sum of the reactive power values in each quarter of time $\sum Q^2$ was calculated in order to determine the most advantageous variant, generating the lowest active and reactive power losses on the transformer.

Table 3. Analysis results for different variants of the capacitor bank operation

Variant description	Battery power [MVAr]	Battery schedule	∑Q2 (value affecting active power losses)
Current status (according to the recorded battery operation in SCADA WN)	1,08	Actual (based on recorded measurements)	15 026
When the battery is completely disconnected	-	battery disconnected	2 410
Status with existing battery operating according to the schedule specified in the network operation program	1,08	On weekdays: continuous work On weekends: continuous work	29 813
Condition with existing battery - working according to the new schedule (optimal, generating the lowest active power losses)	1,08	On weekdays: 7-15 On weekends: continuous work	5 658
Status when changing battery power and schedule (selection of optimal battery power and schedule)	0,216	On weekdays: 7-15 On weekends: continuous work	2 123

5. CONCLUSIONS

During the majority of the operating time in the period from 01.08.2022 to 28.02.2023, section S1 was loaded with reactive power Q of a capacitive nature with an average value of Q_1 = - 0.75 MVAr, which indicates overcompensation with capacitive reactive power of this section.

The simulation results indicate that in the analyzed period with the recorded load in section S1, active and reactive power losses would be smaller with a significantly reduced capacitor bank power and the adoption of a new work schedule or when disconnecting the battery.

In connection with the above, it is recommended to disconnect the capacitor bank as the simplest solution.

In summary, the phase-out of traditional capacitor banks in high-voltage networks is due to the emergence of more advanced and flexible compensation technologies and the changing structure of the power system, in which distributed sources such as photovoltaics play an active role.

ACKNOWLEDGEMENTS

The work was created as part of project based learning - PBL, in the 12th competition under the Initiative of Excellence - Research University, Silesian University of Technology, Gliwice, Poland.

BIBLIOGRAPHY

1. B. Witek, Projektowanie elektroenergetycznych układów przesyłowych, Gliwice 2013,
2. S. Bolkowski, Elekrotechnika, Warszawa 1994,
3. W. Orlik, Badania I pomiary elektroenergetyczne dla praktyków, Krosno 2015,
4. K. Żmuda, Elektroenergetyczne układy przesyłowe i rozdzielcze, Gliwice 2016.

TalentDetector
23th-25th June 2025
Gliwice-Brenna, Poland
DEPARTMENT OF ENGINEERING MATERIALS AND BIOMATERIALS
FACULTY OF MECHANICAL ENGINEERING
SILESIAN UNIVERSITY OF TECHNOLOGY
INTERNATIONAL STUDENTS SCIENTIFIC CONFERENCE

Analiza numeryczna własności mechanicznych wspornika schodowego

Mateusz Szojda[a], Bianka Wyrobek[a], Agata Śliwa[b], Marek Sroka[b]

[a] Akademickim Liceum Ogólnokształcące Politechniki Śląskiej w Gliwicach
email: matiszojda@icloud.com, wyrobek.bianka@gmail.com
[b] Silesian University of Technology, Faculty of Mechanical Engineering, Department of Engineering Materials and Biomaterials
email: agata.sliwa@polsl.pl, marek.sroka@polsl.pl

Streszczenie: Celem niniejszej pracy było wykonanie symulacji komputerowej dopuszczalnych naprężeń mechanicznych powstałych we wsporniku schodowym ze stali S355N. Analiza została wykonana w programie SolidWorks, wykorzystującym metodę elementów skończonych.
Abstract: The aim of this study was to simulate the permissible mechanical stress caused bracket stair steel S355N. The analysis was performed using simulation module of SolidWorks, by applying finite element method.

Słowa kluczowe: SolidWorks, naprężenia mechaniczne, wspornik, stal S355N

1. WPROWADZENIE

Schody wspornikowe to specyficzna konstrukcja. Są to schody, których budowa opiera się na dążeniu tylko do jednego celu, lekkości kompozycji i osiągnięciu minimalizmu. Konstrukcja tych schodów oparta jest na stopniach „wychodzących" ze ściany. Trudność polega na odpowiednim dobraniu konstrukcji wsporczej do każdego stopnia. Tak wykonane schody urzekają niezwykłym wrażeniem, jakby wykonano je wbrew prawom fizyki ze ściany. Doskonale komponują się w połączeniu ze szkłem oraz stanowią wzajemne dopełnienie całości konstrukcji. Unikalny design sprawia, że schody wspornikowe stanowią niezapomniany element wystroju wnętrz to także oszczędność miejsca, ponieważ ich minimalistyczna konstrukcja eliminuje zastosowanie elementów nośnych. Sprawia to, że koszt wykonania schodów o takim charakterze jest niższy niż w przypadku tradycyjnych rozwiązań [1,2].

Ich budowa opiera się na widocznych dla użytkowników stopniach, które odmieniają dotychczasowe postrzeganie typowych konstrukcji (Rys.1). Warto zaznaczyć już na samym początku, że schody wspornikowe stawiają określone wymagania ścianie. Jej minimalna grubość to 24cm. Niestety nie każda ściana jest w stanie je spełnić, co stanowi niejako ograniczenie w zastosowaniu schodów wspornikowych. Wewnątrz ściany umieszcza się belkę, do której montuje się poszczególne stopnie. Jednostronny montaż pozwala na wydobycie oryginalności z tego rodzaju schodów. Belki wykonuje się z żelbetu lub ze stali. Najczęściej

zamontowanie stopni odbywa się na placu budowy, ale można skorzystać także z zakupu gotowej konstrukcji [2,3].

Rysunek 1. Schody wspornikowe [1]
Figure 1. Stairs Cantilever [1]

Przedmiotem analizy wytrzymałościowej jest wspornik przeznaczony do schodów wspornikowych. Wspornik mocowany jest do ściany, stanowi podparcie dla pojedynczego stopnia i został przedstawiony na rysunku 2.

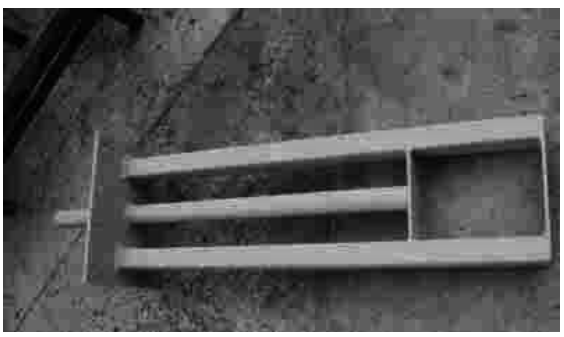

Rysunek 2. Wspornik schodowy [2]
Figure 2. Bracket stair [2]

2. ZAŁOŻENIA MODELOWE

W celu dokonania analizy wytrzymałościowej opartej na elementach bryłowych typu 3D wykonano model CAD wspornika który składa się z dwóch rur o przekroju kwadratowym przyspawanych czołowo do blachy połączonym ze ściana za pomocą śrub. Pomiędzy rurami kwadratowymi wpuszczona jest w blachę rura okrągła stanowiącą usztywnienie konstrukcji i

połączona płaskownikiem z rurami kwadratowymi. Wymiary oraz postać geometryczną wspornika przedstawiono na rysunku 3. Model CAD do analizy wytrzymałościowej został uproszczony poprzez usuniecie zaokrągleń wynikających ze spoin (Rys.4).

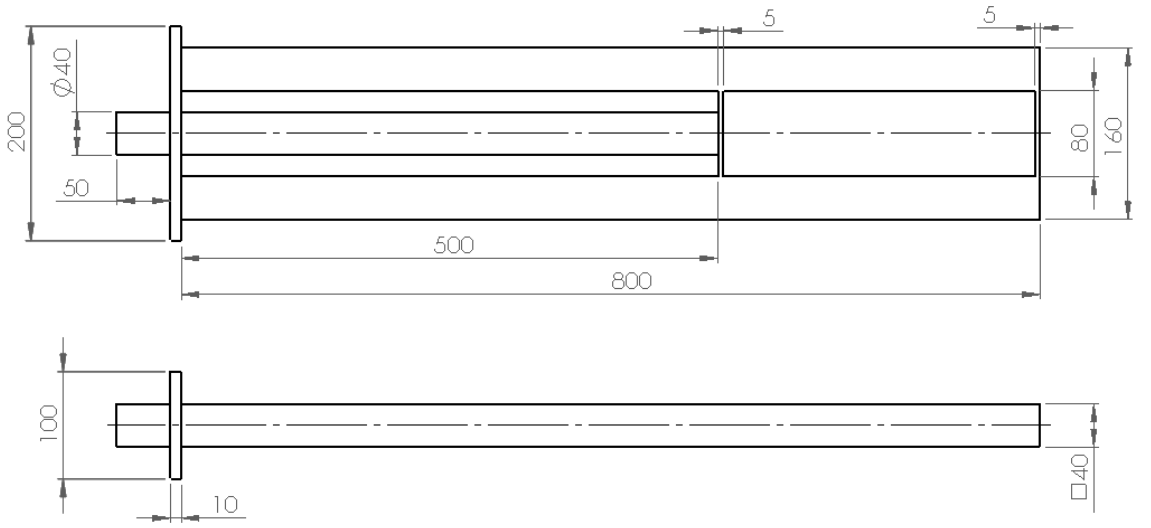

Rysunek 3. Wymiary wspornika schodowego
Figure 3. The dimensions of the bracket staircase

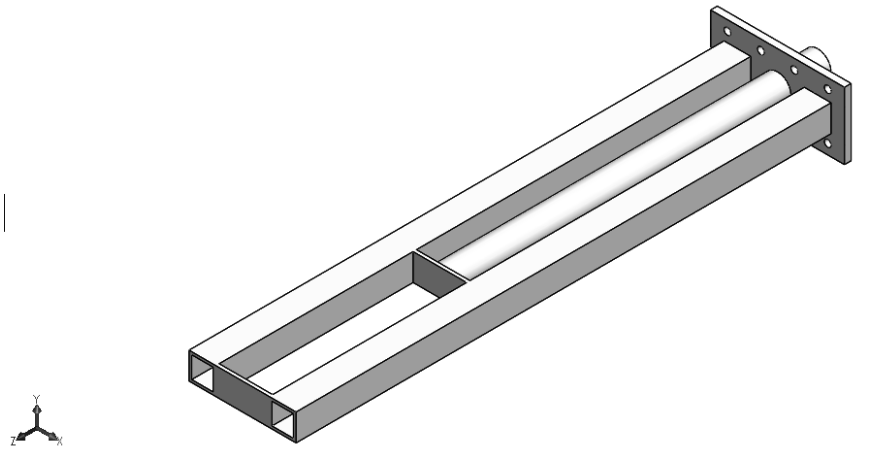

Rysunek 4. Model przestrzenny wspornika schodowego
Figure 4. Model surround bracket staircase

Kolejnym krokiem jest dobór materiału, z którego wykonano wspornik. Na podstawie analizy literaturowej zaproponowano stal konstrukcyjną S355N [4,5].

Parametry stali S355N [5]:
- moduł Younga = 210 GPa
- współczynnik Poissona = 0,28
- gęstość = 7800 kg/m^3
- wytrzymałość na rozciąganie = 450 MPa
- granica plastyczności = 355 MPa

3. ANALIZA ROZKŁADU NAPRĘŻEŃ

Wspornik mocujemy do ściany za pomocą śrub, w tym celu odebrano wszystkie stopnie swobody powierzchniom cylindrycznym w otworach montażowych.

Jako obciążenie wspornika przyjęto masę dwóch osób równą 140 kg. Masa została rozłożona na powierzchni wspornika i dodana jako siła rozłożona na powierzchni czyli ciśnienie (Rys. 5).

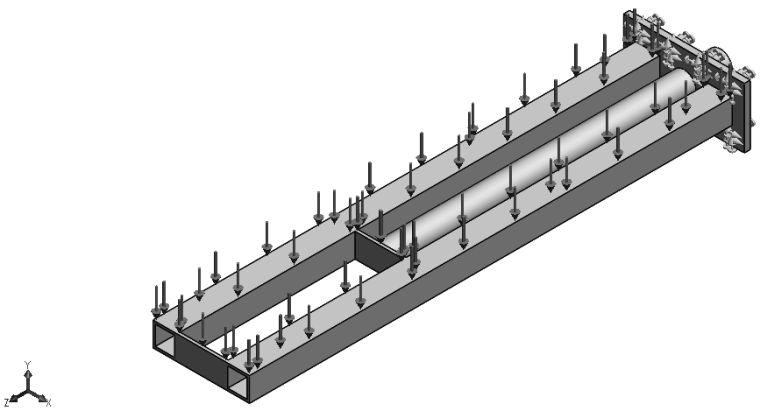

Rysunek 5. Model geometryczny wspornika schodowego z nałożonymi warunkami brzegowymi

Figure 5. Model geometric staircase bracket with imposed boundary conditions

Kolejnym krokiem było nałożenie siatki elementów skończonych na model. Do tego celu użyto element typu tetragonalnego o maksymalnym rozmiarze 10 mm. Dokładne parametry siatki zestawiono w tabeli 1. Na rysunku 6 przedstawiono model geometryczny po dyskretyzacji.

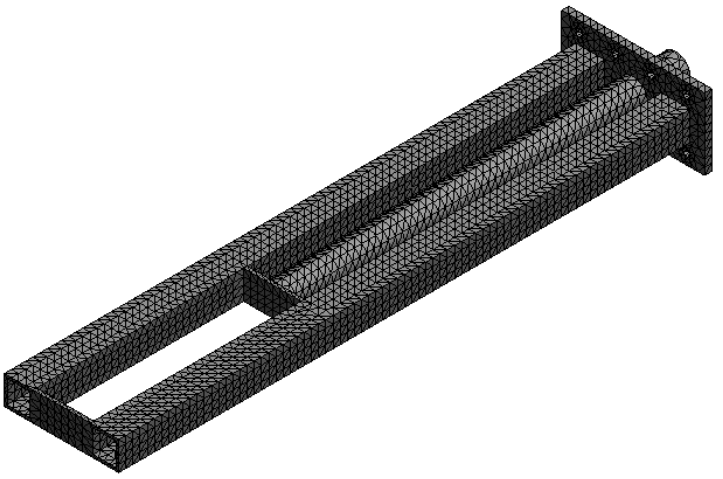

Rysunek 6. Model geometryczna wspornika schodowego z nałożoną siatką elementów skończonych

Figure 6. Model geometric staircase bracket of the applied finite element mesh

Tabela 1. Parametry siatki nałożonej na model geometryczny wspornika schodowego
Table 1. Parameters of the grid imposed on the geometric model of the bracket staircase

Siatka Szczegóły

Nazwa badania	Analiza statyczna 1 (-Domyślna-)
Typ siatki	Siatka bryłowa
Użyty generator siatki	Siatka standardowa
Automatyczne przejście	Wyłączone
Uwzględnij automatyczne pętle siatki	Wyłączone
Punkty jakobianu	4 punktów
Rozmiar elementu	10 mm
Tolerancja	0.5 mm
Jakość siatki	Wysoka
Całkowita liczba węzłów	41024
Całkowita liczba elementów	20713
Maksymalny współczynnik kształtu	11.504
Procent elementów o współczynniku kształtu < 3	67.3
Procent elementów o współczynniku kształtu > 10	0.0193
% zniekształconych elementów (Jacobian)	0
Czas do ukończenia siatki (hh:mm:ss)	00:00:08
Nazwa komputera	JA-KOMPUTER

Na rysunkach 7-12 przedstawiono wyniki analizy MES w postaci map naprężeń oraz przemieszczeń. Na rysunkach 7-8 oraz 11-12 ujęto rzuty izometryczne i boczne. Rysunek 9 przedstawia widok przybliżony w miejscu naprężeń maksymalnych. Fragmenty konstrukcji zilustrowane na rysunku 10 wyraźnie pokazują, że naprężenia zredukowano według teorii Hubera von Missesa przekraczają 36MPa.

Rysunek 7. Mapa naprężeń zredukowanych wg teorii Hubera von Misesa w rzucie izometrycznym

Figure 7. Map of stress reduced by the theory of Huber von Mises isometric

Rysunek 8. Mapa naprężeń zredukowanych wg teorii Hubera von Misesa w rzucie bocznym
Figure 8. Map of stress reduced by the theory of Huber von Mises in a side view

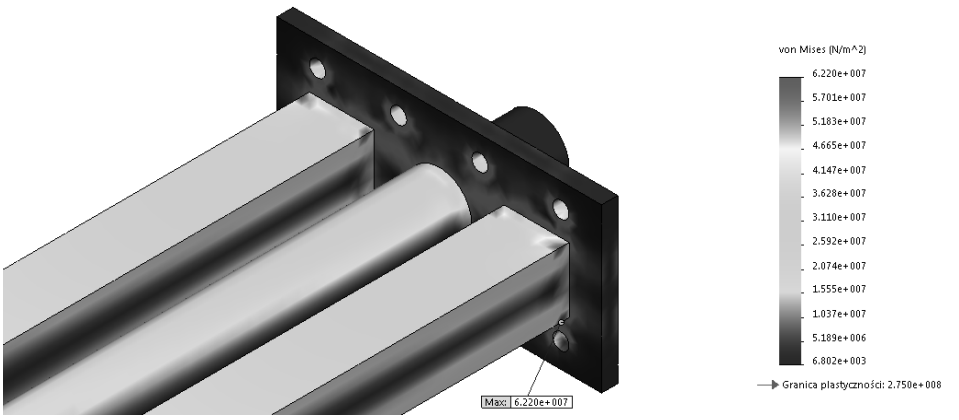

Rysunek 9. Mapa naprężeń zredukowanych wg teorii Hubera von Misesa w widoku przybliżonym na miejsce naprężeń maksymalnych
Figure 9. Map of stress reduced by the theory of Huber von Mises to view the approximate location of maximum stress

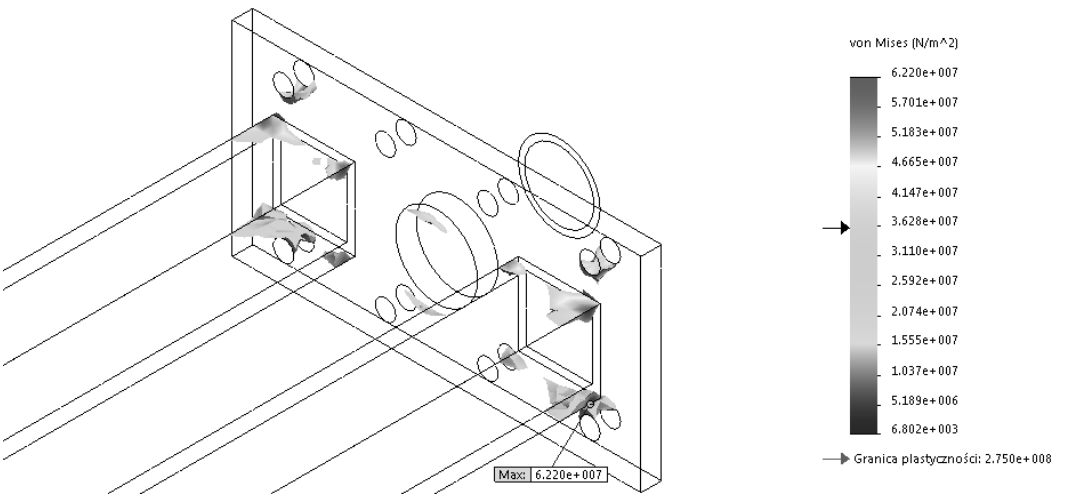

Rysunek 10. Fragmenty konstrukcji, w których naprężenia zredukowane według teorii Hubera von Misesa przekroczyły 36 MPa

Figure 10. Portions of the structure in which the equivalent stresses according to the theory of Huber von Mises exceeded 36 MPa

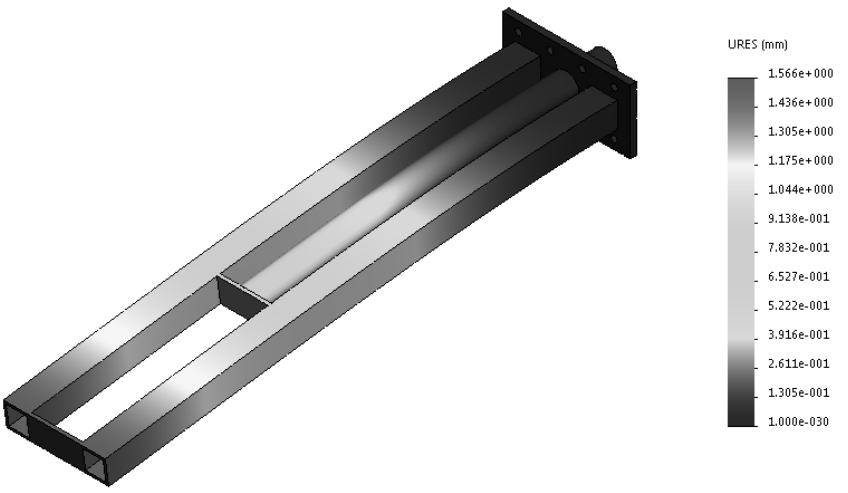

Rysunek 11. Mapa przemieszczeń sumarycznych w rzucie izometrycznym
Figure 11. Displacement map summary isometric

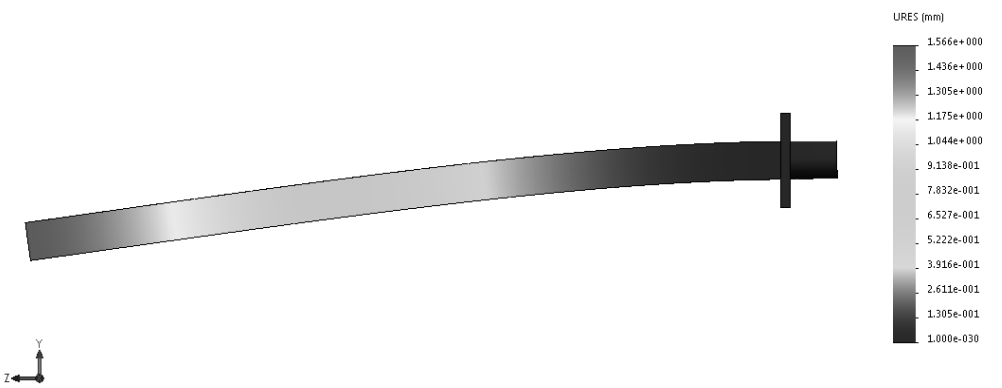

Rysunek 12. Mapa przemieszczeń sumarycznych w rzucie bocznym
Figure 12. Displacement map summary in side view

4. PODSUMOWANIE

W niniejszej pracy przedstawiono analizę wytrzymałościową wspornika schodowego ze stali konstrukcyjnej S355N. Symulację wykonano przy użyciu programu SolidWorks.

Naprężenia maksymalne uzyskane w analizie numerycznej są znacznie mniejsze od naprężeń dopuszczalnych i wynoszą 62 MPa, natomiast maksymalne ugięcie wspornika wynosi 1,5 mm. Współczynnik bezpieczeństwa dla tej konstrukcji wynosi x= 5,7, jest to wartość przewyższająca standardy (od 2 do 2,3), zatem można zastosować materiał o mniejszej granicy plastyczności lub zmienić postać geometryczną wspornika i zredukować masę. Otrzymane wyniki potwierdzają słuszność wyboru stali konstrukcyjnej S355N do produkcji wsporników schodowych.

LITERATURA

[1] http://budujesz.info/artykul/schody-polkowe-wspornikowe-konstrukcja-i-charakterystyka,1575.html
[2]http://www.dom.pl/schody-wewnetrzne-wspornikowe.html
[3]Brzoska Z. Wytrzymałość materiałów. PWN, Warszawa, 1970.
[4]Bąk R, Burczyński T. Wytrzymałość materiałów z elementami ujęcia komputerowego. WNT, Warszawa, 2008.
[5]PN-EN ISO 4957:2004 – Stale narzędziowe.

TalentDetector

23th-25th June 2025
Gliwice-Brenna, Poland

DEPARTMENT OF ENGINEERING MATERIALS AND BIOMATERIALS
FACULTY OF MECHANICAL ENGINEERING
SILESIAN UNIVERSITY OF TECHNOLOGY

INTERNATIONAL STUDENTS SCIENTIFIC CONFERENCE

Influence of tin and niobium on the morphology of calcium phosphate nanowires

Yao M. Tsekpo[a], E. Atioyire[a,b], Weronka Smok[a], Paweł Jarka[a], Tomasz Tański[a]

[a] Silesian University of Technology, Faculty of Mechanical Engineering, Department of Engineering Materials and Biomaterials
[b] Department of Materials Science and Engineering, School of Engineering Sciences, College of Basic and Applied Sciences, University of Ghana, Legon-Accra
email: yao.tsekpo@polsl.pl

Abstract: Calcium phosphate compounds are known to be multifunctional materials with varied applications ranging from biomedicine to pollution remediation. The influence of dopants on the morphology of one-dimensional (1D) structures prepared by the electrospinning technique with non-synthetic calcium as starting material remains understudied. This study employs the use of the sol-gel and electrospinning technique to prepare calcium phosphate nanowires from *Galatea paradoxa* clamshells. The morphology of the resultant nanowires was analyzed using a scanning electron microscope (SEM) and Fourier Transform Infrared Spectroscopy (FTIR). The results obtained revealed that the average wire diameters obtained were between 68 nm – 403 nm. The results imply that the material is suitable for application as a photocatalyst or scaffold for drug delivery.

Keywords: tin, niobium, calcium phosphate and nanowires

1. INTRODUCTION

The scientific community has given calcium phosphate-based nanomaterials considerable attention due to their biocompatibility, osteoconductive properties, and chemical resemblance to human bone [1–3]. These characteristics make them ideal for biomedical applications, such as bioactive coatings, composites, and scaffolds for tissue engineering [4–8]. There are several different types of calcium phosphates (CaPs), including Brushite (DCPD), Monetite (DCPA), Octacalcium Phosphate (OCP), α-Tricalcium Phosphate (α-TCP), β-Tricalcium Phosphate (β-TCP), Amorphous Calcium Phosphate (ACP), Calcium-deficient Hydroxyapatite (CDHA), Hydroxyapatite (HAP), and Tetracalcium phosphate (TTCP) [9]. Because of their apparent significance in orthopaedics and their similarity to bone minerals, hydroxyapatite and tricalcium phosphate have been investigated the most among them [9]. Calcium phosphate compounds promote the use of green chemistry and the circular economy by replacing synthetic calcium precursors with sustainable alternatives. Many techniques for creating calcium phosphate nanostructures with various morphologies have been devised, including the sol-gel technique,

hydrothermal method, solvothermal method, hydrolysis method, precipitation method, electrospinning method, mechanochemical method, and solid-state method [10–13].

A little-known calcium phosphate substance, the HAP nanowires have a variety of uses, including dental applications [14], bone tissue engineering [15], and as bioactive coatings because of their enhanced structural qualities and biocompatibility [16,17]. Interest in this compound has grown as a result of recent research by Tsekpo et al. [18] on the application of tin-doped HAP films for environmental cleanup, particularly for dye removal. The production process affects the morphology, structure, and characteristics of the doped HAP nanowires, much like it does for other calcium phosphate compounds.

Research into generating new morphologies of nanomaterials, notably calcium phosphate compounds, is gaining traction [19–22]. The characteristics of calcium phosphate nanostructures are known to be greatly influenced by their form, and doped HAP structures are no different. Despite the fact that these morphologies are appropriate for drug delivery applications, their manufacturing processes are laborious, time-consuming, and not highly scalable. However, combining the sol-gel and electrospinning techniques simplifies and expedites the preparation of one-dimensional structures, making it suitable for creating one-dimensional doped HAP structures. Since the early 20th century, electrospinning has been used to create ceramic one-dimensional structures because it yields high-quality materials with consistent shape and size distribution and requires minimal post-processing.

In this work, sol-gel and electrospinning methods are used to create Sn and Nb doped HAP nanowires. To comprehend their form and physical characteristics, the nanowires were characterised. *Galatea paradoxa* shells are used in this study as a calcium precursor in a novel way. It looks into how temperature affects the morphology of doped HAP made by electrospinning. The results provide information about the chemical characteristics of doped HAP and point to possible uses in pollution cleanup, biomedicine, and catalysis.

2. MATERIALS AND METHODS

2.1. Materials

Analytic grade orthophosphoric acid (M = 98 g mol^{-1}) of 85% purity was obtained from Przedsiębiorstwo Wielobranżowe B&K, Poland, and was used in this preparation. Clamshells (Galatea paradoxa) were received within a radius of 100 m from the banks of the Volta River, Sogakope, Ghana (GPS coordinates: 5.999602, 0.585249). Ethanol (CH_3CH_2OH, purity 99.8 %, Sigma Aldrich). Poly(vinylpyrrolidone) (PVP, Mw = 1,500,000 g mol^{-1}, Sigma Aldrich).Tin (IV) chloride pentahydrate ($SnCl_4 \cdot 5H_2O$, purity of 98 %) as tin precursor was purchased from Sigma-Aldrich. Ammoniumniobate (V) oxalate hydrate (NbO_xA, $NH_4[NbO(H_2O)_2(C_2O_4)_2]\times xH_2O$, purity 99.9%) as niobium precursor was purchased from Pol-Aura. All other chemicals were of analytical grade. De-ionized water was used in the resining and preparation of solutions in this study.

2.2. Method

$CaCO_3$ was converted to calcium oxide (CaO) by calcining the clamshell powder for one hour at 1200 °C. In order to create the nanowires, the calcined powder was used as a calcium precursor.

This was accomplished by making a 1 M solution of the calcined shell powder, adding 10 wt% of the Sn and Nb precursors, and reacting with a 0.6 M solution of phosphoric acid (H_3PO_4). Known as the precursor solution, the mixture was left to react for the entire night. To create the spinning solution, 2 g of PVP was added to 18 mL of ethanol and swirled for 30 minutes after they had been combined with 2 mL of the precursor solution.

The spinning solution was electrospun using a DOXA Microfluidics Electrospinning Startup Machine under optimal conditions. The setup involved a 15 cm gap between the nozzle and the flat collector, a 20 kV potential difference, and a solution feed rate of 0.7 mL/h through the machine's nozzle. Aluminium foil was used to collect the resulting fibrous polymer-ceramic mats.

Subsequent high-temperature thermal processing was carried out in a Czylok chamber furnace under an air atmosphere. The fibrous polymer-ceramic mats were subjected to calcination for 1 hour at 600 °C (Nb-HAP 600 and Sn-HAP 600) and 700 °C (Nb-HAP 700 and Sn-HAP 700), respectively, followed by cooling inside the furnace. The heating rate was maintained at 2 °C min^{-1}.

2.3. Characterization

To characterise the one-dimensional nanostructures, two studies were carried out using advanced research techniques. A scanning electron microscope (SEM, SUPRA 35 by ZEISS, Germany) with the EDAX Trident XM4 series X-ray spectrometer (EDX) was used to observe the morphology and chemical composition of the samples. The state of the chemical bonds in the samples was analysed using Fourier-Transform Infrared Spectroscopy (Nicolet 6700 from Thermo Scientific, USA) in the Attenuated Total Reflectance (ATR) mode.

3. RESULTS AND DISCUSSION

Figure 1 depicts the SEM analysis of the composite nanofibres after heat treatment. Heat treatment at 600 ºC (Figure 1A and 1B) formed multiple ceramic nanostructures, resulting in a one-dimensional configuration with a consistent diameter along the entire length of the nanowire. The nanowires were observed to be cylindrical and decorated with particles along its length. The diameters of these one-dimensional nanostructures were measured using SEM images, and a histogram of the diameter size distribution was generated. This examination of the diameter size distribution made it easier to determine the diameter range of all acquired nanowire samples, which ranged from 68 to 153 nm for Sn-HAP 600 and 60 to 403 nm for Nb-HAP 600. Sn doped HAP is seen to have narrower diameters as compared to Nb-HAP and this is because the addition promotes structural refinement[18].

Conversely, with the heat treatment at 700 ºC (Figures 1C and 1D), the one-dimensional structure is seen to degenerate, and sintering begins with the particles having varying oblong and circular shapes for Nb-HAP 700 (Figure 1C) however Sn-HAP 700 (Figure 1d) is seen to remain stable at this temperature with minimal changes to the structure which is indicative of thermal stability.

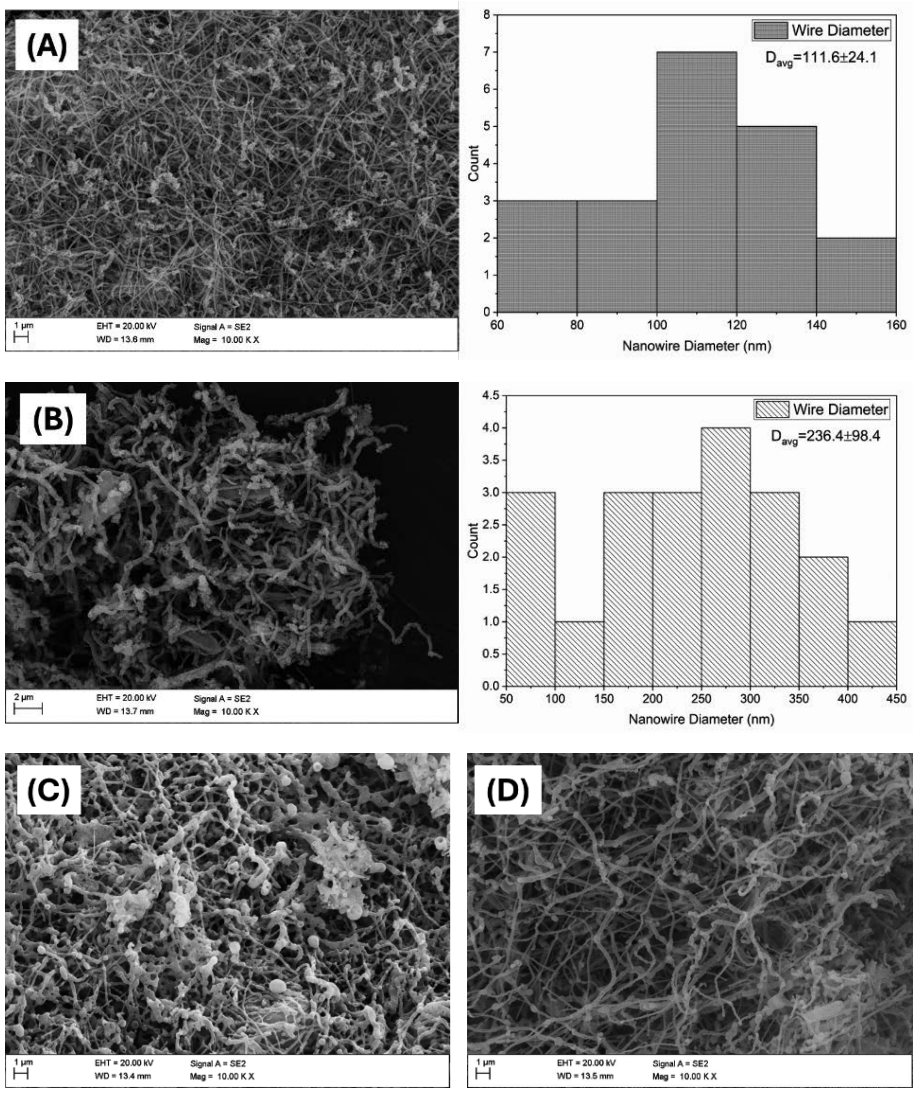

Figure 1. Image and Wire distribution of Sn-HAP 600(A), Image and Wire distribution of Nb-HAP 600(B), Nb-HAP 700 (C) and Sn-HAP 700(D)

Figure 2, shows the FTIR spectra of in-doped hydroxyapatite (Sn-HAP) samples sintered at 600°C (Sn-HAP600) and 700°C (Sn-HAP700). The spectral bands in the range 500–1200 cm^{-1} are characteristic of phosphate (PO_4^{3-}) vibrational modes. Specifically, the stronger and more well-defined peaks in Nb-HAP700 indicate an increase in crystallinity, whereas the broader and weaker peaks in Sn-HAP600 suggest lower crystallinity [23].

The ν_4 bending vibration mode of PO_4^{3-} is observed at ~570 cm^{-1} for all samples [24]. For Sn-HAP700, the peaks at 935 cm^{-1} correspond to P—O symmetric stretching vibrations (ν_1), while the peaks at 1018 cm^{-1} and 1080 cm^{-1} represent the P—O asymmetric stretching vibrations (ν_3) of PO_4^{3-} ions [24,25]. These peaks are relatively sharper and more defined in Sn-HAP700 compared to Sn-HAP600, suggesting enhanced crystallinity. Additionally, the peaks at 1153 cm^{-1} and 1209 cm^{-1} are attributed to the bending vibrations of P—O—H [26].

The presence of carbonate (CO_3^{2-}) groups is confirmed by bands appearing around 1400–1600 cm^{-1}. The peaks at 1540 cm^{-1} and 1606 cm^{-1} correspond to the ν_4 bending vibrations of carbonate

ions [27], which are more pronounced in Sn-HAP600. This suggests a higher carbonate content in Sn-HAP600, which decreases with increasing sintering temperature [28].

The peaks around 3000 cm^{-1} and 3500 cm^{-1} correspond to hydroxyl (HO^{-1}) stretching vibrations [28]. The decreasing intensity of these peaks with increasing temperature suggests the removal of surface and lattice water as well as carbonate decomposition.

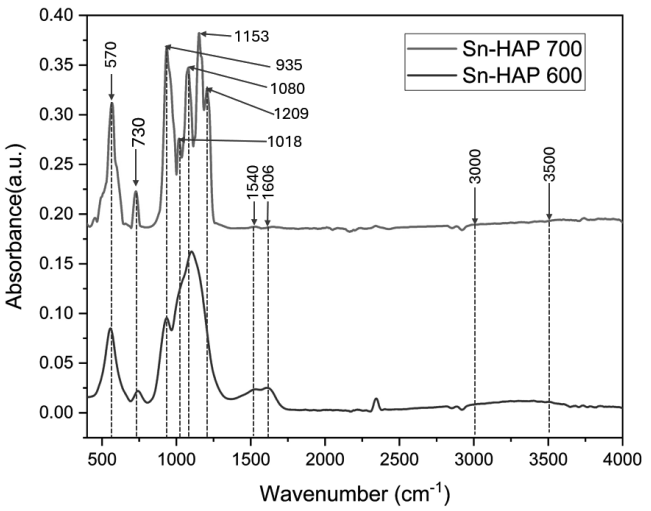

Figure 2. FTIR spectra of Sn-HAP

Figure 3 presents the FTIR spectra of niobium-doped hydroxyapatite (Nb-HAP) samples sintered at 600°C (Nb-HAP600) and 700°C (Nb-HAP700). The spectral bands in the range 500–1200 cm^{-1} are characteristic of phosphate (PO_4^{3-}) vibrational modes. Specifically, the stronger and more well-defined peaks in Nb-HAP700 indicate an increase in crystallinity, whereas the broader and weaker peaks in Nb-HAP600 suggest lower crystallinity [23] similar to the trends observed in Sn-HAP samples.

The ν_4 bending vibration mode of PO_4^{3-} is observed at $\sim 570\ cm^{-1}$ for all samples [24]. For Nb-HAP700, the peaks at 930 cm^{-1} correspond to P—O symmetric stretching vibrations (ν_1), while the peaks at 1020 cm^{-1} and 1074 cm^{-1} represent the P—O asymmetric stretching vibrations (ν_3) of PO_4^{3-} ions [24,25].Additionally, the peaks at 1151 cm^{-1} and 1207 cm^{-1} are attributed to the bending vibrations of P—O—H [26].

The presence of carbonate (CO_3^{2-}) groups is confirmed by bands appearing around 1400–1600 cm^{-1}. The peaks at 1520 cm^{-1} and 1610 cm^{-1} correspond to the ν_4 bending vibrations of carbonate ions [27], which are more pronounced in Nb-HAP600. This suggests a higher carbonate content in Nb-HAP600, which decreases with increasing sintering temperature [28].

In addition to phosphate and carbonate absorption bands, the hydroxyl (HO^{-1}) stretching vibrations are detected in the regions of 3000 cm^{-1} and 3500 cm^{-1} [28]. The decreasing intensity of these peaks with increasing temperature suggests the removal of surface and lattice water as well as carbonate decomposition, which is consistent with the behavior observed in the Sn-HAP samples.

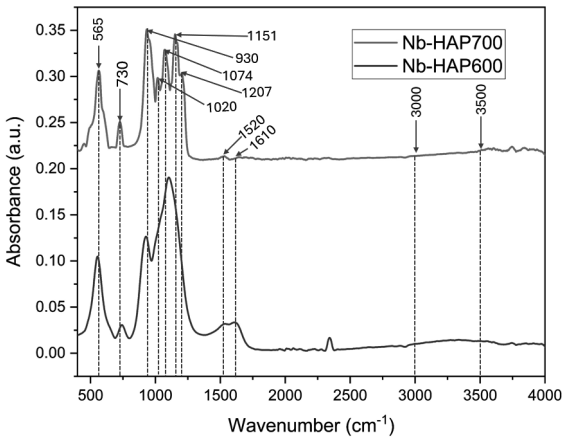

Figure 3. FTIR spectra of Nb-HAP

4. CONCLUSION

This study presents a method for synthesizing novel doped HAP one-dimensional nanowires using sol-gel and electrospinning techniques, emphasising green chemistry and the circular economy for biomedicine, catalysis, and pollution remediation. Findings confirms the formation of ceramic doped HAP nanowires from *Galatea paradoxa* shell powder as a calcium precursor, with diameters ranging from from 68 to 153 nm for Sn-HAP 600 and 60 to 403 nm for Nb-HAP 600. The study highlights temperature sensitivity in nanowire formation. While focusing on *Galatea paradoxa* shell powder as an alternative to synthetic calcium precursors, the research encourages future exploration of bio-derived materials in electrospinning for various nanostructures. The main contribution lies in creating nanoscale doped HAP structures using cost-effective, scalable technology for applications in bone regeneration, photocatalyst and pollutant adsorption. Despite investigating the physical and chemical properties of the nanowires, unanswered questions remain, including the effects of time on formation, additional characterisation of optical and dielectric properties, and influences of dopants, which could enhance material understanding and propose new applications.

REFERENCES

[1]S.A. Shah, M. Sohail, P. Nakielski, C. Rinoldi, S.S. Zargarian, A. Kosik-Kozioł, Y. Ziai, M.A. Haghighat Bayan, A. Zakrzewska, D. Rybak, M. Bartolewska, F. Pierini, Integrating Micro- and Nanostructured Platforms and Biological Drugs to Enhance Biomaterial-Based Bone Regeneration Strategies, Biomacromolecules (2024). https://doi.org/10.1021/ACS.BIOMAC.4C01133/ASSET/IMAGES/LARGE/BM4C01133_0008.JPEG.

[2]X. Tan, S.B. Shabestari, B. Noshadi, A. Ghorbani, F. Iranmanesh, A. Asefnejad, A New Approach to Ceramics Based on the Tissue Reaction: A Versatile Ceramic for Pharmaceutical, Dental and Ancient Artifacts Applications Using Machine Learning (ML) Modeling, Nanomedicine Research Journal 9 (2025) 283–297. https://doi.org/10.22034/NMRJ.2024.03.006.

[3]T.S.S. Carvalho, J.H. Belo, J.C.C. Abrantes, M. Bañobre-López, D. Lopes, A. V. Kovalevsky, A. Kaushal, J.P. Araújo, S.M. Olhero, P.M.C. Torres, Magnetic and thermo-responsive microparticles based on calcium phosphates with high potential to produce structures for bone regeneration and local hyperthermia, Mater Res Bull 185 (2025) 113274. https://doi.org/10.1016/J.MATERRESBULL.2024.113274.

[4]C. Feng, Y. Wu, Q. Li, T. He, Q. Cao, X. Li, Y. Xiao, J. Lin, X. Zhu, X. Zhang, C. Feng, Y. Wu, T. He, Q. Cao, X. Li, Y. Xiao, J. Lin, X. Zhu, X. Zhang, Q. Li, A Novel Hollow-Tube-Biphasic-Whisker-Modified Calcium Phosphate Ceramics with Simultaneously Enhanced Mechanical Strength and Osteogenic Activity, Adv Funct Mater 32 (2022) 2204974. https://doi.org/10.1002/ADFM.202204974.

[5]S. Mofakhami, E. Salahinejad, Biphasic calcium phosphate microspheres in biomedical applications, Journal of Controlled Release 338 (2021) 527–536. https://doi.org/10.1016/J.JCONREL.2021.09.004.

[6]Y. Zhang, J. Li, M. Soleimani, F. Giacomini, H. Friedrich, R. Truckenmüller, P. Habibovic, Biodegradable Elastic Sponge from Nanofibrous Biphasic Calcium Phosphate Ceramic as an Advanced Material for Regenerative Medicine, Adv Funct Mater 31 (2021) 2102911. https://doi.org/10.1002/ADFM.202102911.

[7]A. Das, S. Ghosh, T. Ringu, N. Pramanik, A Focus on Biomaterials Based on Calcium Phosphate Nanoparticles: an Indispensable Tool for Emerging Biomedical Applications, Bionanoscience 13 (2023) 795–818. https://doi.org/10.1007/S12668-023-01081-6/FIGURES/5.

[8]A. Díaz-Cuenca, D. Rabadjieva, K. Sezanova, R. Gergulova, R. Ilieva, S. Tepavitcharova, Biocompatible calcium phosphate-based ceramics and composites, Mater Today Proc 61 (2022) 1217–1225. https://doi.org/10.1016/J.MATPR.2022.01.329.

[9]S. V. Dorozhkin, Biphasic, triphasic and multiphasic calcium orthophosphates, Acta Biomater 8 (2012) 963–977. https://doi.org/10.1016/J.ACTBIO.2011.09.003.

[10] A. Diez-Escudero, M. Espanol, M.-P. Ginebra, High-aspect-ratio nanostructured hydroxyapatite: towards new functionalities for a classical material, Chem Sci 15 (2024) 55–76. https://doi.org/10.1039/D3SC05344J.

[11] B.-Q. Lu, Y.-J. Zhu, One-dimensional hydroxyapatite materials: preparation and applications, Can J Chem 95 (2017) 1091–1102. https://doi.org/10.1139/cjc-2017-0144.

[12] B. Ma, S. Zhang, F. Liu, J. Duan, S. Wang, J. Han, Y. Sang, X. Yu, D. Li, W. Tang, S. Ge, H. Liu, One-Dimensional Hydroxyapatite Nanostructures with Tunable Length for Efficient Stem Cell Differentiation Regulation, ACS Appl Mater Interfaces 9 (2017) 33717–33727. https://doi.org/10.1021/acsami.7b13313.

[13] B. Ma, S. Zhang, F. Liu, J. Duan, S. Wang, J. Han, Y. Sang, X. Yu, D. Li, W. Tang, S. Ge, H. Liu, One-Dimensional hydroxyapatite nanostructures with tunable length for efficient stem cell differentiation regulation, ACS Appl Mater Interfaces 9 (2017) 33717–33727. https://doi.org/10.1021/ACSAMI.7B13313/SUPPL_FILE/AM7B13313_SI_001.PDF.

[14] P.G. Ittycheria, T. George, M. John, G. Meenu, V. Thomas, S. Aswathy, R. Kuriakose, J. Thomas, Application of Hydroxyapatite in Regenerative Dentistry, in: P. Vizureanu, M.S. Baltatu (Eds.), Novel Biomaterials for Tissue Engineering, IntechOpen, Rijeka, 2024. https://doi.org/10.5772/intechopen.112387.

[15] S. Shaikh, S. Gupta, A. Mishra, P.A. Sheikh, P. Singh, A. Kumar, Laser-assisted synthesis of nano-hydroxyapatite and functionalization with bone active molecules for bone

regeneration, Colloids Surf B Biointerfaces 237 (2024) 113859. https://doi.org/10.1016/J.COLSURFB.2024.113859.

[16] F. Barbosa, F.F.F. Garrudo, P.S. Alberte, L. Resina, M.S. Carvalho, A. Jain, A.C. Marques, F. Estrany, F.J. Rawson, C. Aléman, F.C. Ferreira, J.C. Silva, Hydroxyapatite-filled osteoinductive and piezoelectric nanofibers for bone tissue engineering, Sci Technol Adv Mater 24 (2023) 2242242. https://doi.org/10.1080/14686996.2023.2242242.

[17] J. Wu, C. Jiao, H. Yu, H. Liang, J. Zhao, Z. Tian, C. Wang, D. Wang, L. Shen, A tailored hydroxyapatite/magnesium silicate 3D composite scaffold: Mechanical, degradation, and bioactivity properties, Ceram Int 49 (2023) 35438–35447. https://doi.org/10.1016/J.CERAMINT.2023.08.221.

[18] Y.M. Tsekpo, T. Tański, W. Smok, P. Jarka, A. Kołkowska, D. Łukowiec, Superhydrophililc tin doped hydroxyapatite films using Galatea paradoxa shells, Surf Coat Technol 505 (2025) 132087. https://doi.org/10.1016/J.SURFCOAT.2025.132087.

[19] C. Combes, C. Rey, Amorphous calcium phosphates: Synthesis, properties and uses in biomaterials, Acta Biomater 6 (2010) 3362–3378. https://doi.org/10.1016/J.ACTBIO.2010.02.017.

[20] K. Lin, C. Wu, J. Chang, Advances in synthesis of calcium phosphate crystals with controlled size and shape, Acta Biomater 10 (2014) 4071–4102. https://doi.org/10.1016/J.ACTBIO.2014.06.017.

[21] V. Sokolova, M. Epple, Biological and Medical Applications of Calcium Phosphate Nanoparticles, Chemistry – A European Journal 27 (2021) 7471–7488. https://doi.org/10.1002/CHEM.202005257.

[22] S. V. Dorozhkin, Synthetic amorphous calcium phosphates (ACPs): preparation, structure, properties, and biomedical applications, Biomater Sci 9 (2021) 7748–7798. https://doi.org/10.1039/D1BM01239H.

[23] J. Reyes-Gasga, E.L. Martínez-Piñeiro, G. Rodríguez-Álvarez, G.E. Tiznado-Orozco, R. García-García, E.F. Brès, XRD and FTIR crystallinity indices in sound human tooth enamel and synthetic hydroxyapatite, Materials Science and Engineering C 33 (2013) 4568–4574. https://doi.org/10.1016/j.msec.2013.07.014.

[24] I. Rehman, W. Bonfield, Characterization of hydroxyapatite and carbonated apatite by photo acoustic FTIR spectroscopy, Journal of Materials Science: Materials in Medicine 8 (1997) 1–4. https://doi.org/10.1023/A:1018570213546.

[25] S.N. Kane, A. Mishra, A.K. Dutta, Preface: International Conference on Recent Trends in Physics (ICRTP 2016), Journal of Physics: Conference Series 755 (2016). https://doi.org/10.1088/1742-6596/755/1/011001.

[26] A. Mokhtari, H. Belhouchet, A. Guermat, In situ high-temperature X-ray diffraction, FT-IR and thermal analysis studies of the reaction between natural hydroxyapatite and aluminum powder, Journal of Thermal Analysis and Calorimetry 136 (2019) 1515–1526. https://doi.org/10.1007/s10973-018-7812-8.

[27] W. Korzeniewski, A. Witkowska, Dissolution of Nb-doped hydroxyapatite prepared via low-temperature mechanochemical method: Spectroscopy studies, Nuclear Instruments and Methods in Physics Research, Section B: Beam Interactions with Materials and Atoms 545 (2023). https://doi.org/10.1016/j.nimb.2023.165149.

[28] M. Safarzadeh, C.F. Chee, S. Ramesh, M.N.A. Fauzi, Effect of sintering temperature on the morphology, crystallinity and mechanical properties of carbonated hydroxyapatite (CHA), Ceramics International 46 (2020) 26784–26789. https://doi.org/10.1016/j.ceramint.2020.07.153.

TalentDetector
23th-25th June 2025
Gliwice-Brenna, Poland
DEPARTMENT OF ENGINEERING MATERIALS AND BIOMATERIALS
FACULTY OF MECHANICAL ENGINEERING
SILESIAN UNIVERSITY OF TECHNOLOGY
INTERNATIONAL STUDENTS SCIENTIFIC CONFERENCE

Energy saving technologies for obtaining high purity neon and helium

Irine Ugrekhelidze[a], Tamaz Isakadze[b]

[a,] Technical University of Georgia, Faculty of Transport Systems and Mechanical Engineering, Academic Department of Industrial Engineering and Technologies
E-mail: i.ugrekhelidze@gtu.ge
[b,] Technical University of Georgia, Faculty of Transport Systems and Mechanical Engineering, Academic Department of Industrial Engineering and Technologies
E-mail: tamazisakadze@gmail.com

Abstract: The article discusses the classical technology of recycling neon-helium concentrate. In order to obtain light inert gases, the need to reduce specific energy costs is substantiated. In recycling the neon-helium gas stream, reserves have been identified to reduce operating costs. It is proposed to include a membrane module in the scheme, where the neon flow is simultaneously separated and the mixture is enriched with helium. The efficiency of the technology of receiving neon and helium increases by increasing the duration of the operation cycle of cryogenic adsorbents and reducing the number of compressors.

Key words: neon, helium, separator, compressor, absorber, membrane module.

1. INTRODUCTION

Raw materials for extraction of light inert gases (Ne and He) are obtained simultaneously with the release of oxygen from the atmosphere. Typically, large rectifiers can produce neon-helium mixture products with a content of about 50%. Nitrogen and hydrogen prevail in the concentrate. Purification of H_2 is usually carried out by the oxidation reaction რეაქციით $2H_2 + O_2 \rightarrow 2H_2O$. Neon and helium are inert gases, so they can only be separated by physical methods. Enrichment processes and purification are carried out at temperature T = 30...78K. Cryogenic provision of separation at such temperature levels is associated with significant operating costs. In the conditions of increased competition and increasing costs of energy carriers, the use of energy saving technology is very relevant.

Technological sequence of obtaining high-purity neon

The individual stages of neon and helium production are shown schematically in Figure 1. The process can be divided into several stages.

I. Obtaining cylinders with initial mixture supplied from several sources (usually from oxygen plants of metallurgical enterprises).

II. Purification of the mixture from hydrogen by chemical methods. Absorption and removal of reaction product (H_2O) by condensation and adsorption methods at ambient air temperature.
III. Enrichment of the mixture by condensation of the nitrogen contained in it in a dephlegmator at a temperature of T = 68...77.4 K.
IV. IV. Deep (final) cleaning of the mixture from nitrogen and other impurities in adsorbers at liquid nitrogen temperature (T = 77.4 K).
V. V. Separation of the neon-helium mixture in the column at a temperature of T 30 K, accompanied by the separation of pure neon and helium (yHe 80 %).
VI. VI. Treatment of the flow in the adsorber at the temperature of liquid nitrogen (T = 77.4 K), which is accompanied by the production of pure helium and neon concentrate (yNe 75%).

The schematic diagram of the apparatus for separating the neon-helium mixture is shown in Figure 2.

A purified neon-helium mixture with a natural percentage composition (about 75% Ne and 25% He) and a pressure of P = 0.13 MPa (abs.) enters the circulation compressor K1. After compression at a pressure of P = 2.5 MPa, the flow is gradually cooled in the recuperative heat exchanger TO1 in the nitrogen bath AB and in the low-temperature heat exchanger TO2 at a temperature below 40 K. Under these conditions, neon is partially compressed in the flow of the required mixture. The process of cooling the mixture at temperature T = 30...31 K takes place in the heat exchanger TO3, and then in the IR valve. As a result of the thermal contact of the RK cube of the rectification column with the boiling neon, a large part of the mixture goes into a liquid state. The vapor-liquid mixture of neon and helium is separated in the separator ΦC. As a result, neon gas with a concentration of 20% Ne and the remaining 80% helium is absorbed at the top of the separator as a by-product. In the separator, the helium stream is compressed in the K3 compressor and collected in the high-pressure receiver RVD 1 for further processing.

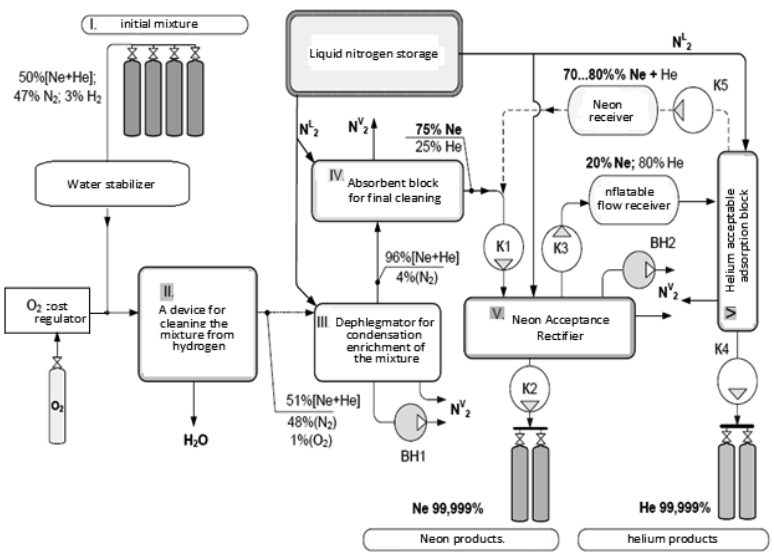

Figure 1. A simplified scheme of the technological sequence of recycling the neon-helium mixture, K1...K5 - membrane compressors, BH1...BH2 - vacuum pumps, N2L - liquid nitrogen, N2 V gaseous nitrogen

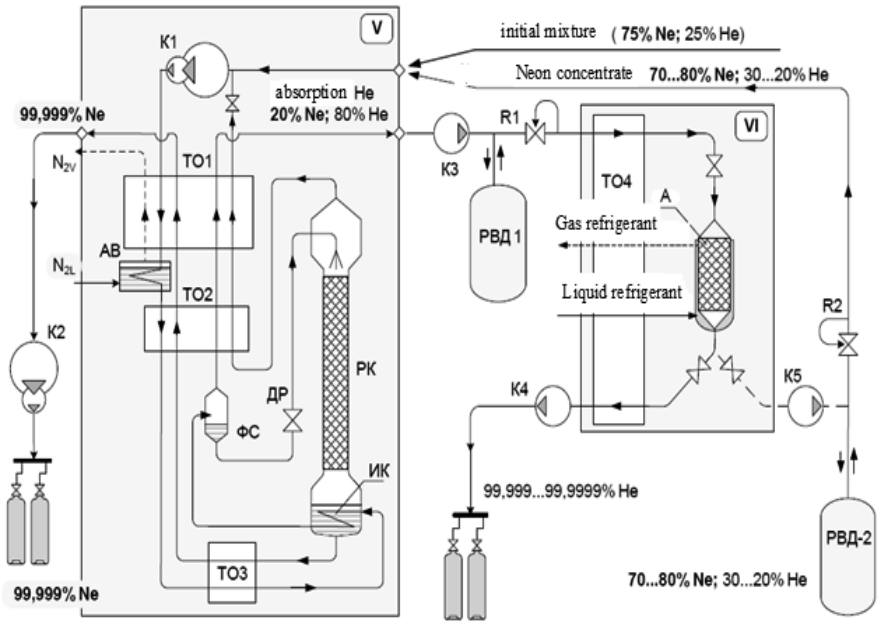

Figure 2. A classic scheme of a complex for the production of high-purity neon and helium

Table 1 – Neon production quality and waste content, (%)

neon	Ne	99,999
hydrogen	H_2	0,00005
helium	He	0,0005
nitrogen	N_2	0,0001
oxygen	O_2	0,00005
carbon monoxide	$CO+CO_2$	0,0001
water	H_2O	0,0001

A liquid is released from the top part of separator ФС, 98% of which is neon, the remaining 2% is helium. The neon-enriched mixture is throttled at the ДР valve and supplied to the contact space РК of the rectification column. The helium-enriched gas flow from the upper part of the rectification column РК enters the inlet of the circulation compressor К1. Pure product neon is obtained in the РК cube of the rectification column, which is vaporized in the low-temperature heat exchanger ТО3, and then successively closed in the heat exchangers ТО2 and ТО1 at the temperature T = 260...280 K. ТО2 and ТО1 heat exchangers also pass the flow of gas coming from the separator ФС and the flow of helium coming out of the rectification column РК.

Optimization of the temperature level of receiving helium by the adsorption method

As can be seen from Figure 2, when taking neon, helium with a composition of 80% is formed. This gas leaves the unit and is collected in the high-pressure receiver РВД 1. The processing of this flow through rectification in block V is ineffective. The return of the

extracted gas to the V circuit for processing will lead to the accumulation of helium and the decrease in the performance of the rectification column PK. This mixture is utilized by adsorption in a separate block VI. Pure helium is obtained during the flow of helium mixture A in the cooling adsorber. Neon, which is absorbed into the sorbent in the mixture stream. After saturation of the adsorber, it is heated and 70...80% neon concentrate is obtained. This charge product is then returned to Unit V to obtain high purity neon.

CONCLUSION

The use of the technology presented in the article allows for a significant increase in the economic performance of He-Ne mixture processing. This positive effect is realized through the multi-stage separation of the neon-helium mixture in the membrane module, where the adsorbers are included. Thus, the introduction of such technology in cryogenics will bring significant energy efficiency to a number of sectors of the public economy.

BIBLIOGRAPHY

1. T.Megrelidze, Z.Jafaridze, S.Suladze, G.Gugulashvili, G.Goletiani, A.Tefnadze, G.Kvirikashvili, Z.Omiadze. Refrigerator machines (Piston compressors). Technikuri Universiteti. Tbilisi: 2009. pp. 52-53.
2. T.Megrelidze, E.Sadagashvili, G.Beruashvili, G.Gugulashvili. Study the optimal working regimes of refrigerator machines with difficult cikle. Transactions of Technical University of Georgia. Tbilisi. Technikuri Universitety. 2011. # 2 (480). Pp. 91-96.
3. Meyer. Training Manual Refrigeration-AC, ICCT, 2004.
4. System Trouble Shooting Measuring Instruments. Danfoss A/S (RC-SM/MWA), 09-2002.
5. Refrigerant Properties Honeywel. Honeywell International Inc., USA, 2006.
6. A.S. Bernshtein Thermoelectric Generators
7. A. Regel Thermoelectric Generators
8. A. I. Karchevsky Thermoelectric materials.
9. A. G. Samoilevich Thermoelectric and thermomagnetic methods of energy conversion.

TalentDetector

23th-25th June 2025
Gliwice-Brenna, Poland

DEPARTMENT OF ENGINEERING MATERIALS AND BIOMATERIALS
FACULTY OF MECHANICAL ENGINEERING
SILESIAN UNIVERSITY OF TECHNOLOGY

INTERNATIONAL STUDENTS SCIENTIFIC CONFERENCE

Laser tattoo removal by Q-switch lasers

Martyna Urbańska[a], Kinga Stępska[b], Mirosław Bonek[c]

[a] Student of Production and Management Engineering, e-mail: mu309689@student.polsl.pl
[b] Student of Production and Management Engineering, e-mail: ks309686@student.polsl.pl
[c] Silesian University of Technology, Faculty of Mechanical Engineering, Department of Engineering Materials and Biomaterials

Abstract: The article shows the use of Q-switch lasers in the process of tattoo removal, taking account the mechanism of biophysical interaction of laser light with tissues. The theory of selective photothermolysis is presented as the basis for effective and precise destruction of pigment without damaging the surrounding tissues. In addition, a non-ablative method is described, consisting in breaking down the pigment without the skin surface. Particular attention is paid to the construction and principle of operation of Q-switched lasers, which generate short, high-energy pulses that enable an effective breakdown of ink molecules. In the article it also includes an overview of the most used types of lasers used depending on the type and colour of pigment.

Keywords laser tattoo removal, Q-switch, the non-ablative method, selective photothermolysis theory, ruby laser, alexandrite laser, Nd: YAG laser

1. INTRODUCTION

A tattoo is a form of permanent decoration of the body that involves the insertion of ink or pigment into the deeper layers of the epidermis using special needles. Tattooing has a very long history – the first traces of this practice is noticing five thousand years back. They were in various cultures around the world and were used for both ritual and aesthetic purposes. [1].
Today, tattoos are a trendy way to express oneself, but the end of the results do not always meet expectations. In such cases, more and more people decide to remove them. There are several methods of tattoo removal, but the most effective and commonly used method is laser tattoo removal.

Laser tattoo removal involves the use of precise, intense pulses of light that break down the pigment in the skin.
One of the most used devices is the Q-switch laser (Quality-Switching). In physics and optics, the Q factor refers to the quality of the resonator (the ability to store energy in the form of light over time). The Q-switch laser allows for temporary energy storage in the laser resonator and then its rapid release in the form of a truly short (nanosecond) and intense light pulse. As a result, the dye is broken down into small fragments, which the body gradually removes. [2]

Although the process requires several treatments, modern technologies results with minimal risk of skin damage.

2. AIM OF THE ARTICLE

The following article aims to present one of the applications of lasers in aesthetic medicine, which is tattoo removal with particular emphasis on the principle of operation and construction of Q-switch lasers.

3. BIOPHYSICAL IMPACT

In the process of tattoo removal, the key factor which enables the operation is the delivery of the right amount of energy to a specific depth in the skin. The absorption of energy in the tissue is possible due to the presence of specific chromatophores.

Chromatophores are the substances which they have the ability to absorb a specific wavelength of radiation. This is the group of atoms in a molecule that absorbs light in the UV-VIS, thanks to which a given compound has a specific colour. Such substances are water, hemoglobin, proteins, or melanin. Each of the above-mentioned substances absorb a different range of radiation.

The chromatophores mentioned above are the basis for the theory of selective thermolysis. In turn, on the basis of this theory, laser tattoo removal is possible.

4. SELECTIVE PHOTOTERMOLYSIS THEORY

The theory has the beginning back to 1983, and its originators were R. Anderson and J.A. Paarish. Interestingly, at first none of the scientific publications were interested in publishing an article on the subject.

Their work was based on two chromatophores melanin and oxyhemoglobin, contained in vessels. [3]

The essence of the therapy was to induce thermal injury in the target structures in an area defined in terms of location and size. In order to avoid excessive heating of the surrounding tissues, the pulse duration should be selected in such a way that it is equal to or shorter than the thermal relaxation time. [4]

Thermal relaxation time is a physical phenomenon in which a heated object loses their heat through conduction to the environment. Its time is different depending on the individual characteristics of a given tissue and its size. As is known, small areas cool down faster than larger ones, which is caused by the fact that the thermal relaxation time is directly proportional to the square of the volume of the irradiated structure. During the phenomenon, a so-called thermal block that occurs achieved by rapid heating of the tissue. Then the diffusion of heat is still limited, thanks to which the energy remains at the place of the pulse. Achieving it will enable selective thermal destruction of the structure. The main factor influencing the occurrence of the phenomenon is the thermal relaxation coefficient, which depends, among other things, on the absorption coefficient and the heat diffusion coefficient. [4]

In short, thermal relaxation is the time it takes to heat the chromophore and dissipate half of the absorbed heat from the surrounding tissues. [5, 6]
In order for the selective photothermolysis theory to occur, the following conditions must be met: [3,6]

1. A wavelength that is better absorbed by the target structures than by the surrounding tissues must be used.
2. The energy density that is delivered must be high enough to achieve the desired temperature in the target structure.
3. The pulse duration must be shorter than or equal to the time needed to cool the target structures.

Based on the above information, we can therefore formulate a definition - the theory of selective photothermolysis consists in the thermal destruction of tissues using generated heat. Its selectivity is achieved by appropriately selecting the wavelength, the energy of which is best absorbed by a specific dye and not by the surrounding tissues.

Due to the thermal relaxation mentioned above, the heat transferred to the surrounding tissues will be minimal only when the pulse time is less than or equal to TRT.
Proper use of the descriptive theory and after selecting the appropriate parameters, limits the likelihood of scarring and other adverse effects.

5. NON-ABLATIVE METHOD

In laser tattoo removal techniques, two types of methods are distinguished – ablative and non-ablative. [1]

Since this article focuses exclusively on laser tattoo removal using Q-switch lasers, information about the ablative method will not be expanded (the ablative method is performed using CO2 lasers).

The non-ablative method involves the selective removal of ink without damaging the surrounding tissues, using a Q-switch laser (nanosecond pulses). The laser energy is selectively absorbed by the dye. [3]

It should be remembered that each colour absorbs different wavelengths. For this reason, in this method, depending on the dye, lasers such as ruby, alexandrite or Nd: YAG are used which will be described in more detail later in the work.

The right selection of laser and parameters is crucial to perform the procedure in a safe and effective way. Before the first procedure, it is recommended to perform a laser test on the skin which helps to determine the above-mentioned parameters and also checks the tissue's reaction. [3, 4]

During the procedure, Q-switch lasers send nanosecond pulses that hit specific tissues. The high rate of pulses causes photomechanical/photoacoustic breakdown of the dye into smaller particles that can be more easily removed from the body. [3,4]

The photomechanical effect (also called photoacoustic) is a process during which light that is absorbed by a material generates acoustic waves. This is caused by an increase in temperature, then an increase in pressure, which ultimately leads to the creation of an acoustic wave that causes so-called micro explosions of pigment molecules. It is the speed at which these lasers operate that causes the energy to be transformed into a shock wave instead of heating the tissue. [7]

Immediately after the tattoo pigment is broken down, some of the particles are immediately removed from the body through micro-damage to the epidermis, while the rest, which is in deeper layers of the skin, is removed by phagocytosis. [3-5]

Phagocytosis is a biological process during which pathogens; dead cell fragments and small particles are absorbed by cells called phagocytes. Thanks to it, cells have the ability to get rid of unnecessary or dangerous elements. It is mainly used by cells of the immune system and also belongs to the mechanisms of innate immunity. Phagocytosis is also of significant importance for maintaining homeostasis. [8]

This involves surrounding the particle with a fragment of the phagocytic cell membrane, and then the cell draws it into its interior. Such a vesicle, containing the particle, is called a phagosome. Its contents are digested using various enzymes and chemicals. [8]

The non-ablative method is characterized by the lack of thermal damage to tissues, which carries a minimal risk of complications. Discoloration, discoloration, and changes in skin texture are rarely encountered. This process is very precise and also allows tattoo removal from delicate areas such as the face or neck. [6]

Unfortunately, the process of tattoo removal using the above method is long-term - it can take several months, and not every color of the dye reacts properly. Some of the most difficult dyes to remove are white and yellow. [5]

6. CONSTRUCTION AND OPERATION OF Q-SWITCHED LASERS

The operation of Q-switch lasers is based on so-called quality factor switching, or Q-switching. The letter “Q” refers to the optical quality of the laser's resonant cavity, specifically to its ability to retain and store energy. By controlling this parameter, it is possible to precisely control the laser's energy emission.

The mechanism of Q-switching involves temporarily blocking the emission of laser radiation, allowing a large amount of energy to accumulate inside the resonator. When the accumulated energy reaches a maximum level, Q-switching occurs, leading to an immediate release of energy in the form of a truly short but extremely intense light pulse. [9,10]

6.1 Q-switching methods

Q-switched lasers can be divided according to the different pulse switching methods used:

1. Rotating mirror Q-switching: In this method, one of the laser's mirrors is mounted on a rapidly rotating axis, allowing light to be emitted only when the mirror is in the correct position.
2. Electrooptic Q-switching: It involves the use of an electro-optical crystal that changes its optical properties under the influence of a voltage, allowing the laser to switch quickly.
3. Acoustooptic Q-switching: In this method, acoustic waves generate changes in the refractive index, which leads to modulation of the light flux.
4. Passive Saturable-Absorber Q-switching: This method involves using a material that absorbs light until it reaches a saturated state and then allows the stored energy to be rapidly released as a pulse.
5. Thin-film Q-switching: In this case, a thin layer of absorber material (such as metallic) is placed on a substrate. When the laser power is increased, this layer burns off quickly, leading to the release of a pulse.

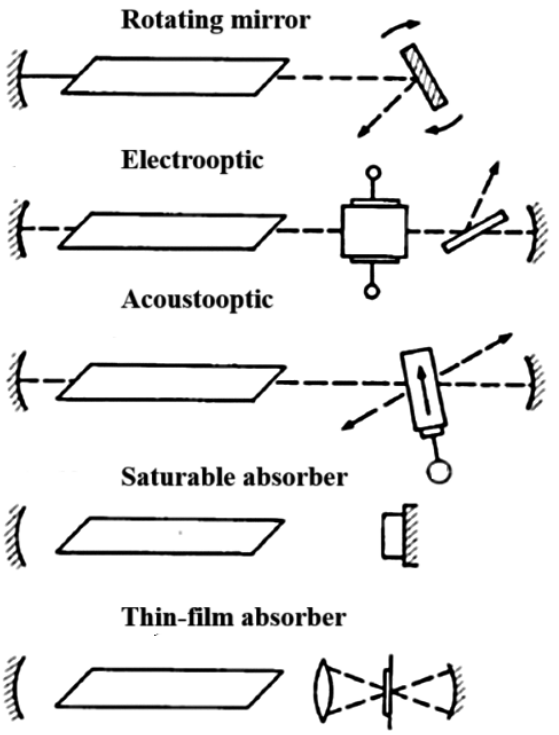

Figure 1. Types of Q-switching [17]

The most common methods used in tattoo removal are electrooptic Q-switching, which provides precise pulse control, and acoustooptic Q-switching, which, although slightly less precise, is useful for lower-power applications. Other methods, such as rotating mirrors, saturable absorber, and thin-film absorber, are rarely used in this technology because of their limited precision and pulse control, which can result in lower efficiency and danger in laser tattoo removal. [12,13,17]

6.2 Principle of active Q-switch lasers

Switching using an external modulator - electrooptic or acoustooptic is used for Active Q-switching. These modulators act as a blocker, stopping the emission of light, and the energy accumulates in the amplification medium. When the stored energy reaches a certain value, the modulator opens, allowing the energy to be released in the form of a strong light pulse. With this process, it is possible to precisely control both the timing, duration, repetition rate and synchronization of the pulses. This system ensures stability and predictability. The principle of Q-switched active lasers can be illustrated with the help of the corresponding diagrams (Figure 2).

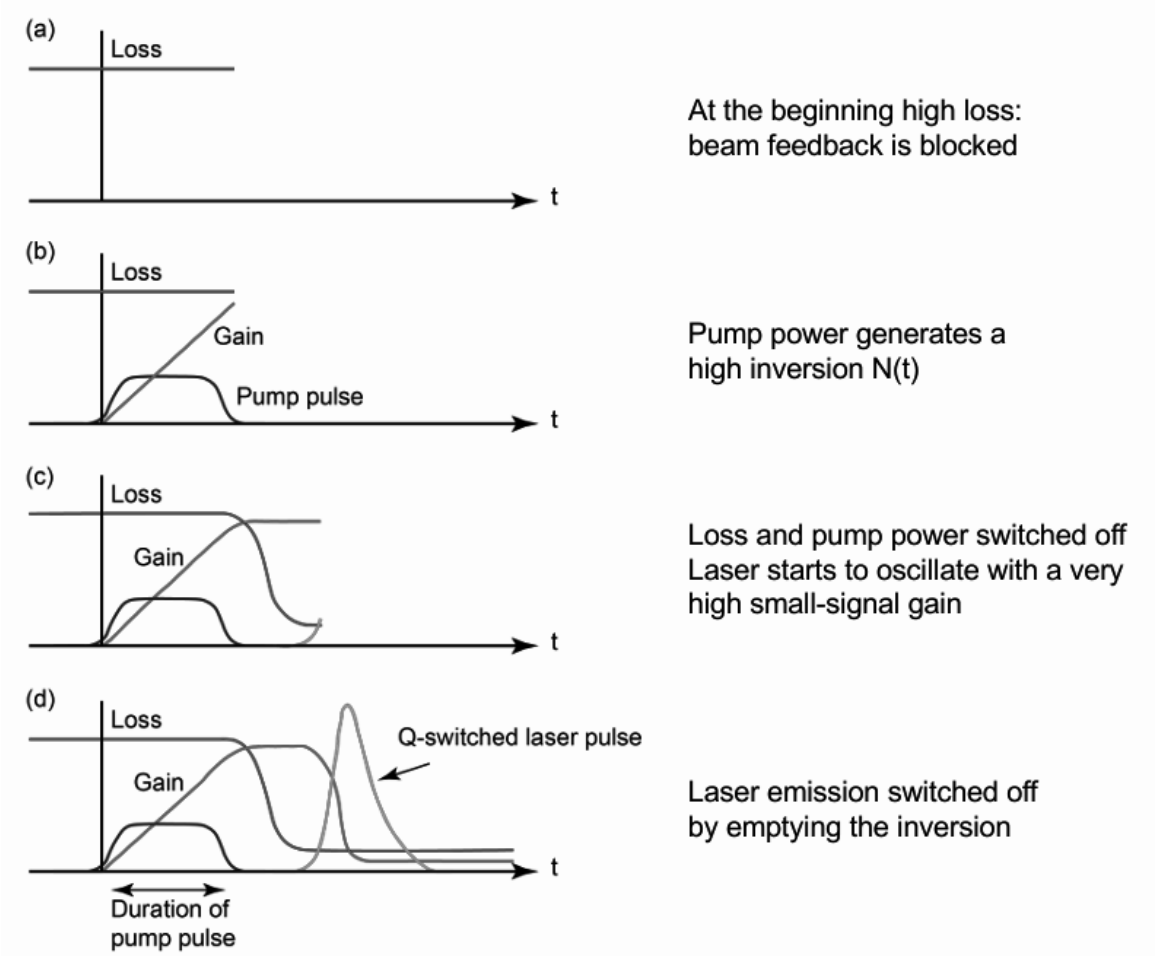

Figure 2. Stages of operation of Active Q-switch lasers [14]

1. Beginning - high loss in the resonator

At the beginning of laser operation, the resonator is deliberately set in high optical loss mode - the quality factor of the resonator (Q) is extremely low. This can be implemented by blocking one of the mirrors or using an Active Q-switch (e.g., electrooptic or acoustooptic). In this phase, the system does not generate laser radiation, because the gain in the active medium is less than the loss.

2. Pumping phase - energy storage

Although no light emission occurs yet, pumping is ongoing – energy from an external source excites atoms in the active medium, leading to a buildup of population inversion. This means that more and more electrons are in an excited state, ready to emit photons. At this stage, the active medium acts as an energy reservoir. The system gain gradually increases, but it is still limited by high losses.

3. Q-switching – sudden drop in losses

When the gain exceeds the losses, a sudden Q-switching event occurs – the losses in the resonator are drastically reduced. This can be achieved by unblocking the mirrors or deactivating the loss modulator. The quality factor (Q) of the resonator increases sharply, and conditions become favorable for laser emission.

4. Laser pulse – rapid energy release

Within a truly short time, a giant laser pulse is generated, characterized by high power and extremely short duration – from nanoseconds to several tens of nanoseconds. The accumulated energy is released abruptly: the population inversion is rapidly depleted (i.e., the active medium "discharges"), the gain drops below threshold, and the emission stops as quickly as it started. The entire emission process lasts significantly less than the pumping time. [14–18]

7. TYPES OF LASERS DEPENDING ON THE PIGMENT BEING REMOVED

Laser tattoo removal is a precise method of eliminating pigment from the skin; however, the effectiveness of the procedure primarily depends on selecting the appropriate laser for the ink color. Each color absorbs light at a different wavelength - therefore, there is no universal laser capable of removing all pigments. Incorrect parameter selection may result not only in ineffective pigment fragmentation or tattoo darkening, but also in skin damage, burns, or scarring.

Before beginning the procedure, it is important to determine what type of pigment was used in the tattoo. This can be particularly challenging with amateur tattoos, as they often contain non-standard pigments. For this reason, a test treatment on a small area of the tattoo is recommended. This helps assess the pigment's and skin's reaction, and allows for optimal device settings to be selected. [19]

A simplified classification of laser applications for tattoo removal, based on different pigment colors, is presented below (Table 1):

Table 1. Types of lasers depending on their application in pigment removal

Laser Type	Wavelength of emitted radiation [nm]	Application (target pigments)
Nd: YAG	1064	Black, dark navy blue, graphite
Nd: YAG (+ KTP)	532	Brown, red, orange
Alexandrite	755	Green, blue
Ruby	694	Green, blue, black-blue

The most used laser is the Nd: YAG laser, which emits radiation at a wavelength of 1064 nm in the infrared range. This wavelength penetrates deeply into the skin and is relatively weakly absorbed by melanin, making this laser safe for use on individuals with darker skin phototypes. It is particularly effective in removing dark pigments, such as black, graphite, and dark navy blue.

When a KTP crystal is used, the energy of the Nd: YAG laser can be converted to a 532 nm wavelength, which falls within the visible light spectrum. This allows for the removal of lighter pigments, especially red and orange. [5,22]

An alternative to the Nd: YAG lasers are ruby and alexandrite lasers, which are more effective at removing pigments in cool color tones. However, due to their higher melanin absorption, their use in individuals with darker skin tones carries a greater risk of hypopigmentation and skin complications. The ruby laser, which emits light at a wavelength of 694 nm, is particularly

effective in removing blue and green pigments. It achieves the best results in removing black-blue pigments, but may be less effective with red pigments, for which better results are obtained using the Nd: YAG 532 nm laser. The alexandrite laser, operating at a wavelength of 755 nm, is also used for removing cool-toned pigments, including green, turquoise, and blue. [5,20–23]

In the case of multicolored tattoos, removal can present additional risks. These types of tattoos often contain a mixture of various pigments, each of which may absorb light energy differently. A common phenomenon observed during treatment is pigment color change, which occurs when the laser wavelength is not properly matched to all the pigment colors present in the tattoo. For example, pigments containing iron oxides, often found in red and brown inks, may darken when exposed to the laser - sometimes even turning black. A similar reaction can occur with pigments that contain titanium. Such chemical reactions make the outcome of the procedure more difficult to predict and require an individualized approach for each case. [24]

Another limitation of this method is the difficulty in removing very light-colored inks, such as white and yellow. These pigments have a high light reflectance and low energy absorption at the wavelengths commonly used in lasers. This limits their ability to absorb radiation and thus impairs the breakdown of the ink by heat. [5,24]

8. SUMMARY

A modern method of laser tattoo removal based on Q-switch technology enables effective and precise elimination of pigment from the skin without damaging it. The key phenomenon used in this technology is selective photothermolysis, which means destroying the pigment through short laser pulses that are absorbed mainly by the pigment, not by the surrounding tissues. The foundation of the process are chromophores - molecules that absorb light of a specific wavelength, such as melanin or hemoglobin.

The effect of the laser is based not only on thermal energy but also on photomechanical fragmentation of the pigments—thanks to which pigment particles become removable by the immune system (so-called phagocytosis).

In Q-switch technology, energy is accumulated in the laser and suddenly released in the form of a very short, intense pulse. Unlike the ablative method, the non-ablative technique allows precise removal of ink from the skin without damaging the surrounding tissues. The procedure is safe and suitable even for sensitive areas such as the face or neck.

The effectiveness of the treatment depends on the appropriate choice of laser and parameters—different wavelengths are absorbed by different pigment colors. Most commonly, the Nd: YAG laser (1064 nm) is used for dark pigments, and with the addition of the KTP crystal (532 nm) for lighter colors like red or orange. In more difficult cases, ruby lasers (694 nm) and alexandrite lasers (755 nm) are also used, which better handle cool colors such as green and blue.

The advantage of this method is a low risk of complications, high precision, and the possibility of using it on delicate skin areas. The downside remains the long duration of therapy (several months) and the difficulty in removing some colors, such as white or yellow.

ACKNOWLEDGEMENTS

The work was created as part of project of Students Scientific Circle of Laser Surface Treatment under the Initiative of Excellence - Research University, Silesian University of Technology, Gliwice, Poland.

BIBLIOGRAPHY

[1] https://77ink.pl/blog/skad-sie-wziely-i-jak-ewoluowaly-wzory-i-techniki-tatuazu-historia-tatuazu/
[2] https://vici.clinic/zabiegi/usuwanie-tatuazu/?srsltid=AfmBOopGy8wxf3fta9DZbwtFA3RayKIn3xpYUmiREucpSo-I62H4mAx9
[3] A. Mańkowska, *Laserowe usuwanie tatuaży,* Wyższa Szkoła Edukacji i Terapii w Poznaniu, Kosmetologia estetyczna/1/2013/vol.2
[4] https://shar-pol.pl/b/mechanizm-usuwania-tatuazu-laserem-pikosekundowym
[5] A. Mańkowska, *Rozprawa doktorska: Laseroterapia wysokoenergetyczne w wybranych problemach dermatologicznych i kosmetycznych – doświadczenia własne,* Poznań, 2010
[6] S. Malinowska, R. K. Mlosek, *Lasery i IPL – źródła światła stosowane w gabinetach kosmetologicznych i medycyny estetycznej,* Medycyna estetyczna, 2016
[7] https://www.sciencedirect.com/science/article/pii/S2213597919300175
[8] https://www.poradnikzdrowie.pl/zdrowie/uklad-odpornosciowy/fagocytoza-czym-jest-i-jak-przebiega-rola-fagocytozy-w-organizmie-aa-oo2N-qDPY-CEZF.html
[9] https://pl.meta-laser.com/news/passive-q-switched-laser-vs-active-q-switched-74052508.html
[10] https://iviter.pl/encyklopedia/dobroc-ukladu
[11] https://www.fiberoptics4sale.com/blogs/wave-optics/laser-q-switching
[12] https://pl.meta-laser.com/news/passive-q-switched-laser-vs-active-q-switched-74052508.html
[13] https://eng.libretexts.org/Bookshelves/Electrical_Engineering/Electro-Optics/Book%3A_Ultrafast_Optics_%28Kaertner%29/04%3A_Laser_Dynamics_%28single-mode%29/4.04%3A_Q-Switching
[14] https://ethz.ch/content/dam/ethz/special-interest/phys/quantum-electronics/ultrafast-laser-physics-dam/education/lectures/ultrafast_laser_physics/lecture_notes/6_Q-switching.pdf_
[15] https://ocw.mit.edu/courses/6-974-fundamentals-of-photonics-quantum-electronics-spring-2006/resources/chapter7/
[16] https://spie.org/publications/spie-publication-resources/optipedia-free-optics-information/fg14_p10-11_q-switching
[17] https://www.fiberoptics4sale.com/blogs/wave-optics/laser-q-switching
[18] http://kcl.digimat.in/nptel/courses/video/104101122/lec30.pdf
[19] https://artofbeauty.com.pl/powiklania-po-laserowym-usuwaniu-tatuazy/
[20] K. Gemza, A. Surgiel-Gemza, *Metody obrazowania efektów zabiegów laserowego usuwania pigmentów zdeponowanych w skórze z uwzględnieniem zabiegów wykonanych laserem pikosekundowym,* Specjalistyczna Praktyka Lekarska Medycyna Estetyczna/4/2020/vol. 9
[21] https://novagroup.pl/wp-content/uploads/NanoStar-broszura-2022.pdf
[22] A. Zapała, *Laserowe usuwanie tatuażu i makijażu permamentnego, cz. I. Podstawy teoretyczne*, Kosmetologia estetyczna/2/2017/vol. 6
[23] https://artofbeauty.com.pl/powiklania-po-laserowym-usuwaniu-tatuazy/
[24] https://klinikaurody.net.pl/zabiegi/usuwanie-tatuazu-makijazupermanentnego/

TalentDetector
23th-25th June 2025
Gliwice-Brenna, Poland
DEPARTMENT OF ENGINEERING MATERIALS AND BIOMATERIALS
FACULTY OF MECHANICAL ENGINEERING
SILESIAN UNIVERSITY OF TECHNOLOGY
INTERNATIONAL STUDENTS SCIENTIFIC CONFERENCE

Study of strength properties of components made of recyclate doped filaments

Martyna Urbańska[a], Kinga Stępska[b], Jan Wypiór[c], Olaf Pradelok[d], Krzysztof Olszak[e], Vojtěch Macejko[f], Eliška Posmyková[g], Mariusz Król[h], Jiří Hajnys[i]

[a] Politechnika Śląska, Wydział Mechaniczny Technologiczny, Inżynieria Produkcji i Zarządzania, email: mu309689@polsl.pl
[b] Politechnika Śląska, Wydział Mechaniczny Technologiczny, Inżynieria Produkcji i Zarządzania, email: ks309686@polsl.pl
[c] Politechnika Śląska, Wydział Mechaniczny Technologiczny, Inżynieria Produkcji i Zarządzania, email: jw309692@polsl.pl
[d] Politechnika Śląska, Wydział Mechaniczny Technologiczny, Automatyka i Robotyka Przemysłowa email: op307516@polsl.pl
[e] Politechnika Śląska, Wydział Mechaniczny Technologiczny, Automatyka i Robotyka Przemysłowa, email: ko302591@polsl.pl
[f] VSB - Technical University of Ostrava, Faculty of Mechanical Engineering, The Department of Machining, Assembly and Engineering Metrology
[g] VSB - Technical University of Ostrava, Faculty of Mechanical Engineering, The Department of Machining, Assembly and Engineering Metrology
[h] Politechnika Śląska, Wydział Mechaniczny Technologiczny, Katedra Materiałów Inżynierskich i Biomedycznych, e-mail: mariusz.krol@polsl.pl,
[i] VSB - Technical University of Ostrava, Faculty of Mechanical Engineering, The Department of Machining, Assembly and Engineering Metrology

Abstract: This paper presents the results of our own research, which aimed to develop 3D printing filaments doped with recyclate, extrude them and print samples AND test their strength properties. The filaments were made in three ratios of PLA and recyclate mixture: 80/20, 60/40 and 40/60. The project was carried out within the framework of PBL teamwork and included the entire process - from material preparation to extrusion of the filaments, to the performance of mechanical tests.

Keywords: Filament, extrusion, recyclate, PLA, 3d printing, mechanical properties,

1. WSTĘP

3D printing technology was developed by American scientist Charles Hull in the late 20th century. Initially, the 3D printing system was unattainable for most people due to the high cost of implementation, but this has changed over time. Today, the use of 3D printing in everyday life continues to grow. Nowadays it is one of the most popular topics in the world of new

technologies. The market for printing devices is constantly growing, and the demand for prints is increasing. This is otherwise known as additive technology, which allows the production of components with complex shapes without the need for injection molds. Among the range of incremental methods available, the Fused Filament Fabrication (FFF) technique, also referred to as Fused Deposition Modeling (FDM), has gained popularity due to its relatively low operating costs, wide availability of materials and simplicity of equipment operation. Each device has a relatively fixed and similar design. We can change settings thanks to a control panel and a control board is responsible for monitoring the correctness of the print. These two components are the most important [1]. In addition, several other parts necessary for 3D printer operation can be listed [7]:

- extruder - its main function is to introduce the filament, or filament-like material, into the head, where it is plasticized,
- frame - a rigid housing, prevents vibrations that affect the quality of printing,
- head - a component equipped with heat sinks and fans, so you can change the temperature of the extruded filament,
- motors, guides - allow movement
- working table- on it prints are created, often flexible, removable which makes it easier to peel off finished models.

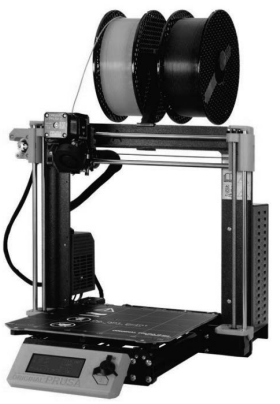

Figure 1. Original Prusa MK3S+ 3D printer [7].

The model can be designed, for example: in SOLIDWORKS. The printing process is based on applying successive layers of polymer according to the user's CAD file. An indispensable step is the preparation of the file in the “slicer” program which translates the printing parameters (temperature, extruder speed, head path distribution) into printer control signals [2-4].

Despite the significant advantages of 3D printing, there are some limitations related to the amount of material used. Although 3D printing uses less material than classic manufacturing methods and is considered more environmentally friendly, there is still room for improvement in the process. Increasing pressure from EU sustainability regulations is prompting the search for alternative sources of raw material. Solutions that would reduce the negative impact on the environment. In this context, the use of recyclate, i.e. recycled polymer waste, as a component of the filament becomes important. Through mechanical recycling of plastics (shredding of waste in special schredders), the raw material is obtained in the form of regranulates. If properly prepared, it can retain satisfactory mechanical and aesthetic properties. The need to optimize the consumption of non-renewable resources through the use of recyclate at the same time fits into the concept of a closed-cycle economy. According to studies, the admixture of even several

percent of regranulate to a pure polymer (e.g. PLA) lowers the carbon footprint of the printing process. Nevertheless, obtaining a homogeneous blend of PLA with recyclate requires precise dosing and control of extruder parameters during filament extrusion [5, 6].

2. PURPOSE AND SCOPE OF THE STUDY METHODOLOGY

The work of the project focused on an attempt to produce a filament for 3D printing technology (FDM) with varying additions of recyclate, formed from grinding, and then determine the strength properties of the newly developed material. It was decided to produce a filament with admixture of recyclate in three proportions:

- 40% PLA granulate and 60% recyclate,
- 60% PLA granulate and 40% recyclate,
- 80% PLA granulate and 20% recyclate.

3. RESEARCH METHODOLOGY

A Felfil Shredder (Model 750) was used to obtain recycling. It is an advanced shredder designed to shred the acquired PLA waste created during failed FDM prints. The device is capable of shredding PLA, PETG and other plastics up to 4 kg per hour, among others. The machine consists of 12 interchangeable blades with different profiles, and the maximum thickness of the material is up to 20 mm [9].

A Felfil Evo Extruder was used to extrude the filament, which is designed to produce a new filament with a fixed diameter. It makes it possible to create your own recycled filament from pellets and recyclate. The device is compatible with many materials such as PLA, ABS and PVA. It is characterized by such parameter values: filament diameter of 1.75 mm or 2.85 mm; extrusion speed of about 1.15 m/min and the operating temperature range reaches up to about 250 C [9].

Once the new filament was developed, test samples were printed using the Prusa i3 MK3S+ printer, which offers a 250 × 210 × 210 mm workspace with a magnetic heated table and a removable PEI-coated steel plate for excellent adhesion and easy print removal. The unit supports a wide range of materials, including PLA, PETG, ASA, ABS, PC, nylon and flexible TPU. The maximum nozzle temperature is 300°C, and the table temperature is 120°C. The printer offers advanced features such as automatic table leveling, filament detection, print recovery after power failure and layer offset compensation, which translates into reliability and versatility in 3D printing [10-12]. In the next step, standardized specimens (5 each) were printed for strength testing.

4. TEST EQUIPMENT, MATERIAL AND METHODOLOGY

The work on the project included a few basic assumptions and sub-points. It was decided to extrude three different filaments, which consisted of different proportions of mixed PLA material along with admixtures of recyclate. The following are the proportions,
from which the mentioned filaments were made:

- 40% PLA granulate and 60% recyclate,
- 60% PLA granulate and 40% recyclate,
- 80% PLA granulate and 20% recyclate

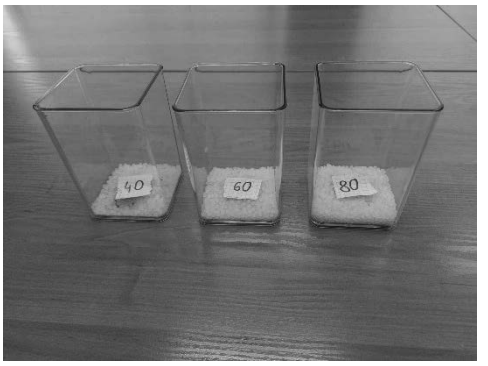

Figure 2. Prepared pellets in proportions of 40%, 60% and 80%

The research methodology was the same in each case. The first stage of the work was the preparation of the recyclate. Recyclate was obtained and processed from old, failed prints and from supports. The collected material was ground three times (to obtain a fine fraction) in a Felfil Shredder Model 750. After the recyclate was properly ground, it was subjected to drying for 1h at maximum temperature (70º C) in a dryer.

a) b) c)

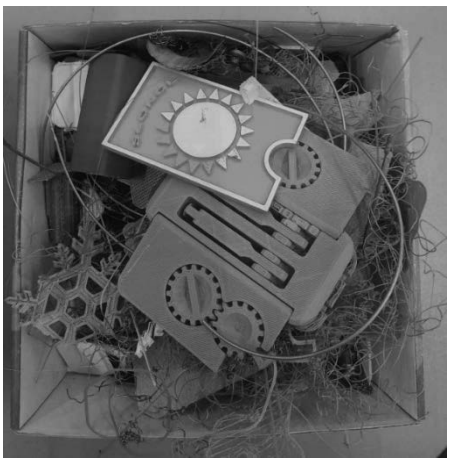

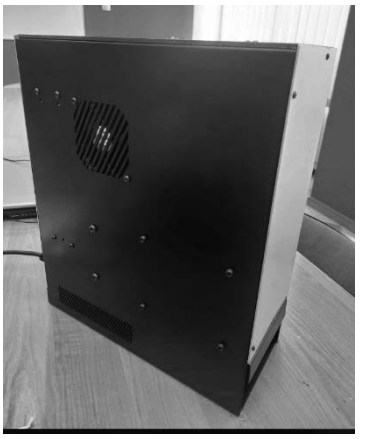

d) e)

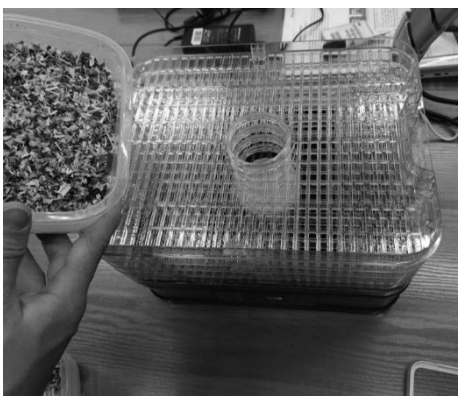

Figure 3. a) recyclate material b) Fellfill Shredder Model 750 c) center of Fellfill Shredder Model 750 d) dryer e) ground and dried recyclate

The next step was to prepare the materials for extrusion, that is, to measure the proportions of the materials. Each filament material was measured to 200g in the appropriate proportions.

Figure 4. Mixed granulate with recyclate in the ratio of 80% PLA 20% recyclate

The mixture was then poured into the Felfil Evo Extruder, where the extrusion process of the new filament was carried out. For this, extrusion parameters such as temperature, extrusion speed, winding speed and filament diameter had to be properly selected and stabilized.

The process of making the filament proved to be complex and challenging. At the initial extrusion stage, it was necessary to pull the heated, prone to curling filament through the appropriate holes of the cooling system and through the winding rollers.

The initial stage was also made difficult by the uneven heating of the machine components and the irregular structure of the recyclate, which led to the formation of thickenings and folds on the surface of the filament. As a result, the first meters of material produced did not meet the required standards and had to be rejected.

Due to the lack of publicly available data on the processing parameters of PLA and recyclate mixtures in specific proportions, it was necessary to establish them through experiments and numerous tests.

a) b)

Figure 5. a) Felfil Evo Extruder b) Fellfil Spooler

Despite constant monitoring and adjustment, the diameter of the filament varied from 1.65-1.80 mm. This was the result of unstable process conditions and the inhomogeneity of the

recyclate, which proved difficult to eliminate completely under laboratory conditions. This range was considered acceptable for the project.

Finally, the optimal parameters to produce the filament were determined for the various proportions of PLA and recyclate. These parameters yielded properties closest to those assumed in the project and are shown in Table 1.

Table 1 Filament manufacturing parameters

Type of mixture	Pull speed [m/min]	Extrusion temperature [°C]	RPM [obr./min]	Filament diameter [mm]
40 % PLA 60 % recycled	0,93	196	6	1,75
60 % PLA 40% recycled	0,85	199	7	1,75
80 % PLA 20 % recycled	0,85	200	7	1,75

The printed filaments were used to print standardized specimens (according to PN-EN ISO 527:1998) for static tensile testing to compare the effect of recyclate contribution on the strength properties of the components.

Models of the shapes were designed in SolidWorks and then imported into PrusaSlicer software version 2.9.2, where detailed printing parameters were determined. A 100% density fill was used in the form of parallel lines. Based on the density of standard PLA filament (1.24 g/cm³), the program estimated the material consumption needed to print one batch of five samples at 50.18 g, which corresponds to about 16.82 meters of 1.75 mm diameter filament. On this basis, the appropriate amount of material was prepared.

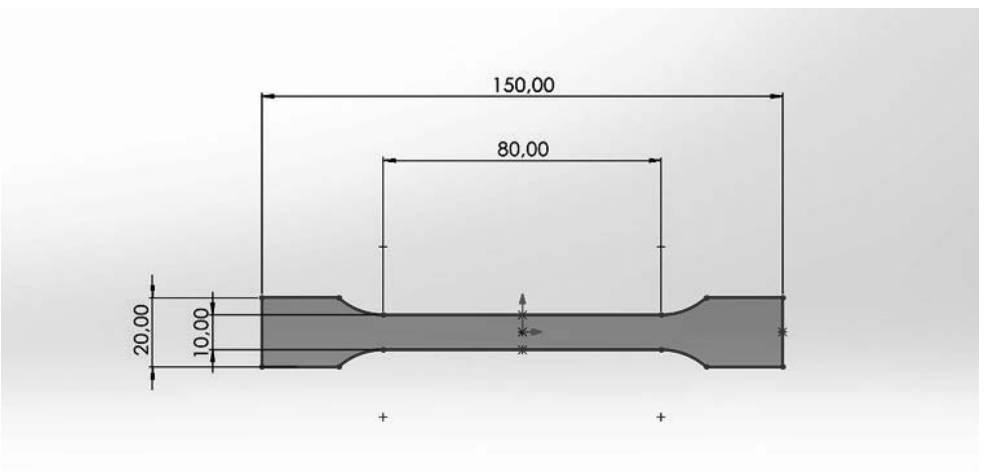

Figure 6. Static tensile test specimen

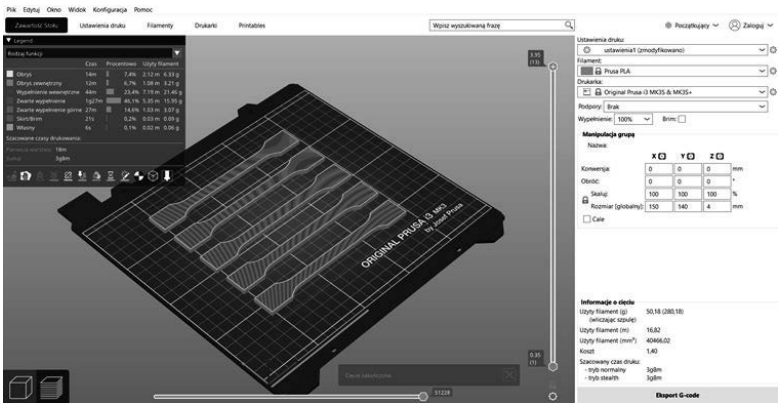

Figure 7. Model analysis in PrusaSlicer 2.9.2

The height of the first layer was set at 0.35 mm, while the other layers were set at 0.3 mm. The temperature of the print head was 215 °C, and the working table was 60 °C. The total printing time for one series of samples was 3 hours. The process was carried out using an Original Prusa i3 MK3S+ printer.

5. RESULTS

Mechanical tests on the obtained specimens were carried out in accordance with the current PN-EN ISO 527:1998 standard, which specifies the methodology for carrying out static tensile testing for plastics, taking into account, among other things, the requirements for the shape of the specimens, the strain rate and the interpretation of the obtained results. For the analysis, we used a Zwick Roell Z020 testing machine, which allows precise measurement of stresses and strains in specimens until failure. The study focused on two key mechanical parameters: stress at break [MPa] and relative elongation [%].

Figure 8. Zwick Roell Z020 strength machine

For each of the three blends of PLA granules with the addition of recyclate (20%, 40%, 60%), we conducted 5 independent tests, in addition, we performed analogous tests for samples made with pure PLA (100% PLA granules, 0% recyclate) as the reference material. All samples were prepared according to the same procedure and tested under identical conditions, so we obtained consistency and comparability of the obtained results placed in Table 2 and located in Figure 9.

Table 2. Tensile strength tests

Type of mixture	Sample no.					Mean value [MPa]
	1	2	3	4	5	
40 % PLA 60 % recyclate	27,8	26,3	26,8	27	28,6	27,3
60 % PLA 40% recyclate	28,5	32,1	31,2	32	29,2	30,6
80 % PLA 20 % recyclate	15,3	16,4	16	16,9	16,4	16,2
100 % PLA 0 % recyclate	51,2	52,9	54,2	55,2	55,6	53,8

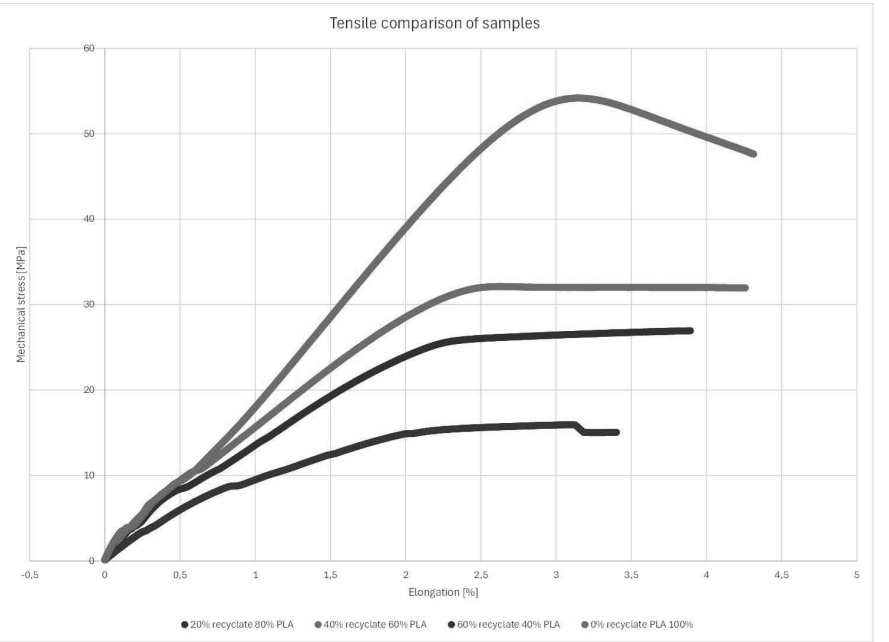

Figure 9. Comparison of tensile strengths of averaged specimens

6. CONCLUSIONS

The characteristics of the stress-strain plots of the 80/20, 60/40 and 40/60 and 100 PLA samples indicate the typical behavior of polymeric materials subjected to tensile testing - an initial elastic section, followed by a gradual transition to plastic deformation and rupture. Differences in the graphs periodize the influence of varying proportions of recyclate admixture in the material. An increase in the proportion of recyclate has a negative effect on the consistency of the material's structure. Despite the noticeable differences, even filaments with a high

proportion of recyclate show satisfactory mechanical properties, confirming the potential for their use in less stressed structural components. The results confirm that doping with recyclate can be an effective way to reduce waste and costs, but it requires careful selection of proportions and control of production parameters to maintain the mechanical properties of the filament.

ACKNOWLEDGEMENT

The present study was produced as part of the activities of the Student Research Group "GYROID" operating at the Department of Engineering and Biomedical Materials at the Faculty of Mechanical Engineering, Silesian University of Technology in Gliwice.

Publication supported by the Excellence Initiative - Research University program implemented at the Silesian University of Technology, 2025.

BIBLIOGRAFIA

1. https://mws.pl/artykul/co-to-jest-druk-3d-i-jakie-daje-mozliwosci-krotki-poradnik/
2. https://get3d.pl/2024/01/16/programy-aby-rozpoczac-druk-3dporadnik
3. https://zadar.pl/programy
4. https://3d.edu.pl/najlepsze-programy-typu-slicer/
5. https://fibometry.com/ekologia-w-druku-3d-mniej-odpadow-i-wiecej-mozliwosci/
6. https://3d.edu.pl/
7. https://outlet3d.eu/pl/fdm/1873--drukarka-3d-original-prusa-i3-mk3s-.html
8. https://felfil.com
9. https://zadar.pl/drukarka-3d-original-prusa-i3-mk3s-plus
10. https://strongmocha.com/vetted/prusa-i3-mk3s-review-3d-printing-excellence/
11. https://top3dshop.com/blog/original-prusa-i3-mk3s-3d-printer-review
12. P. Falkowska, Sz. Jędrzejewski, D. Tatar, A.J. Nowak, M. Król, *Badania własności wytrzymałościowych filamentów domieszkowanych recyklatem,* Talent Detector, 27th January 2023
13. P. Falkowska, Sz. Jędrzejewski, D. Tatar, A.J. Nowak, M. Król, *Badanie własności wytrzymałościowych filamentów domieszkowanych recyklatem,* Talent Detector, 27th January 2023
14. https://www.zwickroell.com/products/static-materials-testing-machines/universal-testing-machines-for-static-applications/allroundline/
15. https://www.zwickroell.com/pl/branze/tworzywa-sztuczne/termoplastyczne-i-utwardzalne-masy-formierskie/proba-rozciagania-iso-527-1-2/
16. https://tenslab.pl/proba-rozciagania-wg-iso-527

TalentDetector
23th-25th June 2025
Gliwice-Brenna, Poland
DEPARTMENT OF ENGINEERING MATERIALS AND BIOMATERIALS
FACULTY OF MECHANICAL ENGINEERING
SILESIAN UNIVERSITY OF TECHNOLOGY
INTERNATIONAL STUDENTS SCIENTIFIC CONFERENCE

Microstructure and Hardness Evaluation of Additive Materials Applied by Hardfacing by Welding Technology

Monika Vargová[a], Miroslava Ťavodová[b]

[a,b]Technical University in Zvolen, Faculty of Technology, Department of Manufacturing Technology and Quality Management
email: [a]monika.vargova@tuzvo.sk, [b]tavodova@tuzvo.sk

Abstract: The article focuses on the evaluation of the microstructure and hardness of UTP BMC and PlasWeld Ferro 55 additive hardfacing materials. These hardfacing materials were applied to the tool body material for crushing unwanted growths 16MnCr5. These tools operate in a highly heterogeneous environment and are subject to rapid wear. The aim of the modification is to increase the service life of these tools. Microstructural evaluation and Rockwell hardness testing were performed on the prepared samples. It can be concluded that the PlasWeld Ferro 55 hardfacing material achieved satisfactory results. There were no defects in the microstructure that would affect the quality of the hardfacing. The hardness of this hardfacing material was 2.65 times higher than the hardness of the 16MnCr5 material and 1.5 times higher than the hardness of the hardened UTP BMC harfacing material. On the basis of these results, it is planned to verify the suitability of the hardfacing materials also in real operating conditions.

Keywords: crushing tool, hardfacing by welding, microstructure, hardness

1. INTRODUCTION

Forests have an important productive and public utility function. They are capable of generating wood, creating and protecting fertile soil, producing oxygen, filtering air, and capturing and collecting clean water. Forests therefore need to be sustainably managed. However, this requires mechanisation, which is subject to wear over time. The working parts of the machinery - the tools that come into direct contact with the cultivated soil and woodland - are also subject to this wear.

Tools used for environmental modification in planting and establishing forests are subject to high loads in an inhomogeneous working environment. They are subject to rapid abrasive wear and wear due to the action of strong impacts. Their frequent replacement causes economic and technical problems for forestry companies. It is therefore necessary to search for solutions to increase their service life. One of the methods to increase the service life of the tools is the technology of hardfacing by welding of additive materials.

Additive materials used for hardfacing by welding commercially available in a wide range. Additive materials with a microstructure composed of carbides in an austenitic matrix are often

used for applications where abrasion resistance is required and are usually classified according to expected hardness [1,2]. However, the abrasive wear resistance of additive materials depends on many other factors such as the type and shape of hard phases and toughness [3]. Chromium-rich additives are often used due to their low cost and availability, but tungsten- or vanadium-rich additives offer better performance due to a good combination of hardness and toughness [1].

The correct choice of an additive material, which by its structure and properties can better withstand the effects of a heterogeneous working environment, is a prerequisite for increasing the service life of the tools for crushing unwanted growths.

2. MATERIAL AND METHODS

Tools for crushing unwanted growths operate in a strongly heterogeneous environment. In their work, they come into contact with the processed wood mass. The second component is the soil, on the surface of which minerals and rocks are found. All these factors have an impact on the rapid wear of the tools used for shredding unwanted growth. Also, the high rotor speed of the base machine adapter on which the tools are mounted contributes to the wear of these tools.

The tools themselves are constructed as a composite - a tool body to which a wolfram-carbide (WC) tip is soldered (Figure 1). In practice, it often happens that after some time in service, due to environmental heterogeneity and dynamic loading of the tool, the tip is lost and the tool body is further worn and deformed. This is due to the cyclic repetition of the plastic deformation of the tool micro-surface layers under conditions of intense abrasion, which leads to significant material loss. This process of wear is reflected in a short period of time by a significant degradation of the tool, resulting in loss of functionality and premature decommissioning of the tool. The increased frequency of tool changes and the associated long-term downtime of technical equipment consequently represent a significant economic problem for forestry operators [4].

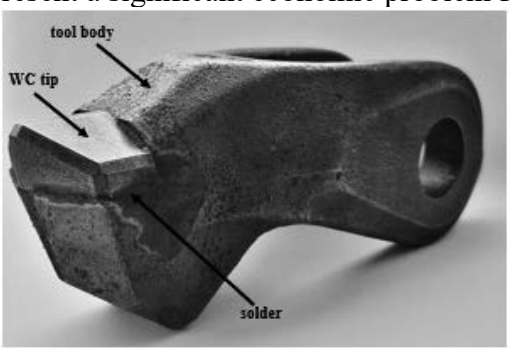

Figure 1. Tool for crushing unwanted growth

Based on previous research, it was found that the body of the tools for crushing unwanted growths is made of 16MnCr5 steel. This is a ferritic-perlitic steel in the unheat-treated state [5]. It is a manganese-chromium based structural steel designed for cementing. The material has good formability in hot forming and, after soft annealing, in cold forming. The steel is characterised by good technological properties, particularly in terms of machinability and weldability. It is suitable for machining components for hardening up to 35 *mm* diameter, for cementing with high core strength. Typical applications include shafts, gears, camshafts, valve lifters, piston pins and gear couplings. The chemical composition of 16MnCr5 steel is given in Table 1 [6].

The samples for microstructure evaluation and hardness test were formed by applying the additive material to the tool body material 16MnCr5 by the hardfacing by welding technology.

The additive materials were selected based on the type of wear to which the tool is subjected, the desired composition and also based on the recommendations of the additive manufacturers. Two surfacing materials were selected:

- Electrode UTP BMC - harefaced on 16MnCr5 material by manual arc welding. Used for hardfacing by welding parts subjected to high pressure and impact in combination with abrasive wear. After hardficing, it forms an austenitic structure. The chromium in these hardfa ing material increases the resistance to abrasive wear and corrosion. It is mainly used in the mining industry, quarries, cement industry, for hardfacing of crushers, etc. The hardness achieved in the second layer after impact hardening is 48 to 53 HRC. The chemical composition of this electrode is given in Table 1 [7].
- PlasWeld Ferro 55 powder - hardfaced on 16MnCr5 material by plasma welding technology. The laser and plasma hardfacing powder is specially designed for hardfacing by welding parts subject to high abrasive wear and pressure in combination with moderate impacts. The weld deposite can be machined by grinding. After hardfacing, it forms a ferritic-martensitic structure. The hardness achieved in the second layer is 53 to 58 HRC. The chemical composition of the powder is given in Table 1 [8].

Table 1. Chemical composition of tool body material 16MnCr5 and hardfacing materials

Element, wt. [%]	C	Si	Mn	Cr	Mo	P	S	Fe
16MnCr5	0.14 – 0.17	0.17 – 0.37	1.1 – 1.4	0.8 – 1.1	-	max. 0.035	max. 0.035	balance
UTP BMC	0.6	0.8	16.5	13.5	-	-	-	balance
PlasWeld Ferro 55	0.35	0.3	1.1	7.0	2.2	-	-	balance

The two additive materials were hardfaced by welding in two layers rotated 90° to each other. The hardfacing was carried out by certified welders at Valtec s.r.o. (Zvolen, Slovakia). Before the hardfacing by welding, the surfaces were cleaned with a wire brush mounted in an angle grinder, and were degreased with an industrial solvent. Next, the welding parameters were adjusted on the welding machine according to the data given in the technical data sheets of the electrode and powder. Prior to hardfacing each subsequent weld line, the sample was always cleaned to prevent inclusions from impurities in the weld metal. After hardfacing, the samples were allowed to cool freely in air to room temperature and then cleaned.

BMC UTP electrodes dried in a 196L chamber drying oven at 300°*C* for 2 hours. The hardfacing current for all layers was chosen to be $I = 120\ A$ and the voltage $U = 80\ V$. It was important to minimize the heat input during the hardfacing process. After each 20 *mm* section, it was necessary to measure the interpass temperature using a touch thermometer. The interpass temperature is prescribed by the manufacturer to be 250°*C*, but due to the small size of the samples, the temperature was reduced to 200°*C*. The samples with the UTP BMC thread are shown in Figure 2a,b.

For the next experiment, one sample with a UTP BMC hard deposit (Figure 2b) was hardened by intense impacts of the surface of the deposit for 2 *min*, to produce intense plastic deformation on a PRAKO KAP 40 ram with a ram weight of 40 *kg* and a maximum stroke of 220 *mm*. By this process, we attempted to simulate the impact loading of the tool in service. The sample with a hardened UTP BMC hardfacing material is shown in Figure 2c.

Argon was used as a shielding gas for the har facing by welding with PlasWeld Ferro 55 powder. Helium was used as the plasma gas. The welding current for all layers was chosen to be

I = 90 A. The plasma gas flow rate was 1.2 $l.m^{-1}$. A sample with the PlasWeld Ferro 55 coating is shown in Figure 2d.

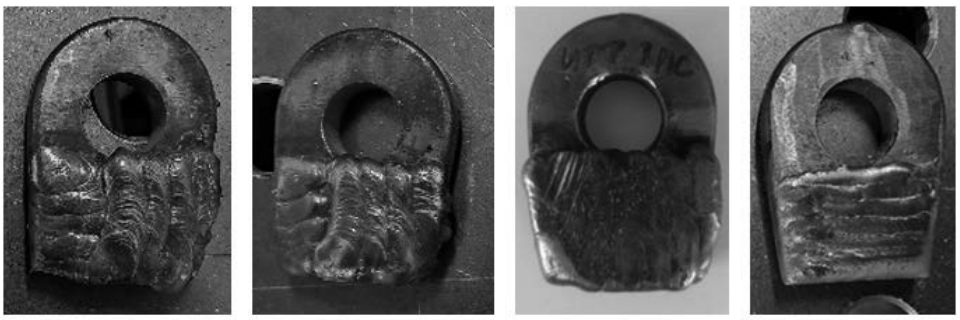

Figure 2. Samples with hardfacing materials; a) sample with UTP BMC hardfacing material; b) sample for hardening of the UTP BMC hardfacing material, c) sample with hardened UTP BMC hardfacing material, d) sample with PlasWeld Ferro 55 hardfacing material

The Rockwell hardness was measured on the prepared samples according to ISO 6508-1:2016 [9] and the Universal Hardness Tester UH250 was used, with a loading force of F = 1,471 N.

Samples for microscopic analysis were prepared according to the standard procedure for the preparation of metallographic samples. The etchant 2% Nital (2 *ml* HNO_3, 98 *ml* ethyl alcohol) was used to induce the microstructure of the base material 16MnCr5 and the etchant Cor (120 ml CH_3COOH, 20 *ml* HCl, 3 *g* picric acid, 144 *ml* CH_3OH) was used for the hardfacing material. For light microscopy, an OLYMPUS GX71 light microscope with an OLYMPUS DP12 camera was used. The microscope used accessories for observation in polarized light and using differential interference contrast.

3. RESULTS AND DISCUSSION

Samples for microstructure evaluation and hardness testing were prepared by abrasive water jet machining (AWJM). The abrasive water jet machining technique was chosen to avoid thermal influence on the observed surfaces. Each sample was prepared to best characterize the condition of the material under examination. The samples taken were prepared in dentacrylic, ground on 240, 400, 600 and 800 grit sandpaper, moistened with water, polished with 1/0 grit diamond paste on satin, moistened with kerosene, washed and rinsed with petroleum alcohol.

3.1. Evaluation of the microstructure of hardfacing materials

In Figure 3a we can see the microstructure of the hardfacing material, the mixing zone and the base material (BM). In Figure 3b, we can see a more detailed view of the microstructure of the BM, the mixing zone, and the UTP BMC hardfacing m In Figure 3c, we can see a more detailed view of the build zone and the microstructure of the hardfacing material. We can conclude that there is sufficient mixing of the BM and the hardfacing material. The structure of the hardfacing material itself is composed of larger austenitic grains, which is consistent with this type of hardfacing material. Some of the fine carbides have been expelled along the grain boundaries and some are found in the austenitic grain itself. It is due to the chromium carbides

that the wear resistance is increased in the hardfacing materials At the same time, however, grain boundary cracks can occur which can not only affect the cohesiveness of the hardfacing material and the BM, but also propagate further into the BM.

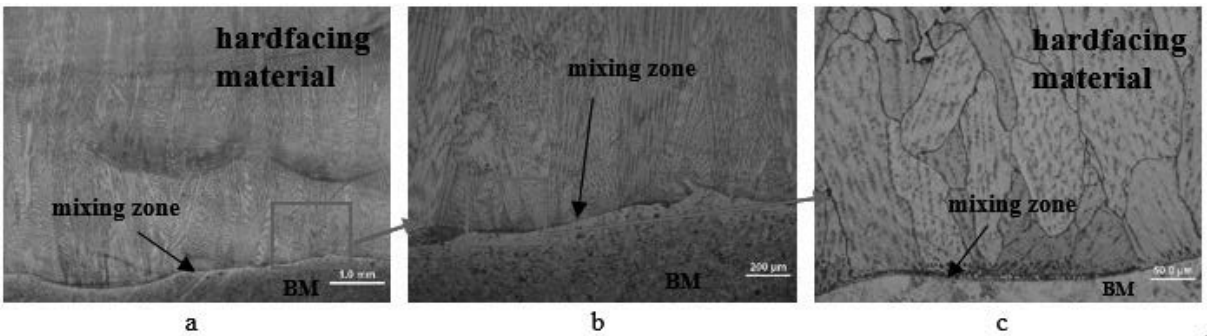

Figure 3. Microstructure of UTP BMC hardfacing material; a) BM - mixing zone – hardfacing material, b) detail of BM – mixing zone – hardfacing material, c) microstructure of the first layer of the hardfacing material

In Figure 4a, we can see the microstructure of the UTP BMC hardfacing material that was impact strengthened for 2 *min*, the mixing zone and the microstructure of the BM in the area without visible defects. The mixing zone is diffuse. Compared to the UTP BMC hardfacing material that was not impact strengthened, we can also see areas with different types of cracks leading through the hardfacing material to the BM (Figure 4b,c). The cracks are either simple, propagating along the grain boundary (Figure 4c) or branching, observed in the mixing zone (Figure 4b). This condition can significantly affect the lifetime of the tool so modified. It can be concluded that the hardfacing material forms an austenitic structure.

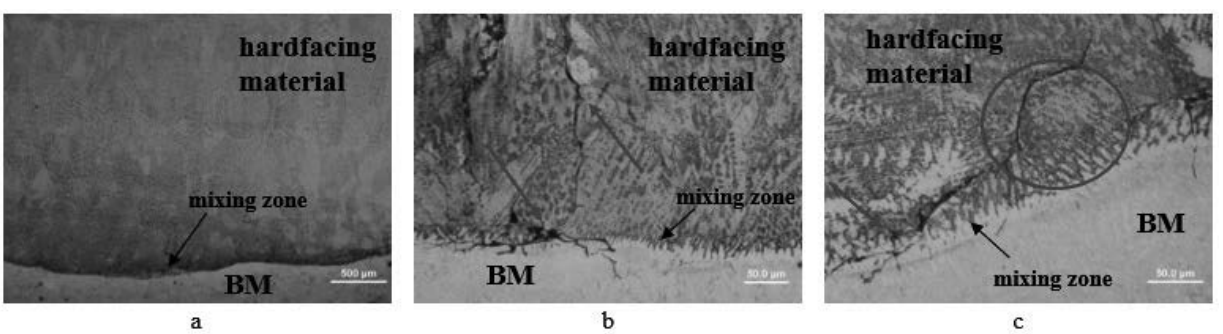

Figure 4. Microstructure of hardened UTP BMC hardfacing material; a) area without visible defects, b) branched crack in the mixing zone, c) a simple crack along the grain boundary

In Figure 5a we can see the microstructure of the BM, the mixing zone and the microstructure of the PLASweld Ferro 55 hardfacing material. The intermixing of the BM and the hardfacing material was diffusive, with no visible defects that would affect the quality of the joint. The structure of the hardfacing material is partially dendritic (Figure 5b). In Figure 5c, we can observe a detail of the structure of the hardfacing material with the presence of martensite in the base grain. The dendrite itself does not contain any defects or cracks.

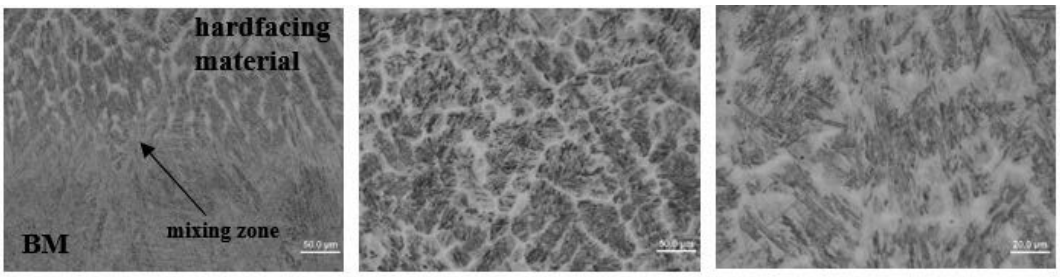

Figure 5. Microstructure of PlasWeld Ferro 55 hardfacing material; a) BM – hardfacing material, b) mixrostructure of hardfacing material, c) detail of microstructure

Based on the data obtained, it can be concluded that sufficient, satisfactory diffusive mixing with BM occurred for each hardfacing material. No defects were observed that could affect the cohesiveness of these materials. However, for the UTP BMC hardfacing material, for which we attempted to simulate the operating conditions of the tool, there was a failure of this hardfacing material. Cracks were observed in the microstructure that led through the strand to the BM (Figure 4b,c). Such defects in the hardfacing material may not only affect the wear resistance, but may also cause breakage of part of the material due to impact loading [10,11].

Studies that address the wear resistance of materials differ in their views on the suitability of the microstructure that could best withstand the effects of the working environment [12,13,14,15]. It was therefore necessary to carry out further tests to confirm or exclude the suitability of the selected hardfacing materials.

3.2. Hardness test according to Rockwell

Rockwell hardness measurements according to ISO 6508-1:2016 were performed on the samples. The measured hardness values are shown in Table 2.

Table 2. Measured Rockwell hardness values

Material		**Hardness [HRC]**					
		1.	**2.**	**3**	**4.**	**5.**	**Avarage**
16MnCr5		20	21	21	20	20	**20**
UTP BMC	non-hardened	20	24	25	21	24	**23**
	hardened	31	34	39	36	33	**35**
PlasWeld Ferro 55		50	55	53	55	54	**53**

In the graph (Figure 6) we can see a comparison of the hardness results measured by Rockwell. The highest hardness compared to the tool body material, 16MnCr5, was achieved by the PlasWeld Ferro 55, namely 53 HRC. This hardness is also declared by the powder manufacturer itself. The UTP BMC hardness was 23 HRC, which is almost comparable to the hardness of the 16MnCr5 material. However, after impact hardening for 2 *min*, this hardfacing material reached a hardness of 35 HRC. The manufacturer declares a hardness after hardening of 48 to 53 HRC, but does not specify the exact conditions under which such a hardness can be achieved. However, it can be assumed that higher loading (hardening) of this hardfacing material may also increase its hardness. This presumption follows from the fact that the BMC UTP hardfacing material that was not impact hardened reached a hardness of only 23 HRC.

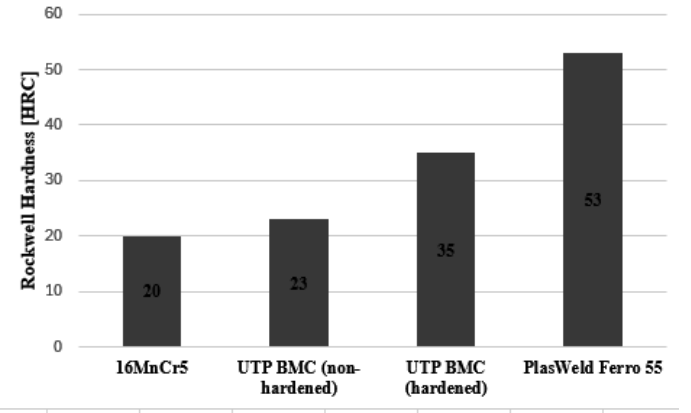

Figure 6. Comparison of Rockwell hardness results

Some authors report that hardness correlates strongly with abrasive wear resistance [16,17]. Thus, based on the results from hardness measurements, we can predict that the hardfacing material with the highest hardness will best resist the effects of an abrasive environment. However, other authors, in turn, have reported in their studies that hardness has no effect on wear resistance [18,19]. Therefore, it would be advisable in further research to also perform abrasive wear resistance tests.

4. CONCLUSION

Tools for crushing unwanted growths are subject to high wear. For this reason, they are rapidly being decommissioned, causing economic and technical problems for forestry companies. The price of one tool is around € 100-120. For this reason, it is necessary to look for solutions to increase their service life. On the basis of the results, we can conclude the following:

- The declared microstructure of the UTP BMC and PlasWeld Ferro 55 hardfacing materials was achieved. For the UTP BMC hardfacing material, which was impact strengthened, cracks appeared in the hardfacing material which could affect the quality of the hardfacing itself. However, it should be noted that such hardening does not accurately simulate the working conditions of the tools themselves.
- The highest hardness according to Rockwell was achieved by PlasWeld Ferro 55 hardfacing material, 53 HRC. Compared to 16MnCr5, this is 2.65 times higher hardness. The UTP BMC hardfacing material reached a hardness of 35 HRC after hardening, which is low compared to the hardness declared by the manufacturer. However, the electrode manufacturer does not specify the exact hardening conditions of this hardfacing material at which the hardness declared by the electrode manufacturer can be achieved after hardening.

In order to verify the resistance of the hardfacing materials to abrasive wear, further laboratory tests and measurements need to be carried out in future research. Based on these tests, it will then be possible to select the additive materials to be applied directly to the tool. Subsequently, the tools thus modified should be tested under real operating conditions.

ACKNOWLEDGEMENTS

The research was supported by the Visegrad Fund fellowship No. 62510157.

BIBLIOGRAPHY

1. Pari, L., Suardi, A., Santangelo, E., García-Galindo, D., Scarfone, A., Alfano, V., Current and innovative technologies for pruning harvesting: A review. Biomass and bioenergy 107 (2017) 398-410. ISSN 0961-9534.
2. Catalogue of tools, Kingkong tools, https://www.kingkong-tools.com/company, 2025
3. Ťavodová, M., Kalincová, D., Hodnotenie stavu nástrojov mulčovača po vyradení z prevádzky. Zvyšovanie životnosti nástrojov a konštrukčných častí mechanizmov: vedecký recenzovaný zborník (2016) 118-124. ISBN 978-80-228-2862-8
4. Hnilica, R., Messingerová, V., Stanovský, M., Slugeň, J., Hnilicová, M., Ferenčík M. Možnosti mechanizácie prác pri zakladaní a výchove lesa: Vedecká monografia. Zvolen: Technická univerzita vo Zvolene (2015) 99. ISBN 978-80-228-2722-5
5. Ťavodová, M., Kalincová, D., Kotus, M., Pavlík, Ľ., The possibility of increasing the wearing resistance of mulcher tools, Acta technologica agriculturae 21, 2 (2018) 87-93. ISSN 1338-5267.
6. Steel 16MnCr5, JKZ, https://www.jkz.cz/cs/produkty/konstrukcni-oceli/csn-14-220-17131-16mncr5/, 2025
7. UTP BMC. Valtec, https://www.valtec.sk/obchod_homedir/data/2616/prilohy/L1_25345_en__U_UTP%20BMC_se_en_v1.pdf, 2025
8. PLASweld Ferro 55, Voestalpin, https://weldingshop.voestalpine.com/DE/en/documents/download/RGF0YXNoZWV0IFBMQVN3ZWxkIEZlcnJvNTUucGRmfE9ubGluZXx2b2VzdFByb2R1Y3RDYXRhbG9nMDkyMA==?inline=true, 2025
9. ISO 6508-1:2016. Metallic Materials—Rockwell Hardness Test—Part 1: Test Method. International Organization for Standardization: London. 2018.
10. Chotěborský, R., Hrabě, P., Müller, M., Savková, J., Jirka, M., Navrátilová, M., Effect of abrasive particle size on abrasive wear of hardfacing alloys, Research in Agricultural Engineering 55, 3 (2009) 101-113. ISSN 1805-9376.
11. Tavodova M., Falat, L., Skultetyova, V., Laboratory analysis od hardfacing material applies by plasma and TIG welding, MM Science Journal (2020) 3826-3831 ISSN 1803-1269.
12. Rojacz, H., Katsich, C., Kirchgaßner, M., Kirchmayer, R., Badisch, E., Impact-abrasive wear of martensitic steels and complex iron-based hardfacing alloys, Wear 492-493 (2022) 204183. ISSN 0043-1648.
13. Nagentrau, M., Tobi, A. M., Sambu, M., Jamian, S., The influence of welding condition on the microstructure of WC hardfacing coating on carbon steel substrate. International Journal of Refractory Metals and Hard Materials 82 (2019) 43-57. ISSN 0263-4368.
14. Badisch, E., Ilo, S., Polak, R. Multivariable modeling of impact-abrasion wear rates in metal matrix-carbide composite materials, Tribology letters 36 (2009) 55-62. ISSN 1573-2711.
15. Coronado, J. J., Caicedo, H. F., Gómez, A. L., The effects of welding processes on abrasive wear resistance for hardfacing deposits, Tribology International 42, 5 (2009) 745-749. ISSN 0301-679X.
16. Kováč, I., Mikuš, R., Žarnovský, J., Drlička, R., Harničárová, M., Valíček, J., Kadnár, M., Increasing the wear resistance of surface layers of selected steels by TIG electric arc surface remelting process using a powder based on $CaCN_2$, The International Journal of Advanced Manufacturing Technology 123, 5 (2022) 1985-1997. ISSN 1433-3015.
17. Slota, J., Kubit, A., Gajdoš, I., Trzepieciński, T., Kaščák, Ľ., A Comparative Study of Hardfacing Deposits Using a Modified Tribological Testing Strategy, Lubricants 10, 8 (2022) 187. ISSN 2075-4442.

18. Brziak, P. et al., Materiály a ich správanie sa pri zváraní, VÚZ, Bratislava, 2003. ISBN 80-88734-10-X
19. Falat, L., Džupon, M., Ťavodová, M., Hnilica, R., Ľuptáčiková, V., Čiripová, L., Homolová, V., Ďurišinová, K., Microstructure and abrasive wear resistance of various alloy hardfacings for application on heavy-duty chipper tools in forestry shredding and mulching operations, Materials 12, 13 (2019) 2212. ISSN 1996-1944.

TalentDetector

23th-25th June 2025
Gliwice-Brenna, Poland

DEPARTMENT OF ENGINEERING MATERIALS AND BIOMATERIALS
FACULTY OF MECHANICAL ENGINEERING
SILESIAN UNIVERSITY OF TECHNOLOGY

INTERNATIONAL STUDENTS SCIENTIFIC CONFERENCE

Vplyv veľkosti plastickej deformácie a teploty rekryštalizačného žíhania na tvrdosť a štruktúru vybraných konštrukčných materiálov

Jozef Vicena[a], Milan Uhríčik[a], Mirosław Bonek[b]

[a] Žilinská Univerzita v Žiline, Strojnícka Fakulta, Katedra materiálového inžinierstva, Univerzitná 8215/1, 010 26 Žilina, Slovak Republic
[b] Silesian University of Technology, Faculty of Mechanical Engineering, Department of Engineering Materials and Biomaterials, ul. Konarskiego 18A, 44-100 Gliwice, Poland
email: vicena4@stud.uniza.sk milan.uhricik@fstroj.uniza.sk

Abstrakt: Príspevok popisuje vplyv veľkosti plastickej deformácie po rekryštalizačnom žíhaní vzoriek austenitických ocelí AISI 304, AISI 316Ti a medi (čistota viac ako 99,8%) na tvrdosť podľa Vickersa a štruktúru.

Veľkosť plastickej deformácie má priamy vplyv na tvrdosť a mikroštruktúru materiálov, pričom rekryštalizačné žíhanie umožňuje obnoviť pôvodné vlastnosti. Experimentálne výsledky potvrdzujú teoretické predpoklady o deformačnom spevnení a procese rekryštalizácie.

Bolo preukázané, že pri austenitických oceliach dochádza so zvyšujúcou sa deformáciou k nárastu podielu deformačného martenzitu, zmenšovaniu zŕn a úbytku dvojčiat. V prípade ocele AISI 316Ti boli navyše pozorované karbidy titánu. Pri medi bolo zaznamenané zjemnenie zŕn, výskyt precipitátov a pri vysokých deformáciách aj dynamická rekryštalizácia. Najvyššie hodnoty tvrdosti podľa Vickersa boli namerané pri najväčších stupňoch deformácie - konkrétne 45 % pre AISI 304, 50 % pre AISI 316Ti a 60 % pre meď. Po rekryštalizačnom žíhaní došlo k postupnému poklesu tvrdosti až na stabilné hodnoty, približne 55 HV pre meď a 100 HV pre ocele. Plastická deformácia spôsobila orientačnú reorganizáciu zŕn, zníženie počtu dvojčiat a pri oceliach aj vznik deformačného martenzitu. Rekryštalizačné žíhanie následne viedlo k obnove jemnozrnnej mikroštruktúry.

Kľúčové slová: Plastická deformácia, rekryštalizačné žíhanie, austenitické ocele, meď, tvrdosť Vickersa, mikroštruktúra.

1. ÚVOD

Austenitická oceľ je definovaná ako vysokolegovaná oceľ s vysokým obsahom chrómu a niklu, čo jej zabezpečuje austenitickú mikroštruktúru. Táto mikroštruktúra je stabilná pri všetkých teplotách, čo odlišuje austenitické ocele od ostatných typov nerezovej ocele, ako sú feritické alebo martenzitické. Charakteristické prvky austenitickej ocele sú predovšetkým nikel a chróm, kde chróm zaisťuje odolnosť proti koróznemu napadnutiu a nikel prispieva k udržaniu austenitickej štruktúry pri nízkych teplotách. Ocele s austenitickou štruktúrou obsahujú malé

množstvo uhlíka (menej ako 0,10 %), veľa chrómu (16-22 %), niklu (8-40 %) a môže v nich byť aj trochu molybdénu (do 5 %), rovnako ako ďalšie prvky ako dusík, titán, niób, meď alebo kremík. Tieto ocele majú síce nižšiu pevnosť pri ťahaní (230-300 MPa), ale sú veľmi húževnaté (až 240 $J \cdot cm^2$ pri -196 °C) a dobre sa tiahnu (45-65 %), čo z nich robí ideálny materiál na spracovanie za studena. Austenitické ocele nie sú magnetické.

Štandardná klasifikácia austenitických ocelí sa riadi podľa systému AISI/ASTM, kde sú najčastejšie používané typy ako 304 (AISI 304) alebo 316 (AISI 316). Oceľ AISI 304 je najpoužívanejšia austenitická chrómniklová oceľ s veľmi dobrou odolnosťou voči korózii, tvárnosťou za studena a zvárateľnosťou. Oceľ AISI 316Ti je austenitická nehrdzavejúca oceľ stabilizovaná titánom. Materiál sa vyznačuje veľmi dobrou odolnosťou proti korózii v prírodnom prostredí s nízkym obsahom chlóru a soli.

2. EXPERIMENTÁLNA ČASŤ

Pre experimentálne merania boli použité materiály vo forme tyčových valcovaných polotovarov - dve austenitické nehrdzavejúce ocele AISI 304 a AISI 316Ti a čistá meď (Cu > 99,8 %). Chemické zloženie ocelí bolo stanovené atómovou emisnou spektroskopiou pomocou prístroja Spektromaxx. Výsledky kontroly ocelí sú uvedené v tab. 1 a tab. 2 a porovnané s požiadavkami normy EN 10088. Atómová emisná spektroskopia funguje na princípe excitácie atómov pôsobením vysokej teploty, pri ktorej atómy emitujú žiarenie s charakteristickou vlnovou dĺžkou. Na základe týchto údajov je možné presne určiť typ a množstvo prvkov vo vzorke. Analýza až na % obsah Mn a Mo potvrdila súlad chemického zloženia s normou.

Tab. 1 Chemické zloženie ocele AISI 304
Table 1. Chemical composition of AISI 304 steel

Vzorka	Chróm (Cr) %	Nikel (Ni) %	Uhlík (C) %	Kremík (Si) %	Mangán (Mn) %	Fosfor (P) %	Síra (S) %
AISI 304	18.85	7.82	0.0742	0.536	1.37	0.0139	0.0215
Norma	17-19,5	8,0-10,5	<0,07	<1,0	<2,0	<0,045	<0,015

Tab. 2 Chemické zloženie ocele AISI 316Ti
Table 2. Chemical composition of AISI 316Tiel

Vzorka	Chróm (Cr) %	Nikel (Ni) %	Uhlík (C) %	Kremík (Si) %	Molybdén (Mo) %	Mangán (Mn) %	Titán (Ti) %
AISI316Ti	16,54	10,77	0,0616	0,871	1,89	0,0117	0,0515
Norma	16-18,5	10-13,5	<0,08	<1,0 %	2-2,5	<2,0	<0,07

Z tyčových polotovarov austenitických ocelí AISI 304 a AISI 316Ti s priemerom 12 mm bolo ručne odrezaných šesť vzoriek s dĺžkou 20 mm. Rovnako bolo pripravených šesť vzoriek z čistej medi (Cu > 99,8 %) s priemerom 15 mm a rovnakou dĺžkou. Vzorky boli najprv nahrubo zarovnané sústružením a následne jemne dobrúsené do lesku.

Následne boli vzorky podrobené počiatočnému tepelnému spracovaniu - žíhaniu v mufflovej peci LAC, s cieľom eliminovať vnútorné napätia vzniknuté počas výroby polotovarov. Vzorky z austenitických ocelí boli žíhané pri 1050 °C počas 30 minút, zatiaľ čo medené vzorky pri 650 °C

rovnako po dobu 30 minút. Ochladzovanie prebiehalo vo vode s teplotou 50 °C a následne na vzduchu pri izbovej teplote 25 °C. Po tepelnom spracovaní bolo z každého materiálu (AISI 304, AISI 316Ti, meď) vybraných päť vzoriek na deformáciu a jedna bola ponechaná ako nedeformovaná referenčná vzorka. Plastická deformácia za studena bola aplikovaná hydraulickým lisom v rôznych stupňoch. Stupeň deformácie (%) sa vypočítal podľa vzorca:

$$St.plastickej\ deformácie\ (\%) = \frac{l_0 - li}{lo} \times 100 \qquad (1)$$

Rozsah deformácií a zodpovedajúce zmeny dĺžky vzoriek na základe aplikovaného stupňa deformácie boli: oceľ AISI 304: 5 - 45 % (dĺžky: 19 - 11 mm); oceľ AISI 316Ti: 7,5 - 50 % (dĺžky: 18,5 - 10 mm); meď: 5 - 60 % (dĺžky: 19 - 8 mm).

Po aplikácii plastickej deformácie bolo realizované sekundárne tepelné spracovanie - rekryštalizačné žíhanie. Po každom žíhaní nasledovalo morenie v roztoku zloženého z 15 ml kyseliny fluorovodíkovej (HF), 2 ml kyseliny dusičnej (HNO_3) a destilovanej vody doplnenej do objemu 100 ml, pričom morenie sa robilo pri teplote 50 °C po dobu 10 minút kvôli odstráneniu oxidov z povrchu vzoriek. U austenitických ocelí začínalo sekundárne tepelné spracovanie na teplote 600 °C s výdržou 20 minút. Teplota žíhania sa následne zvyšovala po 20 °C, až na konečných 1040 °C. Celkovo bolo vykonaných 23 cyklov žíhania (po 25 minút) s následným morením.

Bezprostredne po tepelnom spracovaní nasledovalo meranie tvrdosti podľa Vickersa (HV5). Výsledné hodnota merania tvrdosti pre vzorky AISI 304 a AISI 316Ti uvedená v tab. 3 a tab. 4 je priemerom z 5 meraní na každej jednej vzorke. Grafické znázornenie vplyvu teploty rekryštalizačného žíhania na zmenu tvrdosti podľa Vickersa ocelí AISI 304 a AISI 316Ti pri rôznych stupňoch deformácie je dokumentované na obr. 1 a obr. 2.

Tab. 3 Výsledky meraní tvrdosti AISI 304 po rekryštalizačných žíhaniach
Table 3. Results of hardness measurements of AISI 304 after recrystallization annealing

°C	0%	5%	17,5%	25%	35%	45% Stup.def.
600	120,00	144,00	171,00	180,33	199,33	207,67
620	130,33	165,33	190,33	196,33	200,67	210,00
640	128,27	147,77	170,67	191,33	191,67	200,33
660	118,67	160,57	163,67	185,90	190,87	198,33
680	130,67	164,67	180,67	184,00	205,67	212,33
700	126,00	160,00	175,33	201,00	204,00	211,67
720	120,00	161,17	180,00	184,67	195,33	205,67
740	126,17	159,57	167,33	183,67	190,67	200,00
760	118,60	152,67	182,67	190,67	189,33	210,00
780	126,87	148,33	158,33	175,33	187,33	194,87
800	118,33	134,83	149,93	182,67	175,40	181,67
820	124,00	141,93	150,77	161,87	174,67	190,67
840	122,03	143,73	142,03	160,07	173,67	173,33
860	117,97	132,00	144,87	136,83	149,93	171,33
880	116,23	126,33	148,47	141,97	150,57	150,40
900	112,43	130,37	136,83	134,07	146,00	157,33
920	108,40	115,57	134,20	124,53	128,30	131,20
940	106,63	118,80	130,20	125,37	126,57	137,53
960	100,63	102,20	107,37	120,03	124,73	124,30
980	100,60	106,63	109,27	108,30	116,90	120,20
1000	92,83	95,07	101,30	111,07	115,53	114,27
1020	106,73	108,40	110,67	110,40	107,60	112,57
1040	101,53	104,30	104,97	108,43	110,90	110,13

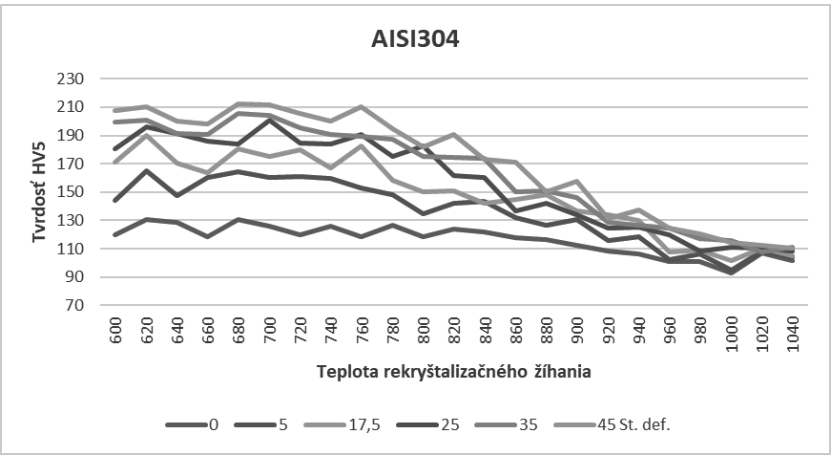

Obr.1 Vplyv teploty rekryštalizačného žíhania na zmenu tvrdosti podľa Vickersa ocele AISI 304 pri rôznych stupňoch deformácie
Figure 1. Effect of recrystallization annealing temperature on the change in Vickers hardness of AISI 304 steel at different degrees of deformation

Tab. 4 Výsledky meraní tvrdosti AISI 316Ti po rekryštalizačných žíhaniach
Table 4. Results of hardness measurements of AISI 316Ti after recrystallization annealing

°C	0%	7,5%	20%	30%	40%	50% Stup.def.
600	105,33	148,67	158,33	198,00	207,67	211,00
620	112,67	151,00	173,00	204,00	227,00	233,67
640	116,87	165,67	175,33	199,00	200,00	208,33
660	110,67	160,33	165,27	201,33	205,00	219,00
680	114,33	160,87	162,67	196,67	205,00	218,67
700	128,33	169,33	174,33	201,00	200,67	226,67
720	115,67	152,30	174,33	189,33	192,33	210,00
740	111,67	150,00	157,20	189,00	209,33	208,00
760	107,67	157,93	174,00	174,10	208,33	201,00
780	114,17	152,00	171,67	182,67	194,33	190,67
800	120,83	147,63	169,33	185,33	204,33	192,67
820	110,60	159,17	160,07	165,00	165,00	169,33
840	114,80	153,70	149,13	160,87	170,67	163,17
860	108,17	132,47	140,77	154,47	162,33	164,20
880	120,87	130,27	129,10	138,27	168,00	145,63
900	119,93	114,83	136,50	134,40	160,67	123,00
920	105,67	116,73	133,10	135,47	130,67	142,63
940	115,67	110,93	132,60	139,33	127,87	150,77
960	121,03	112,40	107,33	106,33	130,83	125,97
980	98,20	110,90	95,07	94,23	93,83	112,90
1000	102,17	99,90	106,87	103,93	109,53	102,17
1020	111,00	110,67	111,73	114,57	107,87	108,37
1040	108,40	110,63	109,53	108,23	111,00	109,40

Výsledky meraní tvrdosti austenitických ocelí ukazujú, že vzorky s najvyšším stupňom deformácie (45 % pri AISI 304 a 50 % pri AISI 316Ti) dosiahli najväčšiu tvrdosť po prvotnom rekryštalizačnom žíhaní. Tvrdosť klesala s nižšou deformáciou, čo potvrdzuje závislosť medzi mierou plastickej deformácie a tvrdosťou, resp. pevnosťou. Grafy zároveň ukazujú negatívnu koreláciu medzi tvrdosťou HV5 a teplotou žíhania - s rastúcou teplotou rekryštalizačného zíhania tvrdosť klesala.

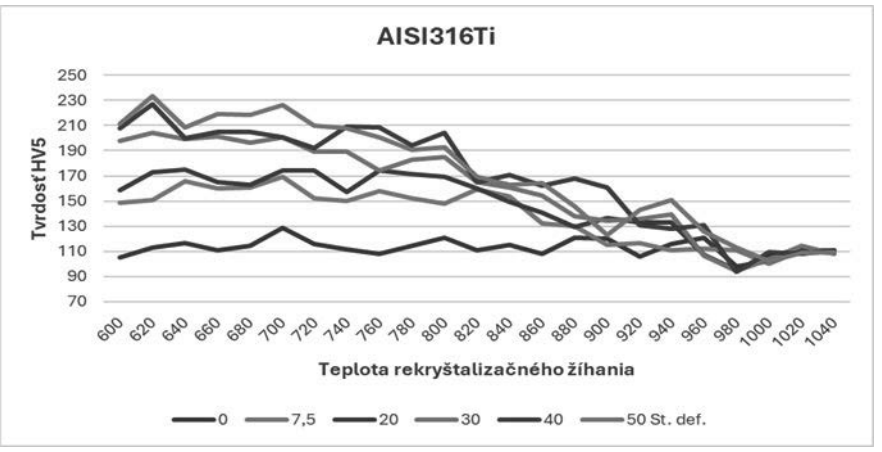

Obr.2 Vplyv teploty rekryštalizačného žíhania na zmenu tvrdosti podľa Vickersa ocele AISI 316Ti pri rôznych stupňoch deformácie
Figure 1. Effect of recrystallization annealing temperature on the change in Vickers hardness of AISI 316Ti steel at different degrees of deformation

Na vzorkách čistej medi (Cu > 99,8 %) bolo realizované rozpúšťacie žíhanie v intervale teplôt 160 - 460 °C, v krokoch po 20 °C, pričom po každom cykle bola meraná tvrdosť HV5 (výsledná hodnota uvedená v tab. 3 je priemer z piatich meraní). Výsledky meraní sú uvedené v tab. 5 a znázornené graficky na obr. 3.

Tab. 5 Výsledky meraní tvrdosti medi po rekryštalizačných žíhaniach
Table 5. Results of hardness measurements of cooper after recrystallization annealing

°C	0%	5%	20%	35%	45%	55%	60% Stup.def.
160	51,30	56,03	72,27	80,50	84,43	86,20	90,93
180	42,67	54,90	64,63	77,70	80,97	82,57	94,63
200	48,13	53,97	62,97	80,93	83,60	86,83	93,67
220	43,03	53,30	63,97	75,90	80,43	85,20	92,83
240	46,50	53,43	62,83	83,60	88,40	92,93	95,20
260	45,73	56,00	67,77	75,17	84,20	84,63	60,57
280	41,50	57,70	66,03	81,57	84,13	56,03	54,83
300	43,30	53,27	58,63	74,17	56,53	62,27	54,63
320	41,80	58,80	65,67	77,63	60,87	60,33	56,17
340	42,07	54,23	61,87	52,80	52,57	52,90	53,17
360	42,37	56,10	62,00	51,23	52,03	52,80	52,03
380	44,73	57,17	61,87	44,67	45,80	46,27	46,13
400	42,47	52,80	58,17	48,37	48,13	48,13	48,27
420	44,00	51,87	55,13	47,00	46,00	44,00	46,00
440	43,00	51,30	51,57	45,00	44,00	45,00	43,00
460	42,00	56,57	55,10	44,00	45,00	44,00	44,00

Výsledky merania tvrdosti v závislosti od teploty rozpúšťacieho žíhania a stupňa deformácie (tab. 4) ukazujú, že vzorka medi so 60 % plastickou deformáciou dosiahla najvyššiu tvrdosť, zatiaľ čo nedeformovaná vzorka najnižšiu.

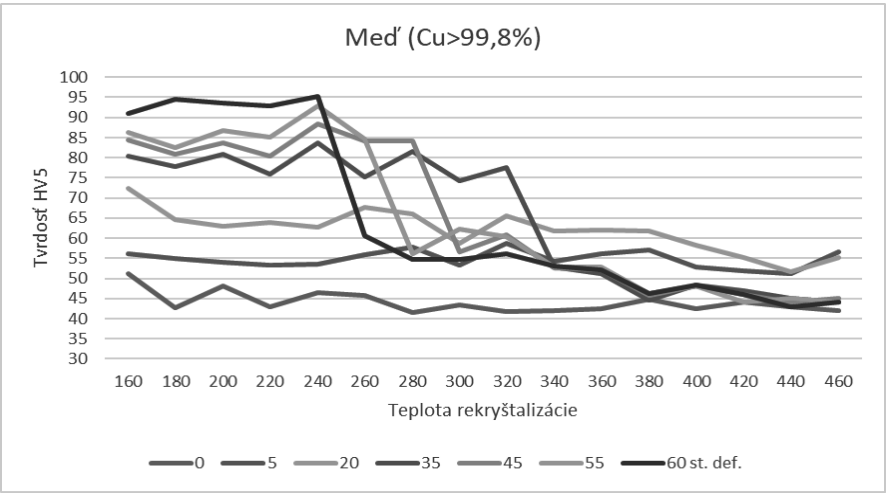

Obr.3 Vplyv teploty rekryštalizačného žíhania na zmenu tvrdosti podľa Vickersa medi pri rôznych stupňoch deformácie
Figure 1. Effect of recrystallization annealing temperature on the change in Vickers hardness of cooper at different degrees of deformation

Rovnako ako pri vzorkách AISI 304 a AISI 316Ti, vyšší stupeň deformácie výrazne zvyšuje tvrdosť materiálu. Grafy znázorňujú pokles tvrdosti so zvyšujúcou sa teplotou rekryštalizačného žíhania. Zvýšenie tvrdosti je dôsledkom deformačného spevnenia, ktoré vzniká akumuláciou dislokácií v kryštálovej mriežke - čím je ich viac, tým je materiál tvrdší a odolnejší voči ďalšej deformácii. Tento jav potvrdzujú aj grafy na obr. 1, obr. 2 a obr. 3.

Metalografické hodnotenie vzoriek je dokumentované na obr. 4 až obr. 7. Vzorky boli pripravené štandardne, t.j. rezanie, preparácia, brúsenie, leštenie a leptanie lept. Kallings2.

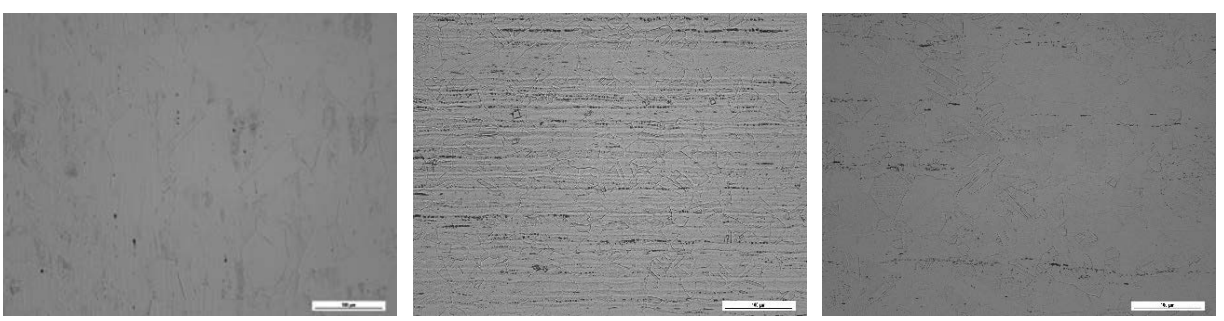

a) AISI 304 *b) AISI 316Ti* *c) meď*

Obr. 4 Mikroštruktúra vzoriek vo východiskovom stave po prvotnom tepelnom spracovaní bez deformácií; lept. Kallings 2
Figure 4. Microstructure of samples in the initial state after initial heat treatment without deformation;etch. Kallings 2

Metalografické hodnotenie sa robilo najprv na vzorkách po počiatočnom tepelnom spracovaní bez deformácií, následne aj na vzorkách po vybraných stupňoch deformácie. Rovnako sa postupovalo aj pri hodnotení po sekundárnom (rekryštalizačnom) tepelnom spracovaní.

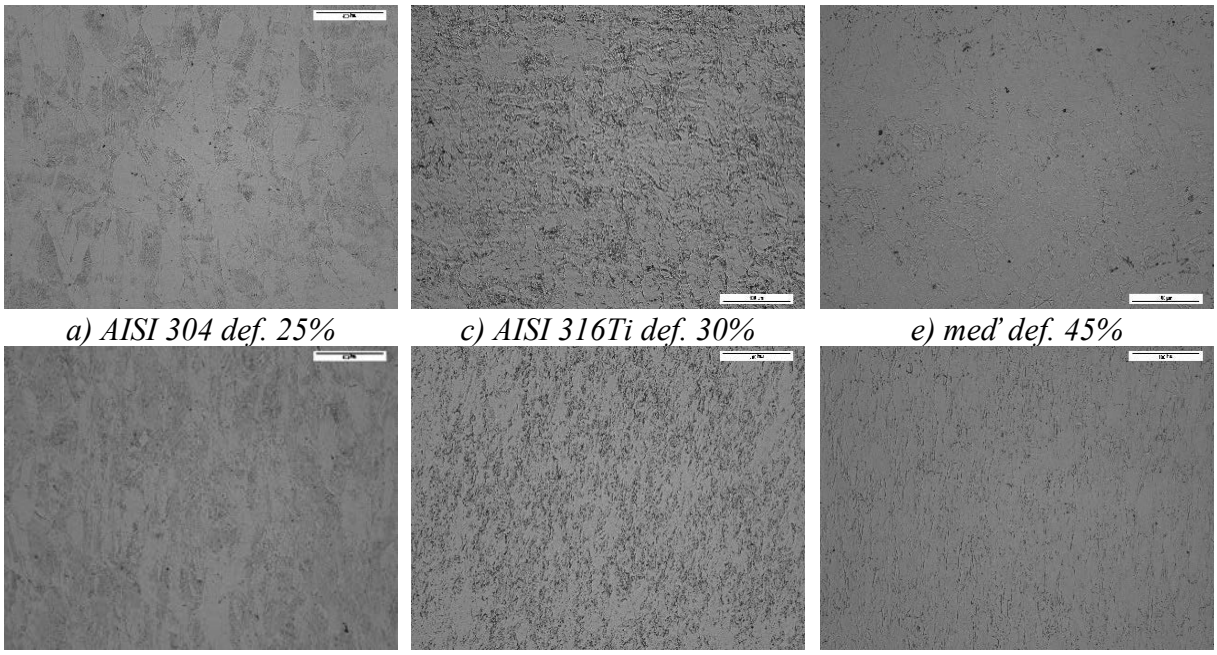

a) AISI 304 def. 25% *c) AISI 316Ti def. 30%* *e) meď def. 45%*

b) AISI 304 def. 45% *d) AISI 316Ti def. 50%* *f) meď def. 60%*

Obr. 5 Mikroštruktúra vzoriek vo východiskovom stave po prvotnom tepelnom spracovaní a vybraných stupňoch deformácie; lept. Kallings2
Figure 5. Microstructure of samples in the initial state after initial heat treatment and selected degrees of deformation; etch. Kallings2

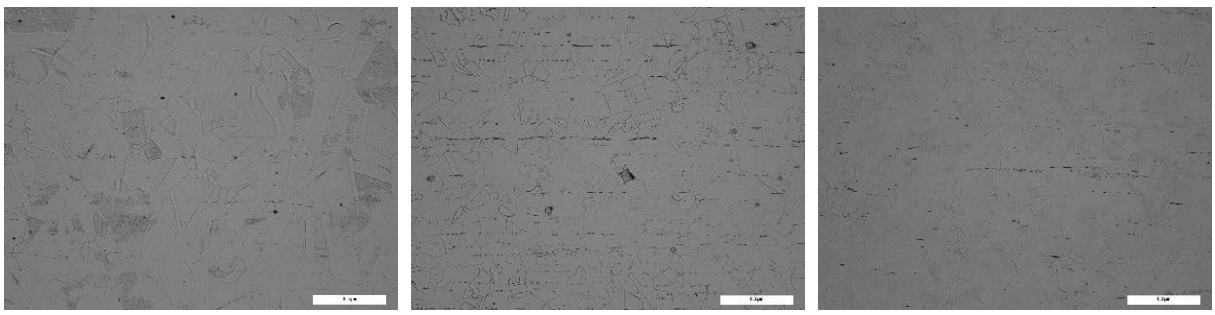

a) AISI 304 *b) AISI 316Ti* *c) meď*

Obr. 6 Mikroštruktúra vzoriek po sekundárnom tepelnom spracovaní bez deformácie; lept. Kallings2
Figure. 6 Microstructure of samples after secondary heat treatment without deformation; etch. Kallings2

Z výsledkov metalografického hodnotenia vyplýva, že plastická deformácia významne ovplyvňuje mikroštruktúru materiálu, najmä veľkosť zŕn a počet dvojčiat, pri vyššej deformácii ich počet klesá. U austenitických ocelí sa v dôsledku deformácie tvorí deformačný martenzit, čo potvrdzujú aj štúdie autorov Stokłos (2008) a Sohrabi (2008). Tmavšie oblasti v mikroštruktúre poukazujú na vyšší obsah deformačného martenzitu. Tvorba martenzitu a deformačné spevnenie prispievajú k nárastu tvrdosti a odolnosti voči ďalšej deformácii [1-3].

Mikroštruktúra medi (99,8%) je tvorená zrnami alfa fázy. Po aplikácii deformácie pozorujeme zjemnenie hustoty zŕn. Po tepelnom spracovaní je na hraniciach možné pozorovať začiatok dynamickej rekryštalizácie.

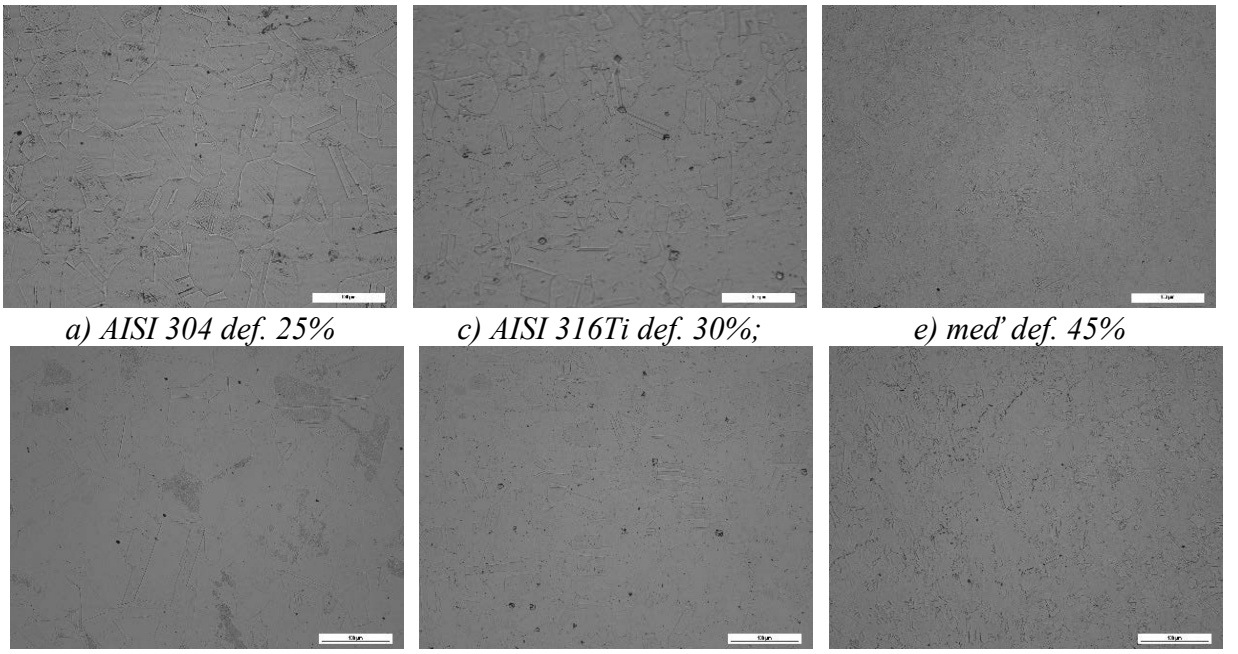

a) AISI 304 def. 25% *c) AISI 316Ti def. 30%;* *e) meď def. 45%*

b) AISI 304 def. 45%; *d) AISI 316Ti def. 50%;* *f) meď def. 60%*

Obr. 7 Mikroštruktúra vzoriek po sekundárnom tepelnom spracovaní s vybranými stupňami deformácie; lept. Kallings2
Figure 7. Microstructure of samples after secondary heat treatment with selected degrees of deformation; etching Kallings2

POĎAKOVANIE

Príspevok vznikol v rámci riešenia spoločného slovensko-poľského projektu Project Based Learning ako výsledok spolupráce medzi Politechnikou Slaskou, Gliwice a Žilinskou univerzitou v Žiline a projektov KEGA č. 004ŽU-4/2023 a KEGA č.009ŽU-4/2023.

BIBLIOGRAFIA

1. Oravcová, M. Štruktúra a vlastnosti vybraných biomateriálov pre endoprotézy. Diplomová práca. Žilinská univerzita v Žiline, 2014, 82 str.
2. Skočovský, P. a kol. Konštrukčné materiály. Žilina: EDIS - vydavateľstvo Žilinskej Univerzity, 2000. ISBN 80-7100-608-4.
3. Bokůvka, O. Prednášky z predmetu Materiály I a Materiály II, 2022.
4. Stokłos, Z. a kol. Mechanické a magnetické vlastnosti nehrdzavejúcej ocele valcovanej za studena, Katowice, ISBN 1897-2764
5. Sohrabi, M. J., Naghizadeh, M., Mirzadeh, H. 2020 https://www.researchgate.net/ publication/344329512_Deformation-induced_martensite_in_austenitic_stainless_steels.

TalentDetector
23th-25th June 2025
Gliwice-Brenna, Poland
DEPARTMENT OF ENGINEERING MATERIALS AND BIOMATERIALS
FACULTY OF MECHANICAL ENGINEERING
SILESIAN UNIVERSITY OF TECHNOLOGY
INTERNATIONAL STUDENTS SCIENTIFIC CONFERENCE

Určenie príčiny a následný návrh náhrady poistnej skrutky v kolennej endoprotéze

Richard Vidrich[a], Ronald Bašťovanský[b], Peter Palček[a], Mirosław Bonek[c]

[a] Žilinská univerzita v Žiline, Strojnícka fakulta, Katedra materiálového inžinierstva, Univerzitná 8215/1, 010 26 Žilina, Slovak Republic
[b]Žilinská univerzita v Žiline, Strojnícka fakulta, Katedra konštruovania a častí strojov, Univerzitná 8215/1, 010 26 Žilina, Slovak Republic
[c] Silesian University of Technology, Faculty of Mechanical Engineering, Department of Engineering Materials and Biomaterials, ul. Konarskiego 18A, 44-100 Gliwice, Poland
email: vidrich@stud.uniza.sk, ronald.bastovansky@fstroj.uniza.sk peter.palcek@fstroj.uniza.sk

Abstract: Príspevok analyzuje poruchu skrutkového spoja v oblasti kolennej endoprotézy, ku ktorej došlo v dôsledku únavového lomu skrutky z titánovej zliatiny TiAl6V4. Porucha nastala približne dva roky po operácii. Analýza lomu bola realizovaná pomocou riadkovacieho elektrónového mikroskopu. Chemické zloženie materiálov skrutky a drieku endoprotézy bolo určené spektrometrom SPECTRO xSORT. Driek bol vyrobený zo zliatiny Co-Cr-Mo. Na základe výpočtov napätí v krute a ťahu pre rôzne uťahovacie momenty bolo preukázané, že nesprávny uťahovací moment počas operácie môže významne prispieť k predčasnému poškodeniu spoja. Výsledkom bol návrh možného riešenia - optimalizácia skrutkového spoja s cieľom predísť podobným poruchám v budúcnosti.

Keywords: Únavový lom, skrutkový spoj, endoprotéza, titánová zliatina TiAl6V4, Co-Cr-Mo zliatina

1. ÚVOD

Degeneratívne kĺbové ochorenie je najčastejším ochorením pohybového aparátu u dospelých, a preto je tiež významným zdrojom morbidity so všetkými dopadmi na pacienta a spoločnosť. Artróza je skupina ochorení kĺbu, pri ktorom je najnápadnejším znakom úbytok kĺbovej chrupavky, subchondrálna skleróza a prítomnosť kostných cýst. Ochorenie postihuje súčasne aj kĺbové väzy, puzdro, synoviálnu membránu a periartikulárne svaly. Artróza je teda komplexné biologické a mechanické zlyhávanie kĺbu.

Implantácia umelej kĺbovej náhrady je dnes u pokročilejších stupňov artrózy metódou voľby. Totálna endoprotéza kolenného kĺbu (TEP) u pokročilej artrózy prináša okolo 85 % vynikajúcich výsledkov. Pomocou umelých kĺbových náhrad sa dajú docieliť uspokojivé výsledky, kedy sa pacient zbaví bolesti, získa dostatočný, funkčný rozsah pohybu kĺbu a zvýši sa tak kvalita jeho života.

Implantáty môžu byť podľa fixácii ku kosti cementové, necementové a hybridné. Cementové sú ku kosti fixované kostným cementom, čo umožňuje včasné zaťaženie končatiny. Fixácia necementových endoprotéz prebieha pomocou osteointegrácie, čo znamená priame vrastenie kosti do upraveného povrchu implantátu. Podmienkou necementovej fixácie je dobrá kvalita kosti. Výhodou necementových endoprotéz je dlhšia životnosť a väčšia odolnosť voči infekciám, nevýhodou je finančná náročnosť a náročnejšia rehabilitácia s dlhším odľahčením končatiny. Hybridné endoprotézy sú kombináciou cementovej a necementovej fixácie, kedy jeden komponent je fixovaný cementovým a jeden necementovým spôsobom.

2. EXPERIMENTÁLNA ČASŤ

Jedným z kritických komponentov kolenných endoprotéz sú skrutkové spoje, ktoré zabezpečujú pevnú fixáciu endoprotézy v kosti, prípadne dvoch častí endoprotézy. Poškodenie týchto skrutiek počas uťahovania alebo únavovým procesom predstavuje problém, ktorý môže viesť k narušeniu stability a funkcionality kolennej endoprotézy.

Na experimentálne práce bola použitá poškodená kolenná endoprotéza. Poškodenie nastalo únavovým porušením skrutky v pacientovom kolene. Cieľom experimentálnych prác bolo na základe analýzy poškodenej endoprotézy navrhnúť optimalizované konštrukčné riešenie zmeny poistenia skrutkového spojenia.

Na obr. 1 je prierez kolennou endoprotézou. Zostava sa skladá z piatich súčastí: pánt kolennej endoprotézy (1.), skrutka M6 s dierou pre poistný kolík (2.), poistný kolík (3.), driek s vnútorným závitom (4.) a puzdro (5.). Driek (4.), ktorý má v sebe vnútorný závit, sa vsunie do puzdra (5.). Driek sa upevní v puzdre pomocou momentového kľúča uťahovacím momentom 10 Nm. Na vrch puzdra sa priloží pánt (1.). Skrutka M6 (2.) sa cez otvor v pánte (1.) zaskrutkuje do drieku (4.) vopred stanovením uťahovacím momentom 5 Nm. Skrutka sa pri doťahovaní natočí do pozície, v ktorej je možné skrutku poistiť poistným kolíkom (3.). Táto skrutka slúži ako uzavretie skrutkového spoja, nemá teda nosný charakter. Umožňuje spojenie medzi pántom (1.) a driekom (4.).

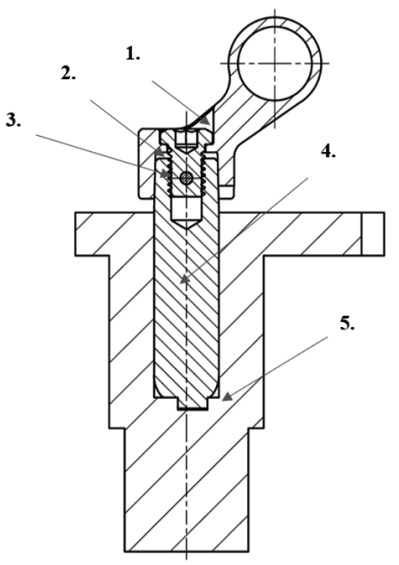

Obr. 1 Prierez zostavou kolennej endoprotézy
Figure 1. Cross-section of a knee endoprosthesis assembly

Skrutkový spoj sa počas svojho používania opotrebuje vplyvom okolitej teploty, tlaku, rôznych síl, ktoré vyplývajú z pohybu pacienta a hlavne únavou materiálu. Únava materiálu spôsobuje problémy pre pacienta, pretože môže dôjsť k lomu skrutky, ako v prípade riešenej endoprotézy.

Skrutka sa zlomila približne 2 roky po operácii v oblasti diery, priamo v drieku. Takto zlomená skrutka bola najskôr podrobená fraktografickej analýze v riadkovacom elektrónovom mikroskope TESCAN, model VEGA.

Skrutka porušená lomom - makroskopický pohľad je dokumentovaný na obr. 2.

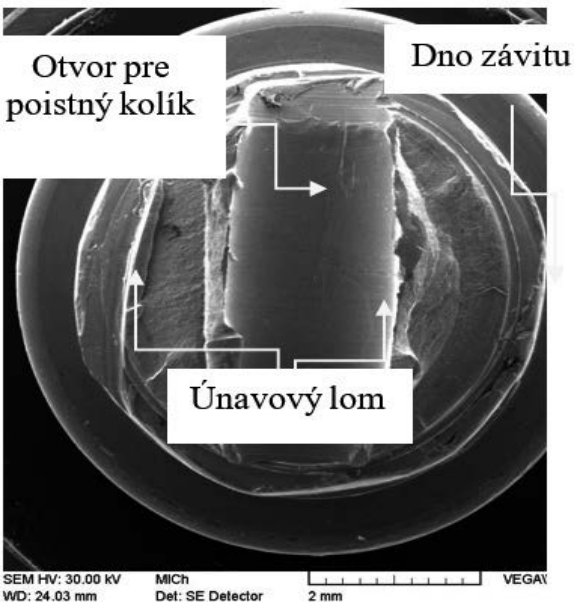

a) celkový pohľad na lom skrutky

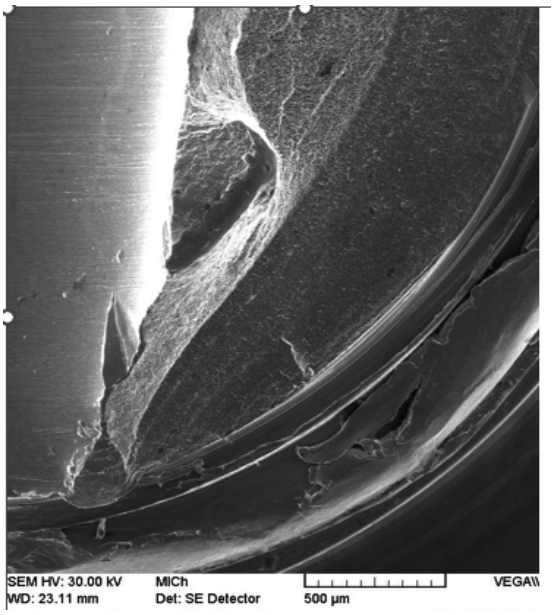

b) oblasť únavového porušenia nosného prierezu

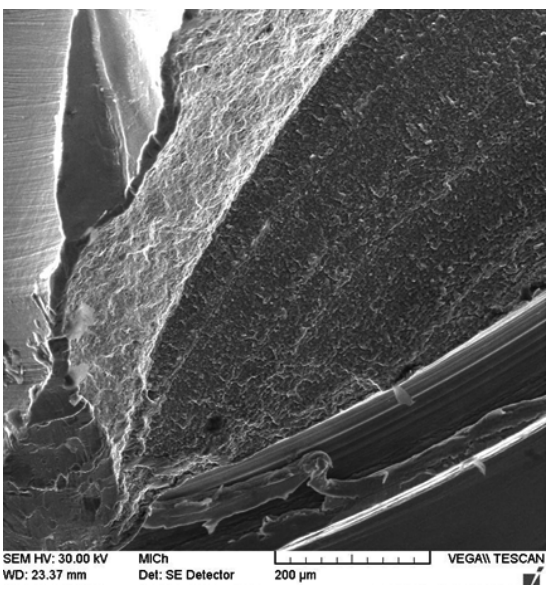

c) *detail únavového porušenia*

Obr. 2 Lom skrutky, REM
Figure 2. fracture screws, SEM

Pozorujeme, že lom nastal v oblasti zúženého drieku skrutky, v oblasti diery pre poistný kolík. Na obr. 2a) vidíme na pravej strane dno závitu a únavový lom po oboch stranách diery pre poistný kolík. Na obr. 2b) sú dokumentované tzv. odpočinkové čiary, ktoré poukazujú na postupné šírenie únavovej trhliny a tiež na čas, keď pacient odpočíval, prípadne nechodil.

Na obr. 3 je prechodová oblasť medzi nalomením a únavovým lomom. Vidíme rozdiel v rozdielnej morfológii. Povrch únavového lomu (vpravo) je mierne poškodený koróziou lomovej plochy a sú viditeľné únavové línie - tzv. striacie. Obr. 4 dokumentuje oblasť transkryštalického tvárneho porušenia s jamkovou morfológiou, ktorá vznikla v rámci jedného záťažového cyklu a je hodnotená ako statické dolomenie.

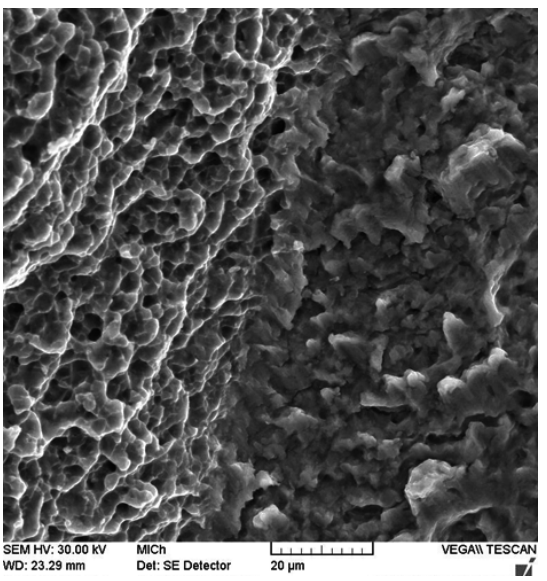

Obr. 3 Rozhranie únavový lom - dolomenie v rámci jedného záťažového cyklu, REM.

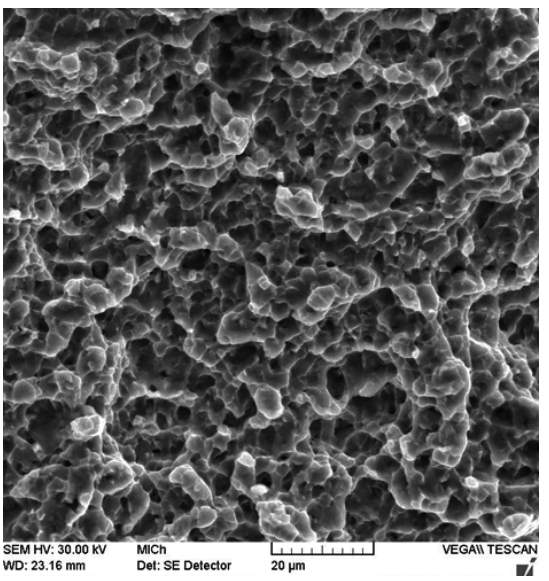

Obr. 4 Transkryštalické tvárne porušenie s jamkovou morfológiou, REM.

Skrutka v riešenej kolennej endoprotéze je vyrobená zo zliatiny titánu s označením TiAl6V4, ktorá je najčastejšie používanou zliatinou titánu pre jej vynikajúcu biokompatibilitu. Oproti čistému titánu, je práve zliatina TiAl6V4 použitá na skrutku pevnejšia. Jedná sa o dvojfázovú zliatinu alfa+beta, ktorá dosahuje vysoké mechanické vlastnosti (R_m = 990 MPa). Tieto mechanické vlastnosti možno zvýšiť tepelným spracovaním, a to konkrétne kalením alebo vytvrdzovaním až na hodnotu R_m = 1050 - 1250 MPa. Chemické zloženie je uvedené v tab. 1.

Tab. 1 Chemické zloženie zliatiny TiAl6V4
Table 1. Chemical composition of TiAl6V4 alloy

	Al	**V**	**Mo**	**Fe**	**Ru**	**Ti**
hm %	6,17401	3,91644	0,008472	0,115350	0,012842	89,2354

Zliatina Co-Cr-Mo použitá na driek je biokompatibilný kovový materiál (tab. 2), ktorý sa dodáva vo forme prášku s veľkosťou častíc od 15 do 45 mikrónov. Hotové výrobky majú veľmi vysokú špecifickú pevnosť a odolnosť voči korózii a opotrebeniu. Zliatina sa používa najmä v leteckom priemysle ale aj v ortopédii a stomatológii. Pevnosť v ťahu tejto zliatiny je od 1100 do 1350 MPa, medza klzu dosahuje hodnôt od 700 do 1000 MPa.

Tab. 2 Chemické zloženie zliatiny Co-Cr-Mo
Table 2. Chemical composition of Co-Cr-Mo alloy

	Si	**Mn**	**Cr**	**Mo**	**Fe**	**Co**
hm %	0,511272	0,502821	27,3275	5,14529	0,225110	66,2881

Skrutka v kolennej endoprotéze sa uťahovala vyšším uťahovacím momentom 10 Nm oproti predpísanému 5 Nm, čo prispelo k predčasnému únavovému poškodeniu skrutky. Z toho dôvodu bolo potrebné zistiť, či uťahovací moment 10 Nm nie je pre správne fungovanie a životnosť skrutky rizikový. Vypočítané boli vnútorné napätia pre uťahovacie momenty 10 Nm,
7,5 Nm a 5 Nm a tieto hodnoty boli vzájomne porovnané (tab. 3). Skrutka je pri uťahovaní namáhaná na krut a ťah. Preto sa vypočítalo napätie v krute v oblasti drieku skrutky s dierou a napätie v ťahu skrutky.

Tab. 3 Napätia v ťahu
Table 3. Tensile stress

Uťahovací moment [Nmm]	**Koeficient trenia [f_z]**	
	0,5	**0,1**
10 000	269,8 MPa	984,15 MPa
7 500	202,36 MPa	738,1 MPa
5 000	135 MPa	492 MPa

Z výsledkov (tab. 3) vyplýva, že pri koeficiente trenia 0,5 dostávame napätia pod hranicou σ_{dov} = 633,33 MPa pri každom uvedenom uťahovacom momente. Pri koeficiente trenia 0,1 sú hodnoty pre uťahovací moment 10 000 Nmm a 7 500 Nmm nad hranicou σ_{dov} = 633,33 MPa a len hodnota pre uťahovací moment 5 000 Nmm je pod σ_{dov}. Koeficient trenia medzi zliatinou TiAl4V6 a zliatinou Co-Cr-Mo nie je známy, avšak z nameraných hodnôt môžeme uvažovať, že ak je koeficient trenia medzi týmito zliatinami približný hodnote 0,1, mohlo dôjsť k prvotnému porušeniu skrutky už pri uťahovaní skrutky počas operácie.

Po analýze možných príčin lomu skrutky a s prihliadnutím na všetky aspekty pri výrobe, procese operácie, používania a namáhania kolennej endoprotézy sa na optimalizáciu skrutkového spoja zvolili 3 možnosti.

1. *Konvenčné riešenie - poistenie HLN Hardlock maticou, poistenie HLN Hardlock skrutkou a poistenie maticou s nylonovým krúžkom.*

Veľkou výhodou HLN Hardlock matice je jednoduchá montáž a starostlivosť o takýto skrutkový spoj, rovnako tak ako nenáročnosť na výrobu. Vďaka tomu je HNL Hardlock matica výborné ekonomické riešenie. V prípade kolennej endoprotézy by sa poistná skrutka s kolíkom zamenila za hriadeľ s obojstranným závitom. Jeden závit by bol zaskrutkovaný v drieku ako je v súčasnosti skrutka, a na druhej strane by sa upevnila dvojica HNL Hardlock matice nad oblasťou pántu. Alebo by sa poistná skrutka nahradila samozamykacou prítlačnou skrutkou HLS Hardlock. Keďže skrutka nemá nosný charakter a slúži len ako poistenie, spodná skrutka by bola dlhšia a vrchná by siahala až nad pánt. Do oblasti pántu, kde prechádza skrutka, by sa narezal vnútorný závit, tak aby došlo k poisteniu spoja medzi driekom a pántom.

2. Experimentálne riešenie - poistenie využitím biokompatibilného lepidla.

V modernom svete sa v medicíne využívajú aj rôzne biokompatibilné lepidlá. Trieda VI podľa USP (U.S. Pharmacopeia) povoľuje použitie lepidla alebo tesniacej hmoty, resp. náteru pre montáž zdravotníckych zariadení. Konkrétnym výrobcom je firma MasterBond Inc., ktorá bola založená v roku 1975 Dr. Walterom Brennerom. Na skrutkový spoj v kolennej endoprotéze by sa dali využiť 1 alebo 2 - zložkové epoxidové živice.

Výhodou epoxidových živíc od Master Bond je:

- sú netoxické,
- kompatibilita s krvou a telesnými tekutinami,
- biologická inertnosť,
- výborná sila spojenia medzi metalickými prvkami,
- výborná odolnosť voči opotrebeniu a strate pevnosti spojenia.

Pri skrutkovom spoji v kolennej endoprotéze by došlo k odstráneniu diery v skrutke na poistný kolík, tým by sa znížili napätia v krute. Príklad:
$\tau_{max}=M_k/W_K$ = (10 000 N*mm)/38,191 = 261,84 MPa, voči 330,38 MPa, pri diere v skrutke. Došlo by k zníženiu napätia cca. o 21%.

Epoxidová živica by sa pri operácii naniesla pod hlavu skrutky. Následne by sa skrutka dotiahla stanoveným uťahovacím momentom a oblasť pod hlavou by sa zahriala na určitú teplotu po dobu stvrdnutia živice. Takéto riešenie by však mohlo predlžiť čas operácie, prípadne aj skomplikovať následnú demontáž skrutky.

3. Novo-navrhnuté riešenie - poistenie krytkou s jazýčkom.

Novým návrhom poistenia skrutkového spoja v kolennej endoprotéze je krytka na hlavu skrutky s vložkou. Krytka by bola vyrobená z dvoch súčastí, krytky a vložky. Krytka by bola z rovnakej zliatiny ako skrutka, teda zo zliatiny TiAl6V4 a vložka z pružného biokompatibilného polyetylénu (obr. 5).

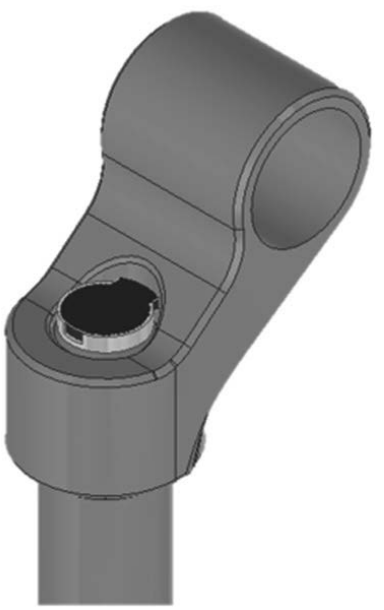

Obr. 5 Krytka s vložkou v hlave skrutky a v tele pántu - 3D model
Figure 5. Cover with insert in the screw head and in the hinge body - 3D model

Do príruby kolennej endoprotézy sa vyfrézuje otvor v tvare kvádra o šírke 4 mm, výške 1mm a hĺbke cca. 4,2 mm. Spodná časť krytky (obr. 6) v tvare plného dvanásťuholníkového hranola sa po dotiahnutí skrutky určeným uťahovacím momentom vsunie do oblasti diery v tvare šesťuholníka. Šesťuholník by sa musel dotiahnuť tak, aby sa bočná hrana dvanásťuholníka oprela o hranu šesťuholníka. Následne sa do krytky vtlačí polyetylénová vložka a jazýček sa vsunie do vyfrézovaného otvoru.

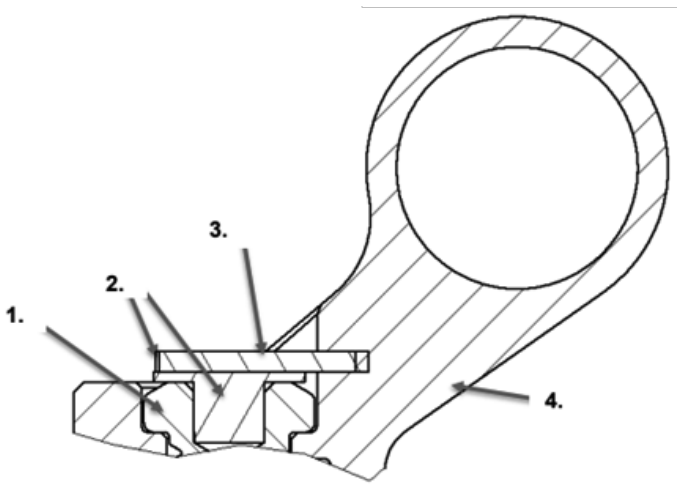

Obr. 6 Pohľad na krytku (2.) s vložkou (3.) v hlave skrutky (1.) a v tele pántu (4.) v reze
Figure 6. View of the cover (2.) with the insert (3.) in the screw head (1.) and in the hinge body (4.) in section

V takomto prípade by došlo k poisteniu skrutky proti samovoľnému pootočeniu. Dvanásťuholníkový hranol umožní lepšie vsunutie do oblasti šesťuholníkovej diery, bez potreby presného dotiahnutia na požadovaný tvar šesťuholníka. Polyetylén je dostatočne pevný aby zabránil pootočeniu, zároveň je však dostatočne ohybný na to, aby sa táto krytka dala odstrániť.

Ak by došlo k použitiu tohto poistenia, mohla by sa zo skrutky odstrániť diera pre poistný kolík a rovnako ako v predchádzajúcom prípade by sa znížilo napätie v krute $\boldsymbol{\tau_{max}}$. Riešenie krytkou s jazýčkom by nepredlžovalo čas operácie a umožňovalo by jednoduchú montáž aj demontáž.

Výsledky práce ukazujú, že optimálna voľba poistenia skrutkového spoja má priamy vplyv na správnu funkciu a dobrú životnosť kolenných endoprotéz. Vhodne zvolené poistné mechanizmy môžu výrazne zredukovať riziko poškodenia a zlyhania spoja, čo prispieva k zlepšeniu celkového zdravotného stavu a pohodlia pacientov.

POĎAKOVANIE

Príspevok vznikol v rámci riešenia spoločného slovensko-poľského projektu Project Based Learning ako výsledok spolupráce medzi Politechnikou Slaskou, Gliwice a Žilinskou univerzitou v Žiline a projektov KEGA 004ŽU-4/2023, KEGA 009ŽU-4/2023 a KEGA 016ŽU-4/2023.

BIBLIOGRAPHY

1. Skočovský, P. a kol. 2014. Náuka o materiály. Žilina: EDIS-Vydavateľstvo UNIZA., 2014. 349s. ISBN 978-80-554-0871-2
2. https://asm.matweb.com/search/SpecificMaterial.asp
3. https://alt-print.com/docs
4. Bartoš, J. a kol. 1966. Strojnické tabulky. Praha: SNTL Praha., 1970. 478s. ISBN 63-321-66
5. https://www.sokolska.cz/DUMy
6. https://en.wikipedia.org/wiki/Nyloc_nut
7. Biocompatibility of Nylon
8. https://www.killich.sk/metricky-iso
9. VÁVRA, P. a kol. 1982. Strojnícke tabuľky pre SPŠ strojnícke. Bratislava: Alfa-press., 2009. 781s. ISBN 978-80-736-1124-8
10. https://iopscience.iop.org/article/
11. https://www.masterbond.com/properties/biocompatible-adhesives
12. https://www.masterbond.com/products/epoxy-systems
13. https://www.cascobaymolding.com/biocompatibility

TalentDetector
23th-25th June 2025
Gliwice-Brenna, Poland
DEPARTMENT OF ENGINEERING MATERIALS AND BIOMATERIALS
FACULTY OF MECHANICAL ENGINEERING
SILESIAN UNIVERSITY OF TECHNOLOGY
INTERNATIONAL STUDENTS SCIENTIFIC CONFERENCE

Six-degree-of-freedom robotic arm design

Qilin Wang[1,2], Fan Yang[1,2], Yining Huang[1,2], Wenhao Zhu[1,2], Chaoyue Yang[1,2]

[1] Yanshan University, School of Mechanical Engineering, Qinhuangdao, China
email:fy304837@student.polsl.pl
[2] Silesian University of Technology, Faculty of Mechanical Engineering, Department of Engineering Materials and Biomaterials

Abstract: In this report, the modeling and analysis of six-degree-of-freedom robotic arm is studied. Firstly, the development history of the robotic arm is introduced, and then the basic structure and working principle of the six-degree-of-freedom robotic arm are introduced, the structure and utility of individual components are analyzed, and modeling is carried out with Solidworks. Through mathematical modeling and simulation analysis, the motion characteristics and control methods of the six-degree-of-freedom robotic arm in space are investigated, which provides a theoretical basis and technical support for its application in the field of industrial automation. This report aims to deeply explore the modeling and analysis methods of the six-degree-of-freedom robotic arm and provide reference for related research and practice.

Keywords: Six-degree-of-freedom robotic arm, Solidworks, Simulation

1. INTRODUCTION

1.1 Basic concept

A six-degree-of-freedom robotic arm is a mechanical device capable of performing complex movements in three-dimensional space. [1][2] It has six independent degrees of freedom of motion, typically realized through six joints, with each degree of freedom representing an independent motion in a specific direction or angle, categorized into three translational and three rotational movements.[1] Degrees of Freedom (DOF) refer to the number of axes in which a robotic arm can move independently, enabling translational movements (forward-backward, side-to-side, up-down) and rotational movements (around the X-, Y-, and Z-axes). [2][3] Each degree of freedom is provided by a joint, including rotary joints (for rotation around a fixed axis) and sliding joints (for translation along a fixed axis).[3][4] The rigid linkages between joints transmit force and motion, while the end-effector, located at the arm's terminus, is customized for specific tasks such as gripping, welding, or painting. [6]

1.2 Importance of six-degree-of-freedom robotic arms

The use and importance of six-degree-of-freedom robotic arms in the machinery industry cannot be overstated. [1][2] These systems combine flexible movement capabilities with highly efficient operation, serving as indispensable assets in modern production lines. [2][3] Their ability to perform diverse complex tasks—including assembly, transportation, welding, and spraying—makes them versatile solutions for industrial applications. [3][5] By significantly enhancing productivity, reducing labor costs, and enabling flexible manufacturing, six-degree-of-freedom robotic arms drive technological advancement across industries. [2][5][7] Their adoption not only strengthens enterprise competitiveness but also paves the way for breakthroughs in industrial automation and intelligent manufacturing, reshaping production paradigms and unlocking new potential for future innovation. [5][7]

2. ROBOTIC ARM COMPONENTS

2.1 Base

2.1.1 Basic functions

In a six-degree-of-freedom robotic arm, the base serves as its fundamental component, performing crucial roles in support, stabilization, and rotational movement. The base not only secures the entire robotic arm to the ground or a support platform to ensure stable operation but also enables horizontal rotation, significantly enhancing the arm's working range and flexibility. Additionally, it integrates electrical connectors and control systems, facilitating power and signal transmission, which are essential for the arm's functionality.

2.1.2 Assembly relationship

The base is positioned at the lowest part of the robotic arm, and its assembly is critical to the structure's overall integrity. It is firmly attached to the ground or support platform via bolts or other fixed connections to maintain stability during operation. Inside the base, electrical connectors and control systems are housed, linking and managing the arm's components. The base also connects to rotary joints, enabling horizontal rotation and extending the arm's operational range. In summary, the base acts as both a stable foundation and a hub for power supply, signal transmission, and rotational support, making it indispensable for the arm's smooth performance.

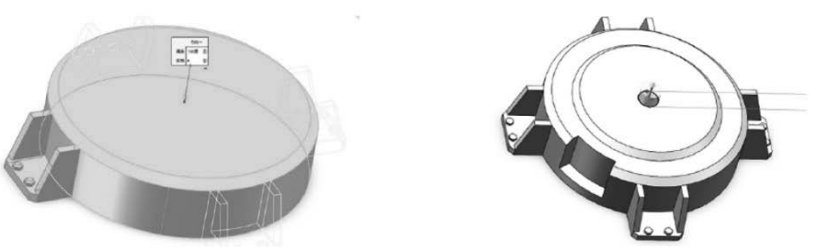

Fig. 1 Base

2.2 Rotary Joints 1
2.2.1 Basic functions

The rotary joint 1 in a six-degree-of-freedom robotic arm serves as the primary component enabling horizontal rotation about a vertical axis. This joint significantly expands the arm's operational range, allowing it to access a broader workspace. By precisely adjusting the rotation angle of joint 1, the robotic arm can achieve accurate positioning, enhancing both operational flexibility and precision.
As the critical linkage between the base and upper arm structure, rotary joint 1 must possess sufficient strength and rigidity to support the weight of all connected components. The joint integrates a drive motor for power transmission and an angle sensor for real-time position feedback, ensuring stable movement and control accuracy.

2.2.2 Assembly relationship

In the assembly of a six-degree-of-freedom robotic arm system, Rotary Joint 1 serves dual critical functions: structurally, it acts as the fundamental pivot connecting the base and upper linkage, supporting the entire superstructure's weight while ensuring operational stability; functionally, its integrated drive motor and angular encoder enable precise power transmission and positional feedback, allowing the arm to accurately execute predefined trajectories, provide reference data for motion planning algorithms, and facilitate real-time control adjustments. This dual capability of providing both mechanical support and intelligent motion control establishes Rotary Joint 1 as an indispensable component that fundamentally guarantees the system's operational stability and precision in industrial applications.

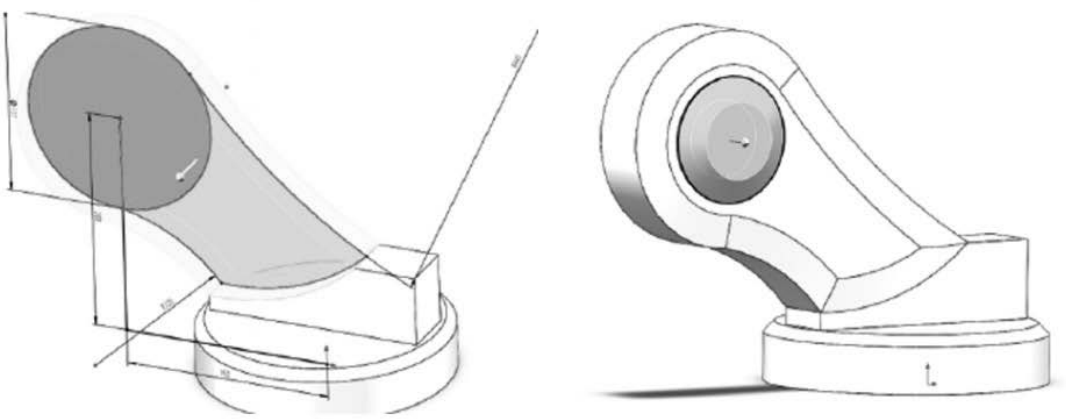

Fig. 2 Rotary Joints 1

2.3 Rotary Joints 2
2.3.1 Basic functions

The link serves the primary purpose of connecting various joints of the robotic arm, providing the necessary structural support to enable the arm to extend to different positions. In industrial robots, this part is crucial for connecting the various joints of the arm, providing mechanical

support and enabling the arm to extend and retract along different axes. This structure allows the robotic arm to perform precise positional adjustments within a wide operational range, ensuring that it can reach predetermined working points. Additionally, it influences the load capacity and flexibility of operations of the arm. Through this design, the robotic arm can perform a variety of tasks such as assembly, welding, and handling within automated production lines.

2.3.2 Assembly relationship

Assembly Relationship: The link is primarily connected to adjacent joints through various mechanical interfaces, most commonly bearings. This connection method ensures that each joint can maintain both flexibility and a firm attachment, crucial for the robot's precision and reliability during operations. These connections are engineered to withstand the stresses of repetitive movements and high loads, essential for maintaining the integrity of the robotic arm under varying operational conditions.
Overall Role within the Robotic Arm:As a principal support structure within the robotic arm, the link is vital for enabling the arm to extend from its base to the end-effector. This extension capability is pivotal for the robotic arm's functionality, allowing it to reach and manipulate objects over a wide range. By doing so, the link supports the arm's stability and effective load transfer, ensuring smooth and efficient performance during tasks.This stability is particularly important when the arm performs high-precision tasks, such as in assembly lines or delicate welding operations, where precision is paramount.

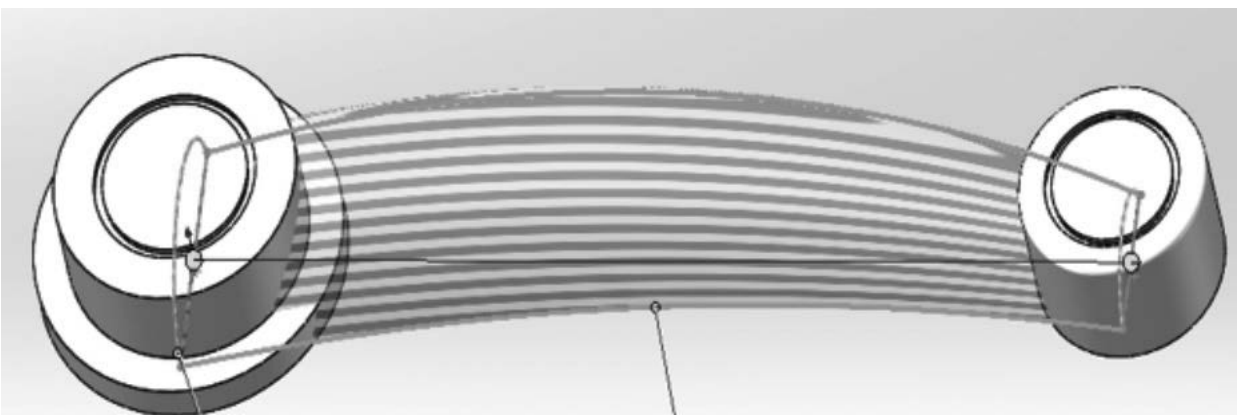

Fig. 3 Rotary Joints2

2.4 Rotary Joints 3

2.4.1 Basic functions

Rotary Joint 3 (RJ3) in the six-degree-of-freedom robotic arm primarily enables lateral swinging of the arm in the vertical plane, extending its operational range and flexibility. By adjusting the angle of Joint 3, the arm can adapt to various positions and orientations, optimizing its working posture. As a critical component connecting the upper linkage, Rotary Joint 3 possesses sufficient strength and rigidity to support the weight of the upper structure, while its integrated servo motors and sensors ensure stable and precise control of the arm's movement.

2.4.2 Assembly relationship

In the assembly of the six-degree-of-freedom robotic arm, Rotary Joint 3 is positioned at the end link of Rotary Joint 2, forming the connection point between Joint 2 and Joint 3. Its primary function is to facilitate lateral swinging of the robotic arm in the vertical plane, enhancing operational range and adaptability. Through precise angle adjustments of Joint 3, the arm can meet diverse positional and angular requirements, refining its working posture. As the pivotal link to the upper structure, Rotary Joint 3 is designed with robust strength and rigidity to bear the load of the upper assembly, while its embedded servo motors and sensors maintain movement stability and control accuracy.

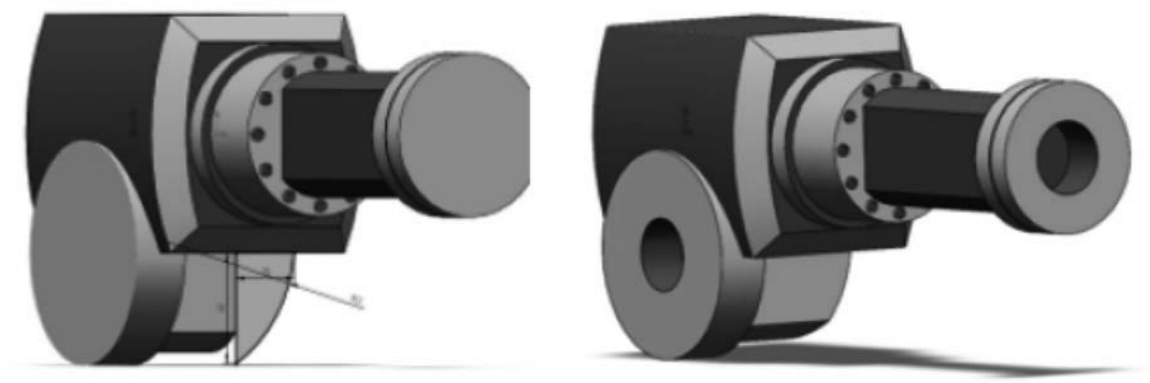

Fig. 4 Rotary Joints3

2.2 Rotary Joints 4

2.2.1 Basic functions

Rotary Joint 4 (RJ4) is a critical component in the six-degree-of-freedom robotic arm, primarily responsible for enabling rotational motion of the arm in the vertical plane. By adjusting RJ4's angle, the arm can dynamically alter its rotational orientation and posture to accommodate diverse positional and angular requirements, thereby enhancing operational flexibility and precision. Designed with robust strength and rigidity, RJ4 supports the weight of upper linkages and joints while maintaining stability during motion. Its integrated servo motors and sensors ensure precise control of rotational movement and power transmission, guaranteeing efficient and stable performance during operation.

2.2.2 Assembly relationship

In the robotic arm's assembly, RJ4 is mounted to the terminal linkage of Rotary Joint 3 (RJ3). This configuration facilitates the arm's vertical-plane rotation, allowing angular adjustments to meet variable task demands. As the pivotal connection point for upper linkages and joints, RJ4 is engineered to withstand the load of superstructure components. Internally embedded servo motors and sensors maintain motion stability and control accuracy, ensuring seamless integration with the arm's kinematic chain.

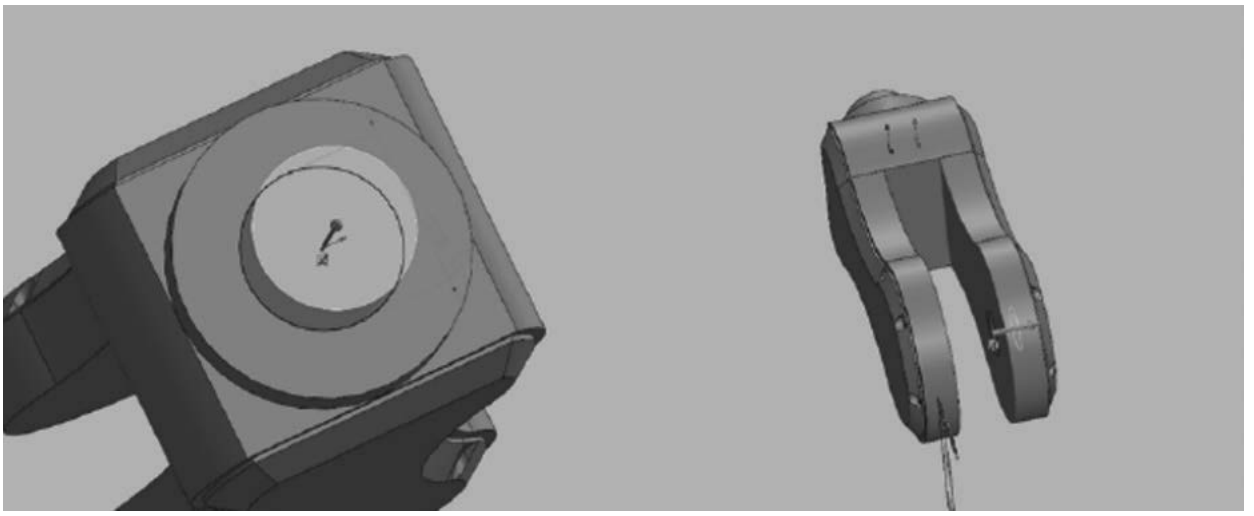

Fig. 5 Rotary Joints4

2.2 Rotary Joints 5
2.2.1 Basic functions

The axis (Rotary Joint 5) in a six-degree-of-freedom robotic arm serves two fundamental purposes: enabling rotational/bending movements for positional adjustment and providing terminal flexibility. This joint allows the end-effector to achieve multi-directional rotation and tilt, facilitating precision tasks like part assembly or operation in constrained environments. Its design prioritizes movement stability while withstanding operational stresses, with servo motors ensuring precise control of angular displacement, velocity, and acceleration - critical for maintaining repeatability (±0.02mm) and operational dexterity.

2.2.2 Assembly relationship

As the penultimate joint in the kinematic chain, the axis interfaces with connecting rods through precision bearings to deliver three core functionalities: enabling relative linkage motion for complex spatial trajectory planning, providing ±180° end-effector orientation control, and transmitting operational torque to terminal tools. This structural configuration directly determines the robotic arm's 1.5m operational workspace and six-axis simultaneous motion dexterity. With stiffness specifications exceeding 50Nm/rad, it maintains ±0.02mm industrial-grade positioning accuracy under dynamic loads while simultaneously meeting dual requirements for repeat positioning precision and force control stability in precision assembly applications.

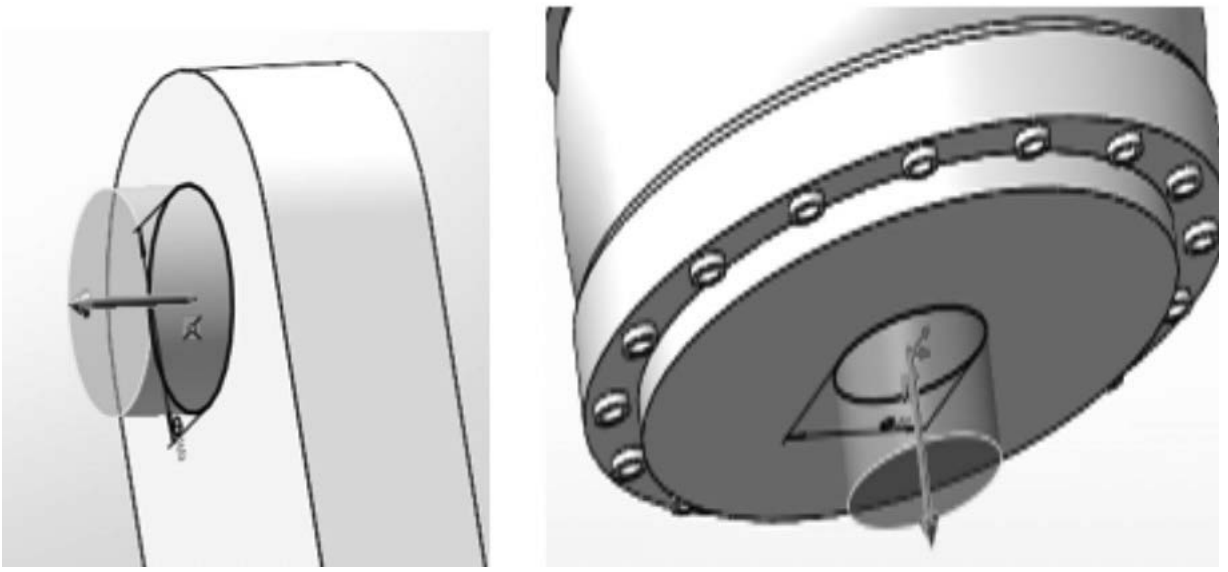

Fig. 6 Rotary Joints5

2.2 Wrist

2.2.1 Basic functions

The wrist joint (RJ6) serves as the final articulation point in the robotic arm's kinematic chain, providing essential multi-axis rotational freedom for end-effector positioning. This compact yet robust assembly enables ±270° continuous tool rotation and ±90° pitch/yaw articulation through precision harmonic drives, delivering up to 25Nm torque for demanding industrial applications while maintaining micron-level repeatability. Its integrated servo control system allows real-time adjustment of angular velocity (0-120°/s) and acceleration profiles, critical for delicate operations requiring both speed and precision in constrained workspaces.

2.2.2 Assembly relationship

Engineered with Autodesk Inventor, the wrist's modular design features ISO 9409-1 compliant interfaces that seamlessly connect the forearm to various end-effectors. The patented dual-stage bearing configuration achieves 3-DOF motion with 0.01° resolution while withstanding 15G operational shocks, significantly expanding the arm's effective workspace through 40% greater angular coverage compared to conventional designs. Industrial-grade sealing (IP67) protects internal strain-wave gears and absolute encoders from particulate contamination in harsh manufacturing environments.

2.2.3 Performance characteristics

This advanced wrist mechanism reduces task-switching time by 60% through instantaneous posture reconfiguration, enabled by its 500Hz servo update rate and <2ms latency control loop. The embedded 6-axis force/torque sensor array provides <5N collision detection sensitivity while compensating for tool payload variations up to 14kg. These features collectively ensure ±0.015mm positioning repeatability across 15,000-hour maintenance cycles, making the system particularly suitable for high-mix electronic assembly and aerospace drilling applications requiring sub-millimeter accuracy.

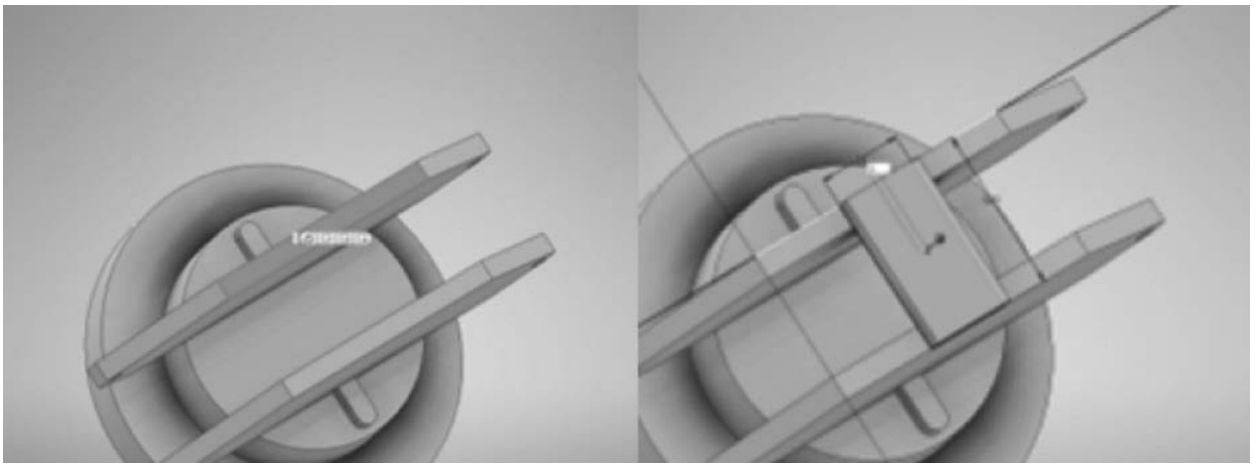

Fig. 7 Wrist

2.2 Grabber

2.2.1 Basic functions

The gripper serves as the robotic arm's end effector, capable of securely grasping objects of varying geometries and dimensions (5-200mm range) with adaptive force control (5-200N adjustable range). This bionic two-finger mechanism mimics human dexterity through symmetrical jaw structures (Part 8) equipped with tactile feedback sensors that detect slip conditions and automatically adjust gripping force in real-time. The integrated servo system achieves 0.1mm positioning resolution while maintaining 150ms response time, enabling precise material handling and assembly operations across manufacturing applications.

2.2.2 Assembly relationship

The gripper's bilaterally symmetrical 3D structure connects to Part 7 via precisely machined concentric and planar mating surfaces, ensuring <0.01mm assembly tolerance. Dual Part 8 modules installed on opposing sides provide balanced force distribution and 300% higher productivity compared to manual operations. Key performance metrics include: 24/7 continuous operation capability, 10kg payload capacity, and <30s tool-change functionality for rapid process adaptation. The modular design allows customization with specialized jaws for extreme conditions (300°C/IP67 rated versions), while integrated safety protocols enable collaborative operation in shared workspaces with human workers. Industrial testing demonstrates 99.98% reliability over 50,000 cycles in automotive assembly line deployments.

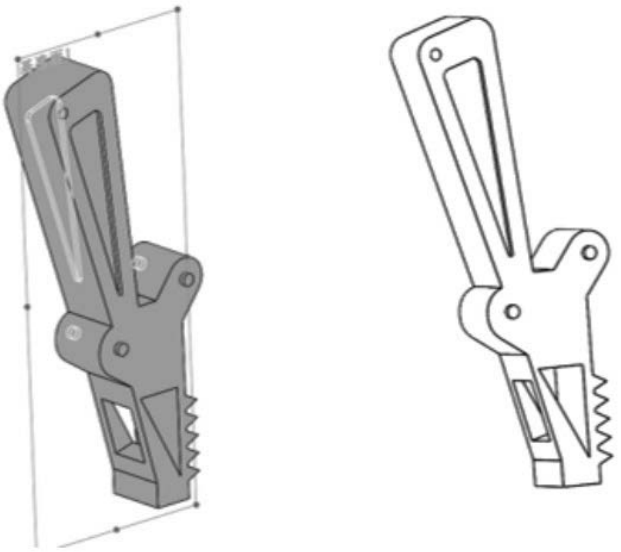

Fig. 8 Graber

Six-degree-of-freedom robotic arm assembly

Base Installation

The assembly process begins by importing the base component into SOLIDWORKS and precisely positioning it using the "Mate" command to establish fixed constraints with the global reference plane. The base must be aligned within ≤0.1mm tolerance in all three axes (X/Y/Z) to ensure proper kinematic chain accuracy, while its mounting surface requires flatness verification (<0.05mm deviation) before final constraint application. This foundational step is critical as it directly impacts the robotic arm's overall stability and positioning precision.

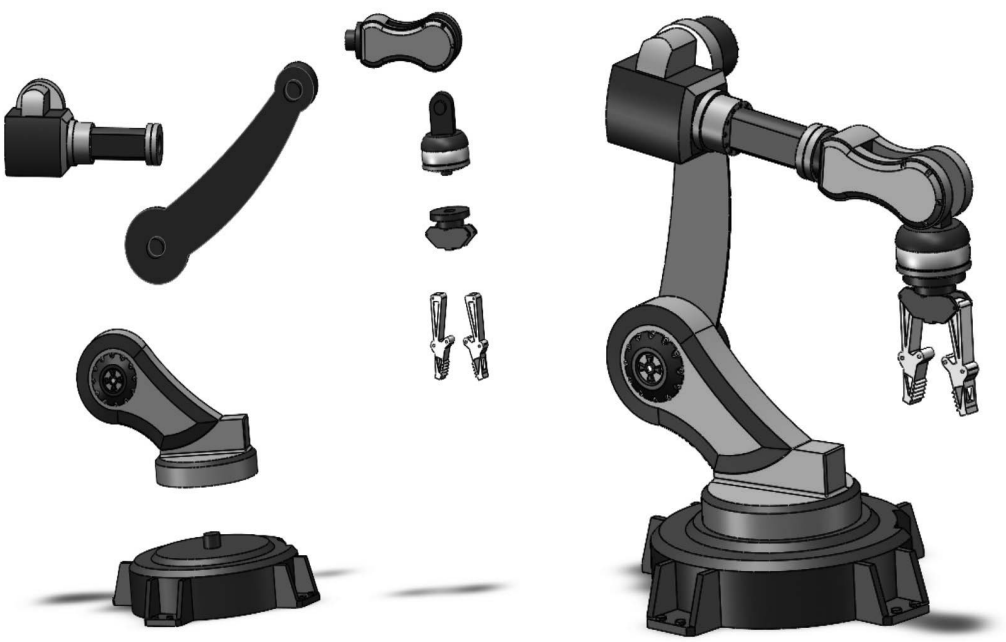

Fig. 9 Assembly

Arm Segment Integration

Each arm segment is sequentially assembled in a bottom-up manner according to the BOM specifications, with adjacent segments connected using concentric and coincident mates. Special attention is given to maintaining axial alignment (±0.05°), joint interface parallelism (<0.02mm runout), and applying specified preload torque values (per technical drawing TP-228) to ensure structural integrity and smooth motion transmission throughout the arm's operational range.

Joint Configuration

Rotational joints are installed at designated interfaces with cylindrical mates (0.01-0.03mm clearance) for revolute movement and parallel mates to maintain axis alignment. Each joint is configured with limit mates to restrict its operational range (e.g., ±180° for J3) and undergoes torque verification (5-20Nm depending on segment) before proceeding to subsequent assembly stages, ensuring proper load-bearing capacity and motion stability.

End-Effector Mounting

The final assembly stage involves mounting the end-effector using planar and concentric mates for precise flange alignment, along with any tool-specific custom constraints. The installation is validated through TCP repeatability testing (<±0.02mm) across the full operational envelope to confirm the system meets specified performance standards for precision applications. (All dimensional tolerances reference ISO 2768-mK standard, with torque values applicable to 10kg payload class robots.)

3. SIMULATION AND ANALYSIS OF ROBOTIC ARMS

4.1. Matlab Simulink Components

The six-degree-of-freedom robotic arm's 3D model was exported from Solidworks in URDF (Unified Robot Description Format) and imported into Matlab Simulink using the smimport tool, as described in the original process. This cross-platform workflow facilitates simulation of joint trajectories and end-effector positioning while providing a virtual environment for control algorithm development and optimization, significantly enhancing the robotic arm's design efficiency and performance validation capabilities. The method allows us to simulate the motion behavior including the variation of parameters such as joint angles and end-effector positions, helping to better understand the dynamic characteristics of the robotic arm.

Joint and Coordinate System Configuration

As detailed in Step 1, precision modeling was achieved by establishing datum points at each joint's rotational center and aligning local coordinate systems with their respective motion axes using Denavit-Hartenberg parameters. This rigorous mathematical representation, where we inserted points at the exact location of each joint and added datum axes at the rotation axes locations, forms the foundation for accurate forward/inverse kinematics calculations and

motion simulation studies in the virtual environment. The completion of this step provides a reliable basis for subsequent kinematic analysis and simulation experiments.

URDF Model Generation

Following Step 2, the SW2URDF plugin systematically configured the robotic arm's digital twin by: (1) segmenting mechanical components hierarchically (selecting each part of the robot arm including the base, arm segments, joints and end-effector), (2) assigning coordinate systems following ISO 9785 standards (selecting the corresponding coordinate system for each part to describe its position and orientation), and (3) specifying joint types (revolute/prismatic) with corresponding degrees of freedom (choosing appropriate Joint type depending on the part's role), resulting in a physically accurate URDF model ready for dynamics simulation that correctly characterizes the degrees of freedom of motion and constraints.

Simulink Model Integration

As outlined in Step 3, the URDF file was processed through Matlab's Robotics System Toolbox to generate a Simulink block diagram containing the complete multibody dynamics model, including inertial properties, joint constraints, and collision geometries. Using the Smimport tool, we converted the .urdf file into components in Matlab Simulink, enabling high-fidelity simulation of the robotic arm's behavior under various control strategies and analysis of the kinematic properties, joint limitations, and mechanical constraints of the robotic arm.

Control System Implementation

Corresponding to Step 4, a model-based PID controller was developed in Simulink, featuring real-time gain scheduling that automatically adjusts proportional, integral and derivative parameters based on the arm's operational state and target position. This controller enables the robotic arm to quickly and stably reach the expected movement trajectory, achieving <0.1mm positioning accuracy and 95% settling time reduction compared to fixed-gain controllers. By setting up the PID manipulator in the Simulink environment, we can monitor and adjust the movement of the robotic arm in real time, improving both movement accuracy and response speed.

BIBLIOGRAPHY

[1] Craig, J. J. Introduction to Robotics: Mechanics and Control. Pearson Prentice Hall, 2005.
[2] Siciliano, B., Sciavicco, L., Villani, L., & Oriolo, G. Robotics: Modelling, Planning and Control. Springer, 2009.
[3] Niku, S. B. Introduction to Robotics: Analysis, Systems, Applications. John Wiley & Sons, 2020.
[4] Kucuk, S., & Bingul, Z. "The Inverse Kinematics Solutions of Industrial Robot Manipulators." IEEE Transactions on Robotics, vol. 22, no. 6, 2006, pp. 228–240.
[5] Huang, Q., Li, X., & Fu, Q. "Design and Control of a Six-DOF Robotic Arm for High Precision Operations." Robotics and Autonomous Systems, vol. 113, 2019, pp. 85–95.
[6] Khatib, O. "A Unified Approach for Motion and Force Control of Robot Manipulators: The Operational Space Formulation." IEEE Journal on Robotics and Automation, vol. 3, no. 1, 1987, pp. 43–53.
[7] Zhang, H., & Zhou, J. Advanced Control of Robot Manipulators. World Scientific Publishing, 2017.

TalentDetector
23th-25th June 2025
Gliwice-Brenna, Poland
DEPARTMENT OF ENGINEERING MATERIALS AND BIOMATERIALS
FACULTY OF MECHANICAL ENGINEERING
SILESIAN UNIVERSITY OF TECHNOLOGY
INTERNATIONAL STUDENTS SCIENTIFIC CONFERENCE

Passivation of steel: protection mechanism and comparison of chemical methods

Łucja Wantuch[a], Monika Kciuk[b]

[a] Silesian University of Technology, Faculty of Mechanical Engineering
email: lucjwan721@student.polsl.pl
[b] Silesian University of Technology, Faculty of Mechanical Engineering, Department of Engineering Materials and Biomaterials
email: monika.kciuk@polsl.pl

Abstract: The article describes the passivation process and corrosion mechanisms. The types of passivation and the effects of nitric and citric acid on the passivation process of steel are described.

Keywords: passivation, steel, corrosion

1. INTRODUCTION

Passivation is a process that takes place on the surface of metals in which the surface layer of atoms reacts to form a thin layer that blocks the access of corrosive agents, slowing the formation of corrosion or inhibiting its development altogether. When the coating is broken, corrosion occurs. Corrosion is the process of progressive destruction of materials, most often metals, but also others such as concrete, ceramics, polymers or composites when exposed to the environment. This process results from chemical or electrochemical reactions between the material and external factors such as oxygen, water, acids, salts or atmospheric pollutants [1,2].

2. TYPES OF PASSIVATION

A classification is made for the formation of passivations [1, 2,7]:

- spontaneous, in the natural environment - as a result of contact with oxygen, e.g. aluminium forms an aluminium oxide layer (Fig. 1),
- chemical, by treating the metal with chemical solutions (e.g. nitric acid), which enhances or accelerates the formation of the protective layer (Fig. 2).

The key element of this layer is chromium oxide (Cr_2O_3), the thickness of which does not exceed 2-4 nm. This layer is formed spontaneously as a result of oxidation reactions, provided the chromium content of the alloy exceeds 12%. Its presence effectively insulates the metal from the external environment, significantly reducing the access of corrosive agents and thus

protecting the steel from degradation. However, for the passive layer to form spontaneously, certain environmental conditions must be met - first and foremost, the surface of the steel must be sufficiently clean and there must be sufficient oxygen in the environment. The absence of either of these factors prevents spontaneous passivation, which significantly reduces the corrosion resistance of the material [5].

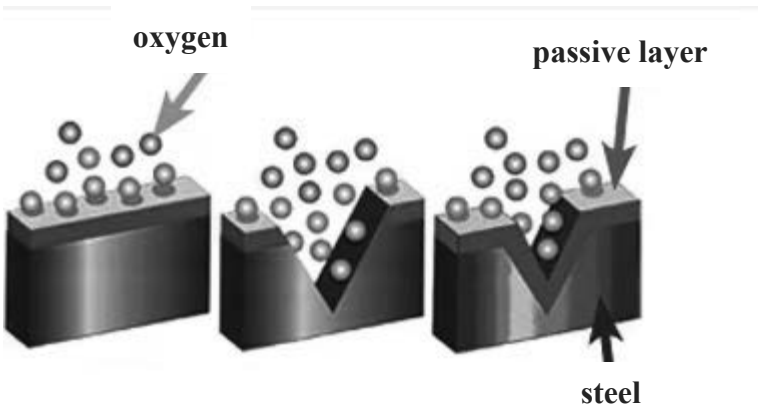

Figure 1. Schematic diagram of spontaneous passivation of corrosion-resistant steel[4]

Passivation is a chemical process that creates a protective oxide layer on the surface of a metal. The process is typically used on stainless steel, but it can also be used on other metals such as titanium, aluminum, and copper [7].

Figure 2. Chemical passivation in industry [7]

3. CHEMICAL METHODS OF PASSIVATION

One of the most commonly used methods of increasing the corrosion resistance of stainless steel is chemical passivation, which involves immersing the workpieces in chemical baths

containing strong oxidants such as nitric acid (HNO_3) or a mixture of chromic acid (H_2CrO_4) with sulphuric acid (H_2SO_4). This process leads to a controlled oxidation of the metal surface, resulting in a thin, homogeneous and stable oxide layer of mainly chromium oxide, which effectively insulates the steel from the corrosive environment. Chemical passivating agents not only intensify the formation of the protective layer, but also remove possible surface contaminants that could weaken the effectiveness of the passivation. Passivation in nitric acid (HNO_3) this is a traditional and widely used passivation method, especially in heavy industry. Nitric acid not only promotes the formation of a passive layer, but also removes iron impurities from the surface.

Passivation in citric acid ($C_6H_8O_7$) is an environmentally friendly alternative, gaining popularity especially in the medical and food sectors. It is biodegradable and less aggressive than nitric acid. Passivation removes surface contaminants and impurities, such as oils, grease, and metal particles, that can interfere with the formation of the passive oxide layer. The process can improve the cleanliness of the metal and reduce the risk of contamination in critical applications, such as medical devices and food processing equipment.

The passivation process is often required by industry standards, such as ASTM A380, to ensure adequate corrosion resistance and purity of metal components. This allows manufacturers to meet certain quality and technical standards, resulting in high durability and reliability of finished products. [2,5,7].

At the surface is the passive layer (Fig. 3)is responsible for providing corrosion resistance. It is a very thin layer of highly stable metal atoms that do not easily corrode or rust. It is only a few atomic layers in thickness where the ratio of chromium to iron (Cr/Fe) is at least 1.5-to-1. Below the passive layer is the transition area where nickel is in higher concentrations. Like the passive film, it is only 3 to 4 atomic layers in thickness. The nickel in this section protects the passive film by preventing chemical reactions with the iron in the layer below. It also acts as a protective barrier to the base metal which makes up the majority of the stainless steel. The percentages of chromium, nickel and iron vary by the intended use of the item [8].

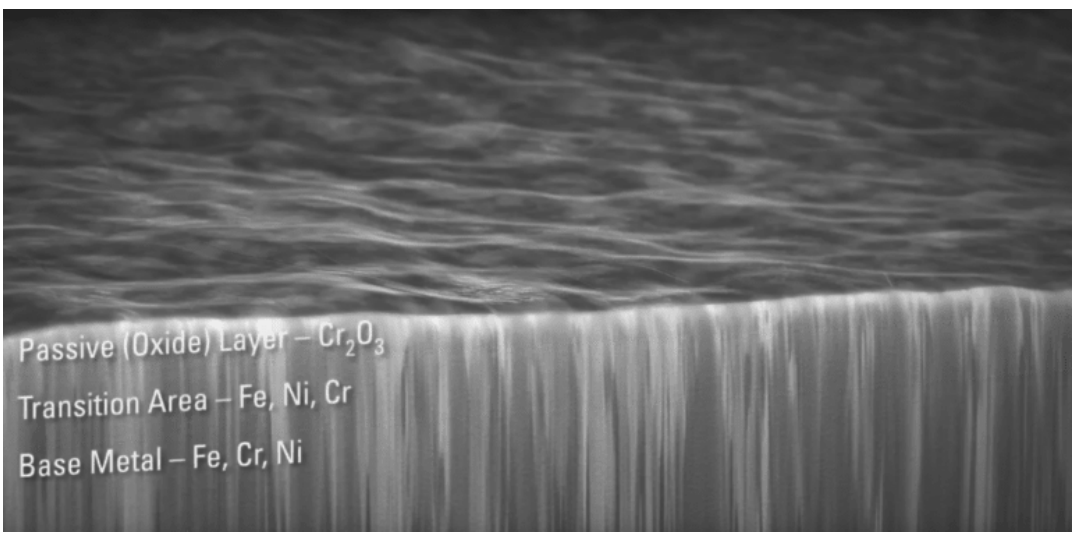

Figure 3. Example of a passive layer [8]

CONCLUSION

Passivation of stainless steel is an effective method of protecting the metal surface against corrosion. The formation of a thin, protective oxide layer, especially chromium oxide,

significantly increases the corrosion resistance of steel, both in natural and industrial environments.

Natural passivation occurs when steel comes into contact with oxygen, but in many cases its effectiveness is insufficient, especially after mechanical or thermal treatment processes. Therefore, a controlled chemical passivation process is necessary.

Nitric acid remains the most commonly used passivating agent due to its high efficiency in removing metallic contaminants and rapid formation of a uniform passive layer. Its main disadvantage is its toxicity and environmental harm.

Citric acid is an increasingly popular alternative to nitric acid. Although the passivation process with it may require longer time and higher temperature, its non-toxicity, biodegradability make it more environmentally friendly and safe for food and medical applications.

BIBLIOGRAPHY

1. B. Surowska, Wybrane zagadnienia z korozji i ochrony przed korozją, Politechnika Lubelska, Lublin 2002
2. https://www.cynkowniapatelscy.pl/blog/pasywacja-metalu-charakterystyka-procesu
3. R. Levchenko, Korozja metali, Archiwum Wiedzy Inżynierskiej, tom. 7, nr.1, 2022, 13-16
4. https://www.rywal.com.pl/pasywacja-i-trawienie-stali-antox/
5.http://www.commercialelectroplating.com/stainless-steel-electropolishing-passivation-services.html
6. Gümpel, P., Leu, F., Burkert, A., & Lehmann, J. New Lean Alloy Alternatives for 300 Series Stainless Steels – a Corrosion Perspective. *Applied Science and Engineering Progress*, *5*(4), 2013, 29–42
7.https://capablemaching.com/blog/comparing-electropolishing-and-passivation-which-surface-treatment-is-right-for-your-needs/
8. What is the Passivation Process? | Astro Pak

TalentDetector
23th-25th June 2025
Gliwice-Brenna, Poland
DEPARTMENT OF ENGINEERING MATERIALS AND BIOMATERIALS
FACULTY OF MECHANICAL ENGINEERING
SILESIAN UNIVERSITY OF TECHNOLOGY
INTERNATIONAL STUDENTS SCIENTIFIC CONFERENCE

AGV auto levelling system for autonomous floor mapping

Krzysztof Witek[a], Krzysztof Paszek[b], Ernest Antolak[c], Justyna Paszek[d]

[a] Silesian University of Technology, Faculty of Automatic Control, Electronics and Computer Science, Computer Science Student
[b] Silesian University of Technology, Faculty of Automatic Control, Electronics and Computer Science, Department of Telecommunications and Teleinformatics
email: Krzysztof.Paszek@polsl.pl
[c] Silesian University of Technology, Faculty of Automatic Control, Electronics and Computer Science, Department of Electronics, Electrical Engineering and Microelectronics
[d] Silesian University of Technology, Faculty of Mining, Safety Engineering and Industrial Automation, Department of Geoengineering and Resource Exploitation

Abstract: This paper presents an AGV (automated guided vehicle) system for autonomous floor mapping. The system collects data on floor heights relative to a reference level. The AGV integrates multiple sensors and systems for safe navigation and sampling. The key component is the auto-levelling system, which ensures accurate detection of the reference level using a laser. The collected data helps in developing a floor map to evaluate floor irregularities.

Keywords: AGV, auto levelling system, mobile application

1. INTRODUCTION

Floor flatness and levelness are critical factors across various sectors, from industrial settings to healthcare facilities [1]. In industries, precise machinery relies on a stable foundation to operate effectively, while in homes and healthcare environments, uneven surfaces can lead to accidents and injuries. Modern technologies, such as professional laser scanners and smartphone cameras, can be used to create 3D models of spaces, although the accuracy of consumer devices may be limited [2–3]. Professional laser scanners provide the high accuracy and precision needed for larger areas, but analysing the data collected during room or floor scanning is time-consuming and expensive. Integrating measurements from different sources is often challenging, highlighting the importance of using the right tools and methods for accurate floor mappings [4].

The floor scanning process can be carried out in various ways and for different purposes, such as detecting the type of surface, assessing its quality, and analysing its texture [5]. The data obtained can be used to take appropriate actions in the field of floor repair, maintenance, or vehicle path modification. Laser scanners or depth cameras mounted on drones or AGVs allow for the automation of the process of tedious manual measurements and collection of data about the floor [6].

This article presents an AGV whose task is to collect data on the floor surface in relation to the reference level. The aim was to create an inexpensive AGV that enables data collection in rooms with complex structures. The collected information enables the development of a floor map, which facilitates the assessment of its unevenness. The scanning process can be fully automatic or at points specified by the operator.

2. AGV PLATFORM DESCRIPTION

The prepared platform (see Figure 1) integrates multiple sensors and systems, the primary purpose of which is to enable safe movement around the room and collect data on the floor. An important aspect of the vehicle is manoeuvrability, which will allow scanning room floors with complex shapes without unnecessary manoeuvring. To meet this requirement, four omnidirectional wheels with a diameter of 100 mm were used. The use of omnidirectional wheels allows the platform to move in any direction regardless of the AGV's orientation. The wheel drive is powered by four independent 12V brushed DC motors, equipped with a 30:1 metal gearbox, and a torque of 1.37 Nm. Each motor is connected to a separate driver, which allows for the detection of its overload. Quadrature encoders integrated into the motors, with 64 counts per revolution, enable ongoing control of the vehicle's movement and the detection of slippage in each wheel separately.

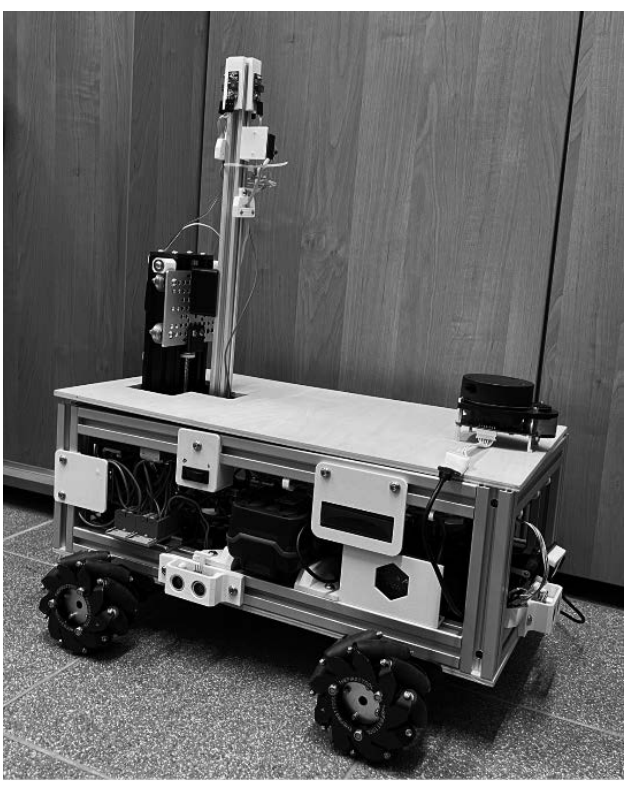

Figure 1. The AGV with an auto levelling system

The vehicle's position within the room is determined based on LiDAR point cloud data and a SLAM (simultaneous localisation and mapping) algorithm. LiDAR data is used to create

a room map, allowing the vehicle to identify measurement points. The vehicle can either create a room map before beginning measurements or construct one while taking measurements.

2.1. AGV levelling system

The automatic levelling system is a crucial component of the AGV, enabling accurate detection of the reference level designated by a laser. To level the AGV, information about the roll and pitch of the AGV is required. This information is determined based on the IMU (inertial measurement unit), in particular the accelerometer and gyroscope. The system processes accelerometer and gyroscope data using a Kalman filter to determine the current roll and pitch of the AGV. This information adjusts the leg extension, keeping the vehicle level on uneven surfaces. A level AGV ensures the measuring probe stays perpendicular to the reference level set by the cross laser.

The levelling system utilises 3 extendable legs. Figure 2 shows the designed 3D model of one of the legs. On top of the leg is a stepper motor with the shaft pointing down. A trapezoidal screw is mounted to the motor shaft using a flexible clutch. The trapezoidal screw, with a trapezoidal nut screwed to the extendable part of the leg, transfers the rotary motion of the motor to the linear motion of the leg.

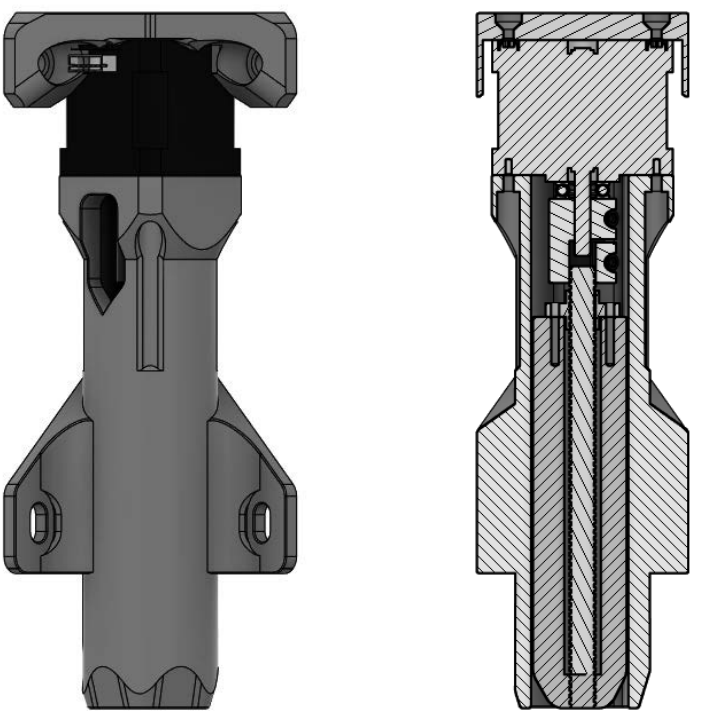

Figure 2. The auto levelling system leg

Each leg is driven by a separate stepper motor (JK42HS40-0504), which is controlled by the control unit through the Bigtreetech TMC2209 v1.3 controller. The motor drivers are connected to the control unit via a dedicated Bigtreetech EXP-MOT V1.0 expansion module.

The control unit is responsible for controlling vehicle movement, the measuring probe, and the automatic AGV levelling system. The control unit is based on the Arduino Due, which utilises the 32-bit ARM Cortex-M3 architecture. Wireless (Wi-Fi) communication with the mobile

application is carried out via the Raspberry Pi, which serves as the location and communication unit. The control unit is connected to the location and communication unit via UART. The location and communication unit receives commands sent from the mobile application and then sends them to the control unit (see Figure 3).

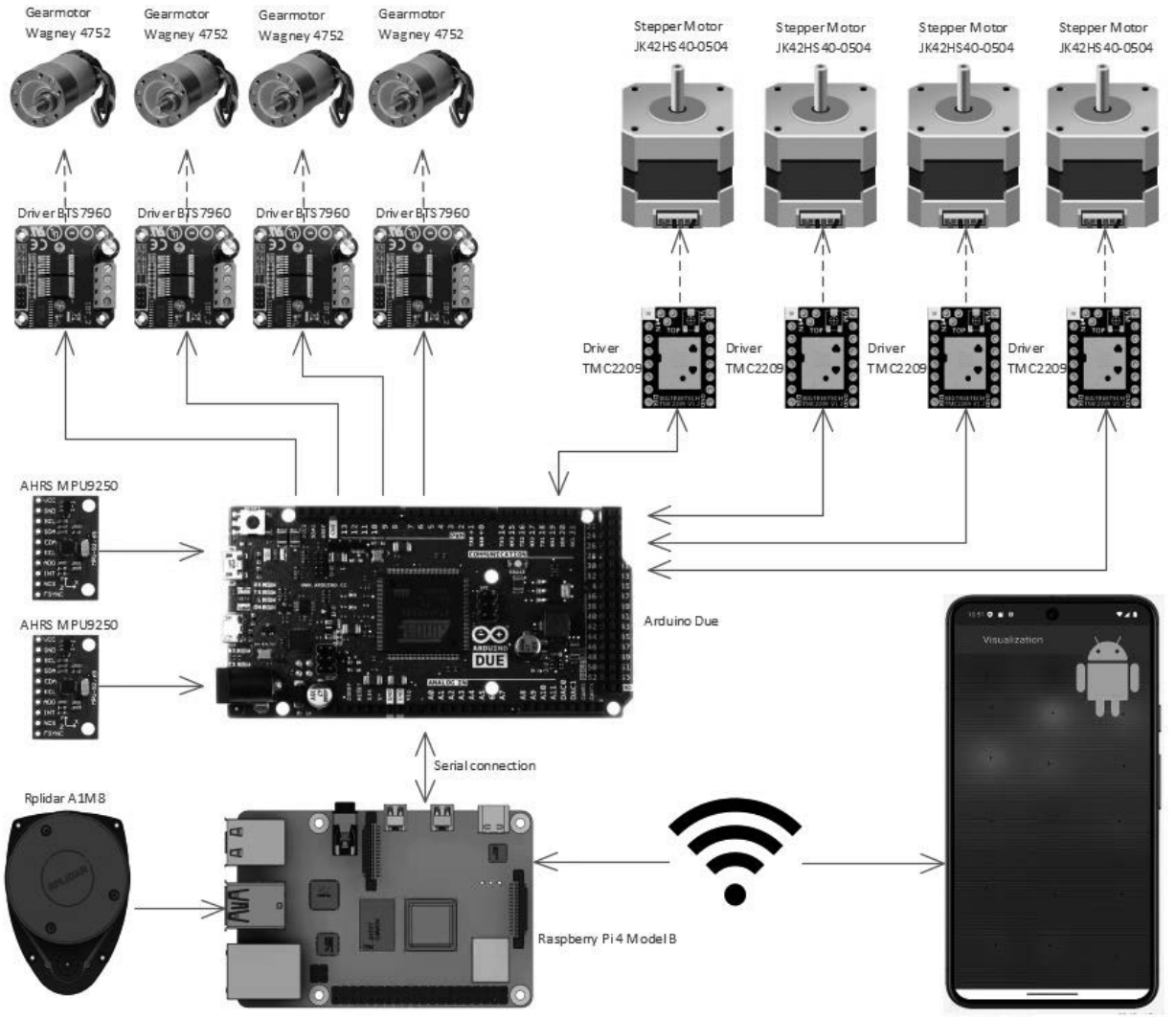

Figure 3. System components

2.2. AGV levelling algorithm

The algorithm works by moving the platform to an elevated position and then repeatedly reading the pitch and roll angles. If these angles exceed a small threshold m, the algorithm computes how much each motor should move to reduce the tilt, using a proportional control strategy. The correction for each motor is derived from how pitch and roll can be influenced by the movement of each motor (see Figure 4).

The acceptable level of tilt m defines when the platform is considered level and the algorithm stops. The proportional gain k scales the correction step based on the pitch or roll angle. A larger k results in more aggressive correction. If k is too large, it will overshoot. If k is too small, convergence will be slow.

If the platform moves too low (legs are fully retracted) and the system is still not level, the algorithm considers levelling failed and aborts further movement.

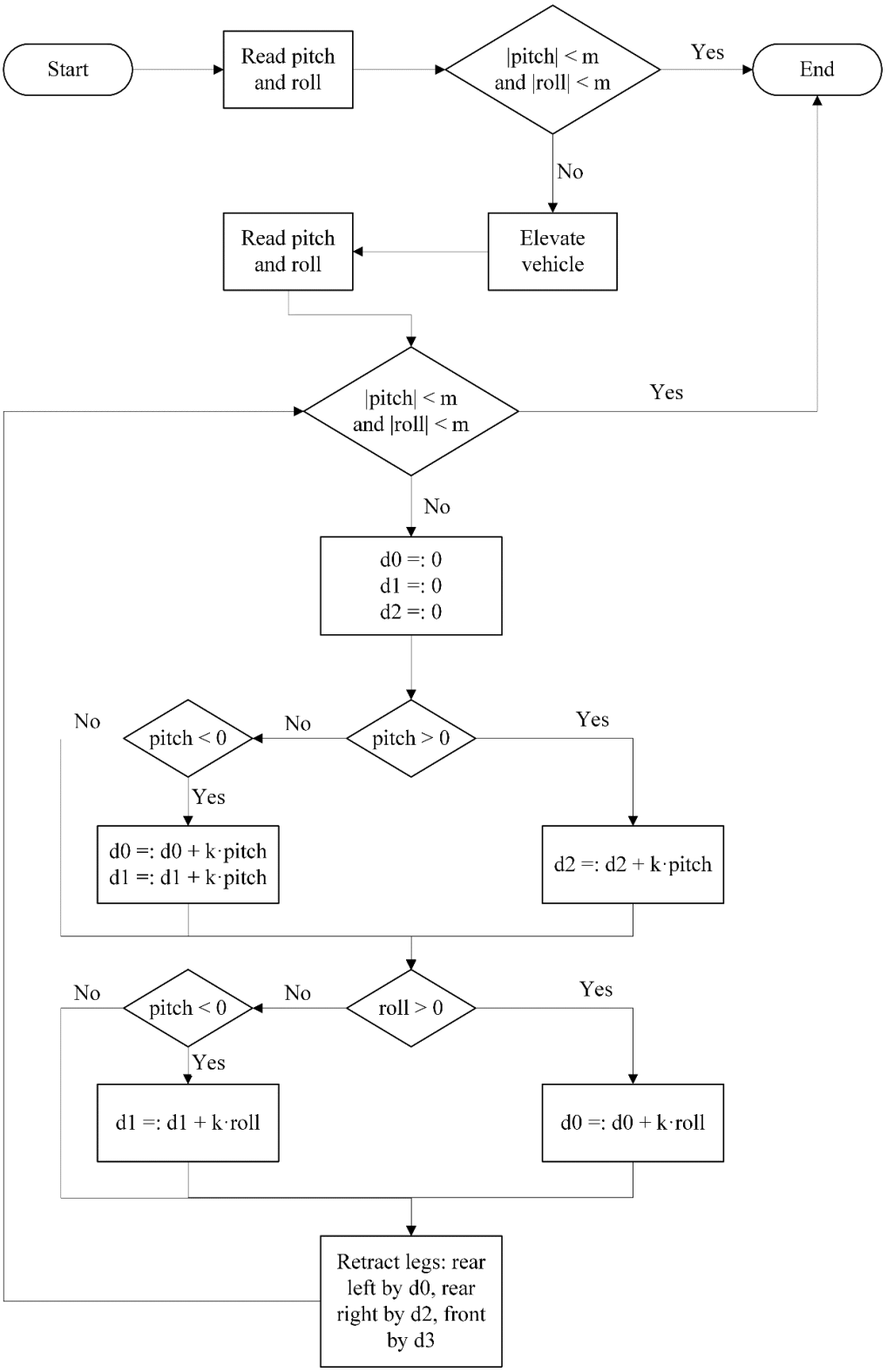

Figure 4. The block diagram of the AGV levelling algorithm

2.3. Reference level detection

The reference detection module (measuring probe – Figure 5) utilises LDRs (light-dependent resistors) to measure light intensity and detect the laser. When light intensity increases, resistance decreases, which leads to a change in voltage output. The setup includes four LDRs mounted on a moving sampling probe, which is controlled by a stepper motor that enables precise vertical movement along the rail. A microswitch, mounted at the end of the probe, detects the floor level. The distance from the laser level to the floor is calculated based on the number of rotations of the stepper motor, providing accurate level detection.

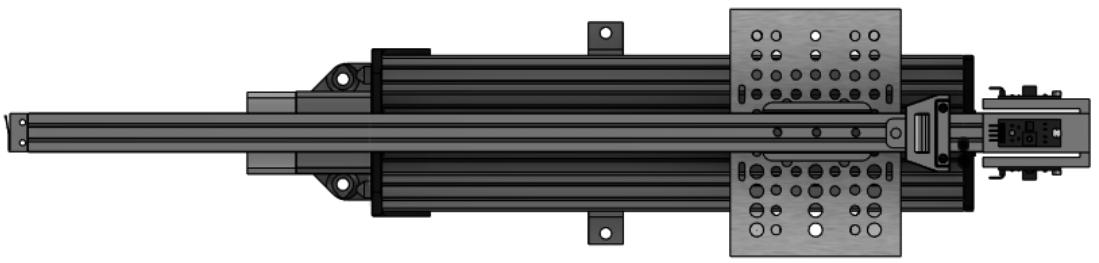

Figure 5. The level detection probe

The sampling process (see Figure 6) begins with automatic AGV levelling (discussed in Subsection 2.2). Then the probe goes down to detect the floor and then moves up to detect the reference level (laser light). This sequence allows the measurement of the distance between the floor and the reference level marked by a cross-line laser

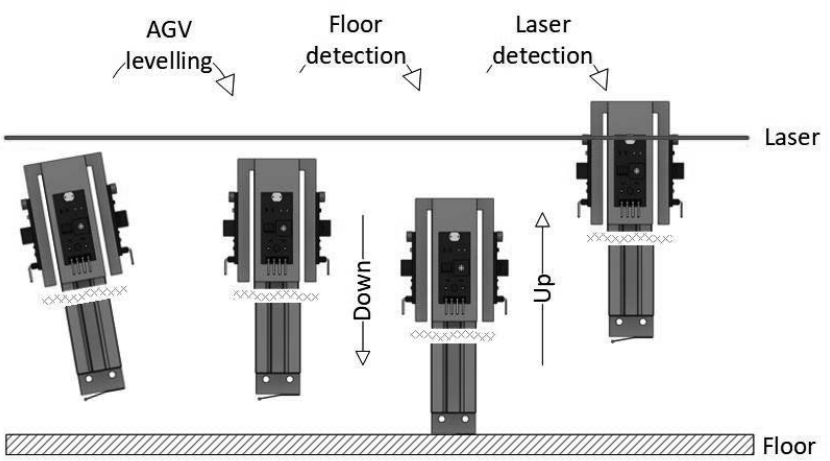

Figure 6. AGV levelling and sampling process

3. FLOOR MAPPING

An android mobile application (see Figure 7) controls AGV by sending appropriate messages that are recognised and processed by the localisation and communication unit. Depending on the selected mode – automatic or manual – the application sends different sets of commands that determine the movement and actions of the AGV. In automatic mode, the user selects a measurement point in the mobile application. Then, the localisation and communication unit collects the current position of the AGV, determines the path to the destination, and generates

a list of commands that it sends to the control unit via the serial port. In manual mode, single commands are sent to the localisation and communication unit and executed by the AGV.

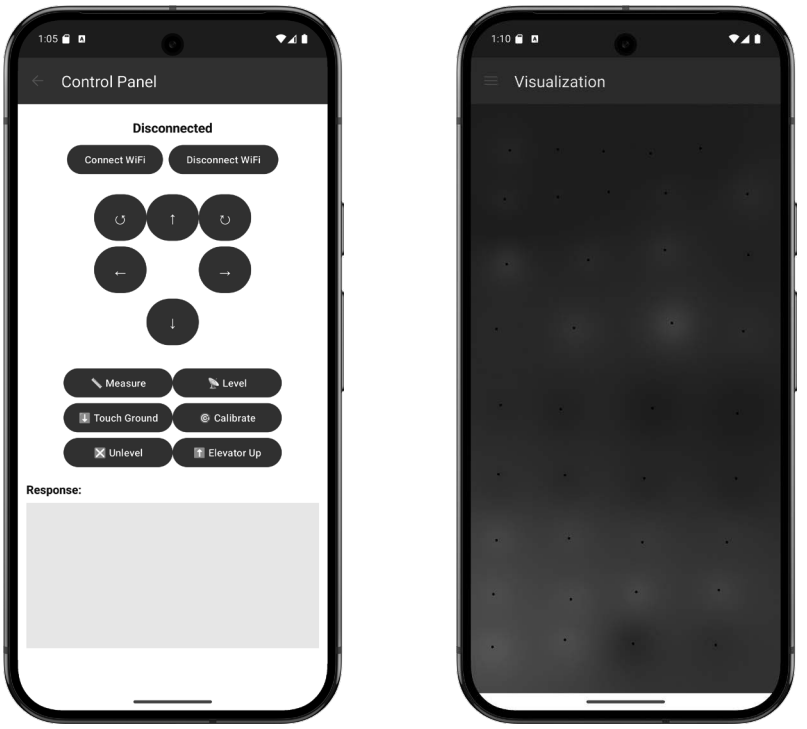

Figure 7. The mobile application – control panel (on the left), sampled floor view (on the right).

The application visualises measurement points as a heightmap. This approach makes the data representation intuitive, reflecting the actual surface layout. Each added point is stored as a triple (X, Y, Z). To provide visual continuity, interpolation is used between measured points.

The interpolation method applied is IDW (inverse distance weighting), which estimates height values in between measured points based on their distance. Closer points have more influence on the interpolated value, resulting in a realistic gradient across the entire surface. Data about the floor presented in this way allows for quick analysis at the measurement site. Accurate data collected is saved in a database, which allows for its precise later analysis.

4. CONCLUSION

The integration of multiple sensors and systems on the AGV board ensures safe navigation and precise data collection. The auto-levelling system ensures that the sampling probe is perpendicular to the reference level, allowing for accurate detection of the laser and then the accurate calculation of the distance between the reference level and the floor. The ability to create detailed floor maps facilitates the evaluation of surface irregularities, which is crucial for various applications, from industrial settings to healthcare environments. The use of omnidirectional wheels enhances the AGV's manoeuvrability, allowing it to navigate complex room structures efficiently. The implementation of a mobile application for control and data visualisation enhances the system's usability.

The presented AGV system offers a cost-effective and efficient solution for floor mapping in complex environments.

ACKNOWLEDGEMENTS

This research was partially funded by the Polish Ministry of Science and Higher Education partially by Statutory Research, and partially by Young Researchers funds of the Faculty of Automatic Control, Electronics and Computer Science, Silesian University of Technology.
This research was supported by the Excellence Initiative – Research University program at the Silesian University of Technology 2025.

BIBLIOGRAPHY

1. F. Bosché and E. Guenet, Automating surface flatness control using terrestrial laser scanning and building information models, Automation in Construction, 44 (2014) 212–226, doi:10.1016/j.autcon.2014.03.028.
2. M. Lemmens, Terrestrial Laser Scanning, Geo-information (2011), 101–121, doi:10.1007/978-94-007-1667-4_6.
3. YaNan Hao, Y.C. Tan, V.C. Tai, X.D. Zhang, E.P. Wei and S.C. Ng, Review of key technologies for warehouse 3D reconstruction, Journal of Mechanical Engineering and Sciences, 16 (2022) 9142–9156, doi:10.15282/jmes.16.3.2022.15.0724.
4. K. Pavelka, P. Raeva, K. Pavelka Jr., M. Kýhos and Z. Veselý, Analysis of Data Joining from Different Instruments for Object Modelling, The International Archives of the Photogrammetry, Remote Sensing and Spatial Information Sciences, (2022) 853–860, doi:10.5194/isprs-archives-XLIII-B2-2022-853-2022.
5. S. Wilson, J. Potgieter and K. Arif, Floor surface mapping using mobile robot and 2D laser scanner,. 2017 24th International Conference on Mechatronics and Machine Vision in Practice (2017), 1–6, doi:10.1109/M2VIP.2017.8211508.
6. S. Wilson, J. Potgieter and K. M. Arif, Robot-Assisted Floor Surface Profiling Using Low-Cost Sensors, Remote Sensing, 11 (2019), doi:10.3390/rs11222626.

TalentDetector
23th-25th June 2025
Gliwice-Brenna, Poland
DEPARTMENT OF ENGINEERING MATERIALS AND BIOMATERIALS
FACULTY OF MECHANICAL ENGINEERING
SILESIAN UNIVERSITY OF TECHNOLOGY
INTERNATIONAL STUDENTS SCIENTIFIC CONFERENCE

The influence of sea water on the properties of ship steel covered with a protective coating

Anna Włodarczyk-Fligier[a], Magdalena Polok-Rubiniec[a], Aneta Kania[a]

[a]Silesian University of Technology, Faculty of Mechanical Engineering, Department of Engineering Materials and Biomaterials
email: anna.wlodarczyk@polsl.pl

Abstract: The article discusses the results of research on the effect of sea water on the surface of ship steel coated with epoxy resin with the addition of copper in comparison to conventional coatings commonly used in the shipbuilding industry, clean steel and steel coated with epoxy resin and resin with the addition of copper.

Keywords: ship steel, epoxy resins, protective coatings

1. INTRODUCTION

The growing development of materials engineering as a field of technical science requires searching for increasingly optimal solutions using new materials. This is made possible by the development of research techniques, material manufacturing technologies and the constantly expanding knowledge of specialists in this field. Modern science leads to the production of materials with properties that will fulfill their task in the designated conditions and will be reliable and durable.

Counteracting lichens occurring in sea waters is based on enriching paint systems with special, toxic additives to paints that stop or completely prevent lichens and microorganisms (algae, shells, mussels or seaweed) from adhering to steel used in shipbuilding. The most important toxic additives added to paint systems are compounds such as: copper (copper oxide), organometallic compounds, e.g. biocides and tributylcoccine. Over time, however, the system loses its efficiency and, depending on the aggressiveness of the environment, requires renewal. The above-described compounds are gradually being abandoned due to the constantly growing requirements for environmental protection. As a result of these activities, various types of coatings are used. Epoxy resins as a material for protective coatings are often used due to their versatility in use and relatively cheap production and application technology. Using appropriate chemical elements, the properties of such coatings can be appropriately directed, improving their mechanical and physical properties [1-7].

1.1. Research material

The test material was ship steel, which was sandblasted and then the sample surfaces were cleaned. The steel samples were then coated with
epoxy resin, copper-based epoxy resin and conventional shipbuilding paint, the last batch was retained without any coatings for comparison purposes as a reference material.
The sample with Epidian 5 resin was enriched with copper in the form of a powder with a grain size of 0.063 mm. The resin layer was applied manually with particular attention to the uniformity of the resin distribution on the surface of the material. The steel samples coated with the conventional shipbuilding paint consisted of a layer of Intershield 300 primer, a layer of Intergard 263 paint and a third layer of Interswift 6600.

1.2. Research process

Batches of samples with different coatings were placed in a salt chamber and exposed to 5% brine for 7 days and then 14 and 21 days (PN-EN ISO 9227) [8]. Each batch of samples, after being removed from the salt chamber simulating the conditions of steel in seawater, was examined using a stereoscopic microscope (Zeiss Discovery v12, at x8 magnification) and a surface roughness measuring device (Surtronic 25 profilometer). Computer software connected to the profilometer generated surface roughness and waviness graphs for each batch of samples. The measurement was performed using the elementary section Le, which is determined by the PN-EN ISO 1302:2004 standard [9]. The length of the elementary section was determined at 8 mm. Scratches were made on the samples, down to the parent material, in order to visualize differences in the results.

1.3. Research results

Based on the photos taken of the samples after corrosion tests, differences in the surface topography of the surface layer covering the ship's steel can be observed between the different layers. The epoxy resin layer is characterized by high surface roughness compared to the sample covered with resin with the addition of copper and the sample covered with paint. The sample covered with a layer of resin with the addition of copper is distinguished by significantly greater porosity than the sample covered with resin alone and the sample covered with paint. The sample covered with a layer of paint is characterized by the smoothest surface and the lowest porosity. After the experiment, the steel sample was very much destroyed by the progressing corrosion. The sample covered with resin alone is invariably filled with corrosion products in the pores and discoloration around these areas. The sample covered with epoxy resin with the addition of copper stopped resisting the adhesion of oxidation products and was covered with them to a large extent. Additionally, it was evenly discolored over the entire surface. Light discoloration is also visible, suggesting degradation of the epoxy coating. The sample coated with shipbuilding paint began to show clearly visible pores in random areas of the sample, as well as significant discoloration (Fig. 1).

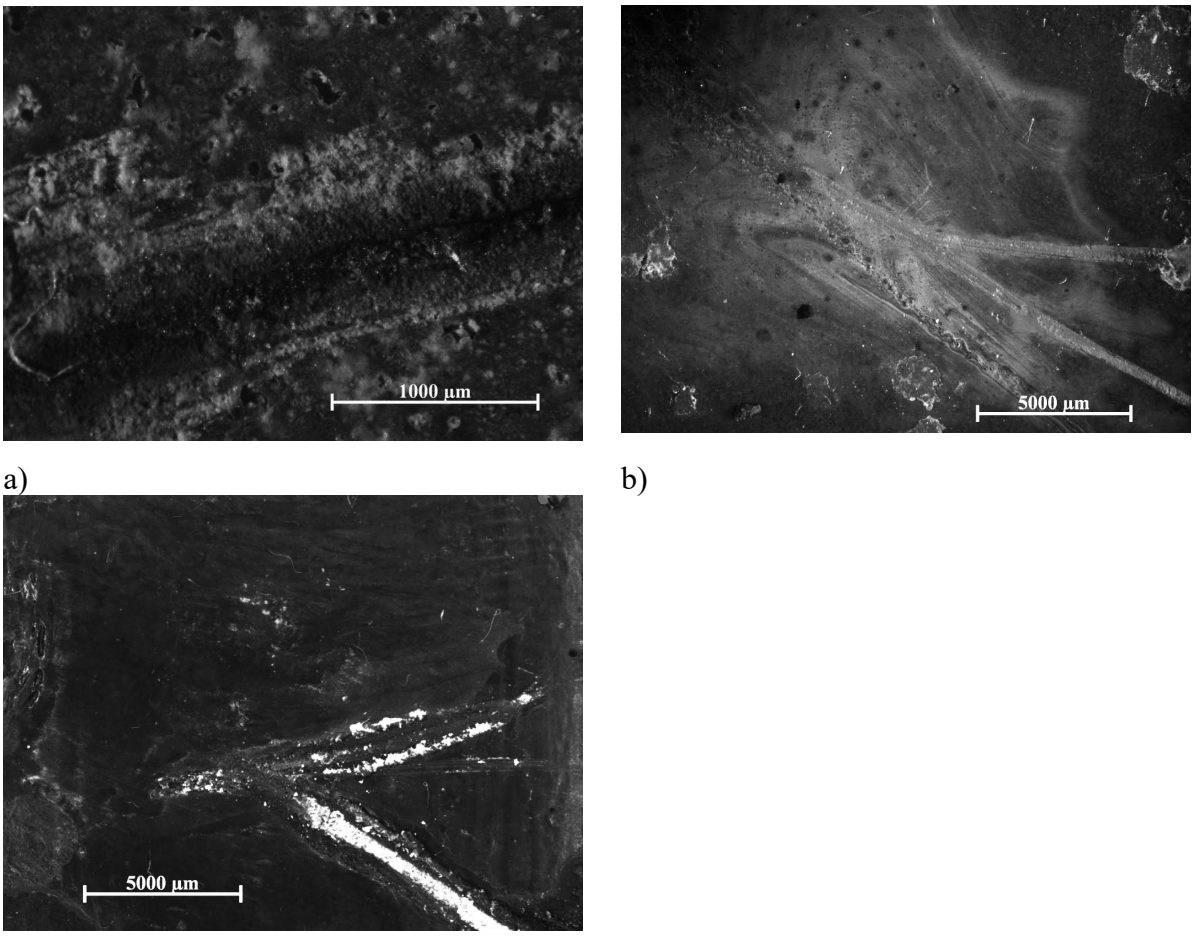

a) b)

c)

Rysunek 1. Zdjęcia próbek po przeprowadzaniu badań z wykorzystaniem komory solnej: a) z powłoką z żywicy epoksydowej, b) z powłoką z żywicy epoksydowej z dodatkiem miedzi, c) z powłoką z farby, przy powiększeniu x8

Figure 1. Photos of samples after testing using a salt spray chamber: a) with an epoxy resin coating, b) with an epoxy resin coating with the addition of copper, c) with a paint coating, at x8 magnification

The results of surface roughness measurements using a profilometer confirm the observation of photographs taken on the samples. The sample with the applied resin coating was initially characterized by high roughness, on a par with the sample covered with resin with the addition of copper. From the beginning of the tests, the sample gradually began to show lower roughness results due to the pores on the sample surface being filled with oxidation products. The filled pores eventually led to the leveling of the surface layer of the coating (Fig. 2). However, this is an undesirable phenomenon due to the fact that the pores are filled with corrosion products. The sample with the applied epoxy resin coating with the addition of copper is also characterized by high roughness at the initial stage of the tests (Fig. 3). Over time, it behaves similarly to the sample covered with pure resin, with the difference that the surface resists the corrosion adhering to the pores for much longer, which may suggest that the addition of copper to the coating counteracts this phenomenon. The sample coated with the shipbuilding paint system behaves in a more predictable manner than the resin-coated samples.

The coating maintains a relatively low surface roughness measurement from the beginning of the test to the end (Fig. 4).

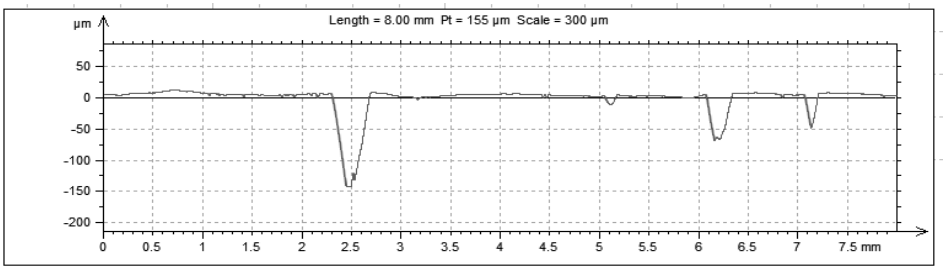

Rysunek 2. Wykres chropowatości próbki pokrytej żywicą epoksydową na odcinku 8mm, po 21 dniach ekspozycji w komorze solnej

Figure 2. Roughness graph of the sample coated with epoxy resin over a section of 8 mm, after 21 days of exposure in a salt chamber

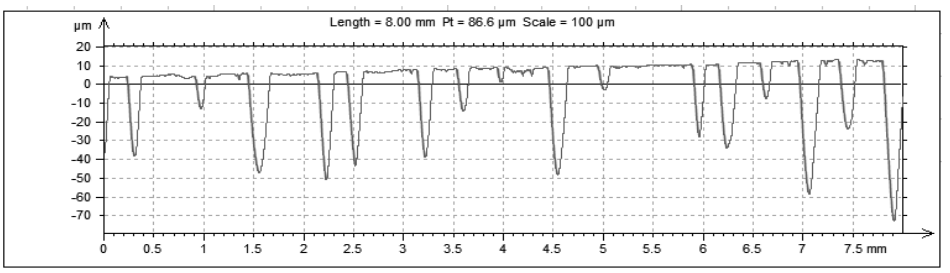

Rysunek 3. Wykres chropowatości próbki pokrytej żywicą epoksydową z dodatkiem miedzi na odcinku 8mm, po 21 dniach ekspozycji w komorze solnej

Figure 3. Roughness graph of the sample coated with epoxy resin with the addition of copper over a section of 8 mm, after 21 days of exposure in a salt chamber

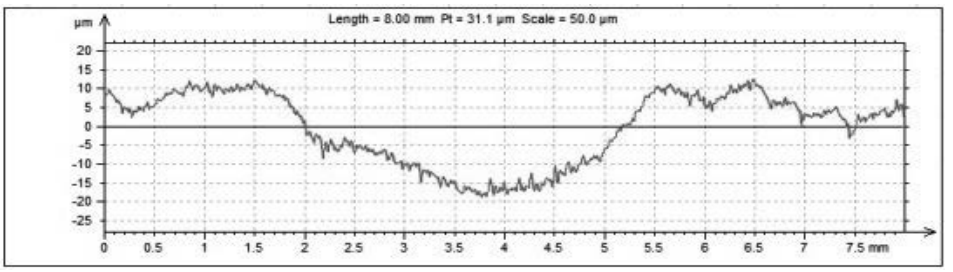

Rysunek 4. Wykres chropowatości próbki pokrytej farbą na odcinku 8mm, po 21 dniach ekspozycji w komorze solnej

Figure 4. Roughness graph of the sample covered with paint over a distance of 8 mm, after 21 days of exposure in a salt chamber

CONCLUSIONS

Based on the conducted research, it can be concluded that the coating with the applied paint system is the best application from the point of view of surface roughness and preventing adhesion of lichens and unnecessary products to the external coating. Samples with applied resin coatings and resins with the addition of copper are characterized by high surface porosity, which allows for the filling of pores with various types of lichens, microorganisms (in the

marine environment) and rust. The use of copper addition to the resin slows down the covering with sediments, as evidenced by the results of both visual tests based on observation of photos and the results of surface roughness. Based on the observation of photos of samples taken with a stereoscopic microscope, it can be concluded that protective coatings are a necessary condition for the presence of steel in the marine environment. However, the appropriate selection of coatings and the characteristics of their surfaces are important.

BIBLIOGRAPHY

1. J. Haponiuka, Tworzywa sztuczne w praktyce, wyd. Verlag Dashofer Gdańska, Gdańsk 2010.
2. Z. Brojer, Żywice epoksydowe. Wydawnictwa Naukowo-Techniczne, Warszawa 1982.
3. M. Cicholska, Metaloznawstwo okrętowe, wyd. Akademia Morska w Gdyni, Gdynia 2013.
4. L.A. Dobrzański, Podstawy nauki o materiałach i metaloznawstwo, WNT, Warszawa, 2002.
5. M. Hetmańczyk, Podstawy nauki o materiałach, Wydawnictwo Politechniki Śląskiej Gliwice 1996.
6. S. Tkaczyk, Powłoki ochronne, opracowanie zbiorcze, Wydawnictwo Politechniki Śląskiej
7. J. E. Hunter, Antifouling Coatings and the Global Environmental Debate, Protective Coatings Europe; 1997
8. PN-EN ISO 9227 Badania korozyjne w sztucznych atmosferach.
9. PN-EN ISO 1302:2004 Oznaczania chropowatości powierzchni.

TalentDetector
23th-25th June 2025
Gliwice-Brenna, Poland
DEPARTMENT OF ENGINEERING MATERIALS AND BIOMATERIALS
FACULTY OF MECHANICAL ENGINEERING
SILESIAN UNIVERSITY OF TECHNOLOGY
INTERNATIONAL STUDENTS SCIENTIFIC CONFERENCE

Finite Element Analysis of Single-Cell Ti6Al4V and TiZrNb Structures: Investigating Thickness and Porosity Effects for Scaffold Design Applications

Sichale Worku Fita [a], Mirosław Bonek [b], Sebastian Sławski [c], Anna Woźniak [d]

[a] Silesian University of Technology, Faculty of Mechanical Engineering, Department of Engineering Materials and Biomaterials, email: Sichale.fita@polsl.pl, miroslaw.bonek@polsl.pl
[c] Silesian University of Technology, Faculty of Mechanical Engineering, Department of Theoretical and Applied Mechanics, email: sebastian.slawski@polsl.pl
[d] Silesian University of Technology, Faculty of Mechanical Engineering, Materials Research Laboratory, email: awozniak@polsl.pl

Abstract: Titanium and its alloys are among the most commonly used materials due to their biocompatibility, corrosion resistance, and favorable mechanical properties. This study focuses on a finite element analysis (FEA) of a single-cell titanium alloy to investigate how changes in wall thickness and porosity affect its mechanical performance. ANSYS software is used for simulating different design variations. Results include stress-strain relations, deformation patterns, and the correlation between single-cell porosity and equivalent stress. The findings provide quantitative insights to support the design of single cells as building blocks for bone implant applications.

Keywords: FEA, Titanium Alloy, Thickness, Porosity, Mechanical Performance, ANSYS.

1. INTRODUCTION

Titanium alloys, particularly Ti6Al4V and TiZrNb, are gaining recognition for their potential in orthopedic applications, particularly for cancellous bone replacement. Ti6Al4V is commonly used because of its advantageous mechanical characteristics and biocompatibility. Ti6Al4V shows outstanding strength and corrosion resistance, making it suitable for load-bearing applications[1]and has demonstrated good biocompatibility. While TiZrNb alloys have a lower elastic modulus, hence reduces the possibility of stress shielding and increasing compatibility with natural bone. Based on this, recent research indicates that TiZrNb alloys may enhance osteointegration and bone regeneration properties, positioning them as a viable option.
The mechanical performance of scaffolds is greatly influenced by their geometry, especially thickness and porosity. These parameters are crucial in determining scaffolds' strength, stiffness, and biological integration, vital for effective tissue regeneration. Additionally, Variations in strut thickness directly influence the mechanical properties of single cells used as the basis for scaffold structures.. Thicker struts typically improve strength and stiffness, aligning scaffold characteristics more closely with those of native bone[2]. Also, Height-to-diameter ratios

promote compressive strength and stiffness, enhancing load transmission during physiological activity. On the other hand, since larger porosity reduces mechanical qualities, 40% porosity scaffolds are frequently preferred for mechanical strength and biological integration. Additionally, Specific pore geometries (e.g., spherical, cubic, and others) promote cell growth and integration and affect mechanical behavior and biological response[3]. Also, structural features such as geometry, strut thickness, and porosity critically influence their mechanical performance and biological integration. Investigating the response of a single unit cell provides foundational insight that can inform the design of more complex scaffold architectures.

FEA is essential for optimizing scaffold design by simplifying the prediction of mechanical behavior and informing the development of implants for tissue engineering. Computer modeling is used to simulate different scaffold shapes and materials, allowing the design of structures that fulfill particular biomechanical criteria. This method not only improves comprehension of scaffold efficacy but also helps in the development of patient-specific implants. So, FEA helps to analyze mechanical properties, material selection, and design iteration in general. This study uses FEA to evaluate how these structural variables affect mechanical behavior, using two titanium alloys—Ti6Al4V (Grade 5) and TiZrNb—as material models to inform future experimental work.

2. LITERATURE REVIEW

The mechanical behavior of Ti-based scaffolds, specifically Ti6Al4V and TiZrNb, is important for medical implants. For instance, Orthopedic implants made from Ti6Al4V are popular due to their biocompatibility and mechanical properties. While pore size, scaffold architecture, and manufacturing methods affect these scaffolds' stress-strain performance, which has to replicate human bone mechanical properties for osteointegration. For instance, Deshmukh et al.[4] suggests Ti6Al4V scaffolds behave like human bone, modifying porosity and pore size for strength and biological performance, and pore diameters of 600 μm and up to 65% porosity balance mechanical strength with cell ingrowth. Eventhogh it is not clearly stated, TiZrNb scaffolds are known for their biocompatibility and mechanical properties. The addition of zirconium and niobium increases corrosion resistance and decreases elastic modulus, making them suitable for medical applications.

According to Akbari et al. [2] scaffolds with lower porosity typically have improved mechanical strength and stiffness, as evidenced by their cubic scaffolds with lower porosity that showed higher mechanical properties.While, Khajehmohammadi et al.[5] Suggests scaffolds having around 50% porosity showed best cell proliferation and vitality, as evidenced by research involving human foreskin fibroblast cells. on the other hand, Onal et al. [6] Suggested particular pore geometries, of gyroid and diamond, increase cellular adhesion and proliferation due to increased surface roughness. In general, Ti6Al4V scaffolds are well-documented for their mechanical and biological performance, while TiZrNb alloys might offer advantages in some applications due to their unique material properties, making it necessary for more investigation and comparison.

Computational approaches, especially FEA, have significantly improved scaffold analysis. FEA allows to simulate and optimize scaffold designs by forecasting mechanical reactions under diverse stress circumstances, hence minimizing the necessity for extensive experimental trials. This synthesis emphasizes the utilization of FEA in both single-cell and whole structural scaffolds. For instance, according to Hassan et al.[7] FEA simulates the mechanical environment

around individual cells, increasing an understanding of how scaffold properties affect cell proliferation and differentiation. Additionally, simulates dynamic loading conditions, which are essential for simulating physiological settings and promoting cellular activity.

3. MATERIALS AND METHODS

3.1 Material Selection

Titanium (Ti) is a commonly used material that possesses several remarkable characteristics, including high strength, lightweight nature, robust flexibility, resistance to corrosion, and favorable biocompatibility[1] . Consequently, it is widely used in the production of artificial bone defect fillers and internal fixation screw systems[8]. The mechanical properties used in the simulation are listed in Table 1 below.

Table 1: Mechanical properties of Ti-6Al-4V and TiZrNb used in simulation

£ 4	¢ ã¢ffj2ã 6	Ë4 —¢3 $ 4 ˙n—6—4 _ ° ã	° 4 2444 ¢ 4 0ã¢24	Ë2ffj̃n 4¢0ffj̃ 3¢Ø ¢ ° ã	Affj̃ 4 2Δ 3 Ŧ$
	ø2 6 Á				
	ø2Ò£ Ŋ				
	° —0ffjø2				

3.2 Model Design

A single cubic lattice unit cell of the gyroid is modeled in SolidWorks and imported into ANSYS Workbench. Five (5) different thicknesses (0.2mm, 0.25mm, 0.3mm, 0.35mm, and 0.4mm) of the unit cell were used. Those thicknesses are named Model 1-Model 5, as shown in Figure 1 below.

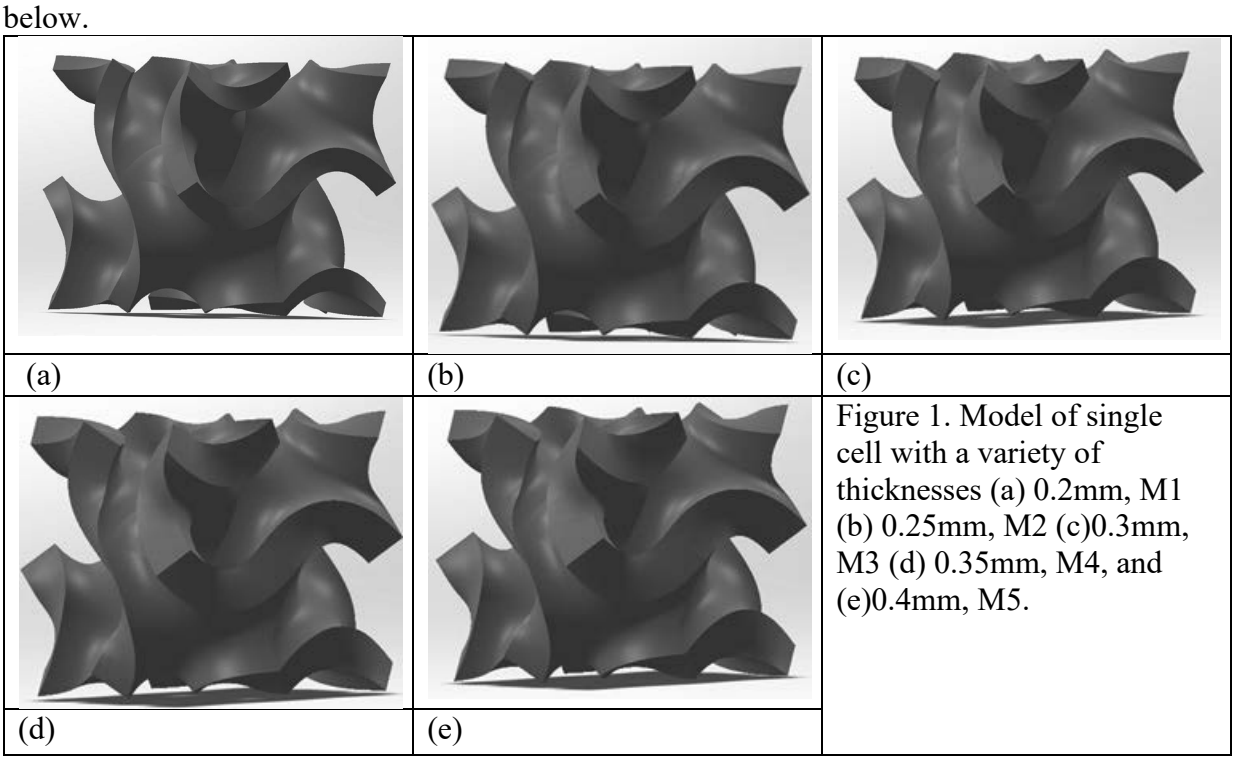

Figure 1. Model of single cell with a variety of thicknesses (a) 0.2mm, M1 (b) 0.25mm, M2 (c)0.3mm, M3 (d) 0.35mm, M4, and (e)0.4mm, M5.

3.3 Boundary Conditions

It was assumed to be a homogeneous, isotropic, and linearly elastic material with time-invariant properties. A single-cell model was used for the simulation, with one side fixed and external loads of 9.81 N, 50 N, and 100 N applied in the opposite direction to represent physiological forces. For analyses focused on osseointegration and internal stability, lower forces below 1 N were also considered appropriate[9]ANSYS was used to perform a static structural analysis, evaluating output parameters such as Von Mises stress, total deformation, strain energy, and directional deformation. Both alloys were analyzed under the same boundary conditions.

4. RESULTS AND DISCUSSION

4.1 Relationship Between Thickness and Porosity

As strut thickness increases, porosity decreases nonlinearly due to unit cell geometry, affecting strength and permeability essential for osseointegration. Generally, increasing wall thickness enhances properties such as strength and toughness. However, this also leads to a decrease in pore density, potentially hindering nutrient transport and cell growth[10]. The analysis indicates that as thickness increases, porosity decreases, as illustrated in Figure 2

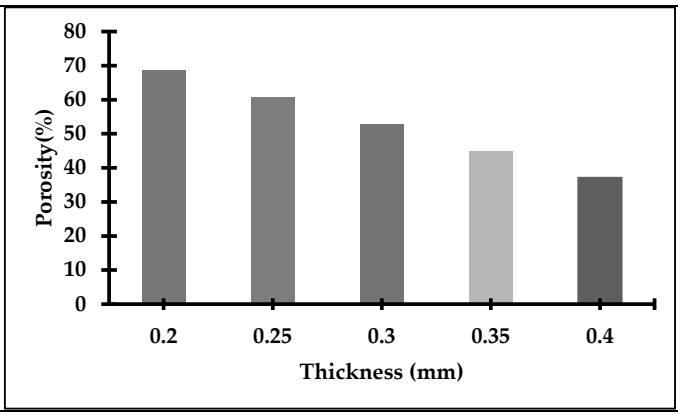

Figure. 2: Relation between the thickness of a single cell and porosity

4.2 Stress-Strain Behavior

Compression stress-strain curves indicate that increased thickness can withstand increasing loads without failure[11]. For Ti6Al4V (Grade 5), as indicated in Figure 3(a), Model 1 (0.2 mm thickness) showed the highest stress response at 774.05 MPa with 0.0067 mm strain under 100 N, while Model 5 (0.4 mm) exhibited the lowest 184.47 MPa. Under a smaller load of 9.81 N, Model 1 again showed the highest stress (75.93 MPa), and Model 5 the lowest (18.10 MPa), both with a strain of 0.0034 mm. while For TiZrNb, as illustrated on Figure 3 (b) Model 1 (0.2 mm thickness) exhibited the highest stress under 100 N, reaching 833.81 MPa with 0.0093 mm strain, while Model 5 (0.4 mm) showed the lowest 223.16 MPa. Under a 9.81 N load, stress values ranged from 21.89 MPa (Model 5) to 86.46 MPa (Model 1), both with 0.0015 mm strain.
For cancellous bone replacement materials with moderate stiffness and higher strain capacity are preferred. Based on the average stress-strain values, Ti6Al4V (Grade 5), Model 1, which exhibits

the highest stress and strain, is not ideal due to the risk of fracture and mechanical failure under high stress while Models 2 and 3 are more suitable, offering moderate stress levels and higher strain capacity. While for TiZrNb, Models 1 and 2, having the highest stress and strain values, are unsuitable for implantation due to the increased risk of fracture and mechanical failure. Models 3 and 4 are preferred, as they demonstrate moderate stress and relatively high strain, making them more appropriate for bone replacement applications.

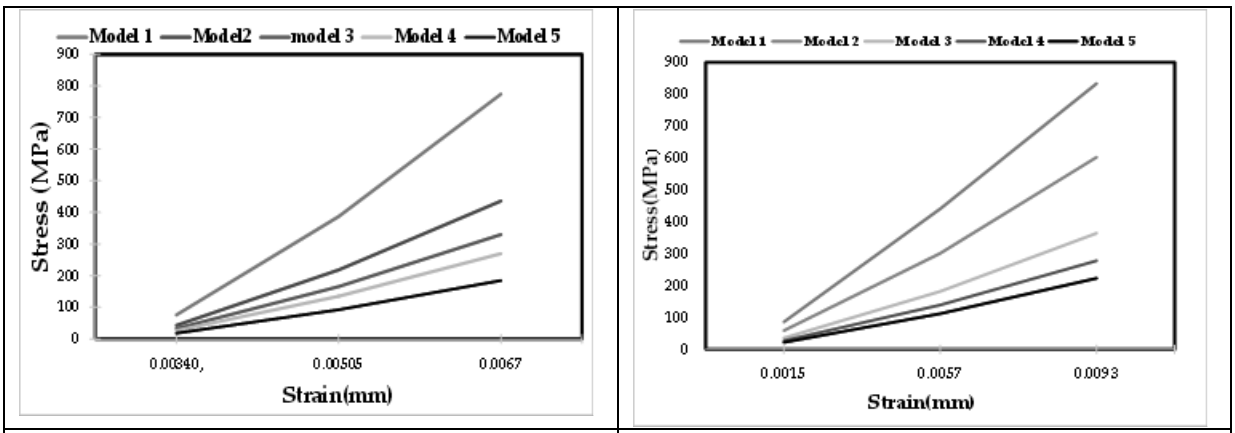

(a) (b)

Figure 3. Stress-Stran Relation (a) Ti6Al4V(Grade 5) and (b) TiZrNb

4.3 Deformation and Stress Distribution

Deformation and von Mises stress analyses are key insights to analyze performance under load. Stress concentrations, particularly in notched regions, highlight localized failure risks[12]. This analysis shows varied deformation across the geometries[13]. Figures 4 compare the responses of Ti6Al4V and TiZrNb under 9.81 N, 50 N, and 100 N. To show up, model 3 (0.3 mm) was used for trend generalization. Directional deformation increased with force in the negative Y-direction, indicating tension-compression asymmetry. Meanwhile, Ti6Al4V exhibited lower deformation (0.0008–0.008 mm) than TiZrNb (0.0011–0.011 mm), suggesting greater stiffness. Thus, Ti6Al4V is more suitable for bone applications due to its superior mechanical resistance.

Additionally, equivalent stress and maximum principal stress are investigated. As force application increases, their values also increase for Ti6Al4V(Grade 5), equivalent stress ranges between 32.393 MPa- 330.2 MPa, while for TiZrNb, equivalent stress values range between 32.495 MPa - 331.24 MPa. From this result, we see a small difference with a higher value of around 1MPa. Both titanium alloys demonstrate mechanical properties that closely resemble those of human bone, which is essential for reducing stress-shielding effects in implants. Both materials show similar equivalent stress ranges. The maximum principal stress ranges between 28.783 MPa and 293.4 MPa for Ti6Al4V(Grade 5) and 28.693 MPa - 292.49 MPa for TiZrNb. So slightly higher maximum principal stress was observed on Ti6Al4V(Grade 5). A higher maximum principal stress indicates a greater capacity to bear loads. But TiZrNb provides a reduced elastic modulus, hence reducing stress-shielding effects in bone[15], which makes it a better choice.

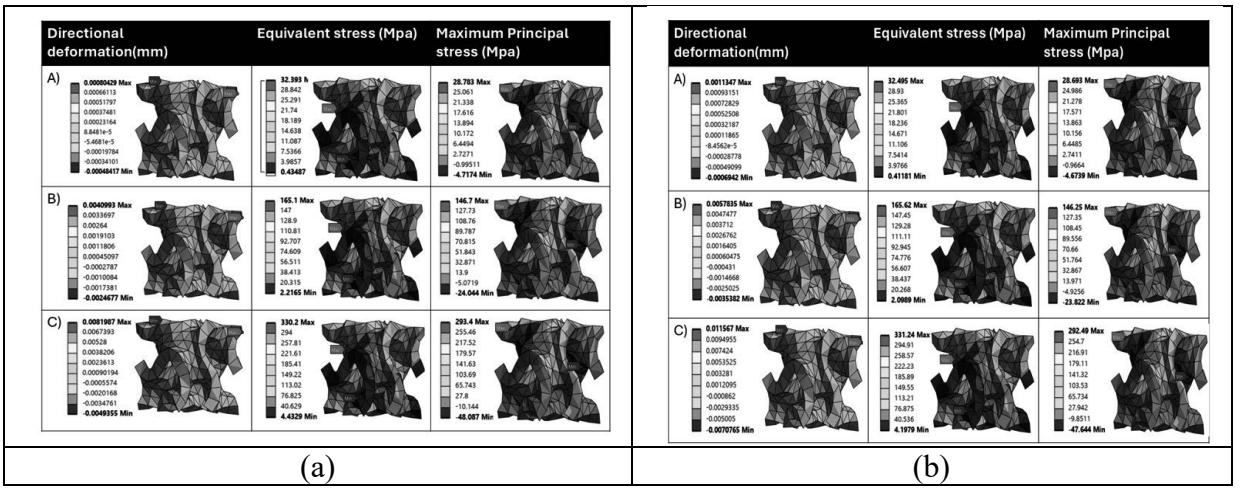

(a) (b)

Figure 4 (a) Figure of Comparison between directional deformation, equivalent (von-Mises) stress, and Maximum Principal stress of Ti6Al4V(Grade 5) for Model 3 (0.3mm thickness). (b) Comparison between directional deformation, equivalent (von-Mises) stress, and Maximum Principal stress of TiZrNb for Model 3 (0.3mm thickness).

On the other hand, the mechanical response of the models is strongly influenced by strut thickness. As thickness increases, resistance to deformation improves, resulting in lower directional deformation under higher loads. This indicates that a thicker model possesses greater structural stiffness. This trend is illustrated in Figure 5, where models with increased thickness show reduced deformation despite rising force levels. Similarly, Figure 6 demonstrates that equivalent (von Mises) stress increases with applied force across all models, reflecting a consistent stress response pattern relative to structural geometry.

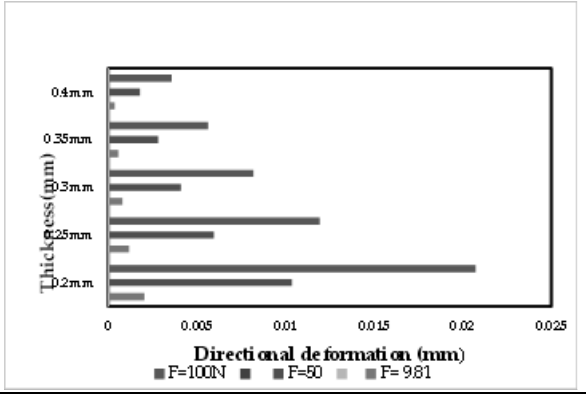

Figure 5. Force-directional deformation Image

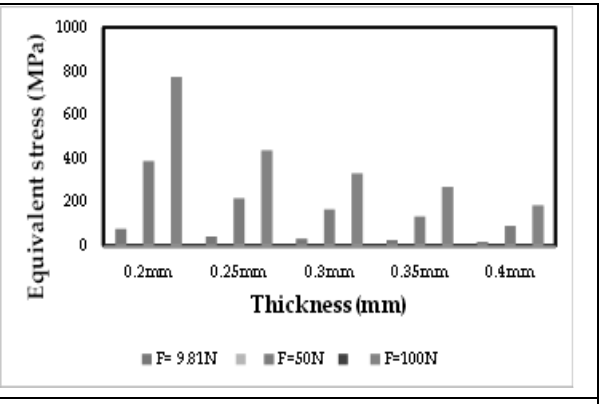

Figure 6. Force-Equivalent stress Image

5. DISCUSSION

A comparative analysis of five models was conducted to evaluate their mechanical performance under loading using ANSYS simulations. The focus was on assessing equivalent stress and directional deformation in structurally critical regions, excluding non-deformed areas. Notably, no model exhibited failure during the simulations, indicating adequate mechanical stability

within the tested conditions. Among the models, Models 2, 3, and 4 demonstrated moderate stress levels coupled with higher strain, suggesting their suitability for bone applications. Model 3, with a strut thickness of 0.3 mm, emerged as the optimal design due to its balanced mechanical response. Although thicker models such as Model 1 and Model 5 showed higher resistance to deformation, their reduced porosity could impair nutrient transport, limiting biological integration. Porosity and equivalent stress analyses further supported the selection of Models 3 and 4. Overall, Model 3 paired with Ti6Al4V alloy is recommended for cancellous bone replacement in hemiarthroplasty, owing to its favorable combination of mechanical strength, biocompatibility, and potential to support osteogenesis.

6. CONCLUSION

This research applied finite element analysis to assess how changes in thickness and porosity affect the mechanical performance of single-cell Ti6Al4V and TiZrNb scaffolds. The findings indicate that while increasing thickness enhances structural strength, it also reduces porosity, potentially affecting biological compatibility. Ti6Al4V showed higher stiffness, whereas TiZrNb minimized stress shielding. Among the models, the 0.3 mm thickness (Model 3) provided the most effective compromise between mechanical strength and flexibility, making it ideal for bone implant design.

BIBLIOGRAPHY

[1]M. Geetha, A. K. Singh, R. Asokamani, and A. K. Gogia, “Ti based biomaterials, the ultimate choice for orthopaedic implants–A review,” *Prog. Mater. Sci.*, vol. 54, no. 3, pp. 397–425, 2009, Accessed: May 22, 2025. [Online]. Available: https://www.sciencedirect.com/science/article/pii/S0079642508001126?casa_token=A-FRdISd1S0AAAAA:q2-jRI_bI6yykfIWhL3Ocj3WTSg0Yt_uRLYWd25UAe1-keD9aVyKZth_iusb3tdXcLkJaEwDJgXh

[2]S. Akbari and P. Khazaeinejad, “Geometrical and mechanical analysis of polylactic acid and polyvinylidine fluoride scaffolds for bone tissue engineering,” *Eng. Comput.*, vol. 39, no. 6, pp. 4153–4165, Dec. 2023, doi: 10.1007/s00366-023-01902-y.

[3]A. Gryko, P. Prochor, and E. Sajewicz, “Finite element analysis of the influence of porosity and pore geometry on mechanical properties of orthopaedic scaffolds,” *J. Mech. Behav. Biomed. Mater.*, vol. 132, p. 105275, 2022, Accessed: May 23, 2025. [Online]. Available: https://www.sciencedirect.com/science/article/pii/S1751616122001898

[4]S. Deshmukh, A. Chand, and R. Ghorpade, “Bio-mechanical analysis of porous Ti-6Al-4V scaffold: a comprehensive review on unit cell structures in orthopaedic application,” *Biomed. Phys. Eng. Express*, vol. 10, no. 6, p. 062003, 2024, Accessed: May 23, 2025. [Online]. Available: https://iopscience.iop.org/article/10.1088/2057-1976/ad8202/meta

[5]M. Khajehmohammadi, R. Azizi Tafti, and H. Nikukar, “Effect of porosity on mechanical and biological properties of bioprinted scaffolds,” *J. Biomed. Mater. Res. A*, vol. 111, no. 2, pp. 245–260, Feb. 2023, doi: 10.1002/jbm.a.37455.

[6]E. Onal, J. E. Frith, M. Jurg, X. Wu, and A. Molotnikov, “Mechanical properties and in vitro behavior of additively manufactured and functionally graded Ti6Al4V porous scaffolds,”

Metals, vol. 8, no. 4, p. 200, 2018, Accessed: May 23, 2025. [Online]. Available: https://www.mdpi.com/2075-4701/8/4/200
[7]C. R. Hassan, Y.-X. Qin, D. E. Komatsu, and S. M. Uddin, "Utilization of finite element analysis for articular cartilage tissue engineering," *Materials*, vol. 12, no. 20, p. 3331, 2019, Accessed: May 23, 2025. [Online]. Available: https://www.mdpi.com/1996-1944/12/20/3331
[8]L. E. Murr *et al.*, "Microstructures and mechanical properties of electron beam-rapid manufactured Ti–6Al–4V biomedical prototypes compared to wrought Ti–6Al–4V," *Mater. Charact.*, vol. 60, no. 2, pp. 96–105, 2009, Accessed: May 22, 2025. [Online]. Available: https://www.sciencedirect.com/science/article/pii/S1044580308002076
[9]S. Su *et al.*, "Facile Fabrication of 3D-Printed Porous Ti6Al4V Scaffolds with a Sr-CaP Coating for Bone Regeneration," *ACS Omega*, vol. 7, no. 10, pp. 8391–8402, Mar. 2022, doi: 10.1021/acsomega.1c05908.
[10] P. Niksiar, Z. Meng, and M. M. Porter, "Multidimensional Mechanics of Three-Dimensional Printed and Micro-Architectured Scaffolds," *J. Appl. Mech.*, vol. 88, no. 10, p. 101004, 2021, Accessed: May 22, 2025. [Online]. Available: https://asmedigitalcollection.asme.org/appliedmechanics/article-abstract/88/10/101004/1109382
[11] O. A. Ntousi *et al.*, "Mechanical Evaluation of Bone Scaffolds' Behavior under Compression," in *2024 46th Annual International Conference of the IEEE Engineering in Medicine and Biology Society (EMBC)*, IEEE, 2024, pp. 1–4. Accessed: May 22, 2025. [Online]. Available: https://ieeexplore.ieee.org/abstract/document/10781954/
[12] L. dos S. Pereira, G. H. B. Donato, and M. Mattar, "Assessment of the von Mises stresses and stress triaxiality in notches using modified tensile specimens," *Mater. Res.*, vol. 26, no. suppl. 1, p. e20220572, 2023, Accessed: May 22, 2025. [Online]. Available: https://www.scielo.br/j/mr/a/53xh333KNqXdWtntZVnJxgG/
[13] R. Rahmani, M. Antonov, L. Kollo, Y. Holovenko, and K. G. Prashanth, "Mechanical behavior of Ti6Al4V scaffolds filled with CaSiO3 for implant applications," *Appl. Sci.*, vol. 9, no. 18, p. 3844, 2019, Accessed: May 22, 2025. [Online]. Available: https://www.mdpi.com/2076-3417/9/18/3844
[14] S.-H. Kim, S.-H. Bae, S.-B. Park, H. Seonwoo, and S.-E. Shin, "Friction and Wear Behavior of Selective Laser Melted Ti6Al4V-Equine Bone Nanocomposites," *Korean J. Met. Mater.*, vol. 62, no. 5, pp. 351–359, 2024, Accessed: May 22, 2025. [Online]. Available: http://kjmm.org/journal/view.php?number=1090
[15] C. A. F. Salvador, H. P. Van Landeghem, and R. A. Antunes, "Selection of Ti Alloys for Bio-Implants: An Application of the Ashby Approach with Conflicting Objectives," *Adv. Eng. Mater.*, vol. 25, no. 22, Nov. 2023, doi: 10.1002/adem.202301169.

TalentDetector

23th-25th June 2025
Gliwice-Brenna, Poland

DEPARTMENT OF ENGINEERING MATERIALS AND BIOMATERIALS
FACULTY OF MECHANICAL ENGINEERING
SILESIAN UNIVERSITY OF TECHNOLOGY

INTERNATIONAL STUDENTS SCIENTIFIC CONFERENCE

Numerical analysis of the load on the surface of a wood chipping tool

Zuzanna Zielińska[a], Łukasz Lomania[a], Katarzyna Ptasznik[a], Kajetan Kojm[a], Wiktoria Borowiec[a], Wojciech Mikołejko[a], Agata Śliwa[a], Marek Sroka[a], David Varholík[b], Peter Očovský[b], Miroslava Tavodova[b]

[a] Silesian University of Technology, Faculty of Mechanical Engineering, Department of Engineering Materials and Biomaterials
email: zz304779@student.polsl.pl, lukalom979@student.polsl.pl; kp309682@student.polsl.pl, kajekoj367@student.polsl.pl, wiktbor155@student.polsl.pl, wojciech.mikolejko@polsl.pl, agata.sliwa@polsl.pl, marek.sroka@polsl.pl
[b] Technical University in Zvolen, Faculty of Technology, Department of Manufacturing Technology and Quality Management
email: xvarholik@is.tuzvo.sk, xocovsky@is.tuzvo.sk, tavodova@tuzvo.sk

Abstract: Forest cutters (also known as mulchers) represent a key technological tool in forestry, primarily used for stand maintenance, processing of post-harvest residues, and site preparation for reforestation. These machines are capable of shredding woody material—such as shrubs, invasive trees, branches, or stumps—directly on site, thereby increasing operational efficiency while reducing environmental impact. Technological advancement has led to the development of a wide range of forest cutters, from smaller mounted models to robust tracked machines designed for demanding terrain. The choice of equipment depends on specific site conditions and the requirements of forest management. With the growing emphasis on cutting efficiency, increasing attention is being paid to the cutting elements themselves. The shape, material, and configuration of these components significantly influence both the effectiveness of the work and its impact on the environment. Examining these tools offers valuable insights for the further development and sustainable application of forestry technology.

Keywords: Forest cutter; cutting tools; tool geometry; tool material

1. FOREST CUTTERS

Forestry mulchers are robust, heavy-duty machines designed for efficient land clearing and vegetation management. Equipped with powerful rotating blades or hammer tools, they effectively shred trees, shrubs, and other plant material into smaller fragments, facilitating easier handling and natural decomposition. Available in a range of sizes and configurations—including skid-steer attachments, tractor-mounted units, and self-propelled machines—these devices are adaptable to various terrains and vegetation densities.

While their primary function is to clear land for agricultural, industrial, or development projects, forestry mulchers also play a crucial role in fire risk reduction, habitat management for wildlife, and the promotion of forest health by controlling the accumulation of dead and combustible vegetation. Their use minimizes soil disturbance compared to traditional clearing methods, helping to preserve soil structure and reduce erosion. Additionally, mulching returns valuable organic matter to the soil, enhancing nutrient cycling and supporting ecosystem sustainability.
[1]

Figure 1 Forestry mulcher: FORST (INO) [2]

The intensity of impact from these machines is higher compared to mulchers and chippers. Unlike them, the working tools can penetrate significantly below ground level, often disturbing the root systems of vegetation. These machines are also used for milling stumps and entire trees. The cutting tools are securely attached to a rotor. Forestry mulchers are equipped with a wood-feeding device, which can be either fixed or hydraulically controlled, often paired with a rear guard. During operation, the vegetation is pressed down and shredded, with the resulting chips mixing into the soil and incorporated into the surface layer. [3]

2. TOOLS OF MULCHERS

Tools used in mulchers, shredders, and soil milling machines undergo significant abrasive wear when operating in varied and rough environments. Abrasive wear happens when particles detach from the tool's working surface due to friction with harder, rougher materials or abrasive particles. Generally, two main types of abrasive wear are recognized based on how materials interact. The most common type involves the impact between abrasive particles and the tool surface, typical in applications like soil cultivation and raw material extraction.

Currently, there is no clear agreement on which material structure best resists abrasive wear. Some experts advocate for austenitic-carbide structures, while others prefer martensitic-carbide types. This divergence stems from the complexity of wear mechanisms and the variety of working conditions encountered.

The overall wear resistance of the tool material depends on the combined effect of its microstructural components. When it comes to abrasive wear, two stages are critical: first, the penetration of abrasive particles into the surface, where hardness plays a crucial role; second, the degradation of the surface, influenced by the strength of atomic bonds and the cohesion between grains in the material's structure.

a) b)

Figure 2 Types of tools a) Tool with a single WC tip [5], b) Tool with two WC

Abrasive wear significantly affects operational efficiency, leading to increased downtime for repairs or replacements and potentially lowering work quality. One key factor in accelerated wear of soil-working tools is the presence of hard silicon dioxide (SiO_2) particles, which have hardness levels between 900 and 1280 HV.Apart from other factors, the microstructure of the material greatly influences its wear resistance, making precise predictions challenging.

Several approaches can enhance the durability of these tools, including:

- Attaching tungsten-carbide tips by brazing, which is currently the most popular method;
- Applying weld overlays to the exposed parts of the tool while maintaining the brazed tips;
- Using heat treatment on the tool surface to improve wear resistance;
- Repairing worn tools by welding to restore lost carbide tips;
- Completely replacing tool materials, such as with HARDOX steel. [4]

2.1 Materials of tools for mulchers

Mulcher tools, particularly the cutting teeth, are typically manufactured from robust materials designed to withstand high mechanical loads, impact forces, and abrasive wear during operation in forestry and land-clearing environments. Two commonly used material systems are high-strength alloy steel and tungsten carbide-tipped steel bodies.

Standard mulcher teeth are made from high-quality alloy steel, which provides good toughness and mechanical strength. These teeth generally feature four sharp cutting points, allowing them to efficiently cut through vegetation and collect debris from the ground. Steel teeth are known for their aggressive cutting performance. However, they require frequent sharpening and rotation to maintain cutting efficiency and prolong their service life.

For more demanding and abrasive environments, tungsten carbide-tipped mulcher teeth are commonly used. In this case, a carbide cutting tip is welded onto a forged steel body, resulting in a tool with exceptional wear resistance and extended service life. These teeth retain their sharpness for a significantly longer period, reducing the need for maintenance. When worn or damaged, the entire tooth is usually replaced. [7]

Advantages of carbide teeth:
- excelent durabilty and wear resistance
- longer lifespan, even when working in rocky or sandy conditions
- lower maintenance requirements
- consistent cutting performance over time
- suitable for cutting trees, thick brush, and stumps

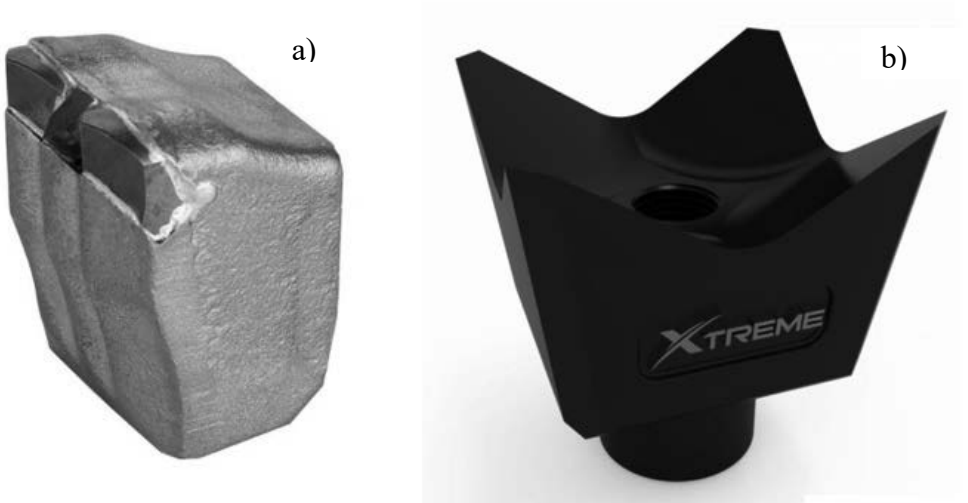

Figure 3 Comparision of mulcher tools a) Carbide mulcher teeth [8], b) Steel mulcher teeth [7]

3. MODELS USED IN COMPUTER SIMULATION

The numerical analysis of the tool was prepared in the Ansys Workbench 2024 R2 environment, in the Mechanical module. The aim of the study was to provide a computer representation of the behaviour of a mulching flail tool under the influence of the force acting on it - taking into account actual operating conditions.
In the first stage of the analysis, a geometrical model of the tool was developed, which is shown in Figure 1. Thanks to the accurate representation of the tool's shape, it was possible to carry out a detailed analysis of its ergonomics and functionality. This was the basis for further computer simulation.

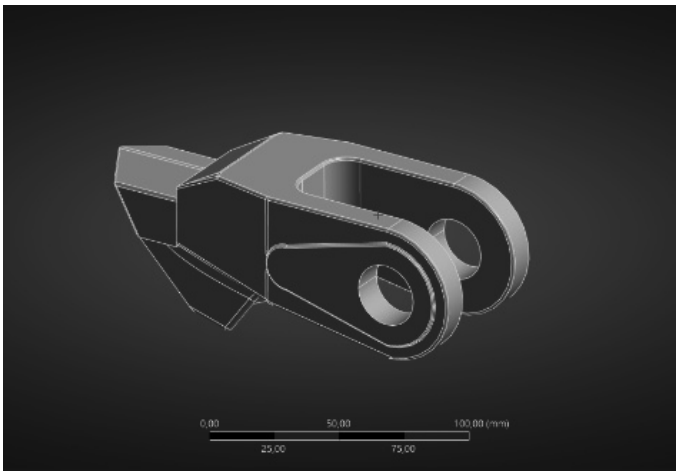

Figure 3 Geometric model of the tool

The next step was to apply a finite element mesh (FEA), as shown in Figure 2, using the PrimeMesh method. The elements used were 2 mm in size, which allowed the intricate geometry of the model to be accurately represented. By applying the FEA method, it is possible to break down the solids into small, simple elements and solve the mechanics equations for the entire model.

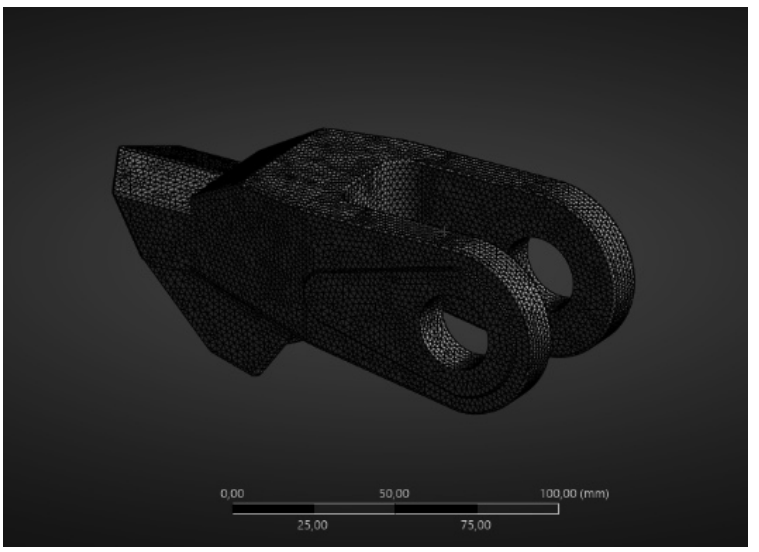

Figure 4 Geometric model of tool with superimposed finite element mesh

The material properties are then assigned according to the parameters in the table shown in Figure 3. The material data are key to determining the actual response of the structure under loading conditions.

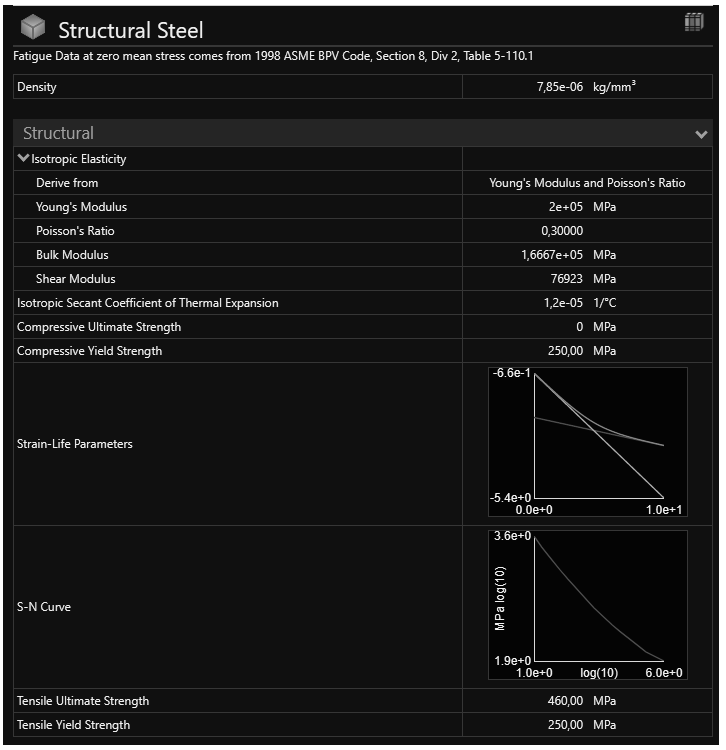

Figure 5 Material used

The model was braced in simulation space using a boundary condition of Fixed Support type, as shown in Figure 4. This type of fixation means that the displacements in all directions (X,Y,Z) are zero, simulating a permanent connection to a foundation or other immovable structure.

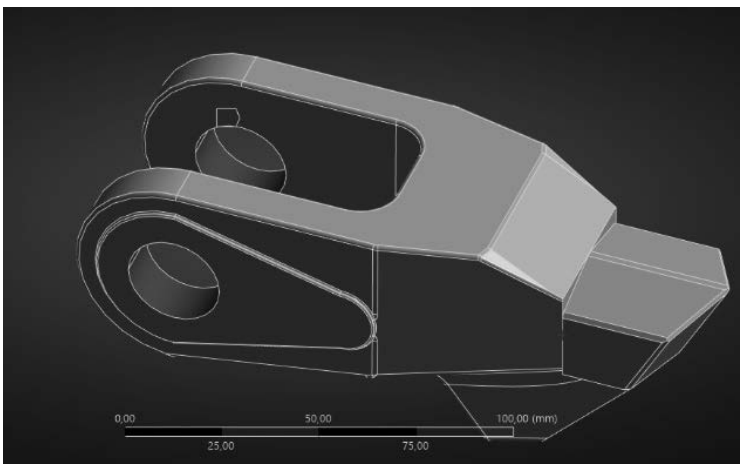

Figure 6 Fixed Support location implemented in the model

Figure 5 shows the point of application of the force - Force type load. The force of 17,800 N was estimated on the basis of the torque resulting from the operating conditions of the beater. The course of this force is shown in Figure 6. As can be seen, the force increases linearly from 0 to a maximum value and then stabilises at 17,800 N.

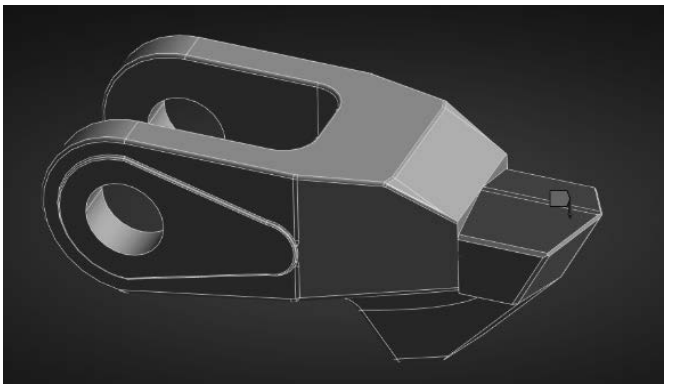

Figure 7 Force application point marked in red

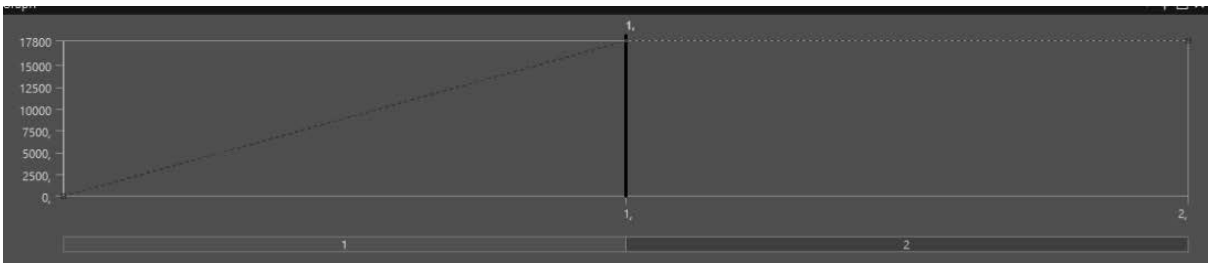

Figure 8 Diagram of the effect of force

Before the next step of the analysis, running the solver, the "Large Deflection - On" option was activated. This makes it possible to relativise non-linear deformations in the structure, thereby increasing the accuracy of the simulation results.
The following figure (Fig. 7) shows the results of the Von-Mises stress distribution. These are used to assess the stresses on the material. This type of analysis is essential for the design of components subjected to several or many forces simultaneously.

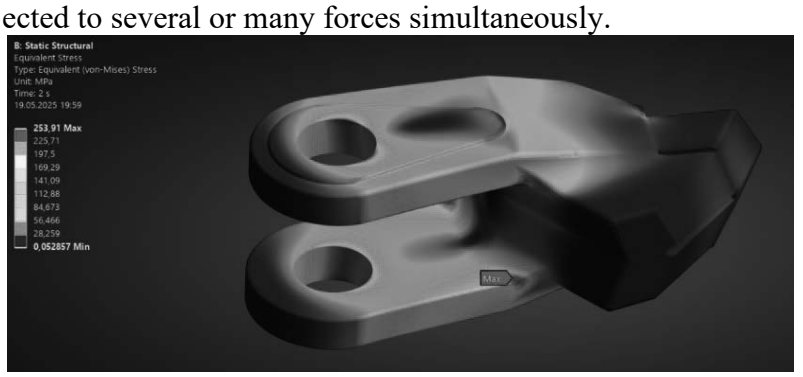

Figure 9 Von-Mises stresses

4. CONCLUSIONS

The finite element analysis conducted using SolidWorks enabled precise identification of high-stress zones within the tool structure, particularly in the regions of fixture and force application. These areas may serve as potential initiation sites for material fatigue. The displacement distribution analysis also revealed locations that may require additional structural reinforcement, emphasizing the necessity of accounting for nonlinear deformations in the design of tools operating under significant dynamic loads.

The obtained results confirm that the wear resistance and operational durability of the tool strongly depend on the appropriate selection of material. Tips made of cemented carbide exhibit significantly improved wear resistance under harsh operating conditions; however, their performance is also influenced by the method of mounting and the adequacy of structural support.

The application of finite element analysis (FEA) in the Ansys Workbench environment enabled a realistic representation of the tool's behavior under actual operating conditions. Such simulations constitute a valuable asset in the design process - they support the optimization of component geometry, allow for performance prediction, and help reduce costs associated with the development and testing of physical prototypes.

5. SUMMARY

Forestry mulchers are powerful machines used for land clearing, forest management, and fire prevention. They shred vegetation into mulch while minimizing soil disturbance. Their tools face extreme abrasive wear, especially in harsh, rocky environments.

To improve durability, tools are made from alloy steel or reinforced with tungsten carbide tips, which offer superior wear resistance and longer lifespan. Enhancements like brazing, overlays, and specialized steels further extend tool life.

A simulation in Ansys Workbench modeled tool behavior under real loads, identifying stress and displacement zones. The study confirmed that tool performance depends on material choice and design, with simulations helping optimize durability and reduce development costs.

ACKNOWLEDGEMENT

The current study was conducted as part of the collaborative activities of the Student Research Group 'B@jt' at the Department of Engineering and Biomedical Materials, Faculty of Mechanical Engineering, Silesian University of Technology in Gliwice.
Publication supported by the Excellence Initiative—Research University program implemented at the Silesian University of Technology, year 2025.

LITERATURE

1. MARKET RESEARCH INTELLECT, 2024, Available at: https://www.marketresearchintellect.com/blog/the-digital-forest-advances-in-mulching-technology-and-software-integration/
2. SIPSK, 2025, Available at: https://www.sipsk.com/lesne-frezy-forst-ino
3. Ján KOVÁČ, Jozef KRILEK, Ján JOBBÁGY a Jiří DVOŘÁK. *Technika a mechanizácia v lesníctve: vysokoškolská učebnica*. Zvolen: Technická univerzita vo Zvolene, 2017. ISBN 978-80-228-3021-8.
4. Miroslava ŤAVODOVÁ, Daniela KALINCOVÁ, Martin KOTUS, Ľubomír PAVLÍK, The Possibility of Increasing the Wearing Resistance of Mulcher Tools, from Journal: Acta Technologica Agriculturae (pages: 87-93), Available at:

https://www.researchgate.net/publication/326401109_The_Possibility_of_Increasing_the_Wearing_Resistance_of_Mulcher_Tools
5. FECON, 2025, Available at: https://fecon.com/product/bull-hog-mulching-teeth/
6. FECON, 2025, Available at: https://fecon.com/product/bull-hog-rotors/
7. KONECARBIDE, 2023, Available at: https://konecarbide.com/mulcher-teeth-steel-or-carbide/
8. SKID STEER SOLUTIONS, 2025, Available at: https://www.skidsteersolutions.com/double-carbide-mulching-tooth-adapter-promac/

TalentDetector

23th-25th June 2025
Gliwice-Brenna, Poland

DEPARTMENT OF ENGINEERING MATERIALS AND BIOMATERIALS
FACULTY OF MECHANICAL ENGINEERING
SILESIAN UNIVERSITY OF TECHNOLOGY

INTERNATIONAL STUDENTS SCIENTIFIC CONFERENCE

Analysis of the properties of multilayer composite materials dedicated for yacht hulls

Zuzanna Żaczek[1], Agnieszka J. Nowak[2]

[1] Student Science Club "HEAD TO HEAD" operating at the Department of Scientific and Didactic Laboratory of Nanotechnology and Material Technologies at the Faculty of Mechanical Engineering, Silesian University of Technology in Gliwice, Poland
[2] Scientific and Didactic Laboratory of Nanotechnology and Material Technologies, Silesian University of Technology, Konarskiego 18A, 44-100, Gliwice, Poland

Abstract: The paper presents a review of the literature on polymer matrix composite materials. The focus was on considering their use in the maritime industry and, in particular, their role in constructing a yacht's hull, the types of which are also presented in the work. Eight batches of multilayer composite materials were produced, and their selected properties were determined. The research conducted in this work allowed for the development of an appropriate material dedicated to yacht hulls. The obtained results can be used for further analyses, allowing the observation of the behaviour of materials in a specific application.

Keywords: Composite materials, polymer matrix composite materials, multi-layer laminates, glass fiber, aramid fiber, basalt, fiber marine

1. INTRODUCTION

Composite materials are undoubtedly an inseparable element of the industry. Due to their extensive properties, they enjoy great interest, considering their mechanical strength, low density and considerable elasticity. Thanks to this, composites are used in the aviation, construction, automotive, medical and even marine industries. In marine, polymer matrix composites, which cover decks and build masts or yacht hulls, enjoy particular interest. A commonly used material used to produce a yacht hull is a multilayer laminate. The production of the materials mentioned above allows for the comfortable use of the product and extends its service life compared to conventional methods. The aim of this work is to develop a multilayer composite material dedicated to yacht hulls. The work developed diversified composite materials in terms of the reinforcement phase system and matrix material. Finally, EPIDIAN 652 epoxy resin (matrix material), glass fiber, aramid fiber, and chopped basalt fiber (reinforcement) fabrics were used. The laminates were manufactured using manual moulding technology with appropriately selected hardeners. Eight batches of multilayer composite material samples were produced to develop an optimal material for dedicated applications. The batches of samples were made in the

form of sheets, cut and tested by applicable standards. The test results were discussed, and conclusions were drawn.
The planned and implemented tests of the multilayer composite material dedicated to yacht hulls allow us to determine which produced materials will be optimal for yacht operation. An important aspect of this work is the addition of cut basalt fiber to the multilayer composite material, which will improve the durability of the hull while facilitating the disposal of the used part of the boat.

2. RESEARCH MATERIAL

Two types of fibers in the form of fabric were used to produce the laminate dedicated to the yacht's hull: glass with a grammage of 163 g/m^2, aramid with a grammage of 173 g/m^2 and chopped basalt fibre. (Fig 1) .

Epoxy resin - EPIDIAN 652 was used as the matrix. This substance has a medium viscosity and a light yellow colour, and its form is clear. The properties of epoxy resin EPIDIAN 652 are presented in Table 1. Two hardeners were used to extend the research and select the optimal solution. IDA, i.e., hardeners for epoxy resins, EPIDIAN, guarantee high mechanical properties and are chemically resistant. The properties of hardener IDA are presented in Table 2. The second hardener used for epoxy resin is hardener DECO. It is a dedicated hardener for epoxy resin EPIDIAN with high transparency, aesthetics and high chemical and mechanical resistance.

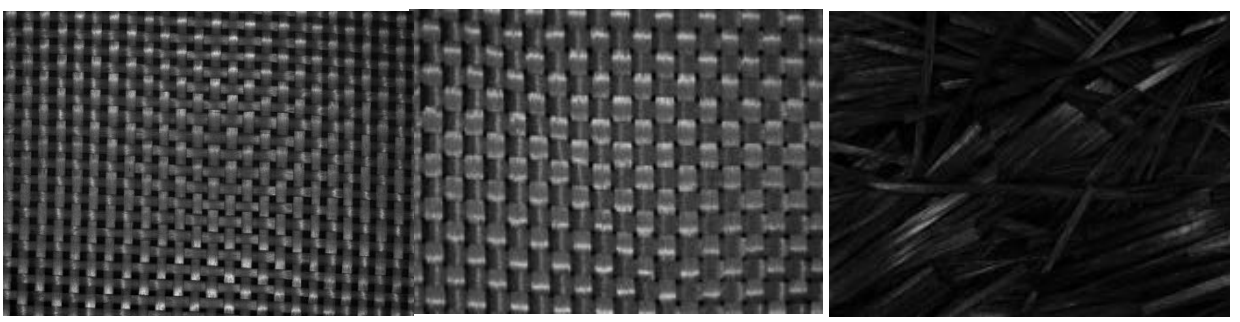

Figure 1. *Fabric made of (from left) glass, aramid and basalt fibers*

Table 1. *Properties of epoxy resin EPIDIAN 652*

Density, g/cm^3	1,10
Epoxy number, mol/100g	0,48-0,51
Viscosity, 25°C – mPas	500-900

Table 2. *Properties of IDA hardener*

Gęstość, g/cm^3 w 20°C	1,01-1,03
Liczba aminowa, KOH/g	200-350
Lepkość, 25°C – mPas	150-350

2.1 Sample preparation

The first stage of sample preparation for testing was the preparation of selected materials constituting the components of the base laminates of materials used for testing. First, sheets were cut out of fabrics and arranged in the order of impregnation. Eight batches of samples were prepared from previously cut fabric forms. Resin compositions reinforced with materials in the

form of glass and aramid fiber fabrics in various configurations and cut basalt fiber placed on the outer layer of the sheet were prepared. The composition and designations are presented in Table 3. After preparing eight batches of samples for testing, the manual moulding process was performed on silicone moulds.

Manual moulding began with the correct protection of the mould with Vaseline. Then, the impregnation solution was prepared following the proportions indicated by the manufacturer. The base materials were impregnated with a solution of EPIDIAN 652 (E652) epoxy resin and DECO hardener in the proportion of 100 g of resin – 50 g of hardener. During impregnation, 25g cut basalt fiber weighed on an analytical balance was used as the first layer to stop UV radiation and improve recycling properties. The entire process was repeated with IDA hardener - in a 100g resin - 50g hardener ratio. Forming was performed using a small grooved roller. The sheets prepared this way were pressed to remove excess resin and air from the system and left under load for seven days to achieve complete impregnation and hardening. After seasoning, the samples were cut into 80x10mm rectangles using a guillotine, and the resulting beams were sent for strength and impact tests.

Table 3. *Composition and designations of the composite materials produced.*

	The order of arrangement of fiber fabrics	**Composition**	**Designation**
1.	Glass - glass - glass - basalt	E652+DECO	SSS_DECO
2.	Glass - aramid - glass - basalt	E652+DECO	SAS_DECO
3.	Glass - aramid - aramid - glass - basalt	E652+DECO	SAAS_DECO
4.	Glass - aramid - glass - aramid - glass - basalt	E652+DECO	SASAS_DECO
5.	Glass - glass - glass - basalt	E652+IDA	SSS_IDA
6.	Glass - aramid - glass - basalt	E652+IDA	SAS_IDA
7.	Glass - aramid - aramid - glass - basalt	E652+IDA	SAAS_IDA
8.	Glass - aramid - glass - aramid - glass - basalt	E652+IDA	SASAS_IDA

3. RESEARCH METHODOLOGY

3.1 Hardness tests

The materials selected in the work, constituting the multilayer composites matrix, were sent for hardness tests. EPDIAN 652 and two types of hardeners, i.e. DECO and IDA, were used in the work. The unused matrix's remains were poured into a mould at the composite production stage and left to cross-link. After seven days, the 5 mm thick disks for hardness testing were removed and secured. Then, five measurements were taken for each matrix variant on a Zwick 3106 D-89079 Ulm hardness tester from Zwick/Roell. Hardness tests were performed following ISO 2039-1 Hardness tests of plastics.

3.2 Static three-point bending test

The static three-point bending test was performed to assess the strength properties. The tests were performed on the SHIMADZU AGX-V2 device following the PN-EN ISO 178 standard "Plastics - determination of bending properties". Five samples from each developed material series were used for the tests (Table 3).

3.3 Impact tests

Impact tests were performed following the PN-EN ISO 179 standard "Plastics. Charpy impact strength determination". The tests were performed on a Zwick/Roell HIT25P device. The impact strength was calculated using formula no. 1 based on the average fracture energy obtained during the test.

$$R_e = \frac{E_c}{a*b} * 10^3 \quad (1)$$

Where:
R_e – impact strength, kJ/m^2
E_c – average fracture energy, J
a - -Average thickness of the test sample, mm
b - Average width of test sample, mm

4. DISCUSSION OF RESEARCH RESULTS

4.1. Hardness tests

The average hardness results with the DECO and IDA hardeners used are presented in Table 4. The load for all tests was 132 N. On this basis, it can be concluded that the resin with the DECO hardener has higher hardness. The hardness tests are graphically presented in figure 2.

Table 4. *Hardness results of epoxy resin with IDA and DECO hardener*

	Height of the recess, mm	Hardness, N/mm^2	Standard deviation
IDA	0,33	60,54	1,48
DECO	0,16	24,14	2,65

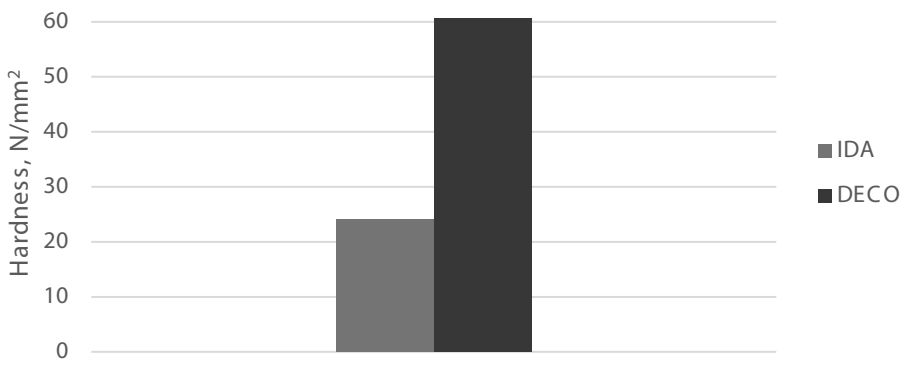

Figure 2. *Comparison of average hardness measurements for resin with DECO and IDA hardener*

4.2. Static three-point bending test

The static tensile test allowed for determining the bending strength, deformation for maximum bending force, bending stresses and Young's modulus. The results are presented in Table 5. Based on them, laminates with the addition of aramid fibre have better-bending strength properties than the DECO hardener used, while the SAAS_DECO laminate has the highest bending strength. Similarly to the deformation for maximum bending force, the multilayer composite material marked SAAS_DECO shows the best properties. The SAS_IDA laminate shows the highest bending stress. The SAS_DECO laminate characterizes the highest Young's modulus. The stress-elongation graph is presented in Figure 3, while the appearance of the samples after the static three-point bending test is presented in Table 5.

Table 5. *Result of the static three-point bending test.*

	Bending strength, MPa	**Deformation for max force,%**	**Bending stress, MPa**	**Young's modulus, MPa**
SSS_IDA	74,18	2,43	65,56	2605,02
SSS_DECO	62,65	2,13	27,85	2874,56
SAS_IDA	74,78	2,69	94,09	3291,43
SAS_DECO	82,86	2,12	58,91	3840,06
SAAS_IDA	31,97	2,29	28,09	1709,61
SAAS_DECO	85,1	2,93	38,07	1361
SASAS_IDA	55,62	2,54	33,22	2109,95
SASAS_DECO	66,93	2,23	69,28	2759,78

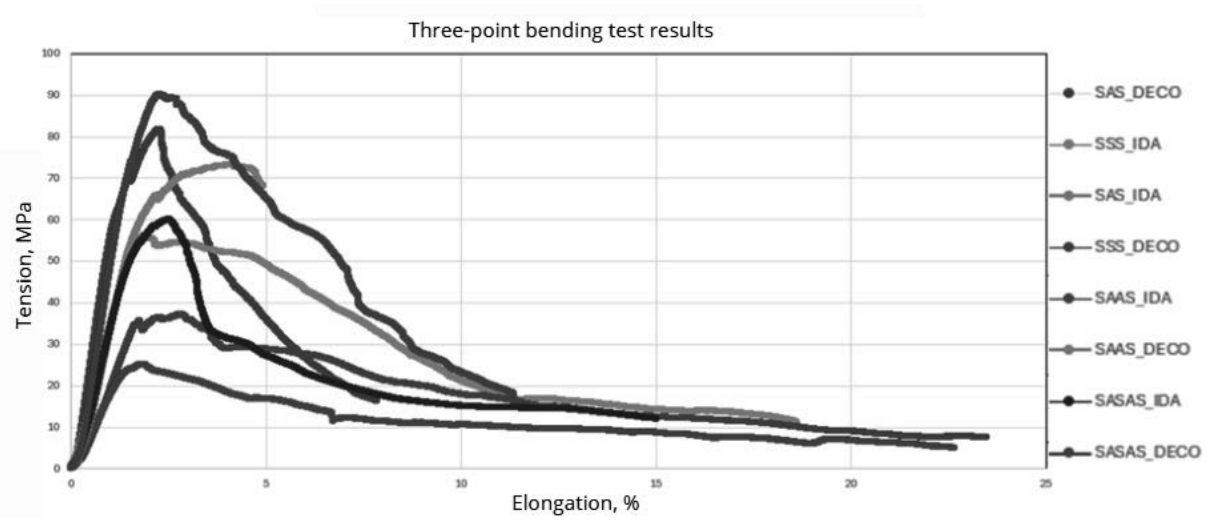

Figure 3. *Example graphs of developed material variants*.

4.3. Impact tests

Impact tests allowed for a clear determination of the force needed to break the samples. The results are presented in Table 6. After the test, it can be observed that the continuity of the samples was maintained, and none of them was completely broken. Delamination occurred in some of the

tests, most often in the layer with cut basalt fibers that promote delamination. The tests clearly show that the highest impact strength is possessed by the multilayer composite material designated SAAS_IDA (Fig. 5). Example photos after impact testing of the manufactured material variants are presented in Table 7.

Table 6. *Impact test results*

	Medium thickness, mm	**Medium width, mm**	**Average energy broken, J**	**Impact strength, kJ/m^2**
SSS_IDA	2,69±0,2	19,82±0,7	5,53	104,52
SSS_DECO	2,73±0,45	19,19±0,45	6,19	121,12
SAS_IDA	2,73±0,33	21,02±0,35	3,37	57,92
SAS_DECO	3,25±0,17	14,94±0,94	4,3	90,39
SAAS_IDA	3,46±0,42	20,15±0,29	10,71	163,86
SAAS_DECO	3,82±0,09	19,90±0,70	7,49	100,86
SASAS_IDA	3,00±0,08	17,89±0,2	6,25	116,45
SASAS_DECO	3,70±0,11	20,34±0,40	6,41	86,88

Table 7. *Sample photos after impact testing of manufactured material variants.*

SSS_IDA	**SAS_DECO**
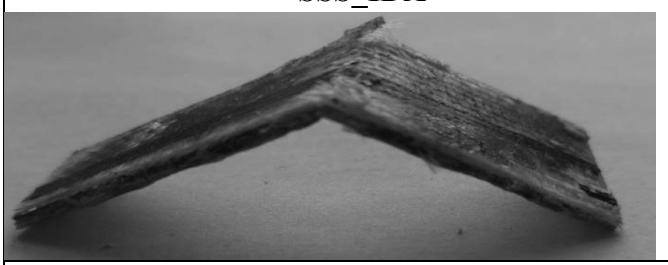	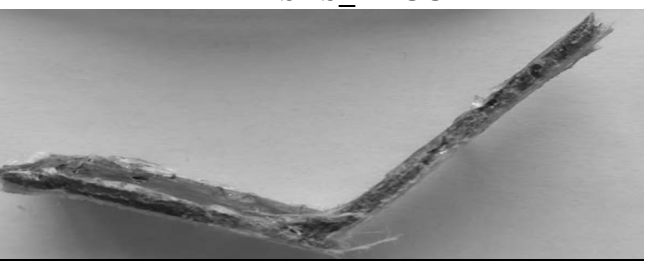
SAS_IDA	**SAAS_DECO**
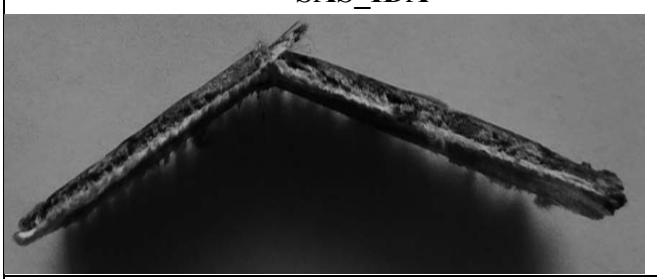	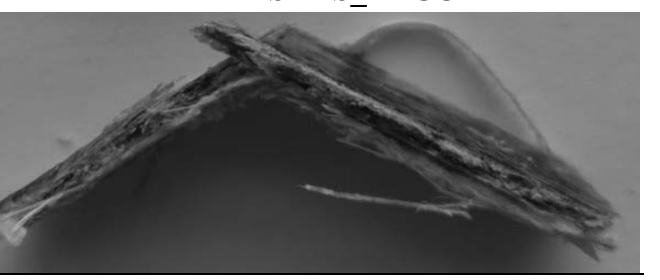
SAAS_IDA	**SASAS_DECO**
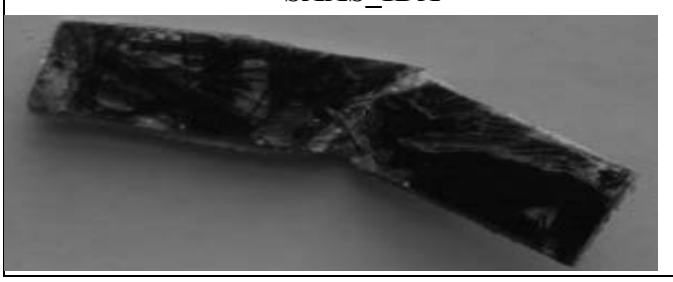	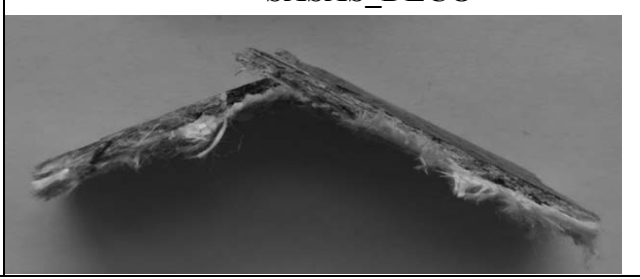

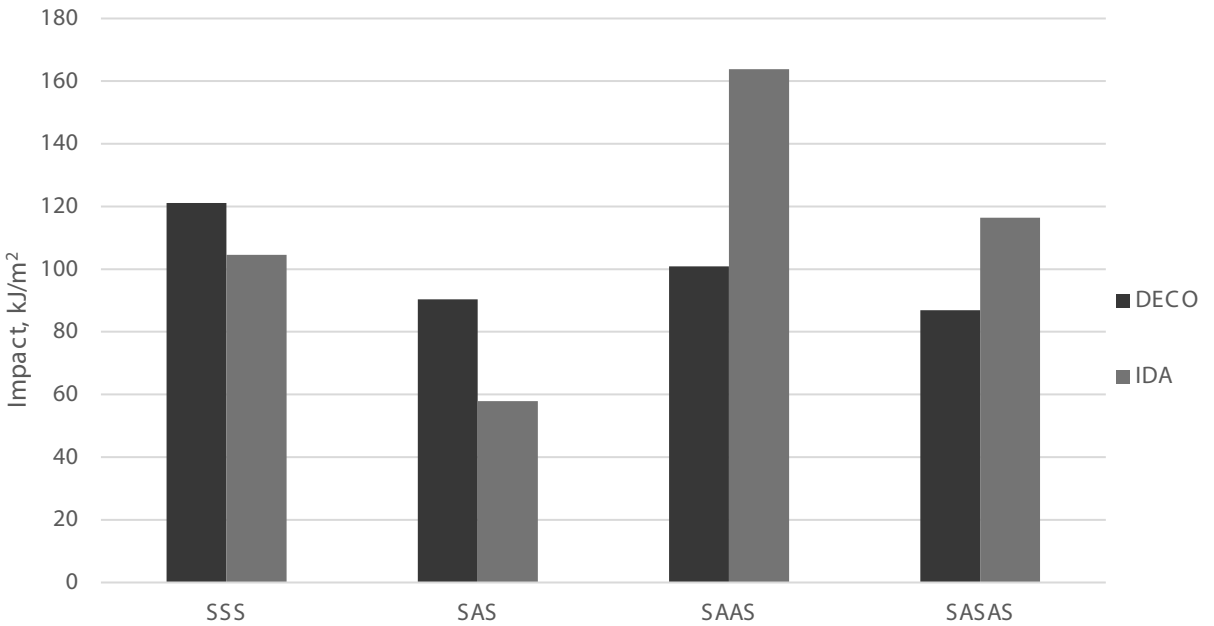

Figure 5. *Graphical representation of averaged impact test results*

5. CONCLUSION

The subject matter discussed in the work provides an answer to the problems that the marine industry is currently struggling with in the context of producing yacht construction elements from composite materials. The research carried out allows for an unambiguous assessment and development of a multilayer composite material dedicated to marine use. The research carried out in the project allowed for the assessment of the mechanical and physical properties of all laminate compositions presented in the project.

The hardness tests of the resin composition show that the resin (EPIDIAN 652) with the DECO hardener is characterized by better hardness; the marked result is better by 151% than the IDA-hardened resin.

The laminate demonstrates the best bending strength in three-point bending with the composition of the reinforcing phase in fabric: glass - aramid - aramid - glass - and chopped basalt fiber with the DECO hardener used. This result is 53% better than the laminate with the same fabric composition with IDA cross-linked resin and 166% better than the worst bending strength result recorded for the material with the fabric composition: glass - aramid - glass - chopped basalt fiber with IDA hardener.

The best impact properties were recorded for the laminate with IDA hardener with the composition of glass fiber fabrics - aramid - aramid - glass - chopped basalt fiber, giving a result 62% higher than the corresponding laminate with DECO hardener and 183% higher than the worst result recorded for the laminate with the composition of glass fiber fabrics - aramid - glass and chopped basalt fibers with the IDA hardener used. The high impact strength was also recorded for the material with the composition of glass fiber fabrics - glass - glass - chopped basalt fiber, giving a result 35% lower than the best result recorded in the study. The material for which the best bending strength was recorded (SAAS_DECO) is characterized by an impact strength 62% lower than the best impact measurement (SAAS_IDA).

The research carried out in the project allows for the development of a multilayer composite material dedicated to the yacht hull. Laminates with IDA hardener show better mechanical properties, and in particular, a multilayer composite material consisting of glass fiber fabrics - aramid - aramid - glass - cut basalt with IDA hardener, obtaining the best impact properties. The research carried out can be treated as an introduction to further corrosion and ageing studies, determining the effect of the seawater environment on the condition of samples in terms of dedicated applications.

ACKNOWLEDGEMENT

The present study was produced as part of the activities of the Student Science Club "HEAD TO HEAD" operating at the Department of Scientific and Didactic Laboratory of Nanotechnology and Material Technologies at the Faculty of Mechanical Engineering, Silesian University of Technology in Gliwice.

BIBLIOGRAPHY

1. Dobrzański LA.' Non-metallic engineering materials. Silesian University of Technology Publishing House (2008).
2. Website: havel–composite.pl index.php/menu/produkty/type/tkaniny_szklane Date of access: 20.12.2024
3. Grabian J., Ślączka W., and Przetakiewicz W.; Multifunctional layered composite materials for hulls of selected units operated in inland navigation conditions; *Advances in Mechanical and Materials Engineering* 35.298 (3) (2018): 297-308.
4. Jastrzębska M., and Jurczak W.; Modern composite materials for the production of sports and recreational equipment; Logistics 3 (2012).
5. Błędzki Andrzej K., Gorący K., and Urbaniak M.; Possibilities of recycling and utilization of polymer materials and composite products; *Polimery* 57.9 (2012): 620-626.

TalentDetector
23th-25th June 2025
Gliwice-Brenna, Poland
DEPARTMENT OF ENGINEERING MATERIALS AND BIOMATERIALS
FACULTY OF MECHANICAL ENGINEERING
SILESIAN UNIVERSITY OF TECHNOLOGY
INTERNATIONAL STUDENTS SCIENTIFIC CONFERENCE

Characterisation of materials used in construction for damp-proofing and waterproofing

Ewelina Kaputa-Kuc[a], Ewa Jonda[b] *, Marek Sroka[b]

[a] Łukasiewicz Research Network - Warsaw Institute of Technology Branch in Katowice, Al. W. Korfantego St. 193A, 40157 Katowice, Poland,
email: ewelina.kaputa-kuc@wit.lukasiewicz.gov.pl
[b] Department of Engineering Materials and Biomaterials, Silesian University of Technology, Konarskiego St. 18a, 44100, Gliwice, Poland
email: *ewa.jonda@polsl.pl, marek.sroka@polsl.pl

Abstract: The concepts of damp and waterproof insulation are related to the protection of buildings against moisture and water and are often confused with each other. The purpose of this study is to present the division and characteristics of materials used in construction for damp and waterproof insulation and to indicate the differences between them resulting from their intended use. Waterproofing, which provides protection for the underground part of the building, is necessary to protect its structure from destruction as a result of environmental factors. Damp insulation is performed to protect the building from moisture coming from the ground or air, e.g. when the building is built on permeable soil (e.g. loose). In turn, waterproof insulation is usually used, among others, when the building is located on cohesive soil (e.g. clay) and its foundations are below the groundwater level and may be exposed to the adverse effects of water.

Keywords: materials, laser treatment, polimers

1. INTRODUCTION

The impact of water occurring in nature in various forms on buildings is a harmful and undesirable phenomenon. Materials used in construction are absorbent, do not constitute a tight barrier for water, and are also destroyed by water. Water can be an indirect cause of the destruction of materials. In the presence of moisture, harmful fungi develop in a very short time, which can very quickly lead to the complete destruction of wooden elements of the building. In addition, moisture and fungi in the building create harmful conditions for the health of people and animals staying in it, reducing or even eliminating the utility value of rooms or entire buildings. Therefore, waterproofing and damp-proofing are key elements in construction, aimed at protecting structures against the harmful effects of water and moisture [1].

The purpose of a damp proof course is to prevent water from rising from the ground up the wall, to prevent water from moving from one part of the wall to another and to prevent water from draining from the internal wall of a cavity wall structure to the outside of the building.

Damp proof courses can also be used in masonry chimneys and parapet walls to protect the interior of the building from water running down from above. They should be designed in conjunction with flashings and waterproofing sheets, including roofing sheets and damp proof sheets, to provide a continuous barrier and should deflect water away from the building so that it can drain away safely [2].

Waterproofing is designed for use in wall structures on or under floors or slabs set in the ground to protect against water exerting hydrostatic pressure, passing from the ground to the interior or from one part of the structure to another. Here, waterproofing and membranes are key and must ensure tightness [3].

Depending on the location and method of placing the insulation, we speak of horizontal insulation /on surfaces with an inclination of 0° to 2°/ or vertical insulation /on vertical surfacesand close to vertical/ [1].

1.1. Asphalt roofing felts

Roofing felts are a traditional waterproofing material, mainly used as horizontal and vertical insulation (Fig. 1). Modern roofing felts, which are modified with e.g. SBS elastomer (styrene-butadiene-styrene) or APP plastomer (atactic polypropylene) are characterized by much better flexibility, resistance to low temperatures and greater durability compared to classic asphalt roofing felts. Modified roofing felts are most often thermo-welded or self-adhesive. They are produced with different types of matrix, and most often it is:

- polyester non - woven fabric, glass fleece insert, glass fleece insert with non-woven fabric [4], [5]. The requirements for these products are specified in Polish standards: PN-EN 13969:2006 [6]; PN-EN 14967:2007 [7]; PN-EN 13707+A2 [8],

Figure 1. Asphalt roofing felt [9]

- asphalt binders, asphalt solutions, asphalt masses and asphalt emulsions. These are liquid materials most often applied cold or hot, which after hardening create a flexible, jointless waterproofing coating (Fig. 2). They are mainly used in vertical insulation of foundations. They create a strong moisture barrier [10]. Adhesives - asphalt-based adhesive materials used for gluing roofing felts and making moisture insulation. Masses - thick mixtures of asphalt with additives (e.g. latex, fibers), creating flexible, thick-layer insulation. Asphalt solutions - liquids created by dissolving asphalt in organic solvents. Asphalt emulsions - water dispersions of asphalt with emulsifiers, non-toxic and solvent-

free [10]. These products must meet the requirements of the Polish standards: PN-B-24620:1998 [11]; PN-B-24006:1997 [12], PN-B-24000:1997 [13]; PN-B-24002:1997 [14], PN-B-24003:1997 [15].

Figure 2. Bituminous insulation [16]

2.2. Bentonite waterproofing mats

This is a modern solution used to protect underground parts of buildings against water ingress. Used to insulate foundation slabs, backfilled walls, tunnels, underground passages, flood embankments and other structures exposed to water. Bentonite mats marked in standards with the symbol GBR-C (geosynthetic clay barrier) are a type of composite, i.e. a product made of one or more geosynthetics and swelling clay. These include, among others [16 – 18]:

- •geotextile or geotextile (top layer),
- •powdered or granulated bentonite, or loose nonwoven fabric filled with bentonite (middle layer),
- •geotextile (bottom layer).

Mainly sodium bentonites are used for the production of mats, but also calcium, activated calcium or chemically modified sodium bentonites. In accordance with the requirements of the PN-EN 13491 standard [19] (Fig. 3).

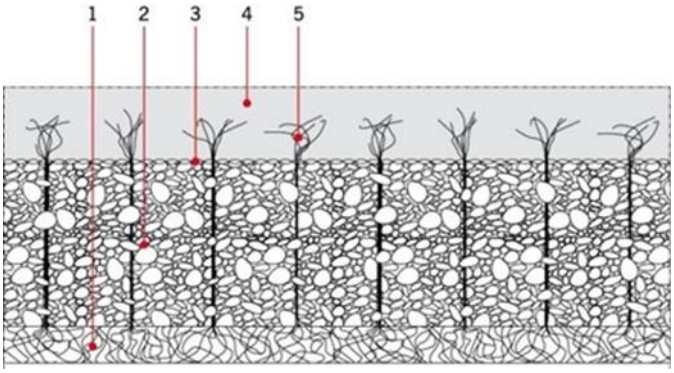

Figure 3. Bentonite needle mat: 1 - PP non-woven fabric, 2 - granulated bentonite, 3 - PP fabric, 4 - concrete, 5 - adhesion fibers [20]

2.3. Foils and membranes

These are popular choices for moisture insulation. They are made of plastics such as polyvinyl chloride (PVC), polyethylene (PE) in HDPE or LDPE versions, polypropylene (PP), EPDM synthetic rubber (ethylene-propylene-diene rubber) or thermoplastic polyolefins (TPO) and are a modern alternative to traditional moisture insulation solutions. Polymer foils are used as both horizontal and vertical insulation [10]. As horizontal insulation, they are used to separate the wall above ground from the foundation wall, which is its base but has no contact with the ground. The use of this type of insulation protects the walls from moisture rising from the ground. Vertical insulation, on the other hand, is used between the footings and the foundation walls, as well as at the junction of the foundation and external walls of the building. Its main task is to protect against capillary rise: the drawing of moisture through the walls and its transfer upwards to the walls of the building. Due to their high flexibility and chemical resistance, foils and membranes are particularly suitable for insulating large surfaces and at high groundwater levels [10, 21, 22]. Figures 4 and 5 show the appearance of sample foils used for waterproofing in construction.

Depending on the type and purpose of the foil or membrane (vapour barrier, damp-proofing, waterproofing, roofing), various standards specifying technical requirements are used, including: PN-EN 14909 [2]; PN-EN 13967 [23]; PN-EN 13956 [24]; PN-EN 13984 [25]; PN-EN 13970 [26].

Materials compliant with the requirements of the PN-EN 13967 [23] standard are classified as type A - intended for damp-proofing, classified as type T - for waterproofing. Materials for damp-proofing are classified as type V - a ventilation or drainage product.

According to the ITB recommendations [27] in accordance with the PN-EN 14909 [2] standard, PE foils (polyethylene foil) and PP foils (polypropylene foil) used for moisture insulation cannot be thinner than 2 mm, PVC foils (polyvinyl chloride) cannot be thinner than 1 mm. In the case of foils meeting the technical requirements of the PN-EN 13967 [23] standard:

- for waterproofing, the thickness of the PE and PP foil must not be less than 1 mm, and the thickness of the PVC foil must not be less than 1.5 mm (with a tightness of at least 0.2 MPa for 24 hours),
- for moisture insulation, the thickness of the PVC foil must be at least 1 mm [28].

Figure 4. Waterproofing foil [29]

Figure 5. Dimpled waterproofing foil [30]

In recent years, the environmental aspect related to the recycling of polymer materials and their reuse in the production process has become increasingly important. Manufacturers are increasingly introducing recycled components into their products – both from internal recycling (post - production waste) and external recycling (post-consumer waste). Recyclates are most often used:

- in the internal layers of membranes, not directly exposed to UV radiation and mechanical damage, in products with reduced aesthetic requirements (e.g. ground membranes),
- as admixtures to PE or PVC foils in controlled proportions.

The use of recyclates may affect [21, 31, 32]:

- mechanical strength – may be reduced if the appropriate quality of the recyclate is not maintained,
- dimensional stability and chemical resistance – some admixtures may negatively affect the stability of the material in the long term,
- resistance to ageing and UV radiation – recyclates may be less resistant to external factors, which requires the use of protective layers or stabilizers.

SUMMARY

Damp and waterproof insulation is an important element of protecting underground parts of buildings from the harmful effects of water. Modern technological solutions provide a wide range of materials, from traditional asphalt felts, through bituminous masses and bentonite mats, to innovative foils and membranes made of plastics. In recent years, the use of recycled components has become a significant trend in the design of waterproofing materials. The use of recyclates, primarily in polymer products such as PE and PVC, allows for a reduction in the consumption of primary raw materials and a reduction in the negative impact of the construction industry on the environment. However, it should be remembered that these materials may be characterized by lower durability, variability of physical properties and reduced resistance to external factors. Therefore, their use requires special care in the selection, design and quality control, especially in structures exposed to intensive moisture or pressurized water.

BIBLIOGRAPHY

[1] S. Matławski, Z. Wczelik, Wykonywanie izolacji przeciwwilgociowych, ARKADY, wydanie III poprawione, 1967r.
[2] Polska Norma PN-EN 14909:2012, „Elastyczne wyroby wodochronne - Wyroby z tworzyw sztucznych i kauczuku do poziomej izolacji przeciwwilgociowej -- Definicje i właściwości".
[3] Materiały firmy SUEZ, Baza wiedzy.
[4] A. Śmiałek, G. Gładkiewicz„ Czym się różnią papy", 09.09.2009r, www. murator.pl.
[5] Kazimierowicz, M. Rokiel, murator.pl, „Papa termozgrzewalna na dach i fundament. Rodzaje pap i ich zastosowanie", 10.07.2018r.
[6] Polska Norma PN-EN 13969:2006/A1:2007, „Elastyczne wyroby wodochronne -- Wyroby asfaltowe do izolacji przeciwwilgociowej łącznie z wyrobami asfaltowymi do izolacji przeciwwodnej części podziemnych -- Definicje i właściwości".
[7] Polska Norma PN-EN 14967:2007, „Elastyczne wyroby wodochronne -- Wyroby asfaltowe do poziomej izolacji przeciwwilgociowej -- Definicje i właściwości".
[8] Polska Norma PN-EN 13707+A2:2012, „Elastyczne wyroby wodochronne -- Wyroby asfaltowe na osnowie do pokryć dachowych -- Definicje i właściwości".
[9] Materiały informacyjne - Izolacja Jarocin S.A., Warszawa.
[10] M. Rokiel, „Właściwości i rodzaje materiałów do hydroizolacji", 06.04.2011r, www. izolacje.com.pl.
[11] Polska Norma PN-B-24620:1998+PN-B-24620:1998/Az1:2004 „Lepiki, masy i roztwory asfaltowe stosowane na zimno".
[12] Polska Norma PN-B-24006:1997, „Masa asfaltowo-kauczukowa".
[13] Polska Norma PN-B-24000:1997, „Dyspersyjna masa asfaltowo-kauczukowa".
[14] Polska Norma PN-B-24002:1997, „Asfaltowa emulsja anionowa".
[15] Polska Norma PN-B-24003:1997, „Asfaltowa emulsja kationowa".
[16] K. Franczuk, Materiały budowlane, kb.pl, 01.12.2023.
[17] Francke, „Nowoczesne hydroizolacje budynków, Zeszyt 1. Zabezpieczenia wodochronne części podziemnych budynków", Wydawnictwo Naukowe PWN, Warszawa 2021.
[18] R. Ruhnau, „Abdichtung mit Bentonit in „Lufsky Bauwerksabdichtung", Teubner, Wiesbaden, 249 – 264, 2006
[19] Francke, „Warunki Techniczne Wykonania i Odbioru Robót Budowlanych. Część C: Zabezpieczenia i izolacje. Zeszyt 5: „Izolacje przeciwwilgociowe i wodochronne części podziemnych budynków", Instytut Techniki Budowlanej, Warszawa 2019.
[20] Polska Norma PN-N 13491:2006/A1:2007, „Bariery geosyntetyczne - Właściwości wymagane w odniesieniu do wyrobów stosowanych jako bariery nieprzepuszczalne dla płynów do budowy tunelów i budowli podziemnych".
[21] B. Monczyński, Izolacje 3/2022, „Materiały stosowane do wtórnej hydroizolacji budynków – membrany z tworzyw sztucznych i kauczuku", 16.04.2022r.
[22] B. Monczyński, Izolacje 3/2022, „Materiały stosowane do wtórnej hydroizolacji budynków – membrany z tworzyw sztucznych i kauczuku", 16.04.2022r.
[23] Materiały informacyjne, hermetiksystem.pl.
[24] Polska Norma PN-EN 13967+A1:2017-05, „Elastyczne wyroby wodochronne -- Wyroby z tworzyw sztucznych i kauczuku do izolacji przeciwwilgociowej łącznie

z wyrobami z tworzyw sztucznych i kauczuku do izolacji przeciwwodnej części podziemnych -- Definicje i właściwości".
[25] Polska Norma PN-EN 13956:2013-06, „Elastyczne wyroby wodochronne -- Wyroby z tworzyw sztucznych i kauczuku do pokryć dachowych -- Definicje i właściwości".
[26] Polska Norma PN-EN 13984:2013-06, „Elastyczne wyroby wodochronne -- Wyroby z tworzyw sztucznych i kauczuku do regulacji przenikania pary wodnej -- Definicje i właściwości".
[27] Polska Norma PN-EN 13970:2006/A1:2007, „Elastyczne wyroby wodochronne -- Wyroby asfaltowe do regulacji przenikania pary wodnej -- Definicje i właściwości"
[28] Komentarz do normy PN-EN 14909:2012, „Elastyczne wyroby wodochronne. Wyroby z tworzyw sztucznych i kauczuku do poziomej izolacji przeciwwilgociowej. Definicje i właściwości wraz z zaleceniami ITB dla wyrobów objętych normą", ITB, Warszawa 2011.
[29] M. Rokiel, Izolacje 1/2020, „Hydroizolacje rolowe-wybrane zagadnienia".
[30] Materiały informacyjne www. nexeoplastics.com.
[31] GUTTA, Materiały prasowe, www.gutta.pl.
[32] Materiały informacyjne, , „Wpływ recyklingu tworzyw termoplastycznych na zmiany właściwości materiału i proces przetwarzania", www. dopak.pl.
[33] Journal of Polymers and the Environment, Development of an Engineering Material with Increased Impact Strength and Heat Resistance from Recycled PET", 31, 5296 - 5308, 2023.

TalentDetector
23th-25th June 2025
Gliwice-Brenna, Poland
DEPARTMENT OF ENGINEERING MATERIALS AND BIOMATERIALS
FACULTY OF MECHANICAL ENGINEERING
SILESIAN UNIVERSITY OF TECHNOLOGY
INTERNATIONAL STUDENTS SCIENTIFIC CONFERENCE

Surface Morphology and Composition of Cobalt-Chromium (Co-Cr) powder used in Dental implantology before and after Selective Laser Melting (SLM)

Maryam Soleimani[a], Wojciech Sitek[a], Magdalena Szindler[b]

[a] Silesian University of Technology, Faculty of Mechanical Engineering, Scientific and Didactic Laboratory of Nanotechnology and Material Technologies, email: maryam.soleimani@polsl.pl, wojciech.sitek@polsl.pl
[b] Silesian University of Technology, Faculty of Mechanical Engineering, Department of Engineering Materials and Biomaterials,
email: magdalena.szindler@polsl.pl

Abstract: This study investigates the surface characteristics of cobalt-chromium (Co-Cr) dental implants fabricated via Selective Laser Melting (SLM) using different laser modes. Implant geometries were modeled using computer-aided design (CAD). Surface morphology and elemental composition were analyzed using Scanning Electron Microscopy (SEM) and Energy Dispersive X-ray Spectroscopy (EDS). The results highlight the influence of laser parameters on surface quality, contributing to improved implant performance and manufacturing precision.

Keywords: additive manufacturing, Co-Cr, SLM, 3D printing, dental implants

1. INTRODUCTION

Dental implants are widely recognized for their ability to restore both the function and appearance of natural teeth. Unlike conventional solutions such as dentures or bridges, implants closely replicate the structure of a real tooth by using biocompatible materials that are surgically inserted into the jawbone [1]. These materials serve as artificial roots, providing a secure and lasting foundation for the replacement tooth. This enables individuals to eat, speak, and smile with confidence, as the implant functions and feels like a natural tooth. In addition to their functional and aesthetic advantages, dental implants play a vital role in maintaining oral health [2]. Tooth loss can lead to jawbone deterioration due to lack of stimulation, but implants help prevent this through a process called osseointegration, which supports bone preservation and strength [3]. Although titanium (Ti) is primarily used in the field of implantology, cobalt-chromium (Co–Cr) alloys are the favored choice in dental prosthodontics. They are widely regarded as the preferred material for fabricating base-metal frameworks due to their reliable clinical performance, affordability, biocompatibility, and strong mechanical characteristics. Regarding the method used to fabricate frameworks, the lost-wax casting technique has traditionally been employed for base-metal restorations. While this approach is cost-effective for dental practitioners, it is also intricate and labor-intensive [4]. As a result, computer-aided

design and manufacturing (CAD-CAM) technologies have emerged as a promising alternative, offering greater efficiency by minimizing human error and variability in laboratory procedures. Additive manufacturing, a 3D printing technology recently introduced for producing base-metal dental implants, offers an environmentally friendly alternative and has demonstrated promising outcomes in this application [5]. A key process in applying powder bed fusion technology to prosthetic dentistry is selective laser melting (SLM). This technique enables the direct fabrication of metal components by precisely and rapidly fusing layers of metal powder using a high-powered laser beam. The SLM process enables the creation of intricate 3D structures and offers material efficiency, as unused powder can be recycled for future production, minimizing waste [6,7]. The aim of this study is to perform a comparative analysis of the surface characteristics of cobalt-chromium samples fabricated using selective laser melting (SLM). Specifically, the research focuses on evaluating samples produced under two different laser modes to determine how variations in SLM processing parameters influence surface roughness. By identifying the mode and parameters that result in improved surface quality, the study seeks to contribute to the optimization of SLM techniques for dental implants applications.

2. MATERIAL AND METHODS

The MEDILOY S-CO cobalt-chromium (Co-Cr) alloy powder, classified as a Type 5 cobalt-based dental alloy, was sourced from BEGO Company (Co 63.9%, Cr 24.7%, W 5.4%, Mo 5.0%, and Si 1.0%.). The powder and sample's morphology and chemical composition were analyzed using a Zeiss scanning electron microscope (SEM) equipped with an energy-dispersive spectroscopy (EDS) system (EVO 15 MA). The specimens were fabricated using Selective Laser Melting (SLM) with the TruPrint 2000 printer, employing both continuous and pulsed laser modes at 0° and 45° build orientations to assess surface quality and optimize laser processing parameters.

2.1 Powder Analysis

The SEM analysis presented in Figure 1 (a, b) reveals that the powder particles are mainly spherical, exhibiting a clear range of particle sizes. A well-graded particle size distribution also enhances powder flowability, which is crucial for achieving consistent layer deposition during the printing process and minimizing defects in the final build.

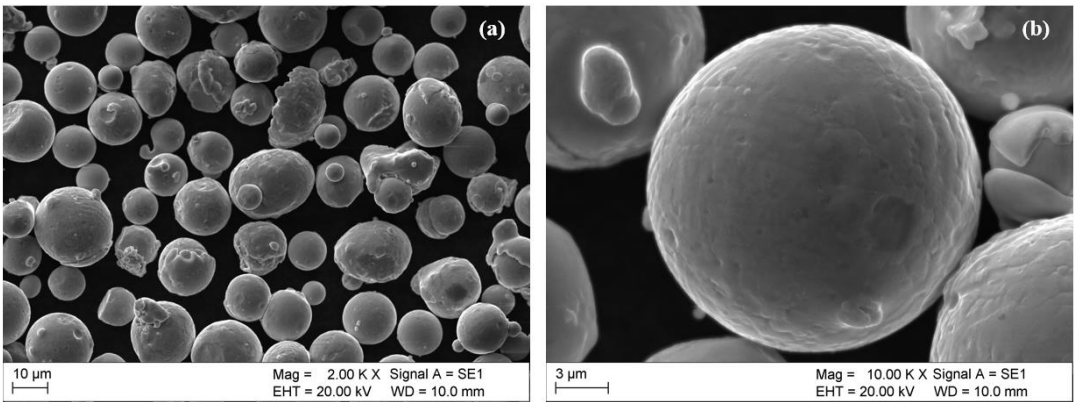

Figure 1. SEM images of Co-Cr powder MEDILOY S-CO, Bego company, with 2.00KX (a), and 10.00 KX (b) magnification

The elemental composition of the powder, as shown in Figure 2 (a-g), through EDS analysis, confirms cobalt (Co) and chromium (Cr) as the major elements, with smaller amounts of other elements also present. The percentages of the elements in different points (p2, p3, p4) marked on Figure 3, are shown in Table 1.

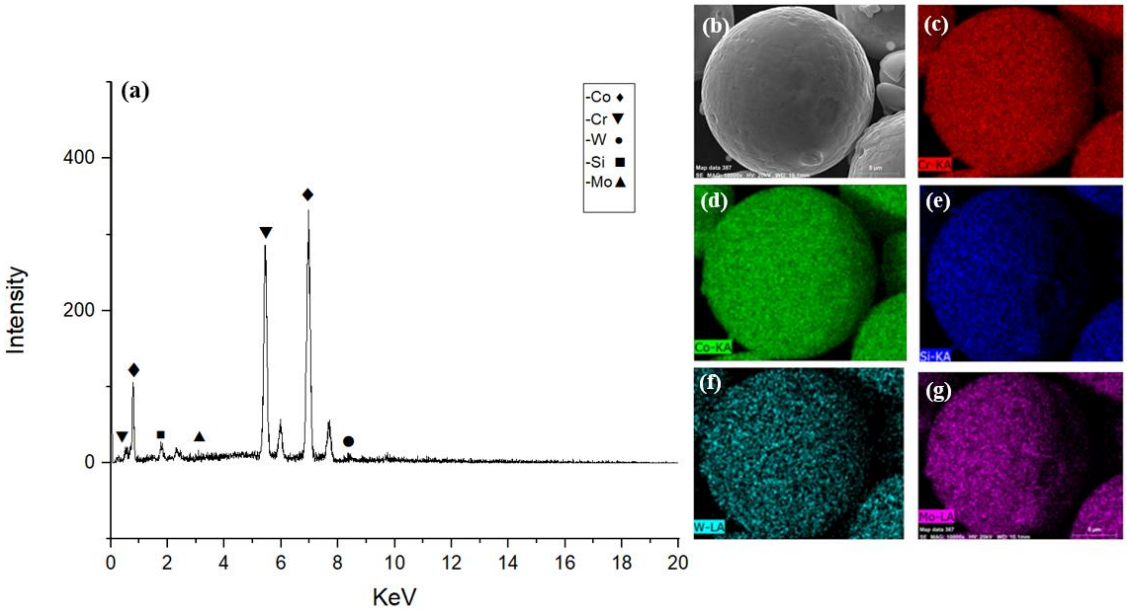

Figure 2. Spectrum of the elements in the powder (a), SEM images of Co-Cr powder from Bego Company (b), EDS results Mapping of sample composition: Chromium (c), Cobalt (d), Silicone (e), Tungsten (f), Molybdenum (g)

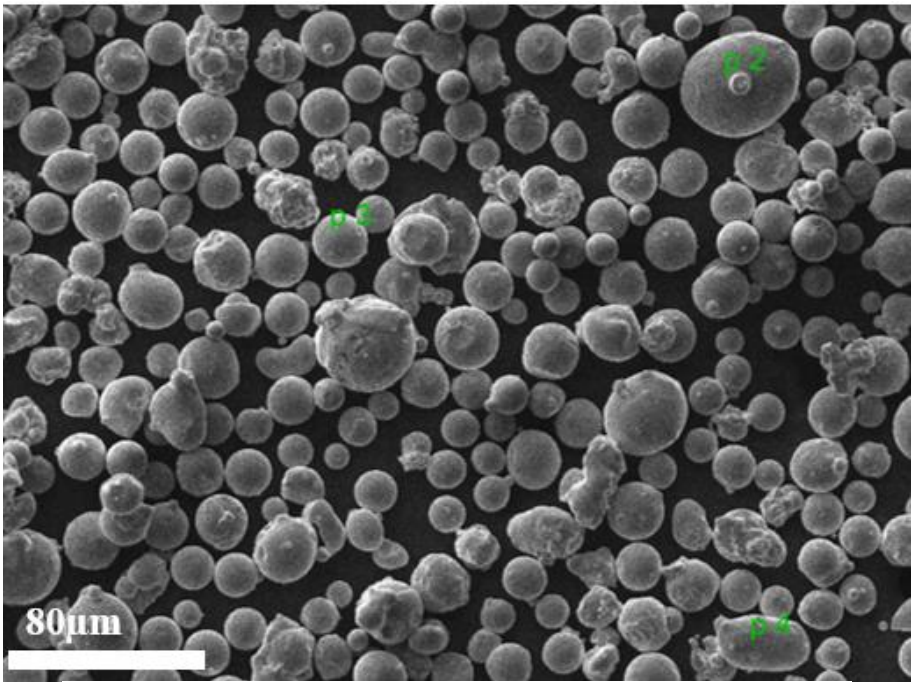

Figure 3. EDS Spectrum at Selected Point on Powder Sample

Table 1. Weight Percent (wt%) of Elemental Presence from Point EDS Analysis

Element	p2 [wt.%]	p3 [wt.%]	p4 [wt.%]
Co	65.38	66.80	65.90
Cr	27.63	25.51	26.55
W	6.78	5.62	6.52
Si	0.01	0.21	0.11
Mo	0.20	1.87	0.91

2.2 Surface Morphology Analysis

After printing the samples, shown on Figure 4, to evaluate how 3D printing parameters influence surface morphology, Scanning Electron Microscopy (SEM) was utilized. As shown in Figure 5 (a), the pulsed laser mode at a 0° build orientation produced printed layers with noticeable overlap. In contrast, the continuous laser mode resulted in vertically aligned layers with little to no overlap Figure 5 (b). Additionally, printing at a 45° angle yielded a smoother surface compared to the 0° setup, highlighting the significant influence of build orientation on surface quality Figure 5 (c, d). These observations emphasize the importance of examining the mechanical properties of specimens fabricated with different laser settings and orientations. This is especially critical for dental implants, where mechanical performance must adapt to varying positions and angles in the oral cavity.

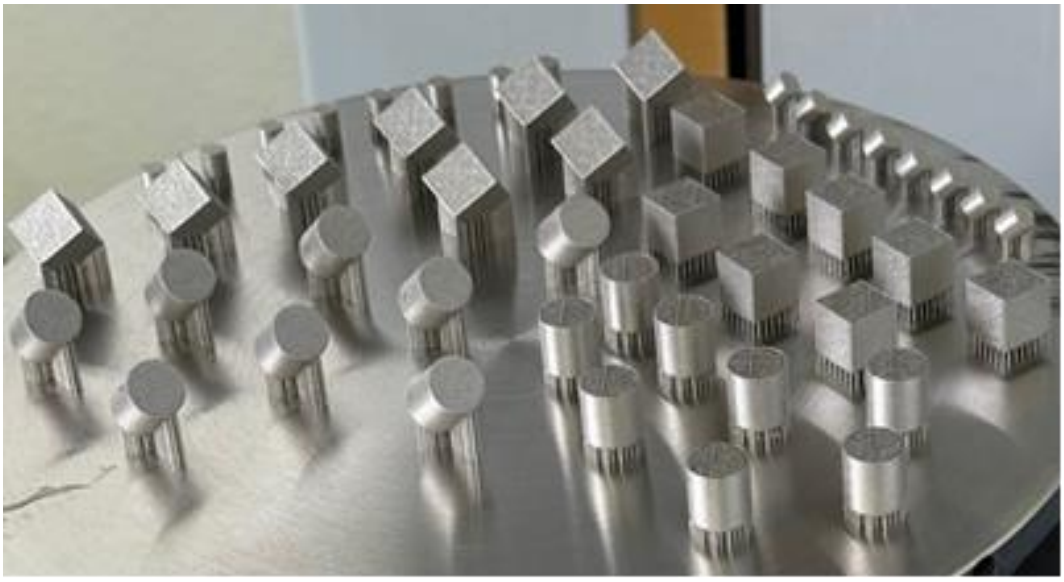

Figure 4. 3D-printed specimens prior to removal from the build platform

To verify that the Selective Laser Melting (SLM) process did not alter the material's elemental composition, a supplementary Energy Dispersive Spectroscopy (EDS) analysis was performed on the printed surface. As illustrated in Figure 6 (a-g), cobalt (Co) and chromium (Cr) remain the dominant elements, confirming that the printing process preserved the original chemical composition. This is beneficial because maintaining the intended alloy composition ensures that the mechanical, corrosion-resistant, and biocompatible properties of the material, especially critical for applications such as dental implants, are retained after printing.

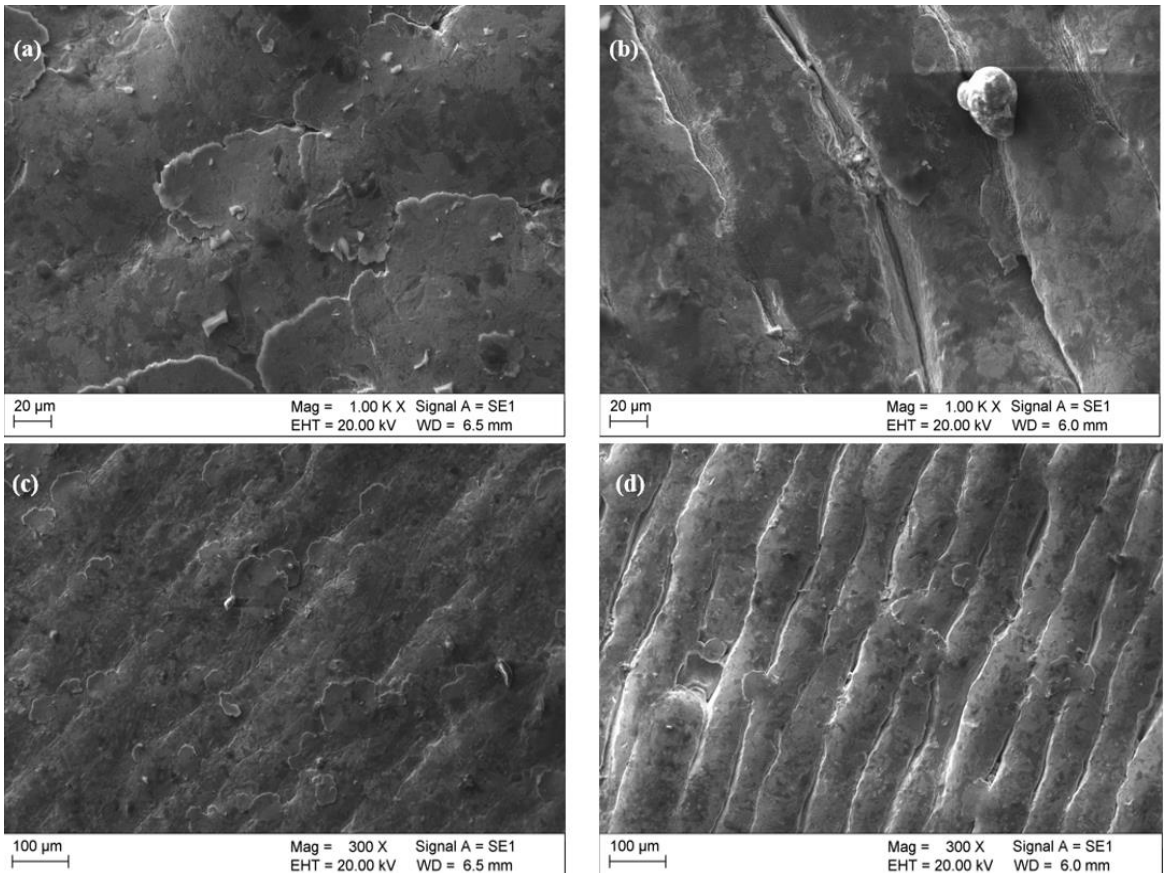

Figure 5. SEM images of samples SLM printed in: 0° angle with Pulsed laser (a); 0° angle with Continues laser (b); 45° angle with Pulsed laser (c); 45° angle with Continues laser (d)

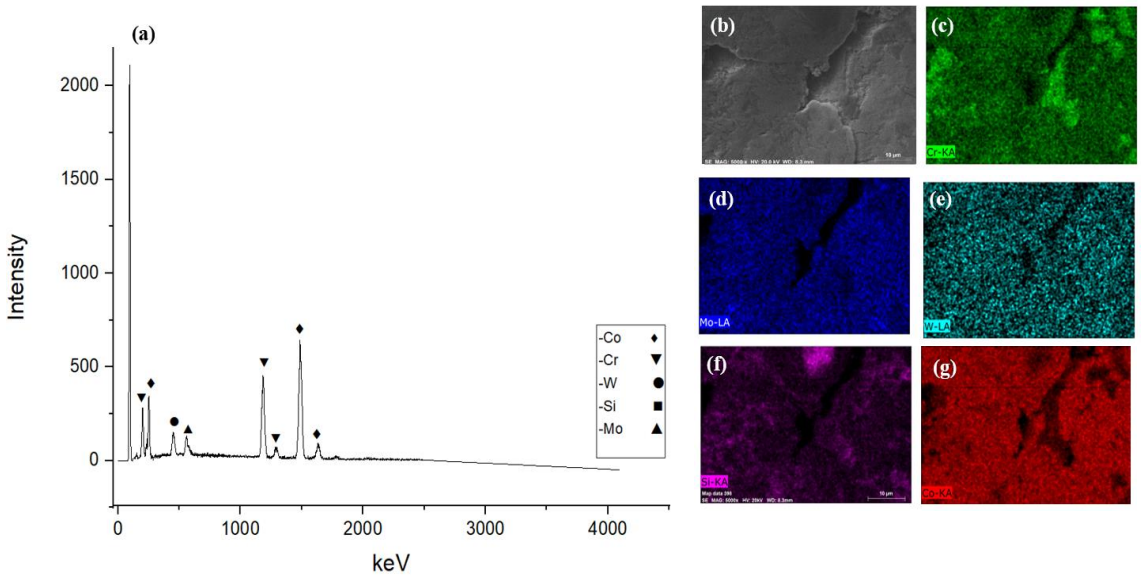

Figure 6. Spectrum of the elements in sample prepared by SLM (a), SEM images of sample surface (b), EDS results Mapping of sample composition: Chromium (c), Molybdenum (d), Tungsten (e), Silicon (f), Cobalt (g)

3. CONCLUSION

These results highlight the crucial impact of advanced manufacturing methods, like Selective Laser Melting (SLM), in improving product quality in the dental field. By carefully adjusting the printing parameters, significant enhancements in surface finish can be achieved, leading to more accurate and dependable implant fabrication. The alloy powder used showed consistent quality and a favorable elemental composition, which was confirmed to be retained in the printed samples, demonstrating excellent material stability and suitability for both dental applications and modern 3D printing processes. This research illustrates how the combination of cutting-edge technologies facilitates the production of high-performance, patient-specific implants. Future studies will focus on an in-depth analysis of the microstructure and mechanical properties of the printed parts to further refine surface quality and broaden the application potential of this technique in the industry.

BIBLIOGRAPHY

1. Gupta, R., Gupta, N., & Weber, K. K. (2023). Dental implants. In StatPearls [Internet]. StatPearls Publishing.
2. Sotova, C., Yanushevich, O., Kriheli, N., Grigoriev, S., Evdokimov, V., Kramar, O., ... & Peretyagin, P. (2023). Dental implants: modern materials and methods of their surface modification. Materials, 16(23), 7383.
3. Jambhulkar, N., Jaju, S., Raut, A., & Bhoneja, B. (2023). A review on surface modification of dental implants among various implant materials. Materials Today: Proceedings, 72, 3209-3215.
4. Saha, S., & Roy, S. (2022). Metallic dental implants wear mechanisms, materials, and manufacturing processes: a literature review. Materials, 16(1), 161.
5. Molinero-Mourelle, P., Roccuzzo, A., Yilmaz, B., Lam, W. Y. H., Pow, E. H., Highsmith, J. D. R., & Gómez-Polo, M. (2022). Microleakage assessment of CAD-CAM Cobalt-Chrome and Zirconia abutments on a conical connection dental implant: A comparative in vitro study. Clinical oral implants research, 33(9), 945-952.
6. Elhadery, S. S., Alhajj, M. N., Yunus, N., Ibrahim, N., Abidin, Z. Z., Ahmad, S. F., & Salleh, N. M. (2024). Adaptation of cobalt chromium frameworks fabricated by conventional versus selective laser melting techniques: An in vitro and clinical assessment. The Journal of Prosthetic Dentistry.
7. Albaijan, R., Vohra, F., Alnassar, T. M., Robaian, A., Alnafaiy, S. M., Murayshed, M. S., ... & Gufran, K. (2024). Comparison of surface micro-roughness and adaptation of titanium and cobalt chrome implant abutment fabricated by selective laser melting and conventional techniques. Clinical Implant Dentistry and Related Research, 26(6), 1303-1312.

TalentDetector
23th-25th June 2025
Gliwice-Brenna, Poland
DEPARTMENT OF ENGINEERING MATERIALS AND BIOMATERIALS
FACULTY OF MECHANICAL ENGINEERING
SILESIAN UNIVERSITY OF TECHNOLOGY
INTERNATIONAL STUDENTS SCIENTIFIC CONFERENCE

Influence of external friction on amplitude dependences of internal friction of steel

Yuliia Sokolan[a], Kateryna Sokolan[b], Oleg Polishchuk[c], Mirosław Bonek[d]

[a] Khmelnitskyi National University, Faculty of Engineering Mechanics, Khmelnitskyi, Ukraine email: sokolan.julia@gmail.com.
[b] Khmelnitskyi National University, Faculty of Engineering Mechanics, Khmelnitskyi, Ukraine email: sokolan.kateryna @gmail.com .
[c] Khmelnitskyi National University, Faculty of Engineering Mechanics, Khmelnitskyi, Ukraine email: opolishchuk7l@gmail.com.
[d] Silesian University of Technology, Faculty of Mechanical Engineering, Gliwice, Poland email: miroslaw.bonek@polsl.pl.

Abstract: The conditions of development and character of manifestation of strengthening and de-strengthening mechanisms of relaxation of contact stresses at external friction of metals are studied insufficiently and constitute an important problem in metallophysics of contact strength. In the article by methods of internal friction the change of relaxation ability of carbon steel in connection with influence of heat treatment and modes of external friction on amplitude dependences of internal friction is studied. Steel 45 after different heat treatment regimes was investigated. Subsequently, the samples were subjected to the influence of external friction and the amplitude dependences of internal friction were investigated. It was found that steel friction always initiates relaxation (dissipative) processes that affect the formation of friction bonds and their dissipative properties. It was also shown that external friction of low-tempered steel leads to the summation of thermal hardening and dynamic strain aging, which causes an additional increase in relaxation resistance. Friction of high-tempered steel and with increasing sliding velocity the mobility of dislocations decreases.
Keywords: steel heat treatment, internal friction, external friction, amplitude dependences of internal friction, dislocations, energy dissipation, oscillation decrement, stress relaxation.

1. INTRODUCTION

In the case of sliding friction of metal surfaces in machine assemblies, the effective local contact stresses are usually much lower than the yield strength of the mating materials. Under such conditions, the processes caused by long-term dynamic loading of actual contact spots (e.g., fatigue, delamination, etc.) should be closely related to inelastic stress relaxation phenomena, on which the dynamic stress of friction contact surfaces depends.

It is known [1] that stress relaxation directly in the process of force action can be accompanied by de-strengthening, unchanged mechanical properties or hardening (elasticity growth). The result depends on the degree of stability of the metal structure and temperature-velocity mode of deformation. Under cyclic dynamic loading, stress relaxation processes in

metals are closely related to internal friction, having the same mechanisms. Therefore, the measure of the relaxation capacity of the material and the degree of stress relaxation can be the level of internal friction or the height of its relaxation maxima corresponding to a given amplitude of cyclic stresses and deformation temperature.

Of particular interest are the processes of stress relaxation during dynamic strain aging (DSA) and stress tempering - dynamic aging (DA). In the first case, diffusive rearrangement leads to hardening due to blocking of fresh dislocations induced by deformation by atmospheres and segregations of impurity atoms (carbon and nitrogen). In the second type of aging in metastable systems (e.g., after quenching), in addition to DSA, a heterogeneous structure is formed with the release of finely dispersed excess phases (carbide and nitride particles) that impede ductile flow (relaxation hardening) [2, 3]. The efficiency of the development of these relaxation phenomena depends on the consistency of the diffusion processes of introduction atoms and dislocation rearrangement, which, in turn, depend on the strain rate and temperature regime. On the other hand, relaxation de-strengthening with the growth of dissipative capacity can occur, for example, when large-dispersed (coagulated) particles of the excess phase are released.

The conditions of development and character of manifestation of strengthening and de-strengthening mechanisms of relaxation of contact stresses at external friction of metals are studied insufficiently and constitute an important problem in metallophysics of contact strength. In the article by methods of internal friction the change of relaxation ability of carbon steel in connection with influence of heat treatment and modes of external friction on amplitude dependences of internal friction is studied. Such statement of the question becomes actual in the context of the problem of creation of tribotechnical materials possessing high ability to energy dissipation at preservation of sufficient strength. This applies, for example, to friction units operating without lubrication (friction clutches, friction dampers and shock absorbers, braking devices).

2. FORMULATION OF THE PROBLEM

In [4] the influence of triboactivation of steel on hardening and relaxation properties of surface layers was studied. The study of these parameters does not provide a complete picture of the effect of external friction on the dissipative properties of steel and dynamic relaxation processes of hardening. In this connection, the task of studying the influence of external friction on the amplitude dependences of internal friction becomes urgent.

3. PRESENTING MAIN MATERIAL

Steel 45 was studied in the state of hardening (in water from the temperature of 850 ºC), as well as after tempering at temperatures of 200, 400 and 600 ºC for an hour. Substructural changes in steel caused by heat treatment and external friction were investigated by the method of amplitude-dependent internal friction on a torsion pendulum type machine (Fig. 1). Tribotechnical tests were carried out on a friction machine (Fig. 2).

The sample 3 (Fig. 3), fixed in the clamp 2 and centering support 8, is driven into rotation at a preset speed by the electric motor 1. Friction is carried out between the narrow working part of the sample and abrasive pad 5 (P500), which is pressed with a controlled force to the cylindrical surface of the sample by the enveloping fixture 4, on which a pressing load is applied from the weights 6 placed on the suspension 7.

4. THE RESULT OF WORK

Fig. 4 shows the effect of external friction on the amplitude dependences of the steel oscillation decrement after four heat treatment regimes.

a)

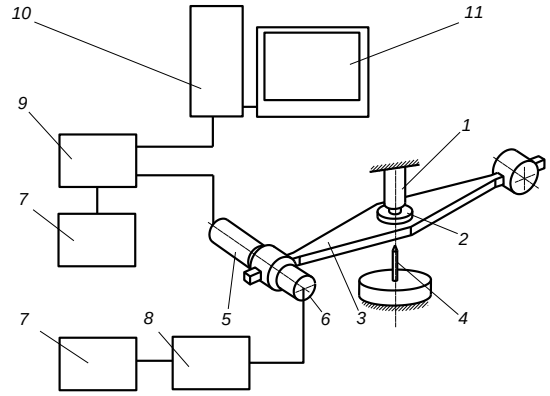

b)

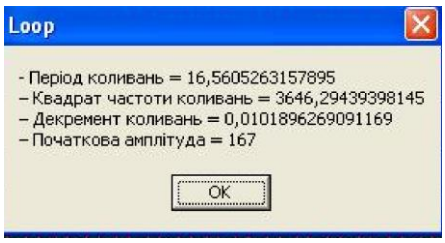

c)

d)

Figure 1 - General view (a), schematic diagram of the installation (b), measurement results output window (c) and working unit (d):
1 - stationary sample; 2 - moving sample; 3 - pendulum; 4 - support (needle);
5 - displacement sensor; 6 - oscillation excitation coil; 7 - power supply units; 8 - pulse forming unit; 9 - analog-to-digital converter; 10 - computer system unit; 11 - monitor

a)

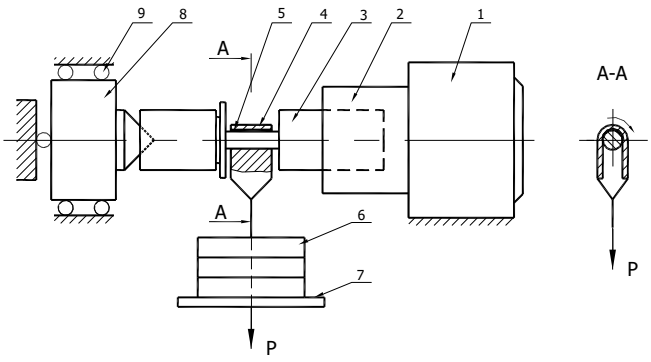

b)

Figure 2 - General view (a) and scheme of the friction machine (b): 1 - electric motor; 2 - clamping device (collet); 3 - sample; 4 - counterbody; 5 - abrasive pad; 6 - weights; 7 - suspension base; 8 - movable axial support (centering); 9 - ball bearing supports

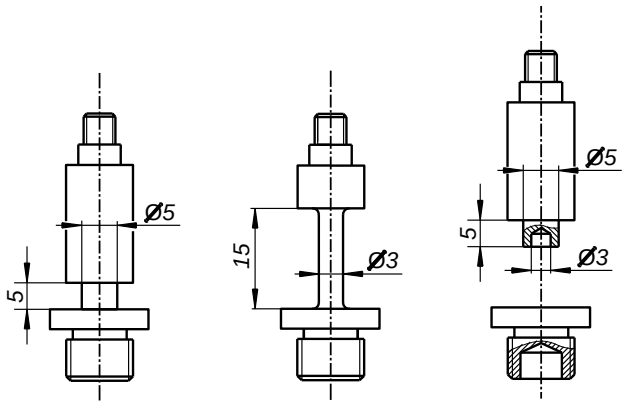

a) b) c)

Figure 3 - Samples for measuring volumetric internal friction (a, b) and frictional contact (c)

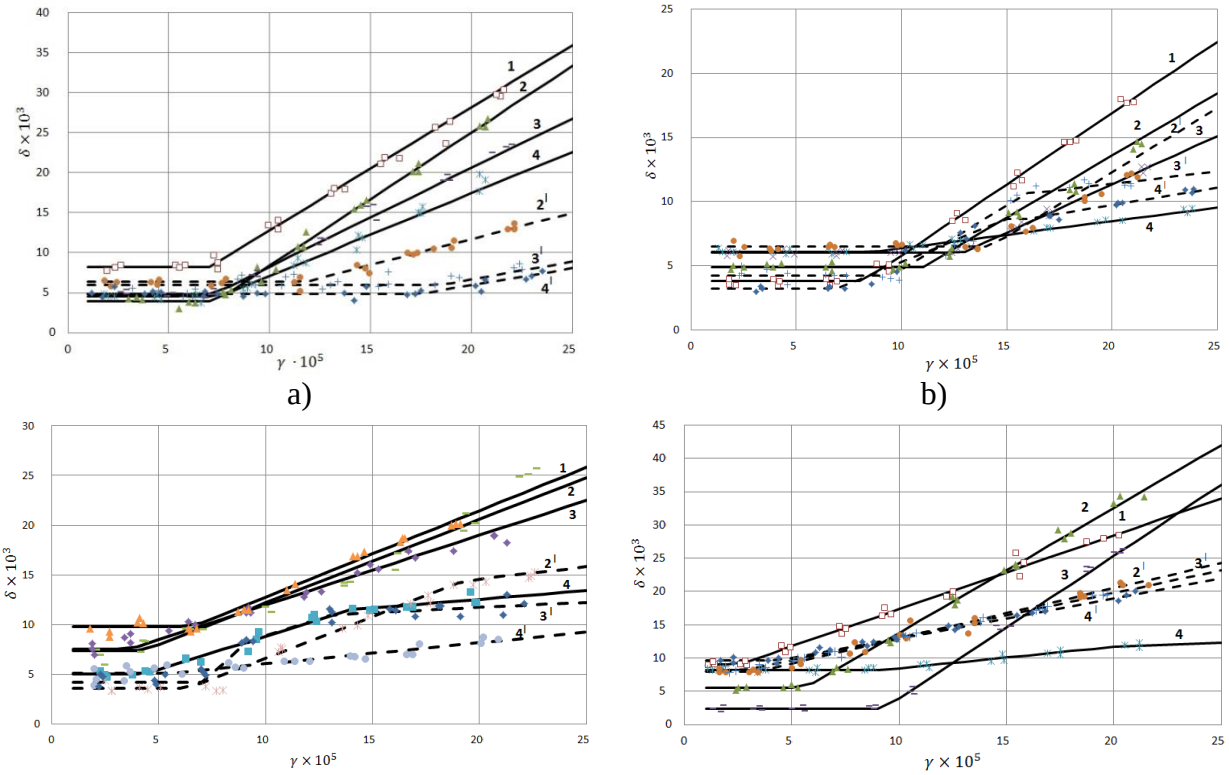

a) b)

c) d)

Figure 4 - Influence of external friction on amplitude dependences of oscillation decrement δ of steel 45: hardening (a); tempering 200 ºC (b); tempering 400 ºC (c); tempering 600 ºC (d) (1 – initial state; 2, 2$^{|}$ – V = 0,08 m/s; 3, 3$^{|}$ – V = 0,21 m/s; 4, 4$^{|}$ – V = 0,34 m/s; 2, 3, 4 – P = 10 N; 2$^{|}$, 3$^{|}$, 4$^{|}$ – P = 5 N)

The amplitude-dependent internal friction (ADIF) carries information about the dislocation structure of metals, the interaction of dislocations with impurity atoms, and the mechanisms of mechanical energy dissipation under cyclic loading [5, 6, 7]. The amplitude-independent region of internal friction (AIDIF) corresponds predominantly to losses due to oscillations of short dislocation segments of length L_c located between the nearest impurity atoms locally anchoring dislocations (background of internal friction). Energy dissipation is related to the phase lag of

deformations from applied stresses during periodic bending of such dislocation segments. The strain after which the internal friction becomes dependent on its amplitude corresponds to the beginning of dislocation detachment from impurity atmospheres. At the same time, dislocations remain fixed in the nodes of the dislocation mesh, causing losses in the oscillatory motion of LN segments (dislocation hysteresis). When the strain amplitude increases further, dislocations break away from the nodes of the dislocation grid, forming dislocation loops, the movement of which causes microplastic deformation.

The values of decrement and square of frequency of oscillation at fixed relative strain $\gamma = 20\ \ 10^{-5}$ were compared (Fig. 5). It follows from the obtained data that at both contact loads with increasing sliding velocity in the investigated range for all types of heat treatment there is a general tendency to decrease the level of ADIF to values below the initial one. Only in the case of highly tempered steel (Fig. 5 d, curve 1) at increased load (P = 10 N) the decrease in the decrement of oscillations is preceded by its initial growth at minimum sliding velocity (V = 0.08 m/s). An increase in friction velocity causes a rapid decrease in decrement. As a rule, a more significant decrease in the level of ADIF occurs at a reduced load P = 5 N. For low tempered steel (T_{temp} = 200 ºC), the effect of contact pressure on ADIF is insignificant (Fig. 5 b).

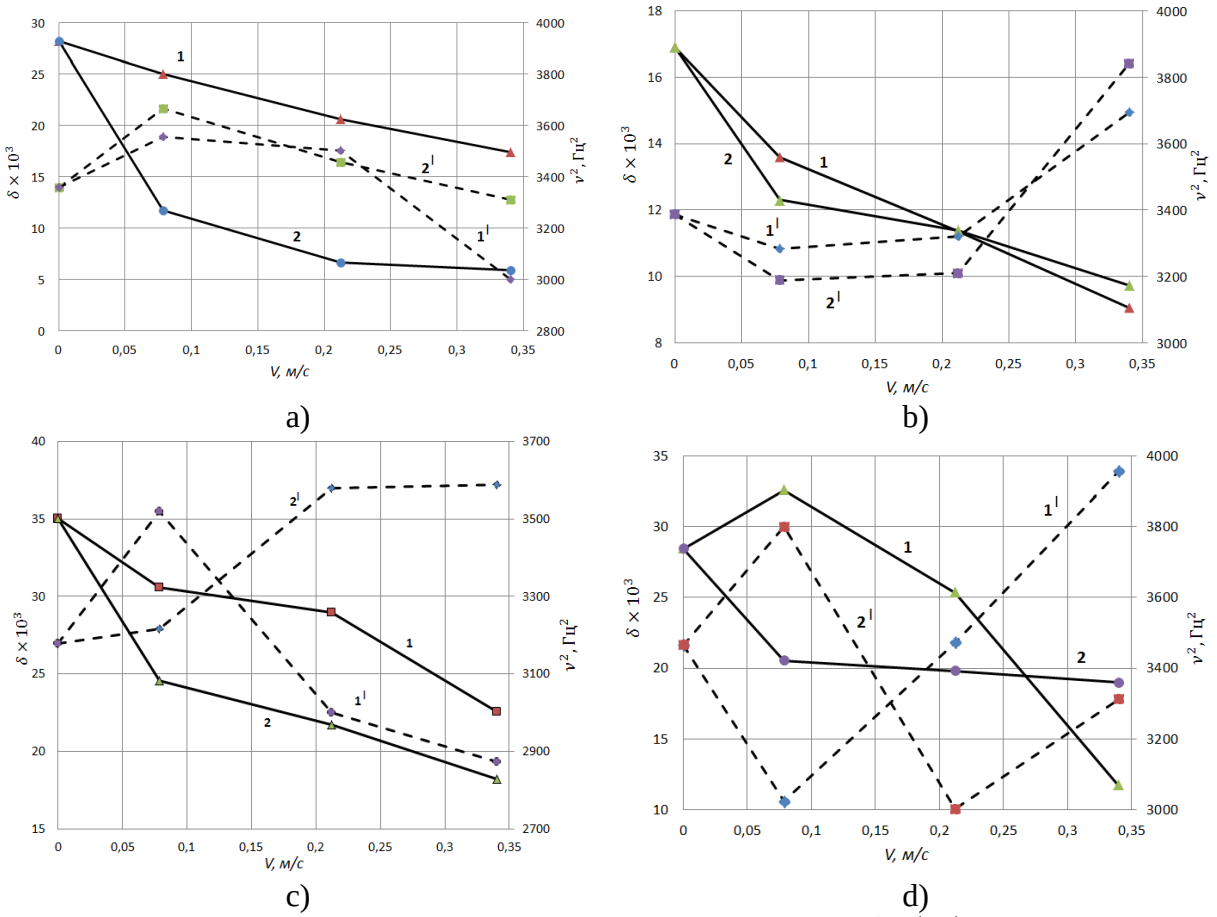

Figure 5 - Dependence of decrement δ (1,2) and frequency square ν^2 (1', 2') of oscillations at $\gamma = 20 \cdot 10^{-5}$ on external friction velocity V and heat treatment mode: hardening (a); tempering 200 ºC (b); tempering 400 ºC (c); tempering 600 ºC (d)
(1, 1' – P = 10 N; 2, 2' – P = 5 N)

The level of ADIF is influenced by the processes of substructural rearrangement in the frictional contact zone. The observed initial growth of the oscillation decrement in friction of highly tempered steel (Fig. 5 d) is caused by an increase in the density of mobile dislocations, which have the possibility of long-range movement, as well as by the migration of impurity atoms along the dislocations to the nodes of their attachment, which leads to an increase in the size of dislocation segments L_c.

Decrease of decrement in the ADIF region, accompanying, as a rule, the hardening of metal, occurs due to a decrease in the mobility of dislocations. This is facilitated by:

- formation of a low-mobility dislocation grid in the process of their interaction (when critical density is reached) with reduction of the distance between LN nodes;

- development of dynamic strain aging (DSA), as a result of which generated ("fresh") dislocations are blocked by impurity atoms of introduction (C+N) migrating to them, their atmospheres and segregations. The dissipative capacity of the structure decreases due to the reduction in the length of dislocation segments (L_c) and a decrease in the total mobility of dislocations. Optimal conditions for the development of DSA are created at such friction velocities and temperatures, when the velocity of dislocation motion becomes commensurate with the diffusion velocity of impurity atoms. DSA is controlled by diffusion processes, which under friction are significantly accelerated due to the temperature rise and due to a significant increase in the dislocation density.

Note that according to the applied test methodology, the specimens were subjected simultaneously with friction to a certain action of cyclic loads (bending with rotation). Therefore, the possible superposition of two factors should be taken into account: volumetric (fatigue) and contact (tribological). The role of the fatigue factor increases with increasing contact load and decreasing strength of the specimen, which leads to an increase in the deflection of its working part. Thus, friction of highly tempered steel (T_{temp} = 600 ºC) at velocity V_1 = 0.08 m/s and P = 10 N is accompanied by an initial increase in decrement due to the fact that in these conditions the factor of mobile dislocation multiplication prevails (Fig. 5 d, curve 1). Due to the low concentration of introduction atoms (C+N) in the solid solution, steel in the state of high tempering, which stabilizes the structure, is less susceptible to DSA. Therefore, the observed subsequent decrease in the energy dissipation capacity with increasing sliding velocity seems to be mainly due to the formation of slow-moving dislocation "scaffold" complexes.

At reduced load (P = 5 N) in all cases the tribological factor comes first: the rate of multiplication of mobile dislocations decreases, and the processes of their inhibition (mainly due to DSA) already at low friction velocity (V_1 = 0.08 m/s) become dominant, leading to a sharp decrease in the ability of the material to dissipate energy. With increasing sliding velocity, the dynamics of frictional interaction grows with a simultaneous increase in temperature in the contact zone, as a result of which the level of internal friction, decreasing, tends to stabilize due to the equalization of the action of the factors of propagation and anchoring of dislocations.

Judging by the intensity of decreasing decrement with increasing external friction velocity, hardened steel is the most susceptible to hardening under the studied conditions (Fig. 5 a). Quenching, forming a metastable structure with a high concentration of impurity atoms (C+N) in the solid solution, contributes to the strengthening of the DSA effect in friction. This accelerates the decomposition of martensite and transformation of residual austenite with the release of highly dispersed carbide particles. This causes the so-called stress tempering

(dynamic aging), which results in structural relaxation due to diffusion redistribution of impurity atoms with the formation of new phases [3]. The carbide particles released in this process have a high dispersity and increased concentration due to an increase in the number of nucleation centers of the carbide phase. As a result, the resistance of steel to small plastic deformations increases and the relaxation resistance increases as a result of relaxation of stresses generated in the process of martensitic transformation. Compared to conventional tempering, the temperature of dynamic aging, which forms the maximum elastic limit, is 50-100 °C lower [3].

5. CONCLUSIONS

Increase of friction velocity of hardened steel with corresponding increase of contact temperature intensifies stress relaxation, which is caused by:

- diffusion redistribution of carbon and nitrogen atoms in the field of cyclic stresses, as well as displacement of weakly anchored dislocations (de-strengthening factor);
- structural relaxation (physicochemical reactions of decomposition of supersaturated solid solution - martensite and transformation of residual austenite);
- dynamic strain aging and dynamic tempering, causing a decrease in the mobility of dislocations and hindering viscous flow along the interfaces (hardening factor).

These mechanisms of stress relaxation during friction of hardened steel prevail over the usual nucleation, which is typical for normalized and highly tempered steel.

The specified mechanisms of stress relaxation at friction of hardened steel prevail over the usual naklep, which is characteristic for normalized and highly tempered steel.

Low tempered steel (T_{temp} = 200 ºC) at all friction speed regimes showed a monotonic decrease in the decrement of oscillations to values below the initial one, indicating the predominance of the DSA factor caused by contact interaction (Fig. 5 b). Low tempered steel shows the lowest ability to dissipate mechanical energy and the greatest stability of relaxation properties in the studied friction conditions.

Thus, steel friction always initiates relaxation (dissipative) processes that affect the formation of friction bonds and their dissipative properties. The intensity and mechanisms of dissipation depend on the structural state of steel, load-velocity regime and temperature of contact interaction. Depending on the heat treatment of the steel and the friction regime, relaxation during dynamic strain aging (DSA) reduces the dissipative capacity of the material to a greater or lesser extent. The result depends on the saturation of the solid solution with impurity atoms, as well as on the amount of precipitates and their morphology (dispersity, shape). By increasing the resistance of steel to small plastic deformations and at the same time maintaining sufficient relaxation capacity of the material, DSA should contribute to the growth of wear resistance.

Hardening of steel, forming a metastable structure with a high concentration of impurity atoms in solid solution, enhances the effect of dynamic strain aging, which together with dynamic tempering under load causes relaxation of peak microstresses directly in the process of friction, thus reducing the risk of brittle microcracks and increasing the energy intensity of steel.

Friction of low-tempered steel (T_{temp} = 200 ºC), which has high elasticity and relaxation resistance in the initial state, leads to the summation of thermal strengthening and dynamic

strain aging, which causes an additional increase in relaxation resistance (reduction of viscosity and dissipative capacity).

In friction of highly tempered steel (T_{temp} = 600 ºC), which is not prone to DSA, the initial increase in internal friction (dissipative capacity) is due to the increase in the density of generated mobile dislocations. With increasing sliding velocity and density of dislocations their mobility decreases, mainly due to mutual blocking, leading to a decrease in viscosity and embrittlement.

To ensure tribosystem operability directly at macroelastic friction modes (for example, at the stage of running-in) it is necessary to bring steel to such a structural state by heat treatment and realize such temperature-velocity tribotechnical conditions under which strengthening mechanisms of diffusion and structural relaxation will develop.

The leading strengthening and loosening dynamic relaxation mechanisms change with the change of steel structure as a result of heat treatment, as well as depending on the load-velocity modes of friction. The formation of relaxation (dissipative) ability of steel in the process of friction is influenced by diffusion activity of introduction atoms, mobility of dislocations and the possibility of viscous flow along the interfaces. Dissipative ability (energy capacity) and wear resistance of steel can be increased by implementing favorable dynamic mechanisms of stress relaxation directly in the friction process.

The leading strengthening and loosening dynamic relaxation mechanisms change with the change of steel structure as a result of heat treatment, as well as depending on the load-velocity modes of friction. The formation of relaxation (dissipative) ability of steel in the process of friction is influenced by diffusion activity of introduction atoms, mobility of dislocations and the possibility of viscous flow along the interfaces. Dissipative ability (energy capacity) and wear resistance of steel can be increased by implementing favorable dynamic mechanisms of stress relaxation directly in the friction process.

BIBLIOGRAPHY

1. Borzdyka A. M. Stress relaxation in metals and alloys / A. M. Borzdyka, L. B. Getsov. - M: Metallurgy, 1978. - 256 p.
2. Babich V. K. Deformation aging of steel / V. K. Babich, Y. P. Gul, I. E. Dolzhenkov. - M: Metallurgy, 1972. – 320 p.
3. Pastukhova J. P. Dynamic aging of alloys / J. P. Pastukhova, A. G. Rakhshtadt, Y. A. Kaplun. - M.: Metallurgy, 1985. - 320 p.
4. Sokolan Iu. Effect of steel triboactivation on hardening and relaxation properties of surface layers / Iu. Sokolan, K. Sokolan, P. Maidan, S. Matiukh, O. Polishchuk, M. Bonek // International students scientific conference “Talent Detector 2025”. - 31th January, 2025, Gliwice, Poland. - p. 537 – 549
5. Krishtal M. A. Internal friction and structure of metals / M. A. Krishtal, S. A. Golovin. - Moscow: Metallurgy, 1976. - 376 p.
6. Shevelya V., Sokolan J., Kupiec B., Korenivskiy M. Effect of Viscoelastic Properties of Treated Steel on the Rheology and Dissipative Properties of Frictional Contact / V. Shevelya, J. Sokolan, B. Kupiec, M. Korenivskiy. // Archives of Foundry Engineering. – 2014. – Vol. 14, Special Issue 1. – p. 193-198
7. Shevelya V. V. Dynamic relaxation processes in steel friction under the action of heat treatment / V. V. Shevelya, Yu. S. Sokolan. // Strength of Materials. – 2015. – Vol. 47, No. 4. – p. 524-531